This is an electronic reprint of the original article.
This reprint may differ from the original in pagination and typographic detail.

Mahmoodi, Bayazid; Tamadonfar, Parsa; Bhattacharya, Atmadeep; Kaario, Ossi

# LES-TFM modeling of hydrogen combustion in internal combustion engines

*Published in:*
THIESEL 2024 Conference on Thermo- and Fluid Dyamics of Clean Propulsion Powerplants

Published: 02/09/2024

*Document Version*
Publisher's PDF, also known as Version of record

*Published under the following license:*
CC BY-SA

*Please cite the original version:*
Mahmoodi, B., Tamadonfar, P., Bhattacharya, A., & Kaario, O. (2024). LES-TFM modeling of hydrogen combustion in internal combustion engines. In *THIESEL 2024 Conference on Thermo- and Fluid Dyamics of Clean Propulsion Powerplants* (pp. 713-716). Editorial de la Universitat Politècnica de València. http:///10.4995/Thiesel.2024.679601

This material is protected by copyright and other intellectual property rights, and duplication or sale of all or part of any of the repository collections is not permitted, except that material may be duplicated by you for your research use or educational purposes in electronic or print form. You must obtain permission for any other use. Electronic or print copies may not be offered, whether for sale or otherwise to anyone who is not an authorised user.

**CONFERENCE PROCEEDINGS**

# THIESEL 2024

CONFERENCE ON THERMO–AND FLUID DYNAMICS PROCESSES FOR

# Clean Propulsion Powerplants

10th – 13th September 2024
Valencia (Spain)

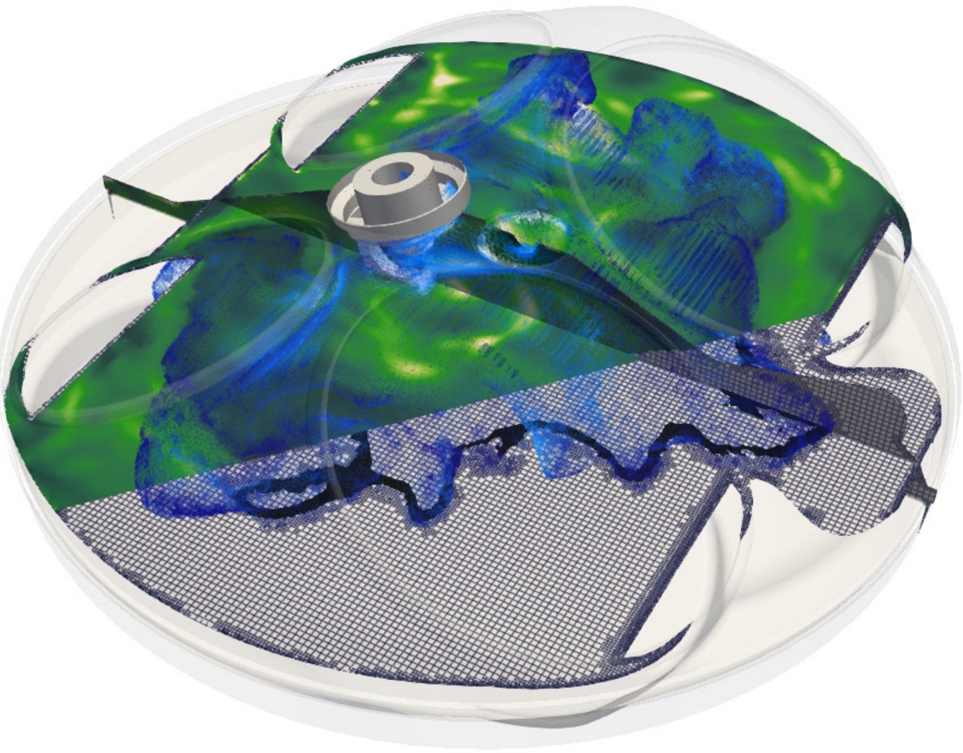

UNIVERSITAT POLITÈCNICA DE VALÈNCIA

Clean Mobility & Thermofluids

GENERALITAT VALENCIANA
Conselleria de Educación, Universidades y Empleo

# OVERVIEW AND OBJECTIVES

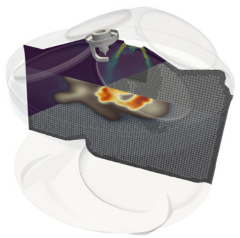

The twelfth edition of the THIESEL Conference on Thermo-and Fluid Dynamics of Clean Propulsion Powerplants in 2022 marked a turning point in its history by integrating fully in its topics the electrification of automobiles. Its success indicates that the renewed Steering and Organising Committees made the right choices. THIESEL 2024 is now the **thirteenth edition,** and since we are non-superstitious scientists and engineers, we are sure no one will see any bad omen in this, quite the opposite!

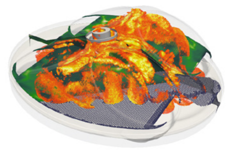

As its name states, the THIESEL 2024 Conference focus is on the thermo-and fluid dynamic processes occurring in propulsion powerplants, which include thermal and noise challenges in electric components, energy optimization in the global electrified propulsion system, new injection/combustion concepts based on hydrogen, ammonia, renewable-fuels and not excluding any other clean propulsion approach.

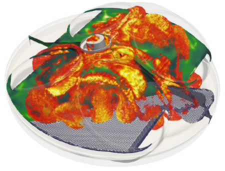

Since research in all these areas is in full swing, the aim of the THIESEL 2024 Conference is to facilitate the exchange of ideas and experiences between Industry, Universities and Research Centres, as well as to create a discussion forum for the most recent advances and for the identification of future lines of research.

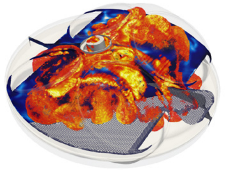

## LIST OF CONTENTS

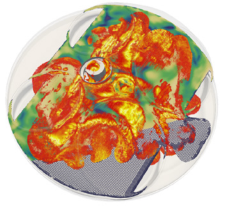

OVERVIEW and OBJECTIVES
ORGANISING and SCIENTIFIC COMMITTEES
CONFERENCE SESSIONS
  Session 1.1 ANALYSIS TECHNIQUES OF H2 ENGINES
  Session 1.2 H2 COMBUSTION CHAMBER DESIGN
  Session 1.3 AMMONIA FUEL FOR MARINE TRANSPORT
  Session 1.4 AMMONIA COMBUSTION TECHNIQUES
  Session 2.1 THERMAL MANAGEMENT
  Session 2.2 AFTERTREATMENT
  Session 2.3 THERMAL RUNAWAY
  Session 2.4 DATA-DRIVEN CONTROL AND OPTIMIZATION
  Session 3.1 SUSTAINABLE POWERTRAINS
  Session 3.2 COMBUSTION EMISSIONS
  Session 3.3 SPRAYS & COMBUSTION
POSTERS' ABSTRACTS
AUTHORS' INDEX
CREDITS

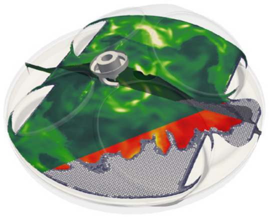

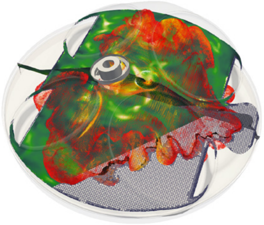

# COMMITTEES

## STEERING COMMITTEE

**Prof. Raúl Payri**
CMT. Universitat Politècnica de València – SPAIN

**Prof. José Ramón Serrano**
CMT. Universitat Politècnica de València – SPAIN

**Dr. Christian Angelberger**
IFP Energies Nouvelles – FRANCE

**Prof. Choongsik Bae**
KAIST - KOREA

**Prof. Thomas Koch**
IFKM. Karlsruher Institut für Technologie - GERMANY

**Dr. Paul Miles**
Sandia National Laboratories – USA

**Prof. Jiro Senda**
Doshisha University – JAPAN

**Dr. Jim Szybist**
Oak Ridge National Laboratory - USA

## CONFERENCE COORDINATOR

**Dr. Xandra Margot**
CMT. Universitat Politècnica de València - SPAIN

## LOCAL ORGANISING COMMITTEE

CMT. Universitat Politècnica de València – SPAIN

**Prof. Alberto Broatch**
**Dr. Antonio García**
**Dr. Xandra Margot**
**Dr. Ricardo Novella**
**Dr. Pedro Piqueras**
**Dr. Benjamín Plá**

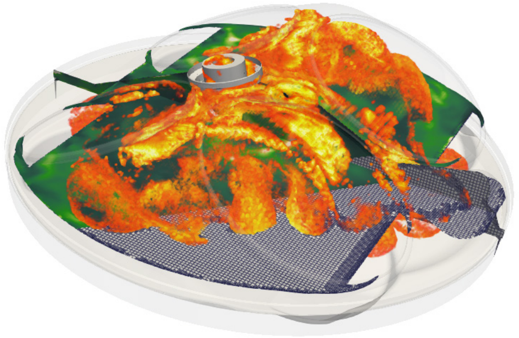

## ADVISORY AND SCIENTIFIC COMMITTEE

Dr. Philipp Adomeit. FEV – Germany
Dr. Amin M. Andwari. University of Oulu - Finland
Dr. Rosario Ballesteros. UCLM Ciudad Real - Spain
Dr. Michele Bardi. IFP Energies nouvelles - France
Dr. Chris Bitsis. Southwest Research Institute - USA
Dr. Maximilian Brauer. TU Berlin - Germany
Dr. Tristan Burton – Convergent Science - USA
Dr. Aaron Costall. Cranfield University - UK
Dr. Gabin Dober. BorgWarner - Luxembourg
Prof. Pilar Dorado. Universidad de Córdoba - Spain
Dr. Georgios Fontaras. European Commission Joint Research Centre - Italy
Prof. Jinwu Gao. Jilin University - China
Dr. M. Reyes García Contreras. UCLM Toledo - Spain
Prof. Avelina García García. Universidad de Alicante - Spain
Dr. Patrick Gastaldi. Aramco Overseas Company - France
Dr. Stéphane Guilain. Ampère - France
Prof. Viktor Hacker. T.U. Graz - Austria
Dr. Takeshi Hashizume. Toyota - Japan
Prof. Zhixia He. Jiangsu University - China
Dr. Ameya Joshi. Corning Inc. - USA
Prof. Hiroshi Kawanabe. Kyoto University - Japan
Prof. Grigoris Koltsakis. Aristotle University Thessaloniki - Greece
Prof. Federico Millo. Politecnico di Torino - Italy
Prof. Yasuo Moriyoshi. Chiba University - Japan
Prof. Eiichi Murase. Kyushu University – Japan
Prof. Hideyuki Ogawa. Hokkaidou University – Japan
Dr. Noshin Omar. ABEE Group - Belgium
Prof. Angelo Onorati. Politecnico di Milano - Italy
Dr. Steven Pierson. Jaguar Land Rover - UK
Mr. Alain Raposo. ACC Automotive Cells Co. - France
Prof. Guillermo Rein. Imperial College London – UK
Dr. Michael Riess. IAV - Germany
Prof. Giorgio Rizzoni. Ohio State University - USA
Prof. Christine Rousselle. Université d'Orléans - France
Mr. Alexander Seipel. Horiba Europe - Germany
Dr. P. Kelly Senecal. Convergent Science - USA
Dr. Derek Splitter. Oak Ridge national Laboratory - USA
Prof. Athanasios Tsolakis. University of Birmingham - UK
Dr. Bianca Vaglieco. CNR-STEMS - Italy
Dr. Olivier Varnier. Jaguar Land Rover – U.K
Dr. Alberto Vassallo. Punch Torino - Italy
Dr. Timothy Watling. Johnson Matthey - UK
Prof. Margaret Wooldridge. University of Michigan - USA
Dr. Yahui Zhang. Yanshan University - China
Dr. Peng Zhao. University of Tennessee – USA

# CONFERENCE PAPERS

## Session 1.1 ANALYSIS TECHNIQUES OF $H_2$ ENGINES

# Ultra-Lean Mixture Formation and Combustion of a Hydrogen-Fuelled High-Performance DI-SI Engine: an Experimental and Numerical Study

F. Mortellaro[1], R. Tonelli[1] and M. Medda[1]

[1]Ferrari S.p.A. – R&D Department. Viale Abetone Inferiore,4 – 41053 – Maranello, Italy.
E-mail: fabiosanti.mortellaro@ferrari.com
Telephone: +(39) 0536 949111

**Abstract**. The combustion of hydrogen (H2) in internal combustion engines represents a compelling and promising solution towards achieving carbon neutrality in future transportation. When compared to traditional fuels such as gasoline and diesel, hydrogen (H2) emerges as a cleaner and more ideal alternative. In the complete combustion of H2 in air, the primary products are water, with only minimal amounts of oxides of nitrogen and particulate matter being generated. Consequently, research aimed at the realisation of efficient and clean combustion in hydrogen internal combustion engines (H2 ICEs) has emerged. This paper presents a study of a high-performance direct-injection spark ignition engine fuelled by hydrogen. The engine rotational speed is 7500 rpm, it is operated at a high load, and at an ultra-lean air-to-fuel ratio, in order to achieve maximum efficiency. Firstly, test bench data is collected and analysed in order to determine the effect of the start of injection timing on combustion performance and efficiencies. Secondly, a computational fluid dynamics (CFD) model is calibrated to replicate the experimental evidence. Subsequently, the CFD model is employed to virtually evaluate the potential for hardware modifications to achieve the highest efficiency calibration of the engine without any working issues related to combustion instabilities. Finally, the new hardware is subjected to experimental testing, which serves to corroborate the CFD prediction in terms of combustion performance enhancement.

## 1. Introduction

The International Energy Agency (IEA) has devised the Net-Zero Emissions Scenario by 2050 (NZE) with the objective of limiting the global temperature increase to a level well below 2°C with respect to pre-industrial levels, as agreed in the Paris Agreement (COP21). The IEA has identified the production of hydrogen as a pivotal aspect of decarbonisation across a number of industrial sectors, including the automotive industry and the production of low-carbon hydrogen, which is categorised as green, pink, blue, or turquoise. The production and consumption of this hydrogen will undergo a significant increase in the coming years, as evidenced by projections [1].

Although fuel cell (FC) technology has been more widely commercialised in the road transportation sector, there is considerable potential for hydrogen-fuelled internal combustion engines ($H_2$ ICEs) [2], [3], [4]. A plethora of research activities have been initiated, with several prototype vehicles constructed, including those designed for use in passenger cars, heavy duty vehicles, and sports cars [5], [6]. The benefits of the $H_2$ ICEs over FC include a higher tolerance to fuel impurities, greater flexibility in switching between fuels, reduced reliance on rare materials and a reduced thermal load [7]. A key limitation of the $H_2$ ICEs compared to the FC is the generation of tailpipe emissions, predominantly nitrogen oxide (NOx), alongside minor amounts of carbon monoxide (CO), carbon dioxide ($CO_2$), hydrocarbons (HC) and particulate matter (PM) resulting from the combustion of lubrication oil.

The current standard for passenger cars is compressed hydrogen with a 700 bar tank, while for race cars, a hydrogen liquid tank may be a solution. It should be noted that the specific energy and energy density of hydrogen storage are inferior to that of gasoline storage, as documented in references [8] and [9]. In order to successfully achieve targets for an on-road sport car, the hydrogen-fuelled ICE powertrain must face a number of specific challenges [10]. These include achieving performance comparable to that of a gasoline engine, maintaining high efficiency and developing effective strategies for emission management.

Hydrogen has distinctive physical and chemical characteristics that differentiate it from conventional fossil fuels. With a lower heating value (LHV) of 120MJ/kg, hydrogen can provide nearly three times as much energy by mass compared with gasoline (41-44MJ/kg). It should be noted, however, that hydrogen has a higher stoichiometric ratio, with a value of 34.3 compared to 14.5 for gasoline [3]. The combination of the two characteristics results in a lower calorific value of the air-fuel mixture under stoichiometric conditions, which is higher in the case of hydrogen. Consequently, the mass of air required for the same fuel power is approximately 15% less for hydrogen than for gasoline [3], [7].

The density of hydrogen is approximately one order of magnitude lower than that of gasoline. The volumetric efficiency advantage of direct injection over port injection in the case of hydrogen is therefore greater than for gasoline. Assuming that there is sufficient mixing time and combustion is stable and efficient, the optimal strategy for minimising the charging system is a direct injection with closed intake valves. The flammability range of hydrogen is considerably wider than that of gasoline, spanning lambda from 0.14 to 10 [2] , [3] in ambient conditions, as opposed to the range of 0.25 to 1.42 for gasoline. This suggests that a hydrogen internal combustion engine will exhibit greater stability in a highly diluted environment, potentially leading to lower emissions and increased engine efficiency [11].

At stoichiometric ratios, hydrogen exhibits a markedly elevated flame speed, approximately one order of magnitude faster than gasoline. In the stoichiometric condition, the minimum energy required to ignite a hydrogen-air mixture under atmospheric conditions is notably lower than that required for gasoline [11]. Therefore, $H_2$ ICEs operating in stoichiometric condition is subject to the risk of pre-ignition from hotspots or residues in the combustion chamber [4], [12]. In the case of an ultra-lean air-to-fuel ratio (2.5-2.8 times over stoichiometric ratio), the minimum energy required for ignition is significantly higher, while the laminar flame speed is significantly reduced [11], [13].

In these conditions, combustion temperature remains low enough to prevent the formation of NOx; thus, NOx can be considered insignificant, and dedicated after-treatment is not required [10]. Furthermore, a lean condition reduces the risk of pre-ignition [4], [12]. In ultra-lean conditions, air dilution reduces heat losses, thereby enabling higher thermodynamic efficiency than that observed in the stoichiometric case to be achieved [3], [10].

The objective of developing a high-performance $H_2$ ICE is to achieve high specific power output while maintaining the highest possible efficiency. This is a challenging goal, as the two objectives are often in conflict. As highlighted in [10], achieving high specific power output would require the engine to operate at high revolutions per minute (RPM) and with a high amount of flowing air. Nevertheless, the design of a sport car imposes strict boundary conditions on the powertrain, such as limited space for the installation of peripherals (e.g., cooling radiators, charging system, aftertreatment), a thrilling transient response (imposing limited dimensions of the charging system), and the need to comply with low-emissions requirements set by the regulatory body (providing dedicated NOx after-treatment). Given the lack of clarity regarding the scenario and the absence of detailed specifications for the aforementioned conditions, the research conducted by the development group has been focused on achieving the highest possible power output with a hardware that can operate within the constraints imposed by the high efficiency requirements. These include a high compression ratio and an ultra-lean mixture, which must be maintained at 7500 revs per minute. Consequently, the maximum specific power that can be achieved in ultra-lean conditions is constrained, and it is crucial to enhance the $H_2$ ICE ability to handle ultra-lean conditions. This can be achieved by developing technical solutions that optimize the efficiency of the combustion process and the volumetric efficiency.

In previous works [10], [14], the authors conducted an analysis of both experimental and numerical data to assess the benefits and drawbacks of a late injection strategy. This strategy involves initiating the injection of fuel into the combustion chamber during the compression stroke, with the intake valves closed. Late Start Of Injection (SOI) has been demonstrated to enhance volumetric efficiency, as hydrogen has a significantly lower density than air. Therefore, it is not advisable to inject with open valves. The late injection strategy results in a reduction in compression work, as for a significant duration of the compression stroke, only air is present in the chamber. This reduces the mixture temperature at the end of compression, which has a positive impact on knock resistance and pre-ignition risks. The primary drawback of late injection is the potential for incomplete mixture homogenisation, which can result in the emission of hydrogen and nitrogen oxides at the exhaust. The aforementioned analysis demonstrated that, in stoichiometric conditions, the advantages of late SOI outweigh the disadvantages. In the case of lambda ultra lean, the advantages of late SOI on volumetric efficiency and compression losses are expected to be lower than in the case of stoichiometric mixture due to the greater ratio between air and hydrogen [2]. Furthermore, in ultra lean conditions the risk of abnormal combustion is reduced. When compared to stoichiometric conditions, the risk of problems with combustion stability is higher in the case of lambda ultra lean. Therefore, the importance of ensuring homogeneity of the mixture increases. Furthermore, other studies indicate that direct injection with closed valves may be a strategy to optimise engine efficiency even in lean conditions [15].

In this scenario, Computational fluid dynamics (CFD) tools play a fundamental role to reduce development costs and time to market. They can support the engine design development, providing reliable simulations. In particular, in-cylinder simulations can be proficiently adopted to estimate the gas exchange process, the injection phase, the mixture formation quality, combustion and, finally, auto-ignition of the end-gas. Fuel-air mixing is crucial for achieving stable ignition and ensuring a clean and efficient combustion process in $H_2$ ICEs. Computational Fluid Dynamics (CFD) can effectively aid in optimizing injector configuration and injection strategies to enhance the mixing process.

In this study, the authors conducted an experimental investigation on a single-cylinder engine fueled with hydrogen and equipped with a high-pressure direct injector. The experimental campaign demonstrated that the start of injection (SOI) has a significant impact on the combustion characteristics of the mixture. However, the objective of achieving the highest possible efficiency is precluded by combustion instability issues. Secondly, the software CONVERGE [16] was employed to construct a comprehensive 3D CFD model to investigate these engine operating conditions, both in terms of mixture stratification and combustion performance. Thirdly, a virtual validation of hardware modifications is conducted to ensure that the maximum efficiency condition is reached and combustion instability issues are resolved. Finally, one of the proposed solutions was validated at the test bench, thereby confirming the prediction of the model.

## 2. Engine and measuring apparatus description

The engine analysed in the subsequent paragraphs is a direct-injection spark-ignition single cylinder engine (SCE). The combustion chamber layout and design are derived from a production series gasoline direct injection (GDI) engine. The main geometric characteristics are typical of a modern gasoline fuelled engine, having four valves, pent-roof, tumble intake ports, central-mounted injector, spherical bowl piston shape. A schematic layout of the combustion system is represented in Fig. 1. The engine Further specifications are listed in Table 1.

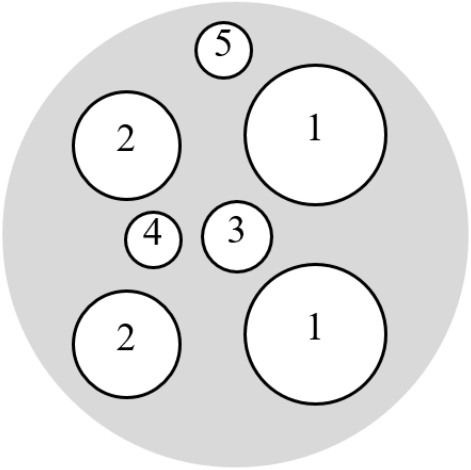

**Fig. 1.** SCE schematic head layout: (1) Intake valves, (2) Exhaust valves, (3) Hydrogen injector, (4) Spark plug, (5) Pressure Transducer

Intake and exhaust valves are moved by means of a double overhead camshaft (DOHC). Variable Valve Timing (VVT) is actuated using hydraulic actuators both on intake and exhaust camshafts; however, in the operating conditions explored in this work they are not actuated, thus using the engine at fixed valve timings.

The fuel is injected by a dedicated $H_2$ injector. The design is a solenoid-controlled outwardly opening nozzle. The working pressure range is 5 to 40 bar, with a static mass flow rate of approximately 13 g/s @ 24 bar. The hydrogen pressure is regulated through external pressure regulator connected directly to a high-pressure vessel, while its temperature is kept constant at 50°C.

The air that is flown by the charge system is refrigerated and enters the intake plenum at a fixed temperature, which is maintained by an air conditioning system.

The mixture is ignited by a cold heat range spark plug. The design is adapted for an hydrogen engine, having the electrodes with very limited protrusion. This is beneficial in order to avoid abnormal combustion phenomena, as discussed in [4].

Combustion chamber is instrumented with a piezoelectric pressure transducer (Kistler 6045b) placed between intake and exhaust valves on the side. Intake and exhaust runners pressure are measured through integrated pressure transducer (Kistler 4007 and Kistler 4049). To measure hydrogen flow, a Coriolis Endress+Hauser Promass A (max flow 100kg/h) is used. Exhaust hydrogen concentration (dry) is measured through a V&F HSense Mass Spectrometer. Lambda is measured indirectly through emission measurement and directly through a Bosch LSU5.2 series gasoline lambda probe. For heat release calculation, a thermodynamic method with constant polytropic coefficient (1.4 compression, 1.3 expansion) is used. Each steady state measurement consists in 1000 engine cycle for indicated data and 30s average for test bench measurements. A representative scheme of the measuring instruments is pictured in Fig. 2.

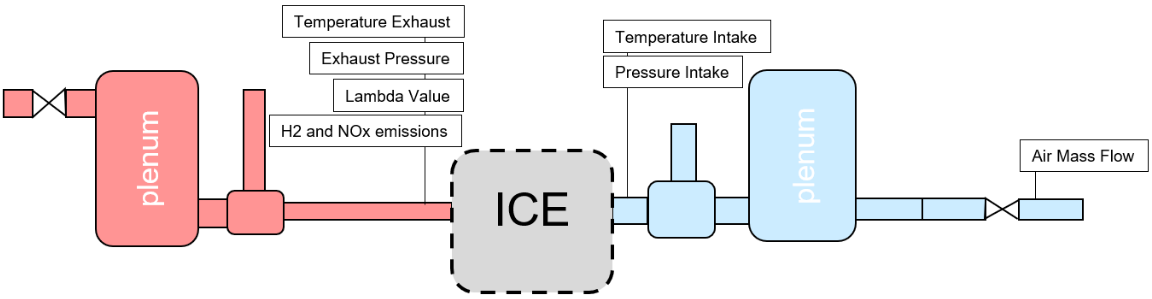

**Fig. 2.** Example of figure legend (font point 9. Line should not end with a dot)

**Table 1**. Engine specifications

| | |
|---|---|
| Displacement | 498 cc |
| Bore / Stroke | 88 / 82 mm |
| Compression ratio | 14 |
| Number of Valves | 4 |
| Injector | Low-pressure direct injection |
| Ignition | Cold grade M12 spark plug |
| Intake Cam Width | 195 CAdeg |
| Exhaust Cam Width | 240 CAdeg |

## 3. Experimental tests

### 3.1 Investigated conditions

In [14], the injection timing that resulted in the highest efficiency was the late injection (LI) timing, when compared with the intermediate injection (II) and the early injection (EI). This ensured the highest indicated efficiency and the highest volumetric efficiency.

The objective of the subsequent investigation is to replicate the aforementioned study, varying the start of injection timing while maintaining the new operating conditions and hardware (specifically the compression ratio of the piston). The highest load reached was constrained by the structural limitations of certain components of the engine. Further specifications are provided in Table 2.

**Table 2**. Test specifications

| | |
|---|---|
| Engine speed | 7500 rpm |
| IMEPH | 20 bar |
| Lambda | 2.5 |
| Charge air temperature | 65° C |
| Hydrogen temperature | 50° C |
| IVO (@ 0.6 mm) | -15 CAdeg aTDC |
| EVC (@ 0.6 mm) | 10 CAdeg aTDC |
| Injection Duration | 2 ms |
| Injection Pressure | 27 bar |

### 3.2 Test results

A sensitivity to hydrogen injection timing is performed by varying the actuation of the SOI during the thermodynamic cycle. Through accurate analysis of the cylinder pressure, it has been demonstrated that there is a delay between the electrical input of the start of injection (SOI) timing imposed by the ECU and the effective injection of the hydrogen inside the cylinder. The delay is due to the physics involved in the injector construction, which is caused by the energising time of the solenoid that actuates the needle and the movement of the needle itself. In Fig. 3, the pressure trace plotted with the engine operated with SOI = -360 CAdeg aTDC; during the intake stroke shows a discontinuity, where the effective injection takes place, before returning to the mean value of the intake manifold. The injection delay is estimated at 1.1 milliseconds, which corresponds to approximately 50 CAdeg at 7500rpm.

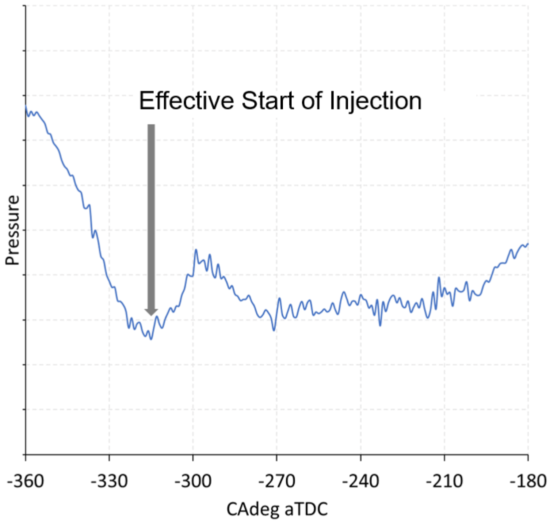

**Fig. 3.** In-cylinder pressure trace during the intake stroke. Electrical signal SOI=-360 CAdeg aTDC

The primary outcome of the test is that it is not possible to run the engine with a LI calibration due to the variation of the combustion, as measured by the coefficient of variance (CoV) of the gross indicated mean effective pressure (IMEPH). This resulted in misfire and abnormal combustion. Even with the II, the engine exhibited a high CoV of IMEPH, despite the low incidence of misfire cycles that permitted the acquisition of data. As an illustration, Fig. 4 depicts the pressure trace of five subsequent cycles, demonstrating a 20% variation in the maximum pressure. This is clearly unacceptable in the context of normal engine operation. Consequently, the range of SOI under investigation is -360CA < SOI < -180CA, and the main findings are discussed below.

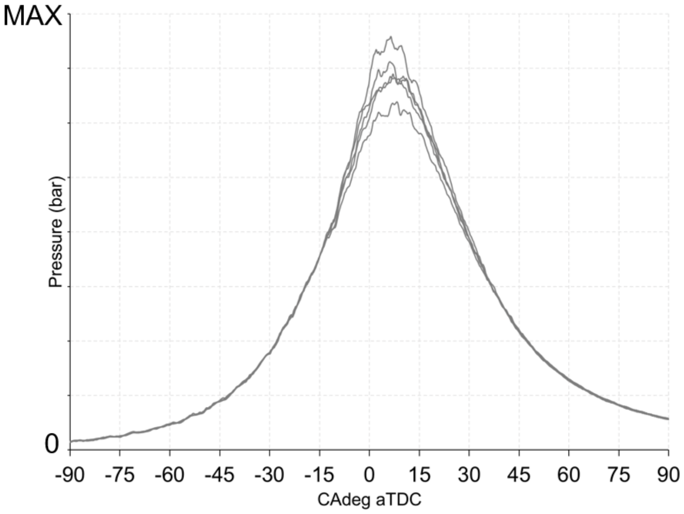

**Fig. 4.** In-cylinder pressure traces with engine operated with Intermediate Injection (SOI=-180 CA aTDC)

In Fig. 5, the CoV is plotted against the SOI at a constant IMEPH. The last point which does not see a critical instability or misfire event is the SOI = -240 CAdeg. It can be observed that injection phasing affects the manifold volumetric efficiency, leading to higher values when the hydrogen is injected after intake valve closing. Filling capacity reaches an asymptotical maximum at SOI = -240 CAdeg, indicating that the hydrogen injection occurs entirely after the intake valve has closed. This is due to the injection activation delay.

The concentration of unburned hydrogen (H2) measured at the exhaust demonstrates a distinct pattern. Advancing the hydrogen injection leads to a reduction in the quantity of emissions. This is likely due to the formation of a more homogeneous mixture at the time of ignition. Hydrogen is more flammable than gasoline (see paper on prop H2), and thus able to complete the flame surface propagation even in the presence of rich or lean mixture pockets within the combustion chamber.

Regarding the combustion performance indicators, Fig. 5 presents the CAdeg at 50% of the Mass Fraction Burnt (MFB 50%), the burn duration (MFB 10-90%) and the burn delay (MFB 0-10%). It should be noted that the quantitative values have been omitted for reasons of confidentiality. In order to reach knocking conditions, combustion phasing is regulated. The acquisitions reported in Fig. 5 are therefore the limited spark advance that precedes knock. Knock takes place in an internal combustion engine when a region of unburned charge, commonly referred to as end-gas, auto-ignites before the flame front initiated by the spark plug has sufficient time to consume it. Further details concerning the analysis of knock amplitude and the calculation of the MFB can be found in [17].

The occurrence of knocking is contingent upon the injection strategy employed, with the II cycle exhibiting the most delayed injection. Nevertheless, the advancement of the injection (EI) allows for more efficient operation, which is consistent with the conclusions drawn in [14].

The duration of the burn is only minimally affected by the injection strategy. This may be attributed to comparable turbulence levels at TDC firing with the distinct injection timings. It is notable that the SOI = -180 is particularly susceptible to the effects of mixture inhomogeneity, exhibiting a notable elongation of the flame propagation duration.

The burn delay does not exhibit an univocal trend. In fact, the injection timings with the most advanced injection timing, which should result in a homogeneous mixture, and with a lambda value in the volume next to the spark plug similar to the mean value of the combustion chamber, have the longest burn delay. This is to be expected, given that the laminar flame speed at ultra-lean values of lambda is relatively low compared to the stoichiometric value [18]. Retarding the injection is likely to result in the formation of a richer pocket of mixture in the volume adjacent to the spark plug, which in turn will lead to a faster MFB 0-10%. Finally, when the injection continues to be delayed, the combustion stability is affected, resulting in misfire events. This indicates that the mixture has a lambda value outside the flammability region. This outcome is of significant relevance since it demonstrates that burn delay is not invariably proportional to the coefficient of variation of the IMEPH and, therefore, the combustion stability, in contrast with the findings of a previous paper on a gasoline engine [19].

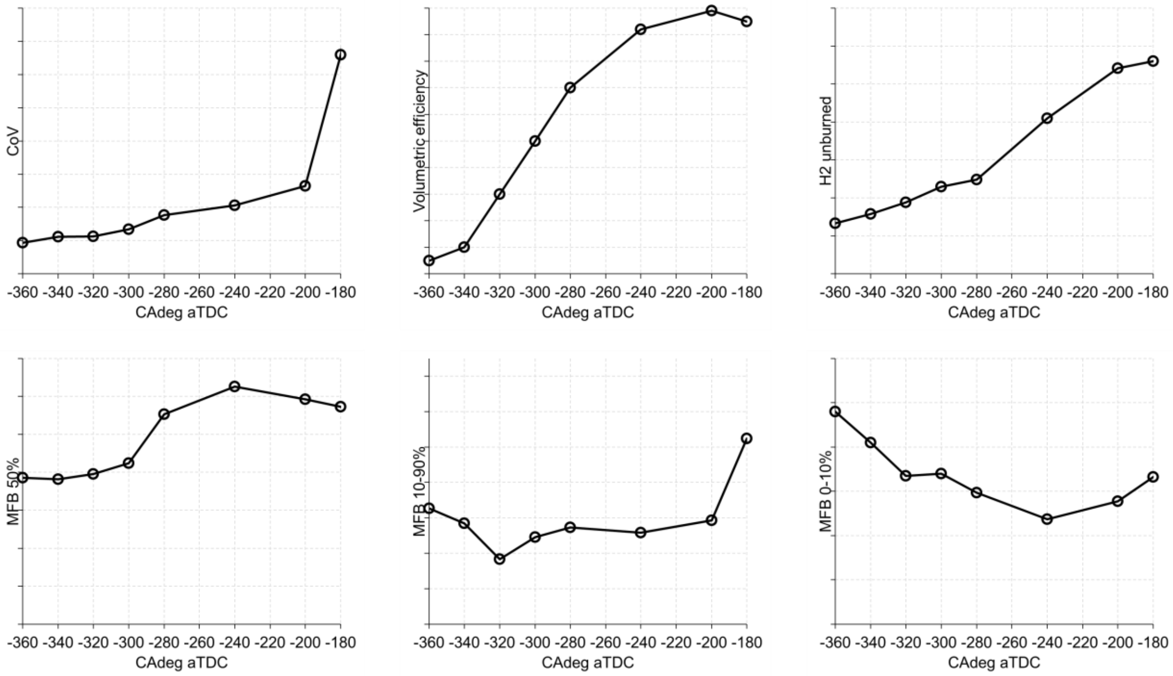

**Fig. 5.** Test bench results varying the SOI

This information is of value when attempting to ascertain which calibration is the most fruitful in the context of designing a complete powertrain system layout. It is evident that volumetric efficiency has an appreciable impact upon the design and operation of the engine's charging and cooling systems. It is therefore essential to ascertain which injection strategy the engine will operate under in order to select the most appropriate peripherals. In order to select the most effective calibration, the Fig. 6 reports the product of the volumetric efficiency and the indicated efficiency. The injection timing with the greatest retardation has the highest value, despite exhibiting the lowest indicated efficiency. This clearly defined the objective of optimising the combustion system with a SOI of -180°CAdeg.

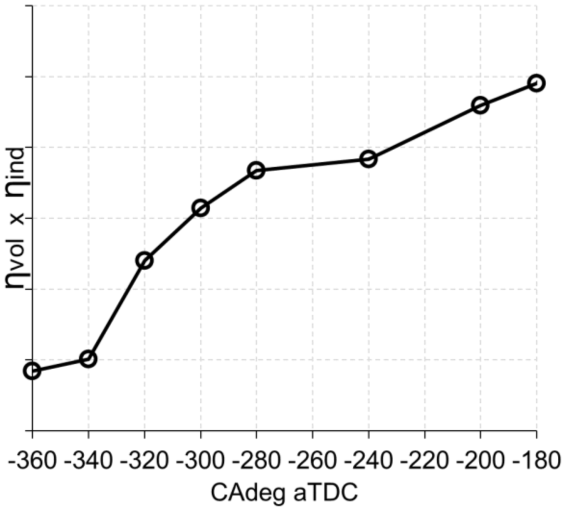

**Fig. 6.** Product of volumetric efficiency and indicated efficiency varying the SOI

## 4. CFD Simulations

In order to gain a deeper understanding of the results presented in the preceding paragraph, it is necessary to acquire knowledge regarding the root causes of the malfunctioning when retarding the injection timing. Furthermore, in order to develop the combustion system to achieve the greatest possible efficiency, CFD simulations must be carried out.

The methodology employed in the modelling process is outlined in paragraph 4.1. In order to reduce the computational effort associated with the points available from the SOI sweep, only three values are selected: -360CA, -240CA and -180CA. The combustion process is then correlated with the experimental data and the result described. Subsequently, virtual validation is employed to propose hardware modifications that will enable the combustion stability of the system to be maintained even when the SOI timing is retarded.

### 4.1 Numerical modeling

The commercial CFD software CONVERGE (version 3.0.28) was used for the simulations. The code makes use of a modified cut cell Cartesian mesh, in conjunction with Adaptive Mesh refinement (AMR) [16]. The computational domain comprises the combustion chamber and intake and exhaust ports. Geometrical symmetry is exploited; thus, only one-half of the domain is simulated, thereby reducing the computational effort.

In the domain, the largest cell size was 4 mm within the intake and exhaust ports, and 1 mm inside the combustion chamber. Targeted refinements achieved 0.5 mm on the combustion chamber walls, 0.125 mm at the spark, and 0.0625 mm around the hydrogen injector poppet valve. The subgrid-scale (SGS) refinement of cells by AMR ensures a high resolution (0.25mm) to capture the complex gas exchange processes occurring through the intake/exhaust valves, hydrogen injection and subsequent combustion. The total number of fluid cells is approximately 1e6 at BDC, increasing to 2.5e6 during the injection phase due to embedded and adaptive mesh refinements. Fig. 7 provides an example of the resulting mesh at BDC.

The injector characterisation is not included here, as it follows the methodology presented in [14].

The approach to turbulent flow involves the k-ε RNG model for compressible flows, which is commonly used in engine simulations. The Redlich-Kwong equation of state is employed to close the set of Reynolds-averaged Navier-Stokes (RANS) equations. The diffusion coefficient is calculated as the weighted average of the molecular mass diffusivity for each species. The specific heat and thermal conductivity are dependent on temperature, and expressed as polynomial functions. At solid walls, a non-slip condition is imposed, and a fixed temperature value is assigned, which depends on the specific boundary and is obtained from a combination of experimental evidence and thermo-structural simulations results. The near-wall flow is modelled via a high-Reynolds approach, with the adoption of wall functions both for velocity and thermal boundary layers. With respect to the former, a standard law of the wall is employed. With respect to the latter, the GruMo-UniMORE thermal wall function is selected as it has been validated on gasoline engines with comparable load and rotational speed [20].

The timestep is set between 1e-6s and 1e-8s in order to maintain the CFL number to a value close to 1. The PISO solution algorithm and second-order numerical scheme are employed for the transport equations of momentum, temperature, and turbulent quantities.

The time-dependent pressure and temperature boundary conditions are derived from a GT-Power 1D model. The model has been provided with phenomenological models for turbulence and combustion, and has undergone extensive validation against experimental measurements.

The combustion process is represented by the Extended Coherent Flamelet Model (ECFM) [21], which is a general-purpose combustion model capable of simulating the complex mechanisms associated with turbulent mixing and flame propagation, which are characteristic of modern internal combustion engines. The flame surface density (FSD) transport equation serves as its governing principle, regulating the turbulent premixed flame propagation process. In order for the FSD equation to account for the local thermodynamic state and composition of the mixture, it must also include a term for the speed of the laminar flame. In order to model the interaction between the flame and local turbulence, an additional source term is introduced into the turbulent stretch term in the flame surface density (FSD) equation. In the present simulation, the intermittent turbulent net flame stretch (ITNFS) [22] is employed.

The spark plug is represented by the Imposed Stretch Spark Ignition Model (ISSIM) [23]. ISSIM, developed for the simulation of the combustion process, is used to simultaneously simulate the electrical energy deposited in the circuit and the surface and mass deposition of the flame.

A tabulated approach, which employs detailed chemistry, is employed to model auto-ignition and laminar flame speed. In this simulation, the tables were generated using the GRI3.0 mechanism [24] and the CONVERGE chemistry tools. These tables were constructed to cover a pressure range of 10bar – 200bar in intervals of 10 bar, a temperature range of 500K – 1200K in intervals of 100K, an equivalence ratio range of 0.3 – 2 in intervals of 0.1, and an EGR fraction ranging from 0 – 0.2 in intervals of 0.05.

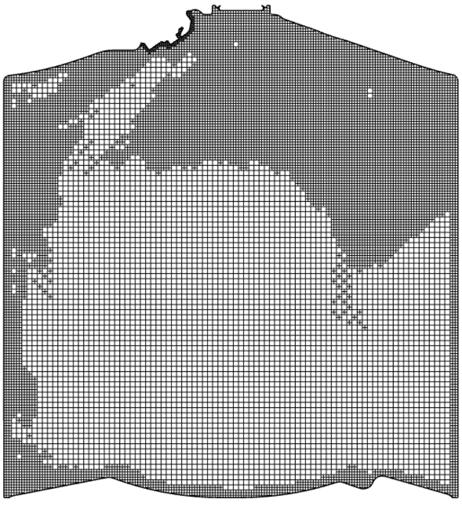

**Fig. 7.** Example of a section on symmetry plane of the computational mesh at BDC

### 4.2 Simulation results

As previously stated, three SOI calibrations are replicated. The following values were considered: -360CA, -240CA, and -180CA. The quantity of hydrogen injected is identical in all three cases, as is the calibration at the test bench. The inlet pressure is varied in order to obtain the mean lambda value. In order to validate the CFD simulation, it must be demonstrated that the mean experimental results ob-tained during gas exchange can be adequately predicted by the numerical model. Fig. 8 contains a number of important characteristic quantities that are useful for evaluating the mixture status inside the combustion chamber. For purposes of comparison, the only black curve represents the intake valve lift profile, which is identical across the three cases. The remaining lines are coloured, with the SOI = -300 case in orange, SOI = -240 in red, and SOI = -180 in blue. With regard to the lambda value, all three cases fall within the experimental range of ±0.5%, which corresponds to a value of 2.5. The hydrogen mass flow rate injection profiles are presented in graphical form. It can be observed that the actual lift of the injector needle is adjusted in accordance with the findings discussed in the previous section. It is noteworthy that the SOI = -240 case initiates its injection shortly before the intake valve closes, with no discernible impact on the intake pressure at the inlet manifold. In contrast, the SOI = -300 case neces-sitates a higher pressure to ensure consistent airflow and lambda. This is in accordance with the test bench results, as the two cases with the latest injections have an equal volumetric efficiency.

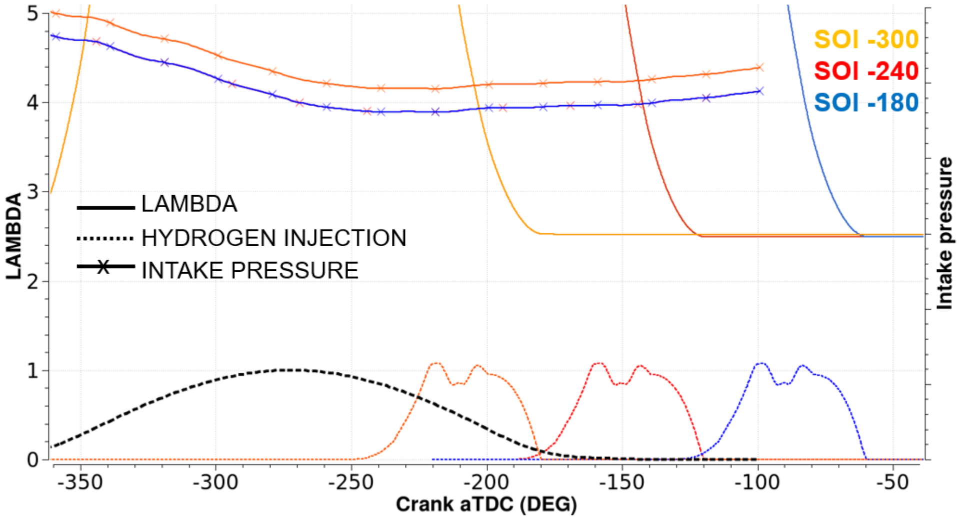

**Fig. 8.** Lambda, intake pressure, and hydrogen mass flow rate for the three simulated cases. Dashed black curve represents the intake valve lift profile

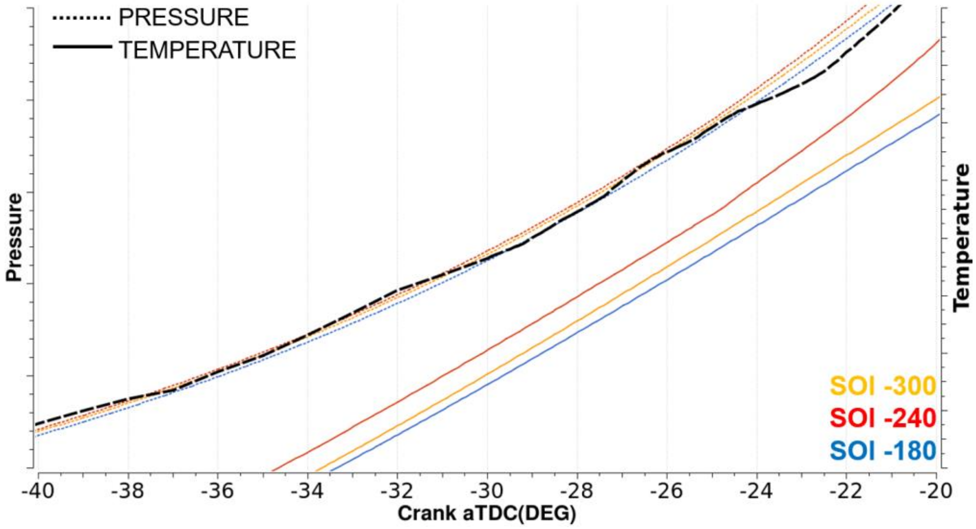

**Fig. 9.** Pressure and temperature inside the combustion chamber before TDC firing. Dashed black curve represents the experimental data for SOI=-240

In Fig. 9, the pressure and temperature line plots inside the cylinder towards the end of the compression stroke are presented. The SOI value of -240 was selected as the reference case, and in addition to the CFD simulations, the experimental acquisition of the pressure trace was plotted. The comparison indicates a satisfactory correlation between CFD and test bench data at the end of the compression stroke, provided that pressure and temperature are representative. A clear trend emerges when the three cases are analysed in terms of pressure and temperature of the charging mixture. The SOI=180 case exhibits the lowest temperature value, whereas that of the SOI=240 case displays the highest. This phenomenon provides a plausible explanation for the divergent knock resistance observed at the test bench. In particular, the SOI=240 case exhibited the highest MFB50% at knock-limited spark advance.

It may be reasonably expected that the three cases will exhibit considerable disparity in terms of mixture stratification and homogenization quality, due to the differing SOI. Fig. 10 presents the equivalence ratio among the three cases, in the brief interval preceding spark plug actuation, with the piston positioned near the top dead center (TDC). It can be observed that the injection with the most recent injection has the poorest mixture stratification. This is evidenced by the presence of pockets of both rich and lean fuel around the combustion chamber, with the majority of the fuel located at the periphery. Conversely, the core volume remains devoid of hydrogen. This is corroborated by the line plot displayed in Fig. 11, in which the values represented are the volume-averaged lambda around the spark plug, considered to be a sphere with a radius of 4 mm. It is observed that the SOI=-180 case exhibits the least amount of fuel, which is near the upper limit of flammability. Conversely, the other two cases demonstrate lambda values of approximately 1.6. The experimental evidence corroborates this observation, demonstrating that the SOI = -180 exhibits the greatest CoV of IMPEH and the highest hydrogen emission at the exhaust. The former is attributed to the extremely lean value, whereas the latter is due to the zones with high $H_2$ mass fractions. With regard to the macroscopic distribution of these cases, it can be observed that the values are similar, with a leaner portion under the exhaust valve than that under the intake valve. Conversely, the SOI = -300 exhibits a notable homogenization. Consequently, the calculated equivalence ratio standard deviation at the instant taken for the contour plots is 34.9%, 29.8% and 18.3% for the SOI=-180, SOI=-240 and SOI=-180 cases, respectively.

Fig. 12 presents a comparison between CFD and the mean experimental pressure trace for case SOI = -240, which is taken as a reference case. The simulation is demonstrated to be capable of accurately predicting the experimental value. It should be noted that the pressure curve deviates from the experimental values in the region close to TDC. In this area, CFD tends to overpredict the pressure in the combustion chamber. The presence of blow-by leakages in the experiment, which are not modelled in the current simulation, could explain this deviation. The numerical setup (with the exception of spark advance) used for this correlation in terms of FSD transport tuning parameters remains unchanged for the other cases. Fig. 13 presents the resulting pressure trace from CFD simulations. Notably, the SOI = -180 case exhibits a markedly attenuated flame propagation, which is consistent with the potential occurrence of a misfire event during testing. The result is a pressure trace that is almost indistinguishable from that of a "cold" cycle, with no evidence of any combustion event.

A comparative analysis was conducted between the various cases, with the results presented in Fig. 14, which compares the combustion indicators expressed in delta CA against the reference case (SOI=-240). The predictions are in qualitative agreement with experimental evidence, particularly in regard to the SOI=-300 case. Although the quantitative discrepancies exist, the model is capable of predicting which configuration burns at a faster or slower rate. Nevertheless, the SOI=-180 case exhibits minimal flame activity, suggesting that the combustion indicators calculation may be misleading, particularly from both the simulation and experimental perspectives. This is likely due to the high CoV of IMEPH.

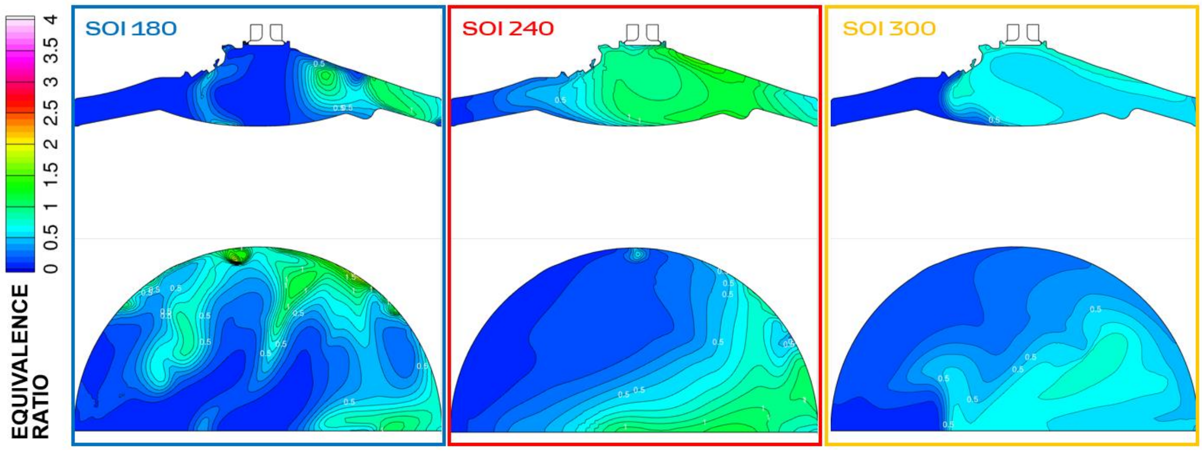

**Fig. 10.** Equivalence ratio distribution contour plot. Upper row displays the symmetry plane; lower row section is normal to the cylinder axis and tangent to the cylinder head

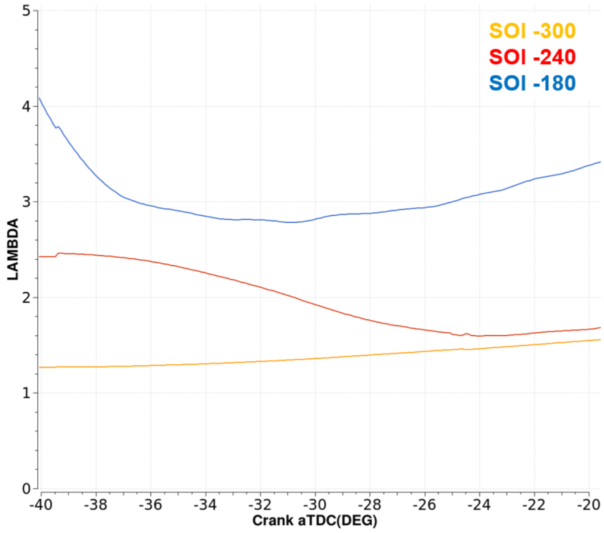

**Fig. 11.** Volume-averaged Lambda values around the spark plug, considering a sphere with a r=4mm radius

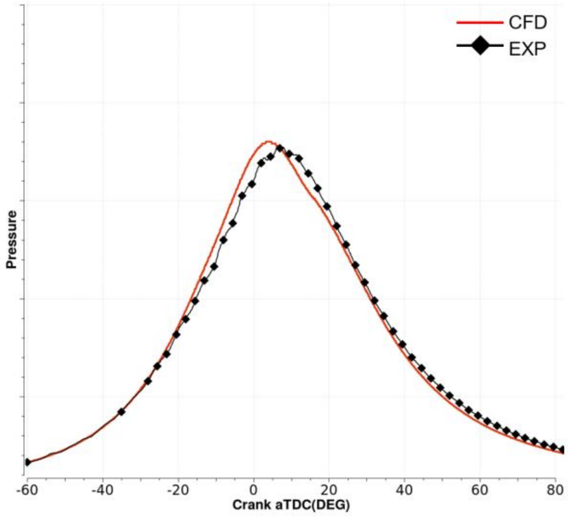

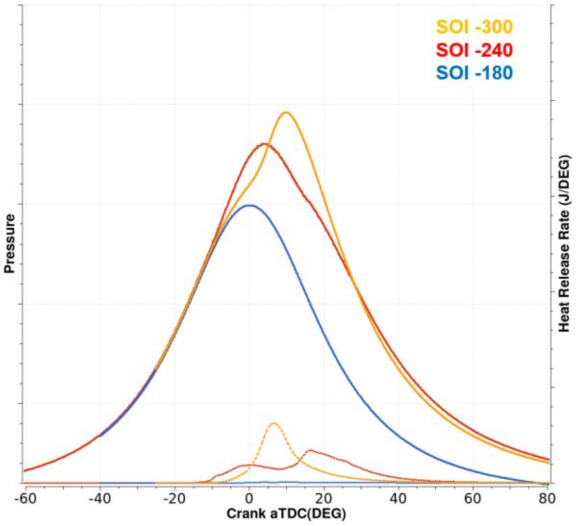

**Fig. 12.** Measured and predicted pressure traces. Case SOI=-240

**Fig. 13.** Comparison of the predicted pressure traces (left axis) and HRR (right axis) for the three cases

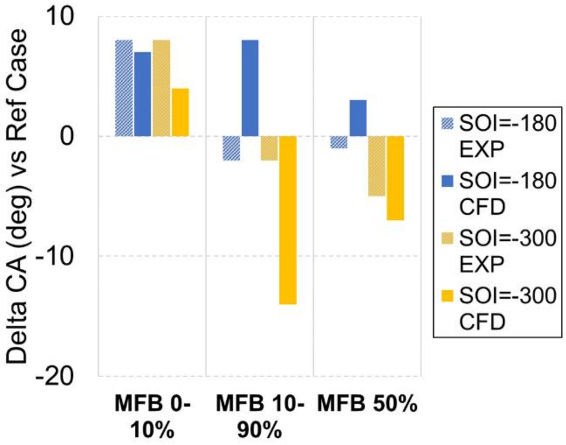

**Fig. 14.** Measured and predicted combustion indicators. Difference with reference case SOI=-240

## 5. Hardware modifications to enable late injection

As previously discussed, the objective of this activity is to enable the engine to operate at the maximum possible efficiency with a late injection. As the analysis of the efficiencies indicated, the objective of the final phase of the project is to modify the combustion system in order to enable the late injection, even in an ultra-lean operational point. The starting point is the SOI=-180 case, which provides a clear illustration of the situation at the spark plug prior to the commencement of combustion. There are essentially two contrasting approaches to modifying the mixture stratification, with the objective of enriching the central portion of the combustion chamber:

A. Achieving the maximum homogenisation, thereby promoting the overall diffusivity of the charge. This method necessitates a higher level of turbulence. The most straightforward method to achieve this is to enhance the tumble vortex during the intake and compression stroke, with the design of a new intake port
B. Searching for a mixture stratification, with the intention of bringing more fuel closer to the spark plug, thereby avoiding the "splashing" effect in the vicinity of the liner, positioning the combustion chamber's richest section centrally. Installing a guiding jet cap at the base of the injector directs the hydrogen jet towards a specified area of the cylinder, in conjunction with the mean flow field, thus enabling the creation of a suitable mixture stratification.

### 5.1 Virtual validation

Proposal A, also designated as 'High Tumble', is activated by a novel intake port that ensures a +66% increase in the absolute value of the peak TumbleY vortex and a +50% increase in the maximum TKE value during the intake and compression stroke. Fig. 15 presents the differences in velocity and turbulence kinetic energy contours on the symmetry plane. Conversely, the pressure at the intake required to achieve the same mass airflow is greater, resulting in a 4% reduction in volumetric efficiency.

In contrast, the proposal B) entails the installation of two distinct jet caps on the baseline configuration (low tumble). Geometry B1 comprises a single-hole jet cap, which directs the hydrogen jet in a direction parallel to that of the tumble vortex in order to enhance the mean flow field anti-clockwise rotation. The geometry B2 is a multi-hole jet cap, comprising nine holes. The aim is to encourage stratification of the fuel mixture by means of the introduction of smaller hydrogen jets, which should result in the fuel being confined to the central portion of the combustion chamber. Fig. 16 illustrates the geometric differences between the two proposed geometries.

The resulting equivalence ratio distribution of the new proposals is presented in Fig. 17. The high tumble solution provides a more homogeneous charge than that obtained with SOI = -180 and a low tumble intake port. Consequently, the augmented turbulence intensity resulted in a positive effect on the additional diffusivity. The stratification is comparable to that observed in the SOI=-240 case, with a region beneath the intake valve exhibiting higher values and the central volume approaching lambda unity. The jet cap B1 confines the hydrogen to the left portion of the combustion chamber, under the direction of the jet hole itself. The volume near the spark plug is near-stoichiometric, as evidenced by the monitored lambda values in a sphere of radius 4 mm, which are proposed for the three new simulations in Fig. 18. Finally, the analysis of the jet cap B2 reveals a stratified charge that is not conducive to the desired outcome. Indeed, the majority of the mixture is concentrated in the outer portion of the combustion chamber, exhibiting a similar distribution as observed in the SOI = -180 without modifications. Upon examination of the mixture distribution, it can be seen that an increase in the number of holes in a jet cap results in a hydrogen jet that is comparable in quality to a standard injector without a cap. It can be concluded that the increased hydrogen diffusion facilitated by multiple holes is not beneficial in this instance, as it does not provide directionality for the hydrogen towards a specific region in order to achieve stratification. Finally, in Fig. 18, the lambda value for the B2 case is so lean that it resides outside the plot range (lambda >>5), which precludes any further analysis.

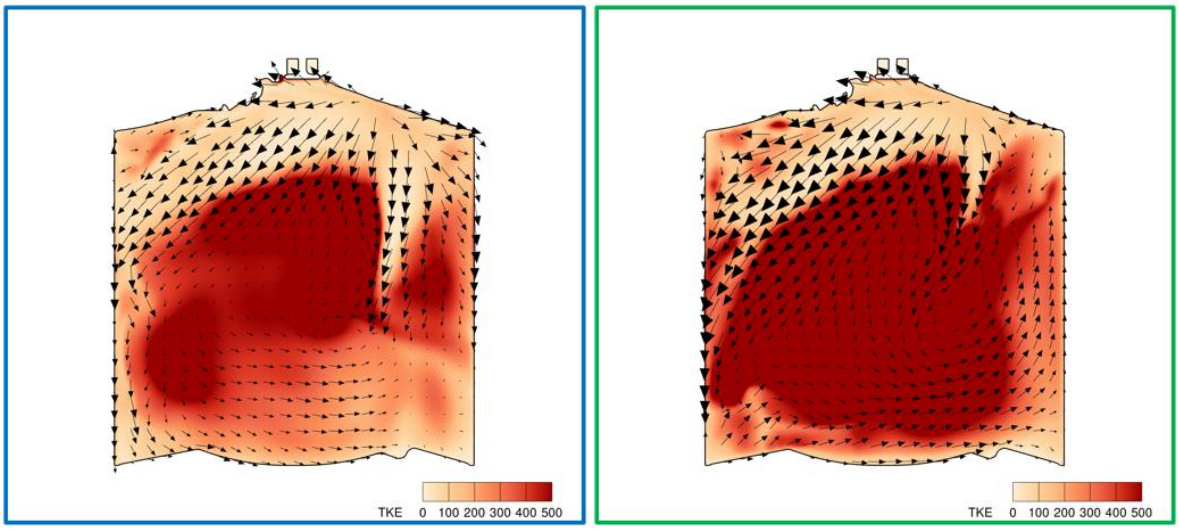

**Fig. 15.** TKE contour and Velocity vector for Low Tumble (blue) and High Tumble (green)

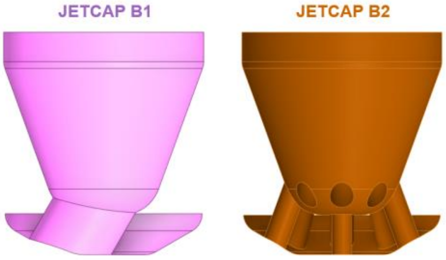

**Fig. 16.** Geometric representation of the two jet caps proposed

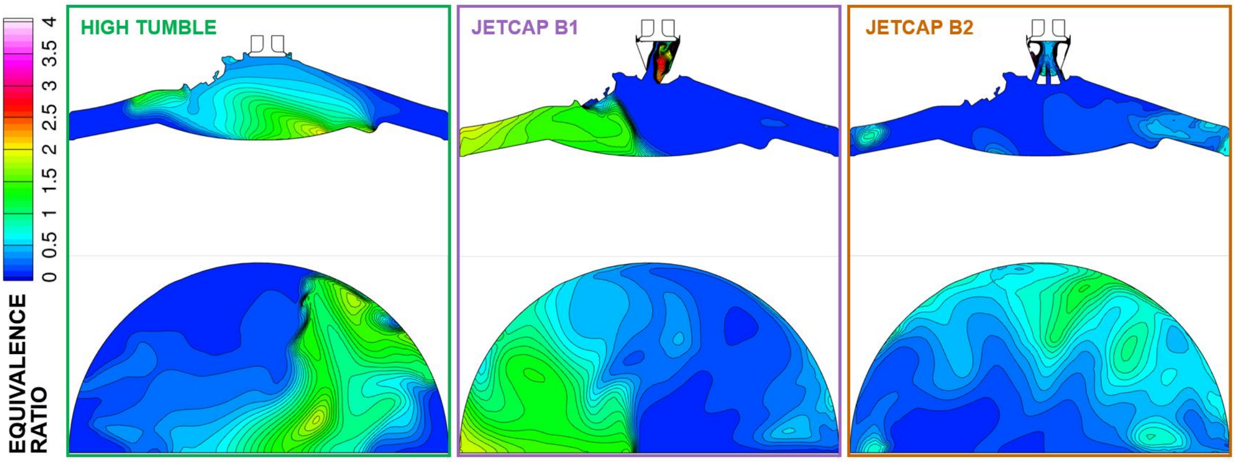

**Fig. 17.** Equivalence ratio distribution contour plot with SOI=-180. Upper row displays the symmetry plane; lower row section is normal to the cylinder axis and tangent to the cylinder head

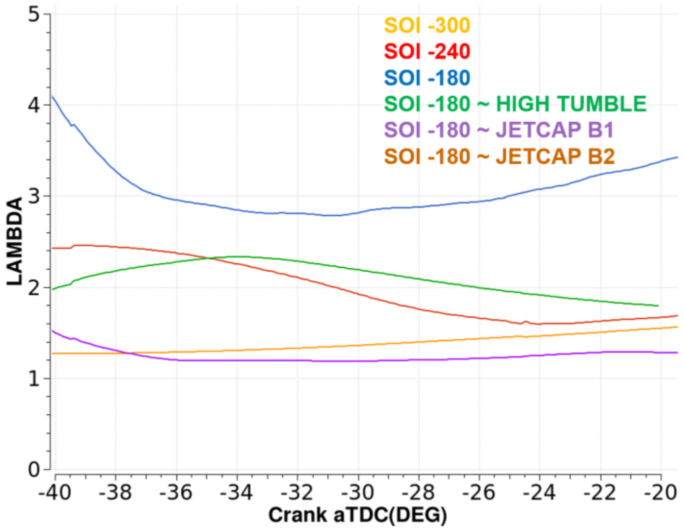

**Fig. 18.** Volume-averaged Lambda values around the spark plug, considering a sphere with a r=4mm radius (Jet cap B2 line is outside of the plotting range)

Finally, the combustion simulation for the three cases is presented in Fig. 19. The spark advance is set to maintain the same IMEPH. As anticipated, the jet cap B2 is not affected by flame propagation due to unfavorable mixture conditions in the vicinity of the spark plug. The mixture stratification of the high tumble and jet cap B1 cases, with a central region that sees stoichiometric conditions, ensures a high flame speed, resulting in both a short burn duration and burn delay.

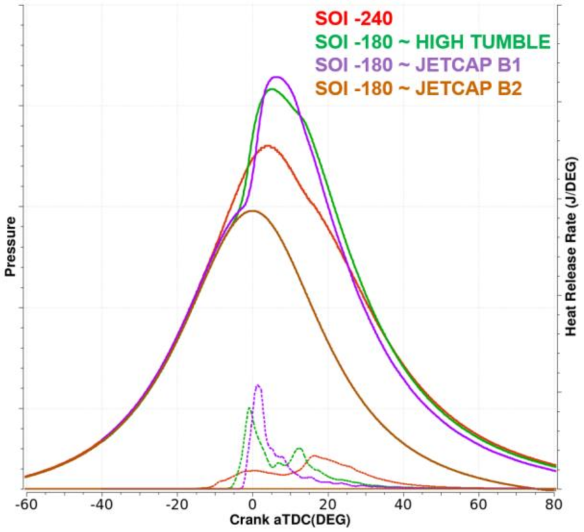

**Fig. 19.** Predicted pressure traces (left axis) and HRR (right axis) from CFD simulations

## 5.2 Experimental assessment

To validate the model's predictive capabilities, a final evaluation of the proposed hardware is conducted. It must be noted that, at the time of drafting this report, the data from the new intake port with high tumble are the only results available.

In the test, the SOI = -180 calibration with high tumble port demonstrated a remarkably low coefficient of variation (CoV) of IMEPH and an absence of misfires. This result is in accordance with the simulation indication, which predicted the formation of an ignitable mixture around the spark plug. In addition, Fig. 20 illustrates the difference in CA between the combustion indicators. The SOI = -240 is retained as the reference case. Once more, the qualitative trends observed in terms of burn duration and burn delay are reflected in the simulation results, although the differences are accentuated by the predictions of the model, repeating what already observed in the quantitative comparison of Fig. 14.

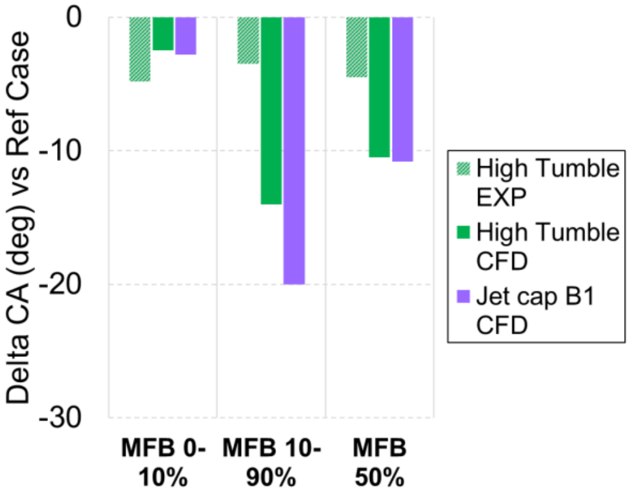

**Fig. 20.** Measured and predicted combustion indicators. Difference with reference case SOI=-240

## 6. Conclusions

This study examines the potential use of hydrogen as a fuel for a single cylinder research engine. The objective of this research is to identify the optimal engine configuration for maximum power output and efficiency. For this reason, this investigation employs a specific operating point, namely high rotational speed (7500 rpm), a high geometric compression ratio (CR=14) and ultra-lean conditions (lambda 2.5). The load is the highest possible, compatible with the structural limits of the engine.

The results obtained at the test bench demonstrate a notable sensitivity to the start of injection (SOI) of the fuel. In particular, late injection strategies are not feasible due to the high coefficient of variation of the IMEPH and the occurrence of misfires. The experimental testing revealed that intermediate or early injection strategies resulted in variations in the volumetric efficiency, combustion duration and unburned hydrogen emission. However, the analysis of efficiencies demonstrates that the highest overall efficiency is achieved through a late injection strategy. As a consequence, further enhancements to the hardware are necessary to ensure the engine operates effectively with the aforementioned calibration.

The test data is employed to validate the efficacy of a 3D CFD model that is capable of predicting differences in mixture stratification and replicating combustion performances in accordance with the SOI. It is notable that misfire events occurring with late injection can be traced back to a very lean portion of the mixture in close proximity to the spark plug, which does not allow for the development of a robust flame kernel.

Subsequently, the virtual validation of hardware modifications has demonstrated the feasibility of implementing a delayed injection strategy through two principal methods: the augmentation of turbulence intensity and the subsequent augmentation of mixing diffusivity; or the stratification of the mixture and the assurance of an optimal lambda value proximate to the spark plug and within the central portion of the combustion chamber. The former method is initiated by actuating a different intake port, which generates a more intense tumble vortex. The latter method involves the installation of a jet cap on the injector. Two different jet caps were evaluated in this experiment, each employing a distinct stratification strategy (single-hole versus multiple-hole). The CFD results demonstrate the considerable potential of two of these proposed solutions (namely the high-tumble intake port and the single-hole jet cap), which are shown to be effective in ensuring stable combustion when a late injection strategy is employed. The proposed intake port was subjected to testing at the test bench, and the outcomes validated the efficacy of the design.

It appears that CFD is an efficacious instrument when employed to design an entire combustion system, furnishing reliable indications regarding the quality of combustion and mixture distribution. It is evident that there is a necessity for improvement to ensure the precision required to provide accurate estimations of final output power in terms of quantitative value. Further analysis will be conducted to determine the origin of this discrepancy.

Future developments will focus on enhancing the precision of the predictions by refining the mixing model in terms of molecular and turbulent diffusivity evaluation and revisiting the combustion model, with a critical examination of the tabulated values of LFS at elevated pressure and temperature.

Another crucial aspect is the emission of NOx under different engine operating conditions. The model may be further developed to include the chemistry of NOx formation, thereby allowing for the simulation of emission levels at the exhaust.

## References

[1] International Energy Agency, «CO2 emissions in 2022,» [Online]. Available: https://iea.blob.core.windows.net/assets/3c8fa115-35c4-4474-b237-1b00424c8844/CO2Emissionsin2022.pdf.

[2] Wimmer, «H2-Direct Injection-A Highly Promising Combustion Concept».

[3] Kapus P., . Heindl, . Weißbäck e . Grabner, Proceedings of the 43rd International Vienna Motor Symposium 27 - 29 April 2022., 2022.

[4] D. Takahashi, . N. Matsubara, . A. Yamashita e . K. Nakata, Proceedings of the 44th International Vienna Motor Symposium 26 - 28 April 2023., 2023.

[5] D.-I. Jan Niklas Geiler, D.-I. Tobias Rabe, D.-I. Erik Schünemann, D.-I. Klaus Moritz Springer, M. Blomberg e D.-I. Markus Kirzinger, 32nd Aachen Colloquium Sustainable Mobility 2023 1 Light Commercial Vehicle with a H2 Engine Hybrid Powertrain.

[6] Wrobel, «Hydrogen Internal Combustion Engine Vehicles: A Review,» *Energies,* 2022.

[7] H. Yip, «A Review of Hydrogen Direct Injection for Internal Combustion Engines: Towards Carbon-Free Combustion,» *Applied Sciences,* vol. 9, n. 22, p. 4842, 11 2019.

[8] A. Sartbaeva, V. L. Kuznetsov, S. A. Wells e P. P. Edwards, «Hydrogen nexus in a sustainable energy future,» *Energy and Environmental Science,* vol. 1, n. 1, pp. 79-85, 2008.

[9] Winklhofer e . Stepan, Proceedings of the 43rd International Vienna Motor Symposium 27 - 29 April 2022.

[10] D. Massimo Medda, D. Vito Calia, D. Michele Di Sacco, D. Fabrizio Gullino, D. Vincenzo Rossi, D. Nicola Silvestri, D. Roberto Tonelli, D. Francesco Zaffino e F. SpA, 32nd Aachen Colloquium Sustainable Mobility 2023 1 Challenges and Opportunities in developing a Hydrogen High Specific Power SCE in the roadmap towards zero net GHG.

[11] C. M. White, R. R. Steeper e A. E. Lutz, «The hydrogen-fueled internal combustion engine: a technical review,» *International Journal of Hydrogen Energy,* vol. 31, n. 10, pp. 1292-1305, 8 2006.

[12] P. Grabner, M. Schneider e K. Gschiel, «Formation Mechanisms and Characterization of abnormal Combustion Phenomena of Hydrogen Engines,» 2023.

[13] S. Verhelst, C. TJoen, J. Vancoillie e J. Demuynck, «A correlation for the laminar burning velocity for use in hydrogen spark ignition engine simulation,» *International Journal of Hydrogen Energy,* vol. 36, n. 1, pp. 957-974, 1 2011.

[14] F. S. Mortellaro, N. Silvestri, F. Zaffino, M. Medda, M. D'Elia, V. Viswanathan e R. Rothbauer, «Effect of Start of Injection in a Hydrogen-Fueled DISI Engine: Experimental and Numerical Investigation,» *SAE Technical Papers,* 2023.

[15] Y. Luo, B. Wu, Q. Li, X. Tang, Z. Yang, C. Wu e T. Wu, «Experimental and simulation research on the lean combustion characteristics of direct-injection hydrogen engine,» *International Journal of Hydrogen Energy,* vol. 68, pp. 398-409, 5 2024.

[16] K. J. Richards, P. K. Senecal e E. Pomraning, Converge 3.0 Manual, Convergent Science, 2022.

[17] Berni F., Mortellaro F., Pessina V. et al., «Modeling of gaseous emissions and soot in 3D-CFD in-cylinder simulations of spark-ignition engines: A methodology to correlate numerical results and experimental data.,» *International Journal of Engine Research,* vol. 24, n. 5, pp. 2149-2174, 2023.

[18] S. Verhelst, C. T′Joen, J. Vancoillie e J. Demuynck, «A correlation for the laminar burning velocity for use in hydrogen spark ignition engine simulation,» *International Journal of Hydrogen Energy,* vol. 36, n. 1, pp. 957-974, 2011.

[19] M. Noguchi, S. Sanda e N. Nakamura, «Development of Toyota Lean Burn Engine,» *SAE Transactions,* vol. 85, pp. 2358-2373, 1976.

[20] F. Berni e e. al., «A modified thermal wall function for the estimation of gas-to-wall heat fluxes in CFD in-cylinder,» *APPLIED THERMAL ENGINEERING,* pp. 1045-1062, 2017.

[21] O. Colin, A. Benkenida e C. Angelberger, «3d Modeling of Mixing, Ignition and Combustion Phenomena in Highly Stratified Gasoline Engines,» *Oil & Gas Science and Technology,* vol. 58, n. 1, pp. 47-62, 2003.

[22] C. Meneveau e T. Poinsot, «Stretching and quenching of flamelets in premixed turbulent combustion,» *Combustion and flame,* vol. 86, n. 4, pp. 311-332, 1991.

[23] O. Colin e K. Truffin, «A spark ignition model for large eddy simulation based on an FSD transport equation,» *Proceedings of the Combustion Institute,* vol. 33, n. 2, pp. 3097-3104, 2011.

[24] G. P. Smith, D. M. Golden, M. Frenklach e e. al., «GRI Mech 3.0,» [Online]. Available: http://www.me.berkeley.edu/gri_mech/.

# Towards $H_2$ICE: Experimental and Computational Characterization of Hydrogen Injection, Mixing, and Combustion

Hong G. Im[1,*], Xinlei Liu[1], Moez Ben Houidi[1], Hao Wu[1], Abdullah Zaihi[1], Kevin Moreno-Cabezas[1], Bin Wu[1], Niraj Panthi[1], Hammam Aljabri[1], Rafael Menaca[1], Mebin Samuel Panithasan[1], Emre Cenker[2,*], Abdullah S. AlRamadan[2], Balaji Mohan[2], Gaetano Magnotti[1], William L. Roberts[1], James W.G. Turner[1]

[1] King Abdullah University of Science and Technology (KAUST), CCRC, Thuwal 23955-6900, Saudi Arabia.

E-mail: hong.im@kaust.edu.sa
Telephone: +(966) 544700186

[2] Saudi Aramco Research and Development Center, Transport Technologies Division, Dhahran, Saudi Arabia

E-mail: emre.cenker@aramco.com
Telephone: +(966) 547531173

**Abstract.** Hydrogen-fuelled internal combustion engines ($H_2$ICE) have great potential as future carbon-free transportation, especially in heavy-duty applications, but the implementation in real vehicles has not yet been demonstrated due to a number of technical challenges. One of the most important issues is the design of hydrogen injector systems that can provide the needed amount of fuel into the combustion chamber with rapid mixing with the main chamber gases to achieve a near homogeneous mixture, in order to ensure stable combustion without combustion anomalies such as pre-ignition and knocking. The present study provides an overview of the ongoing FUELCOM4 project with KAUST and Saudi Aramco in an effort to enhance our knowledge of hydrogen injection, mixing, and combustion characteristics by utilizing high-fidelity laser diagnostics and simulations. First, hydrogen jet injection and mixing characteristics are investigated in a high-pressure constant volume chamber experiment with accompanying simulations for validation. Jet penetration and dispersion characteristics depending on different injector configurations are examined. Recent developments in advanced laser diagnostic techniques to quantify the hydrogen fuel distribution are also discussed. Finally, parametric studies of the effects of jet dispersion and mixing on engine combustion characteristics are presented.

## 1 Introduction

In the pursuit of decarbonizing the energy and transportation sectors, hydrogen ($H_2$) has emerged as a focal point in combustion research. $H_2$ offers promise as a clean energy source for internal combustion engines (ICEs) due to its potential to be produced from water using renewable electricity. Notably, the application of $H_2$ in ICEs necessitates minimal modifications to existing engine hardware, positioning $H_2$ ICEs as a viable solution for future transportation, particularly in heavy-duty applications.

Given its high flame propagation speed and low ignition energy, $H_2$ is better suited for spark-ignition (SI) mode rather than compression ignition (CI) mode. Its wider flammability range compared to gasoline presents an opportunity for ultra-lean combustion, crucial for achieving stable combustion without knocking. However, earlier studies employing the port fuel injection (PFI) method encountered challenges such as flashback and pre-ignition at high loads, alongside reduced net air flow rate and engine power due to $H_2$ expansion. Contrastingly, the direct injection (DI) method has emerged as a solution to mitigate these issues by supplying $H_2$ directly into the combustion chamber, a method increasingly favored in recent $H_2$ ICE combustion research. However, the primary challenge in $H_2$ DI lies in achieving adequate mixing before spark ignition. Poor mixture distribution can lead to misfire or knocking, necessitating systematic optimization of injector design and injection strategy. Additionally, due to $H_2$'s ultra-low density, high injection pressure is required, resulting in choked flow within the nozzle channel and shock wave generation upon expansion into the combustion chamber. The complex transcritical and supersonic mixing process further complicates high-pressure $H_2$ injection, requiring a thorough understanding of optimization.

The FUELCOM project is a long-term research collaboration program between the Clean Combustion Research Center at KAUST and the Transport Technologies Division at Saudi Aramco's Research and Development Center. The partnership aims to develop early-stage technology by improving the science and application of core ideas that pave the road for sustainable mobility. FUELCOM commenced with a number of projects centered around fundamentally characterizing a wide range of fuel components based on their combustion behavior. This was followed by an extensive investigation of emerging engine combustion concepts, including gasoline compression ignition, high-pressure isobaric combustion, and pre-chamber combustion concepts. Since 2023, FUELCOM has been undertaking a new project (FUELCOM4) to advance the knowledge of $H_2$ combustion to achieve stable and efficient operation on heavy-duty engines.

The FUELCOM4 $H_2$ICE research framework is primarily composed of four workstreams interacting efficiently to achieve the ultimate targets of the project, including the research on $H_2$ injection and engine combustion, diluted combustion methods (exhaust gas recirculation and water injection), novel ignition concepts (plasma and pre-chamber combustion), $NO_x$ reduction with catalyst, and lubricant oil combustion. In the current paper, we present an overview of the on-going efforts in investigating the characterization of $H_2$ injection and combustion processes. The main research objectives include:

- Investigation of the effects of ambient conditions (injection and ambient pressures) on the $H_2$ jet development in a constant volume chamber (CVC).
- Development of the computational models for the simulation of $H_2$ injection utilizing hollow-cone and solid-cone injectors.
- Examination of the impact of overall lambda ($\lambda$) and spark timing on the combustion characteristics of $H_2$ on both the metal and optical engines.
- Evaluation of the effects of different chemical kinetics and combustion models on the prediction of $H_2$ engine combustion.

The paper is structured into four main sections. First, the experimental work on $H_2$ injection in the constant volume chamber (CVC) is reported to show the methodology and the main findings. Second, the CFD simulation work for $H_2$ injection is presented to show the modeling setup and validation, followed by an overview of the key understanding related to the mixture formation. Third, the metal and optical engine combustion experiments with both the DI and PFI configurations are reported. Key combustion characteristics of $H_2$ under various $\lambda$ conditions are analyzed and discussed. In the last section, the ongoing studies in assessing the combustion models for $H_2$ engine combustion simulations are briefly discussed.

## 2 Hydrogen injection experiments

### 2.1 Experimental setups

#### *2.1.1 High-speed Z-type schlieren setup*

A high-speed z-type Schlieren imaging method was utilized to visualize the $H_2$ jets in a CVC. The schlieren method operates on the principle that variations in the refractive index of a gas lead to optical inhomogeneity [1]. In the context of jet and flow studies, the density gradient within the flow field is translated into a change in relative light intensity within a plane. By employing high-speed photography, it becomes possible to capture and record the morphology of the jet, as well as its time-resolved evolution. Fig. 1 illustrates the experimental setup schematically. A high-power LED, driven by Thorlabs DC2200 High-Power controller, was used to generate a monochromatic red-light beam with a wavelength of 625 nm. The diverging light beam passed through a 1 mm aperture and was subsequently collimated using an 8-inch diameter f/5 parabolic mirror #1. It was then directed through a constant volume chamber (CVC) to illuminate the $H_2$ jets. Following that, the collimated light was once again focused using parabolic mirror #2. At the focal plane, a knife edge was positioned to partially block the refracted light beams before reaching a focusing lens with a focal length of 400 mm. The transmitted beam was subsequently captured by a high-speed CMOS camera (Photron, FASTCAM SA-X2) with a repetition rate of 100,000 frames per second (100 kHz) and an exposure time of 8.38 μs. The resulting image resolution was 384×264 pixels, providing a spatiotemporal resolution of approximately 0.1087 mm/pixel.

A cube-shaped CVC with an internal volume of around 0.12 L was employed to provide ambient pressure. The observation window of the CVC was made of quartz optical glass, with a visual range diameter of 25 mm and a thickness of 22 mm. The ambient gas used in this experiment was nitrogen, and the temperature of the surrounding environment was maintained at 20 °C. The single-hole high-pressure injector used in this study was obtained by modifying a commercial automotive Bosch HDEV5 GDI solenoid injector. This idea was inspired by the approach of Yip et al. [2], nevertheless, a different modification method was adopted. The original HDEV5 GDI injector features 6 identical holes with a diameter of approximately 0.16 mm and cannot provide a sufficient $H_2$ flow rate for practical engine applications. Therefore, our solution is to increase the flow area of the orifice in the nozzle tip. The solid part between the 6 holes was precisely machined by CNC to form a single coaxial hole with a diameter of 1.2 mm. A polytetrafluoroethylene (PTFE) nozzle gap was placed between the injector tip and cap attachment to minimize the effective sac volume and ensure a tight seal. In addition, the orifice geometry of the obtained single-hole injector can be adaptively customized with PTFE. In this study, the customized PTFE nozzle diameters and lengths are $d$ = 1.0 mm and $L$ = 2.8 mm, respectively. The injector was controlled and triggered through NI DIDS 2003 (National Instruments Direct Injector Driver System). The camera triggering was synchronized with the fuel injection through a digital pulse generator (Stanford research systems DG535).

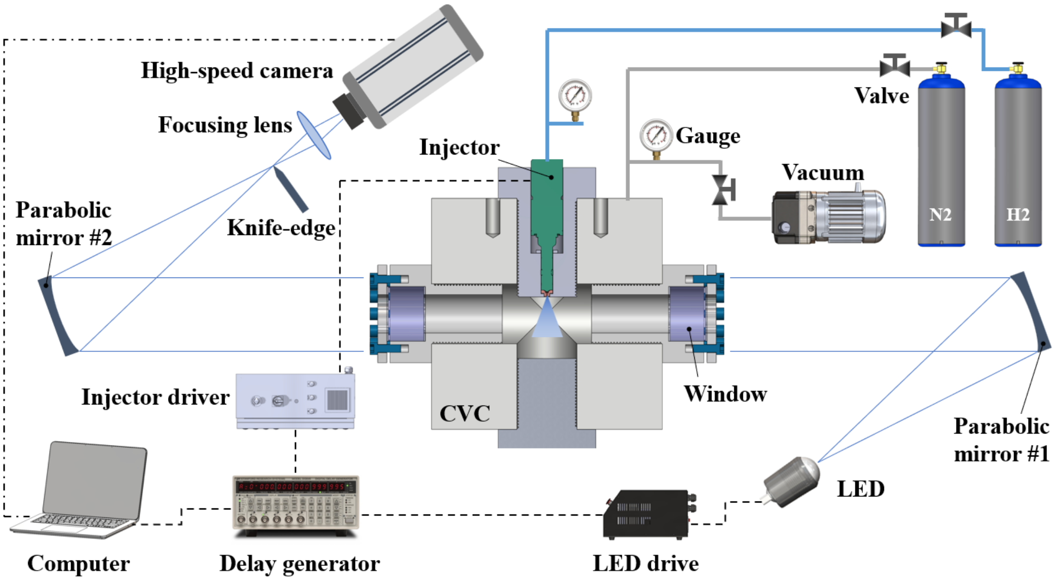

**Fig. 1.** Schematic diagram of high-speed schlieren setup.

### *2.1.2 Laser-induced high-speed Raman imaging setup*

The same CVC and injector setup as described in 2.1.1 was adopted, except the laser inlet window was changed to a sapphire one with a much thinner thickness. The schematic of the optical setup is illustrated in Fig. 2. This section first describes the 1-D Raman setup and then the modifications needed to convert it to 2-D Raman. A pulse-burst Nd:YAG laser (Spectral Energies, QuasiModo 1200) provides a train of frequency doubled 532-nm pulses at a repetition rate of 50 kHz during a 5 ms burst window (~ 250 pulses in total). The pulse duration and energy were set to 100 ns and ~ 13 mJ/pulse to avoid optical breakdown at elevated ambient pressures. A zero-order half-wave plate ensured the vertical polarization of the incident beam. A $f$ = 150 mm AR-coated convex lens focused the beam to a spot size ~ 120 μm (HMFW) at $z$ = 2.6 mm below the injector cap.

An image relay system, formed by a 1-inch $f$ = 30 mm achromatic doublet and a 2-inch $f$ = 100 mm achromat, collected the Raman scattering signal, and reimaged it at the first focal plane, outside the chamber. To maximize the collection efficiency, the first achromat was placed inside the chamber. A wire grid polarizer halved any unpolarized signal, such as fluorescence from the windows while keeping the highly polarized Raman signal unchanged. After recollimation of the signal, a wavelength separation unit suppressed surface and elastic scattering (Rayleigh, Mie) through an OD6 notch filter at 532 nm, then separated the vibrational $N_2$ Raman bands (597.5 ~ 612.5 nm) from the $H_2$ (673.5 ~ 686.5 nm) through a dichroic beamsplitter and two bandpass filters (Semrok, FF01-605/15 for $N_2$ and Semrok, FF01-680/13 for $H_2$). Two identical $f$ = 50 mm camera lenses (Nikon, Nikkor 50 mm f/1.2) focused the two Raman signals on two back-illuminated EMCCD cameras operated in low-noise CCD mode (Princeton Instrument, ProEM HS: 1024BX3). The two cameras are operated in subframe burst gating mode (Spectra Kinetic) [3] to enable a high sampling rate while maintaining the low noise of scientific CCD cameras. By setting the frame exposure time of 300 ns, the recording of 1037 subframes per readout cycle at 50 kHz was achieved. A slit with an opening of 625 μm was located at the first focal plane outside the chamber to block the whole sensor except ~ 12 pixels rows. A 3×1 software binning along the horizontal (laser propagation) direction was applied in postprocessing to improve SNR, resulting in a pixel density of ~ 22 pixels/mm. A delay generator (BNC, model 577) provides synchronization between the cameras and the laser.

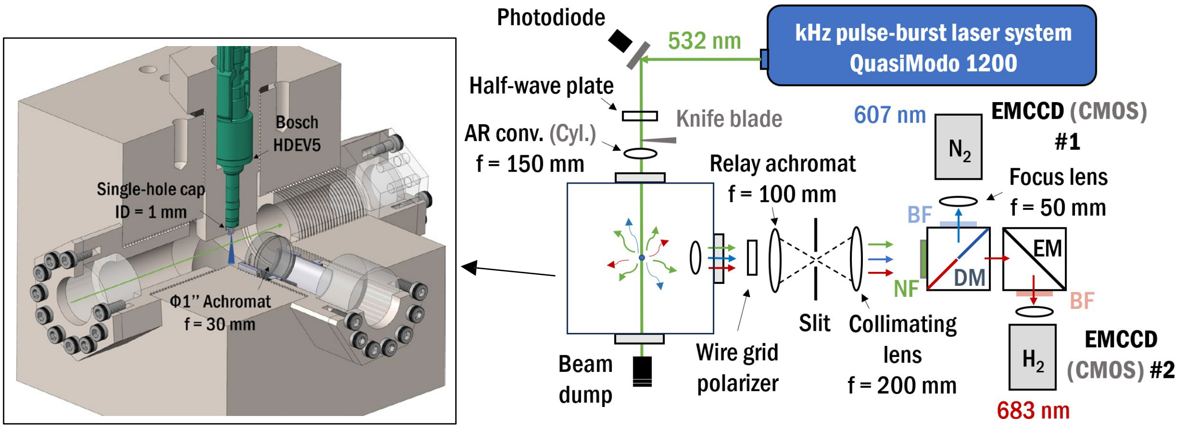

**Fig. 2.** The schematic of the optical setup for high-speed Raman scattering measurements. Different components applied in 2-D are marked in grey.

Several modifications were made to convert the system for 2-D imaging. The pulse-burst laser was operated at 10 kHz, with pulse duration set to 200 ns, resulting in ~ 150 mJ/pulse. An *f* = 150 mm AR-coated cylindrical lens, replaced the spherical lens to form a 7-mm tall, 120-μm thick laser sheet in the center of the chamber. A knife edge placed before the cylindrical lens blocked the top portion of the beam, reducing the laser sheet size to 4.4 mm to avoid ablation of the injector cap while maintaining high leaser energy in its proximity. The upper edge of the laser sheet was ~ 0.5 mm below the injector cap. The slit was removed for 2-D imaging and the Raman signals of $H_2$ and $N_2$ are collected separately by two high-speed CMOS cameras (Photron, FASTCAM SA-X2). The exposure time of each frame was 5 μs and in total 100 subframes were recorded per readout cycle. Software binning of 2×2 was done in postprocessing and resulted in a pixel density of ~ 21 pixels/mm. The spatial resolutions of both $N_2$ and $H_2$ channels were tested with the standard 1951 USAF target (Thorlabs, R1DS1N) and yielded to ~ 90 μm after the software binning.

## 2.2 Hydrogen jet characterization in the CVC

### 2.2.1 Hydrogen jet structure and macroscopic characteristics

Fig. 3 illustrates the morphological changes of $H_2$ jets over consecutive time intervals following the start of injection (ASOI) at various pressure ratios ($R_p$). The pressure ratio is defined as $R_p = P_{inj} / P_b$, where $P_{inj}$ represents the upstream injection pressure and $P_b$ denotes the ambient pressure, which remains constant at 10 bar. The detected edges of the jets are depicted as green lines to provide a visual representation of the jet boundaries. During the early stages of injection, the jet shape is unstable and undergoes constant fluctuations. As the injection time increases, the jet progressively moves downwards and expands horizontally on both sides. Beyond an injection time of 0.4 ms, a cone-shaped structure near the nozzle becomes increasingly prominent. As the jet develops into the far-field, the jet head takes on an irregular spherical configuration. Furthermore, as the pressure ratio increases, the jet evolves at a faster rate and reaches the bottom of the window in less time. An interesting observation is the presence of shadows alongside the $H_2$ jet mainstream. These shadows result from the formation of shock waves caused by the high-speed jet. These shock waves create sharp density gradients in the flow field, which can be captured by a camera. The results regarding the jet structure indicate that, at the same ambient pressure, the shadows created by shock waves become more pronounced with an increasing injection-ambient pressure ratio. Additionally, in the later stages of jet development, all jets exhibit a deviation from the nozzle axis due to the buoyancy effect.

Fig. 4 (a) illustrates the influence of pressure ratio on jet penetration by varying the injection pressure while maintaining a constant ambient pressure of 10 bar. It is important to note that the visible scope of the window imposes a limitation on the maximum jet penetration obtainable from the post-processing of jet images, which does not exceed 25 mm. By examining the plots of jet penetration versus time, it is evident that an increase in pressure ratio leads to greater jet penetration. This finding aligns with the results of previous studies [4-6]. Furthermore, for $R_p = 8$, $P_{inj} = 80$ bar, as well as $R_p = 10$, $P_{inj} = 100$ bar, the difference in jet penetration at the same ASOI time becomes negligible. This suggests that there is a limit to further increasing jet penetration by raising the injection pressure when the ambient pressure is fixed. Fig. 4(b) depicts the jet penetration under different ambient pressures while keeping the injection pressure constant. As expected, a larger $R_p$ corresponds to higher jet penetration at the same ASOI time. This can be attributed to the fact that increasing $R_p$ leads to an elevation in injection pressure or a decrease in ambient pressure. Consequently, the jet attains a greater mass flow rate or encounters less resistance from the ambient environment, both of which facilitate its forward propagation.

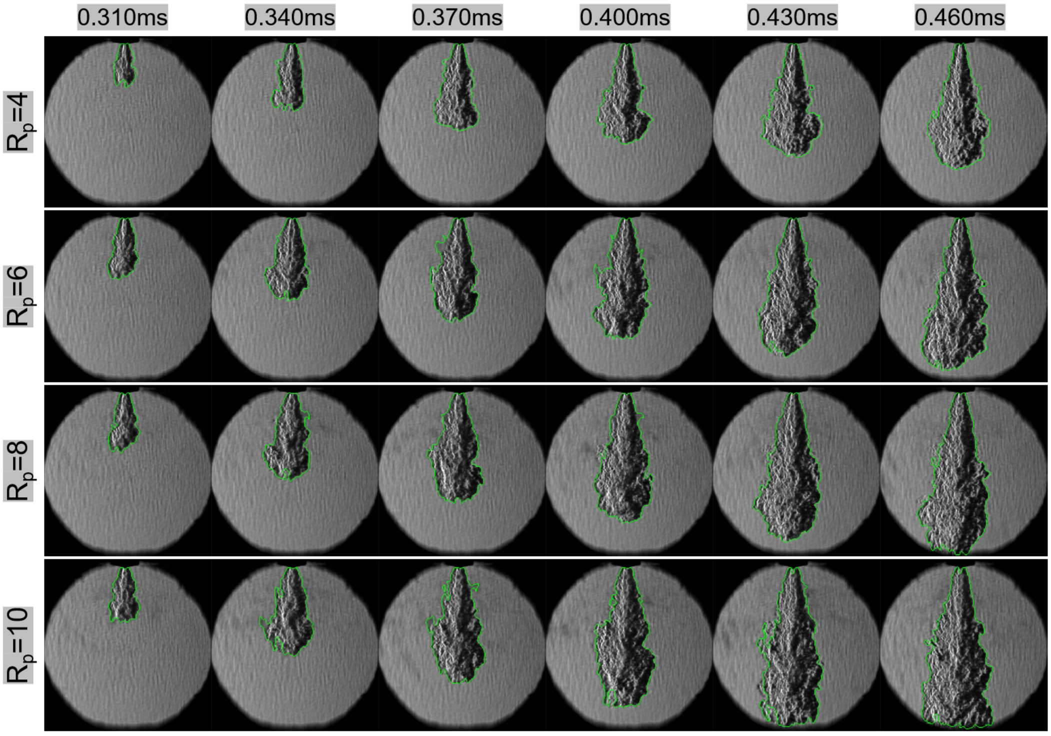

**Fig. 3.** Evolution of $H_2$ jets for $R_p$ ranges from 4 to 10. $P_{amb}$ = 10 bar.

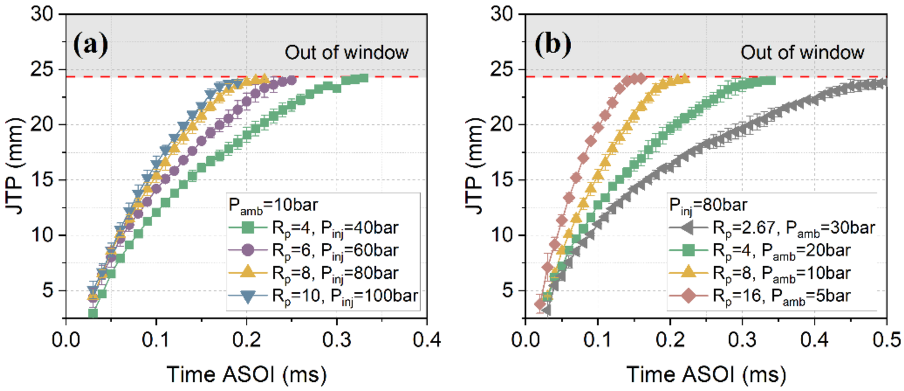

**Fig. 4.** $H_2$ jet penetration for various $R_p$: (a) different $P_{inj}$ under $P_{amb}$ = 10 bar, (b) different $P_{amb}$ under $P_{inj}$ = 80 bar.

Fig. 5 presents the $H_2$ jet projection area as it relates to the pressure ratio, considering variations in both injection pressure and ambient pressure. When the ambient pressure is held at 10 bar, a larger pressure ratio corresponds to a larger jet projection area. This observation can be attributed to the influence of $R_p$ on jet penetration. Specifically, when the injection time remains constant, a larger jet penetration indicates an enhanced spatial diffusion capability of the jet. Similarly, when the ambient pressure is changed while maintaining a fixed injection pressure of 80 bar, the same trend is observed, as depicted in Fig. 5(b). In this case, altering the ambient pressure also affects the jet projection area, with higher ambient pressures resulting in smaller projection areas. In summary, both the pressure ratio and ambient pressure play significant roles in determining the jet projection area. Higher $R_p$ values and lower ambient pressures contribute to larger jet projection areas, indicating improved spatial diffusion capabilities of the jet.

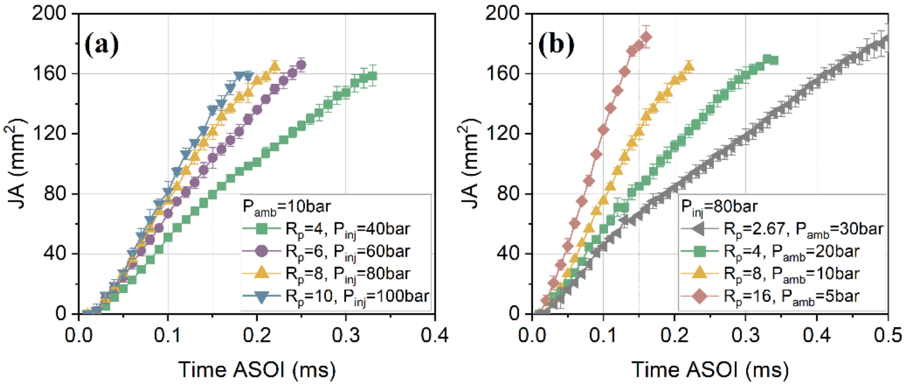

**Fig. 5.** $H_2$ jet area for various $R_p$: (a) different $P_{inj}$ under $P_{amb}$ = 10 bar, (b) different $P_{amb}$ under $P_{inj}$ = 80 bar.

Previous studies [4, 5] have predominantly employed a normalized parameter, namely the pressure ratio, to quantify the characteristics of $H_2$ jets. In our study, we achieved equivalent injection-ambient pressure ratios by manipulating various injection pressures and ambient pressures. To facilitate a straightforward comparison, we selected three sets of pressure ratios ($R_p$ = 2, 4, 8) derived from different combinations of injection pressures and ambient pressures. The jet penetration and jet area were chosen as the parameters for comparison, as depicted in Fig. 6. The data presented in the plot demonstrates that, for a given pressure ratio $R_p$, the jet penetration and jet area obtained from different injection pressures and ambient pressures exhibit similar trends. However, certain minor differences persist, particularly in terms of the jet area.

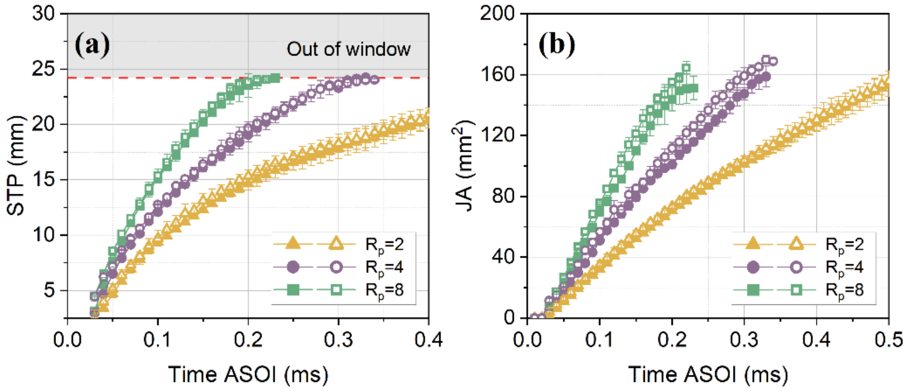

**Fig. 6.** Effects of $R_p$ on $H_2$ jet characteristics: (a) jet penetration, (b) jet area.

When a high-pressure gas is discharged through a nozzle into a low-pressure ambient environment, the gas jet undergoes distinct flow states and transitions. By defining the pressure ratio as the ratio between the nozzle inlet pressure and the ambient pressure, we can identify three primary jet flow states and two transition states. Within a pressure ratio range of 1 to 1.89, a subsonic jet is generated. As the pressure ratio increases to the range of 1.95 to 3.85, the gas jet becomes moderately under-expanded, characterized by the presence of clearly observable shock diamonds or shock units. When the pressure ratio exceeds 4.05, the jet enters a highly under-expanded state. To describe the shock waves formed by these highly under-expanded $H_2$ jets, we employ three characteristic parameters: Mach disk height, Mach disk width, and the triple point angle. Mach disk height refers to the distance between the nozzle exit and the Mach disk. Mach disk width represents the dimensions of the Mach disk. The triple point angle is defined as the angle between the tangent of the expansion wave and the nozzle axis [7]. The variations of Mach disk height are used to calculate the pressure information in the gas nozzle including orifice inlet pressure and orifice outlet pressure by using an empirical equation, as expressed by [8]

$$\frac{!}{"} = 0.67\&\overline{\frac{\#_!}{\#_"}} \qquad (1)$$

Where *H* is the Mach disk height and *d* is the nozzle orifice diameter. $P_i$ is the upstream inlet pressure of the single-hole cap.

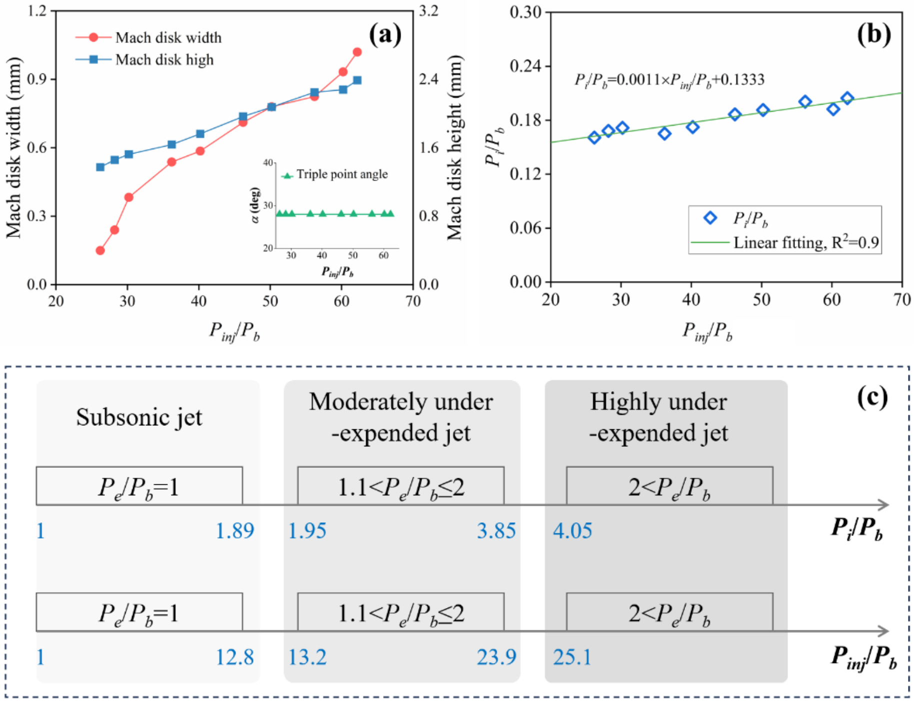

**Fig. 7.** Effects of $R_p$ on $H_2$ jet characteristics.

By employing image post-processing techniques, we can obtain crucial parameters such as Mach disk height, Mach disk width, and the triple point angle, all of which vary with the pressure ratio defined by the injection pressure and ambient pressure, as shown in Fig. 7(a). Furthermore, utilizing the above empirical equation that establishes a relationship between Mach disk height, nozzle diameter, and the pressure ratio between the nozzle inlet and ambient, we can calculate the nozzle inlet pressure and the pressure ratio denoted as $P_i$ divided by $P_b$. We found this pressure ratio shows a linear dependence on the pressure ratio defined by injection pressure divided by ambient pressure, as shown in Fig. 7(b). It can be concluded there is an approximately 80% pressure loss from the upstream supply injection pressure to the nozzle inlet. We hypothesize that this outcome may be attributed to the formation of a Laval structure between the injector needle valve and the seat. As the gas passes through the Laval nozzle, there is a continuous decrease in pressure coupled with an increase in gas flow velocity. Based on our observations, we can establish new pressure thresholds to identify different jet states according to the injection-ambient pressure ratio, as depicted in Fig. 7(c). Specifically, if this ratio falls between 1 and 12.8, the jet is categorized as subsonic. When the pressure ratio lies between 13.2 and 23.9, the jet is considered moderately under-expanded. If we further increase the pressure ratio beyond 25.1, the jet becomes highly under-expanded. Additionally, we have observed that the triple point angle remains nearly constant across different pressure ratios.

### *2.2.2 Hydrogen mixing field quantification using high-Speed 1-D and 2-D Raman imaging*

The high-speed 1-D Raman scattering technique is here applied to investigate the effect of ambient pressure on the $H_2$ mole fraction ($x_{H2}$), 2.6 mm below the single-hole cap. The injection pressure $P_{inj}$ = 60 bar is selected, and the injection duration is set to 2 ms. Results for three ambient pressures, $P_{amb}$ = 25, 12.5, and 1 bar are here discussed. For each injection condition, measurements are repeated 10 times. Between measurements, the chamber is purged, vacuumed, and then filled with $N_2$ up to the desired $P_{amb}$. This lengthy procedure is necessary to prevent the accumulation of $H_2$ in the chamber between consecutive injections. Preliminary measurements show that due to the small volume of the chamber and the high sensitivity of 1-D Raman, three injections are sufficient to raise the residual $H_2$ mole fraction level to 0.5%, 1%, and 13%, for $P_{amb}$ = 25, 12.5, and 1 bar, respectively.

By carefully timing the injection of 2 ms within the 5 ms laser burst using a separate delay generator, instantaneous $x_{H2}$ profiles of transient $H_2$ jets are measured with high temporal and spatial resolutions. Fig. 8(a) shows the single-shot 1-D $x_{H2}$ profiles of injections in $P_{amb}$ = 25 bar at selected ASOIs. The first profile, (ASOI of 0.33 ms) shows a narrow $H_2$ jet (FWHM < 1 mm) sided by two peaks attributed to the leading vortices of the starting jet. $N_2$ is entrained rapidly, and the peak $H_2$ mole fraction is ~ 0.9 in the central jet and ~ 0.4 on the side peaks. At ASOI of 0.35 ms, the $H_2$ jet profile becomes broader, ~ 2 mm in FWHM, with a nearly flat region with $x_{H2}$ ~ 0.9 followed by a rapid decrease as it approaches the shear layer. The leading vortices have moved out of the probe region and are no longer visible. The jet quickly reaches a quasi-steady state, with no large variations in the overall profile, but the side peaks oscillate in radial positions as the turbulent jet entrains the surrounding $N_2$. Profiles at $P_{amb} = 12.5$ bar are similar, and therefore not reported here.

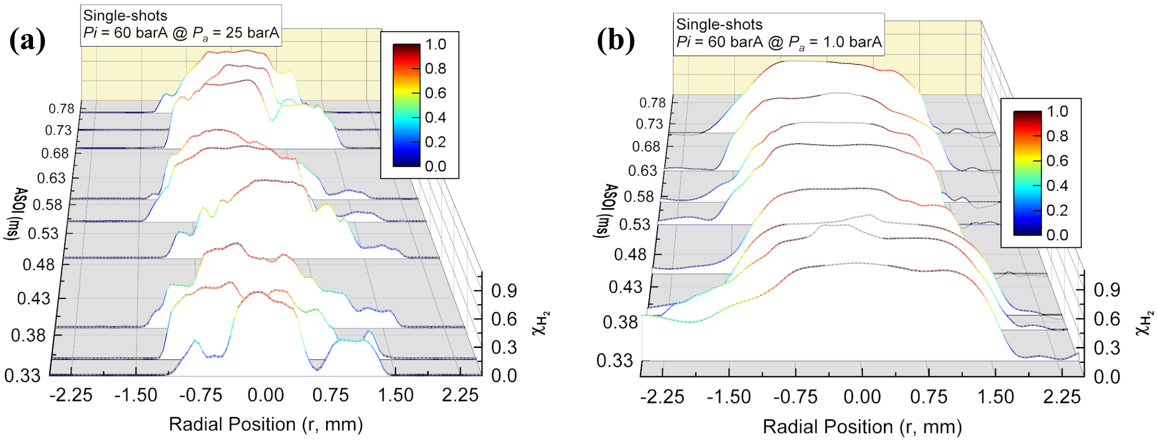

**Fig. 8.** The development of 1-D single-shot $x_{H2}$ of (a) $P_{inj} = 60$ bar and $P_{amb} = 25$ bar, and (b) $P_{inj} = 60$ bar and $P_{amb} = 1$ bar at selected ASOIs.

Fig. 8(b) shows the $x_{H2}$ profiles measured for $P_a = 1$ bar. The large pressure ratio ($R_p = 60$) leads to a highly under-expanded jet, and consequently dramatic difference in the mole fraction profiles. At ASOI of 0.33 ms, the jet features a wide core (~ 2.5 mm) with no $N_2$ entrainment ($x_{H2} = 1$) and a highly asymmetric wing with significant mixing. The high-mixing region is associated with the starting of the jet and disappears by ASOI of 0.39 ms. A quasi-steady state is reached quickly, characterized by a broad region (~ 2 mm) of pure $H_2$ ($x_{H2} = 1$), followed by a sharp transition to pure $N_2$ ($x_{H2} = 0$). Remarkably, Fig. 9 shows a semi-quantitative plot of the measured $H_2$ number density normalized by the one of pure $H_2$ at ambient temperature and pressure. Single-shot number density measurements have an additional source of error in the laser energy fluctuations. Measurements in pure $H_2$ at 1 bar show an average error of ~ 13% in the ROI over the laser pulses. Despite the uniform $x_{H2}$ as measured in the core region, the measurements show a wide variation in $H_2$ number densities due to the shock structure associated with highly under-expanded jets. These shock structures prevent the mixing ($x_{H2} = 1$) in a relatively wide radial range. High-speed measurements of the relative number density, allow for monitoring the temporal and spatial evolution of the shock structure, and the formation of the shock cell. The arrows in Fig. 9 describe the evolution of the location of the shock waves, as they first move outward, and then inward until reaching a relatively steady state. An embedded picture of Schlieren imaging in Fig. 9 conveys an overview of the shock cell using the same cap and at similar $P_{inj}$ and $P_{amb}$. The measurements show that high-speed Raman scattering can provide quantitative mole fractions in the presence of shock waves and temporally resolves the shock cell evolution. Strategies to include temperature measurements by probing additional $H_2$ transition will be the object of future studies.

This section discusses the means, standard deviations, and coefficient of variance of the collected $x_{H2}$ profiles. Statistics are computed based on 10 individual measurements, for each time of ASOI. A quantitative comparison of the 1-D $x_{H2}$ profiles at $z = 2.61$ mm for all three injection conditions is summarized in Fig. 10. Results are drawn for the starting of the jets at ASOI 0.33 ms (Fig. 10(a) and (b)), and at a time during the quasi-steady period near the end of the injection of ASOI 1.91 ms (Fig. 10(c) and (d)). The left column presents the single-shot measurements of $x_{H2}$, and the right column gives the corresponding statistics over repeated injections. By comparing the statistical results in Fig. 10(b) and (d), a more axisymmetric shape in the burst-averaged $x_{H2}$ profiles is easily noticed for all the cases in the quasi-steady period. A comparable mixing level is achieved at the centerline for both $P_{amb} = 25$ and 12.5 bar with the averaged $x_{H2} \sim 0.9$, while nearly pure $H_2$ of $x_{H2} \sim 1$ is measured for the $P_{amb} = 1$ bar as a result of the shock cell. In the quasi-steady state at 1.91 ms, much smaller standard deviations are measured near the core of the jets, in contrast to the outer radial positions of the mixing layer, where much higher turbulent intensities should be expected. The standard deviation based on 10 bursts, measured on the centerline during the steady state is ~ 0.01, 0.05, and 0.02 for $P_{amb} = 25$, 12.5, and 1 bar, respectively.

The possibilities and limitations of high-speed 2-D Raman imaging for $H_2$ jet characterization are also investigated. Due to lower SNR, as a result of lower laser energy and the use of CMOS cameras, measurements are limited to a high chamber pressure of $P_{amb} = 25$ bar. Results for $P_{inj} = 60$ bar are presented here. The measurements are repeated 30 times. Results are here limited to mole fractions, removing the need to measure the spatial and temporal energy profile, a major advantage of Raman scattering compared to Rayleigh or fuel-tracer PLIF as discussed in [9]. The 2-D WATR denoising is performed and the effective Raman cross-section ratio of $\sigma_{!\ \$}/\sigma_{\%\$} \approx 2.066$, obtained from the 1-D line measurement is used for the 2-D $x_{H2}$ calculations. The development of the transient $H_2$ jet of $P_{inj}$ = 60 bar and $P_{amb}$ = 25 bar is depicted in Fig. 11 with a spatial resolution of ~ 90 µm, capable of resolving some of the turbulent structures in the shear layer. At ASOI 0.31 ms, the pair of leading vortices only inferred in the 1-D measurements appear clearly in 2-D. The jet rapidly develops into a quasi-steady turbulent jet as previously observed in the 1-D Raman measurement in Fig. 8(a).

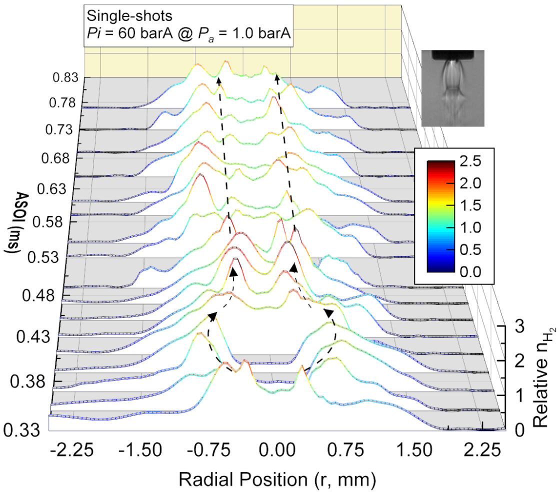

**Fig. 9.** The development of 1-D single-shot relative number density of $H_2$ of $P_{inj}$ = 60 bar and $P_{amb}$ = 1 bar at selected ASOIs. The formation process of the stabilized shock structures is indicated by the arrows.

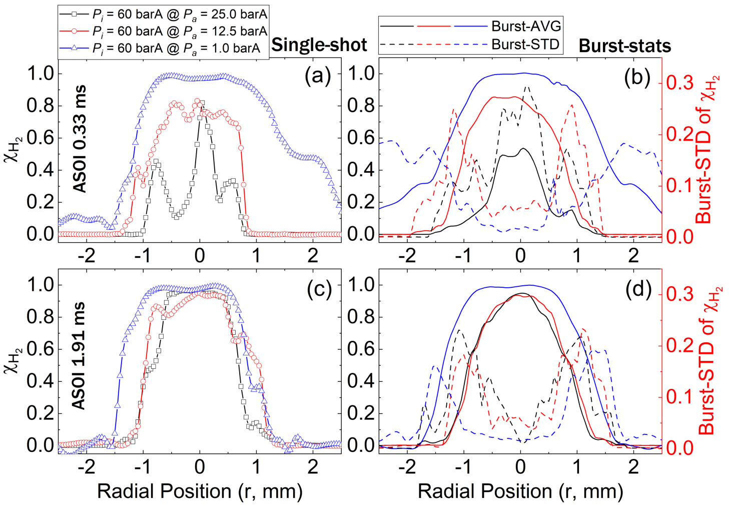

**Fig. 10.** The quantitative comparison of 1-D $x_{H2}$ at z = 2.61 mm of $P_{inj}$ = 60 bar and $P_{amb}$ = 25 (black), 12.5 (red), and 1 (blue) bar, (a) the single-shots and (b) burst-statistics at ASOI 0.33 ms; (c) the single-shots and (d) burst-statistics at ASOI 1.91 ms.

Fig. 12 extends to 2-D imaging the analysis of mean and standard deviations shown for the 1-D profiles in Fig. 10. Average of 30 images at 0.31 ms ASOI in Fig. 12(a), obtained for $P_{inj}$ = 60 bar shows clearly the leading vortices surrounding the central jet indicating good repeatability of the experiment. Turbulent mixing and the repeatability of the experiment are responsible for the large standard deviations at the edge of the $H_2$ jet, and a smoother interface in the mean, compared to the single-shot image in Fig. 11. Fig. 12(c) and (d) show the average and standard deviation at ASOI of 1.91 ms based on 30 bursts. Fig. 12(e) and (f) compute the average and the standard deviation, based on 14 acquisitions during the steady-state period of the jet within a single injection. The two average pictures are qualitatively similar, with minor differences in the width of the jet and centerline mole fraction. Centerline standard deviations based on repeated measurements at ASOI of 1.91 ms in Fig. 12(d) are significantly larger than those based on multiple frames from a single injection (~ 0.05 to 0.1) in Fig. 12(f). The increased variability over multiple measurements is attributed to the repeatability of the injections and small fluctuations in the background and flare. Instrument precision contributes to the standard deviation along the centerline in Fig. 12(f). As a comparison measurement in pure $H_2$ over the same time window (ASOI 0.61 to 1.91 ms) show a standard deviation of 0.04 to 0.06 along *r* = 0 in a single burst. The regions of high standard deviation on the side of the jet, indicative of the turbulent mixing layer, are thin near the nozzle and then grow significantly between *z* = 3 and 4 mm.

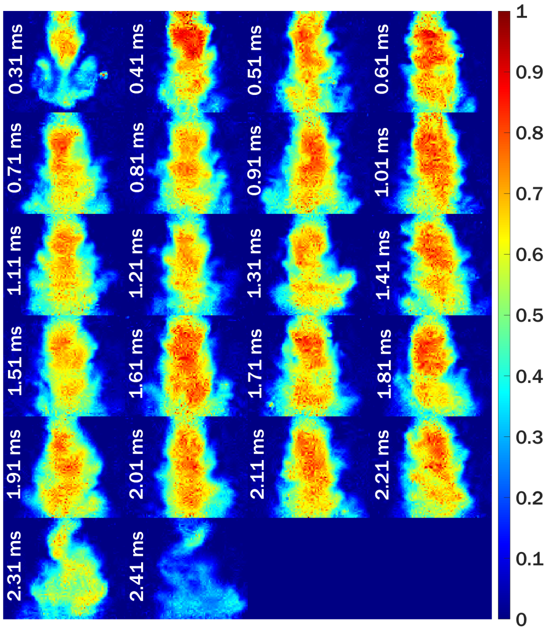

**Fig. 11.** The time-sequenced single-shot 2-D $x_{H2}$ of $P_{inj}$ = 60 bar and $P_{amb}$ = 25 bar, the time in ASOI of each frame is implanted in white. The ROI size of each frame is 3.88 (H)×4.76 (W) mm$^2$.

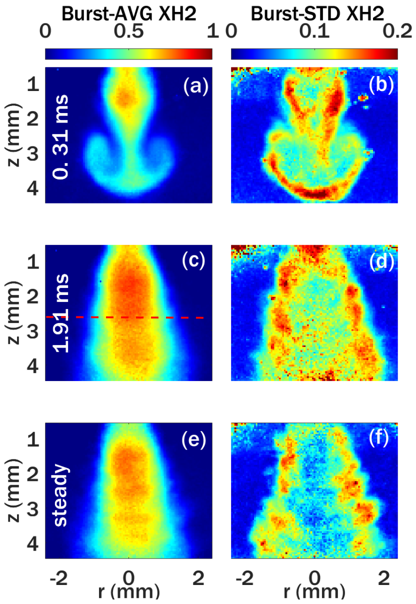

**Fig. 12.** The burst-statistics of 2-D $x_{H2}$ of $P_{inj}$ = 60 bar and $P_{amb}$ = 25 bar, (a) the burst-AVG and (b) burst-STD of $x_{H2}$ at ASOI 0.31 ms, (c) the burst-AVG and (d) burst-STD $x_{H2}$ at ASOI 1.91 ms, (e) the time-AVG and (f) time-STD $x_{H2}$ of #15 injection ASOI 0.61 to 1.91 ms.

To examine the accuracy of the 2-D imaging at 10 kHz, a 1-to-1 assessment at the same ASOI is conducted between the 1-D and 2-D burst-statistics of $P_{inj}$ = 60 bar and $P_{amb}$ = 25 bar at *z* = 2.61 mm. The relative location of the 1-D probe volume is indicated by the red dashed line in Fig. 12(c), and the comparison is demonstrated in Fig. 13.

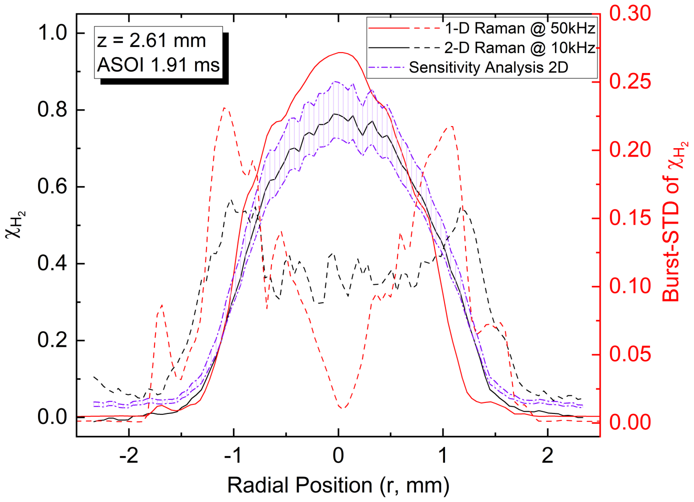

**Fig. 13.** The comparison of burst-statistics between 1-D (red) and 2-D (black) $x_{H2}$ of $P_{inj}$ = 60 bar and $P_{amb}$ = 25 bar at ASOI 1.91 ms and $z$ = 2.61 mm. Consequent variation by ± 2 counts/pixel in the flare of burst-averaged $x_{H2}$ of 2-D measurement is shown by the dash-dot line (purple).

It is found that a maximum deviation of ~ 15% in the burst-averaged results appears near the jet centerline, with the 1-D measurement rendering $x_{H2}$ ~ 0.94 while the 2-D measurement giving $x_{H2}$ ~ 0.79 at the same location. The standard deviation at $r = 0$ is ~ 0.01 for the 1-D measurements and ~ 0.10 for the 2-D. The observed difference is due to the low SNR of the 2-D measurements, and the increased relative importance of the flare noise. The peak signal in $N_2$ at $P_{amb}$ = 25 bar is only 30 counts/pixel in the current setup, and the flare signal is up to 10 counts/pixel, making the measurements very sensitive to small errors in accounting for this contribution. The dash-dot purple lines in Fig. 13 indicate that a ± 2 counts/pixel change in the flare, varies the burst-average $x_{H2}$ by about ± 10% in the vicinity of $r = 0$. The effect of the flare diminished significantly for $x_{H2}$ in the 0.1 to 0.5 range and becomes prominent again as $x_{H2}$ approaches 0. The results explain why a large discrepancy is observed near the centerline, but 1-D and 2-D results agree better for lower values of $x_{H2}$.

## 3 Hydrogen injection simulations

### 3.1 Computational setup

This research utilized CONVERGE, a computational fluid dynamics software, to run simulations aimed at solving fluid flow governed by conservation equations of mass, momentum, and energy. To tailor the study for engine simulation applications, the Reynolds-averaged Navier-Stokes (RANS) RNG $k$-$\varepsilon$ turbulence model [10] was employed. Thermodynamic and transport properties were derived from the $H_2/O_2$ kinetic mechanism developed by Burke [11].

Simplified geometries were constructed based on the modeled geometry used for model validation. These simplified geometries consisted of hollow-cone and solid single- and multi-cone injectors, designed for comparison under uniform conditions and to assess the influence of jet geometry on the mixing process. The external geometry and jet angle from the HDEV4 injector used for validation were retained in the new geometries. The simulation conditions are detailed in Fig. 14, and an example of this geometry and the mesh implemented in the CONVERGE code is depicted in Fig. 14.

The diagram depicts the computational domain's geometry near the injector tip within the cylindrical CVC, specifically for the case of the multi-hole injector with six nozzles. The mesh displayed consists of a structured base mesh size of 1 mm applied uniformly across the entire domain. To ensure precise flow resolution in confined regions like inside the injector nozzles, fixed embedding up to level 6 is employed. Furthermore, a level 3 adaptive mesh refinement (AMR) strategy is utilized to automatically refine the mesh based on a 0.01% $H_2$ mass fraction within the domain, resulting in a minimum mesh size of 15.625 μm. The variable mesh size, determined by local AMR, fixed embedding, and generated flow velocity, also regulates the time step, set variably to satisfy the unity CFL condition. In terms of boundary conditions, the upstream boundary within the injector is defined as an inflow of total pressure. The lateral and bottom walls of the chamber are treated as outflow boundaries with a constant pressure equal to ambient pressure. Additionally, all solid walls, including the injector, and the upper surface of the chamber adhere to the logarithmic law of the wall.

The figure illustrates the geometry of the computational domain near the injector tip within the cylindrical CVC, specifically for the case of the multi-hole injector with six nozzles. The mesh shown comprises a structured base mesh size of 1 mm that is consistently applied across the entire domain. To ensure accurate flow resolution in confined regions, such as inside the injector nozzles, fixed embedding up to level 6 is implemented. Furthermore, a level 3 adaptive mesh refinement (AMR) strategy is employed to automatically refine the mesh based on a 0.01% $H_2$ mass fraction within the domain. This refinement results in a minimum mesh size of 15.625 μm. The variable mesh size, determined by the local AMR, fixed embedding, and generated flow velocity, also controls the time step. It was set up as a variable to satisfy the unity CFL condition, as shown in Table 1. In terms of boundary conditions, the upstream boundary within the injector is defined as an inflow total pressure, as specified in Table 1. The lateral and bottom walls of the chamber are treated as outflow boundaries with a constant pressure equal to the ambient pressure. Additionally, all solid walls, including the injector, and the upper surface of the chamber follow the logarithmic law of the wall.

**Table 1.** Simulation conditions [12].

| **Injector type** | **Hollow-cone** | **Solid-cone** |
|---|---|---|
| Jet angle | 85° | |
| Needle opening lift | 85 μm | N/A |
| Nozzle diameter | N/A | 1.098 mm single hole<br>0.511 mm four holes<br>0.418 mm six holes<br>0.323 mm ten holes |
| Injection pressure | 20 $bar_{abs}$ | |
| Ambient pressure | 1 $bar_{abs}$ | |
| Injection and ambient temperature | 300 K | |
| Injection profile | Step profile | |
| Injection duration | 2 ms | |
| Injected mass | 1.803 mg | |
| Ambient gas | $N_2$ | |
| Simulation duration | 3 ms | |
| CFL number | <1.0 | |

To simplify the model and accommodate the rapid response and quick opening characteristics of piezoelectric injectors, the movement of the injector needle was disregarded. This omission eliminated transient effects across various injector setups. Consequently, flow control was artificially managed by allowing or restricting flow from the internal nozzle region to the chamber, resulting in a square profile for the mass flow rate across all configurations. The injector pressure remained constant at 20 bar absolute for all cases, with both injected and ambient gas temperatures set at 300 K to induce a shocked sonic flow. To ensure uniformity in mass flow rate across all configurations, nozzle diameters were adjusted, as detailed in the table. For each solid-cone configuration, the nozzle diameter was determined by simulating the initial stages of injection until reaching a steady state. This process enabled the determination of the mass flow rate at the specified nozzle diameter, which was then iteratively adjusted to match the mass flow rate of the reference hollow-cone geometry. These specific values for needle lift and injection pressure were chosen to achieve an $H_2$ injection mass flow rate suitable and realistic for light-duty engine applications.

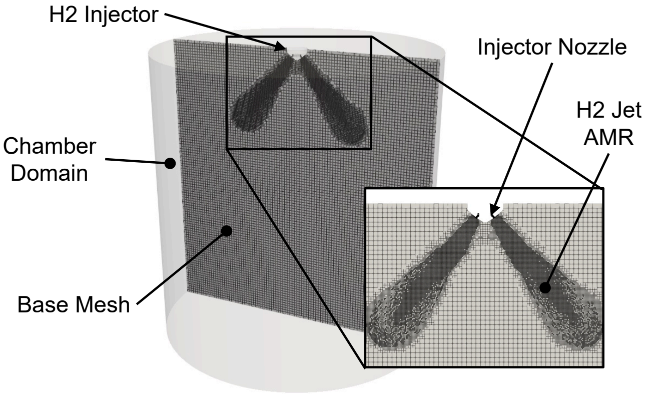

**Fig. 14.** Injector tip geometry and mesh [12].

## 3.2 Validations against the measured data for the hollow-cone injector

Fig. 15 shows the snapshots of experiments, that were conducted in KAUST laboratory, and simulations at 0.4 ms with various injection pressures. The injection pressure has a proportional effect on jet penetration length and area. Note that the postprocessing of the experiment and simulation images were done differently, meaning that the simulation images represent the plane schlieren while the experiment images express the Z-type schlieren. A reasonable match between the experiments and simulations has been achieved in terms of jet behavior. At 0.4 ms, the jet has already reached the visual domain limit for both high injection pressures. The experimental snapshots domain is limited to achieve a higher resolution. Fig. 16 shows a good match in jet penetration length of the simulations and KAUST experiments at distinct injection pressures.

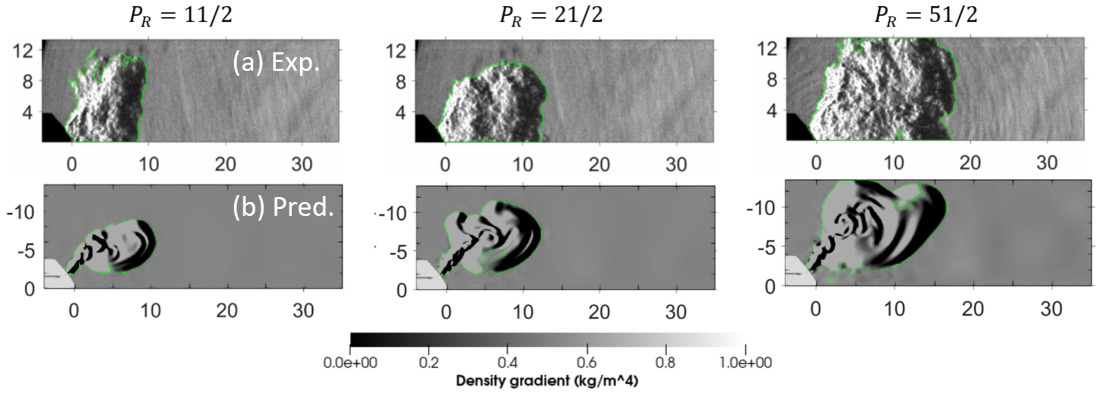

**Fig. 15.** Qualitative comparison between experimental and numerical results at 0.4 ms and different injection pressure [13].

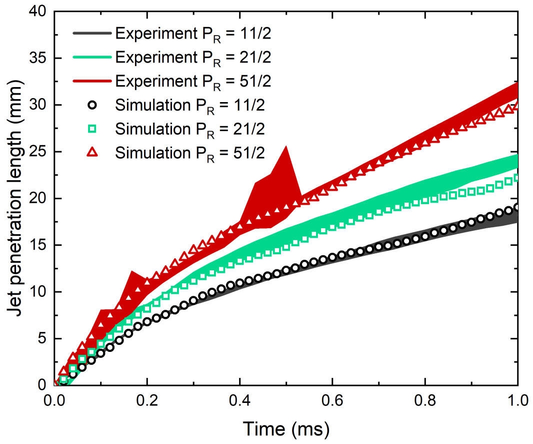

**Fig. 16.** Prediction of jet penetration length at various injection pressures [13].

## 3.3 Comparison of hollow- and solid-cone injectors

Fig. 17 shows the maximum penetration length over time for all injector configurations. It's clear from the figure that solid-cone configurations achieve a longer maximum jet penetration compared to the hollow-cone case. This discrepancy arises because, in the hollow-cone configuration, $H_2$ disperses evenly in all directions during injection, whereas in solid-cone configurations, $H_2$ gas is concentrated and directed in a specific orientation.

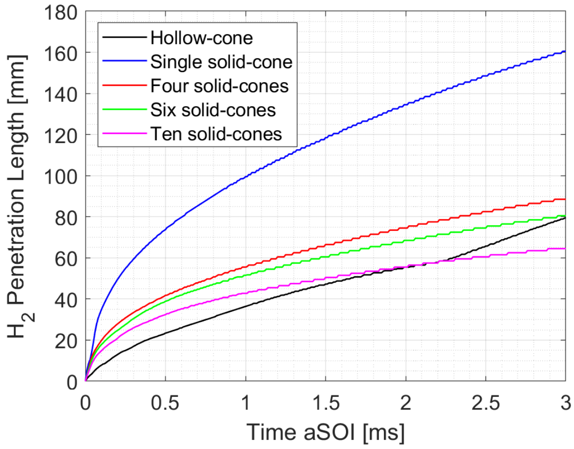

**Fig. 17.** Maximum penetration length for different inj. configurations [12].

In the case of the single solid-cone jet, its penetration nearly doubles that of the other solid-cone configurations. This discrepancy arises because the single jet aligns directly along the injector axis, whereas the other configurations are angled at 85°, as shown in Table 1. This angular orientation, as previously mentioned, was derived from the reference hollow-cone injector and applied consistently across all simplified geometries. As for the penetration length in multi-hole injectors, it diminishes with an increase in the number of holes. This reduction is attributed to the lower inertia of the compressible flow, where the same mass flow at identical pressure is distributed among more holes. Consequently, this division leads to a decrease in velocity and an increase in the shear interaction of the smaller jets with the surrounding gas in the chamber.

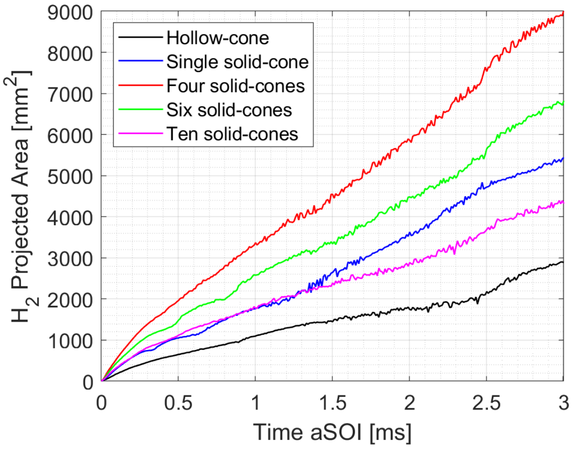

**Fig. 18.** Projected jet area for different inj. configurations [12].

In Fig. 18, the $H_2$ projected area of the jet is depicted, offering a general insight into mixing dynamics and illustrating how the gas diffuses within the chamber. This measure is derived by calculating the projected area onto a plane along the line of sight within the isocontour of 0.1% $H_2$ mass fraction. Fig. 18 reveals that the hollow-cone configuration displays the smallest projected area. This outcome can be attributed to the uniform distribution of flow around the injector, resulting in the formation of a compact yet robust toroidal recirculation region with high vorticity. Such a phenomenon is engendered by the shear forces between gases in the internal part of the cone, which remain relatively stationary near the nozzle. Consequently, the transportation and mixing of $H_2$ become challenging within this confined space. Further downstream, a larger but weaker vortex and recirculation region develop in the outer part, characterized by a lower magnitude of vorticity. This region facilitates the transportation of $H_2$, aiding in its mixing with the ambient $N_2$. These flow structures are presented in Fig. 19, with green arrows denoting the smaller and stronger vortex, while orange arrows indicate the larger and weaker vortex.

For solid-cone injectors, the absence of a small yet potent recirculation region near the nozzle is notable, replaced instead by the generation of a larger, weaker vortex termed a "vortex ball", as shown in Fig. 19 for both single and six solid-cone configurations. This characteristic allows solid-cone configurations to expand the jet more effectively compared to the hollow-cone configuration. This trend is consistent across all multi-hole configurations as well. Fig. 18 shows a decrease in the projected area as the number of holes increases for solid-cone configurations, attributed to overlapping jets in the line of sight, thereby limiting the efficacy of the projected area as a metric for the degree of mixing.

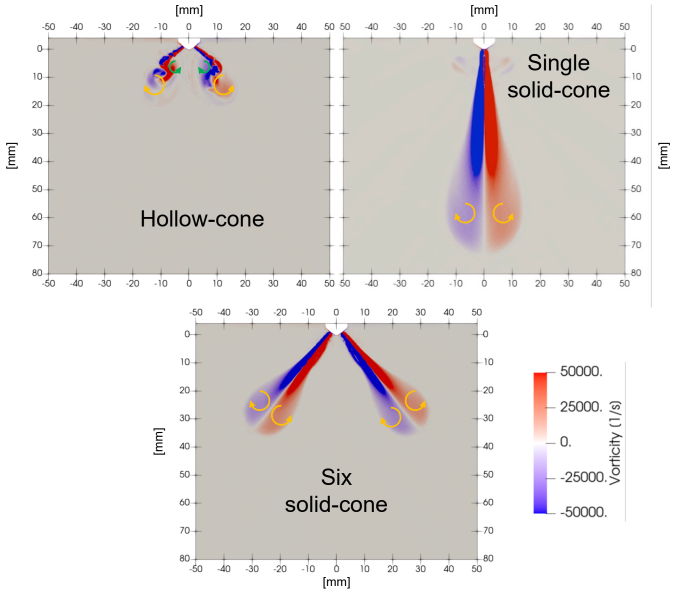

**Fig. 19.** Vorticity and flow patterns in a midplane for the hollow-cone, single, and six solid-cone configurations at 0.5 ms aSOI [12].

The vortices and flow patterns shown in Fig. 19 also shed light on the post-injection increase in penetration observed at 2 ms for the hollow-cone configuration, as presented in Fig. 17. Throughout injection, a robust vortex strives to confine the injected gas along the injector axis and near the tip. With the cessation of injection, this vortex dissipates, allowing the larger vortex's influence to predominate, thereby transporting the $H_2$ further from the injector. Notably, the analyzed solid-cone cases exhibit no discernible spray collapse due to jet-to-jet interaction, a phenomenon observed with gas generated from vaporized liquid jets under specific conditions like flashing boiling. It is expected that with an increase in the number of holes, this effect will approximate the behavior of the multi-hole injector toward the hollow-cone configuration, indicating the presence of a robust vortex near the injector tip. This suggests a resemblance between the behavior of the hollow-cone jet and that of a solid-cone jet with an infinite number of holes.

The turbulent kinetic energy in the chamber over time for different injector configurations is illustrated in Fig. 20. Typically, turbulent kinetic energy escalates during injection as the jet stirs the bulk mass. However, upon injection cessation, viscous effects dissipate the energy, causing its value to decline across all cases. As previously discussed, the hollow-cone configuration demonstrates the lowest value, confined to a small region near the injector tip. In contrast, all solid-cone configurations exhibit notably higher turbulence intensity, nearly double that of the hollow-cone case. With an increase in the number of holes, a decrease in turbulence level is observed, as mentioned earlier. This phenomenon arises because the less forceful jets from smaller nozzles fail to transfer and dissipate as much turbulent kinetic energy to the surrounding gas, resulting in a lower average turbulent kinetic energy in the domain. These findings suggest that solid-cone configurations are more adept at inducing turbulent fluctuations.

Fig. 21 shows the turbulent length scale. Initially, turbulence in the chamber surges as $H_2$ is injected, with length scales diminishing, indicating a predominance of energy in small-scale eddies. Following this, small eddies dissipate, and larger vortices become prevalent, leading to an increase in the turbulent length scale. Upon injection cessation, a slight drop in the turbulent length scale or an inflection point occurs as flow inertia transitions to smaller scales before diffusion. Subsequently, the turbulent length scale rebounds. Notably, the hollow-cone configuration generates the largest scales, which tend to increase owing to the larger vortex until injection cessation. At this point, the jet expands, and turbulence structures dissipate into smaller ones due to the jet's recirculation near the injector tip. In the case of the single solid-cone configuration, the jet extends further and interacts more with the ambient gas, intensifying turbulence at smaller scales. However, as shown in Fig. 19, the jet generates two large vortices that boost the turbulent length scale before injection cessation, occurring roughly after 1.3 ms.

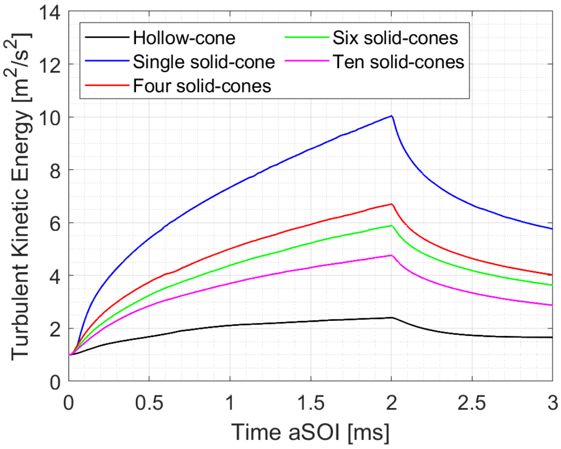

**Fig. 20.** Average turbulent kinetic energy in the chamber for different inj. configurations [12].

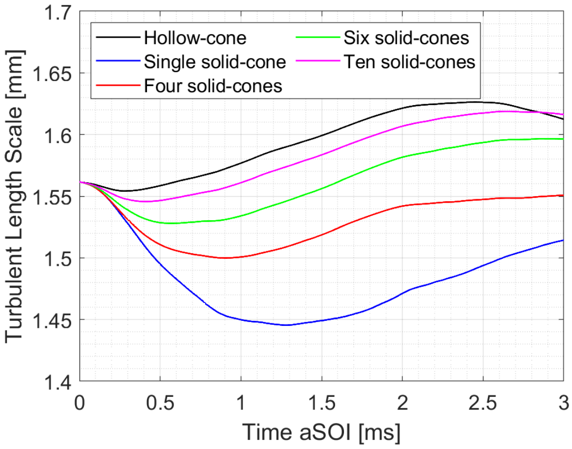

**Fig. 21.** Average turbulent length scale in the chamber for different inj. configurations [12].

Additionally, as shown in Fig. 21, an increase in the number of holes leads to the formation of larger-scale eddies containing the majority of the energy. The expansion of the vortex ball to larger scales for each jet contributes to a subsequent rise in the turbulent length scale. This phenomenon is consistent with the observed dissipation of turbulence levels, as shown in Fig. 20. Overall, these findings highlight that solid-cone jets introduce more turbulence compared to hollow-cone jets, resulting in smaller, high-energy eddies that enhance the diffusion and mixing of the fuel.

Fig. 22 presents the probability density function (PDF) distribution of the equivalence ratio in the jet region for the hollow-cone injector at different time steps. Lighter-colored lines represent the early moments of injection, while darker lines represent later time steps. The jet region is defined as the volume where the mass fraction of $H_2$ exceeds 0.1%. At the onset of injection, the jet is small, with only a limited mass of $H_2$ mixed with the ambient. This explains why, in Fig. 22 at 0.01 ms, the PDF exhibits a high value extending beyond the graph's limit for equivalence ratios higher than two. Simultaneously, the small amount of diffusing and mixing $H_2$ accounts for less than 15% of the injected mass, resulting in an equivalence ratio of less than 0.5.

Fig. 22 shows the progressive mixing of $H_2$ over time, resulting in a relatively constant mass fraction below 5% with an equivalence ratio between 0.5 and 2. At time steps of 0.5, 0.75, and 1.0 ms, more $H_2$ is diffused and mixed, leading to a concentration peak around equivalence ratios between 1 and 1.5. Subsequently, $H_2$ continues mixing towards leaner equivalence ratios than stoichiometric. Following the end of injection at 2.0 ms, the injected fuel diffuses further, and the PDF peak shifts towards lean mixtures between 0.5 and 1.

The PDF distribution of the equivalence ratio for the solid-cone configurations is presented in Fig. 23. It's apparent that for all solid-cone cases, the PDF resembles the hollow-cone case during the initial stages of injection, with mass fraction values exceeding the displayed range for equivalence ratios higher than 2. This is because the injected fuel has not yet fully mixed, resulting in an equivalence ratio lower than 0.5. As time progresses and more $H_2$ is injected, there is a more uniform distribution of the equivalence ratio, with a maximum PDF fraction of 10% in all cases. Over time, the PDF quickly rises to higher values, reaching a maximum of 30% at equivalence ratios lower than 0.5 for all cases. Notably, for the ten solid-cone configuration, there is a peak similar to a normal distribution, converging to an equivalence ratio of 0.15.

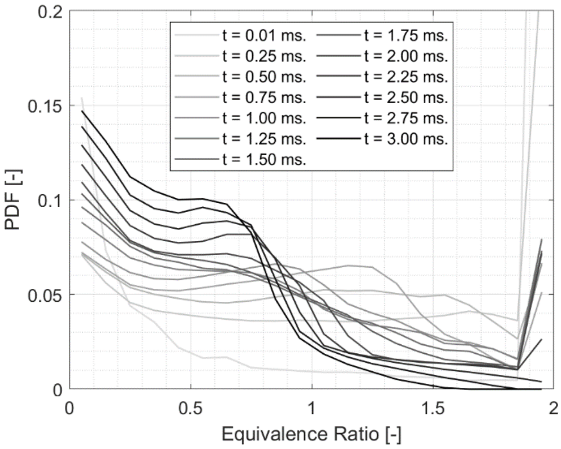

**Fig. 22.** PDF evolution in time for the hollow-cone injector [12].

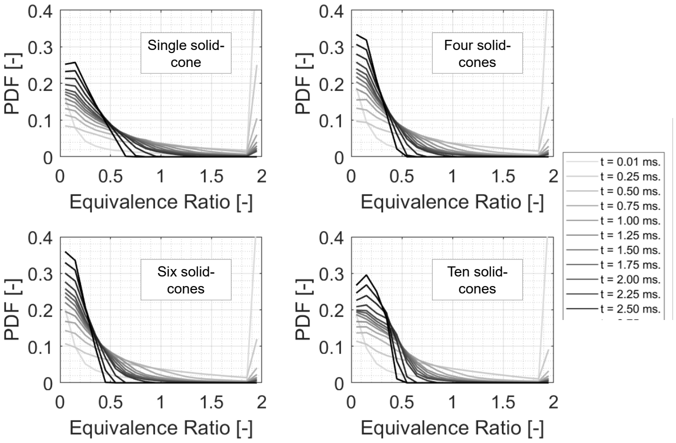

**Fig. 23.** PDF evolution for the solid-cone injector configurations [12].

Comparing Fig. 22 and Fig. 23 allows for a comprehensive analysis and conclusion based on the jet projected area depicted in Fig. 18. In Fig. 18, all solid-cone cases suggest better mixing than the hollow-cone configuration. When analyzing the PDF considering the entire volume in the three-dimensional domain, the maximum PDF value in the lean region and after injection cessation is approximately 0.3 for all solid-cone configurations, twice the value obtained for the hollow-cone configuration, indicating more efficient mixing for solid-cone cases. While Fig. 23 does not distinctly determine the superior solid-cone configuration, the results in Fig. 18 suggest that the four-hole configuration would achieve better mixing as it covers a larger region.

Once again, this highlights that solid-cone configurations achieve faster and more effective mixing compared to the hollow-cone configuration. Therefore, depending on the application, a solid-cone injector should be preferred if faster and more homogeneous mixing is required. However, this conclusion is limited to the ambient conditions, and further analysis should be conducted in the future under actual engine configurations.

# 4 Hydrogen engine combustion experiments

## 4.1 Metal engine measurements

### *4.1.1 Metal engine setup*

A heavy-duty six-cylinder diesel engine from Volvo Trucks underwent modification to operate in a single-cylinder configuration. This involved deactivating five cylinders and utilizing a modified intake manifold. The specifications of the test engine are detailed in Table 2, with a schematic provided in Fig. 24.

The engine head was originally designed to accommodate three DI injectors, as depicted in Fig. 25. With injector positions N1, N2, and N3 are located near the intake, at the center, and near the exhaust side, respectively. This configuration was modified from CI mode to SI mode by replacing the central injector (N2) with a spark plug and substituting the side diesel injector closer to the intake side (N1) with a gasoline injector. Furthermore, the intake manifold design was modified to accommodate multiple port injectors for port fuel injection. $H_2$ cylinders were connected to the injectors via a mass flow meter to precisely measure the $H_2$'s flow rate. Additionally, a flashback arrestor was installed in the fuel line connected to the PFI injectors to mitigate backfire issues. For engine control and monitoring purposes, a National Instrument’s (NI) data acquisition system was dedicated to handling all aspects of engine control and monitoring throughout the study.

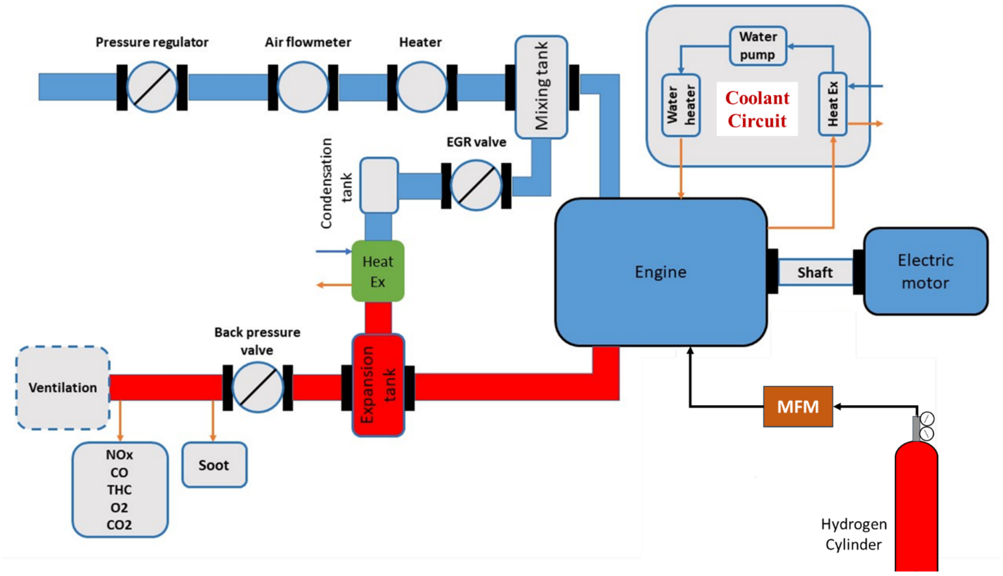
Pressure regulator
Air flowmeter
Heater
Mixing tank
Water pump
Water heater
Coolant Circuit
Heat Ex
EGR valve
Condensation tank
Heat Ex
Engine
Shaft
Electric motor
Back pressure valve
Ventilation
Expansion tank
MFM
NOx
CO
THC
O2
CO2
Soot
Hydrogen Cylinder

**Fig. 24.** Schematic diagram of the experimental setup for the single-cylinder metal engine.

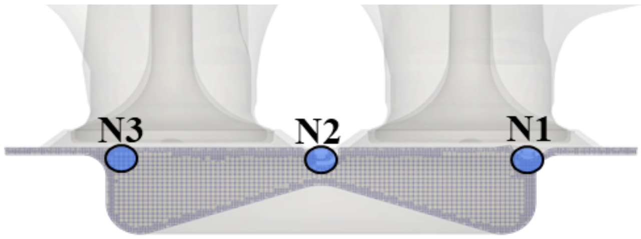

**Fig. 25.** Injector positions on the cylinder head.

**Table 2. Engine specification of the single-cylinder metal engine.**

| | |
|---|---|
| Engine model | Volvo D13 |
| Valve mechanism | Single overhead cam |
| Number of valves | 2-Intake 2-Exhaust |
| Bore (mm) | 131 |
| Stroke (mm) | 158 |
| Connecting rod length (mm) | 255 |
| Compression ratio | 17:1 |
| Displacement (Single Cylinder) (L) | 2.13 |

### *4.1.2 PFI study*

$H_2$ was injected into the intake port using multiple Bosch port fuel injectors. The use of more than one injector was necessary due to the engine's higher cubic capacity. A fixed upstream pressure of 11 bar was maintained for the port fuel injection. Detailed testing points were outlined in Table 3, encompassing two speeds, three loads, and three $\lambda$ points. Load control was achieved by adjusting the injection duration, with injection pulse width ranging from 10.8 to 16 ms for load variations between 4 to 6 bar gross indicated mean effective pressure (IMEPg). This led to the injection duration of nearly 115 CAD at 1200 rpm and 87 CAD at 900 rpm. Injection timing was standardized for all operations at 330 CAD bTDC to ensure completion before the intake valve closing time of 170 CAD bTDC. Injecting fuel alongside intake air contributed to improved mixing and aided the combustion process.

**Table 3.** Engine operating conditions.

| | |
|---|---|
| Engine Speed [rpm] | 900, 1200 |
| IMEPg [bar] | 4.2, 5.2, 6.2 |
| $\lambda$ [-] | 3.7, 4.7,5.7 |
| EGR [%] | 0, 10, 20 |
| Injection pressure [bar] | 11 (PFI) |
| Start of Injection [°CA bTDC] | 71 (DI) |

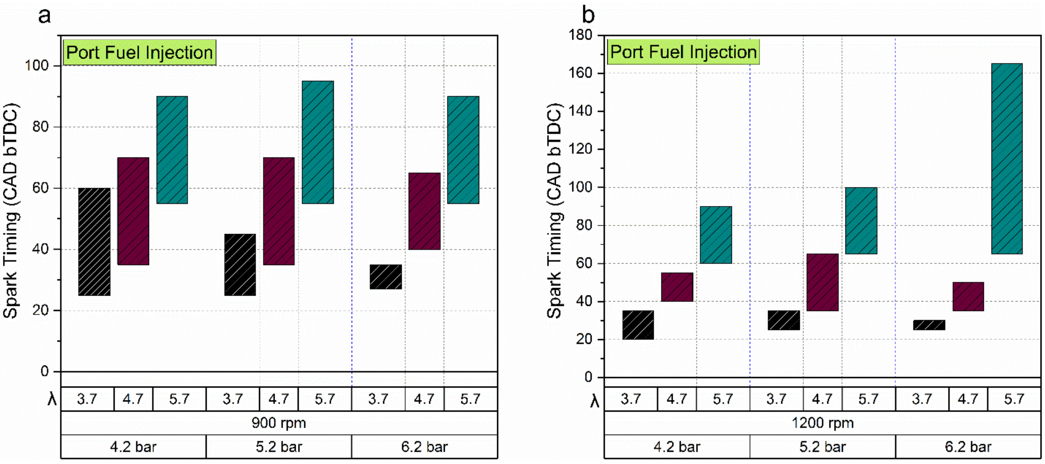

**Fig. 26.** Spark timing sweep limits at different loads, speeds, and $\lambda$: a) 900 rpm; b) 1200 rpm.

Fig. 26a and b illustrate the spark timing sweep achieved under various $\lambda$, load, and speed conditions without employing EGR. The spark timing sweep was constrained either by misfire resulting in a higher coefficient of variation (COV) of IMEPg ($COV_{IMEP}$) value exceeding 5% or by the occurrence of knock. Observations indicate that as $\lambda$ values increase, spark timing needs to be advanced due to excessive dilution rates. At 900 rpm, spark sweeps for all variations exhibited similar windows, except for $\lambda = 3.7$ at 6.2 bar, which displayed a notably shorter window. However, at 1200 rpm, this window was reduced overall, except for the $\lambda = 5.7$ at 6.2 bar, which demonstrated a considerably larger spark sweep window.

### *4.1.3 DI study*

The DI experiments were conducted using a central spark plug and side injector configuration, with a Bosch gasoline direct injector utilized for $H_2$ injection. The upstream $H_2$ pressure was maintained at approximately 71 bar, enabling higher loads by injecting more $H_2$ into the engine cylinder. Injection timing was set at 280 CAD bTDC to compensate for the extended injection duration, which reached up to 17 ms, significantly exceeding the recommended 5 ms for the injector. All other experimental conditions were consistent with those used for the PFI study.

Fig. 27 illustrates the spark timing window for the direct injection experiments under various load, speed, and $\lambda$ conditions. Notably, the spark sweep window for $H_2$ DI experiments was considerably smaller compared to port fuel injection experiments. Additionally, there are instances where spark timing windows were not recorded, particularly at $\lambda = 5.7$, 6.2 bar at 900 rpm, and multiple points at 1200 rpm. This is attributed to significantly higher occurrences of misfire or knocking at these points, making it challenging to record even a single stable point. Stratification of the charge mixture is identified as a primary factor affecting combustion stability in these instances.

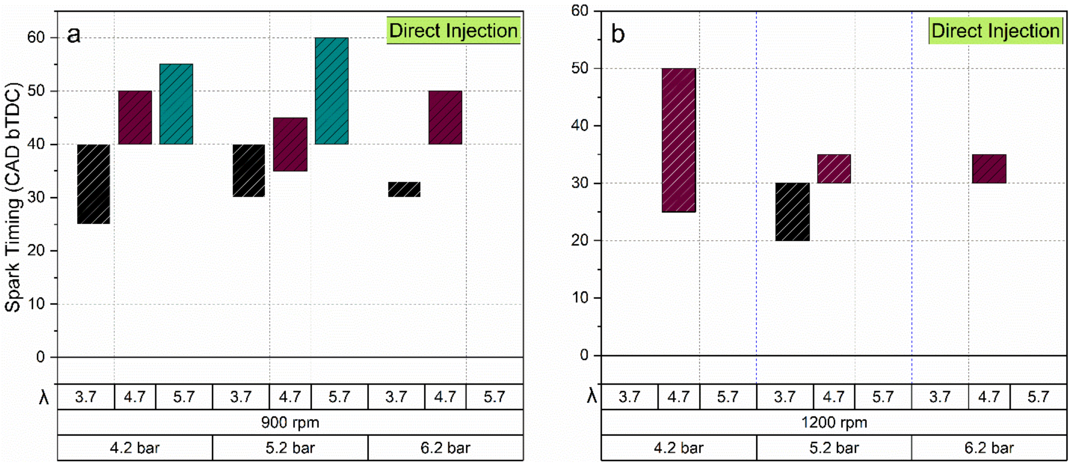

**Fig. 27.** Spark Timing window for $H_2$ DI experiments at different load, speed, and $\lambda$ conditions. a) 900 rpm, b) 1200 rpm

The spark window is notably narrower for the 0% EGR condition and the lowest efficiency recorded at 48.5% with a spark timing of 30 CAD bTDC. However, upon introducing EGR, a substantial increase in gross efficiency is observed, accompanied by an expansion of the spark timing window. This enhancement is primarily attributed to the EGR flow improving the air-fuel mixture within the combustion chamber, thereby enhancing gross efficiency and promoting combustion stability, resulting in a wider spark timing window. The gross efficiency peaks at 52% with a spark timing of 30 CAD bTDC under the 20% EGR condition.

#### *4.1.4 Emissions*

Despite encountering numerous challenges in establishing $H_2$ engine operation, there are notable benefits evident in the emissions outcomes. As a carbon-free fuel, $H_2$ yielded no emissions of CO, $CO_2$, or HC in the exhaust. While $NO_x$ emissions have historically presented a significant challenge with $H_2$ engines, the current experimental campaign yielded nearly zero $NO_x$ emissions. This outcome could be attributed to the exceptionally high dilution rates, which effectively reduced the combustion peak temperature, thereby mitigating $NO_x$ emissions.

### 4.2 Optical engine measurements

#### *4.2.1 Optical engine setup*

The same engine that was employed for the measurement of $H_2$ DI was used for the combustion measurement. The diesel fuel injector was replaced with a spark plug (NGK 2862 ER10EH) and the port-fuel gas injectors were installed in the intake manifold. The schematic of the experimental setup for $H_2$ SI combustion is shown in Fig. 28. The engine was operated at 1200 rpm using an AC motor in a throttled operation with an intake air pressure of 0.7 bar adjusted using mass flow controllers. A range of pressure sensors and thermocouples were installed in the cooling water system, lubricating oil circuit, fuel line, intake, and exhaust lines for the constant monitoring of local pressure and temperature. The piezoelectric pressure sensor (AVL GH01D) installed in the windows holder, in combination with a charge amplifier (AVL FI PIEZO) was used to measure the in-cylinder pressure data using a rotary encoder (Linde RSI 503) with a crank angle resolution of 0.2 degrees. The intake air and coolant/oil temperature were maintained at 25°C and 30°C respectively. The $H_2$ gas was delivered at -360°CA aTDC in the intake stroke using a port-fuel injection system for the duration of 25 ms. Bosch NGI2 injectors are used to inject the $H_2$ gas. Mass flow controllers set the flow rates for air and $H_2$, to achieve the desired $\lambda$. Safety components such as solenoid valves and flashback arrestors were also installed. The experiments were conducted at varying spark timing (ST) on lean excess-air ratios of 3. The engine was operated in a 5/20 skip firing mode, i.e., five fired cycles followed by twenty motored cycles. A LabVIEW FPGA-based real-time embedded control system (NI 9038 CompactRIO) was used to drive the engine and collect data. A Photron SA-X2 fast camera equipped with a Nikon 50 mm, f/1.2 lens captured the line-of-sight integrated high-speed natural combustion luminosity from the bottom view of the combustion chamber. The frame rate and exposure time of the camera were set to 36,000 frames per second and 5 μs, respectively.

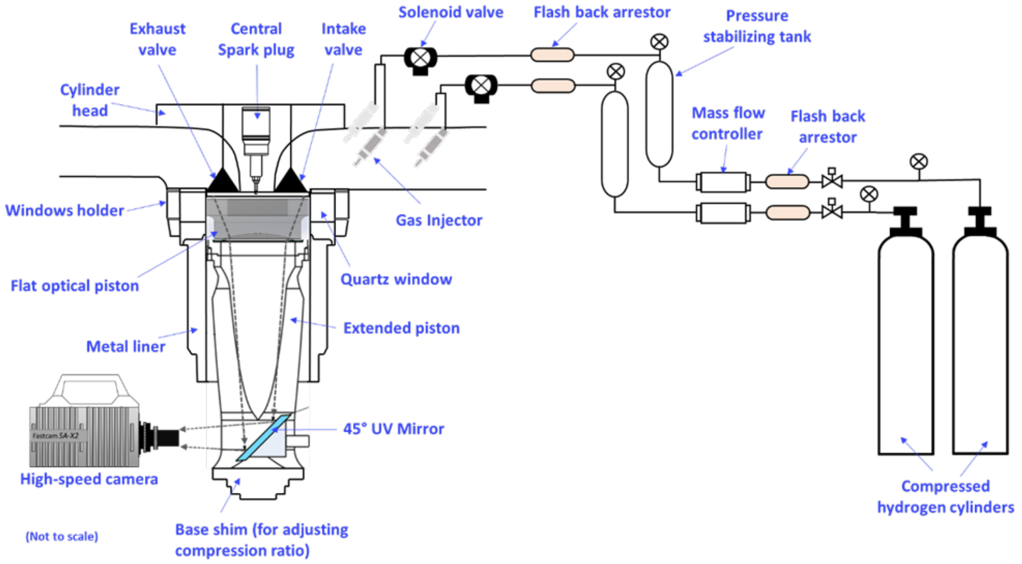
Exhaust valve
Central Spark plug
Intake valve
Solenoid valve
Flash back arrestor
Pressure stabilizing tank
Cylinder head
Mass flow controller
Flash back arrestor
Windows holder
Gas Injector
Flat optical piston
Quartz window
Extended piston
Metal liner
45° UV Mirror
High-speed camera
Fastcam SA-X2
Compressed hydrogen cylinders
(Not to scale)
Base shim (for adjusting compression ratio)

**Fig. 28.** Schematic of the optical engine and line-of-sight integrated high-speed natural combustion luminosity bottom view imaging system for $H_2$ combustion [14].

### 4.2.2 Measurements

Fig. 29 shows (a) In-cylinder pressure and rate of heat release (ROHR), (b) Combustion parameters and (c) Gross indicated mean effective pressure (IMEPg) and $COV_{IMEP}$ of pure $H_2$ combustion at the air-excess ratio of 3. The raw in-cylinder pressure traces obtained using a piezoelectric transducer were further post-processed using standard techniques such as pegging, TDC offset correction, averaging, and filtering to obtain the cycle-averaged in-cylinder pressure trace. The ROHR was calculated based on the first law of thermodynamics while the quadratic assumption of in-cylinder temperature was considered for the estimation of specific heat ratio. The peak cylinder pressure and RoHR increase with the advance in spark timing. The COV of IMEPg is a marker of cycle-to-cycle variations and is useful to indicate engine combustion stability. In this work, a COV of the IMEPg less than 5%, is considered stable combustion.

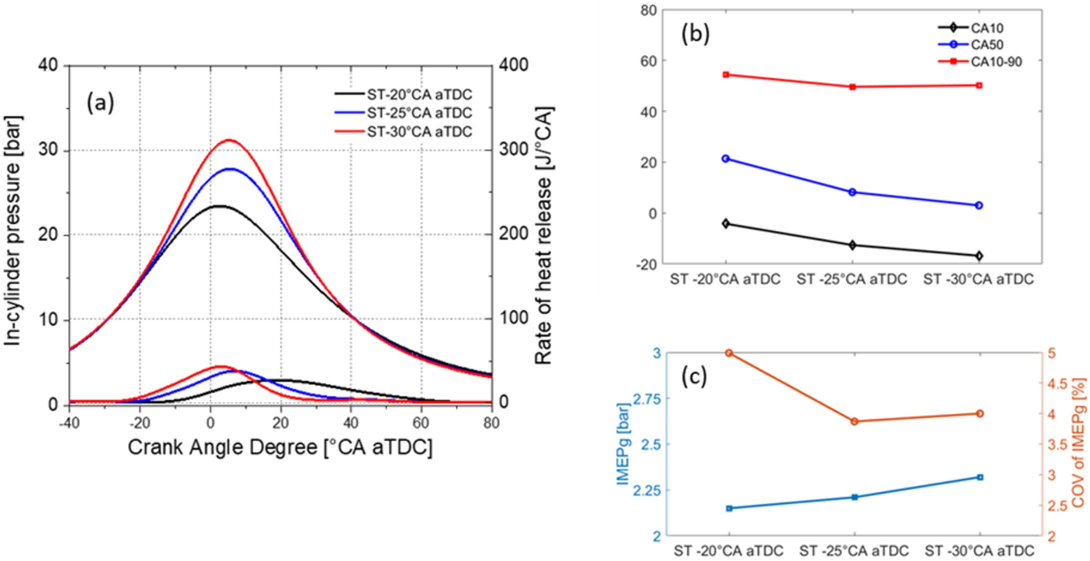

**Fig. 29.** (a) In-cylinder pressure and RoHR, (b) Combustion parameters, and (c) IMEPg and coefficient of variation (COV) of IMEPg of pure $H_2$ combustion at $\lambda = 3$ [14].

Results show that the IMEPg increases with the advance in spark timings. For example, at $\lambda = 3$ for ST of -20°CA aTDC, the mean IMEPg was 2.15 bar. With the advance in spark timing to -30°CA aTDC, the IMEPg was slightly increased to 2.32 bar. The COV of IMEPg shows a minimum at ST of -25°CA aTDC for $\lambda = 3$, with the corresponding values as 3.87. CA10, CA50, and CA90 were defined as the crank angle corresponding to 10%, 50%, and 90% of the cumulative heat release, respectively. The combustion duration was defined as the difference between CA10 and CA90. Results show that the CA10 and combustion phasing (CA50) decrease as the spark timing advances. The minimum combus-tion duration (CA10-90) was observed at ST of -25°CA aTDC for $\lambda$ = 3, suggesting a faster combustion process. Results show that the minimum combustion duration case correlates well with the minimum COV of the IMEPg case, thereby indicating the optimal configuration of spark timing for $\lambda$ = 3 of pure $H_2$ combustion.

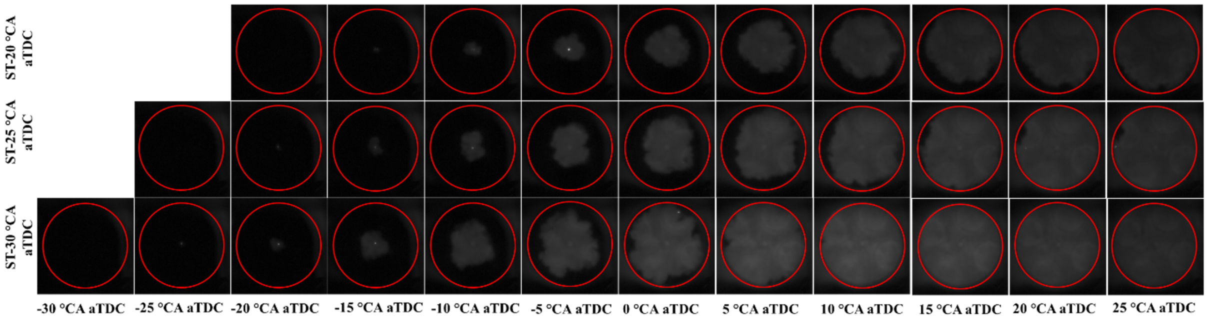

**Fig. 30.** High-speed natural combustion luminosity images of pure $H_2$ combustion at $\lambda$ = 3 [14].

Fig. 30 shows the high-speed natural combustion luminosity images of pure $H_2$ combustion at $\lambda$ = 3. The red circle in these images represents the piston bowl-wall boundary. Optical diagnostics help to understand the overall flame development process by providing the spatial and temporal evolution of flames. At $\lambda$ = 3 for ST of -20°CA aTDC, initial flame kernels were formed between -15 and -10°CA aTDC. With the advance in spark timing, the location of initial flame kernels also moves forward i.e., for ST of -30°CA aTDC, initial flame kernels were formed between -25 and -20°CA aTDC. This shows that the initial flame kernel appears to advance at a similar pace with an advance in spark timing. After the initial flame kernel formation, the flame develops radially towards the piston bowl wall as it propagates. The flame size is increasing rapidly with an advance in spark timing as seen in Figure 3. This suggests that the advance in spark timing enhances the combustion process along with improved thermal efficiency as can be seen from IMEPg results (Fig. 29).

In summary, thermodynamic analysis and optical diagnostics were carried out to study the behavior of pure $H_2$ combustion in a heavy-duty single-cylinder optical diesel engine converted to run in a spark-ignition operation. The results showed that the flame propagation was dominant and no knocking or abnormal combustion behavior was observed during the entire combustion process for the tested lean burn condition of pure $H_2$ combustion. $H_2$ has unique combustion characteristics that lead to a different combustion behavior compared to hydrocarbons, especially under lean conditions. The optical $H_2$ engine data including in-cylinder pressure traces and combustion luminosity images serves as a crucial tool for calibrating and validating the combustion models including reaction kinetics, turbulence, and heat transfer contributing to the efficient design of $H_2$-powered internal combustion engines.

## 5 Hydrogen engine combustion simulations

### 5.1 Computational setup

A similar computational setup to the previous $H_2$ injection modeling study was employed for $H_2$ engine combustion modeling. Two different combustion solvers were tested and evaluated, including the detailed combustion solver SAGE [15] and the G-equation model [16]. Four distinct chemical kinetic mechanisms were examined using SAGE. Additional details of them are listed in Table 4. Note that the SAGE multi-zone well-stirred reactor model used an energy source to capture ignition, depositing 0.06 J of energy and achieving a maximum temperature of 50000 K within a spherical region with a radius of 0.5 mm for a duration of 0.5 CAD. These energy parameters were carefully selected to elevate the mixture temperature at the spark location to its adiabatic flame temperature, thus ensuring effective combustion. On the other hand, for the G-equation model, ignition is accomplished using passive source modeling with a G=0 surface initialized at the spark location. Details about the computational domain and mesh resolution are available in Table 5 and Fig. 31.

**Table 4. The chemical mechanism used in the simulations.**

| Mechanism | Number of species | Number of reactions |
|---|---|---|
| Burke [11] | 9 | 23 |
| C3 [17] | 12 | 37 |
| Creck [18] | 21 | 62 |
| Aramco [19] | 39 | 34 |

**Table 5.** Grid details.

| Mesh refinement technique | Value |
|---|---|
| Base grid | 4 mm |
| AMR (velocity and temperature) | Level 3 (min. grid of 0.5 mm) |
| Fixed embedding (intake and exhaust valves, piston, liner, and cylinder head) | Level 3 |
| Fixed embedding (spark plug) | Level 5 (min. grid of 0.125 mm) |

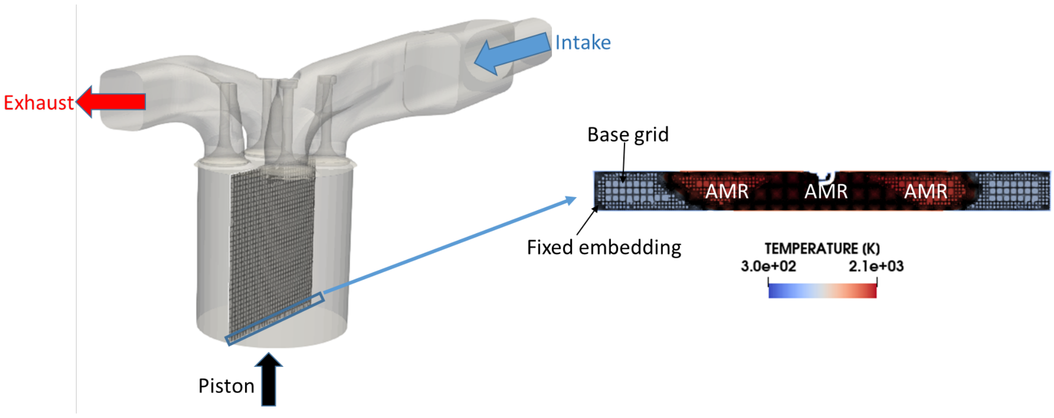
Intake
Exhaust
Base grid
AMR
AMR
AMR
Fixed embedding
TEMPERATURE (K)
3.0e+02
2.1e+03
Piston

**Fig. 31.** Computational domain and mesh details [20].

## 5.2 Comparison of four $H_2$ mechanisms using the SAGE combustion model

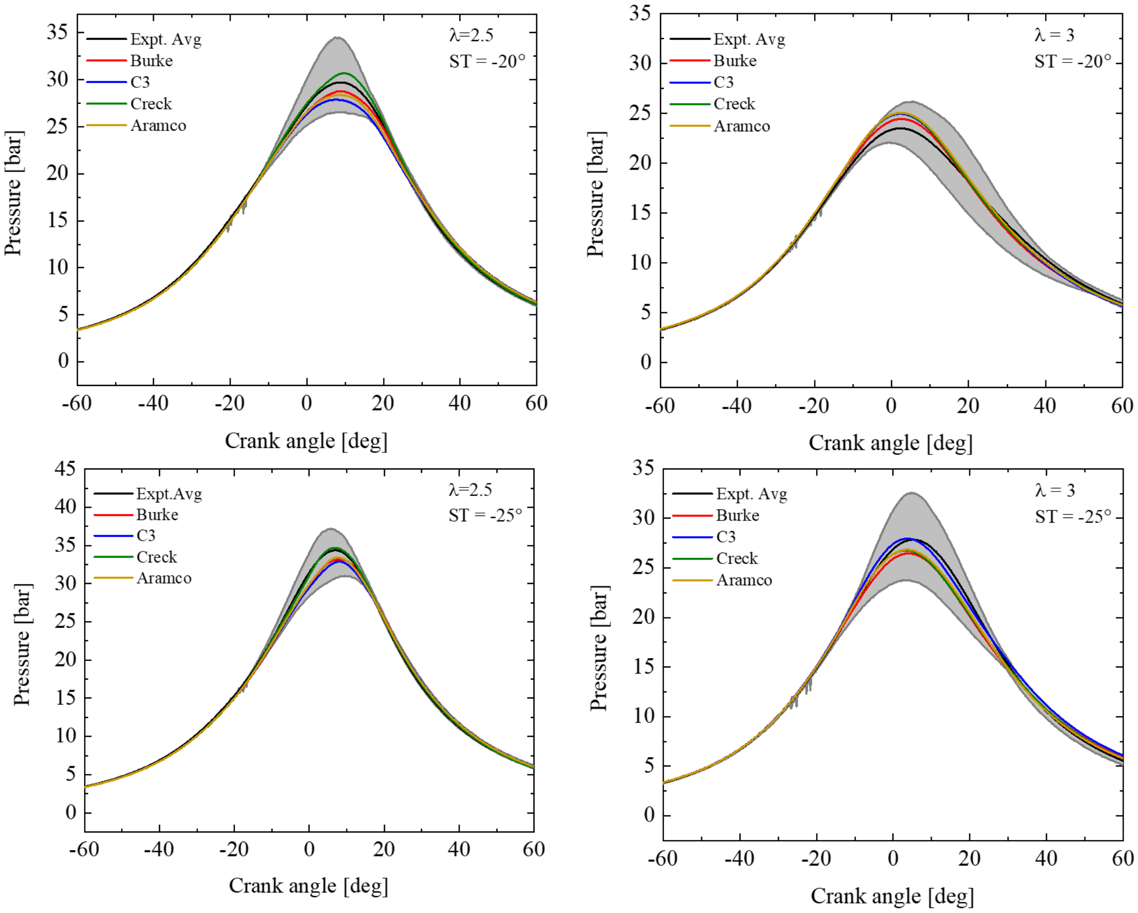

**Fig. 32.** Comparison of experimental pressure trace and prediction using different chemical mechanisms at different λ and ST [20].

The impact of employing different chemical mechanisms on the pressure trace during combustion is illustrated in Fig. 32. At $\lambda = 2.5$, all mechanisms demonstrate reasonable agreement with the experimental pressure trace, falling within the range indicated by the grey area. A closer examination reveals that Burke, C3, and Aramco mechanisms exhibit similar behavior during the combustion phase. Conversely, the Creck mechanism tends to produce a slightly higher pressure trace compared to the others, although it remains within the measured pressure trace range. Additionally, at $\lambda = 3$, it is observed that C3 yields the highest pressure trace, yet remains well within the experimental range. Overall, all mechanisms perform satisfactorily under these conditions, suggesting any mechanism could effectively predict the experimental data. Consequently, the Burke mechanism was selected due to its comparatively lower number of species and reactions, thereby expediting the simulations. Fig. 33 compares the measured and predicted flame development using the Burke mechanism. An overall good agreement between the predicted flame surface and isosurface of temperature at 1800 K is observed.

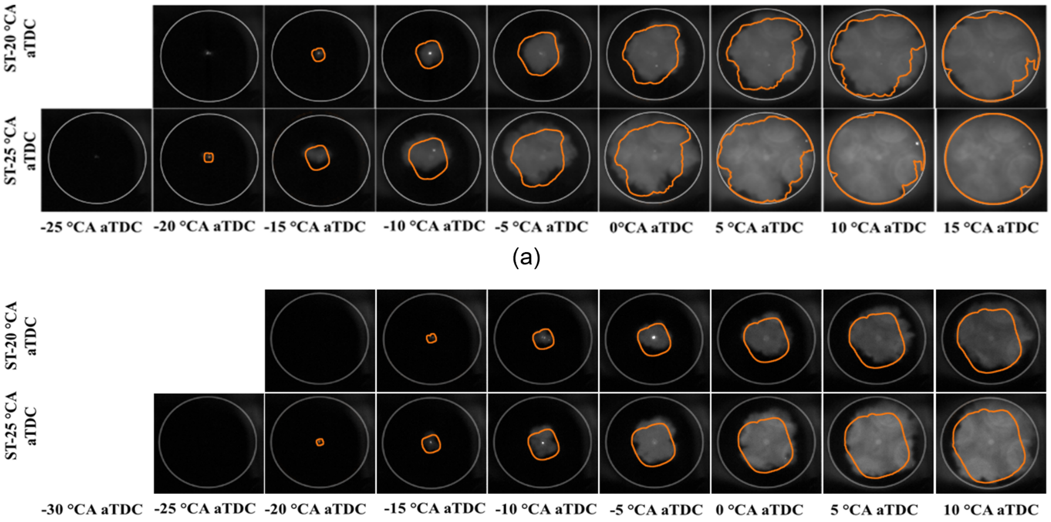

(a)

(b)

**Fig. 33.** Comparison between the experimental high-speed natural combustion luminosity images and prediction using temperature iso-surface of 1800 K for (a) $\lambda = 2.5$ and (b) $\lambda = 3$ [20].

## 5.3 Evaluation of the b₁ constant value with the G-equation combustion model

In the G-equation combustion model, the turbulent flame velocity is calculated by

$$S_{\&} = S_{,} + u^{(}\text{-} - \frac{)\#^{*}\$^{\%}}{\$^{*}{}_{\&}} Da + 12\frac{)\#^{*}\$^{\%}}{\$^{*}{}_{\&}} Da3^{\$} + a_{+}b_{,}^{\$} Da5^{-/\$}\ 6 \qquad (2)$$

In Equation 2, the $b_1$ constant signifies the large-scale turbulence constant, which plays a crucial role in influencing the rate of turbulent flame propagation. Increasing the value of the $b_1$ constant artificially boosts the turbulent flame speed, a necessary adjustment to accurately capture the intricate dynamics of combustion. This adjustment becomes particularly relevant in cases where the model initially underestimates the flame speed due to the assumption of the unity of the Lewis number.

It's important to recognize that the $b_1$ constant is just one parameter within the broader turbulence model framework. Turbulence levels are primarily determined by various other parameters and factors such as $\lambda$. Thus, while augmenting the $b_1$ constant can impact turbulent flame speed, it does not directly alter turbulence levels. To address the heightened flame speed induced by thermo-diffusive instabilities, it's recommended to increase the $b_1$ constant, as depicted in Fig. 34, where a value of 2.5 proves suitable under these conditions. Furthermore, it's evident from the figure that using a value of 2.5 aligns well with both the SAGE and G-equation models. For additional validations, Fig. 35 explores different values of $\lambda$ to assess the applicability of the $b_1$ value across varied $\lambda$, yielding consistent results akin to $\lambda = 2.5$. Note that the impact of increasing the $b_1$ constant diminishes as the mixture leans towards a lower fuel-to-air ratio. This is attributed to the decreasing laminar flame speed term mentioned in Equation 2. Fig. 36 offers a comparison between experimental natural combustion luminosity images and predictions obtained with SAGE and G-equation models. It shows that by adjusting the $b_1$ constant, a commendable agreement between SAGE and G-equation combustion models was achieved.

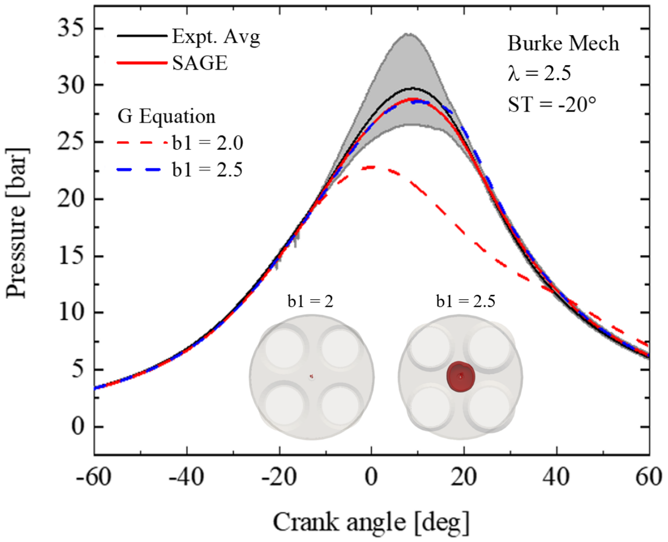

**Fig. 34.** Effect of changing the value of the constant b1 on the predicted pressure trace using SAGE and G at $\lambda = 2.5$. The flame front (G = 0) iso-surface at -10°CA aTDC [20] is also included for comparison.

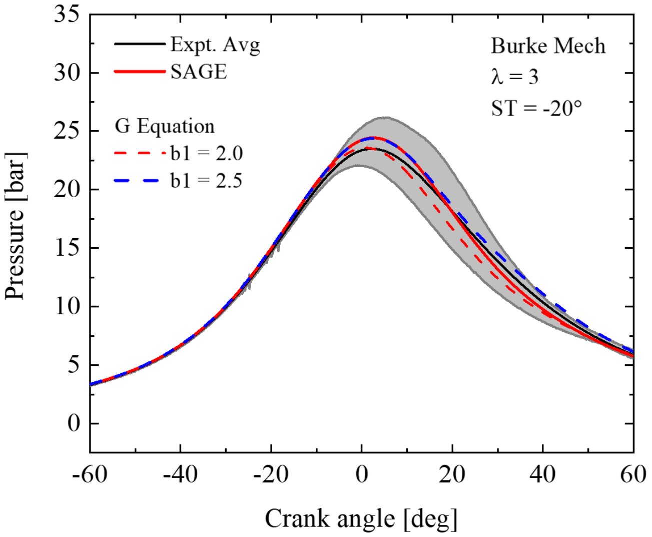

**Fig. 35.** Comparison between the experimental pressure and the simulation using SAGE and the G-equation at $\lambda = 3$ and ST = -20°CA aTDC [20].

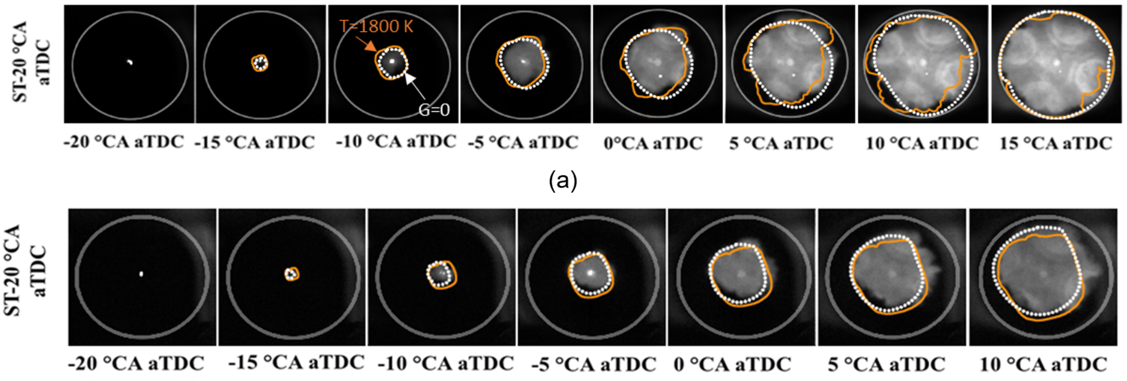
ST-20 °CA aTDC
T=1800 K
G=0
-20 °CA aTDC
-15 °CA aTDC
-10 °CA aTDC
-5 °CA aTDC
0°CA aTDC
5 °CA aTDC
10 °CA aTDC
15 °CA aTDC
ST-20 °CA aTDC
-20 °CA aTDC
-15 °CA aTDC
-10 °CA aTDC
-5 °CA aTDC
0 °CA aTDC
5 °CA aTDC
10 °CA aTDC

(a)

(b)

**Fig. 36.** Comparison between the experimental natural combustion luminosity images and prediction using SAGE (in yellow) and G-equation (in white) for (a) $\lambda = 2.5$ and (b) $\lambda = 3$ [20].

## 6 Concluding remarks

In the ongoing FUELCOM4 project, the $H_2$ injection and engine combustion characteristics are being investigated using experimental and computational methods. Experiments are performed on constant volume chamber and single-cylinder metal/optical engines. Sophisticated optical diagnostics such as Schlieren and Raman are utilized to visualize the transient mixing field of $H_2$ jet. The measured results demonstrate the high sensitivity of the mixing quality of $H_2$ to the boundary conditions and in-cylinder transient flow motion. These measured data supported the validation of CFD simulations, which interactively helped optimize the injection strategy and hence improve the engine performance.

The major findings through the project thus far are summarized as follows:

(1) Increasing the injection-ambient pressure ratio results in greater jet penetration. However, there is a limitation to further increasing jet penetration by raising the injection pressure when the ambient pressure is fixed. Considering the relatively lower peak mass flow rate for the hollow-cone HDEV-4 injector, which is restricted by its unique internal geometry, it would be challenging to implement it for heavy-duty applications. For such cases, a larger mass flow rate injector would be more suitable.

(2) The pressure ratio, defined as the ratio of the nozzle inlet pressure to the ambient pressure ($P_i/P_b$), shows a linear dependence on the ratio of the injection to ambient pressure ($P_{inj}/P_b$). For the injector under study, a significant level of pressure loss was observed from the upstream supply injection pressure to the nozzle inlet.

(3) By combining a powerful 50 kHz pulse-burst laser with highly sensitive, low-noise EMCCD cameras operating in subframe burst gating, the instrument provides spatially and temporally resolved measurements with better than 0.01 precision in mole fraction. In addition, semi-quantitative measurements of the relative number density of $H_2$ reveal the temporal evolution of the shock structures, never observed before with Raman scattering. The technique can be expanded to get other scalar quantities, such as pressure and temperature in this shock region.

(4) At the same mass flow rate, solid-cone configurations in general exhibit longer penetration lengths compared to the hollow-cone case. However, the penetration length decreases as the number of holes increases due to the introduction of an angle, which results in reduced velocity for each jet. Comparatively, the solid-cone configurations significantly outperform the hollow-cone configuration in efficiently mixing hydrogen with the nitrogen atmosphere within a shorter timeframe. This suggests that a multi-hole cap may be preferred for hollow-cone injectors to improve mixture uniformity.

(5) To adjust the engine load, spark timing needs to be advanced as $\lambda$ increases due to excessive dilution rates. The spark sweep window for $H_2$ DI experiments is considerably smaller compared to PFI experiments, primarily due to the increasingly cyclic uncertainties in mixing and combustion processes. Due to the high CR of the current Volvo engine configuration, relatively high engine thermal efficiency was attained, albeit at the expense of a higher knocking tendency, significantly restricting the engine operating range. As a result, a modified piston design yielding a smaller CR is required to promote engine stability and reliability.

(6) For the combustion closure model in CFD application, the multi-zone well-stirred reactor SAGE model effectively predicts the performance of $H_2$ SI engines, yielding good agreement in pressure patterns and combustion luminosity images. The flamelet-type G-equation combustion model using the standard flame speed correlations exhibits errors, mainly attributed to the significant thermo-diffusive instability inherent in $H_2$ combustion at lean-burn conditions. Further investigation is needed to capture the lean turbulent hydrogen flame propagation characteristics.

In closing, there are additional challenges to be addressed in the next stage of this project. For example, to overcome the drawbacks of the injector and piston shape issues, a larger mass flow rate injector and a new piston shape with a smaller CR will be implemented, which are anticipated to enhance engine performance over a wider range of engine loads. Furthermore, given that the tumble and swirl motions for this Volvo prototype diesel engine are not strong enough, further optimization of the injector configuration and injection strategy etc. is needed, where high-fidelity CFD will play an important role in designing the optimal configuration. In the meantime, qualitative measurements of in-cylinder mixture distribution and combustion evolution on the optical engine will be conducted, providing valuable validation datasets for refinement and validation of various submodels in CFD simulations.

## 7 Acknowledgments

This paper is based on work supported by the Saudi Aramco Research and Development Center FUELCOM program under Master Research Agreement Number 6600024505/01 and the FLEET consortium. FUELCOM (Fuel Combustion for Advanced Engines) is a collaborative project between Saudi Aramco and KAUST intended to address the fundamental aspects of hydrocarbon fuel combustion in engines, and develop fuel/engine design tools suitable for advanced combustion modes.

## References

[1] G.S. Settles, Schlieren and shadowgraph techniques: visualizing phenomena in transparent media, Springer Science & Business Media, 2001.

[2] H.L. Yip, A. Srna, X. Liu, S. Kook, E.R. Hawkes, Q.N. Chan, Visualization of hydrogen jet evolution and combustion under simulated direct-injection compression-ignition engine conditions, Int. J. Hydrogen Energy 45 (2020) 32562-32578.

[3] Y. Krishna, A.M. Mahuthannan, D.A. Lacoste, G. Magnotti, 50-kHz-rate Rayleigh and filtered Rayleigh scattering thermometry using a pulse-burst laser, AIAA Scitech 2021 Forum, 2021.

[4] M. Yeganeh, Q. Cheng, A. Dharamsi, S. Karimkashi, J. Kuusela-Opas, O. Kaario, M. Larmi, Visualization and comparison of methane and hydrogen jet dynamics using schlieren imaging, Fuel 331 (2023) 125762.

[5] X. Wang, B.-g. Sun, Q.-h. Luo, L.-z. Bao, J.-y. Su, J. Liu, X.-c. Li, Visualization research on hydrogen jet characteristics of an outward-opening injector for direct injection hydrogen engines, Fuel 280 (2020) 118710.

[6] Z.A. Kuensch, S. Schlatter, K. Keskinen, T. Hulkkonen, M. Larmi, K. Boulouchos, Experimental investigation on the gas jet behavior for a hollow cone piezoelectric injector, SAE Technical Paper, 2014, 2014-01-2749.

[7] Q. Dong, Y. Li, E. Song, C. Yao, L. Fan, J. Sun, The characteristic analysis of high-pressure gas jets for natural gas engine based on shock wave structure, Energy Convers. Manage. 149 (2017) 26-38.

[8] J. Yu, V. Vuorinen, H. Hillamo, T. Sarjovaara, O. Kaario, M. Larmi, An experimental study on high pressure pulsed jets for DI gas engine using planar laser-induced fluorescence, SAE Technical Paper, 2012, 2012-01-1655.

[9] B. Wu, P. Sharma, T. Yu, L. Palombi, H. Wu, M.B. Houidi, N. Panthi, W. Roberts, G. Magnotti, High-Speed 2-D Raman and Rayleigh Imaging of a Hydrogen Jet Issued from a Hollow-Cone Piezo Injector, SAE Technical Paper, 2023, 2023-24-0019.

[10] Z. Han, R.D. Reitz, Turbulence modeling of internal combustion engines using RNG κ-ε models, Combust. Sci. Technol. 106 (1995) 267-295.

[11] M.P. Burke, M. Chaos, Y. Ju, F.L. Dryer, S.J. Klippenstein, Comprehensive H2/O2 kinetic model for high-pressure combustion, Int. J. Chem. Kinet. 44 (2012) 444-474.

[12] K.M. Cabezas, A. Zaihi, X. Liu, B. Aljohani, H. Wu, M.B. Houidi, W.L. Roberts, H.G. Im, Numerical Analysis and Comparison of Different Hydrogen Jet Injection Configuration in a Constant Volume Chamber, SAE Technical Paper, 2024, 2024-01-2693.

[13] A. Zaihi, K. Cabezas, X. Liu, M. Houidi, B. Aljohani, W. Roberts, H.G. Im, Hydrogen Spray Simulation with a Hollow-Cone Injector, ILASS Europe, 2023, 1-7.

[14] N. Panthi, P. Sharma, A.S. AlRamadan, E. Cenker, G. Magnotti, Hydrogen Combustion using Port-fuel Injections in a Heavy-Duty Optical Diesel Engine Converted to Spark Ignition Operation, SAE Technical Paper, 2023, 2023-32-0043.

[15] P. Senecal, E. Pomraning, K. Richards, T. Briggs, C. Choi, R. McDavid, M. Patterson, Multi-dimensional modeling of direct-injection diesel spray liquid length and flame lift-off length using CFD and parallel detailed chemistry, SAE Technical Paper, 2003, 2003-01-1043.

[16] J. Ewald, N. Peters, A level set based flamelet model for the prediction of combustion in spark ignition engines, Interdisciplinary Aspects of Turbulence, 2005, 68-76.

[17] S. Dong, S.W. Wagnon, L. Pratali Maffei, G. Kukkadapu, A. Nobili, Q. Mao, M. Pelucchi, L. Cai, K. Zhang, M. Raju, T. Chatterjee, W.J. Pitz, T. Faravelli, H. Pitsch, P.K. Senecal, H.J. Curran, A new detailed kinetic model for surrogate fuels: C3MechV3.3, Appl. Energy Combust. Sci. 9 (2022) 100043.

[18] E. Ranzi, A. Frassoldati, R. Grana, A. Cuoci, T. Faravelli, A.P. Kelley, C.K. Law, Hierarchical and comparative kinetic modeling of laminar flame speeds of hydrocarbon and oxygenated fuels, Prog. Energy Combust. Sci. 38 (2012) 468-501.

[19] W.K. Metcalfe, S.M. Burke, S.S. Ahmed, H.J. Curran, A hierarchical and comparative kinetic modeling study of C1-C2 hydrocarbon and oxygenated fuels, Int. J. Chem. Kinet. 45 (2013) 638-675.

[20] H. Aljabri, Computational Studies of Isobaric and Hydrogen Internal Combustion Engines, King Abdullah University of Science and Technology, 2023.

# Characterization of Double Injection Hydrogen Jet using Acetone- PLIF in a Constant Volume Chamber

J.J. Kim[1*], S-Y. Lee[2], Y. Ki[1], J. Hwang[3], and C. Bae[1†]

[1]Mechanical Engineering, Korea Advanced Institute of Science and Technology, 34141 Daejeon, South Korea

E-mail: justinjkim@kaist.ac.kr
Telephone: +(82) 10 8247 2883

[2]Mechanical Engineering, Michigan Technological University, 49931 Michigan, USA

E-mail: sylee@mtu.edu
Telephone: +(1) 906 487 2559

[3]Mechanical Engineering, Mississippi State University, Mississippi, USA

E-mail: hwang@me.msstate.edu

## Abstract

As global warming intensifies, hydrogen is increasingly recognized as a viable alternative to traditional fossil fuels due to its potential for clean combustion. However, the application of hydrogen in internal combustion engines is hindered by challenges such as elevated NOx emissions, which are influenced by hydrogen's unique combustion properties. A crucial aspect of mitigating these emissions is understanding the local equivalence ratio of hydrogen, which significantly impacts combustion efficiency and pollutant formation. This study focuses on examining the distribution of hydrogen and the effects of single and double injections using the Planar Laser-induced Fluorescence (PLIF) technique, traditionally applied to fossil fuels. Given hydrogen's high diffusivity, acetone was used as a doping agent to enhance measurement accuracy. The experimental setup involved a 266 nm Nd-YAG pulse laser to excite the acetone, with the fluorescence captured by a high-speed color camera. Additionally, Schlieren imaging was utilized to validate the PLIF measurements and to check for any slipping between the acetone and hydrogen, which is critical for measurement precision. The findings were promising, showing a strong correlation between the PLIF and Schlieren images, confirming that the adapted PLIF method effectively captures the hydrogen jet distribution with minimal interference from the gas's high diffusivity. These results suggest that PLIF, when used with acetone, can reliably measure hydrogen distribution and potentially assess the local equivalence ratio in jet formations. Despite these encouraging outcomes, further research is necessary to fully validate this method, especially in actual engine settings. This study contributes to the ongoing efforts to optimize hydrogen as a clean fuel alternative for internal combustion engines, an essential advancement in reducing greenhouse gas emissions and addressing the challenges of climate change.

## 1. Introduction

Recent research on internal combustion engines (ICEs) is increasingly exploring the use of alternative fuels such as hydrogen, methanol, and ammonia, driven by the urgent global imperative to address climate change. As the severity of climate impacts has escalated over recent decades, there has been a worldwide push among governments to achieve net-zero emissions by 2050 [1][2]. This goal is critical to mitigate the emissions of greenhouse gases (GHGs), which are the primary drivers of global climate change. Traditional fossil fuels, such as gasoline and diesel, are major contributors to GHG emissions, releasing significant amounts of carbon dioxide ($CO_2$) and carbon monoxide (CO), along with other harmful pollutants like nitrogen oxides (NOx) and particulate matter (PM).

Despite concerted international efforts, GHG emissions continue to rise. For instance, the transport sector alone emitted 7.98 Gt of $CO_2$ in 2022, accounting for about twenty percent of the global total of 36.8 Gt $CO_2$, with the road subsector emitting 5.87 Gt $CO_2$ [3][4]. While electrification is a burgeoning trend within the transport sector, certain high-energy-demand sectors such as long/medium-haul trucking, aviation, and shipping continue to rely on ICEs due to their higher energy density compared to electric batteries. Given that batteries currently offer about 50 times lower energy density [5], these sectors are projected to depend on ICEs into the foreseeable future. The transition from fossil fuels to alternative fuels is thus essential for reducing GHG and toxic emissions in a cost-effective manner.

Notably, hydrogen emerges as a leading alternative fuel, offering the advantage of zero greenhouse gas emissions during combustion since it contains no carbon. However, hydrogen's adoption is not without challenges. It tends to produce higher levels of NOx due to its high combustion temperature. Addressing this issue involves strategies such as high dilution with excess air or integrating after-treatment systems in the engine exhaust [6][7][8]. Utilizing existing technologies like the fuel injector to limit NOx production could be more cost-effective.

Visualizing the formation of the hydrogen mixture during combustion is a critical first step in managing local NOx levels, as understanding the fuel distribution is key. Moreover, many researchers and developers focusing on hydrogen engines are prioritizing direct injection due to issues like backfiring and low volumetric efficiency associated with port injection [9]. Direct injection supports a lean stratified charge combustion strategy, beneficial for several reasons [10]. Despite hydrogen’s small quenching distance leading to higher heat transfer losses through the engine walls, this approach helps mitigate such losses and reduce pumping losses by allowing the engine to operate with a wide-open throttle, even under low to medium load conditions.

According to Lee [10], the timing of the mixture formation—from the start of injection to the start of ignition—significantly influences combustion behavior, affecting heat release, flame speed, and rise time. The changes in the local equivalence ratio, influenced by the duration of the mixture formation, are crucial in driving these variations in combustion behavior. Additionally, the hydrogen stratified charge approach can encounter difficulties in reaching the spark plug at the start of ignition due to the significant contraction of the fuel jet under high ambient pressure conditions when using the hollow cone injector [10].

The lean stratified charge combustion strategy significantly enhances the efficiency and effectiveness of ignition by injecting fuel during the compression stroke, which optimizes the distribution and timing of fuel for ignition [10]. This method is particularly useful when high ambient pressures inside the engine cylinder are present, conditions under which traditional single-injection strategies often lead to misfiring [10]. To further address the limitations inherent in stratified charge systems, a double injection strategy has been suggested. This approach not only reduces jet penetration but also increases jet width, thereby improving the likelihood that a flammable mixture adequately reaches the spark plug [10].

Despite these technical advancements, ignition failures may still occur if the flammable mixture does not adequately accumulate at the spark plug. This persistent challenge is exacerbated by limitations in current measurement technologies, such as Schlieren imaging. While Schlieren technology is instrumental for visualizing density variations within transparent media and is routinely used to evaluate the fuel-air mixing distribution, its line-of-sight measurement approach can inadvertently provide misleading information about the actual spray distribution. Schlieren imaging's primary drawback is its dependence on line-of-sight data, which only captures a two-dimensional projection of complex three-dimensional flow fields. This limitation becomes particularly acute when trying to understand fuel distribution near the spark plug—a crucial zone for ignition.

Given the narrow spatial volume of the spark plug's ignition location, accurately capturing this area becomes challenging with Schlieren technology due to the broad width of the spray formation it typically visualizes. This spatial mismatch can lead to significant inaccuracies in determining whether a sufficient flammable mixture has reached the ignition site, potentially leading to ignition failure despite apparently optimal conditions. Therefore, while recent innovations in injection strategies have significantly improved the delivery and distribution of fuel, the effectiveness of these advancements remains constrained by the capabilities of existing visualization tools. This underscores a pressing need for more advanced measurement techniques capable of providing detailed three-dimensional spatial information. Such advancements would not only address the current limitations of line-of-sight measurements but also ensure more reliable ignition by accurately assessing the presence and distribution of flammable mixtures at the critical point of ignition.

This paper, therefore, seeks to observe and analyze the impact of the double injection strategy using the planar laser-induced fluorescence (PLIF) technique with acetone, and to evaluate the feasibility of this methodology for high-diffusivity gases by comparing the cross-sectional views of nitrogen, helium, and hydrogen.

## 2. Methodology

### 2.1 Experiment Apparatus and Optical Setup

The experimental apparatus centers on a 1.4-liter constant volume chamber (CVC) designed with a hexahedral shape, as illustrated in Fig. 1. This chamber is outfitted with a precision valve control system that enables pressurization to predefined levels of 5, 10, and 15 bar. An electrical heating system ensures the chamber temperature remains steady at 323 K to provide a consistent experimental environment. Additionally, the chamber features quartz windows on several sides, which are essential for employing sophisticated imaging techniques such as Planar Laser-Induced Fluorescence (PLIF) and z-type Schlieren imaging. These techniques are integral for detailed observation of the fuel's structural dynamics within the chamber.

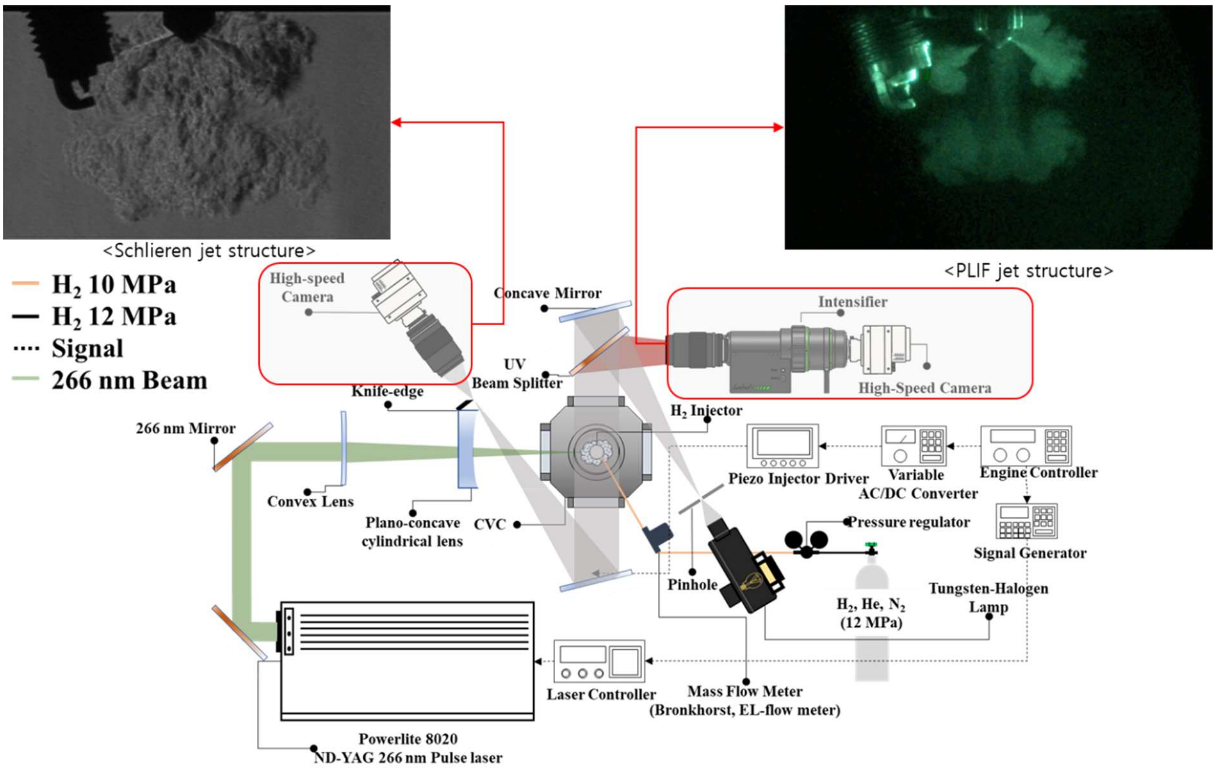
<Schlieren jet structure>
<PLIF jet structure>
— H₂ 10 MPa
— H₂ 12 MPa
···· Signal
— 266 nm Beam
High-speed Camera
Concave Mirror
Intensifier
UV Beam Splitter
High-Speed Camera
Knife-edge
H₂ Injector
266 nm Mirror
Piezo Injector Driver
Variable AC/DC Converter
Engine Controller
Convex Lens
Plano-concave cylindrical lens
CVC
Pressure regulator
Signal Generator
Pinhole
H₂, He, N₂ (12 MPa)
Tungsten-Halogen Lamp
Laser Controller
Mass Flow Meter (Bronkhorst, EL-flow meter)
Powerlite 8020 ND-YAG 266 nm Pulse laser

**Figure 1: Combustion chamber, PLIF and Schlieren optical setup.**

In the setup for acetone PLIF, light from a frequency-quadrupled Nd:YAG laser, emitting at 266 nm, is shaped into a two-dimensional thin laser sheet at the center of the chamber. This is accomplished using a convex lens with a 1.0 m focal length and a cylindrical lens with a -25 mm focal length. These lenses work in tandem to vertically bisect the chamber. A UV beam splitter, strategically placed within the z-shaped Schlieren configuration, facilitates the simultaneous capture of both PLIF and Schlieren images on the same plane. This setup allows for a direct comparison between the two imaging methods, thereby enhancing the analysis of the combustion process. For capturing PLIF images, the configuration includes a UV camera lens coupled with an intensifier and a high-speed color camera. This arrangement is specifically tuned to detect wavelengths between 325 and 500 nm [13], using a bandwidth filter to sharpen the imaging output. Simultaneously, the Schlieren setup utilizes two concave mirrors and a tungsten-halogen lamp, along with a high-speed gray-scale camera. Both high-speed cameras were set at 17000 fps as frame speed and 58 μs as exposure time.

The injection system in the experimental setup incorporated a conventional hollow-cone-shaped gasoline direct injection (GDI) injector. This injector was strategically mounted atop the chamber using a bespoke head adapter designed to secure and align it precisely. The choice of a hollow-cone-shaped injector was deliberate, aimed at optimizing the volumetric flow rate of gaseous fuel, which is crucial for achieving desired combustion characteristics under controlled experimental conditions. In contrast to this setup, multi-hole injectors, which are predominantly used for liquid fuels, prioritize the enhancement of fuel atomization. They achieve this by increasing the velocity at which the fuel is injected and by designing smaller holes in the injector tips. These modifications help to create a finer mist of fuel, which can improve the mixing of fuel and air and thereby enhance combustion efficiency.

Given the inherent challenges associated with ensuring a tight seal when using hydrogen—a gas that is notably difficult to contain due to its low molecular size—the Schlieren imaging system was integral to the setup. This system was continuously employed to monitor the GDI injector for any potential leaks. The Schlieren system is particularly well-suited for this task as it is highly sensitive to variations in gas density, which enables it to detect and visualize even minute leaks of hydrogen gas from the injection system. This continuous monitoring is essential for maintaining the integrity of the experimental conditions and ensuring the safety and accuracy of the combustion experiments.

### 2.2 Acetone Seeding System

The diagram presents a high-pressure fuel-acetone seeding system, primarily used for research, designed to produce a mixture of fuel (hydrogen, helium, or nitrogen) and acetone vapor under controlled conditions. The system's core component, an acetone delivery tank, contains liquid acetone and is submerged in a water bath held at 288 K (15°C) to ensure stable vaporization rates by maintaining constant temperature despite environmental fluctuations. Hydrogen, helium, or nitrogen, pressurized to 120 bar, bubbles through this acetone, becoming saturated with vapor before exiting the tank at a controlled 100 bar. This setup includes a primary component known as the bubbler, where the vaporization occurs and a bypass route equipped with a check valve to prevent acetone backflow during system pressurization or depressurization, enhancing safety and ensuring consistent vapor delivery.

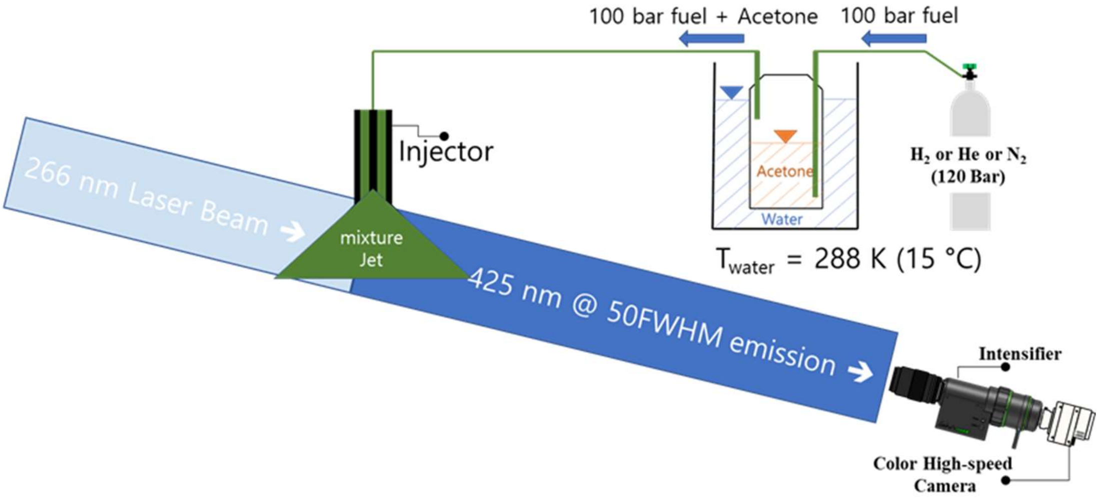

**Figure 2: Diagram of the acetone seeding chamber integrated with the fuel delivery line.**

Temperature is monitored by two thermocouples: one tracking the liquid acetone's temperature and the other the temperature of the exiting gas stream, crucial for maintaining optimal conditions for vapor production. The system also incorporates valves and pressure control mechanisms to maintain these pressures, optimizing gas flow and vapor pickup. Safety features such as pressure relief valves and monitoring systems, although not depicted in the diagram, are included to ensure safe operational parameters. This setup's simplicity and reliability minimize mechanical complexity and potential failure points, making it a robust and dependable choice for generating consistent, controlled acetone vapor streams in experimental setups. The continuous, stable output of acetone-enriched gas is vital for experiments requiring high precision and repeatability.

### 2.3 Test Conditions

Test conditions were standardized to ensure optimal consistency in the test results, as detailed in Table 1. Critical parameters such as injection duration, ambient temperature, fuel temperature, injection pressure, and ambient pressure were consistently maintained across all experiments. These included an injection duration of 1000 ms, an ambient temperature of 323 K, a fuel temperature of 288 K, an injection pressure of 10 MPa, and an ambient pressure of 15 MPa. Additionally, to investigate the impact of the split ratio on the distribution and behavior of the fuel jet, the ratio between the first and second injections in the double injection setup was varied. Three configurations were tested: 3:7, 5:5, and 7:3.

**Table 1. Test conditions**

| Parameter | Value |
|---|---|
| Injection duration [μs] | 1000 |
| 266nm laser timing [after end of 2nd injection μs] | -200, 0, 200, 400 |
| Ambient temperature [K] | 323 |
| $H_2$, $N_2$, He temperature [K] | 288 |
| Injection pressure [MPa] | 10 |
| Ambient pressure [MPa] | 1.5 |
| Split ratio | 3:7, 5:5, 7:3 |
| Dwell time [μs] | 200, 600, 1000 |

The dwell time, which is the interval between the first and second injections, was varied across three different durations—200, 600, and 1000 ms—to further explore its influence on hydrogen distribution. In the single injection setup, fuel was injected continuously for 1000 ms without division. Laser firing times were strategically scheduled at -200, 0, 200, and 400 ms relative to the end of the second injection. This timing was selected to capture the dynamics of hydrogen distribution both before and after the second injection, providing insights into the temporal evolution of the fuel's dispersal. The specific moments of these laser firings are detailed in Fig. 3 6, clearly showing the timing of observations relative to the injection events.

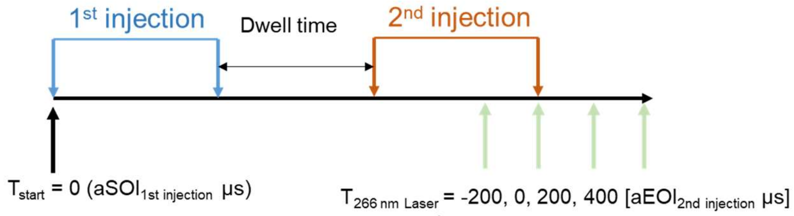
1st injection
Dwell time
2nd injection
$T_{start}$ = 0 ($aSOI_{1st\ injection}$ μs)
$T_{266\ nm\ Laser}$ = -200, 0, 200, 400 [$aEOI_{2nd\ injection}$ μs]

* Injection duration = 1st injection duration + 2nd injection duration

**Figure 3: Detailed Diagram of Injection Sequence and Laser Firing Timing.**

## 3. Results and Discussion

### 3.1 Successful Ignition (Fig 4) and Misfire (Fig 5) Scenarios for a Single Hydrogen Jet

The sequence of images provided in Fig. 4 offers a compelling visual documentation of the ignition phases within a high-pressure environment (15 bar), specifically involving a flammable hydrogen mixture. These images are integral to understanding the temporal dynamics of hydrogen ignition, with each frame pinpointing specific moments following the start of injection (aSOI) during the single jet injection. This detailed temporal breakdown captures the evolution from non-reactive conditions to active combustion, highlighting critical factors such as timing and mixture positioning relative to the spark plug.

The first frame, recorded just 0.2 ms after injection, illustrates a non-reactive state within the combustion chamber where the hydrogen mixture has not yet reached the spark plug. This moment is crucial as it represents the prepared but inactive state of the mixture, setting the stage for ignition. Subsequent frames captured at 0.83, 0.88, and 0.94 ms show the development of the ignition arc stretching towards the hydrogen spray. This elongation of the arc indicates that the initial spatial alignment of the flammable mixture and the spark plug was suboptimal, necessitating the extension of the spark to effectively reach the hydrogen. The dynamic extension of the arc highlights the adaptive response of the ignition process to spatial discrepancies in mixture placement. By 0.99 ms, the arc discharge successfully contacts the hydrogen, initiating combustion. The frame at 1.65 ms confirms the onset of stable combustion, characterized by a notable change in the visual properties of the mixture—signifying that the combustion has become self-sustaining and is propagating through the fuel mixture.

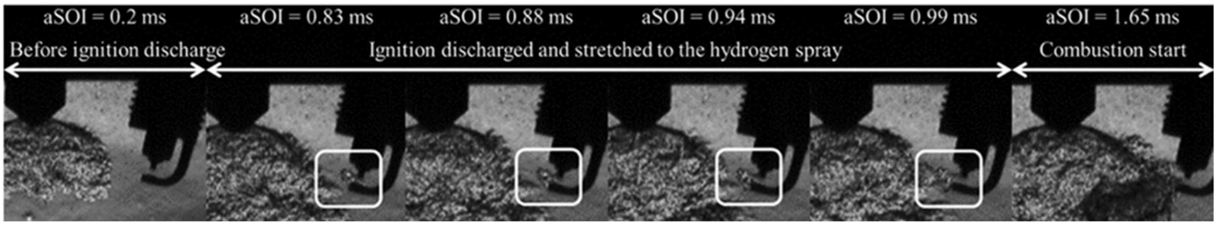

**Figure 4: Successful ignition demonstrated by optimal location and timing of ignition [10][11].**

The detailed analysis of these frames underscores the critical role of precise timing and accurate mixture positioning for effective ignition, especially in a high-pressure condition. This observation is particularly relevant for hydrogen and similar high-diffusivity fuels, which present unique challenges in combustion management. The ability of the spark to adapt and extend toward the hydrogen spray is indicative of the dynamic processes involved in achieving efficient combustion under such conditions. The insights gained from this visual sequence are vital for the optimization of ignition systems, aiming to enhance fuel efficiency and reduce emissions. Understanding the interplay between spark reach and mixture distribution enables the refinement of engine designs to accommodate the fast diffusivity and specific ignition requirements of hydrogen-based fuels.

Figure 5 presents a sequence of Schlieren images documenting the misfiring behavior of a hydrogen mixture in a combustion setup. These images are designed to visualize the failure of the spark to ignite the flammable mixture at the planned moment. Misfiring can occur due to various factors. One common issue is the timing of the spark; if it occurs when the hydrogen concentration is outside the flammable limits near the spark plug, effective ignition is compromised. Additionally, the mixture may be unevenly distributed or insufficiently concentrated around the spark plug. Other potential issues could include a weak spark or a spark plug positioned such that it does not effectively intersect with the path of the flammable mixture.

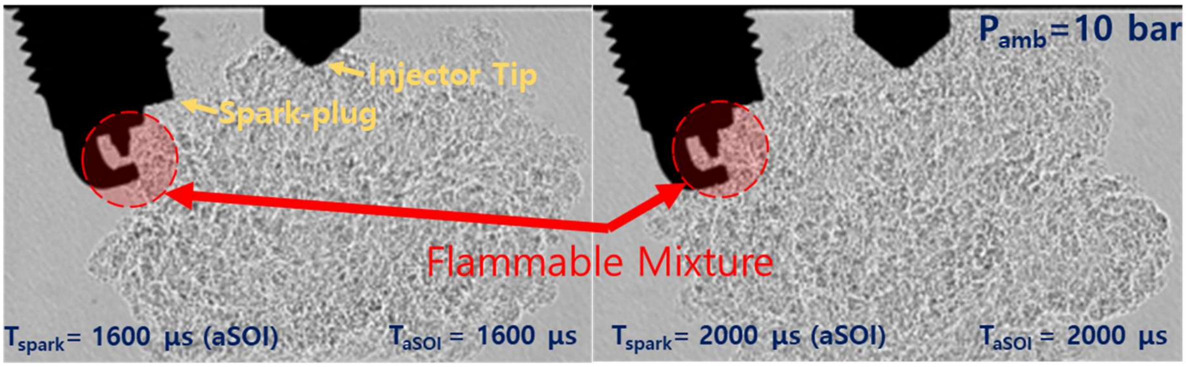

**Figure 5. Misfiring example of hydrogen mixture when the flammable mixture was formed at the spark-plug and spark-plug ignited according to the Schlieren images. ($T_{spark}$=spark-plug ignition timing, $T_{aSOI}$=time after start of injection, $P_{amb}$=ambient pressure)**

### 3.2 Double Injection Jets

Figure 6 presents a series of high-resolution images captured using both Schlieren and PLIF techniques, depicting the behavior of a gas jet from an injector tip to the vicinity of a spark plug in a chamber experiment. The first image on the left shows a raw Schlieren capture, which highlights density variations in the gas flow as white areas against a grey background, indicating the intricate flow dynamics near the injector tip. The center image, captured using PLIF, illuminates the hydrogen distribution in green hues, facilitated by the fluorescence of the gas under laser stimulation, pinpointing the concentration and movement of hydrogen around the spark plug. The rightmost image combines these two techniques into a post-processed overlap, where the Schlieren data provides a grey-scale background and the PLIF data overlays it in a color-coded format, with red indicating denser hydrogen concentrations and green showing lesser concentrations. This composite view allows for an integrated analysis of both flow dynamics and chemical composition at a critical moment in the combustion process, offering valuable insights into the interaction between the gas jet and the spark necessary for ignition.

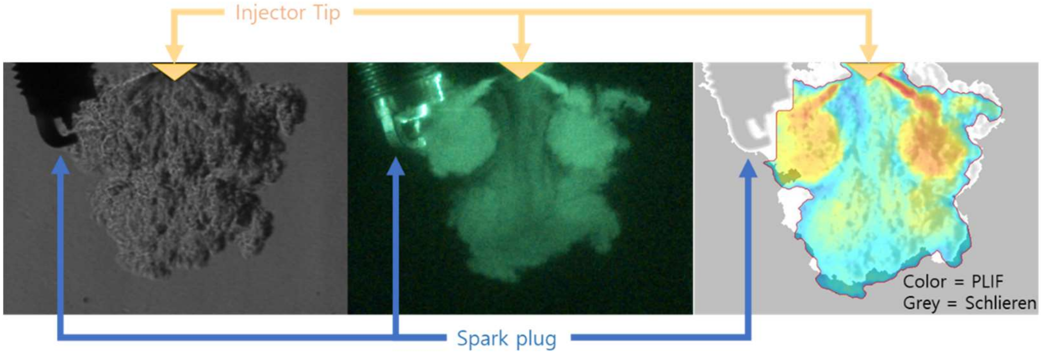

**Figure 6: Raw Schlieren Image (left), PLIF Image (center), and Post-Processed Overlapped Image (right). Overlap images are not from the left and center images. Fix this problem.**

Figure 7 displays a plot comparing the measured areas of a single injection hydrogen jet using two different imaging techniques. The data points, represented by red circles for Schlieren areas and black squares for PLIF areas, indicate the extent of the hydrogen jet captured by each method at various experimental conditions. The plot demonstrates that the areas measured by PLIF are consistently smaller compared to those measured by Schlieren, suggesting that while Schlieren imaging captures a broader range of density variations in the gas flow, PLIF provides a more concentrated view, focusing on the regions with significant hydrogen concentrations. This difference is significant for understanding the distribution and concentration of hydrogen in experimental setups, highlighting the complementary nature of these imaging techniques in capturing detailed dynamics of the hydrogen jet during injection processes.

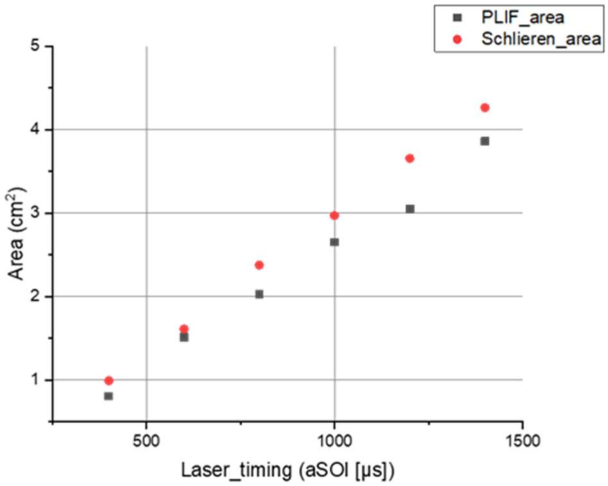

**Figure 7: Measurement of the area of a single hydrogen jet injection using Schlieren and PLIF.**

Further observations of hydrogen jet structures have elucidated the emergence of a toroidal vortex ring similarly observed in Lee [10] as seen in Figure 8. This ring-shaped vortex forms due to the pressure differentials at the edges of the hollow-cone-shaped jet and is typically observed ascending post-injection. Despite hydrogen's high diffusion rate, the structure tends to collapse and contract more significantly under elevated atmospheric pressure conditions. This phenomenon is likely due to the hydrogen's relatively low structural rigidity, which makes it more susceptible to external pressure influences.

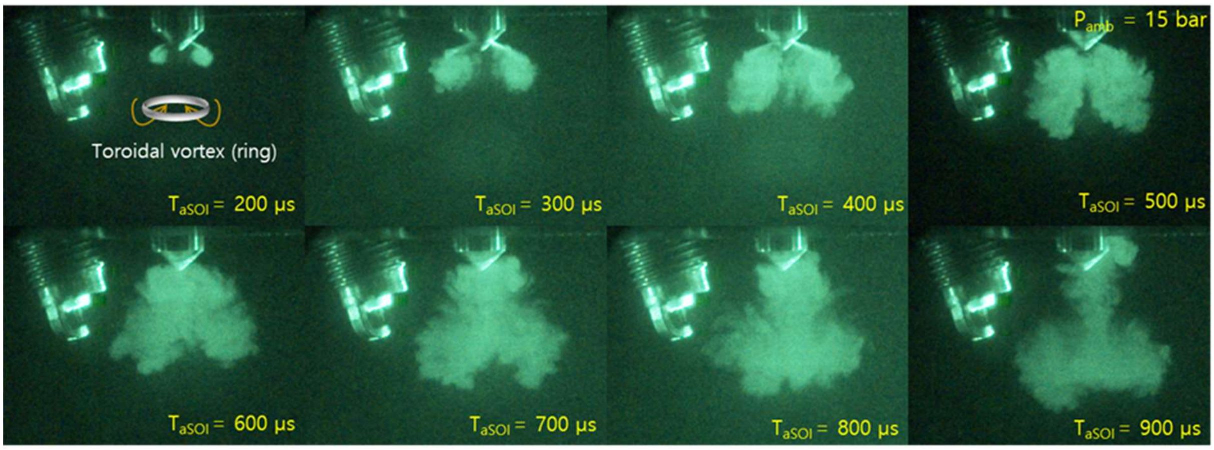

**Figure 8: Sequence of single jet acetone-PLIF images under conditions of an ambient pressure of 1.5 MPa, injection pressure of 10 MPa, and injection duration of 1000 μs. Note: The images represent multiple events, not a single continuous jet.**

Figure 8 also illustrates the time-resolved evolution of an acetone-seeded hydrogen jet ejected from a hollow cone injector. This sequence of images, recorded at incremental times from 200 to 900 ms post-injection, provides a detailed view of the dynamic formation and expansion of a toroidal vortex within the jet. The images show the transformation of the hydrogen jet, which is initially tight and focused, into a broader, ring-shaped structure as it propagates through the ambient environment. The distinct green fluorescence of the acetone allows for clear visualization of the jet's morphology and the vortex dynamics. This evolution is captured under specific experimental conditions with an ambient pressure of 1.5 MPa and an injection pressure of 10 MPa. The detailed progression reveals insights into the fluid mechanics of gas injection and mixing, highlighting the effects of injector design and pressure differential on the spatial distribution and behavior of the jet. This visual documentation is crucial for understanding the complexities of hydrogen dispersion and mixing in combustion applications.

Figure 9 (left) illustrates the area covered by hydrogen as a function of laser timing relative to the end of injection (aEOI), across various split ratios in double injection and a single injection scenario. The single injection (black line) serves as a baseline, showing a steady increase in hydrogen spread from -200 μs to 400 μs aEOI. In contrast, the double injection with a 3:7 split ratio (green line) starts with the lowest coverage but experiences a significant expansion as the cycle progresses, likely due to a greater volume being injected later, enhancing late-stage mixing. The 5:5 split ratio (red line) demonstrates a balanced expansion, starting moderately and finishing with the highest coverage by 400 μs, suggesting that an even split optimizes hydrogen dispersion throughout the cycle. Meanwhile, the 7:3 split ratio (blue line) starts strong due to a larger initial injection volume, with a sharp increase up to 200 μs, after which it plateaus, indicating early cycle saturation. The trends suggest that a balanced 5:5 ratio might provide the most effective hydrogen coverage, enhancing combustion efficiency, while the skewed ratios (3:7 and 7:3) could be optimized for specific engine dynamics to target early or late injection benefits.

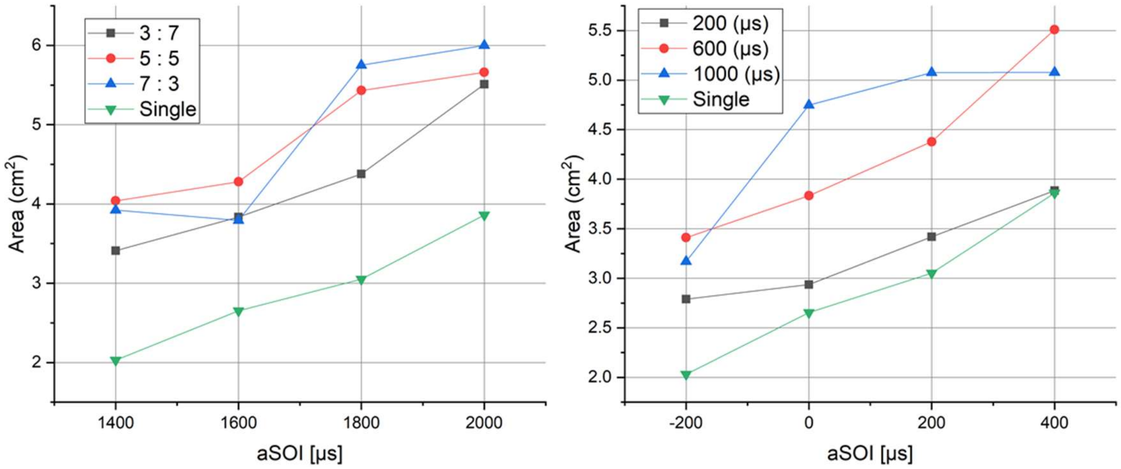

**Figure 9: Calculation of jet area from PLIF images, analyzed by split ratio (left) and dwell time (right). Measurements were taken under conditions of 1.5 MPa ambient pressure, 10 MPa injection pressure, and an injection duration of 1000 μs. The right panel specifically examines area evolution under various dwell times at a constant split ratio of 3:7.**

Figure 9 (right) demonstrates how the area affected by a changes in the dwell time between two injections at different end-of-injection (EOI) timings. It features curves for different dwell times: 200 μs, 600 μs, 1000 μs, and a single pulse configuration. In the single pulse setup, there is a steady, moderate increase in area from -200 μs to +400 μs aEOI, illustrating a consistent expansion effect. For the 200 μs dwell time in double injections, the area shows a linear and gradual increase, eventually equating to the single shot area at an aEOI of 400 μs. This suggests that while shorter dwell times influence the early stages of jet formation, their long-term impact is minimal. In contrast, the 600 μs and 1000 μs settings show more pronounced increases in area, particularly from 0 μs to +400 μs aEOI. The longer dwell times facilitate clearer and more effective impacts, attributed to the interaction where the second injection significantly influences the expansion caused by the first, due to slower dynamics. Overall, this graph highlights that longer dwell times enhance the impacted area, likely due to more favorable fluid dynamics and the maximization of injection momentum.

The PLIF area measurements conducted using surrogate fuels alongside single injections of helium and nitrogen provided valuable insights into the interaction between acetone and fuel diffusivity. Figure 10 provides a comparative analysis of the area affected when using different gases as spray mediums: hydrogen (H2), nitrogen (N2), and helium (He). It clearly shows that the area increases with the timing of laser activation (aSOI in μs) across all three gases. However, the growth patterns and final areas slightly vary by medium.

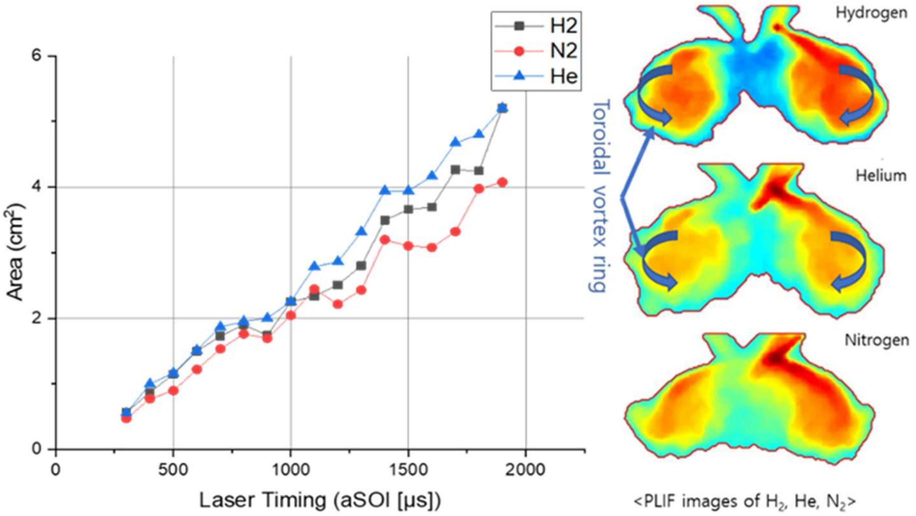

**Figure 10: Jet area variation (left) with different surrogate medium and PLIF structures (right).**

Helium demonstrates the steepest increase in area, particularly noticeable beyond 1000 μs, suggesting it is the most reactive or has the highest expansion rate under these conditions. Nitrogen displays moderate growth, maintaining a steady progression throughout the range. In contrast, hydrogen, although initially following a pattern similar to nitrogen, begins to show a slightly slower increase in area beyond 1500 μs. This analysis indicates that the physical properties of the gas, such as density and atomic/molecular structure, influence the expansion and distribution of the spray when interacting with the laser.

Although hydrogen, with a diffusivity of $1.04 \times 10^{-5}$ Pa/s at 374 K, exhibited the highest diffusivity, its jet area was smaller than that of helium ($2.32 \times 10^{-5}$ Pa/s) but larger than nitrogen ($2.12 \times 10^{-5}$ Pa/s). These findings suggest the potential for using helium and nitrogen as surrogate fuels for hydrogen in non-combustion applications to reduce the risks associated with hydrogen's explosive nature.

The acetone PLIF images in Figure 10 (right) reveal distinctive jet structures for the three different spray gas media: hydrogen, helium, and nitrogen. In the case of hydrogen, the jet structure is notably expansive and exhibits a clear toroidal vortex, indicative of high reactivity and rapid mixing characteristics. Helium, in the middle image, also shows a pronounced toroidal vortex structure but with slightly less spread than hydrogen, suggesting efficient but somewhat lesser mixing compared to hydrogen. This is likely due to helium's lower density and higher diffusion rate. Lastly, the nitrogen image at the bottom depicts a more compact and less defined jet structure, with reduced visible vorticity and a smoother gradient in the color mapping, implying slower mixing dynamics and a denser spray compared to the other gases. This variation in jet structure across the gases highlights the significant impact that the physical properties of different media have on the dynamics and morphology of jet sprays.

## 4. Conclusions

The utilization of PLIF with acetone has proven highly effective in visualizing hydrogen distribution during double injection experiments, confirming acetone's suitability as a tracer for hydrogen vapor and offering valuable insights into cross-sectional distribution, a capability lacking in Schlieren imaging. Implementing a double injection strategy appears promising for augmenting jet area and facilitating flammable mixture formation under elevated ambient pressures. Additionally, PLIF imaging suggests that surrogate fuels like helium and nitrogen provide safer alternatives to hydrogen in non-combustion experiments, with helium recommended for its ability to replicate hydrogen's toroidal vortex ring. While PLIF enables qualitative assessments of fuel distribution, quantitative analysis requires a fixed reference point for precise measurements. This research not only underscores PLIF's effectiveness but also sets the stage for future investigations into injection strategies and safety protocols in hydrogen applications. Furthermore, the analysis of single jet ignition scenarios highlights the critical importance of precise timing and accurate mixture positioning for effective combustion, with implications for optimizing ignition systems to enhance fuel efficiency and reduce emissions. Conversely, misfire scenarios underscore the challenges in achieving reliable ignition, emphasizing factors crucial for maximizing combustion efficiency in hydrogen-based systems. Observations of toroidal vortex ring formations deepen understanding of fluid mechanics in hydrogen dispersion, aiding in injector design and pressure management strategies to improve combustion performance. Further comparisons of jet expansion dynamics under different injection conditions guide optimization strategies, while evaluations of surrogate fuels emphasize the need for reliable reference data to refine combustion models and advance hydrogen-based combustion system efficiency and sustainability.

## References

[1] Curran, S., Onorati, A., Payri, R., et al., "The future of ship engines: Renewable fuels and enabling technologies for decarbonization," International Journal of Engine Research, Vol 25(1), 85-110, 2024. doi:10.1177/14680874231187954.

[2] International Energy Agency, "Global Energy and Climate Model Report," 2023.

[3] International Energy Agency, "CO2 Emissions in 2022 Report," 2023.

[4] International Energy Agency, "Greenhouse Gas Emissions from Energy," 2023.

[5] Hydrogen Storage Tech Roadmap, USDRIVE, Department of Energy, US Government, 2017.

[6] Ma, D., Sun, Z.Y, "Progress on the studies about NOx emission in PFI-H2ICE," International Journal of Hydrogen Energy, Vol 45 (17), 10580-10591, 2020.

[7] Waldron, T., Brin, J., Seitz, H., "Hydrogen Internal Combustion Engine Dyno Test Results with a Driven-Turbo," 11th International Engine Congress 2024.

[8] Muller, A., Feldhaus, F., Thannimmotil, R., Huthwohl, G., Szolak, R., Beutel, P., Rummele, F., "Efficieny emission reduction by the thermal management system CatVap with conventional and synthetic fuels," 11th International Engine Congress 2024.

[9] Stepien, Z., "A Comprehensive Overview of Hydrogen-Fueled Internal Combustion Engines: Achievements and Future Challenges," Energies, Vol 14 (20), 6504, 2021.

[10] Lee, S., Kim, G., Bae, C., "Effect of mixture formation mode on the combustion and emission char-acteristics in a hydrogen direct-injection engine under different load conditions," Applied Thermal Engineering, Vol 209, 118276, 2022.

[11] Lee, S., Kim, G., Bae, C., "Lean combustion of stratified hydrogen in a constant volume chamber," Fuel, Vol 301, 121045, 2021.

# Session 1.2 $H_2$ COMBUSTION CHAMBER DESIGN

# A 1D-3D Numerical Study of a Pent-Roof Spark-Ignition Engine Fueled with Hydrogen Lean Mixtures

L. Sforza[1], F. Ramognino[1], T. Cerri[2], G. G. Gianetti[1], G. D'Errico[1], A. Onorati[1], J. Gomez-Soriano[3], R. Novella[3]

[1]Department of Energy. Politecnico di Milano. Via Lambruschini 4a, 20156 Milano, Italy

[2]Sursum-Mi s.r.l. Via Durando 38, 20158 Milano, Italy

[3]CMT – Clean Mobility & Thermofluids, Universitat Politècnica de València. Camino de Vera s/n, 46022 Valencia, Spain

E-mail: lorenzo.sforza@polimi.it
Telephone: +(39)0223993811

**Abstract.** The spark-ignition (SI) engine technology represents a flexible and low-cost solution to deal with the ongoing decarbonization of the transportation sector. Among the possible energy carriers, hydrogen ($H_2$) is extremely attractive by virtue of theoretical $H_2O$-only emissions at the tailpipe. However, harmful pollutants like nitrogen oxides ($NO_x$) can be easily produced if stoichiometric air-fuel mixtures are used. Therefore, differently from conventional fuels, ultra-lean operations represent a feasible option to hinder $NO_x$ production, thanks to the wide $H_2$ flammability range. In this study, a combined 1D-3D computational fluid dynamics (CFD) investigation is carried out on a research pent-roof SI engine, fueled with premixed $H_2$-air lean mixtures. The 1D study is performed on the full engine layout for a complete characterization of the thermal and fluid-dynamic processes in intake and exhaust systems. Then, a 3D analysis is accomplished focusing on the combustion chamber and a small portion of the intake/exhaust manifolds, where at open ends time-varying boundary conditions are imposed from 1D simulations. Different levels of mixture dilution and load are investigated at constant engine speed. The purpose is twofold: validating the adopted numerical methods and providing insights on the engine design in terms of gas-exchange process and hydrogen lean-combustion development. The achieved results showed a significant impact of the dynamic effects inside the intake/exhaust systems on the cylinder gas-exchange process, in terms of exhaust gases recirculation and evolution of the identified tumble motion. A preliminary combustion investigation on three selected lean conditions showed the capability of both 1D and 3D models in predicting the experimental in-cylinder pressure and heat release traces. Despite a numerical-experimental difference in terms of trapped mass at closed-valves seemed the major source of discrepancy, the reliability of the employed 1D-3D combined approach was demonstrated.

## 1. Introduction

The rapid evolution of the transport sector towards a complete environmental sustainability compels the usage of renewable and carbon-free energy carriers. In this context, the SI engine technology presents several benefits for the $H_2$ employment in powertrains. However, several challenges need to be addressed when hydrogen is used as fuel for internal combustion engines (ICEs) in place of conventional hydrocarbons. For example, pre-ignition or knocking phenomena could be detected within the combustion chamber [1], with the sequential progression of pre-ignition and backfire into the intake manifold.

According to the literature, the exploitation of wide ranges of charge dilution with air or exhaust gas recirculation (EGR), and even water injections, proved to be advantageous in mitigating knock susceptibility and nitrogen oxides ($NO_x$) emissions [2,3], while enhancing engine performance and efficiency [4]. Although hydrogen direct injection into the cylinder is the most attractive option, because it overcomes limitations regarding the volumetric efficiency [5, 6] and a higher probability of abnormal combustion events [7], the port fuel injection (PFI) solution is still nowadays a largely studied approach. First, it allows the usage of less specialized and cheaper engine components [8, 9], enabling faster and more cost-effective the retrofitting of an already existing engine configuration. Second, the PFI eases the study and optimization of the combustion process inside metal engines, thanks to the reduced uncertainties in terms of $H_2$-air stratification.

Numerical approaches are extremely helpful tools to support the experimental research on $H_2$ ICEs. Indeed, numerical calculations can clarify several thermophysical phenomena that are difficult to be understood, especially in metal engines.

According to the literature, numerical investigations were carried out since the start of the twenty-first century. Ma et al. [10] used a zero-dimensional model to calculate the effects of variations in ignition timing and compression ratio, on the performance of a vehicle's hydrogen engine. Full-cycle simulations with a cryogenic PFI strategy were carried out by D'Errico et al. [11,12] with 1D gas dynamic calculations and a quasi-dimensional combustion model.

Concerning 3D-CFD numerical investigations, França et al. [13] selected two lean operating conditions ($\lambda$ = 1.7 at part-load and $\lambda$ = 2.5 at full-load) to assess the capability of the SAGE model in predicting the reaction rate. The effect of injection timing and duration on the homogeneity of $H_2$-air mixtures was investigated through 3D-CFD simulations by Pasa et al. [14] on a PFI flat-head four-cylinder SI engine.

In this work, a numerical investigation of a single-cylinder pent-roof SI engine, where $H_2$ is introduced with a PFI strategy, is carried out by means of a combined 1D-3D CFD analysis. Ultra-lean mixture conditions, with different levels of air dilution and load, are investigated at constant engine speed. Purpose of this study is, first, to validate the selected 1D-3D methodology. Then, to clarify how the engine architecture and the selected operating conditions affect the hydrogen lean-combustion development and the gas-exchange process in terms pressure, trapped mass, flow and turbulence features evolution inside the cylinder.

## 2. Experimental setup

The experimental data used to validate the numerical simulations were gathered from tests conducted on a single-cylinder SI research engine, previously employed in other research endeavors [5,6]. Table 1 provides an overview of the engine main specifications.

**Table 1:** Engine specifications.

| | |
|---|---|
| Number of cylinders | 1 |
| Displaced volume | 454.2 $cm^3$ |
| Cylinder diameter | 82.0 mm |
| Stroke | 86.0 mm |
| Compression ratio | 10.7 |
| Connecting rod length | 144.0 mm |
| Injection systems | PFI & DI |
| Ignition system | Spark plug |
| Valves per cylinder | 2 intake, 2 exhaust |
| Intake Valve opening (IVO)* | 340 CAD |
| Intake valve closing (IVC)* | -135 CAD |
| Exhaust valve opening (EVO)* | 120 CAD |
| Exhaust valve closing (EVC)* | -338 CAD |

**with respect to the firing TDC (0 CAD)*

This paper focuses exclusively on the PFI configuration. In particular, the injector used is a Zavoli JET Injector designed for gaseous fuels, featuring a maximum working pressure of 4.5 bar, a working temperature range from -40°C to 120°C, and a discharge nozzle diameter of 3 mm.

Hydrogen was stored in pressurized tanks and routed through a pressure discharge control system before being delivered to the injector. The injector discharge passes through a 4 mm diameter, 100 mm long tube before being connected to the intake manifold via a T-junction.

The test cell configuration, including pressure and temperature measurement points, fuel injection, and positioning of additional control and measurement instruments, is depicted in Fig. 1. In-cylinder pressure was monitored using a Kistler piezoelectric transducer, while piezoresistive pressure sensors were employed to measure average flow pressures. Air mass flow was quantified using a Kromschroeder volumetric airflow meter, and hydrogen mass flow was tracked utilizing a Bronkhorst F-113AC-1M0-AAD-55-V sensor.

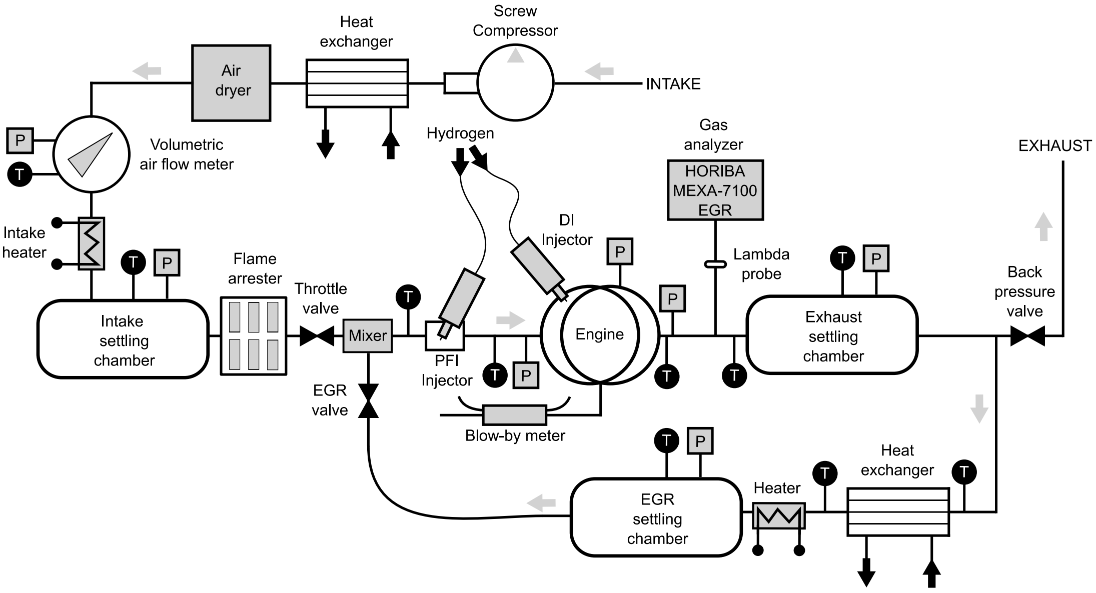
Heat exchanger
Screw Compressor
Air dryer
INTAKE
P
T
Volumetric air flow meter
Hydrogen
Gas analyzer
HORIBA MEXA-7100 EGR
EXHAUST
Intake heater
DI Injector
Lambda probe
Flame arrester
Throttle valve
Back pressure valve
Intake settling chamber
Mixer
PFI Injector
Engine
Exhaust settling chamber
EGR valve
Blow-by meter
Heat exchanger
Heater
EGR settling chamber

**Figure 1:** Test bench layout.

The experimental setup incorporates an online combustion diagnostic software (INDICOM). This software enables real-time monitoring and maintenance of stable values for critical combustion parameters such as indicated mean effective pressure (IMEP), heat release rate (HRR), and combustion phasing (CA50). Further details regarding the test facility equipment and testing methodology can be found in the relevant literature citations.
The set of operating conditions outlined in Table 2 was specifically chosen for the numerical investigation presented in this work.

**Table 2:** Set of operating points used in this study.

| **Operating conditions** | **Engine speed** | **Engine Load** | | $\lambda$ | **Spark-timing** |
|---|---|---|---|---|---|
| **(OC)** | **[rpm]** | **type** | **IMEP [bar]** | **[-]** | **[CAD]** |
| L2.6LL | 1500 | Low load (LL) | 5.1 | 2.6 | -20 |
| L2.4ML | 1500 | Mid load (ML) | 8.5 | 2.4 | -24 |
| L2.6ML | 1500 | Mid load (ML) | 8.5 | 2.6 | -26 |
| L3.0ML | 1500 | Mid load (ML) | 8.7 | 3.0 | -32 |
| L3.4ML | 1500 | Mid load (ML) | 8.6 | 3.4 | -36 |
| L2.6HL | 1500 | High load (HL) | 11.2 | 2.6 | -30 |

# 3. Numerical models

## 3.1. 1D thermo-fluid dynamic model

A discrete system of 1D pipes, characterized by variable cross-sections, is selected to model the entire engine configuration. The unsteady behaviour of the compressible and reacting flow, which evolves inside the engine, is described by solving conservation equations for mass, energy, momentum and species mass fractions, assuming the fluid as a mixture of ideal gaseous species. This quasi-linear hyperbolic system of partial differential equations is solved by means of shock-capturing numerical methods [12, 15].

Combustion is modelled according to a Two-Zone model [16], which considers the closed-valves domain as divided into two homogeneous control volumes: the burned and unburned mixtures.
The ignition delay is predicted through a polynomial function, which takes into account the effect of the mixture composition and whose coefficients were identified in previous studies performed on SI engines fuelled with hydrogen [12, 17].
The heat released by the premixed flame propagation is modelled as source term of burned mixture:

$$\dot{\omega}_b = \rho_u A_l S_t \tag{1}$$

where $A_l$ is the unstretched laminar flame surface and $\rho_u$ the unburned gas density. $S_t$ is the turbulent flame speed, which is estimated according to Zimont correlation [18]:

$$S_t = A \frac{u'^{0.75}}{\alpha_u^{0.25}} L_t^{0.25} \sqrt{S_u} \tag{2}$$

Here, $\alpha_u$ is the unburned mixture thermal diffusivity, $u'$ the turbulence intensity and $L_t$ the integral length scale, while $A$ is a model constant which requires a slight calibration. The laminar flame speed $S_u$ is estimated as:

$$S_u = C_0 S_{u0} \tag{3}$$

where the unstretched laminar flame speed $S_{u0}$ value is retrieved from a lookup table on the basis of the local thermodynamic conditions and mixture properties. The lookup table is built from 1D laminar flame speed calculations at constant-pressure conditions. The parameter $C_0$, instead, is introduced to model the strong hydrodynamical instability observed on lean $H_2$-air flames under typical engine conditions [19]. According to Berger [20], $C_0$ is calculated

$$C_0 = 1 + \left( \left. \frac{S_u}{S_{u0}} \right|_r - 1 \right) \left( \frac{\phi}{\phi_r} \right)^{\gamma_\phi} \left( \frac{T_u}{T_{u,r}} \right)^{\gamma_{T_u}} \left( \frac{p}{p_r} \right)^{\gamma_p} \tag{4}$$

as function of the local air-to-fuel ratio $\phi$, unburned mixture temperature $T_u$ and pressure $p$, on the basis of the following reference conditions: $\left.\frac{S_u}{S_{u0}}\right|_r$ = 2.7 m/s, $\phi_r$ = 0.5, $T_{u,r}$ = 298 K and $p_r$ = 1 bar.
Inside the combustion chamber, the wall heat transfer (WHT) is modelled by means of Woschni approach [21].

### 3.2. 3D model for gas-exchange and combustion

The 3D-CFD simulations are carried out by means of an unsteady Reynolds-averaged Navier-Stokes (U-RANS) approach, in which transport equations for mass, momentum, energy, turbulence and species mass fractions are solved. Time-varying boundary conditions of pressure and temperature are imposed at the open surfaces of the 3D domain, on both the intake and the exhaust pipes. This allows to mimic the dynamics of the average-cycle gas exchange process, without modeling the whole engine schematic.
Fig. 2 depicts the structure of the employed combustion model for 3D-CFD simulations.
The flame front propagation is modelled by solving a transport equation for the regress variable $b$ (unburned gas fraction) [22]

$$\frac{\partial \rho \tilde{b}}{\partial t} + \nabla \cdot \left( \rho \tilde{\mathbf{U}} \tilde{b} \right) + \nabla \cdot \left( \mu_t \nabla \tilde{b} \right) = \rho_u \tilde{S}_u \tilde{\Xi} |\nabla \tilde{b}| + \dot{\omega}_{ign} \tag{5}$$

where $\mu_t$ is the turbulent dynamic viscosity, while $\mathbf{U}$ is the flow speed.
Ignition is included in Eq. 5 by the additional source term

$$\dot{\omega}_{ign} = \frac{C_s \rho_u b}{\Delta t_{ign}} \tag{6}$$

according to the simplified deposition model employed in [23]. The parameters $C_s$ and $\Delta t_{ign}$ allow to calibrate both the strength and the time-duration of the energy released by the ignition system, respectively.

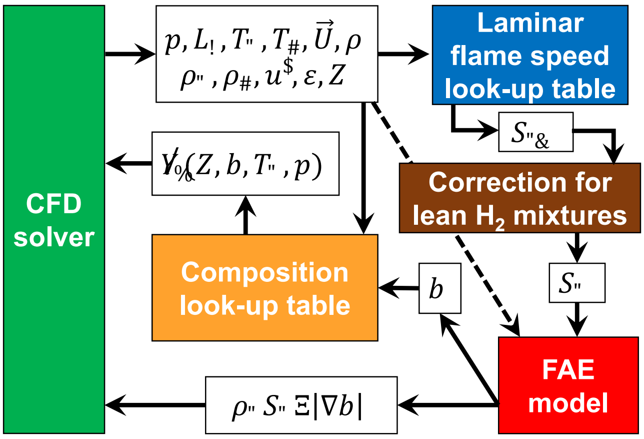
CFD solver
Laminar flame speed look-up table
Correction for lean H2 mixtures
Composition look-up table
FAE model
b

**Figure 2:** Structure of the 3D model used for the combustion stage prediction.

The reaction rate of the premixed combustion is modelled in Eq. 5 (first right hand side term) according to the flame area evolution (FAE) model. Here, the flame wrinkle factor $\Xi$, which represents the turbulent to laminar flame speed ratio $S_t/S_u$, is modelled according to the one-equation approach [24]:

$$\Xi = f \cdot \Xi_{eq} \tag{7}$$

The laminar-to-turbulent transition process, taking place after the ignition event, is modeled by the $f$ parameter, whose value is computed according to Herweg and Maly [25] and where the kernel radius evolution is estimated through the simplified 0-D sub-model proposed by Sforza et al. [23].
The equilibrium wrinkle factor $\Xi_{eq}$ of Eq. 7 is modelled according to Peters [26]:

$$\Xi_{eq} = 1 - \frac{a_4 b_3^2}{2b_1}\frac{L_t}{\delta_l} + \left[\left(\frac{a_4 b_3^2}{2b_1}\frac{L_t}{\delta_l}\right)^2 + a_4 b_3^2 \frac{u'}{S_u}\frac{L_t}{\delta_l}\right]^{1/2} \tag{8}$$

where $a_4 = b_3 = 0.78$ and $b_1 = 2.3$ are model constants taken from [26] and slightly calibrated.
The $S_u$ value is predicted consistently to the 1D approach displayed in previous sub-section (Eqs. 3 and 4), while the chemical composition is estimated as

$$Y_i = b \cdot Y_{u,i} + (1-b) \cdot Y_{b,i} \tag{9}$$

where the mass fraction of each species is calculated as function of its values in the burned $Y_b$ and unburned state $Y_u$, according to the local $b$ value. Both $Y_b$ and $Y_u$ are retrieved from a specific lookup table, where the $Y_b$ value is recovered at equilibrium conditions.

## 4. Numerical setup

The 1D study of the selected SI engine is carried out with Gasdyn, a software developed by the authors and already validated also on $H_2$-fuelled ICEs [12, 27].
The 1D engine schematic is built according to the experimental test bench of Fig. 1, but including a few simplifications on both the intake and exhaust systems. Fig. 3 displays a portion of the 1D model schematic as shown by the software graphical user interface (GUI).
The 1D computational grid is characterized by different resolutions along the engine schematic. In particular, a base cell size of 10 mm is employed over all intake and exhaust pipes, while a specific refinement is applied in between the $H_2$ PFI and the cylinder, where the mesh grid is reduced to 2.5 mm.
All 1D simulations are carried out by imposing pressure and temperature boundary conditions at both inlet and outlet ends of the engine, resorting to the available measured values. Similarly, the wall temperatures of the combustion chamber (piston, cylinder head and liner) are retrieved from experimental

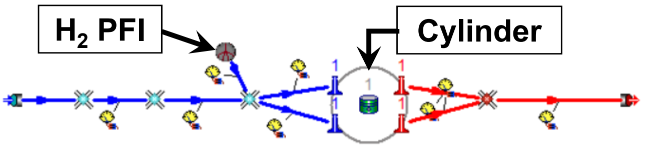

**Figure 3:** 1D model schematic used on Gasdyn software: zoom over the cylinder and the PFI location of hydrogen.

measurements. In particular, 15 consecutive engine cycles are simulated for each operating condition of Table 2, imposing as simulations target the experimental $\lambda$ value.

For what concerns the power-cycle simulation, turbulence is considered by means of the K-k model [28], while pressure is assumed homogeneous inside the whole closed-valves domain.

The lookup table for the $S_{u0}$ calculation (Eq. 3) is generated through a series of 1D laminar flame speed calculations performed in the OpenSMOKE framework [29] at constant pressure $p$, unburned gas temperature $T_u$ and fuel-to-air equivalence ratio $\phi$ conditions. The $p$, $T_u$ and $\phi$ values are then varied within the following a-priori defined intervals, in order to cover all thermodynamic states of the investigated operating conditions. As preliminary assumption, the EGR effect on the $S_{u0}$ calculation is neglected.

The 3D gas-exchange process is simulated inside a domain which includes only the cylinder and a small portion of both intake and exhaust manifolds, as shown by Fig. 4a. The dynamic behaviour of the whole engine system is properly considered by imposing 1D time-varying pressure and temperature conditions at the open ends of the considered volume (*inlet* and *outlet* sections of Fig. 4a). Moreover, an additional saving of the computational effort is achieved by exploiting the symmetrical features of Fig. 4a region, with respect to the Y-normal plane crossing the spark-plug. The resulting halved 3D domain, which is used in this work, is represented over two views in Fig. 4b, with the piston positioned at the top dead center (TDC).

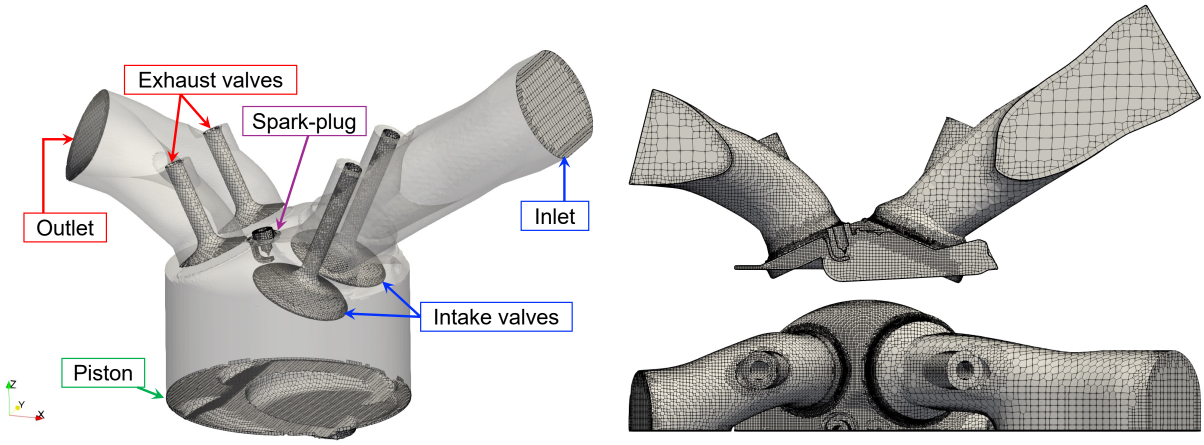

**(a)** **(b)**

**Figure 4:** Overview of the numerical 3D domain selected for the gas-exchange simulations. (a) Full-domain representation. (b) Actual domain used for CFD simulations, represented with the piston at the TDC: side and top views.

A multi-mesh approach is employed to simulate the gas-exchange process. This methodology consists of two different steps, which are handled with a semi-automatic routine. First, a series of meshes is created to cover the whole engine cycle. Then, 3D-CFD simulations are carried out over each mesh previously generated. For more details about this methodology, the reader is referred to [30].

The power-cycle stage, instead, is simulated with a mesh confined to the closed-valve domain, with a dynamic addition/removal of cells layers to mimic the piston motion.

For the gas-exchange simulations, a hex-dominant base mesh size of 4 mm is employed over the whole selected domain and maintained in both intake and exhaust ducts, far from the valves. Then, several refinements are applied to adequately capture the engine geometrical details and the main flow features in narrow gaps, as well as inside the combustion chamber. In particular, according to previous studies [31, 32], inside the cylinder a maximum cell size of 1 mm is ensured to properly model all flow and turbulence scales. Moreover, inside the gap between each valve and its seat, at least five cells are guaranteed along the perpendicular direction to the flow velocity field. To satisfy this limit, the smallest cell dimension is reduced to $\approx 50$ $\mu$m at the minimum lift position, which is assumed equal to 0.25 mm according to Nodi et al. [32]. Finally, a boundary layer of 1 cell is applied to all boundaries of the considered CFD domain.

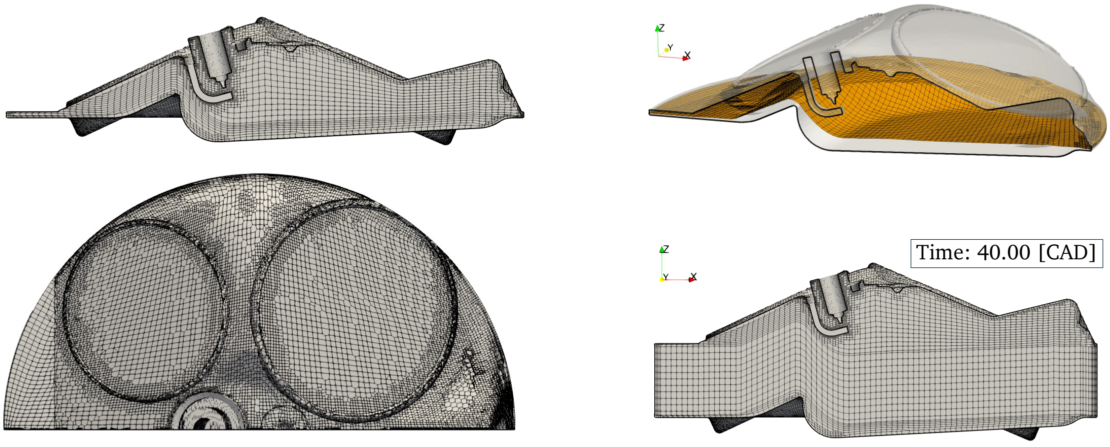

**(a)** **(b)**

**Figure 5:** Mesh employed for the 3D power-cycle simulation. (a) Actual domain used for CFD simulations, represented with the piston at the TDC: side and top views. (b) Piston motion simulation: mesh surface where layers of cells are added/removed (top); mesh with piston at 40 CAD after TDC (bottom).

The modeling of the power-cycle, instead, is carried out with a computational domain confined to the in-cylinder region, as depicted in Fig. 5a. To maximize the consistency with the gas-exchange modeling, the engine symmetry with respect to the spark-plug crossing plane is exploited, and a hex-dominant mesh is generated at the TDC. To accommodate the piston displacement, the dynamic addition/removal of cells layers is applied from the mesh surface highlighted in the top Fig. 5b. An example of the mesh structure with the piston positioned far from the TDC is shown by the bottom picture of Fig. 5b.

The gas-exchange simulations are all started at the exhaust valve opening (EVO). At this time instant, the in-cylinder pressure and temperature values are initialized according to the results retrieved from 1D simulations, which are carried out prior the 3D analysis and considering the whole engine schematic. A similar strategy is used for the intake and exhaust manifolds, but pressure and temperature values sampled nearby the valves seats are used. For what concerns the mixture composition, fully burned products from perfect oxidation are initialized inside the cylinder and the considered exhaust manifold. A perfectly homogeneous premixed air-fuel mixture, instead, is assumed inside the intake duct, because the PFI process is not modelled in this 3D investigation. Both fresh and burned mixtures compositions are varied over each operating condition, according to $\lambda$ values reported in Table 2.

As previously mentioned, time-varying boundary conditions of pressure and temperature are imposed at the open inlet and outlet sections, according to 1D simulations results. The experimental values of wall temperatures are used inside the combustion chamber, while for the intake and exhaust manifold the wall temperatures assumed during the 1D analysis are adopted.

Turbulence is modelled by means of the standard k-ε model, using the coefficients suggested in the literature [16]. Scalable wall-functions are applied at the single-cell boundary layer, to model the near-wall behaviour of turbulence and thermal diffusivity. The same lookup table used for the 1D analysis is adopted for the $S_{u0}$ calculation (Eq. 3), while the lookup table for the burned mixture composition (Eq. 9, $Y_{b,i}$ values) is generated with homogeneous reactor calculations, as described by Lucchini [33].

The mesh generation and all 3D CFD simulations are carried out with Lib-ICE, which is a set of solvers and libraries based on the OpenFOAM® open-source platform and where the presented numerical models are implemented by the authors.

# 5. Results and discussion

## 5.1. Gas-exchange process

### *5.1.1. Cylinder pressure*

To deeply clarify the engine behaviour in terms of in-cylinder pressure evolution, the operating condition (OC) *L2.6ML* is selected as reference, because almost central with respect to Table 2 conditions in terms of both air-fuel ratio ($\lambda$) and load (IMEP) variations.

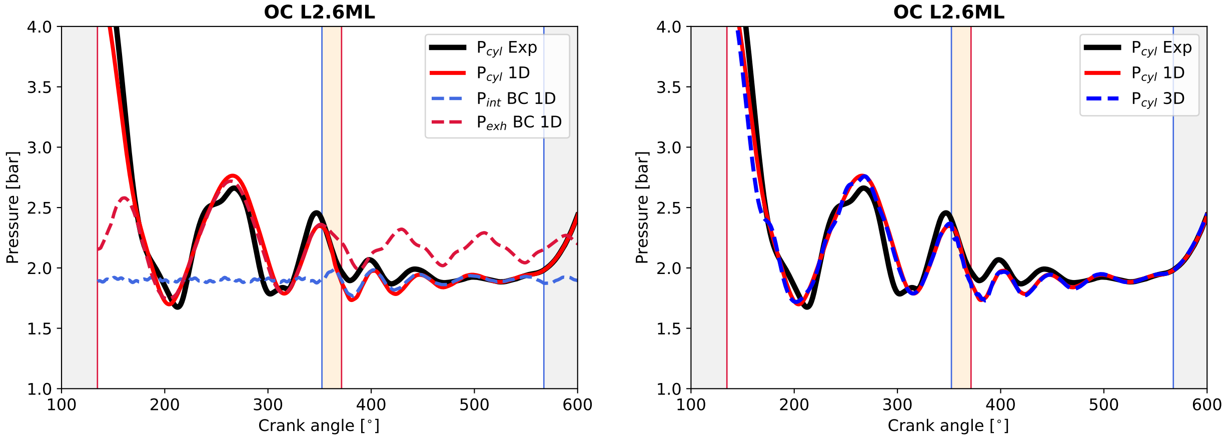

**(a)** **(b)**

**Figure 6:** OC L2.6ML: evolution of the in-cylinder pressure during the gas-exchange process. (a) Comparison between measured (Exp) and 1D calculated traces, together with 1D pressure evolution nearby intake ($P_{int}$ BC) and exhaust ($P_{exh}$ BC) valves. (b) Comparison between measured (Exp), 1D and 3D calculated traces. Vertical red lines identify EVO and exhaust valve closing (EVC) instants, while blue ones intake valve opening (IVO) and intake valve closing (IVC) times (from left to right, respectively). The overlap stage is identified by the orange area, while the closed-valve phase is highlighted in grey.

Fig. 6a compares the experimental against the 1D pressure traces inside the cylinder, during the gas-exchange process. As it can be observed, a satisfactory agreement is achieved between measurements and calculations. The 1D model seems able to capture the dynamic effects produced by both intake and exhaust systems on the in-cylinder behaviour. In fact, during the exhaust stage (in between the two vertical red lines), the spontaneous discharge process seems to trigger a high-intensity wave effect inside the exhaust pipe, as predicted by 1D calculations immediately after the exhaust valves (red dashed line, with initial pressure oscillation amplitude of $\approx$ 0.5 bar). This phenomenon, which is gradually damped over time, strongly affects the in-cylinder pressure value until the first part of the intake stage. Indeed, by observing the 1D pressure evolution predicted immediately upstream the intake valve (blue dashed line), a signal oscillation is started after the IVO instant (first vertical blue line, from left). This generates a dynamic effect on the intake pipe, which affects the cylinder filling during almost all the intake process. Finally, it is worth to notice how the in-cylinder pressure value is higher than the intake one during almost the whole overlap stage (orange area). Therefore, a significant back-flow of exhaust gases is expected to be conveyed into the intake manifold.

Fig. 6b compares the experimental and the 1D in-cylinder pressure traces against the 3D results. The 1D-3D agreement is excellent, demonstrating how the selected approach for the 1D-3D coupling is reliable for this engine configuration.

All previous observations discussed for the OC L2.6ML can be similarly extended to other conditions of Table 2. In particular, 1D simulations demonstrated to be essential in clarifying the dynamic effects of both exhaust and intake manifolds. These phenomena are observed to be significant for the present engine configuration and they must be properly captured to replicate the in-cylinder pressure trace.

### *5.1.2. Trapped mass*

Following the same approach for the in-cylinder pressure analysis, the OC L2.6ML is selected as reference condition for a detailed analysis of the in-cylinder total trapped mass evolution.

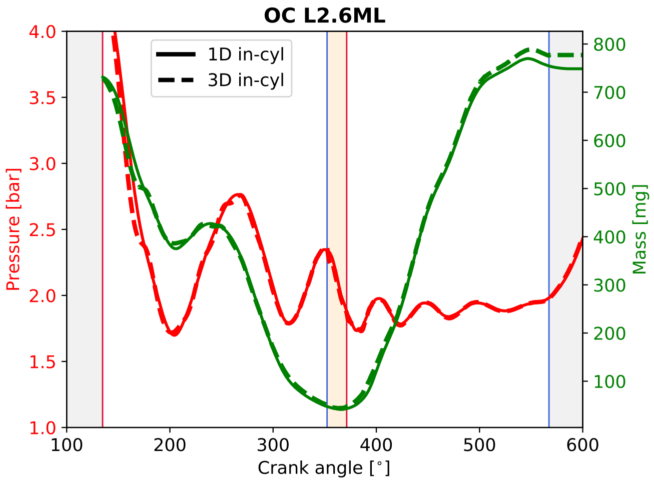

**Figure 7:** OC L2.6ML: comparison between numerical 1D (solid lines) and 3D (dashed lines) evolution of the in-cylinder trapped mass (in green), together with the in-cylinder pressure trace (in red), during the gas-exchange process. Vertical red lines identify EVO and EVC instants, while blue ones IVO and IVC times (from left to right, respectively). The overlap stage is identified by the orange area, while the closed-valve phase is highlighted in grey.

Fig. 7 shows both 1D and 3D results in terms of in-cylinder trapped mass evolution during the gas-exchange process (green curves). An overall agreement between 1D and 3D results is observed, proving the consistency of the employed 1D-3D coupling. This is true despite a small discrepancy is detected nearby the IVC (vertical blue line on the right), which can be attributed to differences in terms of discharge coefficient across the intake valves seats.

Focusing, instead, on the exhaust stage (in between the two vertical red lines), after the spontaneous discharge process (from EVO to 200 CAD) an in-cylinder mass increase can be observed in the 200-230 CAD time frame. This is caused by the pressure dynamic effect in the exhaust pipe, previously observed in Fig. 6a, which reverses the flow direction back to the cylinder, causing the pressure rise shown by the red curves between 200-250 CAD (Fig. 7).

Another aspect that needs to be clarified is the cylinder scavenging during the overlap stage. Looking at the orange area of Fig. 6a, it can be observed a positive pressure drop from the exhaust to the intake pipes (from red dashed line to the blue dashed line, respectively) over the whole phase. This generates a recirculation of the in-cylinder exhaust gases into the intake manifold, encompassing the entire overlap stage. As a consequence, the in-cylinder volume scavenging is not properly fulfilled, with an internal EGR amount estimated by 1D calculation between 3% and 4.7% for the selected operating conditions (Table 2).

Finally, by observing the green lines of Fig. 7 near the IVC time (vertical blue line on the right), a weak reverse flow back to the intake pipes can be noticed. This is caused by the combined influence of an in-cylinder pressure increase (compression stroke has started) and a negative phasing of the dynamic effects inside the intake pipe (local descending pressure), as shown by Fig. 6a near the vertical blue line on the right.

The present phenomenon, as well as previous observations discussed for the OC L2.6ML can be extended to other conditions of Table 2.

Fig. 8 compares the measured and the calculated in-cylinder trapped mass values over each OC, showing how the experimental trend (black bars distribution) is consistently captured by both 1D and 3D numerical simulations. From a quantitative point of view, computed results always overestimate the measured value. As reported in Fig. 8b, 1D simulations over-predict the experimental in-cylinder trapped mass in between 2% (L2.6ML) and 7% (L2.6LL). This differences are mirrored to 3D simulations, on the basis of the 1D-3D coupling. In fact, the blue bars trend is consistent with the red bars one, but

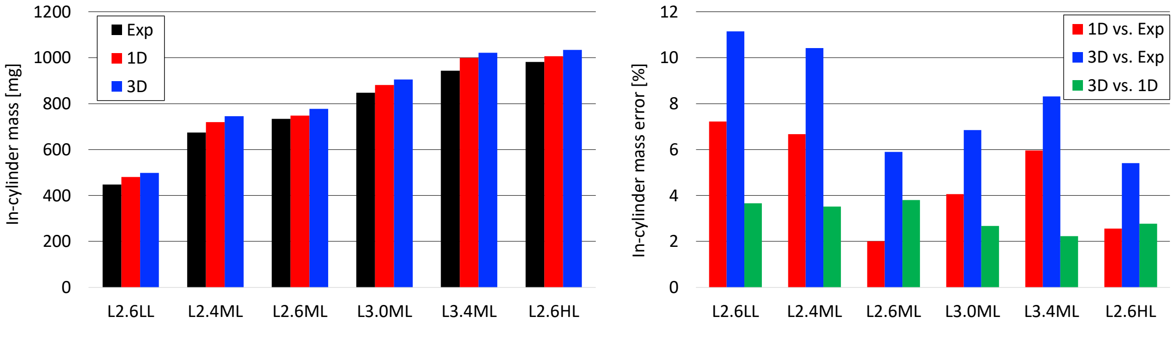

(a) (b)

**Figure 8:** Comparison between values of in-cylinder total trapped mass. (a) Comparison between measured (Exp.), 1D and 3D calculations. (b) Relative discrepancies of 1D-Exp, 3D-Exp and 3D-1D values.

characterized by a higher discrepancy towards the measured reference. This aspect is motivated by the 1D-3D misalignment previously discussed for the OC L2.6ML near the IVC (green lines of Fig. 7), which slightly varies between 2.2% (L3.4ML) and 3.8% (L2.6ML) among the studied conditions (green bars).

### *5.1.3. Cylinder flow and turbulence features*

In accordance to previous discussions, the OC L2.6ML is selected as reference condition for a deep understanding of the in-cylinder flow motion and the related turbulence evolution.

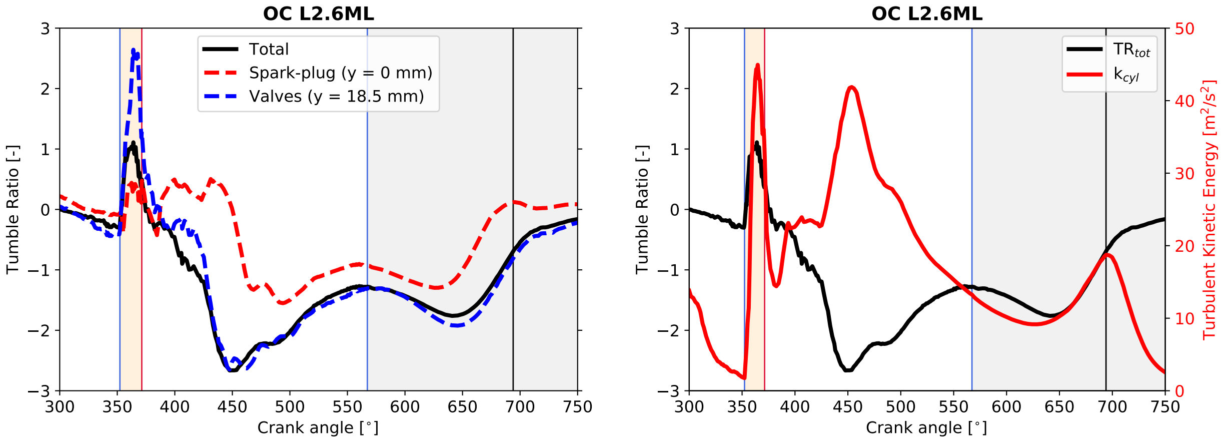

(a) (b)

**Figure 9:** OC L2.6ML. (a) Comparison between the tumble ratio calculated on the: 3D-CFD cylinder domain of Fig. 4b (black); plane crossing the spark-plug (red); plane crossing the exhaust/intake valve axis (blue). (b) Comparison between the tumble ratio calculated on the overall cylinder domain (black) and the average in-cylinder turbulent kinetic energy (red). The vertical red line identifies the EVC instant, while blue vertical lines the IVO and IVC times (from left to right, respectively). The vertical black line spots the spark-timing. The overlap stage is identified by the orange area, while the closed-valve phase is highlighted in grey.

Fig. 9a reports the tumble ratio (TR) evolution inside the cylinder, shown from the IVO (first vertical blue line, on the left) to the spark-timing (vertical black line). In particular, different approaches and positions for calculating the TR are employed and compared. The total tumble value (black line), calculated considering the energy of the whole 3D-CFD cylinder domain of Fig. 4b, is plotted against the TR (red line) computed on the plane crossing the spark-plug (namely, the symmetry plane of Fig. 4b) and the TR (blue line) evaluated on the plane crossing the exhaust/intake valve axis (shifted of 18.5 mm from the symmetry plane of Fig. 4b).

First, during the overlap stage (orange area), a significant discrepancy is observed among the three values, with the most intense tumble motion detected under the exhaust/intake valves plane. This is caused by a clock-wise tumble motion, which is generated prior the EVC (vertical red line of Fig. 9a).

After the EVC, instead, the evolution of the total tumble ratio becomes fully consistent with the one calculated on the valves plane, with a reversal of rotation if compared to the overlap phase (change of sign). On the other hand, the TR value estimated on the spark-plug plane is always lower than the total one, becoming almost negligible at the spark-timing (Fig. 9a, vertical black line). This demonstrates how the overall tumble features of this 4-valve engine architecture, calculated considering the total domain energy, are mainly driven by the flow characteristics under the exhaust/intake valves group from EVC to spark-timing.

Fig. 9b compares the evolution of the turbulent kinetic energy inside the cylinder (red line), together with the total TR trace (black line). As it can be observed, three different peak values can be detected. The first, during the overlap phase, is related to the generation of the clockwise rotating tumble. The second, in the middle of the intake stage ($\approx$450 CAD), is produced by the formation of the counter-clockwise rotating tumble. The third one, instead, is observed near the spark-timing and it is caused by the gradual decay of the tumble motion created during the intake process (Fig. 9b, between 650 and 700 CAD).

The present results, as well as previous observations discussed for the OC L2.6ML can be similarly extended to other conditions of Table 2.

### 5.2. Combustion analysis

In the light of the discrepancies in terms of in-cylinder trapped mass between computed results (both 1D and 3D) and experimental measurements, previously identified by Fig. 8b, a preliminary analysis of the combustion process is carried out only on selected OCs. The purpose is to clarify if the employed 1D and 3D numerical combustion models are able to mimic the experimental observations in presence of lean hydrogen-air mixtures, while a comprehensive analysis of all conditions of Table 2 is left to a future work.

In particular, to maximise the numerical-experimental consistency in terms of energy amount available in the cylinder during the closed-valves phase, the 3D temperature field at the IVC is re-scaled to match the experimental total trapped mass value. On the other hand, 1D power-cycle simulations (15 consecutive cycles) are performed without any modifications on IVC conditions, to assess the model capabilities in predicting the overall steady-state behaviour of each OC of Table 2.

Top row images of Fig. 10 compare the measured pressure traces inside the cylinder against 1D and 3D results, in presence of an increasing air dilution (from left to right). For the sake of clarity, here crank-angles are shifted of 720 CAD with respect to previous figures, to center the 0 CAD value with the studied TDC of firing.

First, from experiments, it can be observed an almost similar pressure evolution over the three selected OCs, in terms of phasing and magnitude of each peak value, as well as general shape of the curve. This is consistent with the target of the experimental campaign, where modifications on the spark-timings (Table 2) and of the intake/exhaust conditions are applied to fulfill the same IMEP. Concerning the numerical results, both 1D and 3D approaches seems able to replicate with a satisfactory accuracy the experiments, despite a few discrepancies.

To clarify the 1D-3D predicting capabilities of the different stages of the combustion process, also identifying possible aspects that need improvement, the AHRR traces are reported in the bottom row images of Fig. 10. These results are calculated by means of the same post-processing approach on both experimental and numerical pressure traces, to ensure consistency.

The prediction of the laminar-to-turbulent transition stage seems much more accurate in 3D simulations, with a smooth initial ramp-up of the heat release rate. On the contrary, a sharper variation is detected on 1D results.

Moving to the turbulent combustion stage, observed over all cases in the -20/0 CAD interval, both 1D and 3D models show a tendency in underestimating the AHRR growth rate by increasing the air dilution (moving from picture (d) to (f)). This can be ascribed to an underestimation of the laminar flame speed under such air dilution values. In fact, the correlation proposed by [20] (see Eq. 4), used to model the thermo-diffusive instability effects of lean hydrogen flames, was developed for air-fuel ratios limited to $\lambda \leq 2.5$.

It is worth to observe how the AHRR peak values estimated by 3D simulations are much more consistent to experimental data, if compared to the 1D model predictions. In particular, the most significant 1D-

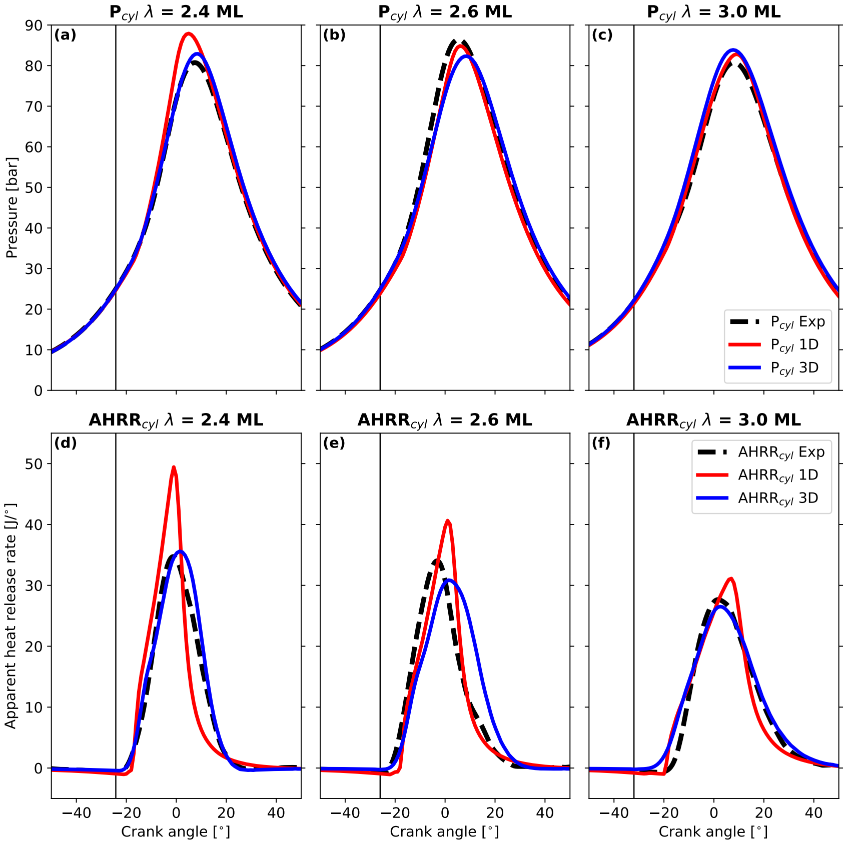

**Figure 10:** Impact of the air-dilution on the combustion process at fixed load conditions ($\lambda$ effect at mid load). Comparison between experimental measurements (dashed black lines), 1D (red lines) and 3D (blue lines) results in terms of pressure trace (top row) and apparent heat release rate (AHRR) (bottom row) evolution. The air dilution is increased from left - (a) and (d) images - to right - (c) and (f) images. The vertical black line spots the spark-timing.

experimental discrepancy is detected for the OC L2.4ML (Fig. 10d). This aspect can be attributed to differences in terms of in-cylinder energy content, being condition L2.4ML characterized by the highest $\lambda$ value and the maximum total trapped mass error (see Fig. 8b, red bars) among medium load conditions. Finally, the modeling of the combustion completion stage seems significantly affected by the accuracy in reproducing the previous turbulent combustion stage and the related peak value of AHRR. This is demonstrated by the numerical results of Fig. 10d, where the 3D-experimental agreement is excellent, while 1D results are significantly affected by the longer turbulent combustion stage, hence higher AHRR peak.

According to the achieved results, this preliminary analysis showed an overall satisfactory capability of both 1D and 3D models in predicting the experimental combustion process, when lean hydrogen mixtures are employed. Nevertheless, the 1D-experimental discrepancy in terms of total in-cylinder trapped mass showed to be the most impacting aspect on the results accuracy. Therefore, this issue must be addressed by future works.

## 6. Conclusions

In this work, an hydrogen-fuelled SI engine, characterized by a pent-roof architecture and a PFI strategy, is studied with a combined 1D-3D CFD investigation. The 1D analysis involved the entire engine layout, while 3D simulations are carried out on a confined domain including the combustion chamber and a small portion of the intake/exhaust manifolds. The 1D-3D coupling is fulfilled by imposing 1D time-varying boundary conditions at the open ends of the 3D domain.

The selected approach is validated against experimental measurements of in-cylinder pressure evolution and total trapped mass at closed valves of six different operating conditions, where variations of air dilution ($\lambda$) and load (IMEP) are separately studied. Despite 1D simulations over-predict the experimental in-cylinder trapped mass in between 2% and 7%, the agreement in terms of pressure evolution during the gas-exchange process is rather satisfactory.

The employed strategy to couple 1D and 3D simulations demonstrated to be reliable for this engine configuration. Both 1D and 3D in-cylinder pressure trends showed to be almost identical during the gas-exchange process. A small discrepancy is only observed in terms of total trapped mass at the IVC, which can be attributed to differences in terms of discharge coefficient across the intake valves seats.

Therefore, the achieved 1D-3D results are used to provide insights on the engine design in terms of gas-exchange process and hydrogen lean-combustion development. During the gas-exchange phase, the dynamic effects of both exhaust and intake manifolds play a significant role in terms of exhaust gases recirculation and evolution of the identified tumble motion. In particular, the in-cylinder volume scavenging is not properly fulfilled during the overlap stage, because a negative phasing of the pressure wave inside the intake pipe produces a back-flow of exhaust gases into the intake manifold. This generates a clock-wise tumble motion inside the cylinder, prior the EVC. Afterwards, when the fresh air-hydrogen mixture starts to flow inside the cylinder, a reversal of tumble rotation is observed. The tumble ratio TR value, estimated on different planes, demonstrated how from EVC to spark-timing the overall tumble features are mainly driven by the flow characteristics under the exhaust/intake valves plane, instead those under the central spark-plug.

The combustion process is finally investigated on selected operating conditions, characterized by the same load but different air dilution values. This preliminary analysis showed an overall satisfactory capability of both 1D and 3D models in predicting the experimental observations in terms of pressure and heat release rate evolution, which demonstrated to be almost similar over the three selected operating conditions. Despite the thermo-diffusive instability effects seem underestimated on the computed laminar flame speed enhancement, especially when $\lambda > 2.5$, the major source of discrepancy is believed to be introduced by the 1D-experimental difference in terms of total in-cylinder trapped mass. However, both aspects must be addressed by future works.

## 7. Acknowledgments

This work has been supported by the project ”Digital Twin Technology for the Development of LP-DI Hydrogen engine for heavy-duty applications (DHyCE-HD)”, funded by the MIUR Progetti di Ricerca di Rilevante Interesse Nazionale (PRIN) 2022 - grant 2022W2FEZ8.

## References

[1] CM White, RR Steeper, and AE Lutz. The hydrogen-fueled internal combustion engine: a technical review. *International journal of hydrogen energy*, 31(10):1292–1305, 2006.

[2] Muhammad Khristamto Aditya Wardana and Ocktaeck Lim. Investigation of ammonia homogenization and NOx reduction quantity by remodeling urea injector shapes in heavy-duty diesel engines. *Applied Energy*, 323(June 2021):119586, 2022.

[3] Winklhofer, Ernst, Jocham, Bernhard, Philipp, Harald, Kapus, Paul, Leitner, Daniel, Heindl, Rene, and Diniz-Netto, Nilton. Hydrogen ice combustion challenges. In *16th International Conference on Engines Vehicles*. SAE International, aug 2023.

[4] Sebastian Verhelst and Thomas Wallner. Hydrogen-fueled internal combustion engines. *Progress in Energy and Combustion Science*, 35(6):490–527, 2009.

[5] S Molina, R Novella, J Gomez-Soriano, and M Olcina-Girona. Impact of medium-pressure direct injection in a spark-ignition engine fueled by hydrogen. *Fuel*, 360:130618, 2024.

[6] V De Bellis, M Piras, F Bozza, E Malfi, R Novella, J Gomez-Soriano, and M Olcina-Girona. Development and validation of a phenomenological model for hydrogen fueled pfi internal combustion engines considering thermo-diffusive effects on flame speed propagation. *Energy Conversion and Management*, 308:118395, 2024.

[7] Sebastian Verhelst. Recent progress in the use of hydrogen as a fuel for internal combustion engines. *International Journal of Hydrogen Energy*, 39(2):1071–1085, 2014.

[8] Andy Thawko, Shalom Adam Persy, Amnon Eyal, and Leonid Tartakovsky. Effects of Fuel Injection Method on Energy Efficiency and Combustion Characteristics of SI Engine Fed with a Hydrogen-Rich Reformate. *SAE Technical Papers*, (2020):1–12, 2020.

[9] G Maio, A Boberic, L Giarracca, D Aubagnac-Karkar, O Colin, F Duffour, K Deppenkemper, L Virnich, and S Pischinger. Experimental and numerical investigation of a direct injection spark ignition hydrogen engine for heavy-duty applications. *International Journal of Hydrogen Energy*, 47(67):29069–29084, 2022.

[10] Jie Ma, Yongkang Su, Yucheng Zhou, and Zhongli Zhang. Simulation and prediction on the performance of a vehicle's hydrogen engine. *International Journal of Hydrogen Energy*, 28(1):77–83, 2003.

[11] G. D'Errico, A. Onorati, S. Elgas, and A. Obieglo. Thermo-Fluid Dynamic Simulation of an Single-Cylinder $H_2$ Engine and Comparison with Experimental Data. *ASME Paper*, ICES2006-1311, 2006.

[12] Gianluca D'Errico, Angelo Onorati, and Simon Ellgas. 1d thermo-fluid dynamic modelling of an s.i. single-cylinder $h_2$ engine with cryogenic port injection. *International Journal of Hydrogen Energy*, 33(20):5829–5841, 2008.

[13] França, Louise Bomfim Magalhães, Pasa, Bruno Roberto, Fagundez, Jean Lucca Souza, Pereira, Juliano Silveira, Martins, Mario Eduardo Santos, Lanzanova, Thompson Diórdinis Metzka, and Salau, Nina Paula Gonçalves. Validation of a cfd hydrogen combustion model on an pfi si engine under lean combustion. In *SAE Brasil 2023 Congress*. SAE International, jan 2024.

[14] Pasa, Bruno Roberto, Fagundez, Jean Lucca Souza, Martins, Mario Eduardo Santos, Salau, Nina Paula Gonçalves, Cogo, Vitor Vielmo, Prante, Geovane Alberto Frizzo, and Wittek, Karsten. Numerical analysis of the influence of soi and injection duration on the homogenization of hydrogen-air mixtures in a pfi si engine under lean operation. In *SAE Brasil 2023 Congress*. SAE International, jan 2024.

[15] A. Onorati, G. Ferrari, and G. D'Errico. 1d unsteady flows with chemical reactions in the exhaust duct-system of s.i. engines: Predictions and experiments. *SAE Transactions*, 110:738–752, 2001.

[16] T. Poinsot and D. Veynante. *Theoretical and Numerical Combustion*. Edwards, 2005.

[17] S. D. Hires, R. J. Tabaczynski, and J. M. Novak. The prediction of ignition delay and combustion intervals for a homogeneous charge, spark ignition engine. In *1978 Automotive Engineering Congress and Exposition*. SAE International, feb 1978.

[18] A. N. Lipatnikov and J. Chomiak. Turbulent Flame Speed and Thickness: Phenomenology, Evaluation and Application in Multi-Dimensional Simulations. *Progress in Energy and Combustion Science*, Vol. 28:pp. 1–73, 2002.

[19] Hongchao Chu, Lukas Berger, Temistocle Grenga, Zhao Wu, and Heinz Pitsch. Effects of differential diffusion on hydrogen flame kernel development under engine conditions. *Proceedings of the Combustion Institute*, 2022.

[20] Lukas Berger, Antonio Attili, and Heinz Pitsch. Intrinsic instabilities in premixed hydrogen flames: parametric variation of pressure, equivalence ratio, and temperature. part 2 – non-linear regime and flame speed enhancement. *Combustion and Flame*, 240:111936, 2022.

[21] G. Woschni. Universally Applicable Equation for the Instataneous Heat Transfer Coefficient in the Internal Combustion Engine. *SAE Paper*, 670391, 1967.

[22] H. G. Weller, G. Tabor, A. D. Gosman, and C. Fureby. Application of a Flame-Wrinkling LES Combustion Model to a Turbulent Mixing Layer. *Proceedings of the Twenty-Seventh Combustion Symposium (International)*, 1998.

[23] L. Sforza, T. Lucchini, G. Gianetti, and G. D'Errico. Development and validation of si combustion models for natural-gas heavy-duty engines. *SAE Technical Papers*, 2019.

[24] Lorenzo Sforza, Tommaso Lucchini, and Gianluca D'Errico. 3d-cfd methodologies for a fast and reliable design of ultra-lean si engines. In *CO2 Reduction for Transportation Systems Conference*. SAE International, jun 2022.

[25] R. R. Maly and R. Herweg. A Fundamental Model for Flame Kernel Formation in SI Engines. *SAE Paper*, 922243, 1992.

[26] N. Peters. *Turbulent Combustion*. Cambridge University Press, 2000.

[27] Alberto Ballerini, Tarcisio Cerri, Andrea Massimo Marinoni, and Angelo Onorati. Advances in 1d thermo-fluid dynamic simulation of si hydrogen-fueled engine. *Journal of Physics: Conference Series*, 2385(1):012055, dec 2022.

[28] G. D'Errico, G. Ferrari, A. Onorati, and T. Cerri. Modeling the Pollutant Emissions From a S.I. Engine. *SAE Paper*, 2002-01-0006, 2002.

[29] Alberto Cuoci, Alessio Frassoldati, Tiziano Faravelli, and Eliseo Ranzi. Numerical modeling of laminar flames with detailed kinetics based on the operator-splitting method. *Energy & Fuels*, 27(12):7730–7753, 2013.

[30] Tommaso Lucchini, Gianluca D'Errico, Hrvoje Jasak, and Zeljko Tukovic. Automatic mesh motion with topological changes for engine simulation. *SAE Paper*, 2007.

[31] T. Lucchini, G. D'Errico, D. Paredi, L. Sforza, and A. Onorati. CFD Modeling of Gas Exchange, Fuel-Air Mixing and Combustion in Gasoline Direct-Injection Engines. *SAE Technical Papers*, 2019.

[32] Nodi, Alessandro, Sforza, Lorenzo, Lucchini, Tommaso, Onorati, Angelo, Buttitta, Marco, and Marmorini, Luca. Cfd modeling of conventional and pre-chamber ignition of a high-performance naturally aspirated engine. In *WCX SAE World Congress Experience*. SAE International, apr 2024.

[33] T. Lucchini, Gianluca D'Errico, Angelo Onorati, Alessio Frassoldati, and Alessandro Stagni annd Gilles Hardy. Modeling non-premixed combustion using tabulated kinetics and different flame structure assumptions. *SAE International Journal of Engines*, 2(10):593–607, 2017.

# Investigating Combustion Chamber Design Parameters for Hydrogen Adaptation of Diesel Engines: 3D CFD Study

B. Suatean[1], R. Bayet[2], S. Guilain[3] and G. de Paz[4]

[1]Horse Romania S.A. - Str. Preciziei 3G, 062204, Buhcarest, Romania.
E-mail: bogdan-niculae.suatean@renault.com
Telephone: +40752303873

[2]AVL-LMM – 5 – 9 rue Benoît Frachon, F- 91127 Palaiseau, France
[3]Ampere – Centre Technique de Lardy. 1, Allée Cornuel, 91510 Lardy, Fance.
[4]Horse Spain – AV DE Madrid 72, 47008, Valladolid, Spain.

**Abstract.**

The need to reduce CO2 emissions is pushing worldwide authorities into tightening emission standards, especially for the transportation sector. If Battery electric vehicles is probably the best solution of passenger cars, utility vehicles with its high energy demand are looking for other solutions. While keeping the assets of internal combustion engines, researchers are studying many alternative fuels to Diesel. Hydrogen, which is the most abundant element in nature, and which can be obtained with renewable energy sources, and, most importantly, can be tuned with the very low emission values, is regarded as the fuel of the future.

HORSE is preparing the adaptation of current Diesel 2L engines to hydrogen in a very lean combustion mode (lambda >2). In this paper, the effects of some combustion chamber design parameters are studied. Unlike gasoline fuel, combustion speed does not have to be improved with hydrogen as the laminar combustion speed is high. Thus, the optimization is more focused on hydrogen mixing process. Indeed, a good mixing allows to decrease auto-ignition risks and engine out NOx formation, the two Achilles heels of Hydrogen Internal Combustion Engine. Thus, we define some key metrics to qualify the mixing while keeping an eye on turbulence production close to the ignition event. We describe how we survey the rich zones, and especially close to hot surfaces – as they must be minimized.

After reproducing hydrogen jets characteristics in bombs, a parametric optimization of the combustion system (location of injector, combustion chamber shape, piston shape, intake ports, injector cap) is performed using unsteady 3D Computational Fluid Dynamics calculations with physical models developed and calibrated for hydrogen injection. We are describing the detailed effects of some design parameters on the mixing during compression stroke and their consequences on the key criteria.

In conclusion, such 3D Computational Fluid Dynamics process is proven as a great tool to provide valuable information of the entire hydrogen mixing process and to select the most promising configurations.

## Notations

| | |
|---|---|
| *ICE* | *Internal combustion engine.* |
| *LCV* | *Light commercial vehicle* |
| *PEMFC* | *Proton-Exchange Membrane Fuel Cells* |
| *CFD* | *Computational fluid dynamics* |
| *CR* | *Compression Ratio* |
| *TKE* | *Turbulent Kinetic Energy* |
| $\mu(x)$ | *Mean value of x parameter* |
| $\sigma(x)$ | *standard deviation of x parameter* |
| $\varphi$ | *Richness in H2 of mixture* |
| $\lambda=1/\varphi$ | *Air excess of the mixture* |
| *TDCF* | *Top Dead Center Fire* |
| $V$ | *Combustion chamber volume* |
| $V_{\lambda\leq 1.6}$ | *Volume in combustion Chamber where local* $\lambda \leq 1.6$ |
| $\varpi$ | *Angular speed* |
| $L$ | *Angular momentum* |

## 1. Introduction

As technology advances, there's a global surge in the number of vehicles on the roads. However, a considerable portion of these vehicles still relies on fossil fuels. This reliance has triggered a surge in fossil fuel consumption, resulting in a rapid depletion of these resources. Consequently, developed nations, facing high energy demands, are exerting increased pressure on countries abundant in fossil fuel reserves to meet their energy needs, often leading to destabilization in these regions [1,2].

The utilization of alternative fuels in internal combustion engines has gained increasing significance in contemporary times. This trend is primarily driven by the rising demand for fuel alongside the proliferation of vehicles, coupled with the introduction of emission standards by certain countries. Among the various alternative fuels under investigation by researchers, hydrogen stands out as a promising candidate. It is the most abundant element in nature and can be procured from renewable energy sources, offering exceptionally low emission levels. For instance, projections from the French oil market report suggest that by 2050, approximately 25% of passenger vehicles and 20% of non-electric rail transport could be powered by hydrogen, potentially reducing daily oil consumption by up to 20% [3,4]. Similar initiatives promoting the use of hydrogen are evident in other nations as well. However, the widespread adoption of low-carbon or carbon-free alternative fuels like hydrogen necessitates the establishment and commercialization of adequate infrastructure. Hydrogen not only serves as a source of energy capable of mitigating carbon-based emissions but also boasts high energy efficiency. Moreover, aside from its role as an energy carrier, hydrogen is poised to emerge as a viable alternative to petroleum in the foreseeable future, owing to its ability to be generated from renewable energy sources [5] [6] [7]. ICE engine with hydrogen could be an economical solution interesting for LCV as it is using the same industrial assets of current Diesel or gasoline thermal engines while achieving the requested high power. Moreover, H2 ICE have less purity demand than the alternative solution, PEMFC. In this framework, HORSE company that is developing worldwide ICE has decided to launch advanced engineering activities to adapt current Diesel engines to hydrogen combustion. The aim is to keep as much as possible the industrial asset while achieving very stringent emissions levels (CLOVE B), best-in-class performance and efficiency [8][9].

This research, part of this optimization, aims to employ computational fluid dynamics to observe the progression and enhancement of hydrogen injection, mixing, and combustion within the cylinder. Our goal is to gain a deeper understanding of in-cylinder flow dynamics and combustion behavior. Through this investigation, we intend to gather fundamental parameter data crucial for controlling combustion and emissions in pure hydrogen internal combustion engines (ICE). Additionally, we aim to propose innovative strategies to advance the practical implementation and development of hydrogen ICE technology.

The current state of the art in hydrogen internal combustion engine (H2 ICE) technology is marked by a degree of confusion regarding the optimal methodology for transitioning a conventional internal combustion engine (ICE) into one that operates on hydrogen. This study endeavors to address this gap by meticulously investigating several key parameters of design. The primary objective is to delineate a comprehensive strategy for achieving optimal mixing conditions necessary for the successful transformation outlined within the conditions. By systematically exploring various parameters and their interrelationships, this research aims to contribute valuable insights toward the development of effective methodologies for transitioning ICEs into H2 ICEs [10].

By systematically exploring these parameters, the study aims to:

- Develop a Comprehensive Design Framework: A guideline for engineers to follow when converting traditional ICEs to operate on hydrogen, incorporating best practices and optimal settings for each parameter.
- Enhance Performance and Efficiency: Insights on how to achieve higher power outputs and better fuel efficiency without compromising on safety or increasing emissions.
- Reduce Emissions: Strategies for minimizing harmful emissions, particularly NOx, through optimal design and operational adjustments.
- Advance Technological Understanding: A deeper understanding of the interdependencies between various design parameters and their collective impact on engine performance.

## 2. Modeling and key criteria

### 2.1. Engine specifications

The base of the study is a 2.0L automotive diesel 4 stroke engine with a flat roof cylinder head, a direct central injector, intakes ducts design for a swirl aerodynamic motion and a classical diesel bowl piston. The adaptation of this engine to a H2ICE contains the introduction of a direct H2 injector, an H2 spark plug, and the adaptation of CR. **Table 1** contains information on the engine details that have been fixed.

**Table 1** Fixed parameters of the 2.0L turbo-charged direct-injection hydrogen engine.

| Parameter | Value |
|---|---|
| Engine Capacity(cc) | 2000 |
| Bore | 85 mm |
| Stroke | 88 mm |
| Conrod | 155.5 mm |
| Piston crank offset | 0.5 mm |
| Cylinders | 4 |
| Stroke/Bore | 1.03 |
| Compression ratio | 11:1 |
| Ignition | Spark Ignition |
| Engine speed | 1000 – 4500 rpm |

### 2.2. CFD modeling and boundary conditions

The CFD aero and mixing modeling method is based on CONVERGE software and has been developed to be a compromise between fidelity and computation. The mesh development starts with a base size of 0.5mm where we add various mesh refinement levels. The different region of our dataset is illustrated in **Fig. 1(b)**, with corresponding scales detailed in **Table 2**. Employing distinct refinement scales within serves to minimize computational expenses and time requirements, all the while upholding accuracy in computations specially developed for the hydrogen injection. The automatic mesh is limited to 15 million cells.

**Table 2** Mesh refinement scales

| **Region/physic** | Scales |
|---|---|
| H2 injector region | 4 |
| H2 Jet cylinder embedding | 4 |
| Adaptive Mesh Refinement for Velocity | 2 |
| Adaptive Mesh Refinement for H2 species | 3 |

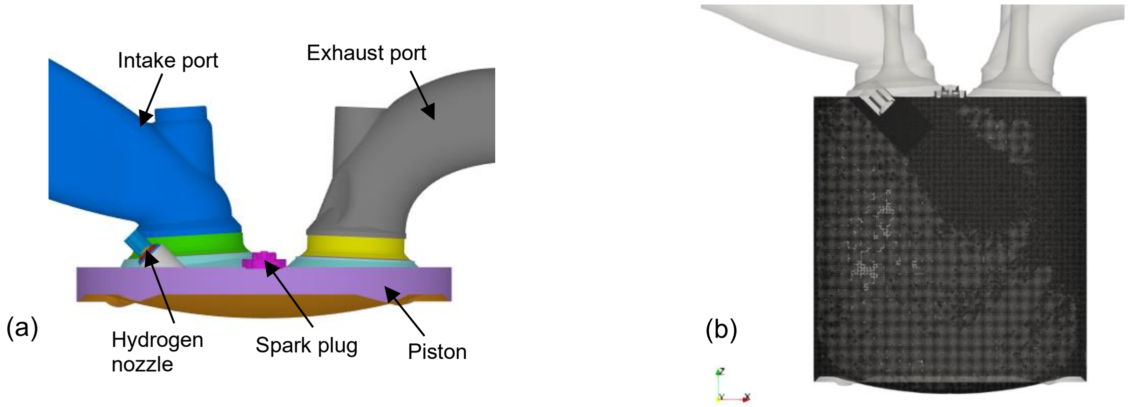

**Fig. 1** (a) Example of schematic diagram of pure hydrogen ICE 3D model

(b) Example of mesh refinement regions for 3D simulation domain

The solver employed in this study is a widely used RANS k-epsilon model, with adaptation specifically designed for hydrogen. These adaptations encompass all the unique characteristics and requirements of hydrogen, ensuring the solver effectively captures the intricacies of hydrogen behavior within the system [11].

In addressing boundary conditions within specified limits, the adaptation for hydrogen injection involves employing a pressure inlet featuring a real valve law to accurately replicate the hydrogen mass flow rate and flow dynamics. Our findings demonstrate that optimizing nozzle pressure, while accounting for injector pressure loss, and refining cell sizes, contribute significantly to representing the hydrogen jet with fidelity. Additionally, the simulation's other boundary condition is tied to the operational parameters, as detailed in **Table 3**. Specifically, our analysis focuses on the operating point, at 3500 RPM, aligning with the rated power operating point of our engine. Notably, we exclusively consider the pure lean lambda 2.5 condition, recognizing its pivotal role as the most constraining condition from a mixing perspective. This point is chosen as the worst case for mixing process, less time and high hydrogen quantity.

**Table 3** Engine Boundary conditions

| Operating point | Rated Power |
|---|---|
| BMEP | 21 bars |
| Rpm | 3500 |
| P admission | GT Power output fix |
| P exhaust | GT Power output fix |
| T admission | GT Power output fix |
| T exhaust | GT Power output fix |
| EGR | 0% |
| Lambda | 2.5 |
| Wall Boundary temperature | GT Power output fixed |
| Valve lifts | As Diesel ones |
| SOI | After IVC: 570°CA |

### 2.3. Hydrogen (H2) mixing and combustion quality Indicator

To evaluate the effectiveness of different conceptual approaches under scrutiny, it is imperative to employ indicators that can assess the quality of mixing [12]. Following examination, four relevant indicators have been identified:

1. **Aero level of motion**: This usual indicator evaluates the level of tumble or swirl present in the system, depending on the specific case being studied. A higher level of aero motion at the start of mixing could indicate a better mixing potential and/or a better turbulence production when the high level is close to TDC. Swirl and Tumble value are calculation are directly based on Converge Formula as angular speed ratio.
$$swirl = \frac{\varpi_z}{\varpi_{crankshaft}} (1) \; \& \; tumble = \frac{\varpi_x}{\varpi_{crankshaft}} \; (2)$$
The angular speed on x and z are calculated from the angular momentum, $L_i$, and the moment of inertia, $I_i$, as:
$$\varpi_i = \frac{L_i}{I_i} \; (3)$$
2. **Turbulent Kinetic Energy** (**TKE): TKE** assesses the turbulence within the combustion chamber, primarily to gauge the conversion of aero motion into energy for combustion. Consequently, it serves as an indicator for the combustion process; higher TKE values signify quicker combustion. The value is calculated with Converge formula description as the mass average transported TKE, as we use a k-epsilon RANS turbulence model.

3. **Homogeneity index of the mixture**: This indicator measures the homogeneity of mixture within the combustion chamber. As the mixture distribution, near the TDCF, follows a normal distribution, the formula is:
$$Homogeneity_{index} = 1 - \frac{\sigma(\varphi)}{\mu(\varphi)} \qquad (4)$$
A value closer to 1 indicates better homogeneity, suggesting statistical proximity to a perfect mixture.

4. **High Equivalence Ratio:** This indicator quantifies the presence of rich pockets in the combustion chamber using the formula**:**

$$High\ Equiv\ Ratio\ H2\ = \frac{V_{\lambda \leq 1.6}}{V} \qquad (5)$$

From literature [13- 17], it is established that the autoignition probability is increasing a lot when lambda is below 1.6. This indicator is aiming to check that the mixing process decrease these rich pockets as fast as possible to not let the ignition process to occur during the compression stroke. Lower values of this indicator are then preferable close to TDCF, with 0 indicating the absence of rich zones.

## 3. Effects of design parameters

This research is expected to make significant contributions to the field of H2 ICE technology by providing a clear and evidence-based roadmap for transitioning conventional diesel ICEs to hydrogen fuel.

### 3.1. Tumble vs. Swirl.

Starting from a Diesel engine and considering a transition to a different air motion configuration can be a complex endeavour. In this case, the focus is on conserving the swirl motion, a crucial aspect in engine performance. The initial question revolves around whether maintaining this swirl motion is feasible or if a shift to a tumble duct design is necessary, particularly concerning the engine's air motion into a flat head configuration.

To address this, a comprehensive parametric study becomes essential. This study encompasses various factors such as adapting the original port to accommodate the hydrogen injector, optimizing the placement of the spark plug, exploring different injection methods (central or lateral), and even experimenting with alterations in piston shape.

Through meticulous analysis and testing, it becomes evident that the optimal swirl design diverges significantly from the reference tumble design.

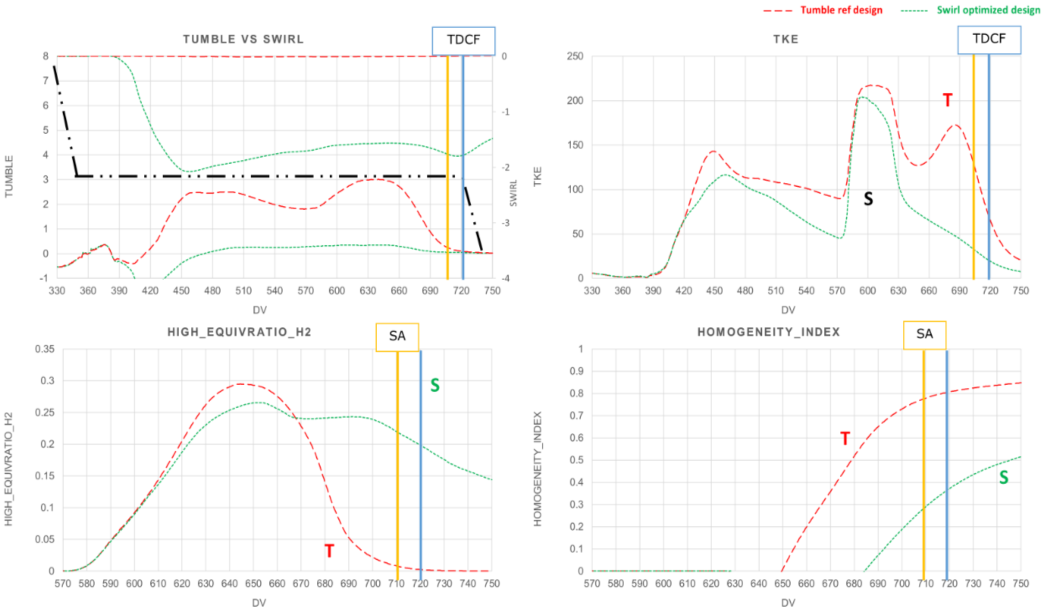

**Fig. 2** Comparison between an optimized swirl design and a tumble duct design on H2 mixing.

This conclusion is vividly illustrated in **Fig.2**, which graphically demonstrates the substantial deviation in mixing efficiency between the identified swirl design and the traditional tumble reference design. In essence, this parametric study underscores the complexity of engine design optimization and highlights the importance of adaptability and innovation in achieving superior performance and efficiency.

In the case of maintaining a swirl motion within the engine, it's crucial to consider its impact on the mixing of hydrogen with air. One significant observation is that the piston motion doesn't disrupt the aerodynamic flow, which, unfortunately, doesn't aid in effectively mixing the hydrogen with the air. Consequently, a substantial portion of the mixture remains excessively rich, as indicated by the High Equivalence Ratio indicator. Additionally, the Homogeneity Index of the richness indicates poor uniformity throughout the mixture.

Another notable finding is the low Turbulent Kinetic Energy (TKE) during the end of the compression stroke. This signifies that the aerodynamic motion is conserved and doesn't transform into turbulence. While this may seem beneficial in some regards, it can potentially impact combustion speed. Although this effect is less pronounced in the case of hydrogen combustion, it remains a factor to consider in overall engine performance and efficiency.

These observations underscore the intricate balance between aerodynamic flow, mixing efficiency, and combustion dynamics in engine design. Achieving optimal performance requires careful consideration and adjustment of these factors to ensure efficient fuel-air mixing and combustion, ultimately leading to improved efficiency and reduced emissions.

### 3.2. Lateral vs central injection

As established the most effective aerodynamic motion in this context is the tumble, this chapter focuses on comparing the impacts of lateral injection and central injection within the same technical framework. Specifically, we maintain a constant flat cylinder head, identical piston specifications, and the same port design across all simulations.

**Fig.3** clearly demonstrates that lateral injection results in more effective mixing of hydrogen within the tumble motion compared to central injection. This finding is consistent and reproducible across various types of tumble duct designs. The alignment of the injection jet with the direction of the tumble motion significantly amplifies the tumble effect. This enhancement is observed not only during the injection phase but also throughout the subsequent conversion of tumble into turbulence. This amplification appears to play a critical role in achieving optimal mixture preparation.

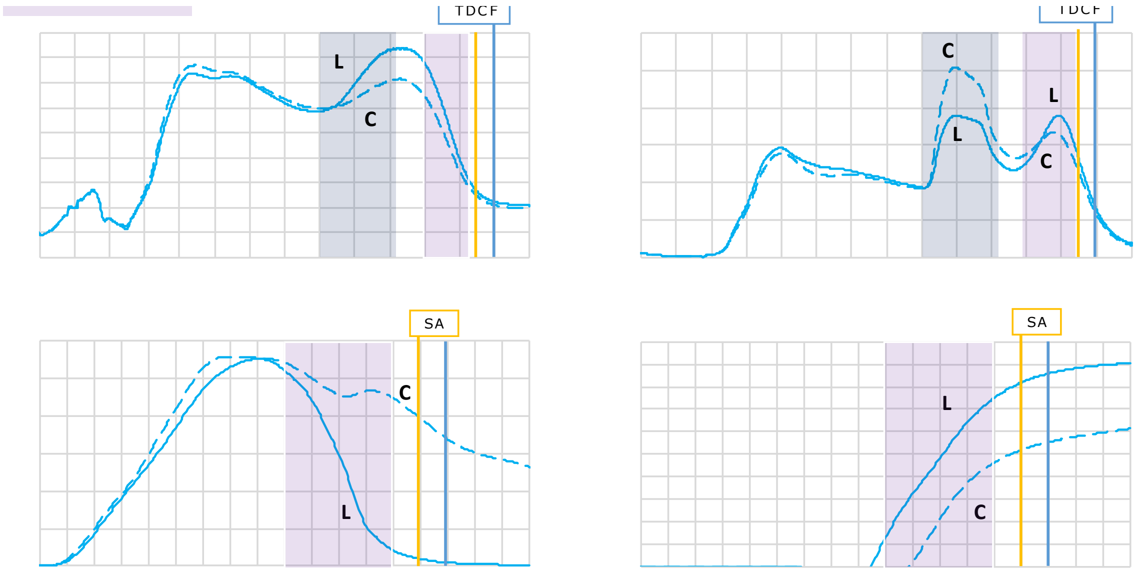

**Fig. 3** Comparison between lateral and central injection for a same intake duct on H2 mixing.

In particular, the high equivalence ratio (indicating regions of overly rich mixtures) decreases substantially during the compression phase. Concurrently, the Richness Homogeneity Index, which measures the uniformity of the fuel-air mixture, shows significant improvement. These observations suggest that the orientation and method of injection profoundly influence the efficiency and quality of the combustion process, with lateral injection offering distinct advantages over central injection in enhancing tumble motion and ensuring better fuel mixture preparation.

### 3.3. **Impact of aero motion level**

In this chapter, we examine the impact of the aerodynamic motion level, specifically focusing on tumble motion. To illustrate this parameter, we analyse different tumble levels generated by various tumble ports (**Fig.4**), all using the same lateral injector position, the same piston designs, and a flat cylinder head combustion chamber.

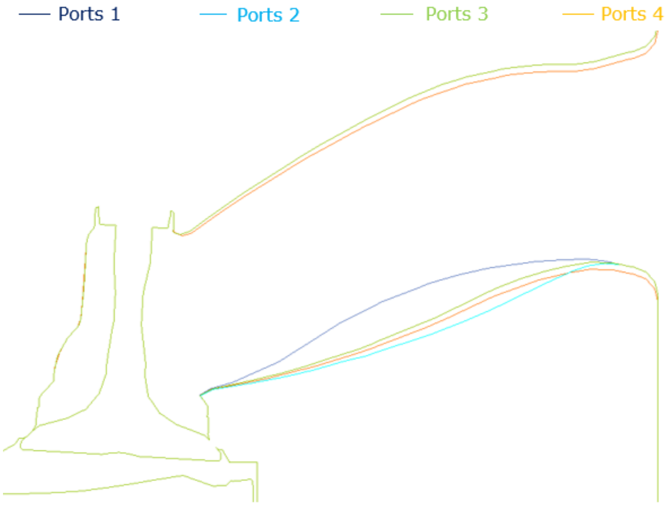

**Fig. 4** Various intake ports designs

**Fig. 5** demonstrates that port 1 performs significantly worse compared to the other solutions presented; it produces the poorest mixing, with the highest number of rich pockets and the lowest richness homogeneity index. In contrast, ports 2, 3, and 4, despite generating similar levels of tumble, show differences in mixing quality. This indicates that the injection process must be well-coordinated with the tumble generated by the duct design. Our findings suggest that duct design is closely linked to injector placement in achieving optimal homogeneity.

In addition to studying tumble, we also investigate variations in swirl motion and other aerodynamic parameters. Our conclusions are consistent across these different types of aero motion: initially, higher levels of aerodynamic motion improve mixing quality. Subsequently, small variations in aero motion must be aligned with the injection process to maximize the benefits of aerodynamic motion in generating a well-mixed fuel-air mixture.

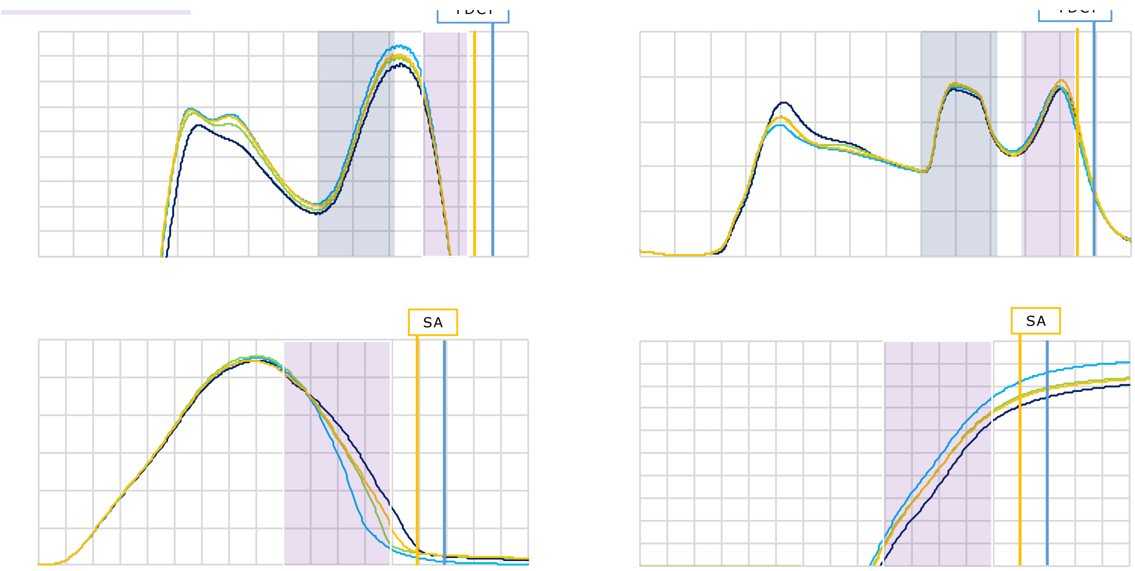

Overall, our study indicates that both the design of the ports and the positioning of the injector play crucial roles in optimizing the mixture preparation in hydrogen ICEs. By carefully tuning these parameters, it is possible to achieve significant improvements in combustion efficiency and performance.

**Fig. 5** Tumble level impact for a same lateral injection flat head and piston condition on H2 mixing.

### 3.4. Piston shape design

It is well-documented that the lenticular piston is optimal for a pent roof design. In this chapter, we extend this analysis to flat roof configurations. To verify this, we conducted comparative tests involving three different piston designs: Piston 2 with a flat bowl (yellow), Piston 3 with a smooth diesel bowl (red), and a deep impact piston based on the Piston 1 shape (green). These designs are illustrated in **Fig.6**. [18].

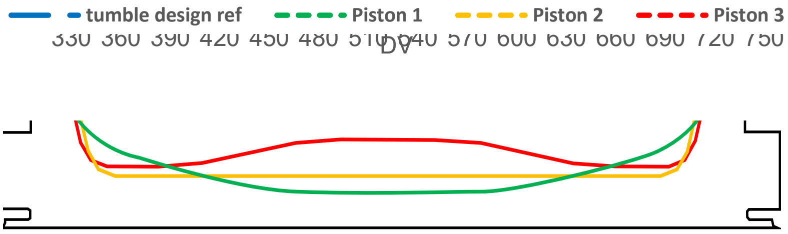

**Fig. 6** Piston bowl illustration

All tests were performed under identical conditions, maintaining the same tumble port configuration, lateral injector position, and a constant compression ratio (CR) of 11. Piston positions were adjusted to ensure these parameters were consistent.

The variation in piston shapes resulted in different levels of tumble. Our analysis indicates that increased tumble correlates with a higher Homogeneity Index and a lower High Equivalence Ratio indicator. These findings confirm that variations in piston shape significantly impact tumble levels, thus affecting the overall performance. Specifically, the results underscore the suboptimal performance associated with certain piston shapes [19].

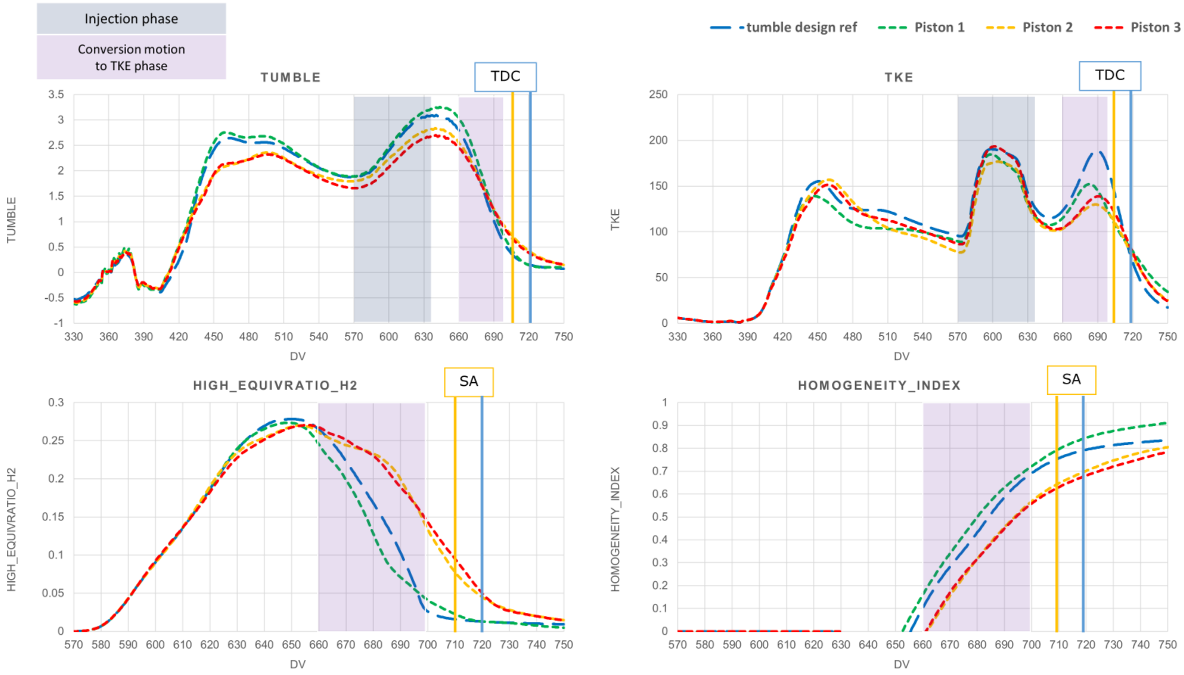

**Fig. 7** Piston shape impact on H2 mixing.

Simulation results, illustrated in **Fig.7**, reveal significant differences in tumble levels, TKE, high equivalence ratio, and homogeneity index generated by each piston shape. The tumble profiles (top left graph) show that all piston designs generate a substantial tumble motion, with Piston 1 (green) producing the highest tumble peak just before top dead center (TDC). The TKE profiles (top right graph) indicate that Piston 1 (green) maintains higher TKE levels during the critical injection phase, suggesting more effective energy transfer from tumble motion. The high equivalence ratio profiles (bottom left graph) show that Piston 1 (green) results in a lower high equivalence ratio, indicating fewer rich mixture zones and thus a more favorable combustion environment. The homogeneity index profiles (bottom right graph) reveal that Piston 1 (green) achieves the highest homogeneity index, indicating the most uniform hydrogen-air mixture. Overall, Piston 2 (green) demonstrates superior performance in generating higher tumble and TKE, leading to better hydrogen mixing and more homogeneous air-fuel distribution.

This study extends the understanding of piston design impact from pent roof to flat roof configurations, emphasizing the importance of optimizing piston shapes for better hydrogen mixing. Piston 1, with its flat bowl design, showed the most promising results, enhancing tumble, TKE, and mixture homogeneity, thus improving overall combustion efficiency. Future work should explore additional piston geometries and their effects under various operating conditions to further enhance the efficiency and performance of hydrogen-fueled internal combustion engines.

### 3.5. Coanda effect

In the extant literature, investigations have uniformly employed a fixed nozzle penetration depth, precipitating the manifestation of Coanda effects upon the hydrogen gas flow. This phenomenon results in a fraction of the hydrogen gas adhering to the cylinder head, as evidenced in **Fig. 8(a)**. It can have a big drawback for pre-ignition propension as it puts hydrogen close to hot surfaces (spark plug and exhaust valves). An augmentation of the nozzle penetration to 8 mm, illustrated in **Fig. 8(b)**, is posited to obviate the Coanda effect, thereby permitting a subsequent evaluation of its influence on the gas mixing dynamics [20], [21].

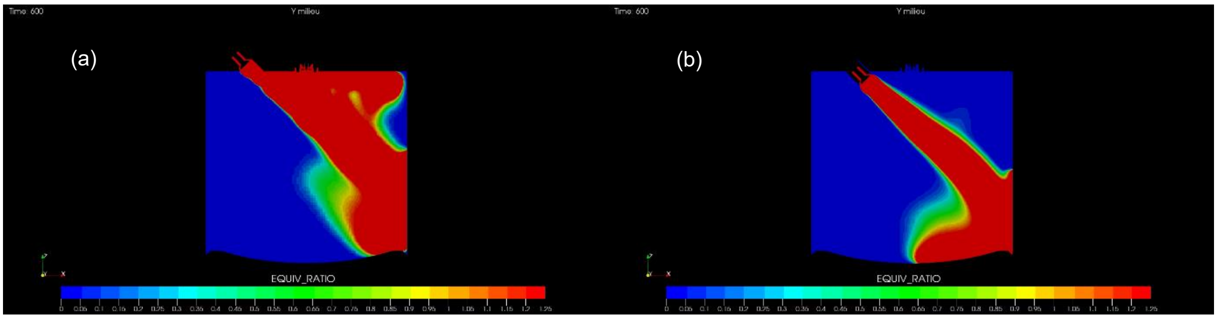

**Fig. 8** Illustration of the Coanda effect reduction by nozzle penetration on the richness reparation 10°CA after injection / (a) reference nozzle penetration (b) + 8mm nozzle penetration

In the context of identical intake ports featuring the same level of tumble, mitigating the Coanda effect has been found to enhance mixing efficiency, as presented in **Fig. 9**. Despite the hydrogen jet experiencing less modification, it fails to generate increased tumble both during and post-injection. Concurrently, reducing the Coanda effect maintains turbulence within the flow throughout injection, resulting in higher turbulent kinetic energy (TKE).

During the tumble TKE conversion phase, a greater proportion of tumble energy is channelled into hydrogen mixing, leading to a notable decline in the High Equivalence Ratio (ER) indicator and a faster increase of the richness homogeneity index. This improved efficiency during the conversion phase is attributed to an increased velocity of hydrogen, as evidenced in **Fig. 8**. Consequently, nearing spark advance, slightly superior H2 mixing is achieved without any Coanda.

However, while a deeper penetration may yield a reduction in the Coanda effect, it poses challenges in terms of temperature on the hydrogen injector nozzle. Alternative solutions such as injector caps or deflectors offer viable means to alleviate the Coanda effect, thereby ensuring injector compliance and optimal performance.

## 3.6. Pent-roof vs flat roof

Pent-roof combustion chamber is often preferred in modern high-performance engines due to its efficiency in airflow, heat retention, and the ability to accommodate more valves for better breathing of the engine. The flat roof design, while simpler and potentially less expensive to manufacture, does not offer the same level of performance benefits [22-23].

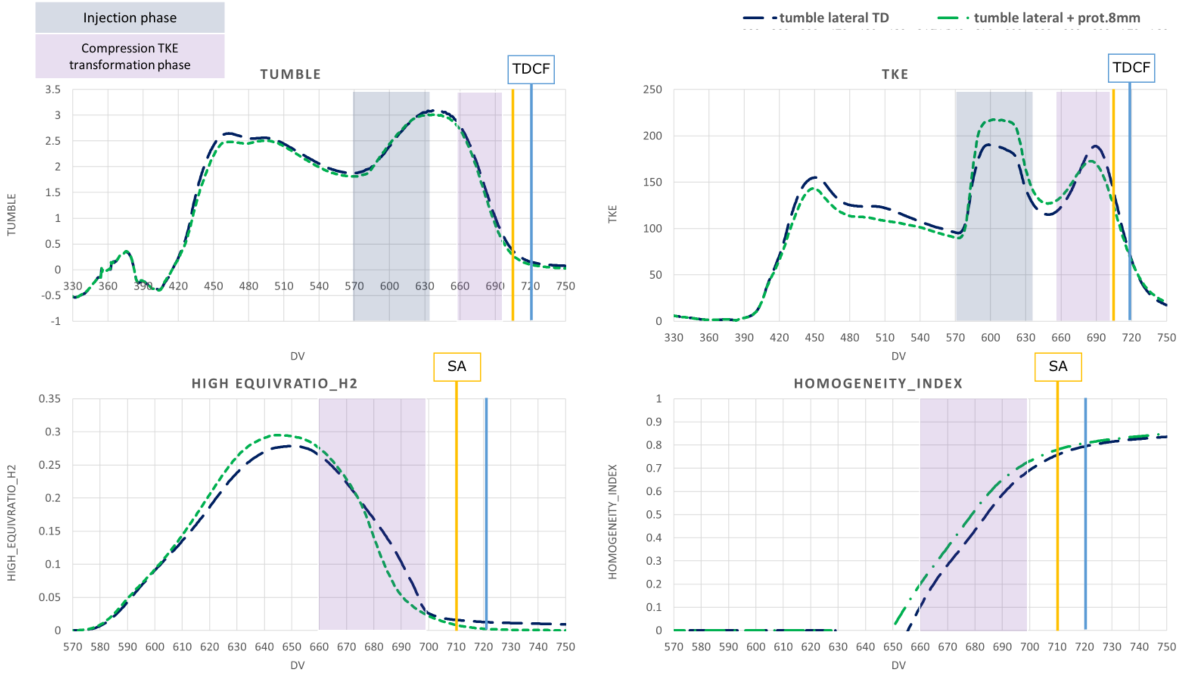

**Fig. 9** Coanda effect impact on H2 mixing.

This chapter provides a comparison between the previously discussed flat roof cylinder head illustrated in **Fig.10(a)** and a conventional pent roof cylinder head, commonly used for tumble flow design. An alternative technical configuration for a hydrogen internal combustion engine (H2 ICE) was developed to facilitate this comparison. This configuration incorporates a duct connected to the pent roof cylinder head and features a centrally located injector and spark plug, as illustrated in **Fig. 10(b)**. It is the only way to construct the cylinder head with valve train, injector and spark plug in such a pent-roof configuration. To ensure a more equitable comparison, several parameters were standardized across both designs, including the piston, compression ratio (CR), injector nozzle. Intake ports and roof chamber are then different.

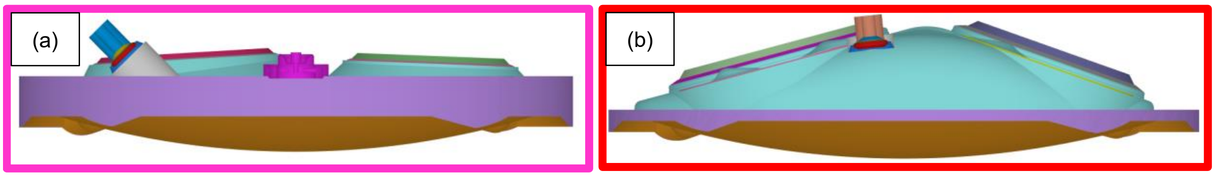

**Fig. 10** (a) flat head combustion chamber (b) pent roof combustion chamber

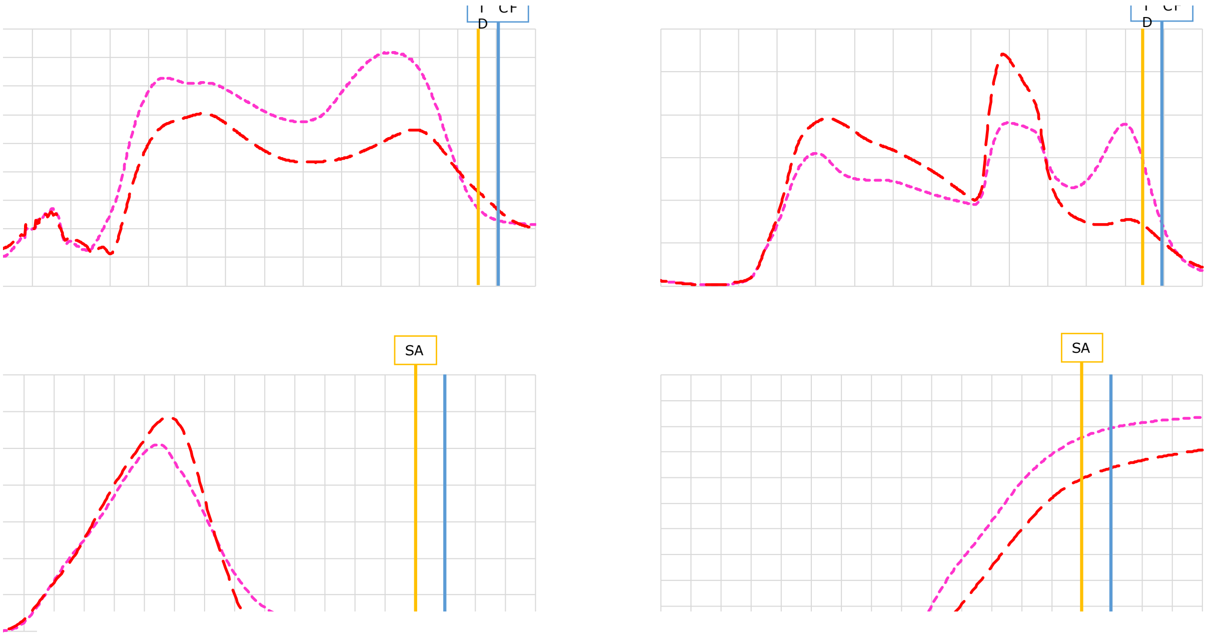

**Fig. 11** Comparison between flat and pent roof cylinder head design on H2 mixing.

The comparison in **Fig.11** indicates that the ports adapted to the pent roof cylinder head generate lower tumble. Consequently, it is challenging to determine whether the poor homogeneity results are more attributable to the pent roof design itself or to the reduced tumble observed with this configuration compared to the flat roof design. The high increase of TKE during injection is due to the central injector position as shown in paragraph 3.2 but that is not helping for the mixing. Conversely, it is noted that the high equivalence ratio achieved with the pent roof is not unfavorable, as it was zero with the flat roof. Thus, it is difficult to conclusively determine if one design is superior to the other. The pent-roof design should be optimized further: tumble level, injector cap, could me the main features. However, in the context of a diesel engine conversion, this suggests that utilizing a flat roof head with a well-designed tumble duct could be a viable solution for hydrogen mixing.

## Conclusions

Hydrogen internal combustion engines (ICEs) have emerged as a significant research focus, and their future development represents a reliable pathway to achieving zero-carbon emissions for ICEs. Moreover, the large-scale application of hydrogen ICEs is a crucial strategy for leveraging the mature industrial infrastructure of ICEs to support energy transition and carbon emission reduction goals. The study concludes that converting a 2L passenger car Diesel ICE into a pure lean H2 ICE requires specific best practices to enhance hydrogen mixing, reduce preignition, improve combustion flame development, and lower NOx formation. The diesel ICE transformation includes:

- Intake port change: Transforming the ports from a swirl to a tumble design and optimizing for the highest possible tumble level.
- Injection and spark plug: Using a lateral injection with a central spark plug, designed to interact effectively with the generated tumble.
- Piston Design: Employing a lenticular piston shape with an adaptable depth to improve mixing.
- Mitigating Coanda Effect: Avoiding the Coanda effect that could have an impact on hydrogen levels at the spark plug by protrusion, a cap or nozzle deflector.
- Head Design: Maintaining a flat head design seems possible to achieve efficient mixing process however the cooling will be a key factor to avoid hot points and pre-ignition.

These measures collectively support the optimal conversion of a diesel engine to operate efficiently and cleanly on hydrogen.

## References

[1] Damon Matthews H, Tokarska KB, Rogelj J, Smith CJ, MacDougall AH, Haustein K, et al An integrated approach to quantifying uncertainties in the remaining carbon budget. Communications Earth & Environment 2021; 2:1e11

[2] Stolarski J , Warmin ski , rzyz a niak , lbaeZie˛ ty , Stachowicz P Titl Energy consumption and heating costs for a detached house over a 12-year period Renewable fuels versus fossil fuels. Energy 2020; 204:117952

[3] Li L, Lin J, Wu N, Xie S, Meng C, Zheng Y, et al. Review and outlook on the international renewable energy development. Energy and Built Environment; 2020.

[4] Sughayyer M. Effects of hydrogen addition on power and emissions outputs from diesel engines. 2016.

[5] Lof J, MacKinnon C, Martin G, Layzell D. Survey of heavy-duty hydrogen fuel cell electric vehicles and their fit for service in Canada. The Transition Accelerator; Sep. 2020.

[6] Verhelst S. Recent progress in the use of hydrogen as a fuel for internal combustion engines. Int J Hydrogen Energy 2014;39:1071e85.

[7] Boretti A. Advances in hydrogen compression ignition internal combustion engines. Int J Hydrogen Energy 2011;36:12601e6.

[8] awood, F , nda, , and Shafiullah, , " ydrogen Production for nergy: n v erview," nter national Journal of Hydrogen Energy 45, no. 7 (2020): 3847-3869, doi:10.1016/j. ijhydene.2019.12.059.

[9] Turner, J., Sverdrup, G., Mann, M.K., Maness, P.-C et al , " ene wable y drogen Production," nt J. Energy Res. 32 (2008): 379-407, doi:10.1002/er.1372.

[10] Szwaja S, Grab-Rogalinski K. Hydrogen combustion in a compression ignition diesel engine. Int J Hydrogen Energy 2009;34:4413e21.

[11] ’ ourke PJ, msden he ab e thod for numerical calculation of spray droplet breakup; 1987. p. 872089.

[12] on o mer, , Fink, , ett, et al , “ ptimization of the ixture Formation in y drogen Combustion ngines by o dified njector oz zle es ign”, Presentation at S international HYDROGEN INJECTION & COMBUSTION IN ENGINES, May 2022.

[13] Heffel, J.W. NOx emission and performance data for a hydrogen-fueled internal combustion engine at 1500 rpm using exhaust gas recirculation. Int. J. Hydrogen Energy 2003, 28, 901–908.

[14] Saravanan, N.; Nagarajan, G. Performance and emission studies on port injection of hydrogen with varied flow rates with Diesel as an ignition source. Appl. Energy 2010, 87, 2218–2229.

[15] Li, H.; Karim, G.A. Hydrogen-fueled spark-ignition engines predictive and experimental performance. Trans. ASME J. Eng. Gas Turbines Power 2006, 128, 230–236.

[16] Antunes, J.G.; Mikalsen, R.; Roskilly, A.P. An investigation of hydrogen fueled HCCI engine performance and operation. Int. J. Hydrogen Energy 2008, 33, 5823–5828.

[17] Mohammadi, A.; Shioji, M.; Nakai, Y.; Ishikura, W.; Tabo, E. Performance and combustion characteristics of a direct injection SI hydrogen engine. Int. J. Hydrogen Energy 2007, 32, 296–304.

[18] Fu Y, Feng L, Long W, Tian H, Tian J, Leng X. Investigation of the performance of double-layer diverging combustion chamber in a single-cylinder diesel engine. Fuel 2020;268:117165.

[19] Lee S, Jeon J, Park S. Optimization of combustion chamber geometry and operating conditions for compression ignition engine fueled with pre-blended gasoline-diesel fuel. Energy Convers Manag 2016;126:638e48.

[20] Saravanan N, Nagarajan G. Performance and emission studies on port injection of hydrogen with varied flow rates with Diesel as an ignition source. Appl Energy 2010;87:2218e29.

[21] Tripathi G, Sharma P, Dhar A, Sadiki A. Computational investigation of diesel injection strategies in hydrogen-diesel dual fuel engine. Sustain Energy Technol Assessments 2019;36:100543.

[22] Jaichandar S, Annamalai K. Influences of re-entrant combustion chamber geometry on the performance of Pongamia biodiesel in a DI diesel engine. Energy 2012;44:633e40.

[23] emizer , € Cihan Analysis of different combustion chamber geometries using hydrogen/diesel fuel in a diesel engine. Energy Sources, Part A Recovery, Util Environ Eff 2021;43:17e34.

# Preliminary Development of a Dome Combustion Chamber Dedicated to Hydrogen Direct Injection Engines

P. Gastaldi[1], D. Kumar[1], G. Milan[2], M. Chandelier[3], R. Drevet[4], G. Dober[5]

[1]Aramco Fuel Research Center, Rueil-Malmaison, France.
[2]Federal-Mogul Powertrain, A Tenneco Group Company, Carpi, Italy
[3]Federal-Mogul Ignition Products SAS, A Tenneco Group Company, Chazelles-sur-Lyon, France
[4]Phinia Inc., Blois, France
[5]Phinia Inc., Belvaux, Luxembourg

[1]E-mail: patrick.gastaldi@aramcooverseas.com
[1]Telephone: +(34) 0698866792

**Abstract**

The imperative to reduce greenhouse gas emissions is compelling the road transport industry to explore various solutions in addition to electrification. A pivotal step in this direction involves adopting low-carbon footprint fuels such as hydrogen, ammonia, and e-fuels for vehicles powered by internal combustion engines.

Hydrogen classifies itself as a promising candidate for spark-ignited internal combustion engines (ICEs) due to its high laminar burning velocity, wide ignitability range in terms of equivalence ratio, and increased resistance to auto-ignition. However, it also exhibits a very low minimum ignition energy, increasing the likelihood of pre-ignition events during engine operation. Therefore, the design of the combustion system and operational strategy must be tailored to achieve stable and efficient hydrogen combustion across various loads and engine speeds.

This article introduces a Dome-shaped combustion chamber designed specifically for hydrogen combustion targeting high specific performance. The Dome is integrated into a robust four-valve flat cylinder head at the central position facilitating the placement of both the medium pressure hydrogen injector and a spark plug specifically designed for $H_2$ operation near the cylinder axis, in cooperation with a straightforward piston design.

Preliminary test results obtained at 2000 rpm x 16 bars of IMEP on a 500cc single cylinder engine are reported. Variations in equivalence ratios and spark timings demonstrated robust and excellent combustion stability until an equivalence ratio of 0.40 and achieved a gross indicated thermal efficiency of 46%. Subsequently, the 3D-CFD simulations were carried out at 2000 rpm x 16 bar, incorporating the hydrogen injection and combustion modelling. The CFD results demonstrated a satisfactory agreement with the experimental in terms of in-cylinder pressure and apparent heat release rates. Finally, the CFD simulations are utilized to evaluate the potential high load performance of the Dome engine at 6000 rpm of engine speed, emphasizing the effect of a split injection strategy.

Keywords: CFD, combustion, Dome engine, Hydrogen

## Notations

| | | | |
|---|---|---|---|
| *AMR* | *Adaptive mesh refinement* | *IMEP* | *Indicated mean effective pressure* |
| *BEV* | *Battery electric vehicle* | *IMEPg* | *Gross Indicated mean effective pressure* |
| *BDC* | *Bottom dead center* | *M/C* | *Main chamber* |
| *bTDC* | *Before top dead center* | *RANS* | *Reynolds-averaged Navier–Stokes* |
| *CFD* | *Computational fluid dynamics* | *RON* | *Research octane number* |
| *CA50* | *Crank angles corresponding to 50% fuel mass burnt* | *SA* | *Spark advance* |
| *CAX* | *Crank angles corresponding to X % fuel mass burnt* | *SCE* | *Single cylinder engine* |
| *DI* | *Direct injection* | *SOI* | *Start of injection* |
| *FCEV* | *Fuel cell electric vehicles* | *SI* | *Spark ignition* |

| | | | |
|---|---|---|---|
| *GDI* | *Gasoline direct injection* | TDC | Top dead center |
| *GHG* | *Green house gas* | *TKE* | *Turbulent kinetic energy (m2/s2)* |

## 1 Introduction

The growing recognition of the impacts of global warming on life has led to an increased focus on greenhouse gas emissions (GHG) over the past few years. Despite only accounting for 15% of total GHG emissions in 2019 (Fig. 1), the transport sector, which includes road, sea, and air travel, must play a significant role in transitioning to cleaner energy sources and reducing reliance on fossil fuels.

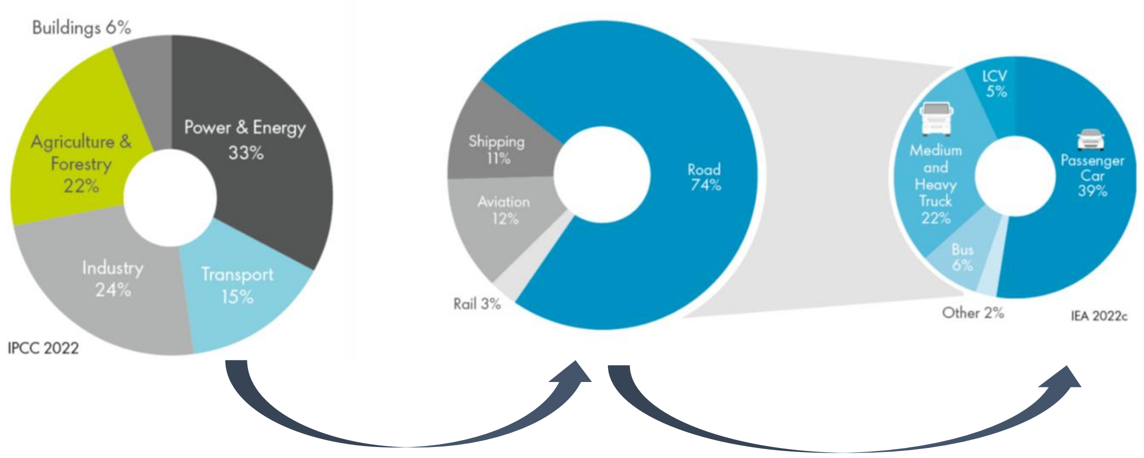

**Fig. 1.** Global GHG emissions per sector 2019 [1]

In parallel, as Fig. 1. clarifies the contribution of each sector, Fig. 2 illustrates an undisputable trend for increasing the number of vehicles between today and 2030, emphasizing the necessity to strongly reduce the emissions per vehicle and particularly the carbon dioxide ($CO_2$) emissions.

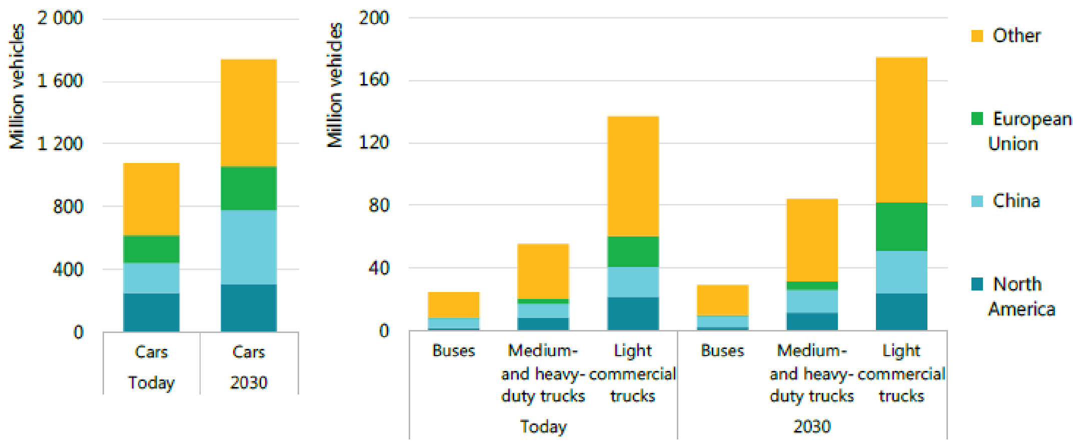

Source: IEA 2019. All rights reserved.

**Fig. 2.** Evolution of road transportation between today and 2030 [2]

Battery Electric Vehicles (BEVs) are undoubtedly effective in reducing greenhouse gas (GHG) emissions. However, their limited usability guides the automotive industry to develop alternative solutions based on substitutes for hydrocarbon fuels. Among these alternatives, hydrogen ($H_2$) and $H_2$-derived fuels, also known as electro-fuels or e-fuels, are gaining significant attention. Ammonia ($NH_3$), a simple electro-fuel derived from combining $H_2$ with nitrogen ($N_2$) from the air, is considered a promising candidate [3]. Additionally, pure $H_2$ remains a key player in this transition. For this reason, Aramco invests highly to reach a production of 2 million metric tons per annum of blue $H_2$ by 2030 and thereby accelerate the infrastructure deployment for use in both passenger cars and light commercial vehicles.

As a fuel, $H_2$ can be used either in conventional internal combustion engines (ICE) or in fuel cell electric vehicles (FCEVs). Fig. 3 illustrates that ICEs offer an interesting compromise in terms of cost-to-power ratio, with the economic and social advantage of utilizing existing production infrastructure.

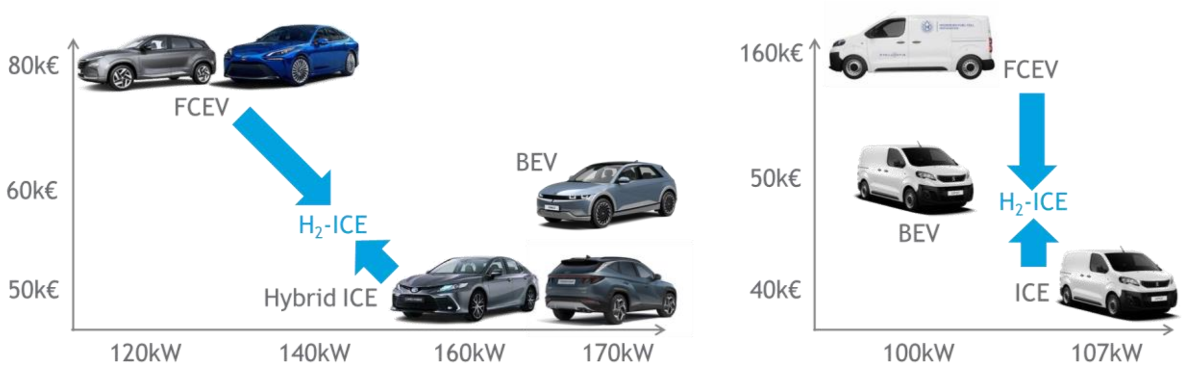

**Fig. 3.** Cost to power comparison between $H_2$ICE, hybrids and BEV

Paradoxically, the concept of utilizing hydrogen as a fuel in internal combustion engines (ICE) is not entirely new. In 1807, in Switzerland, François Isaac de Rivaz developed a prototype that used compressed hydrogen gas and oxygen, which was electrically ignited (refer to Fig. 4 (a). Subsequently, research activities began worldwide, including efforts by for instance Roger Billings in the USA or the Musashi Institute of Technology in Tokyo during the 1970s.

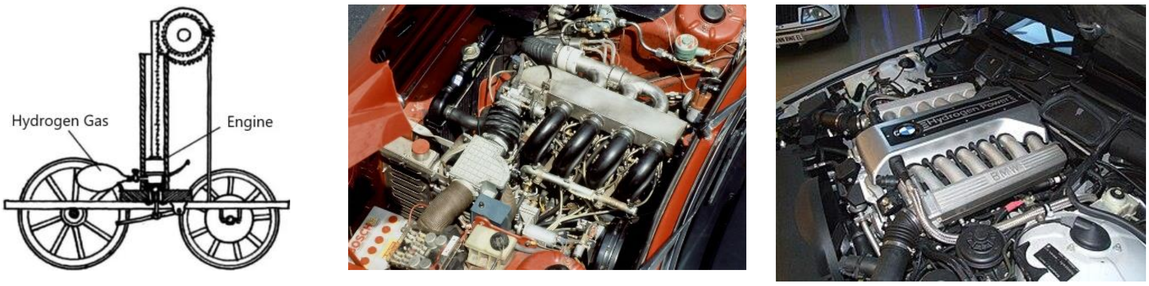

(a) (b) (c)

**Fig. 4.** François-Isaac de Rivaz vehicle [4] and BMW $H_2$ engines [5]

Particularly, BMW made significant advancements in 1979 with a class 5 sedan and later a V12 class 7 vehicle (Fig. 4 ) utilizing liquid hydrogen storage. Mercedes also made strides from 1984 using compressed gas. Despite promising developments, these efforts faced challenges due to high costs and poor power density compared to conventional engines running on inexpensive fossil fuels. A very interesting application was the use of a dual gasoline/hydrogen racing V12 Aston Martin Engine during the 24 hours of Nürburgring [6] in 2013 (see Fig. 5), Developed by the Institut für Verbrennungskraftmaschinen und Thermodynamik in Graz, the turbocharged engine achieved a power density of more than 50 kW/l in hydrogen mode.

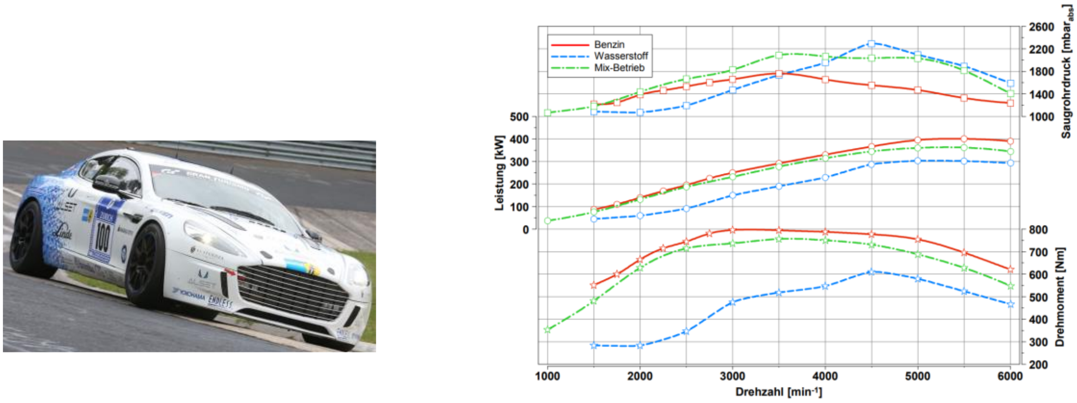

**Fig. 5.** V12 engine, comparison between gasoline, hydrogen and mixed operation at full load [6]

In 2015, the Paris Agreement on climate change set up new rules and led the road transportation industry to intensively find alternatives to fossil fuels. Hydrogen appeared to be one solution and previously scheduled or completely new activities were supported in different ways; the simplest one consisted of retrofitting existing Diesel engines by adding an $H_2$ port fuel injection (PFI) and slightly adapting the piston design and the compression ratio [6]. More intensive investigations were followed using a medium pressure direct injection (DI) in almost every vehicle class, from passenger cars like Hyundai [8], light commercial vehicles like Stellantis [9] and Renault [10], or even very high performances models as Porsche [11] and Ferrari [12]. Thanks to DI, air filling was very much improved compared to PFI with very few risks of backfire in the intake port, allowing it to reach power densities comparable to conventional Diesel or gasoline engines with a high thermal efficiency. For all these applications, intensive use of simulation, including 3D computational fluid dynamics (CFD) and 1D modeling, alongside engine tests, was realized to optimize aerodynamics, hydrogen-air mixing, and combustion processes.

This paper is an outcome of collaboration between Aramco, Phinia, and Tenneco; it aims at presenting an innovative DI combustion system design adapted to high power density serial production engines. Single cylinder engine (SCE) test results obtained at 2000 rpm and 16 bars IMEP are presented and discussed and the performance projection on higher engine speed has been achieved thanks to CFD.

### 1.1 Hydrogen fuel characteristics

Table 1 compares the fuel properties of hydrogen with gasoline. Hydrogen possesses a wide flammability range and extremely fast laminar burning velocity. This suggests that a stable ignition and combustion is possible even with ultra-lean or highly stratified locally rich charge. It also inherits a comparatively higher auto-ignition temperature, which makes it less susceptible to knocking. On the other hand, its very low minimum ignition energy strongly increases the risk of pre-ignition in the combustion chamber. Hydrogen flame can sustain close to the walls due to a smaller quenching distance, on one hand, this could ensure more complete combustion, but it would result in increased wall heat loss. Thus, an efficient and controlled combustion of hydrogen in ICE remains quite challenging.

**Table 1**. Properties of different fuels in comparison with hydrogen

| Fuel species | | Gasoline | Hydrogen |
|---|---|---|---|
| Stoichiometric A/F ratio | [-] | 14.6 | 34.2 |
| Lower calorific value | [MJ/kg] | 42.5 | 120 |
| Flammability range (equivalence ratio) | [-] | 0.62–3.89 | 0.09 – 6.81 |
| Laminar burning velocity | [m/s] | 0.40 | 2.30 |
| Auto-ignition temperature | [°C] | 230-450 | 595 |
| Minimum ignition energy | [mJ] | 0.24 | 0.02 |
| Quenching distance | [mm] | 2 | 0.64 |
| Approximate RON | [-] | 95 | >120 |

## 1.2 State of the art DI hydrogen combustion systems

The choice of a combustion system dedicated to serial production engines not only depends upon performance or thermal efficiency but also upon the investment necessary for upgrading industrial facilities, especially for the cylinder head machining.

In recent years, the down-sizing strategy led to equip passenger cars with moderate displacement volume gasoline engines, usually lower than 2.0l; as for high-performance sports cars, a pent-roof cylinder head combined with a tumble air motion generated by the intake ports was preferred. Keeping the baseline architecture of gasoline direct injection (GDI) engines, customized versions for $H_2$ICE's are restricted to variations in the injector and spark plug placements. These components can be positioned centrally or laterally on the intake or exhaust sides. Furthermore, adjusting the intensity of the tumble motion is also part of optimizing the combustion system. In this context, some examples have been provided by Hyundai with a 1.6l four-cylinder engine in Fig. 6 or by Ferrari for a 3.0l V6 as shown Fig. 7.

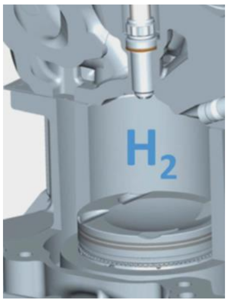

| Engine type | [-] | In-line 4 cylinder |
|---|---|---|
| Displacement volume | [cm$^3$] | 1.598 |
| Bore x Stroke | [mm] | 75.6 x 89 |
| Valves/cylinder | [-] | 4 |
| Spark plug | [-] | Centrally located |
| Hydrogen injector | [-] | Laterally located |
| Compression ratio | [-] | 10.5:1 |
| Power | [kw] | 132 |
| Torque | [Nm] | 265 |

**Fig. 6.** Hydrogen engine proposed by Hyundai, Bosch and Aramco [13]

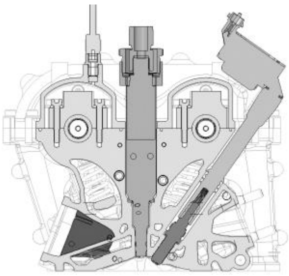

| Displacement volume | [cm$^3$] | 498.7cc |
|---|---|---|
| Bore x Stroke | [mm] | 82 x 88 |
| Valves/cylinder | [-] | 4 |
| Spark plug | [-] | Quite Centrally located |
| Hydrogen injector | [-] | Centrally mounted |
| Compression ratio | [-] | 10.5:1 to 14:1 |

**Fig. 7.** Hydrogen engine proposed by Ferrari [12]

For light commercial vehicles which require a high low-end torque, a low fuel consumption and a high mileage reliability, the retrofitting choice was mainly focused on Diesel engines architecture with cylinder displacement generally higher than 2.0 liter, preserving the use of a flat cylinder head and vertical valves (Fig. 8) with the associated industrial tool.

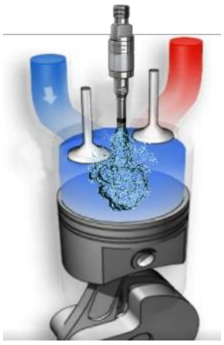

**Fig. 8.** Hydrogen engine proposed by PHINIA [14]

Their optimization for hydrogen is thereafter also limited to the location of the injector -central or side- and the spark plug, as the chosen air motion generally remains swirl.

As the choice between the two architectures is mainly governed by industrial constraints, very few investigations have compared them in terms of power density capability and efficiency.

### 1.3 Combustion strategies

Besides a high combustion velocity and a high resistance to knock characterized by a fine Research Octane Number (RON), hydrogen combustion is nevertheless susceptible to pre-ignition phenomena, i.e., a local ignition before the spark generation, initiated by factors such as hot spots in the chamber, lubricant oil droplets, or local regions possessing both near-stoichiometric mixtures and high temperatures. Mitigating these factors and thereby reducing the occurrence of pre-ignition can be achieved by different ways:

- an ultra-lean homogeneous H2-air mixture avoiding any local equivalence ratio higher than roughly 0.70; the minimum ignition energy of the mixture therefore strongly increases as shown in Fig. 9, reducing the risk of pre-ignition. This strategy also has the advantages of, on one hand lowering the combustion temperature, reducing the wall losses and thereby the wall temperature and the risk of hot spots on metallic parts of the chamber, and on the other hand, maintaining NOx emissions at a low level.
- a late $H_2$ injection during the compression stroke, in order to reduce the mixture temperature at firing Top Dead Center (TDC).
- the use of exhaust gas recirculation to lower the combustion temperature as it is achieved on conventional Diesel and gasoline engines.
- the use of water injection to cool down the in-cylinder mixture.

A large part of the published application is based on the first strategy, optimizing the mixture homogeneity via both an early injection -during or just after the intake stroke- and a strong bulk air motion generated by the intake ports, e.g. swirl with Diesel like flat cylinder heads or tumble with pent-roof architectures.

This choice is nevertheless restricted by the air flow necessity when high power is required because of the low port permeability and the size and complexity of the air system -turbochargers and intercoolers. In parallel, the late injection strategy is limited by the necessity to secure a sonic flow at the $H_2$ injector hole.

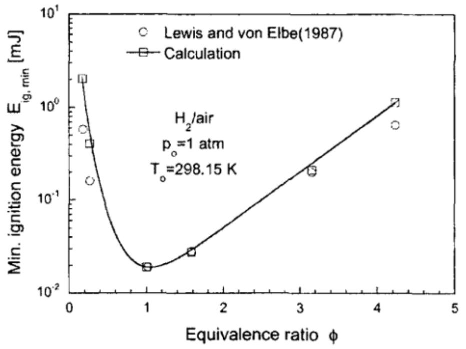

**Fig. 9.** Evolution of the minimum ignition energy versus equivalence ratio [15]

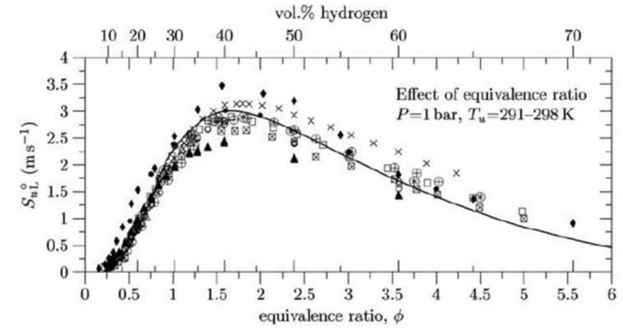

**Fig. 10.** Evolution of the laminar flame velocity versus equivalence ratio [16]

## 2 The Dome $H_2$ICE and engine testing

### 2.1 Engine design Description

This section presents the design and technical specifications of the single-cylinder, direct injection internal combustion engine (ICE) incorporating the innovative Dome combustion chamber. The engine base aims at achieving a high specific power while concurrently ensuring structural robustness. Central to this design is a four-valve flat cylinder head incorporating a Dome-shaped structure, which accommodates both the hydrogen injector and spark-plug. The direct injection hydrogen injector and spark-plug are specifically developed for hydrogen combustion in ICE’s and their particularities are discussed in the next section.

It's crucial to emphasize that the hydrogen injector is decisively mounted on the Dome with an injector recess of 2 mm. This setup allows to maximize the hydrogen jet penetration in the main chamber by minimizing the Coanda effect and simultaneously decreases the jet contact with the hot spark plug electrodes, as illustrated by the 3D simulation results in Fig. 12.

Given the risk of potential pre-ignition in $H_2$ICE, paramount importance is placed on efficient thermal management of engine components; this is achieved notably through a simple piston configuration to ensure its homogenous and effective cooling. The sodium-filled intake and exhaust valves are considered for their superior heat transfer characteristics. Furthermore, the water jackets are carefully integrated to envelop the Dome, injector, and spark-plug to enhance their respective cooling efficiency.

The intake ports are designed to facilitate maximum airflow without inducing any specific bulk flow phenomena, such as swirl or tumble.

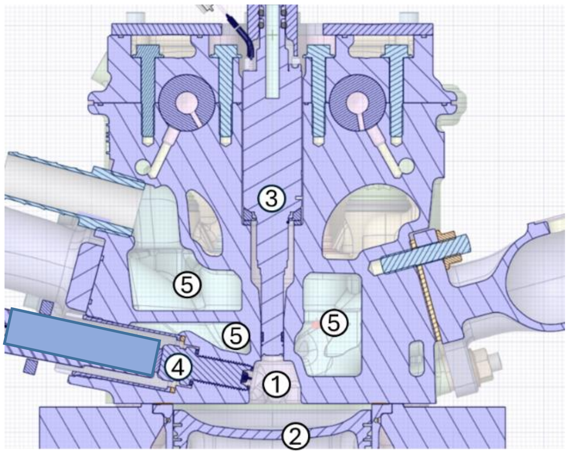

**Fig. 11.** Single cylinder engine layout with Dome (1), piston (2), hydrogen injector (3), spark-plug (4) and cooling water jackets (5)

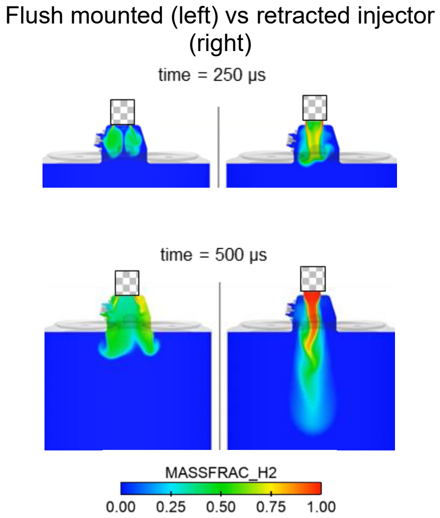

**Fig. 12.** Hydrogen jet penetration from CFD simulations with flush mounted injector (left) and with injector recess of -2 mm (right) at the two different timings after the start of the injection

The choice of an oversquare geometry with an 88 mm bore representative of the current high performance V6 engines benchmark allows potential high engine speeds over 7000 rpm; meanwhile, a compression ratio of 10.5 has been set for these first investigation as a good trade-off between potential efficiency and knock resistance. The detailed engine specifications are listed in the Table 1.

**Table 2.** Engine characteristics of Dome engine

| Parameter | Units | Value |
|---|---|---|
| Displacement volume | [$cm^3$] | 506 |
| Bore x Stroke | [mm] | 88 x 83.5 |
| Connecting rod length | [mm] | 152.5 |
| Compression ratio [-] | [-] | 10.5:1 |
| Valves/cylinder | [-] | 4 |
| Spark plug | [-] | Surface discharge type from Tenneco |
| Hydrogen injector | [-] | DI-CHG15 injector from Phinia |
| Injection pressure | [bar] | Up to 40 bar |

### 2.2 Ignition system

Tenneco's Champion® have developed and provided specific ignition components for use with engines specified to run on Hydrogen fuel. Both coil and spark plug have been designed to operate on engines specified to run with hydrogen application.

The HY2Fire™ plug top coil supplied for this test is a high-energy coil equipped with an energy damper circuit. The objective is twofold. From one side to prevent unwanted spark at start of charge and from the other side to prevent random uncontrolled sparks due to residual energy in the coil after the main spark ends and in-cylinder pressure decreases. The phenomena addressed with this technology are ghost sparks that lead to backfire. This is a must for a hydrogen PFI engines and a plus for DI engines. The solution has already been validated through endurance tests and has entered mass production ramp-up early 2024.

**Fig. 13.** Spark plugs and coil (source Tenneco / Champion®)

The spark plugs supplied are also adapted for hydrogen use. The main target was to keep the spark plug operating temperature as cold as possible to prevent any hot spot that could generate abnormal combustion. Temperatures over 600°C will cause uncontrolled ignition with hydrogen. To do so, the heat range of the spark plug is selected from the racing scale and the ground electrode projection limited as much as possible. In fact, one design has a retracted spark position by 2.5 mm and the other is using a non-projected ground electrode (0 mm spark position). In both cases, thermal modeling was performed to have a back-to-back comparison between the designs. A recent dyno study (single-cylinder engine specifically developed to operate with hydrogen), also confirmed the behavior of the designs under several operating conditions. Voltage demand and electrode temperature were measured. The impact of spark plug design on abnormal combustion was evaluated (misfire, pre-ignition, knocking). The catalytic effect of Platinum, leading to uncontrolled combustions was measured and confirmed. The two designs used during the testing campaign are compliant with this approach. This means they were not only cold-rated but also platinum-free.

### 2.3 Injection system

A Direct-Injection Compressed Hydrogen Gas (DI-CHG) injector (Fig. 14) was provided by PHINIA. This solenoid-driven injector is an outward-opening type, whose key benefits are to provide a higher mass flow rate than inward-opening injectors within the same packaging envelope and are also able to maintain injector sealing against high in-cylinder pressures with a relatively low fuel pressure. The injector operates within a pressure range of 20 to 40 bar which is chosen to balance the need for high injection rates and high utilization of the hydrogen stored in the tank system without the requirement for a compressor. The highest injection pressure is used when high static flow rates are required at high engine loads. The lowest pressure is used to improve the control over small injection quantities at light loads. For this study, a DI-CHG15 was utilized, providing a mass flow rate of 15 grams per second at a H2 injection pressure of 40 bar. The direct injection system allows injection after the intake phase, avoiding the impact of Hydrogen injection on the volumetric efficiency. The H2 control system was also provided by PHINIA which optimises the injector drive current profile according to the operating hydrogen pressure.

The flow curves of the used injector are depicted in Fig. 14 . These measurements showed good stability of the injection rate for both 40 bar and 20 bar injection pressure allowing an accurate control of the injected hydrogen quantity for low and high load.

Fig. 15 depicts the hydrogen jet exiting the DI-CHG15 injector. The gaseous jet initially develops as a hollow cone (Fig. 15 (a)) because of the outward opening pintle and the deflector cap geometry. As the injection progresses, the jet angle reduces due to the pressure drop inside of the jet induced by the momentum exchange between the hydrogen and the air inside of the hollow cone [17]. This leads to the formation of a collimated narrow jet as shown in Fig. 15 (b) which has a high penetration rate in the combustion chamber.

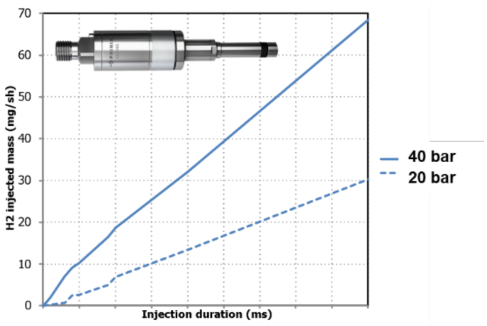

**Fig. 14**. DI-CHG15 Flow curves

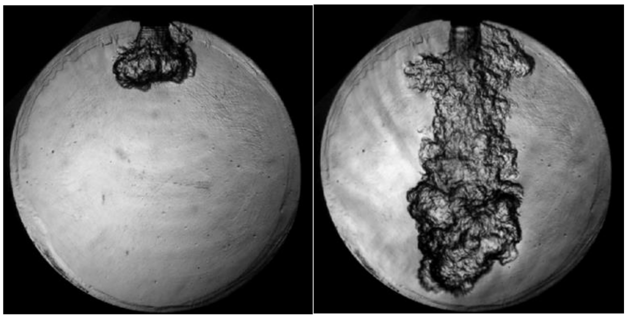
(a) Early phase (b) Fully developed

**Fig. 15.** Hydrogen jet development [17]

### 2.4 Potential advantages of the Dome engine design

The potential advantages of present combustion chamber can be listed as follows:

- The engine is equipped with a robust flat cylinder head which can continuously sustain exceedingly high peak in-cylinder pressures (up to 180 bar) expected from the hydrogen combustion.
- The Dome design allows to locate the DI injector and the spark-plug close to each other and ensures their central positioning with respect to the cylinder head. This was expected to facilitate achieving a desired charge stratification in M/C, Dome, and in the vicinity of the spark-plug. The CFD simulations (section 4.2 and 4.3) confirm that the present design can maintain a relatively richer mixture in the Dome and in the proximity of the spark-plug compared to the main chamber (M/C).
- With a stoichiometric air-fuel ratio of 34:1 for hydrogen, lean combustion necessitates substantially higher intake boost pressures compared to traditional spark ignition engines. Hence, the engine is purposefully designed with straight intake ports to minimize port flow losses and enhance their permeability.
- Due to the smaller flame quenching distance associated with hydrogen, higher wall heat losses can be expected. The current engine design features a flat cylinder head with straight intake ports, resulting in a relatively weak, unstructured bulk flow motion within the combustion chamber compared to its swirl or tumble dominated counterparts. Even if this might slow down the mixing rate, it can be advantageous for minimizing the convective heat losses to the combustion chamber walls.
- Owing to its distinctive design, the engine exhibits versatility in employing various injection and combustion methodologies:
    - Fully homogeneous combustion by injecting hydrogen early during the intake or during the compression stroke, based on the engine operating speed.
    - Stratified combustion by injecting hydrogen late during the compression stroke. This strategy can be particularly interesting at low load conditions and can be used for reducing parasitic losses such as pumping work and heat losses.
    - Partly homogeneous combustion by employing the split injection strategy. For instance, the first injection might be performed during the intake stroke to maintain a relatively homogeneous, ultra-lean mixture in the main chamber, supplemented by a subsequent late injection to sustain a relatively richer mixture in the Dome chamber.

## 3 Engine test bench description

The engine speed of SCE is limited to 4500 rpm, and it is balanced until the second order. The auxiliary components such as water and oil pumps are electrically driven. During these first tests, a commercially available lubricant oil designed for high performance gasoline engines was used. However, in the future, an in-house developed formulation that aims to reduce the occurrence of the pre-ignition will be evaluated.

### 3.1 Test bench

The engine is associated to an electric generator whose power and torque performances are illustrated in Fig. 16. The bench synoptic with the main control and measurement devices is presented in Fig. 17.

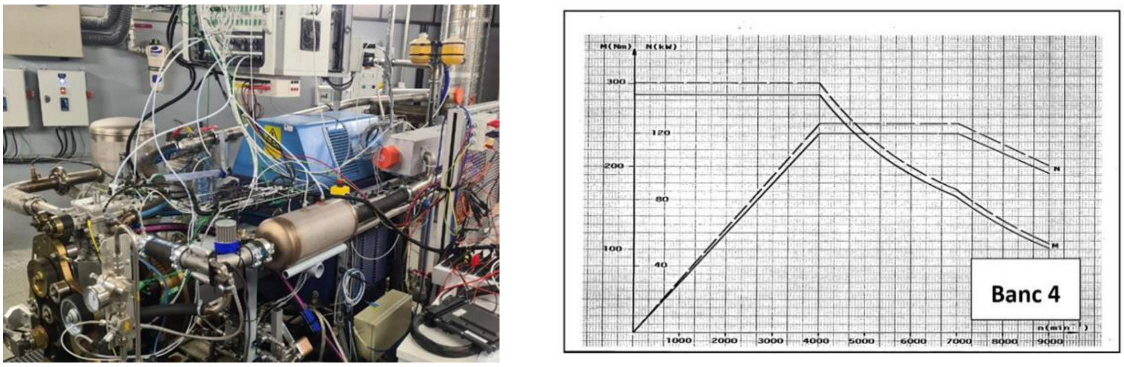

**Fig. 16.** Single cylinder engine (SCE) on the bench (left) and performances of the electric machine (right)

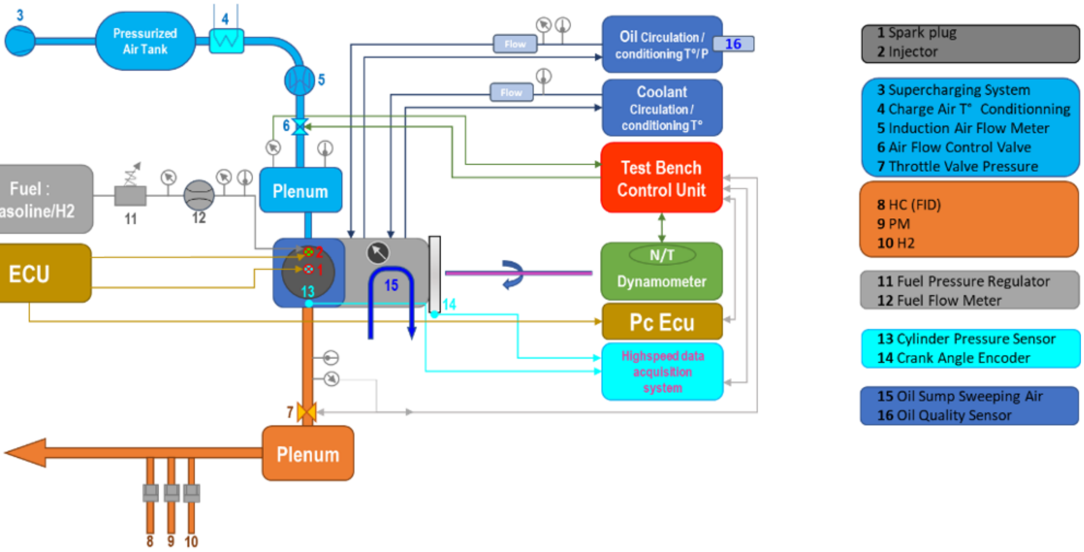
3
Pressurized Air Tank
4
5
6
Flow
Flow
Oil Circulation / conditioning T°/P
16
Coolant Circulation / conditioning T°
Test Bench Control Unit
Fuel : Gasoline/H2
11
12
Plenum
ECU
2
1
13
15
14
N/T
Dynamometer
Pc Ecu
Highspeed data acquisition system
7
Plenum
8
9
10
1 Spark plug
2 Injector
3 Supercharging System
4 Charge Air T° Conditionning
5 Induction Air Flow Meter
6 Air Flow Control Valve
7 Throttle Valve Pressure
8 HC (FID)
9 PM
10 H2
11 Fuel Pressure Regulator
12 Fuel Flow Meter
13 Cylinder Pressure Sensor
14 Crank Angle Encoder
15 Oil Sump Sweeping Air
16 Oil Quality Sensor

**Fig. 17.** Engine test bench synoptic

The bench was equipped with all the standard monitoring systems, with particular attention given to the measurements of hydrogen mass flow rate and unburnt concentration at the exhaust. Bronkhorst's Coriolis-based mass flow meters were used, with F-106BI for the air and F-113AI for hydrogen and the provided data were used to calculate the equivalence ratio. The obtained results were compared against another methodology based on the oxygen measured in the dry exhaust gases (see formula in Fig. 18). This comparison revealed a linear relationship, with a small deviation- around 5% on the current example- observed during lean operation.

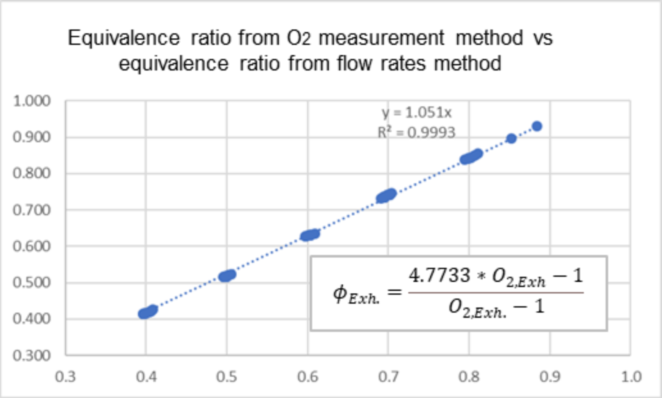

**Fig. 18.** Comparison between equivalence ratio calculation methodologies

One important item to consider is that the flow meters only reflect the equivalence ratio upstream of the combustion chamber. This measurement does not take into account any air leakage in the intake ducts or the blow-by at the beginning of the compression stroke, which only affects air until the hydrogen is injected.

On the contrary, measuring the oxygen concentration in the exhaust gases reflects the equivalence ratio during combustion, but disregards unburnt fuel, resulting in an underestimation of fuel consumption. Therefore, neither of these two methods is entirely satisfactory but they can be sufficient for a first analysis. To conclude, we have decided to use the mass flow information for evaluating the equivalence ratio and the hydrogen consumption, thereby the efficiency.

### 3.2 Test methodology and combustion characterization

This research program followed on the single cylinder engine aims to evaluate the potential of the hydrogen ICE in terms of power density and efficiency at high loads. Consequently, the primary focus is not on $NO_x$ emissions. The program will explore three different combustion strategies, the first one centered on lean combustion, and the other two integrating exhaust gas recirculation (EGR) and water injection, respectively. However, this paper focuses only on the first strategy.

For this paper, a high load operating point at 2000 rpm and 16 bars has been selected to characterize the combustion system.

The test results are focused on two sweeps, the first one involving a variation of the equivalence ratio between 0.40 and 0.80. Then, for each equivalence ratio, a variation of spark advance (SA) was conducted. The spark-timing variation was limited by knock, unstable combustion, or a significant decrease in thermal efficiency. The origin of ignition timing was chosen at the combustion top dead center (TDC), negative values mean that ignition is set before TDC.

Combustion stability was characterized by the normalized standard deviation of the IMEPg (COV IMEPg) over 300 consecutive cycles, with a stability limit set at 3% for the chosen operating point. The combustion process is illustrated by of course its stability but also by the quite conventional criteria based on CA10, CA50, CA90. The apparent heat release was calculated based on the first law of thermodynamics without considering the wall heat losses. During the compression stroke, a specific heat ratio of 1.40 was used, while during the expansion stroke, a specific heat ratio of 1.30 was applied. In order to have a better understanding of the ability to burn ultra-lean mixtures, we have included the standard deviation of the CAXX in this analysis.

The engine operating conditions are highlighted in the Table 3.

**Table 3.** Engine operating conditions

| | |
|---|---|
| Engine speed | 2000 rpm |
| Engine load, IMEPg | 16 bars IMEPg |
| Intake air temperature | 40°C |
| Hydrogen temperature | ~25°C (not controlled) |
| Water in temperature | 90°C |
| Lube oil in temperature | 85°C |

| | |
|---|---|
| Exhaust back pressure P3 versus air intake pressure P2 | 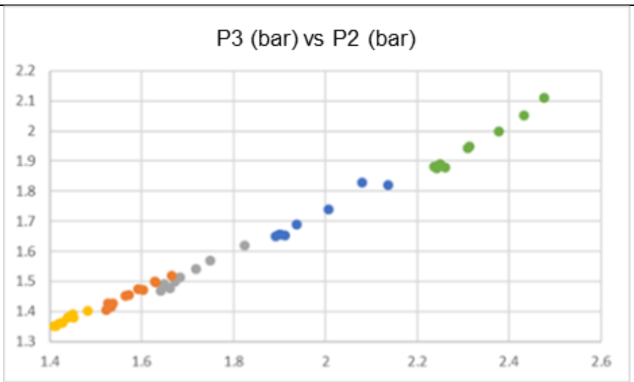 |
| Injection pressure | 25 bar |
| Start of Injection (SOI) | 140° bTDC |

### 3.3 Engine test results

All the tests have been governed by combustion stability. Fig. 19 (a,b) illustrate the results obtained from spark advance (SA) sweeps for different equivalence ratios between 0.40 and 0.80. For advanced spark timings, limitations were primarily imposed by knock or a significant decline in thermal efficiency. Overall, the combustion stability remained extremely good, well below the defined threshold of 3%; for the two richest mixtures, it was independent of the spark timing, even when the ignition point was delayed late during the expansion stroke (Fig. 19 (a)).

The best indicated thermal efficiency of 46% was obtained for ultra-lean mixture with equivalence ratio of 0.40 and very early ignition; it might be emphasized that this efficiency could be improved by reducing the knock propensity, for instance by reducing the water temperature down to 65°C. Fig. 19 (b) clearly shows that the efficiency decreases when the combustion is delayed, is more sensitive with the leanest mixtures, in fact, 0.40 and 0.50 equivalence ratio, and particularly 0.40. This behavior is probably due to a higher sensitivity of ultra-lean mixture to the mixture temperature decrease during the expansion stroke.

Fig. 21. summarizes the effect of the equivalence ratio on the efficiency, showing the potential of ultra-lean burn combustion.

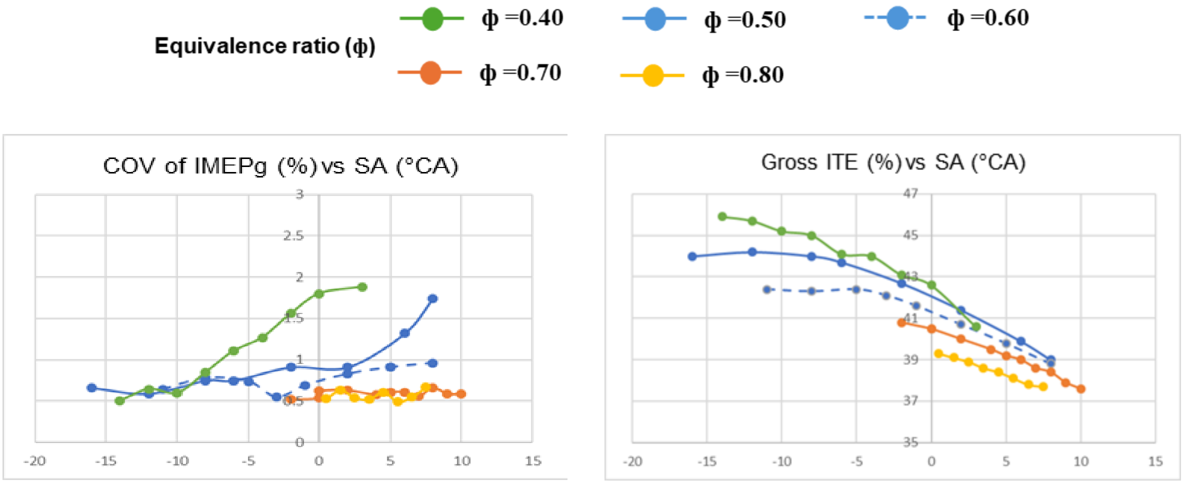

(a) (b)

**Fig. 19.** Combustion stablity (COV IMEPg) and gross indicated thermal efficiecny (ITE) vs spark advance (SA) at different equivalence ratios (ϕ)

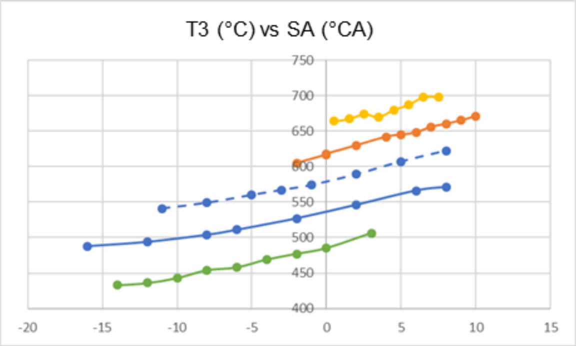

**Fig. 20.** Exhaust temperature (T3) vs spark advance (SA)

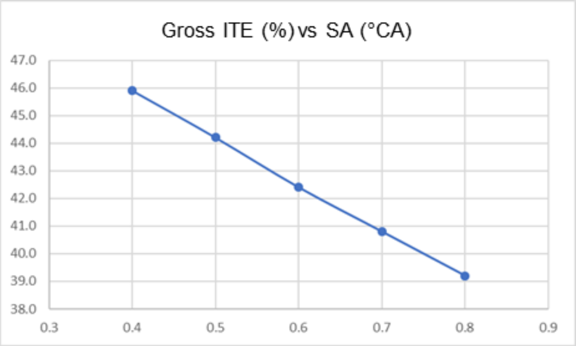

**Fig. 21.** Gross indicated efficiency (ITE) vs equivalence ratio (ϕ)

Fig. 22 provides some information concerning the mechanical stress applied to the combustion chamber as the continuous peak pressure was limited to 150 bars to preserve the piston. The pressure gradient always remained under 9 bars/°CA whatever the equivalence ratio or the ignition timing were.

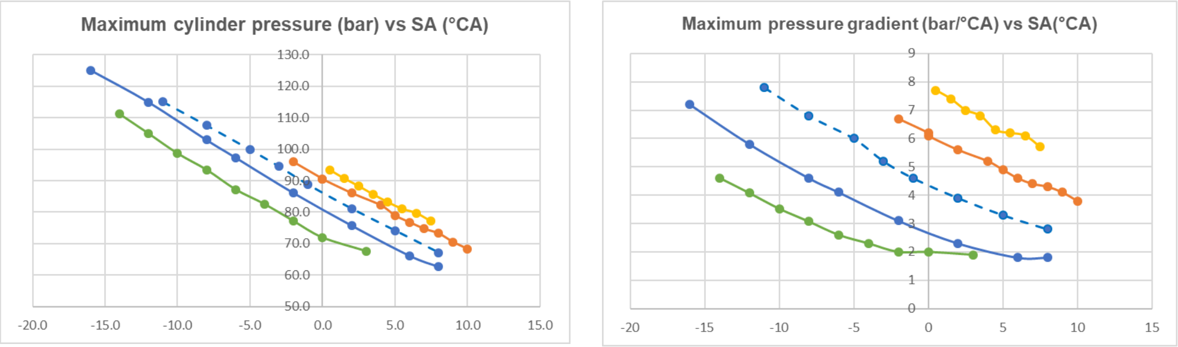

(a) (b)

**Fig. 22.** Maximum in-cylinder pressure vs spark advance (a) and maximum pressure gradient (bar/°CA) vs spark advance (b)

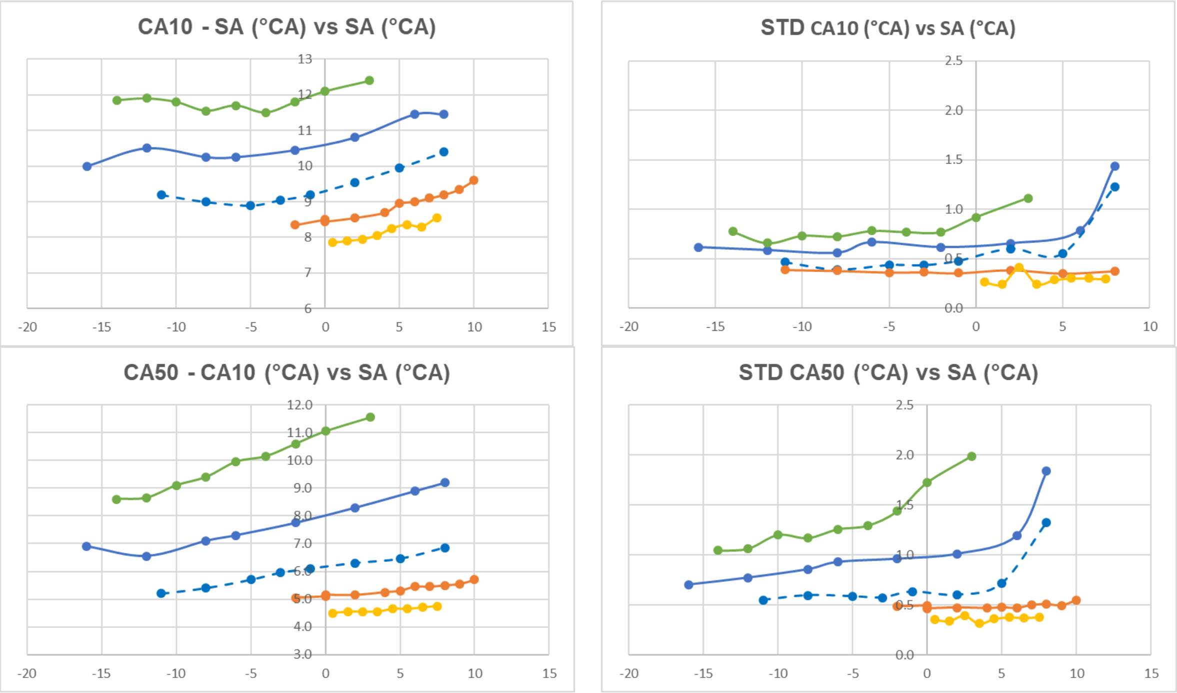

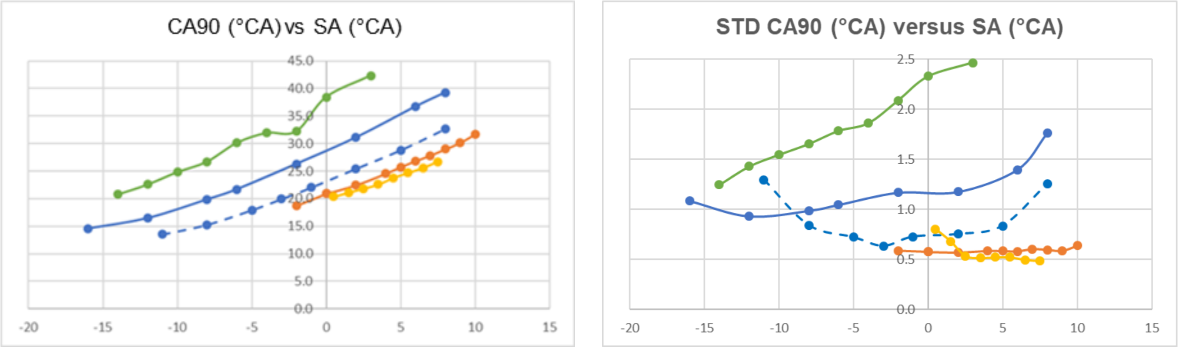

**Fig. 23.** Engine combustion analysis represented by burn angles (CAXX) and their standard deviation from 300 engine cycles vs spark advance (SA)

Following a first-order combustion analysis ignoring wall heat losses, it appears that the start of combustion denoted by CA10-SA is quite stable (standard deviation of CA10 < 1°CA) and only marginally depends upon the spark advance, i.e., the thermodynamic conditions at ignition and the global equivalence ratio, reflecting stratification.

Differences are much more important during the flame propagation (CA50-CA10) and the end of combustion (CA90), where the influence of the equivalence ratio becomes more noticeable. For equivalence ratio 0.40, combustion is clearly slowing down because of a high influence of the in-cylinder temperature decrease during the expansion stroke. Nevertheless, as it is illustrated in Fig. 24 with a comparison of the CA90 PDF distribution for equivalence ratios 0.40 and 0.50, the increase in standard deviation with the leanest mixture is not linked to any “very long” combustion (only very few cycles have a CA90 of +2°CA versus the average) but to some dispersion around the mean value.

In conclusion, the combustion system remained robust in ultra-lean mode, allowing to take benefit of the lower heat dissipation to the walls.

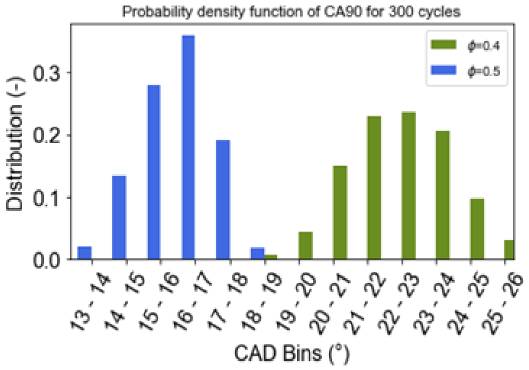

**Fig. 24.** PDF of CA90 at equivalence ratio 0.40 (green) and equivalence ratio 0.50 (blue) at SA=-12°CA

### 3.3.1 *Brief comparison with a pent-roof combustion chamber*

Fig. 25 and Fig. 26 compare the engine test results of the Dome engine to a conventional pent-roof chamber, both having identical dimensions, engine components (piston, injector etc.) and compression ratios. Thanks to a high tumble motion and a significantly higher turbulent kinetic energy (TKE), combustion is significantly quicker with the pent-roof design, especially during the flame propagation until CA90. Nevertheless, this potential advantage is not reflected by any improvement in terms of thermal efficiency or combustion stability, probably due to significantly higher wall losses associated with the pent-roof design. In future, this comparison is planned to be established on more engine operating conditions.

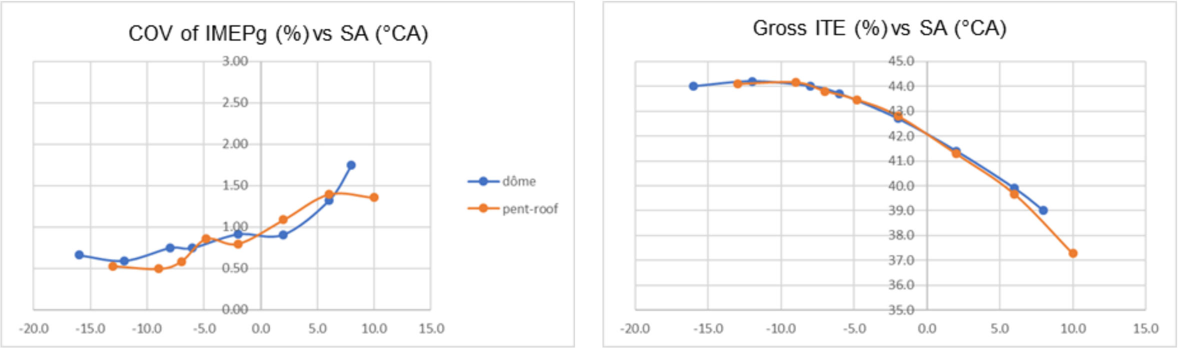

**Fig. 25.** Combustion stability (COV IMEPg) and gross indicated thermal efficiency (ITE) vs spark advance (SA) at equivalence ratio 0.50 for Dome (blue) and Pent-roof (orange) engines

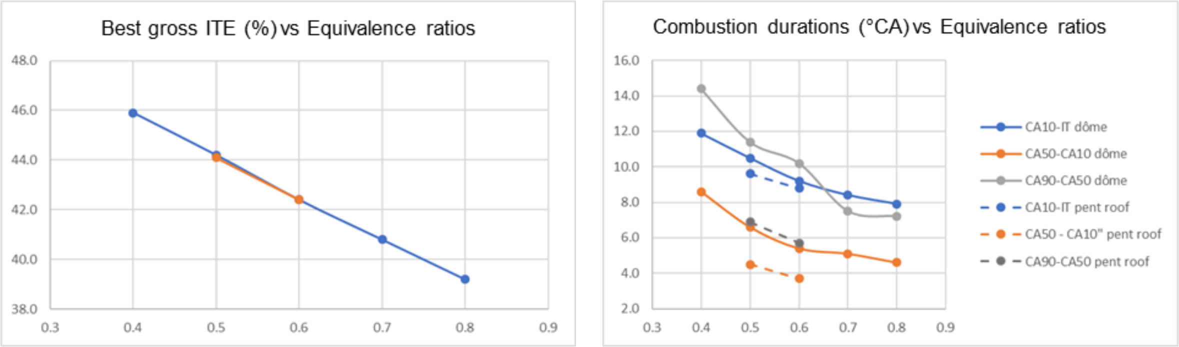

**Fig. 26.** Indicated efficiency comparison between Dome and Pent-roof engines at individual best spark-advances (SA)

## 4 3D CFD modelling

### 4.1 Simulation setup

In this study, the computational work was carried out employing the commercial Computational Fluid Dynamics (CFD) software CONVERGE [18,19]. The engine simulations were performed using the full-cycle approach with calculations commencing at the exhaust valve opening. The initial conditions inside the combustion chamber at the exhaust valve opening were derived from a dedicated one-dimensional GT-Power three-pressure analysis (TPA) simulation.

Mesh generation was executed dynamically by CONVERGE during runtime, with grid size adjustments made throughout the simulation. A base grid size of 2.5 mm was used which was supplemented by fixed embedding and adaptive mesh refinement (AMR) inside the whole computational domain.

During the hydrogen injection, the grid size was refined to 78 μm in the injector needle seat area using the fixed embeddings. Subsequent embedding cylinders were introduced downstream of the injector tip to adequately capture the flow characteristics of the high-velocity hydrogen jet. Furthermore, AMR criteria based on velocity, temperature, and hydrogen mass fraction were used to facilitate grid refinement beyond fixed embedding zones, resulting in a maximum grid count of approximately 3.5 million cells during injection events. This meshing criterion was identified by a separate validation of the $H_2$ jet penetration (longitudinal and lateral) against the dedicated schlieren measurements.

To accurately model ignition initiated by spark deposition, grid refinement to 78 μm was implemented in the vicinity of the spark plug electrodes. The grid size was maintained between 312 μm and 625 μm during the complete combustion event.

The simulation time-step was defined using a variable time step algorithm, with a limit on maximum CFL number at 1. The pressure implicit with splitting of operators (PISO) algorithm [20] was used for resolving the pressure-velocity coupling.

Hydrogen demonstrates real gas behaviour and heats up on expansion. Therefore, the Redlich-Kwong-Soave real gas equation of state was used for the gas simulation. Turbulence was modelled using Renormalization group k-epsilon (RNG k-ε) RANS type turbulence model [21]. Heat transfer between the gas and walls was modelled using Han and Reitz model [22]. To address the high mass diffusivity of hydrogen relative to other fuels and its consequential impact on flame speed, local mixture average diffusion coefficients were computed from a transport.dat file [23]. Finally, the SAGE detailed chemistry solver was opted for modelling the combustion utilizing the chemical kinetics model developed by CRECK modelling group [24,25,26].

In this study, Computational Fluid Dynamics (CFD) simulations were conducted at two distinct engine operating conditions: 2000 rpm x 16 and 6000 rpm x High load. Experimental data was pre-existing for the former condition and was employed to validate the predictive capabilities of the CFD model. Subsequently, the validated model parameters were applied at 6000 rpm x high load to predict the engine performance and associated challenges.

### 4.2 2000 rpm x 16 bar, $\phi$=0.50

At this operating point, the available experimental data was used to define the boundary conditions for the CFD simulation. Thus, the crank-resolved intake and exhaust pressures, along with measured intake and exhaust gas temperatures were applied to the inflow and outflow flow boundaries, respectively. During the engine testing, hydrogen injection was executed at 25 bar of rail pressure, commencing at 140°bTDC. A delay of approximately 0.67 milliseconds was estimated between electrical command and actuation of the injector needle by comparing the measured in-cylinder pressure signal with the isentropic compression curve as shown in Fig. 27. Later on, the same was applied for precising the start of injection timing in the CFD simulations.

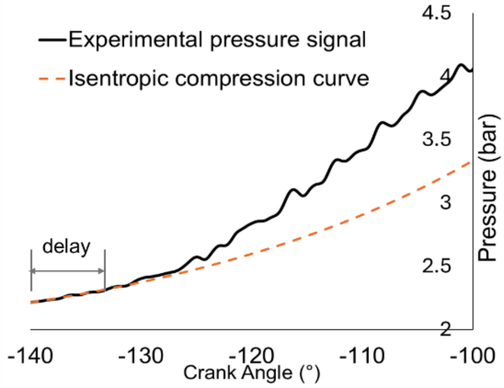

**Fig. 27.** Delay in the actuation of injector needle

Firstly, the cold flow simulations (without hydrogen injection) were performed to clearly understand the air-flow dynamics in the combustion chamber and to anticipate its subsequent impact on air-fuel mixing and combustion. Then, the simulations incorporating hydrogen injection and combustion modelling were performed. Fig. 28. compares the evolution of turbulent kinetic energy (TKE) in the main chamber (M/C) and Dome from the CFD simulations excluding and including the hydrogen injection. During hydrogen injection, the TKE increases in both chambers before gradually dissipating towards the end of the compression stroke, a common observation in flat cylinder head designs. It is worth noting that the TKE near the firing top dead center (TDC) was found to be approximately 2.5 times higher in both chambers with hydrogen injection compared to the fully aerodynamic scenario, which potentially supported the flame propagation during the engine testing at this operating point.

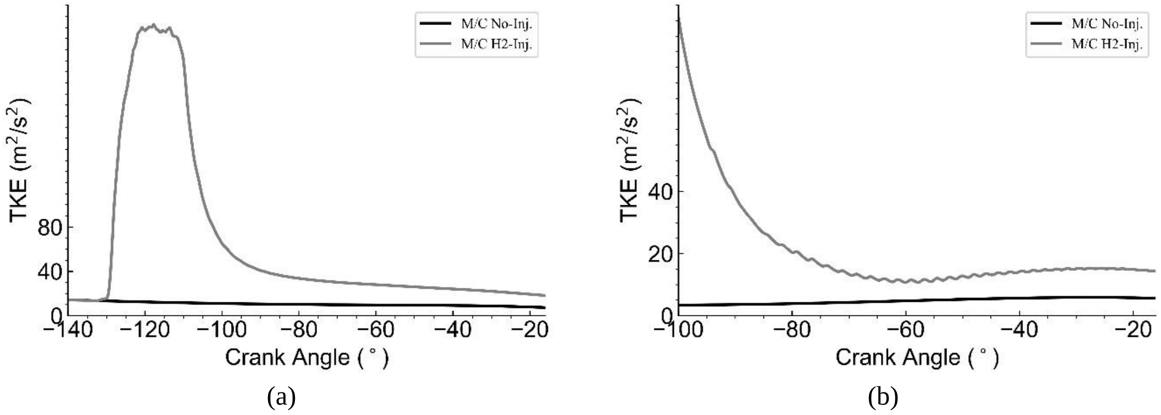

(a) (b)

**Fig. 28.** Turbulent kinetic energy evolution with and w/o $H_2$ injection in M/C (a) and Dome (b)

Fig. 29. depicts the air flow pattern in the M/C and Dome towards the latter stages of the compression stroke. The velocity vectors demonstrate the movement and flow structures highlighting the two key observations: the movement of gases from M/C towards the Dome due to compression and an anti-clockwise rotational flow motion within the Dome. Later on, this flow pattern was identified to influence the trajectory of fuel jet and the transportation of relatively richer mixture from M/C towards Dome (Fig. 30., Crank Angle = -40°, -20°).

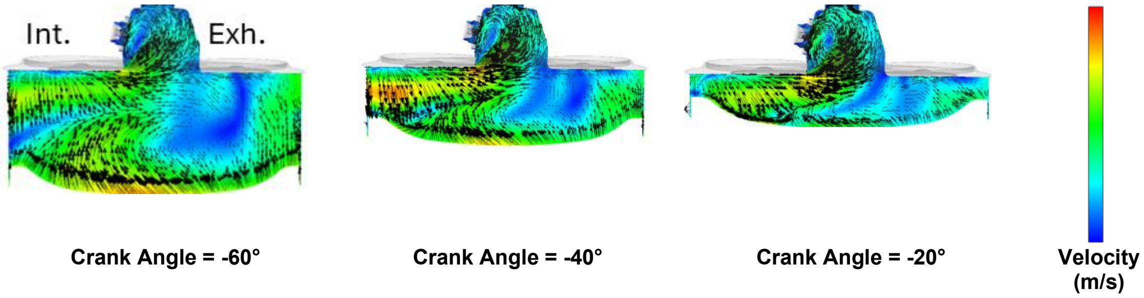

**Fig. 29.** Velocity field and vectors in vertical plane demonstrating the air flow dynamics between M/C and Dome towards the end of compression stroke from a fully aerodynamic simulation without $H_2$ injection

**Fig. 30** focuses on the hydrogen injection and mixture preparation. The hydrogen injection was performed post IVC, between 132°bTDC and 109° bTDC. In the absence of pronounced bulk flow motion and weaker turbulence for this engine, the mixing mechanism predominantly relies on the available mixing time. This mixing window was estimated to be around 9 milliseconds between the end of injection (EOI) and firing TDC. The hydrogen injection and mixing process is represented in Fig. 30 with the help of 2D cut planes. The hydrogen injection takes place at sonic velocity as the ratio of rail pressure and combustion chamber pressure remains beyond 1.90. Consequently, the jet trajectory remains vertical and undisturbed by the mean air-flow pattern in the combustion chamber. Then, it collides with the piston and travels along both the piston and the cylinder liner. As depicted in Fig. 30 (b,c,d), the upward displacement of the jet is more prominent on the intake side (the left part of the combustion chamber) compared to the exhaust side. This was potentially caused by the airflow pattern inside the combustion chamber, as previously described in Fig. 29.

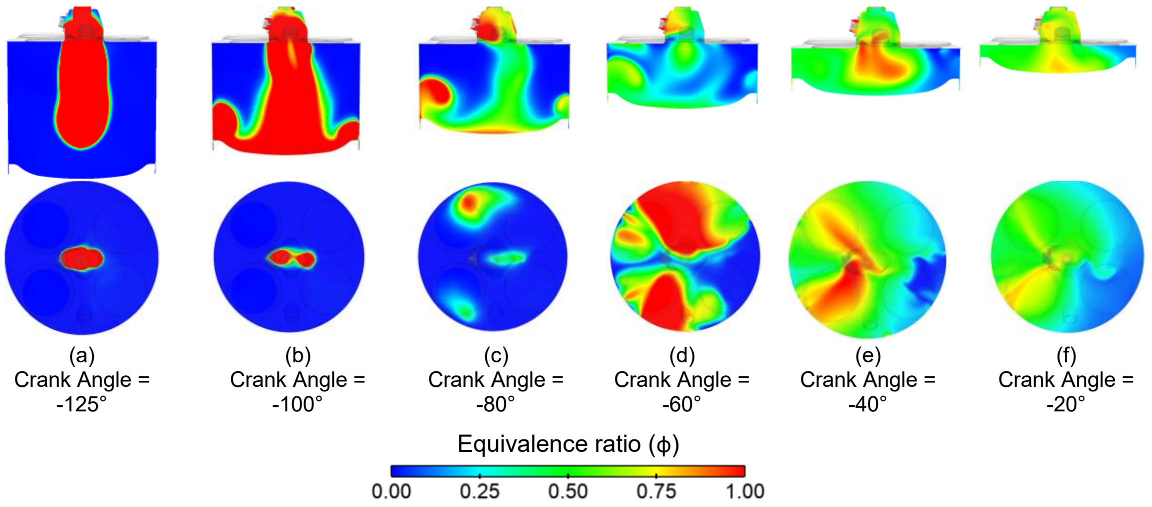

**Fig. 30.** $H_2$-air mixing evolution at various crank angles illustrated by the fuel-air equivalence ratio (ϕ) fields in a vertical plane positioned between the two intake ports (1st row) and horizontal plane placed 2.5 mm below the cylinder head (2nd row)

Overall, the following remarks can be made on mixture preparation based on the analysis of CFD results:

- Qualitatively, the charge remained notably stratified throughout the combustion chamber, even close to firing TDC (Fig. 30 (f)). The mixture was identified to be relatively leaner on the exhaust side, which might have contributed to the mitigation of abnormal combustion phenomena such as pre-ignition and knocking, commonly initiated beneath the hot exhaust valves during test bed experiments.

- Fig. 31 shows the probability density function of the equivalence ratios in the M/C and Dome. It can be seen that the mixture demonstrates a better homogeneity in the Dome region compared to the M/C.
- In Fig. 32., the evolution of mean equivalence ratio in M/C, Dome, and close to the spark-plug is depicted. The mean equivalence ratio (ϕ) in whole the combustion chamber was 0.50 for this operating point. Simulation results indicated a notably higher equivalence ratio (~0.60) in the Dome compared to the M/C (~0.49). Additionally, the equivalence ratio near the spark-plug was consistently identified as around 0.70 on different spark timing (denoted with circles), providing favorable conditions for a stable ignition.

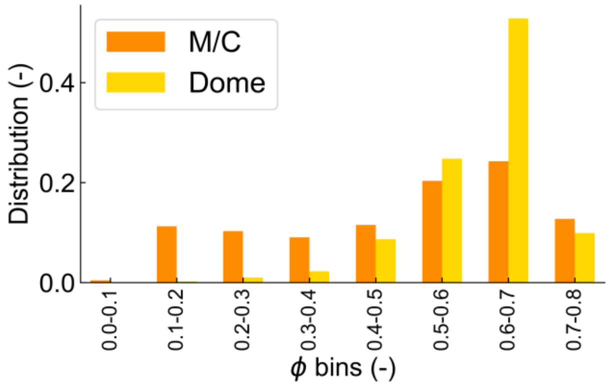

**Fig. 31**. Distribution of equivalence ratio (ϕ) in M/C and Dome at 12° bTDC

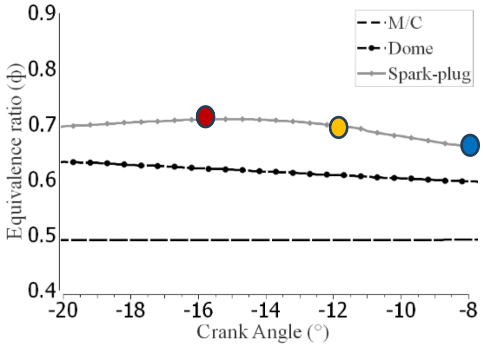

**Fig. 32.** Evolution of average equivalence (ϕ) ratio in M/C, Dome and close to spark-plug electrodes

Finally, the combustion modelling was realized on three different spark-timings using the SAGE detailed chemistry solver. Fig. 33. presents a comparison between the experimental and CFD results. Despite notable mixture heterogeneity in the combustion chamber, the CFD simulations satisfactorily captured the evolution of in-cylinder pressures with varying spark timing (Fig. 33 (a)). Fig. 33. (b-d) compare experimental in-cylinder pressure and apparent heat release rates from 300 test cycles with the CFD results. The CFD simulations consistently predicted higher peaks of heat release and notably a shorter end-of-combustion. One possible reason for this difference could be the lack of accuracy of the RANS CFD models in predicting the hydrogen and air mixing. On this aspect, we plan to validate the mixing prediction by CFD utilizing advanced optical diagnostics in the near future. Additionally, the state of the art chemical kinetics mechanisms are not validated for laminar flame speed at engine-relevant thermodynamic conditions which could be another potential reason for these discrepancies. Overall, the present CFD results could be considered in good agreement with test results demonstrating a reasonable model predictivity.

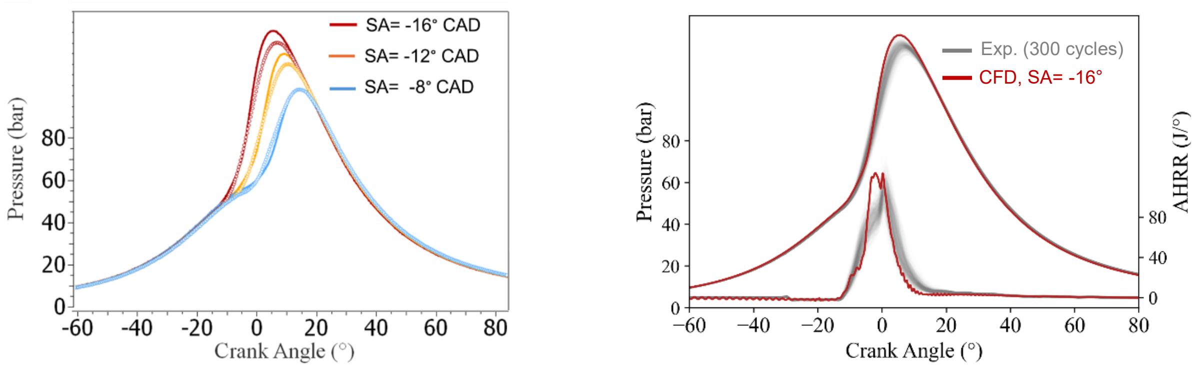
Comparison of in-cylinder pressure obtained from Exp. average cycle (o o o) and CFD (— ) at diffent spark-timings

(a) (b)

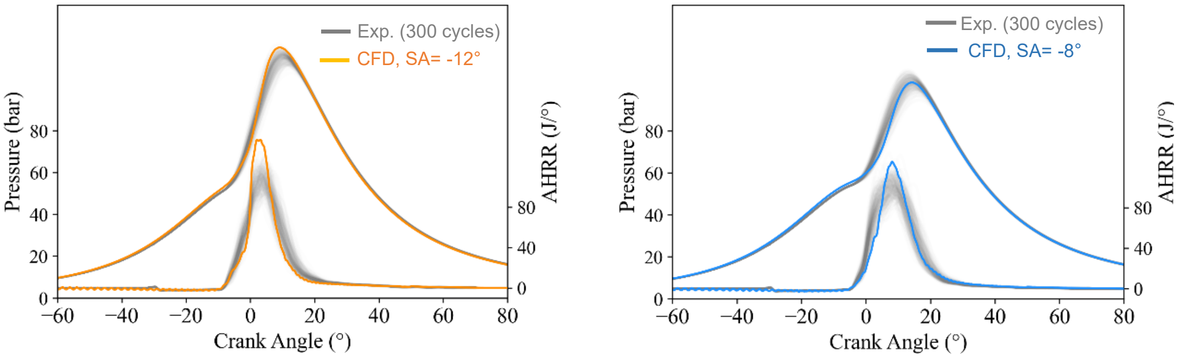

(c) (d)

**Fig. 33.** Comparison of Experimental and CFD results in terms of in-cylinder pressure and apparent heat release rates

### 4.3 6000 rpm x High load, ϕ=0.53

On this engine operating condition, the experimental data was not available, therefore, a constant intake pressure of 2.60 bar and intake temperature of 40°C were applied as inflow boundary conditions. The hydrogen injection was performed at 40 bar of rail pressure and an average equivalence ratio of 0.53 was targeted in the combustion chamber to achieve a potential IMEP of 22 bar. The CFD model settings were maintained identical to validated 2000 rpm x 16 bar configuration.

The objective of this task was to estimate the engine performance and associated challenges at high engine speed and high load using CFD simulations. Therefore, different injection strategies were numerically investigated to achieve the desired $H_2$-air mixing and combustion. As the injection timing can have an impact on trapped air mass in the combustion chamber, the fuel injection mass was adjusted accordingly in the CFD simulations to compare the different configurations at the same equivalence ratio.

The first numerical test was performed involving a single injection post-IVC (SInj), with injection taking place between 132°bTDC and 68°bTDC. This allowed approximately 1.88 milliseconds of mixing time between the end of the injection and the firing TDC. It must be noted that the same was estimated to be around 9 milliseconds at 2000 rpm x 16 bar.Then, split injection with a split ratio of 70:30 was investigated. For the split injection, the timing of the start of the first injection (SOI-1) was set at 260°bTDC, around the peak intake valve lift. It must be noted that the optimization of the split ratio and the injection timings was not considered in the scope of this work. Following this, the second injection commencing at 80°bTDC (SpInj) was performed. The SOI-2 was estimated to achieve a late injection while still guaranteeing a choked flow from the injector during the complete injection event. Fig. 34. Summarizes the two injection strategies tested via CFD simulations, nominated as SInj and SpInj. The evolution of in-cylinder trapped mass from the two configurations is highlighted in Fig. 35. As anticipated the split injection strategy reduced the in-cylinder trapped air mass by 6.3%.

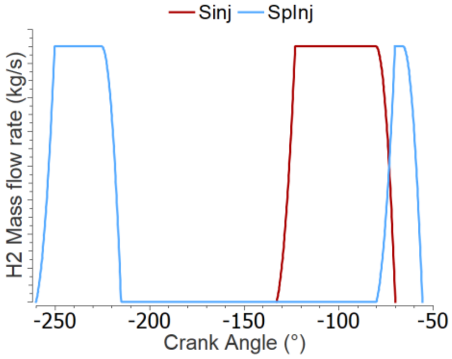

**Fig. 34.** Different Fuel injection strategies

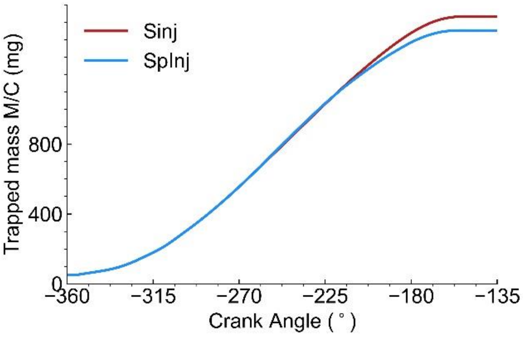

**Fig. 35.** Trapped mass evolution inside the M/C

Previously at 2000 rpm, the hydrogen injection boosted the turbulent kinetic energy (TKE) close to firing TDC in both chambers by 2.5 times, which potentially boosted the fuel burn rate as well. Fig. 36 compares the evolution of TKE in M/C between the different simulated configurations. Compared to pure aerodynamic configuration, the gain in TKE in M/C was identified as 9 % when all the hydrogen was injected during a single injection (SInj). However, in the case of split injection, where only a portion of the total fuel was injected during the second injection, the increase in TKE was not observed.

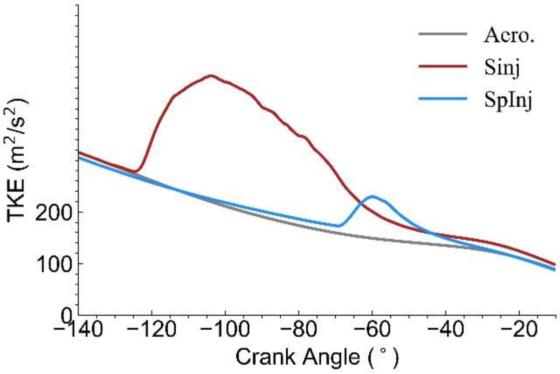

**Fig. 36.** Turbulent kinetic energy (TKE) evolution in M/C

A Comparison of hydrogen injection and mixing mechanisms for two injection strategies is illustrated through 2D visualization planes in Fig. 37. (a,b). For single injection (SInj) configuration, the hydrogen injection occurred between 132°bTDC and 68°bTDC. During this interval, the pressure in the combustion chamber increased from 3.7 bar to 10 bar, whereas the fuel injection pressure was 40 bar. This meant the complete injection event occurred respecting a choked flow condition. In 2D visualizations, we can observe a vertical fuel jet impinging on the piston (Fig. 37 (a)). Overall, the mixing mechanism and trajectory of the fuel jet appear quite similar to the previously discussed 2000 rpm x 16 bar case. However, a notably higher mixture heterogeneity was observed as depicted in Fig. 38 (a) due to the limited mixing time available at 6000 rpm. It's important to note that 28% of the charge in the M/C comprised an equivalence ratio between 0.70 and 1.60, which might lead to abnormal combustion. In summary, the single injection after IVC (SInj) did not provide a substantial boost in TKE close to firing TDC and additionally, it produced a highly heterogeneous mixture in the combustion chamber.

A potential remedy for improving the mixture homogeneity could be early injection during the intake stroke. However, apart from having a penalty on volumetric efficiency, this approach could be more susceptible to the risk of pre-ignition as it would increase the residence time of unburnt fuel in the combustion chamber. Therefore, a split injection strategy was investigated as an alternative solution.

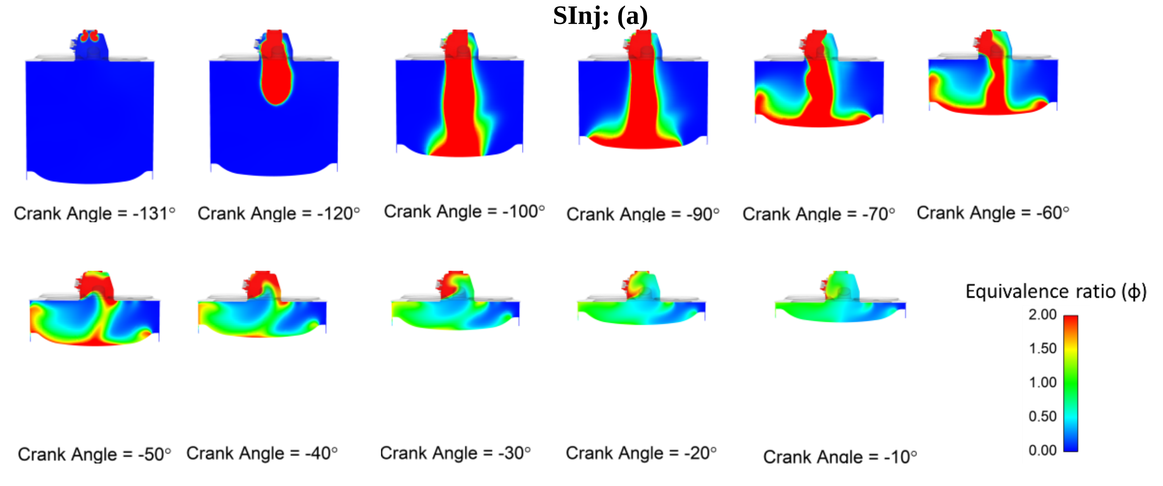

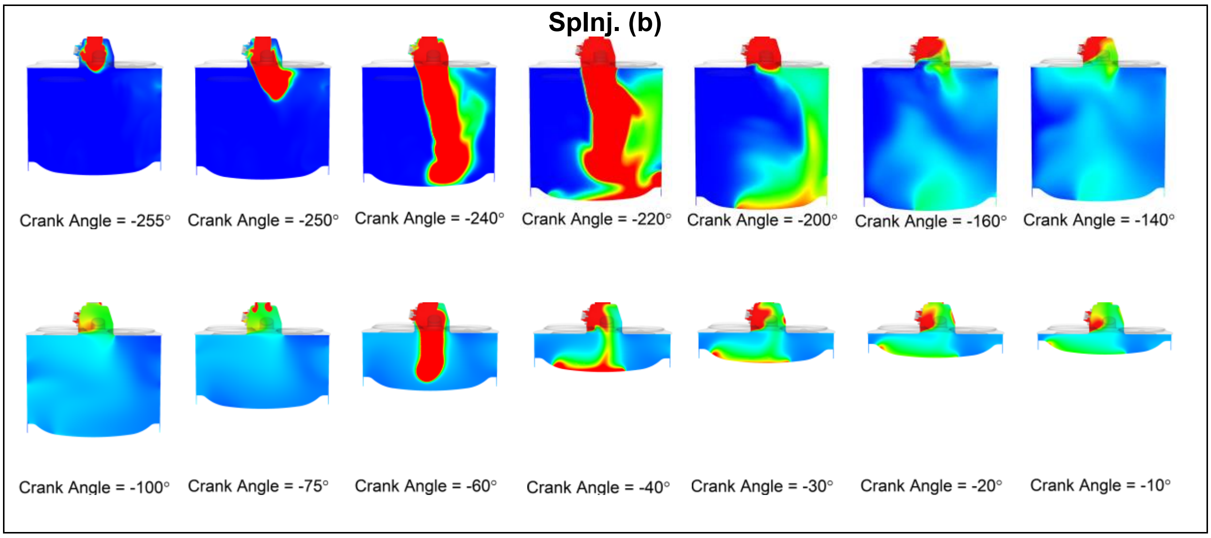

**Fig. 37.** $H_2$ injection and air-fuel mixing evolution at different crank angles illustrated by the fuel-air equivalence ratio (ϕ) fields in a vertical plane positioned between the two intake ports for the different injection strategies

For the split injection configuration (SpInj), the first injection was executed between 260°bTDC and 215°bTDC, when the intake valve was fully open. As a result, the fuel jet was directed towards the exhaust side by incoming airflow from the intake ports as can be visualized in Fig. 37 (b). This method capitalized on the intake air-flow to enhance the mixing rate, while the early injection provided supplementary time for the mixture preparation. Overall, a temporal window of 3.8 milliseconds was available between the end of the first injection and the start of the second injection. Then, the second injection was performed between 80°bTDC and 55°bTDC. In this interval, the pressure in M/C and Dome was rising from 7.5 bar to 15.5 bar due to the piston compression. Consequently, the fuel jet penetration into the M/C was significantly reduced due to high back pressure and a large proportion of injected hydrogen was expected to stay in the Dome.

The distribution of the equivalence ratio in M/C close to firing TDC is plotted in Fig. 38 (a). One can see that the split injection (SpInj) largely improved the mixture homogeneity in the M/C compared to single injection configuration (SInj) and their respective standard deviation of equivalence ratio were reported as 0.19 and 0.32. Additionally it must be noted that the mean equivalence ratio in M/C remained ultra-lean (ϕ = 0.37) before the start of 2nd injection and even after the end of 2nd injection it was identified as lower (ϕ = 0.48) compared to the single injection case (ϕ = 0.50) as presented in Fig. 38 (b). The 2D cut planes comparing the equivalence ratio fields at 10°bTDC for the two configurations are shown in Fig. 39.

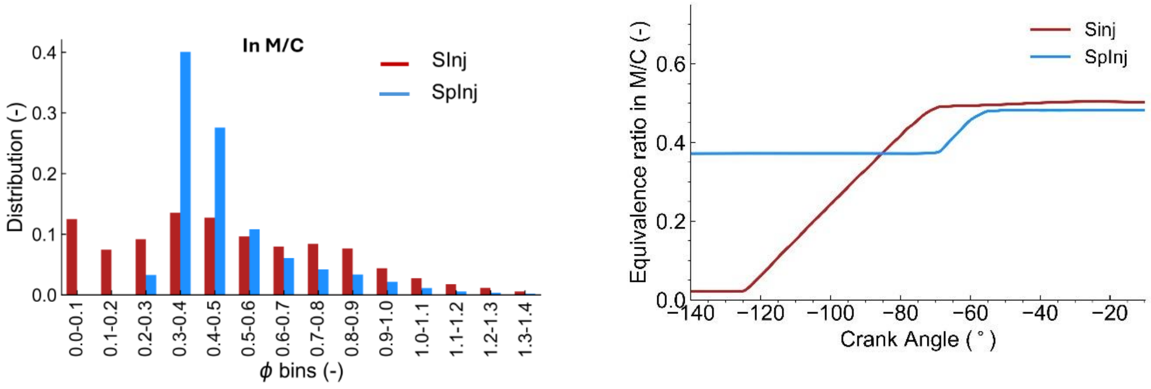

(a) (b)

**Fig. 38.** Distribution of equivalence ratio (ϕ) in M/C (a) at 10°bTDC and evolution of mean equivalence ratio in M/C (b)

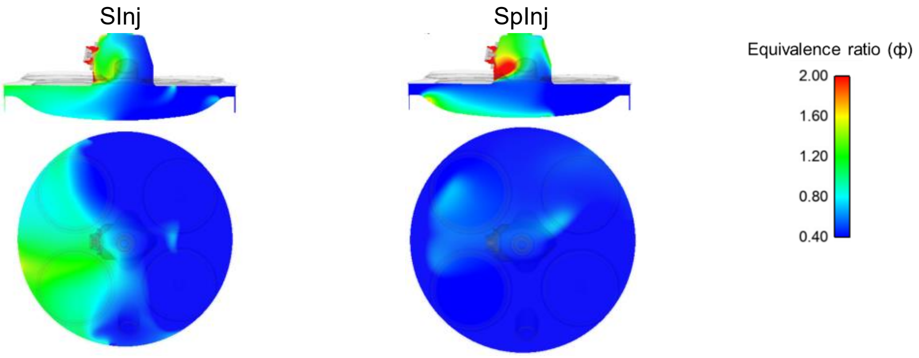

**Fig. 39.** The fuel-air equivalence ratio (ϕ) fields in a vertical plane positioned between the two intake ports (1st row) and horizontal plane placed 2.5 mm below the cylinder head (2nd row) at 10°bTDC

Conversely to M/C, the heterogeneity of the mixture near firing TDC was augmented in the Dome due to the late second injection (Fig. 40(a) and the respective standard deviation of equivalence ratio at 10°bTDC was registered as 0.55 compared to 0.42 for the single injection case. The delayed injection also resulted in a significant portion of the injected hydrogen ($H_2$) being retained in the Dome. At 10°bTDC, the hydrogen mass within the Dome was registered as 3.2 mg, which accounted for nearly 52% of the fuel injected during the delayed second injection. As illustrated in Fig. 40(b), a higher mean equivalence ratio by 24 % was reported in the Dome near the firing TDC.

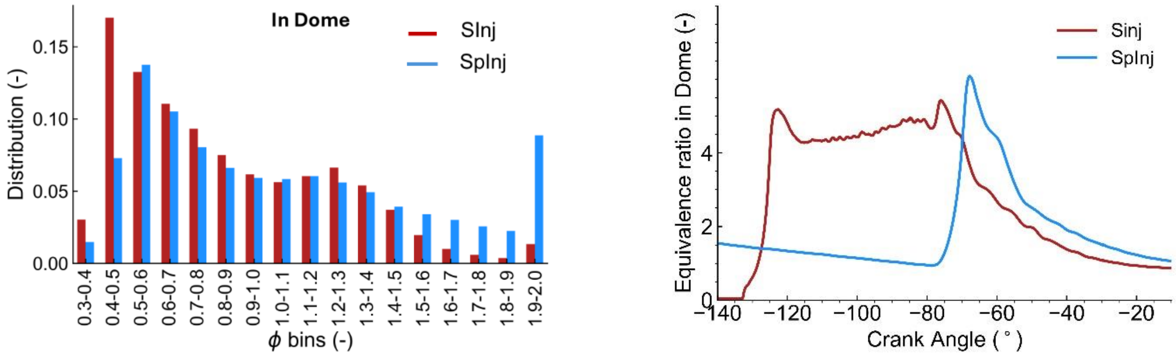

(a) (b)

**Fig. 40.** Distribution of equivalence ratio (ϕ) in Dome (a) at 10°bTDC and evolution of mean equivalence ratio in Dome (b)

It is noteworthy that approximately 17% of the mixture within the Dome exhibited an equivalence ratio exceeding 1.60 (Fig. 40(a)), which was predominantly concentrated close to the spark-plug (Fig. 39). Considering that the peak laminar flame speed of hydrogen-air mixture occurs around an equivalence ratio of 1.60 (Fig. 10), the delayed injection strategy could be anticipated to yield a slower and controlled start of combustion in Dome. The hydrogen was injected in the Dome at a lower temperature compared to the mean gas temperature within it and remained there, it was projected to influence the overall gas temperature within the Dome. As a result, the gas temperature in Dome was identified ~10 K lower with split injection compared to single injection strategy. These chemical and thermodynamic factors were anticipated to govern a slower combustion process within the Dome.

Subsequently, the combustion was simulated for the two configurations by applying the same spark timing of 10° bTDC. Fig. 41 illustrates a comparison of flame propagation between the two configurations, represented by iso-surfaces of gas temperature, deliberately colored according to the local equivalence ratio at the flame front. The visualizations confirm a relatively slower start of combustion and a slower flame propagation in the Dome (Crank Angle = -8 and -6°).

As explained earlier, in M/C, the mixture exhibited significantly improved homogeneity with SpInj compared to SInj, which showed greater heterogeneity and a notably larger volume (on the intake side) occupied by the equivalence ratio between 0.70 and 1.60 at the Dome exit (Fig. 39). This mixture is further compressed by the flame front and undergoes almost spontaneous combustion (-4° CA) consuming all the charge on intake side. Conversely, with SpInj, the flame encounters a more homogeneous and lean mixture at the Dome exit, leading to controlled combustion in M/C.

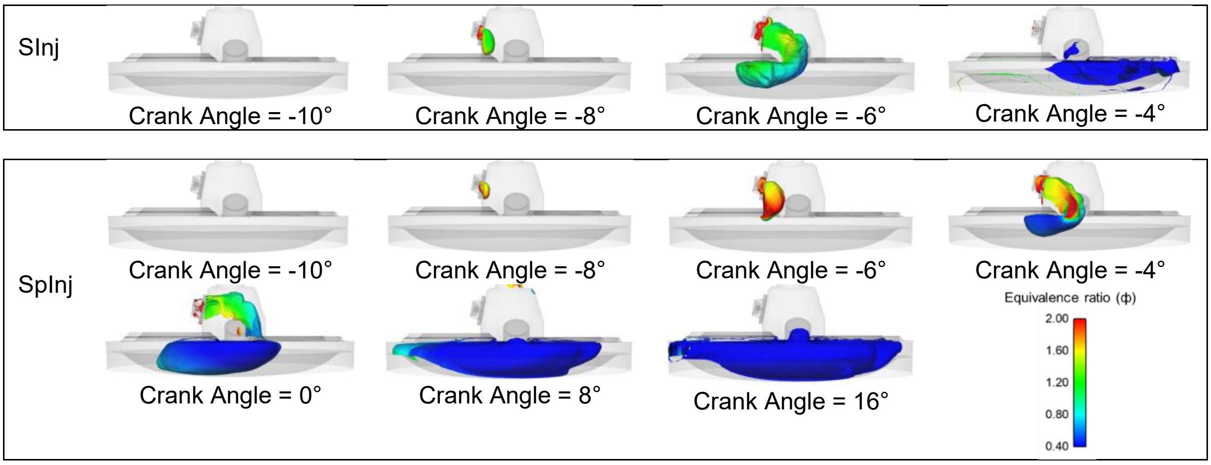

**Fig. 41.** The flame propagation represented by the iso-surface on temperature (=1800K) and colored by the equivalence ratio

The combustion modelling results in terms of In-cylinder pressure evolution are presented in Fig. 42. A noticeable difference is present in the in the cylinder pressure evolution even before the onset of combustion (10 °bTDC) which was caused by the difference in the in-cylinder air trapped mass obtained with the two injection strategies. The combustion modelling predicted an extremely fast combustion with the single injection configuration with peak in-cylinder pressure surpassing 200 bar, whereas a normal combustion was observed with split injection strategy. On the other hand, the split injection strategy produced a controlled combustion with acceptable pressure gradient and peak in-cylinder pressure. The simulation results appeared in good accordance with the observations made during the analysis of mixture preparation in M/C and Dome.

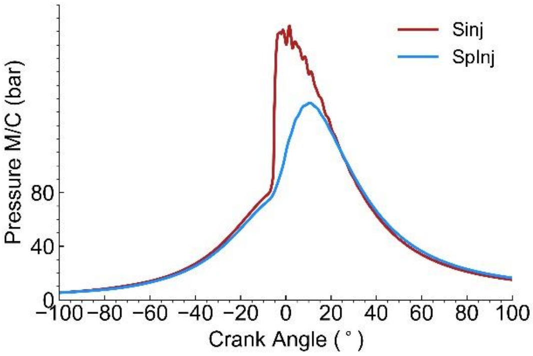

**Fig. 42.** M/C pressure evolution with crank angles obtained from CFD simulation with combustion modelling

In conclusion, the single injection after IVC does not appear to be a good solution for present engine operations at high engine speed. In first place at 6000 rpm, there is a constraint on the available mixing time and in the absence of predefined bulk flow motion for the present engine, the mixing process becomes more challenging. Alternatively, split injection appears to be a better strategy for engine operations at high engine speed and high load and should be investigated during engine testing. Finally, the engine performance was evaluated for simulation results and key performance indicators are highlighted in Table 4.

**Table 4.** Summary of precited engine performance from the 3D simulations at 6000 rpm with SpInj

| **Intake pressure** | **Intake temperature** | **Equivalence ratio (ϕ)** | **Gross IMEP** | **Gross ITE** | **Gross Power** | **CA50** | **$P_{max}$** |
|---|---|---|---|---|---|---|---|
| (bar) | (°C) | (-) | (bar) | (%) | (kw) | (°CAD) | (bar) |
| 2.60 | 40 | 0.53 | 22 | 44 % | 55.8 | 6.8 | <150 |

## 5 Conclusions and perspectives

The paper presented a novel engine design featuring a Dome combustion chamber tailored specifically for hydrogen combustion. This engine aims to achieve enhanced performance by leveraging weak in-cylinder bulk flow motion and charge stratification. During the preliminary experimental campaign at 2000 rpm x 16 bar, the engine demonstrated excellent combustion stability across equivalence ratios between 0.40 to 0.80. Notably, the highest gross indicated thermal efficiency of 46% was attained at an equivalence ratio of 0.40. The engine test results were also compared with a pent-roof engine design of the same dimensions which could be expected to produce completely different aerodynamics (TKE) and mixing behavior. Interestingly, despite having a shorter combustion duration with pent-roof engine, both engines demonstrated nearly identical indicated thermal efficiency when operating at an equivalence ratio of 0.50, most likely due to increased wall heat losses associated with the pent-roof engine architecture.

Subsequently, Computational Fluid Dynamics (CFD) simulations were performed for Dome engine at 2000 rpm x 16 bar, with an equivalence ratio of 0.50. The cold flow CFD simulations highlighted a significant increase in Turbulent Kinetic Energy (TKE) within the combustion chamber due to hydrogen injection, particularly up to firing TDC. Overall, the CFD simulation revealed notably high mixture heterogeneity throughout the combustion chamber, with a relatively richer mixture identified in the Dome compared to the M/C. Following this, combustion was modeled utilizing the SAGE detailed chemistry solver, and the results were compared in terms of in-cylinder pressure and apparent heat release rates. The CFD results demonstrated a satisfactory model predictivity for a variation of spark-advance. These validated model parameters were then applied to estimate the engine performance at 6000 rpm. Given the reduced availability of mixing time at 6000 rpm, two distinct injection strategies were evaluated numerically: single injection after intake valve closing (SInj) and split-injection (Splinj). The split injection was particularly aimed to improve the mixture homogeneity in the main chamber and it was supported by a late second injection after IVC. The detailed analysis of mixture preparation showed that SpInj appeared a more suitable for engine operations at 6000 rpm and combustion modelling predicted a gross indicated thermal efficiency of 44 % associated to a power density higher than 100 kW/l at 6000 rpm.

In the future scope of this work, the objective will be to evaluate the Split injection strategy on the engine test bench. Concerning the CFD, very limited data is available in the literature to evaluate the H2-air mixing from the CFD simulations, we look forward to its quantitative validation thanks to advanced optical techniques. In the present work, the combustion modelling was performed using SAGE detailed chemistry solver, we would like to evaluate the predictivity of flame surface density-based models which simultaneously incorporate the turbulence and chemistry interaction.

## References

[1] Liebig, D., Gao, M., Brombach, J., et al., “Shell's Electrification Journey: From Green Power Production to Charging Solutions for Mobility”, 44th International Vienna Motor Symposium, 2023

[2] Reporting from the International energy agency, 2019

[3] Morel, V., et al.,“Engineering design for ammonia conversion of an existing 2,0L powertrain”, 19th Symposium „Sustainable Mobility, Transport and Power Generation”, Graz 2023

[4] H2 vehicle of François-Isaac de Rivaz (https://medium.com/@reynaertskoenr)

[5] BMW official website (https://www.bmwgroup-classic.com)

[6] Luef, R., Heher, P., Hepp, C., et al., “Konzeption und Entwicklung eines Wasserstoff- / Benzin-Motors für den Rennsport”, 8. Tagung "Gasfahrzeuge", Stuttgart, 2013

[7] Maio, G., Boberic, A., Giarracca, L., Aubagnac-Karkar, D. et al., “Experimental and Numerical Investigation of a Direct Injection Spark Ignition Hydrogen Engine for Heavy-Duty Applications,” International Journal of Hydrogen Energy 47, no. 67, 29069-29084,2022.

[8] Chi, Y., Shin, B., et al., “Hydrogen Engine for a Passenger Car Hybrid Powertrain: Attractive Solution for Sustainable Mobility”, 44th International Vienna Motor Symposium, Vienna, 2023

[9] Beduneau, J., Doradoux, L., Meissonnier. G., et al., “An Affordable CO2 Free Propulsion System – H2ICE on the Road”, 44th International Vienna Motor Symposium”, Vienna, 2023

[10] Libert, C., Perrot, N., Gautrot, G., et al., “HyMot - A H2 Engine optimized for LCV - Simulations & Design”, SIA Powertrain, 2023

[11] Bevilacqua, V., Gallo, A., Böger, M., “Hydrogen Combustion Engine – High Performance, No Emissions”, 44th International Vienna Motor Symposium”, Vienna, 2022

[12] Medda, M., Calia, V., et al., “Challenges and Opportunities in developing a Hydrogen High Specific Power SCE in the roadmap towards zero net GHG”, 32nd Aachen Colloquium Sustainable Mobility, 2023

[13] Pelzetter, R., Claudius, S., et al., “MTZ worldwide”, 2023

[14] Dober, G., Piock, W. et al., “On the road experience with a LCV H2ICE: A practical path to eliminate emissions”, 32nd Aachen Colloquium Sustainable Mobility, 2023

[15] Kim, H. J., et al., “Numerical Calculation of Minimum Ignition Energy for Hydrogen and Methane Fuels”, KSME International Journal, Vol. 18 No. 5, pp. 838~846, 2004

[16] Dahoe, A. E., “Laminar burning velocities of hydrogen–air mixtures from closed vessel gas explosions”, Journal of Loss Prevention in the Process Industries 18 (2005) 152–166

[17] A., Foucher, F., and Doradoux, L., "Hydrogen Jet Characterization of an Internal Combustion Engine Injector Using Schlieren Imaging," SAE Technical Paper 2023-01-0301, 2023

[18] CONVERGE version 3.0 Manual. Convergent Science, 2020

[19] Morel, V., Gorgoraptis, E., Kumar, D., Houillé, S., Dumand, C., Lafetta, O., “Numerical and Experimental Investigations of Spark-Assisted Compression Ignition Combustion Using E10 Gasoline,” Aachen Colloquium Automobile and Engine Technology, 2020

[20] Issa, R., “Solution of The Implicitly Discretised Fluid Flow Equations by Operator-Splitting”, Journal of Computational Physics”, 62,46-65,1986

[21] Yakhot, V., Orszag, S.A., Thangam, S., Gatski, T.B. & Speziale, C.G., "Development of turbulence models foeitz, R.D., “A Temperature Wall Function Formulation for Variable Density Turbulent Flows with Application to Engine Convective Heat Transfer Modeling”, International Journal of Heat and Mass Transfer, 40, 613-625, 1997

[23] Gomez-Soriano, J., Sapkota, P., Wijeyakulasuriya, S., D'Elia, M. et al., "Numerical Modeling of Hydrogen Combustion Using Preferential Species Diffusion, Detailed Chemistry and Adaptive Mesh Refinement in Internal Combustion Engines", SAE Technical Paper 2023-24-0062, 2023.

[24] Kéromnès, A. et al. “An experimental and detailed chemical kinetic modeling study of hydrogen and syngas mixture oxidation at elevated pressures”, Combustion and Flame 160.6 (2013): 995-1011

[25] Metcalfe, W. K., et al. “A hierarchical and comparative kinetic modeling study of C1− C2 hydrocarbon and oxygenated fuels”, International Journal of Chemical Kinetics 45.10 (2013): 638-675

[26] Burke, Sinéad M., et al. “An experimental and modeling study of propene oxidation. Part 1: Speciation measurements in jet-stirred and flow reactors”, Combustion and Flame 161.11 (2014): 2765-278

# Development of a Direct-Injection Hydrogen Combustion System Based on a Flat-Deck Swirling Concept.

D. Gessaroli[1], F. C. Pesce[1], A. Vassallo[1], R. Golisano[2], N. P. Sacco[2], and S. Scalabrini[2],S. Molina[3], M. Olcina-Girona[3],

[1]DUMAREY Torino. Italy

E-mail: davide.gessaroli@dumarey.com
Telephone: +39 334 6402595

[2]PUNCH Hydrocells. Italy

E-mail: roberto.golisano@dumarey.com
Telephone: +39 335 8766211

[3]CMT – Clean Mobility & Thermofluids. Universitat Politècnica de València. Camino de Vera s/n, 46022 Valencia, Spain.

E-mail: cmt@mot.upv.es
Telephone: +(34) 963 877 650

## Abstract.

Decarbonization of the energy and transportation systems is a major effort being pursued through a combination of several technologies, and the usage of hydrogen - both as an energy vector and as a fuel itself for Internal Combustion Engines (ICE) - is considered one of the key players. Concerning hydrogen usage as a fuel for ICE, there are several characteristics that make it suitable as a substitute for traditional fuels: its high calorific power, its good propensity to operate in a wide range of air-fuel ratios, and the complete absence of carbon. In turn, these features significantly reduce $NO_x$ and virtually eliminate HC and CO emissions vs a conventional engine.

Despite such favourable characteristics of hydrogen, controlling its combustion requires extensive knowledge of its properties, such as managing combustion anomalies and employing different strategies to maximize performance and minimize emissions under all operating conditions.

Direct-injection of hydrogen is probably the most important single technology that allows to tackle the above challenges while improving engine performance versus a traditional Port-Fueled injection.

In this paper, the authors discuss the results achieved on a single-cylinder engine fitted with direct hydrogen injection, based on a flat-deck swirling concept. The test campaign highlights the main effects of hydrogen combustion under different engine conditions and different parameter settings such as lambda, EGR and hydrogen injection features (including pressure and phasing). The primary goal is to achieve efficiency and performance levels of a typical Diesel engine combined with significantly lower criteria pollutants emissions.

## Notation (optional)

*CO:* *Carbon monoxide*
$CO_2$: *Carbon dioxide*
$COV_{IMEP}$: *Covariance of IMEP*
*CR:* *Compression Ratio*
*EGR:* *Exhaust Gas Recirculation*
*GHG:* *Greenhouse Gases*
$H_{2Exh}$: *Hydrogen in the exhaust*

| | |
|---|---|
| *HC:* | *Hydrocarbons* |
| *HICE:* | *Hydrogen Internal Combustion Engine* |
| *ICE:* | *Internal Combustion Engine* |
| *IMEP:* | *Mean Indicated Pressure.* |
| *$ISNO_x$:* | *Indicated $NO_x$ emissions.* |
| *MAPO:* | *Maximum Amplitude Pressure Oscillation* |
| *$NO_x$:* | *Nitrogen oxides* |
| *SoI:* | *Start of Injection (CAD after TDC)* |
| *TDC:* | *Top Dead Center* |
| *$T_{exh}$:* | *Exhaust temperature* |
| $\lambda$: | *Air–fuel equivalence ratio* |

## 1. Introduction

In recent years, the quest for sustainable energy solutions has intensified, driven by pressing environmental concerns and the imperative to mitigate climate change. Reducing greenhouse gas (GHG) emissions is crucial to mitigating the global warming effect. At the European Union, the European Green Deal aims to achieve zero net greenhouse gas emissions by 2050. By 2030, the interim target is to reduce GHG emissions by 55% compared to 1990 levels. Transportation represents a substantial source of GHG emissions, accounting for approximately 32% of the carbon dioxide ($CO_2$) emissions in Europe [1].

Consequently, the transportation sector is now confronted with novel challenges concerning stringent vehicle tailpipe emissions and the urgent need to curtail $CO_2$ emissions, thereby propelling the sector towards decarbonization. In response to these imperatives, research within the automotive industry has actively pursued alternative solutions for the medium and long-term horizons. In this pursuit, hydrogen has emerged as a promising alternative fuel with the potential to revolutionize the automotive industry and pave the way towards a carbon-neutral future. Hydrogen offers a compelling solution to the challenges posed by traditional fossil fuels, presenting an opportunity to decarbonize transportation and reduce harmful emissions. Its production can be integrated with renewable energies serving as an energy vector. Moreover, in the transportation sector, it can be used as a fuel in alternative Hydrogen Internal Combustion Engines (HICE), thus allowing the utilization of technology that is available today with certain modifications. Retrofitting changes of gasoline or diesel engines to hydrogen are commonly found in the literature. Additionally, it is also used as an additive as a combustion enhancer for other fuels such as gasoline [2,3] or natural gas [4].

However, the use of hydrogen as a fuel also introduces new challenges for the development of robust and efficient systems. Anomalous combustion events and nitrogen oxides ($NO_x$) emissions are among the primary concerns associated with hydrogen power plants. To address these issues, it is imperative to reduce combustion temperatures to mitigate $NO_x$ emissions and prevent knocking tendencies. Dilution has proven to be a valuable strategy in maintaining these emissions at low levels while optimizing engine performance [5,6].

Another fundamental aspect is mixture formation. In many research papers, authors pointed out that direct injection has noteworthy advantages over a port fuel injection [7], such as higher power output, higher efficiency, the possibility of mixture stratification [8,9,10,11] to control $NO_x$-formation and reduce heat losses and above all to mitigate combustion abnormalities such as back-firing and pre-ignitions. By controlling the timing of the intake valve closing and exhaust valve opening, researchers achieved an impressive 42.2% brake thermal efficiency (BTE) [12]. Despite direct injection help to prevent backfires, the risk of pre-ignition persists [13], particularly due to the low minimum ignition energy of hydrogen [14]. Recently efforts had been made to overcome this situation, a new model for predicting and preventing combustion anomalies was generated [15] to make possible a safe and efficient operation of the hydrogen internal combustion engine. Nevertheless, hydrogen DI technology is on development [16], more research is still needed on the subject.

In this study, two main objectives are pursued. Firstly, the feasibility of achieving high-power points utilizing hydrogen as fuel for ICE while concurrently maintaining low levels of NOx emissions.

Combustion stability and knock mitigation have been relevant parameters which limited engine operating conditions. To achieve this, a comprehensive investigation is conducted, several conditions were tested on a research single-cylinder engine. Secondly, a practical solution to mitigate transient waiting times, which often arise due to the substantial flow rates required to achieve high power levels, is proposed. To address this challenge, the adoption of a post-injection strategy is advocated, which is believed to hold promise in optimizing engine performance and enhancing operational efficiency during transient conditions. Post injection consists of an injection in the expansion stroke with the objective of increasing the temperature of the exhaust gases. By addressing these key factors, this research aims to contribute valuable insights into the development of environmentally sustainable and high-performance hydrogen engines. In this sense, the study brings together current technologies and strategies to be applied and re-adapted to the external factors, contributing to the current knowledge gap.

## 2. Experimental tools

The experiments were conducted on a single-cylinder SI engine with a displacement of 489.1 cm3. The main engine specifications are listed in Table 1 for reference. Engine layout is shown at Fig. 1. The engine is featured an 83 mm bore diameter and a stroke of 90.4 mm, resulting in a compression ratio (CR) of 10.6:1. It operated with a single cylinder and had a rod length of 145 mm. The cylinder was equipped with 2 intake and 2 exhaust valves. Crankcase is ventilated to avoid reach high hydrogen concentration conditions which could ignite. Fuel injection was achieved through direct injection at a maximum pressure of 40 bar, specifically with hydrogen. A conventional spark-plug ignition system was employed for all experimental tests. Fuel delivery was facilitated by a medium-pressure DI injection system with a maximum injection pressure of 40 bar. The DI system ensured that the injection duration was sufficiently short to inject the required fuel quantity as the injection approached the top dead center (TDC). Injection duration served as a parameter for controlling the injected fuel quantity.

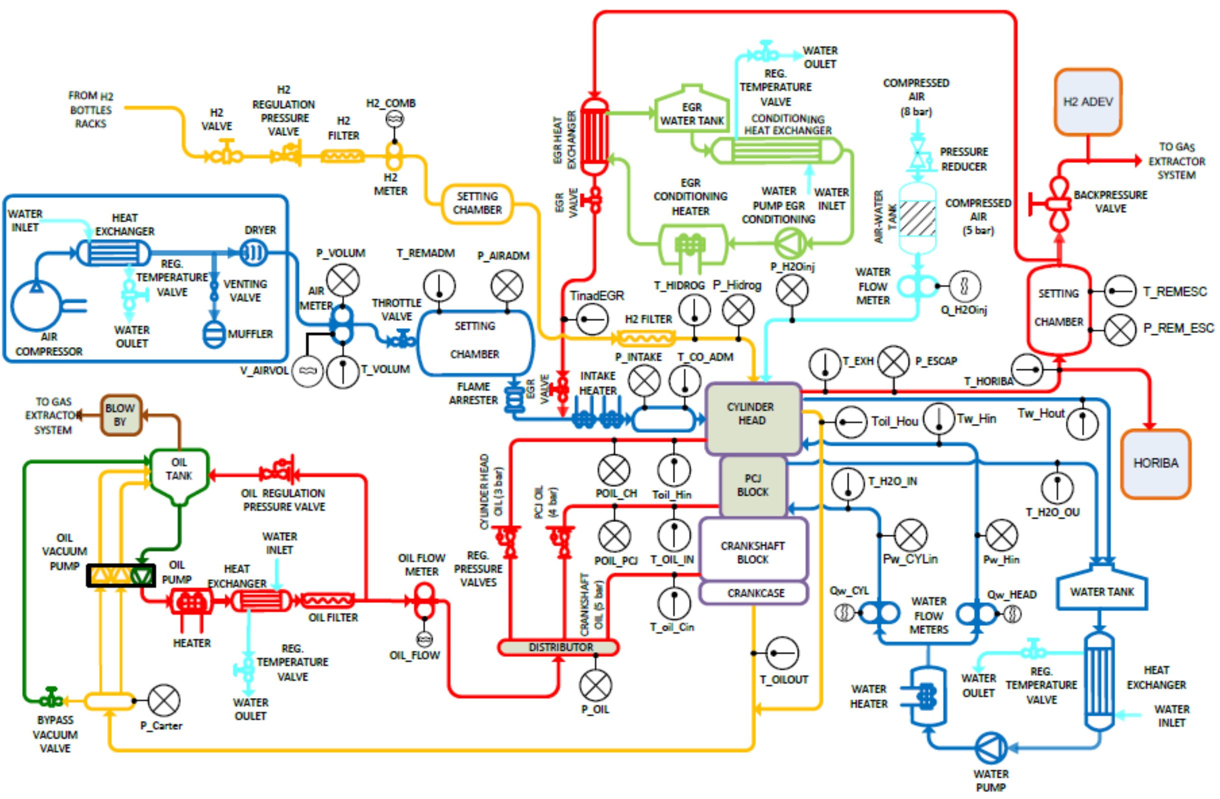
FROM H2 BOTTLES RACKS
H2 VALVE
H2 REGULATION PRESSURE VALVE
H2 FILTER
H2_COMB
H2 METER
SETTING CHAMBER
WATER INLET
HEAT EXCHANGER
DRYER
REG. TEMPERATURE VALVE
VENTING VALVE
WATER OULET
MUFFLER
AIR COMPRESSOR
P_VOLUM
T_REMADM
P_AIRADM
AIR METER
THROTTLE VALVE
SETTING CHAMBER
V_AIRVOL
T_VOLUM
FLAME ARRESTER
EGR VALVE
EGR HEAT EXCHANGER
EGR VALVE
EGR WATER TANK
WATER OULET
REG. TEMPERATURE VALVE
CONDITIONING HEAT EXCHANGER
EGR CONDITIONING HEATER
WATER PUMP EGR CONDITIONING
WATER INLET
COMPRESSED AIR (8 bar)
PRESSURE REDUCER
AIR-WATER TANK
COMPRESSED AIR (5 bar)
H2 ADEV
TO GAS EXTRACTOR SYSTEM
BACKPRESSURE VALVE
TinadEGR
H2 FILTER
T_HIDROG
P_Hidrog
P_H2Oinj
WATER FLOW METER
Q_H2Oinj
SETTING CHAMBER
T_REMESC
P_REM_ESC
INTAKE HEATER
P_INTAKE
T_CO_ADM
T_EXH
P_ESCAP
T_HORIBA
CYLINDER HEAD
Toil_Hou
Tw_Hin
Tw_Hout
HORIBA
TO GAS EXTRACTOR SYSTEM
BLOW BY
OIL TANK
OIL REGULATION PRESSURE VALVE
CYLINDER HEAD OIL (3 bar)
PCJ OIL (4 bar)
POIL_CH
Toil_Hin
PCJ BLOCK
T_H2O_IN
T_H2O_OU
OIL VACUUM PUMP
OIL PUMP
HEAT EXCHANGER
WATER INLET
OIL FLOW METER
REG. PRESSURE VALVES
POIL_PCJ
T_OIL_IN
CRANKSHAFT BLOCK
Pw_CYLin
Pw_Hin
CRANKSHAFT OIL (5 bar)
CRANKCASE
Qw_CYL
Qw_HEAD
WATER FLOW METERS
WATER TANK
HEATER
OIL FILTER
REG. TEMPERATURE VALVE
OIL_FLOW
DISTRIBUTOR
T_oil_Cin
T_OILOUT
WATER HEATER
WATER OULET
REG. TEMPERATURE VALVE
HEAT EXCHANGER
WATER INLET
BYPASS VACUUM VALVE
P_Carter
WATER OULET
P_OIL
WATER PUMP

**Fig. 1.** Test cell layout.

In the experimental setup, the test cell and engine are equipped with essential features to ensure accurate and controlled testing conditions. The dynamometer utilized is the AMK Type ACWA 160, boasting a nominal power output of 60 kW and a maximum torque capacity of 500 Nm, enabling precise measurement and control of engine performance. Furthermore, the oil/water conditioning unit, designed by CMT, ensures optimal operating conditions for the engine throughout testing procedures. This unit is complemented by the Bronkhorst F-113AC-1M0 H2 meter, which facilitates the measurement of hydrogen flow, essential for evaluating the performance of hydrogen-powered systems. Additionally, an external compressor, specifically the Atlas Copco ZA-1, with a maximum pressure of 3.5 bar (abs) and a flow rate of 450 m3/h, is employed to maintain consistent air supply to the engine. To further enhance air quality, an Atlas Copco FD 380W air dryer is integrated into the setup, ensuring that the air provided to the engine is free from moisture and contaminants, thereby contributing to precise and reliable testing outcomes. The gas analysers utilized in our study encompass cutting-edge technology to comprehensively assess exhaust emissions and combustion characteristics. Among these, the Horiba MEXA 7100 DEGR stands out as a versatile instrument capable of measuring a range of critical gases, including $O_2$, CO, $CO_2$, HC, $NO_x$, $N_2O$, and EGR (for hydrocarbon fuels only), providing a holistic understanding of engine performance. Additionally, the $H_2$ exhaust analyzer by ADEV E210126 plays a crucial role in quantifying hydrogen emissions, offering valuable data for evaluating the environmental impact of hydrogen-powered systems. Together, these state-of-the-art gas analyzers form a comprehensive suite of tools, enabling thorough characterization and analysis of exhaust gas composition and engine operation.

Typically, a flat-deck design refers to an engine cylinder head that has a flat surface, as opposed to a more contoured or recessed design. This can influence how air and fuel mix within the combustion chamber. Swirl, organized fluid rotation about the cylinder axis, is usually generated by bringing the air into the cylinder with net angular momentum about the cylinder axis. It is used in smaller higher speed diesel engines to promote more rapid fuel-air mixing, and also in spark-ignition engines to increase the engine's combustion rate.

**Table 1**. Main engine specifications.

| | |
|---|---|
| Number of cylinders | 1 |
| Number of strokes | 4 |
| Bore | 83.0 mm |
| Stroke | 90.4 mm |
| Displaced volume | 489.1 cc |
| Connecting rod length | 145.0 mm |
| Compression ratio | 10.6 |
| Injection systems | DI (max. 40 bar $H_2$) |
| Ignition system | Spark (spark plug) |
| Valves per cylinder | 2 intake, 2 exhaust |
| Geometry | Flat-deck swirling |

## 3. Methodology

The methodology employed in this investigation aimed to assess hydrogen combustion under various operating conditions and injection strategies in a single cylinder SI research engine. For this research, a multitude of data points were collected to determine the most significant effects on the hydrogen engine parameters. To minimize measurement uncertainties, each test was repeated three times. Each test consists of 200 combustion events. The results presented in the following sections represent the average values of the parameters under study.

To ensure consistency and relevance in engine performance analysis, the research activities were conducted under meticulously defined operating conditions. Three distinct engine speed conditions were chosen, each representing high load scenarios:

- High load and low Speed: Operating at 1500 rpm (1500@HL)
- High load and mid Speed: Operating at 2000 rpm (2000@HL)
- High load and high Speed: Operating at 3000 rpm (3000@HL)

Additionally, sweep post-injection activities were conducted under the following condition:

- Low speed & Low load (1500@LL)

## 4. Results

This section presents the outcomes of the studies conducted in the research work. Initially, the results of high load are outlined, followed by an exposition of the findings from post injection analysis.

### 4.1 High load

The scientific literature extensively attests to the merits of lean combustion, encompassing the reduction in thermal losses, $NO_x$ emissions, and decreased susceptibility to knock, among other advantages. With increasing load, $ISNO_x$ experiences a corresponding uptick, attributable to heightened pressure and temperature within the combustion chamber. Higher $\lambda$ values reduce thermal $NO_x$ formation mechanism and helps reaching higher load with low $NO_x$ emission levels. Also, a delayed combustion phasing reduces these emissions. Figure 2 displays the results of the test matrix conducted for high load activities, at different $\lambda$ values and air mass flowrate values. Under high load conditions (IMEP range approx. from 15 to 22 bar), discernible patterns emerged across different operating speeds. $\lambda$ is calculated using air a fuel mass flowrates.

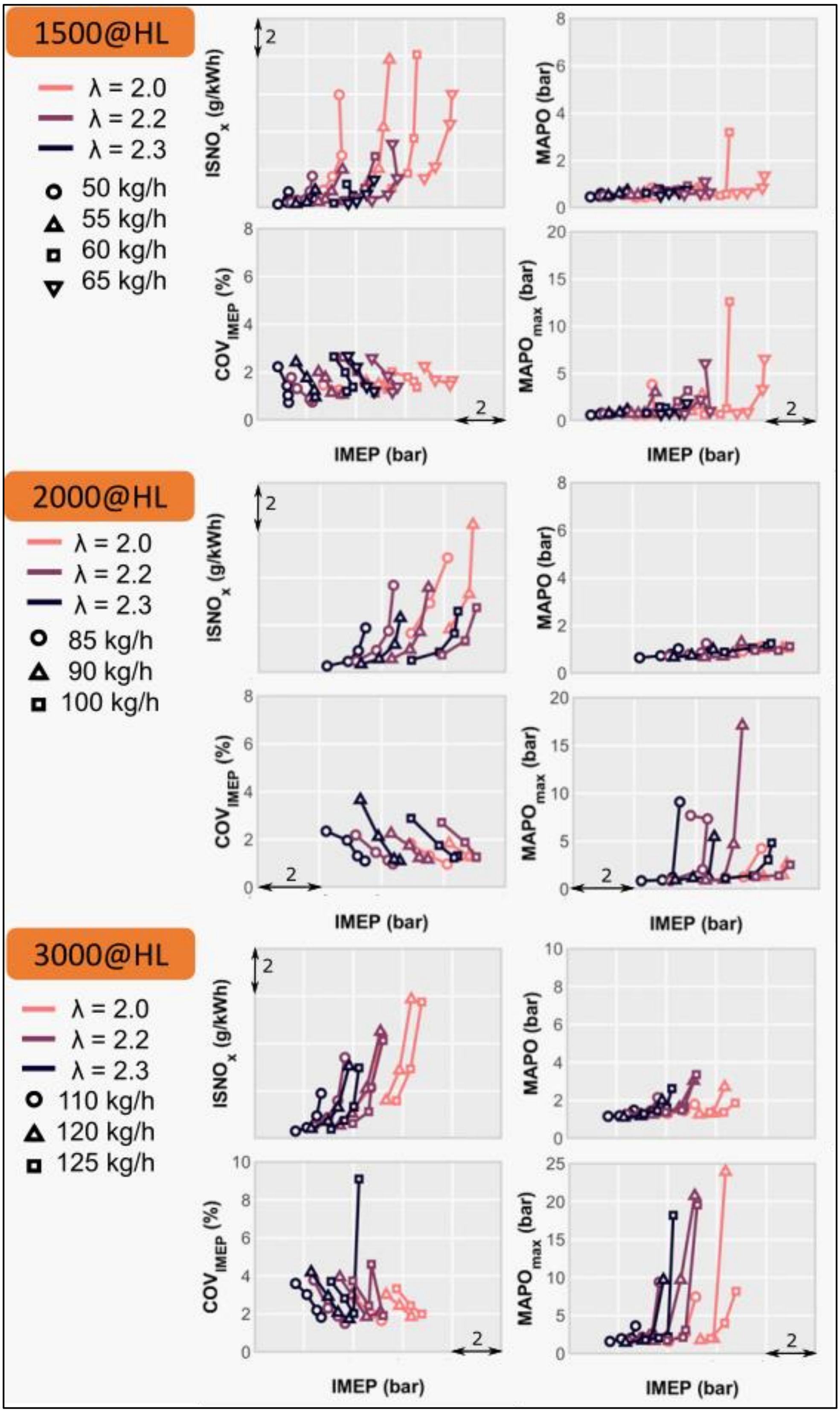

**Fig. 2.** ISNO$_x$ emission levels, COV$_{IMEP}$, and MAPO results under different combustion phasing, λ and air mass flow quantity values.

In this research article, it is delved into critical engine aspects of knocking tendency and stability represented as knocking amplitude (MAPO), and the covariance of IMEP ($COV_{IMEP}$), which play pivotal roles in determining engine safety conditions. It is explored the text matrix finding different conditions of knock tendency and stability, avoiding points which exceed excessive values of these parameters. Mean MAPO values and the maximum MAPO value of each condition are displayed.

As engine speed increase, combustion stability becomes susceptible to disruption, leading to a rise in $COV_{IMEP}$. Lower λ value conditions help in mitigating such instabilities, alongside positioning CAD50 closer to Top Dead Center, thus minimizing combustion irregularities. These effects are widely acknowledged in the domain of engine research. Notably, a significant portion of data points exhibit $COV_{IMEP}$ below 4%, signifying stable combustion conditions.

In terms of knock, the effects of higher engine speed include an increase in the amplitude of knocking cycles. A higher engine speed contributes to reach higher temperature conditions at the engine, which could increase knocking tendency. At maximum MAPO values graph it is shown high amplitude knocking occurring. However, mean MAPO values remain within acceptable thresholds, most of the points present MAPO values below 3 bar, as it possible to observe at Fig. 2. While MAPO max indicates occasional high-amplitude knocking occurrences, it seems infrequent phenomena. Knocking occurs probably induced by a hot spot. At the highest engine speed (3000 rpm), feasibility constraints were encountered in achieving IMEP levels close to 20 bar. Elevated MAPO values were recorded, indicating increased knock activity. Additionally, $COV_{IMEP}$ exhibited higher variability, signifying less stable combustion conditions compared to lower engine speed values. The results underscore the challenges associated with achieving high IMEP levels at elevated engine speed values and emphasize the importance of monitoring knock behavior and combustion stability for optimizing engine performance and emissions.

In pursuit of environmentally sustainable engine operations, optimizing $ISNO_x$, and engine load emerges as a critical focus. This entails achieving high loads while minimizing $NO_x$ emissions. As indicated by the increase in IMEP, $ISNO_x$ experiences a corresponding rise due to heightened pressure and temperature in the combustion chamber. Nonetheless, it is essential to acknowledge the inherent susceptibility to knocking phenomena at high loads. Thus, a delicate balance between load optimization and knock mitigation strategies becomes imperative for achieving desired performance outcomes while adhering to emission standards.

The primary objective of this study is to evaluate the viability of a high-load hydrogen engine. In Figure 3, a selection of data points from the test matrix has been undertaken to minimize $NO_x$ emissions, indicating a concerted effort towards emission reduction. The optimization strategy is focused on the reduction of $ISNO_x$, while also taking into account constraints related to stability and knock amplitude. This approach underscores the multifaceted nature of engine optimization, where considerations for emissions, performance, and operational stability are intricately intertwined.

The selected data points reveal the following trends. As long as the airflow allows for an increase in λ, the engine calibration should prioritize conditions with high λ and delayed CAD50. This approach is suitable for low to medium engine loads. However, for higher loads, it becomes impractical to increase airflow to the same extent. Consequently, λ needs to be reduced, and the combustion timing needs to be advanced. To achieve high load points, a λ value of 2 is targeted, along with advancing CAD50. These conditions result in high $ISNO_x$ emissions. Nevertheless, this effect is only observed at the most demanding operational points.

As a result of this calibration, the majority of the selected conditions demonstrate high λ values, which contribute to maintaining low $ISNO_x$ levels, as well as low MAPO results, even under high loads.

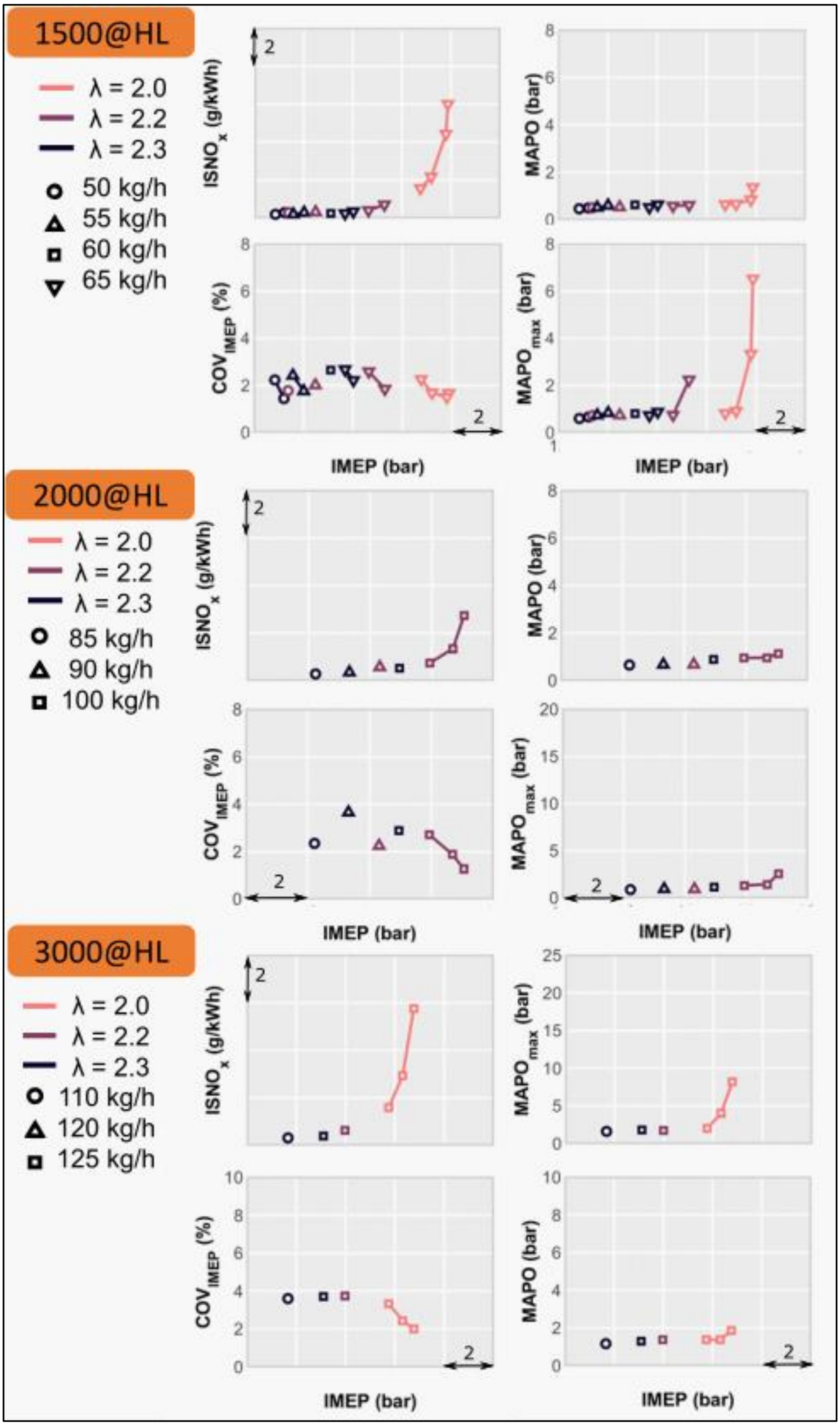

**Fig. 3.** Optimization results of the test matrix.

## 4.2 Post-Injection

These findings provide crucial insights into the performance characteristics of the engine under full load conditions across a spectrum of operating speeds. Particularly noteworthy are the observations that elucidate the intricate trade-offs among emissions, combustion efficiency, and load optimization strategies, thus highlighting the multifaceted nature of engine operation, especially under high load conditions. The optimization process underscores the imperative of charge dilution to mitigate knock tendency and $NO_x$ emissions. From the necessity for quicker control in highly diluted scenarios and the urgency to shorten reaction times between different points, the concept of employing post-injection strategies arises. This method, characterized by an injection during the expansion stroke, serves to elevate the temperature of exhaust gases, thereby supplying the energy necessary to propel the turbocharger at this high λ conditions during transient conditions.

Figure 4 illustrates the significant outcomes of post-injection, notably showcasing a substantial increase in exhaust temperature, which serves as its primary purpose. Remarkably, the rate of temperature change exhibits a peak at the onset of injection. Furthermore, hydrogen presence in the exhaust gases arises from late injections during the expansion stroke, attributed to reduced time and low oxygen levels leading to incomplete combustion. This phenomenon results in a portion of the fuel exiting the cylinder prematurely through the exhaust valve, potentially affecting engine exhaust line systems. Further research is warranted to thoroughly investigate the consequences of high concentrations of hydrogen, taking in to account the Lower Explosion Limit concentrations (LEL). Despite the rise in $NO_x$ levels due to heightened temperatures associated with post-injection, the impact remains relatively modest, highlighting the nuanced effects of this optimization strategy.

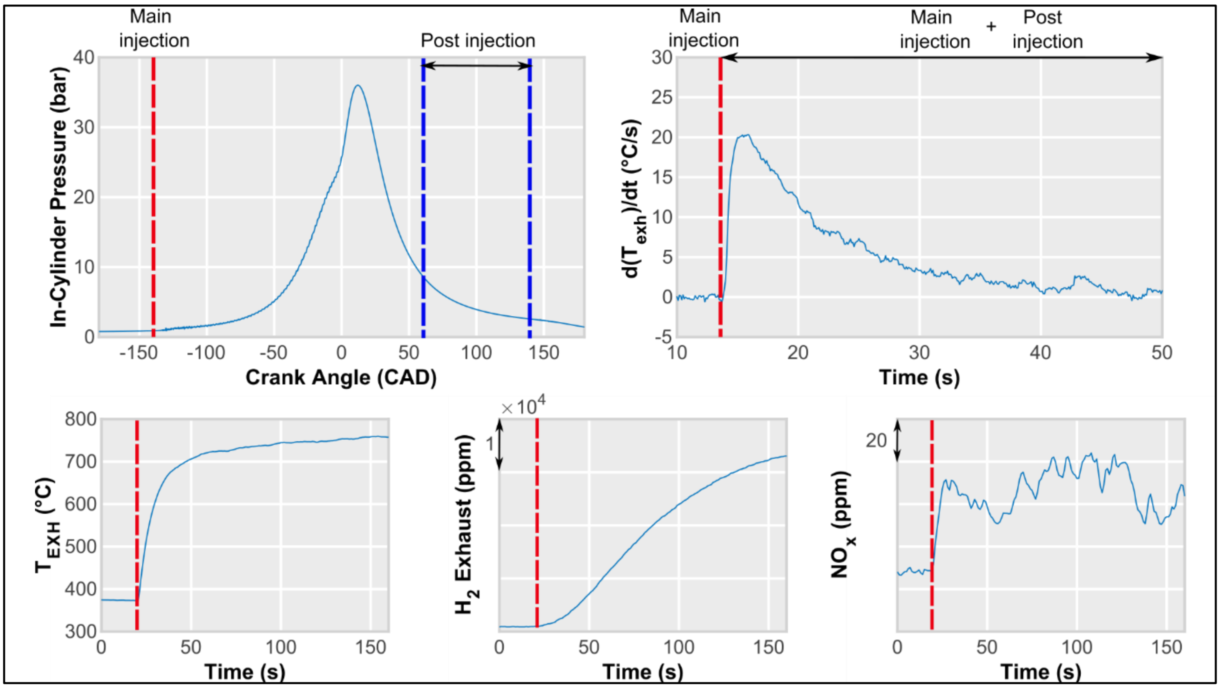

**Fig. 4.** Main effects of post injection.

The research outcomes underscore the significance of key parameters associated with post-injection, notably $\lambda_{total}$, and injection timing. Effects on exhaust temperature ($T_{exh}$), $ISNO_x$, rate of change of exhaust temperature ($\Delta T_{exh}$), and $H_2$ emissions are analyzed.

Exhaust temperature exhibits at Fig. 5 a general increase as reducing $\lambda_{total}$ values. Also, a consistent trend of $T_{exh}$ with SoI is found. Notably reaching the peak at an early Start of Injection for each $\lambda_{total}$ level, as $\lambda_{total}$ is closer to the stoichiometric as early is located the peak. The reduced time to be burned for hydrogen injected on the post injection are probably the main cause of this trend. Exhaust temperature gradient mirrors this pattern closely, reaching the maximum $\Delta T_{exh}$ value at less diluted conditions ($\lambda_{total}$ =1 and 1.1).

In terms of emissions, ISNO$_x$ levels reach their peak at $\lambda_{total} = 1$, showcasing a notable association with significantly delayed SoI values. Furthermore, $H_2$ emissions surge with higher λ values and delayed SoI, reflecting a direct correlation between injection frequency and elevated $H_2$ levels in the exhaust. This phenomenon likely arises from diminished oxygen availability for oxidation and limited time for adequate mixing. These trends require a more in-depth analysis to understand why delaying post-injection leads to an increase in nitrogen oxide emissions.

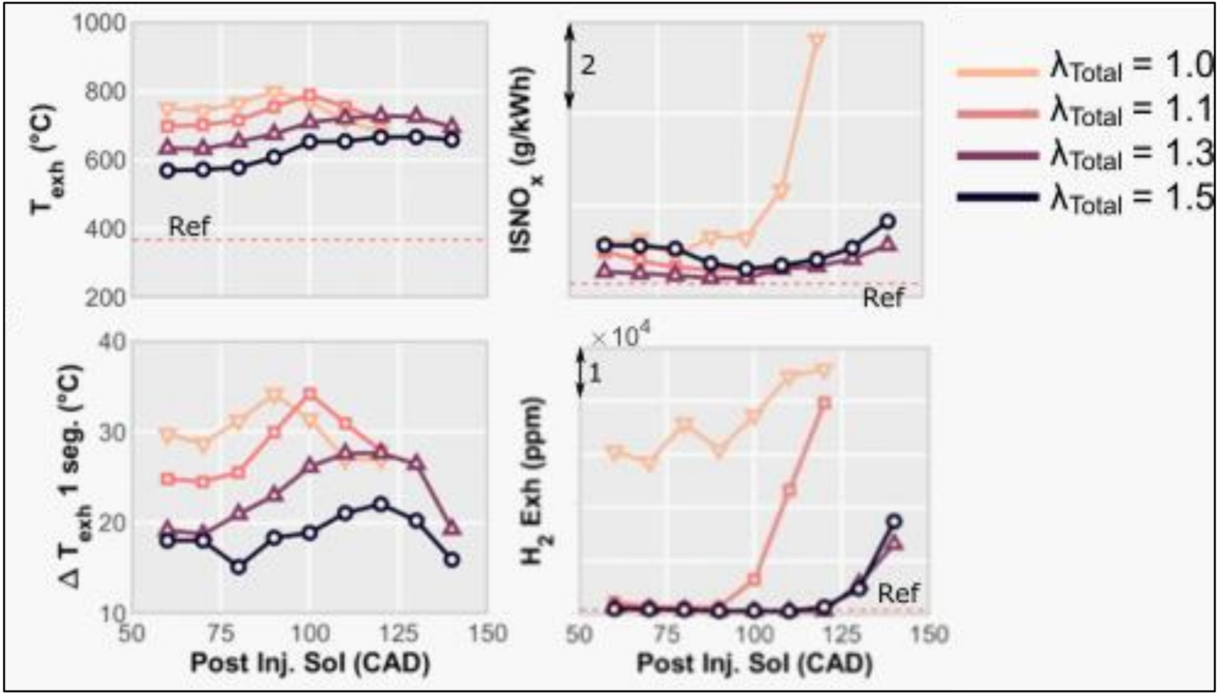

**Fig. 5.** SoI and $\lambda_{total}$ sweep for post injection results.

Table 2. delineates optimal results for SoI concerning $\lambda_{total}$, $T_{exh}$, and $\Delta T_{exh}$, offering crucial insights for potential calibration optimization in this technological realm. Optimal values for SoI which maximize exhaust temperature and increment of temperature are shown. For λ=1.3, SoI =110 and 120 CAD reach similar values.

**Table 2**. Optimal SoI values for different variables, increment of temperature and final exhaust temperature.

| | $\lambda_{Total}$ (-) | | | |
|---|---|---|---|---|
| Optimal SoI (CAD) | 1.0 | 1.1 | 1.3 | 1.5 |
| $T_{exh}$ (°C) | 90 | 100 | 110/120 | 120 |
| $\Delta T_{exh}$ (°C) | 90 | 100 | 110/120 | 120 |

## Conclusions

In conclusion, this research underscores the potential of Hydrogen Internal Combustion Engine with Direct Injection as a promising contender for realizing a carbon-free future power plant. The flat deck swirling concept demonstrates the capacity to deliver high power outputs while maintaining favorable emissions profiles.

A notable finding of this study is the identification of operating points where high load outputs align with low Specific NO$_x$ emissions levels. Through adjustments such as delaying combustion phasing, employing high dilution ratios, it was possible to achieve reduced NO$_x$ emissions while ensuring combustion stability and managing MAPO effectively.

Moreover, the investigation reveals the potential of Post-injection strategies to increase exhaust temperature, and further mitigate $NO_x$ emissions, with acceptable levels of hydrogen ($H_2$) emissions in the exhaust. This underscores the versatility of HICE-DI in addressing emissions concerns across diverse operating scenarios.

While these findings highlight the promise of HICE-DI technology, further research and development efforts are necessary to optimize its implementation. Particularly, addressing challenges related to transient performance and emissions control will be crucial. By advancing HICE-DI technology and continuing to innovate in this field, it can accelerate progress towards a sustainable and environmentally friendly energy landscape.

## References

[1] Fuel Cells and Hydrogen Joint Undertaking (FCH). (2019). Hydrogen Roadmap Europe. https://doi.org/10.2843/249013

[2] Benajes, J., Novella, R., Gomez-Soriano, J., Barbery, I., & Libert, C. (2021). Advantages of hydrogen addition in a passive pre-chamber ignited SI engine for passenger car applications. International Journal of Energy Research, 45(9), 13219-13237

[3] Qian L, Wan J, Qian Y, Sun Y, Zhuang Y. Experimental investigation of water injection and spark timing effects on combustion and emissions of a hybrid hydrogen-gasoline engine. Fuel 2022;322(April):124051. http://dx.doi.org/10.1016/j.fuel.2022.124051

[4] Molina S, Ruiz S, Gomez-Soriano J, Olcina-Girona M. Impact of hydrogen substitution for stable lean operation on spark ignition engines fueled by compressed natural gas. Results Eng 2023;17:100799. http://dx.doi.org/10.1016/j.rineng.2022.100799

[5] Verhelst, S., De Landtsheere, J., De Smet, F., Billiouw, C. et al., "Effects of Supercharging, EGR and Variable Valve Timing on Power and Emissions of Hydrogen Internal Combustion Engines," SAE Int. J. Engines 1(1):647-656, 2009, https://doi.org/10.4271/2008-01-1033.

[6] Molina, S., Novella, R., Gomez-Soriano, J., & Olcina-Girona, M. (2023). Study on hydrogen substitution in a compressed natural gas spark-ignition passenger car engine. *Energy Conversion and Management*, *291*, 117259.

[7] Molina, S., Novella, R., Gomez-Soriano, J., & Olcina-Girona, M. (2024). Impact of medium-pressure direct injection in a spark-ignition engine fueled by hydrogen. *Fuel*, *360*, 130618.

[8] Scarcelli, R., Wallner, T., Matthias, N., Salazar, V., & Kaiser, S. (2011). Mixture formation in direct injection hydrogen engines: CFD and optical analysis of single-and multi-hole nozzles. SAE International Journal of engines, 4(2), 2361-2375.

[9] Salazar, V. M., & Kaiser, S. A. (2010). An optical study of mixture preparation in a hydrogen-fueled engine with direct injection using different nozzle designs. SAE International Journal of engines, 2(2), 119-131.

[10] Salazar, V. M., & Kaiser, S. A. (2010). Influence of the in-cylinder flow field (tumble) on the fuel distribution in a DI hydrogen engine using a single-hole injector. SAE International Journal of Engines, 3(1), 309-325.

[11] Le Moine, J., Senecal, P. K., Kaiser, S. A., Salazar, V. M., Anders, J. W., Svensson, K. I., & Gehrke, C. R. (2015). A computational study of the mixture preparation in a direct–injection hydrogen engine. Journal of Engineering for Gas Turbines and Power, 137(11), 111508.

[12] Ji C, Hong C, Wang S, Xin G, Meng H, Yang J, et al. Evaluation of the variable valve timing strategy in a direct-injection hydrogen engine with the Miller cycle under lean conditions. Fuel 2023;343(October 2022):127932. http://dx.doi.org/10.1016/j.fuel.2023.127932

[13] Gao, J., Wang, X., Song, P., Tian, G. et al., “Review of the Backfire Occurrences and Control Strategies for Port Hydrogen Injection Internal Combustion Engines,” Fuel (2022): 121553.

[14] White, C., Steeper, R., and Lutz, A., “The Hydrogen-Fueled Internal Combustion Engine: A Technical Review,” International Journal of Hydrogen Energy 31, no. 10(2006): 1292-1305

[15] Mendoza, M. G. G., Garcia, A., Molina, S., Olcina-Girona, M., Pesce, F., Gessaroli, D., ... & Sacco, N. (2024). Toy Model: A Naïve Modelling Approach to Hydrogen Combustion Anomalies (No. 2024-01-2608). SAE Technical Paper.

[16] Wittek, K., Cogo, V., & Prante, G. (2023). Development of a pneumatic actuated low-pressure direct injection gas injector for hydrogen-fueled internal combustion engines. International Journal of Hydrogen Energy, 48(27), 10215-10234.

# Development of a Dedicated Hydrogen Combustion System for Heavy Duty Application

D. Serrano[1], V. Giuffrida[1], T. Valin[1], F. Duffour[1] and X. Gautrot[1]

[1]IFP Energies nouvelles, Institut Carnot IFPEN transport Energie, 1 et 4 avenue de Bois Préau, 92852 Rueil Malmaison Cedex, France

E-mail: david.serrano@ifpen.fr
Telephone: +(33) 4 37 70 21 57

**Abstract.**

In the critical context of global warming, the diversification of the energy sources is urgently required. Regarding mobility, in addition to vehicles electrification and advanced biofuels, hydrogen holds the potential to address significant emission reduction for internal combustion engines. This approach preserves the advantages of current fossil fuel engines, such as established and proven technology, long lifespan, controlled costs, and an exceptionally low carbon footprint. Hydrogen is convenient for heavy-duty and off-road applications for which battery capacity is challenging.

Currently, two approaches cohabit in the engineering of hydrogen internal combustion engines: the adaptation of a Diesel-based engine or the design of a brand-new engine dedicated to hydrogen. The main goal of the presented study is to establish the specifications for a dedicated hydrogen direct injection combustion system designed for heavy-duty applications.

The key features of the combustion system have been defined through numerical analysis, focusing on the main challenges of hydrogen combustion engine: fuel/air mixing quality, combustion process, and resistance to abnormal combustions.

The 3D simulation of the final optimized design demonstrates the potential for improved efficiency and low emissions in a dedicated hydrogen direct injection engine, compared to retrofitting a Diesel-based combustion system. A heavy-duty single-cylinder engine equipped with the optimized combustion system has been tested on a test bench using hydrogen. A double-stage turbocharger model has been implemented in the loop to give realistic conditions on air loop for the single-cylinder engine tests. The experimental results confirm the effectiveness of the dedicated combustion system approach that has been highlighted with 3D simulation, particularly in terms of efficiency, low emissions and full-load performance.

## 1. Introduction

Ground transportation is one of the main contributing emitters of Green House Gases (GHG). The limitation in natural resources and the continuous growth of mobility demand imply that Battery Electric Vehicle (BEV) will be only a part of the answer to address the carbon neutrality of ground transportation sector. Hydrogen energy carrier could be an interesting solution, specifically for heavy duty vehicles. Indeed, for these applications (heavy trucks, buses, building and public work), using an electric powertrain could be a real challenge as long range and high energy density are needed, leading to a disproportionate mass of battery and recharging time. However, hydrogen production must be carbon-free. Green $H_2$ produced by water electrolysis is improving and becoming more attractive and it appears in the EU roadmap for 2050 carbon neutrality [1]. Hydrogen can be used in a fuel cell or in an internal combustion engine. This latter solution has many advantages: low-cost compared to fuel cells, re-use of current fossil fuel engine technology, robustness regarding ambient conditions (temperatures, vibrations, dusty environment) and low-purity hydrogen compatibility [2].

Moreover, hydrogen as a fuel has many advantages concerning its intrinsic properties for combustion as shown in Table 1. Its wide flammability range and high flame speed (compared to gasoline and natural gas) allow, with an adapted air loop, ultra-lean combustion yielding low NOx emissions [3]. However, $H_2$ combustion is not free from drawbacks. Gaseous hydrogen has a low density and thus, despite a high mass energy density, a low volume energy density. Those specificities will induce mixing issues and additional compression work. Due to its low ignition energy, hydrogen is prone to abnormal combustion such as for example pre-ignition or backfiring. Additionally, hydrogen internal combustion engines typically operate with a high air-fuel equivalence ratio (λ) to closely monitor NOx emissions, aiming for near-zero levels. Thus, ensuring optimal air/$H_2$ mixture homogeneity becomes crucial, and this mixing process must be optimized thanks to a combination between adapted injection strategy and high turbulence kinetic energy in the combustion chamber.

**Table 1**. Hydrogen physical and chemical properties at 1 bar and 300 K [3]

| Properties | Isooctane (Gasoline) | Methane | Hydrogen |
|---|---|---|---|
| Mass diffusivity in air (cm²/s) | 0,07 | 0,16 | 0,61 |
| Minimum ignition energy (mJ) | 0,28 | 0,28 | 0,02 |
| Minimum quenching distance at λ=1 (mm) | 3,5 | 2,03 | 0,64 |
| Mass lower heating value (MJ/kg) | 42 | 50 | 120 |
| Vol. lower heating value (MJ/m$^3$) | 32000 (liquid) | 35,82 (gas) | 10,8 (gas) |
| Density (kg/m$^3$) | 692 | 0,65 | 0,09 |
| Stoichiometric air-to-fuel ratio (kg/kg) | 14,5 | 17,1 | 34,4 |
| Flammability limits in air (%vol) | 1,1 ➔ 6 | 5 ➔ 15 | 4 ➔ 75 |
| Flammability limits in air (λ) | 1,51 ➔ 0,26 | 2 ➔ 0,6 | 10 ➔ 0,14 |
| Laminar flame speed at λ=1 (cm/s) | 45 | 48 | 290 |

Two approaches cohabit in the engineering of $H_2$ internal combustion engines: retrofitting a current Diesel (or gas) engine or developing a brand-new dedicated $H_2$ combustion chamber [4]. The retrofitting concept means to operate minimum changes to the initial Diesel or gas engine basis, reducing the global cost of this solution. But in this case, the air loop and the combustion chamber are not fully optimized for hydrogen combustion.

In this study, the brand-new dedicated $H_2$ engine approach has been considered. A new combustion chamber dedicated to hydrogen direct injection (DI) combustion has been designed for heavy-duty application, including the piston shape, the compression ratio and the intake and exhaust ducts. Then, the combustion system has been manufactured, and tested on a new single cylinder engine. A previous IFPEN paper [5] presents in detail the first phase of the study with the work done to design the combustion system: this step corresponds to the first descending branch of the "V" design workflow diagram of a combustion chamber displayed on figure 1.

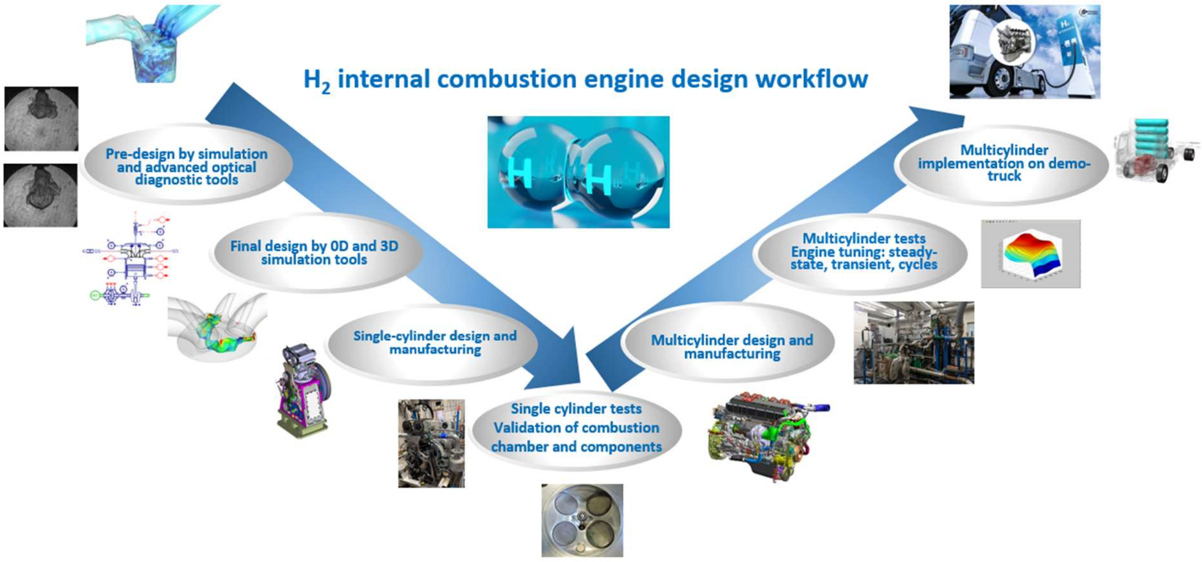
$H_2$ internal combustion engine design workflow
Pre-design by simulation and advanced optical diagnostic tools
Final design by 0D and 3D simulation tools
Single-cylinder design and manufacturing
Single cylinder tests Validation of combustion chamber and components
Multicylinder design and manufacturing
Multicylinder tests Engine tuning: steady-state, transient, cycles
Multicylinder implementation on demo-truck

**Fig. 1.** Design workflow of a combustion chamber

The present article is dedicated to the test campaign results for the single-cylinder engine with this new combustion chamber dedicated to hydrogen combustion. In a first part, the engine and test cell features are described together with the choices made for the engine design. Then, the injection strategy is studied at part load, followed by the process to obtain optimal engine settings supported by simulation. Besides, a methodology for abnormal combustion detection at high load is discussed. The engine tuning strategy to reach full load is then presented. Finally, a full engine map with optimized settings is discussed as a global picture of this study.

## 2. Engine description and experimental Setup

### 2.1 Engine description

The table 2 presents the main characteristics of the engine designed and built according to paper [5]. The tested engine is a single cylinder with a 2.147 L displacement. This engine basis represents a 6 cylinders engine with a 13 L displacement used for heavy-duty trucks. The maximum peak in-cylinder pressure is set to 170 bar for the engine integrity at full load. The compression ratio (CR) has been chosen at 11.8:1. This value comes from previous IFPEN experience [6;7]. For example, 3 different CR (10, 12.4 and 16:1) were tested on a passenger car hydrogen single-cylinder engine, indicating that CR = 12.4:1 is the best trade-off between efficiency and abnormal combustion occurrence [7]. The chosen 11.8:1 compression ratio is obtained thanks to a pent-roof cylinder head and a piston with central shallow bowl facing the direct injector and the spark plug.

$H_2$ is directly injected in the combustion chamber with the injector located between the intake ports. The injector technology is a Phinia outward opening valve nozzle. The injection pressure is set at 40 bar for all the tests, yielding a maximum mass flowrate of 15 g/s in steady state conditions.

The spark plug is supplied by Tenneco and is implemented vertically at the center on the cylinder head, close to the injector. The spark plug is chosen with a high heat range (meaning cold spark plug) and with reduced air gap. The material of the electrodes is platinum-free as this precious metal can be a catalyst for oxidation in presence of hydrogen.

A Miller intake camshaft with Variable Valve Timing (VVT) actuator is implemented. The Intake Valve Opening (IVO) setting range is centered on Top Dead Center (TDC). The interest of using Miller strategy is detailed in the next paragraph. Besides, a standard exhaust camshaft with VVT actuator is implemented. The Exhaust Valve Closing (EVC) setting range is also centered on TDC.

**Table 2**. Engine main characteristics

| | |
|---|---|
| Bore x Stroke | 135 x 150 mm |
| Displacement | 2 147 $cm^3$ |
| Connecting rod length | 235 mm |
| Compression ratio | 11.8:1 |
| Valvetrain | VVT on intake and exhaust camshafts / Miller strategy on intake |
| Air motion | Swumble$^{TM}$ |
| $H_2$ injection | Phinia direct injector / Max mass flowrate = 15 g/s / Injection pressure = 40 bar |
| Ignition | Tenneco cold spark plug with reduced air gap |
| Max. admissible peak cylinder pressure | 170 bar |

A previous IFPEN paper [5] explains that this engine was designed using 0D and 3D simulation tools and IFPEN know-how according to four key points:

- The air motion of the engine is based on the Swumble$^{TM}$ concept which is a combination of slight swirl and high tumble air motion. The two intake ports have been designed together with a pent-roof cylinder head adapted to spark-ignited combustion as shown in figure 2. Hydrogen combustion is done in homogeneous mode. It implies that high turbulence is required to enhance air/$H_2$ mixing and burning velocity. The previous paper [5] compared swirl air motion with a flat roof cylinder head and Swumble$^{TM}$ with a pent-roof cylinder head. It was found that the latter leads to higher Turbulent Kinetic Energy (TKE) and better mixture homogeneity at the vicinity of the spark plug at the combustion activation.
- The use of a cap on $H_2$ injector nozzle changes the jet targeting. The interaction between Swumble$^{TM}$ air motion and supersonic hydrogen jet enhances turbulent kinetic energy leading to improved air/$H_2$ mixing.
- The use of Miller intake valve improves hydrogen combustion behaviour. In the previous study [5], it has been confirmed that Miller intake valve was an interesting trade-off for improved air/$H_2$ mixing, reduced temperature inside the cylinder at firing TDC and reduction of knock tendency.
- The use of aluminium as a material for cylinder head reduces wall temperatures compared to conventional cast iron, leading to reduced knock or even pre-ignition propensity.

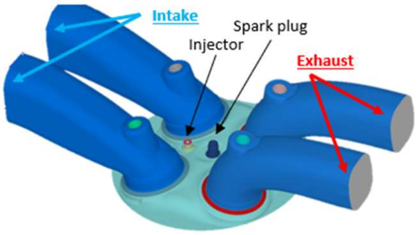

**Fig. 2.** Cylinder head with intake and exhaust ports

## 2.2 Test cell description

The single cylinder engine described in the previous paragraph has been installed on a hydrogen test cell at IFPEN in Solaize, France, to perform a test campaign as illustrated in figure 3. This test bench has been preliminarily modified to be compatible with hydrogen applying the methodology described in the Verhlest and Wallner overview on hydrogen internal combustion engines [8].

Pressurized intake air was provided by an external compressor through a sonic flowmeter. For all the tests, the intake temperature was controlled with an air heater between 30 and 55 °C according to a map depending on engine speed and intake pressure. A flap is used in the exhaust line to simulate the backpressure of a real double-stage turbocharging system. An in-house real-time air loop model is implemented on the test bed supervisor software to evaluate the exhaust backpressure and the corresponding exhaust flap position. The inputs of this double-stage turbocharger system model are intake pressure and air fuel equivalence ratio (also referred as $\lambda_{exhaust}$). The model includes low pressure (LP) and high pressure (HP) compressor and turbine maps that are extracted from a real double-stage turbocharged heavy-duty engine with similar unitary engine displacement. No exhaust gas recirculation (EGR) has been used for these tests and no water injection has been implemented on this engine. These two features will be implemented and tested in the next part of the project. Hydrogen is supplied at 40 bar to the direct injector and the hydrogen flow is measured by a Coriolis mass flowmeter located upstream the injector. Hydrogen is provided by Air Product with a purity > 99.95%. All actuators (ignition, injection, VVT) are controlled with an in-house Electronic Control Unit (ECU). Multiple closed-loop controls are implemented on the supervisor software for controlling Indicated Mean Effective Pressure (IMEP), Crank Angle Degree for 50 % mass fuel burnt (CA50), air fuel equivalence ratio ($\lambda_{exhaust}$), air intake pressure and exhaust backpressure.

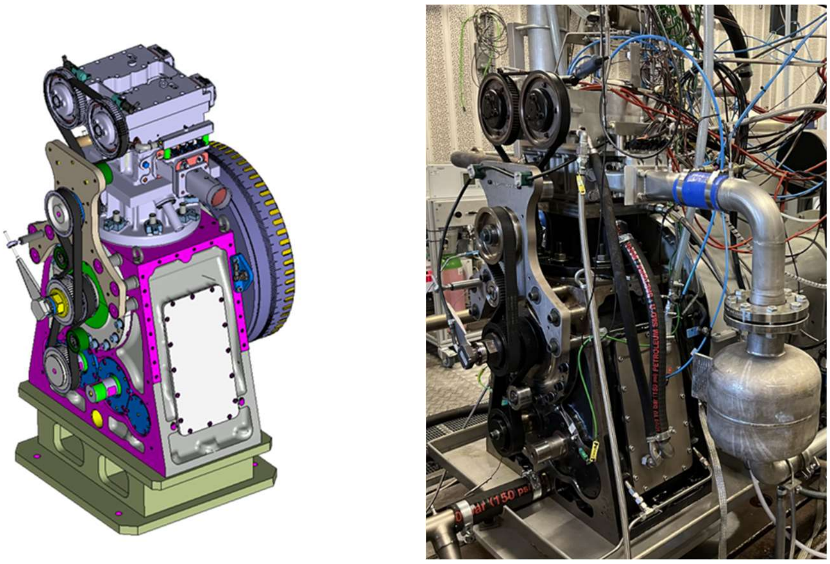

**Fig. 3.** Architecture of the single-cylinder engine and implementation in IFPEN test cell

Real time engine-out emissions (HC, $CH_4$, CO, $CO_2$, $O_2$, NO and $NO_2$) have been measured by Horiba MEXA-7100DEGR analyser. Particle number is measured by SPCS Horiba Mexa 2100. Hydrogen engine-out emissions are measured by a SICK GMS810 gas analyser. The reference relative air-fuel ratio $\lambda_{exhaust}$ is determined based upon the exhaust gas composition making an oxygen atomic balance. This value of $\lambda_{exhaust}$ is also validated with a measure done by a UEGO λ-sensor located in the exhaust line. Oil and coolant were supplied by electrically driven external pumps and temperatures were kept constant for both fluids at 90 °C ± 2 °C. The oil used for this test campaign is a Diesel engine oil referenced as Rubia Optima 1100 FE 10W30 from Total Energies.

Combustion is monitored by an in-cylinder pressure transducer recorded with an angular resolution of 0.1 CAD for 300 consecutive engine cycles. Apparent Heat Release Rate (HRR) and burnt mass fraction are obtained from in-cylinder pressure traces. Moreover, pressure transducers are present at the entrance of the intake port and at the exit of the cylinder head on exhaust port. The objective is to record the engine acoustics, i.e. the pressure oscillations on both intake and exhaust ports during engine tests.

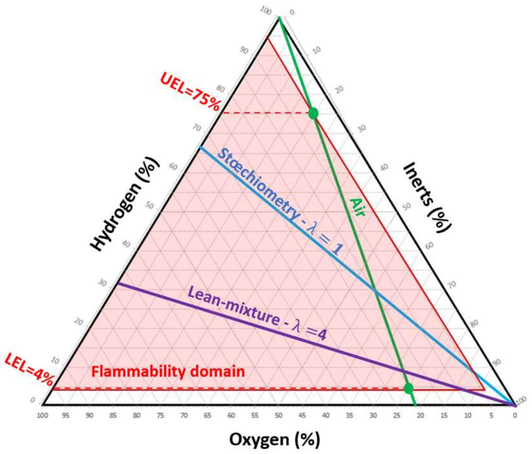

**Fig. 4.** Ternary diagram Lower/Upper Explosive Limits (LEL/UEL) for hydrogen at 20 °C and 1 bar

It is well-known that unavoidable blow-by through piston rings during hydrogen combustion leads to $H_2$ enrichment in the crankcase [9]. The gas composition in the crankcase results from a mixture of gases escaped from the cylinder during intake and combustion-expansion strokes. At any time, it is mandatory not to be in the flammability domain of hydrogen inside the crankcase. This forbidden area is depicted in figure 4 by a ternary diagram as a function of hydrogen, oxygen and inert gases ($N_2$ and $H_2O$) concentrations. At 20 °C, explosive conditions are obtained when Lower Explosive Limit (LEL) is reached, for 4 % of $H_2$ concentration (LEL drops at 3.7 % for 90 °C). To maintain the $H_2$ concentration below this limit in the crankcase, an additional pump aspirates filtered ambient air through the crankcase and the upper part of cylinder head. The mixture of air and blow-by gases passes then through an oil gas/liquid separator.

After installing this single cylinder engine in the described test cell, a full test campaign has been caried out on this engine configuration and the test results are discussed in the next section.

## 3. Engine test results

### 3.1 Injection strategy

During the test campaign, two different injection strategies were tested at part load in steady-state conditions at 1200 rpm engine speed and IMEP = 12 bar with no valve overlap (EVC = 0 CAD ATDC and IVO = 0 CAD BTDC at 1 mm valve lift) and with $\lambda_{exhaust}$ set constant at 2.5 (see figure 5):

- Injection during intake valve opening. The objective is to have sufficient time to homogenize the air and hydrogen in the combustion chamber. Any heterogeneity must be avoided as it leads to NOx emissions and even to pre-ignition. This injection strategy is close to port fuel injection but without having the hydrogen transit in the intake port.
- Injection after intake valve closing. In this case, the time is reduced for air/$H_2$ homogenization and heterogeneities have more probability to be present in the combustion chamber. Moreover, stratification of the fuel can occur if the Start Of Injection (SOI) is too late.

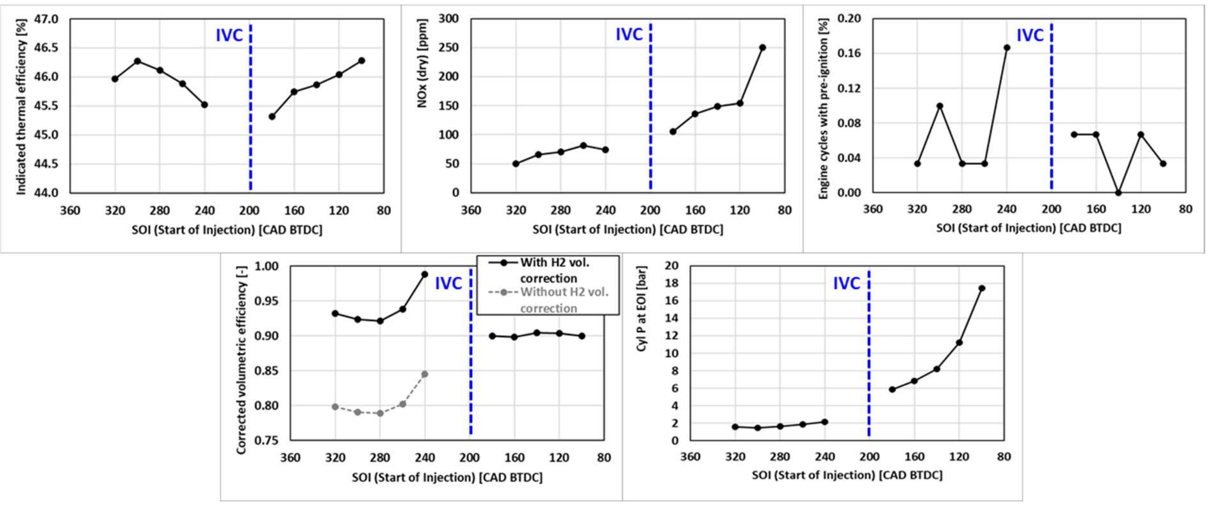

**Fig. 5.** SOI variation at 1200 rpm, IMEP = 12 bar and $\lambda_{exhaust}$ = 2.5

The figure 5 presents the main results of the SOI variation. The spark timing is not kept constant during the variation but set to MBT timing (minimum spark timing for best torque). The Intake Valve Closing (IVC) corresponds to SOI = 200 CAD BTDC as depicted by the vertical blue dotted line. On each chart of the figure 5, results with injection during intake valve opening are on the left part of the curve while those with injection after intake valve closing are on the right part. At any time, the hydrogen jet is supersonic, since the cylinder pressure at the End Of Injection (EOI) is below half of the injection pressure (20 bar in this case). As the SOI varies, the injector backpressure (meaning the cylinder pressure) changes too. The injection duration has then been slightly adapted between 35 to 38 CAD to keep the injected amount of hydrogen constant, whatever the considered SOI.

Whatever the injection strategy, the indicated thermal efficiency is between 45.5 to 46.2 % with an optimum for SOI = 300 CAD BTDC for injection during intake valve opening. The calculation of volumetric efficiency considers the volume of injected hydrogen, when injection is done only during intake valve opening. In figure 5, the volumetric efficiency is depicted in grey dotted line without hydrogen volume correction and in full black line with hydrogen volume correction. Considering hydrogen volume improves volumetric efficiency by 0.12 points during intake valve opening. It is also observed that hydrogen injection during intake valve opening can improve volumetric efficiency compared to the intake of air only, in the case of hydrogen injection after intake valve closing. This volumetric efficiency improvement occurs, when the hydrogen injection generates a favorable pressure oscillation within the combustion chamber, leading to an increment of cylinder pressure at the IVC event.

The ratio of engine cycles with pre-ignition is also estimated thanks to the methodology explained in the following paragraph §3.3. When the ratio of engine cycles with pre-ignition is below 0.1%, the pre-ignition occurrence is considered as not significant, and the pre-ignition becomes prohibitive when this ratio increases over the threshold of 0.1%. In figure 5, whatever the injection strategy, no prohibitive pre-ignition occurrence is noticed except for the SOI = 240 CAD for which the ratio of pre-ignition increases significantly. This corresponds to the hydrogen injection occurring simultaneously with intake valve closing phase. Indeed, the duration of injection is around 36 CAD with a SOI = 240 CAD and IVC is equivalent to SOI = 200 CAD. The explanation of this behaviour is not clarified but it is assumed that supersonic hydrogen jet interacts, in the combustion chamber, with decreasing intake air velocity, coming from intake ports because of intake valve closing phase. The mechanisms of this interaction leading to pre-ignition should be analysed with advanced tools (optical diagnostics or 3D simulation) to be completely explained. As a remark, this trend is experienced in almost all engine tested points.

NOx emissions are higher with injection after intake valve closing. The explanation is the increase of effective compression ratio for this latter injection strategy. A specific test has been done to evaluate the evolution of effective CR for the two different injection strategies. The objective is to have access to the full compression curve between Bottom Dead Center (BDC) and firing TDC by setting the spark timing to -1 CAD ATDC for both injection strategies as shown in figure 6. With a simple calculation of the Laplace law $PV^{\gamma}$ and an assumption on the value of $\gamma$, the effective CR is evaluated. The injection after intake valve closing increases the effective CR by 1.46 points. The rise of effective CR leads to an increase of in-cylinder temperature at firing TDC which can increase knock propensity and can explain the higher NOx emissions with injection after intake valve closing. Furthermore, when SOI decreases for injection after intake valve closing, the NOx emissions continue to increase, and it is assumed to be caused by an air/$H_2$ mixing degradation.

Finally, the optimal injection strategy is during intake valve opening as NOx emissions are lower and indicated thermal efficiency is maintained at a high level.

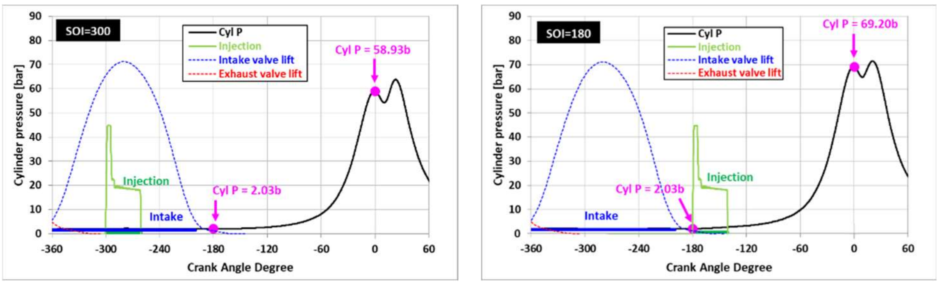

| Injection strategy | Intake valve open | Intake valve closed |
|---|---|---|
| SOI | 300 | 180 |
| Effective CR | 11.82 | 13.28 |

**Fig. 6.** Effective CR evaluation at 1200 rpm IMEP = 12 bar and $\lambda_{exhaust} = 2.5$

### 3.2 Optimal settings at part load

After setting the injection strategy, the other engine control settings are optimized at part load. The first step is to identify the optimal combustion phasing regarding the indicated thermal efficiency. An example is given in Figure 7 at 1200 rpm engine speed and IMEP = 9 bar for $\lambda_{exhaust}$ varying from 1.8 to 3.5. The optimal CA50 is obtained between 3 and 6 CAD ATDC as it corresponds to the highest indicated thermal efficiency. For $\lambda_{exhaust}$ = 1.8 and 2.0, NOx emissions reach high levels, and they are drastically reduced and close to zero for $\lambda_{exhaust}$ higher than 2.5. Besides, unconverted fuel energy (meaning $H_2$ exhaust emissions) is similar for $\lambda_{exhaust}$ in the range of 1.8 to 2.5. For $\lambda_{exhaust}$ = 3.0 and 3.5, the $H_2$ emissions significantly increase as $H_2$ is too diluted for a complete combustion and combustion flame speed is slowed down.

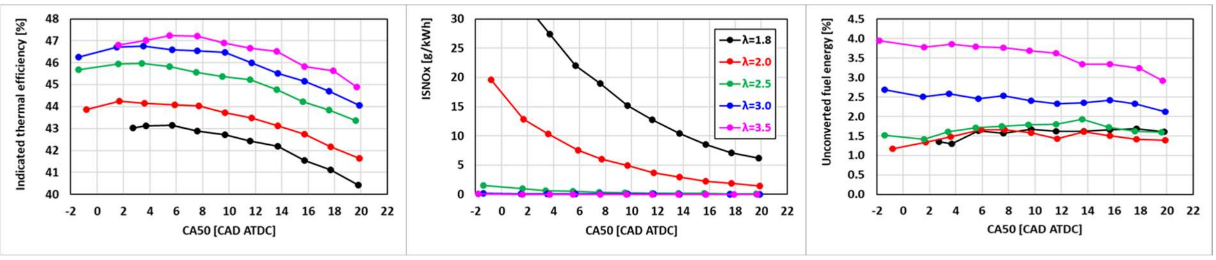

**Fig. 7.** Spark Timing variation at 1200 rpm, IMEP = 9 bar, SOI = 300 CAD BTDC for $\lambda_{exhaust}$ from 1.8 to 3.5

Based on this result of optimal CA50, the figure 8 presents a full map of SOI vs $\lambda_{exhaust}$ for the same operating point at optimal combustion phasing CA50 = 5.5 CAD ATDC. The objective is to identify the optimal SOI and $\lambda_{exhaust}$ settings for this operating point. The range of tested $\lambda_{exhaust}$ is between 1.8 and 3.5, and between 180 and 330 CAD BTDC for SOI. With the VVT set to 0 CAD of valve overlap at 1 mm valve lift, the intake valve opening corresponds to SOI = 200 CAD BTDC and as injection angle duration is around 25 CAD, all the lower parts of the maps for SOI < 225 CAD are considered as injection strategy after intake valve closing. This latter strategy has already been seen as non-optimal at part load.

For this operating point, the optimal $\lambda_{exhaust}$ is around 3.0 as indicated thermal efficiency is very high (around 46.5 %) and NOx emissions are close to 0 g/kWh. $H_2$ emissions are starting to increase but the level of unconverted fuel energy is still moderate.

The optimal SOI is around 300 CAD BTDC as volumetric efficiency is maximized. This effect has already been discussed in the injection strategy section: volumetric efficiency is improved when the hydrogen supersonic jet generates a favourable pressure oscillation within the combustion chamber.

When $\lambda_{exhaust}$ increases, the mixture is more diluted and the maximum of heat release rate decreases: the reduction of max HRR is around 45 % when $\lambda_{exhaust}$ increases from 1.8 up to 3.5. At fixed $\lambda_{exhaust}$, the maximum of heat release rate is almost constant except for very early injection with SOI >

300 CAD BTDC, explaining the fact that SOI = 300 CAD BTDC is the optimum and injection cannot be further advanced. Finally, the optimal settings at 1200 rpm engine speed and IMEP = 9 bar are CA50 = 5.5 CAD ATDC, SOI = 300 CAD BTDC and $\lambda_{exhaust}$ = 3.0. The methodology presented in this section has been applied for the engine tuning on several engine points at part loads.

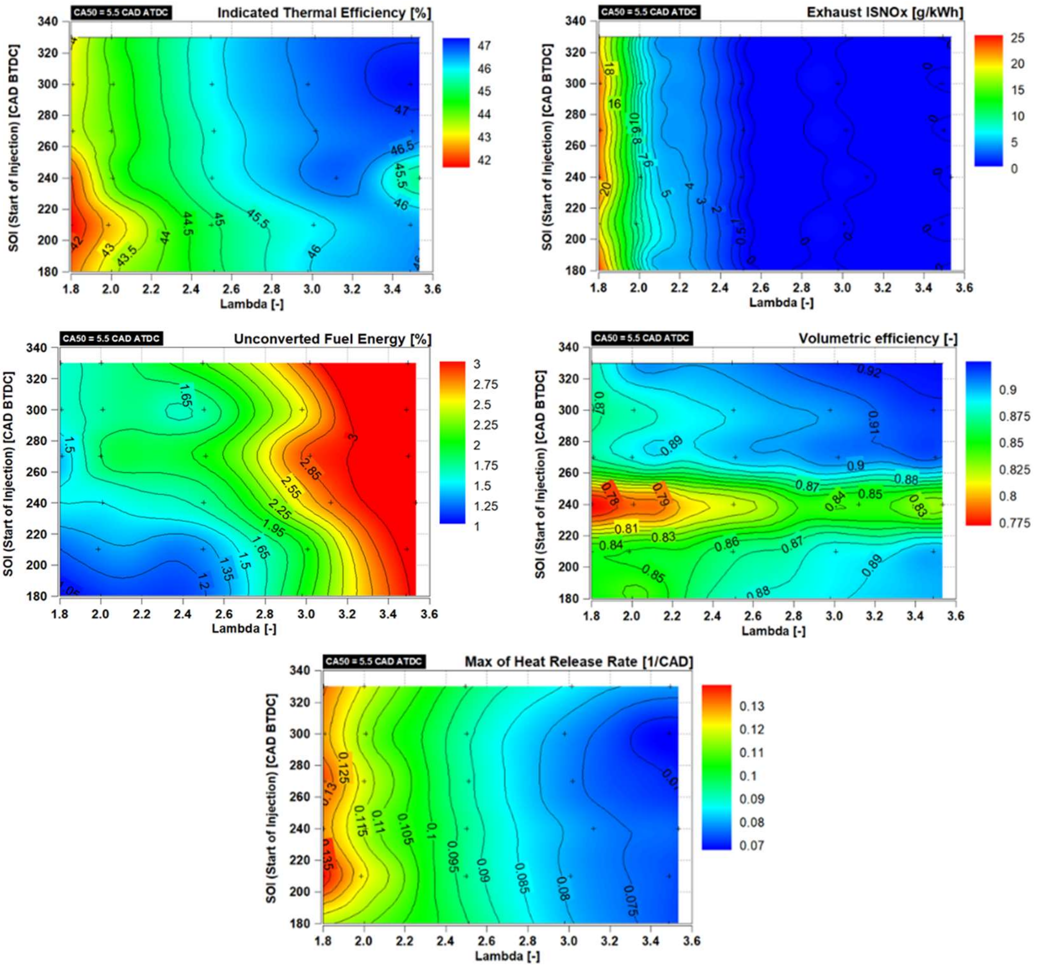

**Fig. 8.** SOI vs $\lambda_{exhaust}$ maps at 1200 rpm, IMEP = 9 bar, CA50 = 5.5 CAD ATDC, EVC/IVO = 0/0 CAD ATDC/BTDC

From these results obtained at part load at 1200 rpm and IMEP = 9 bar, simulation feedback has been realized, with the CFD software CONVERGE$^{TM}$ version 3.1.9, using the setup described by Duffour et al. [5] and according to the conditions operated experimentally for a SOI = 260 CAD BTDC at $\lambda_{exhaust}$ = 2.5. Only one remarkable change is realized in the 3D numerical setup concerning the ECFM combustion model that is now associated to a newly developed turbulent stretching model described by Suillaud et al. [10]. This model is better adapted to high Karvolitz combustion and thus diluted combustion, as for lean hydrogen internal combustion engine.

For the best indicated efficiency operating point at 1200 rpm and IMEP = 9 bar, at SOI = 260 CAD BTDC, the Extended Coherent Flame Model (ECFM) combustion parameter has been calibrated (see figure 9). A good match is observed between experiments and simulation for the mean in-cylinder pressure and for the apparent heat release rate (HRR). The calculated in-cylinder pressure maximum value is almost the same as that from experiment. However, higher peak of heat release rate can be observed in simulation compared to experiments leading to faster combustion.

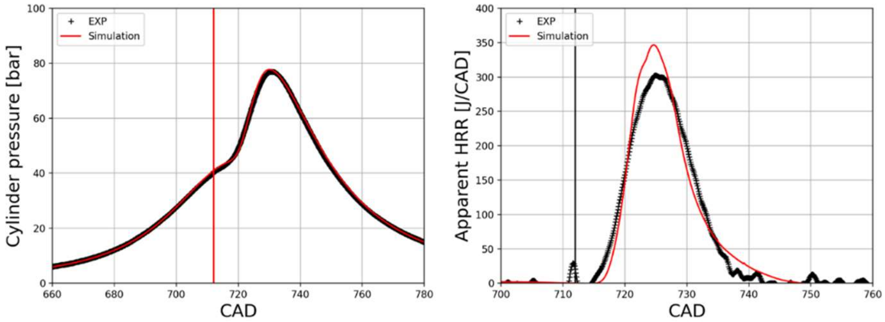

**Fig. 9.** Cylinder pressure and HRR for 3D simulation and experiments at SOI = 260 CAD BTDC

Global data for the combustion such as burn duration and IMEP are presented in table 3. We observe almost same CA50 calibration for both simulation and experiments, a small difference of 0.5 CAD in burn duration (CA90 – CA10). Moreover, all data that concerns the energy losses diagram are compiled inside this table and compared to the experimental results. One can observe the very good match in terms of indicated efficiency, global heat transfer and unconverted percentage of the total fuel energy introduced compared to experimental results. This highlights the validity of the numerical approach used to design this combustion system.

**Tab. 3.** Percentage of the total energy converted in heat losses, indicated efficiency, unconverted fuel energy and burnt duration between simulation and experiments at SOI = 260 CAD BTDC

| | Experiment (EXP) | Simulation |
|---|---|---|
| Unconverted fuel energy [%] | 1.56 | 1.44 |
| Heat losses [%] | 9.15 | 8.47 |
| Other losses (exhaust + pipes) [%] | 41.90 | 42.57 |
| Indicated Thermal Efficiency [%] | 47.38 | 47.52 |
| IMEP [bar] | 9.00 | 9.17 |
| CA10 [CAD ATDC] | 0.4 | 0.8 |
| CA50 [CAD ATDC] | 5.9 | 5.6 |
| CA90 [CAD ATDC] | 12.5 | 13.5 |
| CA90 - CA10 [CAD ATDC] | 12.1 | 12.6 |

Finally, for this operating point 1200 rpm engine speed and IMEP = 9 bar, a Spark Advance (SA) sweep between 14 and 0 CAD BTDC has been realized by simulation and compared to the results obtained experimentally. The results for the in-cylinder pressure and the integrated heat release rate (burnt duration) are presented in figure 10, with experiments in dotted lines and simulation in full line. The results show a good agreement in terms of in-cylinder maximum pressure and burnt duration. Deviation is observed only for delayed spark advance due to the need for more $H_2$ injected mass to compensate the reduction of indicated efficiency and thus keep the same 9 bar IMEP. This was unfortunately not realizable by simulation, due to very high simulation time duration with hydrogen supersonic injection (very low time step) thus, hydrogen injected amount was considered constant for this variation.

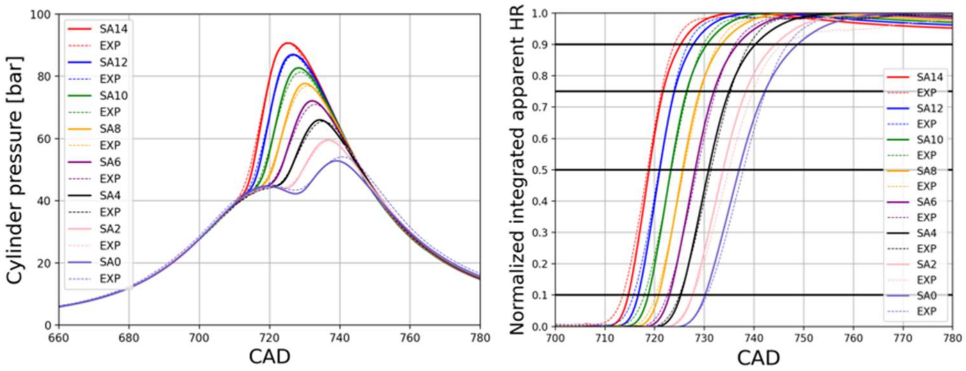

**Fig. 10.** In-cylinder pressure and integrated HRR for 3D simulation and experiments

The dependance of NOx emissions on the spark advance coming from experiments and 3D simulations are compared in Figure 11. These NOx emissions are computed in 3D simulation using extended Zeldovich mechanism [11] and considering that the NOx emissions from $H_2$ ICE are mostly due to thermal NOx. NOx emissions follow the same trend regarding SA variation, but the absolute computed values are lower, by a factor 2 to 2.2. It underlines the need for better understanding and modelling of NOx emissions in $H_2$ ICE.

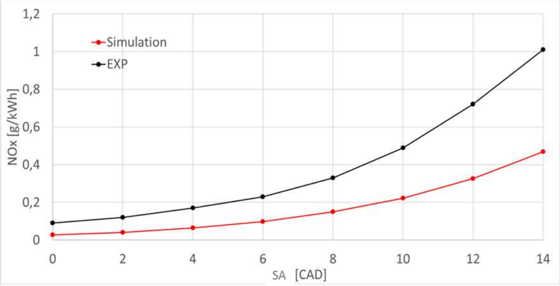

**Fig. 11.** NOx emissions function of spark advance for experiments and 3D simulation

### 3.3 Abnormal combustion characterization at high load

At higher loads (around IMEP > 15 bar), hydrogen combustion can lead to any type of abnormal combustion such as backfiring, knocking or pre-ignition.

As hydrogen direct injection is implemented on this engine, the backfiring has not been experienced during the test campaign. Concerning pre-ignition or knock, they can suddenly occur, in steady-state conditions, without modifying any engine setting. It must be mentioned that pre-ignition can occur with a peak cylinder pressure not exceeding the limit value for this engine (set at 170 bar) as depicted in Figure 12. However, even if these combustion cycles cause no damage to the engine, they must be avoided as much as possible.

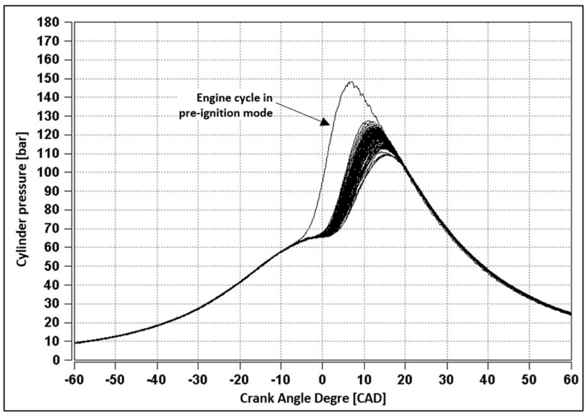

**Fig. 12.** Example of an engine cycle with pre-ignition with “safe” peak cylinder pressure

A test methodology has been set up for pre-ignition and knock detection for high load operating points. At the test cell, detecting abnormal combustion requires to record sufficient samples of engine cycles to properly calculate index statistics. During the tests, the recorded statistical population was set to 3000 consecutive engine cycles to operate the abnormal combustion detection. The left-hand charts on figure 13 illustrate the recording of CA10 and peak cylinder pressure for 3000 consecutive engine cycles at 1200 rpm, IMEP = 16 bar. The CA10 burn mass fraction is obtained from in-cylinder pressure trace using an in-house combustion analysis tool and CA10 is positive when it occurs after firing TDC. On the right-hand charts, the normal distribution is calculated and compared to the cumulative index per value of the statistical population. It is then validated by approximation that recorded CA10 and peak cylinder pressure have a centered and symmetrical normal distribution. The Gauss-Laplace distribution [12] says that 99 % of the population samples of a normal distribution are contained between the boundaries of $\mu(population) \pm 2{,}4.\sigma(population)$ with μ, the mean value and σ, the standard deviation. These boundaries are depicted by dotted blue lines on the charts of figure 13.

For an engine cycle n, the pre-ignition is then set and defined by meeting simultaneously these two conditions:

1. $CA10_n < \mu[Population(CA10)] - 2{,}4.\sigma[Population(CA10)]$
2. $Peak\ Cyl.P_n > \mu[Population(Peak\ Cyl.P)] + 2{,}4.\sigma[Population(Peak\ Cyl.P)]$

Then, the ratio of engine cycles with pre-ignition can be estimated. When the ratio of engine cycles with pre-ignition is below 0.1%, the pre-ignition occurrence measure is considered as not significant, and the pre-ignition becomes damageable when this ratio increases over the threshold of 0.1%.

For knock detection, the methodology is similar by using the Kp_Pk criterion. This index is defined by AVL as the absolute maximum of the rectified knock oscillation superimposed on the cylinder pressure [13]. For an engine cycle n, the damageable knock is then defined by meeting this condition:

$$Kp\_Pk_n > \mu[Population(Kp\_Pk)] + 2{,}4.\sigma[Population(Peak\ Cyl.P)]$$

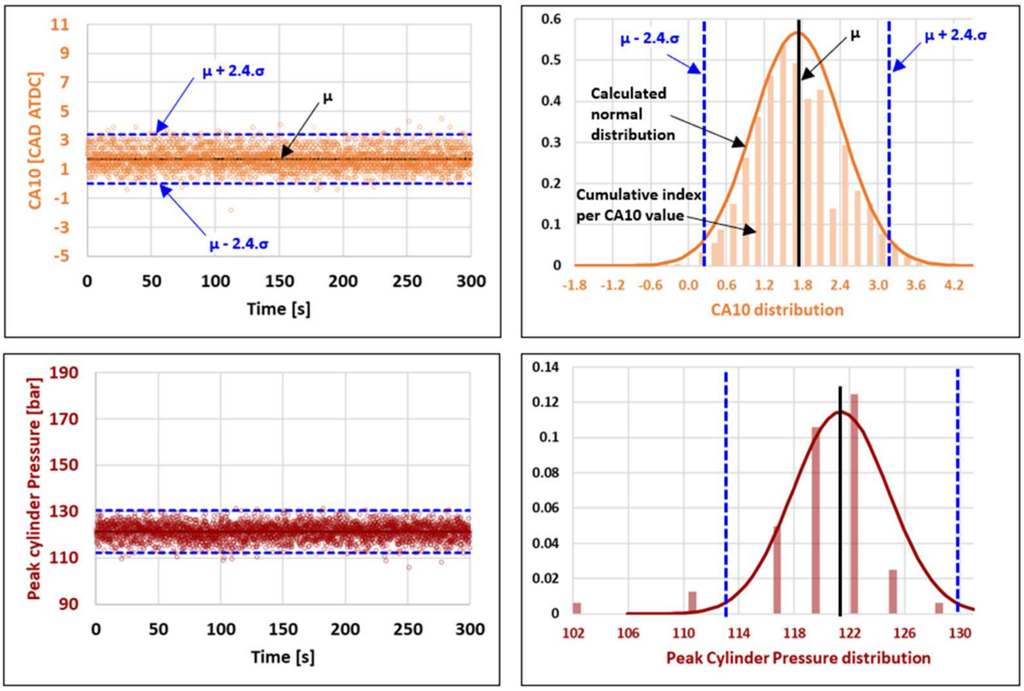

**Fig. 13.** Normal distributions of CA10 and peak cylinder pressure at 1200 rpm, IMEP = 16 bar, SOI = 290 CAD

The figure 14 shows an example of this pre-ignition and knock detection methodology applied to a SOI sweep at 1200 rpm IMEP = 16 bar with VVT actuator set for no valve overlap. The charts display the peak cylinder pressure versus the CA10 for 3000 consecutive engine cycles. The two conditions for detecting pre-ignition are depicted by the blue dotted line rectangle. If the indexes of engine cycles are inside this rectangle, they are symbolized by green circle marks, and it means that combustion is in normal mode without any pre-ignition. If the indexes of engine cycles are outside the blue dotted line rectangle in the upper left side, they are symbolized with red circle marks: the combustion is in pre-ignition mode. Then, the percentage of engine cycles with pre-ignition can be evaluated.

From the test results, we notice that very low rates of unsafe pre-ignition are experienced for earlier SOI between 270 and 310 CAD BTDC. When SOI is delayed from 250 to 230 CAD BTDC, the percentage of engine cycles with pre-ignition increases significantly and overpasses the threshold of 0.1%, meaning that damageable pre-ignition is occurring. For these latest SOI, as injection angle duration is around 48 CAD, the injection occurs simultaneously with the closing of the intake valve. As previously discussed in the injection strategy section, it is assumed that the supersonic hydrogen jet interacts with decreasing intake air velocity coming from the intake ports because of intake valve closing leading to intense pre-ignition. The detailed mechanisms are not clearly identified but the methodology described in this section highlights the correlation between pre-ignition and injection during intake valve closing phase.

Besides, the observation of test results points out that knock occurrence frequency increases with pre-ignition frequency but at a lower rate. This means that some engine cycles with intense pre-ignition lead also to knock detection, but not all of them. Finally, this detection methodology has been applied for the engine settings tuning of all high load operating points.

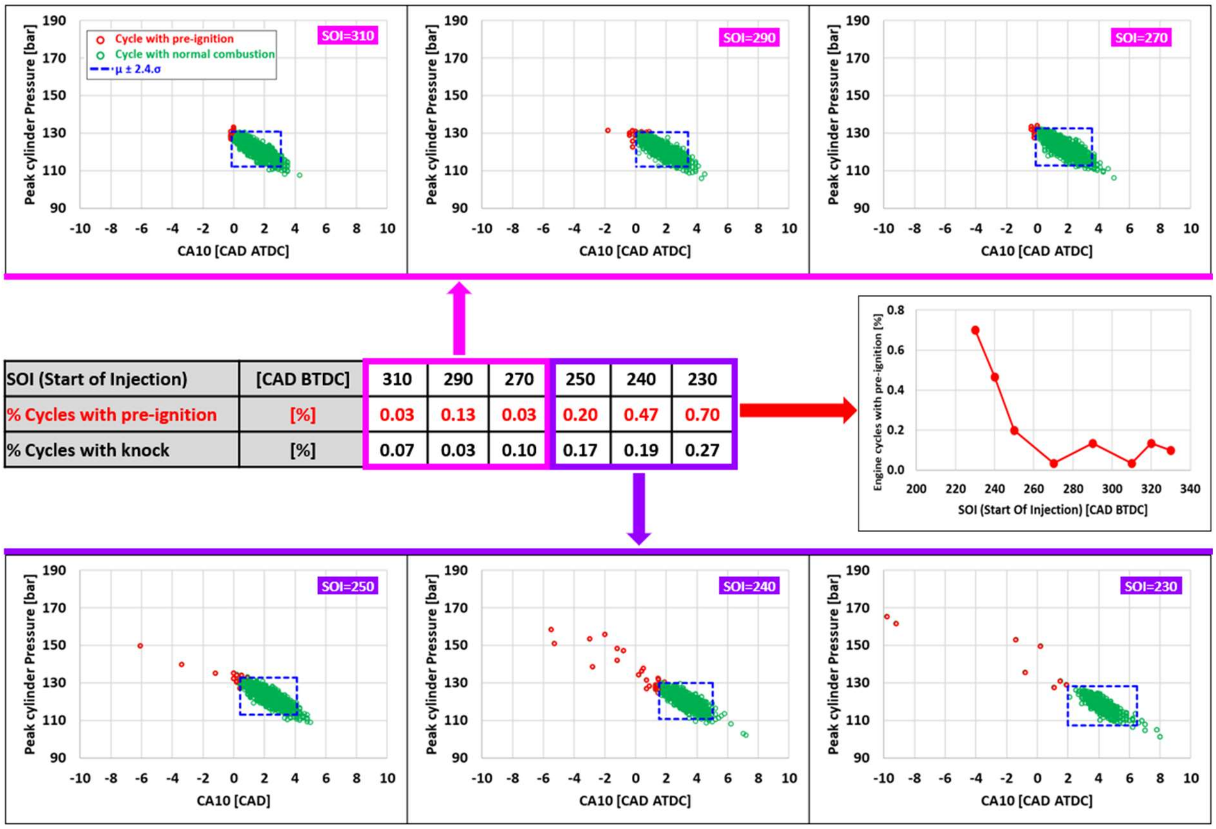

| SOI (Start of Injection) | [CAD BTDC] | 310 | 290 | 270 | 250 | 240 | 230 |
|---|---|---|---|---|---|---|---|
| % Cycles with pre-ignition | [%] | 0.03 | 0.13 | 0.03 | 0.20 | 0.47 | 0.70 |
| % Cycles with knock | [%] | 0.07 | 0.03 | 0.10 | 0.17 | 0.19 | 0.27 |

**Fig. 14.** Detection of engine cycles with pre-ignition and knock for a SOI variation at 1200 rpm IMEP = 16 bar with no valve overlap, EVC/IVO = 0/0 CAD ATDC/BTDC

### 3.4 Full load strategy

The objective of this section is to identify the main limitations of the full load for this hydrogen internal combustion engine. These limitations can vary with a different engine architecture. The engine tuning strategy can then be deduced from the identification of the main boundaries. Considering the abnormal combustion detection methodology described in the previous section, a spark timing variation is performed at 1200 rpm, IMEP = 16 bar for $\lambda_{exhaust}$ = 2.0, 2.5 and 3.0 with positive valve overlap of 20 CAD at 1 mm valve lift. The test results are shown in figure 15. The combustion phasing is limited by three main boundaries shown in the indicating thermal efficiency chart:

1. For early combustions (low values of CA50), the combustion is obviously limited by the increase of the Kp_Pk index indicating a higher knock propensity. The pink area on the low-left hand of the chart represents the prohibitive knock area. The minimum CA50, just before knock limitation, is delayed with the reduction of $\lambda_{exhaust}$.
2. For early combustions and high values of $\lambda_{exhaust}$, the combustion can be limited by the peak cylinder pressure set to 170 bar for this single cylinder engine. The blue area on the upper-left hand of the chart represents the prohibitive peak cylinder pressure area.
3. For delayed combustions (high values of CA50), the combustion is limited by the increasing ratio of engine cycles in intense pre-ignition mode. The purple area on the low-right hand of the chart represents the prohibitive pre-ignition area. The maximum CA50, just before pre-ignition limitation, is advanced with the reduction of $\lambda_{exhaust}$.

Considering these three limitations simultaneously, the possible CA50 combustion phasing range is drastically reduced when $\lambda_{exhaust}$ decreases. When engine load increases, $\lambda_{exhaust}$ must be reduced to decrease air demand, meaning that the turbocharging system can achieve the level of required intake pressure.

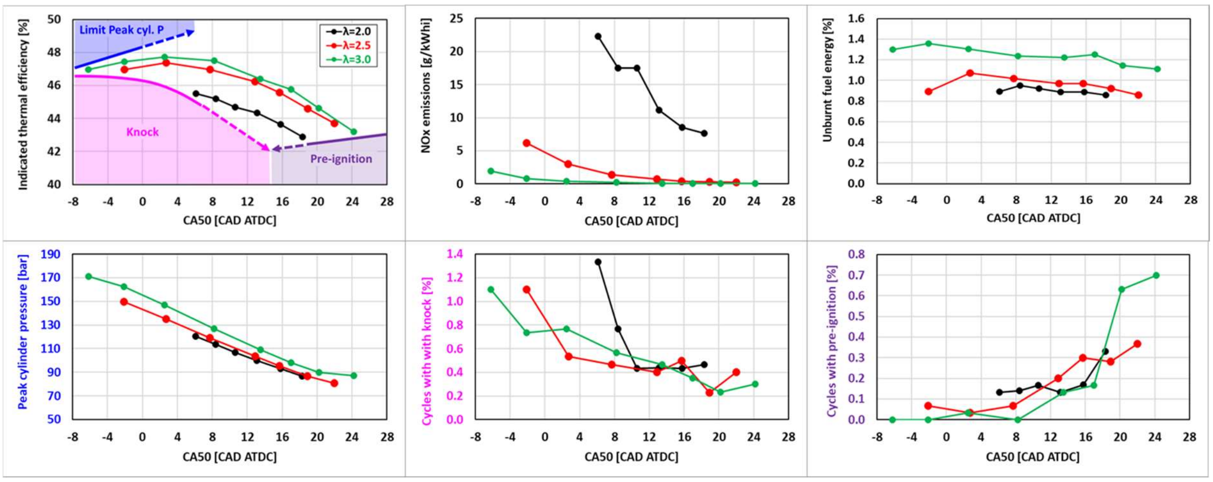

**Fig. 15.** Spark timing sweep for $\lambda_{exhaust}$ = 2.0, 2.5 and 3.0 at 1200 rpm, IMEP = 16 bar, SOI = 300 CAD BTDC with 20 CAD of positive valve overlap (EVC/IVO = 10/10 CAD ATDC/BTDC)

The following step is to operate a load sweep to build up the engine tuning strategy for reaching the full load. An example of load sweep at 1200 rpm engine speed is given in Figure 16. The maximum IMEP reached on this engine configuration at 1200 rpm is IMEP = 23.5 bar with low CoV IMEP and no intense pre-ignition occurrences. The strategy for increasing IMEP can be summarized by the following key points:

- One of the main pre-ignition causes is the high concentrations of residual burnt gases inside the combustion chamber coming from the previous engine cycle. To reduce their concentration, the VVT actuator must be set up for positive valve overlap to allow an efficient air scavenging of the combustion chamber. Indeed, at high load, the double-stage turbocharger model implemented at the test bed results in low exhaust backpressure creating a favourable differential pressure between exhaust and intake. The consequence is an efficient air scavenging during valve overlap as shown in the charts of figure 16. It is interesting to mention that this strategy is only possible with hydrogen direct injection.
- The mixture must be enriched when engine load increases for having achievable intake and exhaust pressures by the turbocharging system, meaning that the double-stage turbocharger is capable to reach the intake pressure demand with a low exhaust pressure. $\lambda_{exhaust}$ is then reduced from 3.0 at IMEP = 10 bar down to around 2.1 at full load. At high loads, as VVT is set up for positive overlap, $\lambda_{exhaust}$ is higher than $\lambda_{in\text{-}cylinder}$ because of the air scavenging.
- The optimal injection strategy is during intake valve opening phase. Besides, optimal SOI at part load is near 300 CAD ATDC. When engine load increases, SOI must be set up earlier so that injection, which lasts longer, ends before the closing of the intake valve. It has already been mentioned in this article that the simultaneity of hydrogen injection and intake valve closing leads to uncontrollable pre-ignition. Obviously, at high load, there is positive valve overlap and SOI must not be set too early and must be done after the EVC. For this engine speed of 1200 rpm, the injection angle duration fits in the intake valve opening phase without any interaction with the intake valve closing phase. Yet, at higher engine speed, 1900 rpm for example, this limitation takes place.

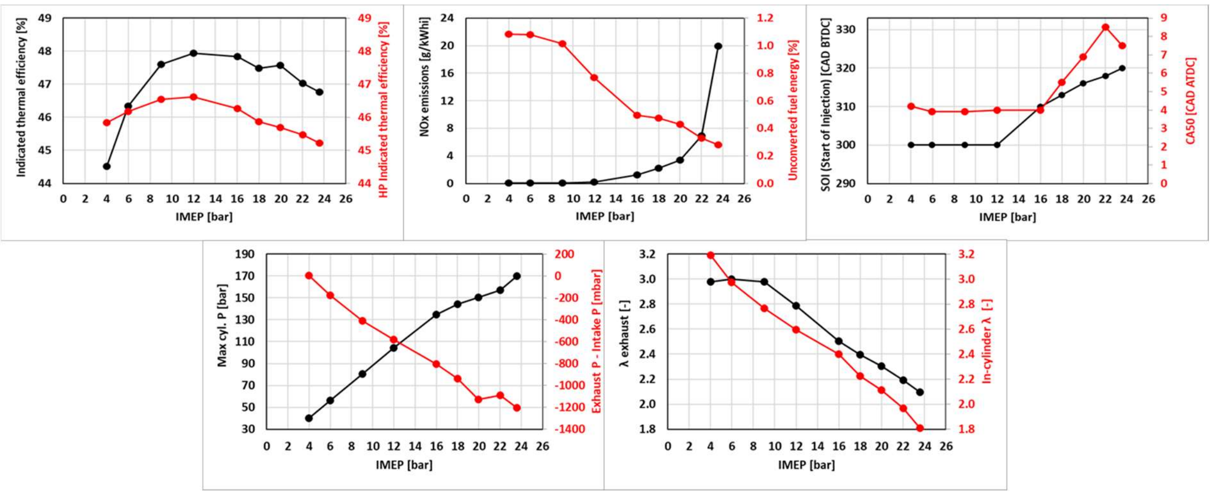

**Fig. 16.** Engine settings, emissions, and efficiencies for IMEP variation at 1200 rpm engine speed from 4 bar IMEP to full load

The indicated thermal efficiency is still very high at full load, around 47 %, close to the maximum of 48 % reached at IMEP = 12 bar (figure 16). Moreover, the HP indicated thermal efficiency is lower by 1 % to 1.5 % compared to indicated thermal efficiency. This gain of 1 % to 1.5 % for indicated thermal efficiency is only due to the double-stage turbocharger positive impact on air loop for these engine operating conditions. Besides, at full load, NOx emissions drastically increase up to 20 g/kWhi as $\lambda_{\text{in-cylinder}}$ decreases. Unconverted fuel energy (or $H_2$ exhaust emissions) drops from 1 % to 0.2 %. This could be explained as $\lambda_{\text{in-cylinder}}$ decreases, combustion efficiency is significantly improved.

Finally, the full load corresponding to 23.5 bar IMEP at 1200 rpm is simultaneously limited by these three boundaries:

- The maximum peak cylinder pressure of 170 bar for engine integrity protection.
- Abnormal combustion occurrences: both knock and pre-ignition. As $\lambda_{\text{exhaust}}$ has been lowered down to 2.1, the possible CA50 combustion phasing range is very narrow, and combustion must be delayed to CA50 = 8 CAD ATDC compared to the optimal phasing between 3 and 6 CAD ATDC as mentioned in section §3.2. If combustion phasing is set earlier than CA50 = 8 CAD ATDC, knock appears; and if combustion is delayed, pre-ignition drastically increases.
- NOx emissions: the level of NOx emissions should stay beyond 4 g/kWhi (and exceptionally higher than this value on the full load curve), to be efficiently converted into $N_2$ by the deNOx exhaust aftertreatment system.

### 3.5 Engine map results

The engine settings have been tuned on load sweeps for four engine speeds: 900, 1200, 1500 and 1900 rpm. Several part load operating points and full load curve have been fully optimized following the previous presented methodologies. The other operating point settings have been extrapolated to get “smooth” map settings. The results are presented in figure 17.

The single cylinder engine has a large area with indicated thermal efficiency higher than 47 % which is directly comparable to similar Diesel heavy-duty engines. The $\lambda_{\text{exhaust}}$ is set at 3.0 from IMEP = 4 bar to 10 bar leading to nearly no NOx emissions and hydrogen unburnt emissions close to 1 to 1.4 % of injected fuel energy. The $\lambda_{\text{exhaust}}$ decreases to 2.5 at IMEP = 16 bar, leading to NOx emissions not higher than 2 g/kWhi and an unconverted fuel energy between 0.6 and 0.8 %. At full load, $\lambda_{\text{exhaust}}$ de-creases down to 2.1 between 1200 and 1500 rpm leading to very high NOx emissions, higher than 10 g/kWhi.

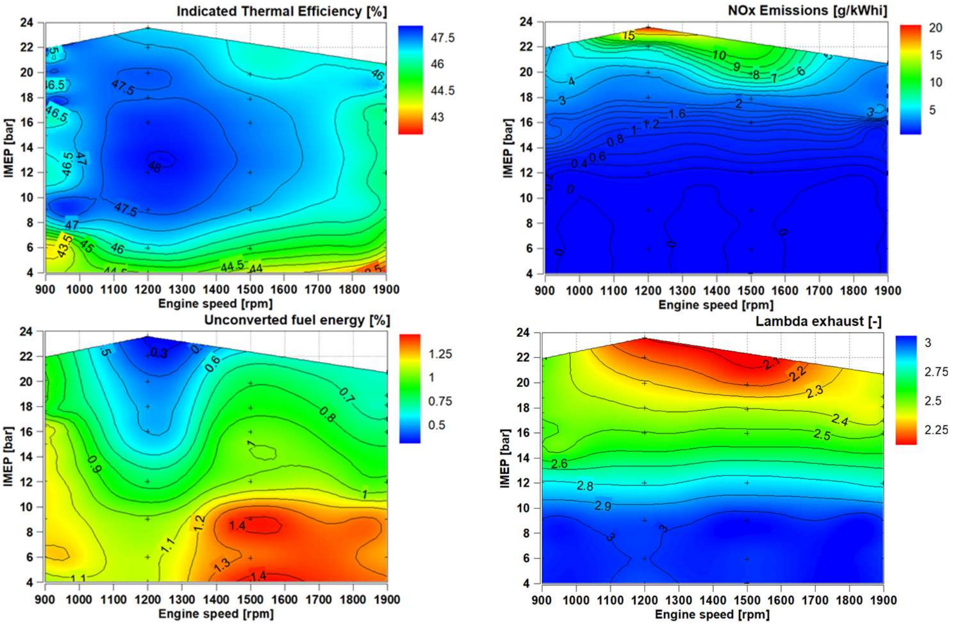

**Fig. 17.** Engine test result maps between 900 and 1900 rpm in terms of efficiency, emissions and $\lambda_{exhaust}$

The double-stage turbocharger model implemented on air loop allows to have a favorable differential pressure between exhaust and intake pressures from -100 mbar at low load up to -1200 mbar at full load (figure 18). Air scavenging with VVT positive valve overlap is applied at low load and massively at full load to mitigate pre-ignition and knock by decreasing the residual gas concentrations inside the combustion chamber. The volumetric efficiency exhibits relatively high values considering the use of Miller intake valve camshaft. The calculation of volumetric efficiency is corrected by considering the volume of hydrogen injected during intake valve opening.

The injection strategy is set for injection during intake valve opening with SOI at 300 CAD BTDC at low load and earlier SOI up to 330 CAD BTDC at full load and high engine speeds. The SOI is set up earlier at full load for the injection angle duration to fit during the intake valve opening, without interfering with intake valve closing phase. This interference has been observed to promote pre-ignition occurrences.

The combustion phasing is optimal between 4 and 6 CAD ATDC for a very large area of the engine map, except for full load conditions between 1200 and 1500 rpm as knock propensity required to delay the combustion.

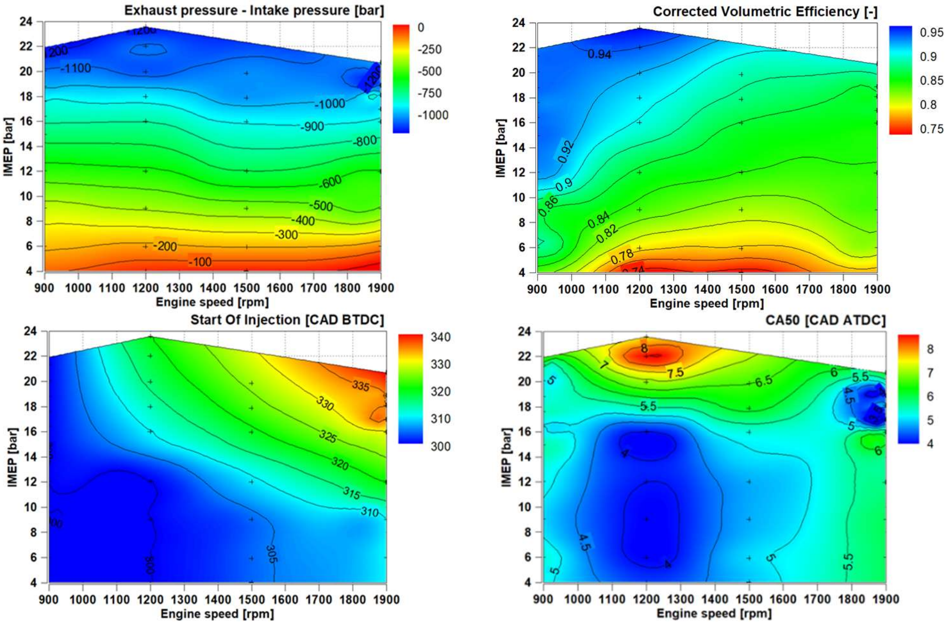

**Fig. 18.** Engine test result maps between 900 and 1900 rpm in terms of air loop, SOI and CA50

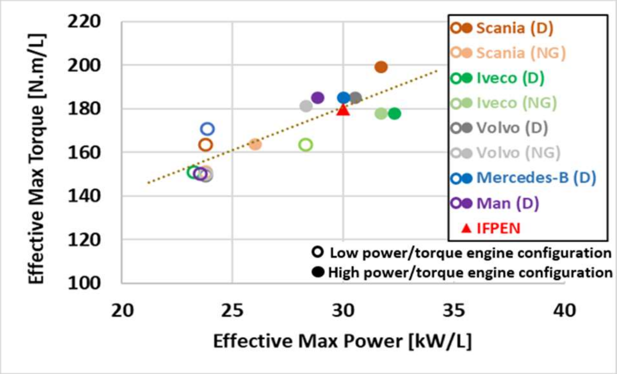

**Fig. 19.** Heavy-duty 13-liter displacement engine benchmark

Finally, the maximum power is reached at 1900 rpm engine speed with 70 kW at IMEP = 20.7 bar and max torque at 1200 rpm with 400 N.m (in indicated conditions, meaning that friction must be subtracted for effective power and torque). This single-cylinder engine represents a 13 liters displacement multicylinder engine. Consequently, the max power of the corresponding multicylinder can be extrapolated to 30 kW/L (kW per liter of engine displacement) and the max torque to 180 N.m/L considering a realistic assumption on engine friction. These values are comparable to the maximum power and torque reached by Diesel or Natural Gas heavy-duty engines of the same displacement, today on the market (respectively between 23 and 32 kW/L and between 150 and 200 N.m/L) (figure 19).

## 4. Conclusions

A hydrogen direct injection single cylinder engine has been designed and manufactured using 0D and 3D simulation tools and IFPEN know-how. The engine has been implemented on an IFPEN test cell and a complete test campaign has been performed to validate the design of the combustion chamber in terms of efficiency, low emissions, and full-load performance. A double-stage turbocharger model has been implemented on the test bed software supervisor, to give realistic conditions on air loop. Different general conclusions on different topics can be drawn:

- The optimal injection strategy is considered to occur during intake valve opening phase. The injection should not happen concomitantly with the intake valve closing phase as pre-ignition can be promoted.
- The optimal SOI at part load is around 300 CAD BTDC as it allows higher volumetric efficiency and better air/$H_2$ homogeneity. The optimal $\lambda_{exhaust}$ at part load is between 2.5 and 3.0, resulting in a good trade-off between high indicated thermal efficiency and low NOx emissions.
- 3D simulation feedback with CONVERGE$^{TM}$ has been realized using last IFPEN development for combustion modeling. The comparison with experiments at part load is consistent in terms of combustion duration and indicated efficiency for a spark advance sweep, showing the validity of the numerical approach used to optimize and design this $H_2$ combustion system.
- A new knock and pre-ignition detection methodology has been developed by using a large population of engine cycles. The cylinder pressure is then processed to evaluate CA10, peak cylinder pressure and Kp_Pk indexes. Statistic calculations on these indexes allow to precisely analyse the impact of engine settings on the appearance of knock or pre-ignition.
- The full load limitations have been identified such as prohibitive pre-ignition, knock and maximum peak cylinder pressure areas. At high load, the double-stage turbocharger model results in lower exhaust pressure compared to intake pressure. This advantage is used to operate air scavenging of the combustion chamber by positive valve overlap leading to a pre-ignition mitigation. Besides, at high load, air/$H_2$ mixture must be enriched for achievable intake pressure by the turbocharging system but with caution as NOx emissions increase significantly.

- The engine settings have been tuned on the whole engine operating range. The indicated engine efficiency is maximum on a large area. NOx emissions are very low from low to mid-load and then increase smoothly in the higher loads area of the map, to finally reach higher values at full load.
- The maximum power and torque obtained are comparable to the performances of Diesel and Natural Gas heavy-duty engines today in the market.

For further engine efficiency or performance improvement, engine configuration should evolve by considering a different double-stage turbocharger model with optimized LP and HP compressor and turbine maps, a different injector cap design and $H_2$ jet targeting allowing for better mixing or a further optimization of engine compression ratio. This process of improvement will be the topic of another article to come.

The authors acknowledge the contribution of their colleagues from IFPEN, A. Nail and J. Terver for the operating of the engine tests.

## Notation

| | |
|---|---|
| $\lambda$ | *Air-Fuel Equivalence Ratio* |
| $\sigma$ | *Standard deviation* |
| $\mu$ | *Mean value* |
| *ATDC* | *After Top Dead Center* |
| *BEV* | *Battery Electric Vehicles* |
| *BTDC* | *Before Top Dead Center* |
| *CA50* | *Crank Angle Degree for 50 % mass fuel burnt* |
| *CAD* | *Crank Angle Degree* |
| *CoV* | *Coefficient of Variation* |
| *CR* | *Compression Ratio* |
| *DI* | *Direct Injection* |
| *ECFM* | *Extended Coherent Flame Model* |
| *ECU* | *Electronic Control Unit* |
| *EOI* | *End Of Injection* |
| *EU* | *European Union* |
| *EVC* | *Exhaust Valve Closing* |
| *GHG* | *Green House Gases* |
| *g/kWhi* | *Unit of mass emissions per kW in indicated conditions* |
| *HP/LP* | *High Pressure* |
| *HRR* | *Heat Release Rate* |
| *ICE* | *Internal Combustion Engine* |
| *IMEP* | *Indicated Mean Effective Pressure* |
| *IVO* | *Intake Valve Opening* |
| *LEL* | *Lower Explosive Limit* |
| *LSPI* | *Low-speed Pre-ignition* |
| *MBT* | *Minimum spark timing for Best Torque* |
| *PFI* | *Port Fuel InjectionSOI Start of Injection* |
| *SA* | *Spark Advance* |
| *TKE* | *Turbulent Kinetic Energy* |
| *VVT* | *Variable Valve Timing* |

## References

[1] European Commission, “A hydrogen strategy for a climate-neutral Europe”, Communication from the commission to the European Parliament, the Council, the European Economic and Social Sommittee and the Committee of the Regions, 301 final, Brussels, COM, 2020

[2] Acar, C. and Dincer, I., “The potential role of hydrogen as a sustainable transportation fuel to combat global warming,” International Journal of Hydrogen Energy 45(5):3396–3406, 2020

[3] Verhlest, S. and Wallner T. “Hydrogen-fueled internal combustion engines”, Progress in Energy and Combustion Science, Elsevier, Volume 35, Issue 6, Pages 490-527, 2009

[4] Snra, A., “Is there a place for H2 internal combustion engines”, Presentation, Webinar H2IQ hour, 2023

[5] Duffour, D., Laget, O., Giuffrida, V., Valin, T., Andre, M., “Optimizing a Heavy-Duty Hydrogen DI combustion system using experimental and numerical workflow”, SIA International Congress: SIA Powertrain & Energy - Rouen 2022

[6] Rouleau, L., Duffour, F., Walter, B., Kumar, R. et al., “Experimental and Numerical Investigation on Hydrogen Internal Combustion Engine,” SAE Technical Paper Series, 15th International Conference on Engines & Vehicles, 2021

[7] Laget, O., Rouleau L., Cordier M., “A comprehensive study for the identification of the requirements for an optimal H2 combustion engine” International Journal of Engine Research. 2023;24(10):4326-4342, 2023

[8] Verhelst, S. and Wallner, T., “Hydrogen-Fueled Internal Combustion Engines”, pp490-527, Progress in Energy and Combustion Science 35, 2009

[9] Fürst, S., Dub, M., Gruber, M. and Lechner, W., “Safety of Hydrogen-Fueled Motor Vehicles with IC Engines”, Engineering, Environmental Science, 1979

[10] Suillaud et al, “Direct Numerical Simulations of high Karlovitz number premixed flames for the analysis and modeling of the displacement speed”, Combustion and Flame, Volume 236, 2022, 111770, ISSN 0010-2180, https://doi.org/10.1016/j.combustflame.2021.111770

[11] Heywood, J.B., Internal Combustion Engine Fundamentals, McGraw Hill, Inc., 1988

[12] Ingrand, P., “Loi normale de Laplace-Gauss”, Journal d'imagerie diagnostique et interventionnelle, Volume 1, Pages S4-S8, ISSN 2543-3431, Supplement, 2017.

[13] Kozlov, A., Terenchenko, A., Zuev, N., Gattarov, I., ”Experimental Research and Computer Simulation of Knock Onset in a Heavy-Duty Si Gas Engine”, International Journal of Innovative Technology and Exploring Engineering (IJITEE), PP: 730-736 | Volume-8 Issue-12, October 2019

# Session 1.3 AMMONIA FUEL FOR MARINE TRANSPORT

# Experimental Investigation of High-Pressure Ammonia Spray and Combustion under Marine Engine-Like Conditions Using Optical Diagnostics

P. Sementa[1], M. Lazzaro[1], C. Tornatore[1], F. Catapano[1], A. Calvo Oliveira[2], L. Thorsen[2], L. Viglione[2]

[1]STEMS: Institute of Science and Technology for Sustainable Energy and Mobility, CNR (Italian National Research Council), via Marconi, 4, 80125 Napoli (Italy)

E-mail: paolo.sementa@stems.cnr.it; maurizio.lazzaro@stems.cnr.it; cinzia.tornatore@stems.cnr.it; francesco.catapano@stems.cnr.it
Telephone: +(39) 081 717 71 23

[2] Wärtsilä, Switzerland

E-mail: alejandro.olivera@wartsila.com; lauge.thorsen@wartsila.com; ludovico.viglione@wartsila.com
Telephone: +(41) 52 550 01 13

**Abstract.** Ammonia could represent a viable alternative to the use of conventional fossil fuels in marine engines as it is carbon-free and can be produced using renewable energy sources. However, the use of ammonia as a marine fuel presents some critical issues, due to its high toxicity, its lower energy density compared to conventional fuels, and its low flammability limits, which make it difficult to burn under lean conditions. To address the latter issue in more detail, experiments were conducted in a constant volume optical chamber designed to inject and burn ammonia under conditions similar to those of 2-stroke marine engines.

The chamber, which mirrors the dimensions of a single-cylinder in a two-stroke marine engine, represents a high-temperature and high-pressure cylinder. Two injectors have been integrated, one for ammonia injection and the other for the supply of conventional fuel to ignite ammonia.

High-precision instruments, including pressure and temperature sensors, as well as a sapphire window for the use of optical methods, such as high-speed imaging, were installed on the chamber. This setup made it possible to collect both thermodynamic and optical data and facilitated the observation of combustion behaviour under various boundary conditions.

Various temperature conditions were investigated in the optical chamber and a sweep of the diesel pilot injection duration was performed. The vaporization of ammonia spray was measured, and the combustion process was studied in detail to better understand the phenomena controlling the process.

The findings from these experiments provide crucial insights for optimizing ammonia combustion for marine engines under various operating conditions. This research supports the development of sustainable propulsion technologies in the maritime sector, addressing critical challenges of ammonia fuel utilization, and contributing to the reduction of greenhouse gas emissions in marine transportation.

## 1. Introduction

The need to move towards sustainable and environmentally friendly energy sources has sparked interest in alternative fuels for marine engines. Among these alternatives, ammonia has emerged as a promising candidate as it is carbon-free and can be produced using renewable energy sources [1, 2]. However, despite its remarkable advantages, the integration of ammonia as a marine fuel shows several challenges.

The main problems with the use of ammonia in marine engines include its inherent properties, particularly its high toxicity, its lower energy density compared to conventional fuels and its low flammability limit [3]. These properties pose significant hurdles, especially when it comes to achieving efficient combustion under lean engine conditions, which is essential for optimizing fuel consumption and reducing emissions [4].

The use of ammonia as alternative fuel for the maritime sector needs to face the challenges of refining engine combustion technologies to optimize its utilization. Within scientific literature, considerable focus has been directed towards pilot-diesel-ignition ammonia combustion modes as a solution to address the inherent challenges associated with this transition [5].

Reiter and Kong [6] demonstrated the operation of a compression ignition engine using ammonia in dual-fuel mode, using diesel as the pilot ignition source. They successfully operated the engine with varying ammonia energy share ratios, achieving reasonable fuel economy and combustion efficiency, although challenges with unburned ammonia emissions remained. Niki et al. conducted extensive research on ammonia fuel in dual-fuel compression ignition engines. Their studies indicated that increasing ammonia supply reduced peak pressures and increased ignition delay, leading to higher unburned ammonia and $N_2$ emissions. They concluded that ammonia could be viable for compression ignition engines with advanced injection strategies and selective catalytic reduction (SCR) technology to control emissions [7]. Scharl et al. conducted experimental studies in a rapid compression-expansion machine that focused on analyzing the ignition and combustion characteristics of diesel-piloted ammonia sprays through heat release rate analysis and optical diagnostics [8, 9]. These studies were conducted under conditions like those of four-stroke marine engines in which the high-pressure dual fuel injectors consist of a single injector body. In the studies, in fact, the distance between the two nozzles was kept small. The investigations showed how sensitive ammonia combustion is to various factors, including the interaction between ammonia and diesel sprays, charge conditions and the characteristics of the diesel pilot. It was found that effective ammonia combustion requires a strong interaction between ammonia and diesel. In addition, poor combustion performance was observed under low load conditions, with a reduction in the amount of diesel pilot leading to delayed ammonia combustion.

This paper investigates the injection and combustion of ammonia under marine engine-like conditions, focusing on overcoming the obstacles posed by the low flammability limit. The experiments were conducted in a customized constant volume optical chamber carefully designed to mimic the conditions in 2-stroke marine engines in terms of dimensions and thermodynamic conditions. Two different injectors are installed in the chamber: one for the injection of ammonia and the other for the supply of conventional diesel fuel to ignite ammonia. Different durations of diesel pilot injections at different chamber temperatures were studied to better understand the impact of this parameter on the optimization of ammonia combustion.

By investigating the complexity of ammonia combustion, this study aims to contribute to the development of sustainable propulsion technologies in the maritime sector. Specifically, the research provides crucial insights into optimizing ammonia combustion for marine engines, addressing the critical issues of its low flammability and ensuring efficient and clean burning under different operating conditions. This work not only advances the understanding of ammonia-diesel dual-fuel systems but also supports the broader goal of reducing greenhouse gas emissions in maritime transportation.

## 2. Experimental setup

Figure 1 illustrates the experimental set-up. The tests were carried out in a constant volume vessel (CVV) designed for operation at pressures of up to 60 bar and temperatures of up to 800°C. The vessel consists of a cylindrical combustion chamber that resembles the combustion chamber of a two-stroke marine engine at the top of the compression stroke, its end is closed by a 118 mm thick flange. The ratio between the chamber length and diameter is 1.3. The cylindrical wall of the combustion chamber is thermally insulated, and the chamber is heated by electric cartridges with a total power of 10 kW. The gas temperature and pressure in the chamber are monitored with K-type thermocouples and static and dynamic pressure sensors, respectively.

Ammonia is stored in liquid phase at 8 bar, then it is compressed at 500 bar by a gas driven pump and then pumped in liquid phase in the chamber through the “main” injector. Diesel fuel is conveyed to the pilot injector by a common rail high pressure diesel pump (not shown in the figure).

Injection and combustion processes were followed by means of high-speed imaging, the setup for application of optical diagnostics is shown in figure 1 (b). To make the CVV optically accessible, the closing flange was provided with two transparent sapphire windows for visualization and illumination, with a diameter of 60 mm and 30 mm respectively. A high-speed camera (Photron FASTCAM SA-X2), equipped with a Nikkor 105mm - f/5 lens, was used for image acquisition. The optical setup included a kind of exploded objective realized by the combination of $L_1$ and $L_2$ lenses with a diameter of two inches and focal lengths of -200mm and 150mm respectively and $L_3$ lens with a diameter of 100mm and a focal length of 250mm. To visualize the injection process, the camera was operated at 10000 fps and the exposure time was set to 0.1 ms. The radiation of a Xenon arc lamp (75W) was used to illuminate the spray by concentrating the light on a glass diffuser flushed in the closing flange. Regarding the combustion process, no illumination was required, and images were recorded at 20000 fps with an exposure time of 0.6 us.

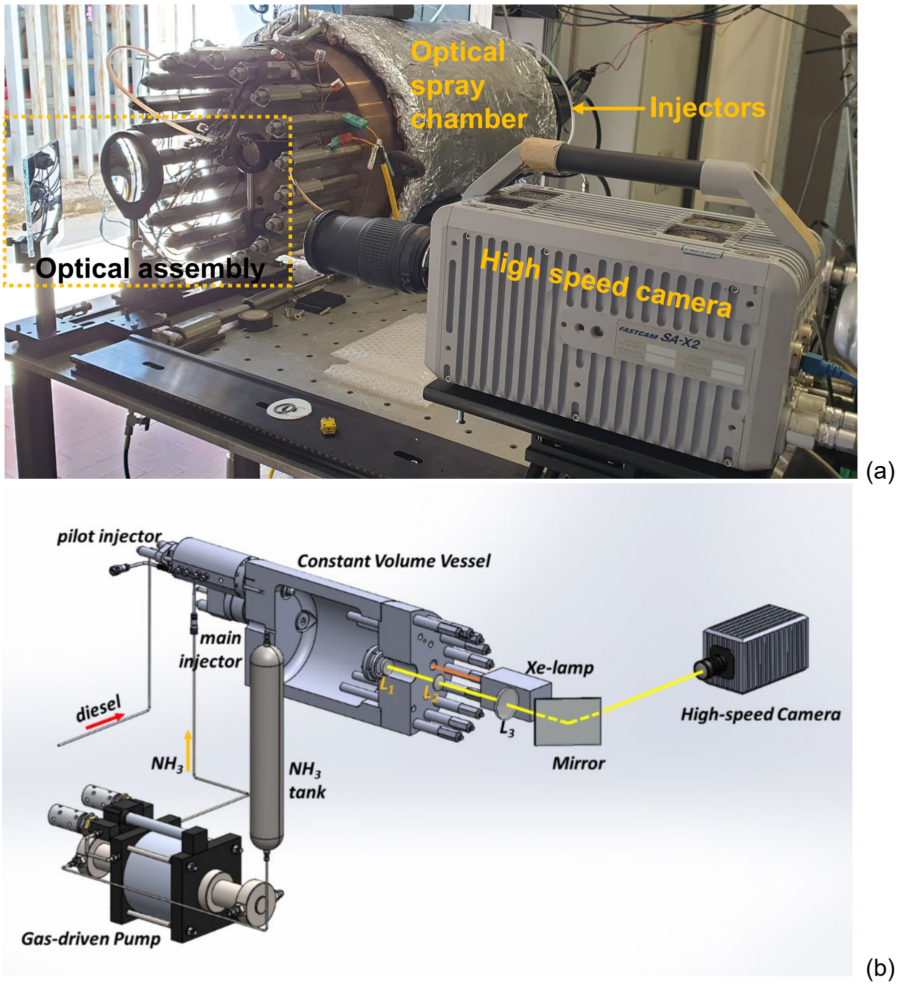
Optical spray chamber
Injectors
Optical assembly
High speed camera
FASTCAM SA-X2
(a)
pilot injector
Constant Volume Vessel
main injector
diesel
Xe-lamp
$L_1$
$L_2$
$L_3$
High-speed Camera
$NH_3$
$NH_3$ tank
Mirror
Gas-driven Pump
(b)

**Fig. 1.** Picture (a) and sketch (b) of the experimental setup

The main and pilot injectors are schematically shown in figure 2 (a). The injectors tips are also shown enlarged in figure 2 (b). The main injector has a five-hole nozzle. The pilot injector tip is normally designed with three holes. However, in the present work two holes have been plugged to allow a better control of the pilot injection timing and flow rate and to obtain a single jet and direct the maximum amount of diesel in the best direction to hit the ammonia jet.

Ammonia and diesel nozzles are mounted on the engine head to resemble the arrangement in a real two-stroke marine engine. A sketch of the injection nozzles' position in the combustion chamber can be found in Figure 2 (c).

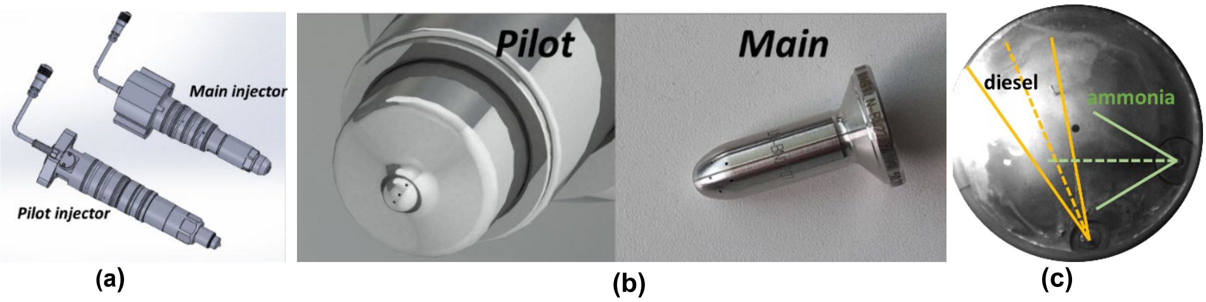
Main injector
Pilot injector
Pilot
Main
diesel
ammonia
(a)
(b)
(c)

**Fig. 2.** Details of main and pilot injectors

The spray images were processed using an in-house image processing method [10] to determine the boundaries of the liquid phase.

The first step of the image processing method consisted of background correction: for each image, the image taken immediately before fuel injection was subtracted to minimize background noise. The corrected images were then adjusted using a fast discrete filter that minimizes the mean curvature and cuts off negative values, resulting in a filtered image for further analysis.

The core of the methodology was image segmentation, which is crucial for identifying the liquid phase boundaries of the spray. An iterative approach was adopted, i.e. Otsu's thresholding method was applied iteratively to successive images, with each image derived from clipping the previous one at the mean value of its foreground class. The iteration was continued until the successive thresholds differed by less than 10%. This ensured that a stable threshold was achieved that effectively captured the liquid phase of the spray.

Throughout the iterative process, the thresholds and mean intensities of the foreground classes were monitored and adjusted accordingly. The final threshold value obtained through this iterative approach was used to binarize the images, extracting the spray boundaries.

The spray parameters, i.e., liquid spray penetration length and cone angle, were then determined as shown in Figure 3.

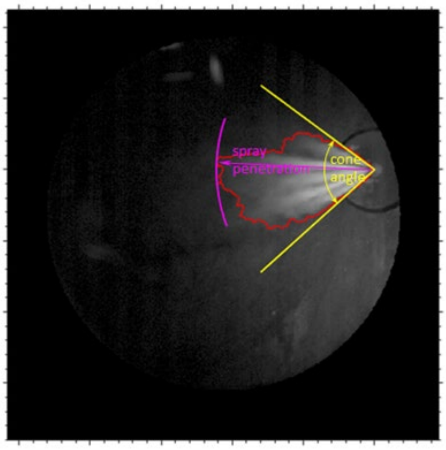

**Fig. 3.** Spray parameters obtained through images post processing method.

The injection tests were carried out at low pressure and temperature (LPT) conditions (5 bar and 30°C) and at different chamber temperatures (from 200°C to 650°C) as well as at two chamber pressures: 20 and 40 bar. The operating conditions are shown synthetically in Table 1.

**Table 1**. Operating conditions for injection tests.

| Chamber Pressure [bar] | Chamber Temperature [°C] |
|---|---|
| 5 | 30 |
| 20 | 200, 400, 480, 650 |
| 40 | 400, 480 |

The combustion tests were all carried out at a chamber pressure of 40 bar. The “pilot injection” (diesel) and the “main injection” (ammonia) were started simultaneously. The pressure of the main and pilot injection was kept at 500 bar.

The following parameters were changed during the tests:

- Duration of diesel injection ($t_{pilot}$): 6/8/12 ms
- Temperature at the start of injection: 500°C and 700°C.

Combustion in the chamber is carried out with a strong excess of air, as is usual in diffusive combustion in two-stroke marine engines. The ratio between the mass of air and the mass of fuel is around 100, and the energy content of diesel compared to ammonia varies between 6.6 and 12.5% depending on the duration of the diesel pilot injection.

## 3. Results and discussion

### 3.1 Ammonia injection tests

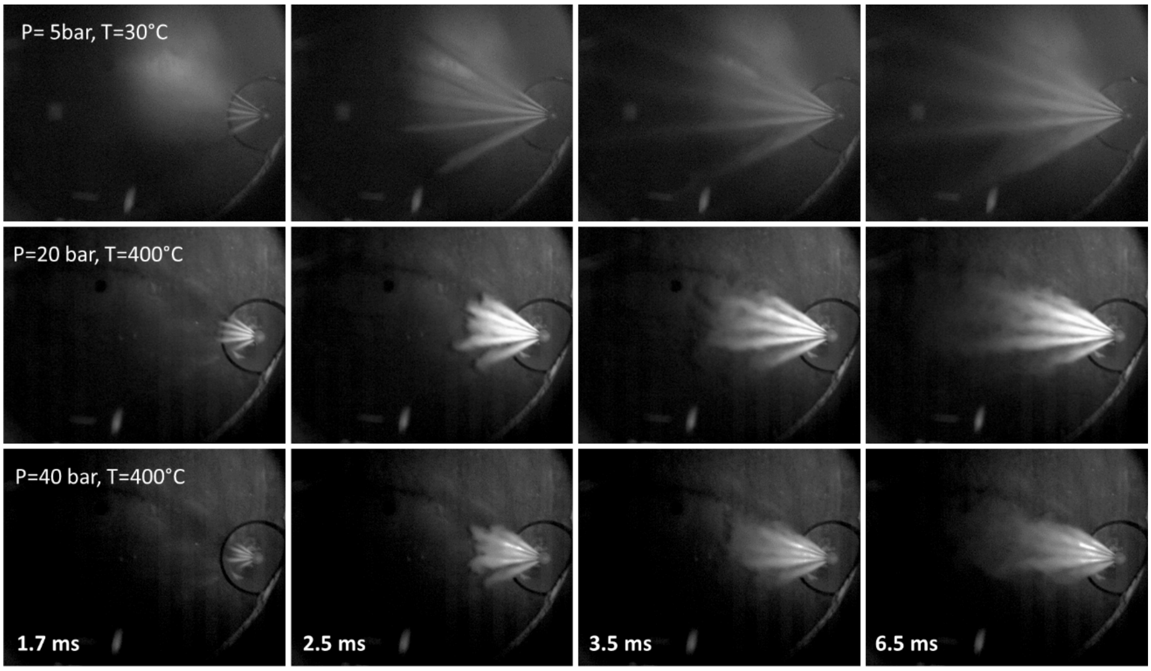

**Fig. 4.** Visualization of the ammonia injection process at 5 bar and 30°C (LPT condition) and at 400 °C and pressure of 20 and 40 bar (time from the electronic start of injection -ESOI)

Figure 4 illustrates the time evolution of ammonia spray under different chamber pressure and temperature conditions, showing spray images at different injection times after the electronic start of injection (ESOI). In the top row, ammonia injection under low pressure and temperature conditions, i.e. 5 bar and 30 °C, was shown as a reference. The images in the center and bottom show the evaporative behavior of the ammonia spray at a temperature of 400 °C and pressures of 20 and 40 bar, respectively. According to the optical data, the effective injection of liquid ammonia into the vessel starts 1.4 ms after the ESOI, which is due to the electromechanical delay of the injector. In the first phase of the injection process (at 1.7 and 2.5 ms after ESOI), 5 distinct jets are clearly visible for all selected conditions. Then the liquid ammonia extracts heat from the environment and starts to evaporate, resulting in the formation of vapor clouds at the edge of the spray.

At 5 bar and 30°C (LPT conditions), ammonia vapor clouds form on the opposite side of the injector (downstream of the spray) and the liquid phase is still visible over a very large distance even at 6.5 ms. This is confirmed by the liquid spray penetration length extrapolated from the visualization of the spray process, which shows that ammonia jets cover about two-thirds of the chamber diameter still in liquid phase. At high temperature (400°C) and intermediate pressure level (20 bar), the behavior of the ammonia spray differs significantly from the LPT conditions, and a faster evaporation is observed. Similarly, at higher pressure of 40 bar, the figure shows how the vaporization of the ammonia starts closer to the nozzle compared to lower pressure condition.

Figure 5 presents the outcomes derived from the analysis of spray penetration length, extrapolated from the spray process visualization. The dashed vertical lines indicate the position of the frames reported in Figure 4.

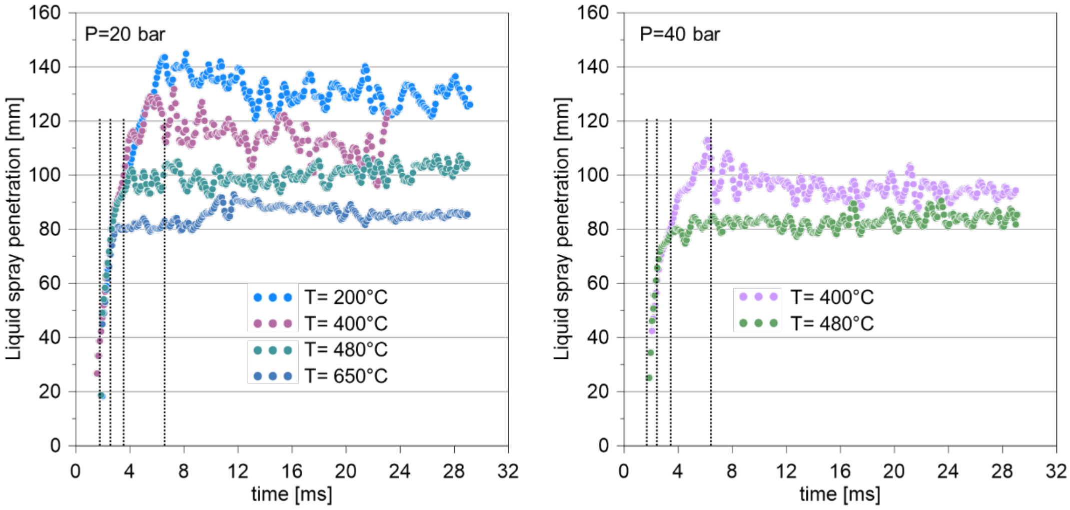

**Fig. 5.** Liquid spray penetration length.

At both pressure levels, namely 20 bar and 40 bar, the penetration of the liquid decreases as the temperature in the chamber increases. This phenomenon is primarily due to the increased vaporization that occurs at higher temperatures. As the temperature increases, the liquid evaporates faster, which reduces the overall penetration of the spray.

When comparing the results obtained at different pressures but the same temperatures, namely at 400 °C and 480 °C, another trend can be observed. At these temperatures, an increase in pressure leads to an increase in air density in the chamber. This higher air density exerts a greater drag force on the liquid jets, slowing them down and reducing the penetration length.

So, while the increase in chamber temperature leads to more significant evaporation and consequently less liquid penetration at both pressure levels, the higher air density at higher pressures induces a reduction in penetration. This dual influence underlines the complex interaction of temperature, pressure, evaporation and air density that determines the behavior of the liquid jets under these conditions.

### 3.2 Ammonia combustion tests

As mentioned in the previous section, the combustion of ammonia with diesel pilot was investigated under various operating conditions with the aid of optical diagnostics and measurement of the pressure curve in the combustion chamber.

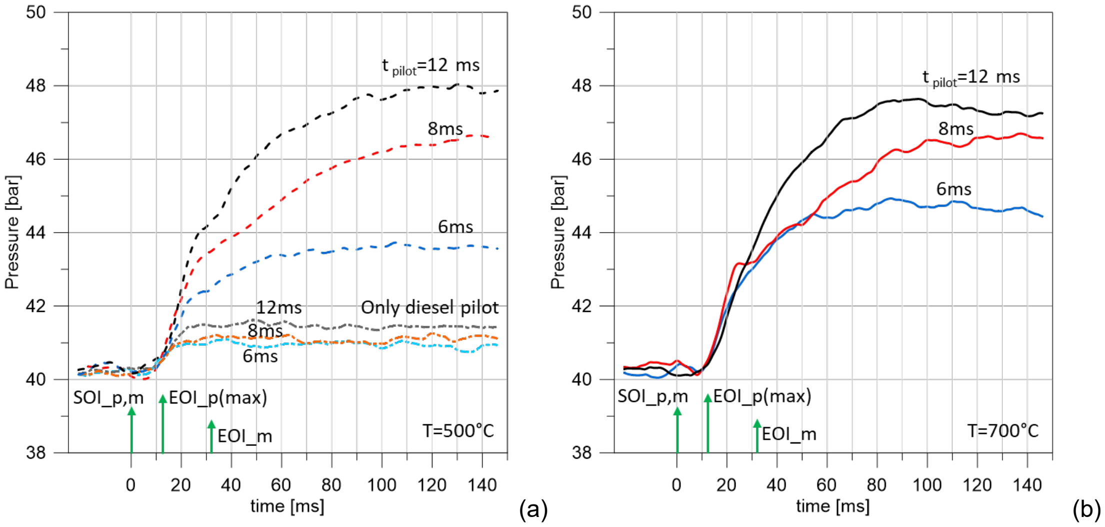

**Fig. 6.** Pressure rise in the combustion chamber at a temperature of 500°C (a) and 700°C (b)

Figure 6 shows the pressure evolution within the combustion chamber at 40 bar and under two different temperature conditions: 500°C in Figure 6(a) and 700°C in Figure 6(b). For each temperature, the three curves correspond to the different durations of the pilot injection: 6 ms, 8 ms and 12 ms, while the ammonia injection duration has been kept constant at 32 ms. The pressure curves are compared with the conditions where only diesel fuel is injected at 500°C. The figure also shows the timing of the electronic signals for: the start of pilot injection (SOI_p); the start of main injection (SOI_m); the end of pilot injection at the maximum value of 12 ms (EOI_p) and the end of main injection (EOI_m).

Few ms after the start of the main and pilot injection, a rapid increase in pressure is measured in the combustion chamber. Heat energy is released during the combustion reactions, which leads to a rapid rise in temperature in the chamber. This in turn leads to a significant increase in pressure as the gases expand to fill the available volume. The pressure continues to rise until the combustion ends that corresponds to a plateau in the curves. The height of the plateau, i.e. the amount of energy released by diesel and ammonia combustion, increases with the duration of the pilot injection at each temperature.

In the cases where only diesel fuel is injected, combustion under these thermodynamic conditions can be considered almost complete and the pressure rise differs by less than 0.5 bar between the shorter and longer injection periods. Therefore, the higher pressure-variation in dual-fuel cases can be mainly attributed to more complete combustion of ammonia enabled by the longer pilot injection.

It is noteworthy that the pressure rise at a higher temperature (700°C) is higher than at 500°C for 6 ms and 8 ms. This indicates that the temperature of 700°C promotes a more complete combustion than at 500°C for these conditions. At a pilot injection duration of 12 ms, no major difference in pressure rise is observed between the two temperatures, suggesting that the combustion of ammonia is almost complete if the pilot injection duration is long enough, and under this condition the chamber temperature does not have a big impact on the process.

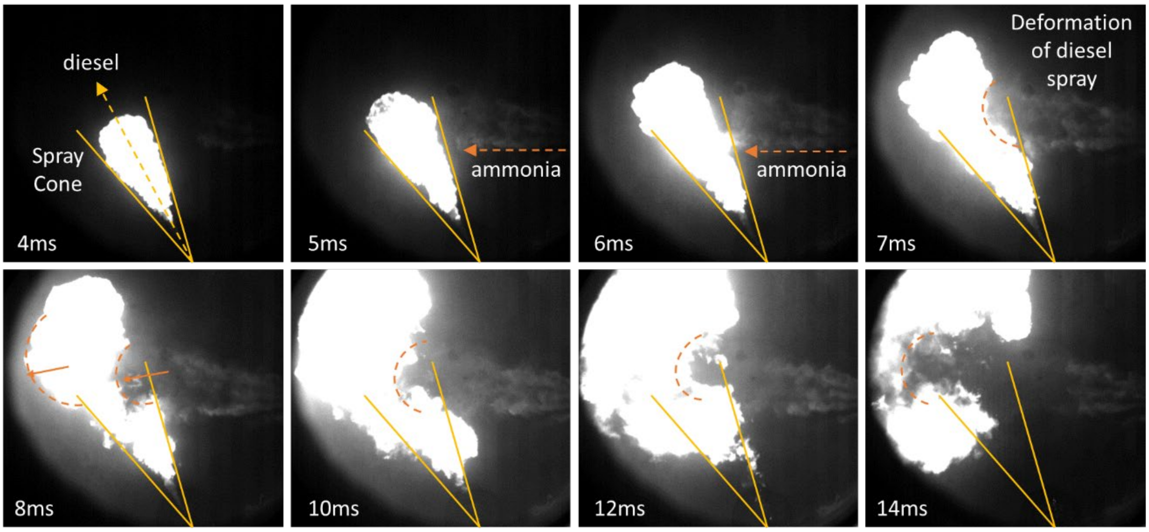

**Fig. 7.** Visualization of the combustion process (temperature of 500°C, duration of pilot injection: 8 ms)

Figure 7 shows the visualization of the combustion process to explain the phenomena that occur when diesel and ammonia are injected simultaneously into the combustion chamber. These data refer to the case of 500°C and a pilot injection duration of 8 ms, but the overall behavior can also be applied to other injection durations and the temperature of 700°C. The time is measured from the electronic start of injection.

The diesel fuel is injected into the combustion chamber through the injection nozzle, which is located at the lower end of the field of view. When the fuel emerges from the nozzle, it is atomized, and the fuel droplets are distributed in a spray pattern in the chamber. The high temperature and pressure conditions in the chamber promote rapid combustion of the fuel-air mixture. This injection can be detected in the combustion chamber from 1.5 ms, which is the electromechanical delay of the injector, determined from the imaging. Ammonia is injected through the main injection nozzle, which is located on the right in the field of view (see Figure 7). The ammonia spray is visible due to the glow of the diesel flame.

As can be seen at 5 ms, the diffusive diesel combustion continues regularly and follows the spray pattern until the ammonia spray meets the diesel spray. The overlap of the two sprays can be observed at 6 ms. This is probably the point at which combustion of the ammonia begins: stoichiometric conditions for ammonia burning and high temperatures prevail in the areas close to the diesel pilot flame, so that combustion of the ammonia can take place. Between 1.5 and 6 ms, the slope of the pressure curves is similar under all conditions, even with single diesel injection, as the pressure increase depends only on the diesel burning rate.

After 6 ms, the diesel pilot injection is strongly influenced and deformed by the ammonia injection, as can be seen in the sequence. Due to the low brightness of its flame, the combustion of ammonia can be recognized in the images only by the strong interaction with the diesel pilot flame. On the other hand, looking at figure 6, at about 10 ms, it is possible to identify an increase in the slope of the pressure curves due to an additional energy release caused by ammonia burning.

Around 10 ms the pilot injection is completed, even if the end of pilot (electronic timing) is at 8 ms. At 12 ms, the flame is in the middle part of the combustion chamber, it shows the trace of the ammonia spray as “negative”.

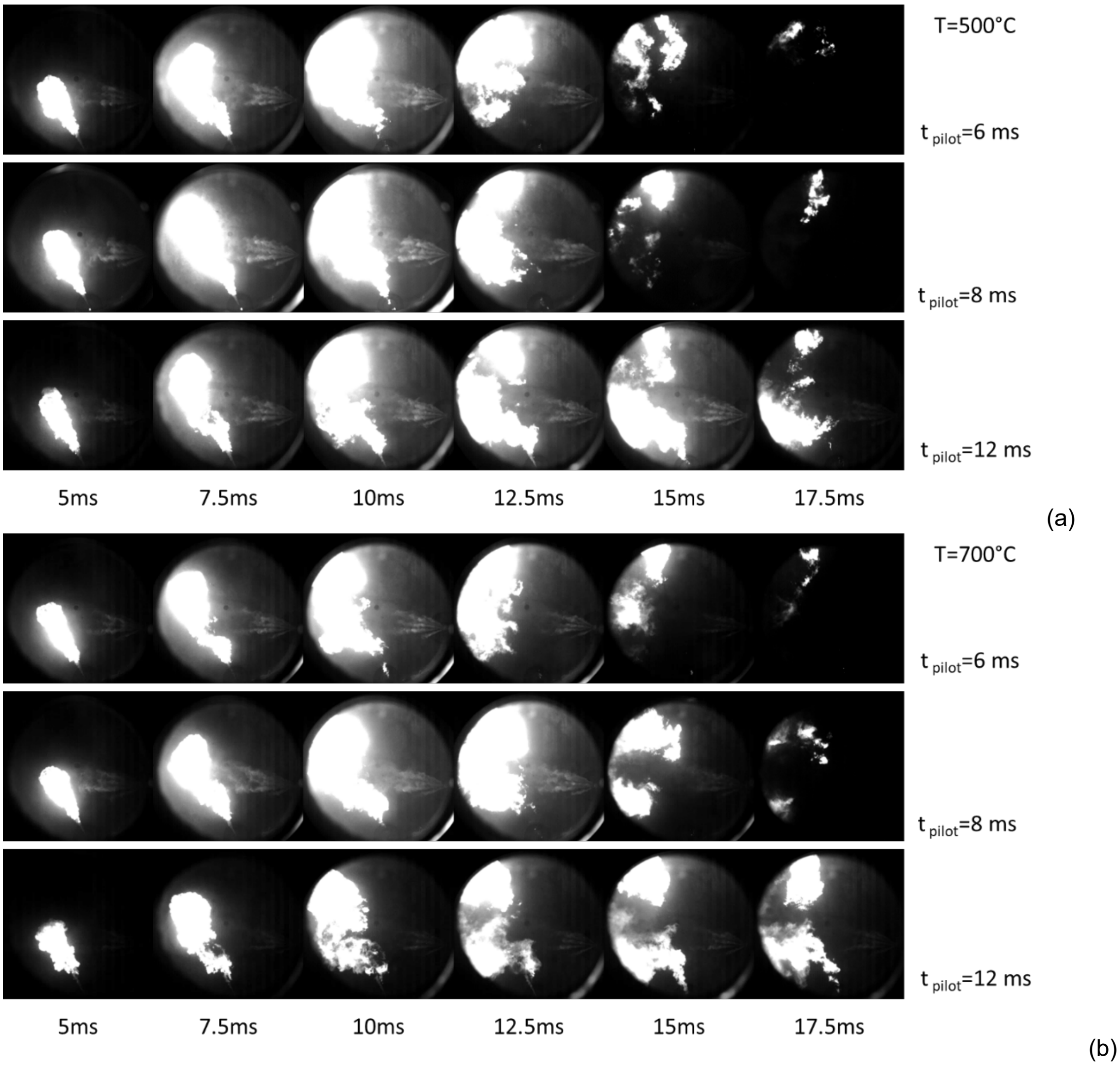

**Fig. 8.** Visualization of the combustion process at 500°C (a) and 700°C (b) for the dif-ferent durations of pilot injection

Figure 8 shows a comparison of the evolution of the combustion process at 500°C (a) and 700°C (b) for the different durations of pilot injection. As can be seen from the images, diesel combustion ends few ms after the injection finished, depending on the duration of the pilot duration in the different cases. More precisely, with this optical method, no flame can be detected in the CCV after 20 ms, but the pressure increase due to the energy release of the ammonia combustion lasts until 70 ms at 6 ms pilot duration at 500°C, and 100 ms at 8 and 12 ms pilot duration at the same temperature. At 700 °C, the energy release is faster and higher at all pilot injection durations, but the evolution of combustion is similar to that of the 500°C case. No combustion is detected after 20 ms and the energy release slows down after this time but continues until about 60 ms at the shorter pilot duration, and until 80 ms at the diesel pilot durations of 8 and 12 ms.

## Conclusions

The paper explores the behavior of ammonia injection in a combustion chamber under different operating conditions. At lower pressure and temperature, the ammonia gradually evaporates, and the visible liquid phase is sustained for a longer period. In contrast, rapid vaporization is observed at higher temperatures and pressures.

The study also examines the combustion of ammonia under different conditions with different pilot injection durations. With a low duration of diesel injection, the increase in temperature enables more complete combustion. At higher pilot injection durations (12 ms), no major difference in pressure rise is observed between 500°C and 700°C, suggesting that the combustion of the ammonia is almost complete. The combustion process was also monitored with optical diagnostics. Due to the low brightness of its flame, the combustion of ammonia could only be detected on the images by the strong interaction with the diesel pilot flame.

The results of this work provide insights into the dynamics of ammonia injection and combustion in dual-fuel marine engines, which has implications for the optimization of combustion efficiency and emission control.

## References

[1] Tornatore C., Marchitto L., Sabia P., de Joannon M. (2022). Ammonia as Green Fuel in Internal Combustion Engines: State-of-the-Art and Future Perspectives. Frontiers in Mechanical Engineering, 8. https://doi.org/10.3389/fmech.2022.944201

[2] Valera-Medina A., Amer-Hatem F., Azad A.K., Dedoussi I.C., de Joannon M., Fernandes R.X., Glarborg P., Hashemi H., He X., Mashruk S., McGowan J., Mounaim Rouselle C., Ortiz-Prado A., Ortiz-Valera A., Rossetti I., Shu B., Yehia M., Xiao H., Costa M. (2021) Review on ammonia as a potential fuel: From synthesis to economics. Energy Fuels. http://dx.doi.org/10.1021/acs.energyfuels.0c03685

[3] Chiong M.-C., Cheng Tung Chong, Jo-Han Ng, Syed Mashruk, William Woei Fong Chong, Nor Afzanizam Samiran, Guo Ren Mong, Valera-Medina A., (2021), Advancements of combustion technologies in the ammonia-fuelled engines. Energy Conversion and Management, Volume 244, 114460, https://doi.org/10.1016/j.enconman.2021.114460

[4] Reggeti S. A., Northrop W. F. (2024) Lean ammonia-fueled engine operation enabled by hydrogen-assisted turbulent jet ignition, Frontiers in Mechanical Engineering, 10. https://doi.org/10.3389/fmech.2024.1368717

[5] Pavlos Dimitriou, Rahat Javaid, (2020) A review of ammonia as a compression ignition engine fuel, International Journal of Hydrogen Energy, 45(11): 7098-7118, https://doi.org/10.1016/j.ijhydene.2019.12.209.

[6] Reiter A.J., Kong S.-C. (2008) Demonstration of Compression-Ignition Engine Combustion Using Ammonia in Reducing Greenhouse Gas Emissions, Energy & Fuels 22 (5), 2963-2971; https://doi.org/10.1021/ef800140

[7] Niki Y., Yoo D.-H., Hirata K., Sekiguchi H. (2016) Effects of ammonia gas mixed into intake air on combustion and emissions characteristics in diesel engine, ASME 2016 internal combustion engine division fall technical conference, Greenville, South Carolina, USA (2016), V001T03A004

[8] Scharl V., Sattelmayer T. (2022). Ignition and combustion characteristics of diesel piloted ammonia injections. Fuel Commun, 11, Article 100068, https://doi.org/10.1016/j.jfueco.2022.100068

[9] Scharl V., Lackovic T., Sattelmayer T. (2023). Characterization of ammonia spray combustion and mixture formation under high-pressure, direct injection conditions. Fuel, 333 (2), 126454, https://doi.org/10.1016/j.fuel.2022.126454.

[10] Lazzaro M., Ianniello R. (2018) Image processing of vaporizing GDI sprays: a new curvature-based approach. Meas Sci Techn 29(1):015402

# Investigation of Four-Stroke Heavy-Duty Marine Engine Fueled by Ammonia and Hydrogen with Active Pre-chamber Ignition, Passive Pre-chamber Ignition and Spark Ignition

Y. Wu[1,2], B. Somers[1], L. Liu[2], Y. Peng[3]

[1] Department of Mechanical Engineering, Eindhoven University of Technology, the Netherlands.

E-mail: l.m.t.somers@tue.nl
Telephone: +(31) 0628832742

[2]College of Power and Energy Engineering, Harbin Engineering University, Harbin, 150001, P.R. China

[3]Shanghai Marine diesel engine research institute, Shanghai, 201108, P.R. China

**Abstract.** The imperative for reducing fossil carbon emissions has garnered global consensus and emerged as a future development objective. Ammonia and hydrogen, as zero-carbon energy carriers, present a highly promising prospect as marine engine fuels. However, their optimal application in maritime engines remain uncertain. The AmmoniaDrive project is studies a concept based on a combination of a fuel cell (FC) and an internal combustion engine (ICE). The FC will be used to generate $H_2$ to run the ICE with a mixture of $H_2$ and $NH_3$ hence needing only a single fuel storage facility. This paper explores the application modes of ammonia and hydrogen in marine engines, with varying energy ratios (ER) of $H_2$ and $NH_3$. To study the optimal, yet constrained ratio, active and passive pre-chamber, and spark plug ignition are studied. The effects of ammonia and hydrogen energy ratio, intake pressures, compression ratios and equivalence ratios on engine combustion, knocking propensity, and $NO_x$ emissions is comprehensively investigated. The ultimate goal is to identify the optimal conditions for achieving optimal engine power, thermal efficiency, $NO_x$ emissions, while preventing knock phenomena with a constrained $H_2$-$NH_3$ ratio. The results reveal that, compared to leaner combustion, stoichiometric combustion in spark plug ignition mode leads to lower $NO_x$ emissions comparable to Tier III standards. For the given intake pressure, it achieves a substantially higher IMEP approximately 23.2 bar, and requires a lower hydrogen energy fraction of around 15%. As such it may relieve some of the concern on power density for lean-burn engines. Nevertheless, the thermal efficiency experiences a slight reduction due to the elevated charge temperature and heat loss. Employing pre-chamber ignition facilitates ultra-lean combustion (equivalence ratio of 0.4), enabling compliance with tier II $NO_x$ emission regulations. Passive prechamber ignition requires a higher hydrogen energy fraction, exceeding 35%, to successfully ignite and achieve satisfactory flame speeds. However, this approach also elevates the risk of knock and makes achieving high compression ratios difficult. Conversely, active prechamber ignition can significantly decrease the required hydrogen energy fraction to approximately 10%, allowing higher compression ratios. Consequently, the highest thermal efficiency reaches 52.8%. Additionally, this approach leads to increase in flame speed due to hot jet energy. Consequently, the $N_2O$ and unburned $NH_3$ emissions are improved.

## 1. Introduction

With the escalating environmental challenges posed by greenhouse gas emissions, the transportation sector, a major contributor to global carbon emissions, plays a crucial role in efforts to reduce carbon emissions. In this context, the International Maritime Organization (IMO) has implemented a strategy with the objective of mitigating greenhouse gas emissions within the maritime sector. This strategy targets a 40% decrease in carbon intensity compared to 2008 levels by the year 2030, followed by a subsequent substantial reduction of 70% by 2050 [1]. Consequently, in recent years, significant efforts have been devoted to the development of low-carbon and zero-carbon emission solutions in the field of marine propulsion systems [2-6].

Hydrogen and ammonia are widely regarded as environmentally friendly fuels, generating only water and nitrogen gas during combustion [7]. Hydrogen, characterized by its rapid flame speed, high calorific value, and wide flammability range, can notably expedite the combustion process and thermal efficiency for internal combustion engines [8]. Nevertheless, significant challenges in transportation and storage hinder its widespread adoption. Additionally, problems such as flashback and knock may occur during hydrogen combustion [9]. In contrast, ammonia exhibits ease of storage and transportation owing to its unique compressibility and liquefaction properties. Moreover, ammonia possesses a higher volumetric energy density [10]. However, owing to its high ignition energy, slow flame propagation speed, and limited flammability range, using ammonia as the sole fuel for internal combustion engines presents challenges such as difficult cold starts, inadequate combustion stability, and low thermal efficiency [11]. The combination of ammonia and hydrogen combustion can leverage their respective strengths and mitigate their individual weaknesses, thereby realizing a viable zero-carbon solution for marine engines. The challenges associated with hydrogen storage and transportation can be addressed through the catalytic hydrogen reforming of ammonia [12] as is also envisaged in the AmmoniaDrive project [13].

Currently, some research has been conducted on the application of ammonia-hydrogen mixtures in internal combustion engines. Wang et al. [14] employed the zero-dimensional software Cantera to explore the fundamental combustion characteristics of ammonia-hydrogen mixtures under high temperature and pressure engine conditions. The parameters such as laminar flame speed, minimum ignition energy, $NO_x$ and ammonia emissions, combustion efficiency, for different hydrogen ratios in the fuel mixture were investigated. The results indicate that NO emissions in stoichiometric ammonia/hydrogen blends may be lower than those in hydrocarbons. Moreover, optimal operational parameters for ammonia/hydrogen mixtures typically fall within an equivalence ratio range of 1.0 to 1.05, with a hydrogen fraction between 40% and 60% (mole fraction). Mørch et al. [15] investigated the impact of varying compression ratio (ranging from 6.23 to 13.58), hydrogen fraction (5-100 vol.%), and equivalence ratio (0.8-1.4) on engine power, thermal efficiency, and $NO_x$ emissions in a small spark-ignition (SI) engine with a cylinder diameter of 82.6mm. They found that the fuel mixture containing 10 vol.% hydrogen exhibits the highest efficiency and brake mean effective pressure (BMEP). Notably, the optimum efficiency is achieved at an excess air ratio slightly above 1, while the peak mean effective pressure is observed at an excess air ratio slightly below 1. Lhuillier et al. [16] investigated the performance and emissions of spark ignition (SI) engines with comparable cylinder diameters across equivalence ratios ranging from 0.6 to 1.2, hydrogen fractions varying from 0% to 60%, and indicated mean effective pressure (IMEP) approximately at 10 bar. The results indicate that the highest indicated pressure and efficiency were obtained with low to moderate hydrogen additions, coupled with slightly fuel-rich and slightly fuel-lean conditions, respectively. Nonetheless, lean mixtures featuring high hydrogen content also demonstrated promising performance. When the hydrogen volume fraction surpasses 40%, the engine demonstrates stable operation under lean-burn conditions with an equivalence ratio of 0.6.

To optimize SI engines often pre-chamber concepts are studied. Several studies [17] [18] [19] have demonstrated that the pre-chamber jet flame ignition can significantly enhance the ignition stability and flame speed of ammonia, enabling the possibility of lean combustion with ammonia. Shawn et al. [20] investigated the impact of varying compression ratios (ranging from 12:1 to 20:1) and equivalence ratios (ranging from 0.5 to 1) on engine performance and $NO_x$ emissions using an 82.5mm bore four-stroke engine equipped with pre-chamber ignition. The equivalence ratio is adjusted by altering the ammonia content of the inlet while maintaining a constant total hydrogen quantity. The findings indicate that, across all compression ratios, the optimal indicated thermal efficiency and minimal unburned $NH_3$ and $N_2O$ emissions are observed at approximately 0.7-0.8 equivalence ratios. Conversely, $NO_x$ emissions are highest at these equivalence ratios. Notably, $N_2O$ formation primarily was found to occur near the wall due to low temperature combustion and quenching, rather than within the propagating flame front.

The studies mentioned above primarily utilize small bore engines with low IMEP. Nonetheless, it's crucial to recognize that larger bore marine engines experience significantly extended flame propagation distances, which markedly influence feasible operating limits. However, there has been limited investigation into suitable ignition modes for utilizing ammonia-hydrogen mixtures in marine engines. Furthermore, the impacts of boundary conditions, including the hydrogen energy ratio, equivalence ratio, compression ratio, and intake pressure on power, thermal efficiency, knock combustion, $NO_x$ and unburned ammonia emissions of marine engines necessitate further comprehensive exploration.

Therefore, this study aims to conduct a numerical investigation into the feasibility of spark ignition, passive pre-chamber ignition, and active pre-chamber ignition on a marine engine. The flammability and knock boundaries under these three ignition modes are explored, considering various conditions such as hydrogen energy ratio, equivalence ratio, compression ratio, and intake pressure. Additionally, their influence on engine power, thermal efficiency, knock, $NO_x$ emissions, and unburned ammonia emissions are examined. Ultimately, the research seeks to determine the optimal solution which achieves the best balance of power, thermal efficiency, and $NO_x$ emissions. The research findings of this paper can provide guidance for the design of marine ammonia-hydrogen fuel engines.

## 2. Numerical methodology

The engine utilized in this investigation is a four-stroke marine medium-speed engine featuring a cylinder bore of 270 mm. Detailed specifications of the engine are outlined in Table 1. The geometry is presented in Figure 1. Ammonia and hydrogen are introduced into the intake manifold during the intake stroke. Subsequently, the fuels mix with air to generate a homogeneous fuel mixture near top dead center, which is then ignited either by a spark plug or jet flame from pre-chamber. The geometric layout of the pre-chamber is depicted in Figure 1. The volume of the pre-chamber is roughly 3% of the volume of the main combustion chamber at top dead center. Six orifices link the pre-chamber and the main chamber. In the case of the active pre-chamber ignition, a small amount of extra hydrogen, constituting approximately 2% of the total energy fraction, is introduced into the pre-chamber at 50° ATDC with a consistent mass flow rate. The injection pressure is maintained around 20 bar. Three ignition methods were explored in this study, namely spark plug ignition, passive pre-chamber ignition, and active pre-chamber ignition. The boundary conditions for each method are presented in Table 2.

**Table 1**. Engine specifications

| | |
|---|---|
| Engine type | Four stroke |
| Bore/(mm) | 270 |
| Stroke/(mm) | 340 |
| Connecting rod length/(mm) | 670 |
| Engine speed/(rpm) | 671 |

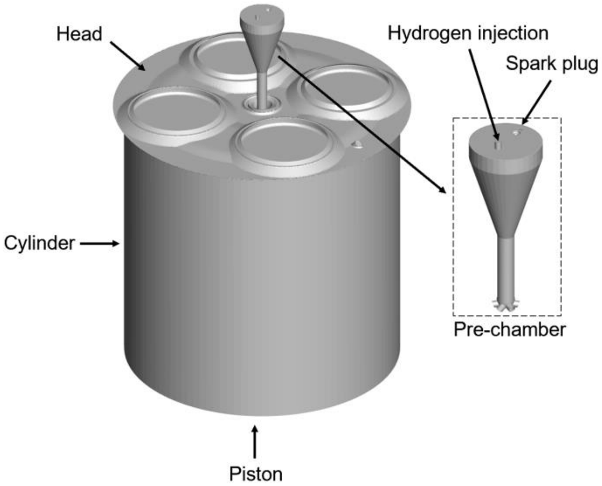

**Fig. 1.** The geometric model of the engine and pre-chamber

**Table 2**. Simulation case set up

| | Spark plug ignition | Passive prechamber ignition | Active prechamber ignition |
|---|---|---|---|
| Compression ratio | 12 | 12-14 | 12-16 |
| $H_2$ energy ratio | 10%-40% | 25%-60% | 0%-30% |
| $H_2$ volume ratio | 13%-47% | 30%-67% | 0%-36% |
| Equivalence ratio | 0.4-1 | 0.4 | 0.4 |
| Spark timing (°ATDC) | -15 | -15 | -10 |
| Intake pressure (bar) | 2 | 3 | 3 |
| Exhaust pressure (bar) | 1 | 2 | 2 |

In this investigation, the three-dimensional computational fluid dynamics (CFD) commercial simulation software CONVERGE is employed. A base grid size of 4 mm is utilized. Additionally, fixed refinement is applied in crucial flow and combustion regions. For instance, spherical refinement is added near the spark plug, employing a fine mesh size of 0.5 mm, while cylindrically shaped refinement is implemented in the pre-chamber, utilizing a fine mesh size of 1 mm. Moreover, refinement grids of 0.5 mm are placed at the interface between the pre-chamber and the main chamber. Adaptive mesh refinement (AMR) is further utilized in regions exhibiting significant temperature and pressure gradients, employing a mesh size of 2 mm. Figure 2 illustrates the mesh for this simulation, encompassing fixed embedding and AMR. By maintaining same AMR and fixed refinement mesh strategies and only altering the base grid, this mesh configuration is tested with pre-chamber ignition cases. Figure 3 illustrates the variation of cylinder pressure with changes in the base grid. It is evident that a base grid of 4 mm adequately satisfies the computational requirements.

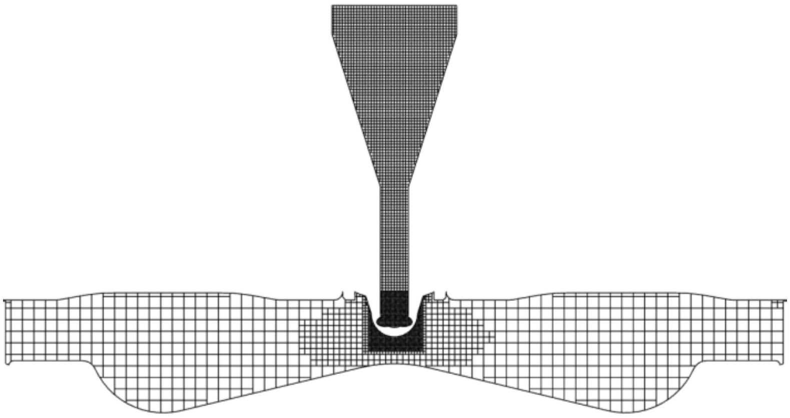

**Fig. 2.** The mesh configuration in this simulation

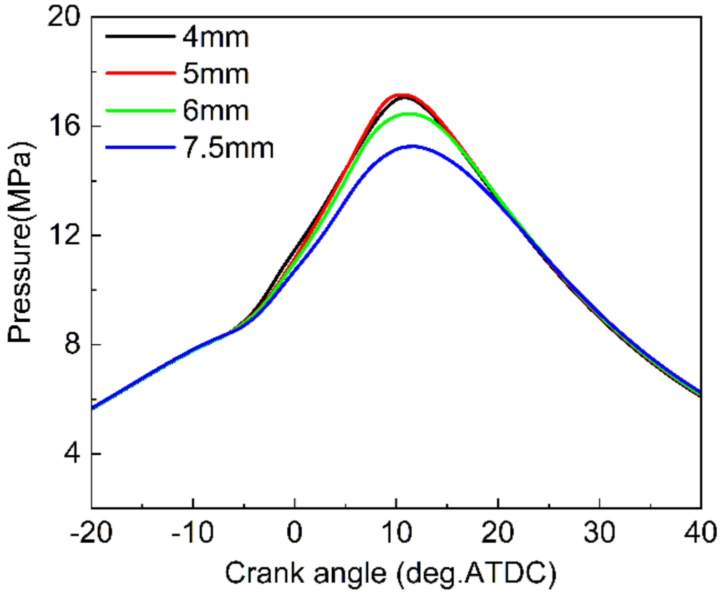

**Fig. 3.** Effect of various base grid sizes on cylinder pressure

The RNG k-ε RANS model is employed to describe the turbulence, while the SAGE combustion model is utilized to simulate the combustion process of ammonia and hydrogen, as shown in Table 3. The reaction mechanism of ammonia-hydrogen developed by Stagni et al. [21], consisting of 31 species and 203 reactions, is employed in this study. The comparison of cylinder pressure and heat release rate between experimental and simulated data under various loads for the original diesel engine is presented in Figure 4. The results indicate that this model can accurately describe the scavenging and combustion processes of the diesel engine under various conditions. Therefore, assuming that the ammonia-hydrogen mechanism is adequately accurate, it can be inferred that this model can effectively describe the combustion process of ammonia-hydrogen mixtures.

**Table 3**. The models adopted in the simulation

| | |
|---|---|
| Turbulence model | RNG k-ε |
| Combustion model | SAGE |

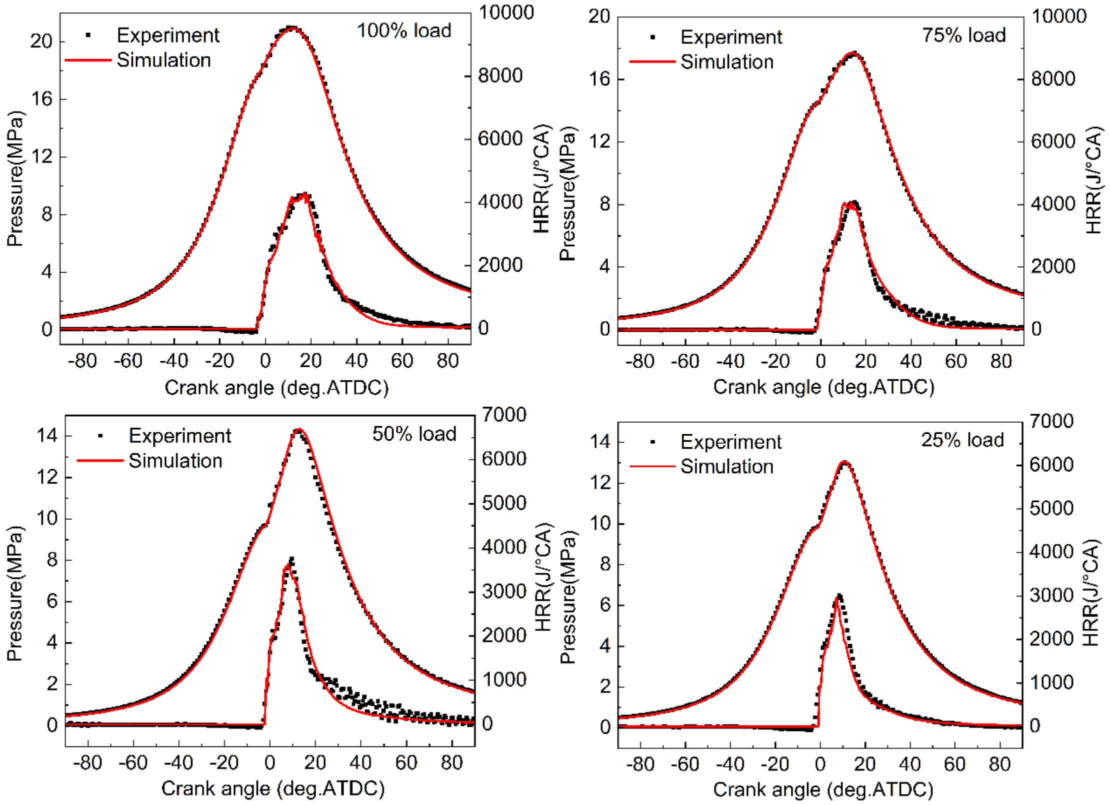

**Fig. 4.** The comparison of cylinder pressure and heat release rate between experimental and simulated data under various loads for the diesel engine

## 3. Results and discussion

### 3.1 Spark plug ignition

Figure 5 illustrates cylinder pressure and heat release rate under different hydrogen energy fractions and equivalence ratios in the spark plug ignition mode. An intake pressure of 2 bar and a compression ratio of 12 were selected to avoid excessively high peak pressure and knock. The spark plug timing was set at -15°ATDC. As expected, an increase in equivalence ratio and hydrogen energy fraction significantly enhances flame propagation speed, peak pressure, and combustion rate. As the hydrogen energy fraction increases, cases with lower equivalence ratios can achieve normal combustion, whereas cases with higher equivalence ratios experience knock. The optimal hydrogen energy fraction ranges between 15% and 40%, and it increases as the equivalence ratio decreases. When the equivalence ratio is reduced to 0.6, the flame speed remains notably slow when the hydrogen fraction is increased to 40%. Furthermore, it is evident that under the current boundary conditions, achieving combustion with extremely lean mixtures (equivalence ratio of 0.4) may necessitate a higher hydrogen energy fraction.

Figure 6 illustrates the feasible boundary conditions for misfire and knock, categorizing engine states into five types: non-ignition (combustion efficiency below 20%), incomplete combustion (combustion efficiency between 20-80%), normal combustion (combustion efficiency above 80% and no knocking), slight knock (MAPO between 0.1-0.2), and heavy knock (MAPO above 0.2). While adjustments to ignition timing or compression ratio can mitigate incomplete combustion and slight knock, addressing severe knock and unburned conditions poses greater challenges. Figure 6 depicts a narrow window for normal combustion conditions, highlighting the sensitivity of flame velocity and engine operation to equivalence ratio and hydrogen energy fraction.

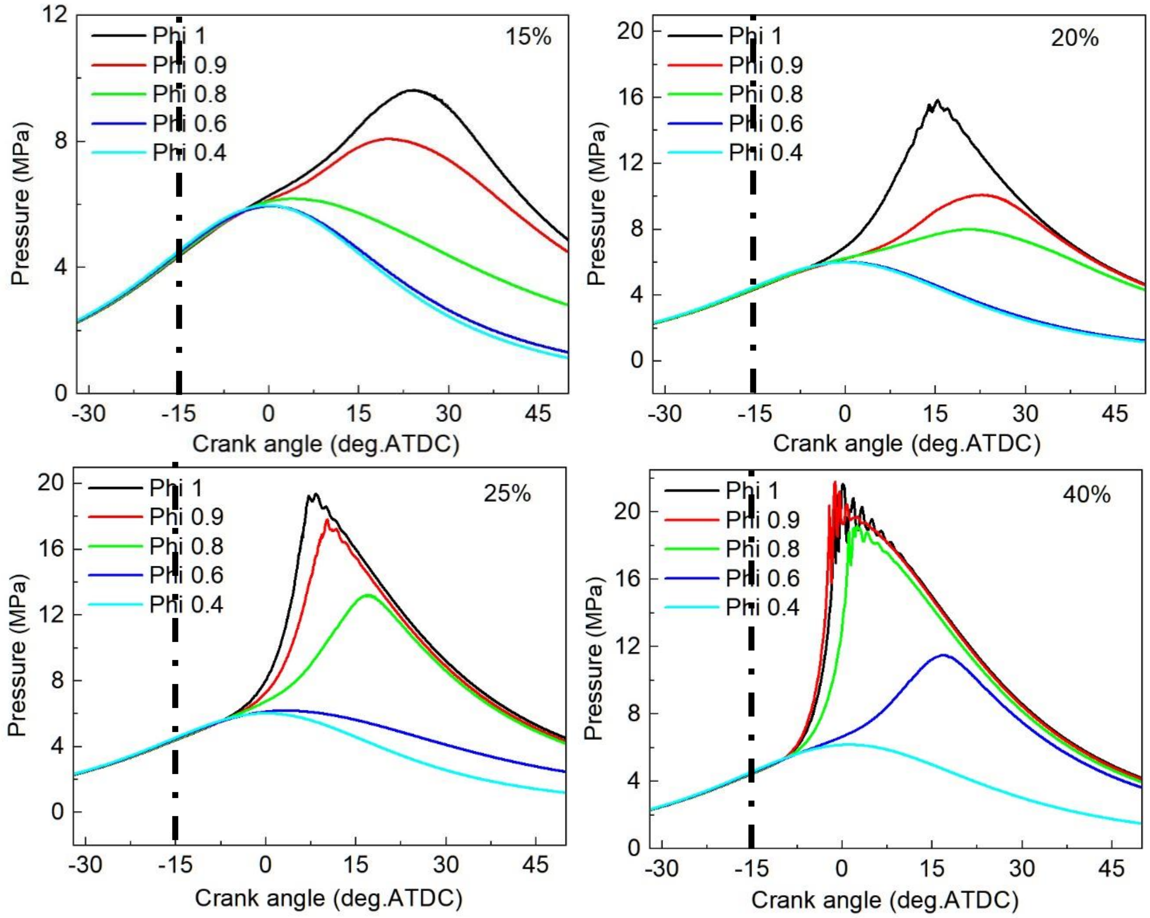

**Fig. 5.** Cylinder pressure and heat release rate curves under different hydrogen energy fractions and equivalence ratios in spark ignition mode. For reference the spark timing is indicated in the figures (dash-dotted line).

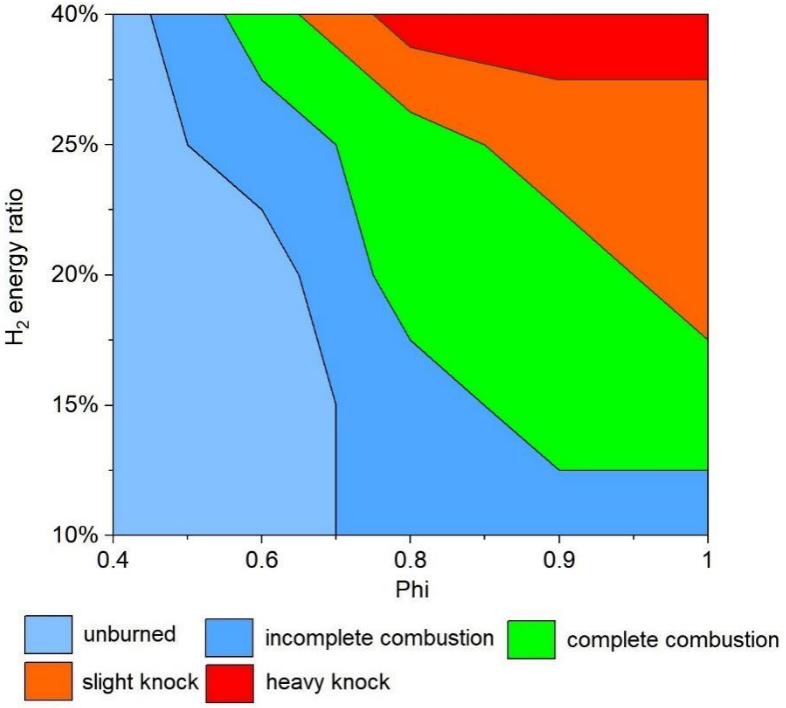

**Fig. 6.** Combustion and knock limits under different hydrogen energy fractions and equivalence ratios in spark ignition mode.

Figure 7 presents the power and thermal efficiency levels across various hydrogen fractions and equivalence ratios, with IMEP indicating the power level. Figure 8 illustrates the emission levels of NO, $N_2O$ and unburned $NH_3$. The normal combustion conditions are highlighted within the dashed box. Notably, the thermal efficiency of normal combustion conditions under spark plug ignition mode predominantly remains below 50% and increases as the equivalence ratio decreases, with a peak efficiency of about 48.7% observed at an equivalence ratio of 0.6. The variation in heat release rate is correlated with the combustion efficiency and combustion phase. IMEP increases with the rise in equivalence ratio and can reach approximately 23.2 bar near the stoichiometric equivalence ratio (normal combustion). With regard to NO emissions, the lowest levels are observed under stoichiometric equivalence ratio conditions, approximately Tier III standard, while the highest emissions occurred in the range of equivalence ratios of 0.6-0.8, even exceeding the level 2 standard. $N_2O$ emissions require special attention due to its greenhouse effect, which is 300 times greater than that of CO2. It is evident that $N_2O$ emission is closely associated with the combustion efficiency. In instances of complete combustion, the presence of $N_2O$ is almost negligible, whereas in cases of incomplete combustion, the quantity of $N_2O$ increases significantly. This phenomenon may be attributed to the lower charge temperature in incomplete combustion cases. Additionally, $N_2O$ and unburned ammonia exhibit a similar trend and an opposite to that of NO emissions, except for stoichiometric equivalence ratios. In summary, to attain lower $NO_x$ emissions with a reduced hydrogen energy fraction, the optimal approach is to apply stoichiometric combustion.

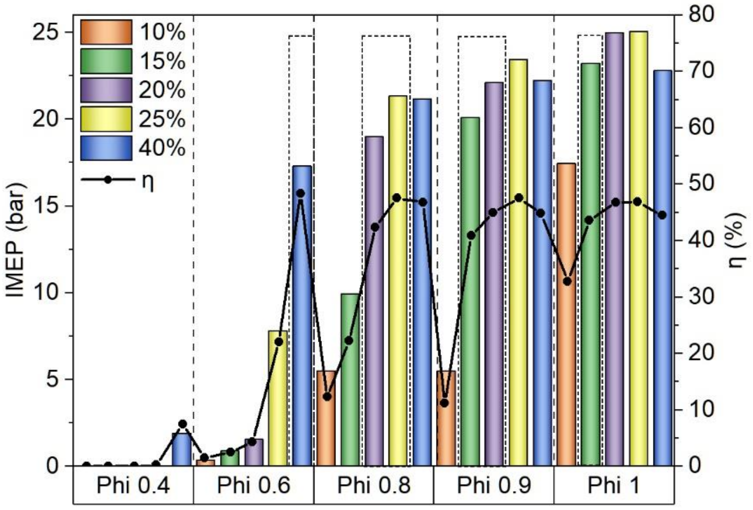

**Fig. 7.** IMEP and thermal efficiency under different hydrogen energy fractions and equivalence ratios in spark ignition mode. The IMEP is indicated with colored bars and the efficiencies with the black line. The dashed boxes indicate normal combustion modes.

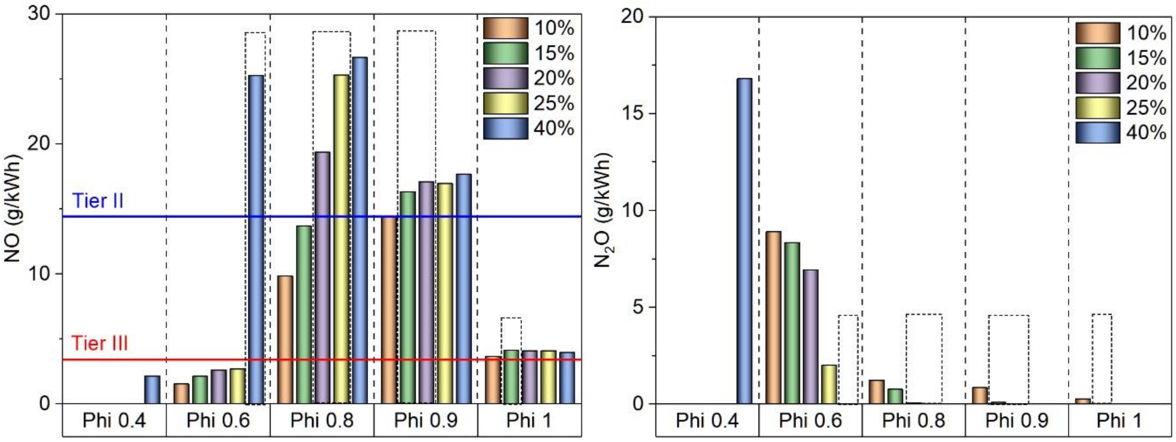

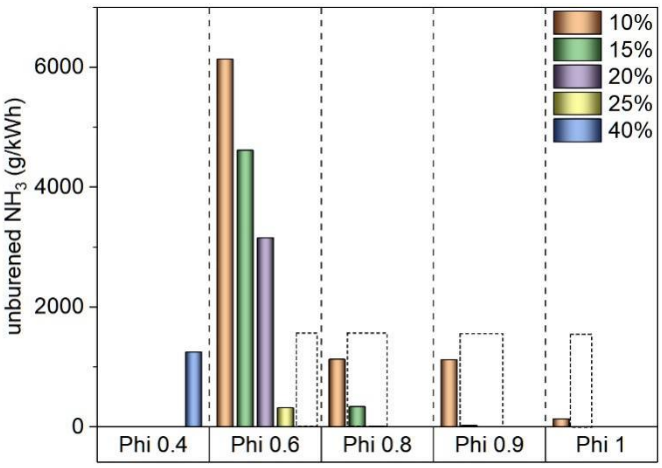

**Fig. 8.** NO, $N_2O$ and unburned $NH_3$ under different hydrogen energy fractions and equivalence ratios in spark ignition mode

Figure 9 illustrates the temperature, NO, and unburned ammonia distributions at CA90 for various equivalence ratios. As anticipated, an increase in the equivalence ratio results in a rise in combustion temperature, which in turn leads to a corresponding increase in thermal NO emissions. Interestingly, at an equivalence ratio of 0.8, the NO concentration is lower than at an equivalence ratio of 1. This implies that under stoichiometric conditions, the fuel NO and prompt NO from ammonia are reduced, especially the prompt NO is closely related to the equivalence ratio. Furthermore, at an equivalence ratio of 0.6, the NO distribution is concentrated at the flame front, unlike in the other two cases where NO is more uniformly distributed over the burned region. Additionally, for an equivalence ratio of 0.6, the slower propagation speed of the flame front results in a substantial amount of unburned ammonia in the peripheral areas.

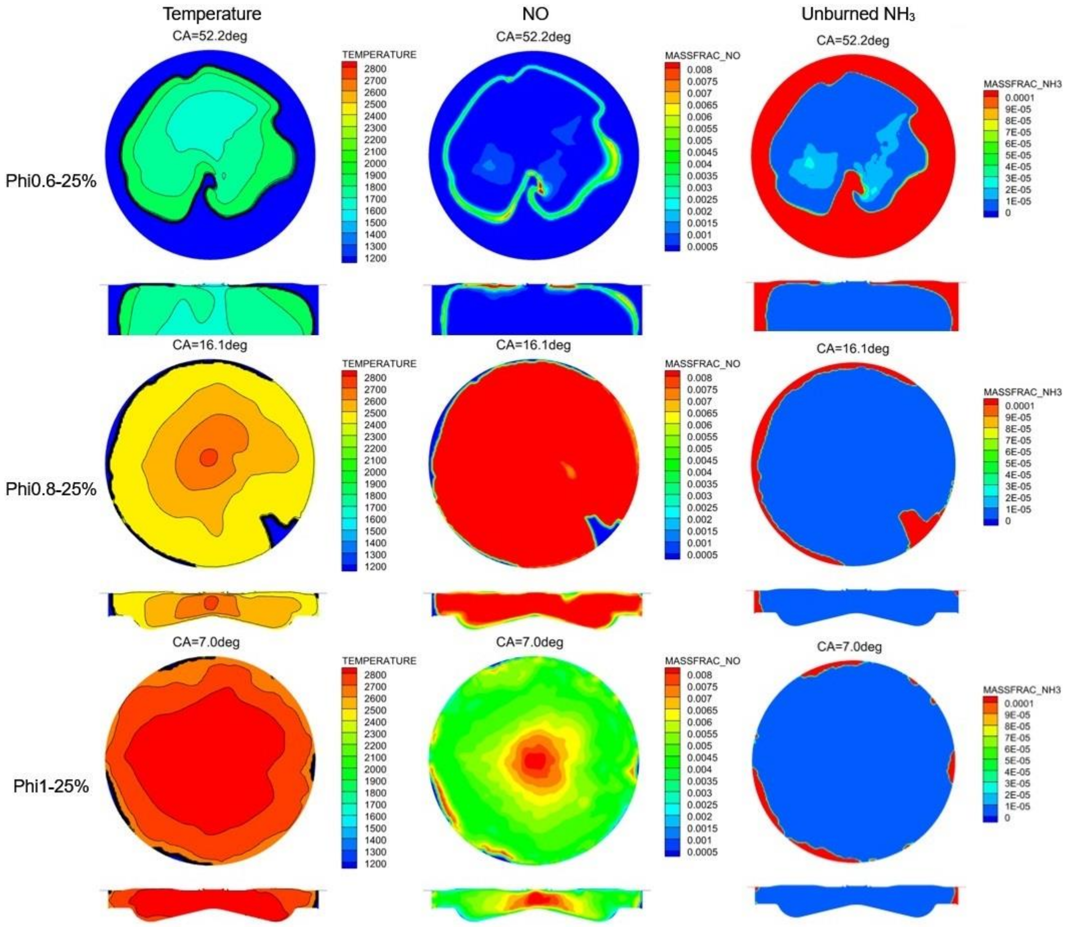

**Fig. 9.** Temperature, NO, and unburned ammonia distributions at CA90 under different equivalence ratios

### 3.2 Passive prechamber ignition

Lean combustion has a promising potential to significantly lower charge temperatures, thereby effectively mitigating the formation of thermal NO. However, achieving lean combustion with spark ignition poses challenges due to the low flame speed, as mentioned earlier. A pre-chamber ignition concept introduces multiple high-velocity hot jets that, on one hand ignite the charge at multiple locations and the other hand increase the turbulence intensity. This leads to a significant improvement in combustion rate compared to the SI mode. Consequently, the pre-chamber ignition mode could extend stable operation towards ultra-lean combustion for ammonia-hydrogen mixtures.

Figure 10 shows lean combustion conditions (equivalence ratio of 0.4) with passive pre-chamber ignition across different hydrogen energy fractions and compression ratios. The intake pressure was raised to 3 bar to attain a 20 bar IMEP, similar to the power output for the SI phi=0.8 condition with 2 bar intake pressure. The spark plug timing remained fixed at -15°ATDC. It is evident that lean combustion at phi = 0.4 is feasible only when the hydrogen energy fraction exceeds 35%. However, the rise in the hydrogen energy fraction also increases the reactivity of the fuel mixture, thereby increasing the knock tendency. Consequently, the operational range for feasible hydrogen energy fractions is quite narrow. Even with a compression ratio surpassing 14, identifying the appropriate hydrogen energy fraction to prevent both knock and misfire can be challenging. Furthermore, even under normal combustion conditions (not knocking and acceptable combustion efficiency), the combustion speed and peak pressure remain low, which adversely affects the power output and thermal efficiency. While advanced spark plug timing can address these issues, the increased likelihood of misfire and knock due to advanced spark plug timing will make it challenging.

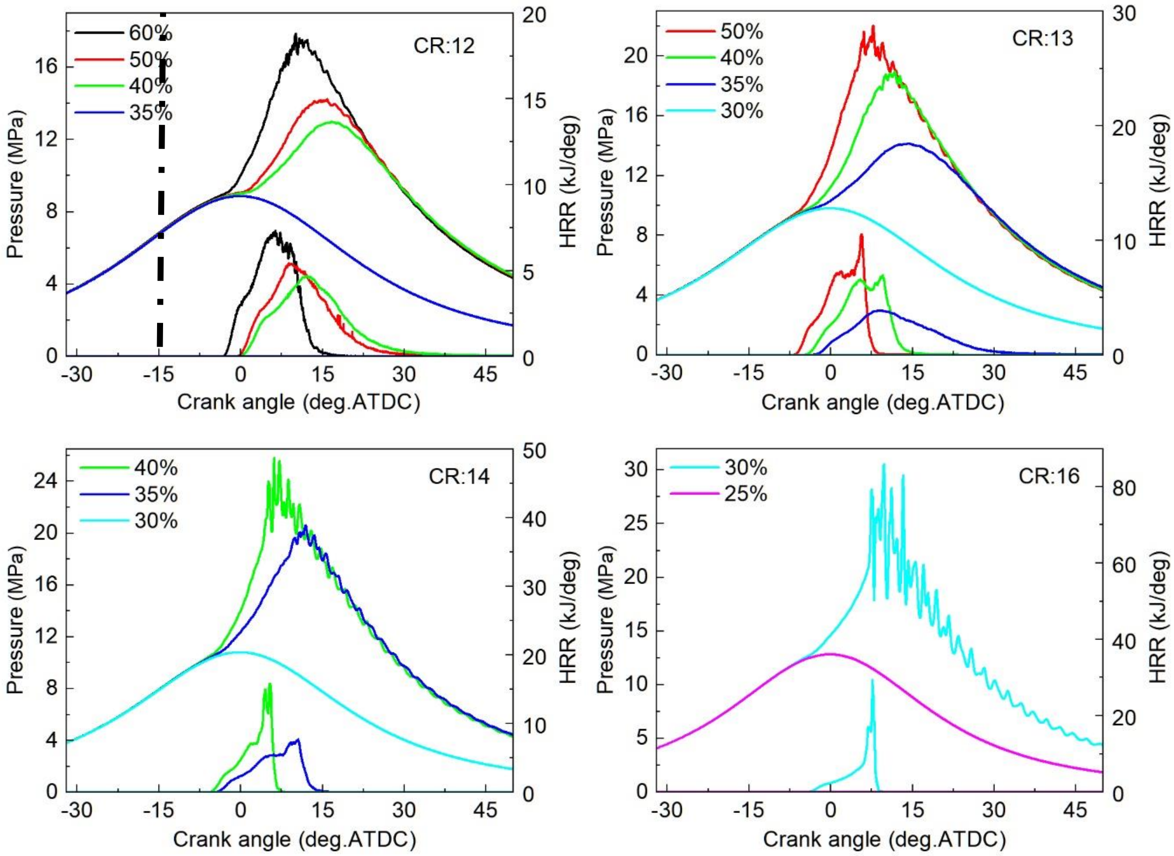

**Fig. 10.** Pressure-volume and heat release rate curves under different hydrogen energy fractions in passive pre-chamber ignition mode at various compression ratios

Figure 11 presents the IMEP and thermal efficiency under different compression ratios and hydrogen fractions, while Figure 12 illustrates the emission levels of NO, $N_2O$ and unburned $NH_3$. The thermal efficiency of the cases with passive pre-chamber ignition exceeds that of spark plug ignition at the same compression ratio, with a maximum increase of up to 2%. This enhancement is attributed to lean combustion, which reduces heat transfer losses on the combustion chamber wall. NO emissions are lower than in most cases under spark ignition mode, except at stoichiometric equivalence ratio. They comply with the tier II standards, particularly in normal combustion conditions, where reduced combustion temperatures significantly lower NO content. However, the $N_2O$ and unburned $NH_3$ emissions exhibit high levels due to the lower combustion rate. Advancing the spark timing may potentially mitigate this phenomenon, nevertheless, excessively advancing the spark timing also poses the risk of knock.

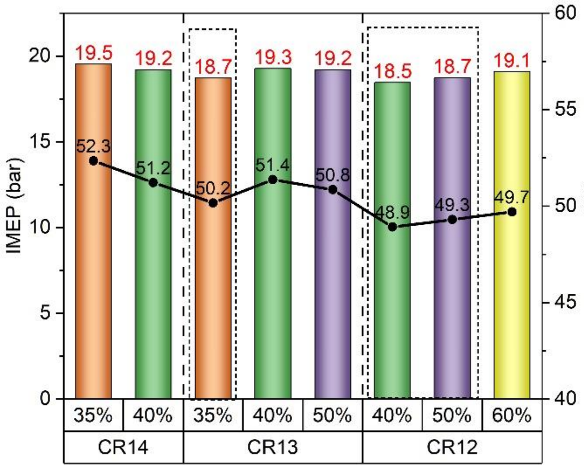

**Fig. 11.** IMEP and thermal efficiency under different hydrogen energy fractions in passive pre-chamber ignition mode at various compression ratios. The line indicates the corresponding efficiency. Dashed box indicates the normal combustion events (no-knock).

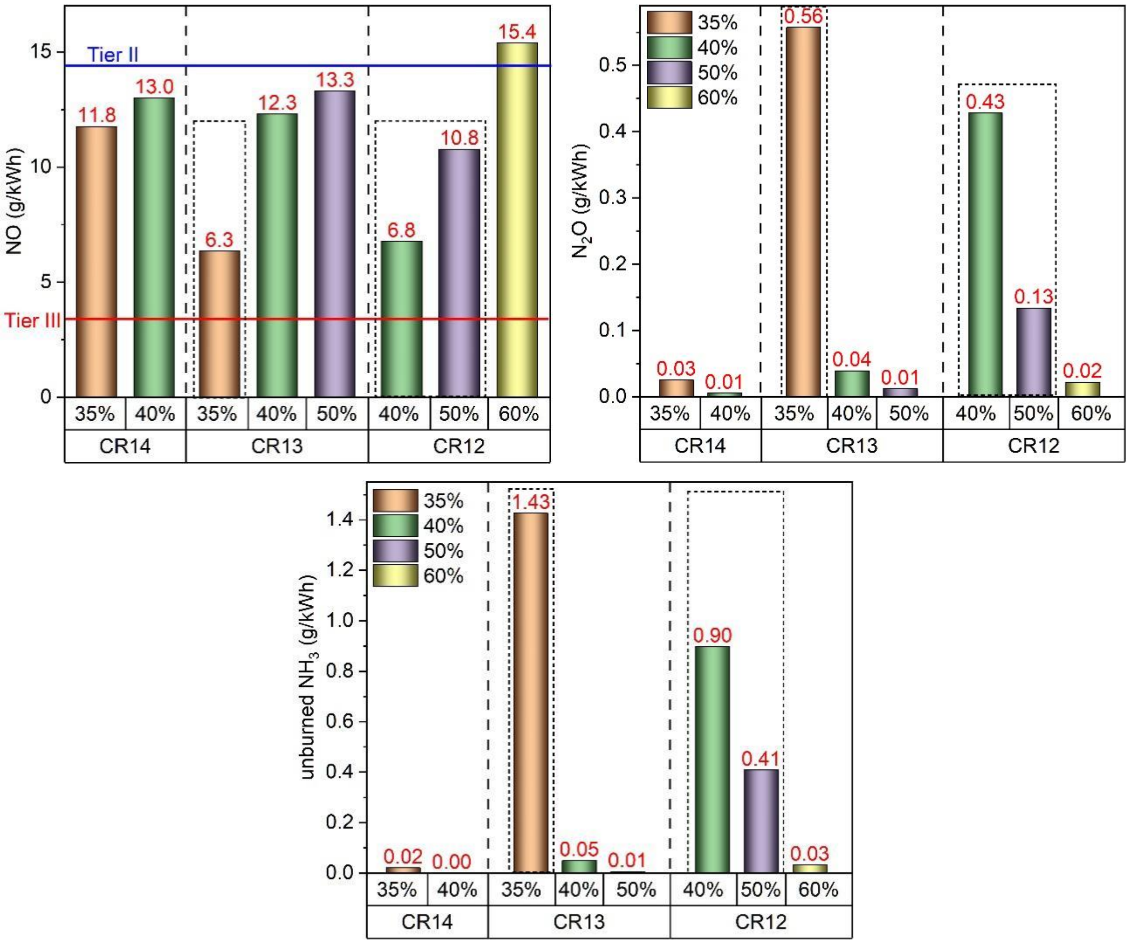

**Fig. 12.** NO, $N_2O$ and unburned $NH_3$ under different hydrogen energy fractions in passive pre-chamber ignition mode at various compression ratios

Figures 13 and 14 present the distributions of temperature and $N_2O$ emissions at various combustion timings for different hydrogen energy fractions under a compression ratio of 12. Higher hydrogen fractions result in elevated combustion temperatures, consequently leading to increased NO emissions.

$N_2O$ is primarily concentrated at the flame front, and its concentration tends to decrease when combustion temperatures increase. Figure 15 illustrates the total $N_2O$ and NO traces as function of CA. It indicates that at higher temperature, $N_2O$ maybe reacts quickly into NO and only at appropriate temperature $N_2O$ is formed and conversion to NO is slow that relevant concentrations remain.

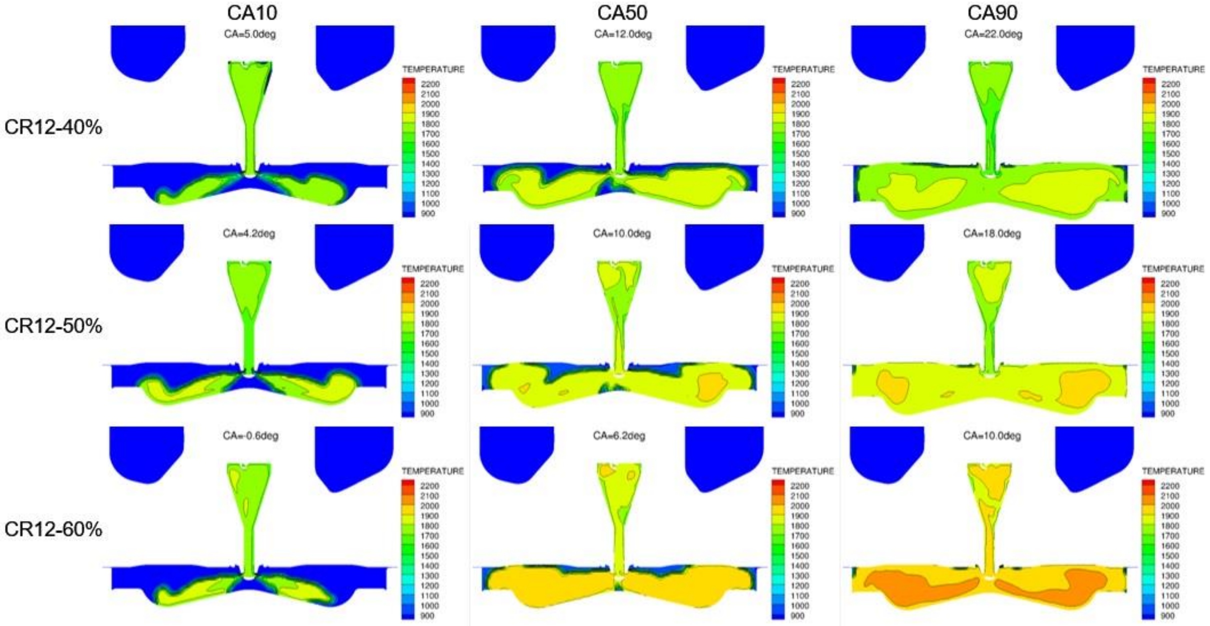
CA10
CA50
CA90
CA=5.0deg
CA=12.0deg
CA=22.0deg
CR12-40%
CA=4.2deg
CA=10.0deg
CA=18.0deg
CR12-50%
CA=-0.6deg
CA=6.2deg
CA=10.0deg
CR12-60%
TEMPERATURE
2200
2100
2000
1900
1800
1700
1600
1500
1400
1300
1200
1100
1000
900

**Fig. 13.** Temperature distributions at different combustion timings under varying hydrogen energy fractions with a compression ratio of 12

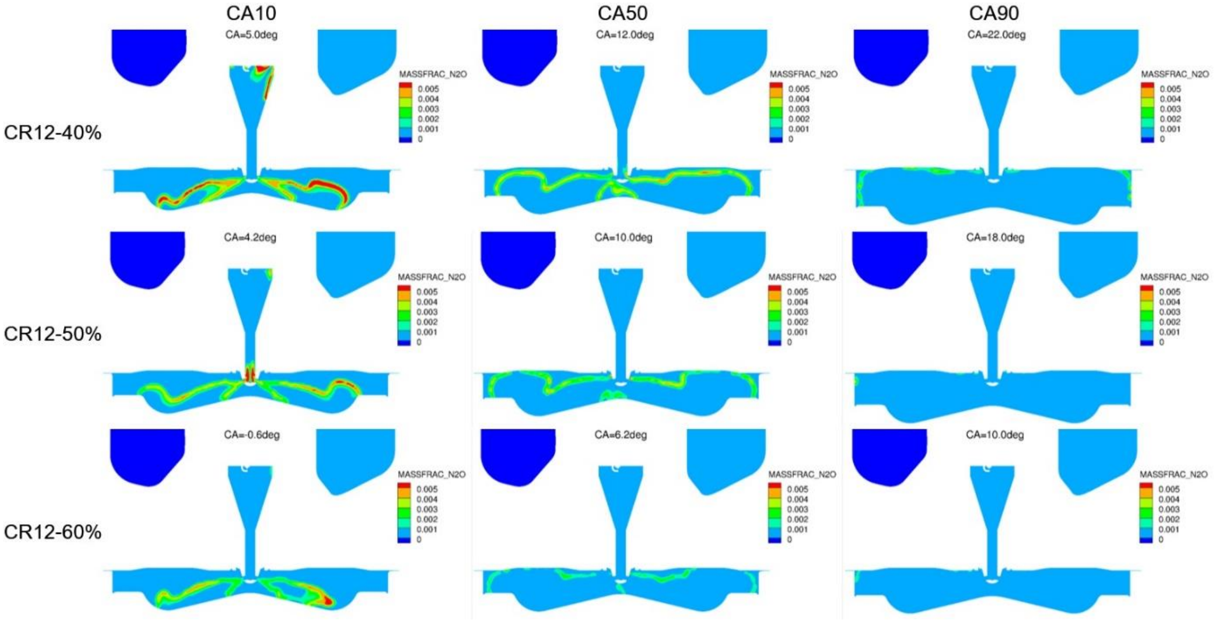
CA10
CA50
CA90
CA=5.0deg
CA=12.0deg
CA=22.0deg
CR12-40%
CA=4.2deg
CA=10.0deg
CA=18.0deg
CR12-50%
CA=-0.6deg
CA=6.2deg
CA=10.0deg
CR12-60%
MASSFRAC_N2O
0.005
0.004
0.003
0.002
0.001
0

**Fig. 14.** $N_2O$ distributions at different combustion timings under varying hydrogen energy fractions with a compression ratio of 12

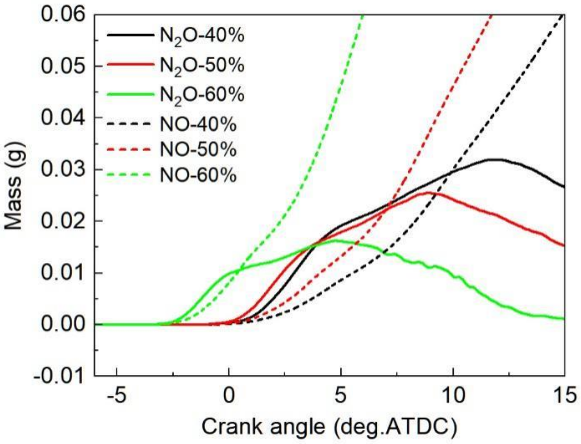

**Fig. 15.** The total $N_2O$ and NO traces as function of CA

### 3.3 Active prechamber ignition

Active prechamber ignition has the capability to increase the temperature in the hot jets, thereby further increasing the flame speed and promoting a more stable ignition process, even at lower hydrogen energy fractions. Figure 16 demonstrates cylinder pressure and heat release rate at various hydrogen fractions and compression ratios with an active pre-chamber. The global equivalence ratio is kept at 0.4 and the intake pressure is 3 bar, equivalent to the settings for the passive pre-chamber. The active pre-chamber is fed with an extra amount of $H_2$, 2% of the total energy input, leading to an equivalence ratio of 0.6 in the pre-chamber. The spark plug timing is retarded to -10°ATDC to mitigate knocking. It is evident that active pre-chamber ignition allows a significant decrease in hydrogen energy fraction in the main chamber to a range of 10% to 25%. Moreover, even after increasing the compression ratio above 14, normal combustion conditions persist. Furthermore, compared to passive pre-chamber ignition mode, active pre-chamber ignition mode exhibits a higher peak pressure and combustion rate without any knock or misfires, despite the delayed spark plug timing, indicating a positive impact on power output.

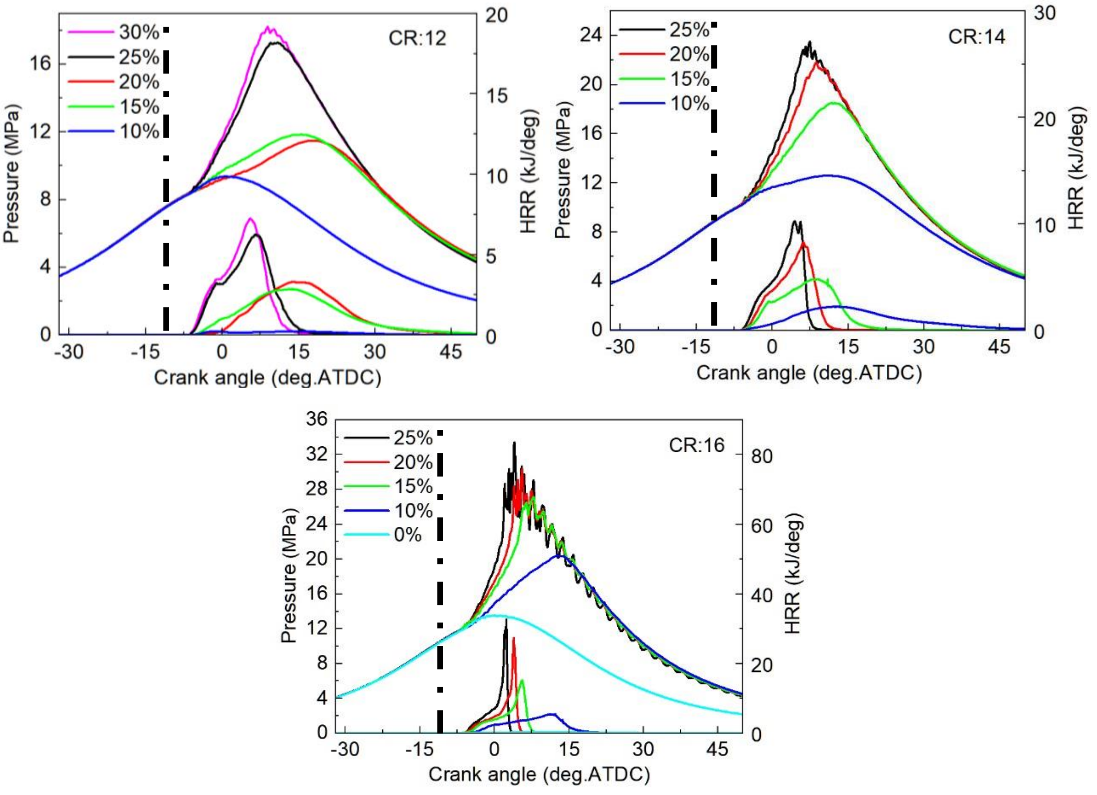

**Fig. 16.** Cylinder pressure and heat release rate curves under different hydrogen energy fractions in active prechamber ignition mode at various compression ratios

Figure 17 illustrates the IMEP and thermal efficiency, while Figure 18 depicts the emission levels of NO, $N_2O$ and unburned $NH_3$. Compared to the passive pre-chamber, the highest thermal efficiency of the active pre-chamber ignition mode is further enhanced, reaching up to 52.8%. This improvement is attributed to an increase in the compression ratio. NO emissions are comparable to those observed in passive prechamber configurations, which comply with Tier II emission standards. Even under normal combustion conditions, NO emissions are slightly higher, possibly due to increased mean combustion temperatures. Conversely, emissions of $N_2O$ and unburned $NH_3$ are substantially decreased, potentially attributed to the increased flame speed.

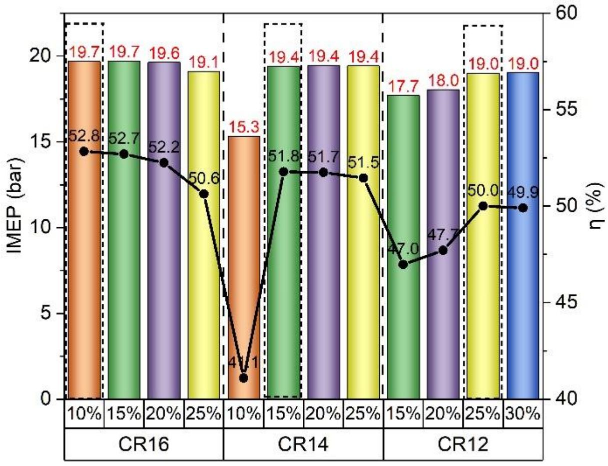

**Fig. 17.** IMEP and thermal efficiency under different hydrogen energy fractions in active pre-chamber ignition mode at various compression ratios

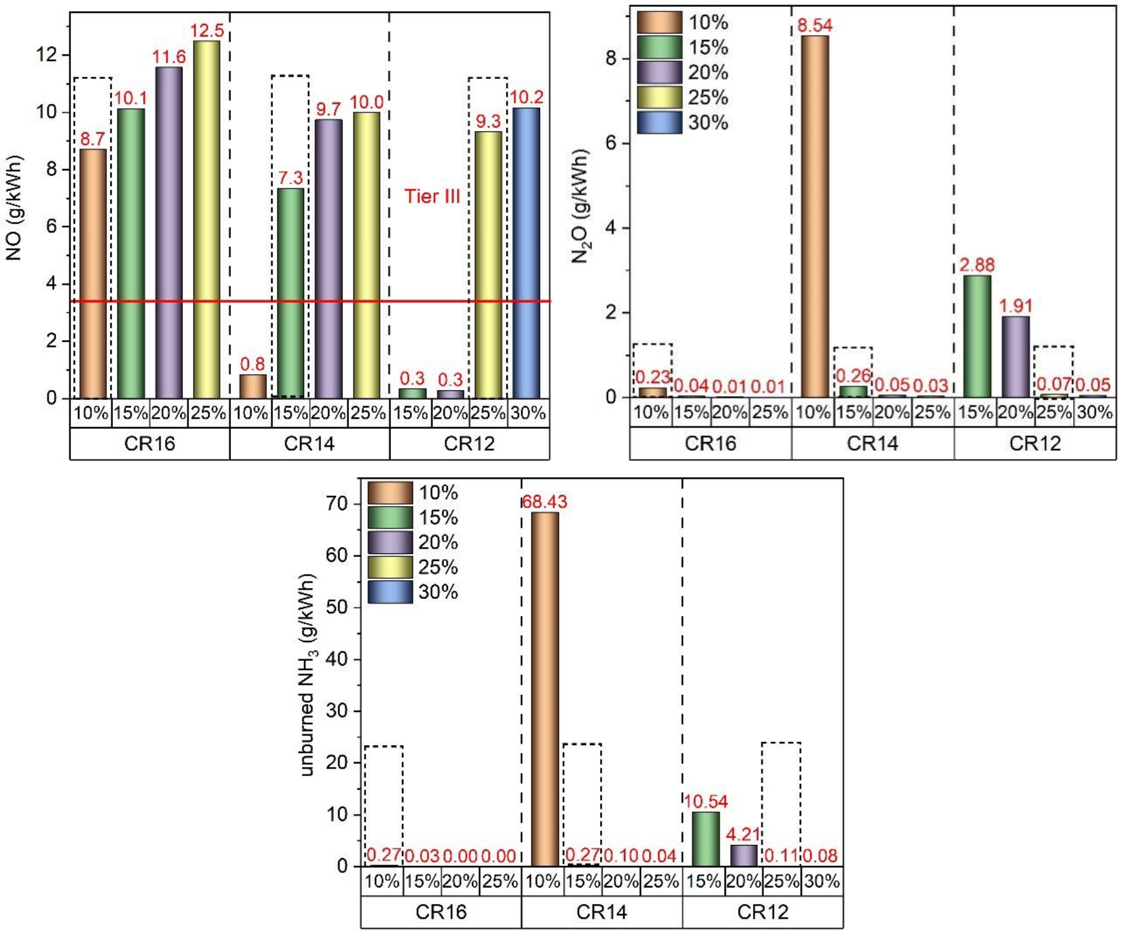

**Fig. 18.** NO, $N_2O$ and unburned $NH_3$ emissions under different hydrogen energy fractions in active pre-chamber ignition mode at various compression ratios

Figures 19 illustrates the distributions of temperature at various combustion timings for different hydrogen energy fractions under a compression ratio of 12. Similar to passive pre-chambers, increasing the hydrogen fraction elevates the overall combustion temperature. However, active pre-chambers differ by exhibiting higher temperatures within the pre-chamber and slightly lower temperatures in the main combustion chamber. This can lead to different distributions of NO emissions compared to passive pre-chambers, as shown in Figure 20. In the passive pre-chamber cases, the main chamber exhibits a higher NO concentration, whereas in the active pre-chamber cases, the main chamber shows an even higher NO concentration.

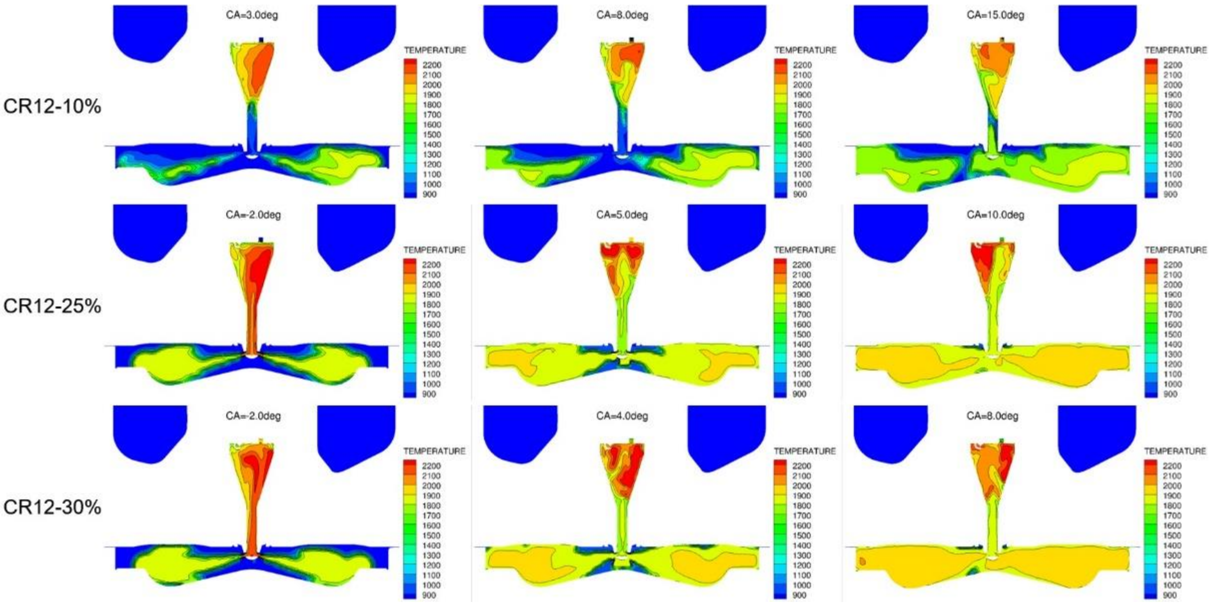

**Fig. 19.** Temperature distributions at different combustion timings under varying hydrogen energy fractions with a compression ratio of 12

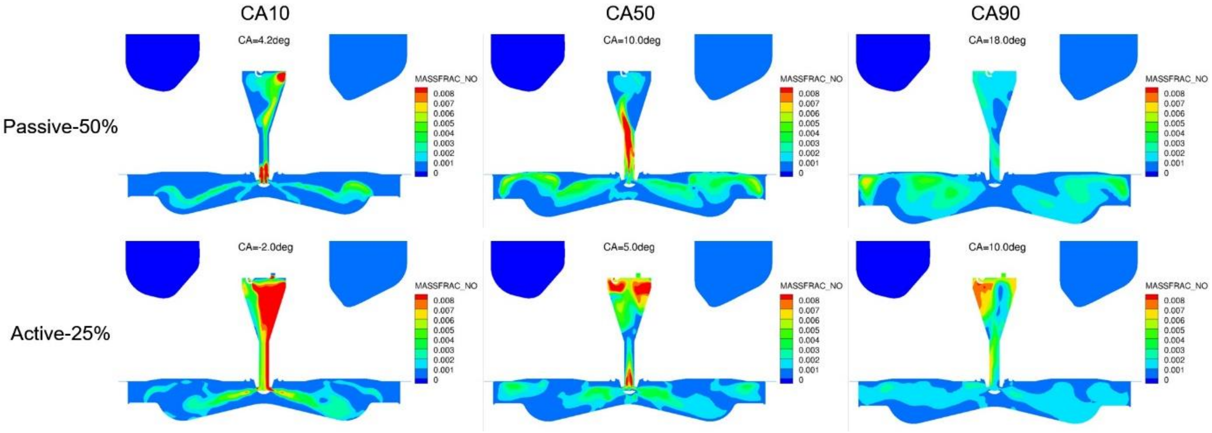

**Fig. 20.** Comparison of NO distribution within the cylinder between active and passive pre-chamber cases

Figure 21 demonstrates the relationship between $N_2O$ and NO, and between $N_2O$ and unburned $NH_3$. It indicates that the concentration of $N_2O$ is inversely proportional to that of NO, which is similar to the $NO_x$-soot trade-off found in diesel engines. Additionally, $N_2O$ appears to be almost directly proportional to the concentration of unburned $NH_3$. The positive correlation between $N_2O$ and unburned $NH_3$ maybe since both are a result of low temperatures. $N_2O$ is typically formed at low temperatures while at these conditions also the flame speed is low leading to incomplete combustion, and thus greater amount of unburned ammonia. Elevated NO concentrations are generally linked to higher charge temperatures, which promote faster combustion and, in turn, reduce $N_2O$ production. Conversely, higher levels of $N_2O$ often indicate incomplete combustion, which tends to correspond with reduced NO concentrations.

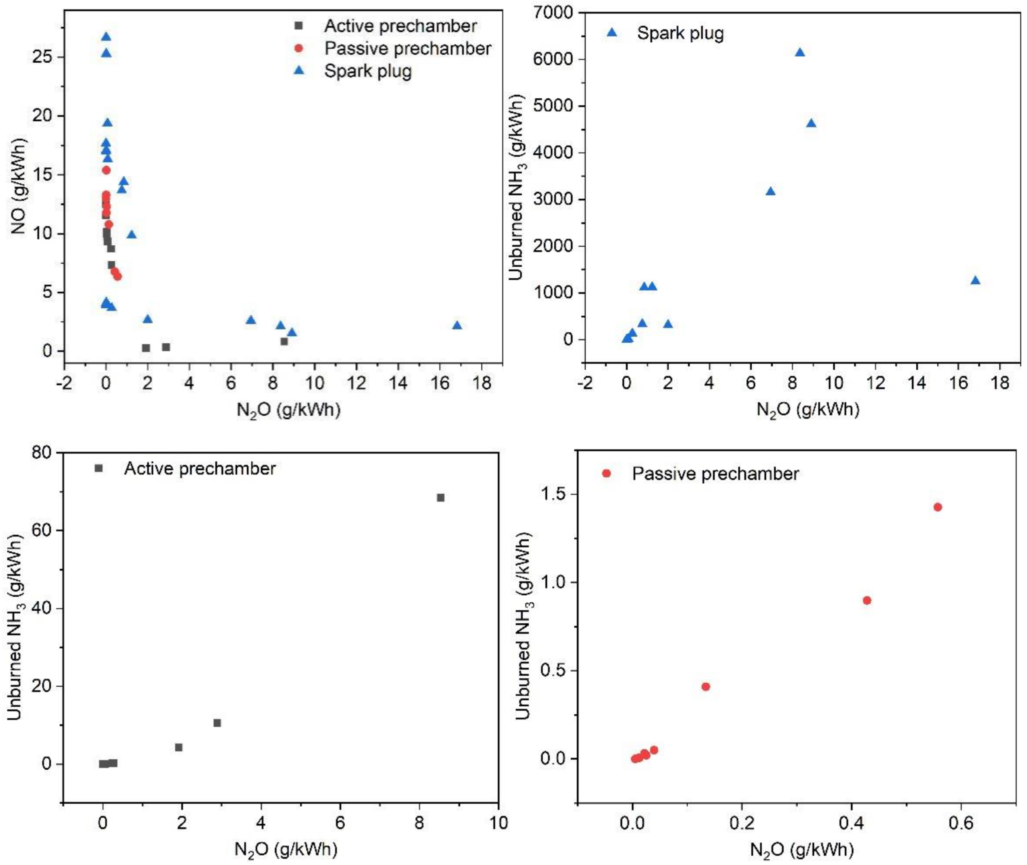

**Fig. 21.** The relationship between $N_2O$ and NO, and between $N_2O$ and unburned $NH_3$

Figure 22 provides a comprehensive comparison of three ignition modes in terms of performance, emissions and hydrogen fraction. Active pre-chamber ignition demonstrates the highest thermal efficiency and achieves the lowest feasible hydrogen fraction. Furthermore, it exhibits excellent emission levels of $N_2O$ and unburned $NH_3$. In contrast, all attributes of passive pre-chamber ignition are the least favorable. Spark ignition under stoichiometric conditions can achieve the lowest emissions of NO, $N_2O$ and unburned $NH_3$. However, its thermal efficiency is significantly reduced due to higher heat transfer losses.

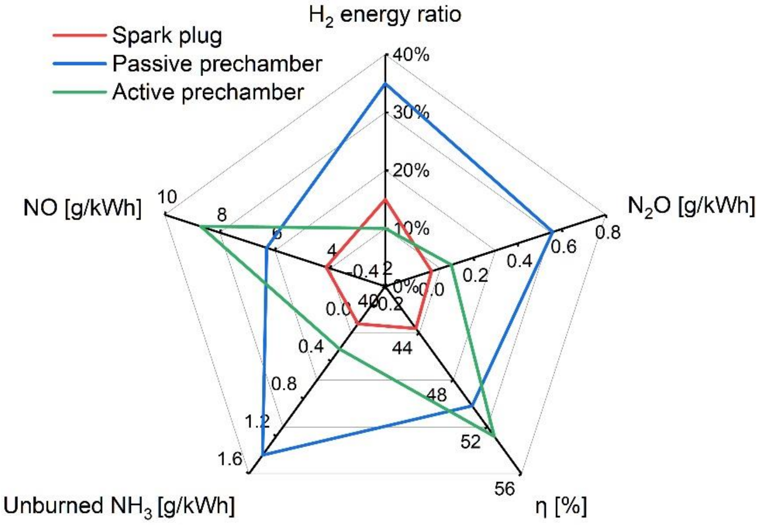

**Fig. 22.** A comprehensive comparison of performance and emissions among spark ignition, passive pre-chamber ignition, and active pre-chamber ignition

## Conclusions

This study investigates and evaluates the feasibility of spark plug ignition, passive pre-chamber ignition, and active pre-chamber ignition for ammonia-hydrogen marine engines, in terms of examining engine performance, emissions, as well as misfire and knock occurrences for a targeted high-load case (approximately 20bar IMEP). Furthermore, optimal operational parameters for guiding engine design are defined, such as compression ratio, equivalence ratio, and hydrogen energy fraction.

The specific conclusions are as follows:

1. Lean combustion is challenging to achieve in spark plug ignition mode due to the lower flame speed and higher ignition energy. $NO_x$ emission is highest in the 0.6-0.8 equivalence ratio range, which can exceed tier II standards. In contrast, stoichiometric combustion yields $NO_x$ emissions near tier III standards, with the lowest hydrogen energy fraction. The optimal hydrogen energy fraction ranges between 15% and 40%. It is found that $N_2O$ emissions are closely linked to the combustion efficiency. In instances of complete combustion, the presence of $N_2O$ is almost negligible. However, in cases of incomplete combustion characterized by lower combustion temperatures, the quantity of $N_2O$ increases significantly for all equivalence ratios.

2. Prechamber ignition can accelerate the flame speed and facilitate lean combustion. However, in the passive prechamber ignition mode, the hydrogen energy fraction needs to be increased to more than 35% to achieve successful ignition. Increasing the compression ratio can reduce the required hydrogen energy fraction. However, this increases the tendencies towards end-gas autoignition and knock. Consequently, achieving normal combustion at high compression ratios becomes challenging.

3. Active prechamber ignition can significantly reduce the hydrogen energy fraction in the main combustion chamber, lowering the risk of spontaneous combustion in the end gas. This allows for a higher compression ratio and leads to a considerable improvement in thermal efficiency. NO emissions are found to be below Tier II. Additionally, the further accelerated flame speed diminishes $N_2O$ and unburned $NH_3$ emissions.

4. In summary, employing spark plug ignition with a stoichiometric equivalence ratio can be used to achieve higher engine power for a given intake pressure and yields minimal emissions of NO, $N_2O$ and unburned $NH_3$. However, this method has a lower thermal efficiency due to increased heat transfer losses (max found is 48.7%). Lean combustion utilizing pre-chamber ignition can achieve a higher thermal efficiency. Especially an active pre-chamber can further enhance thermal efficiency, achieving a maximum of 52.8%, while achieving the lowest hydrogen energy fraction. Both active and passive pre-chambers produce NO emissions at levels compliant with Tier II standards, however, the active pre-chamber demonstrates superior thermal efficiency and lower emissions of $N_2O$ and unburned $NH_3$. This can be attributed to the passive prechamber's higher propensity for knocking and misfires, which hinders its performance.

## References

[1] Chen J, Fei Y, Wan Z. The relationship between the development of global maritime fleets and GHG emission from shipping. Journal of environmental management, 2019, 242: 31-39.

[2] Inal O B, Zincir B, Deniz C. Investigation on the decarbonization of shipping: An approach to hydrogen and ammonia. International Journal of Hydrogen Energy, 2022, 47(45): 19888-19900.

[3] Liu L, Wu Y, Wang Y, et al. Exploration of environmentally friendly marine power technology-ammonia/diesel stratified injection. Journal of Cleaner Production, 2022, 380: 135014.

[4] Liu L, Wu Y, Wang Y. Numerical investigation on the combustion and emission characteristics of ammonia in a low-speed two-stroke marine engine. Fuel, 2022, 314: 122727.

[5] Dimitriou P, Javaid R. A review of ammonia as a compression ignition engine fuel. International Journal of Hydrogen Energy, 2020, 45(11): 7098-7118.

[6] Berwal P, Kumar S, Khandelwal B. A comprehensive review on synthesis, chemical kinetics, and practical application of ammonia as future fuel for combustion. Journal of the Energy Institute, 2021, 99: 273-298.

[7] Hassan Q, Abdulateef A M, Hafedh S A, et al. Renewable energy-to-green hydrogen: A review of main resources routes, processes and evaluation. International Journal of Hydrogen Energy, 2023.

[8] Xing H, Stuart C, Spence S, et al. Alternative fuel options for low carbon maritime transportation: Pathways to 2050. Journal of Cleaner Production, 2021, 297: 126651.

[9] Chiong M C, Kang H S, Shaharuddin N M R, et al. Challenges and opportunities of marine propulsion with alternative fuels. Renewable and Sustainable Energy Reviews, 2021, 149: 111397.

[10] Kurien C, Mittal M. Review on the production and utilization of green ammonia as an alternate fuel in dual-fuel compression ignition engines. Energy Conversion and Management, 2022, 251: 114990.

[11] Chiong M C, Chong C T, Ng J H, et al. Advancements of combustion technologies in the ammonia-fueled engines. Energy Conversion and Management, 2021, 244: 114460.

[12] Elmøe T D, Sørensen R Z, Quaade U, et al. A high-density ammonia storage/delivery system based on Mg (NH3) 6Cl2 for SCR–DeNOx in vehicles. Chemical Engineering Science, 2006, 61(8): 2618-2625.

[13] https://ammoniadrive.tudelft.nl/

[14] Wang D, Ji C, Wang S, et al. Numerical study of the premixed ammonia-hydrogen combustion under engine-relevant conditions. International Journal of Hydrogen Energy, 2021, 46(2): 2667-2683.

[15] Mørch C S, Bjerre A, Gøttrup M P, et al. Ammonia/hydrogen mixtures in an SI-engine: Engine performance and analysis of a proposed fuel system. Fuel, 2011, 90(2): 854-864.

[16] Lhuillier C, Brequigny P, Contino F, et al. Experimental study on ammonia/hydrogen/air combustion in spark ignition engine conditions. Fuel, 2020, 269: 117448.

[17] Liu Z, Zhou L, Zhong L, et al. Reactivity controlled turbulent jet ignition (RCTJI) for ammonia engine. International Journal of Hydrogen Energy, 2023, 48(33): 12519-12522.

[18] Meng X, Zhao C, Cui Z, et al. Understanding of combustion characteristics and NO generation process with pure ammonia in the pre-chamber jet-induced ignition system. Fuel, 2023, 331: 125743.

[19] Liu Z, Zhou L, Zhong L, et al. Enhanced combustion of ammonia engine based on novel air-assisted pre-chamber turbulent jet ignition. Energy Conversion and Management, 2023, 276: 116526.

[20] Reggeti S A, Northrop W F. Lean ammonia-fueled engine operation enabled by hydrogen-assisted turbulent jet ignition. Frontiers in Mechanical Engineering, 2024, 10: 1368717.

[21] Stagni A, Arunthanayothin S, Dehue M, et al. Low-and intermediate-temperature ammonia/hydrogen oxidation in a flow reactor: Experiments and a wide-range kinetic modeling. Chemical Engineering Journal, 2023, 471: 144577.

# Theoretical Analysis of Combustion and Emission Characteristics of Ammonia/Dimethyl Ether Marine Low Speed Engine with High Pressure Dual Fuel Direct Injection

Long Liu[1], Shiyutian Li[1], Haoyu Liu[1] and Yang Wang[1]

[1]College of Power and Energy Engineering, Harbin Engineering University, 150001,PR, Harbin, China

E-mail: liulong@hrbeu.edu.cn
Telephone: +(86) 0451-82568316

Abstract. The use of ammonia as an alternative fuel for marine engines is currently an important method of reducing GHG emissions from shipping, but the poor combustion characteristics of ammonia fuels and more $NO_x$ produced by the emissions make it difficult to be widely used at this stage. Therefore, a simulation model of high-pressure direct-injection ammonia/dimethyl ether (DME) hybrid combustion was developed by coupling chemical reaction kinetics and computational fluid dynamics to analyze the combustion process of ammonia fuel ignited by DME with a low energy ratio(2%-5%), and to study the effect of the active atmosphere brought by DME on the combustion of ammonia. The results show that DME ignites the ammonia fuel by releasing reactive radicals and heat, in this way promotes ammonia combustion. As a result, mixing more DME improves the ammonia combustion characteristics by advancing the combustion phase and shortening the combustion duration. In addition, earlier ammonia injection allows more gas-phase ammonia to be premixed in the cylinder, and the DME flame and the OH it produces are more readily accessible to the ammonia, enhancing the ignition effect and improving engine performance. Comprehensive study of DME injection timing and dual-fuel injection timing intervals, and it was found that when the DME injection timing was too early, the engine worked roughly with large maximum burst pressure and pressure rise rate, which might lead to exceeding the engine strength limit.

## 1. Introduction

The Paris Agreement [1] provided that the increase in global temperatures need to be limited to 2°C in this century, while searching for effective measures that can limit the temperature increase to 1.5°C. However, global temperatures have already risen by 1.1°C compared to pre-industrial temperatures. By today, the climate impact of the greenhouse effect has become increasingly unbearable for everyone. The International Maritime Organisation (IMO) has been done intensive and thoughtful work to reduce carbon emissions in the global shipping industry, which has advanced the global efforts to reduce carbon emissions in the shipping industry and achieved a more significant effect. 80th Marine Environment Protection Assembly conducted by IMO on 7 July 2023 adopted the document "2023 IMO Strategy On Reduction Of GHG Emissions From Ships"[2].In accordance with the principle of a ‘fair and equitable transition', the IMO has alleviated the emissions reduction burden on the shipping industry in underdeveloped countries, and has accelerated the timeline for achieving net zero emissions from the end of this century to 2050.

There are two general approaches to reducing carbon of the shipping industry. Specifically, the first is to increase the thermal efficiency of engines and reduce the use of fossil fuels; the second is to use low-carbon or zero-carbon alternative fuels, such as ammonia, hydrogen, methanol and natural gas. Methanol is one of the excellent low-carbon alternative fuels for marine use, because the molecular oxygen atoms in methanol make it possible for methanol to be self-supplied with oxygen during combustion [3-4], Green methanol is the use of carbon capture technology to produce carbon dioxide in the air to achieve carbon cycling. However, more research is still needed for the large-scale application of methanol in ships because carbon capture technology is very expensive . Hydrogen is considered to be the most promising energy source of this century, and is recognized as an excellent carrier of clean energy as it does not produce $CO_2$ and pollutant emissions when burned [5-6]. However, hydrogen has fatal shortcomings in storage and transportation that are difficult to be solved by existing technologies, making it difficult to popularize today. Ammonia, as a carrier of hydrogen, is easy to produce and store, and has a high octane number [7], making it an ideal zero-carbon fuel for ships. The large cylinder bore and high power of marine low-speed engines can cause irreversible damage to spark plugs when using spark plugs, so spark ignition (SI) is generally not used for ignition. However, ammonia fuel has an ignition temperature of 924 K and a narrow ignition limit (16%-25%) as well as a slow laminar flame speed, and the desire to observe compression ignition of ammonia fuels needs to be achieved in very high compression ratios ranging from 35 to 100. High compression ratios can be overwhelming to the engine and produce more NOx in combustion [8]. Therefore it is necessary to use a more readily self-igniting fuel as a pilot fuel to enable ammonia ignition at lower boundary conditions.

Diesel, being a fossil fuel that has been used for many years, has superior combustion characteristics. Literature [9] investigated the reduction of compression ratio of a compression ignition engine from 35 to 15.2 by igniting ammonia fuel with pilot diesel. After that, it was stated that an ammonia-diesel compression ignition engine with diesel as the pilot fuel can achieve successful operation at 95% ammonia energy share [10]. Since the end of the last century, Dimethyl ether (DME) has been promoted as a diesel alternative [11-16]. DME has the advantages of low NOx emissions, combustion without carbon soot and high cetane number, which makes DME cleaner while igniting ammonia fuels more easily. And DME's low viscosity (viscosity of diesel is 20 times higher than DME) can also be improved with the use of additives. However, DME has a lower calorific value compared to diesel, and more DME needs to be consumed to release the same amount of energy, which leads to the need for larger injectors for use in marine low-speed engines. Therefore a large number of scholars are currently investigating the kinetic modelling of ammonia ignition by low DME ratio. Literature [16] describes the feasibility of direct compression ignition of ammonia/DME mixtures in single-cylinder direct injection diesel engines, makes a series of emission measurements, and analyses the cost of using ammonia/DME fuels. Dai et al. [18] carried out rapid compression machine(RCM) tests to measure the ignition delay time of ammonia fuels ignited by 2% and 5% molar ratios of DME, and a kinetic model for the chemical reaction of ammonia/DME was constructed based on previous studies [19-22]. The authors suggest that the ignition of ammonia fuel by DME is due to the low-temperature oxidation of dimethyl ether at an early stage, the decomposition of which produces reactive factors that contribute to the oxidative exothermic and combustion of ammonia, and that the low-temperature chain-branching reaction of dimethyl ether is important for the ignition of ammonia. Recently, Issayev et al. [23] developed a kinetic model containing 176 substances and 1418 reactions, and Yin et al. [24] improved the kinetic model based on the one developed by Dai and proposed a kinetic model containing 193 substances and 1669 reactions. The two models mentioned above can well predict the $NH_3$/DME/air mixed combustion laminar flame velocity, but they contain too many species and reactions, which will increase a huge amount of computation in 3D simulation and lead to a long computation time. Therefore, this paper adopts the kinetic model developed by Dai et al. with some simplifications, and establishes a simulation model of dual direct injection for a certain type of marine low-speed engine, and investigates the combustion process and combustion characteristics of ammonia ignited by DME with different fraction, so as to provide a technical reference for the development of ammonia marine low-speed engines.

## 2. Model and methodology descriptions

An ammonia/DME dual fuel high pressure direct injection compression-ignition 2-stroke marine engine model based on a low-speed engine of a certain type of ship was constructed and simulated using CONVERGE. The model has three ammonia fuel injectors uniformly distributed around the cylinder head circumference, and the DME injectors are set in a small space in the middle of four exhaust valves. The ammonia injectors have five orifices and the DME injectors have six orifices in a uniformly distributed area. The geometrical model of the engine is detailed in Fig.1, the injection setup is shown in Fig.2, and the parameter settings of the structure are detailed in Table 1.

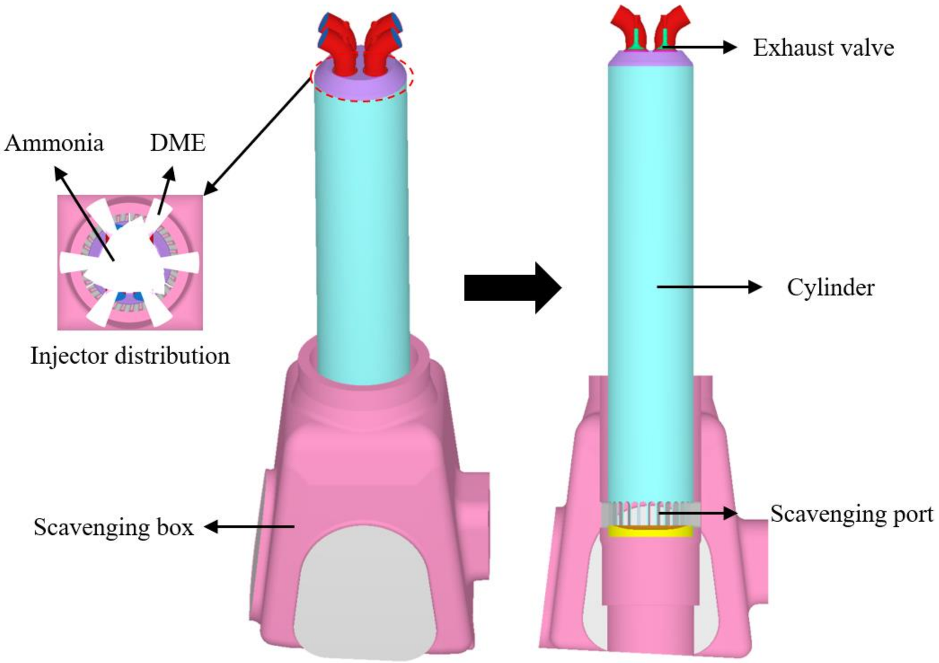
Ammonia
DME
Injector distribution
Scavenging box
Exhaust valve
Cylinder
Scavenging port

**Fig. 1.** Engine geometry model

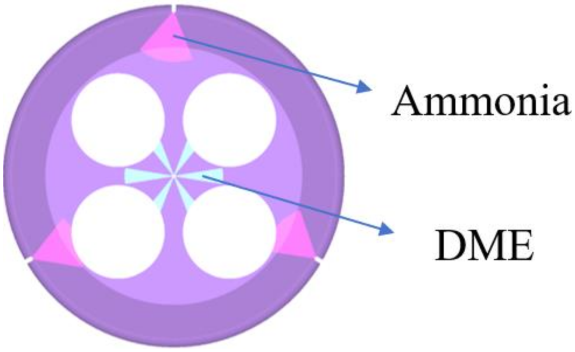
Ammonia
DME

**Fig. 2.** Schematic diagram of oil injection setup

**Table 1.** Engine structural parameters

| Parameters | value |
|---|---|
| Stroke number | 2 |
| Engine speed/(rpm) | 103.2 |
| Bore × Stroke/(mm) | 520 × 1658 |
| Connecting rod length/(mm) | 2658 |
| Compression ratio | 21.8 |
| Number of simulation cycles | 1 |

The injection parameters of the engine are detailed in Table 2, and the sub-models of the simulation model are detailed in Table 3.

**Table 2.** Setting of engine injection parameters

| Parameters | value |
|---|---|
| Number of DME injector | 1 |
| Number of $NH_3$ injector | 3 |
| Injection time of DME/(deg) | -5 |
| Injection time of $NH_3$/(deg) | 0 |
| Energy fraction of DME/(%) | 5/4/3/2 |
| Injection pressure of DME/(MPa) | 70 |
| Injection pressure of $NH_3$/(MPa) | 50 |

**Table 3.** The models adopted in the simulation

| Models | Name |
|---|---|
| Combustion model | SAGE |
| Turbulence model | RNG k-ε |
| Collision model | The NTC collision |
| Droplet breakup model | KH-RT |

Low-speed marine engines are large in size, and the small base mesh cannot be chosen to ensure the computational accuracy and to take into account the computational feasibility. The grid-independence analysis has been completed and the base grid size that can guarantee the accuracy and computational speed has been selected in the previous study, which is described in detail in the literature [2].

The detailed NH3/DME mechanism was developed by Dai and contains 191 species and 1657 reactions, which have been widely adopted and validated. In order to save computational time, a skeleton mechanism was built based on the DRGEP (Directed Relation Graph with Error Propagation) method. The target species of the simplified mechanism were identified as DME, NH3, CO, CO2, H2O, N2, and O2, and the DRGEP ignition delay time errors of 10%, 20%, 40%, and 50% were obtained for four skeleton mechanism mechanisms with species numbers of 75, 61, 61, and 60, which yielded ignition delay time errors of 8.57%, 14.42%, and 14.44%, respectively, 42.8%. Fig. 4 shows the ignition delay time validation results involving different species of skeleton mechanism, which are in sharp contrast to the experimental results. The reaction between NH3 and DME has been less studied and the experimental results are not sufficient. The ignition delay time of the skeleton mechanism at low temperatures is not precise, but the trend is similar, so it is acceptable at this stage. It can be seen that the prediction accuracy of the skeleton mechanism with a species number of 61 is acceptable, and the smaller number of species greatly reduces the computational cost, so the skeleton mechanism with an error of 20% and a species number of 61 was chosen as the final choice.

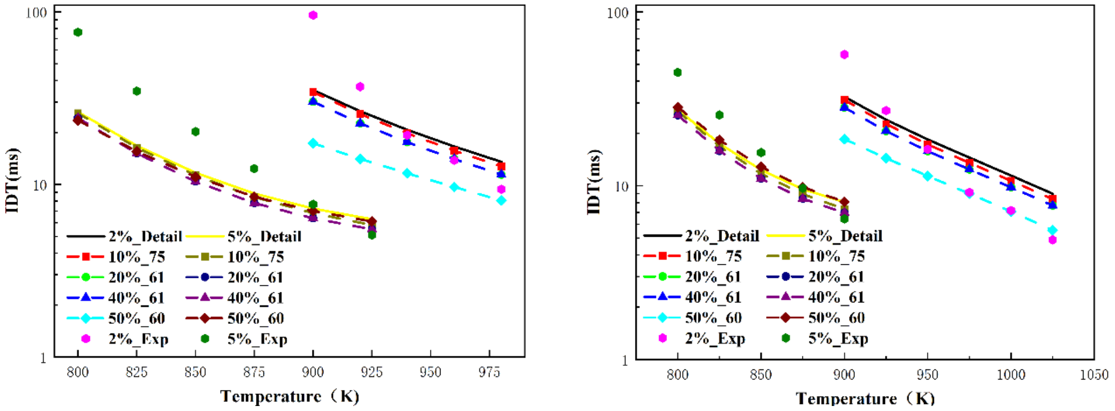

(a)φ=0.5 (b) φ=1

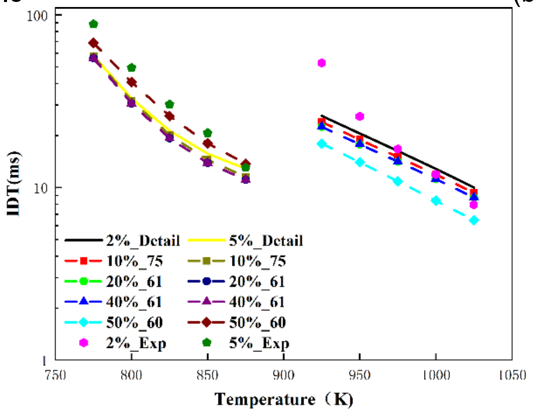

(c) φ=2

**Fig.4.** the ignition delay time validation results

Since there is basically no experimental data on the engine with dual-fuel combustion of $NH_3$ and DME, the cylinder pressure and exothermic rate data of the original engine combusted under four different operating conditions using pure diesel as the fuel are calibrated to be the most accurate at the current conditions, and the comparison is made to obtain the calibration curves as shown in Fig.5.and 6. Therefore the use of diesel experimental data to calibrate this engine model is the most accurate at this stage.

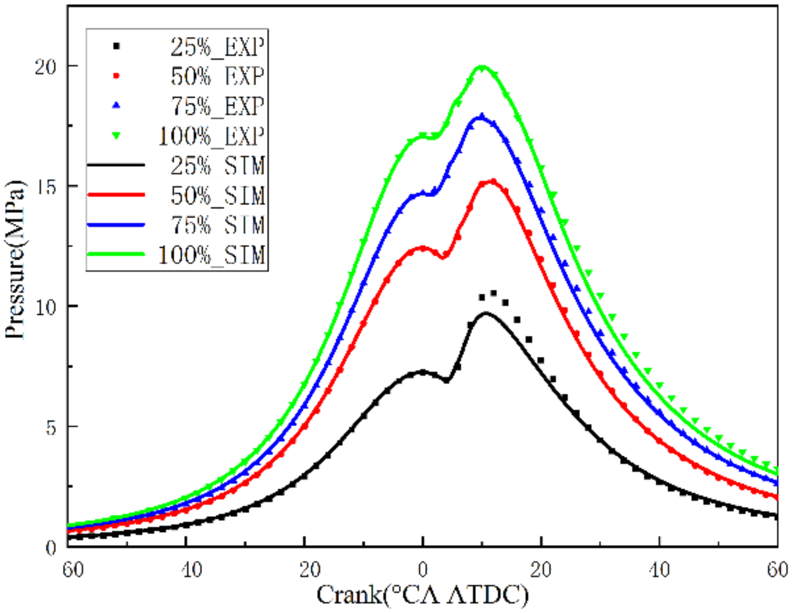

**Fig.5.** Cylinder pressure calibration curves under four different working conditions

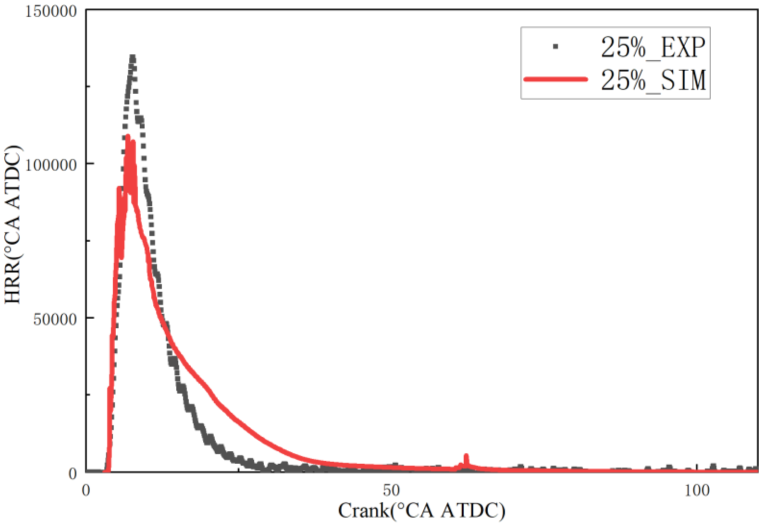

(a)25%load

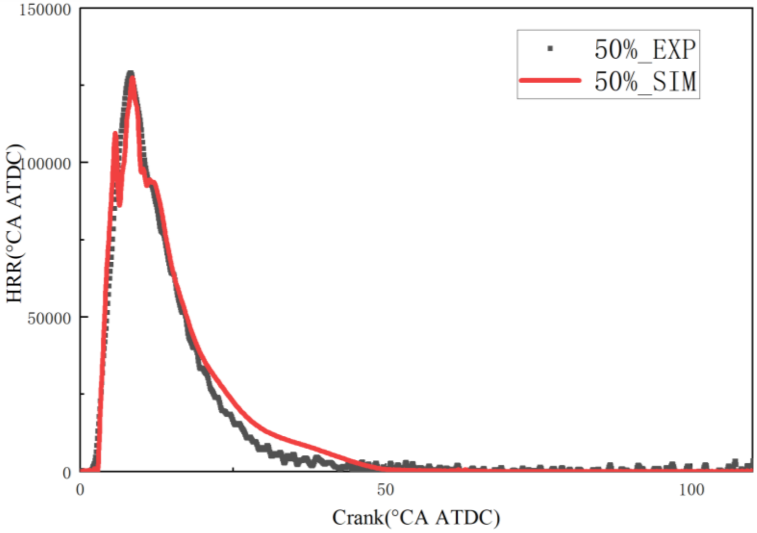

(b)50% load

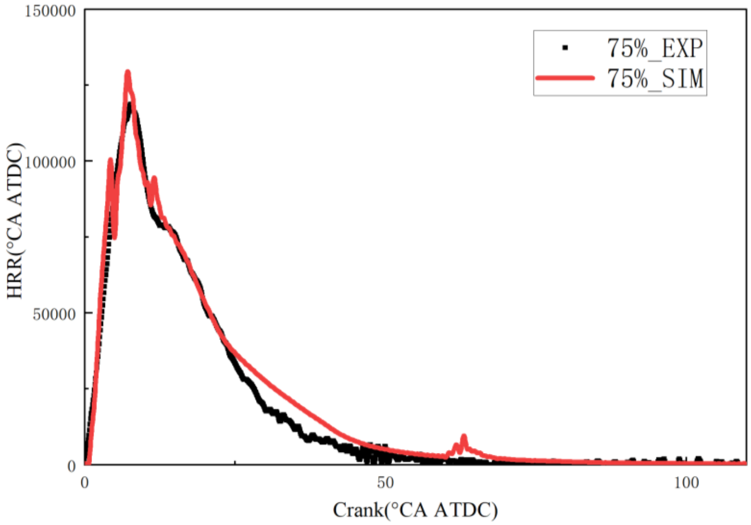

(c)75% load

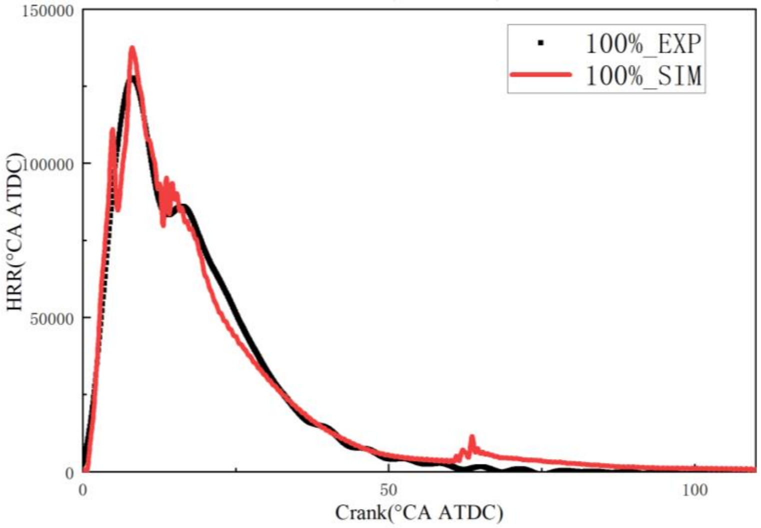

(d)100% load

**Fig.6.** Calibration curves of exothermic rate under four different working conditions

## 3. Results and discussions

### 3.1 Impact of DME energy ratio

DME is a carbon-containing fuel like diesel, so the more DME is used, the more $CO_2$ is produced by combustion, which must be reduced in order to reduce carbon emissions from the engine. However, due to the poor ignition performance of $NH_3$, pilot fuels above a certain energy ratio must be used for ignition. Therefore, the energy share of DME needs to be investigated and the amount of DME used needs to be minimised. Since the skeleton mechanism validates IDT for DME energy ratios of 2% and 5%, DME energy ratios of 2%-5% are currently investigated. In all cases with different DME energy ratios, the combustion in the cylinder presents a typical dual-fuel combustion, as shown in Fig.7. Firstly, the DME combustion was exothermic with a small exothermic peak, which was the first stage of combustion. The first one is the premixed combustion of DME which has time to evaporate before the spontaneous ignition, after which the exothermic rate decreases. The combustion rate then gradually increased as DME was continuously injected until the end of DME injection. After the ammonia was injected into the cylinder, the exothermic rate in the cylinder was almost zero, presumably because the ammonia was ignited by contact with the reactive groups produced by the combustion of the DME. Even so, the ignition delay of the ammonia was long, and the piston travelled some distance downstream before ammonia ignition was achieved, much ammonia fuel accumulated in the cylinder during the time.

After the ammonia ignition, a rapid exothermic phenomenon occurs in a short period of time, which is the second stage of exothermic. As the premixed ammonia burns out, the premixed combustion changes to diffusion combustion. At this time, the rate of ammonia injection into the cylinder and its combustion rate reached a sub-equilibrium, and the exotherm gradually levelled off until the end of the ammonia injection. However, under the conditions of different DME energy ratios, the ignition point of ammonia is almost the same moment, so it can be presumed that ammonia is not exposed to a large number of DME flames. Rather, the ammonia oxidises and burns rapidly after contact with the reactive groups produced by DME oxidation.

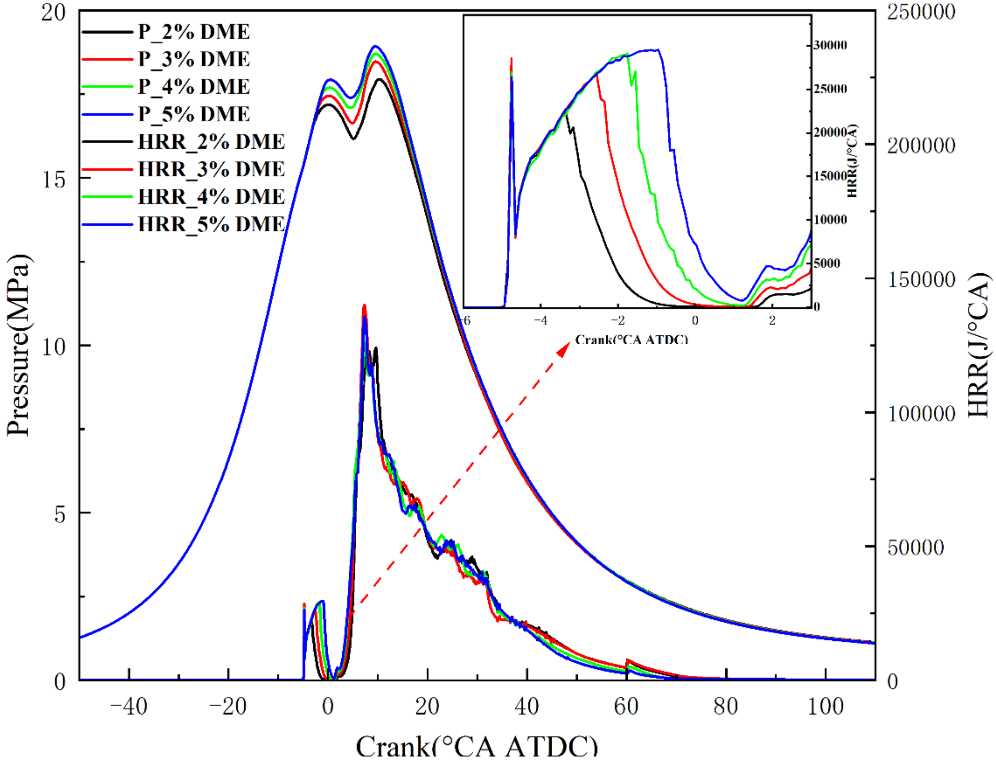

**Fig.7.** Cylinder pressure exothermic rate curves under DME with different energy ratios

According to Dai et al [18], the ignition of ammonia is mainly caused by the contact of OH generated from DME oxidation with ammonia. However, at different DME energy ratios, the ignition point of ammonia was almost at the same moment. In order to observe the ignition process of ammonia more intuitively, cloud maps of temperature and OH mass fraction distributions at the injector height slices were made as Fig.8. The increase of DME ratio resulted in more heat and OH at 1.5°CA after top dead centre (ATDC), which led to more ammonia ignition by oxidation. Therefore, with the increase of DME ratio, the earlier the ammonia ignition point, the earlier the subsequent combustion, the higher the cylinder burst pressure, which presents the phenomenon of the combustion phase histogram shown in Fig.10. From the slice diagram in Fig.8, it can be seen that when ammonia and OH are in contact, most of DME has been finished, and at this time, the flame temperature is lower, the ignition effect is poorer, and the combustion stability is poorer, which is mainly caused by the late timing of ammonia injection Therefore it is necessary to optimize the spray of ignition (SOI) of ammonia and DME. It should be explained that the distribution of OH was non-uniform due to the lower horizontal height of the central DME injector compared to that of the ammonia injector as Fig.9. To facilitate clearer observation of the ammonia ignition process, a slice height corresponding to the horizontal position of the ammonia injector was selected. The intricate combustion and flow within the cylinder led to a minor dispersion of OH to the level of the ammonia injector.

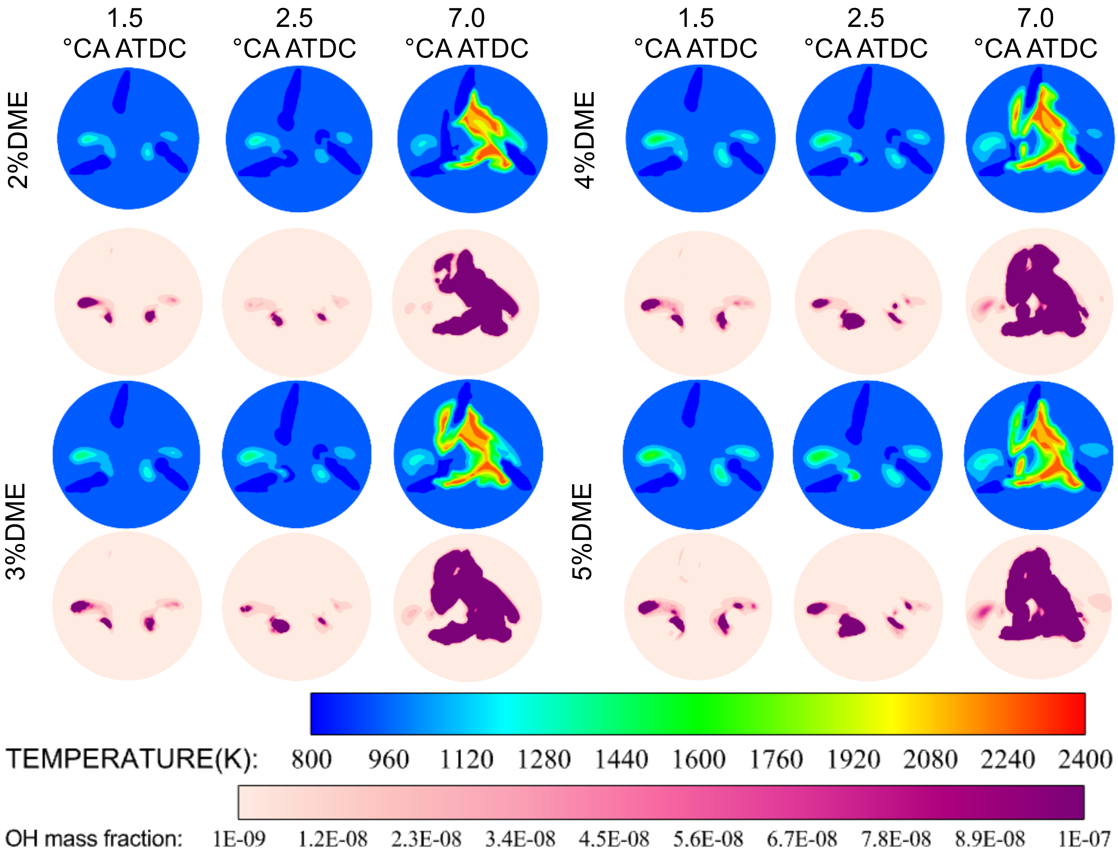

**Fig.8.** Sliced distribution of temperature and OH mass fraction

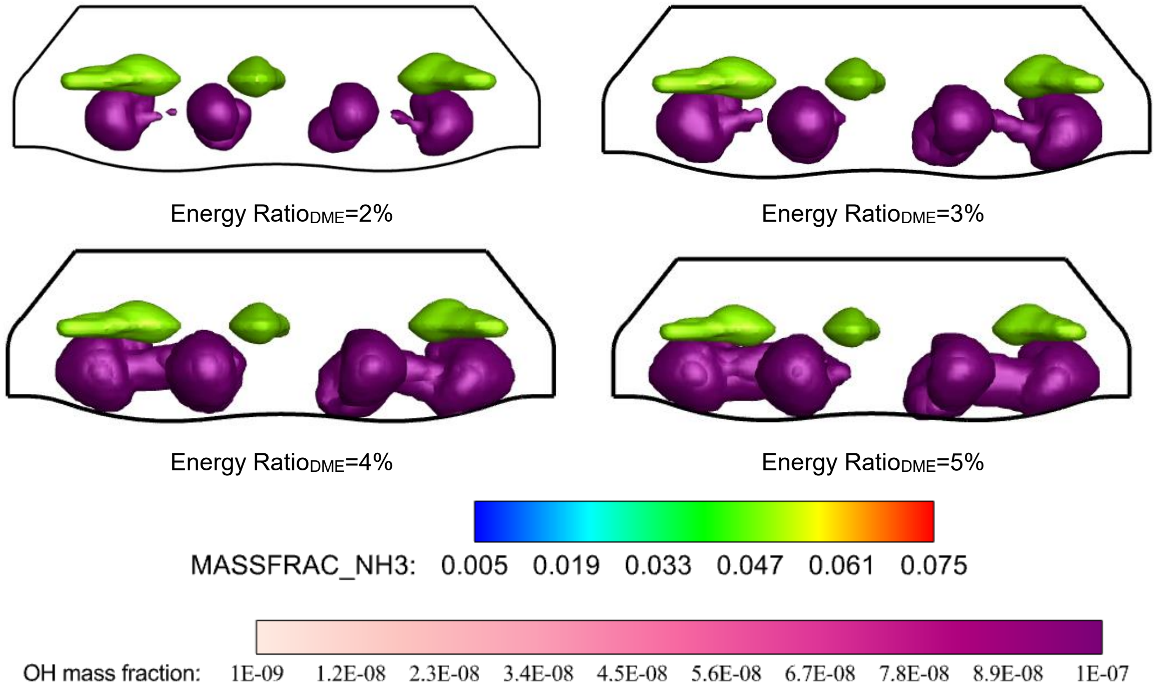
Energy Ratio$_{DME}$=2%
Energy Ratio$_{DME}$=3%
Energy Ratio$_{DME}$=4%
Energy Ratio$_{DME}$=5%
MASSFRAC_NH3: 0.005 0.019 0.033 0.047 0.061 0.075
OH mass fraction: 1E-09 1.2E-08 2.3E-08 3.4E-08 4.5E-08 5.6E-08 6.7E-08 7.8E-08 8.9E-08 1E-07

**Fig.9.** Iso-surfaces of ammonia and DME in the Y-axis plane

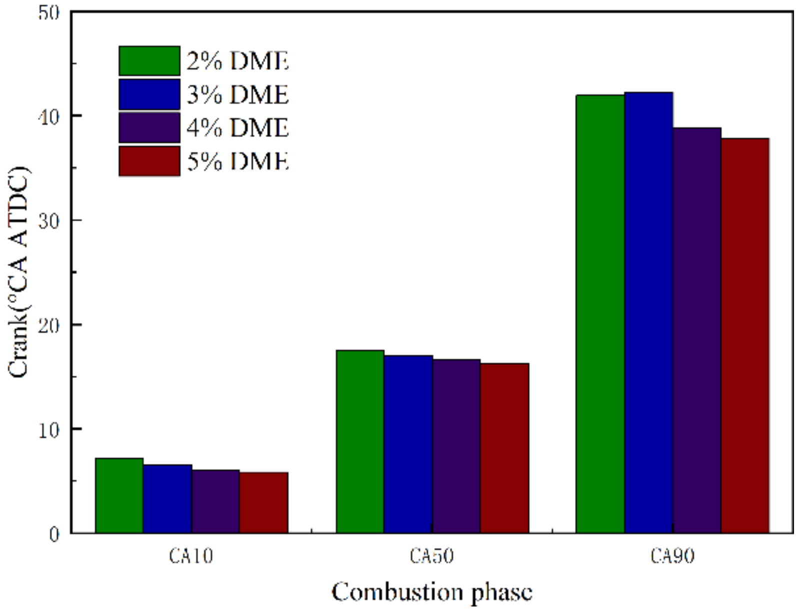

**Fig.10.** Combustion stages at different DME energy ratios(CA10 is defined as the moment when 10% of the total heat release is generated; CA50 is defined as the moment when 50% of the total heat release is generated; CA90 is defined as the moment when 90% of the total heat release is generated)

The combustion of DME produces $CO_2$ and the use of DME should be decreased. Therefore, all subsequent studies were conducted using a DME energy ratio of 2%. Attempts were made to achieve better performance at low equivalence ratio of DME by adjusting the injection strategy.

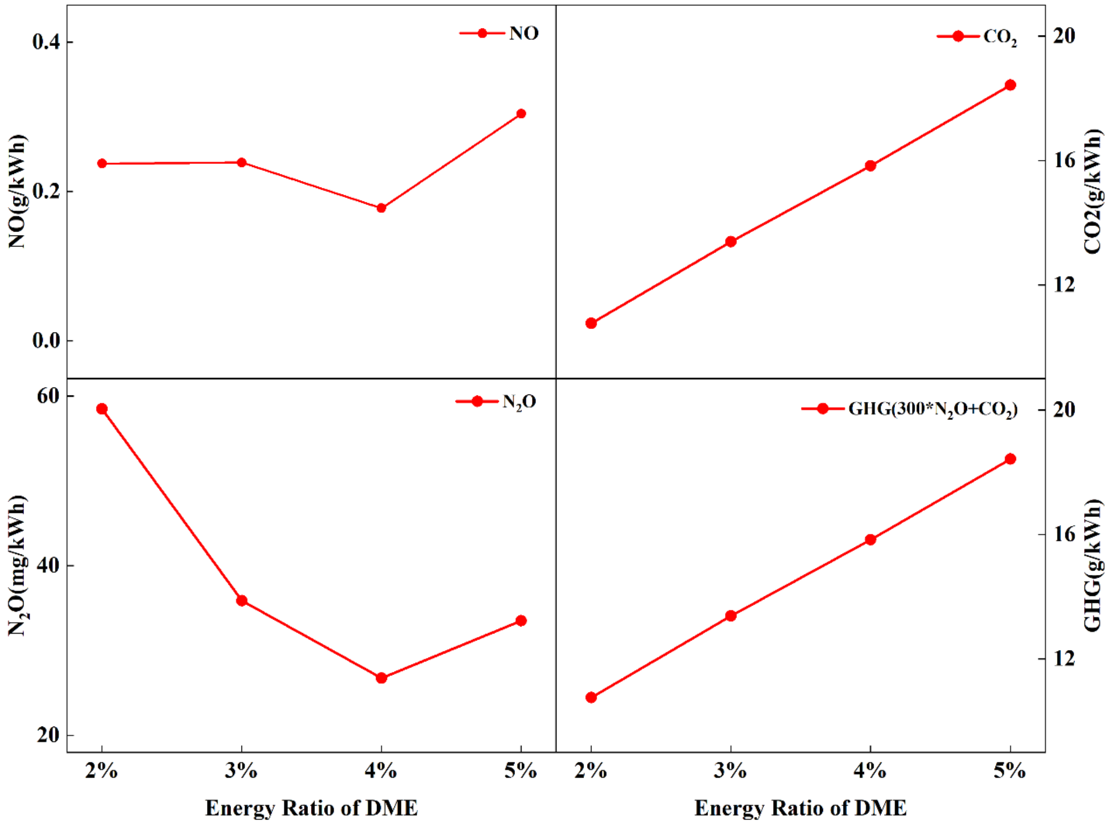

**Fig.11.** NOx and GHG emission at different DME energy ratios (NO accounts for more than 99% of NOx, so NO represents NOx here)

Fig.11 presents the pattern of the effect of different DME energy ratios on NOx and GHG emissions, the energy ratio of DME has little influence on NOx emission, which is mainly due to the long interval between the injection timing of DME and the injection timing of ammonia, resulting in a small difference in ignition effect. Since the greenhouse effect from N2O is about 300 times that of CO2, greenhouse gas emissions can be expressed as $300 \times N_2O + CO_2$. As can be seen from Fig.11, N2O is emitted in smaller quantities and GHG emissions are mainly influenced by CO2 emissions, so the trends and values are similar for both. GHG emissions are increasing with energy ratios ranging from 2% to 5%.

## 3.2 Effect of Injection Timing

### *3.2.1 Effect of Ammonia/DME Injection Intervals*

The above simulation results explored the energy fraction of the pilot DME, and the DME with as low as 2% energy ratio can successfully ignite the ammonia fuel. However, the initial ammonia injec-tion timing was set late, and now the ammonia injection timing is investigated by keeping all the initial conditions unchanged: 103.2 rpm engine speed, 70 MPa DME injection pressure, 50 MPa $NH_3$ injection pressure, and 5°CA before top dead center(BTDC) DME injection timing, while the ammonia injection timing is set to 2.5, 5, and 7.5°CA BTDC, and the cylinder pressure exothermic rate curve is shown in Fig.12, and the temperature curve is shown in Fig.13 The pressure exothermic rate curve is shown in Fig.12 and the temperature curve is shown in Fig.13.After advancing the ammonia injection timing, the burst pressure and pressure rise rate increased significantly, and the ignition point of ammonia was advanced, and the peak exothermic value of ammonia combustion during the rapid combustion period also increased. This is mainly because the ammonia spray oxidation combustion before the accumula-tion of a portion, so the combustion is very violent.

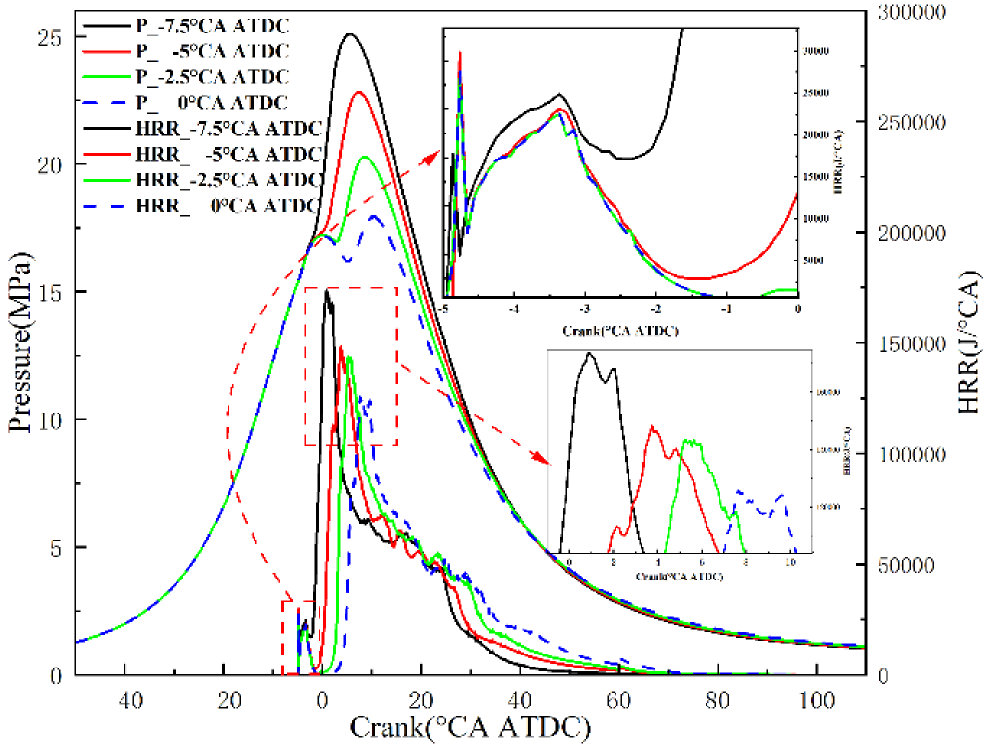

**Fig.12.** Cylinder pressure and heat release rate curves at different injection timing (solid line is the result of adjusted calculation , dashed line is the result of original ammonia injection timing calculation; HRR is heat release rate)

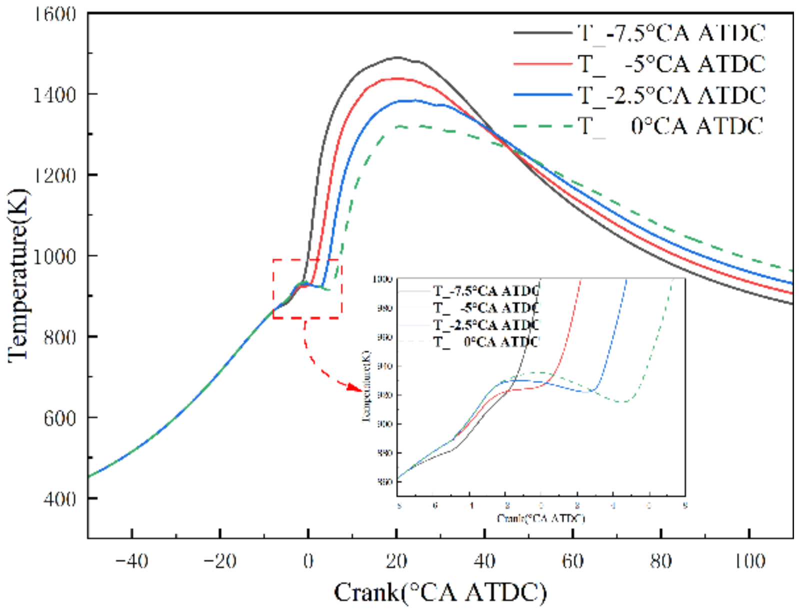

**Fig.13.** In-cylinder temperature curves at different injection timing (solid line is the calculated result after adjustment, dashed line is the calculated result of original ammonia injection timing)

When ammonia injection timing is earlier than DME, the combustion pattern is not the same as in other cases. Since pure ammonia is difficult to be ignited by compression, a portion of the ammonia spray is premixed in the cylinder if the ammonia injection time is early. While DME is easily compressed after being injected, so the DME flame is directly sprayed to the premixed ammonia, and there is a phenomenon of premixed combustion first and then stabilized to diffusion combustion. When DME is injected early, DME forms a flame in the cylinder, and when ammonia is injected into the cylinder, the ammonia spray will be directed to the flame, and the phenomenon of diffusion combustion occurs directly. However, the poor compression ignition characteristics of ammonia and high latent heat of vaporisation make ammonia injected into the cylinder will reduce the temperature of the cylinder, so the ammonia spray will inhibit the combustion of the pilot fuel, pre-injection of ammonia in the example of the combustion stage of the DME exotherm is lower. And according to research, liquid phase ammonia can easily extinguish the flame of pilot fuel[26].When the ammonia is injected late, the liquid ammonia is directly injected into the DME flame, which leads to unstable combustion with large troughs in the exothermic rate in the range of -4°CA ATDC to 0°CA ATDC, which requires adjusting the injection strategy to optimize the ammonia ignition. And when the ammonia is injected early, the internal temperature of the cylinder is higher near the upper stopping point, and after the liquid ammonia is sprayed into the cylinder, the spray edge is rapidly vaporized, and the DME flame can contact more gas-phase ammonia, which results in a better ignition of ammonia by the DME flame. And in order to reduce the inhibition of the pilot flame by liquid ammonia, the DME spray is set so that it does not directly collide with the ammonia spray. Fig.14 demonstrates the ammonia injection moment at -7.5°CA ATDC and -2.5°CA ATDC in the ammonia combustion pre-temperature slice.

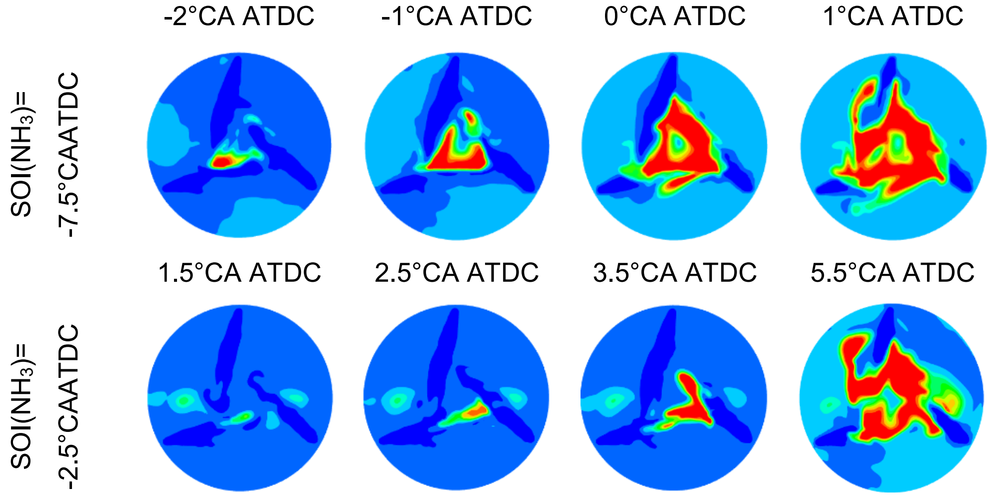

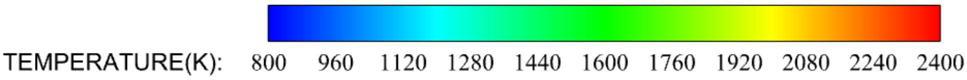

**Fig.14.** Temperature slices at -7.5°CA ATDC and -2.5°CA ATDC at the moment of ammonia injection in the pre-ammonia combustion period.

As can be seen in Fig.14, for uniformity of combustion, one of the three ammonia injectors is offset downwards, the ammonia injected from this injector can easily come into contact with the DME flame that is formed underneath it and thus burn first. Therefore, in the case of the late ammonia injector, the combustion pattern is such that one of the ammonia bundles is ignited and gradually spreads to the other two bundles. In the case of the early ammonia injection, the ammonia combustion is very rapid and occurs simultaneously along the inside of the three ammonia sprays because of premixed combustion. Therefore, the combustion of the pre-injected ammonia case is very intense in the rapid and slow combustion periods, so the maximum burst pressure of the pre-injected ammonia is large, close to 25MPa, and the mechanical strength of the engine cannot withstand such a large pressure. And because the injection timing of DME is -5°CA ATDC, the moment of ignition is earlier than the upper stop, and the upward movement of the piston will do negative work on the exothermic expansion, which requires a coupling study of the injection timing of the fuel and the interval of the dual-fuel injection.

### *3.2.2 DME injection timing and dual-fuel injection interval coupling effects*

The injection timing of DME was set to -10°CA ATDC, -5°CA ATDC and 0°CA ATDC, and the injection timing intervals of ammonia and DME were set to -2.5°CA, 0°CA and 2.5°CA. The effects on ammonia ignition, flame development and emissions were observed. Fig.15 demonstrates the cylinder pressure graphs under the coupled DME injection timing and dual-fuel injection interval conditions, and Fig.16 demonstrates the exothermic rate graphs under different conditions.

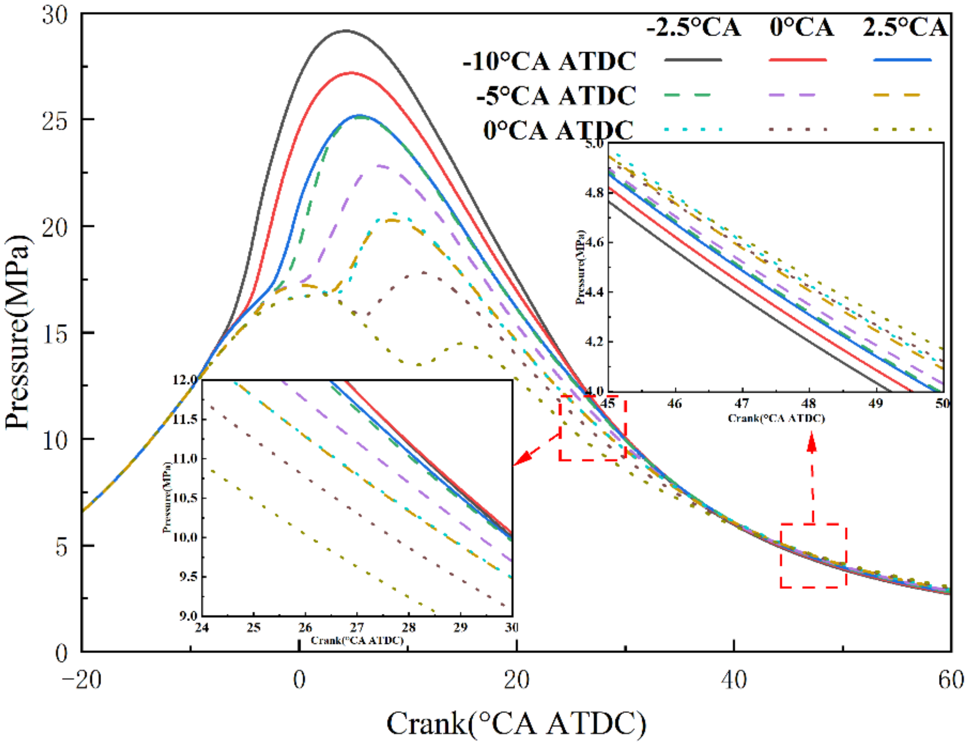

**Fig. 15.** Cylinder pressure curves for different DME injection timing coupled with dual-fuel injection interval conditions (solid line is an example with an injection timing of -10° CA ATDC; dashed line is an example with an injection timing of -5° CA ATDC; dotted line is an example with an injection timing of 0° CA ATDC)

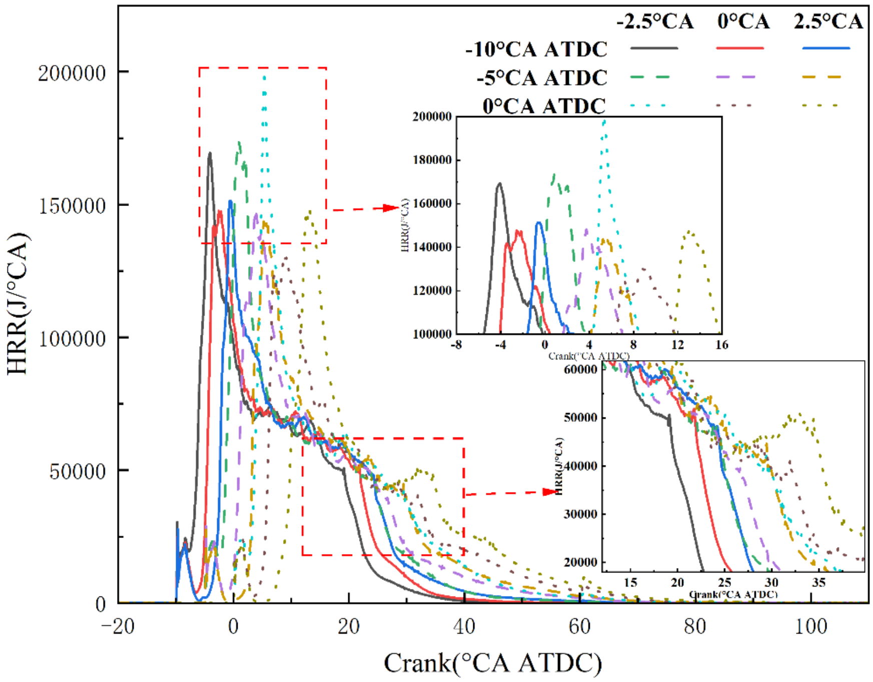

**Fig.16.** Exergy rate plots for different DME injection timing coupled with dual-fuel injection interval conditions (solid line is for the example with injection timing of -10° CA ATDC; dashed line is for the example with injection timing of -5° CA ATDC; dotted line is for the example with injection timing of 0° CA ATDC)

Fig.15 can be found that the earlier injection timing will advance the ignition point, which will increase the pressure rise rate and maximum burst pressure, and the combustion will be violent and work roughly in the rapid and slow combustion periods. And the earlier injection timing counts the afterburning period combustion is more moderate, the exothermic rate is lower. And the piston downward in the afterburning period, the heat dissipation area is enlarged, and the easing of the afterburning period will make the heat loss less, but due to the earlier ignition, it will do a lot of negative work before the upper stopping point, so the output power needs to be further explored. As seen in Fig.16, similar to previous studies, when the DME injection timing is constant, the peak exothermic value decreases and then increases as the ammonia injection moment becomes later and the peak moment is delayed. While the DME injection timing is delayed, the environment inside the cylinder is different at the time of injection, resulting in different combustion of DME. There are two phases of DME combustion exotherm, premixed combustion and diffusion combustion. The cylinder temperature is lower, the evaporation rate of DME oil droplets is slower, more premixed DME burns rapidly after ignition when DME is injected earlier, the peak of premixed combustion is large, and the diffusion combustion time is shorter. This more intense premixed combustion is more effective in igniting ammonia. This may result in faster ignition because the premixed DME has more time to diffuse and more DME diffuses to the setting height of the ammonia injector, and the reactive atmosphere produced by the DME after ignition can reach the injected ammonia spray earlier. In addition, DME injection timing of -10° CA ATDC and -5° CA ATDC have very similar exotherms in the pre-combustion phase of the ammonia combustion, differing only in phase. However, in the later stage of combustion, the exothermic rate decreases faster in the case with early injection timing DME injection timing at 0°CA ATDC and the highest peak exothermic value in the case with an injection interval of -2.5°CA. This is due to the higher pressure and temperature in the cylinder near the upper stop, the DME exotherm is more rapid and the ignition effect on ammonia is better. And since the ignition occurs after the upper stop, the exothermic expansion does basically no negative work on the upward movement of the piston. However, the rate of heat release during the afterburning period is faster compared to the earlier injection timing strategy, which may result in greater heat loss.

Indicated Specific Fuel Consumption (ISFC) is an important metric for judging the performance of an engine, which is defined as the mass of diesel fuel required by the engine to produce 1kWh of output work. Fig.17(a) and 17(b) show the indicated specific fuel consumption and indicated thermal efficiency for different DME injection timing and dual-fuel injection timing interval coupling, respectively.

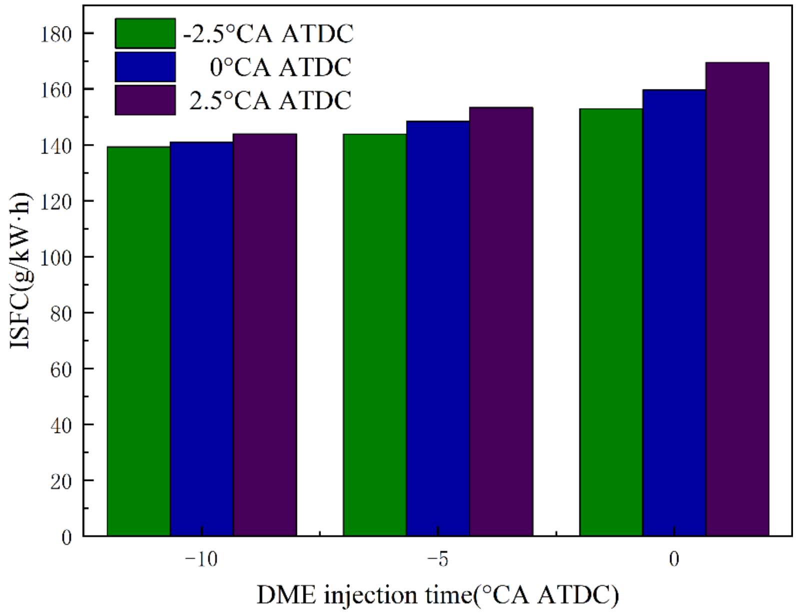

(a)ISFC

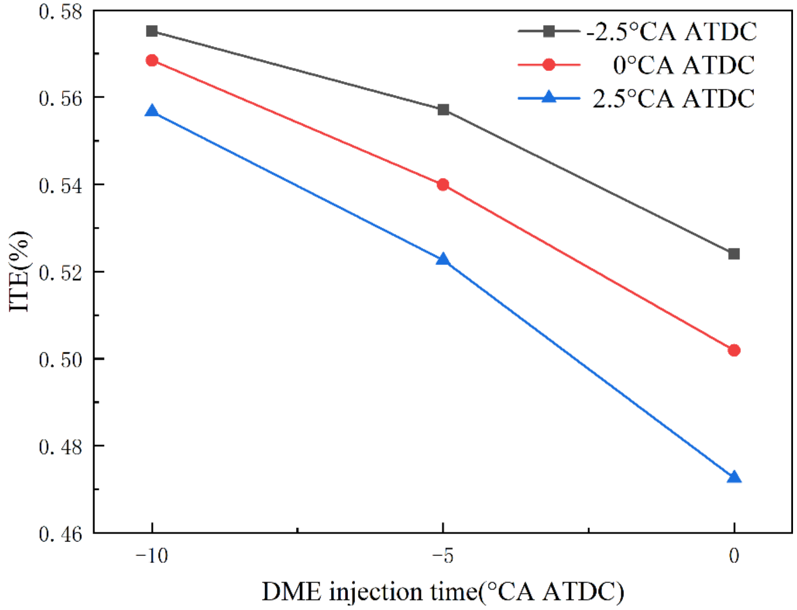

(b)indicated thermal efficiency(ITE)

**Fig. 17.** Indicated Specific Fuel Consumption and Indicated Thermal Efficiency at Different Injection Timing and Injection Timing Intervals

Fig.17 presents a clear pattern, i.e., the fuel consumption gradually increases when the injection interval is varied from -2.5° CA ATDC to 2.5° CA ATDC. While the injection interval is kept constant, the fuel consumption keeps increasing with the postponement of the DME injection timing. Similarly, the ITE decreases with delayed injection timing; and decreases with delayed injection moment. The reduction of fuel consumption by the advance of injection timing is mainly due to the pre-mixed DME in the cylinder realizes multi-point combustion with a faster rate of exothermic heat release, which provides a better thermal atmosphere for the ignition of the ammonia. It makes it easier for ammonia to be ignited and advance the phase of combustion stage. And the reduced fuel consumption with earlier injection interval is mainly affected by the difference between the two combustion methods. When the ammonia is injected in advance, the ammonia gasifies rapidly in the high temperature environment and forms a combustible mixture in the centre of the cylinder. The flame is developed rapidly after DME flame igniting the ammonia/air mixture. And the combustion is mainly concentrated in the centre of the cylinder, where the swirl is weaker and farther away from the cylinder wall, with less heat dissipation and higher thermal efficiency. In addition, the change of both injection strategies will lead to violent combustion or even rough work in the early stage, which decreases the heat release in the later stage which results in a smaller heat loss.

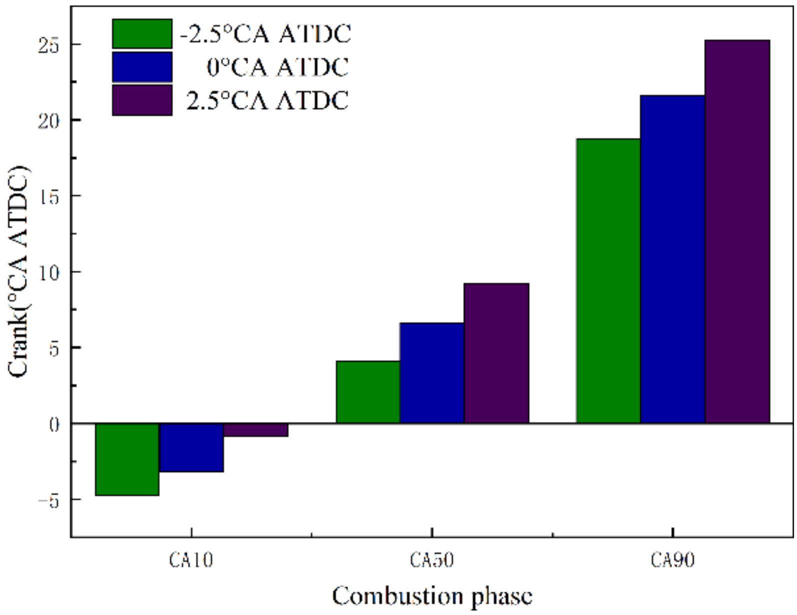

（a）-10°CA ATDC DME Injection

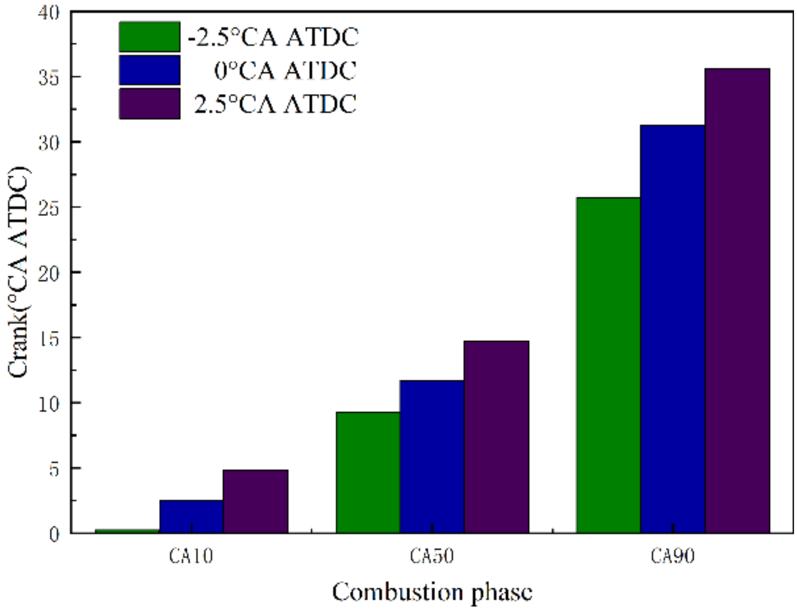

（b）-5°CA ATDC DME Injection

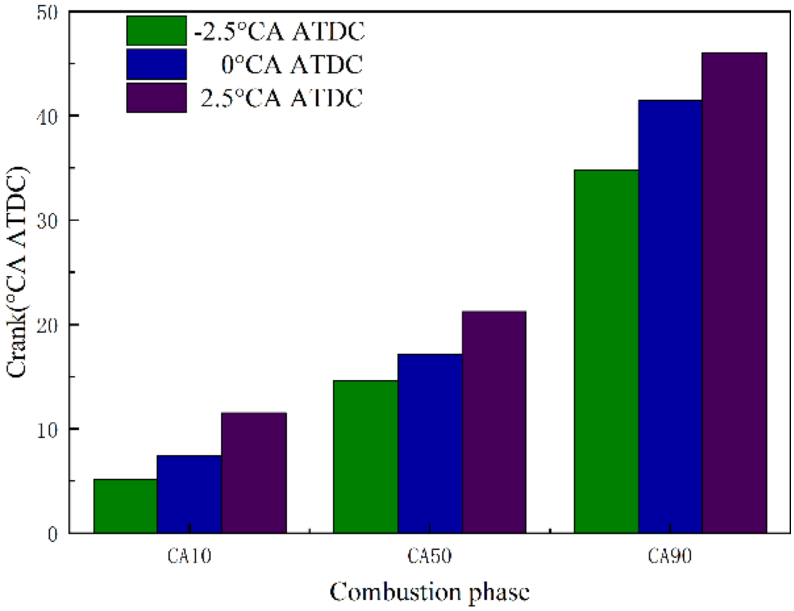

（c）0°CA ATDC DME Injection

**Fig. 18.** Stages of combustion with different injection strategies

Fig.18 shows the combustion stages under different injection strategies, which demonstrates more clearly the effect of different injection strategies on the overall combustion process. When the injection time is advanced, the combustion phase is also advanced, and the CA10 is close to TDC when the injection timing of DME is -5°CA ATDC. In addition, the effect of ammonia injection timing on the combustion phase is similar. The effects of different time intervals of ammonia/DME injection timing on NOx and GHG are illustrated in Fig.19.Earlier injection timing results in more NOx emissions, but lower N2O emissions. Although the injection timing of the -10°CA ATDC produces more NOx emissions, it still does not exceed Tier III emission standards.Liu et al.[27] found that during ammonia combustion, the region of major NO production largely overlaps with the region of high temperatures and low equivalence ratios, and in conjunction with Fig. 13, earlier injection results in higher in-cylinder temperatures, and although ammonia combustion produces mainly fuel-based NOx, it receives less influence from high temperatures than the reactions that generate thermal NOx. Therefore, when the combustion in the cylinder is too intense, more NOx will still be produced. The time interval of ammonia/DME injection timing has a large effect on emissions. If the ammonia injection timing is later, the NOx emissions is lower, but N2O tends to increase with ammonia injection timing delaying.

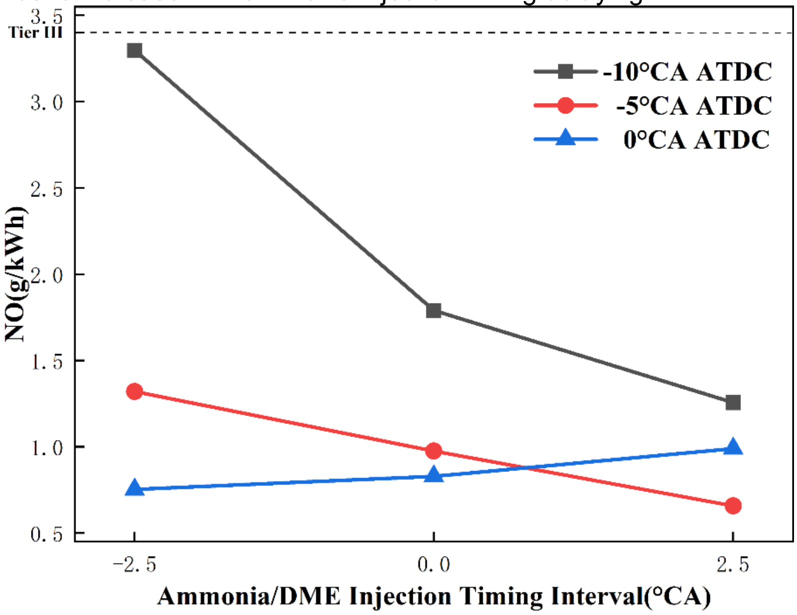

(a)$NO_x$ emission (NO accounts for more than 99% of NOx, so NO represents NOx here)

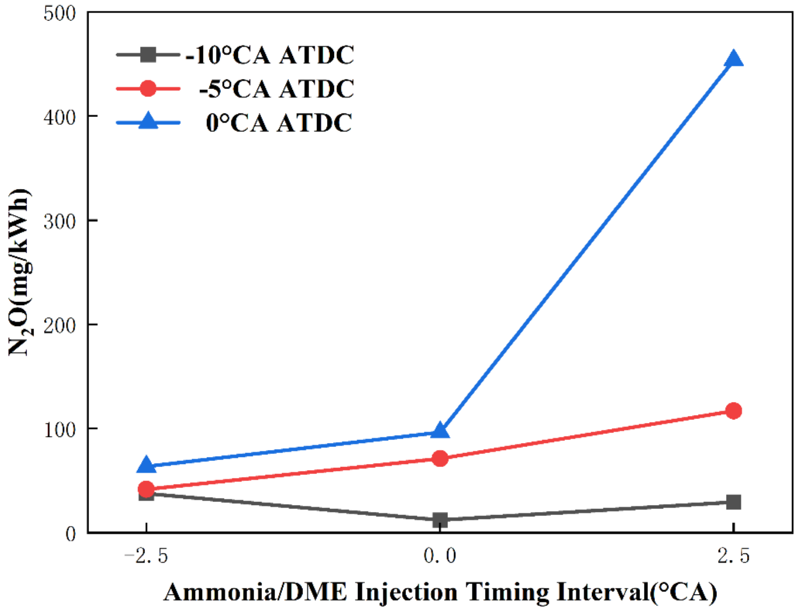

(b)$N_2O$

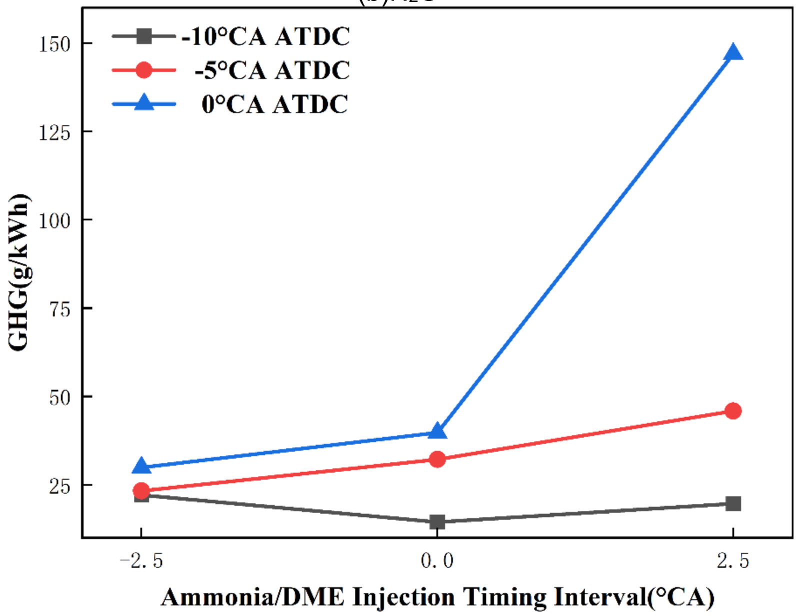

(c)GHG

**Fig. 19.** $NO_x$ and GHG emission at different Ammonia/DME injection timing interval

## Conclusions

In this paper, the ignition process and combustion characteristics of DME-ignited ammonia fuel were investigated, and the following conclusions were obtained:

1. The simulation model constructed in this study enables the ignition of ammonia by DME with an energy ratio as low as 2%. This is due to the fact that the OH and heat produced by DME combustion comes into contact with the head of the ammonia spray, which can quickly oxidise the ammonia spray and cause it to burn.
2. Keeping the DME injection timing unchanged and advancing the ammonia injection timing significantly optimises ignition and combustion. This is mainly due to the premixed gas-phase ammonia in the cylinder, which will not extinguish the DME flame, but will be easily ignited by the pilot flame, and the combustion will be more intense, maintaining the sustainability of the subsequent combustion.
3. When ammonia was sprayed first, the ignition appears in the centre of combustion chamber, which was characterised by premixed combustion. After the premixed flame ignites the three

ammonia oil columns, the combustion changes to diffusion combustion; when ammonia is sprayed later, the ammonia ignites at the head of one of the sprays and gradually ignites the other oil columns, which is characterised by diffusion flame. Appropriate premixed combustion can strengthen the engine performance and improve the thermal efficiency.

4. Advancing the DME injection timing results in an overall advance in the combustion phase and a reduction in fuel consumption. This is due to the lower in-cylinder temperature when injecting earlier, the longer stagnation period of fuel, and the more intense premixed combustion. However, too early injection of DME will lead to rough engine operation, and the mechanical strength of the engine cannot withstand it. Therefore, DME injection timing should be selected after -5°CA ATDC, and ammonia injection timing should be appropriately earlier than DME.
5. The use of DME did not have much impact on NOx emissions, which was mainly due to poor fuel injection strategies. However, premature injection of oil will lead to an increase in NOx emissions.This is mainly due to the fact that premature injection results in more intense combustion, which leads to higher temperatures in the cylinder, thus producing more NOx emissions. On the other hand, N2O is produced mainly at low temperatures, so N2O emissions follow the opposite pattern of NOx emissions. Although the simulation results did not exceed Tie III emission standards, the start of ignition$(SOI)_{DME}$=0°CA ATDC and $SOI_{Ammonia}$=-2.5°CA ATDC solutions produced fewer emissions and greater power performance

## References

[1] UN, Paris Agreement, Paris, 2015.

[2] IMO, 2023 IMO STRATEGY ON REDUCTION OF GHG EMISSIONS FROM SHIPS, Dubai, 2023.

[3] Yeo S J, Kim J, Lee W J. Potential economic and environmental advantages of liquid petroleum gas as a marine fuel through analysis of registered ships in South Korea[J]. Journal of Cleaner Production, 2022, 330: 129955.

[4] Wu S, Wang M, Zou Y. Bidirectional cognitive computing method supported by cloud technology[J]. Cognitive Systems Research, 2018, 52: 615-621.

[5] Midilli A, Ay M, Dincer I, et al. On hydrogen and hydrogen energy strategies: I: current status and needs[J]. Renewable and sustainable energy reviews, 2005, 9(3): 255-271.

[6] Ball M, Wietschel M. The future of hydrogen–opportunities and challenges[J]. International journal of hydrogen energy, 2009, 34(2): 615-627.

[7] Zamfirescu C, Dincer I. Ammonia as a green fuel and hydrogen source for vehicular applications[J]. Fuel processing technology, 2009, 90(5): 729-737.

[8] Liu L, Wu Y, Wang Y. Numerical investigation on the combustion and emission characteristics of ammonia in a low-speed two-stroke marine engine[J]. Fuel, 2022, 314: 122727.

[9] Gray Jr J T, Dimitroff E, Meckel N T, et al. Ammonia fuel—engine compatibility and combustion[J]. SAE Transactions, 1967: 785-807.

[10] Reiter A J, Kong S C. Demonstration of compression-ignition engine combustion using ammonia in reducing greenhouse gas emissions[J]. Energy & Fuels, 2008, 22(5): 2963-2971.

[11] Fleisch T H, Basu A, Gradassi M J, et al. Dimethyl ether: A fuel for the 21st century[M]//studies in surface science and catalysis. Elsevier, 1997, 107: 117-125.

[12] Fleisch T H, Basu A, Gradassi M J, et al. Dimethyl ether: A fuel for the 21st century[M]//studies in surface science and catalysis. Elsevier, 1997, 107: 117-125.

[13] Alam M, Fujita O, Ito K. Performance of NOx reduction catalysts with simulated dimethyl ether diesel engine exhaust gas[J]. Proceedings of the Institution of Mechanical Engineers, Part A: Journal of Power and Energy, 2004, 218(2): 89-95.

[14] Chapman E M. Engine performance and emissions from fuel blends of dimethyl ether (DME) and diesel fuel[M]. American Institute of Chemical Engineers, 2002.

[15] Hansen J B, Mikkelsen S E. DME as a Transportation Fuel[J]. Prepared for the Danish Road Safety and Transport Agency and the Danish Environmental rotection Agency, Lyngby, Denmark, 2001.

[16] Semelsberger T A, Borup R L, Greene H L. Dimethyl ether (DME) as an alternative fuel[J]. Journal of power sources, 2006, 156(2): 497-511.

[17] Gross C W, Kong S C. Performance characteristics of a compression-ignition engine using direct-injection ammonia–DME mixtures[J]. Fuel, 2013, 103: 1069-1079.

[18] Dai L, Hashemi H, Glarborg P, et al. Ignition delay times of $NH_3$/DME blends at high pressure and low DME fraction: RCM experiments and simulations[J]. Combustion and Flame, 2021, 227: 120-134.

[19] Dai L, Gersen S, Glarborg P, et al. Experimental and numerical analysis of the autoignition behavior of $NH_3$ and $NH_3/H_2$ mixtures at high pressure[J]. Combustion and flame, 2020, 215: 134-144.

[20] Glarborg P, Miller J A, Ruscic B, et al. Modeling nitrogen chemistry in combustion[J]. Progress in energy and combustion science, 2018, 67: 31-68.

[21] Hashemi H, Christensen J M, Glarborg P. High-pressure pyrolysis and oxidation of DME and DME/CH4[J]. Combustion and Flame, 2019, 205: 80-92.

[22] Stagni A, Cavallotti C, Arunthanayothin S, et al. An experimental, theoretical and kinetic-modeling study of the gas-phase oxidation of ammonia[J]. Reaction Chemistry & Engineering, 2020, 5(4): 696-711.

[23] Issayev G, Giri B R, Elbaz A M, et al. Ignition delay time and laminar flame speed measurements of ammonia blended with dimethyl ether: A promising low carbon fuel blend[J]. Renewable Energy, 2022, 181: 1353-1370.

[24] Yin G, Li J, Zhou M, et al. Experimental and kinetic study on laminar flame speeds of ammonia/dimethyl ether/air under high temperature and elevated pressure[J]. Combustion and Flame, 2022, 238: 111915.

[25] Liu L, Wu Y, Wang Y, et al. Numerical investigation on the combustion and emission characteristics of ammonia in a low-speed two-stroke marine engine[J]. Fuel, 2022, 314: 122727.

[26] Zhang Z, Long W, Cui Z, et al. Visualization study on the ignition and diffusion combustion process of liquid phase ammonia spray ignited by diesel jet in a constant volume vessel[J]. Energy Conversion and Management, 2024, 299: 117889.

[27] Liu L, Wu J, Liu H, et al. Study on marine engine combustion and emissions characteristics under multi-parameter coupling of ammonia-diesel stratified injection mode[J]. International Journal of Hydrogen Energy, 2023, 48(26): 9881-9894.

# Session 1.4 AMMONIA COMBUSTION TECHNIQUES

# The Role of Ammonia ($NH_3$) Cracking and Heat Recovery in Spark-Ignition Engines

M. Wu[1], A. Cova-Bonillo[1], N.D. Khedkar[1], G. Brinklow[1], J.M. Herreros[1], S. Zeraati Rezaei[1], A. Tsolakis[1](*), P. Millington[2], S. Alcove Clave[2], Andrew P.E. York[2]

[1]The University of Birmingham. Edgbaston, Birmingham, B15 2TT, United Kingdom.
[2]Johnson Matthey Technology Centre, Blount's Court, Sonning Common, Reading, RG4 9NH, UK

(*) Author for correspondence:
E-mail: a.tsolakis@bham.ac.uk
Telephone: +(44) 0121 414 3344

**Abstract.** Write here the abstract of your paper Ammonia ($NH_3$) stands out as a promising zero-carbon fuel for transportation. However, its direct use in internal combustion engines (ICEs) is hindered by its low reactivity. One option to alleviate this challenge is to crack the ammonia into hydrogen ($H_2$) which is much more reactive during its combustion in engines. This study first focused on experimentally studying catalytic ammonia cracking using waste heat from the engine exhaust gas to produce a reformate mixture of hydrogen, nitrogen and ammonia. A tailored catalytic small-scale rig has been coupled to the engine exhaust enabling to decouple and understand the effects of cracking catalyst temperature and residence time. The subsequent part of the study investigated the combustion and emissions characteristics of the reformate mixture to fuel a modern multi-cylinder SI engine by substituting the gasoline fuel up to an energy substitution ratio (ESR) of 30%. Results demonstrated that the fuel's heating value could be increased by up to 13% thanks to the waste energy recovered from the hot engine exhaust gas. The combustion-promoting properties of the hydrogen within the reformate mixture was able to increase combustion stability, thus allowing for leaner operation. Furthermore, the displacement of gasoline from the fuel achieved a reduction in $CO_2$ emissions by a third. Special attention was paid to the formation of $NO_X$ and slip of $NH_3$ which have been reported as key challenges for ammonia and hydrogen combustion systems. These findings provide new knowledge contributing into the implementation of ammonia cracking for ICEs, enhancing overall system efficiency while reducing carbonaceous emissions.

**Notation**

| | |
|---|---|
| *CAD* | *Crank Angle Degree.* |
| *CFR* | *Cooperative Fuels Research.* |
| *CPSI* | *Channels Per Square Inch.* |
| *FTIR* | *Fourier Transform Infrared Spectroscopy.* |
| *GHG* | *Greenhouse Gas.* |
| *GHSV* | *Gas Hourly Space Velocity.* |
| *ICE* | *Internal Combustion Engines.* |
| *LHV* | *Lower Heating Value.* |

## 1. Introduction

The pursuit of sustainable fuels has sparked interest in ammonia ($NH_3$). Its versatility makes it suitable for internal combustion engines (ICEs) and fuel cells [1] [2] [3]. With an appealing zero-carbon footprint, notable energy density, and logistical advantages in production, transportation, and storage, ammonia emerges as a promising future fuel, playing a pivotal role in the transition towards a decarbonized economy [4]. However, challenges related to its high ignition temperature and slow flame propagation, hinder its widespread adoption as a fuel [2]. Different techniques have been explored to overcome these characteristics, among them plasma assisted combustion, oxygen enrichment and hydrogen enrichment [5]. The latter has been extensively studied, as the combustion promoting characteristics of hydrogen can lead to improved combustion of ammonia mixtures [6]. There are challenges associated to combustion of mixtures of different gasses where onboard storage is concerned. Yet, this can be overcome as hydrogen can be produced via electrochemical [7] or via catalytic [8] [9] decomposition of ammonia using waste exhaust heat. This allows for an increase in thermal efficiency due to the recovery of waste heat from the exhaust and eliminates the need to carry separate hydrogen and ammonia storage vessels onboard.

On board ammonia cracking offers a solution to the ammonia combustion challenge by partially converting ammonia into hydrogen to significantly enhance its combustion properties [10]. Ammonia catalytic cracking is a process where ammonia decomposes into hydrogen and nitrogen using a base metal or noble metal catalyst [11] as shown in Equation 1

$$2NH_3 \rightarrow 3H_2 + N_2 \qquad \Delta H = 46.2\ \text{kJ/mol}$$

Equation 1. Ammonia decomposition into hydrogen and nitrogen.

Ammonia cracking is favoured at high temperature and at low pressure owing to its endothermic nature, and higher numbers of moles of products compared to reactants. Thermodynamically, at 1 bar, the process described by equation 1 require at least 350°C to achieve >99% ammonia conversion [11] [12].

The use of hydrogen to improve ammonia combustion in ICEs has been investigated to increase combustion stability, improve engine performance, and reduce emissions. Ryu et al. [13], examined how a ruthenium-coated ammonia dissociation catalyst affected the performance and emissions of a supercharged cooperative fuels research (CFR) engine fuelled with a mixture of ammonia and gasoline. This resulted in increased engine power and reduced emissions, especially at low and medium flow rates. They reported improved combustion efficiency and reduced fuel consumption, with notable reductions in CO, HC, $NH_3$ and NOx emissions. Wang et al. [14] studied the autothermal reforming of $NH_3$ over a ruthenium catalyst by replacing air with diesel engine exhaust gases to provide oxygen for the exothermic reactions. They found that the $O_2/NH_3$ ratio and $NH_3$ concentration significantly influenced the hydrogen yield and reforming efficiency. The introduction of the obtained reformed into the engine intake reduced carbon emissions. However, excessive addition of $NH_3$ caused adverse effects such as increased NOx emissions. Comotti and Frigo [15] developed an on-board hydrogen generation system using a ruthenium-based catalyst to convert ammonia into hydrogen, achieving high system efficiency. The system operates autonomously or in tandem with the engine, optimizing performance and reducing emissions. They noted that while higher $H_2$ flow rates improve fuel economy, they raise NOx emissions, which are mitigated by exhaust aftertreatment. In contrast to the above-mentioned works, Sittichompoo et al [8] used a rhodium-platinum catalyst, previously developed for fuel reforming studies. They produced a $H_2$-$N_2$ mixture with 15% more calorific value than the original ammonia by on-board conversion of ammonia using the engine's exhaust. They were able to replace up to 30% of the gasoline in an SI engine and achieve significant $CO_2$ reduction. In two prior studies, catalytic processes employed temperatures between 450 and 500°C by introducing a small amount of oxygen to promote oxidative reactions and accelerate the ammonia decomposition [16] with a compromise in overall energy efficiency of the process.

This study aims to demonstrate the feasibility of replacing 30% of the energy supply in a gasoline-fuelled spark-ignition (SI) engine with a hydrogen/ammonia mixture produced from an ammonia-cracking device. By harnessing the energy potential of the engine's exhaust gas, the partial dissociation of ammonia using a dedicated catalyst to yield hydrogen was investigated. The impact of this partial substitution at stoichiometric and lean conditions on engine performance and emissions was rigorously evaluated under controlled operating conditions, specifically maintaining a constant engine speed of 2000 rpm and torque of 20 Nm. The findings of this investigation will elucidate the viability and implications of using ammonia cracking for sustainable power generation in SI engines.

## 2. Experimental

### 2.1 Experimental setup

To investigate the feasibility of using reformate mixtures from a catalytic ammonia cracking heat recovery system for combustion, both an ammonia cracking catalyst and a modern SI engine were employed. All testing was completed in the Wyszynski Laboratory at the University of Birmingham. The set-up for both the ammonia cracking and reformate mixture is shown schematically in **Fig. 1** with additional detail provided below.

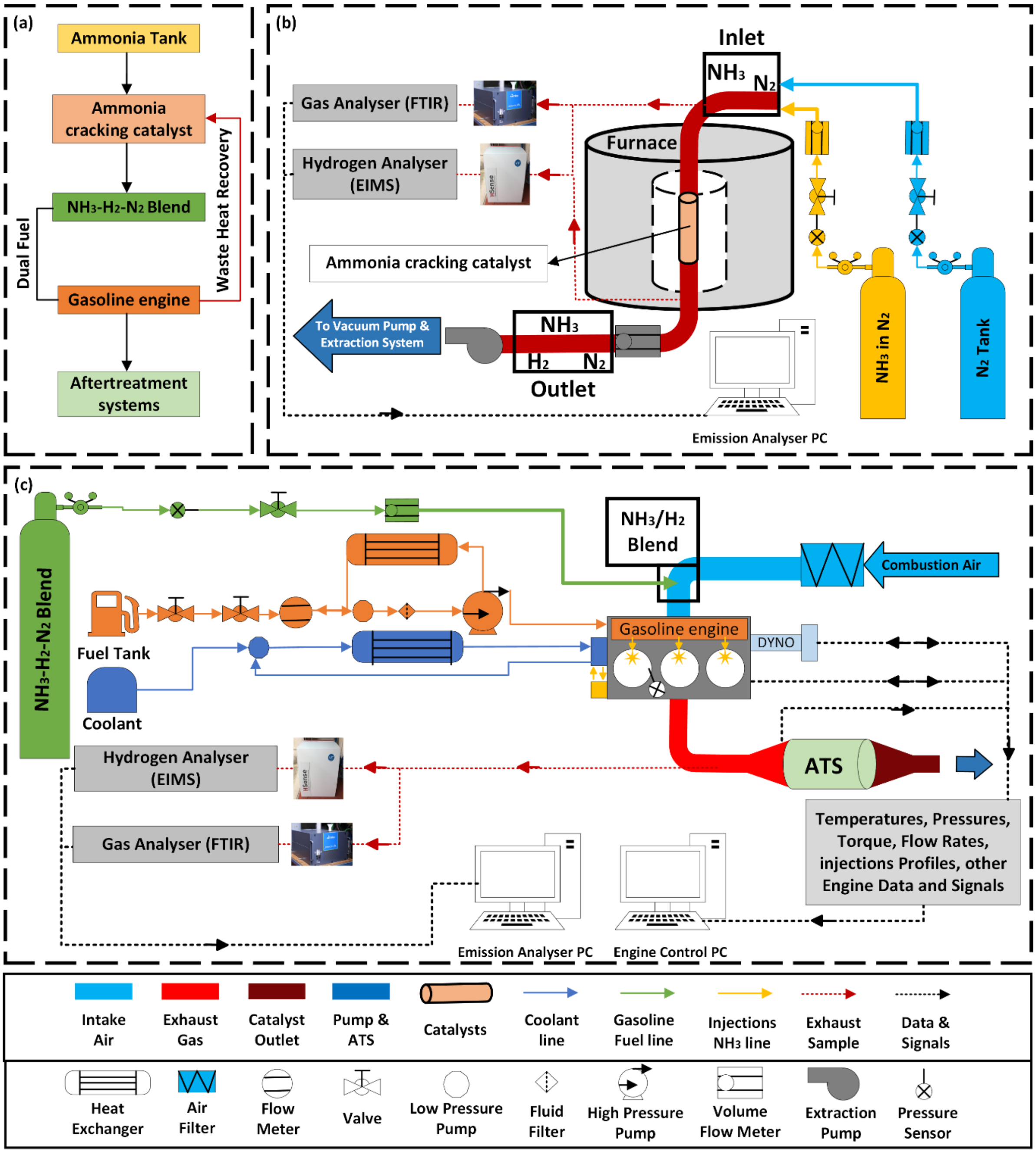
(a)
Ammonia Tank
Ammonia cracking catalyst
NH3-H2-N2 Blend
Gasoline engine
Aftertreatment systems
Dual Fuel
Waste Heat Recovery
(b)
Inlet
NH3
N2
Gas Analyser (FTIR)
Hydrogen Analyser (EIMS)
Furnace
Ammonia cracking catalyst
To Vacuum Pump & Extraction System
NH3
H2
N2
Outlet
NH3 in N2
N2 Tank
Emission Analyser PC
(c)
NH3-H2-N2 Blend
NH3/H2 Blend
Combustion Air
Fuel Tank
Coolant
Gasoline engine
DYNO
ATS
Hydrogen Analyser (EIMS)
Gas Analyser (FTIR)
Temperatures, Pressures, Torque, Flow Rates, injections Profiles, other Engine Data and Signals
Emission Analyser PC
Engine Control PC
Intake Air
Exhaust Gas
Catalyst Outlet
Pump & ATS
Catalysts
Coolant line
Gasoline Fuel line
Injections NH3 line
Exhaust Sample
Data & Signals
Heat Exchanger
Air Filter
Flow Meter
Valve
Low Pressure Pump
Fluid Filter
High Pressure Pump
Volume Flow Meter
Extraction Pump
Pressure Sensor

**Fig. 1.** Engine and exhaust system configuration scheme

## 2.2 Ammonia cracking catalyst setup

The ammonia cracking catalyst used was a ruthenium dioxide catalyst on an alumina support provided by Johnson Matthey with monolith dimensions of 25.4 mm diameter x 76.2 mm length. The catalyst cell density was 400 channels per square inch (CPSI). The catalyst was housed in a vertical reactor within a Carbolite GVA 12/600 3.9 kW tube furnace for precise temperature control (**Fig. 1**b). The setup was instrumented with a K-type thermocouple placed at the inlet to measure catalyst inlet temperature. The volumetric concentrations of the reformate gas out of the catalyst were measuring using an MKS 2030 multi-gas Fourier-transform infrared spectroscopy (FTIR) emission analyser to measure $NH_3$, while a

V&F Electron Impact Ionization Mass Spectrometry (EIMS)-HSense analyser was used to measure $H_2$. Ammonia was supplied to the catalyst via a calibrated flow meter from a cylinder containing 5% ammonia in a balance of nitrogen gas (carrier/diluter gas).

For reference and context, the decomposition equilibrium for ammonia was calculated using the Chemical and Phase Equilibrium Calculation module of Chemkin-Pro. This analysis applied the reaction kinetic mechanism of Stagni et al. [17] (31 species, 203 reactions), a mechanism extensively tested in different scenarios and resulting in a reliable model [18] [19]. A constant pressure and enthalpy setting were applied with a temperature range between 350 °C and 650 °C at a pressure of 1 atm.

### 2.3 Ammonia reformate fuelled engine setup

The effect of the reformate mixtures generated via ammonia cracking on combustion were then tested in a modern 3-cylinder 1.5 litre turbocharged SI engine (details in Table 1). All ICE combustion studies were performed at a constant engine speed of 2000 rpm and a load of 20 Nm. A low load engine operation condition has been studied to represent challenging $NH_3$ combustion conditions (low temperature) which could require the assistance of $H_2$ to limit unburnt $NH_3$. Higher engine loads will increase in-cylinder temperature facilitating $NH_3$ combustion.

**Table** 1. Engine specification

| **Characteristic** | **Value** |
|---|---|
| Displacement | 1.5 l |
| Number of cylinders | 3 |
| Bore | 84 mm |
| Stroke | 90 mm |
| Compression ratio | 11:01 |
| Max power | 136 kW @ 6000 rpm |
| Max torque | 270 Nm @ 1750-3500 rpm |

The hardware of the engine was modified to include injection of mixtures of hydrogen, ammonia and nitrogen supplied via a pressurised gas bottle into the intake manifold. Two different mixtures were used. Mixture 1 (M1) included 5% $NH_3$, 70% $H_2$ and 25% $N_2$ whilst Mixture 2 (M2) contained 10% $NH_3$, 70% $H_2$ and 20% $N_2$ as shown in **Fig. 1c**. The injection of the ammonia reformate mixtures was controlled using a calibrated flowmeter. The air-fuel ratio of the engine was adjusted automatically by the ECU. This was done by adjusting the gasoline injection. The engine speed and load were controlled using a 75 kW AC dynamometer. The engine was instrumented with a piezoelectric AVL GH14P pressure transducer and AVL optical crank angle encoder in order to measure the in-cylinder pressure. This study recorded the in-cylinder pressure data from 200 consecutive cycles and reports the average combustion parameters for each cycle. The heat release rate (HRR) was calculated from the in-cylinder pressure as per Equation 2.

$$HRR = \frac{\gamma}{\gamma - 1} p \frac{dV}{d\theta} + \frac{1}{\gamma - 1} V \frac{dp}{d\theta}$$

Equation 2. Calculation for heat release rate

For Equation 2, the variables *p* and *V* represent the instantaneous in-cylinder pressure and volume, respectively, while $\gamma$ denotes the specific heat ratio (assumed to be 1.33) of the in-cylinder gases. The HRR curve was also normalised to allow for calculation of the 50% cumulative heat release value, which is denoted as MFB50 in this article. During the study, the mixture flow was adjusted while the spark timing of the engine was adjusted using the ATI Vision software to maintain an MFB50 between 3 and 5 CAD aTDC. Engine stability was also observed through calculating the coefficient of variation for indicated mean effective pressure ($COV_{imep}$). **Fig. 2** shows the $COV_{imep}$ for each condition tested. The results show that the $COV_{imep}$ was lower than 2% at each condition. This indicates that the combustion was stable at the operating conditions studied in this work.

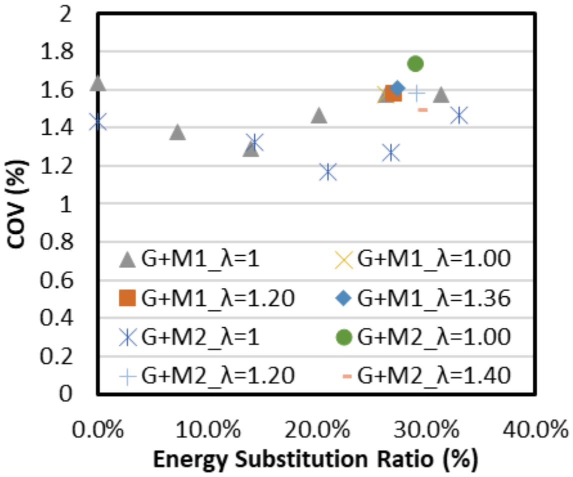

**Fig. 2.** $COV_{imep}$ for energy substitution ratio and air-fuel ratio

### 2.4 Ammonia cracking experimental procedure

Three different levels of gas hourly space velocity (GHSV) and catalyst inlet temperatures were studied, as shown in Table 2. At each GHSV, the flow rate of ammonia at the inlet was varied to ensure that the ammonia concentration at the inlet was the same (approximately 4300 ppm). Temperatures were ramped from 100°C to 550°C at a rate of 5°C/min.

**Table** 2. Experimental methods for ammonia cracking catalysts

| | **5% $NH_3$ in $N_2$** (l/min) | **$N_2$** (l/min) | **Total flow** (l/min) | **$NH_3$** (ppm) | **GHSV** ($h^{-1}$) |
|---|---|---|---|---|---|
| Case 1 | 1.0 | 10 | 11.0 | 4288 | 17,000 |
| Case 2 | 1.5 | 15 | 16.5 | 4206 | 26,000 |
| Case 3 | 2.0 | 20 | 22.0 | 4347 | 34,000 |

For the ammonia cracking reformate combustion tests, pure gasoline was taken as the baseline fuel, i.e. 0% ammonia reformate was used. The two different gas mixture bottles used to simulate the ammonia reformate mixture (M1 and M2) were both tested at the same engine conditions as the baseline. This led to ammonia/hydrogen molar ratios of 0.071 and 0.143 in M1 and M2, respectively, corresponding to conversions of $NH_3$ to $H_2$ of 90% in M1 and 83% in M2. The performance and emissions of the engine with the addition of dual fuel were recorded using the data logged from the ECU and the emissions measured from the MKS FTIR and the V&F HSense. The experimental procedure is summarised in Table 3.

**Table** 3. Dual fuel experimental procedure

| **Mixture composition** | **Mixture ESR (%)** | **Lambda** |
|---|---|---|
| M1: 5% $NH_3$ / 70% $H_2$ / 25% $N_2$ | 7.3 | 1.0 |
| | 14.0 | 1.0 |
| | 20.2 | 1.0 |
| | 26.4 | 1.0 |
| | 31.4 | 1.0 |
| | 27.9 | 1.2 |
| | 27.8 | 1.36 |
| M2: 10% $NH_3$ / 70% $H_2$ / 20% $N_2$ | 14.4 | 1.0 |
| | 21.1 | 1.0 |
| | 26.8 | 1.0 |
| | 33.0 | 1.0 |
| | 29.5 | 1.0 |
| | 29.0 | 1.2 |
| | 28.9 | 1.4 |

### 2.5 Calorific value of the ammonia cracking

**Fig. 3** shows the theoretical change in enthalpy of the ammonia cracking process based on 100% ammonia conversion for an amount of $NH_3$ equivalent to an energy content of 1 MJ. Here it can be seen that since the produced reformate gas mixture of hydrogen and nitrogen contains 1.13 MJ of energy comparted to the 1 MJ of energy contained within the ammonia energy can be recovered to increase the energy content of the fuel by 13%. Since 100% ammonia conversion is not always possible to achieve due to either lack of energy or reaction kinetics often only 80% to 90% conversion is achieved. In this case the increase in energy content is 10.1% and 11.4% respectively. In this study, the ammonia reformate mixtures tested were based on both 80% and 90% ammonia conversion with a flow rate of 50 l/min of products (hydrogen, nitrogen and uncracked ammonia). This requires 0.61 kJ/s and 0.73 kJ/s which equates to approximately 7.3% and 8.8% heat recovery from the waste engine exhaust heat. The magnitude of energy recovery approximately constitutes 3% of the total combustion energy of the fuel.

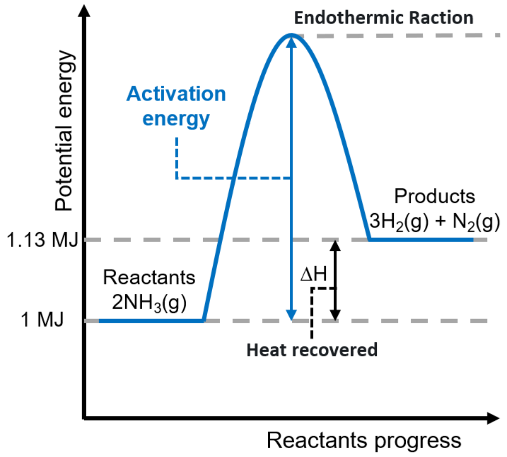

**Fig. 3.** The Heat Recovery of ammonia by endothermic reactions as 100% $NH_3$ cracking

The effect of ammonia conversion rate has a strong influence on the amount of heat that can be recovered. The effect of heat recovered compared to ammonia conversion rate is shown in Table 4. To calculate the lower heating value (LHV) of the mixture Equation 3 was used where $\mathrm{Mixture_{LHV}}$ is the lower calorific values of the ammonia cracking product, with $\mathrm{M_r}$ and $\mathrm{N}$ as the molecular mass and number of moles respectively.

$$LHV_{Mixture} = \frac{(LHV_{H_2} \times M_{r_{H_2}} \times N_{H_2}) + (LHV_{NH_3} \times M_{r_{NH_3}} \times N_{NH_3}) + (LHV_{N_2} \times M_{r_{N_2}} \times N_{N_2})}{(M_{r_{H_2}} \times N_{H_2}) + (M_{r_{NH_3}} \times N_{NH_3}) + (M_{r_{N_2}} \times N_{N_2})}$$

Equation 3. Calculation for heat release rate

**Table 4.** Heat recovery depending upon different ammonia conversion rates

| $NH_3$ Inlet (MJ) | $NH_3$ conversion (%) | Heat recovered (%) | Increase in enthalpy (MJ) | $NH_3/H_2$ products (MJ) |
|---|---|---|---|---|
| 1 | 100 | 13 | 0.13 | 1.13 |
| 1 | 90 | 11 | 0.11 | 1.11 |
| 1 | 80 | 10 | 0.10 | 1.10 |
| 1 | 70 | 9 | 0.09 | 1.09 |
| 1 | 60 | 8 | 0.08 | 1.08 |
| 1 | 50 | 6 | 0.06 | 1.06 |
| 1 | 40 | 5 | 0.05 | 1.05 |
| 1 | 30 | 4 | 0.04 | 1.04 |
| 1 | 20 | 3 | 0.03 | 1.03 |
| 1 | 10 | 1 | 0.01 | 1.01 |
| 1 | 0 | 0 | 0.00 | 1.00 |

## 3. Experimental

### 3.1 Ammonia cracking catalyst analysis

**Fig.** 4a shows that the ammonia conversion ($NH_{3Conv}$) depends on catalyst inlet temperature and GHSV. At approximately 300°C, the catalytic decomposition of ammonia into hydrogen was observed to start. It was also observed that $NH_3$ conversion decreased with increasing GHSV. The light-off temperatures were identified at 398°C, 427°C, and 490°C for GHSVs of 18,000 $h^{-1}$, 25,000 $h^{-1}$, and 35,000 $h^{-1}$ respectively. The point of 90% ammonia conversion occurred at 450°C and 520°C for GHSV of 18,000 $h^{-1}$ and 25,000 $h^{-1}$ respectively. However, at 35,000 $h^{-1}$, 90% ammonia conversion was not achieved at temperatures higher than 550°C. The shade area in the figure “Exhaust temperature window” indicate the actual engine exhaust temperatures available for the ammonia decomposition. **Fig. 4b**, which mirrors ammonia conversion, shows that $H_2$ concentration in the catalyst product increases with temperature but decreases with higher GHSV. At a GHSV of 18,000 $h^{-1}$, the exhaust gas temperature window for low load engine conditions allows for 70-90% $NH_3$ cracking, achieving a $H_2$ concentration 4000-5500 ppm. Further investigation will be required to elucidate the maximum $H_2$ concentration obtained from the cracking process at the various GHSV studied.

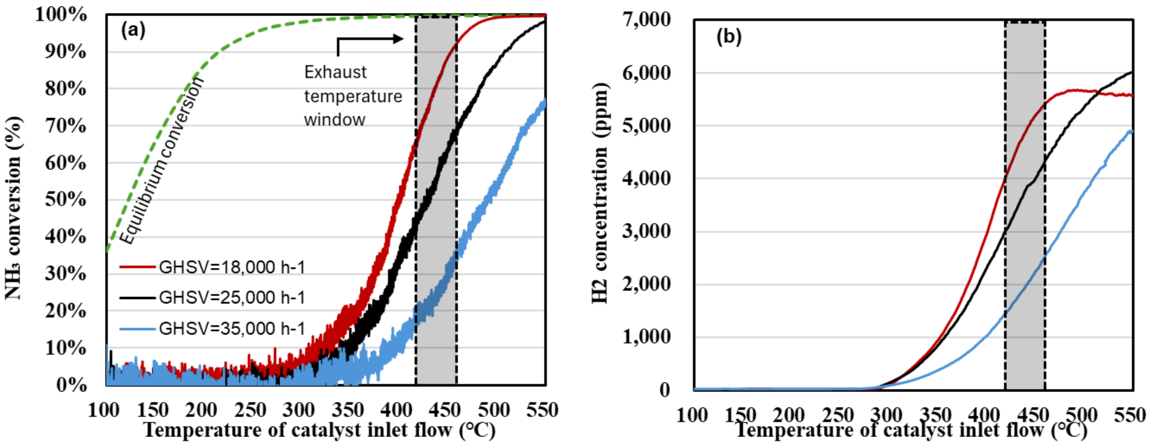

**Fig. 4.** Experimental temperature and gas hourly space velocities (GHSV) dependent compositions of a) Ammonia conversion and b) hydrogen formation

The reaction mechanism occurring at the catalyst surface depends on the nature of the catalyst (the type of metal(s), support, load, the existence or not of promoter). It has been generally accepted that the sequence of reactions that explains the ammonia decomposition process is described through Equation 4 to Equation 9. These reactions describe the initial adsorption of ammonia on an active site of the catalyst (*), followed by successive dehydrogenation and re-combinative desorption to $N_2$ and $H_2$ from the surface to the bulk of the fluid.

$$NH_3 + * \leftrightarrow NH_3(*)$$

Equation 4. Ammonia adsorption

$$NH_3(*) + * \leftrightarrow NH_2(*) + H(*)$$

Equation 5. N-H bond cleavage

$$NH_2(*) + * \leftrightarrow NH(*) + H(*)$$

Equation 6. N-H bond cleavage

$$NH(*) + * \leftrightarrow N(*) + H(*)$$

Equation 7. N-H bond cleavage

$$2H(*) \leftrightarrow H_2(g) + 2(*)$$

Equation 8. Hydrogen recombination/desorption

$$2N(*) \leftrightarrow N_2(g) + 2(*)$$

Equation 9. Nitrogen recombination/desorption

As a general trend [11], it is found that the rate limiting stage is comprised of the $NH_3$ decomposition reactions (Equation 5 and Equation 7), breaking the N-H bonds, for this catalyst configuration ($Ru/Al_2O_3$). The increase in $NH_3$ conversion with temperature is due to the higher kinetic energy of ammonia molecules, which facilitates the breaking of N-H bonds. At higher temperatures, there are more collisions between ammonia molecules and catalyst active sites, increasing the probability of the decomposition reaction occurring. The decrease in $NH_3$ conversion with GHSV is because there is less contact time between ammonia molecules and catalyst and the reaction becomes kinetic limited.

## 3.2 Combustion analysis

### *3.2.1 Effect of gasoline substitution with $NH_3/H_2$ on combustion characteristics*

**Fig. 5** shows peak in cylinder pressure recorded in the expansion stroke rose with gasoline fuel substitution with $H_2$ and $NH_3$ mixture. The maximum pressure for gasoline combustion was 17.5 bar, while 19.0 bar and 18.2 bar were recorded for gasoline with 31.4% M1 and 33.0% M2 mixture respectively. This indicates improved combustion efficiency with higher hydrogen content in the mixtures. Hydrogen has been reported to increase the pool of highly efficient radicals ($OH^{\cdot}$) from the start of combustion, thus accelerating the combustion process. It is important to note that spark timing (ST) was systematically advanced by increasing the ESR to maintain stability and achieve a mid-burning fraction (MBF50) around 4.5 CA aTDC. The slightly lower pressure rise in the Gasoline+M2 mixture (**Fig. 5b**) compared to Gasoline+M1 (**Fig. 5a**) can be attributed to M2 containing twice the ammonia content of M1.

The rate of H-abstraction and radical formation during combustion is influenced by the initial hydrogen concentration [20]. The increasing presence of hydrogen causes more fuel to be involved in the combustion process earlier. This resulted in a higher rate of heat release from the blends compared to gasoline. However, this increase is not well appreciated for the mixture Gasoline+M2, probably because the differences are of the order of the experimental error associated with the pressure measurement and the smaller difference between them discussed above.

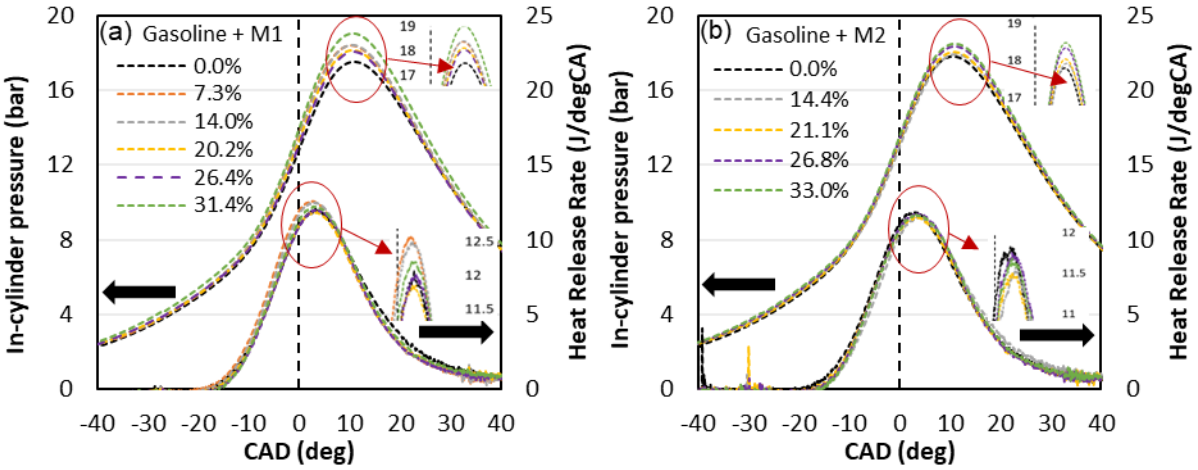

**Fig. 5**. In-cylinder pressure and heat release rate under different energy substitution ratio (from 0 to 33%) for Mixture Gasoline+M1 (a) and Mixture Gasoline+M2 (b) for stoichiometric condition

**Fig. 6** illustrates the impact on combustion duration of the two $H_2$ & $NH_3$ fuel mixtures at various ESR. Please note that the ST timing was retarded to maintain the MFB50 at a constant level. The increase in the ESR due to the incorporation of the zero carbon fuel mixtures gradually decrease the flame development period (CA0-10). The increase in the initial flame combustion speed, indicated by lower CA0-10 period, is attributed to the presence of $H_2$ in the mixture despite the addition of $NH_3$. Lower ignition energy of $H_2$ accelerated the flame development process [21]. The impact of ESR by the zero carbon fuels mixture was less pronounced on the main combustion phase (CA10-50) and the final combustion stage (CA50-90). Therefore, ESR by zero carbon fuels primarily influenced the initial flame development with minimal effects on later combustion stages, results consistent with the effect on HRR shown in **Fig. 5**.

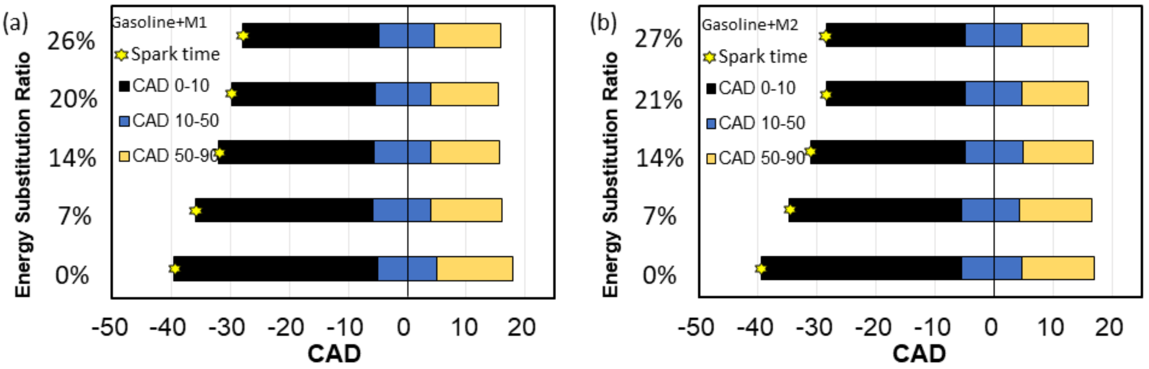

**Fig. 6.** Combustion duration of ESR at different developmental phases for Mixture Gasoline+M1 (a) and Mixture Gasoline+M2 (b) for stoichiometric condition

### *3.2.2 Effect of air-fuel ratio with $NH_3/H_2$ addition on combustion on characteristics*

While lean-burn engine conditions present challenges due to limitations in mixture flammability, they offer a substantial benefit to ICE efficiency. The study maintained the same Gasoline+M1 and Gasoline+M2 blends, preserving their respective energy substitution ratios of 27% and 29%, respectively but adjusted lambda. **Fig.** 7 presents the in-cylinder pressure and heat release rate of the Gasoline+M1 (a) and Gasoline+M2 (b) mixtures under three different lambda conditions. The peak pressure rose as lambda increased. This occurred because the engine throttle angle increased to provide more air to the combustion chamber, which also increased the intake manifold pressure. Hence, the pressure shown for the in-cylinder pressure was higher for the leaner cases even before combustion takes place. Similarly, to maintain an MFB50 between 3 and 5 CAD aTDC, advancement of the spark timing was required.

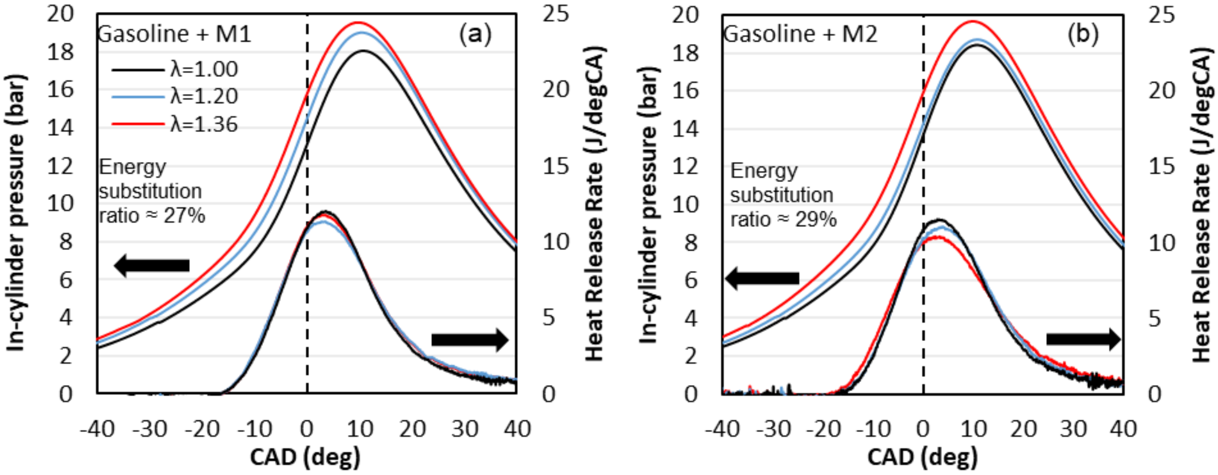

**Fig. 7.** In-cylinder pressure and heat release rate under different air-fuel ratio (from 1 to 1.4) for mixture gasoline+M1 (a) and mixture gasoline+M2 (b)

**Fig.** 8 shows the combustion duration of gasoline+M1 (a) and gasoline+M2 (b) fuel mixtures under three different lambda conditions. As the lambda value increases, the combustion duration gradually increases. Although this was observed at each stage of the process, in particular, the flame development period (CA0-10), was more impacted by the excess air. Shinde & Karunamurthy [22] reported a similar trend in their research. In general, this can be attributed to the lower fuel concentration making more difficult to initiate a stable flame kernel due to the decreased probability of collisions between fuel and oxidant molecules [23]. Furthermore, once initiated, the flame must expand to consume the entire air-fuel mixture, a process that slows down with increased excess air. This is particularly critical in the early stages of combustion. Additional factors such as turbulence intensity integral length scale, thermal diffusivity and laminar combustion speed, density relation and thermal stratification could be contributing to this slowdown [24] [25] [26]. The combined effect of all these factors prolongs the flame development period and, consequently, the overall duration of combustion. Despite this increase, this period remains shorter than that of pure gasoline (at lambda 1, see **Fig.** 6) due to the accelerating effect of hydrogen.

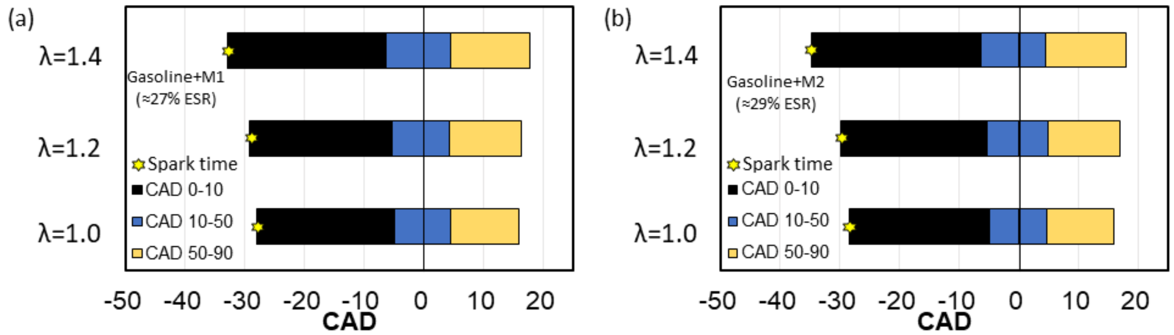

**Fig. 8.** Combustion duration at different developmental phases under different air-fuel ratio (from 1 to 1.4) for mixture gasoline+M1 (a) and mixture gasoline+M2 (b)

## 3.3 Gaseous emissions

### *3.3.1 Effect of gasoline substitution with $NH_3$/$H_2$ on combustion characteristics*

The introduction of a hydrogen-ammonia mixture ($H_2$/$NH_3$) in varying ratios (e.g. Gasoline+M1 and M2) and/or under lean burn conditions reduces the CO and THC emissions (**Fig. 9**). Both CO and THC concentrations decreased proportionally with the increase in the ESR. This behaviour can be attributed to the replacement of a carbon-based fuel (gasoline) with the carbon-free $H_2$/$NH_3$ gas mixture. In contrast, NO and $NH_3$ concentrations exhibited an upward trend with increasing ESR. The literature review indicated a correlation between the rise in NO emissions and the temperature increase caused by hydrogen addition [27] [28]. This suggests enhanced formation of thermal-$NO_X$, but some researchers propose that NO generation from both fuel and thermal pathways might be comparable in magnitude for combustion including ammonia [29]. The higher NO emissions observed in the Gasoline+M2 mixture compared to the Gasoline+M1 mixture confirm a direct link between ammonia concentration and NO formation. NO emissions demonstrate a more pronounced increase of roughly 30% in mixtures containing M2 (higher $NH_3$) compared to those of M1. This suggest that fuel NOx is more dominant than thermal NOx. Furthermore, $NH_3$ slip was more prominent with higher proportions of ammonia within the fuel and was increased monotonically with the increase of the ESR. This finding emphasizes the need for a comprehensive assessment of the trade-offs involved in ESR for SI engines, considering both the positive impact on CO and THC reduction and the potential negative consequences for NO and $NH_3$ emissions. This necessitates the design of new environmental catalysts and exhaust gas aftertreatment systems and their integration withing the engine powertrain.

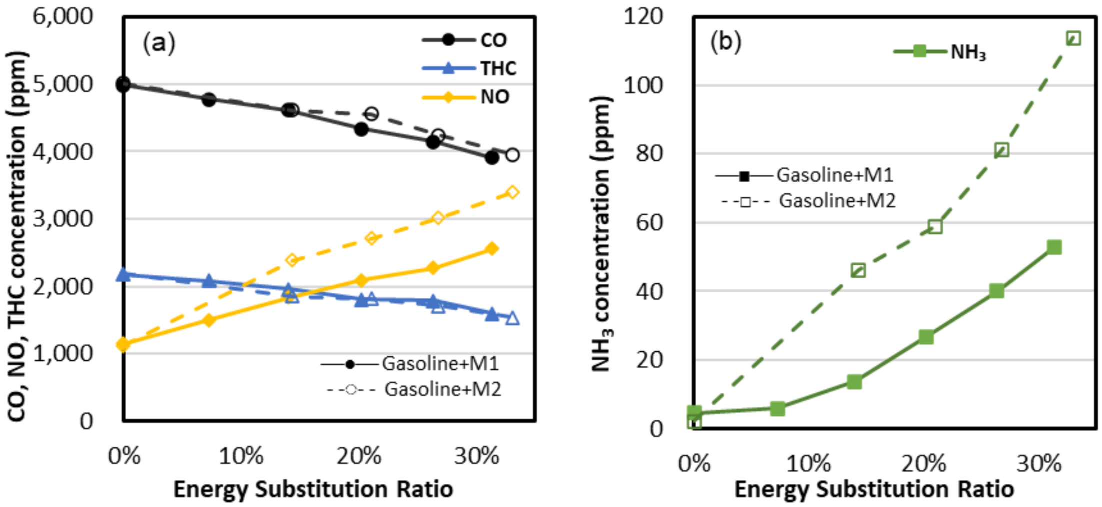

**Fig. 9.** Emissions of CO, THC, NO (a) and $NH_3$ (b) from a SI engine fuelled with Gasoline+M1 and Gasoline+M2 mixtures, shown as a function of energy substitution ratio

The impact of $H_2/NH_3$ blends on emissions of $CO_2$, $CH_4$ and $N_2O$ is shown in **Fig. 10**. These are of particular interest due to their characterisation as greenhouse gases (GHGs). Both $CO_2$ and $CH_4$ decreased because of the replacement of the carbon-based fuel, however, an increase in $N_2O$ was observed due to the increase in the fraction of the $H_2/NH_3$ mixture. It was observed that the production of $N_2O$ was related to the ammonia fraction, since the Gasoline+M2 (more ammonia concentred) mixture produced a higher proportion, in line with the production of NO. $N_2O$ is reported to be produced and consumed from NO through the sequence shown by Equation 10 to Equation 12 [30] [31] [32].

$$NH + NO \leftrightarrow N_2O + H^{\cdot}$$

Equation 10. Nitrous oxide formation

$$N_2O + H^{\cdot} \leftrightarrow N_2 + OH^{\cdot}$$

Equation 11. Nitrous oxide degradation

$$N_2O(+M) \leftrightarrow N_2 + O^{\cdot}$$

Equation 12. Nitrous oxide degradation

According to Equation 10, the increase in NO concentration with ESR leads to a higher production of $N_2O$, which is observed. However, the global warming potential for $N_2O$, in 100 years (GWP100), is 298 times higher than that of carbon dioxide. Methane also exhibits a higher GWP than $CO_2$, though to a lesser extent, at 28 times higher [33]. To accurately assess the impact of the ESR on GHG emissions, the $CO_2$-equivalent approach was employed that takes into consideration both $N_2O$ and $CH_4$. This method allows for a standardised comparison of different GHGs by converting their heat-trapping potential into a common unit based on carbon dioxide. In this way, the emissions of $CH_4$, $CO_2$ and $N_2O$ were determined in terms of mass of $CO_2$ equivalent based on one hour of engine operation.

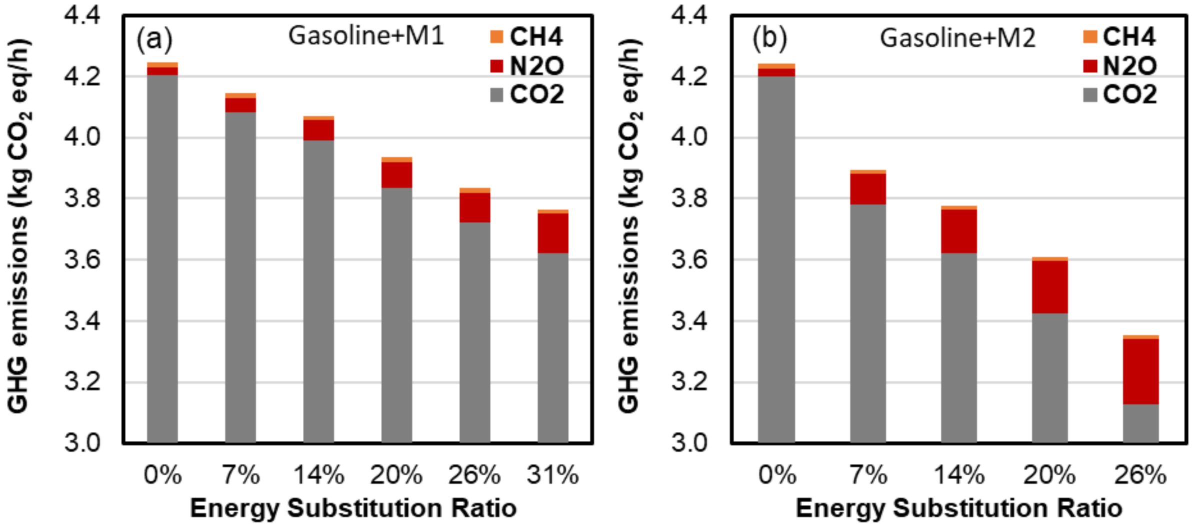

**Fig. 10.** Greenhouse gas (GHG) emissions as function of energy substitution ratio from an SI engine fuelled with Gasoliine+M1(a) and Gasoline+M2 (b) mixtures

The most notable observation from **Fig. 10** is that as ESR increased, there was a consistent decrease in the total potential greenhouse gas emissions, despite the increase in the contribution of $N_2O$. When comparing the Gasoline+M1 and Gasoline+M2 mixtures, it is observed that for the same or similar ESR. $N_2O$ levels were higher for the Gasoline+M2 mixture. This is related to the higher ammonia content in the mixture. However, the total $CO_2$-eq was lower for the Gasoline+M2 mixtures. As a global result, the replacement of gasoline by the mixtures generates a net positive impact by decreasing the concentration of GHG highlighting the potential for ammonia reformate as a fuel to decrease the global warming impact of the transportation sector.

### *3.3.2 Effect of air-fuel ratio on combustion at fixed $H_2$ and $NH_3$*

**Fig.** 11 depicts the emissions of an SI engine fuelled by Gasoline + M1 (a) and Gasoline + M2 (b) under stoichiometric and lean conditions. The bars represent the concentrations of CO, THC, and NO emissions, while the line shows the concentration of unburned ammonia ($NH_3$). The concentration of CO decreased as lambda increased. This was attributed to the increased oxidation of CO to $CO_2$ as more oxygen was available at leaner conditions. The concentrations of HC, NO, and $NH_3$ did not vary significantly, except for a slight increase in NO and a decrease in THC and $NH_3$ around lambda 1.2. This could be explained by the fact that at lambda 1.2 the thermal efficiency was better than at the other A/F ratios, resulting in higher temperatures and therefore higher NO formation, lower THC and therefore lower $NH_3$ slip. When comparing the blends Gasoline + M1 (**Fig.** 11a) and Gasoline + M2 (**Fig.** 11b), it is observed that the latter exhibited higher NO and $NH_3$ production. This was due to the higher $NH_3$ concentration in the fuel (Gasoline + M2).

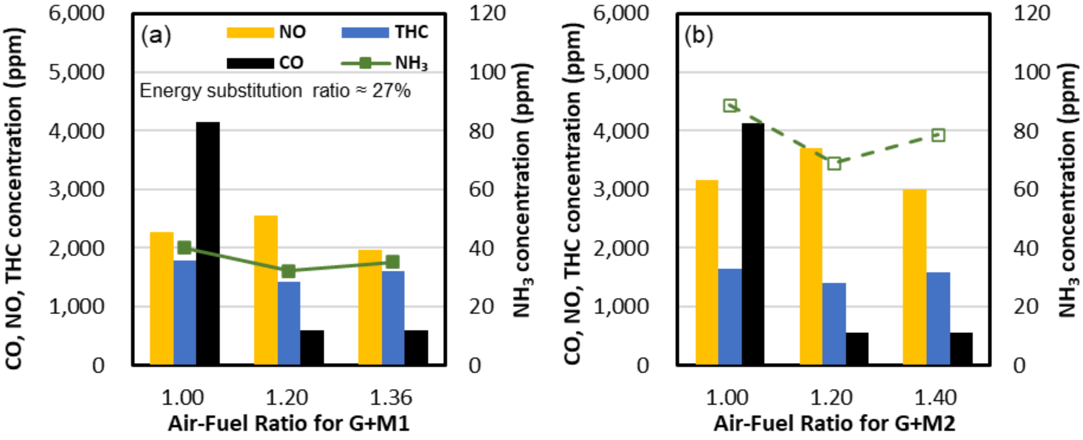

**Fig.** 11. Emissions of CO, THC, NO, and $NH_3$ as a function of air-fuel ratio from a SI engine fuelled with Gasoline+M1 (a) and Gasoline+M2 (b) mixtures

**Fig. 12** plots the variation of $CO_2$, $CH_4$, and $N_2O$ emissions, for stoichiometric and lean combustion with a fixed ESR of 27%. It is important to highlight that the total GHG emissions for $\lambda = 1$ was different due to the different mixture compositions. As with the ESR, the concentration of all these species in emissions decreased with higher lambda values. When comparing Gasoline+M1 and Gasoline+M2 mixture, the trends are similar, although there was a significant increase in $N_2O$ production for blends with a higher $NH_3$ proportion (Gasoline+M2). The decrease with increasing lambda highlights the importance of lean combustion for SI engines fuelled with ammonia reformate to assist in the reduction of the greenhouse gas emissions from the transport sector. In summary, the combustion of gasoline blends with $NH_3/H_2$ leads to the generation of a lower proportion of GHGs, in the lambda range studied.

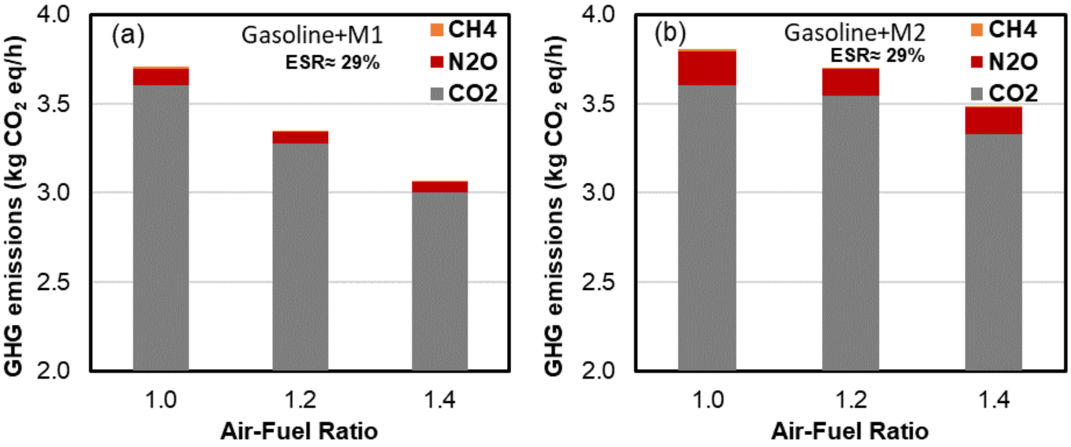

**Fig. 12.** Greenhouse gas (GHG) emissions as function of air-fuel ratio from an SI engine fuelled with (a) Gasoliine+M1 and (b) Gasoline+M2 mixtures

## 4. Conclusions

This study investigated the synergy of using an onboard ammonia cracker to produce hydrogen mixtures (M1 and M2) to reduce the environmental impact and improve SI engine performance. The research focused on two key areas: the effectiveness of ammonia conversion and the subsequent effects on engine behaviour and emissions. The key findings of the study can be summarised as follows:

- A ruthenium catalyst efficiently converts ammonia into hydrogen at elevated temperatures (>350°C). Higher temperatures and lower gas flow rates improved the conversion process. Increasing the gas hourly space velocity reduced ammonia conversion due to less contact time between ammonia molecules and the catalyst.
- Blending gasoline with ammonia-cracking products offered multiple benefits for engine performance. The presence of hydrogen in the blends led to a faster heat release rate. However, to maintain stable combustion, spark timing adjustments become necessary. Additionally, this approach presents the potential for lean burn operation, which can improve both engine efficiency and reduce emissions.
- The addition of ammonia-cracking product blends to gasoline presents a positive effect on engine emissions. Increased the energy substitution ratio decreased harmful pollutants and led to lower overall greenhouse gas (GHG) emissions about 15% to 25%.
- The mixtures with higher ammonia content exhibited a rise in NO emissions. Perhaps most concerning was the significant increase in unburned ammonia ($NH_3$-slip) with increasing ESR, which demands further investigation. Finally, the oxidation of $NH_3$ might lead to a potential increase in nitrous oxide ($N_2O$) emissions. The increase in $N_2O$ offsets a 5% reduction in $CO_2$, but still resulting on an overall reduction on the global warming potential ($CO_2$eq).

## 5. Acknowledgements

The authors wish to thank Johnson Matthey for providing the Ammonia Cracking Catalyst investigated in this study. ESPRC is acknowledged for supporting this work through the MariNH$_3$ project (EPSRC Ref: EP/W016656/1). Special appreciation to the University of Birmingham for providing PhD scholarships and funding to Mengda Wu. Thanks to the dedication of every researcher and technician in the Wyszynski Laboratory at the University of Birmingham, whose hard work ensures the safety of all in the lab.

## References

[1] Mounaïm-Rousselle C, Mercier A, Bréquigny P, Dumand C, Bouriot J, Houillé S. Performance of ammonia fuel in a spark assisted compression ignition engine. International Journal of Engine Research. 2021;23(5). doi:10.1177/14680874211038726.

[2] Lhuillier C, Bréquigny P, Contino F, Mounaïm-Rousselle C. Combustion characteristics of ammonia in a modern spark-ignition engine. SAE Technical Paper 2019-24-0237. 2019. doi:10.4271/2019-24-0237.

[3] Du F, Sun W, Luo H, Li CM. Recent progress in electrochemical synthesis of carbon-free hydrogen carrier ammonia and ammonia fuel cells: A review. Materials Reports: Energy. 2022;2(4):100163. doi:10.1016/j.matre.2022.100163.

[4] Ishaq H, Crawford C. Review and evaluation of sustainable ammonia production, storage and utilization. Energy Conversion and Management. 2024;300:117869. doi:10.1016/j.enconman.2023.117869.

[5] Li T, Duan Y, Wang Y, Zhou M, Duan L. Research progress of ammonia combustion toward low carbon energy. Fuel Processing Technology. 2023;248:107821. doi:10.1016/j.fuproc.2023.107821.

[6] Essmann S, Dymke J, Höltkemeier-Horstmann J, Möckel D, Schierding C, Hilbert M, Yu C, Maas U, Markus D. Ignition characteristics of hydrogen-enriched ammonia/air mixtures. Applications in Energy and Combustion Science. 2024;17:100254. doi:10.1016/j.jaecs.2024.100254.

[7] Ezzat M, Dincer I. Development and assessment of a new hybrid vehicle with ammonia and hydrogen. Applied Energy. 2018;219:226-239. doi:10.1016/j.apenergy.2018.03.012.

[8] Sittichompoo S, Nozari H, Herreros J, Serhan N, da Silva J, York A, Millington P, Tsolakis A. Exhaust energy recovery via catalytic ammonia decomposition to hydrogen for low carbon clean vehicles. Fuel. 2021;285:119111. doi:10.1016/j.fuel.2020.119111.

[9] Fu J, Deng B, Liu J, Wang L, Xu Z, Yang J, Shu G. Study of SI engine fueled with methanol vapor and dissociation gas based on exhaust heat dissociating methanol. Energy Conversion and Management. 2014;79:213–223. doi:10.1016/j.enconman.2013.11.040.

[10] Huo J, Zhao T, Lin H, Li J, Zhang W, Huang Z, Han D. Study on lean combustion of ammonia-hydrogen mixtures in a pre-chamber engine. Fuel. 2024;361:130773.

[11] Zecher-Freeman N, Zong H, Xie P, Wang C. Catalytic cracking of ammonia toward carbon-neutral liquid fuel. Current Opinion in Green and Sustainable Chemistry. 2023;44. doi:10.1016/j.cogsc.2023.100860.

[12] Spatolisano E, Pellegrini LA, de Angelis AR, Cattaneo S, Roccaro E. Ammonia as a carbon-free energy carrier: NH3 cracking to H2. Industrial & Engineering Chemistry Research. 2023;62(28):10813-10827. doi:10.1021/acs.iecr.3c01419.

[13] Ryu K, Zacharakis-Jutz GE, Kong SC. Performance enhancement of ammonia-fueled engine by using dissociation catalyst for hydrogen generation. International Journal of Hydrogen Energy. 2014;39(5):2390-2398. doi:10.1016/J.IJHYDENE.2013.11.098.

[14] Wang W, Herreros JM, Tsolakis A, York APE. Ammonia as hydrogen carrier for transportation; investigation of the ammonia exhaust gas fuel reforming. International Journal of Hydrogen Energy. 2013;38(23):9907-9917. doi:10.1016/j.ijhydene.2013.05.144.

[15] Comotti M, Frigo S. Hydrogen generation system for ammonia–hydrogen fuelled internal combustion engines. International Journal of Hydrogen Energy. 2015;40(33):10673-10686. doi:10.1016/j.ijhydene.2015.06.080.

[16] Matsunaga T, Matsumoto S, Tasaki R, Ogura Y, Eboshi T, Takeishi Y, Honda K, Sato K, Nagaoka K. Oxidation of Ru/Ce0.5Zr0.5O2−x at ambient temperature as a trigger. ACS Sustainable Chemistry & Engineering. 2020;8(35):13369–13376. doi:10.1021/acssuschemeng.0c04126.

[17] Stagni A, Cavallotti C, Arunthanayothin S, Song Y, Herbinet O, Battin-Leclerc F, Faravelli T. An experimental, theoretical and kinetic-modeling study of the gas-phase oxidation of ammonia. Reaction Chemistry & Engineering. 2020;5:696-711. doi:10.1039/C9RE00429G.

[18] Reggeti SA, Kane SP, Northrop WF. Hydrogen production in ammonia-fueled spark ignition engines. Applications in Energy and Combustion Science. 2023;14:100136.

[19] Zhu D, Ruwe L, Schmitt S, Shu B, Kohse-Höinghaus K, Lucassen A. Interactions in ammonia and hydrogen oxidation examined in a flow reactor and a shock tube. The Journal of Physical Chemistry. 2023;127(10):2351–2366. doi:10.1021/acs.jpca.2c07784.

[20] Zhao Y, Wang E, Shi Z. Effects of hydrogen addition on premixed combustion of kerosene in SI engine. Energies. 2023;16(10). doi:10.3390/en16104216.

[21] Gimenez B, Melgar A, Horrillo A, Tinaut FV. A correlation for turbulent combustion speed accounting for instabilities and expansion speed in a hydrogen-natural gas spark ignition engine. Combustion and Flame. 2021;223:15-27.

[22] Shinde BJ, Karunamurthy. Effect of excess air ratio and ignition timing on performance, emission and combustion characteristics of high speed hydrogen engine. IOP Conference Series: Earth and Environmental Science. Chennai, Tamilnadu, India. 2023. doi:10.1088/1755-1315/1161/1/012006.

[23] Derek D. Lean Combustion: Technology and Control. Second ed. Academic Press; 2016. doi:10.1016/C2013-0-13446-0.

[24] Giménez B, Melgar A, Horrillo A, Gabana P. Prediction of the flame kernel growth rate in spark ignition engine fueled with natural gas, hydrogen and mixtures. Fuel. 2023;339:126908. doi:10.1016/j.fuel.2022.126908.

[25] Chu H, Berger L, Grenga T, Gauding M, Cai L, Pitsch H. Effects of turbulence on variations in early development of hydrogen and iso-octane flame kernels under engine conditions. Combustion and Flame. 2023;255:112914. doi:10.1016/j.combustflame.2023.112914.

[26] Luong MB, Luo Z, Lu T, Chung SH, Yoo CS. Direct numerical simulations of the ignition of lean primary reference fuel/air mixtures with temperature inhomogeneities. Combustion and Flame. 2013;160(10):2038-2047. doi:10.1016/j.combustflame.2013.04.012.

[27] Kurien C, Mittal M. Utilization of green ammonia as a hydrogen energy carrier for decarbonization in spark ignition engines. International Journal of Hydrogen Energy. 2023;48(74). doi:10.1016/j.ijhydene.2023.04.073.
[28] Purayil S, Hamdan MO, Al-Omari SA, Selim MYE, Elnajjar E. Review of hydrogen–gasoline SI dual fuel engines: Engine performance and emission. Energy Reports. 2023;9:4547-4573. doi:10.1016/j.egyr.2023.03.054.
[29] Yan Y, Yang R, Liu Z, Liu J. Nitrogen oxides emission characteristics of zero-carbon ammonia-hydrogen fuels for internal combustion engines. SAE Technical Paper 2023-01-0334. 2023. doi:10.4271/2023-01-0334.
[30] Wu B, Wang Y, Wang D, Feng Y, Jin S. Generation mechanism and emission characteristics of N2O and NOx in ammonia-diesel dual-fuel engine. Energy. 2023;284:129291. doi:10.1016/j.energy.2023.129291.
[31] Malte PC, Pratt DT. Measurement of atomic oxygen and nitrogen oxides in jet-stirred combustion. Symposium (International) on Combustion. 1975;15(1):1061-1070. doi:10.1016/S0082-0784(75)80371-7.
[32] Mercier A, Mounaïm-Rousselle C, Bréquigny P, Bouriot J, Dumand C. Improvement of SI engine combustion with ammonia as fuel: Effect of ammonia dissociation prior to combustion. Fuel Communications. 2022;11:100058. doi:10.1016/j.jfueco.2022.100058.
[33] IPCC. Climate Change 2013: The Physical Science Basis. Contribution of Working Group I to the Fifth Assessment Report of the Intergovernmental Panel on Climate Change. Cambridge, United Kingdom and New York, NY, USA. 2013.

# Investigating HCCI Engine Operating Parameters Under the Simultaneous Dual Fueling of Ammonia and Hydrogen Based on Detailed Chemical Kinetics Modelling

F. Balogun[1], A. Vasudev[1], A. Kakoee[1], K. Sirviö[1] and M. Mikulski[1]

[1]Efficient Powertrain Solutions (EPS), School of Technology and Innovations, University of Vaasa, Wolffintie 34, FI65200, Vaasa, Finland.

E-mail: Fatimoh.balogun@uwasa.fi
Telephone: +(358) 29 449 8605

**Abstract.** Challenges associated with the homogeneous charge combustion ignition (HCCI) concept includes combustion phasing control and a narrow operating window. To address the HCCI engine developmental needs, chemical kinetic solvers have been recently included in the commercial engine simulation toolchains like GT-Suite v2022. Their applicability has not been thoroughly tested, especially when less-conventional fuel options have been considered. The purpose of this study is to test the feasibility of kinetic solvers included in the GT-Suite, for simulating HCCI combustion with multi-component fuel blend, consisting predominantly of ammonia, $NH_3$, and hydrogen, $H_2$. The study investigated the effect of fuel blending, air to fuel equivalence ratio, and compression ratio on a dual-fuel 1-cyclinder HCCI engine model. Key combustion parameters such as peak pressure, heat release rate, start of combustion were analyzed. Feasibility of the simulations have been validated by benchmarking the results against the base-line HCCI engine fed with n-heptane (diesel surrogate). The result proved that the solver provides stable simulations for all considered fuel blends/mechanisms. Simulation times with multi-component mechanism of $NH_3$, $H_2$ and n-heptane are on average 32 seconds per cycle with the solver reaching convergence after 6 cycles. The optimization conducted to support the mechanism/solver feasibility study implies optimum performance can be obtained for 90% $NH_3$ to 10% $H_2$ blend ratio, at compression ratio of 20 with lambda value of 2. At optimal operating conditions, indicated mean effective pressure (IMEP) was almost 2.7 times higher, indicated thermal efficiency ($I_{eff}$) is few points higher, and likewise more fuel economical than the baseline HCCI operation with n-heptane. At the same time, all emission quantifiers of the $NH_3/H_2$ HCCI engine, including NOx, were significantly reduced, while keeping the intrinsic advantages of zero-carbon fuel. Finally, it was concluded that the kinetic solver posed great potentials in aiding the HCCI technological advancement, also with the use of $NH_3$ and $H_2$ fuel towards a zero-carbon emission transportation system.

**Notations**

| | |
|---|---|
| $NH_3$ | Ammonia |
| $H_2$ | Hydrogen |
| $\lambda$ | Lambda |
| CA50 | Crank angle at 50% heat release |
| ATDC | After top dead center |
| w/w% | weight by weight percent |
| BR | Blending ratio |
| CR | Compression ratio |
| ER | Equivalence ratio |
| IMEP | Indicated mean effective pressure |
| $I_{eff}$ | Indicated thermal efficiency |
| ISFC | Indicated specific fuel consumption |
| CHR | Cumulative heat release |
| HRR | Heat release rate |
| MFR | Mass flow rate |
| AFR | Air to fuel ratio |

## 1. Introduction

Traditional internal combustion engines (ICE) powered with fossil fuels as its main energy source, has been in use both in power generation and transportation sectors for centuries. However, they have been investigated to produce emissions (including nitrogen oxides NOx, hydrocarbon HC, carbon monoxide CO, and particulate matter PM) which had negative impact on both public health and the environment [1]. Hydrogen ($H_2$) is among the viable option for the replacement of fossil fuels due to its renewable form, higher energy potential and lower ignition temperature [2]. However, due to its high volatility, storage and handling of $H_2$ is challenging, therefore raising debates of its employability in passenger and other transport vehicle [2]. Ammonia ($NH_3$, also from renewable sources) on the other hand, is less volatile and even has a higher energy capacity than $H_2$ [3]. It offers promising alternative fuel in terms of handling, energy density and safety. However, $NH_3$ is poor in combustion due to its high ignition temperature and low flammability (resulting from a slow chemical kinetics in the combustion process). These opposite characteristics of both fuels make them a perfect pair as $H_2$ may be used to enhance the auto-ignition property of ammonia in the $NH_3/H_2$ fuel blend [3].

Due to the advent of more environmental and health friendly options of fuel sources (such as biofuels), ICE optimization to accommodate these newly identified fuel types has led to the progressive research on more efficient combustion concepts [4]. Prospective routes for emission control includes the low-temperature combustion (LTC) enabling alternative fuel source. One option of LTC concept, the homogenous charge compression ignition (HCCI) combustion, has evolved in tandem with biofuel research. HCCI engines combines both elements of spark ignition (SI) and compression ignition (CI) engines. Air-fuel mixture is homogenously mixed before entering combustion chamber (as in SI engine) but ignition occur through compression instead of spark plugs (as in CI engines) [5]. In HCCI combustion mode, ignition is not instigated externally but by compression and autoignition of the air-fuel mixture. Ignition happens when thermodynamic conditions (temperature, pressure, specie concentrations) of the fuel are favorable [6]. This concept allows HCCI the use of different fuels (including biofuels, gasoline, diesel, both neat fuels and fuel blends) and their diverse physicochemical properties to regulate air-fuel autoignition and provides optimized engine operation over a wide range of operating conditions. These fuel flexibility properties of HCCI have prospects to contribute to energy security [7]. LTC and more homogenous mixing of fuel-air, has been investigated to also enable increase in engine performance metrics and a reduction of the emissions generated compared to traditional SI and CI engines. Challenges associated with the HCCI concept includes achieving a consistent combustion and controlling ignition timing under diverse operating conditions [5]. Research to address these challenges are ongoing for a more widespread use of the technology.

In engine performance optimization, the use of fast simulation models may be employed to enable rapid prototyping of robust engine models due to their high comparability [8]. Thereby, enabling applied level engine studies such as optimizing the operating limits of the engine design concept for technology development. HCCI simulation approaches, depending on run-time constraint application, range from Zero-Dimensional (0D) models, to high fidelity 3D models, with detailed Navier-Stokes equations solved using Computational Fluid Dynamics (CFD) [8]. 0D models are typically second law based, and order of magnitude faster than CFD. Fluid motion can be captured phenomenologically by dividing the volume to quasi-dimensional zones (that is, from single to multi-zone models depending on the order of complexity) [8]. Regardless of model fidelity, chemical kinetics is typically employed to simulate HCCI combustion progress. This reflects the reaction-driven nature of the phenomena and to capture ignition properties and combustion characteristics [5].

To address LTC development needs, chemical kinetic solvers have been recently included in the commercial engine simulation toolchains like GT-Suite (v2022 onwards) [9]. The applicability had not been thoroughly tested, especially when less-conventional fuel options are considered. To this end, using a n-heptane fueled single cylinder HCCI engine, Guo et al. [10] compared their experimental measurement with numerical simulations. They observed slight discrepancies in the heat release rate (HRR), in-cylinder pressure and other combustion parameter. This was predicted to be caused by the imperfect assumption of air/fuel homogenous mixing, combustion chamber wall temperature, reaction rates, uniform temperature and pressure, and also the fuel chemistry (level of detail of the applied chemical reaction mechanism applied in modeling). This led to the increment of the inlet temperature by 30 K for modeling HCCI, as recommended by Yelvington et al. [11]. They proposed that the use of 333 K as inlet temperature for the modeled case will allow a reduction in the deviation of the HRR phasing between both experimental and numerical modeling result data.

This study addresses the feasibility of kinetic solvers included in the GT-Suite, for the predictive combustion modeling of HCCI engine with multi-component fuel blend (consisting predominantly of $NH_3$ and $H_2$). This has not been publicly reported till date. To this end a baseline model with a suitable multi-component mechanism is validated over the experimental data available in the previously mentioned study by Guo et al. [10]. The validated model is further extended with $H_2$ and $NH_3$ injectors and benchmarked for combustion and emission performance over a wide range of operating conditions. Simulation convergence study and multi-parameter optimization complete the feasibility study and provide extended insight into the development concerns of advanced, multi-fuel combustion concepts.

## 2. Methods

### 2.1 Setting up the HCCI engine model, including engine specifications, geometry, and boundary conditions

For the HCCI model setup, a 1-cylinder HCCI engine (fueled with n-heptane) was selected from GT-Suite template [12]. This baseline model was calibrated using engine specifications from the single cylinder HCCI engine experiment conducted by Guo et al. [10]. Table 1 has presented the HCCI engine models (both baseline and present study) specifications, geometry, and other initial conditions. For the purpose of this study, a dual fuel 1-cylinder HCCI engine was modeled. $NH_3$ and $H_2$ were the target fuels. The InjRateConn injector type was used to introduce the $H_2$ fuel into the engine model for present study. Engine model specification included standard SI injection timing and valve timing. Combustion object used in the engine cylinder is the EngCylCombHCCI. This object called the EngCylChemGas object to define both the gaseous reaction mechanism and the thermodynamic fluid properties from external files. This automatically created all necessary FluidNASA-LiqGas fluid species reference objects needed for the chemical reaction mechanism. Details on selected chemical reaction mechanism development and validation has been included in subsection 2.2. Combustion was assumed to be truly homogenous. The cylinder Initial state object has been defined by object value "Init-FA", which was used to impose boundary conditions such as absolute pressure, fluid temperature and composition at the start of the simulation. Value for both absolute pressure and temperature have been listed in Table 1. The initial fluid composition defined with the object value "FA-Mixture", which called fluid object "air", "$NH_3$" and "$H_2$" with specified mass fraction as 0.95, 0.04 and 0.01 respectively. For the n-heptane fueled HCCI model, the object value "FA-Mixture" called fluid object "air", and "$NC_7H_{16}$" with specified mass fraction as 0.95 and 0.05 respectively. Exhaust gas recirculation (EGR) intake fraction set to 0.2. Cylinder wall temperature defined by object value "TWall", which defined the head and piston temperature as 575K, and the cylinder temperature as 400K. This represented the temperature of the wall surface directly in contact with the fluid. The heat transfer properties in the cylinder defined by object value "Woshni". This presented the heat transfer model as WoshniGT, overall convection multiplier as 1, head/bore area ratio as 1.3, piston/bore area ratio as 1.03, convection temperature evaluation as hybrid, and enabled the low speed heat transfer enhancement for the heat transfer model. Start of cycle was at -144 °CA at intake valve closing and exhaust valve closing at 140 °CA, replicating the experimental valve timing from Guo et al [10].

**Table 1.** HCCI engine model specifications, geometry, and operating conditions

| Item | Baseline single-fueled HCCI model (experiment) | Dual-fueled HCCI engine (GT-suite) |
|---|---|---|
| Engine specification and geometry | 1-cylinder, four stroke HCCI, bore =82.55mm, Stroke = 114.3mm, displacement=0.6117L, connecting rod length = 254mm, intake valve close (IVC) = -144 °CA, Exhaust valve open (EVO) = 140 °CA, EGR = 20% | |
| Boundary conditions | Temperature = 303 K,<br>Pressure = 95 kPa | Temperature = 333 K,<br>Pressure = 100 kPa |
| Target fuels | n-Heptane | $NH_3/H_2$ blend |
| No of injectors | 1 | 2 |
| Total fuel energy (TFE) | 67,6 MJ | 67,6 MJ |

### 2.2 Chemical kinetics mechanism selection

A reduced chemical kinetic mechanism developed by Patel et al. [13] was used for the baseline model simulation. The reduced mechanism was generated starting from an existing n-heptane mechanism containing 165 reactions and 40 species. The reduced mechanism was generated using SENKIN to produce ignition delay and solution files, and XSENKPLOT to analyze the reduced reaction mechanism. The newly formulated and reduced reaction mechanism was then used to generate new ignition delay data. Finally, kinetic constants in the new mechanisms were adjusted to improve ignition delay and engine combustions to account for diesel fuel cetane number and composition. The newly-reduced mechanism consists of 29 species and 52 reactions, and was validated under constant volume engine conditions. In comparison with a comprehensive mechanism (having 179 species and 1642 reactions), the new reduced mechanism gives similar predictions. Reduced chemical reaction mechanism were often used to enhance the computational efficiency of engine simulations

[13]. Researchers have successfully applied the reduced mechanism developed by Patel et al. in HCCI concepts. Jia et al. [14] implemented an improved phenomenological soot model coupled with the reduced n-heptane chemical mechanism developed by Patel et al., into KIVA-3V code to describe soot formation and oxidation process in a n-heptane HCCI combustion. The model was validated both experimentally and computationally. The results demonstrated satisfactory accuracy on all the studied parameters [14].

For the $NH_3/H_2$ fueled HCCI model, a detailed chemical kinetic mechanism and thermodynamics data file developed by Stagni et al. [15] for low temperature combustion was used for model simulation. Stagni et al. investigated the oxidation of $NH_3/H_2$ blends under low and intermediate temperature conditions using experimental methods in a flow reactor at near atmospheric pressure of 126.7 kPa and using stoichiometric conditions. They also developed a comprehensive kinetic model to interpret the experimental results. Fuel conversion and autoignition at low temperature were confirmed for the fuel blend with a reactivity boost provided by the addition of $H_2$. The kinetic mechanism contained 203 reactions and 31 species. This included a comprehensive list of species involved in the $NH_3$ reaction, including all radicals, intermediates and products. Table 2 presents both fuel type kinetic mechanisms to help understand model fidelity. $NH_3/H_2$ reaction mechanism has also been validated by Xu et al. [16]. The validation was carried out by comparing the results obtained from the mechanism with experimental data. The laminar flame speeds were calculated using CHEMKIN-PRO software with the developed mechanism. The calculated flame speeds were then compared with experimental results obtained by Han et al. [17]. The comparison of these results under different hydrogen content at room temperature and atmospheric pressure demonstrated that the chemical mechanism is reasonable for stimulating the overall combustion rate of $NH_3/H_2$/air mixtures in HCCI concepts.

**Table 2**. Chemical reaction mechanism selection based on target fuel and deired level of detail

| Primary surrogate | Source | No of species | No of reactions | NOx mechanism |
|---|---|---|---|---|
| n-Heptane | Patel, A., Kong, S., and Reitz, R. [13] | 29 | 52 | *NA |
| $NH_3/H_2$ | Stagni et al. [15] | 31 | 203 | Zeldovich -based |

*refers to not applicable

### 2.3. Baseline model validation

To validate the applicability of the baseline model, the operating conditions used for the HCCI engine experiment by Guo et al. [10] was used in GT-power simulation. The experiment was conducted in a single cylinder co-operative fuel research (CFR) engine modified and equipped with an air assist port fuel injector, similar to the single cylinder HCCI baseline model in GT-power. Boundary conditions for the simulation were set in accordance to experimental reference, as follows; Compression Ratio (CR) as 10, intake temperature as 303K, intake pressure as 95 kPa, AFR as 50 and engine speed as 900 rpm. The experiment was tailored towards capturing the n-heptane fueled HCCI engine performance and combustion characteristics at individual parameter sweeps (engine speed and CR particularly). Combustion parameters such as CA50 (crank angle at 50% heat release), IMEP, ISFC, and COVIMEP (coefficient of variation of indicated mean effective pressure) were monitored continuously in four tests to ensure accurate data collection and analysis.

For reproducing this HCCI engine model validation in GT-power, adjustment was made to the intake fluid mixture temperature by an increment of +30 as proposed by Yelvington et al. [12]. This correction was applied to all operating conditions. On this basis, the model was able to replicate the effect of CR and engine speed on the combustion phasing (CA50). The in-cylinder peak pressure and the CA50 measured data from the model were also validated against the experimental data from Guo et al. Results of the validation has been presented in subsection 3.1. This simulation study only considered the results obtained from combustion between IVC and EVO.

### 2.4. Scope of the research

Upon completion of model validation, a second injector was added for delivering $H_2$ fuel to the engine model. Simulations were run to investigate the effect of fuel blending ratio (BR), air-to-fuel ratio equivalence (ER), CR, and engine speed, on the performance, emission and combustion characteristics of an $NH_3$/ $H_2$-fueled HCCI engine in comparison with heptane-fueled HCCI engine model. The selected range of engine operating condition for parametric sweep were as presented in the baseline experimental study. Total fuel energy (TFE) introduced into the new model was kept constant at 67.6 MJ, equating the amount of fuel energy introduced for the baseline model, to enable effective comparison of their results. Table 3 presents the BR for $NH_3/H_2$ from pure $NH_3$ ($NH_3$/100) to 50% $NH_3$ to $H_2$ blend ($NH_3$/50), as a function of their mass flow rate (MFR) and lower heating value (LHV). Based on the initial sweeps, range of operating conditions were refined for further optimization. Parametric sweeps study was done choosing appropriate range and step-size for each parameter. The simulation matrix is presented in Table 4. The results on engine performance metrics and combustion phasing observed as a function of the parametric sweeps. Optimal operating conditions that achieved desired results were selected for iterative refinement. Optimization was realized by fine-tuning the operating conditions to converge towards optimal engine performance, combustion phasing and emissions. Final optimization was made with simulation test 5 as seen in Table 4.

**Table 3.** Blending ratio (BR) for $NH_3/H_2$ fueled 1-cylinder HCCI engines. *LHV_$H_2$ = 120 MJ/g, *LHV_$NH_3$ = 18.8 MJ/g. *Data from Lhuillier et al. [18]

| BR (w/w%) ($NH_3/H_2$) | 100/0 | 90/10 | 80/20 | 70/30 | 60/40 | 50/50 |
|---|---|---|---|---|---|---|
| MFR_$H_2$ (g/s) | 0 | 0.23 | 0.35 | 0.41 | 0.46 | 0.49 |
| MFR_$NH_3$ (g/s) | 2.70 | 2.10 | 1.39 | 0.96 | 0.69 | 0.48 |

**Table 4.** Simulation matrix for $NH_3/H_2$ fueled 4-cylinder HCCI engines. Inlet temperature=333K, Inlet pressure=1bar

| Simulation test | Speed (rpm) | CR | ER (λ) | BR (w/w%) ($NH_3/H_2$) |
|---|---|---|---|---|
| 1 | 900 – 4500 | 20 | 1 | 90/10 |
| 2 | 3500 | 16 – 24 | 1 | 90/10 |
| 3 | 3500 | 20 | 0.8 – 3 | 90/10 |
| 4 | 3500 | 20 | 2 | 50/50 –100/0 |
| 5 | 3500 | 20 | 1-2 | 90/10 |

Fuel-air mixture is among the several causes that may contribute to cycle to cycle variability (CCV). The ER parametric sweep was used in the final optimization in order to achieve optimum solutions. This variability impact combustion timing, maximum pressure and heat release rate. CCV analysis was done by creating scatter plot of CA02/CA50 for all cycles, at selected engine operational point. Results of CCV are presented in subsection 3.3. To run the above case setup, simulation time control was set to periodic, simulation duration was also set to 6 cycles, and in the initialization tab, previous case was set to help the simulation converge faster. HCCI model simulation was initialized and then redirected to GT-Post (an interface for postprocessing and analyzing result data on GT-Power). 5 sets of simulation test were carried out, with test 1 to 4 as main simulation and test 5 as a rerun optimization.

## 3. Results

### 3.1 Baseline Model validation results

According to Fig. 1, GT-power was able to reproduce the experiment results discussed in section 2.3, better while using the proposed simulation temperature 333K. The model was able to capture the combustion phasing in line to the experimental reference, while keeping the same combustion efficiency. CA50 predictions closely matched the experiment at zero-degree ATDC. In-cylinder maximum pressure was adequately reproduced, showing that simulated model reaction pathways were well represented. A difference of 0.5bar may be associated to random errors from the experiments. Low temperature reaction (LTR) predicted to occur earlier in the simulation than in the experiment. Likewise, there was an observable sharp rise in the heat release rate (HRR) at CA50 from the simulated model compare to the experiment. Both over-estimations result primarily from neglects of thermal stratification in 0D, single volume approach. Multizone models are typically able to capture the stratification much better as the kinetic solution progresses slower in the colder zones near the cylinder boundary [19]. The difference is also associated to inaccuracies in determining the boundary conditions on the engine airpath [20] and shortcomings of the incorporated mechanism itself [21]. The mechanism used in this baseline study was generic. Although, the reduced mechanism by Patel et al. was validated on a reference CFR engine, and widely incorporated in various HCCI studies using N-heptane as surrogate.

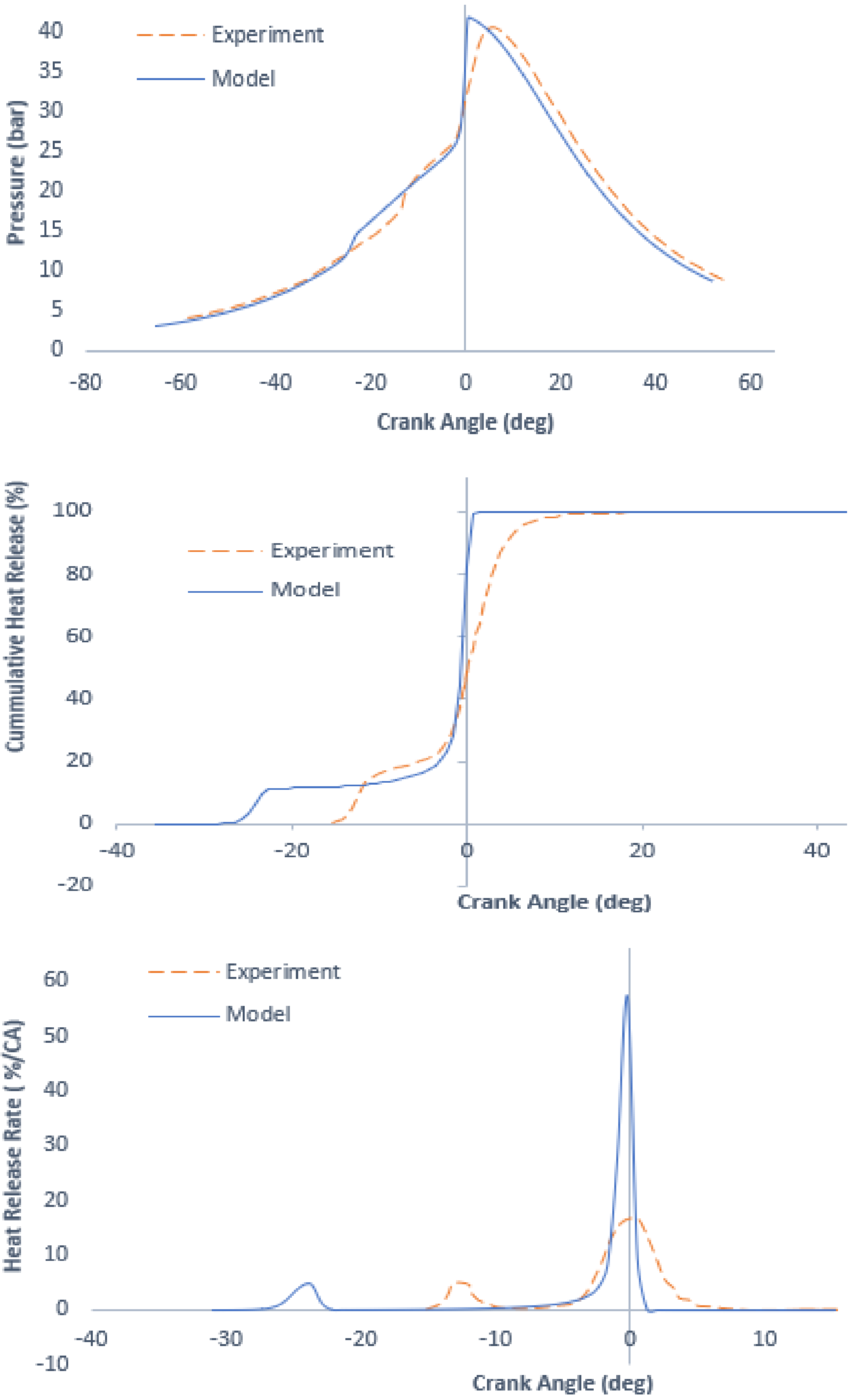

**Fig 1**. Comparison of simulated model (top) in-cylinder pressure (middle) cumulative heat release (bottom) Heat release rate, against the experimental data. AFR=50, CR=10, Intake pressure = 95 kPa.

HCCI is very sensitive to IVC conditions including residual gas temperature and composition, exact fuel make-up (including impurities) and secondary on the thermal in-cylinder stratification. Neither of these parameters were directly available for the baseline engine used in this study and the model calculated the IVC conditions starting from simplified data on the port geometry and valve timing information.

The scope of the research did not deem fit re-tuning the mechanism for this particular experiment (commonly done by studies that show exact HRR match) as this brings bigger risk of over-constraining the predictive features of the model. The approach is considered proper considering the main goal of the study – assessing the functionality for GT-Suite kinetic solver in fast engine simulations. As such, the only tuning parameter was the cylinder-area averaged wall temperature which was not explicitly known from the experiments and used to target the reference CA50. Considering the fidelity of the approach, the resulting performance parameter estimation (main use case of 0/1-D engine models) are more than satisfying, as Pmax, IMEP and engine efficiency are predicted well.

CA10 or CA90 are on the other side, very difficult to predict for HCCI in a computationally efficient 0-D combustion model. This is related to the fact that spatial temperature inhomogeneity is not captured [19]. The model captures the correct trends in this respect, confirming predictivity. On the other hand, CA10 in HCCI is determined majorly by the pre-ignition reactions that do not contribute significantly to the performance and emission formation. The efficiency in HCCI is shaped predominantly by correct combustion onset (CA50) and the amount of energy released due to incomplete combustion. Both of these parameters are captured correctly considering the CHR plots in Fig. 1. As such we consider this model suitable for computationally efficient pre-design, pre-optimisation or control design studies as further substantiated by main body of the result discussion. Table 5 also presents a comparison of baseline experiment versus simulation results of the CA10, CA50 and cylinder maximum pressure.

**Table 5.** Comparison of baseline HCCI engine combustion experiment results (Guo, et al., 2010) versus GT-power model simulation (present study)

| Test | CA10 (ATDC) | CA50 (ATDC) | Maximum Pressure (bar) |
|---|---|---|---|
| Experiment | -12.5 | 0 | 42.5 |
| GT-power simulation model (333 K) | -21.5 | 0 | 42.0 |

The model is able to capture the effect of varying engine speed on CA50, similarly to the experimental data as seen in Figure 2.

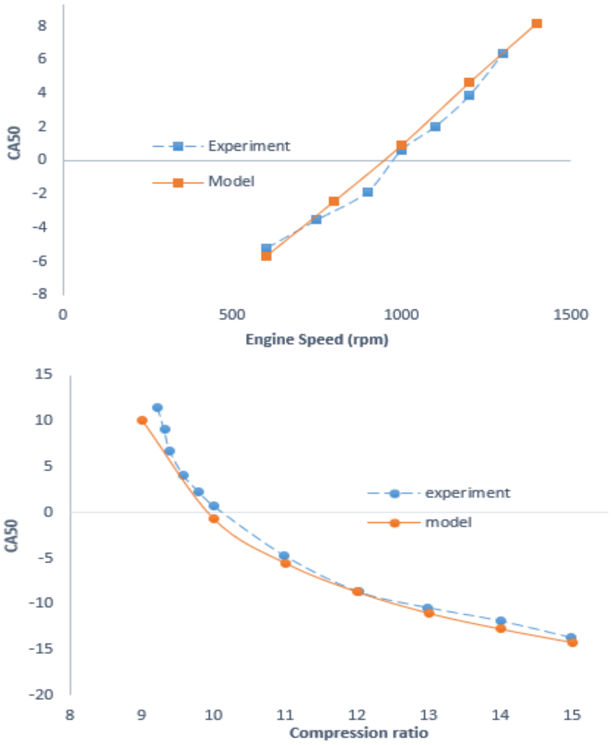

**Fig. 2.** Comparison of experimental CA50 (top) against engine speed, and (bottom) against CR, against GT-power model simulation results. AFR =50, CR=10, P=95 kPa

Simulated engine speed varied from 600 rpm to 1500 rpm and 333K. Resulting data points from the simulated model were almost linear, while those of the experiments showed some deviations even though the trends in both were coherent. CA50 was observed to increase as the engine speed increased, which is understandable as the kinetic timescale of the combustion commences under faster resolving in-cylinder volume. At 900 rpm, CA50 was at zero-degree CA, ATDC. Effect of varying CR on CA50 is further shown in Fig. 2. The observed decrease in CA50 with increased CR, is attributed to shorter combustion duration since kinetically controlled combustion process is faster in this condition [10]. Importantly, both the simulated and experimental trends were coherent. Individual resulting data points were almost corresponding for all cases and error were very minute. Simulation error in CA50 did not exceed 1.5CA for either of the operating points in Fig. 2. Taking to account the above discussion, the predictivity of the modeling framework is considered validated in terms of HCCI phenomenology. Consequently, the model can be further used for extrapolating the combustion concept towards $NH_3/H_2$ fueling, under constraints of the validity of the kinetic mechanism involved.

### 3.2 Analyzing Combustion parameters and performance metrics of $NH_3/H_2$ fueled HCCI engine

#### 3.2.1 Effect of varying engine speed on $NH_3/H_2$ combustion

Simulation test 1 was carried out at inlet conditions of 333 K and 1 bar, and at a constant TFE of 67.6 MJ. As $NH_3$ does not burn readily in its pure form, initial BR used for the simulation was $NH_3$ (90%) (i.e. with 10 w/w% $H_2$). For initial test, CR was set to 20 and engine speed varied from 900 rpm to 3500 rpm. At baseline engine speed of 900 rpm, engine performance and combustion parameters were poor as presented in Table 6 and Fig. 3 respectively. However, between 2000 rpm to 3500 rpm, there was stable combustion. At engine speed higher than 3600 rpm, there was loss of convergence in the simulation. This was perhaps indicative of the range of engine speed upon which the engine can operate, based on the engine specifications and the boundary conditions. Indicated mean effective pressure (IMEP) and indicated thermal efficiency ($I_{eff}$) increased with increasing engine speed. Indicated specific fuel consumption (ISFC) stabilized between 2500 rpm to 3500 rpm as presented in Table 6. In-cylinder pressure (Pmax) also increased with increase in engine speed. This may result from the accumulated heat during compression stroke because of shorter cyclic period as discussed by Hasan et al. [21]. Additionally, with increasing speed, the cumulative heat release (CHR) improved and combustion phasing advanced as illustrated in Fig. 3. This test proved engine speed as an important parameter with significant effect on the combustion and performance of HCCI engines.

**Table 6.** Engine performance metrics for varying engine speed from 900 rpm to 3500 rpm, ER=1, BR=$NH_3$(90%), P=1 bar, T=333K

| Engine Speed (rpm) | 900 | 1500 | 2000 | 2500 | 3000 | 3500 |
|---|---|---|---|---|---|---|
| IMEP (bar) | 0.6 | 2.75 | 5.15 | 6.59 | 7.75 | 8.32 |
| $I_{eff}$ (%) | 1.00 | 7.04 | 15.99 | 23.22 | 28.23 | 31.44 |
| ISFC (g/kW-h) | 3166.86 | 600.48 | 346.82 | 295.7 | 305.3 | 310.54 |

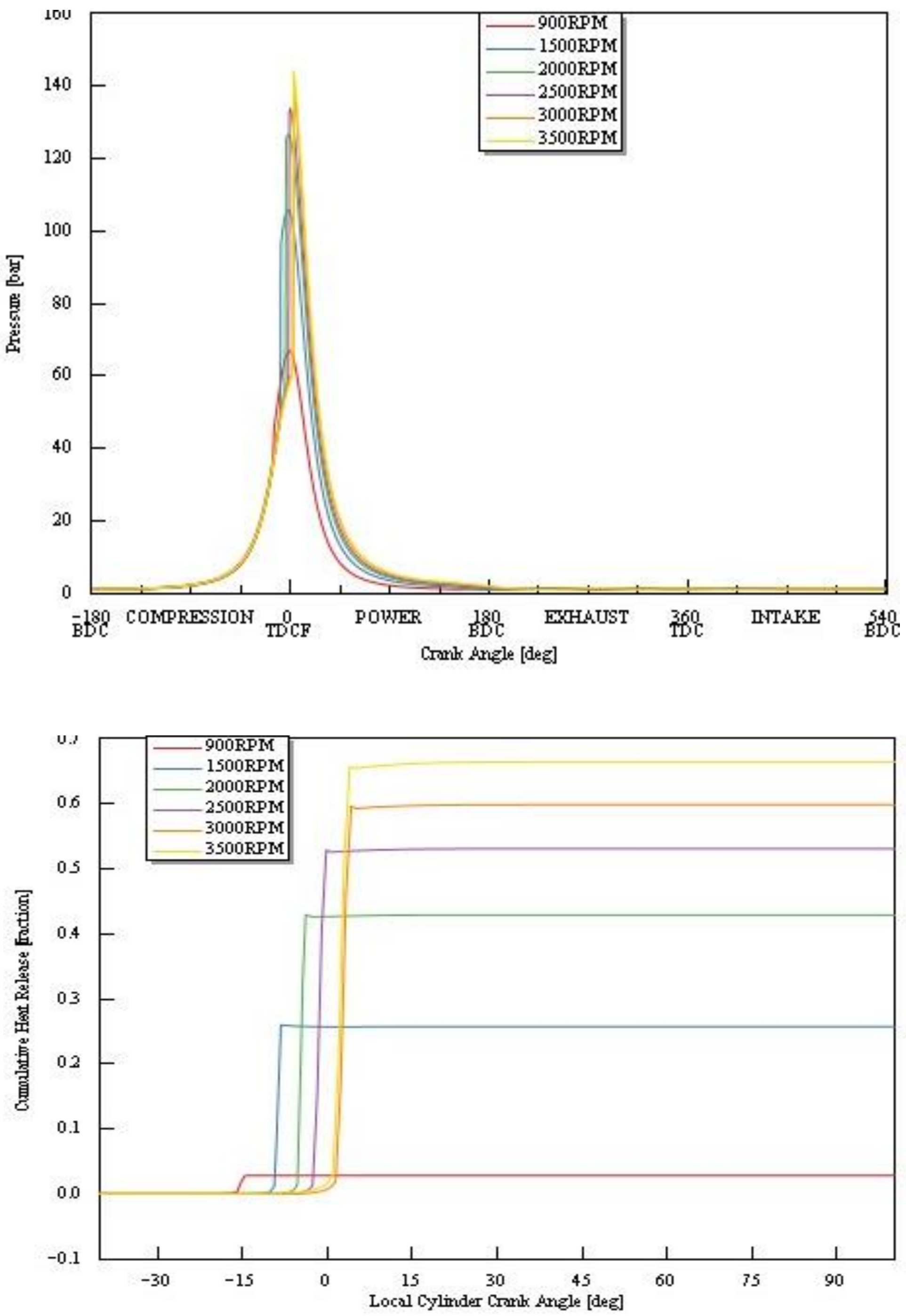

**Fig. 3.** Combustion parameter plots for $NH_3/H_2$ fueled HCCI engine over varying engine speed, (top) In-cylinder Pressure (bottom) Cumulative heat release. Varying engine speed from 900 rpm to 3500 rpm, ER=1, BR=$NH_3$(90%), P=1 bar, T=333K

### 3.2.2. Effect of varying compression ratio on $NH_3/H_2$ combustion

Simulation test 2 was executed with a CR case sweep range of 16 to 24 and incremental step of 2. BR was fixed at $NH_3$ (90%), ER of 1, engine speed of 3500 rpm, inlet temperature and pressure as 333K and 1 bar respectively. At this operating conditions, CR of 22 and 24 proved to be too high and caused excessive Pmax as illustrated in Fig. 4. This trend presents the effect of CR on the combustion characteristics. $I_{eff}$ should conventionally increase with CR. However, here opposite trend is observed. This is mainly because CA50 is unoptimized, occurring nearly $10^0$ CA before TDC. Excessively high in-cylinder pressure can be detrimental to the engine overall efficiency over time. Engine performance metrics were also better at lower CR of 18 and 20 presented in Table 7. Although CR less than 18 gave rise to an unstable combustion where all engine performance were all negative. This implied that at CR lower than 18, compression pressure was not enough for the autoignition of the air-fuel mixture and the thermodynamic conditions were not favorable [6].

**Table 7.** Engine performance metrics for varying CR at constant engine speed=3500 rpm, ER=1, BR=$NH_3$(90%), P=1 bar, T=333K

| CR | 16 | 18 | 20 | 22 | 24 |
|---|---|---|---|---|---|
| IMEP (bar) | - | 8.35 | 7.93 | 7.80 | 7.43 |
| $I_{eff}$ (%) | - | 31.66 | 30.75 | 30.01 | 28.55 |
| ISFC (g/kW-h) | - | 308.68 | 316.69 | 320.42 | 337.37 |

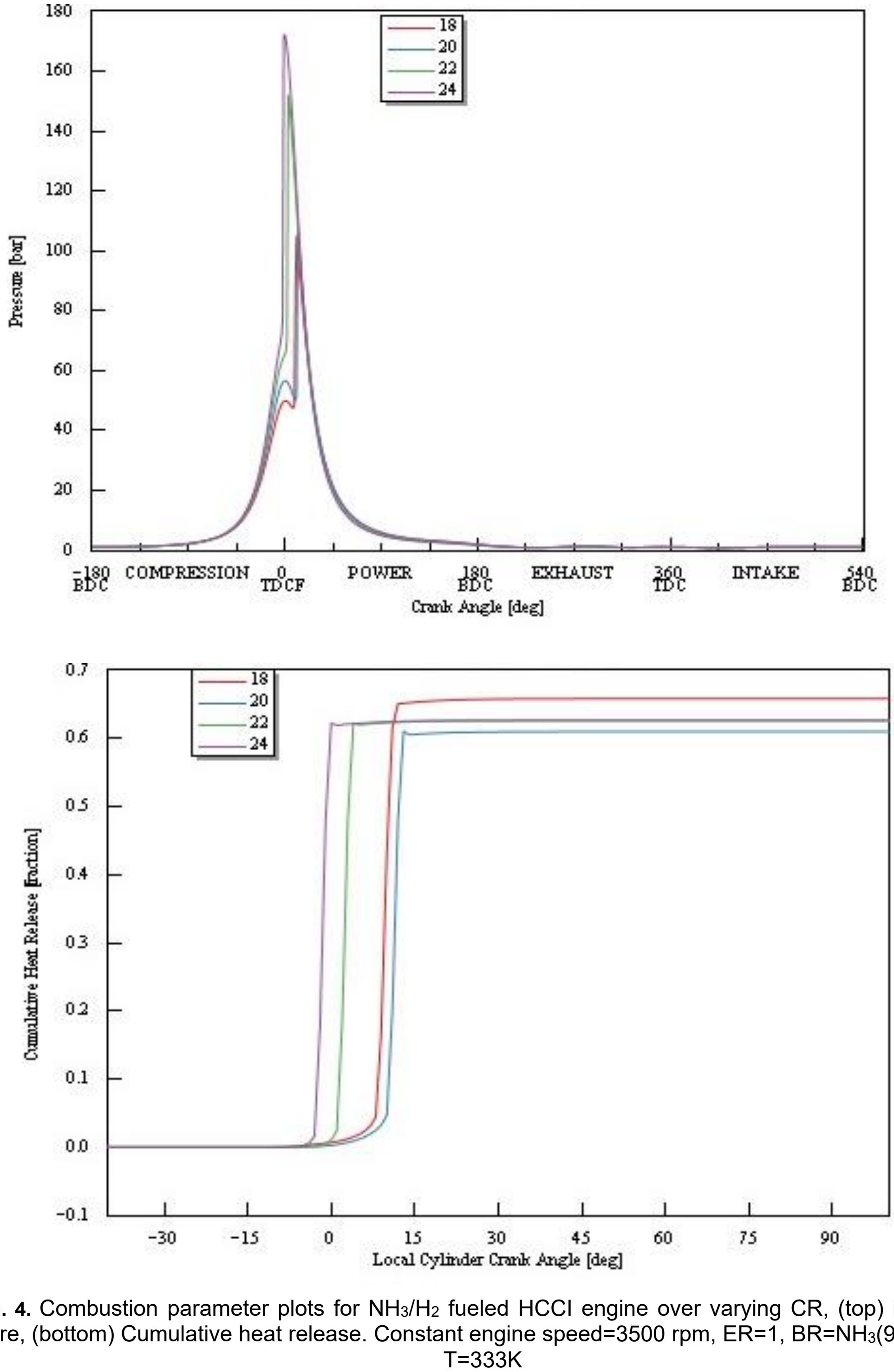

**Fig. 4.** Combustion parameter plots for $NH_3/H_2$ fueled HCCI engine over varying CR, (top) in-cylinder pressure, (bottom) Cumulative heat release. Constant engine speed=3500 rpm, ER=1, BR=$NH_3$(90%), P=1 bar, T=333K

### 3.2.3. Effect of varying equivalence ratio on $NH_3/H_2$ combustion

At fixed TFE of 67,6 MJ, CR at 20, engine speed at 3500 rpm, inlet temperature and pressure as 333 K and 1 bar respectively, the effect of varying ER on the HCCI combustion of $NH_3$ (90%) was investigated. ER (Lambda) was used to quantify the actual air to fuel ratio relative to the stoichiometry required to achieve complete combustion. From the fuel injector introducing $NH_3$ into the engine model, the air to fuel ratio was defined as lambda. This lambda was then varied as a parameter. Simulation test 3 was done with ER case sweep range of 0.8 to 3. ER of 0.8 indicated a rich mixture, while ER of 3 indicated a very lean mixture. Fig. 5 presents the effect of varying ER on Pmax and CHR. Combustion delayed with decrease in lambda. This phenomena was natural as the fuel molecules requires enough air molecules for complete combustion chemistry. At lambda value 0.8 indicating a rich mixture, CHR was lowest, ISFC was highest and, the overall engine thermal efficiency was lowest. Although, 1 is the standard lambda value however optimal CHR, ISFC, and the best thermal efficiency was observed at lambda value 2 for the set operating conditions as illustrates in Table 8. Likewise, combustion phasing parameter CA50, presented better at very lean mixture of lambda 2. The fuel blend might require more air than stoichiometry for better phasing of a complete combustion.

**Table 8.** Engine performance metrics for varying ER at constant engine speed=3500 rpm, CR=20, BR=$NH_3$(90%), P=1bar, T=333K

| ER (lambda) | 0.8 | 1 | 1.5 | 2 | 2.5 | 3 |
|---|---|---|---|---|---|---|
| IMEP (bar) | 7.97 | 8.40 | 8.41 | 8.38 | 7.47 | 6.85 |
| $I_{eff}$ (%) | 26.69 | 31.09 | 38.94 | 42.94 | 40.68 | 38.69 |
| ISFC (g/kW-h) | 408.19 | 325.68 | 196.05 | 149.10 | 137.25 | 131.37 |

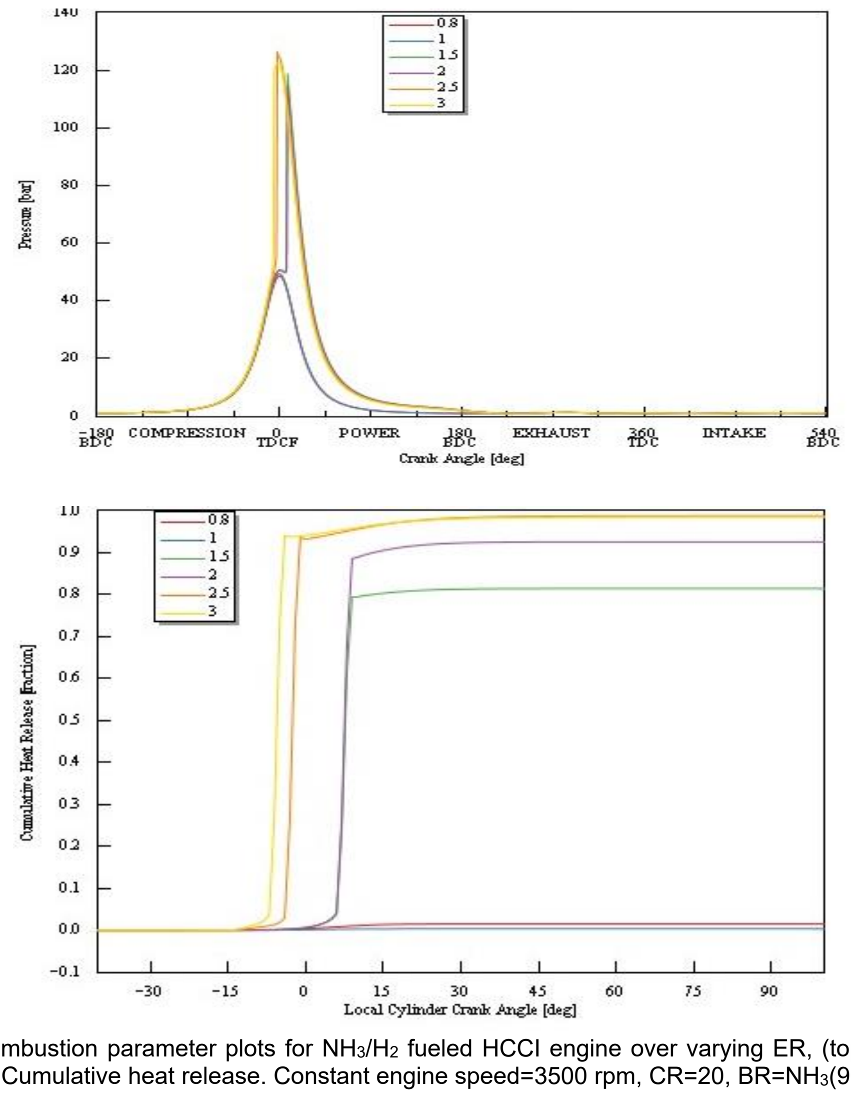

**Fig. 5.** Combustion parameter plots for $NH_3/H_2$ fueled HCCI engine over varying ER, (top) in-cylinder pressure, (bottom) Cumulative heat release. Constant engine speed=3500 rpm, CR=20, BR=$NH_3$(90%), P=1bar, T=333K

### 3.2.4. Effect of varying fuel blending ratio on $NH_3/H_2$ combustion

Table 9 and Figure 6 represents the effect of BR on the HCCI combustion and performance for fixed TFE of 67,6 MJ. For CR at 20, engine speed at 3500 rpm, ER of 2, inlet temperature and pressure as 333 K and 1 bar respectively, simulation test was performed for $NH_3/H_2$ BR of 100/0, 90/10, 80/20, 70/30, 60/40, and 50/50. Table 5 already presented the BRs for $NH_3/H_2$ from pure $NH_3$ to $NH_3$ (50%), as a function of their MFR and LHV. This is to allow for clear presentation of results. Pure $NH_3$ did not combust readily in the engine model as illustrated on the CHR in Figure 6. Pmax at this operating conditions was relatively same for all BR except pure $NH_3$. Engine combustion and performance metrics were optimal at BR of 90. The CHR graph illustrated that, the more $H_2$ fraction in the fuel blend, the earlier combustion was initiated. However, CHR was highest in the fuel blend with the lowest $H_2$ fraction. The effect of the BR can also be seen engine efficiency, as BR of 90 presented the highest $I_{eff}$ and IMEP. This phenomena portrays that $H_2$ was good for improving the ignition properties of $NH_3$. However, heat of combustion of $NH_3$ was above 1.3 times that of $H_2$ fuel [22]. This was reflective from the CHR values for the various BR. An increase in the $NH_3$ percentage fraction from 80 to 90 in the fuel blend, resulted into almost about 30% increase in the cumulative heat release.

**Table 9.** Engine performance metrics for varying BR at constant engine speed=3500 rpm, ER=2, CR=20, P=1bar, T=333 K

| BR ($NH_3/H_2$) | 100/0 | 90/10 | 80/20 | 70/30 | 60/40 | 50/50 |
|---|---|---|---|---|---|---|
| IMEP (bar) | -0.5 | 8.23 | 7.38 | 6.89 | 6.42 | 6.06 |
| $I_{eff}$ (%) | -3.4 | 40.19 | 28.01 | 23.01 | 19.53 | 17.57 |
| ISFC (g/kW-h) | 0 | 173.23 | 168.24 | 184.55 | 205.06 | 219.02 |

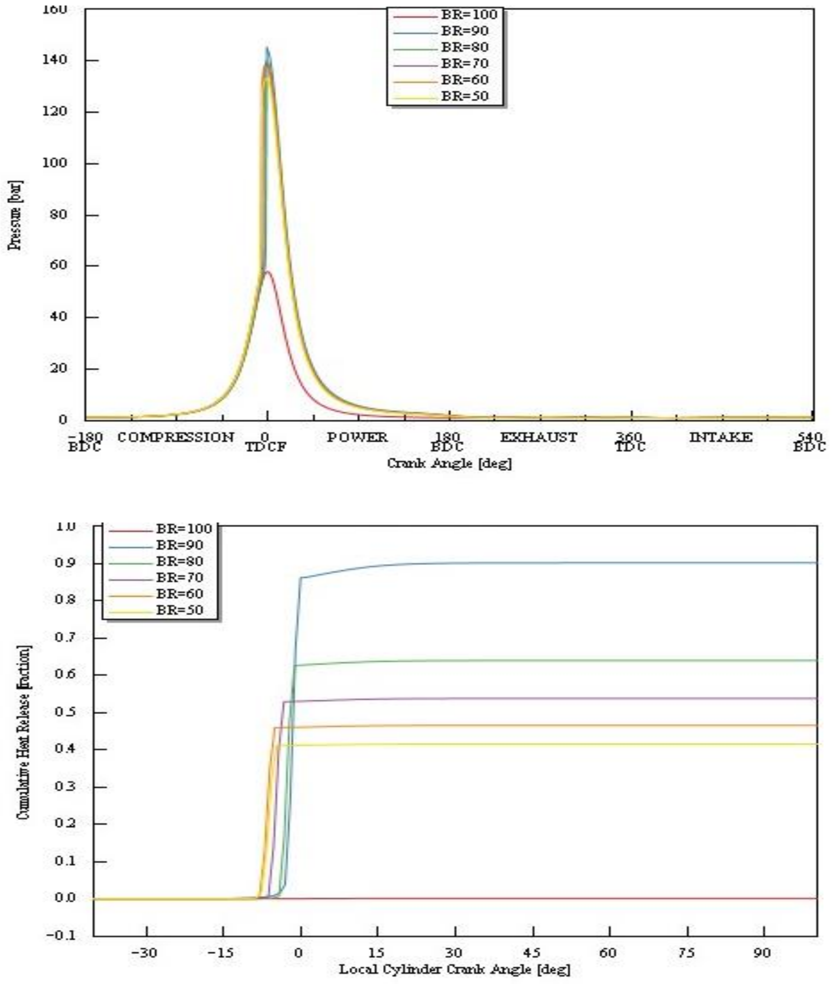

**Fig. 6.** Combustion parameter plots for $NH_3/H_2$ fueled HCCI engine over varying BR, (top) in-cylinder pressure, (bottom) cumulative heat release. Varying BR at constant engine speed=3500 rpm, ER=2, CR=20, P=1bar, T=333K

### 3.2.5. Final round optimization on $NH_3$/$H_2$ combustion engine.

A combination of operating conditions producing optimal engine performance and combustion phasing was used for the simulation of the final round optimization. At fixed engine speed of 3500 rpm, CR of 20, TFE of 67.6 MJ, BR of $NH_3$/$H_2$ as 90/10, inlet temperature and pressure as 333 K and 1 bar respectively, ER was varied between 1 and 2 to compare combustion of stoichiometry mixture, to lean mixture. Table 10 shows that with ER of value 2, engine performance metrics are better. Fig. 7 presents that there was a 35% higher CHR at ER of 2 than 1. This illustrated that there was higher heat of combustion at ER of 2. Although there was zero carbon emissions from both cases, however, NOx emission level was higher at ER value of 2. This might be due to more oxygen radicals forming more bonds with the available nitrogen, as a result of the excess air to fuel ratio from ER value 1 to 1.5 and to 2. This was where the tradeoff occurs. It presents a situation of making a choice between engine overall efficiency or the engine NOx emissions.

**Table 10.** Engine performance and Combustion metric from final round optimization. Engine speed=3500 rpm, CR=20, P=1 bar, T=333 K, BR=$NH_3$(90%)

| ER | IMEP (bar) | $I_{eff}$ (%) | ISFC (g/kW-h) | Pmax (bar) | Tmax (K) | CA50 (deg) | NOx (ppm_emissions) | HC (g/kW-h) | CO, CO2 (g/kW-h) |
|---|---|---|---|---|---|---|---|---|---|
| 1 | 8.2 | 30.8 | 318.6 | 143.5 | 2702 | 1.7 | 42.4 | 0.19 | - |
| 1.5 | 8.4 | 38.9 | 196.1 | 137.6 | 2818 | 4.6 | 180.7 | 0.07 | - |
| 2 | 8.4 | 42.9 | 149.8 | 144.2 | 2896 | 0.5 | 1045.5 | 0.00 | - |

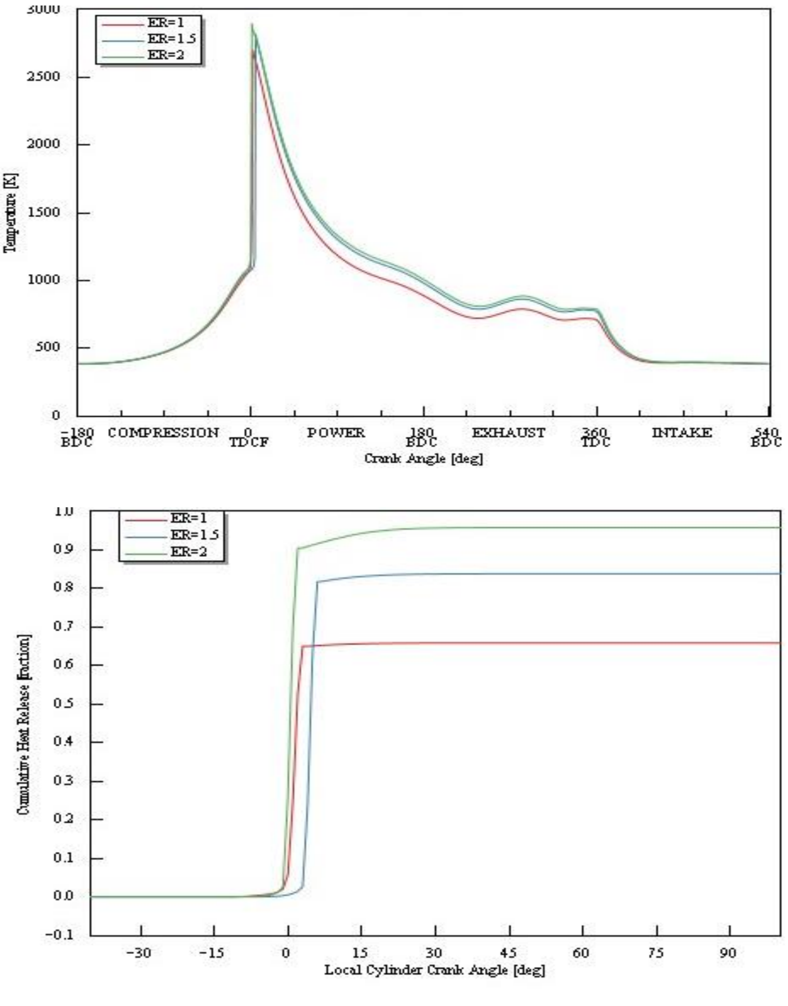

**Fig. 7.** Combustion parameter plots for $NH_3$/$H_2$ fueled HCCI engine over varying ER, (left) cylinder max temperature (right) cumulative heat release. Engine speed=3500 rpm, CR=20, P=1 bar, T=333 K, BR=$NH_3$(90%)

### 3.3. Cyclic variability and engine comparability.

For ensuring stability and reliability of the results, a cycle-to-cycle variability analysis performed for both the current study engine model and the baseline model. The CA02 (crank angle at 2% total heat release) and CA50 investigated against the cycle numbers as illustrated in Fig. 8. This was significant for understanding the combustion stability and assessing how efficiently the fuel combustion is proceeding. The combustion in the baseline model already became stable at cycle number 3 and continued to remain stable for the rest of the cycles. Although combustion phasing was unstable during the first four cycles in the $NH_3/H_2$ engine model, however phasing became stable at cycle number 5 and retained stability until the end.

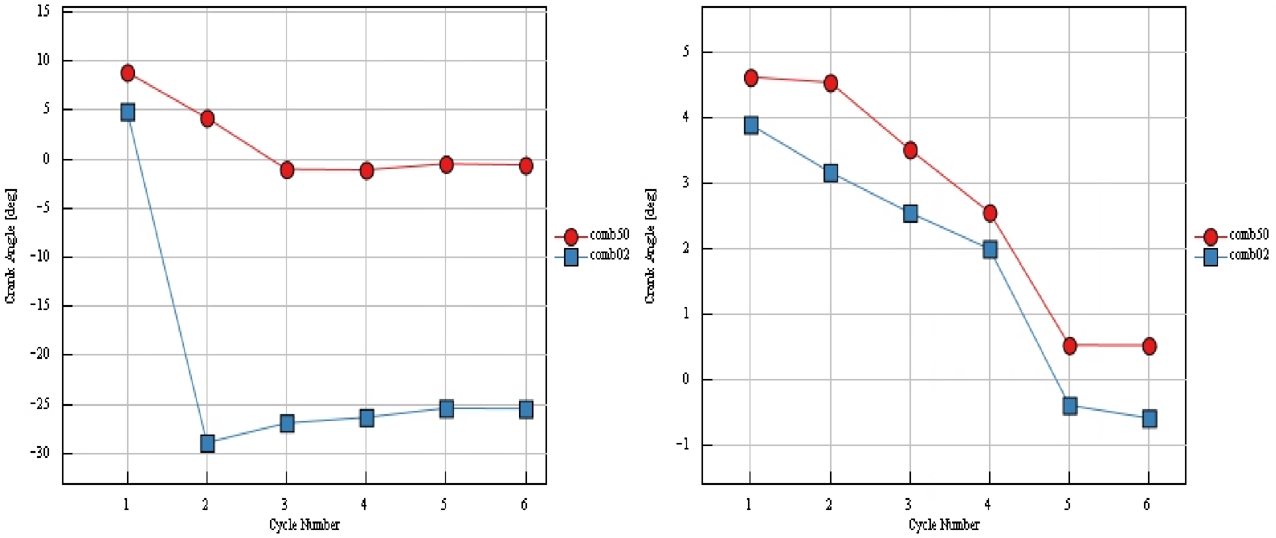

**Fig. 8.** Scatter plot for CA02/CA50 for all cycles in, (left) n-Heptane fueled engine model (right) $NH_3/H_2$ engine model.

## 4. Discussion

### 4.1 Summary of the simulation results and analysis of HCCI combustion behavior

This study investigated the effect of engine speed, $NH_3/H_2$ fuel BR, ER, and CR on the engine performance metrics, combustion phasing and emission characteristics. The study was initiated with BR ratio of 90%/10% for $NH_3/H_2$, respectively, ER of lambda value 1, and CR of 20. Engine speed was varied and observed as a crucial parameter, which significantly had effect on the combustion phasing and engine performance as illustrated in table 6 and Fig. 3. As engine speed increased, the timing of autoignition was better optimized, likewise the engine thermal efficiency and IMEP. The optimized engine speed was 3500 rpm while keeping other operating conditions constant. At engine speed higher than this, the simulation did not reach a convergence. The reason behind the $NH_3/H_2$ fueled HCCI engine, running at faster speed may be that the fuel blend had a faster combustion characteristic compared to heptane fuel. $H_2$ has a high flame speed and can contribute to the faster combustion [23], allowing quicker energy release and enabling the engine run efficiently at higher speeds than that of the n-heptane fueled engine model. The fuel reactivity could play a role in the influence on the engine speed. While keeping other operating conditions constant, CR was varied between 18 to 24. As CR increased, the combustion process advanced, and the peak in-cylinder pressure increased as illustrated in Fig. 4. This trend presented the effect of CR on the combustion characteristics. Although excessively high in-cylinder pressure was detrimental to the engine overall efficiency over time [24]. CR less than 18 gave rise to an unstable combustion where all engine performance were all negative. This implies that at CR lower than 18, compression pressure was not enough for the autoignition of the air-fuel mixture and the thermodynamic conditions were not favorable. Additionally, natural aspiration is considered for the engine operation, warranting higher CR. A value of 20 was observed for CR to be optimal for engine performance and combustion parameters.

The blending of $NH_3$ and $H_2$ fuel depends on specific applications and desired engine performance. Pure $NH_3$ misfired, but with as little as 10% $H_2$ in the fuel energy mix, auto-ignition occurred and performance drastically improved as stated in Table 9 and Fig. 6. However, with increasing fraction of $H_2$ in the fuel blend, there was observable decrease in the cumulative heat release. This could be as a result of the combustion characteristic of $H_2$ fuel. $H_2$ has a faster combustion rate and wider flammability and as a result [24], an increase in the fuel blend fraction will shift the combustion characteristics towards that of $H_2$ which ignites faster but less intense combustion process. This caused CA50 to occur before TDC. It also resulted into an overall lower cumulative heat release as the fraction of $H_2$ increased in the blend. Dilution effect from fuel blend might also affect the overall kinetics and concentration of the reacting species, potentially causing a reduction in the heat release rate, as discussed by Oakley et al. [25] in their study.

The air to fuel ER also had significant effect on the overall engine performance, particularly on the emission characteristics. The heat release rate and cumulative heat release were also higher at a very lean air-fuel mixture, although combustion phasing remained almost at zero-degree crank angle. The intrinsic advantages of zero-carbon fuel was observed for all cases; however, NOx emission level was higher at ER value of 2. NOx Concentration was proportional to peak cylinder temperature. Among the three ER cases, ER of value 2 resulted into the highest in-cylinder temperature. Additionally, formation of more NOx might be due to more oxygen radicals forming more bonds with the available nitrogen as a result of the excess air to fuel ratio from ER value 1 to 1.5 and to 2, while having the best engine performance metric and overall efficiency at ER value as 2. This is where the tradeoff occurs. It presents a situation of making a choice between engine overall efficiency or the engine NOx emissions. This result is corresponding to the study of Meng et al. [26]. They concluded from their study that an increasing inlet pressure with a relatively high ER was favorable for $NH_3$ combustion, although a higher NO formation observed due to high activity of OH and HNO from the chemical kinetics behaviors.

A comparison summary of the performance metrics, combustion parameters and the emission characteristics of both modeled HCCI engines have presented in Table 10. Given the operating conditions as presented in the table, the $NH_3/H_2$ fueled engine enables a higher engine speed. IMEP was almost 2.7 times higher, indicated efficiency ($I_{eff}$) was few points higher, and likewise more fuel economical than baseline engine. Overall emission characteristics was also better than the baseline engine. Although NOx emissions was shown to be more, but very low as values as given in parts per million (ppm) emission. There might also be a high NOx from the baseline engine but the chemical reaction kinetics model used for the baseline engine model did not include a NOx mechanism as presented in Table 2.

**Table 11.** Engine performance and Combustion metric from comparison of the n-Heptane fueled HCCI versus $NH_3/H_2$ fueled HCCI engine. P=1 bar, T=333 K, ncyc = 6

| **Items** | **n-Heptane** | **$NH_3/H_2$ (90/10)** |
|---|---|---|
| Speed (rpm) | 900 | 3500 |
| CR | 10 | 20 |
| AFR | 50 | $\lambda = 2$ |
| IMEP (bar) | 3.10 | 8.43 |
| $I_{eff}$ (%) | 40.1 | 42.9 |
| ISFC (g/kW-h) | 199.7 | 149.8 |
| $P_{max}$ (bar) | 41.2 | 143.1 |
| $T_{max}$ (K) | 1680 | 2831 |
| CA50 (deg) | -0.6 | 0.5 |
| NOx (ppm) | -- | 1045 |
| HC (g/kW-h) | 1.48 e-9 | 0 |
| $CO_2$ (g/kW-h) | 849.7 | 0 |
| CO (g/kW-h) | 3.75 e-4 | 0 |

### 4.2 Remarks on strengths and limitations of GT-Power for chemical reaction kinetic modeling of HCCI

Despite the complexity of low temperature combustion engines such as HCCI, GT-Power provides a user-friendly interface with the availability of the template model, to facilitate detailed thermodynamic modeling capabilities and execution of HCCI simulations, with detailed combustion process analysis even without user's extensive background in computational fluid dynamics (CFD). Being able to study the transient behaviors of engines, especially how engines responds to varying operating conditions against real time performance and emissions predictions makes this software a highly valuable tool for comprehensive powertrain simulations. Ignition timing control is very important in HCCI engines, likewise achieving accurate predictions are challenging. GT-power might have limitations in accurately capturing ignition timing for HCCI engine models. GT-power 0D model disregards in-cylinder thermal stratification – which has been proven necessary to correctly represent HCCI heat release. In real world conditions, model in GT-power may not account fully for these variations non-homogeneity and spatial variations. Additionally, complex and extensive calibration of HCCI engine parameters (such as fuel injection timing, temperature, CR and ER), may limit achieving accurate simulations and as such, experimental calibration could be done to validate the simulation of HCCI in GT-Power. Feasibility of this current study simulations was validated by benchmarking the results against the base-line HCCI engine fed with n-heptane (diesel surrogate). The result proved that the solver provides stable simulations, for all considered fuel blends and their chemical kinetic mechanisms. Simulation times with multi component mechanism of $NH_3$, $H_2$ and n-heptane are on average 32 seconds per cycle with the solver reaching convergence after 6 cycles.

Resulting in-cylinder temperature and pressure of 2831K and 143bar, were relatively high for a HCCI engine and caused increase in engine noise level [27]. Fridhi et al. 2016, studies investigated the effect of intake in inlet air temperate and pressure on the in-cylinder temperature and pressure [28]. They identified that increase in inlet air temperature and pressure reduce the in-cylinder temperature and pressure as well. This could also be studied for further optimization of this $NH_3/H_2$ fueled HCCI engine. More accurate-absolute level concluding on the combustion phenomenology is reserved for higher-fidelity methods like the UVATZ multizone-model developed by Kakoee et al. [20] to supplement on the drawbacks of single-zone kinetic solver offered by GT-Suite. Overall NOx level was also significantly low, and carbon emission was zero as $NH_3/H_2$ fuel blend HCCI engines offer new pathways to zero carbon emission.

## 5. Conclusions

General conclusion regarding the feasibility of GT-suite to investigate the effect of BR, air to fuel ER, and CR on the performance, emission and combustion characteristics of an $NH_3/H_2$ fueled HCCI engine is presented. The study allowed to draw the following conclusions:

- As little as 10 w/w% of $H_2$ in the fuel blend could improve the autoignition properties of $NH_3$.
- Blending $H_2$ with $NH_3$, allowed for an increase in engine speed up to about four times the speed of the n-heptane (diesel surrogate) fuel.
- High CR caused excessively high in-cylinder pressure, which might be detrimental to the engine overall efficiency over time.
- With blending ratio of 10%/90% of $H_2$ /$NH_3$, a lambda as high as 3 can be achieved without significant penalty on $I_{eff}$.
- Combustion of $NH_3/H_2$ blend in excessive air (lean mixture), might present an optimal engine performance and overall efficiency but caused a trade-off effect as engine NOx emissions increased.
- In comparison, the $NH_3/H_2$ fueled engine offered a better engine performance, overall efficiency and emission characteristics than the n-heptane fueled engine model.
- Results from this study proved that GT-suite chemical kinetic solver provides stable simulations, for all considered fuel blends and their chemical kinetic mechanisms

### Acknowledgment

We gratefully acknowledge the Efficient Power Train team, School of Technology and Innovation, of the University of Vaasa, for adequate support, mentoring and collaboration.

## DECLARATION OF INTEREST

The author reports financial support was provided by University of Vaasa. The author reports a relationship with University of Vaasa that includes: employment. The author declare that they have no known competing financial interests or personal relationships that could have appeared to influence the work reported in this paper.

## References

1] Alagumalai, Avinash. "Internal Combustion Engines: Progress and Prospects." *Renewable &; Sustainable Energy Reviews* 38 (2014): 561-571. https://doi.org/10.1016/j.rser.2014.06.014
[2] Onorati, A., Payri, R., Vaglieco, B. M., et al. "The Role of Hydrogen for Future Internal Combustion Engines." *International Journal of Engine Research* 23, no. 4 (2022): 529-540. https://doi.org/10.1177/14680874221081947
[3] Manigandan, S., Je Ir Ryu, T.R Praveen Kumar, and Mahmoud Elgendi. "Hydrogen and Ammonia as a Primary Fuel – A Critical Review of Production Technologies, Diesel Engine Applications, and Challenges." *Fuel (Guildford)* 352 (2023): 129100. https://doi.org/10.1016/j.fuel.2023.129100
[4] Komninos, N.P, and C.D Rakopoulos. "Modeling HCCI Combustion of Biofuels: A Review." *Renewable & Sustainable Energy Reviews* 16, no. 3 (2012): 1588-1610. https://doi.org/10.1016/j.rser.2011.11.026
[5] Xu, Wanying, Meng Zhang, Yifeng Zhang, Jinhua Wang, and Zuohua Huang. "Effects of Temperature and Composition Inhomogeneity on the Ignition Characteristics of $NH_3$/H2 Co-firing Fuels Under HCCI Operating Conditions." *Applications in Energy and Combustion Science* 15 (2023): 100194. https://doi.org/10.1016/j.jaecs.2023.100194
[6] Wang, Binbin, Chuanlei Yang, Hechun Wang, Deng Hu, Baoyin Duan, and Yinyan Wang. "Study on Combustion and Emission Performance of Dual Injection Strategy for Ammonia/Hydrogen Dual-Fuel Engine." *Journal of Physics: Conference Series* 2437, no. 1 (2023). https://doi.org/10.1088/1742-6596/2437/1/012027
[7] P., Rahul Chowta, Krishna Murthy, and Mahesha G.T. "Emission Control Studies in Homogeneous Charge Compression Ignition, Premixed Charge Compression Ignition and Common Rail Direct Injection Engines - a Review." *Biofuels (London)* 12, no. 4 (2021): 363-368. https://doi.org/10.1080/17597269.2019.1657660
[8] Vasudev, Aneesh, Maciej Mikulski, Praveen Ramanujam Balakrishnan, Xiaoguo Storm, and Jacek Hunicz. "Thermo-kinetic Multi-zone Modelling of Low Temperature Combustion Engines." *Progress in Energy and Combustion Science* 91 (2022): 100998. https://doi.org/10.1016/j.pecs.2022.100998.
[9] Gamma Technologies (2024). Available at; https://www.gtisoft.com/. Accessed 20.4.2024.
[10] Guo, Hongsheng, W. Stuart Neill, Wally Chippior, Hailin Li, and Joshua D. Taylor. "An Experimental and Modeling Study of HCCI Combustion Using N-heptane." *Journal of Engineering for Gas Turbines and Power* 132, no. 2 (2010). https://doi.org/10.1115/1.3124667
[11] Yelvington, Paul E., Marc Bernat I. Rallo, Steven Liput, Jefferson W. Tester, William H. Green, and Jialin Yang. "Prediction of Performance Maps for Homogeneous-Charge Compression-Ignition Engines." *Combustion Science and Technology* 176, no. 8 (2004): 1243-1282. https://doi.org/10.1080/00102200490457420
[12]GT-SUITE Engine Performance Application Manual (Version 2022). Page 96-100. Gamma Technologies LLC, Illinois, USA
[13] Patel, A., Kong, S., and Reitz, R., "Development and Validation of a Reduced Reaction Mechanism for HCCI Engine Simulations," SAE Technical Paper 2004-01-0558, (2004), https://doi.org/10.4271/2004-01-0558
[14] Jia, M., Peng, Z.-J., & Xie, M.-Z. Numerical investigation of soot reduction potentials with diesel homogeneous charge compression ignition combustion by an improved phenomenological soot model. *Proceedings of the Institution of Mechanical Engineers, Part D: Journal of Automobile Engineering*, *223*(3), 395–412. (2009). https://doi.org/10.1243/09544070jauto993
[15] Stagni, Alessandro, Suphaporn Arunthanayothin, Mathilde Dehue, Olivier Herbinet, Frédérique Battin-Leclerc, Pierre Bréquigny, Christine Mounaïm-Rousselle, and Tiziano Faravelli. "Low- and Intermediate-temperature Ammonia/hydrogen Oxidation in a Flow Reactor: Experiments and a Wide-range Kinetic Modeling." *Chemical Engineering Journal (Lausanne, Switzerland : 1996)* 471 (2023): 144577. https://doi.org/10.1016/j.cej.2023.144577
[16] Xu, W., Zhang, M., Zhang, Y., Wang, J., & Huang, Z. Effects of temperature and composition inhomogeneity on the ignition characteristics of $NH_3/H_2$ co-firing fuels under HCCI operating

conditions. *Applications in Energy and Combustion Science*, 100194 (2023). https://doi.org/10.1016/j.jaecs.2023.100194

[17] Han, X., Wang, Z., Costa, M., Sun, Z., He, Y., & Cen, K. Experimental and kinetic modeling study of laminar burning velocities of $NH_3$/air, $NH_3/H_2$/air, $NH_3$/CO/air and $NH_3/CH_4$/air premixed flames. *Combustion and Flame*, *206*, (2019). 214–226. https://doi.org/10.1016/j.combustflame.2019.05.003

[18] Lhuillier, Charles, Pierre Brequigny, Francesco Contino, and Christine Rousselle. "Combustion Characteristics of Ammonia in a Modern Spark-Ignition Engine." *SAE Technical Paper Series* October (2019). https://doi.org/10.4271/2019-24-0237

[19] Vasudev, A., Cafari, A., Axelsson, M., Mikulski, M. et al., ”Towards Next Generation Control-Oriented Thermo-Kinetic Model for Reactivity Controlled Compression Ignition Marine Engines, “SAE Technical Paper 2022-01-1033, (2022), http://doi.org/10.4271/2022-01-1033

[20] Kakoee, Alireza, Aneesh Vasudev, Ben Smulter, Jari Hyvonen, and Maciej Mikulski. ”A Predictive 1D Modeling Framework for Reactivity-Controlled Compression Ignition Engines, via a Chemistry-Based, Multizone Combustion Object,” SAE Technical Paper 2023-24-0001, (2023). https://doi.org/10.4271/2023-24-0001.

[21] Hasan, M.M, M.M Rahman, K. Kadirgama, and D. Ramasamy. "Numerical Study of Engine Parameters on Combustion and Performance Characteristics in an N-heptane Fueled HCCI Engine." *Applied Thermal Engineering* 128 (2018): 1464-1475. https://doi.org/10.1016/j.applthermaleng.2017.09.121

[22] Kojima, Y. "Physical and Chemical Properties of Ammonia as Energy and Hydrogen Carriers". In: Aika, Ki., Kobayashi, H. (eds) $CO_2$ Free Ammonia as an Energy Carrier. Springer, Singapore. (2023) https://doi.org/10.1007/978-981-19-4767-4_2

[23] Han, Wang, Peng Dai, Xiaolong Gou, and Zheng Chen. "A Review of Laminar Flame Speeds of Hydrogen and Syngas Measured from Propagating Spherical Flames." *Applications in Energy and Combustion Science* 1-4 (2020): 100008. https://doi.org/10.1016/j.jaecs.2020.100008.

[24] Schneider, Simon, and Georg Wachtmeister. "The Potential of Extremely High Cylinder Pressures in Diesel Engines, Part 2." *MTZ Industrial* 3, no. 1 (2013): 54-60. https://doi.org/10.1007/s40353-013-0072-y

[25] Oakley, Aaron, Hua Zhao, Nicos Ladommatos, and Tom Ma. *Dilution Effects on the Controlled Auto-ignition (CAI) Combustion of Hydrocarbon and Alcohol Fuels*. (2001). https://doi.org/10.4271/2001-01-3606.

[26] Meng, Xiangyu, Chenhan Zhao, Meichao Qin, Mingkun Zhang, Dongsheng Dong, Wuqiang Long, and Mingshu Bi. "Study on Chemical Kinetics and NO Behaviors in Pre-chamber Jet-induced Ignition Mode with Ammonia." *Fuel Processing Technology* 250 (2023): 107876. https://doi.org/10.1016/j.fuproc.2023.107876.

[27] V Akash , Ramanandan H S. “Homogeneous Charge Compression Ignition (HCCI) Engines-A Review on the Technology for Posterity”. *International Journal of Engineering Research & Technology (Ijert)* Volume 09, Issue 06 (June 2020)

[28] Fridhi Hadia, Wadhah Soua, Ammar Hidouri, Omri Ahmed. “Effects of Intake Temperature and Intake Pressure on Combustion and Exhaust Emissions of HCCI Engine.” *International Journal of Mechanical & Mechatronics Engineering*. 10. 1616 (2016).

# Numerical Study of Activity Stratification-Controlled Ammonia-Hydrogen Combined Combustion under Stoichiometric Condition

Zhichao Hu[1], Yanzhao An[1]*, Yiqiang Pei[1], Deyang Zhao[1], Zhanwang Su[2], Hua Zhao[3]

[1] State Key Laboratory of Engines, Tianjin University, Tianjin 300072, China
[2] Guangxi Yuchai Machinery Co., Ltd., Guangxi Yulin 537005
[3] Centre for Advanced Powertrain and Fuels, Brunel University London, Kingston Lane, Uxbridge UB8 3PH, UK.

**Abstract.**

Reducing carbon emissions in the transportation industry requires new technology for engines coupled with carbon-neutral fuels. Ammonia ($NH_3$) and hydrogen ($H_2$) are the promise future zero-carbon fuels. A controlled activity stratification strategy for a large-bore spark ignition engine using $NH_3$-$H_2$ blend fuel is proposed in this study. Under stoichiometric operation, the Split-Channel Supercharge and Fuel-Air Mixing technology (SCS-FAM) is proposed, fuel and air were supplied separately using dou-ble helical intake ports with swirl ratios of 1.2 and 1.4, corresponding to two intake schemes. Different $NH_3$-$H_2$ blend fuel entered cylinder through the high and low swirl ratio intake ports respectively to achieve different mixture stratification. The in-cylinder flow-temperature field, concentration distribution, and key intermediates were compared by simulations. The results showed an upper lean and bottom rich mixture stratification was formed when the $NH_3$-$H_2$ entered through the high swirl port, which does not benefit for in-cylinder combustion. However, an upper rich and bottom lean mixture stratification along with strong swirl was formed in-cylinder that was conducive to ignition and flame propagation when $NH_3$-$H_2$ blend fuel flowed through the low swirl ratio port. The local ammonia-rich regions produced large amounts of $H_2$, H, and other active radicals at the flame front, providing a reaction envi-ronment for ammonia consumption in the low activity zone, which resulted in the shorter combustion duration, improved combustion efficiency, and lower $NO_x$ emissions. With fixed spark timing, Scheme 2 with high swirl air intake exhibited higher indicated thermal efficiency (ITE) compared to Scheme 1 with low swirl air intake over a range of $H_2$ blending ratios from 5 to 20 vol%, achieving a peak ITE of 42.1% at a 15 vol% $H_2$ blend ratio. The engine performance decreased at a high $H_2$ ratio of 30% due to the too fast combustion speed and increased wall heat transfer loss with higher combustion tem-perature. The local $NH_3$-rich auto-thermal reforming, the reaction between excess H radical and $NH_2$/$N_2H_2$ regenerate $H_2$ at the flame front, consequently improving in-cylinder activity distribution. The reaction $N_2O+H=N_2+OH$ was one of the main exothermic reactions and produced much OH radical. $N_2O$ emissions decreased with the increase of the $H_2$ ratio in the $NH_3$-$H_2$ blend fuel. This work aims to achieve efficiently stratified $NH_3$-$H_2$ combined combustion through innovative SCS-FAM technology avoid H2 backfire.

## 1. Introduction

The paradigm shift from fossil fuel reliance towards renewable energy infrastructures is markedly propelled by strides in energy storage innovation [1]. Foreseen as a linchpin within the power framework, the internal combustion engine (ICE) propelled by E-fuels is poised to maintain a central position, particularly within demanding sectors where alternative energy alternatives may encounter impediments [2]. Notably, among the array of zero-carbon fuel options, both ammonia ($NH_3$) and hydrogen ($H_2$) have emerged as focal points, owing to their distinctive attributes and promise in satiating energy requisites whilst ameliorating ecological footprints.

Hydrogen stands as a renowned exemplar of a clean energy reservoir, given its combustion yielding only water as a byproduct. Its rapid flame propagation velocity, expansive combustion range, robust diffusive properties, and low ignition energy confer notable merits for augmenting engine efficacy [3]. Nonetheless, the storage and conveyance of hydrogen in a highly compressed liquid state necessitate ultra-low temperatures, thereby engendering a considerable upsurge in expenses and intricacies [4]. Moreover, the integration of hydrogen into engine systems is frequently hampered by obstacles such as backfire and knock phenomena [5].

In contrast, ammonia emerges as an outstanding carrier of hydrogen, boasting a superior volumetric energy density compared to both hydrogen and methane. Its stable molecular configuration facilitates straightforward storage, rendering it a viable alternative as a fuel source [6]. Nevertheless, ammonia's relatively sluggish flame propagation rate and elevated ignition energy result in heightened cycle-to-cycle variations and combustion instability within engines. Despite these challenges, ammonia perseveres as a promising contender for zero-carbon fuels due to its potential for efficient and safe energy storage. The conversion of ammonia to hydrogen via thermal reforming obviates the need for additional hydrogen provisioning apparatus [7-9]. Researchers have delved into various parameters, including hydrogen fraction [10-13], compression ratio (CR) [14-16], equivalence ratio [17,18], and intake boosting [19], to optimize the performance of ammonia-hydrogen engines. Recently, Zhang et al. [20] conducted numerical investigations into the influence of the combustion chamber on the combus-tion dynamics of heavy-duty lean combustion spark-ignition (SI) natural gas engines. Their findings suggest that augmenting tumble and swirl ratios engenders a favorable in-cylinder flow pattern and heightened turbulence intensity, ultimately curtailing the combustion duration. Porpatham et al. [21] improved engine performance and reduced emissions on a biogas SI engine by enhancing swirl flow. Increasing turbulence in combustion chamber enhances mixing between the combustion and unburned zones, reducing flame extinction in low flame speed fuels. This indicates that the optimization of intake swirl is crucial for enhancing the performance of SI gas engines, especially for large-bore en-gines.

However, for ammonia with very low laminar burning speed, merely increasing the turbulence level in the cylinder is insufficient, and improvement in local mixture reactivity is also required. Liu et al. [22] scrutinized ammonia's behavior within a rapid compression machine, exploring equivalence ratios ranging from 1.75 to 2.25 under high thermodynamic conditions. Notably, the conversion efficiency of ammonia to hydrogen peaked at a stoichiometry ratio of $\varphi = 2$. Nonetheless, higher equivalence ratios led to a diminished reaction yield of $NH_2+H = NH+H_2$, thereby impeding hydrogen generation. Lin et al. [23] conducted numerical simulations to evaluate the performance of a SI engine utilizing a blend of directly injected liquid ammonia and port-injected hydrogen. Their analysis unveiled a notable ammonia stratification upon injection prior to top dead center (TDC). Significantly, hydrogen generated via ammonia-rich combustion played a pivotal role in augmenting flame propagation. These studies emphasize the potential of ammonia to undergo in-cylinder reforming under local high-temperature and pressure conditions to produce hydrogen for improving the local mixture reactivity. Consequently, the optimization of rational flow and mixture stratification in large-bore ammonia-hydrogen engines is imperative to improve combustion performance. Most of the aforementioned studies employ port fuel injection of gaseous ammonia and hydrogen, a method entailing fuel-air premixing prior to cylinder ingress. Such premixed gaseous fuel intake not only diminishes intake volume, thereby reducing power output [24], but also heightens the risk of backfire within intake ports [25].

In this investigation, we propose a controlled activity stratification approach coupled with split-channel supercharge and fuel-air mixing (SCS-FAM) technology for a large-bore SI engine utilizing an $NH_3$-$H_2$ blend fuel. This innovative strategy aims to address challenges related to intake $H_2$ backfire while concurrently enhancing thermal efficiency in $NH_3$-$H_2$ engines. Specifically, it promotes fuel-air mixing and combustion by enhancing the intake swirl. The methodology entails the utilization of two distinct high and low swirl intake ports: one dedicated to delivering supercharged ammonia-hydrogen mixture and the other designated for air induction, thereby engendering differential flow patterns and mixture stratification within the cylinder. The primary objective of this study is to conduct numerical assessments elucidating the impact of hydrogen stratification on combined $NH_3$-$H_2$ combustion dynamics and emission characteristics under high and low swirl intake airflow configurations. Additionally, a detailed investigation into ammonia reforming under localized high thermodynamic conditions is undertaken to bolster the efficacy of controlled activity stratified combustion for ammonia-hydrogen blends. Finally, we delve into the reaction pathway under a 5 vol% $H_2$ condition, delineating the mechanisms underlying local ammonia-rich reforming, the promotional role of $H_2$, and the formation of $NO_x$ emissions.

## 2. Methodology

### 2.1 Engine configuration

The original four-stroke gas SI engine used syngas as fuel for power generation, as shown in Figure 1. $NH_3$-$H_2$ blend fuel is utilized in the current numerical simulations, featuring essential parameters delineated in Table 1. This engine configuration incorporates two distinct intake ports, each specifically allocated for fuel and air induction. The fuel composition entails a blend of various proportions of pre-mixed ammonia and hydrogen. Upon the opening of intake valves, fuel and air ingress through their respective ports and undergo thorough mixing within the cylinder. Consequently, a well-stratified ammonia-hydrogen-air mixture is formed, subsequently ignited by a high-energy spark plug. Notably, it is pertinent to highlight that the swirl ratio of intake port 1 exceeds that of intake port 2.

**Table 1**. Main engine specifications.

| Parameters (units) | Value |
|---|---|
| Bore (mm) | 200 |
| Stroke (mm) | 210 |
| Conrod (mm) | 520 |
| Compression ratio | 9.5 |
| Engine speed (r/min) | 1000 |
| Displacement volume (L) | 105.6 |
| Cylinder Number | 16 |
| Rated power (kW) | 1200 |
| High swirl ratio of intake port 1 | 1.4 |
| Low swirl ratio of intake port 2 | 1.2 |

**Fig. 1.** Engine testing site

## 2.2 Computational models

In this study, a three-dimensional (3D) computational fluid dynamics (CFD) model of the ammonia-hydrogen gas engine was established utilizing Converge v3.0 software. The detailed 3D engine model and 1D GT-power model are depicted in Figure 2. The re-normalization group k-ε turbulence model [26] was employed to simulate turbulence phenomena. For combustion simulation, the detailed chemistry solver SAGE [27], coupled with the Okafor [28] mechanism, was utilized to capture the intricate combustion processes of ammonia and hydrogen. To strike a balance between computational accuracy and time efficiency, a baseline grid resolution of 4 mm was adopted, with grid independence analyses conducted, as depicted in Figure 3a. Fixed embeddings were implemented in the intake and exhaust valves and combustion chamber, with grid refinement to 0.5 mm and 2 mm, respectively. During the ignition phase, the mesh near the spark plug was further refined to 0.125 mm. Moreover, adaptive mesh refinement (AMR) was employed within regions exhibiting high-velocity and high-temperature gradients. Utilizing predefined sub-grid criteria of 15 K for temperature fields and 1 m/s for velocity fields, the grid resolution was adaptively refined to 1 mm and 0.5 mm, respectively, ensuring accurate capture of critical flow features. Figure 3b illustrates the dynamic evolution of grid refinement throughout the simulation process.

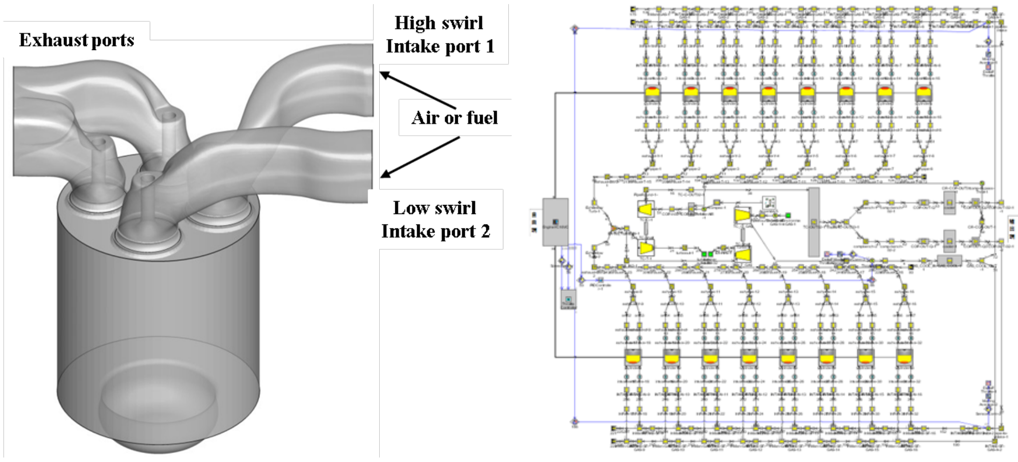
Exhaust ports
High swirl Intake port 1
Air or fuel
Low swirl Intake port 2

**Fig. 2**. 1D and 3D Engine models

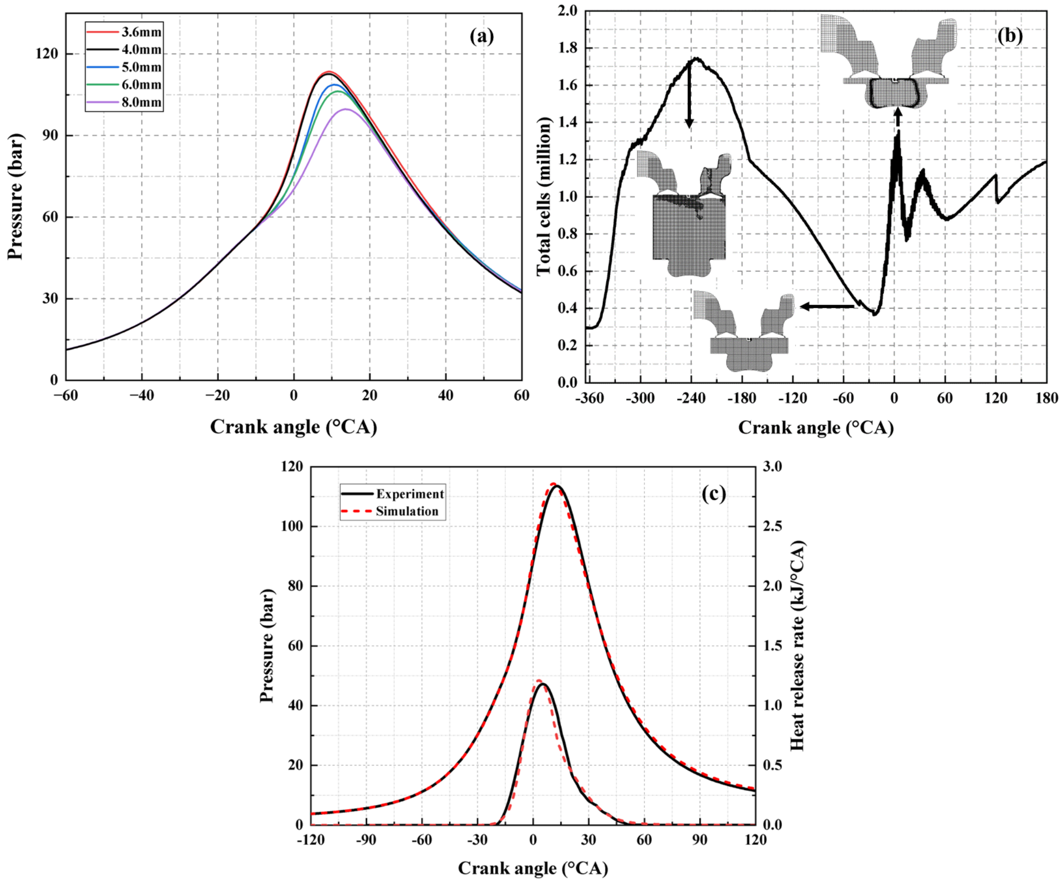

**Fig. 3.** Engine model verification

## 2.3 Model validation

The engine model was calibrated with experimental data for syngas combustion, as depicted in Figure 3c. The specific syngas composition is shown in Table 2 and boundary conditions are shown in Table 3. Fuel enters intake port 1, air enters intake port 2, fuel and air mixes internally to form a mixture with an excess air coefficient (λ) of 1.67. The detailed boundaries and initial conditions for 3D simulation are from experimentally validated 1D GT-power model.

**Table 2.** Gas components used in the experiment

| Gas component | Vol% |
|---|---|
| CO | 69.07 |
| $H_2$ | 6.07 |
| $CO_2$ | 16.59 |
| $O_2$ | 0.47 |
| $N_2$ | 7.8 |
| Low heat value | 2267 Kcal/Nm$^3$ |

**Table 3.** Experimental conditions

| Parameters (units) | Value |
|---|---|
| Intake fuel temperature (K) | 315.5 |
| Intake air temperature (K) | 313.8 |
| Intake air pressure (bar) | 3.348 |
| Intake fuel pressure (bar) | 2.987 |
| Cylinder wall temperature (K) | 433 |
| Cylinder head temperature (K) | 524 |
| Piston wall temperature (K) | 553 |
| Spark timing (° CA ATDC) | -40 |
| Lambda | 1.67 |

## 2.4 Parametric cases

In the current simulations of the ammonia-hydrogen engine, the proposed Split-Channel Supercharge and Fuel-Air Mixing (SCS-FAM) technology is investigated. This technology entails the introduction of fuel and air into the cylinder through distinct intake ports, thereby influencing the flow field, mixture distribution, ignition, and flame propagation. Consequently, two intake schemes are explored based on SCS-FAM. In Scheme 1, $NH_3$-$H_2$ premixed fuels are introduced into intake port 1 with a high swirl ratio, while fresh air is induced into intake port 2 with a low swirl ratio. Conversely, in Scheme 2, $NH_3$-$H_2$ blend fuels are delivered into intake port 2 with a low swirl ratio, and air is supplied to intake port 1 with a high swirl ratio. It is noteworthy that in Scheme 2, a slightly lower $NH_3$-$H_2$ mixture flow into the cylinder occurs as $H_2$ blend ratios change from 5 to 30 vol%, attributable to the weaker intake fuel resistance associated with a low swirl ratio. To maintain a constant in-cylinder mixture concentration of $\lambda=1.0$, adjustments are made to the intake fuel pressure (3.34bar) while keeping the intake air pressure constant, as detailed in Table 4. The ignition timing for all cases is maintained at -30 ° CA aTDC.

**Table 4.** Overview of the intake air and fuel organization schemes

| Scheme 1 | | Scheme 2 | |
|---|---|---|---|
| High swirl intake port 1 for fuel, Low swirl intake port 2 for air, | | High swirl intake port 1 for air, Low swirl intake port 2 for fuel, | |
| $H_2$ (vol%) | Pressure (bar) | $H_2$ (vol%) | Pressure (bar) |
| 5 | 2.893 | 5 | 2.765 |
| 10 | 2.9 | 10 | 2.785 |
| 15 | 2.913 | 15 | 2.793 |
| 20 | 2.925 | 20 | 2.807 |
| 25 | 2.933 | 25 | 2.825 |
| 30 | 2.944 | 30 | 2.838 |

## 3. Result and discussion

### 3.1 Engine performance

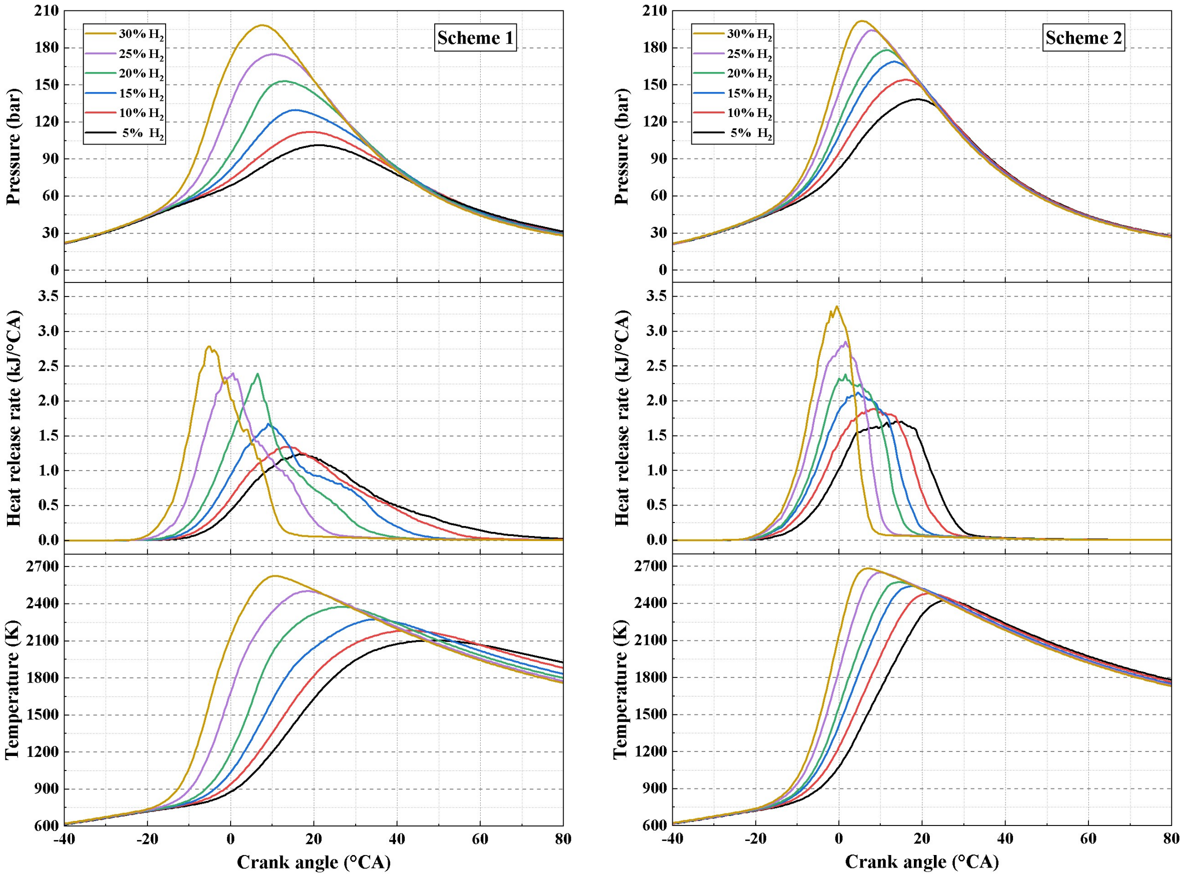

**Fig. 4.** In-cylinder pressure, heat release rate and temperature change with different $H_2$ blend ratios and intake flow strategies

Figure 4 depicts the impact of premixed $NH_3$-$H_2$ fuel on in-cylinder pressure, heat release rate (HRR), and temperature under two distinct intake schemes. Notably, as the blend ratio of $H_2$ increases from 5 to 30 vol%, the in-cylinder pressure, heat release rate (HRR), and temperature, show a clear upward trend with advanced phases. This trend underscores the augmentative influence of $H_2$ on in-cylinder mixture activity and $NH_3$ combustion velocity. Particularly noteworthy is the more substantial enhancement observed in Scheme 1, wherein peak cylinder pressure experiences a remarkable 95.9% increase at 30 vol% $H_2$ compared to 5 vol% $H_2$. Moreover, in-cylinder temperature displays a significant escalation, surpassing 2600 K for both intake schemes at 30 vol% $H_2$ blend ratios, potentially engendering adverse effects on $NO_x$ emissions and heightened heat transfer losses.

The organization of intake flow plays a pivotal role in shaping the $NH_3$-$H_2$ combined combustion process. Compared with Scheme 1, Scheme 2 exhibits even greater enhancements in in-cylinder pressure, featuring a more concentrated and notably elevated HRR occurring around TDC, coupled with rapid temperature increments, all achieved with identical $H_2$ additions. These observations underscore the promotional effect of high swirl intake airflow on $NH_3$-$H_2$ mixture formation and flame propagation, which becomes particularly evident when the $H_2$ blend ratio is below 15 vol%. Conversely, in Scheme 1, a delayed HRR after TDC is evident as the $H_2$ blend ratio diminishes from 15 to 5 vol%, resulting in a slower in-cylinder combustion process and post-combustion. However, HRR curves in Scheme 2 maintain a flattened profile from 3 to 20 °CA aTDC, even at 5 vol% $H_2$, without exhibiting post-combustion effects. Notably, Scheme 2 achieves a peak in-cylinder pressure of nearly 140 bar, representing a substantial 37.2% increase over Scheme 1.

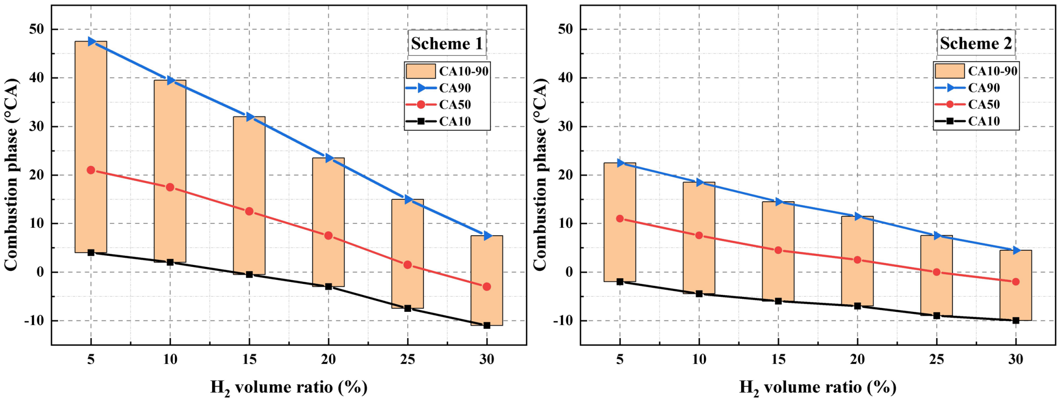

**Fig. 5.** Combustion phase and duration with different $H_2$ blend ratios and intake flow strategies

Figure 5 compares the combustion phase and duration with varying $H_2$ blend ratios under two distinct intake flow schemes. The crank angles of CA10, CA50, and CA90 correspond to the respective 10%, 50%, and 90% of accumulated heat release, serving as pivotal indicators of combustion progression. The combustion duration, delineated as the time interval between CA10 and CA90, offers insights into the temporal extent of combustion events. As the $H_2$ blend ratio escalates, it promotes the spark ignition and flame propagation processes within the cylinder, resulting in earlier combustion phases and shorter combustion durations. With the $H_2$ blend ratio ascending from 5 to 30 vol%, Scheme 1 exhibits a notable 24 °CA reduction in combustion duration, whereas Scheme 2 experiences a reduction of 10 °CA. This discrepancy underscores the profound influence of intake flow fields on the combustion velocity of $NH_3$-$H_2$ mixtures. Scheme 2, characterized by higher intake swirl flow, engenders a more thorough combustion process coupled with markedly advanced combustion phases compared to Scheme 1. Notably, the disparity in combustion duration between the two intake schemes is most pronounced during the CA50-CA90 interval. Introducing 5 vol% $H_2$ to $NH_3$ yields a 25 °CA shorter combustion duration for Scheme 2 relative to Scheme 1; however, as the blend ratio escalates to 30 vol% $H_2$, the discrepancy narrows to 3 °CA. Moreover, Scheme 2 demonstrates swift combustion even with minimal $H_2$ supplementation, underscoring the critical role of well-organized flow fields in large-bore engines. To elucidate these disparities further, an analysis of temperature and $H_2$ concentration distribution within the cylinder is imperative. Subsequent sections provide detailed analyses of these factors, offering insights into how intake flow fields contribute to the observed combustion characteristics.

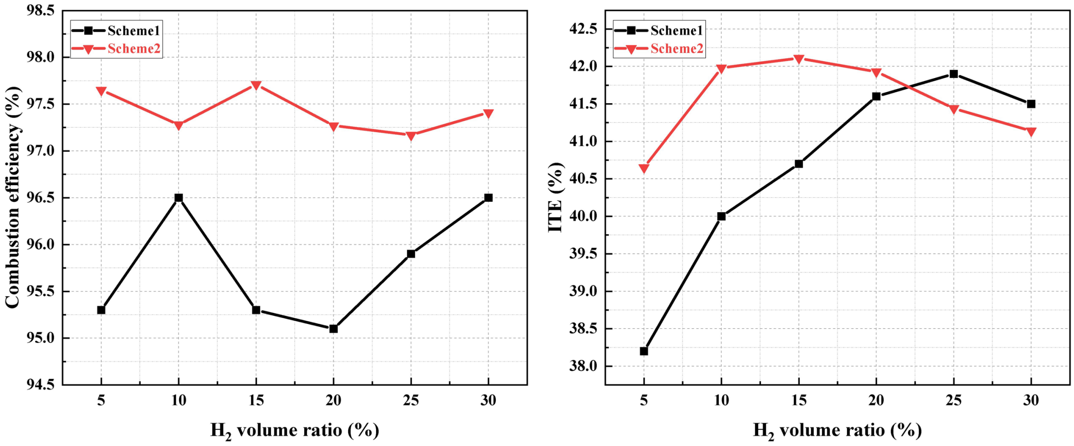

**Fig. 6.** The combustion efficiency and indicated thermal efficiency (ITE) change with different $H_2$ blend ratios and intake flow strategies

Figure 6 illustrates the impact of adding $H_2$ to $NH_3$ on the combustion efficiency and indicated thermal efficiency (ITE) under two distinct intake schemes. It is difficult to control the λ value exactly equal to 1, and there are slight differences in the mixture concentration within the cylinder,resulting in the combustion efficiency not increasing linearly as the increases of H2 proportion. However, it can be observed that the combustion efficiency of Scheme 2 is higher than that of Scheme 1.

The findings reveal a non-linear relationship between ITE and the increasing blend ratio of $H_2$. In Scheme 1, ITE peaks at 41.9% when the blend ratio reaches 25 vol% $H_2$, after which it begins to decline with further increases in the $H_2$ blending ratio up to 30 vol%. This decline in ITE at higher $H_2$ blend ratios may be attributed to elevated heat transfer losses and augmented negative work, as previously noted [29]. Conversely, Scheme 2 attains its maximum ITE of 42.1% at a lower blend ratio of 15 vol% $H_2$. Notably, when the $H_2$ blending ratio falls below 20%, Scheme 2 exhibits significantly higher ITE compared to Scheme 1. This suggests that the high swirl intake airflow characteristic of Scheme 2 is particularly effective in enhancing combustion at lower $H_2$ concentrations.

### 3.2 In-cylinder combustion process

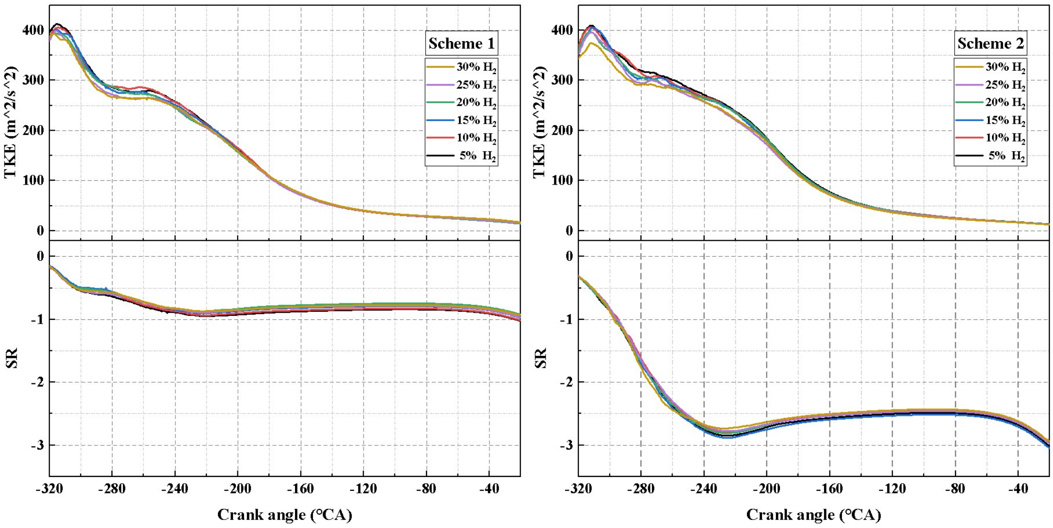

**Fig. 7.** Turbulence kinetic energy (TKE) and swirl ratio (SR) with different $H_2$ blend ratios and intake flow strategies

Swirl serves as a pivotal mechanism in conserving intake kinetic energy and facilitating mixture formation and combustion, particularly crucial when amalgamating with ammonia possessing low laminar flame velocity [30]. When comparing various $H_2$ blend ratios, both intake schemes uphold similar intake port pressures for gas and air respectively, thereby ensuring analogous flow dynamics and velocity fields within the cylinder. Figure 7 depicts the swirl ratio (SR) and turbulent kinetic energy (TKE) profiles of the two intake schemes across different $H_2$ blend ratios. Notably, in Scheme 2, where high-pressure intake air traverses through the high swirl ratio intake port 1, the in-cylinder swirl ratio experiences a substantial augmentation compared to Scheme 1. Despite employing a lower $H_2$ blend ratio, Scheme 2 consistently demonstrates superior $NH_3$-$H_2$ combined combustion performance.

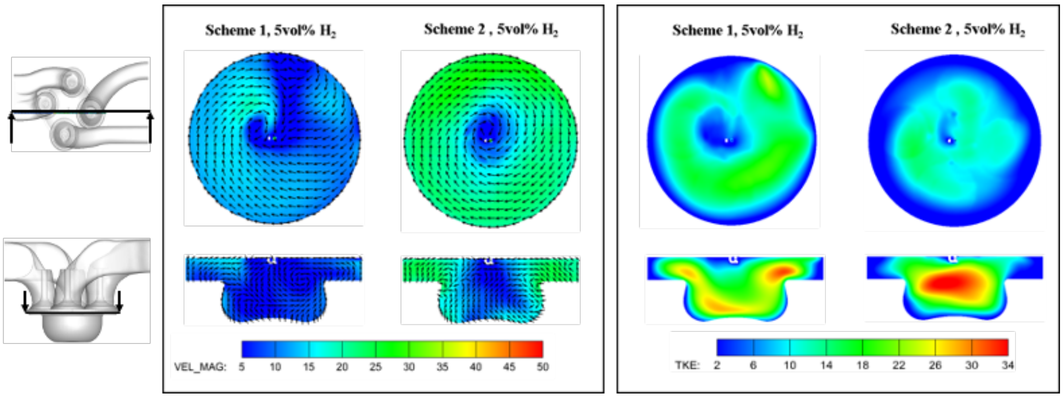

**Fig. 8.** In-cylinder flow field and turbulence kinetic energy distribution under two intake schemes

Figure 8 illustrates the velocity and turbulent kinetic energy (TKE) field distributions near the spark plug under the condition of a 5 vol% $H_2$ ratio. Two cross-sectional slices are compared: one vertical slice intersects the center of the valve seat of intake port 1, while the other horizontal slice intersects the center of the spark plug electrode.

Both intake schemes demonstrate the capability to generate stable swirls within the combustion chamber; however, they exhibit significant disparities in combustion characteristics. In Scheme 1, a significant weak TKE is observed around the spark plug and accompanied by a relatively weaker distribution of swirl within the chamber. This limits the expansion of the flame kernel and subsequent flame propagation, resulting in a gradual rise in combustion pressure, temperature, and HRR, as shown in Fig.3. Contrastingly, Scheme 2 demonstrates a more optimized velocity distribution. During the initial spark ignition period, a lower airflow velocity and TKE are achieved around the spark plug, fostering the stable development of the flame kernel. Subsequently, a higher airflow velocity field is formed around the initial flame kernel along with a higher TKE, which could promote flame propagation to achieve rapid combustion. Moreover, Scheme 2 presents another notable advantage: a heightened airflow velocity is engendered in the squish zone, promoting rapid combustion within this critical region and mitigating post-combustion processes. Consequently, the amalgamation of optimized velocity distribution and enhanced airflow velocity in the squish zone in Scheme 2 renders it a superior choice for fostering rapid and efficient combustion.

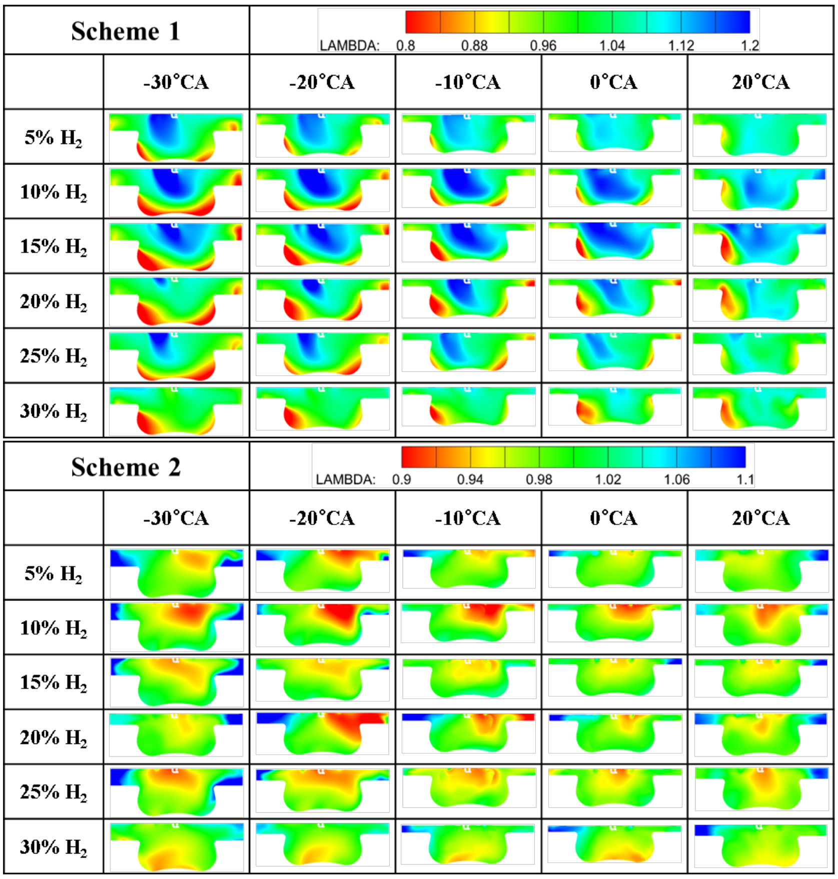

**Fig. 9.** In-cylinder $NH_3$-$H_2$ mixture distribution with different $H_2$ blend ratios under two intake schemes

The $NH_3$-$H_2$ mixture distribution during the combustion process, as depicted in Figure 9, reveals notable differences between Scheme 1 and Scheme 2 across various $H_2$ blend ratios. Scheme 2 consistently demonstrates superior $NH_3$-$H_2$ mixture stratification, characterized by the formation of a rich $NH_3$-$H_2$ mixture ($\lambda < 1$) proximal to the spark plug. This configuration is conducive to rapid in-cylinder flame propagation and combustion efficiency. In contrast, Scheme 1 exhibits poor $NH_3$-$H_2$ mixture stratification, with the rich mixture predominantly distributed in the piston bowl and the squish zone of the combustion chamber. Meanwhile, a lean mixture is observed around the spark plug, even as the $H_2$ blend ratio increases to 30 vol%. Such inadequate stratification hampers the prompt ignition and propagation of the flame front, leading to sluggish in-cylinder combustion kinetics and post-combustion processes.

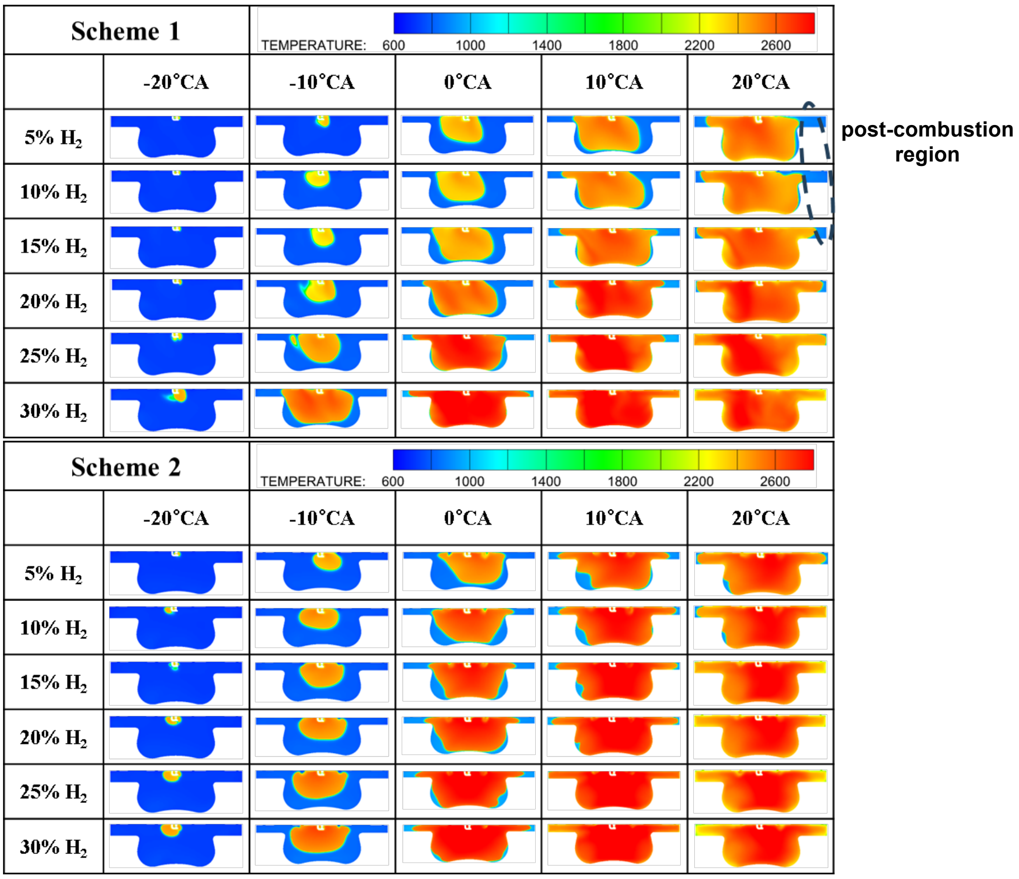

**Fig. 10.** In-cylinder temperature distribution with different $H_2$ blend ratios under two intake schemes

The initiation of flame kernel formation and the early stages of flame development play a pivotal role in shaping subsequent combustion processes [31]. Figure 10 illustrates the evolution of temperature with varying $H_2$ blend ratios under two intake schemes. Owing to the high reactivity and fast laminar burning velocity of $H_2$, $NH_3$-$H_2$ mixtures with higher $H_2$ blend ratios can rapidly form the initial flame kernel, leading to accelerated flame front development and elevated temperatures. This observed trend aligns closely with the changes observed in in-cylinder pressure and HRR. For $H_2$ blend ratios below 25 vol%, both schemes exhibit similar axial flame propagation within the cylinder. However, Scheme 2 demonstrates notably faster radial propagation than Scheme 1, particularly in the squish zone. This discrepancy can be attributed to the intense turbulence present in Scheme 2, which accelerates $NH_3$ flame propagation. Conversely, the sluggish flame propagation observed in the squish zone of Scheme 1 contributes to post-combustion effects, as depicted in Figure 2. Furthermore, the difference in flame propagation velocity between the two schemes diminishes as the $H_2$ blend ratio increases. As the mixture's reactivity increases and reaction rates accelerate, the influence of the flow field on flame propagation becomes less pronounced.

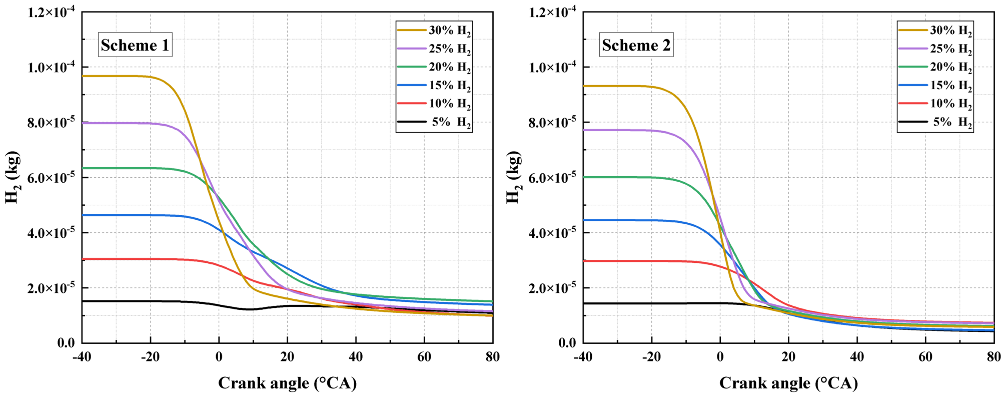

**Fig. 11.** Influence of $H_2$ blend ratios on $H_2$ mass over time under two intake schemes

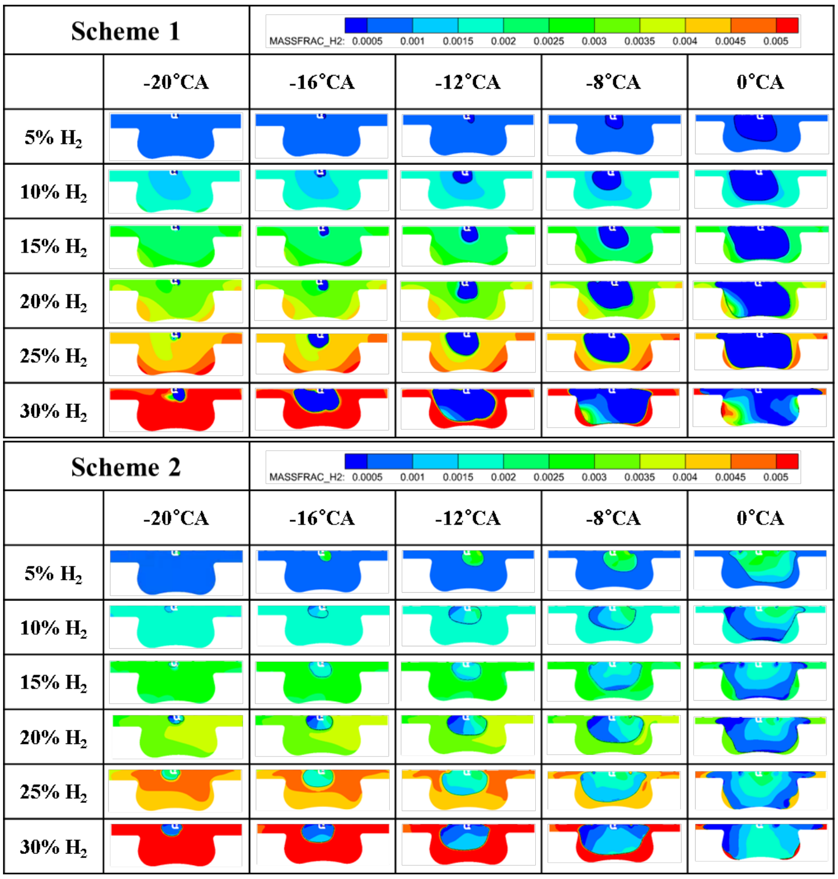

**Fig. 12.** In-cylinder $H_2$ mass fraction with different $H_2$ blend ratios under two intake schemes

Figure 11 illustrates a comparison of $H_2$ mass change across various $H_2$ blend ratios under two intake schemes. In both intake schemes, augmenting the $H_2$ blend ratio accelerates the $H_2$ consumption process, with Scheme 2 exhibiting a notably faster $H_2$ consumption rate compared to Scheme 1. Figure 12 provides a more detailed depiction of the distribution of $H_2$ mass fraction within the cylinder across different $H_2$ blend ratios and intake schemes. The 1500K temperature contour line demarcates the boundary for complete combustion, with a $H_2$ mass fraction below 0.0005 considered indicative of complete combustion. In Scheme 1, as the $H_2$ blend ratio increases from 5 to 30 vol%, the $H_2$ mass fraction remains consistently low (<0.0005) after combustion around TDC. This phenomenon is attributable to the lean $NH_3$-$H_2$ mixture predominant in the upper zone of the combustion chamber. Conversely, Scheme 2 showcases the emergence of additional $H_2$ in the burned zone, particularly pronounced under the 5 vol% $H_2$ condition, where the $H_2$ concentration surpasses even the initial mass fraction of $H_2$. This occurrence can be ascribed to localized ammonia-rich reforming, wherein $NH_3$ within a rich zone ($\lambda$>1) decomposes into $H_2$ under localized high-temperature and high-pressure conditions. This process contributes to the enhancement of in-cylinder activity distribution and stratification. It is noteworthy that despite the generation of additional $H_2$, $H_2$ emissions at later stages of combustion remain low in Scheme 2. This is attributed to the robust swirl movement of the airflow, effectively mixing and dispersing residual $H_2$, coupled with the high combustion efficiency achieved. This observation underscores the effectiveness of the intake scheme and combustion strategy in Scheme 2 in controlling $H_2$ emissions, even in conditions favorable for ammonia-rich reforming.

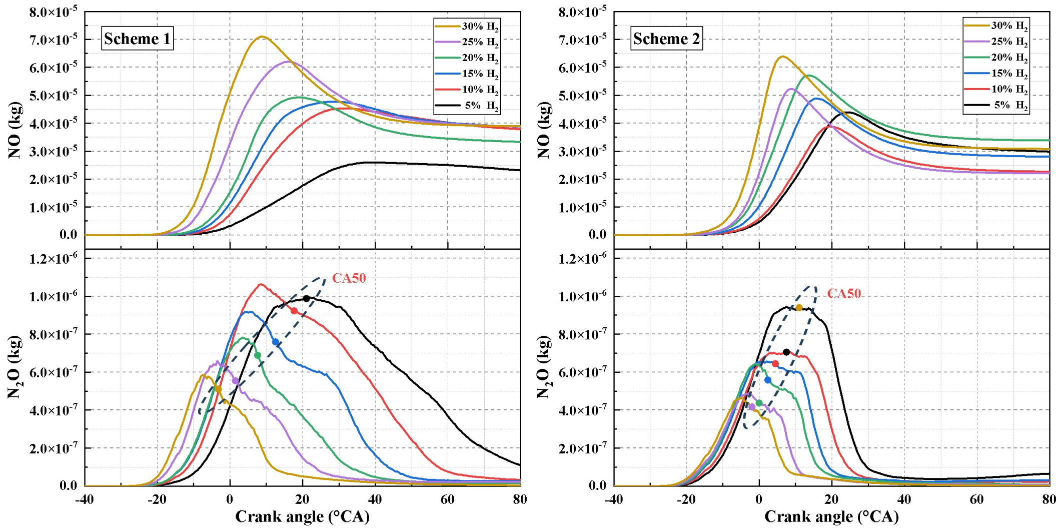

**Fig. 13.** Influence of $H_2$ blend ratios under two intake schemes on $NO_x$ mass over time

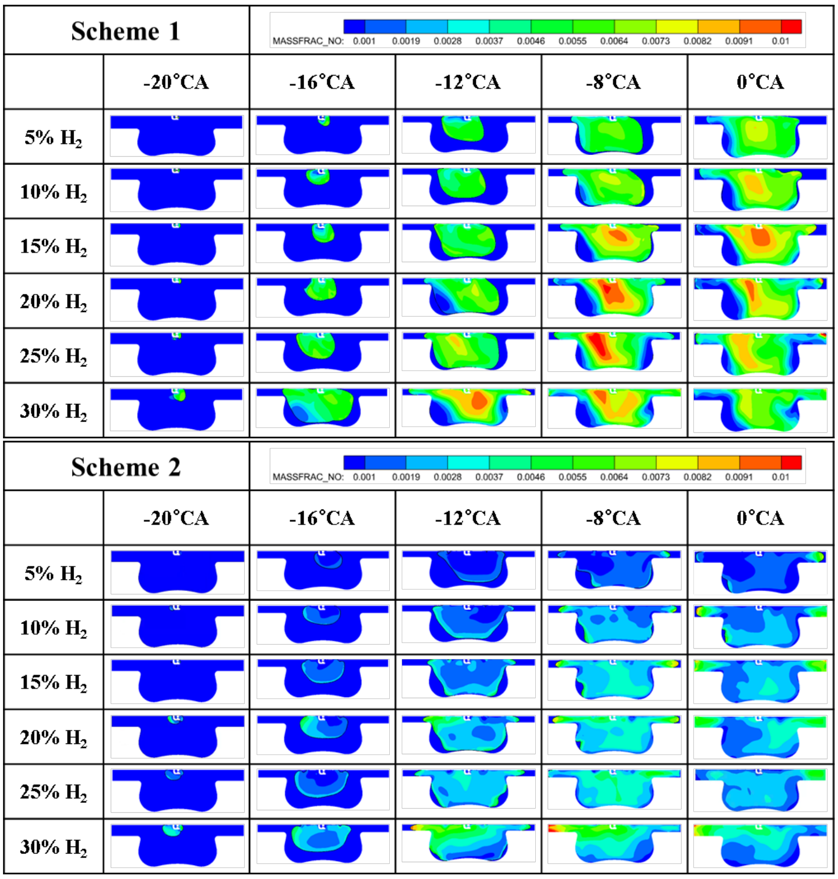
Scheme 1
Scheme 2
MASSFRAC_NO: 0.001 0.0019 0.0028 0.0037 0.0046 0.0055 0.0064 0.0073 0.0082 0.0091 0.01
-20°CA
-16°CA
-12°CA
-8°CA
0°CA
5% H2
10% H2
15% H2
20% H2
25% H2
30% H2

**Fig. 14.** In-cylinder NO mass fraction with different $H_2$ blend ratios under two intake schemes

Figure 13 provides a comparison of NO and $N_2O$ mass evolution with varying $H_2$ blend ratios under two intake schemes. NO, being the primary pollutant, is primarily localized in the flame front and high-temperature combustion zones [32]. Fuel-NO is primarily generated through the interaction of HNO with OH/H radicals [33]. Initially, the NO mass experiences a rapid surge in tandem with the increasing in-cylinder temperature, eventually peaking. Subsequently, during the later expansion stroke, the NO mass gradually diminishes as the in-cylinder temperature significantly decreases. The increase in $H_2$ blend ratio precipitates a rapid escalation in in-cylinder temperature and accelerates the formation of NO and OH/H radicals. However, the peak values and subsequent decrease of NO exhibit no clear pattern, especially in Scheme 2. This can be attributed to the optimized flow field dynamics and $NH_3$-$H_2$ mixture stratification within the cylinder, which contribute to the complex interplay of combustion processes and pollutant formation.

Figure 14 illustrates the distribution of NO within the cylinder for two intake schemes, unveiling a distinct stratification of NO concentration. Interestingly, the two schemes yield diametrically opposed results: in Scheme 1, a higher concentration of NO is observed near the spark plug, whereas in Scheme 2, elevated NO concentration is noted in the squish zone, located farther away from the spark plug. The regions exhibiting lower NO concentration correspond to the ammonia-rich zones depicted in Figure 8, where rich combustion conditions facilitate the suppression of NO generation. This observation underscores the intricate relationship between combustion dynamics, mixture stratification, and pollutant formation. Further analysis of the specific pathways contributing to NO formation and distribution will be conducted in the subsequent section, shedding light on the underlying mechanisms driving these observed phenomena.

The greenhouse effect of $N_2O$ is approximately 300 times stronger than that of $CO_2$, underscoring its significance despite its lower concentration compared to NO [34]. Figure 15 depicts the change in $N_2O$ mass with varying H2 blend ratios under two intake schemes, showcasing the generation of $N_2O$ at CA50 timing. $N_2O$ reaches its peak near CA50 and generates earlier as the hydrogen ratio increases. $N_2O$ primarily forms through the reaction NH + NO = $N_2O$ + H at low temperatures and is distributed across the flame front [32]. Initially, it exhibits rapid increases during combustion and is subsequently pyrolyzed at temperatures exceeding 1300 K [35]. As the $H_2$ blend ratio increases, in-cylinder temperature and H radical concentrations escalate, leading to diminished $N_2O$ mass during the expansion stroke. Scheme 2, characterized by higher combustion temperatures, achieves a more rapid decline in $N_2O$ mass compared to Scheme 1.

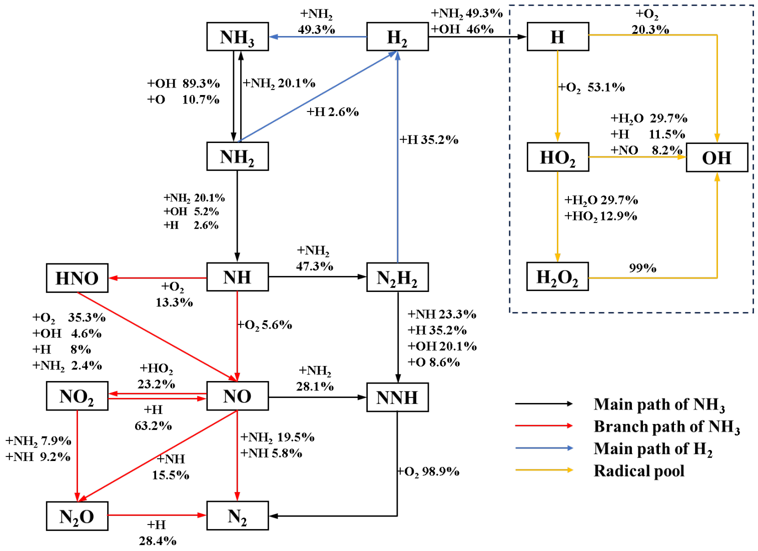

**Fig. 15.** Reaction pathway under 5 vol% $H_2$ condition in Scheme 2

To delve deeper into how the addition of $H_2$ facilitates the combustion process of $NH_3$, a kinetic analysis is conducted on the operating condition with 5 vol% $H_2$ in Scheme 2, as illustrated in Fig.15. The state parameters at CA10 serve as boundaries for this analysis. The percentages presented denote the proportion of species consumed through the specified pathway. Initially, $NH_3$ undergoes dehydrogenation to $NH_2$ via reactions with OH radicals. Subsequently, the primary reaction pathway involves a sequence of transformations: $NH_2$ is converted to NH, then to $N_2H_2$, followed by NNH, ultimately culminating in the formation of $N_2$. Additionally, other branches of NH3 consumption result in the generation of $NO_x$, as depicted by the red lines. Notably, $N_2O$ and $NO_2$ primarily stem from the conversion of NO. In this process, $O_2$ plays a significant role in NO formation. However, in locally ammonia-rich regions, the scarcity of $O_2$ impedes this pathway, leading to a reduction in $NO_x$ generation. Simultaneously, the surplus $NH_3$ promotes NO consumption through the production of NH and $NH_2$ radicals.

The yellow line denotes the contribution of $H_2$ addition to the radical pool. Initially, $H_2$ reacts with $NH_2$ and OH, yielding a substantial amount of H radicals. Notably, the introduction of $H_2$ prompts the reaction $NH_3$ + H = $NH_2$ + $H_2$ to proceed in the opposite direction, inhibiting the decomposition of $NH_3$ in the initial stage. Subsequently, H follows two distinct reaction pathways. In the first pathway, H reacts with $O_2$ to produce OH and O. In the second pathway, H participates in a chain-branching mechanism, leading to the formation of $HO_2$ and subsequently $H_2O_2$, which further decompose to yield additional OH radicals. Both of these pathways significantly contribute to the overall production of OH radicals, thereby enhancing the decomposition of $NH_3$ and promoting the combustion process. The intricate interplay among these reactions underscores the complexity of the combustion process in ammonia-hydrogen engines and emphasizes the pivotal role of $H_2$ addition in altering the reaction kinetics. While H radicals are primarily consumed by $O_2$, in locally ammonia-rich regions, they cannot be entirely depleted. Consequently, the surplus H radicals react with $N_2H_2$ and $NH_2$, resulting in the regeneration of $H_2$, as indicated by the blue lines.

## Conclusions

In our investigation, we introduce the Split-Channel Supercharge and Fuel-Air Mixing technology (SCS-FAM) tailored for implementation in large-bore ammonia-hydrogen engines. This pioneering SCS-FAM approach integrates two distinct intake ports: one dedicated to delivering supercharged fuel and the other responsible for supplying air. Leveraging numerical simulations, we assess the efficacy of the SCS-FAM technology and examine the significant impact of diverse $H_2$ blend ratios on the stratified combustion and emission characteristics of ammonia-hydrogen engines. The key findings from our study are summarized as follows:

1) The introduction of fuel through high and low swirl ratio intake ports respectively leads to distinct flow fields and mixture stratifications within the cylinder. Specifically, introducing $NH_3$-$H_2$ premixed fuels through the low swirl ratio intake port 2, along with air intake via the high swirl ratio intake port 1, generates a rich mixture distribution close to the spark plug. Concurrently, a strong swirl movement is observed away from the spark plug. This configuration effectively promotes the combined combustion of $NH_3$-$H_2$ within the engine, particularly in the squish zone, resulting in a shorter CA50-90 duration.
2) The ITE of the engine does not exhibit a linear relationship with the increase in the proportion of $H_2$. Specifically, Scheme 2 achieves its maximum ITE of 42.1% at a lower blend ratio of 15 vol% $H_2$. However, as the blend ratio surpasses 15%, the ITE decreases due to escalating negative work and heat transfer losses. In comparison to Scheme 1, Scheme 2 demonstrates a higher ITE within the $H_2$ blend range of 5-20 vol%. Notably, even with a 5 vol% $H_2$ blend, Scheme 2 can achieve satisfactory performance.
3) Under stoichiometric conditions, a localized ammonia-rich reforming phenomenon was observed within the cylinder, characterized by the regeneration of $H_2$ in the burned zone, where initially high concentrations of $NH_3$ were present. Remarkably, in Scheme 2, the $H_2$ concentration in the burned zone even exceeded its initial value with a 5 vol% $H_2$ blend. Particularly notable for Scheme 2, this ammonia-rich reforming occurred in close proximity to the spark plug, significantly enhancing the reactivity within the cylinder and thereby facilitating combustion.
4) The initial addition of $H_2$ can indeed exert a certain inhibitory effect on the oxidation of NH3 through the reaction $NH_3+H=NH_2+H_2$. However, the resulting H radicals subsequently generate OH directly or indirectly through two pathways, ultimately reversing the trend and promoting the oxidation of $NH_3$. Moreover, the reaction between H and $NH_2$ or $N_2H_2$ regenerates $H_2$, especially during ammonia-rich combustion.

## References

[1] Kurien, C., & Mittal, M. (2023). Utilization of green ammonia as a hydrogen energy carrier for decarbonization in spark ignition engines. International Journal of Hydrogen Energy.

[2] Qi, Y., Liu, W., Liu, S., Wang, W., Peng, Y., & Wang, Z. (2023). A review on ammonia-hydrogen fueled internal combustion engines. eTransportation, 100288.

[3] Yu, X., Li, Y., Zhang, J., Guo, Z., Du, Y., Li, D., ... & Zhang, J. (2024). Effects of hydrogen blending ratio on combustion and emission characteristics of an ammonia/hydrogen compound injection engine under different excess air coefficients. International Journal of Hydrogen Energy, 49, 1033-1047.

[4] Liu, X., Tang, Q., & Im, H. G. (2024). Enhancing ammonia engine efficiency through pre-chamber combustion and dual-fuel compression ignition techniques. Journal of Cleaner Production, 436, 140622.

[5] Levinsky, H. (2021). Why can't we just burn hydrogen? Challenges when changing fuels in an existing infrastructure. Progress in Energy and Combustion Science, 84, 100907.

[6] Reggeti, S. A., Kane, S. P., & Northrop, W. F. (2023). Hydrogen production in ammonia-fueled spark ignition engines. Applications in Energy and Combustion Science, 14, 100136.

[7] Comotti, M., & Frigo, S. (2015). Hydrogen generation system for ammonia–hydrogen fuelled internal combustion engines. International Journal of Hydrogen Energy, 40(33), 10673-10686.

[8] Ryu, K., Zacharakis-Jutz, G. E., & Kong, S. C. (2014). Performance enhancement of ammonia-fueled engine by using dissociation catalyst for hydrogen generation. International journal of hydrogen energy, 39(5), 2390-2398.

[9] Koike, M., Suzuoki, T., Takeuchi, T., Homma, T., Hariu, S., & Takeuchi, Y. (2021). Cold-start performance of an ammonia-fueled spark ignition engine with an on-board fuel reformer. International Journal of Hydrogen Energy, 46(50), 25689-25698.

[10] Mounaïm-Rousselle, C., Bréquigny, P., Dumand, C., & Houillé, S. (2021). Operating limits for ammonia fuel spark-ignition engine. Energies, 14(14), 4141.

[11] Swift, E., Kane, S., & Northrop, W. F. (2022, October). Operating range and emissions from ammonia-hydrogen mixtures in spark-ignited engines. In Internal Combustion Engine Division Fall Technical Conference (Vol. 86540, p. V001T02A013). American Society of Mechanical Engineers.

[12] Wang, D., Ji, C., Wang, S., Yang, J., & Wang, Z. (2021). Numerical study of the premixed ammonia-hydrogen combustion under engine-relevant conditions. International Journal of Hydrogen Energy, 46(2), 2667-2683.

[13] Lhuillier, C., Brequigny, P., Contino, F., & Mounaïm-Rousselle, C. (2020). Experimental study on ammonia/hydrogen/air combustion in spark ignition engine conditions. Fuel, 269, 117448.

[14] Mørch, C. S., Bjerre, A., Gøttrup, M. P., Sorenson, S. C., & Schramm, J. (2011). Ammonia/hydrogen mixtures in an SI-engine: Engine performance and analysis of a proposed fuel system. Fuel, 90(2), 854-864.

[15] Dinesh, M. H., Pandey, J. K., & Kumar, G. N. (2022). Study of performance, combustion, and NOx emission behavior of an SI engine fuelled with ammonia/hydrogen blends at various compression ratio. International Journal of Hydrogen Energy, 47(60), 25391-25403.

[16] Ji, C., Qiang, Y., Wang, S., Xin, G., Wang, Z., Hong, C., & Yang, J. (2024). Numerical investigation on the combustion performance of ammonia-hydrogen spark-ignition engine under various high compression ratios and different spark-ignition timings. International Journal of Hydrogen Energy, 56, 817-827.

[17] Westlye, F. R., Ivarsson, A., & Schramm, J. (2013). Experimental investigation of nitrogen based emissions from an ammonia fueled SI-engine. Fuel, 111, 239-247.

[18] Yu, X., Li, Y., Zhang, J., Guo, Z., Du, Y., Li, D., ... & Zhang, J. (2024). Effects of hydrogen blending ratio on combustion and emission characteristics of an ammonia/hydrogen compound injection engine under different excess air coefficients. International Journal of Hydrogen Energy, 49, 1033-1047. t

[19] Lhuillier, C. , Pierre Bréquigny, Contino, F. , & Mounam-Rousselle, C. . (2019). Performance and Emissions of an Ammonia-Fueled SI Engine with Hydrogen Enrichment. 14th International Conference on Engines & Vehicles.

[20] Zhang, S., Duan, X., Liu, Y., Guo, G., Zeng, H., Liu, J., ... & Yuan, Z. (2019). Experimental and numerical study the effect of combustion chamber shapes on combustion and emissions characteristics in a heavy-duty lean burn SI natural gas engine coupled with detail combustion mechanism. Fuel, 258, 116130.

[21] Porpatham, E. , Ramesh, A. , & Nagalingam, B. . (2011). Effect of swirl on the performance and combustion of a biogas fuelled spark ignition engine. Energy Conversion and Management, 95(1), 463-471.

[22] Liu, W., Qi, Y., Zhang, R., Zhang, Q., & Wang, Z. (2022). Hydrogen production from ammonia-rich combustion for fuel reforming under high temperature and high pressure conditions. Fuel, 327, 124830.

[23] Lin, Z., Liu, S., Liu, W., Wang, W., Cai, K., Qi, Y., ... & Li, J. (2024). Numerical investigation of ammonia-rich combustion produces hydrogen to accelerate ammonia combustion in a direct injection SI engine. International Journal of Hydrogen Energy, 49, 338-351.

[24] Stępien, Z. A comprehensive overview of hydrogen-fueled internal combustion engines: achievements and future challenges. Energies 2021; 14: 6504.

[25] Sun, Z., Hong, J., Zhang, T., Sun, B., Yang, B., Lu, L., ... & Wu, K. (2023). Hydrogen engine operation strategies: recent progress, industrialization challenges, and perspectives. International Journal of Hydrogen Energy, 48(1), 366-392.

[26] Han, Z., & Reitz, R. D. (1995). Turbulence modeling of internal combustion engines using RNG κ-ε models. Combustion science and technology, 106(4-6), 267-295.

[27] Senecal, P. K., Pomraning, E., Richards, K. J., Briggs, T. E., Choi, C. Y., McDavid, R. M., & Patterson, M. A. (2003). Multi-dimensional modeling of direct-injection diesel spray liquid length and flame lift-off length using CFD and parallel detailed chemistry. SAE transactions, 1331-1351.

[28] Okafor, E. C., Naito, Y., Colson, S., Ichikawa, A., Kudo, T., Hayakawa, A., & Kobayashi, H. (2018). Experimental and numerical study of the laminar burning velocity of CH4–NH3–air premixed flames. Combustion and flame, 187, 185-198.

[29] Dinesh, M. H., & Kumar, G. N. (2023). Experimental investigation of variable compression ratio and ignition timing effects on performance, combustion, and Nox emission of an ammonia/hydrogen-fuelled Si engine. International Journal of Hydrogen Energy, 48(90), 35139-35152.

[30] Hill, P. G., & Zhang, D. (1994). The effects of swirl and tumble on combustion in spark-ignition engines. Progress in energy and combustion science, 20(5), 373-429.

[31] Chen, H., Xu, M., Hung, D. L., & Zhuang, H. (2014). Cycle-to-cycle variation analysis of early flame propagation in engine cylinder using proper orthogonal decomposition. Experimental Thermal and Fluid Science, 58, 48-55.

[32] Zhang, H., Li, G., Long, Y., Zhang, Z., Wei, W., Zhou, M., & Belal, B. Y. (2023). Numerical study on combustion and emission characteristics of a spark-ignition ammonia engine added with hydrogen-rich gas from exhaust-fuel reforming. Fuel, 332, 125939.

[33] Yang, R., Liu, Z., & Liu, J. (2024). The methodology of decoupling fuel and thermal nitrogen oxides in multi-dimensional computational fluid dynamics combustion simulation of ammonia-hydrogen spark ignition engines. International Journal of Hydrogen Energy, 55, 300-318.

[34] Mohammadpour, A., Mazaheri, K., & Alipoor, A. (2022). Reaction zone characteristics, thermal performance and NOx/N2O emissions analyses of ammonia MILD combustion. International Journal of Hydrogen Energy, 47(48), 21013-21031.

[35] Huo, J., Zhao, T., Lin, H., Li, J., Zhang, W., Huang, Z., & Han, D. (2024). Study on lean combustion of ammonia-hydrogen mixtures in a pre-chamber engine. Fuel, 361, 130773.

# Session 2.1 THERMAL MANAGEMENT

# The Hotspot Ignition Nature of Thermal Runaway in Lithium Iron Phosphate Battery Cycled under Low Temperatures

L. Zhang[1], L. Liu[1], A. Terekhov[1], D. Warnberg[1] and P. Zhao[1]

[1]Department of Mechanical, Aerospace & Biomedical Engineering, UT Space Institute, University of Tennessee, Knoxville, Tennessee 37388, USA.

E-mail: pzhao12@utk.edu
Telephone: +(1) 609 933 2463

**Abstract** Thermal runaway remains a major safety issue for lithium-ion batteries (LIBs), causing concerns in their broader adoption in applications such as electric vehicles and energy storage systems. Lithium plating/dendrites, frequently observed in LIBs after low-temperature and/or fast cycling, not only play the role of a major aging mechanism, but also lead to substantial changes in the thermal runaway behavior, thereby presenting a significant challenge to cell performance and reliability. This study focuses on analyzing thermal runaway in aged batteries with dominant degradation from Li plating and dendrite, which is promoted through cycling at low temperatures. We employed the commercial batteries for experiments: 18650 cells with positive electrodes of Lithium Phosphate (LFP) cells were subjected to low temperature cycling until they aged to 60% of cycle life, followed by thermal runaway testing using an accelerating rate calorimeter (EV+ ARC, Thermal Hazard Technology) at 100% state of charge. The results show that thermal runaway of these aged cells occurs earlier than fresh batteries, with a notable decrease in self-heating onset temperature, indicating a higher susceptibility to thermal runaway. The aged cells enter exothermicity much earlier, with a cell surface temperature as early as 55 ℃. Meanwhile, in the early stages of self-heating for LFP batteries, venting gas and white smoke phenomena were prominently observed. This indicates a much higher internal temperature within the cells such that intense electrolyte vaporization and gas generation is feasible. Detailed numerical simulation has been performed to interpret the mode of thermal runaway for cells with lithium dendrite, which bears inherent similarity to hot-spot induced ignition. These observations provide novel understanding of the combustion mode for the thermal runaway of aged cells with plating and dendrites. The contribution of this study are significant for the application and management of secondary life batteries, addressing combined aging and safety challenges. By enhancing the understanding of thermal runaway mechanism in aged LIBs, this research offers critical insights for improving the safety and reliability of LIB applications.

## 1. Introduction

The growing demand for renewable energy and the global trend towards electrification have greatly promoted the development of Li-ion batteries (LIBs) in various fields, especially in electric vehicles (EVs) and energy storage systems. Although lithium-ion batteries are widely adopted and offer many advantages, such as high energy density, low memory effect and long cycle life [1–3], they still have safety concerns, particularly the risk of thermal runaway, a catastrophic failure that can lead to subsequent combustion [4–7]. The initiation of thermal runaway bears inherent similarity to an ignition event, where exothermicity from side reactions, if not dissipated sufficiently fast, can eventually drive the cell temperature to the thermal runaway onset, companioned with very high heat release rate, gas/particle emissions, and even fires. Thermal runaway is being extensively investigated by combining sub-cell, cell, and pack level experiments [8–16], multiphysical modeling and numerical simulation [17–23], and theoretical analysis [24–27] for cells with different materials, aspect ratio, state of charge (SOC), and state of health (SOH). It is worth noting that combustion concepts and research tools can be very helpful in the mechanistic study and prevention of thermal runaway [26,28–32].

Beyond safety, another inherent challenge of battery is that a cell fundamentally suffers from irreversible degradation after hundreds and thousands of cycles, as manifested by reduced cell capacity and increased internal resistance [33–37]. Such degradation frequently involves various physical, chemical and material aspects, for example, loss of active materials [38,39], thickening of solid-electrolyte interphase layer [40–43], lithium plating and dendrite [44–47], and cracking of electrodes [48–54], etc. Concerns on performance decline from cell degradation has attracted interests in battery second life, where dynamic cells approach the end of their automotive life typically with a residual capacity of 70-80%, can still be utilized in less demanding but still effective applications, such as stationary energy storage [49,50,53,54]. The extension of battery second life effectively reduces the overall carbon footprint and increases the renewable energy available to the grid, however, can be challenged even more from thermal runaway and safety concerns. It is highly possible that a degraded cell can lead to easier occurrence of thermal runaway, which of course, depends on the extent and dominant pathway of degradation [5,55–59].

Thermal runaway becomes more concerning in the context of battery second life. A dominant degradation mechanism that is facilitated under low temperature cycling and/or high current fast charging conditions is the production of lithium plating and dendrites, where lithium atoms are deposited on the anode surface, forming metallic lithium instead of being embedded in the anode material [60,61]. Over time, these deposits can grow into dendritic structures that can potentially puncture the separator and cause internal short circuits, increasing the risk of thermal runaway [62–64]. Several key studies have significantly contributed to our understanding of these phenomena. Fleischhammer et al. [65] investigated the safety behavior of high-power 18650 lithium-ion cells subjected to high-rate and low-temperature cycling. They observed that cells aged by low-temperature cycling exhibited significantly lower onset temperatures for thermal runaway, starting as low as 30 ℃, compared to high-rate cycled cells and un-aged cells. This reduction in thermal stability was attributed to lithium plating on the anode, which dramatically increased heat generation during thermal runaway. Wu et al. [66] analyzed the thermal runaway behaviors of Li-ion batteries after low-temperature aging through experimental studies and predictive modeling. They demonstrated that lithium plating during low-temperature aging significantly affects the thermal stability and accelerates the thermal runaway process. Their findings suggested that lithium plating not only reduces the TR onset temperature but also increases the severity of the thermal events. Qi et al. [67] investigated the effect of low-temperature cycling on the thermal and gas production behaviors of NCA/graphite LIBs. Their results indicated that TR onset temperature decreases for aged batteries, primarily due to solid electrolyte interphase (SEI) layer thickening and lithium plating, which accelerate exothermic side reactions. They also found that the amount of gas produced during TR increases with aging, further contributing to thermal instability. Zhang et al. [68] empirically investigated the impact of ambient temperature, charge/discharge rate, and charge/discharge cut-off voltage on the capacity degradation rate and internal resistance growth of commercial 18650 LIBs. They found that low-temperature cycling accelerates aging, primarily due to lithium plating and dendrite formation. Zhao et al. [69] presented a numerical model for thermal runaway in low temperature cycling Nickle-Cobalt-Aluminum (NCA) 18650 cylindrical lithium-ion batteries, including lithium metal reaction, and validated it against oven test results. Wu et al.[70] conducted adiabatic thermal runaway tests on lithium cobalt oxide (LCO) pouch cells cycled at -10 ℃ with varying states of health and developed a model to predict the thermal runaway at different SOH conditions. Kong et al. [71] conducted thermal abuse test of NCA 18650 cells and revealed that lower operating temperatures and higher cycling rates significantly affect the thermal runaway behavior, leading to earlier onset of thermal runaway, and altered venting flame characteristics. Ng et al. [63] explored the effects of low temperature cycling on lithium-ion batteries, focusing on lithium plating and corrosion hazards, where material characterization revealed exacerbate stress in certain regions of the battery, leading to significant lithium deposition, severe gassing, and in some cases, catastrophic failure through thermal and nonthermal runaway. Zhou et al. [72] investigated the critical safety concern of lithium plating in lithium-ion batteries and tried to correlate thermal runaway chemical kinetics with the quantification of lithium plating. Their experiments show that the worst lithium plating scenario is sufficient to cause a secondary thermal runaway ahead of the main thermal runaway event. Despite the useful insights gained from these valuable studies, none of them provide guidance into the combustion mode of thermal runaway of cells with substantial dendrite formation.

This work focuses on the combustion mode of thermal runaway in aging Li-ion batteries with dominant degradation from lithium plating and dendrite, induced by low temperature cycling. The commercial 18650 Lithium Iron Phosphate (LFP) are utilized. Subsequently, a series of thermal runaway tests are conducted by utilizing Accelerating Rate Calorimetry (ARC), following the wait-heat-seek thermal abuse strategy [73]. To further justify the combustion mode, detailed numerical simulations were conducted in the internal hotspot induced thermal runaway, achieving both qualitative and quantitative comparison with the experiment. Our results shed light on the role of dendrites in initiating thermal runaway, which bear similar nature of hot spot induced ignition. The integration of ARC experiments with detailed numerical simulations offers a robust validation framework, highlighting the impact of lithium plating on TR behavior. The findings significant implications for the application and management of secondary life batteries, addressing combined aging and safety challenges.

## 2. Experimental approach

### 2.1 Battery preparation and electrochemical performance test

To understand the thermal runaway behavior of aged batteries with different chemistries under low temperatures cycling, this study utilized the type of 18650 commercial batteries known as the JGNE LFP cell. Table 1 lists the detailed specifications of these test cells.

Before thermal runaway experiments, all cells underwent various preconditioning using a MACCOR 4200 system with an environmental chamber to achieve the required conditions. In this study, both low temperature cycle aging and ambient temperature short-term cycling are considered. The cells were divided into three groups, with the specific cycling protocols detailed in Table 2. Cells 1-2 underwent 50 cycles at low temperature (0 ℃); Cells 3-4 were cycled 50 times at room temperature; Cell 5 served as a fresh cell baseline. After cycling, all cells were subjected to a final standardization process at room temperature to ensure a full charge and a state of charge (SOC) of 100 %. The charging / discharging curves of voltage versus discharge capacity for test cells are illustrated in **Error! Reference source not found.**Fig. 1. It is apparent that the voltage curve of an aged cell is shifted to the left compared to a fresh cell, indicating capacity fading. This transition can be used as an indicator of state of health (SOH), which is commonly used to represent the remaining capacity of a battery relative to its original capacity, and is typically expressed as a percentage:

$$SOH = \frac{Q}{Q_0} \times 100\% \tag{1}$$

where $Q$ is the discharge capacity, $Q_0$ is the initial capacity of the cell. Fig. 2 summarizes the SOH of JGNE LFP cells, showing that Cells 1-2, after undergoing 50 cycles at low temperatures, experienced significant capacity degradation with an SOH slightly below 60%, while the remaining cells maintained an SOH close to 100%.

Following the initialization of all cells, Electrochemical Impedance Spectroscopy (EIS) measurements were conducted using the PARSTAT 4000A system by Princeton Applied Research. This provided key data on the electrochemical properties of the cells, as illustrated by the Nyquist plot in Fig. 3. The Nyquist plot serves as an essential analytical tool for evaluating the electrochemical behavior of cells, offering deep insights into their operational efficiency and internal mechanisms [74]. According to the interpretation based on the Randles cell model, as presented in the Nyquist plot, the point where the semicircle intersects the real axis in the high-frequency domain indicates the ohmic resistance. This resistance is attributed to the combined resistances of the electrolyte, separator, and the battery electronic components. The diameter of the semicircle represents the charge transfer resistance, which reflects the electrochemical reaction kinetics at the electrode interface. Meanwhile, the straight line observed in the low-frequency region is indicative of the diffusion process, demonstrating the movement of ions within the battery. It can be seen that the initial EIS results show that the cells perform very similarly, with only slightly different impedances. As shown in Fig. 3, the EIS results exhibited more pronounced differences after experiencing various cycling conditions, indicating changes in their electrochemical performance. Specifically, cells cycled at low temperatures exhibit not only changes in ohmic resistance but also increases in charge transfer resistance.

**Table 1**. Basic parameters of JGNE LFP test cells

| Parameter (unit) | JGNE |
|---|---|
| Model | HTPFR18650 |
| Chemistry | LFP/Graphite |
| Height (mm) | 65 |
| Diameter (mm) | 18 |
| Rated capacity (Ah) | 1.1 |
| Nominal voltage (V) | 3.2 |
| Charging voltage (V) | 3.65 |
| Discharging cut-off voltage (V) | 2.5 |
| Max. charge/discharge current (A) | 5.5/33 |
| Operating temperature (℃) | 0~55 (Charge)<br>-20~60 (Discharge) |

**Table 2**. Cycling protocol of the JGNE LFP cells

| Battery No. | Test Procedures |
|---|---|
| Cell 1-2 | Step 1: 0.5C Charge/Discharge 2 times at ambient temperature<br>Step 2: 0.5/1/3/5/0.5C Charge/Discharge at ambient temperature<br>Step 3: 1C-Charge 5C-Discharge 50 times at 0℃<br>Step 4: 0.5/1/3/5/0.5C Charge/Discharge at ambient temperature<br>Step 5: 0.1C Discharge-Charge cycle 3 times at ambient temperature |
| Cell 3-4 | Step 1-2: Same as Cell 1-2<br>Step 3: 1C-Charge 5C-Discharge 50 times at ambient temperature<br>Step 4-5: Same as Cell 1-2 |
| Cell 5 | Step 1: 0.1C Discharge-Charge cycle 3 times at ambient temperature |

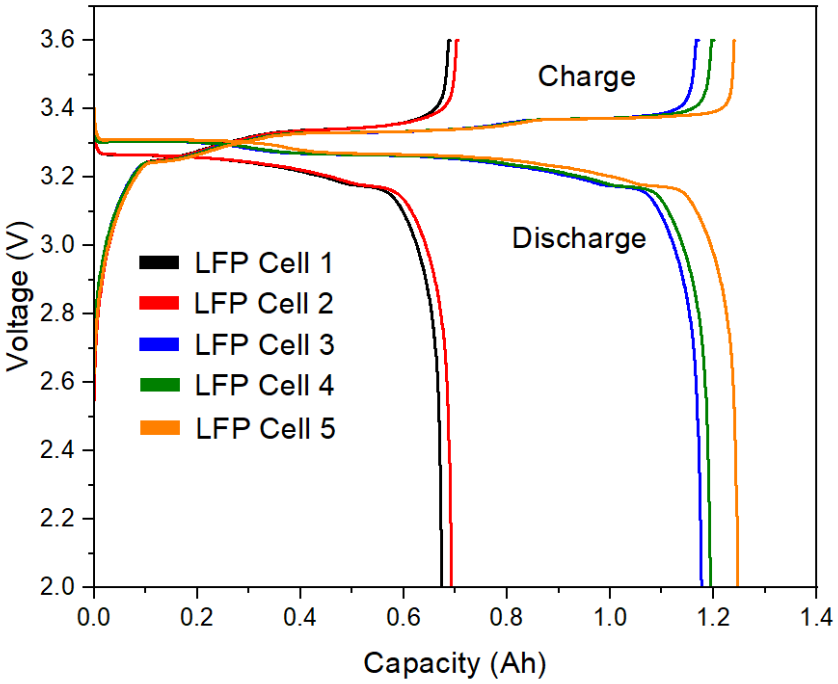

**Fig. 1.** Voltage evolution before ARC test

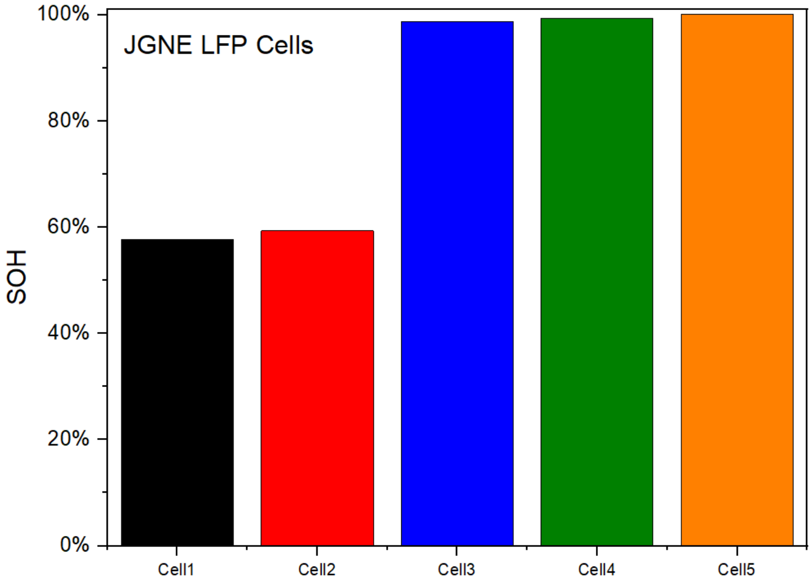

**Fig. 2.** SOH of test cells

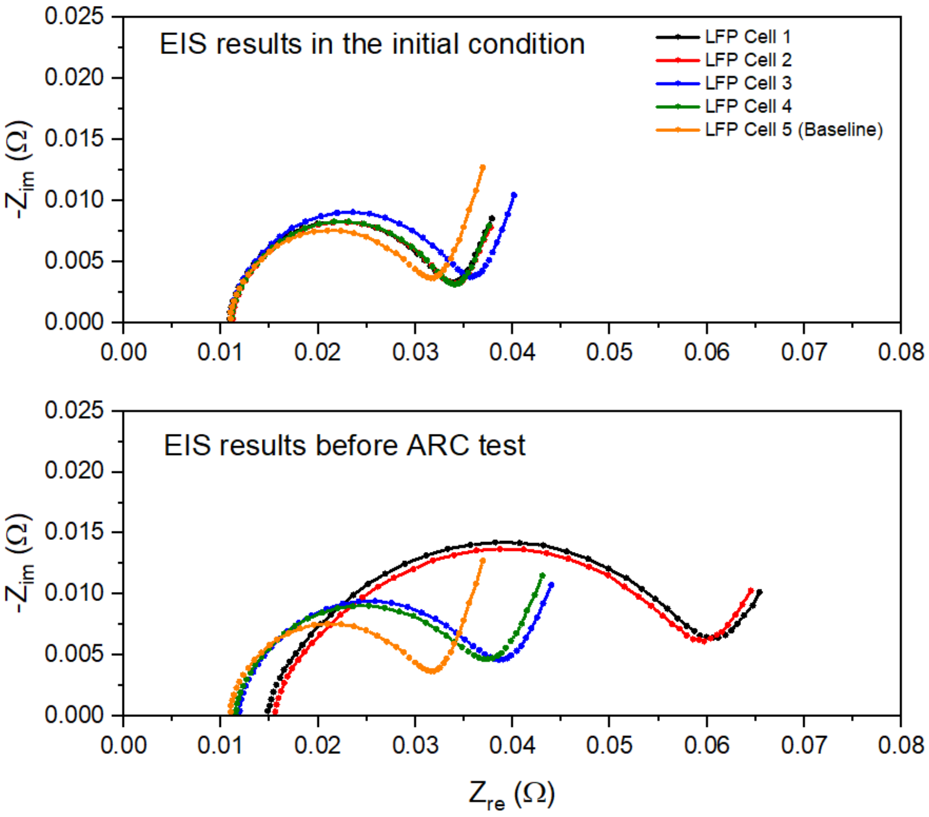

**Fig. 3.** Nyquist plot changes of test cells before cycling and before ARC test

### 2.2 Accelerating rate calorimeter test

In order to study the effect of low temperature cycling on the thermal runaway (TR) characteristics of lithium-ion batteries, the EV+ acceleration calorimeter (ARC), provided by Thermal Hazard Technology (THT), was used to conduct thermal runaway tests. This study aims to evaluate the impact of aging batteries under low temperature cycling on key temperature parameters, including self-heating onset temperature, TR temperature, maximum temperature, and TR delay time. The self-heating onset temperature was determined in all experiments using the established heat-wait-seek (HWS) method, with the detailed method described in our previously published work [73].

### 2.3 Analysis of thermal runaway experimental data

During thermal runaway experiments, we collected data on surface temperature and voltage changes for batteries involved in the tests. The results, as shown in Fig. 4, are compared. This figure illustrates the evolution of temperature and voltage for fresh LFP cells, those cycled at low temperature, and those at ambient temperature. It can be observed that Cell 1 and Cell 2, which were cycled at low temperature, were the first to enter the self-heating mode, at approximately 55 ℃, accompanied by venting gas and the emission of white smoke, as illustrated in Fig. 5. The production of white smoke is primarily attributed to the decomposition of electrolyte and internal materials, resulting in the release of gases and particles from the battery during overheating. However, with the surface temperature of the battery only reaching 55 ℃ at this point, it implies the formation of high temperature spots internally. This leads to a non-homogeneous temperature distribution inside the cell, which in turn causes the observed emission of white smoke from the battery.

From the voltage evolution presented in Fig. 4, it is clear that after reaching a certain temperature, the voltage suddenly drops, but it does not drop to zero immediately. Instead, it stabilizes at a certain level for a while before severe internal short cause the voltage to plummet to 0V, immediately triggering thermal runaway. Additionally, Fig. 4 shows the corresponding temperatures (marked by dots with lines on the graph) when various aged batteries experience sudden voltage drops. It is observed that the cells cycled at low temperatures exhibit a voltage drop first, around 60 ℃, compared to other cells, whose voltage drops at approximately 130 ℃. This suggests that lithium dendrites formed during low temperature cycling create localized hot spots, accelerating internal short circuits.

During thermal runaway testing, three characteristic temperatures are identified to quantify the thermal stability performance of the cells: the self-heating onset temperature (corresponding to 0.02 ℃ /min), TR temperature (corresponding to 1 ℃ /min for JGNE LFP cell), and the maximum temperature. Fig. 6 displays the critical temperatures collected during the thermal runaway experiments. It was observed that for LFP cells, the self-heating onset temperature ranged from 55 to 120 ℃. Cells cycled at 0 ℃ showed a lower self-heating onset temperature, dropping from 120 ℃ to 55 ℃, a difference of approximately 70 ℃. In cells aged at low temperatures, not only is the self-heating onset temperature lower, but the TR onset temperature also shows reduced performance. The decreasing trend in both self-heating and TR onset temperatures indicates a deterioration in the thermal stability of lithium-ion batteries after low temperature cycling. Additionally, the maximum temperature also shows reduced performance, which may be attributed to the loss of active material during the aging process.

In the thermal runaway experiments, we not only obtain characteristic temperature data but also derive the activation energy of the TR reaction and the frequency factor based on the temperature evolution curves and the temperature rise data, following the Arrhenius law [75,76]. The specific expression is shown below:

$$\ln\left(\frac{dT}{dt}\right) \approx \ln(\Delta T_{ad} A) - \frac{E_a}{k_b T} \tag{2}$$

where $\frac{dT}{dt}$ is self-heating temperature rate, $\Delta T_{ad}$ is the difference between the initial self-heating onset temperature and the maximum temperature, $k_b$ is Boltzmann's constant (8.62E-5 eV·K-1), $A$ is frequency factor and $E_a$ is activation energy of TR reactions. Fig. 7 plot ln$\frac{dT}{dt}$ versus $\frac{1000}{T}$ for LFP cells to calculate frequency factor $A$ and activation energy $E_a$ under different conditions. It is observed that the performance of LFP batteries cycled at low temperatures differs significantly from other cells, not showing a linear relationship, thus making it challenging to derive specific values for frequency factor $A$ and activation energy $E_a$ in this study. However, the remaining cells displayed a linear relationship. By linearly fitting the temperature rate curves, the activation energy $E_a$, represented by the slope, and the frequency factor $A$, represented by the intercept, were obtained and summarized in Fig. 8. The bar chart reveals a correlated consistency in the variation of calculated activation energy $E_a$ and frequency factor $A$. Cells with higher activation energy also exhibit larger frequency factors. Since the LFP cells cycled at low temperatures did not yield calculable $E_a$ and $A$ values, they cannot be compared with fresh cells.

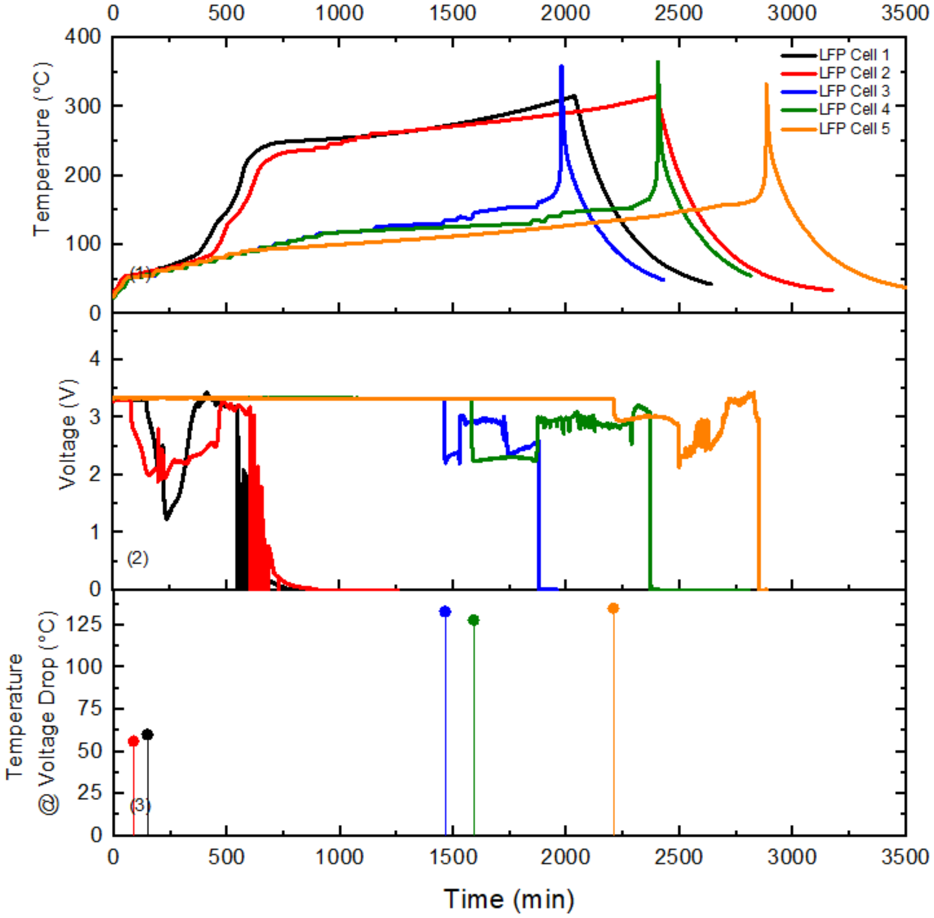

**Fig. 4.** Cell surface temperature, voltage evolution, corresponding temperature during when cell experiences a sudden voltage drop

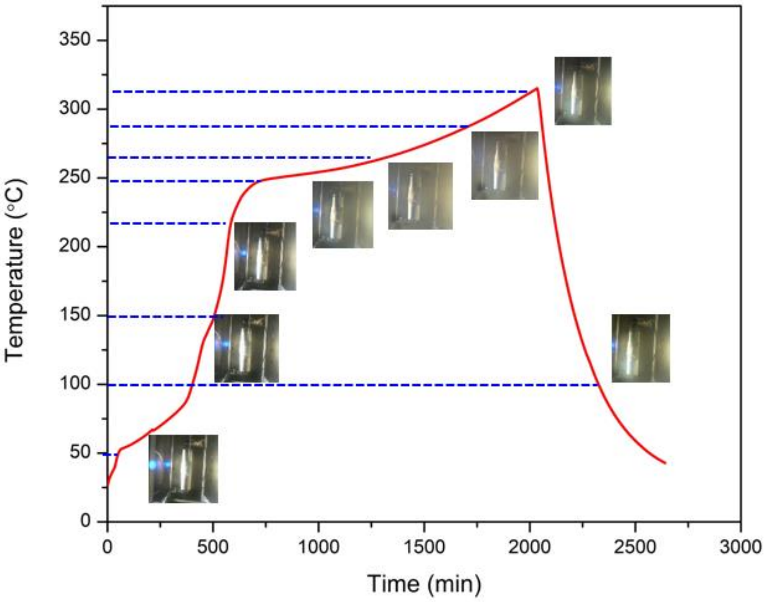

**Fig. 5.** Venting gas and the emission of white smoke observed at around 55 ℃

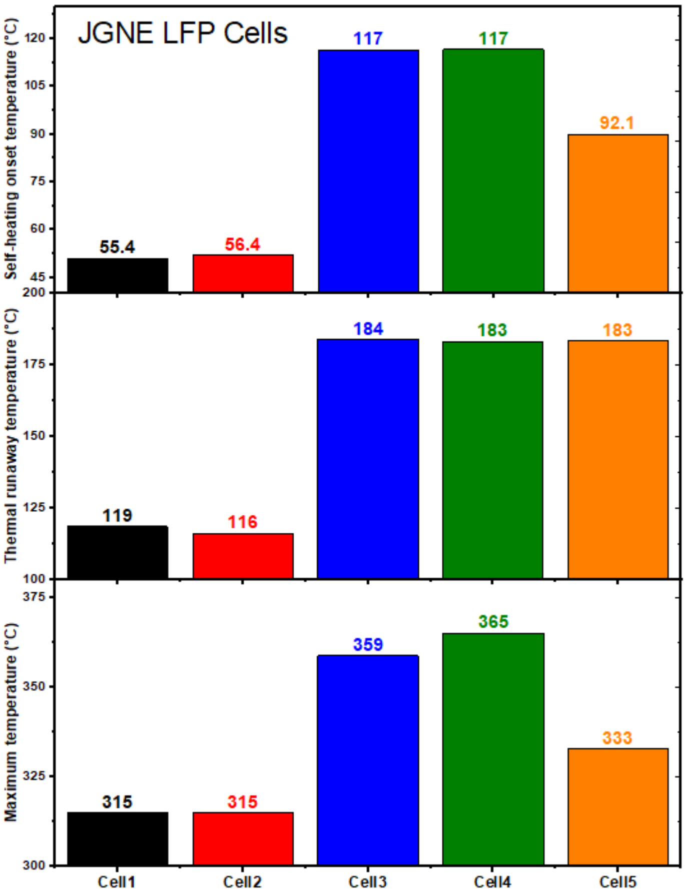

**Fig. 6.** Critical temperatures at different aging conditions

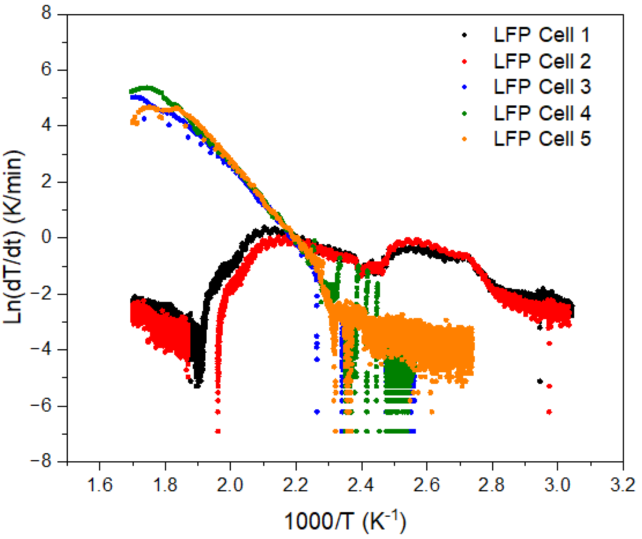

**Fig. 7.** Natural logarithm of the self-heating rate versus inverse of temperature curves

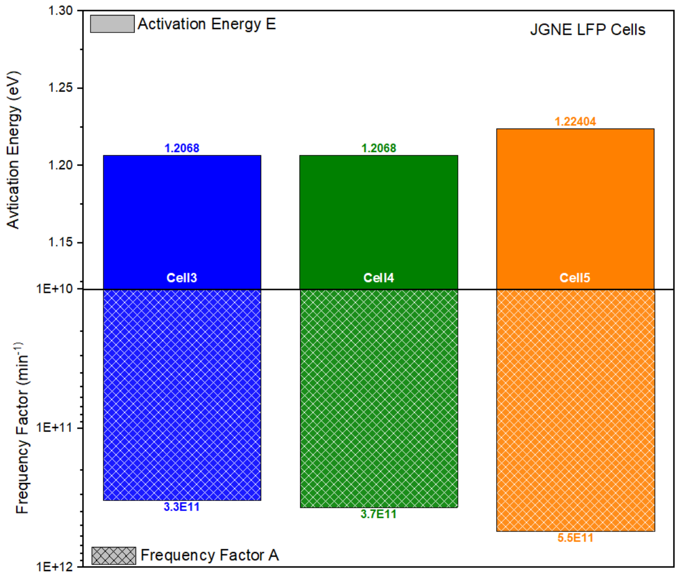

**Fig. 8.** Activation energy and frequency factor of test cells

# 3. Numerical simulation approach

## 3.1 Hot spot simulation strategies

It is well known that short circuits within batteries can create hot spots, leading to thermal runaway. The growth of lithium dendrites can trigger these internal short circuits, thereby forming hot spots within the battery that generate localized high temperatures. The increase in battery temperature also triggers exothermic reactions between the electrolyte, the active material and solid electrolyte interface (SEI), further exacerbating the temperature increase.

Based on the experiments on battery thermal runaway described in the previous Section 2, it was observed that cells undergoing low temperature cycling enter the self-heating mode earlier, a phenomenon particularly evident in LFP batteries. At 55 ℃, these cells entered the self-heating mode, likely due to the formation of lithium dendrites caused by low temperature cycling. As the cell heats up and expands internally, lithium dendrites in some areas may puncture the separator, leading to partial internal short circuits. This forms a local hot spot, triggering the battery to enter the self-heating mode prematurely. To understand how local hot spots affect battery thermal runaway, this study developed a simple thermal runaway model with a local hot spot for a cylindrical 18650 LFP/Graphite cell.

For the numerical simulation, a two-dimensional axisymmetric model (2D) was developed in COMSOL Multiphysics 5.5 to simulate ARC experiments with a hot spot. The energy conservation equation of this model is shown in Table 3. Due to the axisymmetric geometry of the battery, the internal temperature of the battery varies both radially and axially, taking into account both thermal runaway reactions and internal heat conduction.

To better study the impact of local hot spots on thermal runaway, an initial simplified thermal runaway model was used to simulate scenarios without local hot spots. In this study, the LFP Cell 5 serves as a validation tool to ensure the functionality of the model. Based on ARC experimental results, the cell underwent a heating process for up to 700 minutes. During this period, the cell temperature curve from the ARC experiments, as shown in Fig. 9, was applied as a boundary condition to the model, which also considered convection and radiation. The heat transfer coefficient, $h_{conv}$ was set to 20 $W/m^3 \cdot K$, and surface emissivity, $\varepsilon_{rad}$ was set to 0.8. After 700 minutes, the cell entered the self-heating mode, and the thermal boundary conditions of the model were set to adiabatic, with no heat transfer between the cell and the heating system. This adjustment is made based on the operation mechanism of the ARC, when the test cell enters the exothermic mode, the heating system is programmed to trace the temperature of the cell, so that there is no thermal exchange.

The heat source term in the model that triggers thermal runaway comes from four commonly used chemical side reactions [77]. The chemical heat release $Q$, inside the battery stems from four semi-global thermal chemical reactions, including the decomposition of the solid-electrolyte interface (SEI), the reaction between the anode and electrolyte, the reaction between cathode and electrolyte, and electrolyte decomposition. The quantitative characteristics of these reactions depend on the battery material properties, thermal chemical parameters, and temperature. The reaction model, frequency factor, and activation energy describing the kinetics between battery materials have been previously determined by fitting experimental measurements from accelerating rate calorimetry (ARC) and differential scanning calorimetry (DSC) tests [78]. The chemical reaction rates and heat generation are widely recognized in the literature [77,79] and summarized in **Error! Reference source not found.**4.

To validate the thermal runaway model, the four-step reaction model was compared with experimental results from LFP Cell 5, as described in Section 2. The model parameters, summarized in Table 5 and derived from [80], describe a fully charged battery with LFP/Graphite chemistry. As shown in Fig. 10, without any parameter adjustment, reasonable agreement has been achieved between the model and experiment, especially the onset temperature of exothermicity and the thermal runaway time scale. Such agreement provides evidence to the understanding that the thermal runaway in the baseline case bears inherent nature of homogenous autoignition. It should be pointed out that some quantitative discrepancies before the main thermal runaway event can be easily reduced or minimized by further tuning the model parameters. Such a practice, however, is neither necessary or meaningful, given the statistical nature of thermal runaway posed by cell-to-cell variation identified in our previous study [73]. Furthermore, Cells 3 and 4, despite being identical batteries, exhibited slightly different thermal runaway behaviors, as noted in Section 2. Additionally, the temperature curve of the model does not decrease after thermal runaway occurs, contrasting with the rapid decrease in temperature observed in the experimental cells post-thermal runaway. This inconsistency is attributable to the adiabatic boundary conditions of the model. Given that our focus is on the impact of local hot spots on thermal runaway, the deviation of model falls within a reasonable range of acceptance. This model will be utilized further to investigate the effects of local hot spots on thermal runaway.

To understand the impact of local hot spots on thermal runaway, we selected a small area within the battery to simulate the local hot spots, based on the validated model, as illustrated in Fig. 11. The specific meshing parameters for the model are as follows: the minimum element size is set at 1.38E-8 m, the element growth rate for the mesh at 1.4, and the boundary layer properties include 8 layers with a stretching factor of 1.2. The remaining domain size properties are configured with a maximum element size of 6.9E-4 m, a minimum element size of 1.38E-6 m, and an element growth rate of 1.1. The model comprises 15186 domain elements and 654 boundary elements. Based on the preliminary model, we observe the temperature distribution within the battery over time, focusing on the development of hotspots and their impact on thermal runaway. The temperature distribution at different time intervals (0s, 30s, and 60s) is shown in Fig. 12. Fig. 12(a) describes the initial temperature distribution at 0 seconds. As expected, the temperature is uniformly low throughout the battery, indicating no significant heat accumulation at the start. Fig. 12(b) shows the temperature distribution after 30 seconds. At this stage, the hotspot region begins to exhibit apparent increase in temperature, indicating the initial phase of thermal accumulation. Fig. 12(c) illustrates the temperature distribution after 60 seconds. The hotspot has significantly increased in temperature, with the surrounding regions also experiencing a rise in temperature, indicating the potential onset of thermal runaway. Subsequently, we conducted a parametric study and ultimately selected three representative heat source scenarios to apply to the hotspot region, as shown in Fig. 13, to observe the influence of the hot spots on thermal runaway.

**Table 3**. Energy balance equation for 2D axis model

| | 2D axisymmetric Model |
|---|---|
| Assumption | Thermal stratification exists |
| Governing Equation | $\rho c_p \frac{\partial T}{\partial t} = \frac{1}{r}\frac{\partial}{\partial r}\left(k_r r \frac{\partial T}{\partial r}\right) + \frac{\partial}{\partial z}\left(k_z \frac{\partial T}{\partial z}\right) + Q$ |
| Chemical reaction heat | $Q = Q_{sei} + Q_{ne} + Q_{pe} + Q_e$ |
| Boundary condition | $q_{conv}'' = h_{conv}(T - T_{ARC})$ |
| (Heating process) | $q_{rad}'' = \varepsilon_{rad}\sigma(T^4 - T_{ARC}{}^4)$ |
| (Adiabatic process) | $n \cdot q = 0$ |

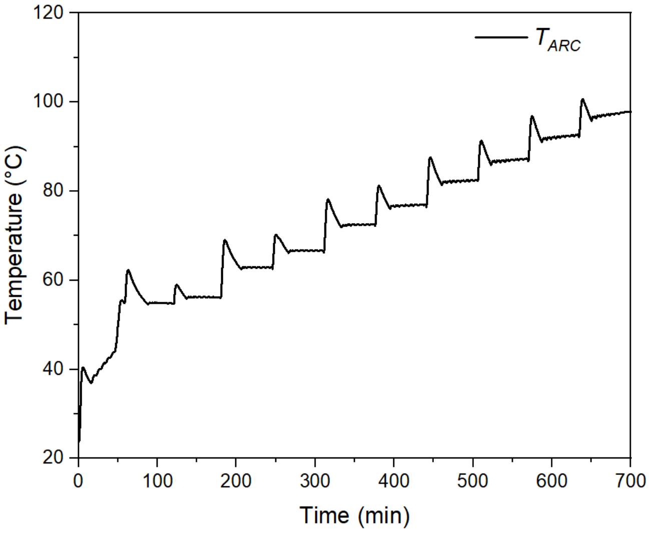

**Fig. 9.** Temperature profile of LFP Cell 5 during the heating process in the thermal runaway experiment

**Table 4**. Reaction rates and heat sources of the four-step thermal abuse model

| Reaction term | Equations | |
|---|---|---|
| SEI decomposition | $\frac{dc_{sei}}{dt} = -A_{sei} exp\left[-\frac{E_{a,sei}}{RT}\right] c_{sei}^{m_{sei}}$ | $Q_{sei} = -H_{sei}W_{sei}\frac{dc_{sei}}{dt}$ |
| Anode-electrolyte reaction | $\frac{dc_{ne}}{dt} = -A_{ne} exp\left[-\frac{t_{sei}}{t_{sei0}}\right] c_{ne}^{m_{ne,n}} exp\left[-\frac{E_{a,ne}}{RT}\right]$ | $Q_{ne} = -H_{ne}W_{ne}\frac{dc_{ne}}{dt}$ |
| | $\frac{dt_{sei}}{dt} = A_{ne} exp\left[-\frac{t_{sei}}{t_{sei0}}\right] c_{ne}^{m_{ne,n}} exp\left[-\frac{E_{a,ne}}{RT}\right]$ | |
| Cathode-electrolyte reaction | $\frac{d\alpha}{dt} = A_{pe}\alpha^{m_{pe,p1}}(1-\alpha)^{m_{pe,p2}} exp\left[-\frac{E_{a,pe}}{RT}\right]$ | $Q_{pe} = -H_{pe}W_{p}\frac{d\alpha}{dt}$ |
| Electrolyte decomposition | $\frac{dc_{e}}{dt} = -A_{e} exp\left[-\frac{E_{a,e}}{RT}\right] c_{e}^{m_{e}}$ | $Q_{e} = -H_{e}W_{e}\frac{dc_{e}}{dt}$ |
| Overall heat generation | $Q = Q_{sei} + Q_{ne} + Q_{pe} + Q_{e}$ | |

**Table 5**. Model parameters of the four-step thermal abuse model

| Symbol | Value | Physical description |
|---|---|---|
| $\rho$ | 2231.2 (kg/m$^3$) | Cell density |
| $c_p$ | 1100 (Jkg$^{-1}$K$^{-1}$) | Heat capacity |
| $k_r$ | 0.7 (Wm$^{-1}$K$^{-1}$) | Thermal conductivity across the layers |
| $k_z$ | 140 (Wm$^{-1}$K$^{-1}$) | Thermal conductivity along the layers |
| $A_{sei}$ | $1.66\times10^{15}$ (1/s) | SEI-decomposition frequency factor |
| $A_{ne}$ | $2.5\times10^{13}$ (1/s) | Anode-electrolyte frequency factor |
| $A_{pe}$ | $2.0\times10^{8}$ (1/s) | Cathode-electrolyte frequency factor |
| $A_e$ | $5.14\times10^{25}$ (1/s) | Electrolyte decomposition frequency factor |
| $E_{a,sei}$ | $1.38\times10^{5}$ (J/mol) | SEI-decomposition activation energy |
| $E_{a,ne}$ | $1.32\times10^{5}$ (J/mol) | Anode-electrolyte activation energy |
| $E_{a,pe}$ | $0.99\times10^{5}$ (J/mol) | Cathode-electrolyte activation energy |
| $E_{a,e}$ | $2.7\times10^{5}$ (J/mol) | Electrolyte decomposition activation energy |
| $c_{sei0}$ | 0.15 | Initial value of $c_{sei}$ |
| $c_{ne0}$ | 0.75 | Initial value of $c_{ne}$ |
| $\alpha_0$ | 0.04 | Initial value of $\alpha$ |
| $c_{e0}$ | 1 | Initial value of $c_e$ |
| $t_{sei0}$ | 0.033 | Initial value of $t_{sei}$ |
| $m_{sei}$ | 1 | Reaction order for $c_{sei}$ |
| $m_{ne}$ | 1 | Reaction order for $c_{ne}$ |
| $m_{pe1}$ | 1 | Reaction order for $\alpha$ |
| $m_{pe2}$ | 1 | Reaction order for $1-\alpha$ |
| $m_e$ | 1 | Reaction order for $c_e$ |
| $H_{sei}$ | $2.57\times10^{5}$ (J/kg) | Reaction heat of SEI-decomposition |
| $H_{ne}$ | $1.714\times10^{6}$ (J/kg) | Reaction heat of anode-electrolyte |
| $H_{pe}$ | $1.947\times10^{5}$ (J/kg) | Reaction heat of cathode-electrolyte |
| $H_e$ | $6.2\times10^{5}$ (J/kg) | Reaction heat of electrolyte decomposition |
| $W_{sei}$ | 598 (kg/m$^3$) | Specific SEI content in jellyroll |
| $W_{ne}$ | 220 (kg/m$^3$) | Specific carbon content in jellyroll |
| $W_p$ | 521 (kg/m$^3$) | Specific positive active content in jellyroll |
| $W_e$ | 335 (kg/m$^3$) | Specific electrolyte content in jellyroll |
| $R$ | 8.314 (J/mol/K) | Universal gas constant |

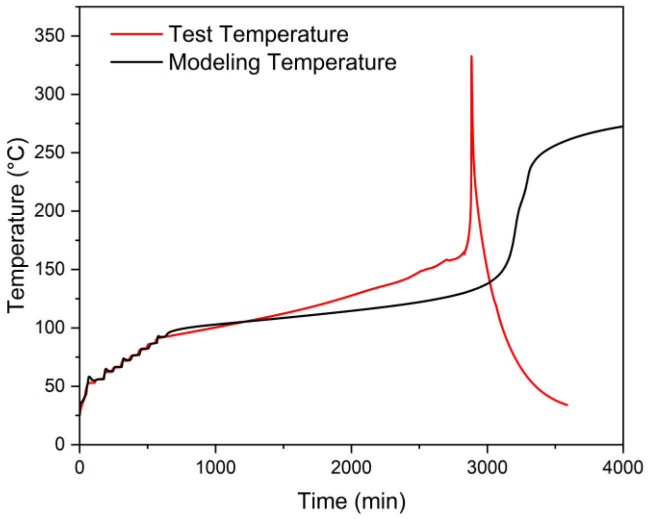

**Fig. 10.** Comparison of temperature profiles: model predictions vs. experimental data for LFP Cell 5

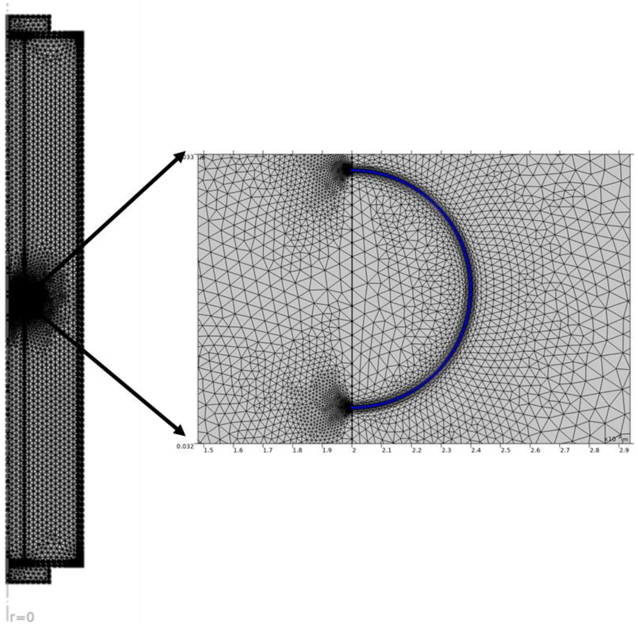
0.033
0.032
1.5
1.6
1.7
1.8
1.9
2
2.1
2.2
2.3
2.4
2.5
2.6
2.7
2.8
2.9
r=0

**Fig. 11.** Numerical simulation model incorporating a small hot spot region

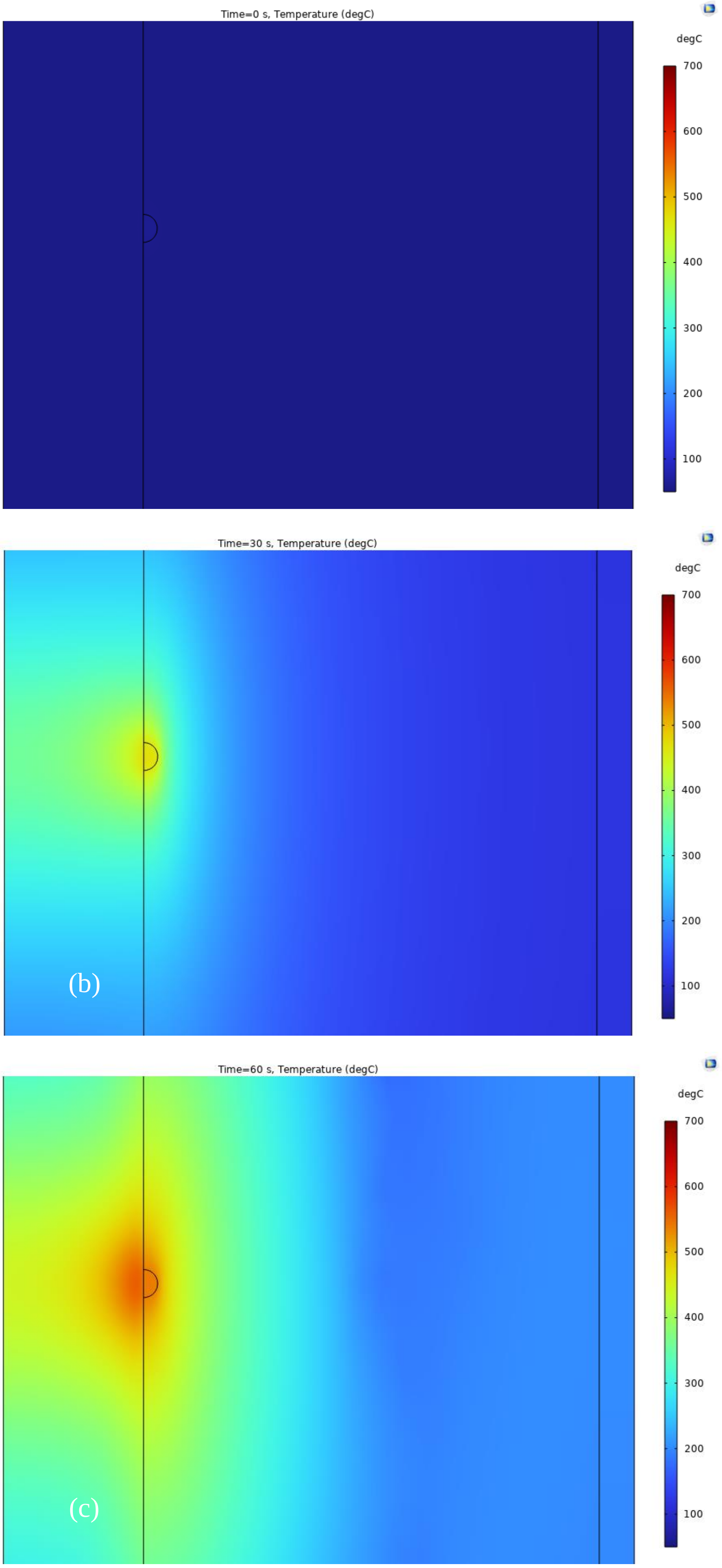

**Fig. 12**. Temperature distribution at (a) 0s, (b) 30s, (c) 60s

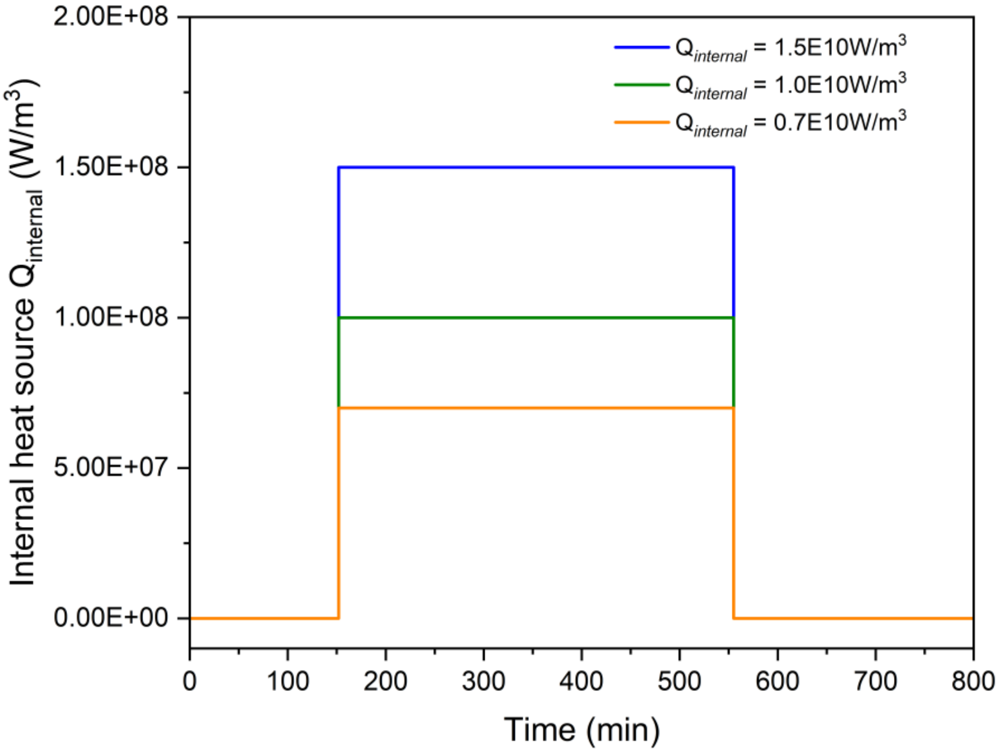

**Fig. 13.** Three different intensities of heat source applied to small hot spot

### 3.2 Hot-spot modeling results

The temperature evolution of the cell after applying a heat source to the small hot spot region is shown in Fig. 14. It can be noted that local heat sources can indeed cause the battery to experience thermal runaway earlier, and the greater the intensity of the heat source, the earlier the thermal runaway occurs. It is observed that when the localized heat source intensity is set to 1.5E8 W/m$^3$, the thermal runaway behavior of model closely mimics the thermal runaway behavior of aged LFP cells cycled at low temperatures. This further confirms that the earlier onset of thermal runaway in LFP cells may be attributed to excessive lithium dendrite formation during the aging process, leading to internal short circuits and hot spots. Additionally, if the localized heat source is particularly small, it does not accelerate the occurrence of thermal runaway. This simplified model provides valuable insights into the impact of local hot spots on thermal runaway.

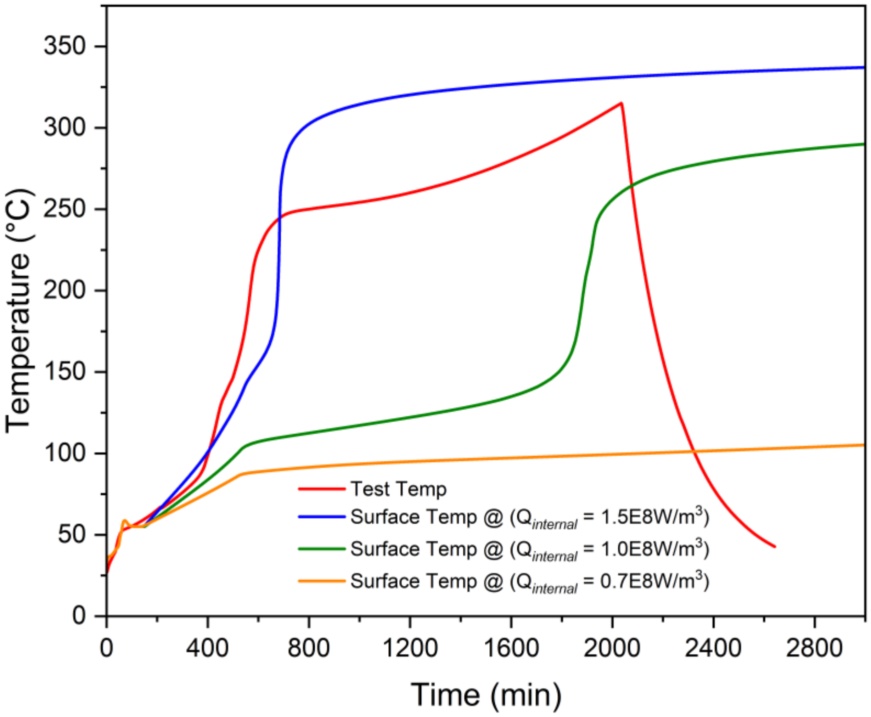

**Fig. 14.** Temperature evolution under different applied internal heat source

## Conclusions

This study investigated the thermal runaway phenomenon in lithium-ion batteries, particularly focusing on the significant effects of lithium plating and dendrites resulting from low temperature cycling. Commercial 18650 LFP cells were employed. It demonstrated an earlier onset of thermal runaway after aging through low temperature cycling compared to fresh cells, which was attributed to the formation of lithium plating and dendrites. Experiments revealed that low temperature cycling significantly accelerated the thermal runaway process. This was apparent in LFP batteries, which entered to the self-heating mode much earlier, around 55°C, indicating that the degree of aging and lithium dendrite formation significantly impacts the thermal stability of the batteries. It is worth noting that the early self-heating mode of LFP is characterized by gas emissions and white smoke, which suggests increased risks associated with aging cells. To better understand the initiation and progression of thermal runaway caused by internal hot spots due to lithium dendrites, the study utilized a simplified model, applying heat sources of varying intensities to a small hot spot within the battery. The model confirmed that while larger heat sources indeed accelerate thermal runaway Although simplified, the results provide valuable insights into the potential effects of localized thermal hot spots on the overall thermal runaway in lithium-ion batteries. This model helps to propose a mechanism of thermal runaway similar to hot spot induced ignition.

## References

[1] J. Wen, D. Zhao, C. Zhang, An overview of electricity powered vehicles: Lithium-ion battery energy storage density and energy conversion efficiency, Renew Energy 162 (2020) 1629–1648. https://doi.org/10.1016/j.renene.2020.09.055.

[2] B. Xu, J. Lee, D. Kwon, L. Kong, M. Pecht, Mitigation strategies for Li-ion battery thermal runaway: A review, Renewable and Sustainable Energy Reviews 150 (2021) 111437. https://doi.org/10.1016/j.rser.2021.111437.

[3] K. Liu, Y. Liu, D. Lin, A. Pei, Y. Cui, Materials for lithium-ion battery safety, (2018).

[4] P. Münster, M. Diehl, J.E. Frerichs, M. Börner, M.R. Hansen, M. Winter, P. Niehoff, Effect of Li plating during formation of lithium ion batteries on their cycling performance and thermal safety, J Power Sources 484 (2021) 0–7. https://doi.org/10.1016/j.jpowsour.2020.229306.

[5] S. Wu, C. Wang, W. Luan, Y. Zhang, Y. Chen, H. Chen, Thermal runaway behaviors of Li-ion batteries after low temperature aging: Experimental study and predictive modeling, J Energy Storage 66 (2023) 107451. https://doi.org/10.1016/j.est.2023.107451.

[6] S. Chavan, B. Venkateswarlu, R. Prabakaran, M. Salman, S.W. Joo, G.S. Choi, S.C. Kim, Thermal runaway and mitigation strategies for electric vehicle lithium-ion batteries using battery cooling approach: A review of the current status and challenges, J Energy Storage 72 (2023) 108569. https://doi.org/10.1016/j.est.2023.108569.

[7] S. Mallick, D. Gayen, Thermal behaviour and thermal runaway propagation in lithium-ion battery systems – A critical review, J Energy Storage 62 (2023) 106894. https://doi.org/10.1016/j.est.2023.106894.

[8] Y. Zheng, Z. Shi, D. Ren, J. Chen, X. Liu, X. Feng, L. Wang, X. Han, L. Lu, X. He, M. Ouyang, In-depth investigation of the exothermic reactions between lithiated graphite and electrolyte in lithium-ion battery, Journal of Energy Chemistry 69 (2022) 593–600. https://doi.org/10.1016/j.jechem.2022.01.027.

[9] S. El Moutchou, H. Aziam, M. Mansori, I. Saadoune, Thermal stability of Lithium-ion batteries: Case study of NMC811 and LFP cathode materials, Mater Today Proc 51 (2021) A1–A7. https://doi.org/10.1016/j.matpr.2022.02.324.

[10] D. Lu, S. Lin, S. Hu, W. Cui, T. Fang, A. Iqbal, Z. Zhang, W. Peng, Thermal behavior and failure mechanism of large format lithium-ion battery, Journal of Solid State Electrochemistry 25 (2021) 315–325. https://doi.org/10.1007/s10008-020-04810-z.

[11] Y. Zhang, S. Cheng, W. Mei, L. Jiang, Z. Jia, Z. Cheng, J. Sun, Q. Wang, Understanding of thermal runaway mechanism of LiFePO4 battery in-depth by three-level analysis, Appl Energy 336 (2023) 120695. https://doi.org/10.1016/j.apenergy.2023.120695.

[12] D. Ren, X. Feng, L. Liu, H. Hsu, L. Lu, L. Wang, X. He, M. Ouyang, Investigating the relationship between internal short circuit and thermal runaway of lithium-ion batteries under thermal abuse condition, Energy Storage Mater 34 (2021) 563–573. https://doi.org/10.1016/j.ensm.2020.10.020.

[13] H. Wang, H. Xu, Z. Zhao, Q. Wang, C. Jin, Y. Li, J. Sheng, K. Li, Z. Du, C. Xu, X. Feng, An experimental analysis on thermal runaway and its propagation in Cell-to-Pack lithium-ion batteries, Appl Therm Eng 211 (2022) 118418. https://doi.org/10.1016/j.applthermaleng.2022.118418.

[14] C.F. Lopez, J.A. Jeevarajan, P.P. Mukherjee, Experimental Analysis of Thermal Runaway and Propagation in Lithium-Ion Battery Modules, J Electrochem Soc 162 (2015) A1905–A1915. https://doi.org/10.1149/2.0921509jes.

[15] L. Yuan, T. Dubaniewicz, I. Zlochower, R. Thomas, N. Rayyan, Experimental study on thermal runaway and vented gases of lithium-ion cells, Process Safety and Environmental Protection 144 (2020) 186–192. https://doi.org/10.1016/j.psep.2020.07.028.

[16] L. Zhang, L. Liu, A. Terekhov, D. Warnberg, P. Zhao, Thermal runaway of Li-ion battery with different aging histories, Process Safety and Environmental Protection 185 (2024) 910–917. https://doi.org/10.1016/j.psep.2024.03.077.

[17] D. Ren, X. Liu, X. Feng, L. Lu, M. Ouyang, J. Li, X. He, Model-based thermal runaway prediction of lithium-ion batteries from kinetics analysis of cell components, Appl Energy 228 (2018) 633–644. https://doi.org/10.1016/j.apenergy.2018.06.126.

[18] S. Abada, M. Petit, A. Lecocq, G. Marlair, V. Sauvant-Moynot, F. Huet, Combined experimental and modeling approaches of the thermal runaway of fresh and aged lithium-ion batteries, J Power Sources 399 (2018) 264–273. https://doi.org/10.1016/j.jpowsour.2018.07.094.

[19] Z. An, K. Shah, L. Jia, Y. Ma, Modeling and analysis of thermal runaway in Li-ion cell, Appl Therm Eng 160 (2019). https://doi.org/10.1016/j.applthermaleng.2019.113960.

[20] S. Bilyaz, K.C. Marr, O.A. Ezekoye, Modeling of Thermal Runaway Propagation in a Pouch Cell Stack, Fire Technol 56 (2020) 2441–2466. https://doi.org/10.1007/s10694-020-00970-6.

[21] C.X. He, Q.L. Yue, Q. Chen, T.S. Zhao, Modeling thermal runaway of lithium-ion batteries with a venting process, Appl Energy 327 (2022). https://doi.org/10.1016/j.apenergy.2022.120110.

[22] A. Kriston, A. Podias, I. Adanouj, A. Pfrang, Analysis of the Effect of Thermal Runaway Initiation Conditions on the Severity of Thermal Runaway—Numerical Simulation and Machine Learning Study, J Electrochem Soc 167 (2020) 090555. https://doi.org/10.1149/1945-7111/ab9b0b.

[23] Y. Zhang, W. Mei, P. Qin, Q. Duan, Q. Wang, Numerical modeling on thermal runaway triggered by local overheating for lithium iron phosphate battery, Appl Therm Eng 192 (2021) 116928. https://doi.org/10.1016/j.applthermaleng.2021.116928.

[24] P. Zhao, L. Liu, Y. Chen, H. Ge, Theoretical and numerical analysis for thermal runaway propagation within a single cell, Int J Heat Mass Transf 181 (2021) 121901. https://doi.org/10.1016/j.ijheatmasstransfer.2021.121901.

[25] M. Parhizi, A. Jain, G. Kilaz, J.K. Ostanek, Accelerating the numerical solution of thermal runaway in Li-ion batteries, J Power Sources 538 (2022) 231531. https://doi.org/10.1016/j.jpowsour.2022.231531.

[26] W. Li, H. Wang, M. Ouyang, C. Xu, L. Lu, X. Feng, Theoretical and experimental analysis of the lithium-ion battery thermal runaway process based on the internal combustion engine combustion theory, Energy Convers Manag 185 (2019) 211–222. https://doi.org/10.1016/j.enconman.2019.02.008.

[27] X. Feng, F. Zhang, J. Feng, C. Jin, H. Wang, C. Xu, M. Ouyang, Propagation dynamics of the thermal runaway front in large-scale lithium-ion batteries: Theoretical and experiment validation, Int J Heat Mass Transf 225 (2024) 125393. https://doi.org/10.1016/j.ijheatmasstransfer.2024.125393.

[28] P. Zhao, A. García, T. Burton, Initiation and propagation of curved reaction front in solids: Insights into solid combustion and battery thermal runaway, Combust Flame 238 (2022) 111951. https://doi.org/10.1016/j.combustflame.2021.111951.

[29] P. Zhao, L. Liu, L. Zhang, Y. Chen, Mitigating battery thermal runaway through mild combustion, Chemical Engineering Journal Advances 9 (2022) 100208. https://doi.org/10.1016/j.ceja.2021.100208.

[30] O. Mathieu, C.M. Grégoire, M.A. Turner, D.J. Mohr, S.A. Alturaifi, J.C. Thomas, E.L. Petersen, Experimental Investigation of the Combustion Properties of an Average Thermal Runaway Gas Mixture from Li-Ion Batteries, Energy and Fuels 36 (2022) 3247–3258. https://doi.org/10.1021/acs.energyfuels.1c04057.

[31] D. Mishra, P. Zhao, A. Jain, Thermal Runaway Propagation in Li-ion Battery Packs Due to Combustion of Vent Gases, J Electrochem Soc 169 (2022) 100520. https://doi.org/10.1149/1945-7111/ac91a7.

[32] Z. Liu, X. Guo, N. Meng, Z. Yu, H. Yang, Study of thermal runaway and the combustion behavior of lithium-ion batteries overcharged with high current rates, Thermochim Acta 715 (2022) 179276. https://doi.org/10.1016/j.tca.2022.179276.

[33] J.S. Edge, S. O'Kane, R. Prosser, N.D. Kirkaldy, A.N. Patel, A. Hales, A. Ghosh, W. Ai, J. Chen, J. Yang, S. Li, M.C. Pang, L. Bravo Diaz, A. Tomaszewska, M.W. Marzook, K.N. Radhakrishnan, H. Wang, Y. Patel, B. Wu, G.J. Offer, Lithium ion battery degradation: what you need to know, Physical Chemistry Chemical Physics 23 (2021) 8200–8221. https://doi.org/10.1039/d1cp00359c.

[34] Y. Preger, H.M. Barkholtz, A. Fresquez, D.L. Campbell, B.W. Juba, J. Romàn-Kustas, S.R. Ferreira, B. Chalamala, Degradation of Commercial Lithium-Ion Cells as a Function of Chemistry and Cycling Conditions, J Electrochem Soc 167 (2020) 120532. https://doi.org/10.1149/1945-7111/abae37.

[35] R. Xiong, Y. Pan, W. Shen, H. Li, F. Sun, Lithium-ion battery aging mechanisms and diagnosis method for automotive applications: Recent advances and perspectives, Renewable and Sustainable Energy Reviews 131 (2020) 110048. https://doi.org/10.1016/j.rser.2020.110048.

[36] D.I. Stroe, M. Swierczynski, S.K. Kær, R. Teodorescu, Degradation Behavior of Lithium-Ion Batteries During Calendar Ageing - The Case of the Internal Resistance Increase, IEEE Trans Ind Appl 54 (2018) 517–525. https://doi.org/10.1109/TIA.2017.2756026.

[37] S. Atalay, M. Sheikh, A. Mariani, Y. Merla, E. Bower, W.D. Widanage, Theory of battery ageing in a lithium-ion battery: Capacity fade, nonlinear ageing and lifetime prediction, J Power Sources 478 (2020) 229026. https://doi.org/10.1016/j.jpowsour.2020.229026.

[38] J. Zhu, M.S. Dewi Darma, M. Knapp, D.R. Sørensen, M. Heere, Q. Fang, X. Wang, H. Dai, L. Mereacre, A. Senyshyn, X. Wei, H. Ehrenberg, Investigation of lithium-ion battery degradation

mechanisms by combining differential voltage analysis and alternating current impedance, J Power Sources 448 (2020) 28–30. https://doi.org/10.1016/j.jpowsour.2019.227575.
[39] Y. Gao, K. Liu, C. Zhu, X. Zhang, D. Zhang, Co-Estimation of State-of-Charge and State-of-Health for Lithium-Ion Batteries Using an Enhanced Electrochemical Model, IEEE Transactions on Industrial Electronics 69 (2022) 2684–2696. https://doi.org/10.1109/TIE.2021.3066946.
[40] A. Sarkar, I.C. Nlebedim, P. Shrotriya, Performance degradation due to anodic failure mechanisms in lithium-ion batteries, J Power Sources 502 (2021) 229145. https://doi.org/10.1016/j.jpowsour.2020.229145.
[41] J. Li, R.G. Landers, J. Park, A comprehensive single-particle-degradation model for battery state-of-health prediction, J Power Sources 456 (2020). https://doi.org/10.1016/j.jpowsour.2020.227950.
[42] F. Zhou, C. Bao, Analysis of the lithium-ion battery capacity degradation behavior with a comprehensive mathematical model, J Power Sources 515 (2021) 230630. https://doi.org/10.1016/j.jpowsour.2021.230630.
[43] G. Dong, J. Wei, A physics-based aging model for lithium-ion battery with coupled chemical/mechanical degradation mechanisms, Electrochim Acta 395 (2021) 139133. https://doi.org/10.1016/j.electacta.2021.139133.
[44] G. Zhang, X. Wei, S. Chen, G. Han, J. Zhu, H. Dai, Investigation the Degradation Mechanisms of Lithium-Ion Batteries under Low-Temperature High-Rate Cycling, ACS Appl Energy Mater (2022). https://doi.org/10.1021/acsaem.2c00957.
[45] S. Sahu, J.M. Foster, A continuum model for lithium plating and dendrite formation in lithium-ion batteries: Formulation and validation against experiment, J Energy Storage 60 (2023) 106516. https://doi.org/10.1016/j.est.2022.106516.
[46] H. Xu, C. Han, W. Li, H. Li, X. Qiu, Quantification of lithium dendrite and solid electrolyte interphase (SEI) in lithium-ion batteries, J Power Sources 529 (2022) 231219. https://doi.org/10.1016/j.jpowsour.2022.231219.
[47] X. Lin, K. Khosravinia, X. Hu, J. Li, W. Lu, Lithium Plating Mechanism, Detection, and Mitigation in Lithium-Ion Batteries, Prog Energy Combust Sci 87 (2021). https://doi.org/10.1016/j.pecs.2021.100953.
[48] T.M.M. Heenan, A. Wade, C. Tan, J.E. Parker, D. Matras, A.S. Leach, J.B. Robinson, A. Llewellyn, A. Dimitrijevic, R. Jervis, P.D. Quinn, D.J.L. Brett, P.R. Shearing, Identifying the Origins of Microstructural Defects Such as Cracking within Ni-Rich NMC811 Cathode Particles for Lithium-Ion Batteries, Adv Energy Mater 10 (2020). https://doi.org/10.1002/aenm.202002655.
[49] M. Shahjalal, P.K. Roy, T. Shams, A. Fly, J.I. Chowdhury, M.R. Ahmed, K. Liu, A review on second-life of Li-ion batteries: prospects, challenges, and issues, Energy 241 (2022) 122881. https://doi.org/10.1016/j.energy.2021.122881.
[50] Y. Tao, C.D. Rahn, L.A. Archer, F. You, Second life and recycling: Energy and environmental sustainability perspectives for high-performance lithium-ion batteries, Sci Adv 7 (2021) 1–16. https://doi.org/10.1126/sciadv.abi7633.
[51] W. Ai, B. Wu, E. Martínez-Pañeda, A coupled phase field formulation for modelling fatigue cracking in lithium-ion battery electrode particles, J Power Sources 544 (2022) 231805. https://doi.org/10.1016/j.jpowsour.2022.231805.
[52] S. Lee, W. Li, A. Dolocan, H. Celio, H. Park, J.H. Warner, A. Manthiram, In-Depth Analysis of the Degradation Mechanisms of High-Nickel, Low/No-Cobalt Layered Oxide Cathodes for Lithium-Ion Batteries, Adv Energy Mater 11 (2021) 1–14. https://doi.org/10.1002/aenm.202100858.
[53] J. Zhu, I. Mathews, D. Ren, W. Li, D. Cogswell, B. Xing, T. Sedlatschek, S.N.R. Kantareddy, M. Yi, T. Gao, Y. Xia, Q. Zhou, T. Wierzbicki, M.Z. Bazant, End-of-life or second-life options for retired electric vehicle batteries, Cell Rep Phys Sci 2 (2021) 100537. https://doi.org/10.1016/j.xcrp.2021.100537.
[54] Y. Zhao, O. Pohl, A.I. Bhatt, G.E. Collis, P.J. Mahon, T. Rüther, A.F. Hollenkamp, A Review on Battery Market Trends, Second-Life Reuse, and Recycling, Sustainable Chemistry 2 (2021) 167–205. https://doi.org/10.3390/suschem2010011.
[55] J.V. Pastor, A. García, J. Monsalve-Serrano, D. Golke, Analysis of the aging effects on the thermal runaway characteristics of Lithium-Ion cells through stepwise reactions, Appl Therm Eng 230 (2023). https://doi.org/10.1016/j.applthermaleng.2023.120685.
[56] T. Gao, J. Bai, D. Ouyang, Z. Wang, W. Bai, N. Mao, Y. Zhu, Effect of aging temperature on thermal stability of lithium-ion batteries: Part A – High-temperature aging, Renew Energy 203 (2023) 592–600. https://doi.org/10.1016/j.renene.2022.12.092.

[57] M. Yang, Y. Ye, A. Yang, Z. Jiang, X. Wang, H. Yuan, M. Rong, Comparative study on aging and thermal runaway of commercial LiFePO4/graphite battery undergoing slight overcharge cycling, J Energy Storage 50 (2022) 104691. https://doi.org/10.1016/j.est.2022.104691.

[58] C. jie Wang, Y. li Zhu, F. Gao, C. Qi, P. long Zhao, Q. fen Meng, J. yong Wang, Q. bing Wu, Thermal runaway behavior and features of LiFePO4/graphite aged batteries under overcharge, Int J Energy Res 44 (2020) 5477–5487. https://doi.org/10.1002/er.5298.

[59] W. Yuan, D. Liang, Y. Chu, Q. Wang, Aging effect delays overcharge-induced thermal runaway of lithium-ion batteries, J Loss Prev Process Ind 79 (2022) 104830. https://doi.org/10.1016/j.jlp.2022.104830.

[60] D. Ren, K. Smith, D. Guo, X. Han, X. Feng, L. Lu, M. Ouyang, J. Li, Investigation of Lithium Plating-Stripping Process in Li-Ion Batteries at Low Temperature Using an Electrochemical Model, J Electrochem Soc 165 (2018) A2167–A2178. https://doi.org/10.1149/2.0661810jes.

[61] T. Waldmann, M. Wohlfahrt-Mehrens, Effects of rest time after Li plating on safety behavior—ARC tests with commercial high-energy 18650 Li-ion cells, Electrochim Acta 230 (2017) 454–460. https://doi.org/10.1016/j.electacta.2017.02.036.

[62] S. Wang, K. Rafiz, J. Liu, Y. Jin, J.Y.S. Lin, Effects of lithium dendrites on thermal runaway and gassing of LiFePO4batteries, Sustain Energy Fuels 4 (2020) 2342–2351. https://doi.org/10.1039/d0se00027b.

[63] B. Ng, P.T. Coman, E. Faegh, X. Peng, S.G. Karakalos, X. Jin, W.E. Mustain, R.E. White, Low-Temperature Lithium Plating/Corrosion Hazard in Lithium-Ion Batteries: Electrode Rippling, Variable States of Charge, and Thermal and Nonthermal Runaway, ACS Appl Energy Mater 3 (2020) 3653–3664. https://doi.org/10.1021/acsaem.0c00130.

[64] P. Xu, J. Li, N. Lei, F. Zhou, C. Sun, An experimental study on the mechanical characteristics of Li-ion battery during overcharge-induced thermal runaway, Int J Energy Res 45 (2021) 19985–20000. https://doi.org/10.1002/er.7072.

[65] M. Fleischhammer, T. Waldmann, G. Bisle, B.I. Hogg, M. Wohlfahrt-Mehrens, Interaction of cyclic ageing at high-rate and low temperatures and safety in lithium-ion batteries, J Power Sources 274 (2015) 432–439. https://doi.org/10.1016/j.jpowsour.2014.08.135.

[66] S. Wu, C. Wang, W. Luan, Y. Zhang, Y. Chen, H. Chen, Thermal runaway behaviors of Li-ion batteries after low temperature aging: Experimental study and predictive modeling, J Energy Storage 66 (2023) 107451. https://doi.org/10.1016/j.est.2023.107451.

[67] C. Qi, Z. Liu, C. Lin, Y. Hu, D. Liu, Z. Li, A. Yi, Study on the effect of low-temperature cycling on the thermal and gas production behaviors of Ni0.8Co0.1Al0.1/graphite lithium-ion batteries, Appl Therm Eng 247 (2024) 123054. https://doi.org/10.1016/j.applthermaleng.2024.123054.

[68] Z. Zhang, C. Ji, Y. Liu, Y. Wang, B. Wang, D. Liu, Effect of Aging Path on Degradation Characteristics of Lithium-Ion Batteries in Low-Temperature Environments, Batteries 10 (2024) 1–17. https://doi.org/10.3390/batteries10030107.

[69] L. Zhao, M. Zheng, J. Zhang, H. Liu, W. Li, M. Chen, Numerical modeling of thermal runaway for low temperature cycling lithium-ion batteries, J Energy Storage 63 (2023) 107053. https://doi.org/10.1016/j.est.2023.107053.

[70] S. Wu, C. Wang, W. Luan, Y. Zhang, Y. Chen, H. Chen, Thermal runaway behaviors of Li-ion batteries after low temperature aging: Experimental study and predictive modeling, J Energy Storage 66 (2023) 107451. https://doi.org/10.1016/j.est.2023.107451.

[71] D. Kong, H. Zhao, P. Ping, Y. Zhang, G. Wang, Effect of low temperature on thermal runaway and fire behaviors of 18650 lithium-ion battery: A comprehensive experimental study, Process Safety and Environmental Protection 174 (2023) 448–459. https://doi.org/10.1016/j.psep.2023.04.017.

[72] H. Zhou, C. Fear, R.E. Carter, C.T. Love, P.P. Mukherjee, Correlating lithium plating quantification with thermal safety characteristics of lithium-ion batteries, Energy Storage Mater 66 (2024) 103214. https://doi.org/10.1016/j.ensm.2024.103214.

[73] L. Zhang, S. Yang, L. Liu, P. Zhao, Cell-to-cell variability in Li-ion battery thermal runaway: Experimental testing, statistical analysis, and kinetic modeling, J Energy Storage 56 (2022). https://doi.org/10.1016/j.est.2022.106024.

[74] W. Choi, H.C. Shin, J.M. Kim, J.Y. Choi, W.S. Yoon, Modeling and applications of electrochemical impedance spectroscopy (Eis) for lithium-ion batteries, Journal of Electrochemical Science and Technology 11 (2020) 1–13. https://doi.org/10.33961/jecst.2019.00528.

[75] C.Y. Jhu, Y.W. Wang, C.Y. Wen, C.M. Shu, Thermal runaway potential of LiCoO2 and Li(Ni1/3Co1/3Mn1/3)O2 batteries determined with adiabatic calorimetry methodology, Appl Energy 100 (2012) 127–131. https://doi.org/10.1016/j.apenergy.2012.05.064.

[76] C.Y. Jhu, Y.W. Wang, C.M. Shu, J.C. Chang, H.C. Wu, Thermal explosion hazards on 18650 lithium ion batteries with a VSP2 adiabatic calorimeter, J Hazard Mater 192 (2011) 99–107. https://doi.org/10.1016/j.jhazmat.2011.04.097.

[77] G.H. Kim, A. Pesaran, R. Spotnitz, A three-dimensional thermal abuse model for lithium-ion cells, J Power Sources 170 (2007) 476–489. https://doi.org/10.1016/j.jpowsour.2007.04.018.

[78] T.D. Hatchard, D.D. MacNeil, A. Basu, J.R. Dahn, Thermal Model of Cylindrical and Prismatic Lithium-Ion Cells, J Electrochem Soc 148 (2001) A755. https://doi.org/10.1149/1.1377592.

[79] D. Ren, X. Liu, X. Feng, L. Lu, M. Ouyang, J. Li, X. He, Model-based thermal runaway prediction of lithium-ion batteries from kinetics analysis of cell components, Appl Energy 228 (2018) 633–644. https://doi.org/10.1016/j.apenergy.2018.06.126.

[80] E. Kwak, J. hyeong Kim, S.H. Hong, K.Y. Oh, Detailed modeling investigation of thermal runaway pathways of a lithium iron phosphate battery, Int J Energy Res 46 (2022) 1146–1167. https://doi.org/10.1002/er.7235.

# In-Cylinder Heat Loss Reduction in a Diesel Engine: Common Principle of a Novel Heat Insulation Structure and a Novel Nozzle Orifice Design

N. Uchida[1], F. Kawaharazuka[1], K. Watanabe[2]

[1]New ACE Institute Co., Ltd. 2530 Karima, Tsukuba-shi, Ibaraki Pref. 305-0822, Japan.
E-mail: n_uchida@nace.jp, f_kawaharazuka@nace.jp
Telephone: +(81) 29 856 1801

[2]DENSO CORPORATION. 1-1 Showa-cho, Kariya-shi, Aichi Pref. 448-8661, Japan.

E-mail: kazumasa.watanabe.j7g@jp.denso.com
Telephone: +(81) 50 1735 8027

**Abstract.** For further increase in thermal efficiency of engines, heat loss reduction becomes to be essential. Many studies to reduce heat loss in a cylinder have been carried out by applying various thermal barrier coating to the piston and/or other in-cylinder surface by utilizing various ceramic materials with lower thermal effusivity. However, their effects on the heat loss of reciprocating engines were mostly very little or sometimes negative. This study firstly investigated the heat insulation layer material and its thickness effects on heat transfer by a one-dimensional unsteady numerical model. As the result, the material of lower heat effusivity doesn’t always reduce heat transfer for diesel combustion by its high surface temperature swing, but rather increase in local heat flux at the “hot spots” near top dead centre (TDC). Such heat flux is also effective not only to increase total heat loss but to reduce indicated work. It is essential to consider not only heat convection, but heat conduction variances. Then, a modified insulation structure with thin aluminium coating overlayed by physical vapor deposition (PVD) on both piston and cylinder head, was tested with a heavy-duty single cylinder engine. Aluminium was initially selected by its high reflectance not to absorb flame radiation at the exposed (with less soot deposits) area, but to selectively absorb at the soot deposit, where flame is interfered, to achieve less local heat convection. Furthermore, the experimental results suggested that the surface temperature at the gas-exposed area is raised by the heat conduction along the aluminium coating layer from the hot spots during and after combustion period. Such surface temperature homogeneity could also be effective for further reduction of cycle-integrated heat loss. The other measure to homogenize the wall temperature distribution or spatial flame distribution, we proposed a novel design of fuel injection nozzle. The experimental result also showed more significant heat loss reduction with the new nozzle.

## Notation

| | |
|---|---|
| AHRR | *Apparent Heat Release Rate (in engine experiments) J/deg.CA (=ROHR)* |
| APS | *Atmospheric Plasma Spraying process.* |
| ATDC | *After Top Dead Centre.* |
| BTE | *Brake Thermal Efficiency %.* |
| $dP/d\theta$ | *In-cylinder pressure change rate MPa/deg.CA.* |
| EGR | *Exhaust Gas Recirculation.* |
| HRR | *Heat Release Rate J/deg.CA.* |
| HTPV | *High Temperature Pressure Vessel.* |
| HVOF | *High Velocity Oxy-Fuel Spraying process.* |
| ITE | *Indicated Thermal Efficiency %.* |
| Ne | *Engine Speed.* |
| Pinj | *Fuel Injection Pressure.* |
| PVD | *Physical Vapor Deposition process.* |
| Q | *Fuel Injection Quantity.* |
| SOC | *Start timing of Combustion.* |
| TBC | *Thermal Barrier Coatings.* |
| TDC | *Top Dead Centre.* |
| $\lambda$ | *Excess air ratio (Lambda).* |
| 8YSZ | *8% Yttria Stabilized Zirconia* ($ZrO_2/Y_2O_3$). |

## 1. Introduction

Drastic heat loss reduction must be an essential measure to increase thermal efficiency of internal combustion engines. Many attempts on heat insulation in the cylinder not only by physically separated flame from the wall, but also by thermal barrier coatings (TBC) have been investigated for several decades [1]. For diesel engines aiming higher thermal efficiency, their compression ratio should be increased rather than increasing in degree of constant volume combustion [2]. Therefore, TBC has been more concerned under the assumption of increased flame-wall interference with limited volume of cavity. To reduce forced convective heat transfer, temperature difference between the wall surface and the working gas is tried to reduce by increasing wall temperature swing synchronous in the instantaneous gas temperature variation especially during compression and expansion strokes [3]. Thermal effusivity, i.e., thermal conductivity and heat capacity of a TBC material, is thought as the dominant factor to determine the temperature swing oscillation [4]. The lower the thermal effusivity, the higher the temperature swing. Even though there are several papers on the heat loss reduction and/or thermal efficiency improvement with low thermal effusivity TBC applied to spark ignition engines [5,6], TBC applied to diesel engines has not been adequately and historically proven its effectiveness.

Binder et al. investigated the effect of 1mm-thick plasma-sprayed yttria stabilized zirconia (YSZ) TBC on the steel piston surface [7]. They concluded from the apparent heat release, volumetric efficiency, heat transfer rate to the oil, surface temperature and the local heat flux, that the combustion is slower in the zirconia coating piston. From the surface temperature measurement data by the laser induced phosphorescence (LIP) technique and the volumetric efficiency, it is revealed that YSZ surface temperature was kept in higher temperature throughout the cycle resulting in the intake gas heating. It could be a cause of the slow combustion. However, ignition delay and initial heat release rate were almost the same probably until the spray impinged on the wall in the experiment. Therefore, the higher working gas temperature is not regarded as the primal cause of slower heat release. Koci et al. discussed on the same phenomena with different thickness: 0.325 mm and surface roughness of YSZ TBC by means of a single cylinder engine and a high temperature pressure vessel (HTPV). That is, the TBC piston tends to make (apparent) heat release rates slower [8]. From the results by Combustion Image Velocimetry (CIV) observed in the HTPV, it was revealed that the polished YSZ coating with the slightly higher surface roughness: Ra = 2.1-5.3 μm (1.0-1.7 μm for the steel piston) reduced the mixing energy. Osada et al. provided the similar comparison of CIV results between a mirror-like polished piston surface of the stainless-steel coating: Ra = 0.04 μm and a baseline metal piston: Ra = 3.2 μm observed through a top-view window of a single cylinder engine, and concluded that no significant difference was observed in the averaged velocity just after flame impingement to the wall [9]. Was it truly the slower heat release caused by the YSZ TBC or the effect of higher heat loss around the top dead centre (TDC)? The cumulative apparent heat release around 60 deg. ATDC of TBC piston in both papers [7,8] indicate clear reduction in comparison with that of the baseline metal piston. If it is caused by only slower heat release of TBC piston, the difference in the cumulative heat release could become smaller around 60 deg. ATDC by relatively higher heat release rate in the late combustion, or carbon monoxide emissions will be increased by the incomplete combustion. This study firstly investigated the effect of thermal conductivity, specific heat, and TBC thickness on the heat flux on the instantaneous and cycle-averaged heat flux calculated by an internally-developed unsteady one-dimensional heat transport model with the boundary condition based on the experimental results.

As a novel coating to reduce heat loss in a diesel engine, we have noticed that the effective utilization of radiation from the luminous flame also plays important role. It has been experimentally confirmed that accumulated soot deposit has a function to improve both heat loss and thermal efficiency simultaneously [10]. We assumed that the soot deposits on the surface, especially at the flame impingement area, selectively absorb the radiation by their very high emissivity resulting in the increase of local surface temperature, which reduces heat transfer at there. For further utilization of this mechanism, the material which has extremely higher reflectance (lower emissivity) and the exact opposite thermal properties to YSZ, namely higher thermal conductivity, was applied to the piston coating. The higher reflectance will increase the selectivity of absorbing radiation at the soot deposit. In addition, the higher thermal conductivity will affect more homogeneous surface temperature distribution.

To compare the novel coating effect with the spatial flame distribution control effect, a new design nozzle was proposed. The nozzle orifice is tangentially drilled to the sac diameter, Ewphum called it as 'offset orifice nozzle' [11]. Since offset orifice nozzle has asymmetrical orifice length, it is assumed that the spray growth is asymmetrical and spray breakup is accelerated. The purpose of this nozzle is to achieve more in-cylinder area-occupied flame, which could also result in the lower heat loss by the homogeneous surface temperature distribution.

## 2. Experimental Setup

### 2.1 Engine specifications

A single cylinder four-stroke direct-injection diesel engine with displacement volume of 2147 $cm^3$ was utilized for engine experiments in this study. Detailed specifications of the engine are listed in Table 1. The engine was designed to have a tolerance up to 35 MPa of peak firing pressure. The test engine simulates turbocharged and after-cooled heavy-duty diesel engines by an externally driven supercharger, exhaust throttling, and air heater/cooler. A hydraulic variable valve actuation system (Sturman Industries, DHVVA) and an electronically controlled high-pressure common rail injection system (Denso G4S modified) which enable a maximum injection pressure of 300 MPa were equipped. To observe in-cylinder combustion phenomena (with the offset orifice nozzle as discussed in 4.1), the other single cylinder transparent (bottom-view) engine was utilized.

**Table 1**. Engine specifications

| Engine type | Single cylinder DI diesel<br>Metal engine | Transparent engine<br>(bottom-view) |
|---|---|---|
| Cylinder bore x Stroke | φ135 mm×150 mm | φ135 mm×140 mm |
| Engine displacement | 2147 $cm^3$ | 2004 $cm^3$ |
| Connecting rod length | 370.46 mm | 250 mm |
| Compression ratio *CR* | 19.2:1 – 27.8:1 | 18:1 |
| Piston cavity type | Toroidal | Pancake |
| Cavity diameter | 98 – 81 mm | 85 mm |
| Valve system | Camless hydraulic VVA x 4 valves (Sturman Industries) | |
| Intake swirl ratio | 1.4 | |
| Fuel injection equipment | Common rail system (DENSO G4S modified) | |
| Max. injection pressure | 300 MPa | |
| Nozzle orifice | φ0.179 mm×9-150° (Baseline, 1750 cc/min)<br>φ0.223 mm×8-156° (High flow, 2500 cc/min)<br>φ0.268 mm×8-156° (Offset orifice, 2500 cc/min) | |
| Fuel specifications | Diesel fuel JIS #2 (Japanese market fuel)<br>Cetane number: 56.8, Sulfur content: 7 ppm (mass) | |

### 2.2 Schematics of experimental system

Figure 1 (Left) shows a schematic of the experimental apparatus and the bottom-view combustion observation layout. This engine system includes an idealized turbocharger/intercooler intake system using an externally driven intake supercharging device. For the metal engine test, intake boost pressure, exhaust back pressure and intake manifold temperature are widely controlled independently at any engine operating points. Intake boost pressure of up to 500 kPa (abs.) is possible with an externally driven supercharger. A standard operating condition without any exhaust gas recirculation (EGR) was to match the exhaust back pressure to the intake boost pressure for eliminating positive pumping work and the effect of turbocharging efficiency variations. In case of increasing (high pressure loop) EGR ratio, exhaust back pressure was slightly increased by throttling the back pressure valve under the same intake boosting pressure. Therefore, the amount of intake fresh air was partly replaced by EGR gas.

Natural luminosity from the in-cylinder flame was observed from the bottom of the piston cavity with a high-speed video camera as shown in Figure 1 (Right). This transparent engine is modified the base metal engine having different stroke and con-rod length from the base metal engine with the extending piston and cylinder block. The extending piston with a pancake cavity (cavity diameter: 85 mm, height: 15.45 mm, compression ratio: 18:1) has a flat faced sapphire window in the bottom of cavity. This cavity shape was designed not to distort the captured image and to maximize the observed area by reducing soot deposit with flame interference on the window. The upper side of the extending cylinder block is equipped with a cooling circuit to limit the maximum temperature of the dry liner to be the same condition of the metal engine. The operating conditions were almost the same, except for the intake temperature which was raised to 373.15 K to achieve the same ignition delay as that with the base metal engine.

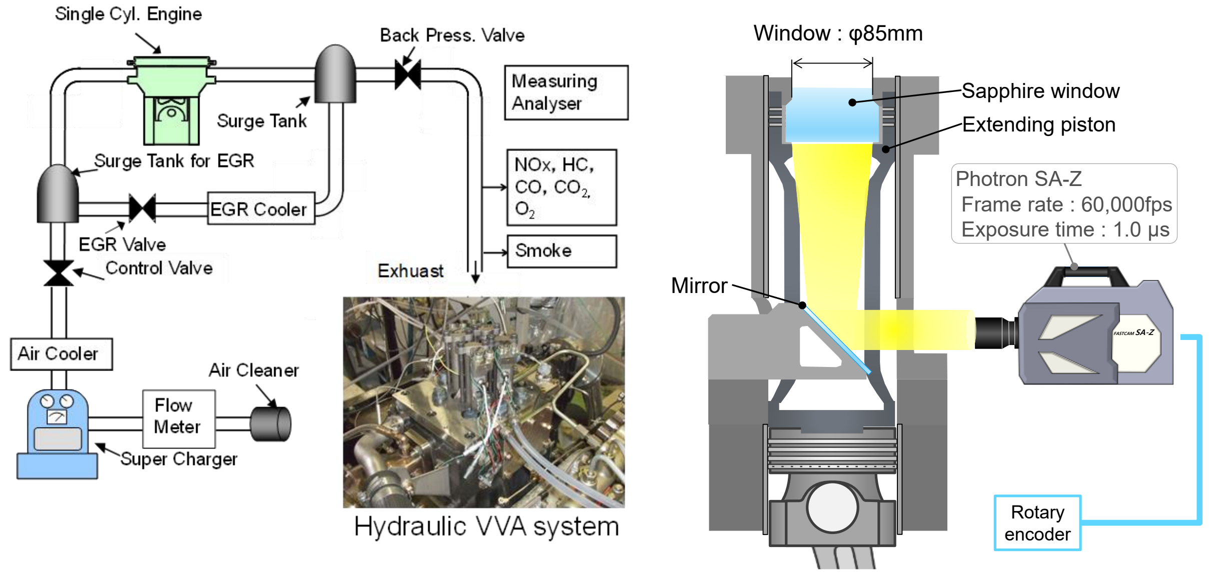
Single Cyl. Engine
Back Press. Valve
Measuring Analyser
Surge Tank
Surge Tank for EGR
NOx, HC, CO, CO2, O2
EGR Cooler
EGR Valve
Control Valve
Smoke
Exhuast
Air Cooler
Air Cleaner
Flow Meter
Super Charger
Hydraulic VVA system
Window : φ85mm
Sapphire window
Extending piston
Photron SA-Z
Frame rate : 60,000fps
Exposure time : 1.0 μs
Mirror
Rotary encoder

**Fig. 1.** Schematic of engine test system and bottom-view transparent engine layout

### 2.3 Measuring instruments

Instantaneous in-cylinder pressure was measured by a water cooled piezo-type pressure transducer (Kistler Type6043AU20SP) which is precisely corrected with the other in-cylinder pressure data during early compression stroke measured by a piezoresistive pressure sensor (Kistler 4075A) mounted on the middle of the cylinder liner. Then, the apparent heat release rate (or described as ROHR: rate of heat release) was analyzed with measured in-cylinder pressure data by utilizing a combustion characteristics analyzer (ONO-SOKKI DS3000 series). Other pressures in the manifolds were measured by piezoresistive pressure sensors (Kistler 4075A). Fuel consumption was measured by AVL 735S+753C. Air flow rate was measured by a Karman vortex flow meter (OVAL VXW040GA). Exhaust emissions, i.e., NOx, CO, and THC were analyzed by a gas analyzer (HORIBA MEXA-ONE). Total energy of unburned THC and CO, latent heat of fuel, and endothermic reaction to form NOx are analyzed in the heat balance as “others” heat loss. Fuel flow rate was precisely measured by a Coriolis type fuel mass flow meter with a temperature control unit (AVL 735S+753C). Smoke emissions in this study was just monitored by a filter paper method instrument (AVL 415S). In-cylinder combustion observation was carried out by utilizing a high-speed camera (Photron FASTCAM SA-Z).

## 3. Re-examination of TBC Coating

### 3.1 One-dimensional heat transport model

The thermal properties of the material are the important factor in reducing heat loss using a heat-insulation layer on the surface. Stainless-steel, SUS316, has been initially selected for the purpose of corrosion prevention for the mirror-polished piston surface to reduce heat transfer coefficient in addition to the lower thermal conductivity characteristics [9]. Therefore, even though it has a potential to reduce heat loss, it is still unclear whether SUS316 will be the optimum material for the thermal properties of the heat insulation structure. In this chapter, such TBC effects are re-examined by utilizing an unsteady one-dimensional heat conduction calculation with various thermal properties. Table 2 shows the calculating conditions. The unsteady one-dimensional heat conduction calculation for infinite plate model was used Fourier's heat conduction equation modified by Enomoto et al. [12]. In order to examine the effect of thermal properties and layer thickness of the material utilized for TBC, the model was divided into two layers, the heat insulation layer, and the base material substrate. The total thickness of the numerical model was fixed to 12 mm (insulation layer is included) assuming the minimum piston wall thickness between cavity surface and cooling side surface used in this study.

The thermal properties of SCM435 for base substrate were used as the properties of the baseline piston material. Thermal properties of the heat insulation layer, arbitrary values were used with reference to the materials examined in the past. Figure 2 shows the thermophysical properties of the materials examined in the past studies. For heat loss reduction, volumetric specific heat and thermal conductivity are both important, whilst it is still unclear to choose the insulation material to achieve the lowest heat loss. Hastelloy and Inconel600 as thermal spray coating on the piston are a kind of stainless-steel alloy, which have slightly higher thermal conductivity than SUS316. To investigate the effect of both lower thermal conductivity and lower specific heat for significantly lower thermal effusivity, aiming higher surface temperature swing, zirconia (YSZ) coating was also examined. Due to the mechanical strength of zirconia coating with binder, we haven't achieved any certain results without material failure. Therefore, titanium could be an alternative for zirconia with the same thermal properties and much material strength. Soot deposit could be the lowest thermal effusivity as an existing material even though it is very difficult to apply as the insulation layer with artificially controlled thickness. In this study, the calculation was performed by changing the specific heat and thermal conductivity within the feasible range of Figure 2.

**Table 2**. One-dimensional calculation model

| | | |
|---|---|---|
| Calculation model | Unsteady one-dimensional heat conduction model | |
| Model size | 12 mm thick in total | |
| Base material | SCM435 | |
| Temperature | Combustion side | *CR* = 27.8:1, 90% load data |
| | Cooling side | 80 deg.C (Same as Lubricant Oil) |
| Heat transfer coefficient | Combustion: Woschni's equation, Cooling: Enomoto's const. | |
| Thermal conductivity | 0.1 – 50 W/m·K | |
| Specific heat | $0.1\times10^6$ – $50\times10^6$ J/m$^3$K | |
| Insulation layer thickness | 0.1 – 0.6 mm | |

The major boundary condition of the combustion side is the instantaneous working gas temperature, which is analyzed as the thermodynamic average temperature with the experimentally measured in-cylinder pressure by utilizing the piston without any insulation layers under the parameters; compression ratio of 27.8:1, engine inlet coolant and the engine oil temperatures of 80 deg.C. For the combustion side heat transfer coefficient, the value obtained from Woschni's equation was used [13]. The heat transfer coefficient of the cooling side was determined as the constant value for engine oil jet cooling condition from the study by Enomoto, et al. [12] Convective heat transfer of cooling side was also calculated by the Newton's law, of which fluid temperature is 80 deg.C (oil temperature). In general, the heat transfer coefficient obtained by Woschni's equation is known as the value which does not correctly express the in-cylinder phenomena of the current diesel engines. In this study, however, the purpose is only to discuss the material properties effects with simplified conditions, so it was not adjusted in the simulation.

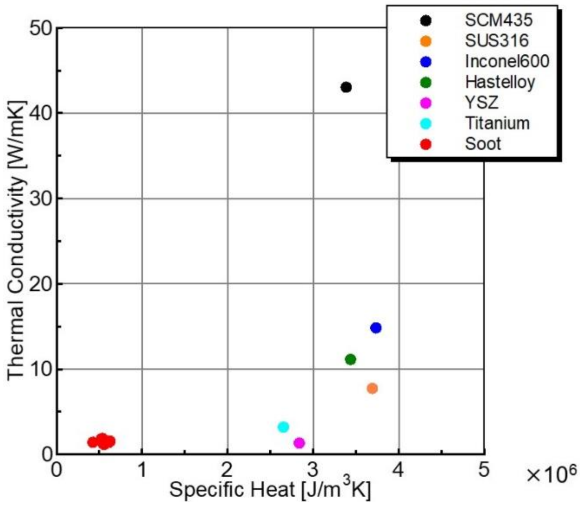

**Fig. 2.** Thermal properties of various materials for heat insulation

The differences in cycle-averaged heat flux for the variation of volume specific heat and thermal conductivity (layer thickness of 0.3 mm) were calculated as in Figure 3. In case of the thermal conductivity of about 30 W/(m·K) or above, there is no difference in heat flux regardless of the difference in insulation layer thickness, which is dominated by the thermal conductivity of the base material SCM435; 44 W/(m·K). In the region where thermal conductivity is 30 W/(m·K) or less, the significant difference in heat flux can be observed. Although the effect of specific heat is smaller than the effect of thermal conductivity, the calculated heat flux also becomes smaller by the concurrent reduction of specific heat with thermal conductivity. Therefore, for the direction to reduce both specific heat and thermal conductivity than SCM435, titanium is selected as a TBC material. In addition to its sufficient mechanical strength as a thin layer coating on the piston, titanium has the similar thermal properties with zirconia.

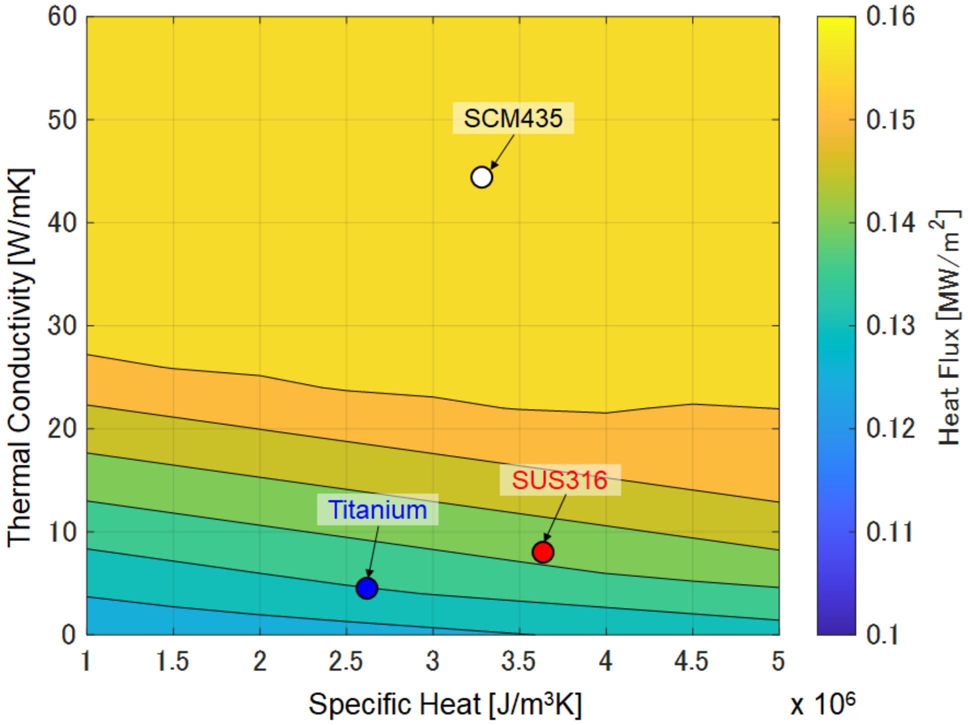

**Fig. 3.** Effect of specific heat and thermal conductivity on ‘cycle-averaged’ heat flux

However, these thermal properties have sometimes negative effect on indicated work in contradiction to the expectation. Figure 4 shows the results of the instantaneous heat flux at the boundary between Titanium layer and the substrate and in-depth temperature comparisons with the same calculation. Focusing on the heat flux, the titanium spraying piston has a negative heat flux (indicating heat transfer from wall surface to working gas) in early compression stroke and late expansion stroke, but the heat flux is much larger than that of the normal (w/o any TBC) piston around TDC. Titanium is a material with lower thermal conductivity and specific heat than SCM435 (piston material). Due to the small specific heat and thermal conductivity, the magnitude of surface temperature swing tends to increase. Nevertheless, instantaneous heat flux at the surface tends to significantly increase around TDC regardless of material porosity and/or surface roughness (such models are excluded in the calculation). Furthermore, the maximum heat loss timing close to TDC resulted in significant reduction of peak in-cylinder pressure and/or indicated work. Increased surface temperature swing only intends to reduce convective heat transfer between gas and material, while heat flux through the material is also varied by the increased temperature gradient. The actual surface temperature will be determined by the equilibrium between these instantaneous heat convection and conduction. As in the study by Binder [7], unchanged oscillation of swing even with YSZ having low thermal effusivity might be caused by the increased heat conduction.

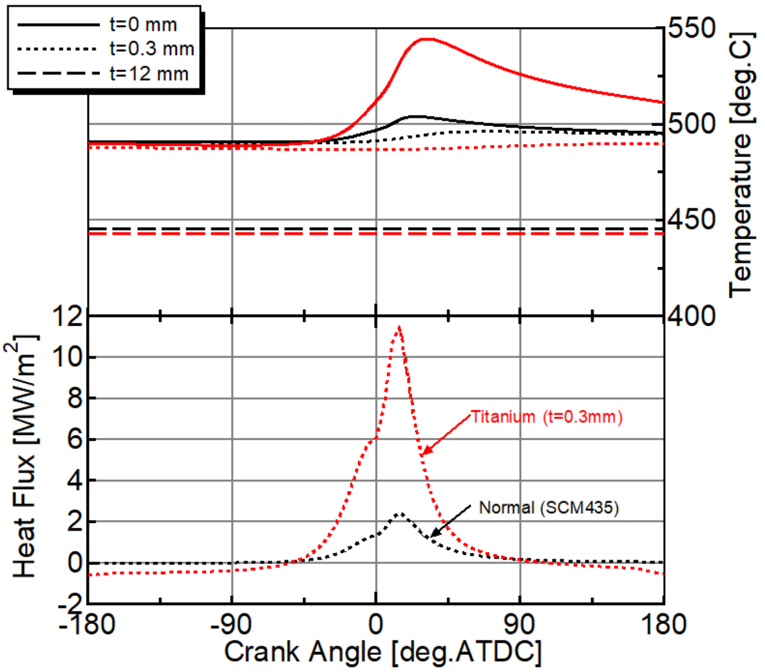

**Fig. 4.** Comparison of heat flux between normal piston and titanium spraying piston (1D simulation)

Experimental comparison of the combustion characteristics and the heat balance analysis [14] between the normal piston and the titanium spraying piston was shown in Figure 5. The result indicated the higher heat loss of about 0.4 %pt. with the titanium spraying piston. The brake thermal efficiency was also 0.2 %pt. lower. Heat release rate of the titanium spraying piston was also decreased around 10deg.ATDC. It was concluded that the titanium thermal spraying piston had a larger heat loss than the normal piston especially around TDC, resulting in the decreased thermal efficiency due to the in-cylinder pressure drop near TDC.

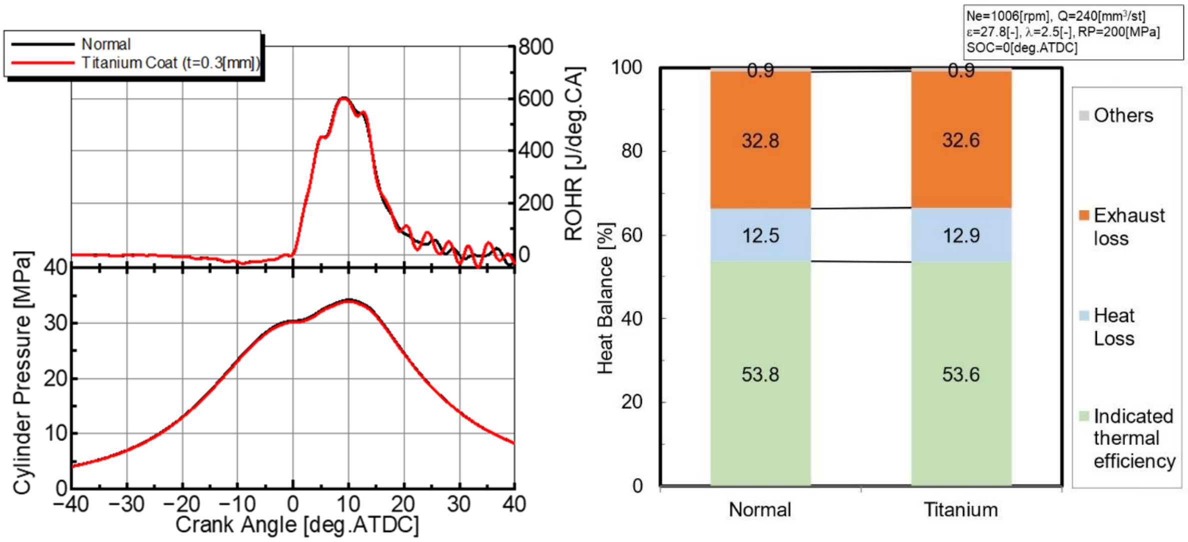

**Fig. 5.** Experimental comparison of combustion characteristics and heat balance between normal piston and titanium spraying piston

### 3.2 New heat loss reduction concept

Most studies on the heat loss in the cylinder commonly discuss only on the effect of heat conduction and/or heat transfer, however, there are few studies on the effect of radiation [15, 16]. In our previous study, it is revealed that the accumulation of soot deposit has a significant effect to reduce heat loss. We assumed that radiative heat transfer will play an important role of its mechanism [10]. If the radiation from luminous flame can be utilized for the active control of the surface temperature, there will be more rooms for the improvement in heat loss during combustion. The mechanism of this phenomenon is assumed that the soot deposits on the combustion chamber, at where spray flame directly impinged, play important role. That is, soot absorbs the radiation from the luminous flame and consequently the local wall surface temperature sufficiently rises before reaching the flame tip to the deposits. If soot deposits selectively absorb the radiation from luminous flame by reducing the absorption at the gas-exposed area, the surface temperature distribution inside the cylinder could be extremely heterogeneous. Heat loss at the gas-exposed wall surface by the lower surface temperature could be compensated by the reduction of the working gas heating, and the heat loss at the soot deposit will be reduced.

To study the heat insulation structure in consideration of radiation, the reflectance of the different material coating on the test piece (substrate material was the same as that of the piston) having the same surface textures as the evaluated pistons were measured. Table 3 shows the pistons with the same surface textures as the measured test pieces. There were four types of pistons that have been compared with the baseline piston; simply mirror-polished raw material of the piston, mirror-polished stainless-steel layer on the piston, titanium spraying on the piston and zirconia spraying on the piston. In addition, a piston coated with thin aluminum layer using PVD method was prototyped as a new measure to improve the reflectance. The reflectance was measured for the above mentioned six test pieces, the same surface textiles of five heat insulation pistons and the baseline pistons (with Parkerizing, surface roughness: Ra=1.6 μm). The measurement was carried out in the range of 250-20000 nm from the ultraviolet region to the far-infrared region. The results are shown in Figure 6.

**Table 3**. Specification of heat insulating test pieces

| Type | Coating | Roughness; Ra μm | Thickness μm |
|---|---|---|---|
| Baseline | Parkerizing | 1.6 | 1-6 |
| Baseline (Polished) | None | <0.1 | - |
| SUS thermal spray | SUS316 HVOF | <0.1 | 300 |
| Titanium thermal spray | Ti APS | <1.0 | 300 |
| Zirconia thermal spray | 8YSZ APS | <6.0 | 300 |
| Aluminum coating | Al PVD | <0.1 | 3-5 |

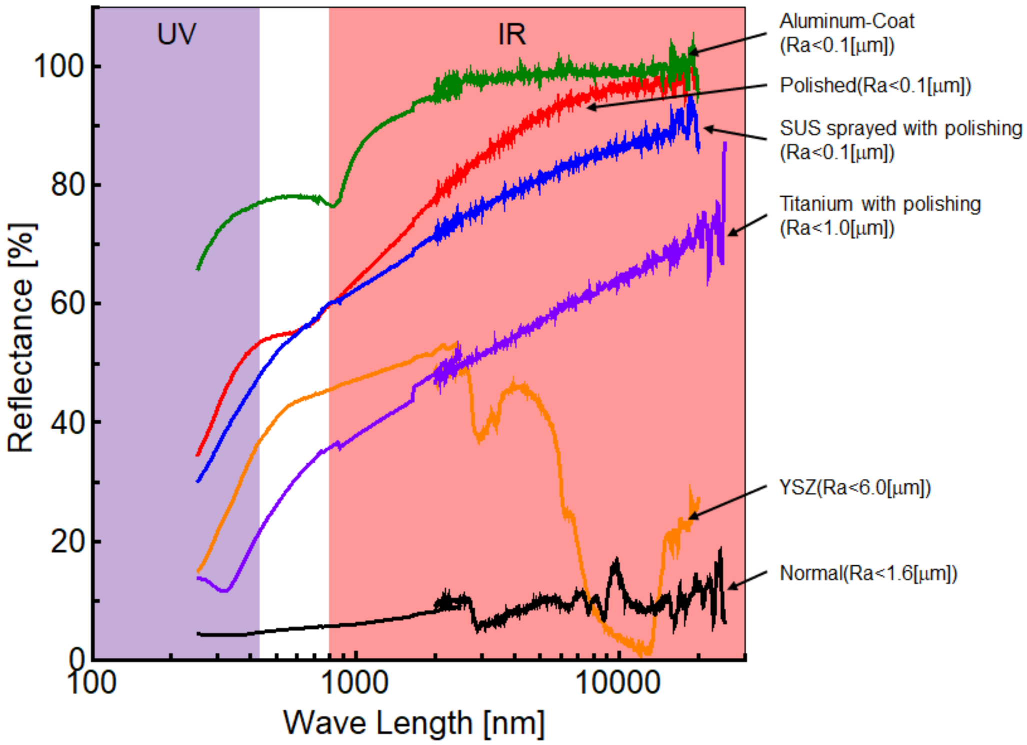

**Fig. 6.** Measured reflectance of six test pieces from UV: Ultraviolet to IR: Infrared

Since the wide range of 200 nm-25000 nm is measured by two measuring instruments with different measurement ranges (from ultraviolet to near infrared and far infrared), some results are shown by the discontinuity lines between the wavelength of 2000 and 2500 [nm] (overlapped region). This is due to the characteristics of the measuring instruments, but since the purpose of this measurement is to confirm the relative value of the reflectance over a wide range, no correction is performed. The reflectance of the standard piston with Parkerizing was about 10% to 20% over a wide range from the ultraviolet region to the far infrared region, whereas the reflectance of the heat insulation structures, the mirror-polished piston and the stainless-steel spraying mirror-polished piston, have almost the same value and higher than the standard piston, and the zirconia or titanium spraying pistons are both lower than the mirror-polished piston and the stainless-steel spraying piston. In comparison with these pistons the aluminum PVD coated piston indicated higher reflectance than any of the heat-insulation structure pistons. In particular, the reflectance in the near infrared region, which is known to have high spectral radiance from the luminous flame according to Planck's law, was about 80%. Therefore, an experiment using the new heat insulation structure minimizing the radiative heat transfer by the aluminum coating was then carried out.

In case of considering radiative heat transfer reduction, increase in the reflectance only on the piston crown side may not be so effective, because radiation could be absorbed elsewhere except for the piston surface, e.g., the fire deck of the cylinder head, valve surfaces. Therefore, two cases were examined (compared with the non-coat condition); one is aluminum coating only on the piston surface, the other is aluminum coating on both piston and cylinder head (exclude mirror polished valve surface). The heat balance analysis results for various excess air ratio under middle and high load conditions are shown in Figure 7.

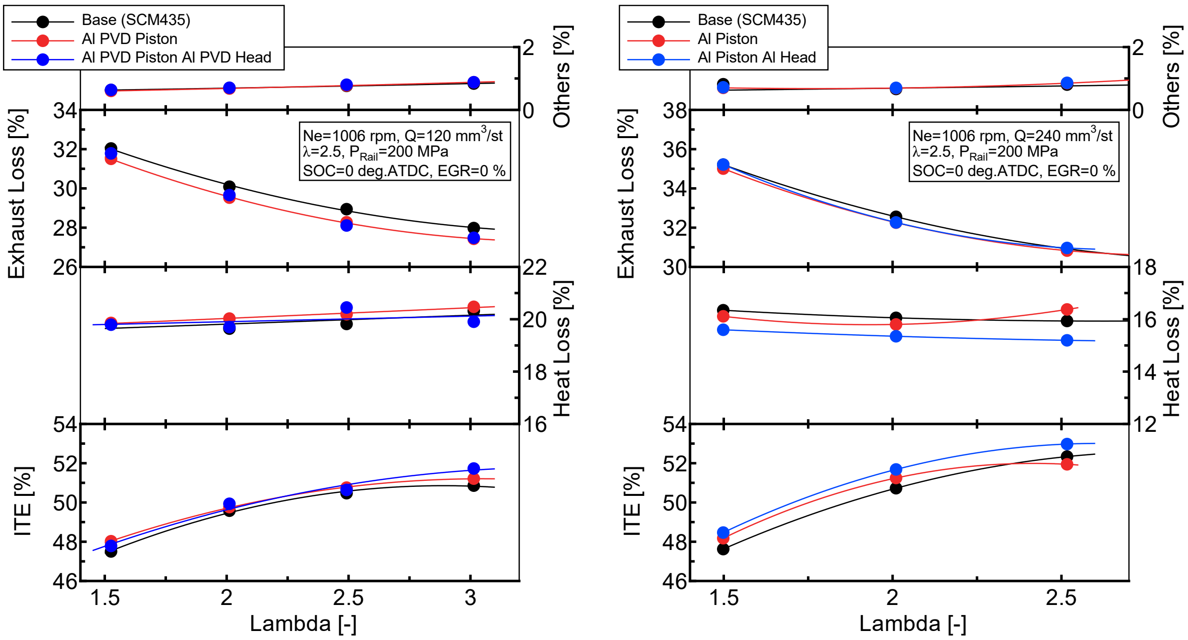

**Fig. 7.** Heat balance comparison between non-coat, piston only Al PVD coat, and piston & head Al PVD coat for excess air ratio (λ) variation under middle (fuel quantity of 120 mm$^3$/st) and high (240 mm$^3$/st) load conditions (compression ratio: 27.8:1)

The engine experimental result indicates the significant improvement in heat loss and indicated thermal efficiency (ITE) with the aluminum coating piston and cylinder head especially at high load condition as show in the heat balance of Figure 7. The engine experiments revealed more remarkable characteristics of the aluminum coating on soot deposit. The baseline and TBC coating (except for aluminum) pistons, soot deposits tend to be firmly seized on the surface by the elevated local surface temperature of the base material, whereas soot deposit on the aluminum coating piston was easily wiped after running the engine under the same operating conditions. It means that the local surface temperature of aluminum coating contacted with the soot deposit could be relatively low in comparison with other baseline and TBC pistons. Thermal penetration depth of soot deposit will be about 1.0 mm based on the Nishiwaki's data [17], which is far larger than actual soot deposit layer thickness (~ 10 μm @ 1000 rpm). That is, instantaneous and large input of heat at the soot surface will be transferred to the lower layer without any effective attenuation. Since the spatial flame distribution should not be significantly changed by the coating, local heat flux at the soot deposit will be the same. The hypothesis for the phenomenon is that the aluminum coating just below the soot deposit can swiftly spread heat not only in-depth but rather along the thin layer to the gas-exposed area adjoining the deposit. Therefore, heat convection at the gas-exposed area could be reduced around TDC by the indirect heat conducting along the aluminum coating. It is concluded that the phenomenon cannot be analyzed by the unsteady one-dimensional heat conduction model. Therefore, we should investigate the effect of surface temperature variation with the specific heat insulation structure from both heat convection (between gas and surface) and heat conduction (two or three dimensional, through solid body) viewpoints. This hypothesis is added to the initial intention of the high reflectance material coating, namely heat loss around TDC was significantly improved by the more homogenous surface temperature distribution. Furthermore, absolute surface temperature difference between piston, valve surfaces and fire deck of cylinder head should also be taken into consideration for the homogeneous surface temperature distribution.

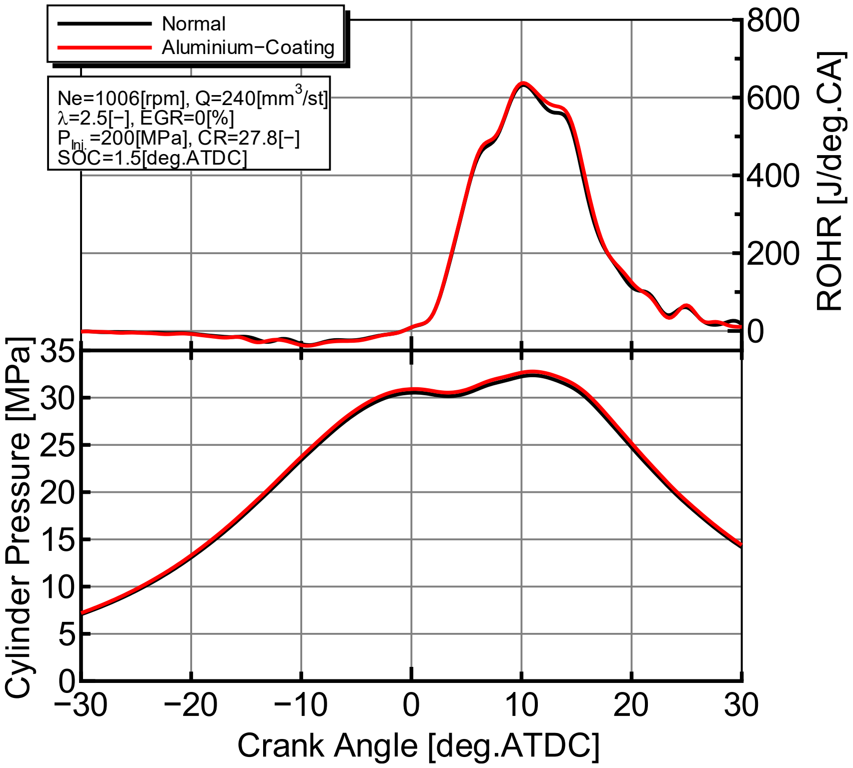

**Fig. 8.** Comparison of combustion characteristics between non-coat (Normal) piston and aluminum coating only on piston surface

Figure 8 compares the combustion characteristics between non-coat and aluminum coating only on the piston. As can be seen in around 12 deg. ATDC (around when the radiative intensity from luminous flame will be the highest), ROHR for aluminum coating was increased, which is supposed the reduced radiative heat loss. Furthermore, from the end of compression stroke, in-cylinder pressure was higher for aluminum coating piston, which is supposed the reduced heat convection with more homogeneous surface temperature distribution.

## 4. Another measure for homogenous surface temperature distribution

Conventional diesel combustion with a center mounted injector has an issue of the air utilization in the cylinder, especially in a higher compression ratio with larger bore size engines. On one hand, if the cavity diameter is reduced, dead volume is increased and cylinder circumference air could not be effectively utilized for the combustion, resulting in the cooler surface temperature of the wide squish area. On the other hand, if the cavity diameter is increased with significant shallow aspect ratio, most combustion is occurred close to cavity peripheral edge and mixing-controlled late combustion is generally retained there in the expansion stroke, resulting in the cooler surface temperature of the cavity center and the bottom of cavity. In both cases, surface temperature distribution (at least for a piston) could become to be heterogeneous, which is closely related to the spatial flame distribution and could be a major cause of heat loss. Although aluminum PVD coating could have a potential to reduce heterogeneity of surface temperature as discussed above, it is not enough for further heat loss reduction especially in lower load condition as shown in Figure 7. To solve it more aggressively, we must find different spatial diffusion flame distribution to occupy much areas in the cylinder for more homogeneous surface temperature distribution. However, only with the conventional injection nozzle and/or conventional cavity design, it could be difficult to control the flame distribution more uniformly in the combustion chamber.

### 4.1 Offset orifice nozzle design and flame observation

Ewphun et al. [11] intended to 'improve mixture formation and shorten spray penetration' by drilling the orifice tangential to the nozzle sac diameter with counter bore to keep the orifice length of the offset orifice nozzle as that of baseline nozzle. In this study, we also intend to improve mixture formation especially upstream the spray to achieve faster and much space consumed flame for homogeneous surface temperature distribution. In addition, asymmetrical spray growth was anticipated by the different orifice length to diameter ratio without counter bore machining. By selecting the orifice direction against the swirl, improved air entrainment into the spray could be possible. Table 4 compares the orifice design of the offset orifice nozzle with that of the radial orifice nozzle. Both nozzle flow rates are 2500 cc/min, about 40 % higher than the baseline nozzle listed in Table 1.

**Table 4**. Specification of utilized nozzle

| Item | Specification | |
|---|---|---|
| Flow rate | 2500cc/min | |
| Nozzle tip | Φ0.223 x 8 -156° | Φ0.268 x 8 -156° |
| Geometry<br>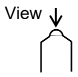<br> | High flow radial orifice | Offset orifice |
| | 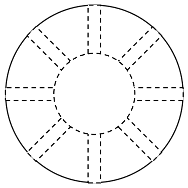 | 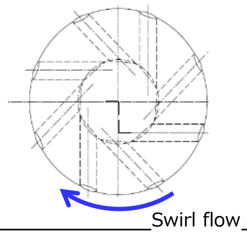<br> |

It is recognized in the preliminary test that flow coefficient of the offset orifice nozzle is significantly lower than radial orifice nozzle with the same orifice diameter. Therefore, the diameter of the offset orifice nozzle was designed to be the same flow rate as the radial orifice nozzle after the same treatment by the abrasive grinding.

As can be seen in the bottom-view combustion observation of Figure 9, anticipated spray asymmetry was not clearly observed, however, luminous flames extended upstream the spray with wider cone angle resulting in the much area occupied flame distribution, whilst no significant flame interference with adjoined sprays was observed. Even though the luminous flame approaches closer to the nozzle orifice, apparent heat release rate (AHRR) as shown in the upper graph in Figure 9 was significantly increased around 9 deg. ATDC resulting in the early disappearance of luminosity. That is, the upstream spray with the offset orifice nozzle was well diluted than that of the radial orifice nozzle even with the wider orifice diameter. This figure also suggested that the spray flame penetration of the offset orifice nozzle could be weaker than radial orifice nozzle, which is assumed by the flame images and apparent heat release rate from 2.0 to 4.0 deg. ATDC.

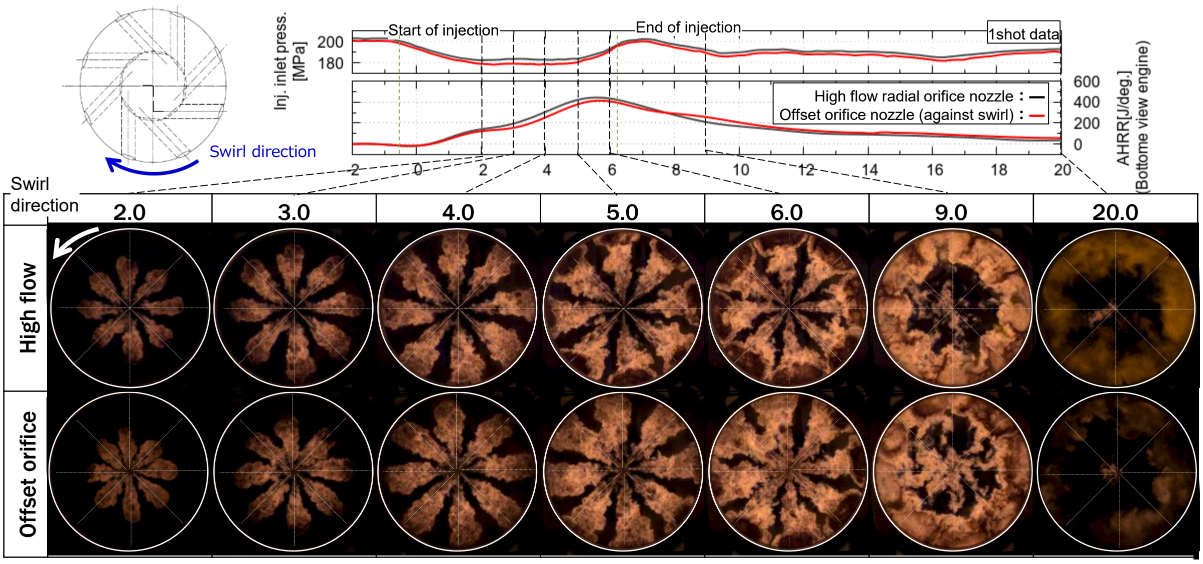
Swirl direction
Inj. inlet press. [MPa]
200
180
Start of injection
End of injection
1shot data
High flow radial orifice nozzle : —
Offset orifice nozzle (against swirl) : —
600
400
200
0
AHRR[J/deg.] (Bottome view engine)
-2
0
2
4
6
8
10
12
14
16
18
20
Swirl direction
2.0
3.0
4.0
5.0
6.0
9.0
20.0
High flow
Offset orifice

**Fig. 9.** Combustion visualization of offset orifice nozzle and high flow radial orifice nozzle

### 4.2 Metal engine performance of offset orifice nozzle

Since compression ratio of the bottom view engine is only 18:1 (limited up to medium load condition), the combustion characteristics' robustness of the offset orifice nozzle was examined by the metal engine with compression ratio of 27.8:1 (toroidal type cavity) under middle and high load conditions. As shown in Figure 10, ROHR was very similar with that of the upper diagram in Figure 9 (pancake cavity), suppressed initial heat release and enhanced late part of heat release with the offset orifice nozzle.

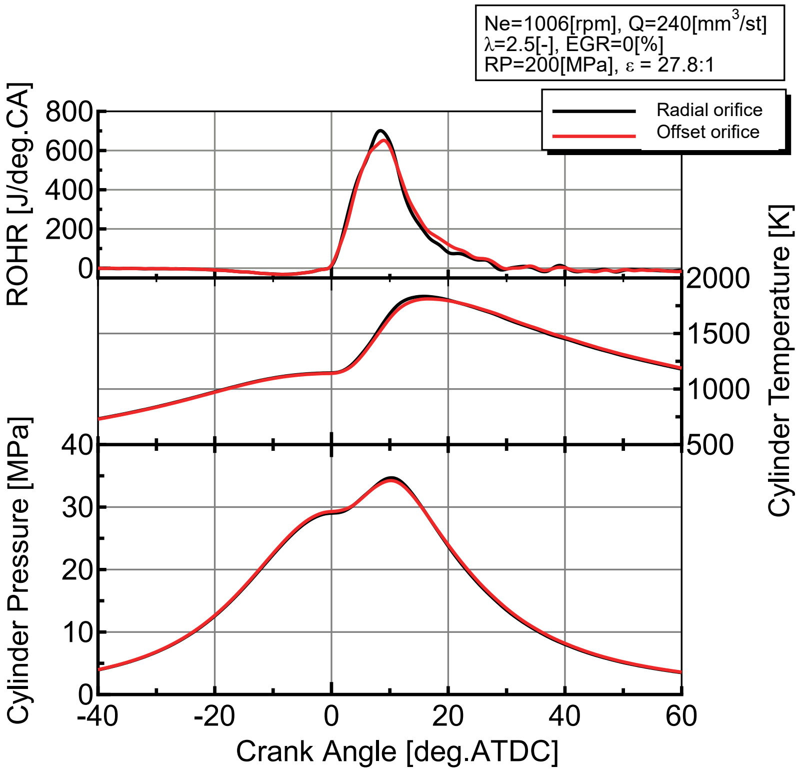

**Fig. 10.** Comparison of combustion characteristics between radial orifice nozzle and offset orifice nozzle @ high load condition

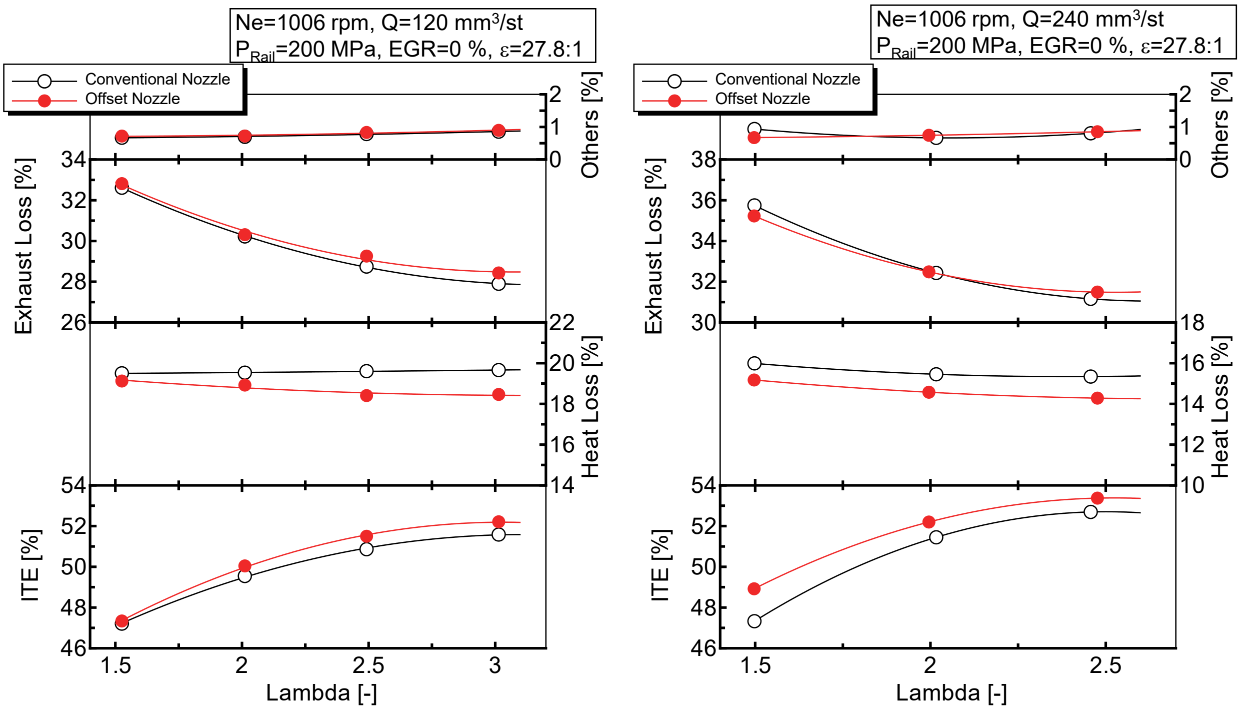

**Fig. 11.** Effect of offset orifice nozzle on energy balance for middle (left) and high (right) load conditions with 27.8:1 of compression ratio for various excess air ratio (Lambda)

It should be noted that the differences in energy balance under medium and high load conditions with the compression ratio of 27.8:1 were much more significant than the aluminum PVD coating as shown in Figure 11. Heat loss was significantly reduced in any cases, which could be a main cause of ITE improvement even though the degree of constant volume combustion was slightly reduced (which is confirmed with the change of ROHR profile). It corresponds with the optimum ROHR profile effect, which has been discussed in our study [18].

Although it has been still a hypothesis without any concrete temperature and/or heat flux measurement data, the cause of heat loss reduction by utilizing the offset orifice nozzle could correspond with that by the aluminum PVD coating. Namely, much homogeneity of the surface temperature distribution. The effect of the offset orifice nozzle has been also experimentally confirmed even with lower compression ratios and/or different cavity shapes, so far. We will measure the instantaneous and local surface temperature variation at several different points on the piston surface to confirm this hypothesis as the next study.

## Conclusions

For the further improvement in thermal efficiency of diesel engines, significant heat loss reduction should be essential under wide operating range, especially high load conditions. Many heat insulation coating techniques mainly on the piston surface have been studied aiming to increase surface temperature swing to reduce convective heat transfer, however, the reduction of heat loss was usually very limited or sometimes negative.

By means of the unsteady one-dimensional heat loss calculation, it is revealed that the instantaneous heat flux around TDC is rather increased with the application of high temperature swing (low thermal effusivity) materials. Therefore, we switched the focus on the utilization of radiative heat transfer not only on the piston but on the fire deck of the cylinder head to reduce heat loss. It is experimentally confirmed that aluminum PVD coating on both surfaces has the potential to improve heat loss and indicated thermal efficiency simultaneously. Furthermore, from the soot deposit observation, it is assumed that this coating also has a function to homogenize the surface temperature distribution. This assumption contradicts the wall temperature control concept which is widely acknowledged as the heat insulation measure with increased surface temperature swing.

As the other aspect of technique to much homogenize the surface temperature distribution, the offset orifice nozzle was proposed. From the spray flame observation, the offset orifice nozzle can achieve wider area consuming flame cluster with a little less penetration. It could result in more homogeneous surface temperature distribution. Experimental results by energy balance analysis confirmed significant decrease in heat loss and increase in ITE for a wider operating range as expected.

## Acknowledgment

The authors are grateful for the financial support offered by the NACE research consortium member companies. This study is also based on results obtained from a project commissioned by Ministry of Land, Infrastructure, Transport and Tourism (MLIT) in Japan.

## References

[1] Uchida N. A review of thermal barrier coatings for improvement in thermal efficiency of both gasoline and diesel reciprocating engines. *Int J Engine Res.* 23(1): 3-19. 2022. doi: 10.1177/1468087420978016.

[2] Uchida N, Watanabe K and Enya K. Achieving Higher Brake Thermal Efficiency under Existence of Peak Firing Pressure Constraint with a HD Diesel Engine. In: *THIESEL 2020 Conference on Ther-mo- and Fluid Dynamic Processes in Direct Injection Engines*. Virtual conference in Microsoft Teams. 8-11 September, 2020. 207-219. CMT-Motores Térmicos.

[3] Wakisaka Y, Inayoshi M, Fukui K et al. Reduction of heat loss and improvement of thermal efficiency by application of ''temperature swing'' insulation to direct-injection diesel engines. *SAE Int J Engines* 9(3): 1449–1459. 2016. doi:10.4271/2016-01-0661.

[4] Assanis D N and Badillo E. Transient heat conduction in low-heat-rejection engine combustion chambers. SAE Technical Paper 870156. 1987. doi:10.4271/870156.

[5] Andrie M, Kokjohn S, Paliwal S et al. Low Heat Capacitance Thermal Barrier Coatings for Internal Combustion Engines. SAE Technical Paper 2019-01-0228. 2019. doi:10.4271/2019-01-0228.

[6] Motwani R, Gandolfo J, Gainey B et al. Assessing the Impact of a Novel TBC Material on Heat Transfer in a Spark Ignition Engine through 3D CFD-FEA Co-Simulation Routine. SAE Technical Paper 2022-01-0402. 2022. doi:10.4271/2022-01-0402.

[7] Binder C, Abou Nada F, Richter M et al. Heat Loss Analysis of a Steel Piston and a YSZ Coated Piston in a Heavy-Duty Diesel Engine Using Phosphor Thermometry Measurements. *SAE Int J Engines* 10(4): 1954-1968. 2017. doi:10.4271/2017-01-1046.

[8] Koci C, Svensson K, Martin G et al. Optical Imaging for Understanding of Thermal Barrier Coated Piston Engine Performance. In: *12th Thermo-and Fluid Dynamic of Clean Propulsion Powertrains (THIESEL 2022)*. Valencia Spain. 13-16 September, 2022. 457-475. CMT-Motores Térmicos.

[9] Osada H, Watanabe N, Onozawa Y et al. Experimental Analysis of Heat-Loss with Different Piston Wall Surface Conditions in a Heavy-Duty Diesel Engine. In: *9th International Conference on Modeling and Diagnostics for Advanced Engine Systems (COMODIA 2017)*. Okayama Japan. 25-28 July, 2017. B204. JSME.

[10] Kawaharazuka F, Uchida N and Osada H. A Novel Piston Insulation Technique to Simultaneously Improve Both Heat Loss and Thermal Efficiency for Diesel Engines. *SAE Int J Adv & Curr Prac in Mobility* 3(5): 2173-2181. 2021. doi:10.4271/2021-01-0453.

[11] Ewphun P-P, Otake M, Nagasawa T et al. Combustion Characteristic of Offset Orifice Nozzle inder Multi Pulse Ultrahigh Pressure Injection and PCCI Combustion Conditions. *SAE Int J Adv & Curr Prac in Mobility* 2(2): 1002-1012. 2020. doi:10.4271/2019-32-0522.

[12] Enomoto Y, Ohya T, Ishii M et al. Study on Analysis of Instantaneous Heat Flux flowing into the Combustion Chamber Wall of an Internal Combustion Engine: Examination in the Case of Consideration of Heat Storage Term and the Temperature Dependency of the Thermocouple's Thermophysical Properties. *Trans JSME Series B* 57(539): 2421-2427. 1991. doi:10.1299/jsmeb1988.35.4_608.

[13] Woschni G, Spindler W, and Kolesa K. Heat insulation of combustion chamber walls – a measure to decrease the fuel consumption of I.C. Engines? SAE Technical Paper 870339. 1987. doi:10.4271/870339.

[14] Uchida N, Galpin J, Watanabe K et al. (Appendix 2 of) Numerical and Experimental Investigation into Brake Thermal Efficiency Optimum Heat Release Rate for a Diesel Engine. SAE Technical Paper 2019-24-0109. 2019. doi:10.4271/2019-24-0109.

[15] Heywood JB. Internal combustion engine fundamentals. 2nd ed. New York: McGraw-Hill. 2018. p.731.

[16] Kuboyama T, Kosaka H, Aizawa T et al. Measurement of convective and radiant heat flux ion DI diesel engines. In: *18th Internal Combustion Engine Symposium (International)*. Jeju Korea. 20–22 December, 2005. Paper No. JSAE 20056099.

[17] Nishiwaki K and Hafnan M. The determination of thermal properties of engine combustion chamber deposits. SAE Technical Paper 2000-01-1215. 2000. doi:10.4271/2000-01-1215.

[18] Uchida N and Watanabe K. Study on novel combustion technologies to achieve "High-heels" heat release rate profile in a higher-compression-ratio diesel engine. *In: 2023 JSAE/SAE Powertrains, Energy and Lubricants International Meeting*. Kyoto Japan. 29 August-1 September, 2023. SAE Technical Paper 2023-32-0077. 2023. doi:10.4271/2023-32-0077.

# Model-Based HVAC Control Unit using a MIL-Concept within BEV Thermal Management Co-Simulation

C. Frühwirth[1], E. Schutting[1], H. Eichlseder[1]

[1]Institute of Thermodynamics and Sustainable Propulsion Systems, Graz University of Technology, Austria.

E-mail: fruehwirth@ivt.tugraz.at

Telephone: +(43) 316 873 30037

**Abstract.** The control of the thermal management system has a key impact on efficiency and lifetime of battery electric vehicles (BEV). Within the BEV thermal management, the electrically powered heating, ventilation and air conditioning (HVAC) components represent the second largest electricity consumer after the electric powertrain. For investigations on an overall system level, a full vehicle co-simulation of a BEV is developed, combining 1D thermal management software KULI and MATLAB/Simulink. In vehicle cabin simulation, a model-in-the loop (MIL) approach is integrated for intelligent HVAC control to resolve the trade-off between efficiency and dynamics.

The KULI model accurately reproduces the entire air path of cabin air conditioning by modeling the fans and heat exchangers based on experimentally measured characteristic curves as well as by modeling the cabin by using a 3D CFD-supported 1D multi-zone cabin model. The overall HVAC system air path is then coupled with this 3D-CFD/1D cabin model based on the setup in a real vehicle. The HVAC system is controlled by applying a MIL concept, where MATLAB/Simulink models are implemented to control KULI HVAC components. This results in an advanced model-based control system concept with continuous exchange of actuator and sensor signals across the data exchange interfaces and enables a comprehensive investigation of the thermal state of the airflow in the HVAC air path.

HVAC controls implemented by OEMs and suppliers are generally based on empirical data and parameterized characteristic curves. In this co-simulation, thermodynamic correlations are developed from system analyses to provide in-depth expertise of the thermal behavior of cabin and air path components. The derived differential equations for thermal behavior mapping are then implemented in a model-based feedforward control system. Based on that, a comprehensive cascaded control of cabin air conditioning with multiple levels considering different target parameters is developed. The analytical models based on thermodynamic correlations enable a fast dynamic response, while feedback loops compensate disturbances and model uncertainties. This concept provides the maximum degrees of freedom in the simulation, enabling the optimal control of heating and cooling power regarding efficiency and dynamics to ensure thermal comfort.

## Formula Symbols

| | | |
|---|---|---|
| $A$ | $m^2$ | *Area* |
| $c_p$ | $J/(kg\ K)$ | *Specific heat capacity at* $p = const.$ |
| $C_D$ | - | *Drag coefficient* |
| $C_p$ | - | *Pressure coefficient* |
| $e$ | $(kW\ h)/(100\ km)$ | *Average electric energy consumption* |
| $E_{Batt}$ | $kW\ h$ | *Battery capacity* |
| $h$ | $J/kg$ | *Specific enthalpy* |
| $\dot{H}$ | $kW$ | *Enthalpy flow rate* |
| $I$ | $W/m^2$ | *Intensity of solar radiation* |
| $k$ | $W/(m^2\ K)$ | *Overall heat transition coefficient* |
| $m$ | $kg$ | *Mass* |
| $\dot{m}$ | $kg/s$ | *Mass flow rate* |
| $n$ | $min^{-1}$ | *Speed* |

| | | |
|---|---|---|
| $N$ | - | *Number of tube rows* |
| $Nu$ | - | *Nusselt number* |
| $p$ | *bar, Pa* | *Pressure* |
| $P$ | *kW* | *Power* |
| $\dot{Q}$ | *kW* | *Heat flow rate* |
| $r_0$ | *J/kg* | *Specific heat of evaporation of water at* $t = 0\,°C$ |
| $Re$ | - | *Reynolds number* |
| $t$ | *°C* | *Celsius temperature* |
| $T$ | *K* | *Thermodynamic temperature* |
| $U$ | *kJ* | *Internal energy* |
| $UA$ | $W/(m^2\,K)$ | *Overall heat transition coefficient* |
| $W$ | *kW/K* | *Heat capacity flow* |
| $x$ | *%* | *Energy consumption share* |
| $x$ | - | *Vapor quantity* |
| $x_{rec}$ | *%* | *Recirculation air ratio* |
| $\alpha$ | $W/(m^2\,K)$ | *Convective heat transfer coefficient* |
| $\alpha$ | ° | *Torsion angle* |
| $\zeta$ | - | *Pressure loss coefficient* |
| $\tau$ | *s* | *Time* |
| $\tau$ | - | *Transmission coefficient* |
| $\varphi$ | - | *Dimensionless flow coefficient* |
| $\varphi$ | *%* | *Relative humidity* |
| $\phi$ | - | *Heat exchanger operating characteristic* |
| $\Phi$ | *kW* | *Heat flow per person* |
| $\psi$ | - | *Dimensionless pressure coefficient* |
| $\Psi_p$ | - | *Number of passengers* |
| $\Omega$ | *kg/s* | *Water vapor emission per person* |

### Indices and Abbreviations

| | | | |
|---|---|---|---|
| *1D* | *One-dimensional* | *CP* | *Pressure coefficient* |
| *3D* | *Three-dimensional* | *d* | *Disturbance variable or signal* |
| *amb* | *Ambience* | *drive* | *Driving share* |
| *auxcon* | *Auxiliary consumers* | *duc* | *Air ducts* |
| *avg* | *Average value* | *D* | *Water vapor* |
| *A* | *Actuator* | *e* | *Control deviation, error signal* |
| *AC* | *Air conditioning* | *el* | *Electrical* |
| *AFLAP* | *Air-side flap* | *elec* | *Electrical* |
| *AHA* | *Air-side auxiliary heater* | *emot* | *Electric powertrain* |
| *ARES* | *Area resistance* | *evp* | *Evaporator* |
| *batt* | *Battery* | *E* | *End of driving cycle* |
| *BEV* | *Battery Electric Vehicle* | *ECU* | *Electronic control unit* |
| *BIR* | *Built-in resistance* | *EM* | *Electric motor* |
| *Body* | *Car body* | *EVP* | *Evaporator* |
| *cold* | *Cold air path* | *flap* | *Temperature mixing flap* |
| *const* | *Constant* | *f* | *Feedforward share* |
| *c* | *Control share* | *F* | *Cross-section; feedforward* |
| *condi* | *Conditioning share* | *FCEV* | *Fuel Cell Electric Vehicle* |
| *C* | *Controller* | *heatex* | *Heat exchanger* |
| *CAB* | *Vehicle cabin* | *hvac* | *Heating, Ventilation and Air Conditioning* |
| *CCR* | *Conduction, convection, radiation* | | |
| *CFD* | *Computational Fluid Dynamics* | *HE* | *Heat exchanger* |
| *CND* | *Condenser* | *HIL* | *Hardware-in-the-Loop* |
| *COP* | *Coefficient of Performance* | *HU* | *Heating unit* |

| | |
|---|---|
| *HVAC* | *Heating, Ventilation and Air Conditioning* |
| *i* | *Summation index* |
| *in* | *Transferred into the system* |
| *init* | *Initialization* |
| *I* | *Air inside cabin; inner media* |
| *ICEV* | *Internal Combustion Engine Vehicle* |
| *Int* | *Vehicle interior* |
| *loss* | *Thermal losses* |
| *ln* | *Logarithmic* |
| *L* | *Dry air* |
| *MAD* | *Mean absolute deviation* |
| *MIL* | *Model-in-the-Loop* |
| *NFAN* | *Variable speed fan* |
| *NTU* | *Number of Transfer Units* |
| *out* | *Transferred out of the system* |
| *O* | *Outer media; surface* |
| *OEM* | *Original Equipment Manufacturer* |
| *p* | *Parallel; passengers; peak* |
| *proj* | *Projecting* |
| *P* | *Passengers; process* |
| *PM* | *Point mass* |
| *rec* | *Recirculation* |
| *Resp* | *Respiration* |
| *RWD* | *Rear-wheel drive* |
| *s* | *Serial* |
| *sim* | *Simulation* |
| *stat* | *Static* |
| *steady* | *Steady-state* |
| *S* | *Solar* |
| *test* | *Testing procedure* |
| *total* | *Total or required value* |
| *TUB* | *Tube* |
| *u* | *Actuating variable or signal* |
| *veh* | *Vehicle* |
| *VTMS* | *Vehicle Thermal Management System* |
| *w* | *Target variable or signal* |
| *warm* | *Warm air path* |
| *WLTC* | *Worldwide Harmonized Light-duty vehicles Test Cycle* |
| *WLTP* | *Worldwide Harmonized Light-duty vehicles Test Procedure* |
| *y* | *Control variable, feedback signal* |
| *Z* | *Actual state variables or signals* |
| *(1+x)* | *Related to dry air* |

## 1. Introduction

In general, improvements in the development of battery electric vehicles are strongly associated with the optimization of the vehicle's thermal management system (VTMS). As the largest system auxiliary energy consumer in BEV, thermal management has a significant impact on achieving the contradictory objectives of dynamically conditioning vehicle components while minimizing energy consumption and maximizing driving range. Regarding cabin air conditioning, demand-based control of heating and cooling performance is particularly important in BEV due to the missing waste heat from the internal combustion engine. Optimizing complex thermal management architectures requires a holistic approach due to the numerous interfaces between cooling circuits and air paths. By using a combination of advanced simulation methods, it is possible to optimize multiple target parameters, such as dynamic conditioning and efficiency, for both overall vehicle and subsystem level investigations.

Research activities at the institute involve the development of a co-simulation environment to investigate the thermal management system of a state-of-the-art battery electric vehicle. This environment integrates comprehensive component-level modeling and simulation technologies in combination with an overall vehicle approach. The application of advanced cabin and battery simulation methodologies, together with highly sophisticated modeling techniques, are used to achieve this. The overall simulation architecture, including the model interfaces, has already been described in detail in [1]. In addition, the battery cooling system is described in depth in [1] with investigations on pack and single cell level including the extension by the use of a hardware-in-the loop (HIL) concept. The development of an innovative automatic HVAC (heating, ventilation and air conditioning) control system and its integration into the overall vehicle simulation are justified by the fact that the ongoing optimization of energy consumption and durability of BEV makes it necessary to consider the cabin air conditioning system in a very detailed manner. This is because the electrically operated components of the HVAC system account for the largest individual auxiliary consumer after the electric powertrain [2]. A precise understanding of the overall system and its control devices is required in order to accurately determine the power demands for dynamic and steady-state heating and cooling processes as well as to provide these through the components in the HVAC air path. By modeling the fans and heat exchangers based on experimental characteristics, as well as by representing the passenger compartment using a 3D CFD-supported 1D multi-zone model, the KULI simulation provides an accurate replication of the overall air path of the HVAC system. The combination of 3D CFD and 1D simulation has proven to accurately predict the thermal behavior of the vehicle cabin in [3]. Within the investigations in [3], the vehicle cabin was modeled only in interaction with the refrigerant circuit, with no consideration of the other HVAC system components. In contrast, this modeling and simulation methodology couples the complete air path of the cabin air conditioning system with the 3D CFD-assisted 1D cabin model utilizing the setup in a real vehicle. The control of the HVAC system is based on a model-in-the-loop (MIL) technique, with implementation of mathematical-physical MATLAB/Simulink models to control KULI HVAC air path components. The controller-plant coupling principle and its benefits have been described in [4], but the modeling of the controller and the plant has not been discussed in detail. This MIL-based co-simulation provides an advanced model-based control framework enabling a comprehensive analysis of the thermal state of the airstream in the HVAC air path. Automatic HVAC system control uses a multi-level cascaded control design which was developed on the basis of the work in [5]. As [5] also states, common HVAC controls developed by automotive OEMs and suppliers use empirical values and parameterized characteristics not available in the public domain. This co-simulation, however, provides thermodynamic equations derived from system analyses to gain extensive knowledge of the thermal behavior of the passenger compartment and HVAC components. In case of the vehicle cabin as a thermodynamic system, a linear coupled differential equation system is formed. Subsequently, these differential equations are integrated into a model-based feedforward control system. Previously, such a control system was applied in [6] for temperature control of a coolant conditioning system, however, only with a single control loop. In this research, a comprehensive multi-level cascaded control of an automotive cabin air conditioning system with different target parameters is designed. Within the overall co-simulation framework, this very precise HVAC modeling and simulation methodology allows the optimal control of the heating and cooling power, also considering potential heat exchange with other fluid circuits.

The present work is structured in such a way that, starting from the overall vehicle thermal management, the cabin air conditioning system is described with a detailed analysis of the vehicle cabin and the HVAC system components. The main focus is on the model-based automatic HVAC control using a MIL concept. The paper first introduces the thermal management system of the BEV under investigation. Here, the architecture of the integral thermal management system is shown. Subsequently, the system-level view is followed by a detailed component-level view of the vehicle's cabin air conditioning system. As the largest individual auxiliary consumer of electrical energy in the BEV, the HVAC system is discussed in an in-depth modeling and simulation perspective. The thermal modeling of cabin and HVAC components in KULI as well as the development of the model-based control system for automatic HVAC control in MATLAB/Simulink are explained in detail. Finally, the results of the full vehicle co-simulation are provided for a representative driving cycle. Results prove the functionality of the model-based HVAC control during a transient cooldown process, focusing on the control of the air duct outlet temperature via the heat flows in the heat exchanger and the electric resistance heater. The additional results address the energy consumption shares of the individual electrical energy consumers in the overall vehicle, as well as the impact of the ambient temperature on the average energy consumption and the average power demand of the HVAC components in the BEV.

## 2. Vehicle Thermal Management System Simulation

### 2.1. Vehicle under Investigation

In order to better illustrate the results described in the course of this research, a general overview of the vehicle investigated in this simulation is provided. The vehicle parameters are basically derived from the BEV Tesla Model 3 Long Range RWD of model year 2018. With respect to cabin air conditioning, this vehicle is equipped with an air-side controlled HVAC unit. The traction battery is made up of a total of 4416 cylindrical battery cells of type 21700. Parallel arrangement of the cells in so-called bricks (46p) and subsequent serial connection in the modules (two modules in 23s and two in 25s arrangement) result in the battery pack with the configuration 46p96s. Some data based on [1] are shown in **Table 1**.

**Table 1.** Excerpt of considered vehicle parameters, based on [1]

| Parameter | Symbol | Unit | Value |
|---|---|---|---|
| Curb weight | $m_{veh}$ | kg | 1726 |
| Drag coefficient | $C_D$ | - | 0.23 |
| Cross-sectional area | $A_F$ | m$^2$ | 2.22 |
| Motor power (peak) | $P_{EM,p}$ | kW | 239 |
| Battery capacity | $E_{Batt}$ | kW h | 75 |

### 2.2. Analyzed Thermal Management System Architecture

**Fig. 1** illustrates the design of the analyzed thermal management system. A dedicated coolant circuit is used for high-voltage battery conditioning. While an electric coolant heater enables rapid heat-up of the battery cells, a plate heat exchanger (chiller) transfers excess heat to the refrigerant circuit for cooling purposes. The electric motor is primarily cooled via an oil circuit; subsequently the dissipated heat of the motor is transferred to the dedicated motor coolant circuit via an oil-to-coolant heat exchanger. For the purpose of waste heat utilization, the heat losses from the electric powertrain can be transferred to the air flow in the HVAC unit via the water-to-air heat exchanger. Another method of recovering waste heat and thus increasing the energy efficiency of the entire vehicle is to couple the coolant circuits of the battery and motor via the 5/2-way valve. In the air-side controlled HVAC unit, the inflowing air from ambient and cabin recirculation is first dehumidified and/or cooled in the evaporator and then reheated to the desired air vent outlet temperature by controlling the temperature mixing flaps. Heat is dissipated at the vehicle front by the motor cooling circuit radiator as well as the refrigerant circuit condenser. [1]

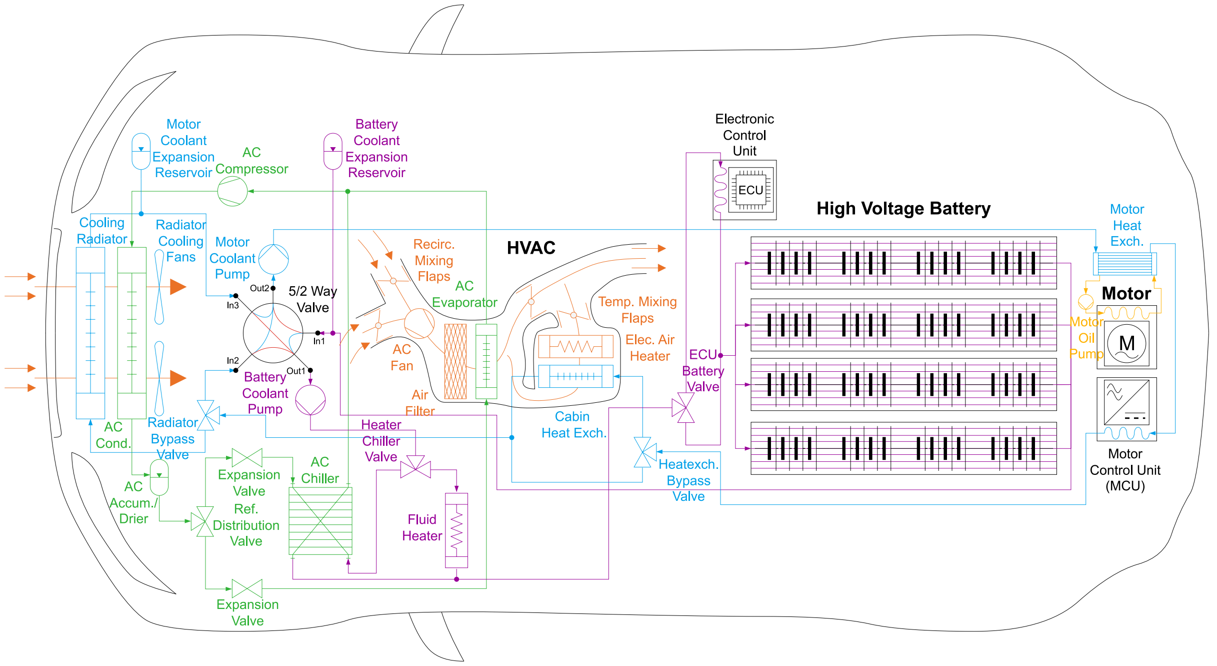
Motor Coolant Expansion Reservoir
AC Compressor
Battery Coolant Expansion Reservoir
Electronic Control Unit
ECU
High Voltage Battery
Motor Heat Exch.
Cooling Radiator
Radiator Cooling Fans
Motor Coolant Pump
Out2
In3
5/2 Way Valve
In1
In2
Out1
Recirc. Mixing Flaps
HVAC
AC Evaporator
Temp. Mixing Flaps
Elec. Air Heater
Motor
Motor Oil Pump
M
AC Fan
Air Filter
ECU
Battery Valve
Battery Coolant Pump
AC Cond.
Radiator Bypass Valve
Heater Chiller Valve
Cabin Heat Exch.
Heatexch. Bypass Valve
Motor Control Unit (MCU)
AC Accum./ Drier
Expansion Valve
AC Chiller
Ref. Distribution Valve
Fluid Heater
Expansion Valve

**Fig. 1.** Analyzed thermal management system architecture, based on [1]

## 3. Modeling and Simulation of the HVAC System

### 3.1. Transient Power Demands of Cabin Air Conditioning

The HVAC system is the largest auxiliary consumer of electrical energy in the battery electric vehicle, second only to the electric powertrain [2]. An automatic air conditioning control system must be designed and optimized with the objective to achieve a trade-off between energy efficiency and dynamics in order to ensure thermal comfort [5].

The energy efficiency of the entire vehicle can be increased by optimizing the interactions between the HVAC system and the refrigerant circuit and the coolant circuit of the electric motor and power electronics via the evaporator and the water-to-air heat exchanger.

How the dynamic heating and cooling power demands for the cabin are calculated and how these components are controlled on demand plays a decisive role in reducing the electrical energy consumption of HVAC components such as fans, the refrigerant compressor and electrical heating devices. This makes it necessary to accurately model the cabin and the HVAC air path.

## 3.2. Cabin Thermal Behavior and Modeling

### *3.2.1. Thermal Behavior*

The thermal state of the cabin is defined by the combined thermal impacts from the environment, the passengers and the air conditioning system. These impacts are illustrated in **Fig. 2**. The air conditioning system has to ensure and maintain thermal comfort through sufficient dynamic control, regardless of the environmental conditions, by balancing the effects of the other impacts mentioned [5].

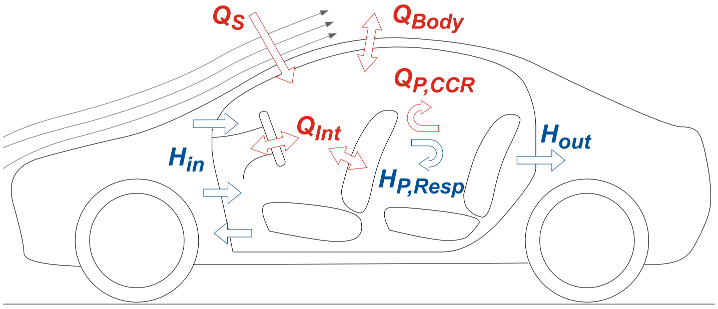

**Fig. 2.** Thermal impacts on the vehicle cabin

The heat and enthalpy flows entering and exiting the cabin must be considered in a cabin model to determine the thermal state of the cabin air volume and estimate the heating and cooling power demands on the air conditioning system. An energy balance in the form of the first law of thermodynamics provides the correlations, i.e., that the change in the internal energy of the cabin air over time $\frac{dU_I}{d\tau}$ is equal to the sum of the entering and exiting enthalpy flows $\sum(\dot{H}_{in} - \dot{H}_{out})$, heat flows exchanged with the car body $\dot{Q}_{Body}$, heat flows exchanged with the interior $\dot{Q}_{Int}$, heat flows entering due to solar radiation $\dot{Q}_S$, heat flows transferred from the passengers by conduction, convection and radiation $\dot{Q}_{P,CCR}$ and the enthalpy flows transferred from the passengers by respiration $\dot{H}_{P,Resp}$. According to [5], ensuring this balance results in the following equation.

$$\sum\ (\dot{H}_{in} - \dot{H}_{out}) + \dot{Q}_{Body} + \dot{Q}_{Int} + \dot{Q}_S + \dot{Q}_{P,CCR} + \dot{H}_{P,Resp} = \frac{dU_I}{d\tau} \tag{1}$$

### *3.2.2. Cabin Modeling*

In order to simulate the thermal behavior of the cabin resulting from these balanced heat and enthalpy flows, an extended multi-zone cabin model is used in the 1D thermal management simulation software KULI. This model integrates predefined vehicle-specific flow field data from the 3D CFD simulation, allowing the estimation of mass flows and diffusion in the vehicle cabin [3] [7]. This approach allows local effects in the cabin to be mapped with high accuracy due to the availability of 3D CFD data and the low amount of computation time required due to the 1D modeling.

The cabin of the considered vehicle was modeled in KULI as a three-row cabin using the multi-zone cabin model [3] [7]. **Fig. 3** shows the general parameters for this model in KULI. In order to consider the influence of the passengers on the cabin air via the terms $\dot{Q}_{P,CCR}$ and $\dot{H}_{P,Resp}$, parameters related to heat and water vapor emissions from humans as reported in [8] are included. Another factor is the proportion of recirculated air, which is relevant for determining the distribution of the entering and exiting enthalpy flows $\sum(\dot{H}_{in} - \dot{H}_{out})$. To calculate $\dot{Q}_S$, data on the intensity of solar radiation are needed. Furthermore, the geometric data for the cabin were estimated to discretize this space into a total of 36 sub-volumes, see **Fig. 4**. This number of sub-volumes results from a grid of 4 cells in x-direction, 3 cells in y-direction and 3 cells in z-direction. Using this grid, the heat propagation within the cabin is calculated, with the coefficients for convection and diffusion being derived from CFD calculations. In this way, temperature and humidity of each individual zone are determined. Detailed information about the interior boundary walls was implemented to calculate $\dot{Q}_{Body}$ and $\dot{Q}_{Int}$ and further specify $\dot{Q}_S$, as shown in **Fig. 5**. Bordering components include the doors, roof, floor, windows, seats and dashboard. Relevant parameters for these include geometric data for their multilayer structure, absorption and emission coefficients, and thermal parameters, such as thermal conductivities and heat capacities.

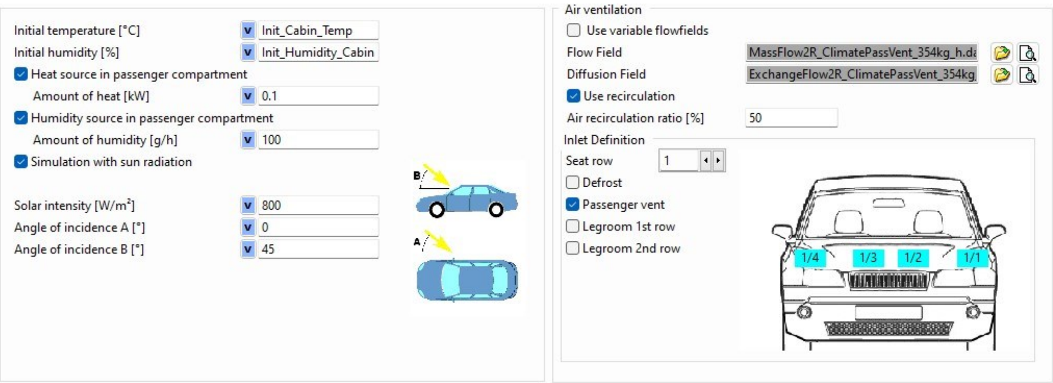

Initial temperature [°C] V Init_Cabin_Temp
Initial humidity [%] V Init_Humidity_Cabin
☑ Heat source in passenger compartment
Amount of heat [kW] V 0.1
☑ Humidity source in passenger compartment
Amount of humidity [g/h] V 100
☑ Simulation with sun radiation

Solar intensity [W/m²] V 800
Angle of incidence A [°] V 0
Angle of incidence B [°] V 45

Air ventilation
☐ Use variable flowfields
Flow Field MassFlow2R_ClimatePassVent_354kg_h.dí
Diffusion Field ExchangeFlow2R_ClimatePassVent_354kg
☑ Use recirculation
Air recirculation ratio [%] 50
Inlet Definition
Seat row 1
☐ Defrost
☑ Passenger vent
☐ Legroom 1st row
☐ Legroom 2nd row

**Fig. 3.** General parameters of the KULI extended cabin model (image extracted from KULI)

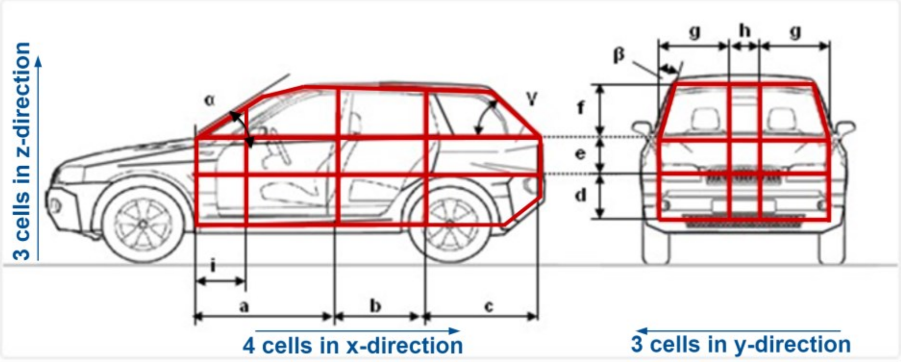

**Fig. 4.** Geometric properties of a multi-zone cabin (image extracted from KULI)

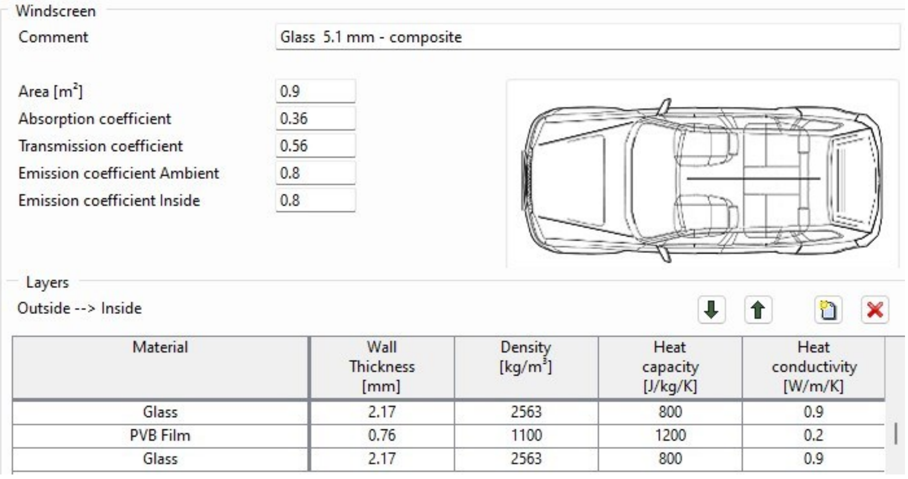

Windscreen
Comment Glass 5.1 mm - composite

Area [m²] 0.9
Absorption coefficient 0.36
Transmission coefficient 0.56
Emission coefficient Ambient 0.8
Emission coefficient Inside 0.8

Layers
Outside --> Inside

| Material | Wall Thickness [mm] | Density [kg/m³] | Heat capacity [J/kg/K] | Heat conductivity [W/m/K] |
|---|---|---|---|---|
| Glass | 2.17 | 2563 | 800 | 0.9 |
| PVB Film | 0.76 | 1100 | 1200 | 0.2 |
| Glass | 2.17 | 2563 | 800 | 0.9 |

**Fig. 5.** Wall properties of interior boundary walls (image extracted from KULI)

## 3.3. HVAC System Layout and Modeling

### *3.3.1. HVAC System Layout*

The main functions of the air conditioning system are to control the temperature and dehumidify the air mass flow as well as to distribute it within the vehicle cabin. A general distinction is made between the water-side and air-side controlled air conditioning systems. According to [9], air-side controlled systems are currently the most common. The schematic structure of such a system is shown in **Fig. 6**.

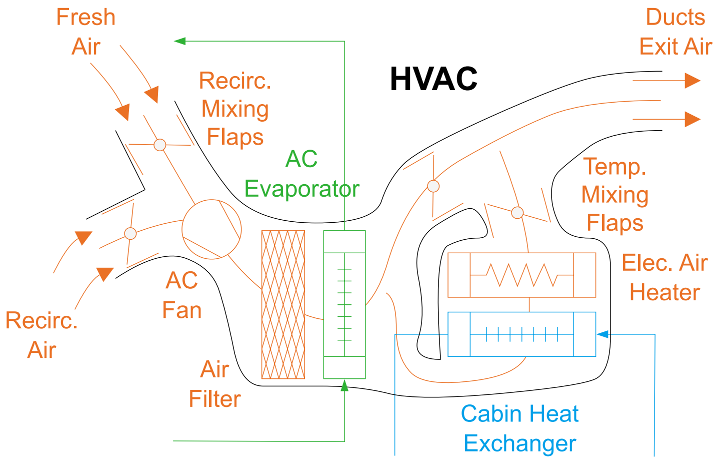
Fresh Air
Recirc. Mixing Flaps
HVAC
Ducts Exit Air
AC Evaporator
Temp. Mixing Flaps
Elec. Air Heater
AC Fan
Recirc. Air
Air Filter
Cabin Heat Exchanger

**Fig. 6.** Components of an air-side controlled air conditioning unit

First, fresh air and recirculated air from the cabin are diverted into the system and mixed by a fan, depending on the portion of recirculated air. In the evaporator, the air flow transfers heat to the refrigerant circuit to either cool or dehumidify it as required, whereby condensed water can be separated. Controlled refrigerant compressors adjust the evaporator exit temperature to cool the air on demand in an energy efficient way. The air flow is then divided to allow one part to pass through a bypass and the other part to pass through the heating devices. The ratio of these air flows can be adjusted by continuously controlling the temperature mixing flap(s). The air heating process in the warm path is basically performed by a water-to-air heat exchanger; i.e., the heat is transferred from the coolant flow of the motor conditioning circuit to the air stream. Here, the motor coolant mass flow through the heat exchanger is independent of the thermal properties of the air. Since the amount of heat dissipated from the powertrain in battery electric vehicles is significantly lower than that in internal combustion engine vehicles (ICEV), an electrical high-voltage heater is also integrated to improve the dynamics (e.g., at low ambient temperatures) [5] [9]. In general, this electrically provided heating power in the high-voltage heater should be minimized to optimize energy efficiency. Cold and warm air are then directed through the ducts so that the specific mixing action results in the desired (i.e., regarding the cabin climate) temperature layering between the foot area, air ducts and windows [5].

Different approaches can be taken to model and parameterize the individual components of the air-side controlled air conditioning unit in KULI. These approaches are described in more detail below. **Fig. 7** shows the overall modelling of the air path in the KULI fluid circuits window. The individual components are initially inserted as blocks and then parameterized via data files. **Fig. 8**, on the other hand, displays the visualization of the air path in the KULI air side window. Here, the components are first interconnected by the user via nodes and then illustrated three-dimensionally for a better overview.

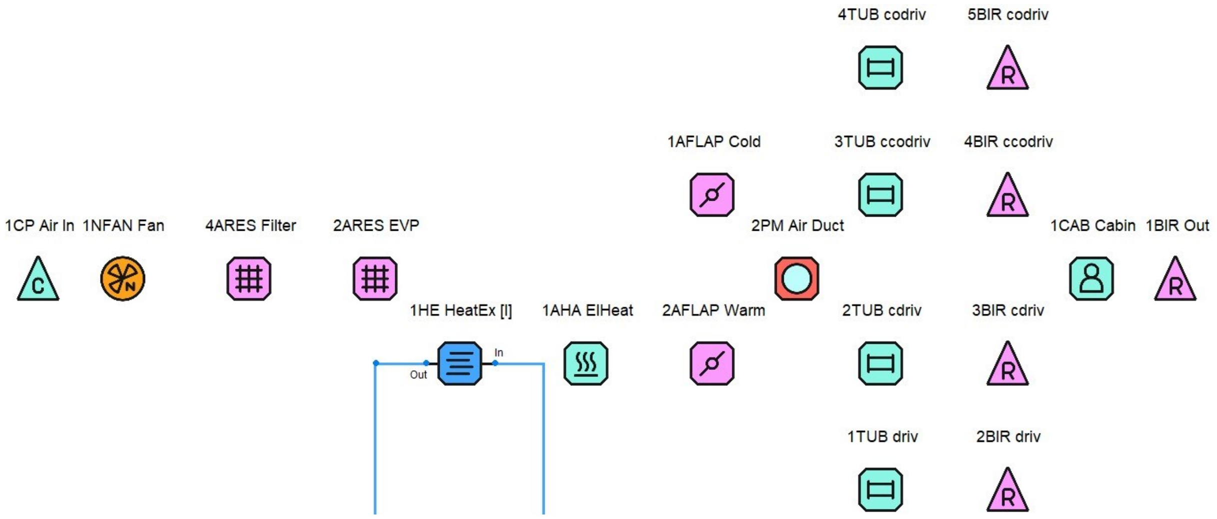
4TUB codriv
5BIR codriv
1AFLAP Cold
3TUB ccodriv
4BIR ccodriv
1CP Air In
1NFAN Fan
4ARES Filter
2ARES EVP
2PM Air Duct
1CAB Cabin
1BIR Out
1HE HeatEx [I]
1AHA ElHeat
2AFLAP Warm
2TUB cdriv
3BIR cdriv
In
Out
1TUB driv
2BIR driv

**Fig. 7.** HVAC air path of the air-side controlled air conditioning unit in the KULI fluid circuits window (image extracted from KULI)

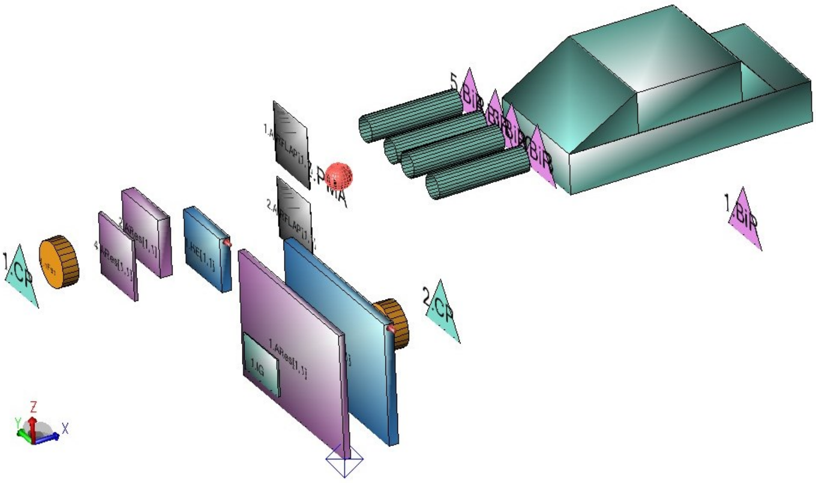

**Fig. 8.** HVAC air path and cooling air path in the KULI air-side window (image extracted from KULI)

### 3.3.2. *Air Inlet and Outlet*

The pressure loss of fresh air flowing into the water box is mapped by a Pressure coefficient block, while the pressure loss of exhaust air flowing out of the cabin is modeled with a Built-in Resistance block [3]. The blocks are labeled 1CP and 1BIR in **Fig. 7**. The Pressure coefficient block is parameterized with a constant dimensionless pressure coefficient $C_p$, for which reference values can be found in [10]. The pressure loss of the Built-in Resistance block is calculated using a quadratic function of the air flow.

### 3.3.3. *Fan*

Characteristic curves from experimental measurements are used to parameterize the variable speed fan [10]. These map the curves of pressure difference $\Delta p$ and electrical power consumption $P_{el}$ as a function of fan speed $n$ and air mass flow $\dot{m}$. Both parameters are further transformed into the dimensionless pressure coefficient $\psi$ and dimensionless flow coefficient $\varphi$ to extend the measured fan characteristics to other speeds and geometries [11]. The fan is represented in **Fig. 7** by the block 1NFAN.

### 3.3.4. *Water-to-Air Heat Exchanger*

The heat exchanger (1HE in **Fig. 7**) is designed as a cross-flow heat exchanger. For electric motor and power electronics conditioning, the coolant flow of the circuit flows through it on the inner side, and the air flow in the air conditioning unit represents the outer medium. The parameterization of the heat exchanger in KULI is basically done with experimentally determined characteristic curves, which are used to map the pressure losses $\Delta p$ of the inner and outer media as a function of the respective mass flow $\dot{m}_I$ or $\dot{m}_O$. Performance curves are also required to determine the exchanged heat flow $\dot{Q}$ between the inner and outer media as a function of the mass flows $\dot{m}_I$ and $\dot{m}_O$, as well as for a given entry temperature difference $ETD$ for the media. However, these curves are only valid for the measured configuration, which has a certain heat exchanger area and certain media inlet temperatures. In order to extend the performance curves to other conditions, the dimensioned curves with $\dot{Q} = f(\dot{m}_I, \dot{m}_O)$ are converted to dimensionless curves with $Nu = f(Re_I, Re_O)$. Subsequently, the operating-characteristic NTU method according to [3], [10] and [12] is used in KULI, where the exchanged heat flow can also be calculated for conditions deviating from the measurement conditions by assuming the following relationship:

$$\dot{Q} = min(W_I, W_O) \cdot ETD \cdot \phi \tag{2}$$

Here, $W_I = \dot{m}_I c_{p,I}$ and $W_O = \dot{m}_O c_{p,O}$ are the heat capacity flows, and $ETD = (T_{I,in} - T_{O,in})$ is the entry temperature difference between coolant and air. The operating characteristic $\phi = f(UA, W_I, W_O, A_O, N)$ is a dimensionless quantity to describe the efficiency of the heat exchanger. It depends on the overall heat transition coefficient $UA$, the heat exchanger surface area $A_O$, and the number of tube rows $N$. A maximum value of 1 is achieved, if the temperatures of outflowing air and inflowing coolant are equal.

To calculate the exchanged heat flow at the current operating point, the Nusselt number $Nu = f(Re_I, Re_O)$ with $Re_I, Re_O = f(\dot{m}_I, T_{I,in}, \dot{m}_O, T_{O,in})$ is first derived from the dimensionless map. Once $Nu$ is known, the heat transfer coefficient $UA$ can be defined, allowing the calculation of the operating characteristic $\phi$ as described. $\dot{Q}$ can then be determined from Equation (2).

### 3.3.5. Evaporator

In general, the refrigerant circuit in KULI can be modeled using a dedicated component library in the KULI HVAC extension. In order to calculate the mass flow as well as the thermal conditions within the closed refrigerant circuit consisting of evaporator, plate heat exchanger, compressor, condenser and expansion valve, equilibrium conditions must be continuously satisfied, and usually for the enthalpy and pressure of the refrigerant [7]. This balancing is an iterative process that requires a significant computational effort. In order to reduce the computation time while further optimizing the co-simulation, the refrigerant circuit in this simulation is implemented as a physical substitute model, where the evaporator, chiller and condenser are considered as idealized heat sources and sinks. For this purpose, area resistances from the KULI library are used, supplied with external heat loads from calculations in physical models. The pressure loss $\Delta p$ due to the flow through the evaporator (component 2ARES in **Fig. 7**) is illustrated in a characteristic diagram from [11] as a function of the air mass flow $\dot{m}$.

### 3.3.6. Mixing Flaps

The temperature mixing flaps are modeled in KULI as two separate air flap components, see blocks 1AFLAP and 2AFLAP in **Fig. 7** as well as scheme in **Fig. 9 (a)**. In the real air conditioning unit, the mass flow distribution can be changed by adjusting the angle of one mixing flap, see **Fig. 9 (b)**. The pressure loss $\Delta p$ that occurs as air flows over the KULI air flaps in the cold and warm air path is parameterized by a characteristic curve that shows the relationship between the respective pressure loss coefficient $\zeta$ and the torsion angle $\alpha$ of the real HVAC unit flap to the mean axis [10]. The explicit correlations of $\zeta_{flap,cold}, \zeta_{flap,warm} = f(\alpha_{flap})$ in simulation are estimated. The angle is adjustable in a range of $-30\,° \leq \alpha \leq 10\,°$ whereby $-30\,°$ means the maximum considered rotation into the cold path, while $10\,°$ means the maximum considered rotation into the warm path.

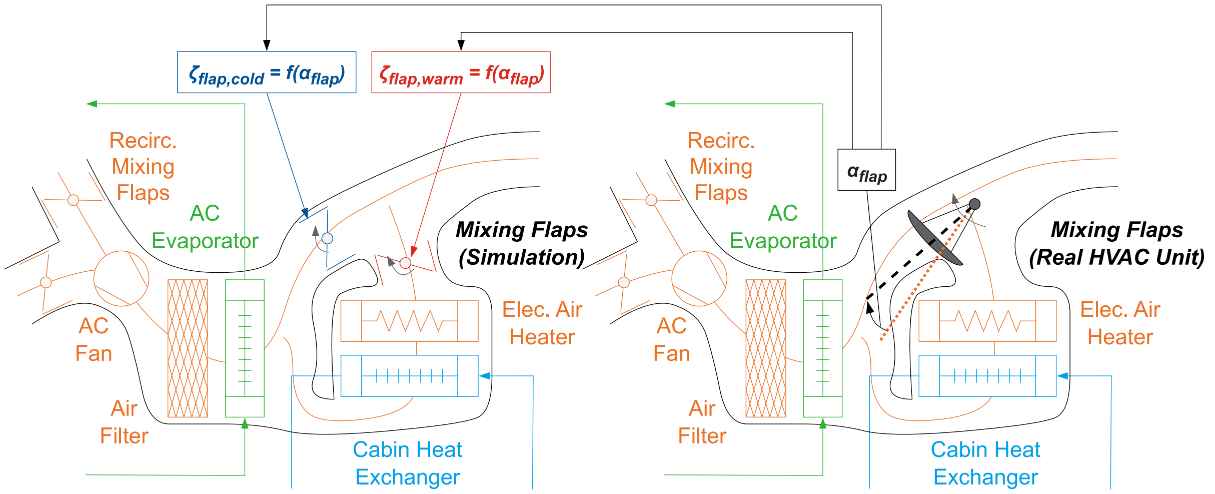

(a) (b)

**Fig. 9.** Temperature mixing flap(s) in simulation (a) and in real HVAC unit (b)

### 3.3.7. Air Ducts

The ducts represent the sections in the HVAC air path, where the air flows from the heating devices to the vehicle cabin. The pressure losses are modelled in KULI with tube components (1TUB, 2TUB, 3TUB and 4TUB in **Fig. 7**), where the pressure losses $\Delta p$ are based on pressure loss coefficients $\zeta$ [10]. In addition, a point mass component (see 2PM in **Fig. 7**) with a representative amount of thermal inertia is integrated into KULI, which determines the convective heat transfer $\dot{Q}$ between the air flow and the ducts according to [13]:

$$\dot{Q} = \alpha A \Delta T_{ln} \tag{3}$$

Here, $\alpha$ is the mean heat transfer coefficient, which is assumed to be approximately constant, while $A$ represents the area of heat transfer. The term $\Delta T_{ln}$ is the logarithmic temperature difference, which considers the inlet and outlet temperatures of the fluid as well as the surface temperature of the duct wall. [13]

## 3.4. Model-based Control of the HVAC System using MIL-Simulation

### *3.4.1. Model-in-the-Loop Concept*

The air conditioning control tasks are performed with the overall objectives of ensuring passenger comfort and safety while simultaneously increasing the system efficiency of the entire vehicle. These specific control tasks require the measurement of actual state variables, such as temperature and relative humidity, at various points in the air conditioning path. These tasks also include the adaption of actuators such as mixing flaps, as well as the demand-based adjustment of heating and cooling powers in heating devices and in the refrigerant evaporator. [5]

The basic structure of a control loop consists of a control unit and a control process [14]. In the specific case of cabin air conditioning, the control process refers to components such as the cabin itself, as well as mixing flaps and heating and cooling devices. Based on sensor values $d$, the control unit specifies the actuating variable $u$ to achieve the control objective, namely to ensure minimum deviation between control variable $y$ and target variable $w$. The specific values or trajectories of the target variable are derived from the control strategies.

In the context of this co-simulation, a model-in-the-loop (MIL) concept as described in [4] is implemented for the control loops of the cabin air conditioning. The principle is shown schematically in **Fig. 10**. Here, the KULI HVAC air path components represent the control process, while models in MATLAB/Simulink represent the control unit. The individual KULI components along the air path in the HVAC system send actual sensor signals via the interface to MATLAB/Simulink. MATLAB/Simulink is then used to calculate the actuator signals on the basis of the measured variables and implemented control strategies. These actuator signals are transferred to KULI simultaneously.

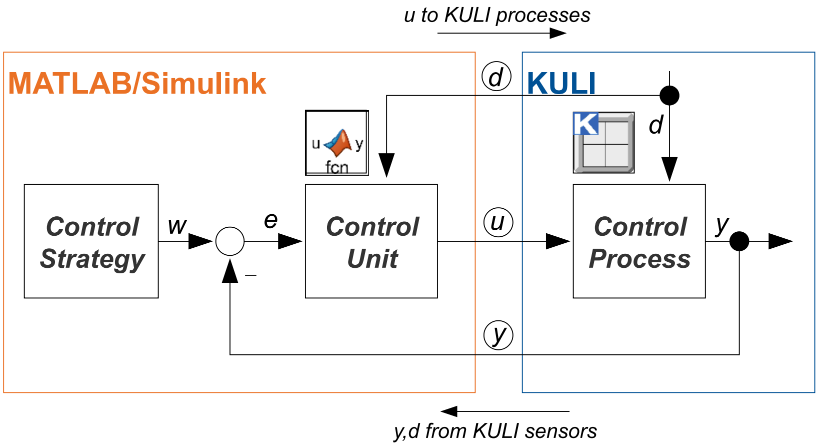

**Fig. 10.** General principle of the model-in-the-loop (MIL) concept in co-simulation

### *3.4.2. Setup of Automatic HVAC Control*

The automatic air conditioning control is set up as a cascaded multi-level control system. That means that multiple control levels are interleaved with each other. This approach is taken generally based on recommendations in [5], although some adaptations have been made.

The control system is shown in **Fig. 11**. It contains a superordinate operating point level, where the trajectory of the target cabin air temperature $T_{I,w}(\tau)$ is implemented as a function of the ambient temperature $T_{amb}$ and time $\tau$. A subordinate regulatory level is used to determine the exit air temperature $T_{duc,out,w}$ from the ducts, which is required to achieve the target cabin air temperature.

Specific control tasks are performed in the heating devices of the air conditioning unit by adjusting the angular position of the (virtual) temperature mixing flap $\alpha_{flap,u}$ to adapt the pressure loss coefficients $\zeta_{cold,u}$ and $\zeta_{warm,u}$. This further enables the regulation of the exchanged heat flow in the water-to-air heat exchanger $\dot{Q}_{heatex,u}$ by changing the mass flow distribution. In addition, the electrical heating power $P_{elec,u}$ is adapted as required.

At the operating point level, the course of the target evaporator exit air temperature $T_{evp,out,w}(\tau)$ is also specified. This temperature is controlled by adapting the dissipated heat flow $\dot{Q}_{evp,u}$ in the evaporator.

The continuous measurement or estimation, for example, of the temperatures $T_{i,d}$, pressures $p_{i,d}$, mass flows $\dot{m}_{i,d}$ and relative humidity values $\varphi_{i,d}$ in the cabin, as well as in individual sections in the HVAC air path, provides the required actual state variables, which also have to be taken into account during the calculation process. These are collectively referred to as $Z_{i,d} = \{T_{i,d}, p_{i,d}, \dot{m}_{i,d}, \varphi_{i,d}, \ldots\}$.

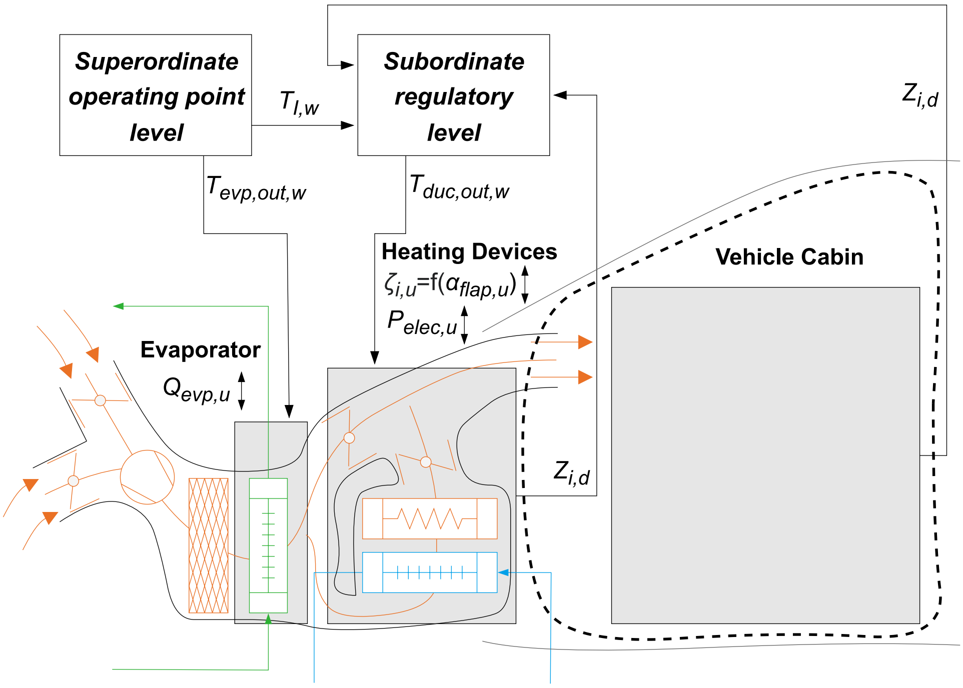

**Fig. 11.** Automatic air conditioning control with operating point level and regulatory level, enabling the adjustment of evaporator and heating devices

This results in the following correlations within the levels of cascaded control of the HVAC system:

Operating point: $$(T_{I,w}, T_{evp,out,w}) = f(T_{amb}, \tau) \tag{4}$$

Regulatory level: $$T_{duc,out,w} = f(T_{I,w}, Z_{i,d}) \tag{5}$$

Heating devices: $$(\alpha_{flap,u}, P_{elec,u}) = f(T_{duc,out,w}, Z_{i,d}) \tag{6}$$

$$\zeta_{cold,u}, \zeta_{warm,u} = f(\alpha_{flap,u}) \tag{7}$$

Evaporator: $$\dot{Q}_{evp,u} = f(T_{evp,out,w}, Z_{i,d}) \tag{8}$$

### *3.4.3. Model-based Feedforward and Feedback Control Design*

Based on the principles of automatic HVAC control, the design of the implemented control concept is now explained in more detail.

The control concept in co-simulation is generally based on a combination of closed-loop feedback control and model-based feedforward control. Feedforward control makes sense because it enables highly dynamic control features when adjusting the control of the system, as changes in the target variable directly impact the determination of the actuating variable [6]. By superimposing the feedforward control and a feedback control loop, the compensation of disturbances and model uncertainties can be ensured, thus minimizing control deviations [14].

The integration of feedforward in HVAC control systems is generally an established method. However, these feedforward controls are usually based on empirical values and characteristic maps, which are kept secret by OEMs [5]. Therefore, in this simulation, a model-based feedforward control was developed using mathematical models based on thermodynamic correlations.

A signal flow diagram of the control principle with model-based feedforward as well as a visualization of the distribution between MATLAB/Simulink and KULI are shown in **Fig. 12**. In the co-simulation, this structure represents the basis for control at the regulatory level, as well as at the level of the heating devices and the evaporator, according to Equations (5), (6), (7) and (8). When the cascaded control is applied, the individual signal flow diagrams for these levels are also interleaved.

In the control unit in MATLAB/Simulink, the trajectory of the target variable $w$ from the control levels is first specified. This serves as the input variable in the feedforward block $F$. The model-based feedforward represents an inverse model of the static control process $P_{stat}^{-1} = F$. For this purpose, the control process – which in this case can represent the evaporator, the cabin, or the heating devices – is analyzed by using thermodynamic equations. These include the first law of thermodynamics as well as mass balances and other correlations. The resulting system of equations is then used to calculate the feedforward control share of the actuating variable $u_F$ as a function of the target variable $w$ and the actual state variables $Z_{i,d}$. These values $Z_{i,d}$ are mainly obtained from the KULI HVAC air path via the co-simulation interface and partly estimated directly in the feedforward. A controller $C$ is superimposed on the feedforward block, which calculates a feedback control share $u_C$ based on the control deviation $e = w - y$. The sum of these values from the feedforward control and feedback control $u_{FC} = u_F + u_C$ is transferred to the control process actuator as the ideal actuating variable. The inertia behavior of the actuator $A$ is also modelled in MATLAB/Simulink, and the signal flow diagram shows an example of a $PT_2T_t$-element. This is required since the actuators in KULI have no inertia. The real actuating variable as output of the actuator $u$ is sent as an input variable to the static process $P_{stat}$, which represents the controlled component in the KULI HVAC air path. The actual control variable $y$ from the dynamic process $P$ in KULI is simultaneously fed back into MATLAB/Simulink through the co-simulation interface.

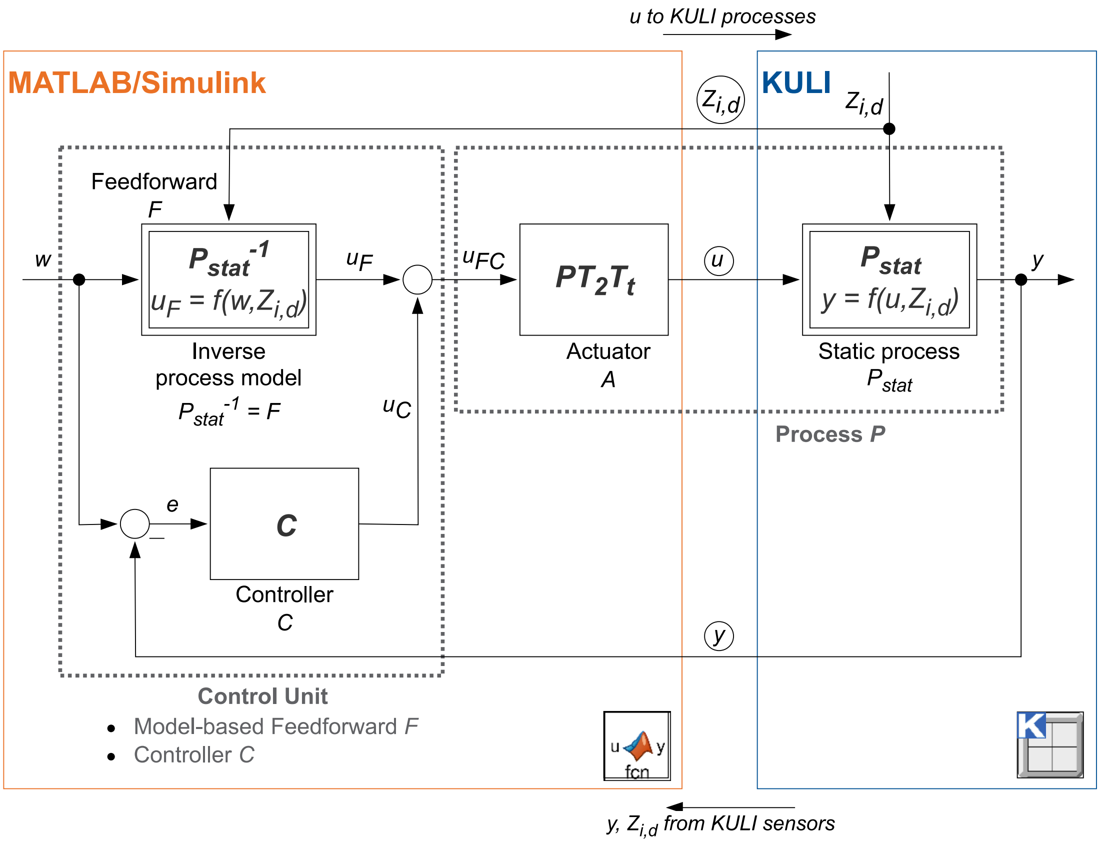

**Fig. 12.** Signal flow diagram of the control principle with model-based feedforward and feedback

### 3.4.4. *Overall HVAC System Control Design*

**Fig. 13** illustrates the signal flow diagram of the entire model-based control system for vehicle cabin air conditioning. This results from the application of the basic control principle in **Fig. 12** to the individual levels of the cascaded automatic HVAC control in **Fig. 11**.

The air target temperatures at the evaporator outlet and inside the cabin are each defined by the superordinate operating point level according to $(T_{I,w}, T_{evp,out,w}) = f(T_{amb}, \tau)$. In the upper section of the diagram, the refrigerant evaporator control is indicated by the relationship $\dot{Q}_{evp,u} = f(T_{evp,out,w}, Z_{i,d})$. The lower section of the diagram shows the subordinate regulatory level for the determination of the required air duct outlet temperature $T_{duc,out,w} = f(T_{I,w}, Z_{i,d})$ as well as the connected heating devices. Here, the position of the temperature mixing flap and the electrically supplied heating power $(\alpha_{flap,u}, P_{elec,u}) = f(T_{duc,out,w}, Z_{i,d})$ are determined.

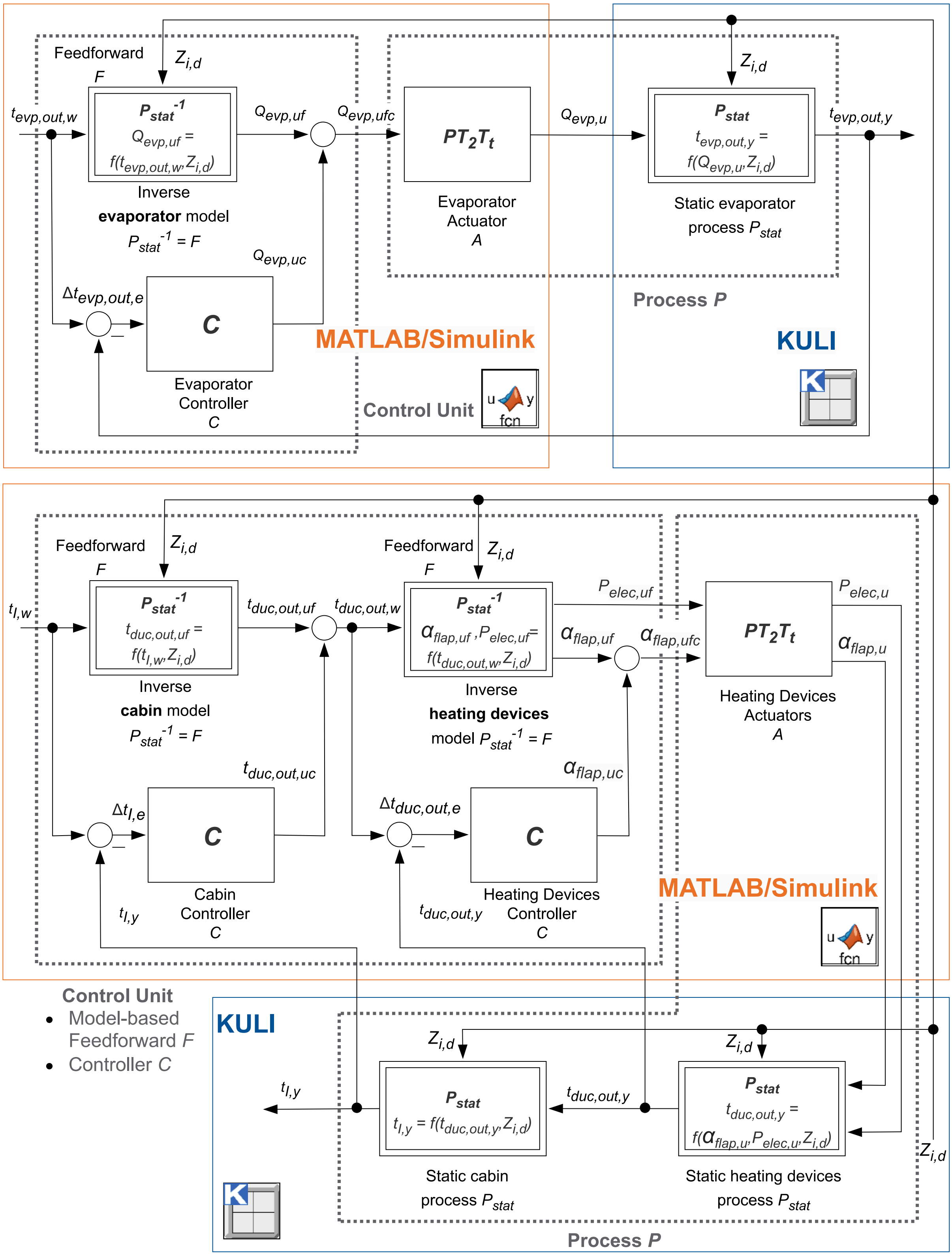
Feedforward F
$Z_{i,d}$
$t_{evp,out,w}$
$P_{stat}^{-1}$
$Q_{evp,uf} = f(t_{evp,out,w}, Z_{i,d})$
Inverse evaporator model
$P_{stat}^{-1} = F$
$Q_{evp,uf}$
$Q_{evp,ufc}$
$Q_{evp,uc}$
$\Delta t_{evp,out,e}$
C
Evaporator Controller C
$PT_2T_t$
Evaporator Actuator A
$Q_{evp,u}$
$P_{stat}$
$t_{evp,out,y} = f(Q_{evp,u}, Z_{i,d})$
Static evaporator process $P_{stat}$
$t_{evp,out,y}$
Process P
MATLAB/Simulink
KULI
Control Unit
u y fcn
Feedforward F
$Z_{i,d}$
$t_{I,w}$
$P_{stat}^{-1}$
$t_{duc,out,uf} = f(t_{I,w}, Z_{i,d})$
Inverse cabin model
$P_{stat}^{-1} = F$
$t_{duc,out,uf}$
$t_{duc,out,w}$
$t_{duc,out,uc}$
$\Delta t_{I,e}$
C
Cabin Controller C
$t_{I,y}$
Feedforward F
$Z_{i,d}$
$P_{stat}^{-1}$
$\alpha_{flap,uf}, P_{elec,uf} = f(t_{duc,out,w}, Z_{i,d})$
Inverse heating devices model $P_{stat}^{-1} = F$
$P_{elec,uf}$
$\alpha_{flap,uf}$
$\alpha_{flap,ufc}$
$\alpha_{flap,uc}$
$\Delta t_{duc,out,e}$
C
Heating Devices Controller C
$t_{duc,out,y}$
$PT_2T_t$
Heating Devices Actuators A
$P_{elec,u}$
$\alpha_{flap,u}$
MATLAB/Simulink
u y fcn
Control Unit
Model-based Feedforward F
Controller C
KULI
$Z_{i,d}$
$t_{I,y}$
$P_{stat}$
$t_{I,y} = f(t_{duc,out,y}, Z_{i,d})$
Static cabin process $P_{stat}$
$t_{duc,out,y}$
$Z_{i,d}$
$P_{stat}$
$t_{duc,out,y} = f(\alpha_{flap,u}, P_{elec,u}, Z_{i,d})$
Static heating devices process $P_{stat}$
$Z_{i,d}$
Process P

**Fig. 13.** Signal flow diagram of the overall HVAC system control design

### 3.4.5. *Control of Cabin Air Temperature on Subordinate Regulatory Level*

To better illustrate the concept from **Fig. 12** and **Fig. 13**, the described approach taken by using the model-based feedforward control will now be related to a concrete example that shows how to determine the target duct exit air temperature $T_{duc,out,w}$ at the regulatory level. For this purpose, the vehicle cabin is investigated thermodynamically, and a differential equation system is set up to describe the thermal behavior based on recommendations in [15]. This results in the inverse cabin model, see **Fig. 13** and **Fig. 14**. In the following equations, temperatures are treated in the degree Celsius scale; therefore, these are written as $t$ in the corresponding equations.

The thermal state in the vehicle cabin was already examined in Equation (1) using the energy balance in the form of the first law of thermodynamics. Here, the air volume within the cabin was defined as a system, and the heat and enthalpy flows supplied (i.e., entering) and dissipated (i.e., exiting) across the system boundaries were balanced. The thermal impacts of the air conditioning system on the cabin air occur in the form of an enthalpy flow that is introduced into the cabin via the air ducts. In order to obtain more detailed information about the correlation between the cabin air temperature $t_I$, actual state variables $Z_i$ in the HVAC air path, and duct exit air temperature $t_{duc,out}$, the individual terms in the energy balance from Equation (1) are formulated in more detail. This procedure is carried out to be able to implement correlations in the feedforward control model at the regulatory level in MATLAB/Simulink.

The entering and exiting enthalpy flows $\sum(\dot{H}_{in} - \dot{H}_{out})$ are calculated by substituting the products of the dry air mass flows $\dot{m}_{i,L}$ and the specific enthalpies related to 1 kg of dry air $h_{i(1+x)}$. This substitution is based on the consideration of humid air as an ideal gas. The air flowing into the vehicle cabin via the ducts (index $duc$), the air flowing out of the cabin in the form of the recirculated air portion (index $rec$) and the exhaust air portion (index $out$) have to be considered:

$$\sum\ (\dot{H}_{in} - \dot{H}_{out}) = \dot{m}_{duc,L} h_{duc(1+x)} - \dot{m}_{rec,L} h_{rec(1+x)} - \dot{m}_{out,L} h_{out(1+x)} \tag{9}$$

The heat flow exchanged with the car body $\dot{Q}_{Body}$ is approximated by considering the overall heat transmitted from the cabin air via the car body and into the environment based on [11]. Transient heating and cooling processes of the car body itself are therefore neglected. The term $kA$ denotes the heat transfer coefficient of the body. For this term, a constant value is taken from the literature [11], resulting in the following relationship:

$$\dot{Q}_{Body} \cong -kA(t_I - t_{amb}) \tag{10}$$

The exchanged heat flow with the interior $\dot{Q}_{Int}$ is neglected in this modelling:

$$\dot{Q}_{Int} \cong 0 \tag{11}$$

The heat flow due to solar radiation $\dot{Q}_S$ is calculated as described in [11] from the products of the projecting areas of the glass panes $A_{proj,i}$, the intensity of the solar radiation $I$ and the transmission coefficients of the glass $\tau_i$. All of the glass panes with the indices $i$ are summed:

$$\dot{Q}_S = \sum_{i=1}^{n} \ (A_{proj,i} I \tau_i) \tag{12}$$

The heat flow of the passengers through conduction, convection and radiation $\dot{Q}_{P,CCR}$ and the enthalpy flow of the passengers through respiration $\dot{H}_{P,Resp}$ are approximated. Here, $\Psi_p$ represents the number of passengers, $\Phi_{CCR}$ denotes the heat flow by conduction, convection and radiation per person, and $\Phi_{Resp}$ characterizes the heat flow by respiration per person. For both quantities, reference values as a function of air temperature are documented in the literature [8]. Taking this approach gives the approximate relationship:

$$\dot{Q}_{P,CCR} + \dot{H}_{P,Resp} \cong \Psi_p(\Phi_{CCR} + \Phi_{Resp}) \tag{13}$$

Assuming a constant pressure $p_I = const.$ and constant volume $V_I = const.$ of the air inside the cabin, the change in internal energy $dU_I$ is equal to the change in enthalpy $dH_I$. Consequently, the change in the internal energy of the air inside the cabin over time $\frac{dU_I}{d\tau}$ can be expressed by replacing the internal energy by the product of the mass of the dry air inside the cabin $m_{I,L}$ and the specific enthalpy of the air inside the cabin as related to 1 kg of dry air $h_{I(1+x)}$. This gives the following relationship:

$$\frac{dU_I}{d\tau} = \frac{d}{d\tau}(m_{I,L}h_{I(1+x)}) \tag{14}$$

The formulated Equations (9), (10), (11), (12), (13) and (14) for the individual terms in the energy balance of the cabin can now be substituted into Equation (1), resulting in the following detailed balance equation:

$$\begin{aligned} &\dot{m}_{duc,L}h_{duc(1+x)} - \dot{m}_{rec,L}h_{rec(1+x)} - \dot{m}_{out,L}h_{out(1+x)} - kA(t_I - t_{amb}) + \sum_{i=1}^{n} (A_{proj,i}I\tau_i) \\ &+ \Psi_p(\Phi_{CCR} + \Phi_{Resp}) = \frac{d}{d\tau}(m_{I,L}h_{I(1+x)}) \end{aligned} \tag{15}$$

In this balance equation, the entering and exiting enthalpy flows $\dot{m}_{i,L}h_{i(1+x)}$ with $i = \{duc, rec, out\}$ can be expressed as a function of the respective temperatures $t_i$ according to the laws applying to humid air as an ideal gas:

$$\dot{m}_{i,L}h_{i(1+x)} = \dot{m}_{i,L}[c_{pL}t_i + x_i(r_0 + c_{pD}t_i)] \tag{16}$$

Here, $c_{pL}$ and $c_{pD}$ denote the specific heat capacities of dry air and water vapor, respectively. The term $r_0$ is the heat of evaporation of water at a temperature of 0 °C, while $t_i$ represents the temperature of the air, and $x_i$ represents the vapor quantity.

Another equation that can be used for the feedforward model is obtained by calculating the specific enthalpy $h_{I(1+x)}$ in Equation (14) as a function of the temperature $t_I$, based on the considerations of humid air as an ideal gas. Furthermore, the product in the equation is derived by applying the rule of Leibniz:

$$\begin{aligned} \frac{d}{d\tau}(m_{I,L}h_{I(1+x)}) = m_{I,L}\, &[c_{pL}\frac{dt_I}{d\tau} + \frac{dx_I}{d\tau}(r_0 + c_{pD}t_I) + x_I c_{pD}\frac{dt_I}{d\tau}] \\ &+ \frac{dm_{I,L}}{d\tau}[c_{pL}t_I + x_I(r_0 + c_{pD}t_I)] \end{aligned} \tag{17}$$

Equation (17) shows that not only the air temperature inside the cabin $t_I(\tau)$ but also the vapor quantity $x_I(\tau)$ are of essential importance [15]. In order to describe the change in the vapor quantity inside the cabin over time $\frac{dx_I}{d\tau}$, the change in the water vapor mass inside the cabin over time $\frac{dm_{I,D}}{d\tau}$ is first written as:

$$\frac{dm_{I,D}}{d\tau} = \frac{d}{d\tau}(x_I m_{I,L}) = \frac{dx_I}{d\tau}m_{I,L} + \frac{dm_{I,L}}{d\tau}x_I \tag{18}$$

Using the mass balances for the dry air and for the water vapor inside the cabin, the temporal change in the vapor quantity $\frac{dx_I}{d\tau}$ can be determined. Regarding the mass balance of the water vapor, the entering and exiting mass flows of water vapor $\dot{m}_{i,D} = x_i\dot{m}_{i,L}$ with $i = \{duc, rec, out\}$ as well as the water vapor emission of the vehicle passengers $\Omega_{Resp}$ must be considered. $\Omega_{Resp}$ describes the water vapor emission per person and is documented in the literature [8] as a function of the air temperature. This results in the following balance equation:

$$\frac{dm_{I,D}}{d\tau} = \sum x_i\dot{m}_{i,L} + \Psi_p\Omega_{Resp} \tag{19}$$

The derived Equations (15), (16), (17), (18) and (19) together with further mass balances and the thermal equation of state for the considered humid air in the vehicle cabin form a coupled linear differential equation system. This fully describes the thermal behavior in the cabin.

This system of equations is now implemented as a feedforward inverse cabin process model (see **Fig. 14**) in MATLAB/Simulink and used to calculate the required duct exit air temperature $t_{duc,out,uf}$ on the regulatory level, and as a function of the target cabin air temperature curve $t_{I,w}$ from the operating point level. For this purpose, the measured cabin air temperature curve $t_{I,y}$ from the KULI extended cabin model as well as measured thermal state variables $Z_{i,d}$ from the KULI HVAC air path are also used in the calculation. The feedforward control value is then superimposed with the control share $t_{duc,out,uc}$ in order to minimize control differences. The resulting accumulated value $t_{duc,out,w} = t_{duc,out,u}$ is finally the input variable of the heating devices for calculating the temperature mixing flap position $\alpha_{flap,u}$ and the additional electrical heating power $P_{elec,u}$.

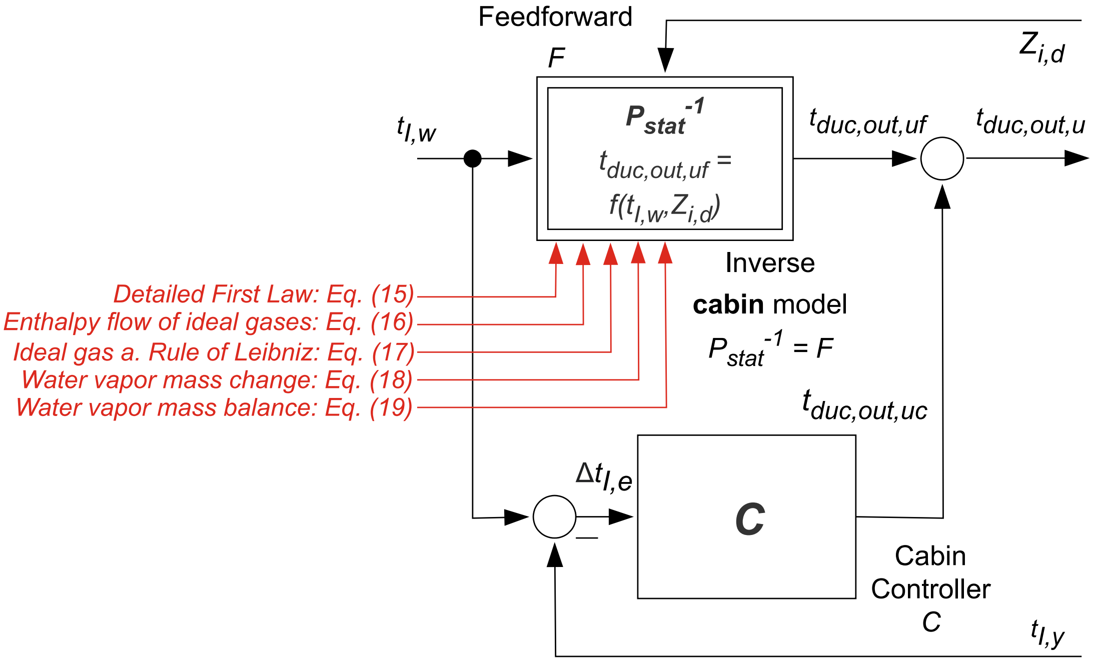
Feedforward
F
$Z_{i,d}$
$t_{I,w}$
$P_{stat}^{-1}$
$t_{duc,out,uf} = f(t_{I,w}, Z_{i,d})$
$t_{duc,out,uf}$
$t_{duc,out,u}$
Detailed First Law: Eq. (15)
Enthalpy flow of ideal gases: Eq. (16)
Ideal gas a. Rule of Leibniz: Eq. (17)
Water vapor mass change: Eq. (18)
Water vapor mass balance: Eq. (19)
Inverse
cabin model
$P_{stat}^{-1} = F$
$t_{duc,out,uc}$
$\Delta t_{I,e}$
—
C
Cabin
Controller
C
$t_{I,y}$

**Fig. 14.** Control structure on regulatory level and equation system of inverse cabin model

## 4. Simulation Results and Discussion

The following chapter describes selected co-simulation results using the model-based control of the HVAC system. These results represent stage 2 of the co-simulation; some of the results from the previous stage 1 were described in [1]. The overall vehicle simulation was performed with the WLTC Class 3 driving cycle. First, the operating conditions “Malaga” with an ambient temperature $t_{amb} = 35\ °C$, a relative humidity $\varphi_{amb} = 40\ \%$ and the solar radiation intensity $I = 500\ W/m^2$ are considered. Additional parameters relevant for cabin air conditioning are a fixed air recirculation rate $x_{rec} = 50\ \%$ and the number of vehicle passengers set to $\Psi_p = 2$. The ambient temperature also represents the initialization temperature for fluids and components in the vehicle such as the cabin, battery and electric motor, so that $t_{init} = t_{amb}$. This enables the determination of results for a dynamic cooldown process.

In this configuration, the HVAC system is discussed first, focusing on the quality of the cabin air temperature control and the composition of the required heating power in the heating devices. In addition, the average energy consumption of the examined vehicle during the simulation is depicted, as well as the distribution of the energy consumption shares among the individual auxiliary consumers.

Furthermore, the full vehicle simulation was also performed for other representative ambient conditions, again using the WLTC Class 3 driving cycle. This enables the determination of the average vehicle energy consumption and the average power demand of the HVAC system as a function of the ambient temperature. A comparison with data from various literature is also performed here in order to validate the results obtained.

### 4.1. Cabin Air Conditioning Control

### *4.1.1. Cabin Air and Duct Exit Temperature*

The target and actual profiles of the air temperature in the vehicle cabin are illustrated in **Fig. 15 (a)**. The target temperature curve $t_{I,w}$ is specified by the superordinate operating point level in MATLAB/Simulink. Starting from the initialization temperature $t_{init} = t_{amb} = 35\ °C$, a continuous adaptation to the steady-state target value of $t_{I,w,steady} \cong 23.5\ °C$ is performed. The actual course of the cabin air temperature $t_{I,y}$, which is determined by the KULI Extended Cabin Model, is shown overlaid. The comparison of the curves shows slight deviations during the first 100 seconds of the transient cooldown process. These can be explained by the start-up inertia of the HVAC components, especially the refrigerant evaporator and the water-to-air heat exchanger. In the signal flow diagrams of the MIL simulation, these are mapped with $PT_2T_t$ elements. [1]

During the continued transient cooldown for $100\,s \leq \tau \leq 600\,s$ as well as during the almost steady-state conditioning from $\tau > 600\,s$, the measured curve from KULI and the target curve of the cabin air temperature from MATLAB/Simulink are approximately equal. A very small mean absolute deviation $\Delta t_{I,MAD} = \frac{1}{\tau_E}\int_{\tau=0}^{\tau_E}|t_{I,y}(\tau) - t_{I,w}(\tau)|d\tau = 0.0935\,°C$ can be determined over the entire driving cycle.

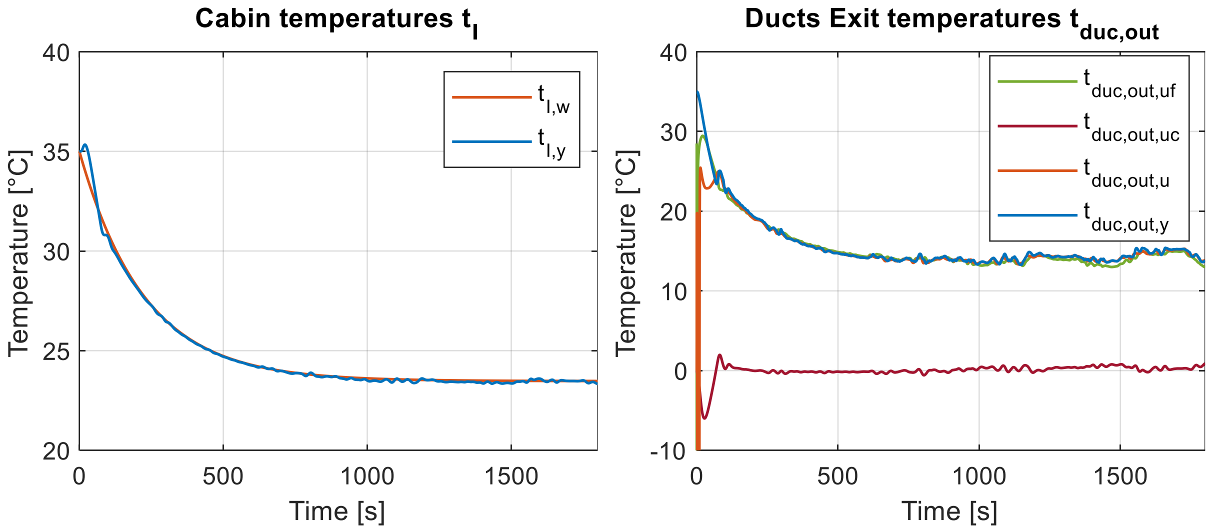

(a) (b)

**Fig. 15.** Cabin air temperature from control strategy and KULI model (a), Air duct exit temperature from model-based control and KULI model (b)

**Fig. 15 (b)** depicts the courses of the air duct outlet temperature. One curve is the proportion of the model-based feedforward control $t_{duc,out,uf}$. This is determined in the inverse process model of the cabin from the differential equation system consisting of Equations (15), (16), (17), (18) and (19) in order to achieve thermal comfort in the vehicle cabin with predefined dynamics. Another curve describes the control share $t_{duc,out,uc}$, which is superimposed with the feedforward control share in order to minimize control differences in the cabin air temperature. This results in the course of $t_{duc,out,u} = t_{duc,out,w}$, which is used to determine the required heating power of the heat exchanger and electric heater at the lower level of the heating devices. The course of the actual air duct outlet temperature in the KULI model $t_{duc,out,y}$ is also shown in comparison.

At the beginning of the simulation ($\tau < 50\,s$), there is a negative control difference $t_{I,w}(\tau) - t_{I,y}(\tau)$, indicating that the measured cabin air temperature in the KULI model is too high. As a result, the aggregated air duct outlet temperature curve $t_{duc,out,u}$ is reduced by a negative control share $t_{duc,out,uc}$ compared to the model-based feedforward control $t_{duc,out,uf}$. From a simulation time of $\tau > 50\,s$, the required control portion is very small. This leads to the conclusion that the inverse process model of the cabin allows the prediction of the required air duct outlet temperature $t_{duc,out}$ with high precision. That implies a good agreement between the implemented process model in MATLAB/Simulink and the KULI Extended Cabin Model, despite certain abstractions.

In addition, it is worth mentioning that the curves of the aggregated air outlet temperature $t_{duc,out,u}$ from MATLAB/Simulink control and the actual air outlet temperature $t_{duc,out,y}$ from KULI are also almost congruent, especially during steady-state conditioning with a value of around $t_{duc,out,y,steady} \cong 14\,°C$. This shows that the composition of the required heating power for reheating the air flow downstream of the evaporator to the desired air duct outlet temperature works very well. More specifically, this confirms the function of the control of the temperature mixing flaps and electric heater at the level of the heating devices.

### *4.1.2. Heat Flows in Heating Unit*

Due to the air flow through the heating devices, i.e., the heat exchanger to the motor coolant circuit and the electric resistance heater, the air flow downstream of the refrigerant evaporator is reheated as needed. Even in the case of high ambient temperatures, such as in the “Malaga” case under consideration with $t_{amb} = 35\ °C$, this measure is necessary, as the evaporator outlet temperature of the air was set to a constant value of $t_{evp,out,w} = 10\ °C$ in the simulation, according to suggestions in [9]. This results in a heating demand to be supplied in order to adjust the air flow temperature to the required air duct outlet temperature.

The exchanged heat flows in the heating devices are shown in **Fig. 16 (a)**. The heating power $\dot{Q}_{total,u}$ is a theoretic value that is calculated in MATLAB/Simulink in the course of model-based feedforward control. This value is determined using the target air duct outlet temperature $t_{duc,out,u} = t_{duc,out,w}$ calculated at the regulatory level and with knowledge of the thermal state upstream of the heating devices $Z_{HU,in,d} = \{T_{HU,in,d}, p_{HU,in,d}, \dot{m}_{HU,in,d}, \varphi_{HU,in,d}, \dots\}$ from the KULI model. The primary objective is the composition of this heat flow by the heat flow $\dot{Q}_{heatex,y}$, which is transferred in the heat exchanger from the motor coolant to the air in the warm path of the HVAC unit, and the heat flow $\dot{Q}_{elec,y} = P_{elec,y}$, which must be supplied electrically in the auxiliary heater. In this way, the specified course of the air duct outlet temperature can be controlled as precisely as possible. The secondary objective is to ensure that the required heat flow is provided to the maximum extent possible via the heat exchanger in order to minimize the electrical energy demand.

The angular position of the temperature mixing flap $\alpha_{flap,u}$, as well as the resulting pressure loss coefficients $\zeta_{cold,u}, \zeta_{warm,u} = f(\alpha_{flap,u})$ in the cold and warm sections of the air path in the HVAC system, are shown in **Fig. 16 (b)**. By controlling these flow resistances, the mass flow distribution between the cold and warm partial air path is defined, which significantly influences the air-side heat transfer in the heat exchanger.

Observing the heat flow curves, a rapid increase in the required heating power to $\dot{Q}_{total,u} \cong 800\ W$ occurs around the time $\tau \cong 100\ s$. By rapidly setting the temperature mixing flap to an angle of $\alpha_{flap,u} \cong -30°$, the flow resistance in the cold partial air path is significantly increased. This allows the transferred heat output in the heat exchanger to be raised. The difference between the required heat output calculated in MATLAB/Simulink and the heat output of the heat exchanger fed back from the KULI model is supplied electrically ($\dot{Q}_{elec,y} = \dot{Q}_{total,u} - \dot{Q}_{heatex,y}$). Due to the continuous increase in motor winding temperature and the associated increase in enthalpy flow of the motor coolant at the inlet of the heat exchanger, the temperature mixing flap must be adapted to an average value of around $\alpha_{flap,u} \cong -8°$ as the cycle progresses. In general, the developed combination of model-based feedforward and feedback control achieves effective coverage of the required heat output with the heat flow that is transferred in the heat exchanger. This results in a very low average electrical heating power of $\dot{Q}_{elec,avg,y} = P_{elec,avg,y} = 12.92\ W$ over the simulated cycle.

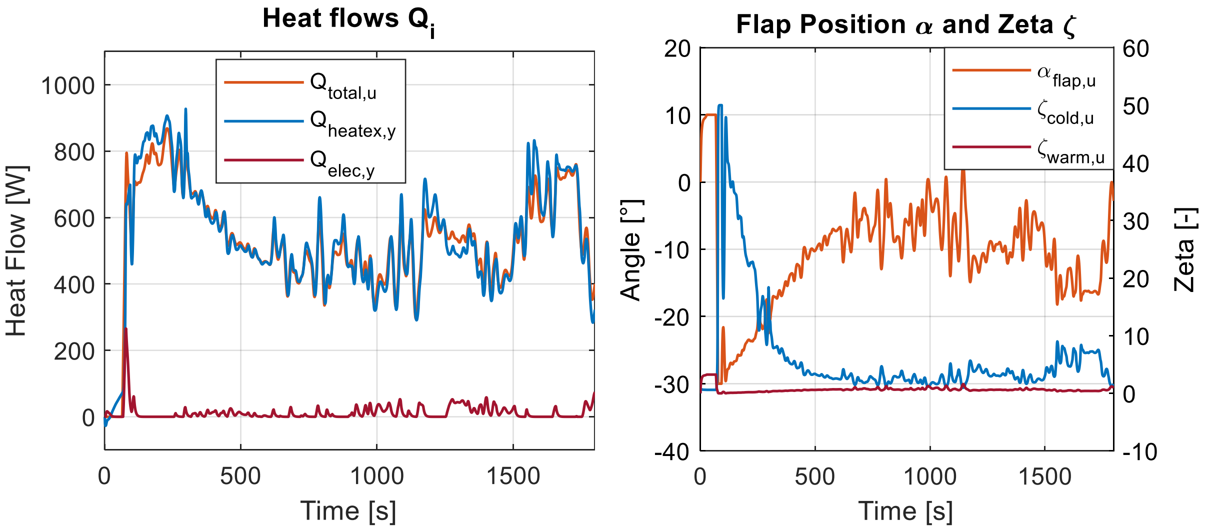

(a) (b)

**Fig. 16.** Heat flows in heating unit (a), Temperature mixing flap angle and pressure loss coefficients (b)

### 4.2. Energy Consumption of the Overall Vehicle and of the HVAC System

#### *4.2.1. Average Vehicle Energy Consumption and Energy Consumption Shares*

**Fig. 17 (a)** provides a comparison between the average energy consumption from the performed simulation and the WLTP (Worldwide Harmonized Light-duty vehicles Test Procedure) manufacturer data. For the "Malaga" operating point with $t_{amb} = 35\,°C$, the current simulation provides a value of $e_{batt,avg,sim,35°C}(\tau_E) = 20.38\,kWh/100km$. In addition, simulation results for the "Frankfurt am Main" operating point with $t_{amb} = 23\,°C$ are also provided and show a slightly lower value of $e_{batt,avg,sim,23°C}(\tau_E) = 19.07\,kWh/100km$. In the course of WLTP, the value obtained for vehicles of the analyzed manufacturer and type is $16 - 18.5\,kWh/100km$ [16], with the variation indicated by dashed lines "min" and "max".

As described in [1], the higher energy consumption in the performed simulation with $t_{amb} = 35\,°C$, compared to the WLTP specification, can be explained by the significant influence of the ambient temperature on the energy consumption of BEV. While WLTP tests are generally conducted at a constant ambient temperature of $t_{amb,test} = 23\,°C$ including preconditioning, the vehicle was simulated at a higher ambient temperature of $t_{amb,sim} = t_{init,sim} = 35\,°C$, which also represented the initial temperature of the cabin, battery, motor and other components. Consequently, this results in higher energy consumption during the steady-state conditioning of the vehicle's subsystems, but above all significantly higher energy consumption during the transient cooldown process if no preconditioning is carried out. Consequently, for validation, the simulated energy consumption at $t_{amb} = 23\,°C$ is also compared with the manufacturer's WLTP data so that the same ambient temperature can be used as a basis. This shows that the simulated value is only slightly above the tolerance range of the test procedure.

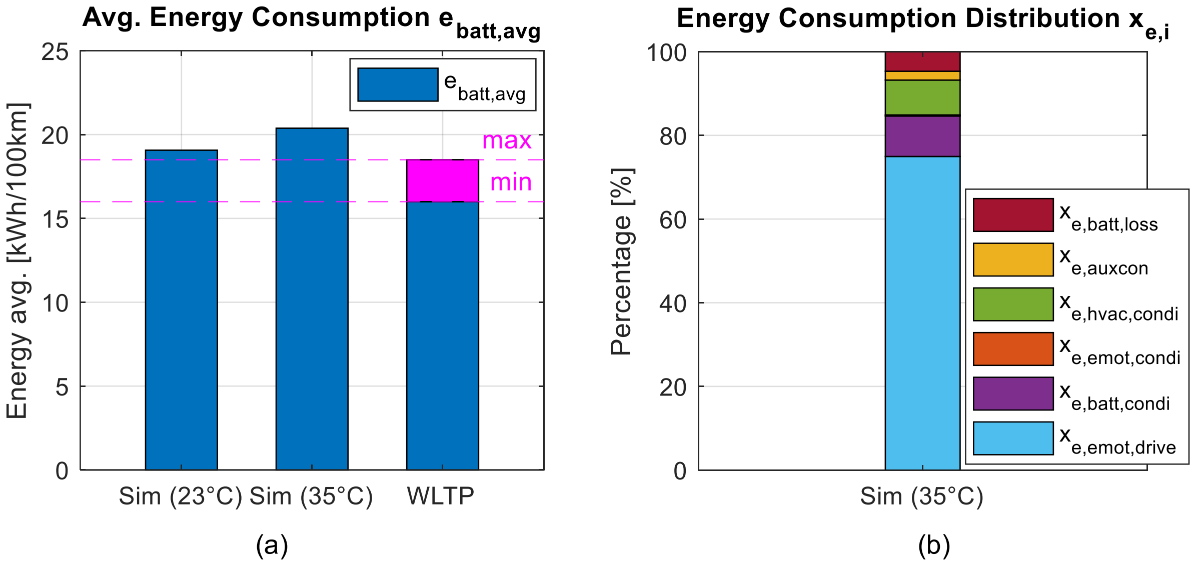

(a) (b)

**Fig. 17.** Average energy consumption (a), Energy consumption shares of electrical energy consumers (b)

The percentage shares of the individual electrical energy consumers in the vehicle in relation to the total electrical energy consumption that were determined during the simulation at $t_{amb} = 35\,°C$ are shown in **Fig. 17 (b)**. Those consumers are the electric powertrain, $x_{e,emot,drive}$, the battery conditioning, $x_{e,batt,condi}$, the conditioning of motor and power electronics, $x_{e,emot,condi}$, the HVAC system, $x_{e,hvac,condi}$, other auxiliary consumers, $x_{e,auxcon}$, and thermal battery losses, $x_{e,batt,loss}$. The energy consumption of the entire thermal management system is the sum of $x_{e,VTMS} = x_{e,batt,condi} + x_{e,emot,condi} + x_{e,hvac,condi}$.

The entire thermal management system accounts for an energy consumption share of $x_{e,VTMS}(\tau_E) = 18.27\,\%$ and is therefore the largest system auxiliary consumer in the BEV alongside the electric powertrain, as also described in [5]. The HVAC system consumes $x_{e,hvac,condi}(\tau_E) = 8.34\,\%$ of the total at the end of the simulation. The share of battery conditioning is slightly higher at $x_{e,batt,condi}(\tau_E) = 9.66\,\%$. This is particularly due to the fact that, assuming an initial battery temperature of $t_{init,batt} = 35\,°C$, there is a very high transient cooling power requirement due to the large thermal mass of the battery. Compared to expansion stage 1 of this simulation in [1], the percentage of cabin air conditioning could also be reduced by further measures. These included increasing the temperature level at the evaporator outlet as needed and reducing the dynamics to achieve thermal comfort in the passenger compartment.

This essentially made it possible to reduce the electrical power of the refrigerant compressor and the electrical power supplied to the auxiliary heater to reheat the air. Under the assumption of a high solar radiation intensity of $I = 500\ W/m^2$ considered here, a relatively low heat output must also be supplied in the heating devices, as the air duct outlet temperature has to be set correspondingly lower.

The achieved results for a transient cooldown process confirm that the electrical energy consumption of the thermal management system is highly dependent on the ambient conditions [17] [18]. The ambient temperature and relative humidity, but also the solar radiation intensity, play a major role in the power demand of the HVAC system. The power requirements for conditioning the motor, power electronics and battery strongly depend on whether preconditioning has been performed as well as on the initial temperature of these components. In particular, the battery with its high thermal inertia significantly impacts the power demand of its thermal management. In the specific case with a high ambient temperature, in addition to the increased operation of the coolant pumps and fans, the increased operation of the refrigerant compressor is primarily responsible for the higher energy consumption. The compressor is operated both to dissipate heat from the battery via the plate heat exchanger and to dissipate heat from the air for cabin air conditioning via the evaporator. [1]

### *4.2.2. Average Vehicle Energy Consumption depending on the Ambient Temperature*

This section, in addition to the results from 4.2.1, focuses on the effect of the ambient temperature on the average total energy consumption of a BEV. For this purpose, the developed BEV co-simulation was performed for the ambient conditions listed in **Table 2** with temperature $t_{amb}$, relative humidity $\varphi_{amb}$, solar radiation intensity $I$ and recirculation ratio $x_{rec}$, in each case for the WLTC Class 3 driving cycle.

**Table 2.** Overview of investigated ambient conditions

| Operating Point | Ambient Conditions | | | |
|---|---|---|---|---|
| | $t_{amb}$ [°C] | $\varphi_{amb}$ [%] | $I$ [W/m$^2$] | $x_{rec}$ [%] |
| Kiruna | -18 | 85 | 0 | 70 |
| Oslo | -5 | 85 | 0 | 70 |
| Graz | 10 | 85 | 100 | 60 |
| Frankfurt am Main | 23 | 55 | 250 | 50 |
| Malaga | 35 | 40 | 500 | 50 |
| Palermo | 40 | 55 | 1000 | 30 |

**Fig. 18** shows the polynomial fitted curve of the vehicle's energy consumption over the ambient temperature. In addition to the curve $e_{avg,TUG,CoSim}$ obtained during this co-simulation, other linear interpolated curves as well as data points from different literature references are also depicted in order to validate the achieved results. The baseline energy consumption data for BEV originate from the studies by Evtimov [19], Liu [20], Yang [21], Hamwi [22], Deng [23] and Hao [24]. In the course of the report by Helms [18], these energy consumption values, determined partly in real driving tests and partly simulated with different test cycles, were converted to the same units and compared.

All available data indicate that energy consumption is lowest in an ambient temperature range of $20\ °C < t_{amb} < 25\ °C$. This is due to the fact that the power demand for the conditioning of the passenger compartment, battery and motor is at its lowest here. The resulting values are around $14 - 19\ kWh/100km$. Energy consumption then increases at both very cold and very warm ambient temperatures, which is due to the increased heating and cooling power requirements of the thermal management system. Generally significant to highlight is the fact that cold ambient temperatures lead to a significantly higher increase in electrical energy consumption than warm ambient temperatures. At $t_{amb} = -10\ °C$, energy consumption is in the range of $24 - 35\ kWh/100km$, while at $t_{amb} = 35\ °C$ it can range between $16 - 24\ kWh/100km$. While the transient heat-up processes of the cabin and battery are largely purely electrical, for the cooling of cabin and battery the required electrical power of the refrigerant compressor is reduced by the coefficient of performance ($COP$) of the heat pump process in comparison to the transferred cooling capacity.

The results of the developed co-simulation with its model-based control of the HVAC system using a MIL concept generally agree with the data from the literature in terms of the qualitative correlation between energy consumption and ambient temperature. All curves reveal the same tendency for energy consumption to increase with a progressive deviation from a moderate ambient temperature $t_{amb} \cong$

$22\ °C$, especially at very cold ambient conditions. As with the previous results, it is important to note that in the performed simulation, the ambient temperature equals the initialization temperature of the vehicle components, so that $t_{amb,sim} = t_{init,sim}$. This assumption applies, for example, to the overall structure of the battery pack including all single cells as well as the casing, which results in a high transient cooling or heating demand in this co-simulation setup. So, the higher energy consumption values from this simulation in the low ambient temperature range may be due to the high power demand for heating the battery with its large electrical capacity and consequently large mass and thermal inertia. It is assumed, in contrast, that the literature data considered pre conditioning of the vehicle components, resulting in different initialization temperatures compared to the performed simulation.

Moreover, the BEV energy consumption is also highly dependent on additional parameters, such as the underlying driving cycle, vehicle type and the integrated thermal management system architecture. In some of the referenced literature, significantly longer cycles than WLTC Class 3 are considered, so that transient power loads have less effect when averaging the energy consumption. A possible deactivation of the HVAC system during the test procedures can also not be completely ruled out.

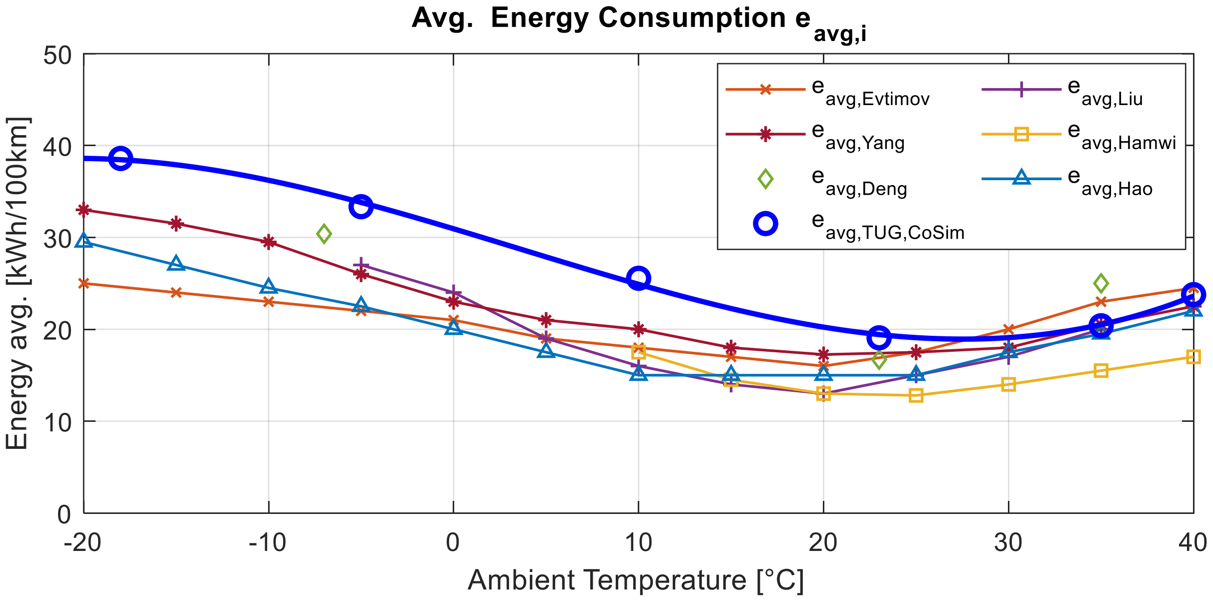

**Fig. 18.** Average Vehicle Energy Consumption depending on the Ambient Temperature

### *4.2.3. Average HVAC Power Demands depending on the Ambient Temperature*

After discussing the influence of the ambient temperature on the total energy consumption, the influence of the ambient temperature on the average power demand of the HVAC system will be addressed. The detailed consideration of the HVAC system in BEV is due to the fact that, compared to vehicles with internal combustion engines (ICEV), the available heat flow of the heat exchanger is significantly lower due to the lower losses of the electric powertrain. Consequently, the electrical power demand of the auxiliary resistance heater increases, which has a major influence on the overall energy consumption.

The data points of the average HVAC power demand $P_{HVAC,TUG,CoSim}$ are plotted over the ambient temperature in **Fig. 19**. For validation purposes, the curve obtained from polynomial fitting of the simulated boundary conditions is also compared with data from literature. These data are derived from Weustenfeld [5]. To be mentioned is that the influence of temperature on HVAC power demand has also been investigated in other literature, but with hardly comparable boundary conditions. Li and Zhu [25] use driving cycles with a duration of 16229 seconds and 5139 seconds respectively, whereby transient power loads are significantly reduced through averaging. The results in Helms [18], which were calculated with the Auxiliary Simulator (AuSim) model package created during the studies in Hausberger [26] and Lohnauer [27], in any case only consider steady-state power requirements of the HVAC system.

Weustenfeld [5] considers a compact class vehicle and also includes the influence of relative humidity $\varphi$ and solar radiation $I$ into the calculation. The derived data are also visualized in **Fig. 19**. While data points $P_{HVAC,Weustenfeld,\varphi\gg,I\gg}$ were determined on the basis of statistically high relative humidity and solar radiation intensity for the respective ambient temperature, data points $P_{HVAC,Weustenfeld,\varphi\ll,I=0}$ refer to statistically low relative humidity and an assumed solar radiation intensity of $I = 0\ W/m^2$. The shaded area indicates the maximum difference between these two data sets of highest and lowest relative humidity and solar radiation. Data points $P_{HVAC,Weustenfeld,avg}$ and the corresponding curve, on the other hand, represent a scenario with statistically expected values for humidity and radiation.

The comparison generally indicates qualitative agreement between the results of the developed BEV co-simulation with model-based control of the HVAC system using a MIL concept ($P_{HVAC,TUG,CoSim}$) and the statistically averaged scenario ($P_{HVAC,Weustenfeld,avg}$) from Weustenfeld [5]. In general, again, it is evident that the lowest power demand can be expected at moderate temperatures of $20\,°C < t_{amb} < 25\,°C$, even when the HVAC system is considered individually. These values are in the range of $400 - 550\,W$ and result from moderate operation of the refrigerant compressor for cooling and potential dehumidification of the inflowing air. The required heating performance for reheating the air up to the required inlet temperature in the cabin can be provided to a large extent by the heat exchanger. At higher ambient temperatures, there is a certain increase in the power requirement, with values between $800 - 2200\,W$ being observed at $t_{amb} = 35\,°C$. Here, the increased operation of the refrigerant compressor for cooling and dehumidifying the inflowing fresh air is the main factor. At low ambient temperatures, the HVAC power consumption is highest, specifically at $t_{amb} = -10\,°C$ the power values are around $3300 - 3900\,W$. Especially after a cold start, the inflowing air has to be heated primarily electrically by the resistance heater, as there is little waste heat from the electric powertrain. In both limiting conditions, increasing the proportion of recirculated air can contribute accordingly to reducing the power demand.

Furthermore, the influence of the investigated relative humidity and solar radiation intensity is important to mention. In the ambient temperature range $-18\,°C < t_{amb} < 10\,°C$, a high relative humidity of $\varphi = 85\,\%$ but low solar radiation intensity of $0 \leq I \leq 100\ W/m^2$ was considered in the applied boundary conditions of the performed co-simulation, see **Table 2**. In the range of increasing ambient temperatures of $10\,°C < t_{amb} < 40\,°C$, a lower relative humidity of $40\,\% \leq \varphi \leq 55\,\%$ but higher solar radiation intensity of $250\ W/m^2 \leq I \leq 1000\ W/m^2$ was assumed in accordance with the described boundary conditions (see also **Table 2**). In Weustenfeld [5], the data points for high ($P_{HVAC,Weustenfeld,\varphi\gg,I\gg}$) and low relative humidity and solar radiation ($P_{HVAC,Weustenfeld,\varphi\ll,I=0}$) spread over a wide range of possible power demands, as the shaded area indicates. Consequently, in addition to the main influencing factor of the temperature, the relative humidity and the solar radiation intensity are also important parameters that are decisive for the HVAC system power demand, especially during cooldown processes. High humidity leads to increased heat capacities of the humid air, while high solar radiation represents an additional heat flow across the cabin, which needs to be balanced out in cooling mode. With respect to certain differences between the simulation results and the literature data, it is important to note that the HVAC power demand is also highly dependent on other boundary conditions such as recirculation ratio and number of passengers but also on the driving cycle and the detailed thermal management system configuration. Here, more detailed information would be required for even better quantitative comparability.

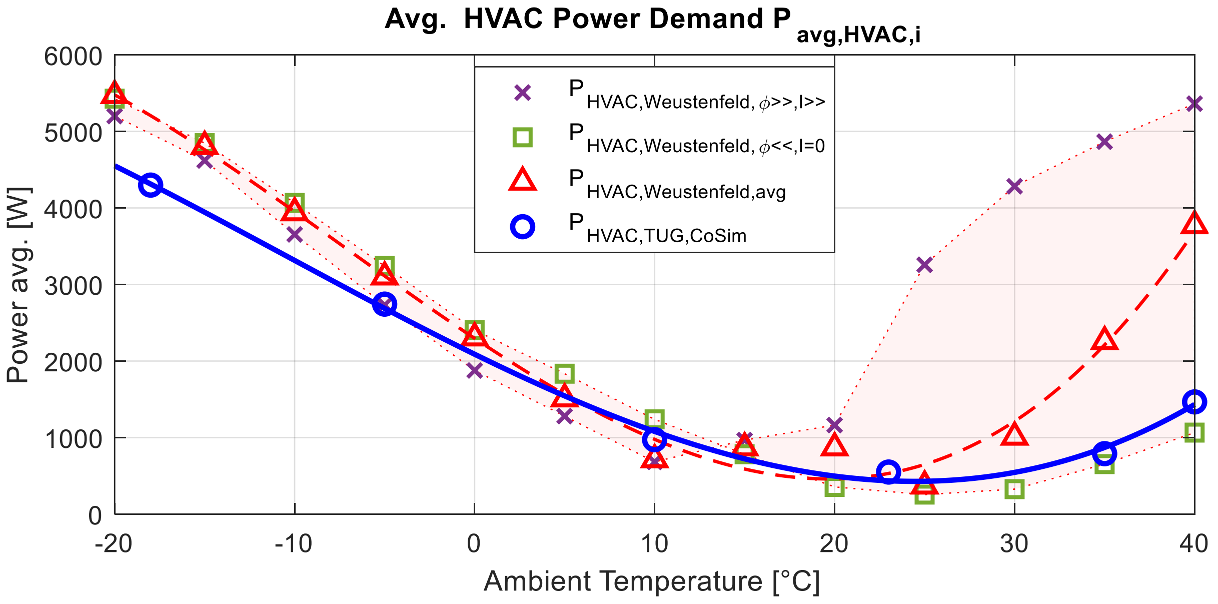

**Fig. 19.** Average Power Demand of the HVAC System depending on the Ambient Temperature

## Conclusions and Outlook

These investigations involved the development of a BEV thermal management co-simulation at overall vehicle system level. By extending the 1D thermal management software KULI with MATLAB/Simulink, a comprehensive range of functions was achieved for precise modeling and simulation at the overall vehicle level and at the thermal management subsystem level, including the passenger compartment, battery and powertrain.

Particularly in the analysis of the HVAC system, a great emphasis was placed on the precise modeling of the vehicle cabin and the HVAC air path components due to their special relevance in BEV. In addition, a model-in-the-loop concept for automatic cascaded control of the HVAC system components was implemented. The cascaded control concept is based on the configuration in real vehicles, but the common empirical characteristics were substituted by a model-based control principle with feedforward control. The mathematical-physical equation systems in the feedforward controls were derived in the course of thermodynamic analyses.

The results demonstrate the highly accurate control of the cabin air temperature to the target temperature profile using the developed control concept. This proves the functionality of the model-based control with feedforward as well as the MIL simulation with KULI and MATLAB/Simulink. Further simulation results also show the significant dependence of BEV energy consumption on the ambient conditions, in particular on the temperature. The simulated results provide basically good qualitative agreement with those from various literature sources. The explicit correlation between the average power demand of the HVAC system and the ambient temperature was also presented, again with good qualitative agreement with an existing simulation. For both considerations, the significant potential increase in the BEV's energy consumption and the HVAC system's power requirement is obvious at very warm, but especially at very cold ambient temperatures. Also worth emphasizing is the significant influence of other boundary conditions on the energy consumption of BEV as well as on the power demand of the HVAC system. In particular, the relative humidity, solar radiation intensity and recirculation ratio on HVAC system level, but also the driving cycle and the thermal management system configuration on overall VTMS level are decisive factors.

Within the scope of ongoing investigations, it is aimed to extend the BEV co-simulation also to a fuel cell electric vehicle (FCEV) at the overall vehicle level. This will be done in order to derive broad findings on thermal management for this vehicle type as well. At the HVAC system level, the investigation of further measures to reduce electrical energy consumption, such as the integration of a heat pump or the continued optimization of the control strategy, is planned as part of the BEV simulation. A further key objective is to derive extensive knowledge about the influence of various other climatic and vehicle-specific boundary conditions on the energy consumption of the vehicle and the power demand of the HVAC system.

## Acknowledgements

The investigations were conducted as part of projects at HyCentA Research GmbH within the Area “Green Mobility” under the “COMET K1” program. Funding for these projects was provided by the Austrian Research Promotion Agency (FFG) of the Federal Ministry for Climate Action, Environment, Energy, Mobility, Innovation and Technology (BMK) and the Federal Ministry for Labour and Economy (BMAW). The author expresses sincere gratitude to these organizations for their support.

Furthermore, the author would like to thank the industrial partner MAGNA ECS (Engineering Center Steyr GmbH & Co KG) for enabling and supporting the use of KULI thermal management simulation software.

## References

[1] Frühwirth, C., Lorbeck, R., Schutting, E., and Eichlseder, H., "Co-Simulation of a BEV Thermal Management System with Focus on Advanced Simulation Methodologies," SAE Technical Paper 2023-01-1609 (2023), doi:10.4271/2023-01-1609.

[2] Shah, S., Vijay, D., and Lehocky, M., "Thermal Management of Electrified Vehicle by Means of System Simulation," SAE Technical Paper 2020-28-0033 (2020), doi:10.4271/2020-28-0033.

[3] Shah, S., "Integration of 1D and 3D CFD Software for Cabin Cool Down Simulation," SAE Technical Paper 2018-01-0773 (2018), doi:10.4271/2018-01-0773.

[4] Boccardo, G., Graziano, E., De Rosa, L., Mrkvica, T. et al., "Virtual BEV Thermal Management Control Development by Means of an Integrated GT-SUITE Model of HVAC and Battery Cooling Circuits," GT-Publication (https://www.gtisoft.com/gt-suite/publications/).

[5] Weustenfeld, T., "Heiz- und Kühlkonzept für ein batterieelektrisches Fahrzeug basierend auf Sekundärkreisläufen," Zugl.: Braunschweig, Univ., Diss., 2017, *Audi-Dissertationsreihe* Band 122, 2017, Cuvillier Verlag, Göttingen, ISBN 978-3-7369-9627-4.

[6] Geneder, S., "Beitrag zur modellbasierten Emulation von Fluidkühlern zur Abbildung der thermischen Zustände des realen Fahrbetriebs am Prüfstand," Dissertation, Fakultät für Elektrotechnik und Informationstechnik, Otto-von-Guericke-Universität Magdeburg, Magdeburg, 2022.

[7] KULI HVAC Manual (Version 16), KULI Software Tool for Thermal Management Simulation, MAGNA Engineering Center Steyr GmbH & Co KG, St. Valentin, Austria, 2022.

[8] Deutsches Institut für Normung, "Raumlufttechnik – Teil 3: Klimatisierung von Personenkraftwagen und Lastkraftwagen," DIN 1946-3, 2006.

[9] Lemmer, K., Jipp, M., Bubb, H., Vögel, H.-J. et al., "Mensch-Technik-Kooperation und Fahrzeuginnenraum," in: Pischinger, S., Seiffert, U. (eds.), *"Vieweg Handbuch Kraftfahrzeugtechnik,"* ATZ/MTZ-Fachbuch, 9th ed. (2021), Springer Vieweg, Wiesbaden, doi:10.1007/978-3-658-25557-2_10.

[10] KULI Theory Manual (Version 16), KULI Software Tool for Thermal Management Simulation, MAGNA Engineering Center Steyr GmbH & Co KG, St. Valentin, Austria, 2022.

[11] Großmann, H., Böttcher, C., "Pkw-Klimatisierung," VDI-Buch, 3rd ed. (2020), Springer Vieweg, Berlin, Heidelberg, doi:10.1007/978-3-662-59616-6.

[12] Schedwill, H., "Thermische Auslegung von Kreuzstromwärmeaustauschern, Fortschr-Ber.," VDI Reihe 6 19, VDI, Germany, 1968.

[13] Gnielinski, V., "G1 Wärmeübertragung bei erzwungener Konvektion: Durchströmte Rohre," in: Stephan, P., Kabelac, S., Kind, M., Mewes, D. et al., *"VDI-Wärmeatlas," Springer Reference Technik*, 12th ed. (2019), Springer Vieweg, Berlin, Heidelberg, doi:10.1007/978-3-662-52989-8_42.

[14] Lunze, J., "Regelungstechnik 1," (Berlin, Heidelberg, Springer Vieweg, 2020), doi:10.1007/978-3-662-60746-6.

[15] Ghebru, D., "Modellierung und Analyse des instationären thermischen Verhaltens von Verbrennungsmotor und Gesamtfahrzeug," Zugl.: Karlsruhe, Univ., Diss., 2013, *Forschungsberichte aus dem Institut für Kolbenmaschinen* Band 2, 2013, Logos Verlag Berlin GmbH, Berlin, ISBN 978-3-8325-3432-5.

[16] Tesla, Inc., "European Union Energy Label," https://www.tesla.com/en_eu/support/european-union-energy-label, accessed July 2023.

[17] Menken, J.-C., "Thermomanagement im batteriebetriebenen Pkw unter Nutzung eines Kaltdampfprozesses mit Sekundärkreislaufsystem," Zugl.: Braunschweig, Univ., Diss., 2016, *Audi-Dissertationsreihe* Band 115, 2016, Cuvillier Verlag, Göttingen, ISBN 978-3-7369-9349-5.

[18] Helms, H., Bruch, B., Räder, D., Hausberger, S., Lipp, S., and Matzer, C.-U., "Energieverbrauch von Elektroautos (BEV)," ifeu – Institute for Energy and Environmental Research gGmbH, and Institute of Thermodynamics und Sustainable Propulsion Systems, 2022, German Environmental Agency (Umweltbundesamt), Dessau-Roßlau, ISSN 1862-4804.

[19] Evtimov, I., Ivanov, R., and Sapundjiev, M., "Energy consumption of auxiliary systems of electric cars," *MATEC Web of Conferences* 133 (2017): 06002, doi:10.1051/matecconf/201713306002.

[20] Liu, K., Wang, J., Yamamoto, T., and Morikawa, T., "Exploring the interactive effects of ambient temperature and vehicle auxiliary loads on electric vehicle energy consumption," *Applied Energy* 227 (2018): 324-331, doi:10.1016/j.apenergy.2017.08.074.

[21] Yang, B., Yao, M., Li, X., Wang, M. et al., "Impact of Thermal Architecture on Electric Vehicle Energy Consumption/Range: A Study with Full Vehicle Simulation," SAE Technical Paper 2021-01-0207 (2021), doi:10.4271/2021-01-0207.

[22] Hamwi, H., Rushby, T., Mahdy, M., and Bahaj, A.S., "Effects of High Ambient Temperature on Electric Vehicle Efficiency and Range: Case Study of Kuwait," *Energies* 15 (2022): 3178, doi:10.3390/en15093178.

[23] Deng, B., Li, L., Ou, Y., Wang, Y., Zhao, Z., Meng, Z., and Zhou, Q., "Study on Environmental Adaptability of Electric Vehicle based on WLTC cycle," *Journal of Physics: Conference Series* 1948, no. 1 (2021): 012087, doi:10.1088/1742-6596/1948/1/012087.

[24] Hao, X., Wang, H., Lin, Z., and Ouyang, M., "Seasonal effects on electric vehicle energy consumption and driving range: A case study on personal, taxi, and ridesharing vehicles," *Journal of Cleaner Production* 249 (2020): 119403, doi:10.1016/j.jclepro.2019.119403.

[25] Li, J., Zhu, Z., "Battery Thermal Management Systems of Electric Vehicles," Master's Thesis, Department of Applied Mechanics, Division of Vehicle Engineering & Autonomous Systems, Road Vehicle Aerodynamics and Thermal Management, Chalmers University of Technology, Göteborg, 2014, ISSN 1652-8557.

[26] Hausberger, S., Stadlhofer, W., Vermeulen, R., Geivanidis, S. et.al., "MAC performance test procedure: Co-ordination of the pilot test phase and follow up towards the drafting of the regulatory text," Final Report performed under Framework Service Contract ENTR/05/18, 2013, European Commission – DG Enterprise and Industry, Delft.

[27] Lohnauer, L., "Einfluss von Anbauteilen und Umgebungsbedingungen auf Real Drive Emission Ergebnisse," Master's Thesis, Institute of Thermodynamics and Sustainable Propulsion Systems, Graz University of Technology, Graz, 2019.

# Session 2.2 AFTERTREATMENT

# Double Gasoline Particulate Filters: A Concept for Reducing Tailpipe PN10 Emissions

C. Larrieu[1], E. Laigle[1], C. Norsic[1], J. Hinault[2], D. Préterre[2] and C. Chaillou[1]

[1]Aramco Fuel Research Center, 232 Avenue Bonaparte, Rueil-Malmaison, 92500, France

E-mail: clement.larrieu@aramcooverseas.com
Telephone: +33 (0)6 46 55 37 84

[2]CERTAM Rouen, 1 Rue Joseph Fourier,76800 Saint-Étienne-du-Rouvray

E-mail: contact@certam-rouen.com
Telephone: +33 (0)2 35 64 37 00

**Abstract.** For several decades, the transportation sector has been improving pollutant emissions to reduce its environmental impact and improve the air quality. Nowadays, exhaust lines commonly include one or more catalysts to convert gaseous pollutants, while solid pollutants (particulate matter, also called soots) are collected using a Particulate Filter (PF). This paper describes how a double PF architecture, one in close-coupled position and one close to tailpipe, is able to significantly reduce the particulate emissions of a gasoline engine.

First, a study on engine bench simulating a severe RDE cycle is conducted to evaluate the Filtration Efficiency (FE) of several combinations of two Euro7-like Gasoline Particulate Filters (GPF) in a row. The engine is a 1.3L Euro6d-temp GDI engine, powered by two types of fuel, designed to maximize and minimize the PN production. The impact of the ambient temperature is also considered by running cycles at 20°C and -10°C. The instantaneous Particulate Number (PN) distribution is measured with three particulate size spectrometers from 6nm to 10µm. The double GPF architecture is then tested by adding a GPF at the tailpipe of a serial Euro6d gasoline passenger car. The PN emissions at intake and after the second GPF are continuously analyzed on a variety of open road trips.

While a single GPF exhibits a FE of 96% on PN10 (Euro7 target), the combination of two GPF allows to reach a FE of more than 99.9% on engine bench with the lowest quality fuel at -10°C. After this first proof-of-concept, the study on passenger car demonstrates the opportunity to reach PN levels lower than ambient concentrations during many trips, validating the relevance of the double GPF technology.

## Notation

| | |
|---|---|
| *A-EAT* | *Advanced Exhaust Aftertreatment Technology* |
| *AQ* | *Air Quality* |
| *ATS* | *After-Treatment System* |
| *B5G* | *5 Gas Analyzer* |
| *BP* | *Back Pressure* |
| *CC* | *Close-Coupled* |
| *CD* | *Chassis Dynamometer* |
| *CO* | *Carbon Monoxide* |
| *Ds* | *Downstream* |
| *ECU* | *Engine Control Unit* |
| *ELPI* | *Electrical Low-Pressure Impactor* |
| *FE* | *Filtration Efficiency;* $(PN_{upstream} - PN_{downstream}) / PN_{upstream}$ |
| *GDI* | *Gasoline Direct Injection* |
| *GPF* | *Gasoline Particulate Filter* |
| *GPS* | *Global Positioning System* |
| *HC* | *Hydrocarbon* |
| *HVAC* | *Heating Ventilation and Air Conditioning* |
| *ICE* | *Internal Combustion Engine* |
| $NH_3$ | *Ammonia* |

| | |
|---|---|
| *NMHC* | *Non-Methanic Hydrocarbons* |
| $NO_X$ | *Nitrogen Oxides (NO, $NO_2$)* |
| *OBD* | *On-Board Diagnostics* |
| *PEMS* | *Portable Emission Measurement System* |
| *PN* | *Particulate Number* |
| *PN10* | *Particulate Number with diameter > 10nm* |
| *PF* | *Particulate Filter* |
| *RDE* | *Real Driving Emissions* |
| *SOA* | *Secondary Organic Aerosol* |
| *TC* | *ThermoCouple* |
| *TP* | *Tailpipe* |
| *Us* | *Upstream* |

## 1. Introduction

### 1.1 Air Quality & Internal Combustion Engines

In some urban areas, the Air Quality (AQ) is a pressing concern due to the dense concentration of population, vehicles, and industries. Some of the pollutant emissions contributing to these concerns proceed from combustion systems (heating systems, industries, transport sector) [1,2,3]. In addition, emissions from other sources such as agricultural practices, solvent use or waste handling can also have a significant impact on air quality. These emissions can be in gaseous or particulate form and can influence both climate change and human health [4,5]. While Internal Combustion Engines (ICE) have an impact on air quality [6], emissions from road vehicles have been improved significantly over the last 30 years due to the introduction of increasingly stringent emission norms [7,8] and the implementation of emission reduction technologies (catalytic systems, particulate filters, better mixture control, hybridization...). The European emission standards currently regulate the following pollutants from the exhaust for most vehicle types, including cars, trucks, locomotives, tractors and similar machinery, barges (but excluding seagoing ships and aeroplanes): Nitrogen Oxides ($NO_X$), Carbon Monoxide (CO), HydroCarbons (HCs), Non-Methanic HydroCarbons (NMHCs), as well as Particulate Matter (PM) in mass and in number (PN). In December 2023, a Euro 7 standard was provisionally agreed upon that includes ammonia ($NH_3$) in exhaust emissions but also non-exhaust emissions such as particulates from tires and brakes [9].

Despite this progress, vehicle emissions remain a contributor to pollutant concentrations in urban areas [5,10,11,12] and many efforts are being made to further reduce emissions and promote vehicles with a low impact on air quality. The generalization of the particulate filter for Diesel vehicles in France resulted in a 72% reduction in PM emissions from road transport between 1990 and 2019 [13]. Recent Diesel vehicles equipped with PF can emit less primary particulate than gasoline vehicles without one [14,15,16]. To reduce particulates emissions even further, a solution that has been generalized is the installation of a PF on almost all ICE-equipped vehicles, including gasoline powered vehicles.

### 1.2 Particulate, GPF and Double GPF technology

Particulate filters have been developed to capture and remove particulates from Diesel and gasoline engine exhaust gases [17,18,19,20]. The PF became effectively (if not in regulation) obligatory in Europe on new Diesel engines on 1 January 2011 in order to reach stricter emission regulations [13]. With the Euro 6 regulation, particulate filters are also becoming widespread on gasoline vehicles, to limit the increase of fine particulates emissions due to direct fuel injection systems [21].

In order to trap particulates, GPF are made of a porous ceramic material with a honeycomb structure. The smallest particulates are trapped by Brownian diffusion (<30 nm), the largest particulates (>200 nm) are trapped by interception and inertial filtration [22,23]. However, the filtration efficiency for intermediate-sized particulates is lower because they are not small enough to be trapped by Brownian diffusion and not large enough for inertial filtration [24]. When the filter is fresh, its efficiency to trap particulates is not maximal, but it increases with mileage due to ash accumulation [25].

Indeed, soot accumulates on the walls of the filter over time and creates an additional layer that improves filtration efficiency. A compromise must also be made between filtration efficiency and induced exhaust back pressure in order to limit the negative effect on fuel efficiency. The compromise depends on different parameters such as the GPF volume, the length/diameter ratio, the open frontal area, the size and porosity of the pores, the wall thickness, and the cell density [26].

GPF have been tested over a wide range of test conditions and most have a PN filtration efficiency (FE) between 60% and over 90%, depending on various factors. For example, in Saito et al. [27], an underfloor GPF is more efficient than a close coupled GPF in the same conditions (92% against 78%). They also found that the higher the number of particulates at the engine out the more efficient the GPF is. The cell design also is an important parameter [27,28]. With Saito et al. conditions, GPF with 300 Cells Per Square Inch (CPSI) and 0.012 inches of wall thickness are more efficient than those with 360 CPSI and 0.005 or 0.008 inches of wall thickness (78% against 61-64%). According to many authors, coated GPF are also more effective than bare GPF [29,30].

Accumulated soot (and ash) in a GPF leads to an increase in back pressure which could lead to an increase in fuel consumption and lowered engine efficiency [31]. Depending on conditions (exhaust temperature and oxygen content), a GPF may or may not need an active regeneration process. During the regeneration process the soot collected on the surface is burned into carbon dioxide, steam and potentially particulates [32, 33]. The regeneration process requires oxygen molecules and temperatures higher than 600°C. However, for most road-going gasoline vehicles, high-temperature, high-oxygen conditions are frequently encountered, for example during a gear shift after a driving speed phase of few minutes. Thus, an active regeneration process is rarely needed for gasoline vehicles.

Because of the potential release of particulates during these regeneration events on conventional PF installations, an opportunity is seen to mount a second GPF serially with the first in order to push FE of the complete system even further. This system is called Double GPF technology.

### 1.3 Advanced-Exhaust Aftertreatment Technology

A-EAT, for Advanced Exhaust Aftertreatment Technology, is an innovative technology concept that Aramco is exploring in an attempt to reduce the amount of direct or indirect emission of pollutants, such as $NO_x$ – particulates – CO – HCs – $NH_3$, from the vehicle tailpipe in order to go beyond upcoming European regulation – Euro 7, with the goal of contributing towards improving urban air quality. The A-EAT relies on innovative integrations of exhaust line architecture and optimized After-Treatment Systems (ATS). A-EAT includes studies of fuels, powertrain technologies, both conventional and innovative ATS, and AQ. AQ investigation is key to point out the main molecules that impact, directly or indirectly, the ambient AQ [34], including SOA formation. The main objective of this approach is to build a vehicle demonstrator with the different studied technologies. This paper is focusing on the ATS part and especially on the double GPF technology. The objective of using two GPF is, as stated, to improve the PN emissions by cumulating the FE of the two GPF and reducing the impact of the regeneration events of the first GPF on tailpipe particulate emissions.

### 1.4 Paper organization

This paper will first present the experimental setups used to evaluate the four samples of particulate filter both in lab and on vehicle. Results will be presented both for individual filters as well as various combinations thereof. An in-depth review of engine bench results will then be presented, articulated around variations of a single parameter as much has possible: tailpipe GPF choice, ambient temperature, fuel. Finally, the last part of the article will be dedicated to a review of tests performed on vehicle, and to the extent to which conclusions from engine bench tests can be confirmed in real use cases.

## 2. Experimental setup

### 2.1 PN Analyzers

Concerning engine bench experiments, number concentration and size distribution of emitted particulates were assessed using three Dekati ELPI+® (Electrical Low Pressure Impactor) having being intercorrelated during the first phase of the experiment on the same sampling point. Sampling was performed using a 45°-bevelled pipe of 6mm inner diameter. Sampling point locations are recapitulated in **Fig. 1**.

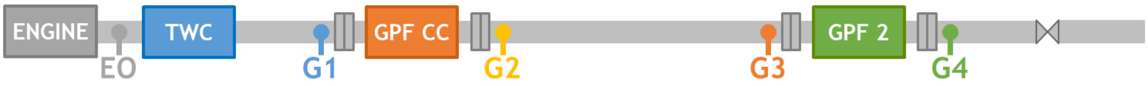

**Fig. 1.** Basic layout of measuring locations for Double GPF testing

The first ELPI+® was used in its High Resolution configuration downstream a fine particle sampler dilution system (Dekati FPS®); sampling point was upstream first particulate filter (G1). Dilution ratio was monitored at 1Hz resolution and was set at 1:25 in order to lower the dew point of the exhaust and to stay in the capacity range of electrometers. The two last ELPI+® were used in High Resolution High Temperature configuration without dilution and were placed upstream and downstream the second particle filter (G3 and G4).

Solid particulates have then been assessed from 6nm to 10µm using 100 virtual classes. Based on observed sensitivity limits (in nb/cm$^3$) of the ELPI, most PN and FE results will be displayed from 10nm up, unless mentioned otherwise.

Concerning chassis dynamometer and on-road testing, two Dekati ELPI+ have been used; the first one sampling in the air intake hose of the engine just before the intake air filter and the second one was placed at the tailpipe.

### 2.2 Fuels

For the campaign, three fuels were used, two of them whose formulations were specifically tailored towards their effect on PN production. Some physical and composition characteristics can be found in **Table 1**. Most of the engine bench campaign was run with a **PN High** fuel, while some tests were conducted with a **PN Low** fuel for comparison.

The PN High fuel is a specialty fuel designed to be representative of a European market commercial fuel in the 90th percentile in terms of PN emissions and has thus been formulated following the EN228 standard with an emphasis on high olefin and heavy aromatics content. As a reminder, higher aromatics content (particularly in the C9+ range) as well as olefin content, to a lesser extent, have been linked with increased PN emissions [35, 36] through the lowering of the distillation curve and higher Final Boiling Point. This fuel is a known reference from a fuel provider.

The PN Low fuel is a tailor-made batch containing only traces of aromatics and olefins.

For vehicle testing, an **E10 CERT** fuel was used, which is an E10 fuel used by OEMs for vehicle certification.

**Table 1.** Fuel characteristics

| Property | unit | PN High | PN Low | E10 CERT |
|---|---|---|---|---|
| RON | - | 95.5 | 96.3 | 96.4 |
| MON | - | 85.0 | 92.5 | 86 |
| Density at 15°C | kg/m³ | 752.7 | 687.4 | 748.9 |
| Vapor Pressure (DVPE @ 37.8°C) | kPa | 61.5 | 62.3 | 57.3 |
| IBP | °C | 30.0 | 32.0 | 35.2 |
| FBP | °C | 205.0 | 181.2 | 189.0 |
| E70 | %v/v | 27.7 | 30.2 | 41.6 |
| E100 | %v/v | 50.2 | 65.6 | 55.3 |
| E150 | %v/v | 79.8 | (1) | 91.5 |
| Olefins | %v/v | 7.5 | 0.2 | 7.0 |
| Aromatics | %v/v | 33.5 | 0.1 | 28.4 |
| Ethanol | %v/v | 0.0 | 0.0 | 9.3 |
| Sulfur | ppm | 2.8 | <3 | 3.6 |

*(1) Not available for this fuel*

### 2.3 Engine bench setup

CERTAM provided a 4-cylinder supercharged direct injection gasoline engine with 1.3L displacement and variable valve timing and lift. After-treatment systems consisted of a close-coupled serial Three-Way Catalyst (TWC) and a first experimental GPF. The exhaust line was prolonged by a 2m long straight tube after which a second GPF was installed, followed by a back-pressure adjustment valve. This can be seen in **Fig. 2**. As such, there was no fully representative effect of external vehicle aerodynamics on the exhaust thermal behavior, nor of backpressure since backpressure is regulated to a constant value for all tests. The GPF studied are summarily described in 2.6. Although the engine was provided with an open ECU, the calibration used for this test campaign was kept standard.

The engine was linked to an asynchronous AVL ELIN charge machine (max power: 120kW, max torque: 500Nm, max rpm: 8000rpm) driven by AVL PUMA software. Simulated vehicle cycles computed from data recorded on chassis dynamometer test bench were applied to the engine. For cold tests, the engine was encased in a cold-box and its fluids (air, liquid, oil) were cooled to -10°C before each experiment, crankshaft temperature initial temperature was -5°C. The cold-box setup is represented in **Fig. 3**. During the cycle, cooling circuit and oil circuit were respectively regulated at 90°C and 110°C. Engine parameters were constantly monitored during the experimentation. Engine out and post TWC exhaust were monitored using five gases HORIBA analyzers. A general overview of the experimental setup is given in **Fig. 4**.

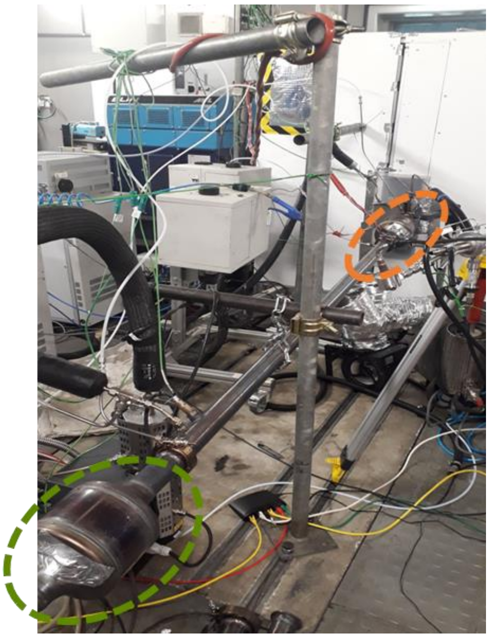

**Fig. 2**. GPF setup for engine bench tests, Close Coupled (CC) GPF in orange, Tailpipe (TP) GPF in green

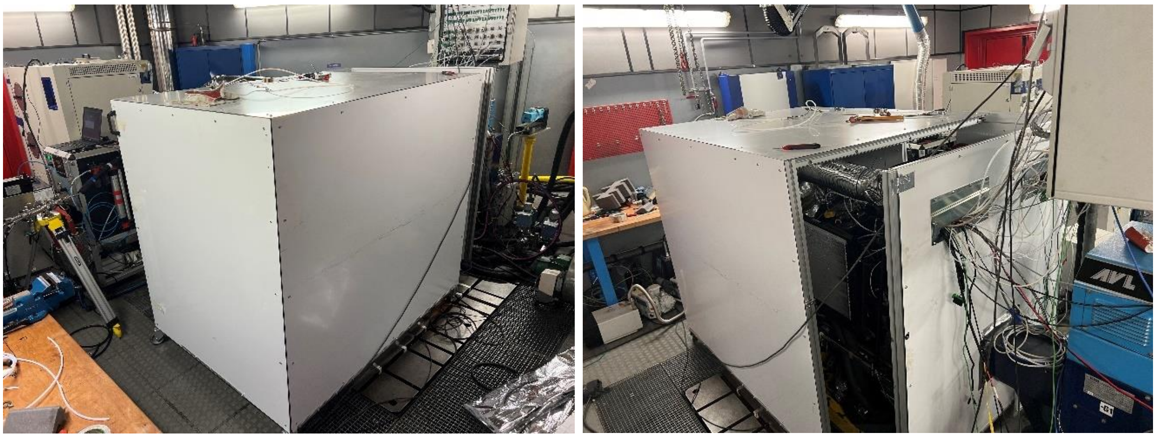

**Fig. 3**. Pictures of cold-box setup for -10°C engine bench tests

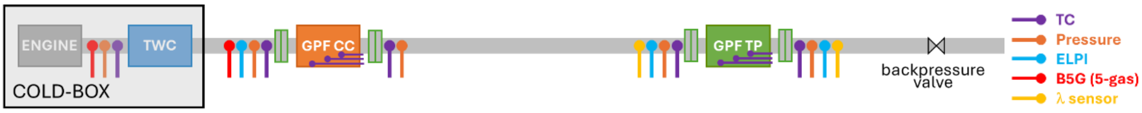
ENGINE
TWC
COLD-BOX
GPF CC
GPF TP
backpressure valve
TC
Pressure
ELPI
B5G (5-gas)
λ sensor

**Fig. 4.** Detail of measuring points and analyzers for engine bench tests

### 2.4 Cycle description

Engine bench tests were run by simulating a purpose-built RDE cycle called **RDE RTS95**.

This RDE cycle is based mainly on components of the RTS95 cycle (whose speed trace is shown in **Fig. 5**), performed with no slope and with slightly altered sections; its speed trace and main dynamic characteristics can be seen in **Fig. 6** and **Table 2** respectively.

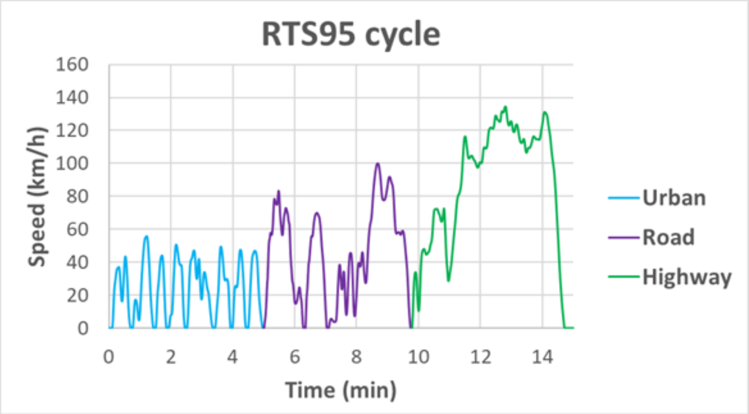

**Fig. 5.** RTS95 cycle speed trace

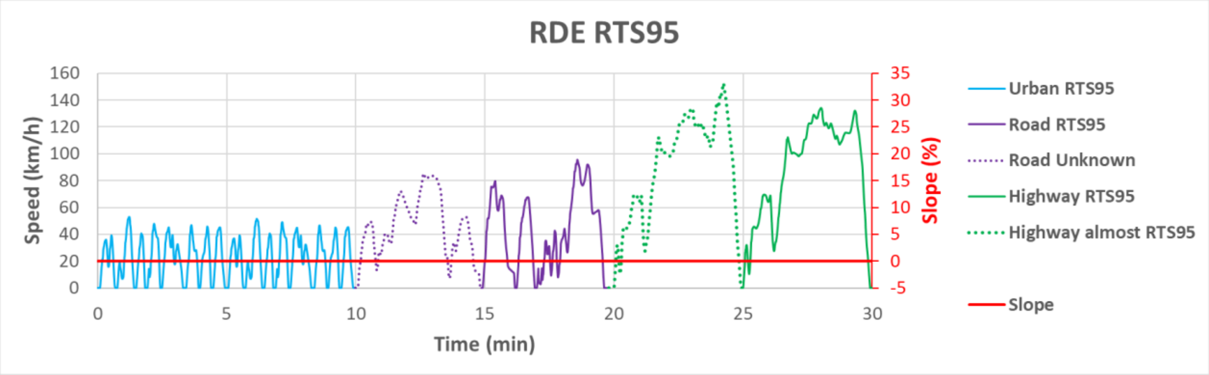

**Fig. 6.** RDE RTS95 cycle speed and slope trace

**Table 2.** RDE RTS95 cycle dynamic characteristics

| Cycle | RDE RTS95 |
|---|---|
| Average speed | 51km/h |
| City rate (1) | 34% |
| Stop time rate | 9% |
| Average acceleration | 0.8m/s² |
| Average deceleration | -0.9m/s² |
| Time in dynamic conditions (2) | 69% |
| Relative Positive Acceleration | 0.24m/s² |
| Speed x Positive acceleration (3) | 18.8m²/s³ |

*(1) Distance below 60km/h*
*(2) Acceleration > 0.2m/s² or deceleration < -0.2m/s²*
*(3) 95th value of speed x position acceleration*

The analysis of results is conducted on the whole cycle as well as on individually identified phases that can be seen in **Fig. 7**. These are:

- The first 42s of the cycle, which correspond to the duration from start to the first stop
- An Urban section composed of two repetitions of the RDE95 Urban phase, *including the first 42 seconds*.
- A Road section composed of a non-specific road subsection immediately preceding the Road section of the original RTS95 cycle.
- A Highway section composed of a non-specific Highway subsection immediately preceding the Highway section of the RTS95 cycle. In this case, the non-specific section is very close to the following RT95 section in profile, with a slightly higher top speed and correspondingly longer acceleration on the last speed peak.

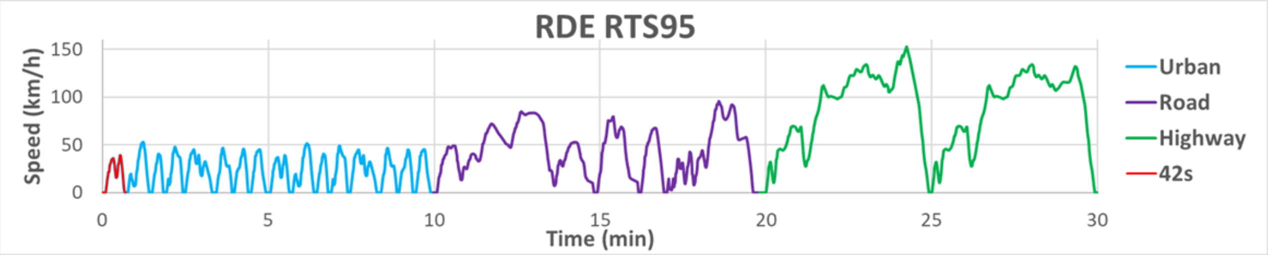

**Fig. 7.** RDE RTS95 cycle speed trace divided by analysis phases

## 2.5 Vehicle testing

### *2.5.1 Vehicle description*

A Euro 6 compliant vehicle, equipped from the factory with 1,2L 3 cylinders engine and close-coupled TWC and GPF, has been prepared in order to have the possibility to add a second GPF placed at the tailpipe, after the muffler. An overview of the experimental setup on vehicle is given in **Fig. 8**.

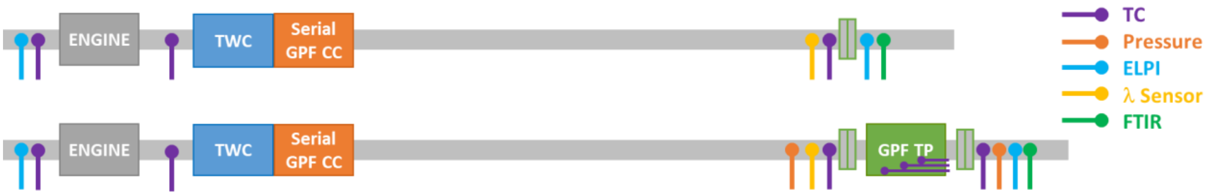

**Fig. 8.** Measuring points and analyzers for vehicle tests, with and without TP GPF

### *2.5.2 Chassis Dynamometer description*

The tests were set up on a chassis dynamometer which is a full HORIBA installation, controlled by STAR VETS operating system, and meets regulatory requirements Euro 6d-Full for gasoline and Diesel engines vehicles.

Dekati ELPI+ measurements were performed in the air intake hose and at the tailpipe with or without the second GPF.

### *2.5.3 Road testing apparatus*

The vehicle was also tested on open road using a trailer equipped with two Dekati ELPI+ and a data logger to record On-Board Diagnostics signals (OBD), GPS, exhaust flow meter, as well as regulated pollutant values from an AVL MOVE Portable Emission Measurement System (PEMS). Particle measurements were performed in the air intake hose and at the tailpipe. The fully equipped trailer with the batteries required for autonomous operation weighed 475 kg and can be seen in **Fig. 9**, along with the tailpipe GPF mounted.

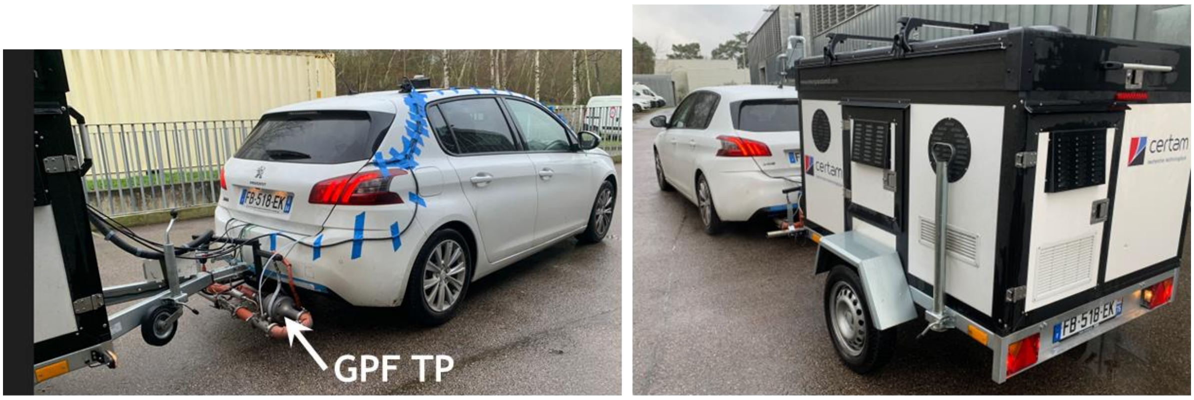

**Fig. 9.** Road test setup

### *2.5.4 Testing conditions*

All vehicle tests were performed in cold-start conditions after resting overnight at ambient temperature.

Coast down tests using the instrument trailer setup were performed in order to implement the same road load for chassis dynamometer tests as for open road tests. Because of safety limitations of the trailer frame, a speed limit of 110km/h is imposed for road tests, which was also implemented in chassis dynamometer cycle traces.

### *2.6 GPF technologies*

The filters tested for the results presented were provided by two different manufacturers. Each manufacturer provided two versions of GPF (A and A+, B and B+) designed for different technical characteristics with regards to their FE to backpressure (BP) trade-off.

These technologies were all tested individually in a single GPF setup. For double GPF setups, different configurations were investigated, first by testing all combinations of A and B (configurations grouped as **Double GPF** in result charts), and then by testing the A+ and B+ samples in tailpipe position combined with either A or B in close-coupled position (grouped as **Double GPF +** configurations).

## 3. Results and discussion

### 3.1 Engine Bench

Tests are conducted with the setup and cycle described 2.3 and 2.4, in various combinations of the aforementioned GPF technologies, also combined with different fuels and different simulated ambient temperatures, as detailed in Table 3. Note that all tests are repeated twice and are numbered following the “Chart N°” references in the table. Tests with A+ or B+ samples in both CC and TP position were also run over the course of the campaign. However, their results are not any better or remarkable than those presented, hence they are omitted from this paper for the sake of brevity.

**Table 3.** Engine bench test matrix for fuels, ambient temperatures and GPFs

| Objectives | Chart N° | Fuel | Tamb | GPF CC | GPF TP |
|---|---|---|---|---|---|
| Single GPF Fuel PN High -10°C | 3 / 4 | PN High | -10°C | A | - |
| | 5 / 6 | | | A+ | |
| | 7 / 8 | | | B | |
| | 9 / 10 | | | B+ | |
| Double GPF Fuel PN High -10°C | 11 / 12 | PN High | -10°C | A | A |
| | 13 / 14 | | | B | B |
| | 15 / 16 | | | A | B |
| | 17 / 18 | | | B | A |
| Double GPF+ Fuel PN High -10°C | 19 / 20 | PN High | -10°C | A | A+ |
| | 21 / 22 | | | B | B+ |
| | 23 / 24 | | | A | B+ |
| | 25 / 26 | | | B | A+ |
| Double GPF+ Fuel PN High 20°C | 35 / 36 | PN High | 20°C | A | A+ |
| | 37 / 38 | | | B | B+ |
| | 39 / 40 | | | A | B+ |
| | 41 / 42 | | | B | A+ |
| Double GPF+ Fuel PN Low -10°C | 43 / 44 | PN Low | -10°C | A | A+ |
| | 45 / 46 | | | B | B+ |
| | 47 / 48 | | | A | B+ |
| | 49 / 50 | | | B | A+ |

PN emissions for all tests in all 3 measurement locations are shown in Fig. 10. Given the high repeatability observed in emissions, and for the sake of result's clarity, results will from now on be averaged by test pairs (3 / 4, 5 / 6, etc) when displaying more than 8 tests (that is, 4 configurations).

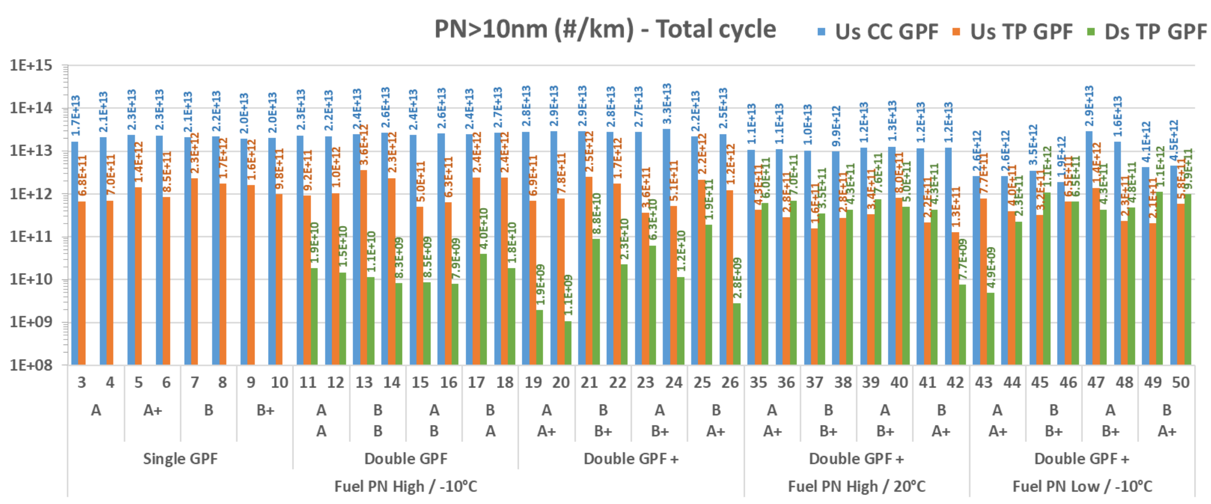

**Fig. 10.** PN emissions on all chassis dynamometer tests

### 3.1.1 Single GPF

First, all filters provided were tested individually in the Close Coupled (CC) position to evaluate their baseline filtration efficiencies. They were tested only with the PN High fuel at an ambient temperature of -10°C.

Filtration efficiency results are presented in **Fig. 11**.

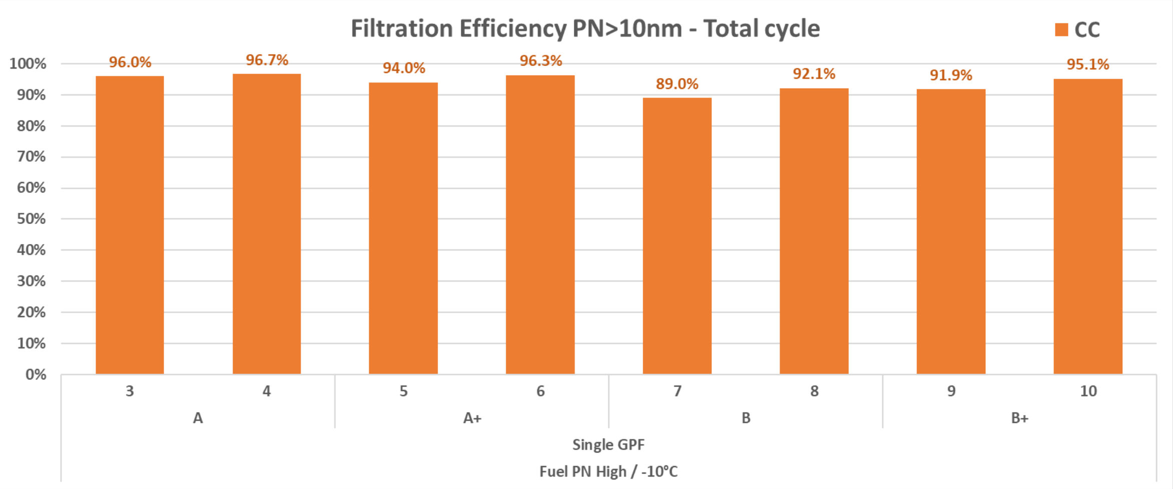

**Fig. 11.** Filtration efficiency for PN10 for all GPF samples individually, Fuel PN High at -10°C

These tests show high filtration efficiency values, consistent with known recent typical GPF technologies. Sample A displays a greater filtration efficiency than B, however samples A, A+ and B+ display very comparable filtration efficiencies.

### 3.1.2 Double GPF

All filters were then tested in configurations **Double GPF** (combinations of A and B samples) and **Double GPF+** (with A+ and B+ samples in tailpipe position) in order to evaluate baseline gains from Double GPF technology as well as further potential gains using improved characteristics GPF samples.

FE Results are presented in **Fig. 12**.

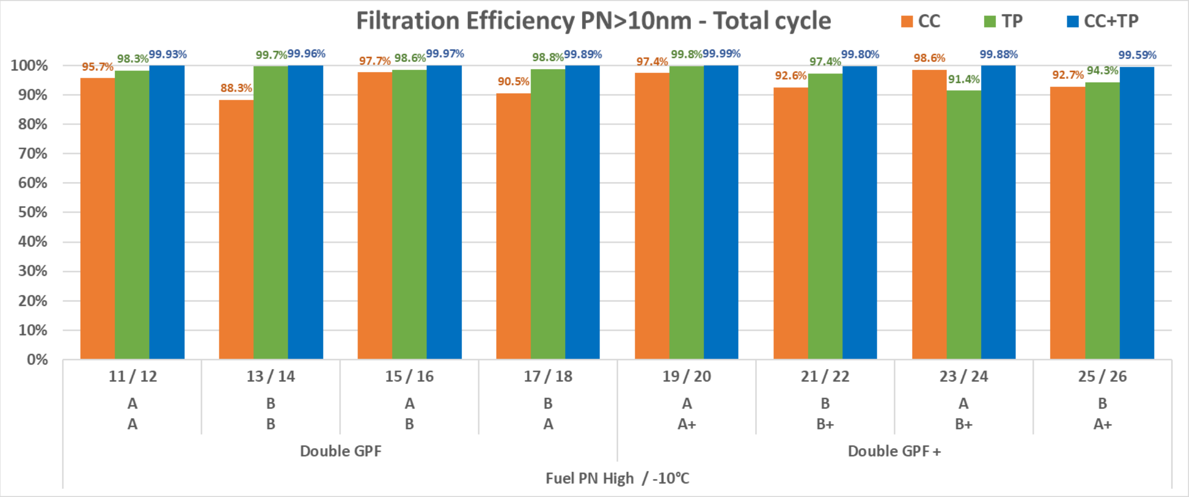

**Fig. 12.** Filtration efficiency for PN10 for all GPF combinations with Fuel PN High at -10°C

All double GPF configurations tested display a high level of filtration efficiency overall, greater than 99.5%, regardless of the exact technologies used for each of the two filters. Except for the A/B+ combination, tailpipe GPF have higher FE compared to CC ones, regardless of whether the tailpipe GPF is an improved sample. All in all, the cumulated effect of both filters shows the potential of the Double GPF technology at the engine bench. Diving deeper into phases, temperatures and oxygen profiles for several tests at the close-coupled and tailpipe positions are displayed in **Fig. 13**. A red shade highlights the zone >600°C where soot combustion is likely to occur in case of availability of oxygen.

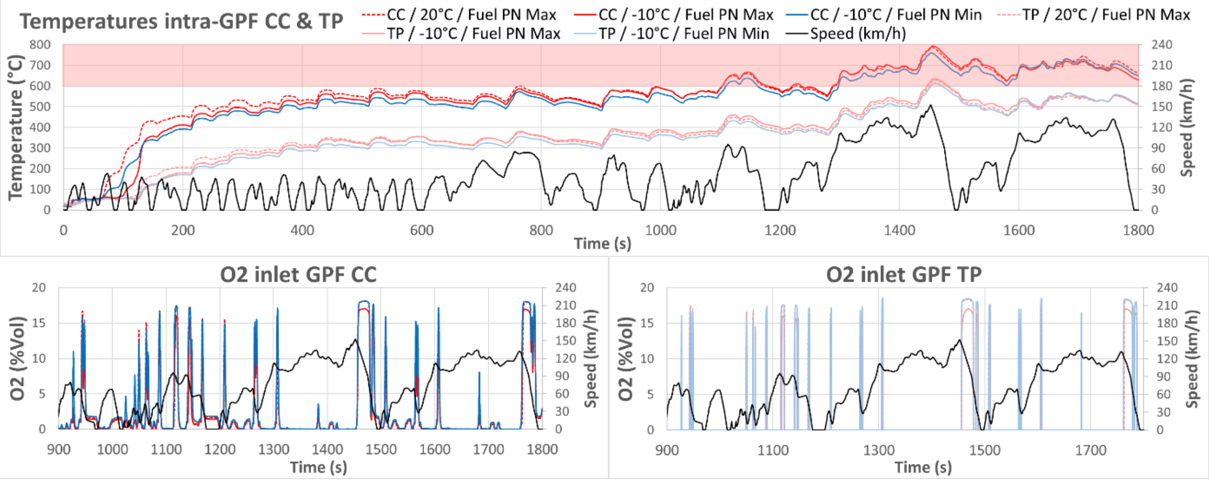

**Fig. 13.** GPF temperature and oxygen profiles for both GPF positions on RDE RTS95

There are multiple occasions for the CC GPF to burn particulate matter starting at 1100s (end of the Road section), and thus to generate additional PN, but there's very little occasion for the tailpipe GPF to initiate soot burning (the only significant window being the accelerator release after the 160km/h speed peak).

To conclude this section, it is generally noted that Double GPF+ configurations perform slightly better overall than their respective Double GPF counterparts and will be the reference point going forward in the article.

### *3.1.3 Impact of temperature and highlight of combustion occurrences*

Tests in Double GPF+ combinations (A or B as closed-coupled filter and A+ or B+ as tailpipe filter) with the reference high PN fuel were also conducted at 20°C. In general for this comparison, engine-out PN emissions are approximately divided by two for tests at 20°C compared to tests at -10°C (as seen on **Fig. 10**). FE results are compared in **Fig. 14**.

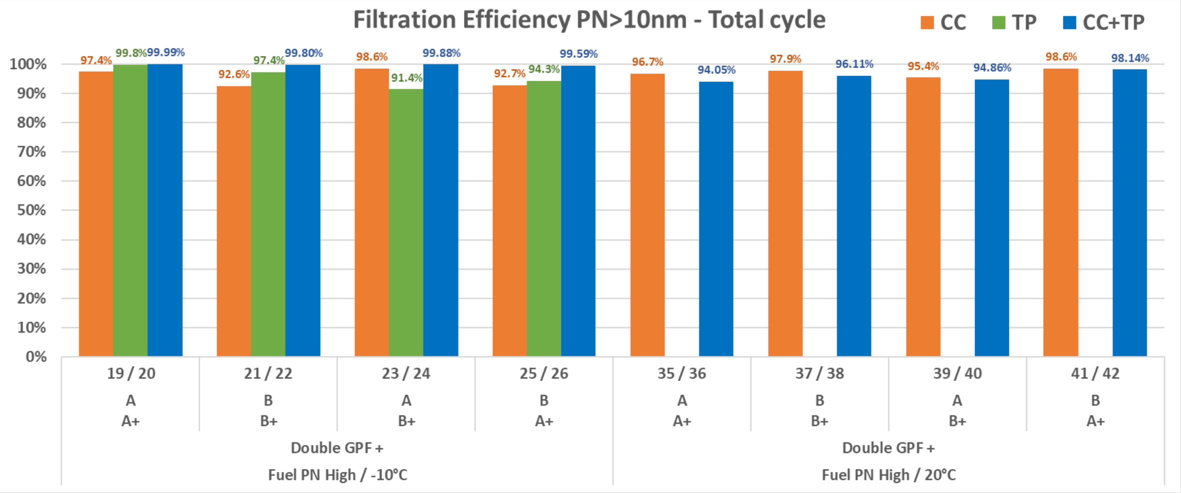

**Fig. 14.** Filtration efficiency for PN10 for Double GPF+ combinations with Fuel PN High at -10°C and 20°C

It is notable that 20°C tests display negative average levels for Tailpipe (TP) PF filtration efficiency, which means the PN count downstream of the TP GPF (G4 position) is higher than the PN count in G3 position, in between the two tested filters. Focusing on phase breakdowns (**Fig. 15** to **Fig. 17**), it appears these negative filtration efficiencies of the TP filter are borne by the Highway phase, and impact negatively the overall filtration efficiency of the full filtration system.

Of note, the Road phase displays reduced filtration efficiency of the CC filter at 20°C compared to -10°C, but the PN release due to combustion is retained by the tailpipe filter and does not significantly impact the overall filtration efficiency. Please also note that some FE results are above 99.995% and are displayed as 100.00% on graphics.

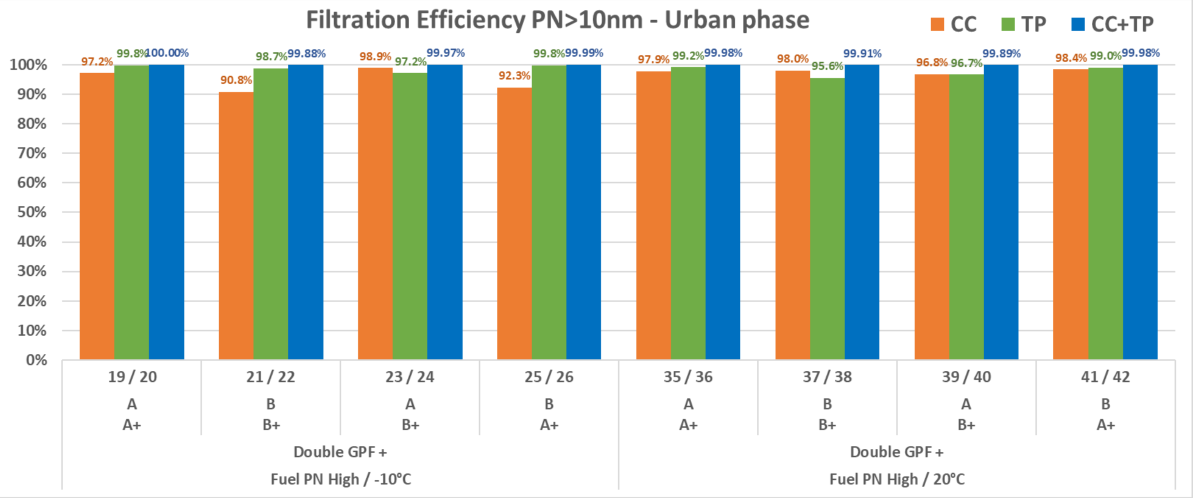

**Fig. 15.** PN10 FE for Double GPF+ combinations with Fuel PN High at -10°C and 20°C – Urban phase

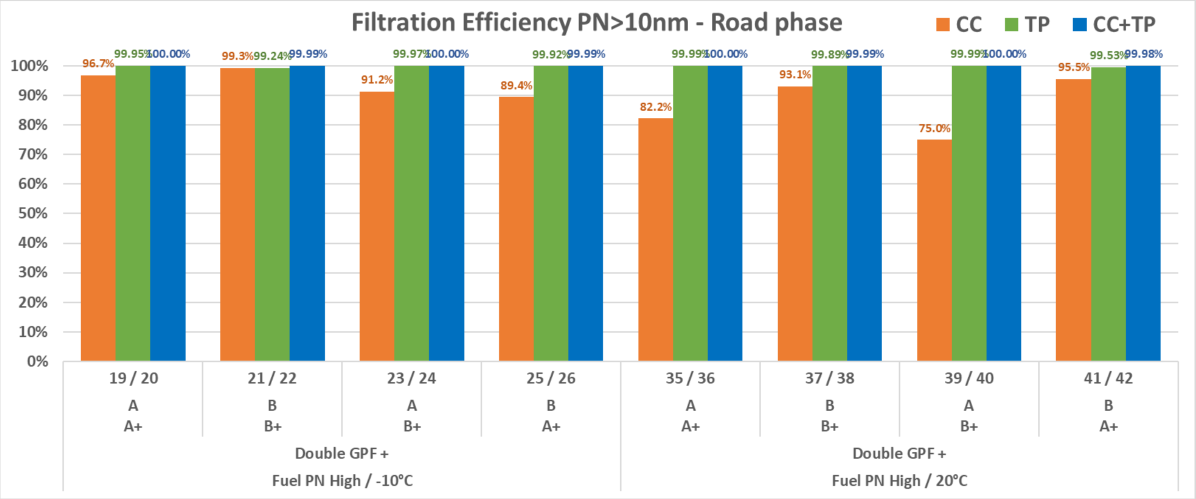

**Fig. 16.** PN10 FE for Double GPF+ combinations with Fuel PN High at -10°C and 20°C – Road phase

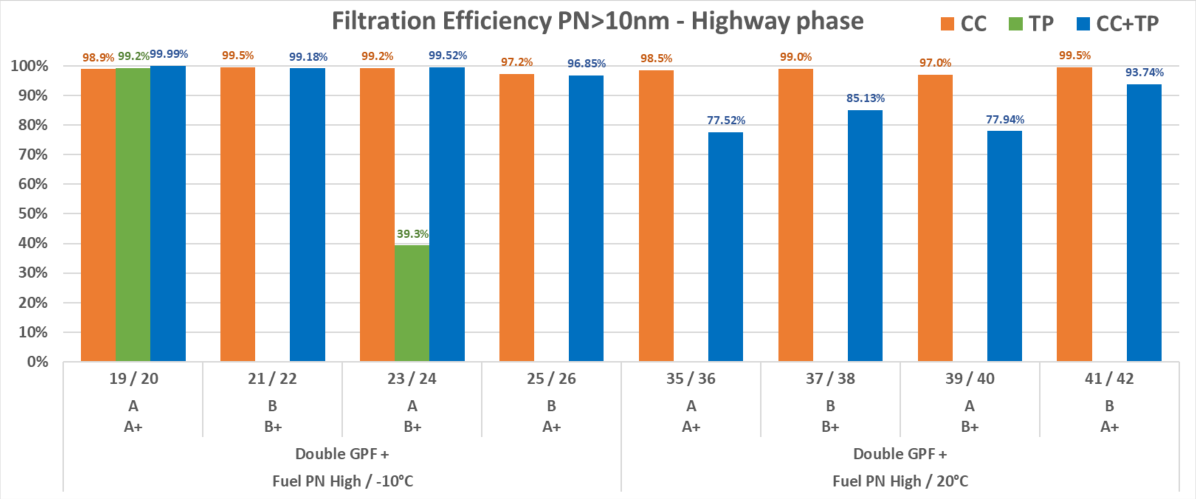

**Fig. 17.** PN10 FE for Double GPF+ combinations with Fuel PN High at -10°C and 20°C – Highway phase

A higher test temperature thus appears to negatively impact FE results primarily insofar as it facilitates soot combustion at the TP filter, despite lower engine-out emissions.

### *3.1.4 Impact of fuel*

Tests in Double GPF+ combinations (A or B as closed-coupled filter and A+ or B+ as tailpipe filter) at -10°C were also conducted with the PN Low fuel in order to compare with equivalent tests done with the reference PN High fuel. PN results in all positions are compared in **Fig. 18**, while FE results are in **Fig. 19**.

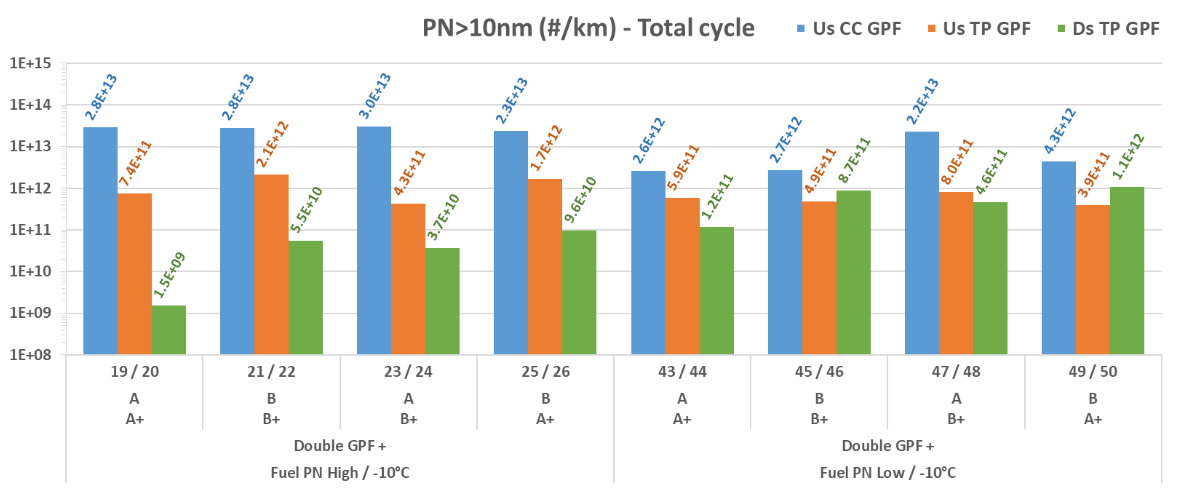

**Fig. 18.** PN10 levels for Double GPF+ combinations with Fuel PN High and Low at -10°C

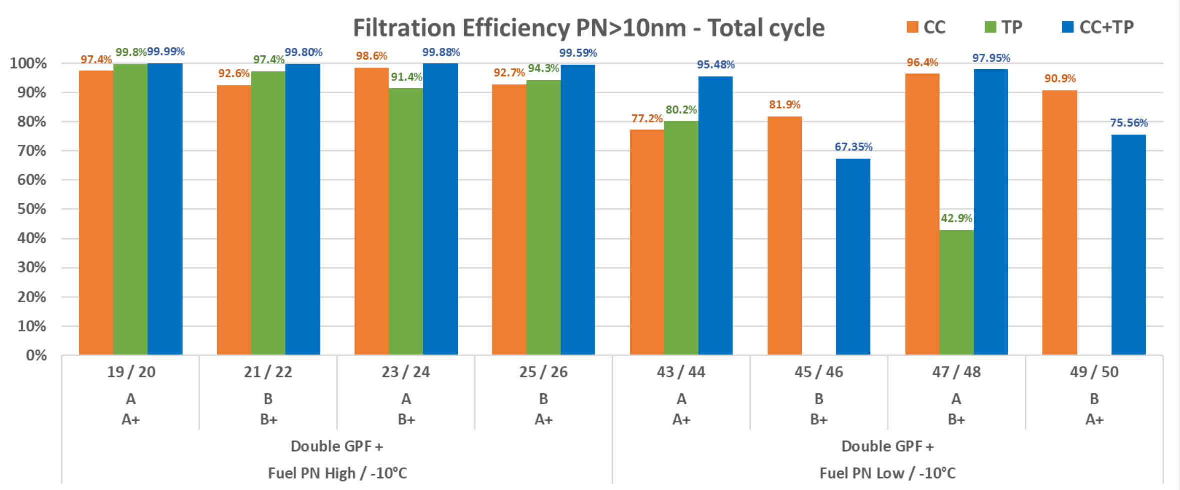

**Fig. 19.** Filtration efficiency for PN10 for Double GPF+ combinations with Fuel PN High and Low at -10°C

It is observed that PN levels are indeed lower at the engine out (by one order of magnitude approximately) when testing with the PN Low fuel. However, tailpipe levels are higher across all tests and the overall filtration efficiency is generally lowered using this fuel. **Fig. 20** shows engine-out PN10 sorted by size averaged over all tests, showing that the PN Low fuel is consistently producing lower PN levels compared to the PN High fuel, across the complete size spectrum, indicating that the effect observed is not due to a skewed PN spectrum distribution.

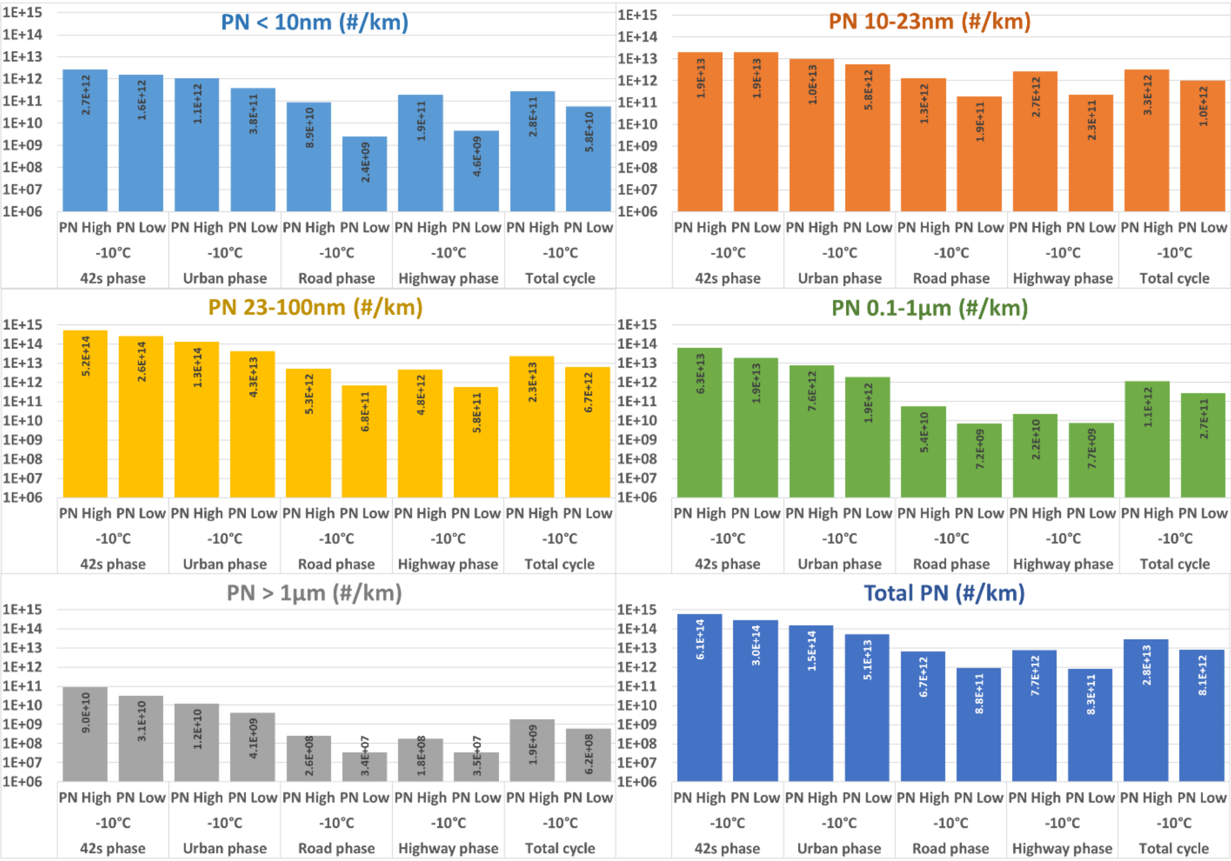

**Fig. 20.** Averaged engine-out PN10 spectrum with Fuel PN High and Low at -10°C

However, on all PN Low tests, more significant amounts of combustion are observed, as can be seen by looking at FE results for Road and Highway phases in **Fig. 21** and **Fig. 22** respectively. This hints at structurally differing particulates based on fuel formulation specifically. At this point, no analysis has been conducted on soot samples to confirm this hypothesis, as this would have required invasive procedures likely to damage the sample filters during the campaign.

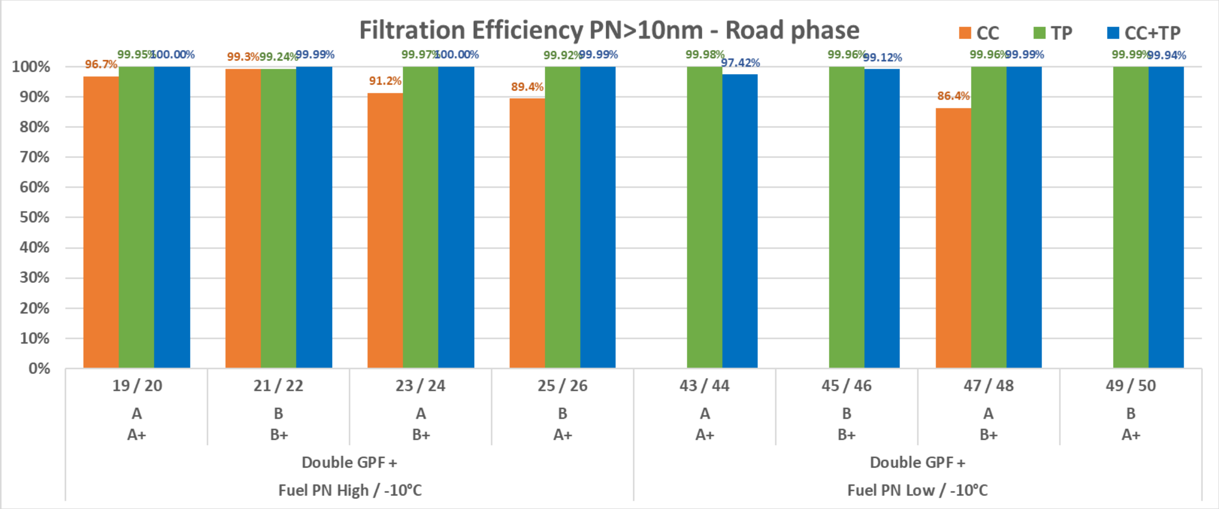

**Fig. 21.** FE for PN10 for Double GPF+ combinations with Fuel PN High and Low at -10°C – Road phase

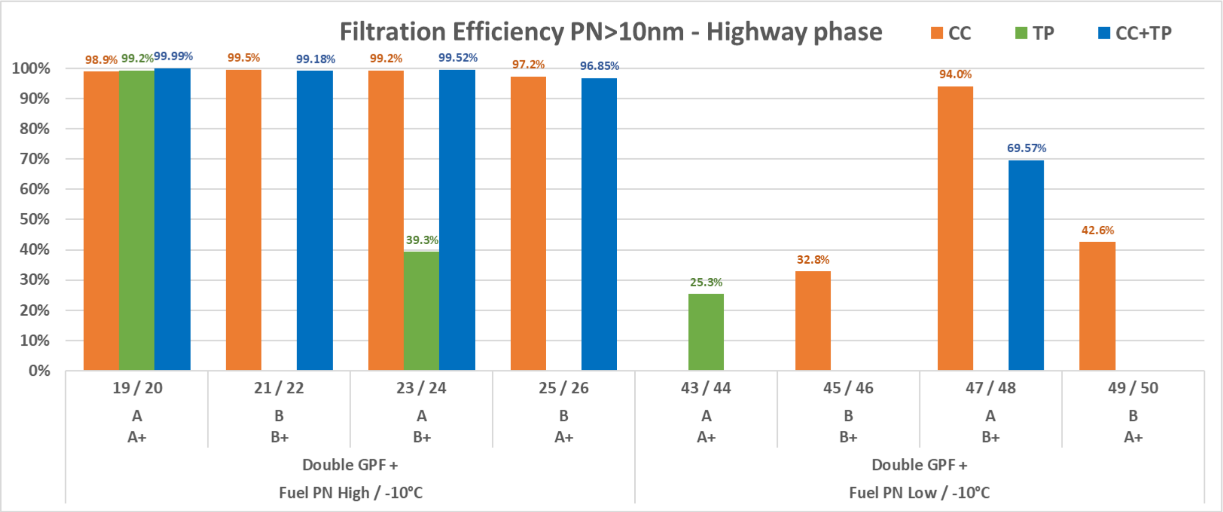

**Fig. 22.** FE for PN10 for Double GPF+ combinations with Fuel PN High and Low at -10°C – Highway phase

Concluding this section, the main hypothesis is that the formulation of the PN Low fuel has an impact on the particulates' composition and structure, and that these differences potentially reduce the soot regeneration temperature. As the formulation is in this case driven by the specific requirements from this specialty fuel (see 2.6; high distillation curve at 100°C and above, low FBP), this may not be an issue for more conventional fuels. Further testing could not be conducted with this fuel over the course of this campaign.

### *3.1.5 PN nucleation phenomenon*

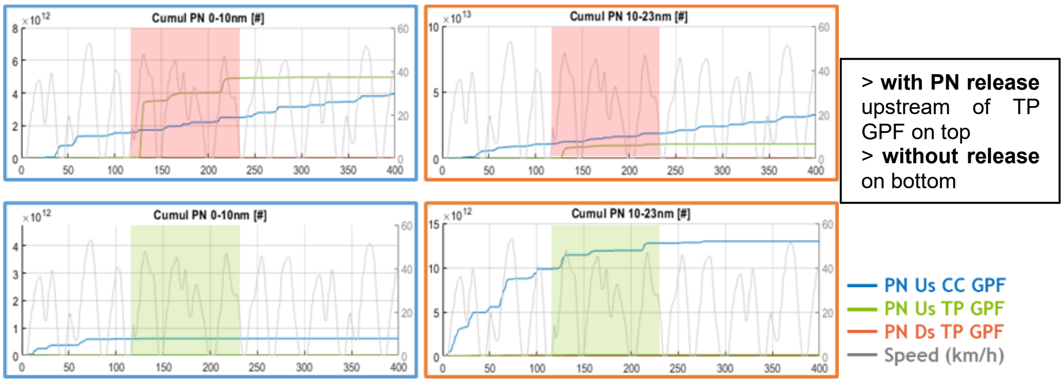

**Fig. 23.** Cumulative PN over time for 2 tests, showing a case of PN release in-between both GPF

Over the course of engine bench testing, some events were observed during which PN of sizes 0 to 23nm appears to be released from the CC GPF at the beginning of the Urban phase (120 to 220s approximately; see **Fig. 23** for examples). These release peaks are not synchronized with inlet peaks and thus do not appear to be linked with a decreased FE at the start of the cycle after regeneration. However, they are highly dependent on fuel and ambient temperature.

Temperatures at the CC GPF are displayed on **Fig. 24** in the bottom graph, with highlights corresponding to the PN release spikes shown on the top graph. Given the temperatures observed coupled with NMHC measurements shown in **Fig. 25** and **Fig. 26** (with coloring based on observed PN release), the most likely explanation is as follows:

- HC condensation: some HC slipping through the TWC at cold-start (based on fuel composition and test temperature) condensates in the GPF.
- Release: HC is released when GPF temperature reaches approximately 350°C.
- Nucleation: additional small-size PN is generated downstream the CC GPF and trapped by the TP GPF.

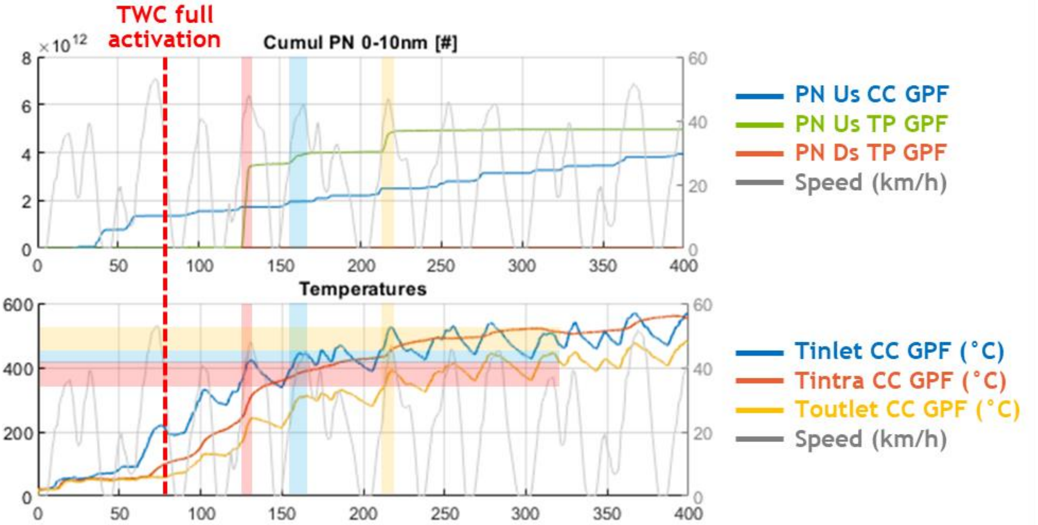

**Fig. 24.** Cumulative PN and temperature over time for a test, displaying a case of PN release; highlights on temperature spikes corresponding to PN spikes downstream of the CC GPF

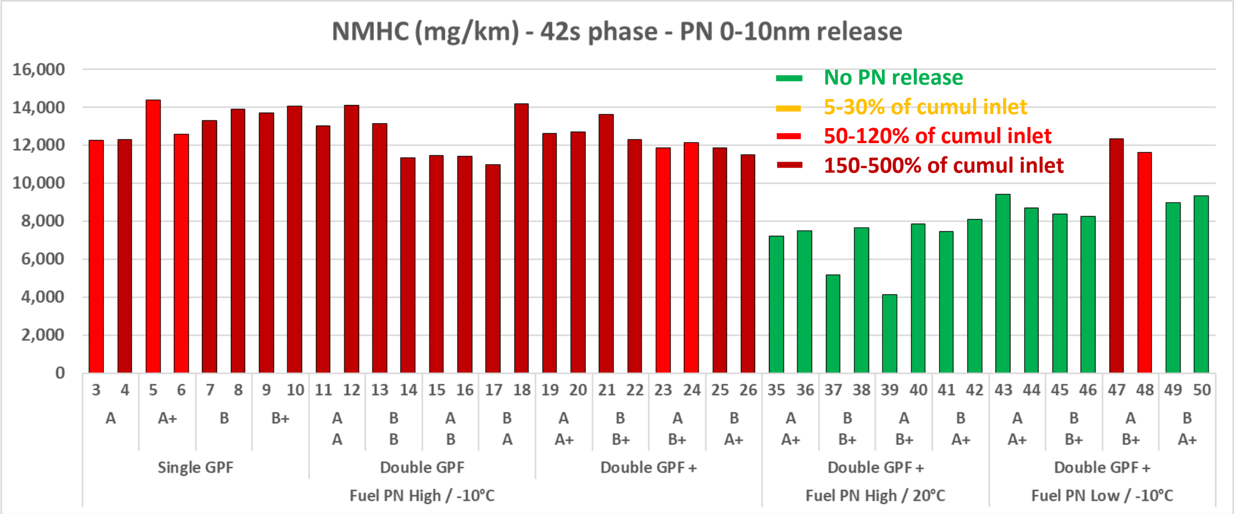

**Fig. 25.** NMHC on 42s phase for all tests, colored by amount of PN released after CC GPF for PN 0-10nm

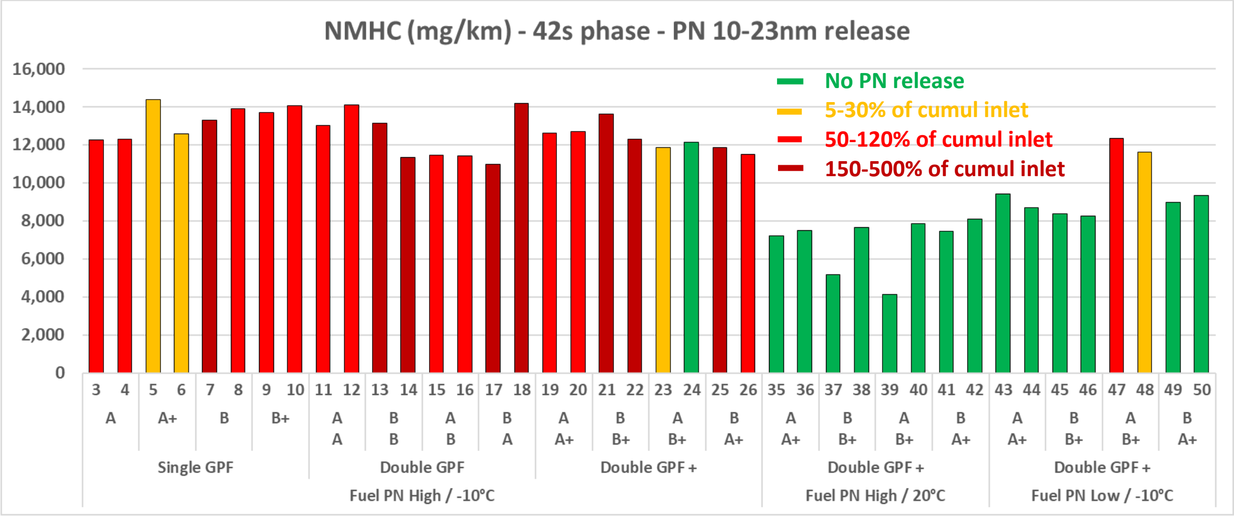

**Fig. 26.** NMHC on 42s phase for all tests, colored by amount of PN released after CC GPF for PN 10-23nm

NMHC emissions at startup thus appear strongly correlated with this phenomenon in cold start conditions. However, this release does not significantly affect global FE in configurations using two GPF, as it is captured by the tailpipe GPF.

### *3.1.6 Optimal technology*

Based on these results, no individual GPF technology appears to perform significantly better with regards to filtration efficiency in a double GPF installation, although some more differences are noted either at 20°C or with a low PN fuel. The most optimal configuration from a FE standpoint appears to be using the GPF sample **A in close-coupled** position combined with the GPF sample **A+ in tailpipe position**.

It is noted that soot burning events on the tailpipe GPF reduce this efficiency significantly, and a validation on vehicle with representative thermal behavior is thus desirable. It is also important to evaluate the impact of additional backpressure on engine performance, which could not be measured with the engine bench setup used.

## 3.2 Vehicle testing

Since passive regeneration of the tailpipe GPF is a rare case in engine bench testing presented in 3.1 due to there being a single regeneration window, and since the test setup is not representative of the tailpipe GPF aerothermal behavior and backpressure (see engine bench conditions described in 2.3), further testing on vehicle is necessary to investigate conditions at the tailpipe GPF and general efficiency of the system. These tests were run in the conditions described in 2.5. Tests were conducted with the vehicle using its factory GPF combined with the A+ GPF installed in a tailpipe position at the back, and all performed with the E10 CERT fuel as described in 2.2.

Types of tests included WLTC and RDE cycles on chassis dyno as well as RDE and Rouen-Paris trips on the open road.

The test matrix is shown in **Table 4**.

**Table 4.** Vehicle test matrix

| Test medium | Test N° | Cycle | GPF CC | GPF TP |
|---|---|---|---|---|
| Chassis Dyno | 1 / 2 | WLTC | Series | - |
| | 3 / 4 | RDE RTS95 | | |
| | 5 / 6 | WLTC | Series | A+ |
| | 7 / 8 | RDE RTS95 | | |
| Open Road | 9 / 10 | RDE CERTAM | Series | A+ |
| | 11 / 12 /13 / 14 | Rouen-Paris | | |

For the sake of analysis and comparison with other tests in the campaign, the WLTC cycle is split into 3 phases rather than the usual 4. The Urban phase as considered for analysis runs from 0 to 590s while the Road phase runs from there until the start of the usual WLTC Extra High phase, which itself constitutes the Highway phase. As a reminder, all cycles are capped at 110 km/h due to safety limitations of the recording trailer. Consequently, chassis dynamometer cycles are displayed in **Fig. 27** with this limitation as well as the specific phase division.

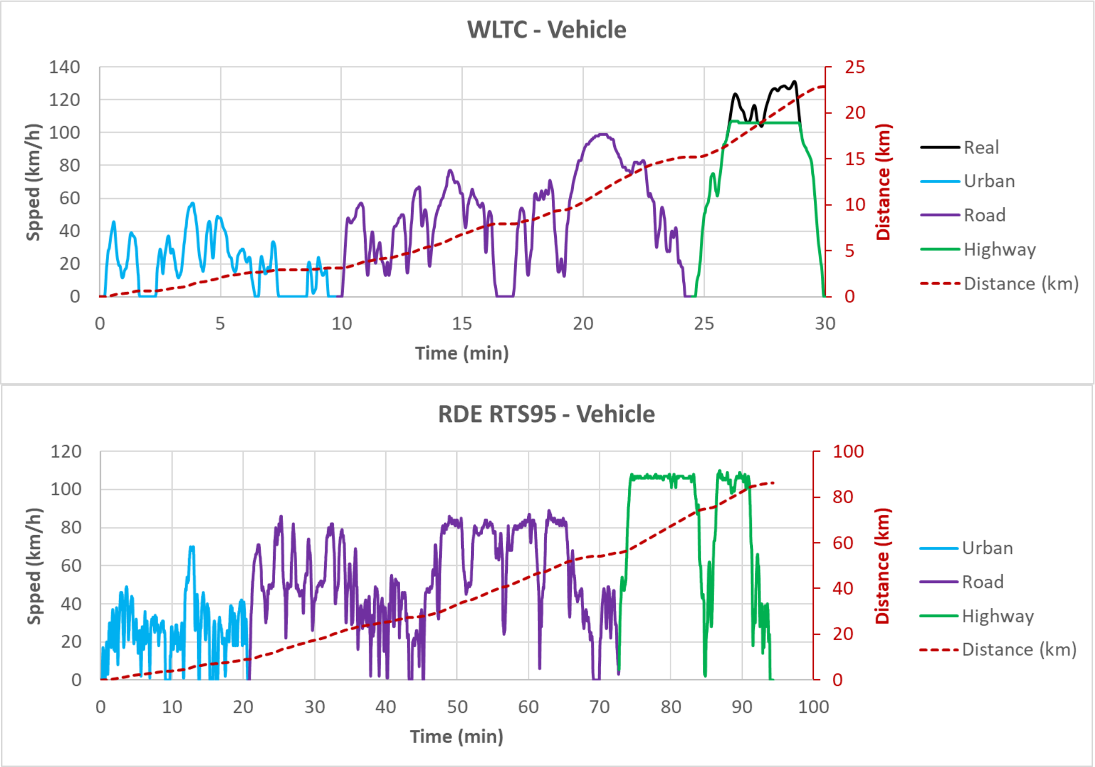

**Fig. 27.** Chassis dynamometer cycle traces with 110km/h speed limitation and specific

Road tests consist of a compliant RDE cycle around CERTAM facilities (86km, 33% urban, 33% rural, 33% motorway; **Fig. 28**), as well as a 270km-long trip from Rouen to Paris and back (**Fig. 29**).

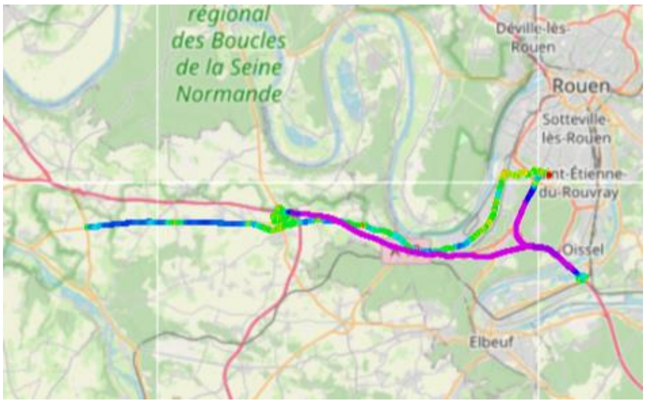
régional
des Boucles
de la Seine
Normande
Déville-lès-Rouen
Rouen
Sotteville-lès-Rouen
Saint-Étienne-du-Rouvray
Oissel
Elbeuf

**Fig. 28**. Road RDE route (source: CERTAM)

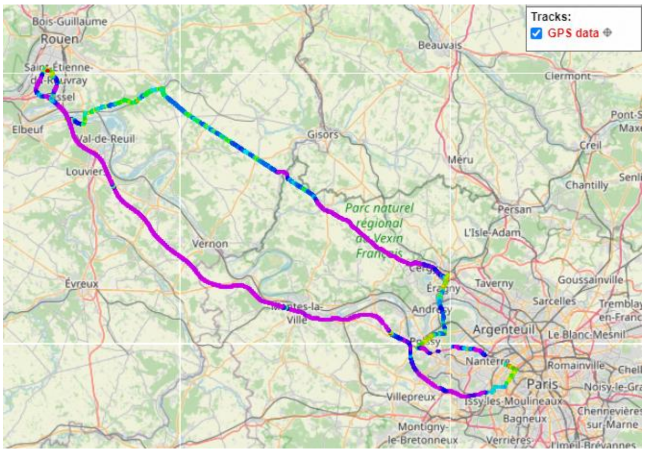
Tracks:
☑ GPS data
Bois-Guillaume
Rouen
Saint-Étienne-du-Rouvray
Oissel
Elbeuf
Val-de-Reuil
Louviers
Beauvais
Clermont
Gisors
Méru
Creil
Chantilly
Persan
L'Isle-Adam
Parc naturel régional du Vexin Français
Vernon
Évreux
Mantes-la-Ville
Cergy
Éragny
Andrésy
Taverny
Sarcelles
Goussainville
Argenteuil
Le Blanc-Mesnil
Poissy
Nanterre
Romainville
Paris
Villepreux
Issy-les-Moulineaux
Bagneux
Montigny-le-Bretonneux
Verrières

**Fig. 29.** Rouen-Paris route (source: CERTAM)

### *3.2.1 Chassis Dynamometer validation and backpressure*

As the test vehicle was not instrumented for measurement of the full exhaust line backpressure, a direct evaluation of backpressures with and without TP GPF could not be carried out. In any case, such measurement would not have been representative of a production-ready solution anyways since the installation of the TP GPF was further out than could be expected, after the unmodified mufflers of the vehicle.

Nonetheless, the vehicle was able to comply with the RDE RTS 95 speed trace and acceleration levels with the added inertia of the measurement trailer, which indicates no major adverse effect on engine power.

Furthermore, Chassis Dynamometer tests were analyzed for fuel consumption in realistic conditions to evaluate any potential impact of backpressure (as a reminder, backpressure was regulated at a fixed value for the engine bench campaign, see 2.3). $CO_2$ results for CD tests are displayed in **Fig. 30**.

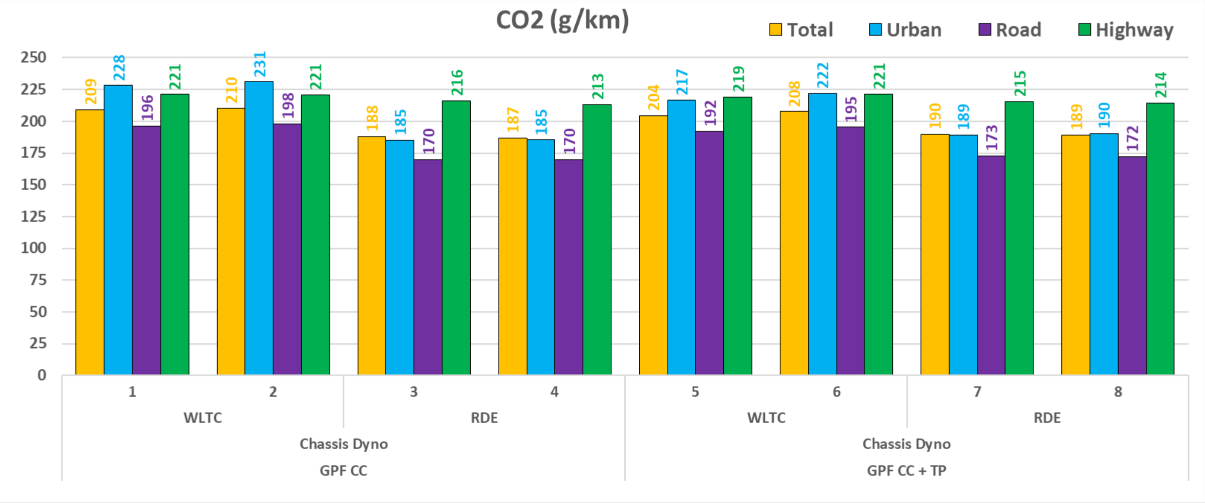

**Fig. 30.** CO2 emissions on chassis dynamometer tests by phase

The results indicate that no increase in fuel consumption was observed using the double GPF setup on vehicle over the course of one cycle. Other gaseous pollutants display no adverse effect from this setup but are not the focus of this article and will not be presented.

### *3.2.2 Overall results on vehicle*

To begin with results analysis, tailpipe GPF temperatures were measured on vehicle tests in order to evaluate the risk of soot burning occurrences. These temperatures are displayed in **Fig. 31** and show that no significant passive regeneration should occur at the tailpipe GPF since temperatures only reach 400°C in this location at the maximum, despite the heavy load incurred by the trailer.

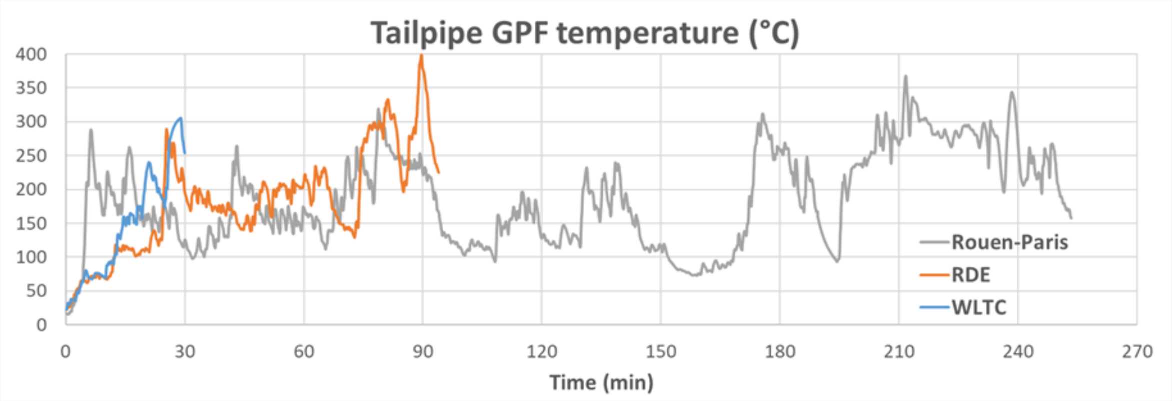

**Fig. 31.** Tailpipe GPF temperatures on vehicle tests

PN results are shown for all vehicle tests in **Fig. 32**, with spectrum in **Fig 33**, both for tailpipe emissions and for PN as measured in the air intake of the engine, upstream of the air filter. Of note, Double GPF tests display consistent tailpipe emission levels between chassis dyno and open road conditions. On the other hand, chassis dyno tests always have significantly lower ambient PN levels than road tests due to the dynamometer facility's Heating Ventilation and Air Conditioning (HVAC) filtering systems. Road tests are showing lower averaged levels of particulates number at the tailpipe compared to ambient ones whatever the cycles.

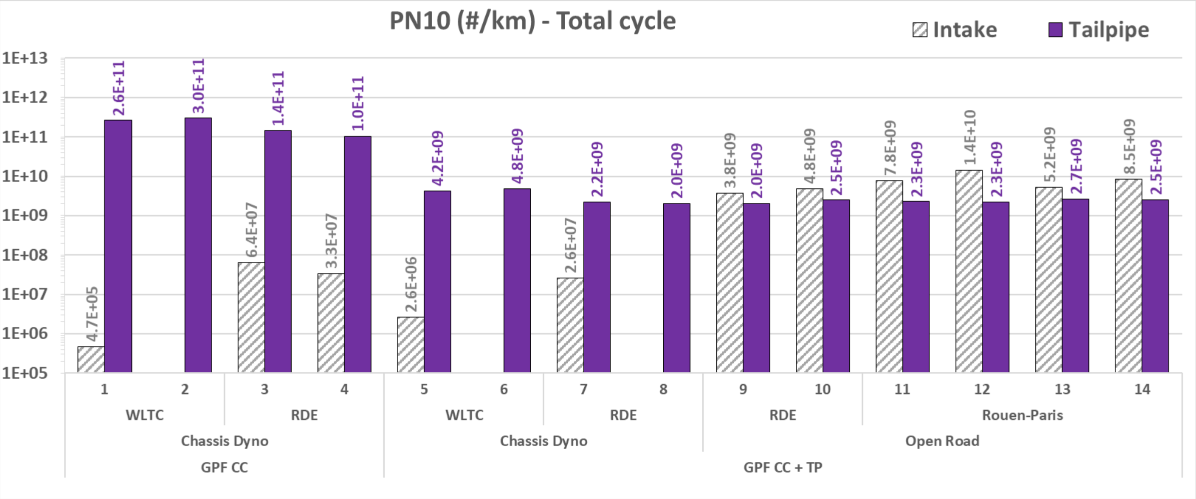

**Fig. 32.** Ambient and Tailpipe PN10 levels for vehicle tests

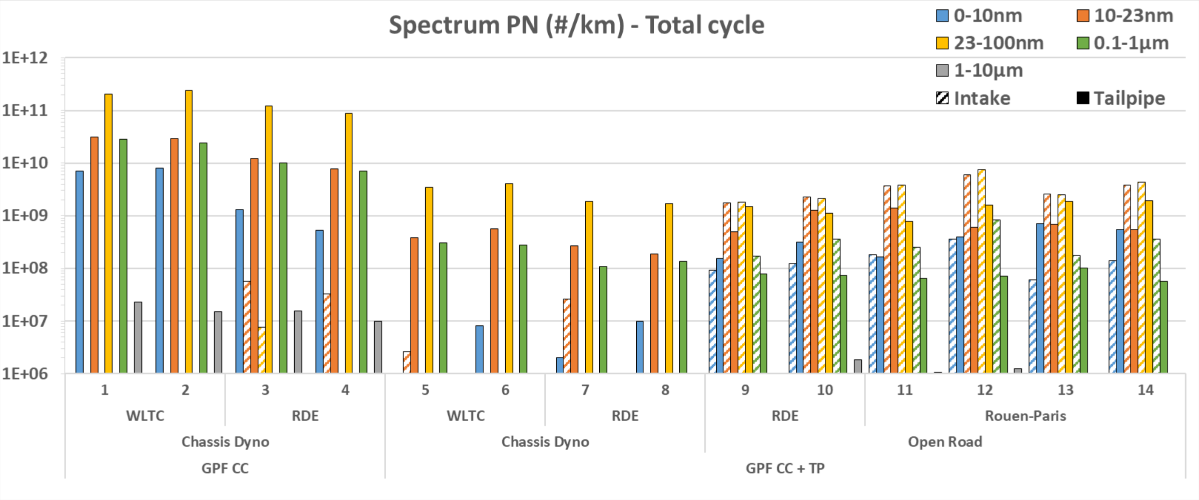

**Fig 33.** Spectrum of ambient and tailpipe PN levels for vehicle tests

Due to the limitations of the testing setup (no possibility to carry intermediate ELPIs to measure PN concentrations upstream of the CC GPF or in between the 2 GPF), a direct FE measurement cannot be performed. However, using a comparison of equivalent Single and Double GPF tests, an estimation of the FE of the tailpipe GPF can be made. This estimation is displayed in **Fig. 34** and shows that the tailpipe GPF alone consistently reaches above 97% FE for PN on most phases and sizes, which is consistent with observations on engine bench.

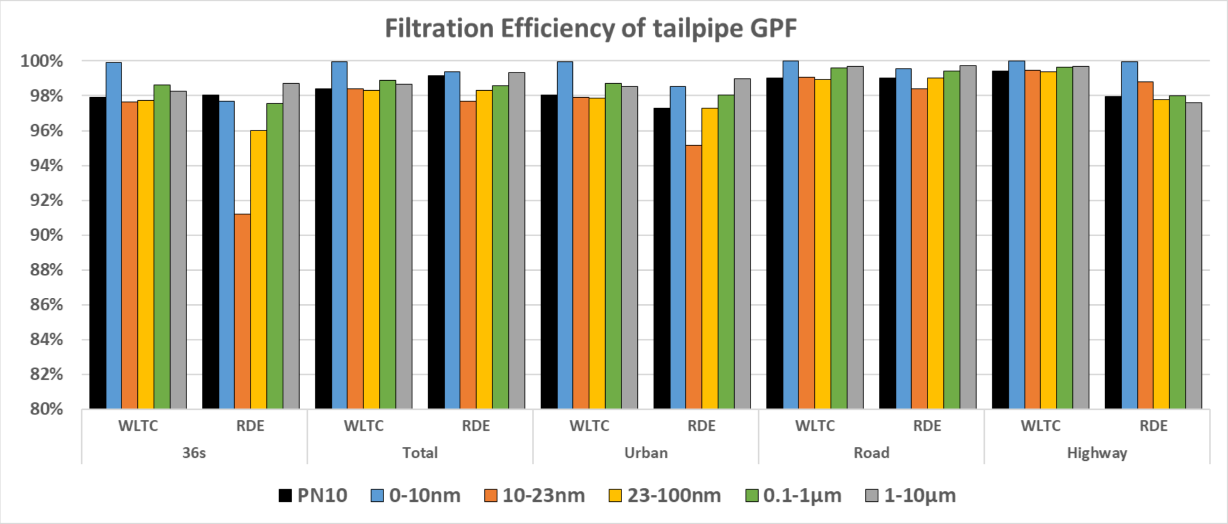

**Fig. 34.** FE estimation of tailpipe GPF in vehicle tests, by spectrum

In **Fig. 35**, PN10 results have been displayed per road segment of the Rouen-Paris route, for each of the four trips performed on this route. It is to be noted that ambient PN10 levels display a high variance. Despite this, all segments except the cold-start segment in two out of the four and one segment of A15 s13 – N184 exhibit lower PN10 levels at the tailpipe compared to ambient levels. In all, 94% of the segments exhibit lower tailpipe PN10 levels compared to ambient ones.

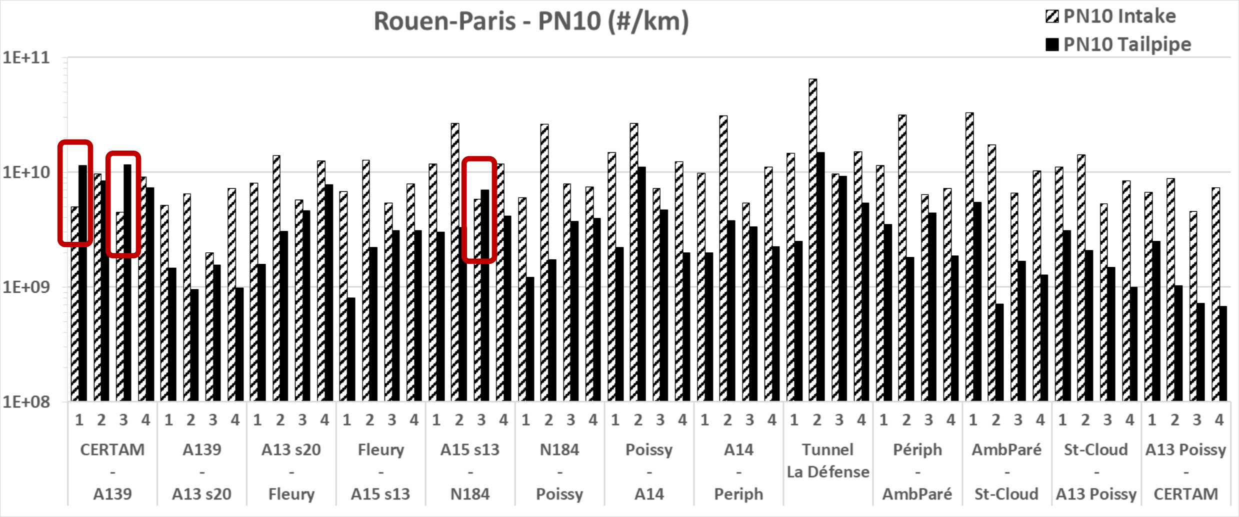

**Fig. 35.** Ambient and Tailpipe PN10 levels for Rouen-Paris tests, by road segment

These results confirm observations from engine bench testing: in the absence of conditions suitable for the regeneration of the tailpipe filter, the FE of the Double GPF system is very high, allowing for consistently lower-than-ambient PN levels at the tailpipe of the vehicle.

## Conclusions

As a conclusion, after displaying encouraging baseline results obtained on engine bench showing that the serial mounting of two GPF could significantly improve the Filtration Efficiency of the particulate filtration system (above 99.5% for reference cases for all filter technologies), the road testing achieved consistently lower averaged tailpipe particulate concentrations compared to ambient ones. For road segments, 49 over 52 segments have lower tailpipe PN emission compared to ambient ones showing the benefit of Double GPF technology. Over the course of this study, some noteworthy points were observed.

First, it seems that the system consistently allows for lower-than-ambient PN levels out of the vehicle tailpipe as long as regeneration events are avoided at the tailpipe filter, as these may be source of additional PN release events. Tests with higher ambient temperatures illustrated this fact by displaying lower FE compared to base cases due to regenerations on highway.

Second, variations in results were observed based on test temperature and fuel which are not attributable to the non-representative aerothermal behavior: notably, increased regeneration occurrences were noted on a low PN fuel despite the exhaust temperatures being generally slightly lower. This in turn led to a decrease in FE and even cases of increased PN emissions at the tailpipe despite lower emissions from the engine. Further investigation into the soot composition could validate or not the hypothesis of particulate composition on the regeneration temperature. However, in the context of a vehicle installation, this is not likely to constitute a development hurdle as tailpipe GPF temperatures were shown to be significantly lower still.

Furthermore, PN release events from the close-coupled GPF at the very beginning of some test cycles were shown to increase with ambient temperature and depending on fuel. A mechanism of TWC slippage, condensation and nucleation for these events has been proposed in the article and might be the subject of a further test campaign.

However, in view of an implementation on vehicle, this raises the question of whether the loading of this tailpipe GPF can become an issue (backpressure and thus fuel consumption), or if volume flow rate is low enough (due to temperature conditions) that it will not be an issue. In any case, further investigation into backpressure levels is required to better understand how a production-ready exhaust with double GPF would impact engine performance. If needed, the second GPF’s regeneration could be dealt with as part of the maintenance schedule given the relatively low particulate mass reaching it compared to what a single GPF would be exposed to. Other solutions could include fitting this tailpipe GPF in a controlled bypass to be able to control its regenerations and limit PN emission peaks, or even using an on-board ozone generator to trigger low-combustion speed, low-temperature regenerations when required. This would require further prototyping and investigation to evaluate the feasibility, controllability, and efficiency with regards to combustion and potential PN release.

Overall, vehicle results displayed in this article are nonetheless highly encouraging in the scope of the A-EAT project in order to provide an exhaust aftertreatment system able to reduce gaseous and particulate exhaust emissions beyond upcoming standards with the goal of contributing towards improving urban air quality.

## Acknowledgement

The authors would like to thank NGK and Corning for providing test samples, as well as HORSE for their invaluable support on the A-EAT project.

HORSE is a global supplier of innovative power solutions. It believes that there is no one-size-fits-all solution to sustainable mobility and so is investing in technologies which will support the automotive industry, and other sectors requiring power generation, in their transition to a sustainable future. Inheriting decades of industrial know-how from Renault Group, HORSE develops, produces and supplies highly efficient full-hybrid, plug-in hybrid and internal combustion powertrains, and cutting-edge technologies (engines, gearboxes, full-hybrid and plug-in hybrid systems, and batteries).

Employing over 9,000 people in seven countries, it is headquartered in Madrid, Spain and has eight manufacturing plants and three R&D centers around the world (Argentina, in Córdoba; Brazil in Curitiba; Chile in Los Andes; Portugal in Aveiro; Romania in Bucharest, Mioveni and Titu; Spain in Seville and Valladolid, and Turkey in Bursa in partnership with Oyak).

## References

[1] Seinfeld, John H. and Spyros N. Pandis. Atmospheric Chemistry and Physics: From Air Pollution to Climate Change. Hoboken, N.J.: J. Wiley, 2006

[2] Gaffney, J.S.; Marley, N.A. The impacts of combustion emissions on air quality and climate—From coal to biofuels and beyond. Atmos. Environ. 2009, 43, 23–36

[3] Yim, S.H.; Barrett, S.R. Public health impacts of combustion emissions in the United Kingdom. Environ. Sci. Technol. 2012, 46, 4291–4296

[4] Préndez, M.; Nova, P.; Romero, H.; Mendes, F.; Fuentealba, R. Representativeness of the particulate matter pollution assessed by an official monitoring station of air quality in Santiago, Chile: Projection to human health. Environ. Geochem. Health 2023, 45, 2985–3001

[5] Megido, L.; Suárez-Peña, B.; Negral, L.; Castrillón, L.; Fernández-Nava, Y. Suburban air quality: Human health hazard assessment of potentially toxic elements in PM10. Chemosphere 2017, 177, 284–291

[6] Luo, Z.; Wang, Y.; Lv, Z.; He, T.; Zhao, J.; Wang, Y.; Gao, F.; Zhang, Z.; Liu, H. Impacts of vehicle emission on air quality and human health in China. Sci. Total Environ. 2022, 813, 152655

[7] An, F.; Sauer, A. Comparison of Passenger Vehicle Fuel Economy and Greenhouse Gas Emission Standards around the World; Pew Center on Global Climate Change: 2004; Volume 25. Available online: https://www.c2es.org/wp-content/uploads/2004/12/comparison-passenger-vehicle-fuel-economy-ghg-emission-standards-around-world.pdf

[8] Li, X.; Nam, K.-M. Environmental regulations as industrial policy: Vehicle emission standards and automotive industry performance. Environ. Sci. Policy 2022, 131, 68–83

[9] De Prez, Matt (19 December 2023). "EU strikes provisional deal over Euro 7 emissions limits". Fleet News. UK. Retrieved 22 December 2023

[10] Cohen, A.J.; Anderson, H.R.; Ostro, B.; Pandey, K.D.; Krzyzanowski, M.; Künzli, N.; Gutschmidt, K.; Pope, C.A., III; Romieu, I.; Samet, J.M. Urban air pollution. Comp. Quantif. Health Risks Glob. Reg. Burd. Dis. Attrib. Sel. Major Risk Factors 2004, 2, 1353–1433

[11] Cruz, I.S.; Katz-Gerro, T. Urban public transport companies and strategies to promote sustainable consumption practices. J. Clean. Prod. 2016, 123, 28–33

[12] Gendron-Carrier, N.; Gonzalez-Navarro, M.; Polloni, S.; Turner, M.A. Subways and urban air pollution. Am. Econ. J. Appl. Econ. 2022, 14, 164–196

[13] Citepa, June 23. Inventaire Des Émissions de Polluants Atmosphériques et de Gaz à Effet de Serre En France—Format Secten. Available online: https://www.citepa.org/wp-content/uploads/publications/secten/2023/Citepa_Secten_ed2023_v1.pdf

[14] Platt, S.M.; El Haddad, I.; Pieber, S.M.; Zardini, A.A.; Suarez-Bertoa, R.; Clairotte, M.; Daellenbach, K.R.; Huang, R.-J.; Slowik, J.G.; Hellebust, S.; et al. Gasoline Cars Produce More Carbonaceous Particulate Matter than Modern Filter-Equipped Diesel Cars. Sci. Rep. 2017, 7, 4926

[15] Giechaskiel, B.; Joshi, A.; Ntziachristos, L.; Dilara, P. European Regulatory Framework and Particulate Matter Emissions of Gasoline Light-Duty Vehicles: A Review. Catalysts 2019, 9, 586

[16] Kostenidou, E.; Martinez-Valiente, A.; R'Mili, B.; Marques, B.; Temime-Roussel, B.; Durand, A.; André, M.; Liu, Y.; Louis, C.; Vansevenant, B.; et al. Technical Note: Emission Factors, Chemical Composition, and Morphology of Particles Emitted from Euro 5 Diesel and Gasoline Light-Duty Vehicles during Transient Cycles. Atmos. Chem. Phys. 2021, 21, 4779–4796

[17] Guan, B.; Zhan, R.; Lin, H.; Huang, Z. Review of the state-of-the-art of exhaust particulate filter technology in internal combustion engines. J. Environ. Manag. 2015, 154, 225–258

[18] Khair, M.K. A Review of Diesel Particulate Filter Technologies. 2003. Available online: https://www.sae.org/publications/technical-papers/content/2003-01-2303/

[19] Stamatellou, A.-M.; Stamatelos, A. Overview of Diesel particulate filter systems sizing approaches. Appl. Therm. Eng. 2017, 121, 537–546

[20] Samaras, Z.; Rieker, M.; Papaioannou, E.; van Dorp, W.; Kousoulidou, M.; Ntziachristos, L.; Andersson, J.; Bergmann, A.; Hausberger, S.; Keskinen, J. Perspectives for regulating 10 nm particle number emissions based on novel measurement methodologies. J. Aerosol Sci. 2022, 162, 105957

[21] Philippe Jacqué, "Pollution : après le diesel, les moteurs à essence au cœur d'une nouvelle bataille européenne" [archive], Le Monde, 26 octobre 2016

[22] Tandon, P.; Heibel, A.; Whitmore, J.; Kekre, N.; Chithapragada, K. Measurement and prediction of filtration efficiency evolution of soot loaded diesel particulate filters. Chem. Eng. Sci. 2010, 65, 4751–4760

[23] Zhong, D.; He, S.; Tandon, P.; Moreno, M.; Boger, T. Measurement and Prediction of Filtration Efficiency Evolution of Soot Loaded Diesel Particulate Filters. SAE 2012-01-0363

[24] Joshi, A.; Johnson, T.V. Gasoline particulate filters—A review. Emiss. Control Sci. Technol. 2018, 4, 219–239

[25] Ravi, S.S.; Osipov, S.; Turner, J.W.G. Impact of Modern Vehicular Technologies and Emission Regulations on Improving Global Air Quality. Atmosphere 2023, 14, 1164

[26] AECC, PDF "GASOLINE PARTICULATE FILTER (GPF) How can the GPF cut emissions of ultrafine particles from gasoline engines?" November 2017

[27] Saito, C.; Nakatani, T.; Miyairi, Y.; Yuuki, K.; Makino, M.; Kurachi, H.; Heuss, W.; Kuki, T.; Furuta, Y.; Kattouah, P.; Vogt, C. New particulate filter concept to reduce particle number emissions. SAE 2011-01-0814

[28] Ito, Y.; Shimoda, T.; Aoki, T.; Yuuki, K.; Sakamoto, H.; Kato, K.; Thier, D.; Kattouah, P.; Ohara, E.; Vogt, C. Next generation of ceramic wall flow gasoline particulate filter with integrated three way catalyst. SAE 2015-01-1073

[29] Richter, J.M.; Klingmann, R.; Spiess, S.; Wong, K.-F. Application of catalyzed gasoline particulate filters to GDI vehicles. SAE 2012-01-1244

[30] Spiess, S.; Wong, K.F.; Richter, J.M.; Klingmann, R. Investigations of emission control systems for gasoline direct injection engines with a focus on removal of particulate emissions. Top. Catal. 2013, 56, 434–439

[31] Czerwinski, J.; Comte, P.; Heeb, N.; Mayer, A. Nanoparticle Emissions of DI Gasoline Cars with/without GPF. SAE 2017-01-1004

[32] Chan, T.W., Saffaripour, M., Liu, F. et al. Characterization of Real-Time Particle Emissions from a Gasoline Direct Injection Vehicle Equipped with a Catalyzed Gasoline Particulate Filter During Filter Regeneration. Emiss. Control Sci. Technol. 2, 75–88 (2016)

[33] Zhongwei Meng, Zhao Chen, Jie Tan, Wei Wang, Zhilin Zhang, Junfeng Huang, Jia Fang, Regeneration performance and particulate emission characteristics during active regeneration process of GPF with ash loading, Chemical Engineering Science, Vol. 248, Part A, 2022, 117114, ISSN 0009-2509

[34] Mehsein, K., Norsic, C., Chaillou, C., Nicolle, A., Minimizing secondary pollutant formation through identification of most influential volatile emissions in gasoline exhausts: Impact of the vehicle powertrain technology. Atmospheric Environment, Vol. 226, 2020,117394, ISSN 1352-2310

[35] Zhu, R., Hu, J., Bao, X., He, L., Zu, L., Effects of aromatics, olefins and distillation temperatures (T50 & T90) on particle mass and number emissions from gasoline direct injection (GDI) vehicles, Energy Policy, Vol. 101, 2017, p. 185-193, ISSN 0301-4215

[36] Yao, C., Dou, Z., Wang, B., Liu, M., Lu, H., Feng, J., Feng, L., Experimental study of the effect of heavy aromatics on the characteristics of combustion and ultrafine particle in DISI engine, Fuel, Vol. 203, 2017, p. 290-297, ISSN 0016-2361,

# Development of a CFD Predictive Methodology for Urea Deposit Risk Assessment

S. Andreoli[1], A. Gallo[1], S. Langridge[2] and R. Schlegel[2]

[1]FPT Industrial S.P.A., Via Puglia 15, 10156 Turin, Italy
[2]FPT Motorenforschung AG, Schlossgasse 2, CH-9320 Arbon, Switzerland

E-mail: alessandro.gallo2@ivecogroup.com
Telephone: --

## Abstract

This article focuses the attention on the approach and methodology to predict the risk of deposits created within an advanced exhaust after-treatment system (ATS) in the automotive field such as Selective Catalytic Reduction (SCR) with urea injection to decrease the emission of pollutants.

The simulation methodologies need to describe the UWS (urea water solution) conversion into ammonia, its mixing with exhaust gases and the possible formation of harmful solid deposits due to incomplete decomposition. Predictive simulations can help to meet the upcoming EU emission regulations in a cost-effective manner, saving time and providing precise results following the industry pace.

The work is carried out with the purpose of developing and validating, using the CFD software CONVERGE, a 3D-CFD methodology which assesses a deposit risk index able to identify the areas of the system where urea deposit formation is expected.

The ATS system used for this study is from off-road applications composed by a diesel oxidation catalyst (DOC) followed by a urea vaporization module (UVM), a UWS injector and four SCR on-filter (SCRoF).

The performance of the ATS system is evaluated in terms of UWS spray modelling, liquid film development, wall temperature and spray-impinged surfaces. The conjugate heat transfer (CHT) approach is used to analyze droplet impingement on walls in detail. Moreover, fixed flow and super-cycling techniques are implemented to accelerate film deposition and to simulate larger physical times in reasonable computational times.

An in-depth sensitivity analysis was conducted on injector modelling, droplet motion and deposit risk index calibration.

The 3D thermal maps, deposit risk index results and deposits' location obtained from the simulations are compared with experimental measurements over five different engine operating points showing reasonable matching.

## 1. Introduction

EU has introduced European Emission Standards, which are legislations imposed on vehicles for coping with the increasing environmental pollution; these standards are defined in a series of European directives, which have become progressively more and more stringent [1].

The Diesel after-treatment system (ATS) structure considered in this work includes three main components. The first two components are a Diesel Oxidation Catalyst (DOC) and a SCRoF (SCR on filter) that permitted to control NOx (nitrogen oxides) through the injection of a urea-water solution (UWS 32.5 wt.-% urea) commonly called AdBlue® or diesel exhaust fluid DEF and at the same time the PM (particulate matter or soot) emissions from diesel engines, on a single substrate [2].

The third component, not considered in this analysis, is a second SCR unit paired with a Clean Up Catalyst (CUC) to limit additional emissions. This approach will also see the introduction of multiple DEF dosing points to increase overall deNOx performance and ensure additional flexibility in the control of the system [2].

To ensure optimal performance of the SCR catalysts, it is crucial to complete the UWS thermolysis reaction within the mixing section of the exhaust system. Failure to achieve its complete decomposition can result in a cascade of undesirable secondary reactions, leading to the formation of solid byproducts like biuret, cyanuric acid or ammelide which can be formed from the liquid film on the walls of the exhaust system [3]. The presence of these solid deposits not only leads to the inefficient utilization of urea but also diminishes the catalyst conversion efficiency, increases back pressure, decreases ammonia uniformity and could potentially cause corrosion of stainless-steel components. Additionally, the deposits can adversely affect the development of the urea spray and the interaction between the spray and the mixing element, further compromising the effectiveness of the nitrogen oxides conversion process [4].

This work has the aim to provide an effective and useful Computational Fluid-Dynamics (CFD) methodology, which can correctly predict the risk of urea deposits generation on the inner walls and mixer surfaces of complex ATS system geometries. Developing a functional predictive methodology can help meet the upcoming emission regulations cost-effectively, thus saving time, and providing more quickly correct results on complex geometry designs [5].

Obtained results must be detailed to predict where the deposits would form and fast enough to follow the design pace. Urea deposit creation is a crucial challenge regarding Diesel exhaust after-treatment systems: producers have ways of dealing with this problem, but currently there is no real solution [4].

The methodology developed in this research will be validated on a complex ATS system designed for off-road applications, using the CONVERGE CFD software.

The study's main objective is to accurately model the UWS spray, liquid film development, wall temperature, and surface impingement to replicate experimental conditions in a simulation environment with high fidelity.

The data collected from the simulation will be compared with experimental measurements taken from five different engine operating points to ensure that the 3D-CFD methodology produces deposits' locations results that are consistent with the experiments.

## 2. Experimental setup: engine test setup

This research concerns the UWS deposit risk evaluation performed on the ATS system adopted in conjunction with an engine for off-road applications.

The engine's primary application is in the agricultural sector powering vehicles such as 4WD tractors, forage harvesters and combines, which need high power and torque values. It is equipped with a high-efficiency SCR exhaust gas aftertreatment system. The layout, depicted schematically in **Fig. 1**, provides that the exhaust gas enters the ATS system from the inlet pipe and then goes through the DOC, the flow is then accelerated by the swirler mounted on the top of the mixer unit (this process is crucial to obtain the proper conditions to inject the UWS spray). The swirled flow can increase the speed of the injected droplets and helps mix them with the exhaust gas, assuring a high efficiency of the system. The mixing of the spray with the flow happens in the inner chamber of the mixer, which is equipped on the outer side with heat exchanger fins. The drops will impact mainly on the walls of this internal part, leading to large temperature drops, deposition of film and, eventually, nucleation of urea deposits.

The flow then passes in the terminal drilled part of the mixer, which permits the exhaust gas mixed with the urea drops to go through the four SCRoF units mounted in the system, capable of enhancing soot oxidation and reduce NOx molecules. Each SCRoF is then followed by an additional SCR combined with a CUC (Clean-Up Catalyst), whose aim is to prevent the unreacted ammonia from slipping from the catalyst and preventing additional undesirable emissions at the tailpipe. These last catalysts are not part of this work, as the computational domain considered ends at the SCRoF outlet.

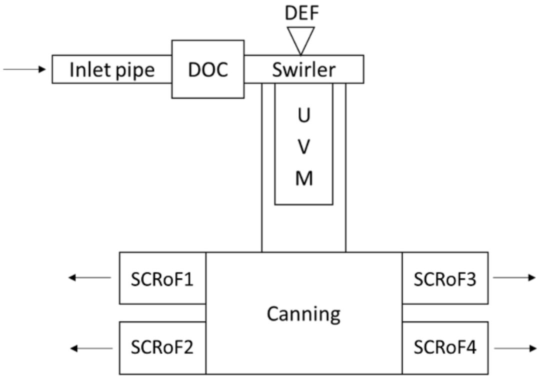

**Fig. 1.** Scheme of the ATS architecture considered in this research

This ATS configuration can greatly reduce the amount of NOx and PM ejected in the atmosphere, which constitutes the main issue with Diesel heavy-duty engines.

However, this system shows a weak point in case of high exhaust mass flow (at high engine speed) combined with high surface spray loading (SSL) of the impinged areas. In fact, in this condition, the spray is deflected towards the inner walls of the mixer by very high centrifugal forces, which are caused by the remarkable swirling effect obtained in the system at high engine speed. This process leads to high film deposition on the walls and to an eventual urea deposit creation, which could lead to considerable drawbacks in DeNOx performance and overall efficiency of the ATS system.

This phenomenon is very difficult to predict efficiently due to the high cost and the long time required for performing detailed experimental measurements in each critical engine operating point. Furthermore, the urea deposit phenomena involve a complex series of chemical reactions that can occur in very different conditions, depending on various combinations of exhaust mass flow, the temperature of the ATS system, UWS dosing and SSL of the walls.

The most functional way to deal with this issue is to adopt the CFD approach: the goal is to obtain useful data performing cost and time-effective simulations, capable of modelling 3D sprays and fluid flows in virtually any condition or engine operating point in a very early phase of the design, thus eliminating the need of expensive test-bench experiments.

The experimental data used to validate this research are collected thanks to a dedicated experimental rig. The mixer unit used for the experiments is instrumented with a set of 36 thermocouples which are positioned at different points of the device giving the possibility of extrapolating a temperature map of the mixer walls necessary for the comparison between bench and simulation results, as shown in **Fig. 2**.

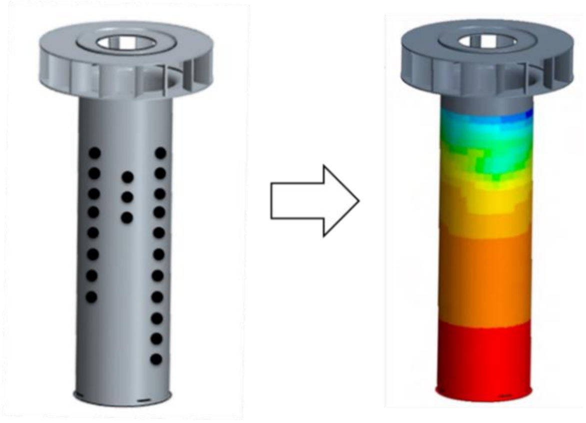

**Fig. 2.** Mixing pipe instrumentation with thermocouples

The inlet of the system, which represents the DOC (diesel oxidation catalyst) outlet, is created using a flanged connection, allowing the hot exhaust gas to flow in the mixer unit installed on the experimental rig. The wires that convey the thermocouples measurements are insulated and leave the module through completely sealed connections.

The data concerning the urea deposits formation and their specific position inside the UVM unit are collected thanks to an endoscope camera and an electric light source, which are mounted on the sides of the UWS injector tip, as shown in **Fig. 3**. The light source is necessary to enlighten the inner chamber, which would otherwise be too dark and would not allow to see the location of the deposits.

An example of the deposit photos that it is possible to capture with this setup is shown in **Fig. 4**, which depicts the mixer unit at the beginning of the test and after 20 min, where the deposits are already clearly visible (white layer on the UVM internal walls).

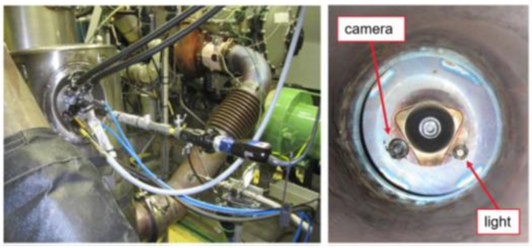

**Fig. 3.** Test bench setup

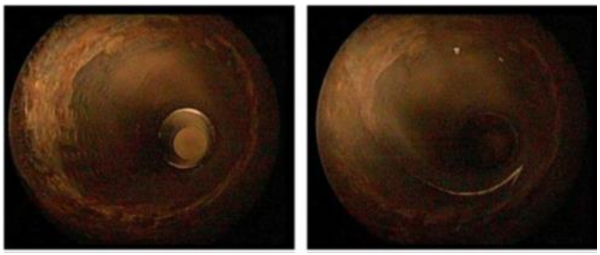

**Fig. 4.** Example of mixing pipe visualization

### 2.1. Experimental data

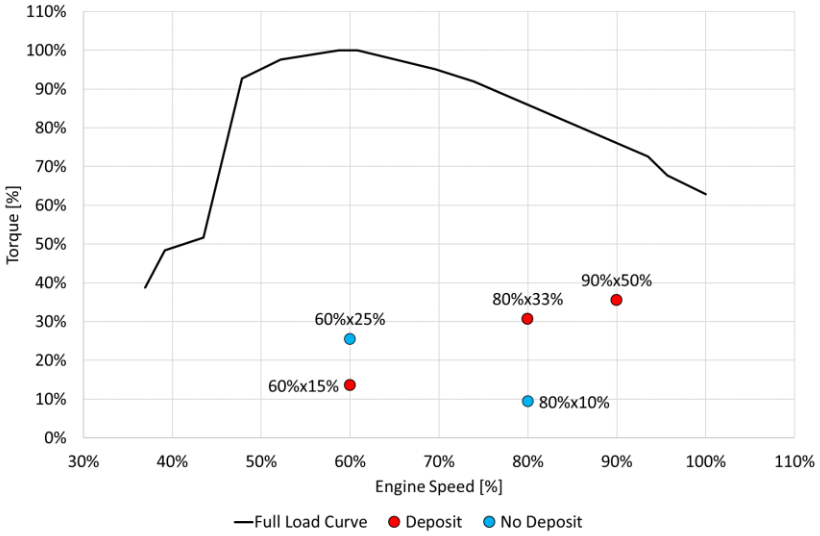

**Fig. 5.** Engine map and operating points

**Table 1.** Operating points

| OP | Engine speed w.r.t. max | Load | Exh Temp °C | Alpha | Deposits observed |
|---|---|---|---|---|---|
| 1 | 90% | 50% | 380 | 1.0 | Yes |
| 2 | 60% | 25% | 380 | 1.0 | No |
| 3 | 60% | 15% | 280 | 1.0 | Yes |
| 4 | 80% | 33% | 380 | 1.0 | Yes |
| 5 | 80% | 10% | 280 | 1.0 | No |

The operating points represented in **Fig. 5** and listed in **Table 1** are characterised by very different values of the exhaust gas mass flow (resulting from the engine speed and torque), Ad-Blue dosing and temperature, to cover a very wide range of operating conditions. Alpha represents the ratio between the injected urea and the theoretical urea to fully reduce the NOx in the exhaust gases.

Starting from a certain constant temperature, due to the vaporization energy the mixer surface temperature declines, dependent on the dosed amount of DEF, the impinged surface area and the heat transfer from the exhaust gas to the spray loaded surface area. This means that a steep decline in temperature can be critical and can lead to urea deposit formation.

Regarding the mass flow, instead, a typical mixer weak point is at low flow condition: this means that the higher the gas speed, the higher the deposit resistance. The UVM unit, instead, shows a completely opposite behaviour, thus a high mass flow condition is critical in the high engine speed point, because the high swirling gas opens the DEF spray resulting in high SSL.

## 3. Virtual model

The fluid dynamics (CFD) consists of the analysis of systems involving fluid flows, heat transfer and resulting chemical reactions employing computer-based simulations run on dedicated software. [6] The simulations on the SCR mixing system architecture previously described was carried out with the commercial CFD code of CONVERGE CFD software.

In these research Adaptive Mesh Refinement (AMR) is used to refine the mesh during the simulation in areas with complex phenomena considering a base grid size and adding fixed refinements in specific locations. A proper mesh has been found to be critical to correctly capture the spray impingement with a base grid size of 12 mm and refinement in critical zone like injector.

RANS equations have been implemented, with RNG (Renormalization Group) k-ε as turbulence model [6].

In simulations of urea-based SCR systems, the wall temperature is fundamental to predict urea-derived deposits, the locations of spray impingement, film accumulation and evaporation rates. Due to the much longer thermal timescale in metal walls compared to gas, a quasi-steady state is not reached in the metal nearly as quickly as in the gas. This gives the chance to adopt a fixed flow approach for the gas phase in order to speed up the simulation [6].

Conjugate heat transfer (CHT) is used when heat transfer occurs simultaneously within and between fluid and solid regions. The predominant mode of heat transfer in fluids is convection, while the predominant mode of heat transfer in solids is conduction, thus 3D CHT models are implemented in the simulations to solve the heat transfer in both the fluid and solid regions [6].

In the case of an exhaust after-treatment simulation with a urea-water solution spray, super-cycling is the proper technique to deal with the widely varying time scales of the phenomena happening during the simulation. For instance, spray transport takes some milliseconds, while wall cooling, film movement, and deposit formation can take from minutes to hours. Super-cycling allows the metal to quickly reach a statistically steady temperature for pulsed sprays without modifying the metal-specific heat at constant pressure (cp) [6].

The UWS injector has been modelled using the information coming from the injector supplier in terms of geometric characteristics, such as number of holes, holes diameter and position, and spray characteristics, such as the Sauter Mean Diameter (SMD) and the spray velocity.

The spray velocity specifically has been found to be critical for this particular application where a strong flow dynamic is involved and required a dedicated calibration in order to correctly match the impingement area. In fact, by using the original value of spray velocity it was not possible to model properly the spray inertia, which was instead correctly obtained by halving the experimental spray velocity.

Two models are commonly considered to simulate urea decomposition: thermal decomposition and molten solid. The thermal decomposition model is based on semi-detailed kinetics and accounts for the decomposition of urea in both the solid and aqueous phases, and it can predict the polymerization of urea decomposition by-products to form solid deposits of biuret, ammelide, melamine and cyanuric acid. The molten solid model, instead, is a simpler model as only two correlations are used: the Frossling correlation models the evaporation of the water contained in the UWS, while an Arrhenius correlation models the decomposition of the urea (NH2)2CO into ammonia (NH3) and isocyanic acid (HNCO). The molten solid model has been selected and used in this activity as it offers the best computational efficiency with an acceptable level of accuracy.

Kuhnke and the Bai-Gosman models have been tested and compared to simulate the droplets-wall interaction, which is crucial to let the urea deposits create on the inner wall surfaces. The tests performed show that even if both models can effectively mimic the spray impingement, the Kuhnke model is able to obtain a faster temperature drop. This allows to obtain very soon the correct temperature range and the near-wall HNCO mass fraction condition in which deposits nucleate.

After the most effective model is selected, a precise calibration of the main parameters that regulate the droplets' behaviour is required. To obtain a CFD setup which can model the spray-wall interaction regardless of the wall temperature in a specific engine operating point, a critical temperature value equal to 1.37 has been chosen for commercial UWS, according to the chemical correlation proposed by Birkhold in 2007. [7]

A User-Defined Function (UDF) is a subroutine used to evaluate the risk of deposit formation on the surfaces impacted by the UWS and the index is evaluated from 1 to 7 considering: wall film pathways, initial footprint, wall film dynamics, wall film thickness, wall film velocity, wall film temperature, urea concentration, HNCO concentration level.

The criteria which establish the risk index are:

1. NO RISK: the liquid film thickness is lower than the critical value and the film temperature is higher than the Leidenfrost temperature (247 [°C]);
2. FILM TRANSPORT: the liquid film velocity is higher than the critical velocity value;
3. CRYSTALLIZATION RISK: the liquid film temperature is lower than 133 [°C] and the urea chemical concentration is lower than the critical value;
4. CRYSTALLIZING UREA the liquid film temperature is lower than 133 [°C] and the urea chemical concentration is higher than the critical value. Since the critical concentration is temperature-dependent it is calculated cell-wise;
5. SLOW UREA DECOMPOSITION: urea decomposes at temperatures above its crystallisation temperature 133 [°C]. However, since a significant urea mass loss is not observed below temperatures of 160 [°C], within these temperature values there is a “slow urea decomposition”;

6. FAST UREA DECOMPOSITION: within wall film temperatures of 160 [°C] and Leidenfrost temperature, urea decomposition rates increase significantly. In this condition, secondary reactions start to become relevant;
7. SECONDARY REACTIONS: within wall film temperatures of 160 [°C] and Leidenfrost temperature, urea decomposition secondary reactions become relevant and the isocyanic acid concentration is higher than the critical level leads to the formation of by-products: biuret, cyanuric acid, ammelide, ammeline and melamine.

Given that the urea deposit risk is considered to be high for the level 7 only, particular attention should be given to the level 6 as well, as the flow condition would potentially result in deposit risk depending on the isocyanic acid concentration. For this activity, a value of 0.0005 has been selected and used for all operating points after calibration with experimental data.

## 4. Model validation: simulations results

### 4.1 Operating Point 1

**Table 2** summarizes the data related to the first engine operating point.

**Table 2.** Operating Point 1

| OP | Engine speed w.r.t. max | Load | Exh Temp °C | Alpha | Deposits observed |
|---|---|---|---|---|---|
| 1 | 90% | 50% | 380 | 1.0 | Yes |

A preliminary analysis of the flow field, as depicted in **Fig. 6**, has been initially performed in order to evaluate the swirl level and the flow dynamic inside of the UVM, which shows a high-speed zone (about 90 [m/s]) in the region immediately after the swirler region.

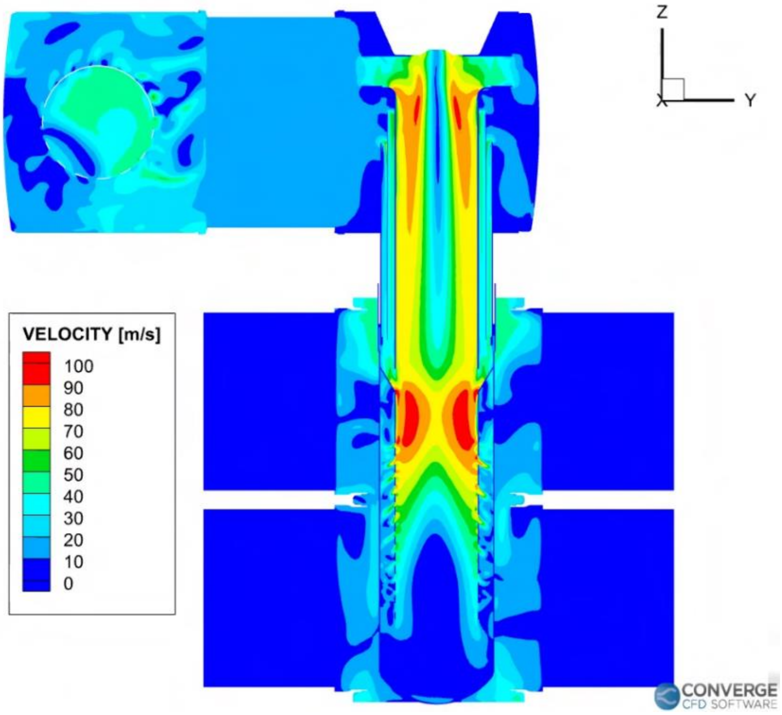

**Fig. 6.** Velocity field of OP1

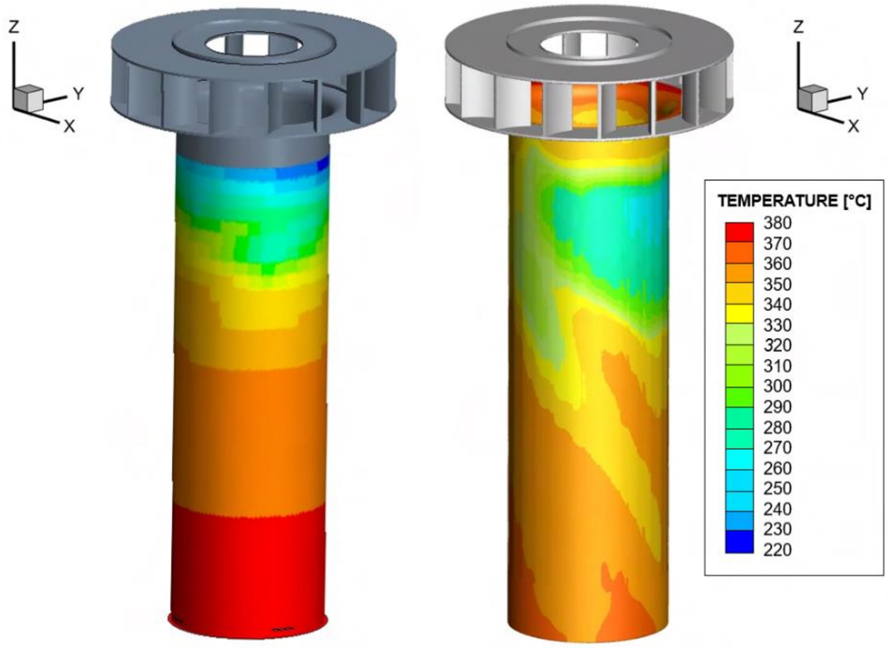

**Fig. 7.** OP1 temperature maps: experiment (left) and simulation (right)

This behavior is correct and can model the droplets' motion after the injection in an acceptable way. They impact on the wall of the UVM internal region at about 120 ÷ 150 [mm] from the top side of the swirler module, which will be used as a reference point to compare the experimental and the simulated deposit location.

The accuracy of the simulated drops impingement is demonstrated by the comparison between the experimental and modelled UVM thermal maps, as shown in **Fig. 7**. To improve the visualization of these results, only the UVM internal part will be shown: it is possible to see that the lower temperature zones, which correspond with the main impinged zones, match correctly, with a slight deviation in the very first part of the mixing pipe.

**Fig. 8** shows, instead, a detailed view of the internal side of the UVM initial zone. In the lower temperature zone, the HNCO mass fraction is higher than the critical value (0.0005 obtained from bench test), thus the conditions that lead to the onset of the deposit are satisfied right at about 120 ÷ 150 [mm] from the top side of the swirler.

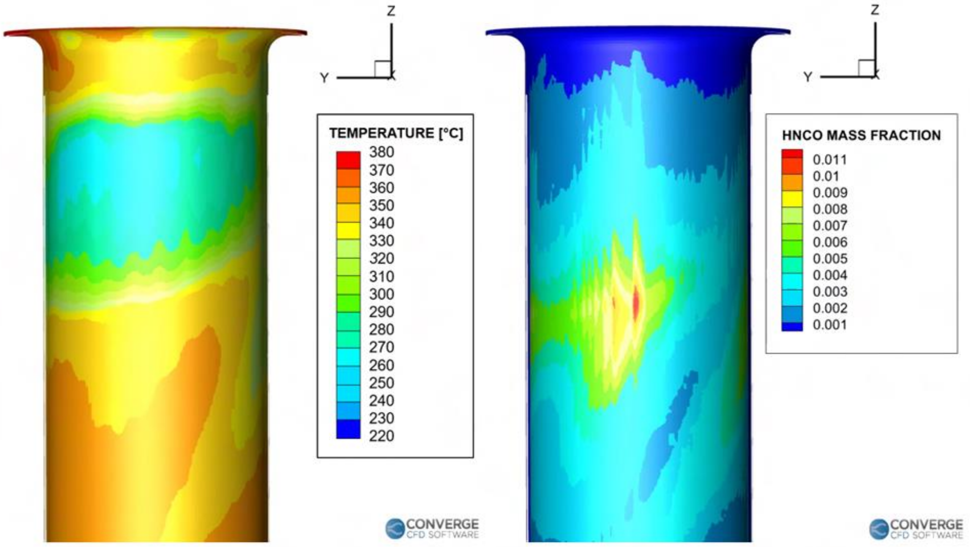

**Fig. 8.** OP1 temperature and HNCO concentration

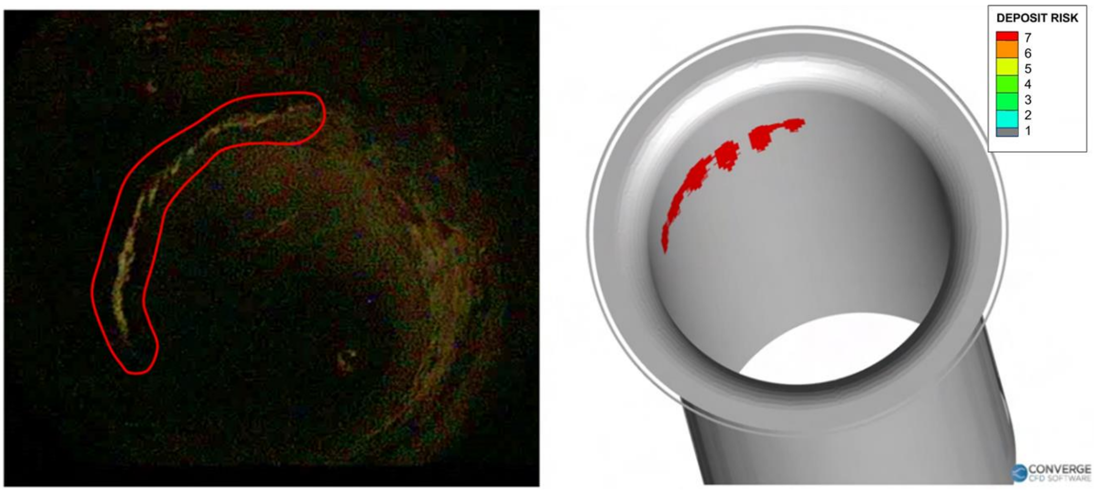

**Fig. 9.** OP1 deposit formation: experimental (left) and simulation (right)

The comparison of the deposits' experimental photos and the visualization of the deposit risk depicted in **Fig. 9** proves that the model has correctly predicted the locations where the urea decomposition secondary reactions take place, highlighted by the red zone.

After ten injections, it can be clearly seen that most of the inner wall surface is at a risk level of 1. This is because the liquid film thickness is lower than the critical value, which means that the wall surface is not well-covered by the liquid film. Additionally, the film temperature is higher than the Leidenfrost temperature, which means that the liquid is boiling off too quickly.

However, in the area with the right temperature and HNCO concentration, which is identified by a risk level of 7, there is a significant presence of secondary reactions and by-products, thus resulting in a high risk of UWS deposits creation.

In the next sections, results will be described less extensively, as general considerations as described in more detail in this section can still apply.

## 4.2 Operating Point 2

**Table 3.** Operating Point 2

| OP | Engine speed w.r.t. max | Load | Exh Temp °C | Alpha | Deposits observed |
|---|---|---|---|---|---|
| 2 | 60% | 25% | 380 | 1.0 | No |

The comparison of temperature field and deposit formation for OP2 is reported in **Fig. 10**.

The temperature map shows that in this case, although the temperature magnitude matches closely, the main impingement area is not perfectly captured, as the simulation shows a higher temperature reduction in an upper area of the mixing pipe. Nevertheless, due to the too high wall temperature, no deposits are observed both in the simulation and in the experiment (**Fig. 11**).

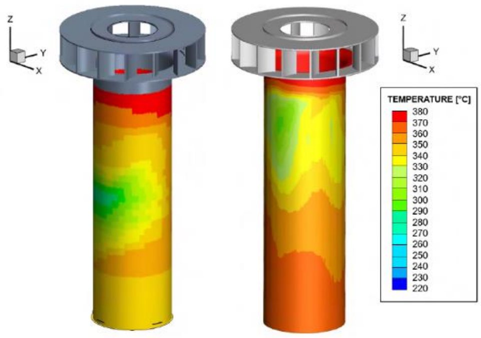

**Fig. 10.** OP2 temperature maps: exp (left) and sim (right)

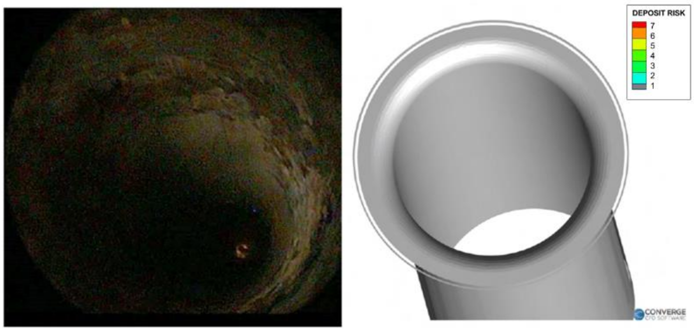

**Fig. 11.** OP2 deposit formation: exp (left) and sim (right)

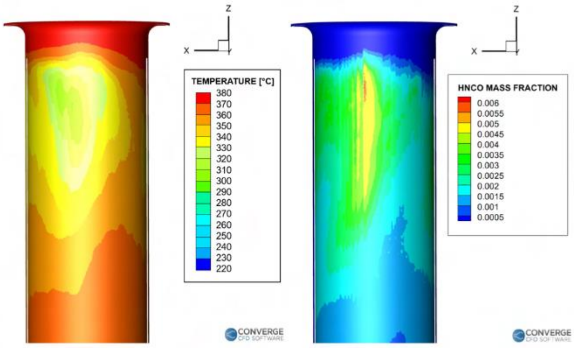

**Fig. 12.** OP2 temperature and HNCO concentration

The internal UVM initial zone is shown in **Fig. 12** for comparison. Although the HNCO mass fraction is higher than the critical one in the lower temperature zone, the temperature level remains higher than the Leidenfrost one, resulting in no deposit nucleation from the wall film.

### 4.3 Operating Point 3

**Table 4.** Operating Point 3

| OP | Engine speed w.r.t. max | Load | Exh Temp °C | Alpha | Deposits observed |
|---|---|---|---|---|---|
| 3 | 60% | 15% | 280 | 1.0 | Yes |

A proper match between the experimental and the simulated temperature field is observed for OP3, both in terms of temperature magnitude and distribution, as shown in **Fig. 13**.

The deposit formation area is also correctly captured, although the simulation shows a wider area (**Fig. 14**).

A focus on the impinged area is shown in **Fig. 15**, which shows how the mass fraction of isocyanic acid is very high due to the simulated conditions, leading to the wide area depicted with deposit risk of level 7.

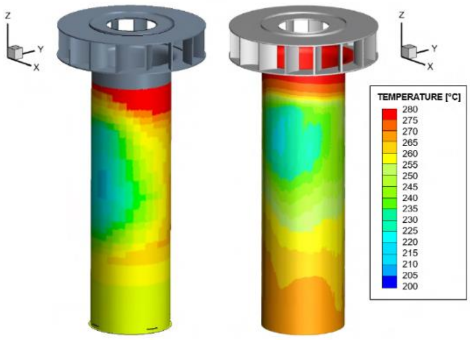

**Fig. 13.** OP3 temperature maps: exp (left) and sim (right)

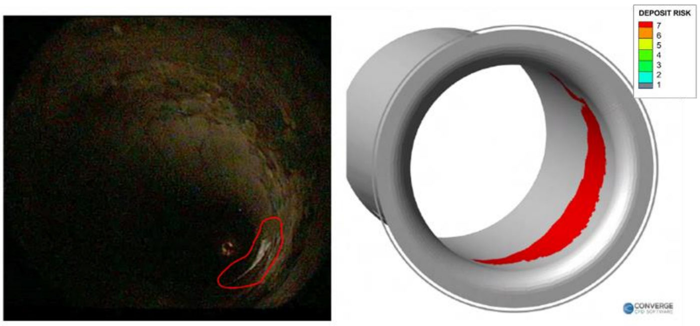

**Fig. 14.** OP3 deposit formation: exp (left) and sim (right)

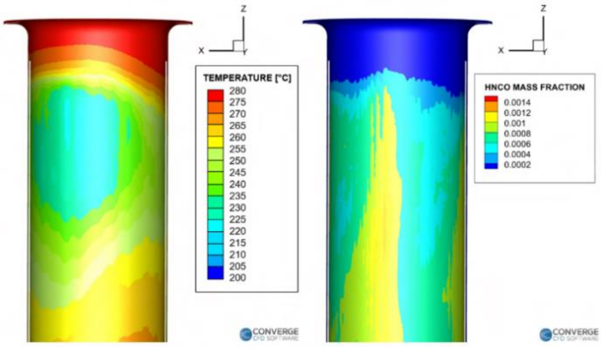

**Fig. 15.** OP3 temperature and HNCO concentration

### 4.4 Operating Point 4

**Table 5.** Operating Point 4

| OP | Engine speed w.r.t. max | Load | Exh Temp °C | Alpha | Deposits observed |
|---|---|---|---|---|---|
| 4 | 80% | 33% | 380 | 1.0 | Yes |

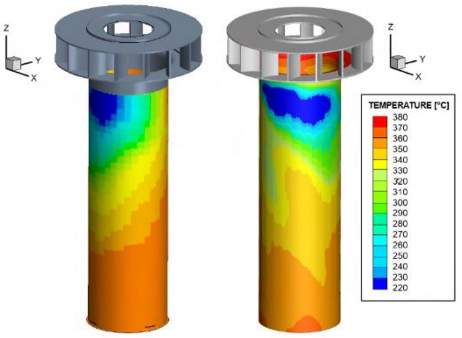

**Fig. 16.** OP4 temperature maps: exp (left) and sim (right)

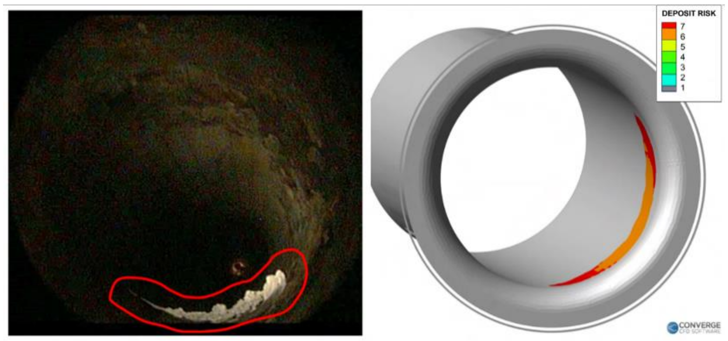

**Fig. 17.** OP4 deposit formation: exp (left) and sim (right)

A nice fit of the temperature magnitude and distribution is observed for OP4 as well, as shown in **Fig. 16**. Also, the presence and position of the deposit formation is well captured (**Fig. 17**).

A focus on the impinged area is represented in **Fig. 18**, where it can be observed that in correspondence of the low temperature area the critical isocyanic acid concentration is also overcome, leading to the deposit risk of level 7. This risk zone configuration suggests that, by significantly increasing the number of injections, the entire risk zone 6 would reach level 7, becoming more representative of the deposits found on the test bench.

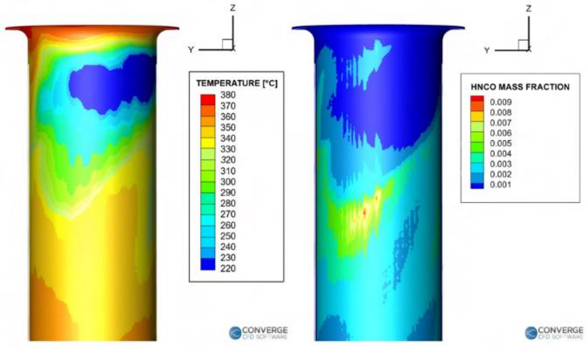

**Fig. 18.** OP4 temperature and HNCO concentration

### 4.5 Operating Point 5

**Table 6.** Operating Point 5

| OP | Engine speed w.r.t. max | Load | Exh Temp °C | Alpha | Deposits observed |
|---|---|---|---|---|---|
| 5 | 80% | 10% | 280 | 1.0 | No |

A good match of the temperature field is observed for OP5 as well (**Fig. 19**).

However, while in the experiments no deposits were observed, the simulation shows an area with risk factor of level 7, as depicted in **Fig. 20**. Anyway, it can be noticed that the area with risk level 6 more than doubles the one with level 7, as a hint that fast urea decomposition is the main phenomenon here.

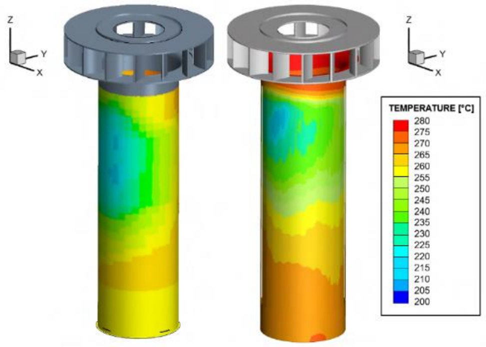
Z
Y
X
TEMPERATURE [°C]
280
275
270
265
260
255
250
245
240
235
230
225
220
215
210
205
200

**Fig. 19.** OP5 temperature maps: exp (left) and sim (right)

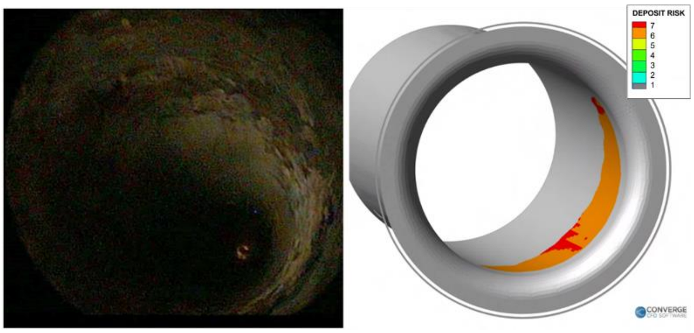
DEPOSIT RISK
7
6
5
4
3
2
1
CONVERGE

**Fig. 20.** OP5 deposit formation: exp (left) and sim (right)

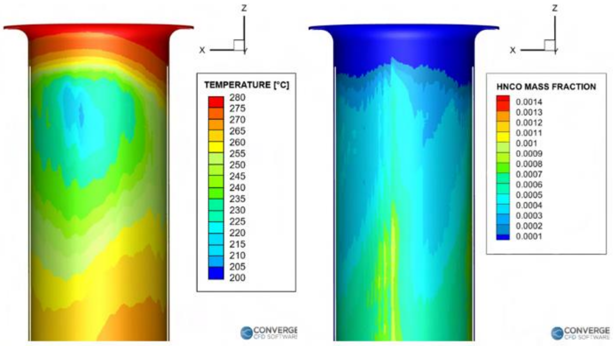
Z
X
TEMPERATURE [°C]
280
275
270
265
260
255
250
245
240
235
230
225
220
215
210
205
200
CONVERGE
HNCO MASS FRACTION
0.0014
0.0013
0.0012
0.0011
0.001
0.0009
0.0008
0.0007
0.0006
0.0005
0.0004
0.0003
0.0002
0.0001
CONVERGE

**Fig. 21.** OP5 temperature and HNCO concentration

The internal UVM zone where the main impingement occurs is shown in **Fig. 21**. Although the temperature level is way lower than the Leidenfrost one, the isocyanic acid concentration remains lower than the critical value in most of the impinged zone, resulting in fast decomposition and therefore no-deposit onset condition from the wall film.

## 5. Conclusions and future development

The purpose of this work was to provide an effective and useful 3D-CFD methodology, which can correctly predict the risk of UWS deposits generation on the inner walls and mixer surfaces of complex ATS system geometries. The presence of deposits implies inefficient utilization of urea, diminished catalyst conversion efficiency and potential corrosion of stainless-steel components.

The proposed CFD methodology has been tested over five different operating points to evaluate the performance of the analyzed ATS system in terms of UWS spray modelling, liquid film development, wall temperature and spray-impinged surfaces and comparing results with test bench.

The comparison between simulation results and experimental measurements has shown a satisfactory and promising coherency. In most of the examined engine operating points, the 3D thermal maps matched closely the data retrieved by the thermocouples positioned on the test ATS geometry. This means that the injected UWS spray has been modelled correctly and that the mesh grid used for the model has been capable of capturing reasonably well the complex droplet motion. Moreover, the deposit risk index outcomes have proven that this CFD methodology can consistently identify the areas of the systems where urea deposit formation is expected, which corresponds to the ones revealed by the deposit photos collected on the test bench. Only the last operating point analyzed did not show a perfect correlation between simulation (high risk) and measurements (no deposits).

The data gathered suggest that there is still room for improvement in the presented methodology. In some operating points, the droplet motion is not completely accurate, and this can be caused by the adopted mesh grid. Even though the ATS geometry was analyzed using an 11.5 million cells mesh, obtained enabling fixed embeddings and adaptive mesh refinements, it’s possible that an even finer grid could be needed to replicate the behavior of the turbulent droplets.

The injector modeling, specifically the initial droplet velocity and droplet diameter, is another area that needs more research. These values have been set to replicate the experimental rig conditions. However, they could completely alter the impingement zone of the UWS spray: this means that, if an injector produced by a company is being simulated, a comprehensive data sheet is required to impose the correct injector characteristics in the simulations.

## References

[1] European Emission Standards Wikipedia page.

https://en.wikipedia.org/wiki/European_emission_standards. Accessed: 2023-09-22 (cit. on pp. 2,3).

[2] T. Selleri, A. D. Melas, A. Joshi, D. Manara, A. Perujo, and R. Suarez-Bertoa. «An overview of lean exhaust denox aftertreatment technologies and nox emission regulations in the european union». In: Catalysts 11.3 (2021), p. 404 (cit. on pp. 4, 6, 10, 11).

[3] Euro 7/VII Emission Standards - AECC Position Paper. AECC. https://www.aecc.eu/. Accessed: 2023-09-22 (cit. on p. 4).

[4] J. Dörnhöfer et al. «A Holistic View on Urea Injection for NO x EmissionControl: Impingement, Re-atomization, and Deposit Formation». In: EmissionControl Science and Technology 6 (2020), pp. 228–243 (cit. on pp. 12, 13).

[5] Selective Catalytic Reduction (SCR). AECC. https://www.aecc.eu/emi ssions-control-technology/catalysts/. Accessed: 2023-11-09 (cit. on p. 11).

[6] K. J. Richards, P. K. Senecal, and E. Pomraning. «CONVERGE (Version 3.1) Manual, Convergent Science Inc». In: Madison, WI (2022) (cit. on pp. 23, 25, 26, 35, 41–46, 48–56, 59, 61–63).

[7] F. Birkhold. Selektive katalytische reduktion von stickoxiden in kraftfahrzeugen:Untersuchung der einspritzung von harnstoffwasserlösung. Shaker Aachen, Germany, 2007 (cit. on pp. 55, 70).

[8] H. Smith, T. Lauer, V. Schimik, and K. Gabel. «Evaluation and prediction of deposit severity in SCR systems». In: SAE International Journal of Engines 9.3 (2016), pp. 1735–1750 (cit. on p. 63).

## Acknowledgments

We want to acknowledge to Fabrizio Cisternino from Politecnico di Torino for his work and support.

# Validation of Different Methods for Exhaust Gas Monitoring in $H_2$ Fueled Internal Combustion Engines

S.C. Eichmann, D. Klenk and M. Schroeder

HORIBA Europe GmbH, Hans-Mess-Str. 6, 61440 Oberursel, Germany.

E-mail: simone.eichmann@horiba.com
Telephone: +(49) 6172 137385

**Abstract.** With the current ongoing global restriction of carbon dioxide ($CO_2$) emissions of internal combustion engines (ICE), vehicle and engine manufacturers are currently looking for alternative forms of energy. Besides electric propulsion and fuel cells, Hydrogen ($H_2$) driven internal combustion engines are expected to play an important role in the near future. The transition from fossil fuelled to $H_2$ fueled engines poses several challenges to automotive manufacturers. Besides the adaption of engines to new fuel properties and the upgrade of test cells to new safety requirements, the different exhaust gas composition also requires a modification in the testing equipment for exhaust gas monitoring and type approval testing. Measurement ranges need to be adapted to different interfering components. Also new components like $H_2$ or water ($H_2O$) might be of interest especially for research and development purposes. Modification of current exhaust gas analyzers will be discussed and validated. Moreover, new methods for additional components will be discussed.

## 1. Introduction

Fossil fueled internal combustion engines will be strongly restricted in the near future for light duty as well as for heavy duty vehicles. For instance, the European Parliament decided that all passenger cars sold from 2035 in the European union need to be carbon dioxide ($CO_2$) neutral [1]. For trucks, busses and heavy duty vehicles $CO_2$ emissions shall be reduced by 90% until 2040 [2]. Moreover, the US and China agreed on a strong reduction of greenhouse gases as well.

For that reason, engine and vehicle manufacturers are currently under big pressure to search for alternative propulsion systems. The light duty market in Europe currently mainly concentrates on electric propulsion; fuel cells, $H_2$ or other alternative fuels play a minor role. In contrast to that, the heavy duty market is more divers. Electrified vehicles will play an important role in urban regions, while for long distances fuel cells and $H_2$ ICE engines enjoy more relevance. Biofuels like for instance methanol are of increasing interest, like for example in the Scandinavian region. For non-road mobile machinery, fossil fueled engines will remain in the near and mid-term future. Various additional fuels like methanol, propane or hydrogen are considered as well, depending on the application. Also electric propulsion is used, for instance for boats or inland ferries. Fuel cells currently play a minor role due to the heavy weight and the high R&D effort.

Hence, $H_2$ ICE engines will especially in the near and mid-term future be a technology of interest, with the global market for $H_2$ ICE engine currently growing with a compound annual growth rate of approximately 10% [3]. One big advantage for engine manufacturers compared to other propulsion systems is the comparatively small development effort and low investment costs for new testing facilities. Nevertheless, there is a number of modifications necessary for the conversion to $H_2$ as fuel. Engine concepts have to be adapted to new fuel properties like density, heat capacity or combustion temperature. This does not only effect the engine performance, but also concentration of different exhaust gas components. For instance, water concentration might reach values up to 35% and also high values of nitrous oxides due to possibly higher combustion temperature can occur.

Conventionally used technologies in exhaust gas monitoring are non-disperse-infrared spectroscopy (NDIR) for carbon monoxide (CO) and carbon dioxide ($CO_2$) measurements and chemiluminescence detection (CLD) for nitrous oxides ($NO_x$) measurements [4,5]. They allow accurate, highly time resolved measurements and are accepted in global regulations for exhaust gas monitoring [6,7].

However, the higher water concentration leads to interference and quench effects [10], which need to be compensated with appropriate methods. Considering also new regulated components like ammonia ($NH_3$) or nitrous oxide ($N_2O$), additional technologies like Fourier-Transformed Infrared Spectroscopy (FTIR) [8,9] or laser-based technologies become relevant [11].

Besides that, additional components like hydrogen ($H_2$) or water ($H_2O$) are of interest. Applications for $H_2$ measurements are for instance the determination of engine performance or the $H_2$ slip. Moreover, it is used for safety measurement at the tailpipe, like for instance described in the Global Technical Regulation 13 for $H_2$ and fuel cell engines [12]. However, methods for $H_2$ monitoring are limited. Infrared spectroscopy does not apply to non-polar molecules like $H_2$, oxygen or nitrogen. Raman spectroscopy [8] is sensitive to $H_2$ but can typically only be applied in the percent range. Gas chromatographs allow $H_2$ monitoring with high accuracy, but show a response time of several minutes and are therefore not suited for automotive applications. The thermal conductivity method is a well-established in process gas analysis, but it also does not meet automotive response time requirements and shows various interferences to all other exhaust gas components. One technology which seems to be beneficial is mass spectroscopy. With its high accuracy, low interference and fast response time, it meets the requirements for automotive applications.

Water measurements are of interest for the determination of exhaust gas recirculation ratio, to get full engine balance, for dry-wet correction or for the interference correction. Capacitive or electrochemical sensors have low costs, but they are limited in respect to response time in the range of minutes. Better suited are infrared based technologies like Fourier-transform infrared spectroscopy (FTIR), quantum cascade laser based infrared spectroscopy (QCL-IR) and non-disperse infrared spectroscopy (NDIR). FTIR is well approved and especially interesting for development cases, as it allows n addition to the standardly measured gases also the detection of various non-regulated components like for instance ethanol, acetaldehyde or various alipthatic or aromatic hydrocarbons. QCL-IR technology shows high accurate measurement, but it is also cost intensive. NDIR is also well suited, and allows the detection of $H_2O$ with good accuracy at much lower price.

In this paper, different technologies for are validated in regard to their applicability to $H_2$ ICE engines. The influence of water as well as the detection limit and repeatability will be compared and discussed. Finally new technologies for the measurement of additional components will be presented.

## 2. Emission monitoring technologies

Different technologies for exhaust gas analyses are available. In the following chapter, a brief overview is given. More details can be found for instance in [13] or [14].

### 2.1 Infrared absorption technologies

Infrared technologies use the property of various gases to absorb light in the near and middle infrared. The ration between light absorption and species concentration *c* is given by the “Lambert-Beer Law”

$$lg\frac{I}{I_0} = c \cdot L \cdot \varepsilon_\lambda \tag{1}$$

with the intensity of incoming light $I_0$, the intensity of transmitted light $I$, the path length $L$, the component concentration $c$ and the wavelength dependent absorption coefficient $\varepsilon_\lambda$.

Moreover, the wavelength of light absorption is specific for a certain molecule. In Fig. 1, absorption lines of various exhaust gas molecules are shown. Data were extracted from the HITRAN database [14]. All displayed components can be detected in the spectral range from 2 to 10 µm. But looking at the absorption lines in more detail, overlaps between the absorption lines of the different molecules occur. This leads to interferences and requires special methods for selective measurement of a certain component in a multi-component mixture.

Different infra-red based technologies are currently used for exhaust gas monitoring. One technology which is already applied since decades is non-disperse infra-red spectroscopy. A principle set-up of this technology is shown in Fig 2 (a). The set-up is divided in a sample side and a reference side. Both sides contain a light source, a gas cell, an optical filter and a detector. The light sources emit light in the infrared, which is partly absorbed in sample gas cell and detected by gas or pyro detectors. The reference cell is filled with nitrogen, so no light absorption occurs. The ratio from both signals corresponds to a certain concentration.

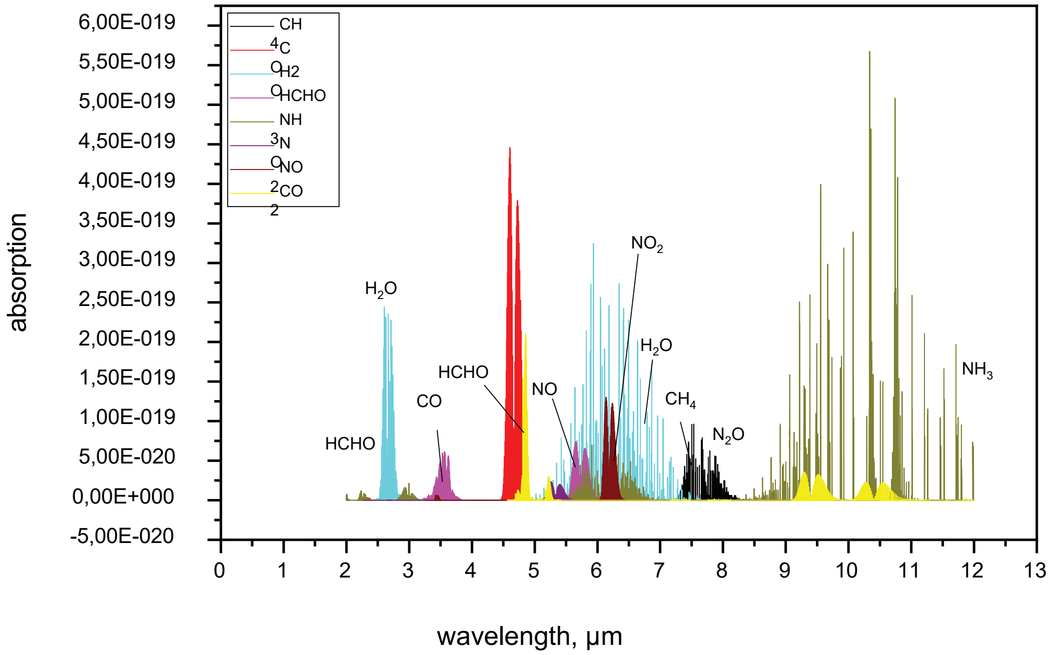

**Fig. 1.** Absorption spectra of various absorption gas components

As in multicomponent mixtures absorption might occur from several gas components, optical filters are used. These are only transmissive for wavelengths where the desired component absorbs, interferences from other components are suppressed. In some cases, it is not possible to suppress interferences completely. For instance, for the detection of $N_2O$, very high interferences from $CO_2$ and water occur. For that reason, NDIR technology is mainly used for carbon monoxide (CO) and $CO_2$ measurement, for other components, more complex methods are applied.

One more sophisticated technology is FTIR [16], see Fig. 2 (b). Like NDIR, this technology is based on light absorption of infrared light by gas molecules and utilizes a light source, a gas cell and a detector. One big difference to NDIR technology is the Michelson interferometer. This unit consists of a beam splitter, a movable and a fixed mirror. A broadband light beam enters the interferometer, is divided into two beams and reflected by the fixed and movable mirror. After the beam splitter, both beams are overlaid. Dependent on the position of the movable mirror, constructive and destructive interference occurs. which results in a time dependent spectral beam profile. The beam passes the sample gas cell, is partly absorbed, measured by the detector and then converted to a wave number dependent signal by Fourier transformation.

FTIR spectrometers for automotive applications typically cover the spectral range from 2 to 10 µm, which allows the detection of multiple exhaust gas components. Moreover, the spectrally solved signal contains more detailed information about various exhaust gas components. This allows better compensation of interference effects as well as a complete exhaust gas analysis. One drawback of the technology is the rather weak signal. To increase signal intensity, a multi-pass cell is commonly used. This kind of gas cells include reflective mirrors, which multiply the length of the beam path inside the cell up to several meters.

One challenge of using FTIR spectroscopy are the various interference effects which occur between different gas components. One reason for that the spectral overlap of absorption lines of the different components. It occurs for instance between $H_2O$ and nitric oxide (NO), nitrogen dioxide ($NO_2$) and $NH_3$, see Fig. 1. More sophisticated post processing algorithms are necessary to consider these effects. In addition, also collision broadening effects between molecules might occur. This leads to different effects like spectral broadening or appearance of new absorption lines [17] and finally to measurement errors. As they the probability of these effects increases with concentration, they mainly have to be considered for $H_2O$ and $CO_2$. For some applications, especially for sampling before after treatment system, additional effects between $H_2O$ and CO or $NH_3$ might be observed.

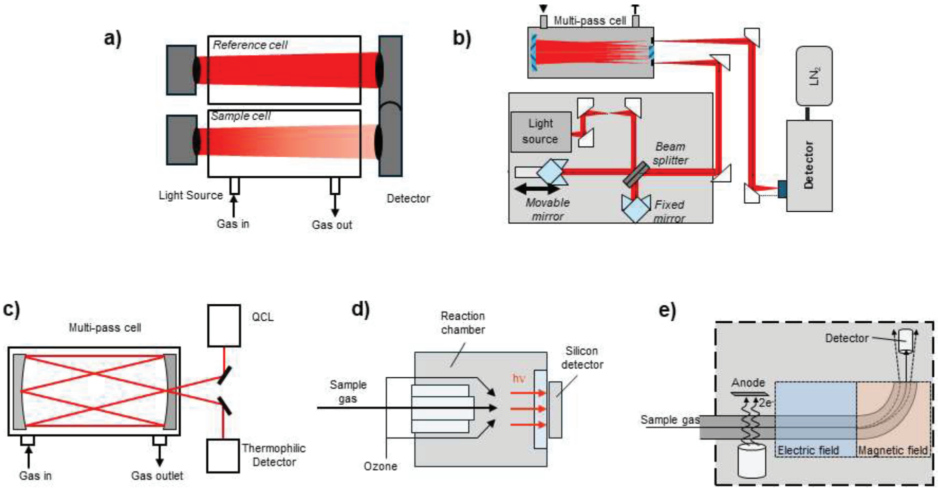

**Fig. 2.** Principle of different methods for exhaust gas monitoring: NDIR (a), FTIR (b), QCL-IR (c), CLD (d), mass spectrometer (e)

With increasing requirements from legislation, also laser-based infra-red technologies become more important. A principal set-up is shown in Fig. 2 (c). As laser sources, tunable diode lasers or quantum cascade lasers [17, 18] are applied. are semiconductor lasers, which emit a very narrow-band light. By changing the temperature of the semiconductor element, the wavelength can be tuned by a few nanometers. This allows the detection of a single absorption line without interference of exhaust gas components. By the use of a multi-pass cell, very high signal intensities can be achieved. This allows the use of very basic detectors like thermophilic detectors or photodiodes [19]. Tunable diode lasers emit light only in the near infra-red spectral region and can therefore only be used for a limited number of components such as $NH_3$, $H_2O$ or $CO_2$. For detection of additional components, quantum cascade lasers can also be used in the mid-infrared and therefore offer the possibility to monitor additional components, such as nitric oxide (NO), nitrogen dioxide ($NO_2$) or $N_2O$. These lasers also allow very high signal intensities, therefore very low detection limits below 1 ppm can be achieved with very simple detectors like a photodiode or thermophilic detectors.

One advantage of QCL-IR technology compared to FTIR is the good suppression of interference effects. Due to low sample pressure and high spectral resolution, signals from the different components are much better resolved, this makes the interference compensation much easier and strongly reduces residual effects.

## 2.2. Chemiluminescence

One standard method for the detection of NO and $NO_2$ is the chemiluminescence detection, see Fig. 2 (d). This measurement principle uses the phenomenon that light emission occurs due to a chemical reaction. The intensity of emitted light correlates to a certain concentration. When NO reacts with ozone to $NO_2$, a small amount of excited $NO_2$ is formed, which leads to chemiluminescence. The emitted light is then measured for instance by a photodiode. In order to monitor also $NO_2$, the analyzer is often equipped with a converter, which reduces $NO_2$ to NO on a carbon-based catalyst. When using this technology for exhaust gas monitoring, collision effects from $CO_2$ and $H_2O$ have to be considered. These collisions can result in a decay of $NO_2$ from excited state to ground state without chemiluminescence and finally result in a reduction of the measurement signal. One possibility to reduce this effect is sample dilution with nitrogen, which reduces the probability of collisions. Another option is to use the measured $CO_2$ value for compensation. With known combustion kinetics and known influence of both components on the $NO_x$ value, $CO_2$ value can be used to compensate quench effect from both molecules.

For the application of an $H_2$ ICE engine, new methods for quenching compensation is required. As $CO_2$ is not present in the off-gas in significant amounts, additional methods are necessary for compensation of $H_2O$ influence. This is possible by different approaches. One possibility is to measure $H_2O$ content in the exhaust gas, for instance by NDIR technology. The quench-corrected NOx concentration can then be calculated by

$$c(NO_{x,corr}) = c(NO_{x,meas}) \cdot \sum_0^n a_0 \cdot c^n(H_2O_{meas}) \qquad (2)$$

with the non-corrected measured $c(NO_{x\,corr})$, the measured $H_2O$ concentration $c(H_2O_{meas})$ an the polynomial coefficients $a_0$.The coefficient are determined by appropriate calibration.

Another way to avoid quench effect is the water removal by a cooler. But as $NO_2$ shows a high solubility of water, $NO_2$ losses in the cooler might occur. Therefore, it is important that the cooler is installed after converter, where no $NO_2$ is present in the sample gas. A schematical sketch of such an analyzer principal is shown in Fig. 3.

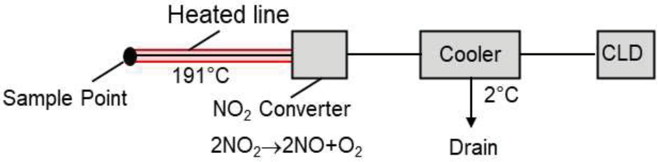

**Fig. 3.** Principal set-up of an CLD analyzer for application at an $H_2$ ICE engine

### 2.3 Mass spectrometry

Mass spectroscopy is an accepted technology for $H_2$ monitoring in automotive applications. This technology uses the deflection of ionized molecules in an electric field. Fig. 2 (e) shows a principle set-up of the measurement. Water molecules are first ionized, accelerated and derived in the magnetic field. The derivation is dependent on the ratio of charge and mass and is unique for certain species. Compared to other technologies like thermal conductivity and gas chromatography, this technology shows fast response time and interferences compared to other exhaust gas components and is therefore perfectly suited for automotive applications.

## 3. Experimental

Several approved technologies were tested for their applicability ICE engines. This includes an NDIR analyzer, an FTIR analyzer an QCL-IR analyzer and a CLD. The NDIR analyzer is equipped with a CO and a $CO_2$ bench. The gas cell as well as the entire sample handling system was heated above 80°C to avoid condensation. Additionally water measurement based on NDIR principle was included for interference correction.

A QCL-IR based analyzer is equipped with QCL lasers analyzers for detection of carbon dioxide (CO), $CO_2$, NO, $NO_2$, $N_2O$ and $NH_3$. An inhouse-designed Heriott cell with an inner volume of less than 50 ml was used. Two beam paths with different path length were used to measure components in different concentration ranges with high sensitivity. A special algorithm based on feature quantity extracted was used which not only reduces residual interferences, but also reduces capacity by factor 10-100 [16].

The FTIR analyzer used had a temperature of 191°C. This allows in principle the detection of more than 20 components. This includes regulated components like CO, $CO_2$, NO or $NO_2$, future regulated components like $NH_3$ or HCHO, but also various saturated, unsaturated or cyclic hydrocarbons. In the following, only results from CO, $CO_2$, NO, $NO_2$, $N_2O$ and $NH_3$ are shown. The analyzer is calibrated for multi ranges and uses signal amplification, to allow measurements from ppm to percent range. To adapt the analyzer to $H_2$ ICE applications, the $H_2O$ measurement range as well as $H_2O$ interference correction were increased to a concentration of 35%. Moreover, a special correction was applied to compensate collision effects with other molecules.

Finally, a CLD analyzer for hot $NO_x$ measurements was used. The influence of water on the measurement was investigated for all units. Moreover, the performance regarding the detection limit and repeatability were compared. Moreover, the possibility to measure additional components with $H_2$ and $H_2O$ was investigated.

### 3.1. Results from proven technologies

Results from performance checks are shown in Table 1. The detection limit was determined by 4 times standard deviation with a set of 100 data points. Nitrogen was used as sample gas. Exemplary, results from CO and NO are shown in Fig. 4 (a) and (b). For CO, similar detection limits of 1.8 achieved for FTIR and QCL IR, see also Table 1. Looking at NDIR measurement, the detection limit was approximately one order of magnitude higher. For additional components, the FTIR detection limits are mostly higher compared to QCL-IR. Only for CO and $CO_2$, much lower values can be achieved. This can be explained by the fact that in contrast to FTIR, only a single range was used and therefore no signal amplification was applied. Looking at the CLD measurement, NO detection limit is similar to QCL-IR.

Repeatability was tested by switching 10 times from zero to span gas. For each measurement of the span gas, the mean value was taken, and repeatability was calculated as maximum deviation of on measured span value divided to the span concentration. The tests were performed for several gas concentrations within the range of the analyzers. Similar repeatability was achieved for both FTIR and QCL. For all units, repeatability was below 1% of the measured value.

Finally, water influence was investigated. Mixtures of $H_2O$ in $N_2$ background with concentrations from 0 to 5, 10, 15, 20, 25, 30 and 35% were applied to the analyzers. Results are shown in Fig. 5. Comparable results for found for NO, $NO_2$, $N_2O$. All measured values were below 1 ppm. For CO and $CO_2$, higher values are observed for the QCL and NDIR measurements. However, both results were within the detection limit of the analyzers.

For the CLD as well as for the NDIR analyzer, no measurable effect was recorded. However, errors up to 7% of the measured value can occur in the presence of $NO_x$ at span point due to quench effects.

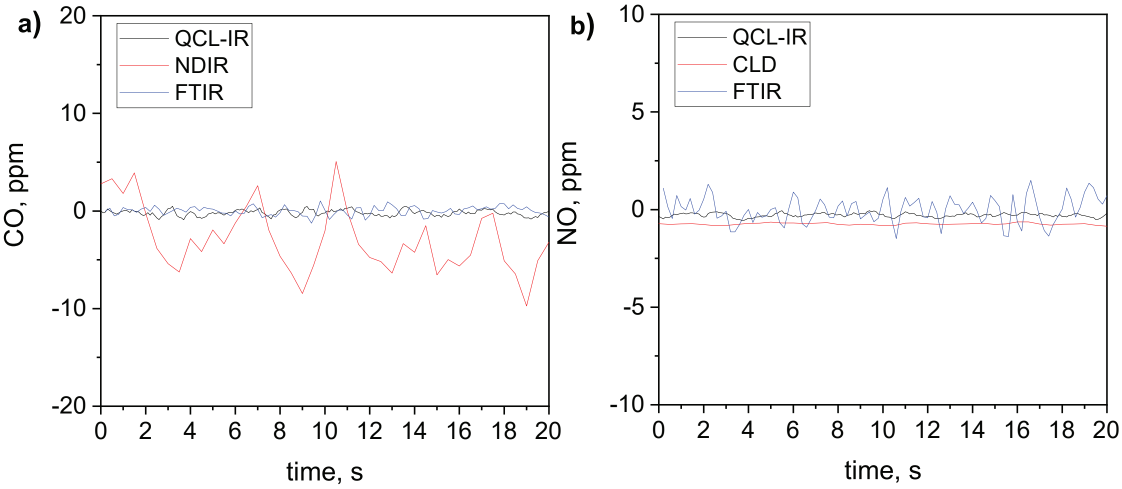

**Fig 4.** Zero noise of CO (a) and NO (b) from different technologies

**Table 1:** Detection limit of different analyzer

| | FTIR | QCL-IR | NDIR | CLD |
|---|---|---|---|---|
| CO | 1.8 ppm | 1.8 ppm | 16 ppm | - |
| $CO_2$ | 1.0 ppm | 200 ppm | 200 ppm | - |
| NO | 2.7 ppm | 0.4 ppm | - | 0.3 ppm |
| $NO_2$ | 0.6 ppm | 0.2 ppm | - | - |
| NO+$NO_2$ | - | - | - | 0.3 ppm |
| $N_2O$ | 0.73 ppm | 0.2 ppm | - | - |
| $NH_3$ | 1.7 ppm | 0.2 ppm | - | - |

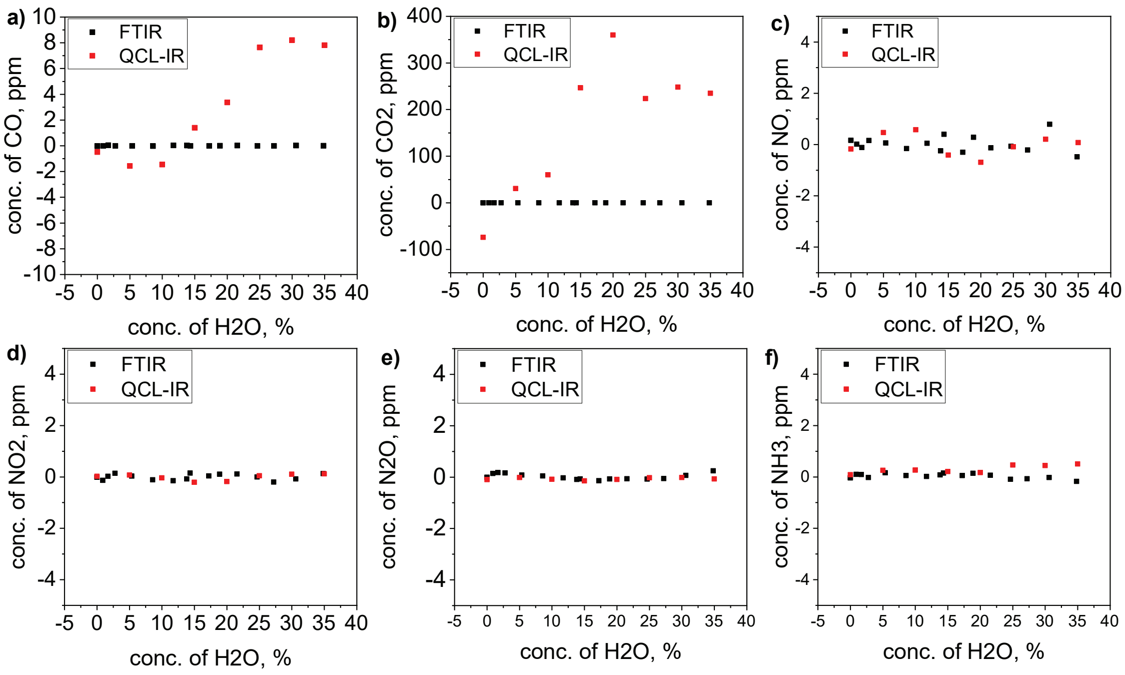

**Fig. 5:** Interference effects at zero point for various components: CO (a), $CO_2$ (b), NO (c), $NO_2$ (d), $N_2O$ (e), $NH_3$ (f)

## 3.2. New methods

### 3.2.1 $H_2$ monitoring solution with mass spectroscopy

A analyzer based on magnetic sector mass spectroscopy was validated. The analyzer is equipped with a sample handling system that operates at 113°C. It is equipped with a complete sample handling system and allows measurements in wet gas. More information of the mass spectrometer can be found in [20]. The mass spectrometer allows measurement in the low ppm range and up to percent level due to multi available measurement ranges from 0-1000 ppm to 0-10%.

For determination of detection limit, range from 0-1000 ppm was chosen. Several mixtures of $H_2$ in the nitrogen background were applied to the spectrometer with concentrations from 0 to 100 ppm, see Fig 6 (a). For all mixtures, the two times standard deviation was below 2 ppm. This allows the detection of small leakages as well as a very accurate efficiency.

For the response time check, a measurement range of 0-5% $H_2$ was used. It was determined by switching from pure nitrogen to 5% $H_2$ in nitrogen background. The data was recorded every 0.1 s, the standard deviation of the measurement determined with 1000 ppm. Response time of the spectrometer is shown in Fig 6(b). $T_{10\text{-}T90}$ time was below 0.2 s. For a complete analyzer with sample handling, the filter and a 12 m heated line, $T_{10\text{-}T90}$ time was below 1s.

In order to test applicability exhaust gas, the influence of a 35% water concentration as well as for various exhaust gas components in reasonable concentrations was tested. This includes for instance 10% CO, 20% $CO_2$, ppm 1000 NO, 200 ppm $NO_2$, but also various hydrocarbons. For all components, the interference was below 30 ppm, which is only slightly above the detection limit of 20 ppm for the applied 5000 ppm measurement range.

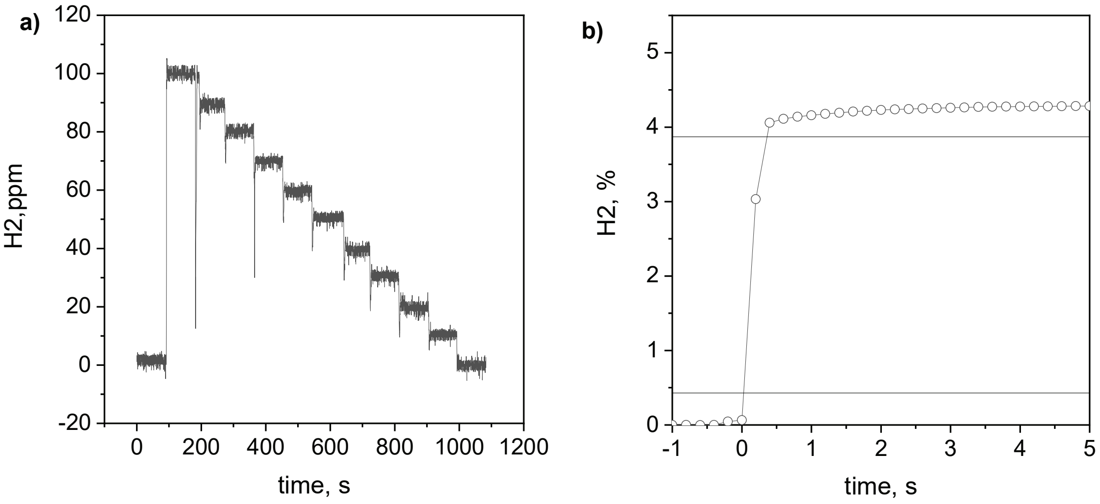

**Fig 6.** Noise (a) and response time (b) of the $H_2$ analyzer

### 3.2.2 $H_2O$ monitoring with NDIR technology

Using NDIR method for water monitoring, two different wavelength regions are suitable: In the near-infrared the spectral range from 2.5 to 2.8 µm or in the mid-infrared the spectral range from 5 to 8 µm. Looking at the range from 2.5 to 2.8 µm, the application is limited to pure $H_2$ ICE applications. It cannot be applied for instance to dual fuel engines or fossil fueled engines as interference from $CO_2$ is expected. In contrast to that, only trace components absorb between 5 at 8 µm, which have no measurable effects for flue gas applications.

The spectral range from 5 to 8 µm was chosen for further investigations. Fig. 7 (a) shows zero noise by a set of 100 data points. The detection limit was determined to less than 65 ppm. For investigation of linearity, a set of mixtures with a water content from 0-35% in instrument air background was generated and applied to the analyzer. A fourth order polynomial was used for linearity correction. Excellent linearity was observed, see Fig. 7 (b). The coefficient of determination was calculated to 0.9996, the maximum deviation from the expected value was less than 0.01% of range.

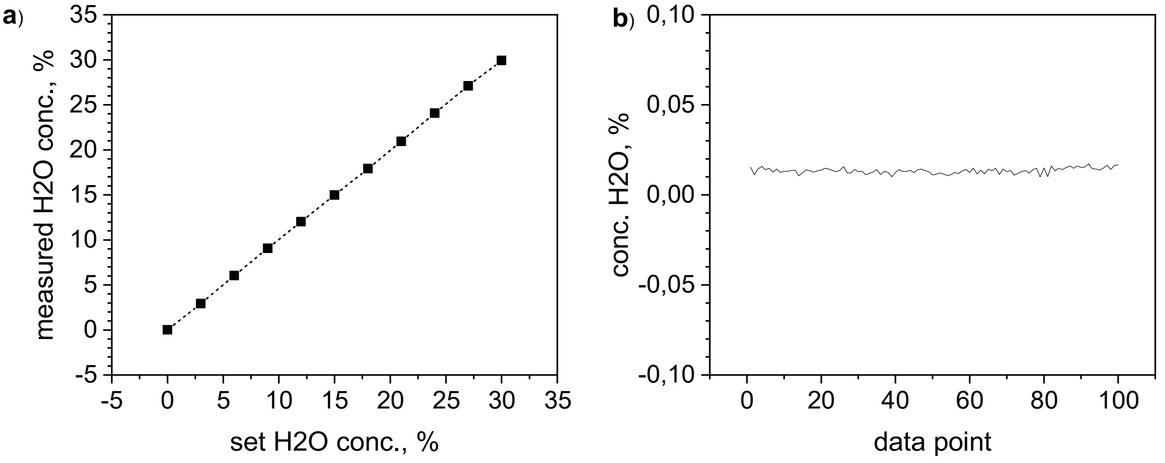

**Fig 7:** Linearity (a) and detection limit (b) of a $H_2O$ analyzer

One big challenge of a water analyzer is the calibration. Although there are devices available in the market, they are very cost intensive and difficult to automize. For that reason, a span calibration using a substitute gas might be advantageous. Several hydrocarbons like ethane, ethylene or propylene absorb at the same wavelength like $H_2$ and are therefore suitable as substitute calibration gas. Propylene was chosen as it is also proposed in the UNR 154 as calibration gas. A gas probe of 10% propylene was applied to the calibration gas. A mean concentration of 16.3 % with a standard deviation of 0.03% was observed.

## 4. Conclusions

Several proven technologies were tested and compared regarding their general performance as well as their applicability to new requirements of ICE engines. According detection limit and repeatability, in principle all units are suitable for exhaust gas measurement and comply current regulations. However, for CO and $CO_2$ monitoring, best detection limit was found with FTIR analyzer. For trace components, better results were achieved with CLD and QCL-IR technology. The water influence was tested up to 35%. For all technologies and components, the measured effect was below detection limit.

As QCL-IR technology is currently only available for limited number of exhaust gas components, an extension to other components is of interest. One possible component of interest is oxygen, which might be of interest for reliable determination of exhaust gas recirculation (EGR) in H2 ICE, as conventional technologies do not allow hot measurements. Also, a reduction of detection limits by extension of the beam path might be interesting for additional applications. Especially in regard to low $NO_x$ limits in US regulations, a reduction of detection limit would increase the applicability of this technology.

## References

[1] https://www.europarl.europa.eu/topics/en/article/20221019STO44572/eu-ban-on-sale-of-new-petrol-and-diesel-cars-from-2035-explained (access April 23. 2024)

[2] https://www.automobil-industrie.vogel.de/eu-co2-emissionen-lkw-busse-einigung-a-84d88d69a881b8ce98cb12e61e4aefbf/?cmp=nl-99&uuid=7876d68fb24b0f613c3e5218586862cb (access April 24, 2024)

[3] https://www.giiresearch.com/report/dmin1382507-global-hydrogen-internal-combustion-engine-market.html (access April 24, 2024)

[4] Barouch Giechaskiel–,*, Anastasios Melas 1 , Jacopo Franzetti 1,2 , Victor Valverde 3 , Michaël Clairotte 1 and Ricardo Suarez-Bertoa, Technologies Vol. 12, pp. 32-52, 2024

[5] Nakamura, H., Kihara, N., Adachi, M., and Ishida, K., "Development of a Wet-based NDIR and Its Application to On-board Emission Measurement System," SAE Technical Paper 2002-01-0612, 2002,

[6] ECE/TRANS/180/ADD15, available online https://unece.org/fileamin/DAM/trans/main/wp29/wp29r-1998agr-rules/ECE-TRANS-180a15e.pdf

[7] Regulation No 49 of the Economic Commission for Europe of the United Nations (UN/ECE), https://eur-lex.europa.eu/legal-content/EN/TXT/PDF/?uri=CELEX:42010X0831(01)

[8] Barouch Giechaskiel and Michaël Clairotte, Applied Science, Vol. 11, 7416-7451

[9] R, Suarez-Bertoa, M. Clairotte, B. Arlitt, S. Nakatani, L. Hill, K. Winkler, C. Kaarsberg, T. Knau5, R. Zijlmans, H. Boertien and C. Astorga, Fuel Vol. 203 pp. 330-340, 2017

[10] M Adachi, H. Nakamura, Engine Emission Measurement Systems. SAE International pp. 73-97, 2011

[11] R. Suarez-Bertao, P. Menoza-Villafuerte, P. Bonnel, V. Lilova, L. Hill, A. Perujo, C.Astergo, Atmospheric Environment, Vol. 139 pp 167-175, 2017

[12] ECE/TRANS/180/ADD13, available online https://unece.org/fileadmin/DAM/trans/main/wp29/wp29wgs/wp29gen/wp29registry/ECE-TRANS-180a13e.pdf (access June 16, 2024)

[13] B. Schrader, Infrared and Raman Spectroscopy. 1st edition, Wiley VCH (2008); pp. 153-161

[14] D. A. Skoog, J.J. Leary, Instrumentelle Analytik. 4th edition, Springer 1996 pp. 84-315; pp. 455-496

[15] available online https://www.spectralcalc.com/spectral_browser/db_data.php

[16] Brian C. Smith, Fundamentals of Fourier transform infrared spectroscopy. 2nd edition, Tylor and Francis Group (2011)

[17] T. Delahaye, X. Landsheere, P. Pangui, F. Huet, J.M. Hartmann, H. Train, Journal of Molecular Spectroscopy, Vol 126, pp. 17-20, 2016

[18] A. Kosterev, G. Wysocki, Y. Bakhirkin, S. So, R. Lewicki, M. Fraser, F. Tittel and R. F. Curl, Application of quantum cascade lasers to trace gas analysis. Appl. Phys. Vol. B 90 (pp. 165–76, 2008

[19] K. Shibuya, A. Podzorov, M. Matsuhama, K. Nishimura, M. Magari, High -sensitivity and low-interference gas analyzer with feature extraction from mid-infrared laser absorption-modulated signal, Measurement Science Technology Vol. 32 035201, 2021

[20] J. E. Lamas, M.C.C. Laedan, K. Hara, JSAE, Conference Proceedings 2022

# Effects of Potential Biofuel Composition on Emission Reduction by a Three-Way Catalyst during Combustion in Direct-Injection Spark Ignition Engine

V. Kärcher[1], P. Hellier[1] and N. Ladommatos[1]

[1] Department of Mechanical Engineering, University College London, WC1E 7JE, UK.

E-mail: p.hellier@ucl.ac.uk
Telephone: +(44) 20 7679 2850

**Abstract.** The displacement of fossil fuel use in transport systems with sustainable alternatives is urgently required to reduce greenhouse gas emissions and address global climate. Advanced biofuels from renewable feedstocks, for example waste biomass, present an opportunity to decarbonise the use of combustion for propulsion but sustainable utilisation of these fuels also requires consideration of impacts on other exhaust pollutants that negatively affect the environment and human health. Therefore, while exhaust after-treatment systems are an established and effective means of emission reduction during combustion of hydrocarbon fuels, there is a need to understand the impacts of biofuel use on the performance of devices including three-way catalysts (TWC) for simultaneous reduction of nitrogen oxides (NOx), carbon monoxide (CO) and unburnt hydrocarbons (THC).

This study therefore investigates the effects of four potential biofuel molecules from sustainable feedstocks, 2-methylfuran (MF), 2-methyltetrahydrofuran (MTHF), gamma valerolactone (GVL) and linalool (LNL), on combustion characteristics, engine-out exhaust emissions and pollutant conversion across a three-way catalyst (TWC) in a gasoline direct injection engine. The potential biofuel molecules were blended with reference gasoline (RGL) at 20 % wt/wt and supplied to a light-duty direct injection spark ignition engine operated at constant speed and load, with gaseous and particulate exhaust emissions measured pre- and post- TWC during catalyst warm-up during engine cold-start and at steady state.

While all of the biofuel blends displayed similar rates of heat release rate relative to gasoline only combustion, the MF blend significantly increased CO and NOx engine-out emissions both during cold-start and at steady state. The use of GVL reduced NOx, while hydrogen ($H_2$) emissions correlated with blend hydrogen carbon ratio. All of the biofuel blends increased the TWC inlet temperature required for pollutant conversion, while MF, LNL and GVL increased $H_2$ levels post-TWC at higher temperatures. LNL exhibited higher particulate levels post-TWC than gasoline only, despite lower engine-out emissions during combustion of the biofuel blend.

## Notation

| | |
|---|---|
| *TWC* | *Three-way catalyst.* |
| *NOx* | *Nitrogen oxides.* |
| $CO_2$ | *Carbon dioxide.* |
| *CO* | *Carbon monoxide.* |
| *THC* | *Unburnt hydrocarbons.* |
| $H_2$ | *Hydrogen.* |
| *MF* | *2-methylfuran.* |
| *MTHF* | *2-methyltetrahydrofuran.* |
| *GVL* | *Gamma valerolactone.* |
| *LNL* | *Linalool.* |
| *RGL* | *Reference gasoline.* |
| *IMEP* | *Indicated mean effective pressure.* |
| $\lambda$ | *Exhaust lambda value.* |
| *PN* | *Particle number.* |
| *PM* | *Particle mass.* |
| *CAD* | *Crank angle degree.* |
| *BTDC* | *Before top dead centre.* |
| *PGM* | *Platinum group metals.* |
| *Ø* | *Diameter.* |
| *cpsi* | *Cells per square inch.* |
| $AFR_{st}$ | *Stoichiometric air fuel ratio.* |
| $T_{boil}$ | *Boiling temperature.* |
| $\sigma$ | *Standard deviation.* |

## 1. Introduction

The urgent need to address global climate change[1] and achieve net-zero carbon emission requires the displacement of fossil fuels in transport with renewable alternatives[2,3]. Liquid fuels from bio-derived feedstocks and synthetic fuels produced from zero-carbon electricity provide an opportunity to progress the decarbonisation of various transport sectors while utilising existing infrastructure and vehicle fleets[4]. However, an important challenge in realising the sustainable use of alternative fuels in internal combustion (IC) engines for transport is the minimisation of pollutant emissions detrimental to air quality and public health[5]. While exhaust after-treatment devices have been optimised for the reduction of pollutant emissions from the use of hydrocarbon-based fossil-derived fuels in compliance with current and upcoming legislative limits, there is a need to understand how the introduction of renewable fuels of varying composition impact the efficiency of these systems[6,7].

The conversion of lignocellulosic biomass to liquid compounds with potential use as drop-in fuels for both spark ignition and compression ignition engines has received significant attention; in the context of production processes[8–12] and also effects on engine combustion and emissions during utilisation[13–16]. Such fuels potentially present lesser impact on land-use and greater net reductions in greenhouse gas emissions than current widely used biofuels, namely ethanol and fatty acid methyl ester biodiesel[17]. Various processes have been developed for the conversion of lignocellulosic biomass to furfural, a platform chemical suitable for onward transformation to various high-value chemicals and potential renewable fuels[18]. The use of furfural as a drop-in fuel is limited by unfavourable physical properties and sequential steps of hydrogenation can be applied to reduce fuel bound oxygen resulting in species including 2-methylfuran (MF) and 2-methyltetrahydrofuran (MTHF)[19]. Other processing routes can result in species incorporating alternative oxygenated functional groups, for example acyclic alcohols and lactones[19,20].

Three-way catalysts (TWC) have been widely utilised for spark ignition engines operating with stoichiometric air fuel mixtures since the introduction of exhaust emissions limits to achieve the simultaneous reduction of nitrogen oxides (NOx) alongside oxidation of carbon monoxide (CO) and unburnt hydrocarbons (THC)[21]. While these were initially developed for non-oxygen bearing gasoline fuels consisting of various hydrocarbon species, several previous studies have investigated the effect of fuel composition on TWC performance, primarily ethanol gasoline blends and for which varying effects of fuel oxygen have been observed[22–24].

Iodice et al. [25] investigated the reduction of pollutants by a TWC with ethanol gasoline blends of varying composition. At hot catalyst conditions increasing fuel ethanol content consistently increased pollutant reduction by TWC, attributed to lower engine out levels via more complete combustion, however, less consistent effects were observed during cold-start, with a 30 % ethanol in gasoline blend increasing CO and HC levels post- TWC. Kärcher et al. [26] investigating the effects of hydrogen ($H_2$) addition upstream of a TWC, and also synergies with fuel composition, found that use of ethanol and butanol gasoline blends resulted in reduced conversion temperatures for up to 1500 ppm $H_2$, while larger and cyclic oxygenates showed an opposing effect. Sinha Majumdar et al.[27] and Ladshaw et al. [28] investigated and modelled the impact of various oxygenates on an aged TWC in a synthetic exhaust flow reactor. Experiments were undertaken with fixed fuel concentrations of 3000 ppmC in the synthetic exhaust gas and oxygen flowrates varied so as to achieve constant lambda values ($\lambda$). The presence of short-chain acyclic oxygenates in the synthetic exhaust gas decreased the light-off temperature of the TWC for conversion of CO, THC and NOx, while increases in TWC light-off temperature were observed with the presence of aromatics and cyclic oxygenates.

This paper presents the results of engine experiments investigating the effects of four novel potential biofuel molecules on TWC emission conversion when present during combustion in a direct-injection spark ignition engine. The potential biofuel molecules included two furans, a lactone ester and long-chain alcohol, representative of a range of potential fuels from lignocellulosic biomass. The molecules were tested during engine warm-up and steady state conditions as 20 % (wt/wt) blends with a fossil gasoline, with measurements of in-cylinder pressure, engine-out emissions, and TWC reduction of regulated pollutants, CO, THC, NOx, particle number (PN) and particle mass (PM), and $H_2$.

## 2. Experimental methodology

### 2.1 Engine and catalyst test facility

All experiments were undertaken with a modified VW 1.4L TSI engine, operated with three firing and one motored cylinder. The engine had been modified for research use with separate intake and exhaust manifolds for the three firing cylinders and single motored cylinder. Fuel was supplied to the three firing cylinders from a 4.3 L fuel tank compressed by nitrogen via the original manufacturer high-pressure fuel pump and common rail. Fuel was injected to each cylinder via 6-hole solenoid injectors (Magneti Marelli) and control of injection parameters determined through the PC interface of the engine control unit (ECU). In-cylinder gas pressure was measured at a resolution of 0.4 CAD by a water-cooled, piezoelectric pressure transducer (Kistler 6061BS31) and recorded by a bespoke data acquisition system (National Instruments Labview). Engine exhaust gas from the three firing cylinders was passed through a TWC with emissions measurement upstream and downstream of the catalyst. A schematic overview of the engine and catalyst test facility is shown in Figure 1, while Table 1 lists the engine specification.

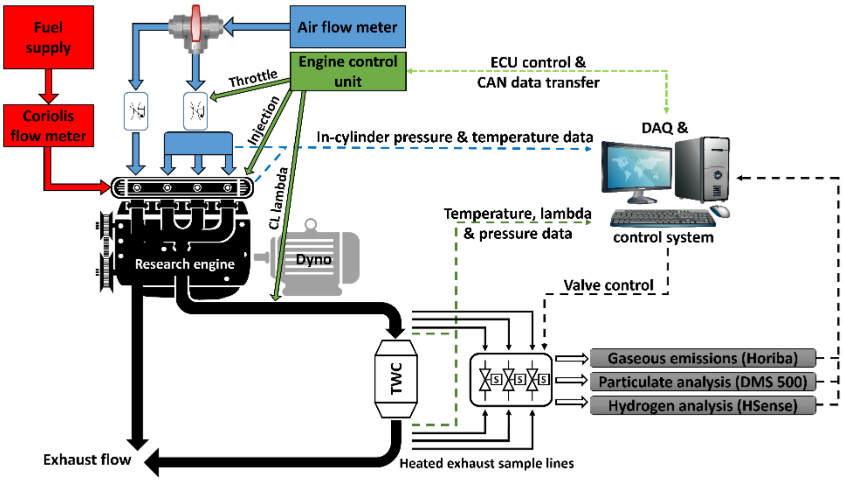
Fuel supply
Coriolis flow meter
Air flow meter
Engine control unit
Throttle
Injection
ECU control &
CAN data transfer
DAQ &
control system
In-cylinder pressure & temperature data
CL lambda
Temperature, lambda
& pressure data
Research engine
Dyno
Valve control
TWC
S
S
S
Gaseous emissions (Horiba)
Particulate analysis (DMS 500)
Hydrogen analysis (HSense)
Exhaust flow
Heated exhaust sample lines

**Fig. 1.** Schematic representation of the engine and catalyst test facility

**Table 1**. Engine specification

| | |
|---|---|
| Number of cylinders | 4 |
| Bore (mm) | 76.5 |
| Stroke (mm) | 75.6 |
| Swept volume/cylinder (cm$^3$) | 347.5 |
| Compression ratio | 10:1 |
| DI fuel injectors | 6-hole solenoid |
| Coolant temperature (°C) | 82 ± 4 |
| Oil temperature (°C) | 80 ± 2 |

A commercially available Euro VI compliant ceramic brick TWC was utilized and had been previously de-greened until steady state performance reached, with Table 2 showing the TWC parameters. Exhaust gas temperature and $\lambda$ were measured at the inlet to the TWC, with measurement and sampling ports placed within 150 mm to 200 mm either upstream or downstream of the TWC. Concurrent measurements of gaseous emissions (CO, $CO_2$, THC and NOx) were made both upstream (pre-) and downstream (post-) of the TWC by Horiba Mexa 9100 and 9400 automotive emissions analyzers via separate PID controlled heated lines at a constant temperature of 190 °C. Measurements of $H_2$ concentration and particulate emissions were undertaken via further heated lines in immediately consecutive experiments (due to analyzer availability) by V&F Hsense electron impact mass spectrometer and Cambustion DMS500 fast particulate spectrometer respectively.

**Table 2**. Properties of the ceramic TWC brick

| | |
|---|---|
| Catalyst type | 3-way – Pd/Rh/Pt |
| Base material | Cordierite |
| PGM ratio | 19/5/1 |
| PGM loading (g) | 15 |
| Ø of element (mm) | 101 |
| Length of element (mm) | 76 |
| Volume (L) | 0.61 |
| Cell density (cpsi) | 400 |
| Wall thickness (mm) | 0.15 |

## 2.2 Fuels investigated

Four potential biofuel molecules, 2-methylfuran (MF), 2-methyltetrahydrofuran (MTHF), gamma valerolactone (GVL) and linalool (LNL), were tested as 20 % gravimetric (wt/wt) blends with a reference gasoline (RGL). The molecules were selected as representative of molecules feasibly achieved from lignocellulosic biomass and also to provide insight into the following effects of fuel molecular structure:

1. Degree of saturation in a furan ring, MTHF relative to MF.
2. Addition of a ketone group, GVL relative to MTHF.

All of the single component molecules were obtained from a chemical supplier (Sigma Aldrich) at an assay of 96 % or greater, while the reference gasoline (Carcal RF-02-03) was fossil derived and obtained from a fuels supplier (Haltermann-Carless). The molecular structure of the potential biofuel molecules is shown in Table 3, while Table 4 lists the properties of all fuels tested.

**Table 3**. Fuel molecular structures

| | |
|---|---|
| 2-methylfuran (MF) | 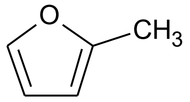 |
| 2-methyltetrahydrofuran (MTHF) | 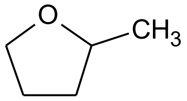 |
| Gamma valerolactone (GVL) | 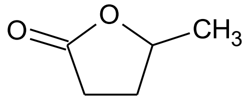 |
| Linalool (LNL) | 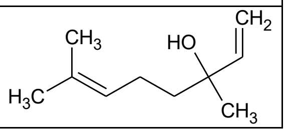 |

**Table 4**. Fuel properties

| **Fuel** | **Molecular formula** | **$AFR_{st}$*** | **H/C** | **Oxygen (%)** | **$T_{boil}$ (°C)**[29] | **Density (kg/dm$^3$)** [29] | **Assay (%)** |
|---|---|---|---|---|---|---|---|
| Reference gasoline | - | 14.22 | 1.73 | 0.92 | - | 0.747 | - |
| 2-methylfuran | $C_5H_6O$ | 10.11 | 1.2 | 19.49 | 65 | 0.913 | 98 |
| 2-methyltetrahydrofuran | $C_5H_{10}O$ | 11.24 | 2.0 | 18.57 | 78 | 0.855 | 99 |
| Linalool | $C_{10}H_{18}O$ | 12.55 | 1.6 | 10.37 | 198[30] | 0.867 | 96 |
| Gamma-valerolactone | $C_5H_8O_2$ | 8.29 | 1.8 | 31.96 | 219 | 1.079 | 99 |

* = calculated according to the method of Spicher[31]

### 2.3 Experimental Conditions

Each of the fuel blends and reference gasoline were tested at constant engine operating conditions of 1600 rpm, 4.7 bar IMEP (indicated mean effective pressure) and exhaust lambda value (λ) of between 0.995 to 0.997. The throttle position was adjusted for each fuel so as to achieve a constant IMEP for all tests of 4.77 ± 0.02 bar, while the engine was operated in a closed-loop lambda mode, with a 1 Hz 2.5% lambda perturbation. For all tests, fuels were injected at a timing of 280 CAD BTDC and pressure of 80 bar with the injection duration determined by the closed loop control. A spark timing of 15 CAD BTDC was used for all tests, while every experiment included a 12 second period of operation on start-up at 900 rpm for stabilization and heating of the closed-loop lambda probe. Measurements were taken both during an initial cold-start phase of 300 seconds following engine start-up for each test and also subsequently at steady-state conditions. A summary of the experimental and engine operating conditions specific to each fuel is shown in Table 5.

**Table 5**. Engine operating conditions for oxygenated fuel blends and gasoline

| Fuel | Injection duration (ms) | | Throttle position (%) | | Lambda (λ) | Fuel flow (g/min) | | IMEP (bar) | |
|---|---|---|---|---|---|---|---|---|---|
| | Mean | 1σ | Mean | 1σ | | Mean | 1σ | Mean | 1σ |
| Reference gasoline | 1.667 | 0.006 | 7.62 | 0.03 | 0.995 | 29.05 | 0.14 | 4.75 | 0.03 |
| 2-methylfuran | 1.738 | 0.0012 | 7.63 | 0.05 | 0.996 | 30.67 | 0.16 | 4.78 | 0.02 |
| 2-methyltetrahydrofuran | 1.718 | 0.015 | 7.56 | 0.05 | 0.995 | 30.29 | 0.22 | 4.79 | 0.06 |
| Linalool | 1.733 | 0.011 | 7.59 | 0.05 | 0.997 | 30.76 | 0.23 | 4.77 | 0.04 |
| Gamma-valerolactone | 1.804 | 0.015 | 7.70 | 0.04 | 0.996 | 32.52 | 0.18 | 4.79 | 0.04 |

## 3. Results and discussion

### 3.1 Combustion characteristics

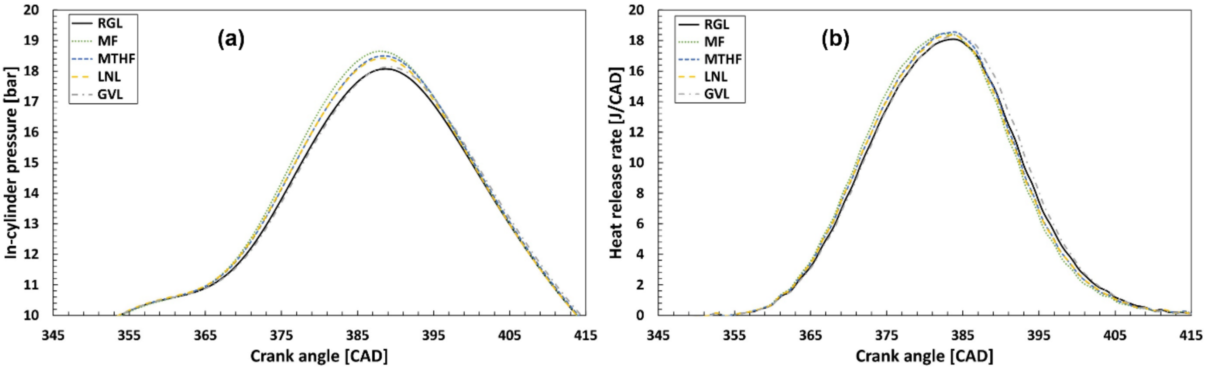

**Fig. 2.** (a) In-cylinder pressure and (b) apparent net heat release rate of 20 % (wt/wt) fuel blends and reference gasoline at steady-state operation following engine cold-start

Figure 2 shows the in-cylinder pressure and apparent net heat release rate of the 20 % potential biofuel molecule blends with gasoline and also the reference gasoline. Readily apparent from Figure 2 is that addition of 20 % of the potential biofuel molecules did not significantly impact combustion phasing, however, it can be seen that, with the exception of the 20% GVL blend, all of the fuel blends resulted in an elevated in-cylinder pressure (Figure 2.a). This is in agreement with the slightly higher engine IMEP during the fuel blend tests (Table 5), however, it is interesting to note that the GVL blend produced the highest relative IMEP (4.79 vs 4.75 bar) and widest opening throttle position. Figure 2.b shows an earlier increasing heat release rate for the potential biofuel blends relative to reference gasoline following ignition, with the exception of the GVL blend and in agreement with the observed lower in-cylinder pressure (Figure 2.a). Of the fuel blends, the fastest increase in heat release rate is apparent in the case of MF (Figure 2.b), in agreement with previous studies of MF as a single component fuel where faster combustion relative to RGL was observed[32,33]. In shock tube experiments by Jouzdani et al.[34], MTHF was found to display longer ignition delay times than MF, attributed to the presence of weaker C-H bonds more susceptible to radical attack in the unsaturated furan and in agreement with the slower rates of heat release rate increase apparent in Figure 2.b. The higher heat release rates of MTHF relative to GVL are in contrast to the study of Talibi et al. [35] where in blends with ethanol and gasoline the furan displayed lower rates of heat release. This work, however, utilized a carburetor for fuel delivery within the engine intake manifold, suggesting a greater influence of the elevated boiling point and density of the lactone relative to the furan in the current study employing high-pressure direct injection of the fuels. Also utilizing a carburetor for fuel delivery, Hellier et al.[30] observed an initial increase in peak heat release rate with the addition of 10 % linalool to gasoline, similar to the increase apparent in Figure 2.b, but a level of peak heat release lower than gasoline with a blend of 40 % LNL.

### 3.2 Engine-out emissions

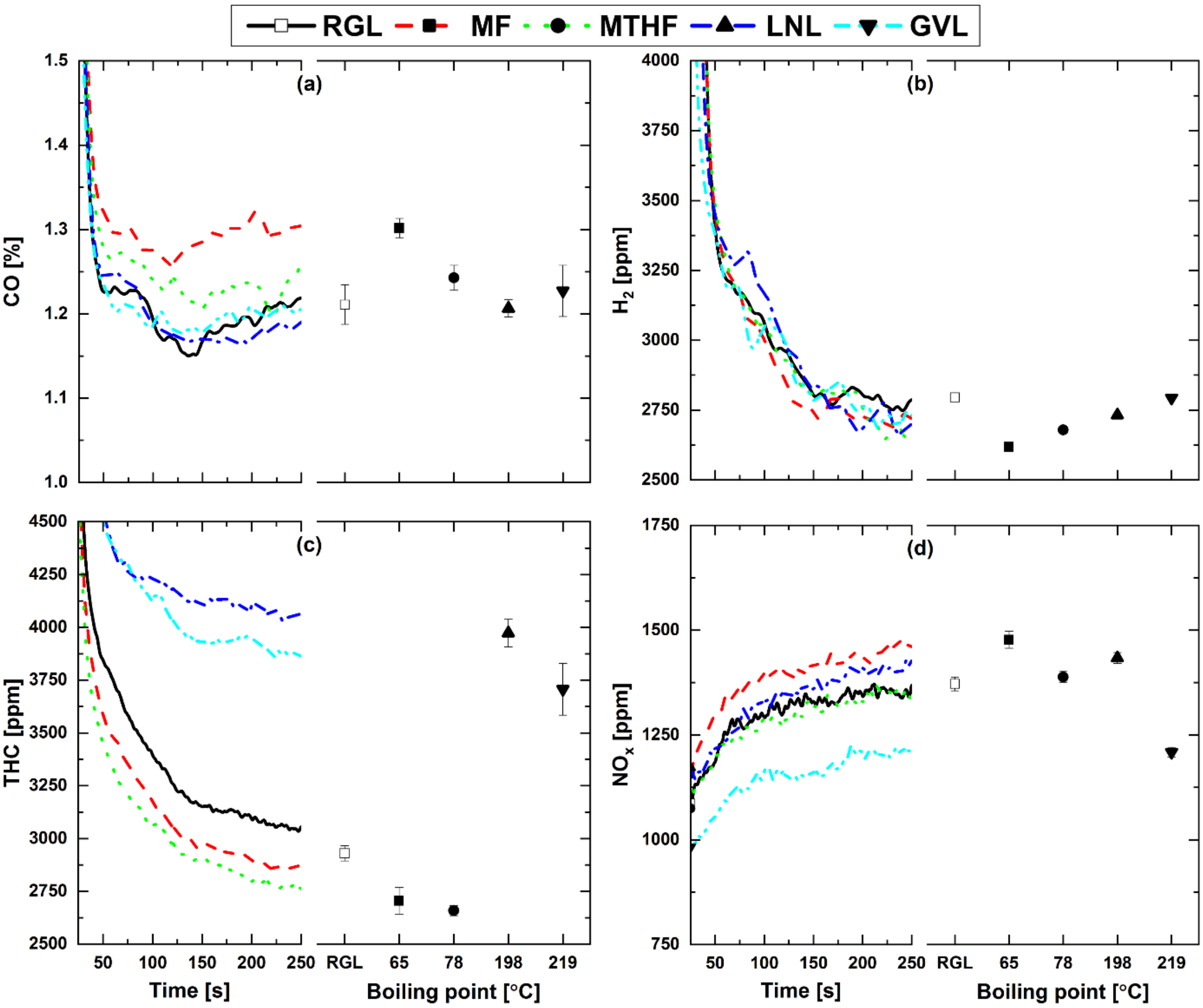

**Fig. 3.** (a) CO, (b) $H_2$, (c) THC and (d) NOx engine out emissions from 20 % (wt/wt) fuel blends and reference gasoline during cold-start and at steady-state operation relative to blend component boiling point

Figure 3 shows the engine-out gaseous emissions from the 20 % fuel blends and reference gasoline during the engine cold-start period, and at steady-state relative to the boiling point of the potential biofuel molecule present in each blend. Where shown in Figure 3 and subsequent figures, the data points indicate mean values and the error bars one standard deviation from the mean. In Figure 3.a, it can be seen both furan blends, those of MF and MTHF, exhibited appreciably higher levels of CO during engine cold-start relative to the LNL and GVL blends, and reference gasoline. Most pronounced are the higher levels of CO emitted by MF, displaying both a lesser initial decrease following engine start-up and a greater increase during 100 to 250 seconds of engine operation. Levels of engine-out $H_2$

(Figure 3.b) were however similar for all fuels tested, with the greatest deviation displayed by the LNL blend between 50 to 100 seconds during cold-start.

Figure 3.c. shows the engine-out measurements of THC, with significantly higher levels emitted by LNL and GVL throughout engine cold-start, while both furan blends produced lower THC than the reference gasoline, as observed in previous tests of MF and MTHF gasoline blends[36,37]. Readily apparent from Figure 3.c. is the correlation between fuel blend component boiling point and THC, with the two molecules of highest boiling point, GVL and LNL, emitting significantly higher levels throughout relative to the lower boiling point furans (Table 4). The higher boiling points of GVL and LNL may have reduced rates of vaporization and efficiency of fuel air mixing during the compression stroke, resulting in a less homogenous mixture and greater persistence of unburnt fuel[38]. In Figure 3.d, it can be seen that for all fuels levels of NOx emitted increased during engine cold-start, with the highest levels throughout displayed by the MF blend and the lowest by GVL. This is in agreement with previous studies of MF[36] and the observed lower peak in-cylinder pressure and slower increase in heat release rate of the GVL blend (Figure 2), with both characteristics likely to reduce the magnitude of in-cylinder temperatures where the majority of NOx is expected to form through thermal oxidation of nitrogen, the rates of which are highly sensitive to temperature[38,39].

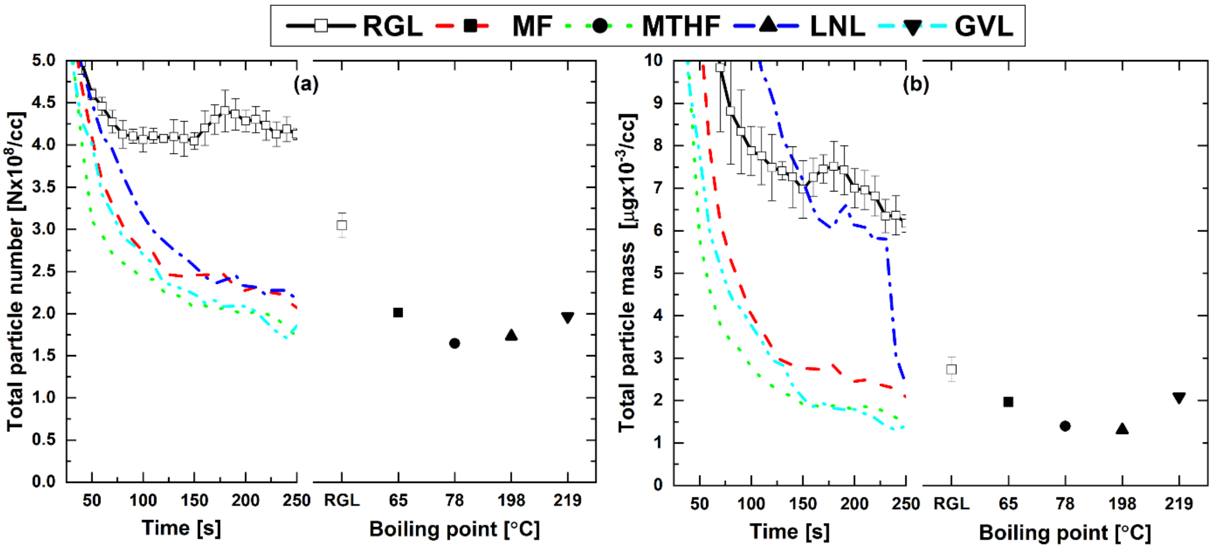

**Fig. 4.** (a) Total particle number and (b) total particle mass engine-out emissions from 20 % (wt/wt) fuel blends and reference gasoline during cold-start and at steady-state operation relative to blend component boiling point

Figure 4 shows the engine-out particulate emissions from the 20 % fuel blends and reference gasoline during the engine cold-start period, and at steady-state relative to the boiling point of the potential biofuel molecule present in each blend. Immediately apparent from Figure 4.a is the significant reduction in particle number (PN) for all of the potential biofuel molecule blends throughout the engine cold-start period relative to RGL, with the largest reductions apparent from GVL and MTHF. It is suggested that the especially high oxygen content of GVL inhibited particle formation through limiting the availability of carbon atoms for production of soot precursors[40], while the greater reduction of PN displayed by MTHF relative to MF can potentially be attributed to the aromatic character of the later[41]. In Figure 4.b, it can be seen that all of the potential biofuel blends exhibited lower particle mass (PM) levels during cold-start relative to RGL, with the exception of LNL. While the blends of MTHF, GVL and MF all displayed a rapid decrease in the level of PM emitted during the first 100 seconds of cold-start, levels of PM emitted by LNL did not show significant decrease until after 100 seconds (later than exhibited by RGL), only reducing to a level below that of RGL between 225 and 250 seconds after engine start.

Figure 5 shows the particle number size distribution measured in the engine-out exhaust during combustion of the 20 % fuel blends and reference gasoline at steady-state, following cold-start. It can be seen that all of the potential biofuel molecule blends exhibited a lower peak particle number than RGL, found at a similar particle diameter of 10 to 20 nm for all fuels tested (Figure 5).

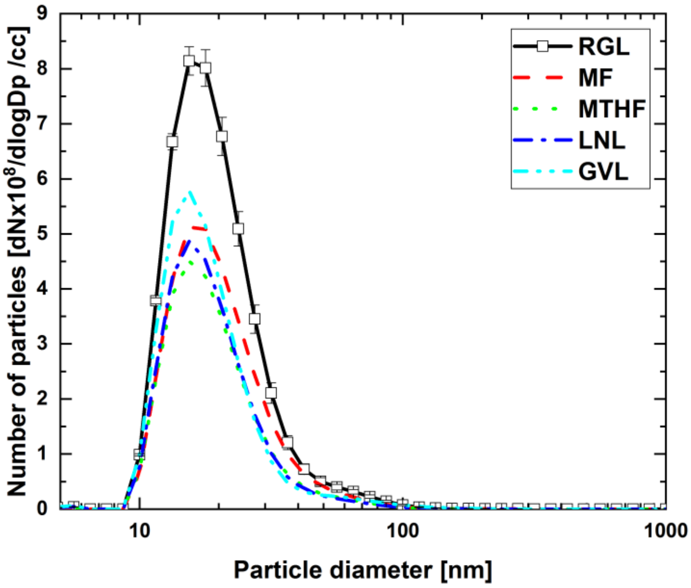

**Fig. 5.** Engine-out particle number size distribution from 20 % (wt/wt) fuel blends and reference gasoline steady-state operation

### 3.2 TWC emissions conversion

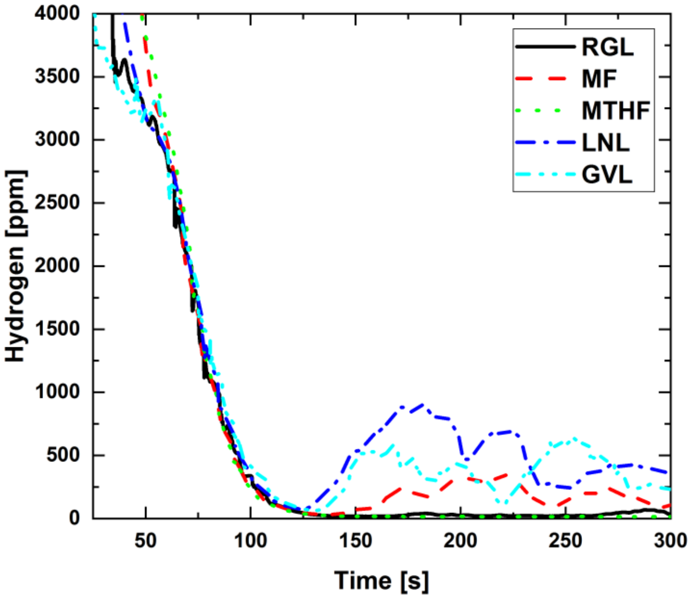

**Fig. 6.** $H_2$ concentrations post- TWC from 20 % (wt/wt) fuel blends and reference gasoline during engine cold-start

Figure 6 shows the exhaust $H_2$ concentration post- TWC during combustion of the potential biofuel molecule blends and RGL during engine cold-start. It can be seen that while $H_2$ levels initially remain similar for all fuels, with near complete conversion by 120 seconds, subsequently levels from LNL, GVL and MF increase appreciably, deviating from RGL and MTHF. The most significant increase is exhibited by LNL, increasing to approximately 800 ppm $H_2$ at 180 seconds, while $H_2$ levels post- TWC from MF decrease to a similar level as exhibited by RGL at 300 seconds (Figure 6). This is in contrast to the engine-out, pre- TWC $H_2$ levels measured (Figure 3.b), which remained similar for all fuels during the cold-start period. It is suggested that the higher densities of LNL, GVL and MF relative to RGL (Table 4) may have reduced access to the active sites within the TWC washcoat, reducing conversion capability. The higher density, and molecular weight, of these molecules may have decreased diffusion rates of these species, impeding access and conversion of $H_2$, especially during lower temperature operation of the TWC earlier in the cold-start period. An additional possibility in the case of LNL and GVL is that higher engine out THC (Figure 3.c) may have increased $H_2$ formation across the TWC (Figure 6) via the water-gas shift reaction[42]. Furthermore, the higher levels of $H_2$ across the TWC during operation with LNL and GVL (Figure 6) may have exacerbated the formation of $NH_3$ and $N_2O$[43,44], especially so LNL which also emitted among the highest levels of engine out NOx (Figure 3.d).

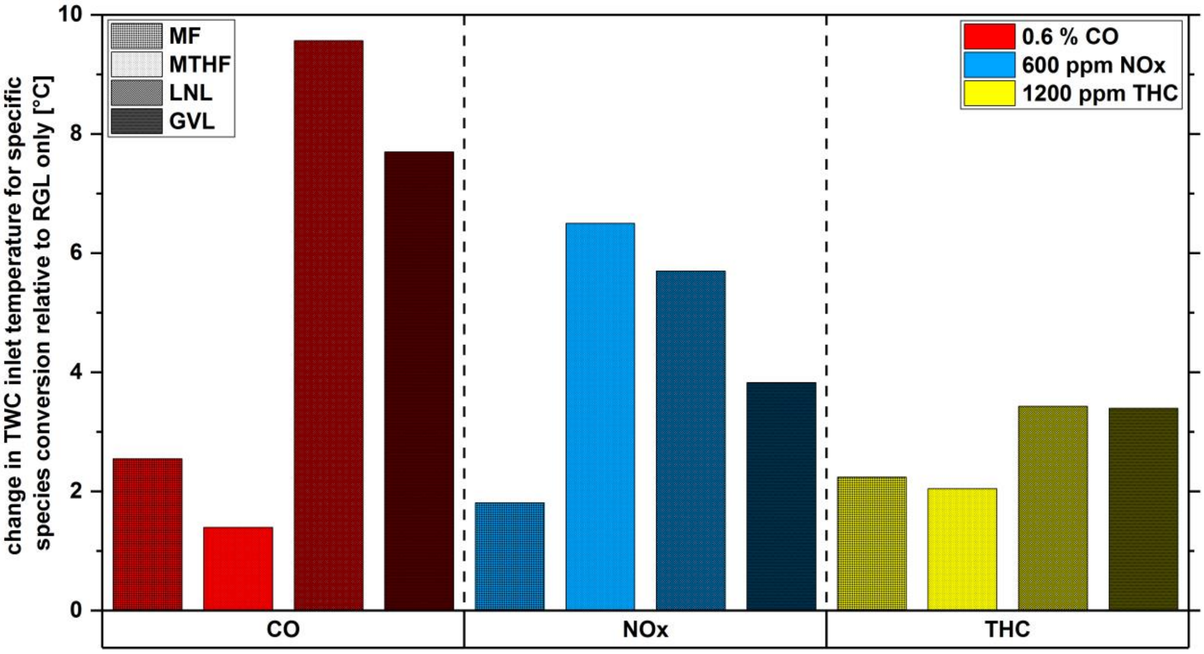

**Fig. 7.** Change in TWC inlet temperature required for consuming 0.6 %, 600 ppm and 1200 ppm of CO, NOx and THC respectively for 20 % (wt/wt) fuel blends relative to RGL

Figure 7 shows the change in TWC inlet exhaust gas temperature required for the conversion of 0.6 % CO, 600 ppm NOx and 1200 ppm THC during combustion of the potential biofuel molecule blends relative to the same level of absolute pollutant species conversion during operation with RGL. It can be seen from Figure 7 that use of all of the potential biofuel molecule blends required an increase in the TWC inlet temperature of between 1 to 9.5 °C for pollutant reduction relative to RGL, suggesting reduced conversion efficiency in all cases. LNL and GVL required the largest increases in TWC inlet temperature of ~9.5 °C and ~7.5 °C for conversion of CO, while the same level of reduction was achieved through increases of 2.5 °C and 1.5 °C for the unsaturated and saturated furans respectively. For conversion of 600 ppm of NOx, the largest temperature increase of ~6.5 °C was required for MTHF, with an increase of only 2 °C necessary for the same conversion with MF (Figure 7). Overall, the increase in TWC inlet temperature required for conversion of 1200 ppm THC relative to RGL was less for all fuel blends relative to that necessary for CO and NOx, with both furans displaying an increase of ~2.5 °C and LNL and GVL showing ~3.5 °C increase.

In comparing Figures 3 and 7, it can be seen that GVL required an increase in the TWC inlet temperature for conversion of 600 ppm NOx despite producing lower engine-out NOx than RGL (Figure 3.d), suggesting a direct effect of fuel composition; as opposed to effects arising from combustion related changes in engine-out exhaust gas composition. A similar observation, albeit to a lesser extent, can be made when considering the lower THC engine-out emissions of both furans relative to RGL (Figure 3.c) with the increase of ~2ºC required in TWC inlet temperature for conversion of 1200 ppm THC (Figure 7).

Figure 8 shows the total PN and PM emissions post-TWC from the potential biofuel molecule fuel blends and RGL during cold-start and at steady-state relative to the fuel component density. In Figure 8.a, it can be seen that PN levels post- TWC decreased throughout the cold-start period for all fuels except LNL and, to a lesser extent, GVL. Also apparent is that from approximately 100 seconds onwards (Figure 8.a), PN levels post- TWC are significantly reduced compared to engine-out, pre- TWC, where the PN concentration for all fuels remained above 1.5 x $10^8$ per cc (Figure 4.a). Figure 8.b shows a similar effect of fuel composition, with higher post- TWC PM from LNL and GVL relative to RGL and both furan blends. With the exception of LNL, a reduction in PM across the TWC is also apparent (Figures 4.b and 8.b), albeit to a much lesser extent than observed in PN, highlighting the greater efficacy of the TWC in the oxidation of smaller nucleation mode particles which impact less on total particle mass[45,46]. No clear effect of fuel component density is apparent in Figure 8, potentially suggesting no significant contribution of liquid fuel droplets in the PN concentrations recorded.

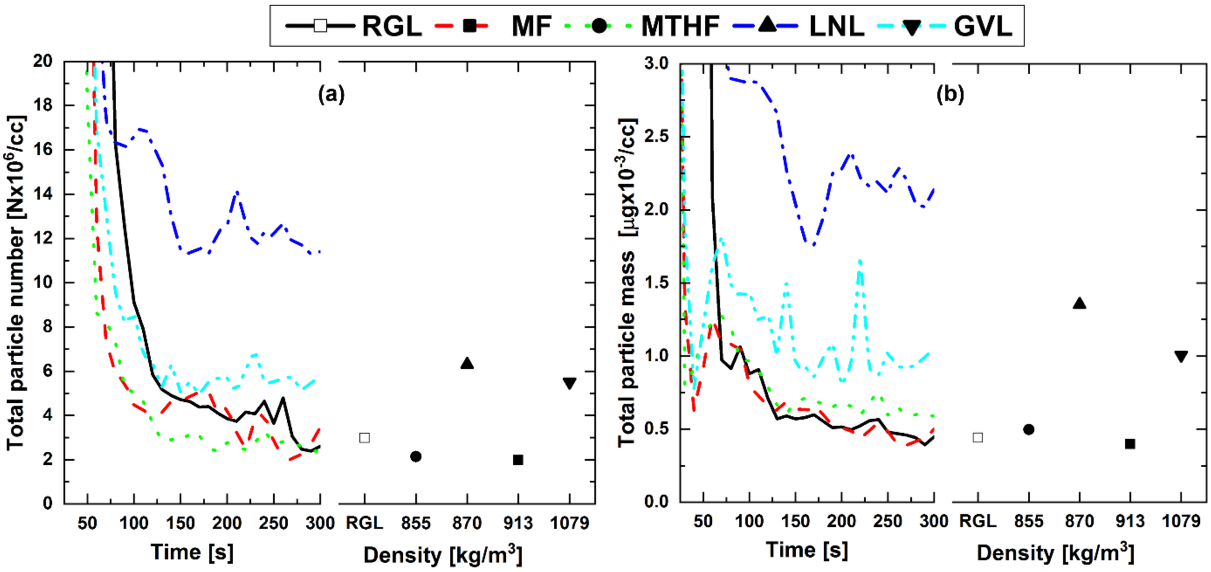

**Fig. 8.** (a) Total particle number and (b) total particle mass post- TWC from 20 % (wt/wt) fuel blends and reference gasoline during cold-start and at steady-state operation relative to blend component density

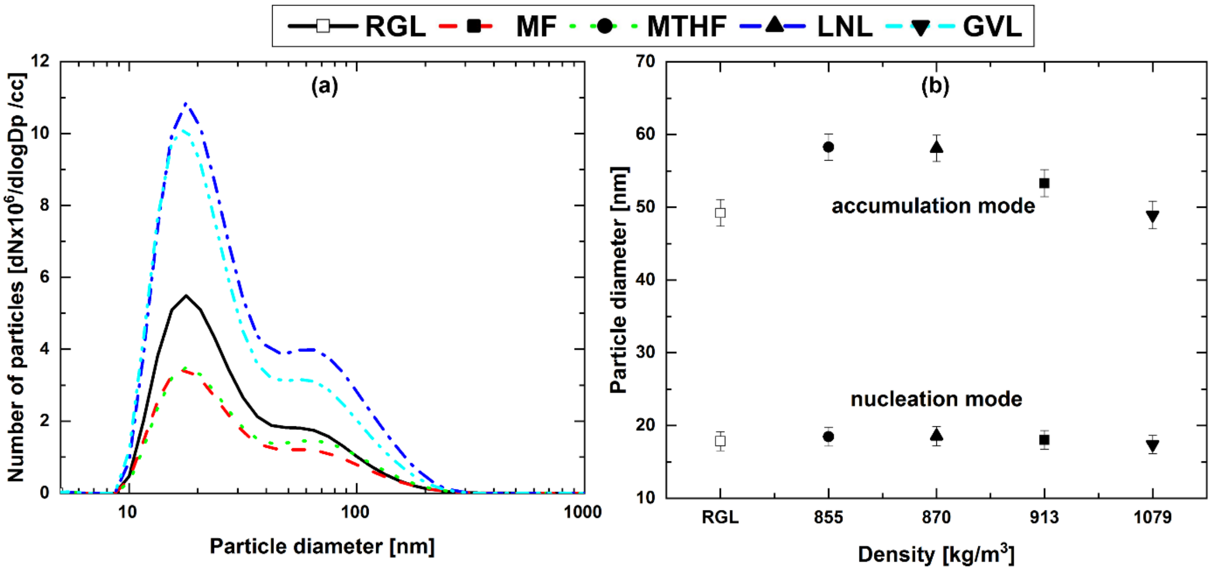

**Fig. 9.** (a) Particle number size distribution and (b) median nucleation mode and accumulation mode particle diameters against fuel component density post- TWC from 20 % (wt/wt) fuel blends and reference gasoline at steady-state operation

Figure 9 shows the particle number size distribution and median nucleation and accumulation mode particle diameters post-TWC from the potential biofuel molecule fuel blends and RGL at steady-state relative. Apparent from Figure 9.a are the larger peak particle numbers from LNL and GVL relative to RGL in both nucleation and accumulation mode size ranges. Both furans, MF and MTHF, however, exhibited lower peak particle numbers, with no clear effect of the furan ring saturation (Figure 9.a). It can also be seen that relative to engine-out, pre-TWC (Figure 5), peak particle numbers in nucleation mode size range are significantly reduced for all blends (Figure 9.a), though this effect is diminished by the presence of 20 % LNL and GVL. Figure 9.b. shows a decrease in accumulation mode median particle diameter with increasing fuel blend component density, with that of the GVL blend similar to RGL only.

## Conclusions

Four potential oxygenated biofuel molecules, MF, MTHF, GVL and LNL, were tested in a direct-injection spark ignition engine as 20 % blends with reference gasoline. From observation of fuel effects during both engine cold-start and steady-state operation, the following specific conclusions in relation to combustion characteristics, engine-out emissions and TWC conversion performance can be drawn:

1. All four potential biofuel molecules resulted in an increase in TWC inlet temperature required for the conversion of absolute amounts of CO, THC and NOx relative to RGL, even when displaying lower engine-out emissions. Post- TWC levels of $H_2$ increased for LNL, GVL and MF following an initial decrease during engine cold-start, attributed to the higher density and molecular weight of the oxygenate molecules.
2. During engine cold-start, PN levels were reduced downstream of the TWC for all fuels, albeit to a lesser extent for LNL, the molecule of lowest oxygen content of those investigated. The peak number of nucleation mode particles was reduced by the TWC for all fuels relative to that of accumulation mode particles, with a fuel effect apparent in GVL and LNL displaying higher peak particle numbers than RGL despite lower engine-out levels.
3. Addition of 20 % MF, MTHF and LNL increased peak heat release rates during combustion relative to RGL. However, the GVL blend reduced combustion speed and delayed peak heat release relative to RGL, with the denser lactone blend requiring a higher fuel flowrate and wider throttle opening position for an equivalent engine IMEP.
4. Both furan blends increased engine-out CO but decreased THC levels relative to RGL, while the use of LNL and GVL appreciably increased THC. Emissions of NOx were primarily influenced by changes in combustion phasing and thermal conditions produced by varying fuel composition, while all of the oxygenated fuels reduced engine-out PN during cold-start.

## References

[1] Falk J, Colwell RR, Behera SK, El-Beltagy AS, Gleick PH, Kennel CF, et al. An urgent need for OP27: confronting converging crises. Sustain Sci 2023;18:1059–63. doi:10.1007/s11625-022-01253-5.

[2] Cheng F, Luo H, Jenkins JD, Larson ED. The value of low- and negative-carbon fuels in the transition to net-zero emission economies: Lifecycle greenhouse gas emissions and cost assessments across multiple fuel types. Appl Energy 2023;331:120388. doi:10.1016/j.apenergy.2022.120388.

[3] Khan MZA, Khan HA, Ravi SS, Turner JW, Aziz M. Potential of clean liquid fuels in decarbonizing transportation – An overlooked net- zero pathway? Renew Sustain Energy Rev 2023;183:113483. doi:10.1016/j.rser.2023.113483.

[4] Duarte Souza Alvarenga Santos N, Rückert Roso V, Teixeira Malaquias AC, Coelho Baêta JG. Internal combustion engines and biofuels: Examining why this robust combination should not be ignored for future sustainable transportation. Renew Sustain Energy Rev 2021;148:111292. doi:10.1016/j.rser.2021.111292.

[5] Yim SHL, Barrett SRH. Public Health Impacts of Combustion Emissions in the United Kingdom. Environ Sci Technol 2012;46:4291–6. doi:10.1021/es2040416.

[6] Morgan C, Goodwin J. Impact of the Proposed Euro 7 Regulations on Exhaust Aftertreatment System Design. Johnson Matthey Technol Rev 2023;67:239–45. doi:10.1595/205651323X16805977899699.

[7] Yanowitz J, Christensen E, Mccormick RL. Utilization of Renewable Oxygenates as Gasoline Blending Components. National Renewable Energy Laboratory: 2011.

[8] Alonso DM, Wettstein SG, Dumesic J a. Bimetallic catalysts for upgrading of biomass to fuels and chemicals. Chem Soc Rev 2012;41:8075. doi:10.1039/c2cs35188a.

[9] Zhou C-H, Xia X, Lin C-X, Tong D-S, Beltramini J, Rodriguez MAR, et al. Catalytic conversion of lignocellulosic biomass to fine chemicals and fuels. Chem Soc Rev 2011;40:5588. doi:10.1039/c1cs15124j.

[10] Rodionova M V., Bozieva AM, Zharmukhamedov SK, Leong YK, Chi-Wei Lan J, Veziroglu A, et al. A comprehensive review on lignocellulosic biomass biorefinery for sustainable biofuel production. Int J Hydrogen Energy 2022;47:1481–98. doi:10.1016/j.ijhydene.2021.10.122.

[11] Okolie JA, Mukherjee A, Nanda S, Dalai AK, Kozinski JA. Next-generation biofuels and platform biochemicals from lignocellulosic biomass. Int J Energy Res 2021;45:14145–69. doi:10.1002/er.6697.

[12] Ashokkumar V, Venkatkarthick R, Jayashree S, Chuetor S, Dharmaraj S, Kumar G, et al. Recent advances in lignocellulosic biomass for biofuels and value-added bioproducts - A critical review. Bioresour Technol 2022;344:126195. doi:https://doi.org/10.1016/j.biortech.2021.126195.

[13] Sudholt A, Cai L, Heyne J, Haas FM, Pitsch H, Dryer FL. Ignition characteristics of a bio-derived class of saturated and unsaturated furans for engine applications. Proc Combust Inst 2015;35:2957–65. doi:10.1016/j.proci.2014.06.147.

[14] Frost J, Hellier P, Ladommatos N. A systematic study into the effect of lignocellulose-derived biofuels on the combustion and emissions of fossil diesel blends in a compression ignition engine. Fuel 2022;313:122663. doi:10.1016/j.fuel.2021.122663.

[15] Tian M, McCormick RL, Ratcliff MA, Luecke J, Yanowitz J, Glaude P-A, et al. Performance of lignin derived compounds as octane boosters. Fuel 2017;189:284–92. doi:10.1016/j.fuel.2016.10.084.

[16] Koivisto E, Ladommatos N, Gold M. Compression Ignition and Exhaust Gas Emissions of Fuel Molecules Which Can Be Produced from Lignocellulosic Biomass: Levulinates, Valeric Esters, and Ketones. Energy & Fuels 2015;29:5875–84. doi:10.1021/acs.energyfuels.5b01314.

[17] Bilal M, Wang Z, Cui J, Ferreira LFR, Bharagava RN, Iqbal HMN. Environmental impact of lignocellulosic wastes and their effective exploitation as smart carriers – A drive towards greener and eco-friendlier biocatalytic systems. Sci Total Environ n.d. doi:10.1016/j.scitotenv.2020.137903.

[18] Adhami W, Richel A, Len C. A review of recent advances in the production of furfural in batch system. Mol Catal 2023;545:113178. doi:https://doi.org/10.1016/j.mcat.2023.113178.

[19] Lange JP, Van Der Heide E, Van Buijtenen J, Price R. Furfural-A promising platform for lignocellulosic biofuels. ChemSusChem 2012;5:150–66. doi:10.1002/cssc.201100648.

[20] Alonso DM, Wettstein SG, Dumesic JA. Gamma-valerolactone, a sustainable platform molecule derived from lignocellulosic biomass. Green Chem 2013;15:584. doi:10.1039/c3gc37065h.

[21] Granger P, Parvulescu VI. Catalytic NOx abatement systems for mobile sources: From three-way to lean burn after-treatment technologies. Chem Rev 2011;111:3155–207. doi:10.1021/cr100168g.

[22] Jin D, Choi K, Myung CL, Lim Y, Lee J, Park S. The impact of various ethanol-gasoline blends on particulates and unregulated gaseous emissions characteristics from a spark ignition direct injection (SIDI) passenger vehicle. Fuel 2017;209:702–12. doi:10.1016/j.fuel.2017.08.063.

[23] Suarez-Bertoa R, Zardini AA, Keuken H, Astorga C. Impact of ethanol containing gasoline blends on emissions from a flex-fuel vehicle tested over the Worldwide Harmonized Light duty Test Cycle (WLTC). Fuel 2015;143:173–82. doi:10.1016/j.fuel.2014.10.076.

[24] Schifter I, González U, Díaz L, Rodríguez R, Mejía-Centeno I, González-Macías C. From actual ethanol contents in gasoline to mid-blends and E-85 in conventional technology vehicles. Emission control issues and consequences. Fuel 2018;219:239–47. doi:10.1016/j.fuel.2018.01.118.

[25] Iodice P, Langella G, Amoresano A. Ethanol in gasoline fuel blends: Effect on fuel consumption and engine out emissions of SI engines in cold operating conditions. Appl Therm Eng 2018;130:1081–9. doi:10.1016/j.applthermaleng.2017.11.090.

[26] Kärcher V, Hellier P, Ladommatos N. Effects of Exhaust Gas Hydrogen Addition and Oxygenated Fuel Blends on the Light-Off Performance of a Three-Way Catalyst. SAE Powertrains, Fuels Lubr 2019:2019-01–2329.

[27] Sinha Majumdar S, Pihl JA, Toops TJ. Reactivity of novel high-performance fuels on commercial three-way catalysts for control of emissions from spark-ignition engines. Appl Energy 2019;255:113640. doi:10.1016/j.apenergy.2019.113640.

[28] Ladshaw AP, Majumdar SS, Pihl JA. Experiments and modeling to evaluate global reaction kinetics of three-way catalyst light off for net-zero carbon fuels and selected fuel blends. Appl Catal B Environ 2023;324:122281. doi:10.1016/j.apcatb.2022.122281.

[29] Awad OI, Mamat R, Ibrahim TK, Hammid AT, Yusri IM, Hamidi MA, et al. Overview of the oxygenated fuels in spark ignition engine: Environmental and performance. Renew Sustain Energy Rev 2018;91:394–408. doi:10.1016/j.rser.2018.03.107.

[30] Hellier P, Al-Haj L, Talibi M, Purton S, Ladommatos N. Combustion and emissions characterization of terpenes with a view to their biological production in cyanobacteria. Fuel 2013;111:670–88. doi:10.1016/j.fuel.2013.04.042.

[31] Spicher U, Bernhardt S, Meinig U, Hannibal W, Knecht A, Stephan W, et al. Ladungswechsel. In: van Basshuysen R, Schäfer F, editors. Handb. Verbrennungsmotor Grundlagen, Kompon. Syst. Perspekt., Wiesbaden: Springer Fachmedien Wiesbaden; 2015, p. 465–532. doi:10.1007/978-3-658-04678-1_10.

[32] Thewes M, Muether M, Pischinger S, Budde M, Brunn A, Sehr A, et al. Analysis of the Impact of 2-Methylfuran on Mixture Formation and Combustion in a Direct-Injection Spark-Ignition Engine. Energy Fuels 2011.

[33] Liu H, Olalere R, Wang C, Ma X, Xu H. Combustion characteristics and engine performance of 2-methylfuran compared to gasoline and ethanol in a direct injection spark ignition engine. Fuel 2021;299:120825. doi:https://doi.org/10.1016/j.fuel.2021.120825.

[34] Jouzdani S, Eldeeb MA, Zhang L, Akih-Kumgeh B. High-Temperature Study of 2-Methyl Furan and 2-Methyl Tetrahydrofuran Combustion. Int J Chem Kinet 2016;48:491–503. doi:https://doi.org/10.1002/kin.21008.

[35] Talibi M, Hellier P, Ladommatos N. Investigating the Combustion and Emissions Characteristics of Biomass-Derived Platform Fuels as Gasoline Extenders in a Single Cylinder Spark-Ignition Engine. SAE Tech Pap 2017;2017-Octob:2017-01–2325. doi:10.4271/2017-01-2325.

[36] Wang C, Xu H, Daniel R, Ghafourian A, Herreros JM, Shuai S, et al. Combustion characteristics and emissions of 2-methylfuran compared to 2,5-dimethylfuran, gasoline and ethanol in a DISI engine. Fuel 2013;103:200–11.

[37] Olalere RK, Zhang G, Xu H. Experimental Investigation of Gaseous Emissions and Hydrocarbon Speciation for MF and MTHF Gasoline Blends in DISI Engine. Int J Automot Manuf Mater 2024:6. doi:10.53941/ijamm.2024.100006.

[38] Heywood JB. Internal Combustion Engine Fundamentals. 2nd ed. 2014. doi:10.1049/oap-cired.2017.1227.

[39] Zeldovich Y. B, Sadavnikov PY, Frank-Kamentskii DA. Oxidation of Nitrogen in Combustion. Acad Sci USSR, Moscow 1947.

[40] Eveleigh A, Ladommatos N, Hellier P, Jourdan A-L. Quantification of the Fraction of Particulate Matter Derived from a Range of 13 C-Labeled Fuels Blended into Heptane, Studied in a Diesel Engine and Tube Reactor. Energy & Fuels 2016;30:7678–90. doi:10.1021/acs.energyfuels.6b00322.

[41] Kholghy MR, Weingarten J, Sediako AD, Barba J, Lapuerta M, Thomson MJ. Structural effects of biodiesel on soot formation in a laminar coflow diffusion flame. Proc Combust Inst 2017;36:1321–8. doi:10.1016/j.proci.2016.06.119.

[42] Whittington BI, Jiang CJ, Trimm DL. Vehicle exhaust catalysis: I. The relative importance of catalytic oxidation, steam reforming and water-gas shift reactions. Catal Today 1995;26:41–5. doi:10.1016/0920-5861(95)00093-U.

[43] de Abreu Goes J, Woo JW, Olsson L. Effects of feed gas composition on fresh and aged twc-coated gpfs loaded with real soot. Ind Eng Chem Res 2020;59:10790–803. doi:10.1021/acs.iecr.0c00654.

[44] Bae W Bin, Kim DY, Byun SW, Hazlett M, Yoon DY, Jung C, et al. Emission of NH3 and N2Oduring NO reduction over commercial aged three-way catalyst (TWC): Role of individual reductants in simulated exhausts. Chem Eng J Adv 2022;9:100222. doi:10.1016/j.ceja.2021.100222.

[45] Bogarra M, Herreros JM, Hergueta C, Tsolakis A, York APE, Millington PJ. Influence of three-way catalyst on gaseous and particulate matter emissions during gasoline direct injection engine cold-start. Johnson Matthey Technol Rev 2017;61. doi:10.1595/205651317X696315.

[46] Whelan I, Timoney D, Smith W, Samuel S. The effect of a three-way catalytic converter on particulate matter from a gasoline direct-injection engine during cold-start. SAE Int J Engines 2013;6:1035–45.

# CFD Based Development Aiding First-Time-Right Design of a Tier-5 Emission Aftertreatment System

Naveen Sridharan[1], Rangesh Pandey[2], Ajay Kumar Maddineni[3]

[1]Principal Engineer, Emission System Development, Donaldson Filtration Solutions, Leuven, Belgium.

E-mail: naveen.sridharan@donaldson.com
Telephone: +(32) 470274724

[2]Senior Engineer, Global Technical Group, Donaldson Filtration Solutions, Gurgaon, India.

E-mail: rangesh.pandey@donaldson.com
Telephone: +(91) 8660613060

[3]Senior Manager – Engineering, Global Technical Group, Donaldson Filtration Solutions, Gurgaon, India.

E-mail: ajay.maddineni@donaldson.com
Telephone: +(91) 9604659636

**Abstract.** This Article highlights the Donaldson's use of CFD tools for analysing, improving, and achieving a first time-right Exhaust Aftertreatment System design. With decades of expertise, we offer high fidelity simulations and accurate CFD indications within short lead times. Donaldson specific, internal parameters and CFD procedures are continuously correlated with inhouse engine bench validation, providing results reflecting real world loads.

Donaldson's system approach ensures EAT design alignment with calibrator needs within packaging constraints. Close-looped calibration system insights contribute to a robust design, incorporating industry partner input for foolproof performance. The analysis is carried out by means of a CFD framework that includes the modelling of exhaust components as a multispecies gas and urea spray as two-component droplets, coupled with momentum and thermal exchange to evaluate the droplet evaporation and species mixing. Reaction mechanism relevant to convert the urea into NH3 via thermolysis process is modelled. Also, the model has been extended to take the conjugate heat transfer and droplet-wall interactions into account via wall film models to identify the deposit risk areas.

The key performance indicators of mixer development include the system backpressure, flow field, catalyst flow uniformity, ammonia uniformity, deposit predictions, and sensor evaluation. In addressing system backpressure, flow & NH3 uniformity, the paper underscores the significance of employing accurate inertial and resistivity coefficients for each substrate. Our internal deposit binning methodology is correlated with our burner rig at over 98% accuracy. This approach enables the development of robust mixers, offering precise predictions on deposit longevity and exact location of reversible crystal initiation.

Collaborating closely with technology partners and the calibration team, we leverage CFD expertise to validate the NOx sensor position post Selective Catalytic Reduction (SCR). This validation ensures optimal sensor signals, closely aligning with analyser readings for utmost accuracy. Furthermore, our upstream duct optimization methods are grounded in a comprehensive understanding of flow fundamentals, incorporating the underlying mathematics and theory of the flow dynamics tool. Often the analysis lead design features are investigated using the surrogate models to facilitate the attainment of an optimal design and enhancing the catalyst utilization efficiency. During the EAT development phase, CFD is also utilized to understand the thermal behaviour including the exhaust gas temperature distribution prior to the substrate locations, at the skin and at the system exit for varied requirements to be met as per the industry standards. The paper provides insights into our continuous development and correlation practices, resulting in an extensive mixer portfolio with industry leading NH3 uniformity index levels.

## Notation (optional)

| | |
|---|---|
| *DOC* | *Diesel Oxidation Catalyst* |
| *DPF* | *Diesel Particulate Filter* |
| *SCR* | *Selective Catalytic Reduction* |
| *SCRoF* | *Coated filter to support NOx conversions and particulate filtration* |
| *cc* | *Close coupled* |
| *NOx* | *Nitrous Oxide* |
| *PM* | *Particulate Matter* |
| *HC* | *Hydrocarbons* |
| *CO* | *Carbon monoxide* |
| $H_2O$ | *Water* |
| *SMD* | *Sorter Mean Diameter* |
| DM | *Dosing Module* |
| AdBlue | *Urea water solution* |
| DEF | *Urea water solution* |
| $1/\alpha$ | *Viscous resistance coefficient of substrates* |
| $C_2$ | *Inertial resistance coefficient of substrates* |
| *PD* | *Pressure drop* |
| $\Delta P$ | *Pressure drop* |
| OP | *Operating boundary condition* |
| $UI_V$ | *Flow uniformity* |
| $UI_{NH3}$ | *Ammonia uniformity* |
| $D_H$ | *Injector hole diameter* |
| $n_H$ | *Number of dosing module injection holes* |
| $D_{10}$ | *Arithmetic mean diameter of droplets.* |
| $r$ | *Spray radius.* |

## 1. Introduction

Since 1997, off-highway tailpipe emissions have been regulated to target pollu-tants such as NOx, HC, PM, and CO. Regulations have evolved from Stage I to the current Stage V in Europe and Tier 4 Final (Tier4F) in the USA, achieving over 95% NOx reduction from engine to tailpipe. The upcoming Tier 5 regulations aim for a conversion efficiency of over 90% from the current limit of 0.4 g/kWh NOx tailpipe emissions. With experience from Stage V and Tier 4F, the off-highway industry has improved its ability to optimize engine and emission calibration, to meet stringent tailpipe targets. While there are multiple technologies proven in market to achieve ultra-low-NOx tailpipe targets of future, ar-riving at the right combination by extensive DoE of system is time & resource consuming and critical.

This paper highlights the need for understanding emission system behaviour in real driving conditions and incorporating specific operating conditions from off-road applications to ensure functionally robust and structurally durable emission systems. While meeting key performance indices (KPIs) set by original equipment (OE) customers across all engine loads is crucial, understanding the connection between the set KPIs to actual system performance is critical. Also, the off-road market demands custom designs for different applications, making performance evaluation essential to meet regulatory targets. To support this, Donaldson has enhanced its CFD work package, achieving over 97% correlation between CFD, engine bench, and field performance.

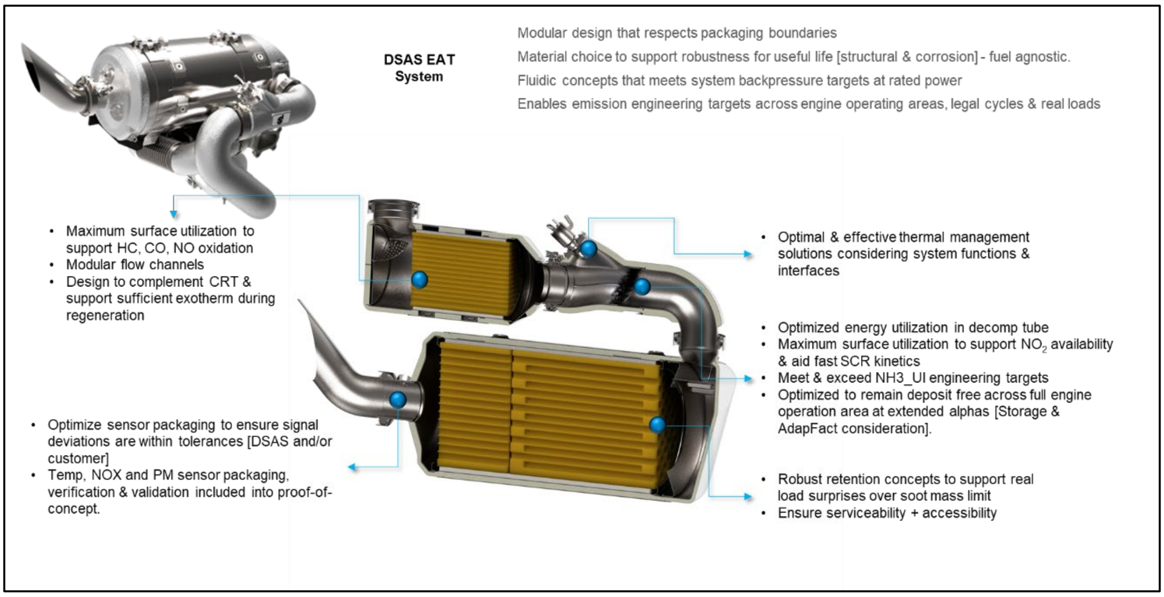
DSAS EAT System
Modular design that respects packaging boundaries
Material choice to support robustness for useful life [structural & corrosion] - fuel agnostic.
Fluidic concepts that meets system backpressure targets at rated power
Enables emission engineering targets across engine operating areas, legal cycles & real loads
• Maximum surface utilization to support HC, CO, NO oxidation
• Modular flow channels
• Design to complement CRT & support sufficient exotherm during regeneration
• Optimal & effective thermal management solutions considering system functions & interfaces
• Optimized energy utilization in decomp tube
• Maximum surface utilization to support NO$_2$ availability & aid fast SCR kinetics
• Meet & exceed NH3_UI engineering targets
• Optimized to remain deposit free across full engine operation area at extended alphas [Storage & AdapFact consideration].
• Optimize sensor packaging to ensure signal deviations are within tolerances [DSAS and/or customer]
• Temp, NOX and PM sensor packaging, verification & validation included into proof-of-concept.
• Robust retention concepts to support real load surprises over soot mass limit
• Ensure serviceability + accessibility

**Fig. 1.** Stage V EAT system with its respective functional necessity

Referring to figure 01, in this paper we brief on the CFD methods and internal KPIs we use to ensure; each functional part of emission system is verified to support the expectations of a calibration engineer and reflects well with his KPIs. This approach ensures first-time-right designs, reducing need for any design changes and supports steadfast development. These advancements and standardizations are achieved after rigorous and continuous internal correlation runs between our engine bench and CFD optimizations. Such engineering services are aimed to add value for our customers, helping them develop industry-leading emission solutions that are simple, effective, and capable of meeting future ultra-low NOx targets.

At Donaldson, our core principle for emission system development prioritizes the use of Computational Fluid Dynamics (CFD) methods. Supported by extensive field data correlations, our CFD approach ensures that our emission systems design not only meet packaging constraints and functional key performance indicators (KPIs) but also align seamlessly with the performance expectations of calibration engineers.

## 2. Emissions System Development Cycle

Within Donaldson Emissions, system development starts from a detailed requirement analysis. The requirement engineering phase is very critical, to understand not just the performance targets and packaging boundaries but to get latent details of the end use of the machine for which the emission system is getting developed for. This information, if not understood in early stage of development, is the reason for design change loops during the calibration phase. Donaldson KPI dashboard is prepared to include all relevant information during the requirement engineering phase and are effectively fed into the concept design, enabling a possibility to arrive at a first-time right design.
In this early stage, we focus in bringing the core strength, best suitable concepts, previous experiences, material choices to suit end usage and right thermal management to retain enthalpy within emission systems. Such wholesome approach is critical to ensure the system meets and exceeds the functional expectations in real loads.

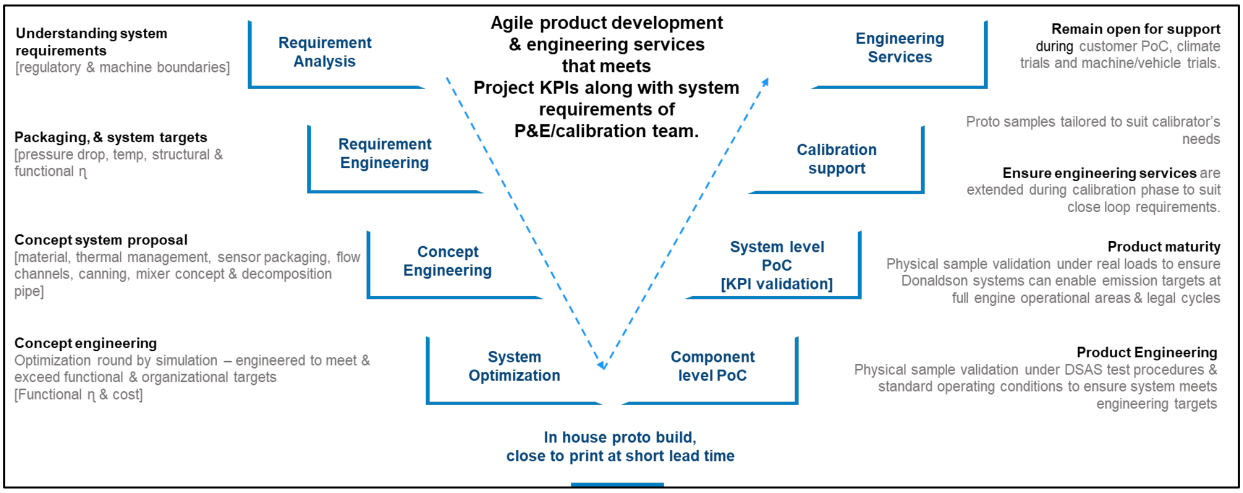
Understanding system requirements
[regulatory & machine boundaries]
Requirement Analysis
Agile product development & engineering services that meets Project KPIs along with system requirements of P&E/calibration team.
Engineering Services
Remain open for support during customer PoC, climate trials and machine/vehicle trials.
Packaging, & system targets
[pressure drop, temp, structural & functional η
Requirement Engineering
Calibration support
Proto samples tailored to suit calibrator's needs
Ensure engineering services are extended during calibration phase to suit close loop requirements.
Concept system proposal
[material, thermal management, sensor packaging, flow channels, canning, mixer concept & decomposition pipe]
Concept Engineering
System level PoC [KPI validation]
Product maturity
Physical sample validation under real loads to ensure Donaldson systems can enable emission targets at full engine operational areas & legal cycles
Concept engineering
Optimization round by simulation – engineered to meet & exceed functional & organizational targets
[Functional η & cost]
System Optimization
Component level PoC
Product Engineering
Physical sample validation under DSAS test procedures & standard operating conditions to ensure system meets engineering targets
In house proto build, close to print at short lead time

**Fig. 2.** Donaldson Emissions System Product Development Approach

Once when the right concepts are brought together, we follow a streamlined approach to keep the design simple, use validated and proven technology. This way, we start with an already matured design which has functional backup from experience design required fine tuning to reach peak efficiency is minimal. With the concept design in place, we aim to meet customer set targets and Donaldson engineering KPIs, derived from working closely with calibration team of our customers and technology partners. Referring to figure 02, through the finetuning process, there is clear documentation of the design changes and the functional responses attributed to each iteration. This gets logged into our design library, allowing us to refer to the Dos & Don'ts for during every requirement engineering phase. The design verification stage matures at concept proofing by simulation methods and is followed by rigorous inhouse bench tests. Once the optimization round is complete, we ensure to use our internal lab infrastructure to get insights on the system performance and the correlation is retained at > 97% for the set KPIs. Such depth and width of understanding around the emission system development allows us to remain agile during the entire product development phase and extend engineering services that meet project KPIs along with system requirements of the performance and emissions team across all operating loads of engine map.

## 3. Industry finest resources

We understand, to be able to extend the finest support to our customers, we need the best mix of experts and tools. Effectively, our Global technical Group is a pool of experts, with functional know-how on emission systems. Our experts constantly take part in the correlation discussions which enable bridging gaps between virtual simulation and physical sample behavior.

### 3.1 EAT System evaluation KPIs focused by CFD

To effectively develop an emission system that has full potential to enable emission regulatory targets at all operating loads over engine map, we focus in detail on the basic performance KPIs and internal engineering set targets. This approach allows Donaldson emission systems to support the complex calibration strategy and react well to the defined algorithms. Modeling and simulation will be playing an important role in the development process to validate various conceptual designs meeting the performance. A commercial CFD tool Ansys Fluent is being used to understand the fluid flow, UWS evaporation and mixing characteristics of the EAT system. A schematic view of the EAT system modeling assumptions is given in the following figure. Fluid flow was modelled in the study could be represented as follows.

$$\rho\partial\varphi/\partial t + \rho div\left(u_j\varphi\right) = -\partial P/(\partial x_i) + div(\tau_i j) + S_\varphi$$

Where $\varphi$is flow variables namely mass ($\varphi$=1), velocity ($\varphi$=u, $\varphi$=v, $\varphi$=w) in the respective direction, and Temperature ($\varphi$=T). $u\_j$ is the velocity vector, $\rho$ is the density of the fluid and P is the pressure. $\tau\_ij$ is the shear stress term and could be expressed as the constitutive equations. $S\_\varphi$ is the source term considering the porous resistivity, centrifugal forces, etc. Exhaust gas is modeled as a multispecies of the diesel combustion byproducts. Choice of turbulence models is critical as the flow path consists of the swirl devices. RANS based k-ε turbulence model with enhanced and scalable wall treatment is used in the current study. Heat transfer from exhaust gases to the ambient through the piping and insulation components are modeled as the convective boundary conditions. Substrates are modeled as a macroscopic porous substrates using the Darcy–Forchheimer equation empirical equation. $\Delta P/L = \mu/\alpha u + C_2\rho/2u^2$

While the exhaust gas is modeled using Eularian approach, UWS solution is modeled using Lagrangian droplets. Discrete phase model is used to model the UWS droplets as a multi component spray via statistically valid parcel approach. The governing equations (Mass, momentum, and energy) of both droplet and gas phases are two-way coupled. Water evaporation of UWS Droplet, urea liquid decomposition and volumetric reaction conversion into NH3 was modeled in accordance with Fluent inbuilt sub routines.

Rosin-Rammler distribution is considered to represent the droplet size distribution per equation

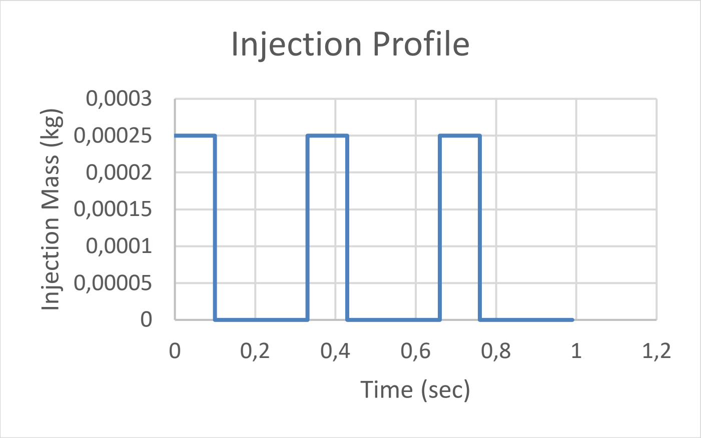

$$Y_d = e^{-K^n}$$

Where,

$$K = d/\bar{d}$$

UWS solution was injected in an unsteady pulsed manner to resemble the real case scenario as shown below.

Further these droplets interactions with wall to predict the deposit formation was evaluated using the Kunkhe impingement model. For this purpose, the mixer surface was treated as a coupled wall to predict the droplet impingement heat transfer and thus the wall film formation. Considering the wall temperature, droplet impingement conditions, droplet material properties and wall film height, impinging droplets on the walls might rebound or thermal breakup at higher temperatures and deposit or splash at lower temperatures. For the wall temperature beyond 265-280 degrees is critical to form the fluid film by means of particle splashing and deposition [15].

The area weighted uniformity indications for flow and species were estimated as follows.

$$\gamma_a = 1 - \frac{\sum_{i=1}^{n}[(\emptyset_i - \emptyset_a)A_i]}{2\emptyset_a \sum_{i=1}^{n} A_i}$$

where, $\gamma_a$ is the area weighted uniformity index $\mathrm{i}$ is the face index of a surface with $\mathrm{n}$ faces and $\emptyset_\mathrm{a}$ is the average value of the variable.

$$\emptyset_a = \frac{\sum_{i=1}^{n} \emptyset_i A_i}{\sum_{i=1}^{n} A_i}$$

Some indices focused during CFD verification at concept proofing stage are;

### 3.1.1 EAT System backpressure [full system and section wise].

- We utilize the online pressure drop tool from our technology partner [NGK] for inputs related to ceramic substrate pressure drops.
- For metallic substrate pressure drops, we rely on the pressure drop tool from our technology partner [EMITEC].
- These inputs are essential for calculating the inertial and viscous resistance coefficients of the substrates, enhancing the correlation between CFD simulations and actual measurements.
- Our development reports consistently include pressure drop indications for bare fresh substrates, along with trends illustrating the impact of soot and ash loading throughout the substrate's useful life.
- This early-stage input is crucial for engine calibration to maintain the necessary EAT pressure drop range.

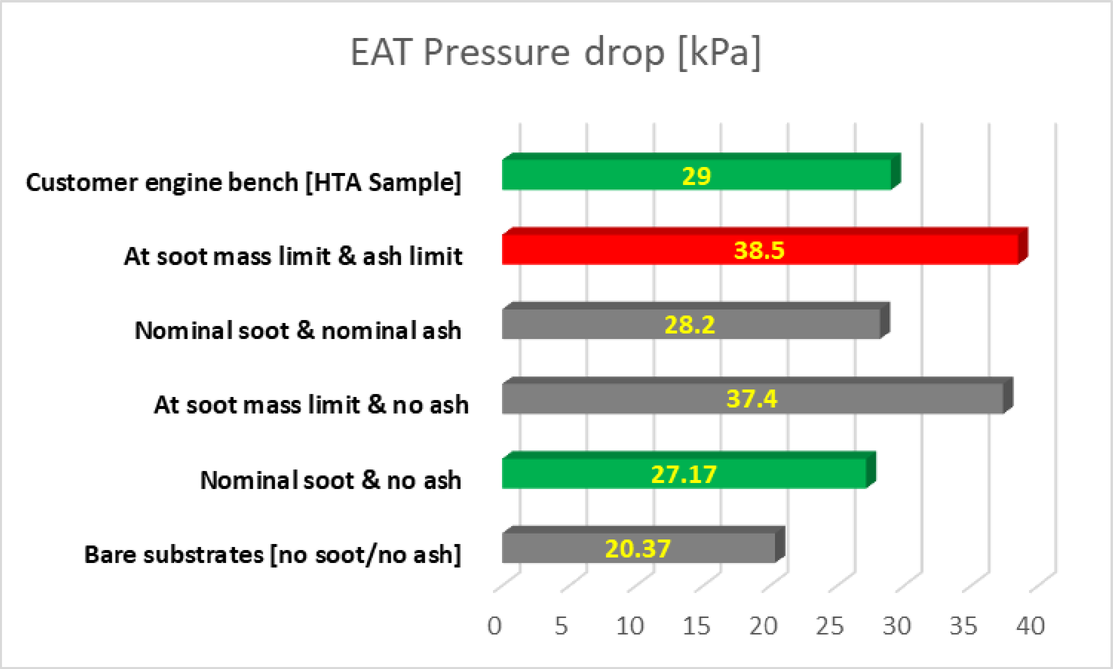

**Fig. 3.** System pressure drop indications as an input for engine calibration [Simulated pressure drop indi-cations, shared for all development projects handled by Donaldson – courtesy NGK online PD tool]

### 3.1.2 Substrates flow uniformity indications

Flow channel design for ensuring full utilization of the catalyst is critical to an EAT system architecture. This allows the respective chemical kinetics or filtration efficiency to reflect set targets across all operational loads across engine map, under different machine operating loads. Within Donaldson emissions, in our CFD verifications, we not only focus on the flow utilization in cumulative average but also go into details of min/max binning to fall withing a calibrated range. This approach helps give clear indication of field behavior and to ensure there are no local hot spot of gas focus, which can eventually disturb respective technology performance degradation over time.

- **For DOC,** the oxidation substrate is coated with platinum group metals, and the efficiency is critical for effective exotherm, conversion of CO, HC and NO2 generation.
- Exothermic reactions, reacting to the induced engine out HC supports in effective regeneration.
- Engine out HC content, if slipped without conversion can poison SCR downstream.
- To maintain a balance of NO2/NOx ratio is critical to ensure higher and fast kinetics at SCR. Lower and higher order of NO2 disturbs the conversion efficiency at SCR, maintaining a range between 0.4 – 0.6 for the ratio remains critical conventionally.
- With DOC being a mechanical component, not protected by any prognosis or close looping, the design of pipes and cone profiles to support full frontal surface utilization is extremely important.

- **For DPF,** to ensure soot and ash filtration are optimal, flow optimization the filtration of soot and ash ensures regulatory norms are met.
- A DPF or an SCRoF enables filtration to >99% and particulate filters are standalone mechanical components to enable such filtration.
- This mandates, gas flow focus should be covering the entire filter frontal surfaces, failing which would mean there is localized soot and ash loading on the particle filter.
- Such behavior would result in frequent regeneration trigger, completely deviating from the soot loading models.

- During hot shut down conditions, if the soot loading is nor distributed evenly, there is high chance of thermal degradation of substrates due to radial temperature differences crossing design threshold.

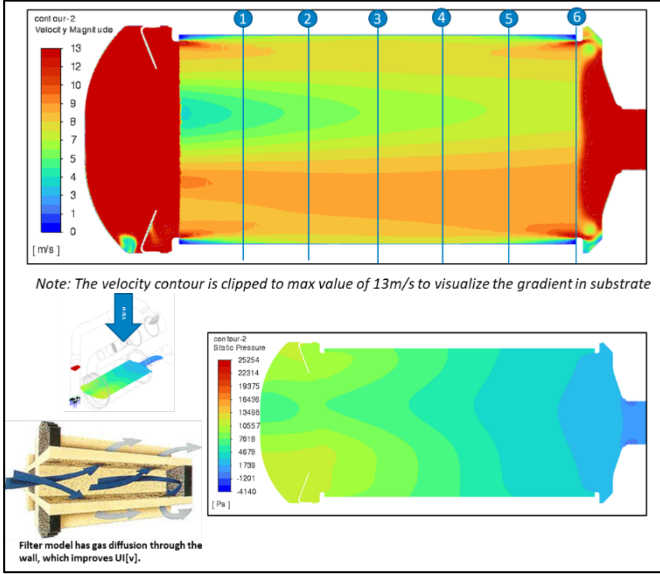

*Note: The velocity contour is clipped to max value of 13m/s to visualize the gradient in substrate*

**Filter model has gas diffusion through the wall, which improves UI[v].**

| Plane # | Location | Flow UI |
|---|---|---|
| 1 | 3inch downstream | 0.986 |
| 2 | 6inch downstream | 0.988 |
| 3 | 9inch downstream | 0.991 |
| 4 | 12inch/ SCRF outlet | 0.992 |
| 5 | 15inch downstream | 0.994 |
| 6 | 18inch/ SCR-outlet | 0.981 |

**Fig. 4.** Understanding and prediction of real time system functioning of a SCRoF technology

- In an ideal closed looping, such frequent trigger for regeneration might force vehicle derate and call for service regeneration.
- Such abnormal field issues, through the life od the filter, can be avoided when packaged with the right flow focus, which is ensured by an effective CFD.

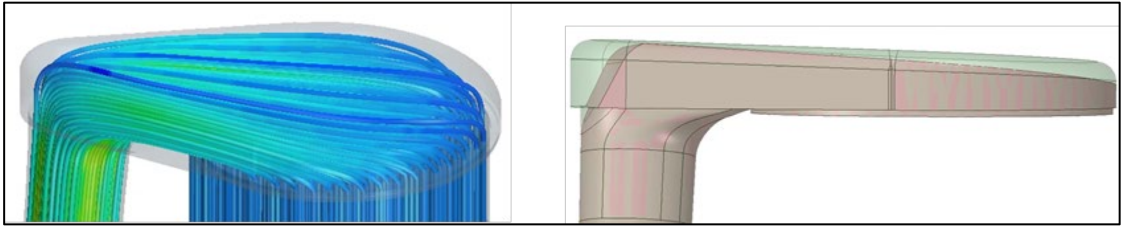

**Fig. 5.** Flow path optimization of an SCR [inlet cone optimization – modularity considered from DOC]

- **For SCR,** general focus during development for NOx conversions are on NH3 uniformity.
- All the proof of concept and field validation are focused towards the NH3 distribution and NOx conversion efficiency.
- While NH3 uniformity is critical, flow uniformity over SCR is equally important to ensure the efficiency of the coated SCR substrates are fully utilized.
- Also, higher flow uniformity would mean lower risk of NH3 slip.
- Stage V EAT architecture, due to huge SCR volume requirements to achieve higher NOx conversion, saw the need for dual leg SCR layouts. For such systems, flow path design s to ensure good mass flow split is critical. By CFD, we ensure gas flow split if focused equally between each SCR sections.

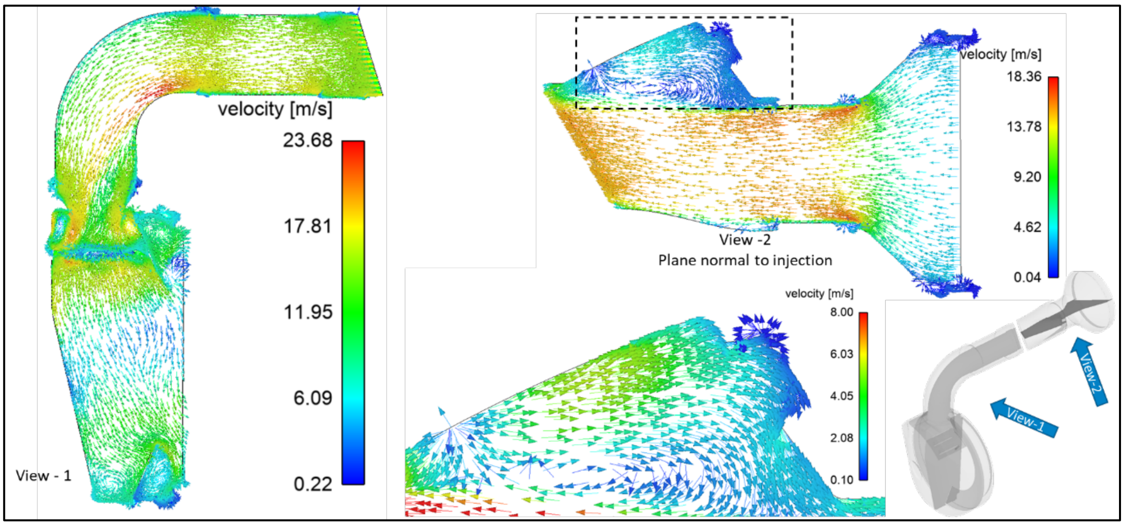

**Fig. 6.** In depth focus at Dosing module packaging to avoid disturbance to urea spray patterns

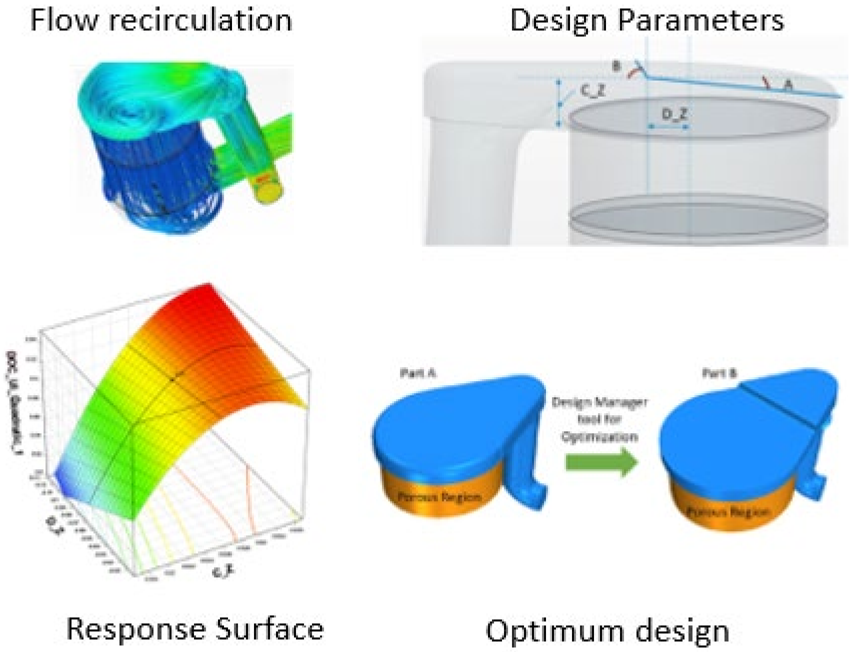
Flow recirculation
Design Parameters
B
C_Z
D_Z
A
DOE_UI_Quantity
D_Z
C_Z
Response Surface
Part A
Part B
Design Manager tool for Optimization
Porous Region
Porous Region
Optimum design

**Fig. 7.** Theoretical and empirical expertise to enable smart system optimization

Computational fluid dynamics (CFD)-based design optimization by coupling it with statistical algorithms is utilized to speedup the product development lifecycle with optimum design. Coupling the statistical tools with CFD was performed for studies like Design of Experiment, response surface creation and optimization.

Case Study: Due to compact space before the substrate, the target flow uniformity of 0.98 was not achieved. Based on the flow fields for base case we identified the recirculation zone. Parametric features introduced in design to break this recirculation. Fig.1 shows the parameters considered. Firstly, we performed the DOE study for screening of the parameters. Out of 4 parameters we identified the 2 critical parameters C_Z and D_Z. Then we performed the Optimization, the Objective of the Optimization is to maximize the uniformity index. Design manager have the single objective as well as multi objective optimization algorithm. There is other important setting for optimization which we defined to make the optimization process efficient like Objective constraints, parameter types, parameter resolution, baseline case, total number of designs to run etc. Considering proper setting for these reduces the optimization time as well as improves quality of the optimization results.

### 3.1.3 NH3 [Ammonia] Uniformity Indices

Mixer efficiency in for of NH3 uniformity is a topic we have correlated to greater extent and our prediction represents >99% correlation to engine bench measurements for both steady state and transient legal cycles. Donaldson Emissions has a huge portfolio of IP protected mixers, which effectively have amassed extreme field experience and proven robust, meeting functional rudiments at all operating loads, in variety of off-road machine applications.

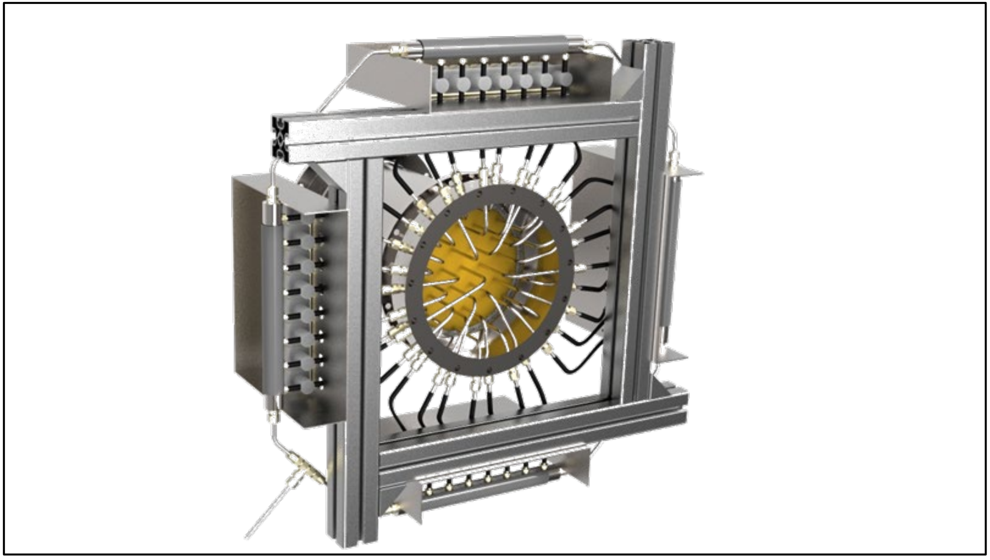

**Fig. 8.** Donaldson in-house developed NH3_UI measurement device and results used for CFD correlation

All of Donaldson mixers are focused for development on CFD, with a parallel correlation run focused in our in-house engine labs. We have developed uniformity measurement devices which can show results in industry best turn around time and use the expertise of our engineers and infrastructure to run engine bench and CFD trials in parallel to keep a clear understating of the concepts and improve correlation as and when possible.

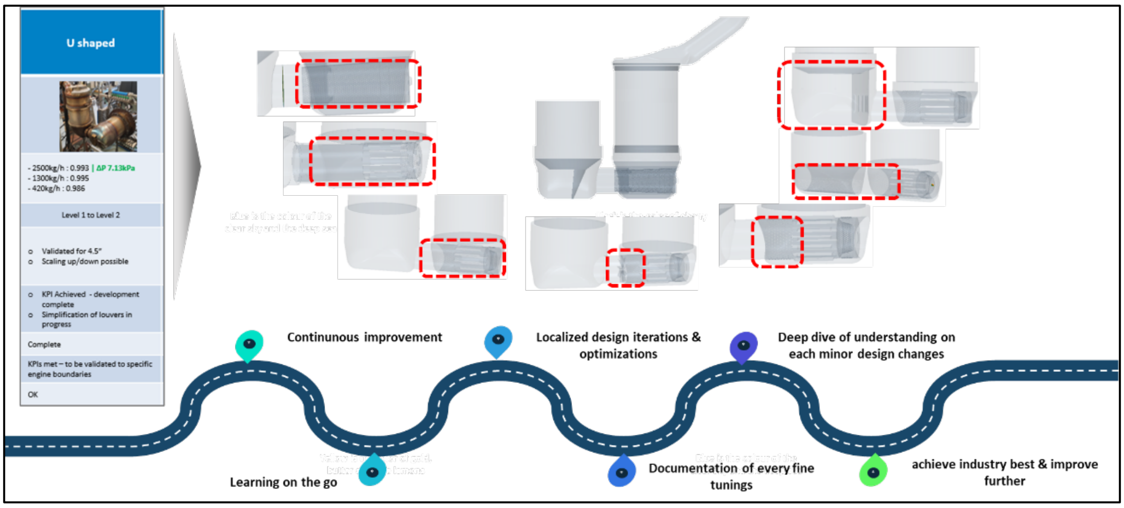
U shaped
- 2500kg/h : 0.993 | ΔP 7.13kPa
- 1300kg/h : 0.995
- 420kg/h : 0.986
Level 1 to Level 2
Validated for 4.5"
Scaling up/down possible
KPI Achieved - development complete
Simplification of louvers in progress
Complete
KPIs met – to be validated to specific engine boundaries
OK
Continunous improvement
Localized design iterations & optimizations
Deep dive of understanding on each minor design changes
Learning on the go
Documentation of every fine tunings
achieve industry best & improve further

**Fig. 9.** Donaldson mixer development strategy with continuous learning and documentation

### 3.1.4 HC uniformity

Tier5 discussions have indicated a need for fuel injection focused into the emission systems, to enable rapid heat up and support cold start. Donaldson, with a proactive approach, reached one of our technology partners [Bosch], understood their HC injection algorithm and development focus by CFD. Donaldson and Bosch CFD engineers had a good discussion which supported HC injection based CFD methods to be one-to-one matching with how Bosch approved its HC injection for regeneration.

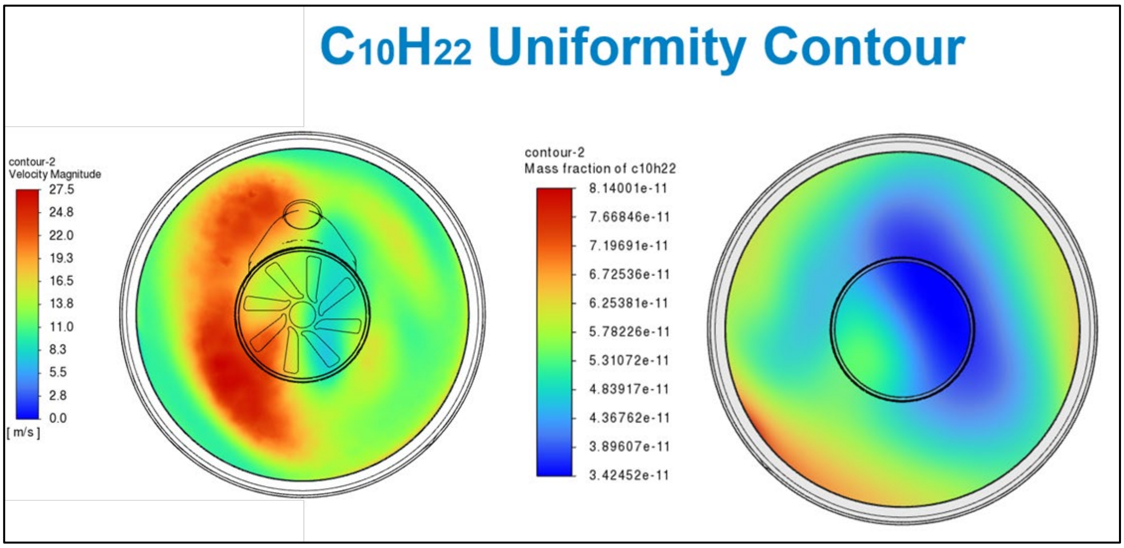
C10H22 Uniformity Contour
contour-2
Velocity Magnitude
27.5
24.8
22.0
19.3
16.5
13.8
11.0
8.3
5.5
2.8
0.0
[ m/s ]
contour-2
Mass fraction of c10h22
8.14001e-11
7.66846e-11
7.19691e-11
6.72536e-11
6.25381e-11
5.78226e-11
5.31072e-11
4.83917e-11
4.36762e-11
3.89607e-11
3.42452e-11

**Fig. 10.** Donaldson hydrocarbon-based injection study [correlation support from Bosch GmbH]

From here, Donaldson continued the verification practices and have developed in depth study possibility to identify when a system would need HC mixer and how to ensure effective utilization of injected HC in exhaust stream over an eHeater or a heat up catalyst.

### 3.1.5 Deposit predictions

First focus of our mixer technology is to keep the system deposit free across all operating loads.

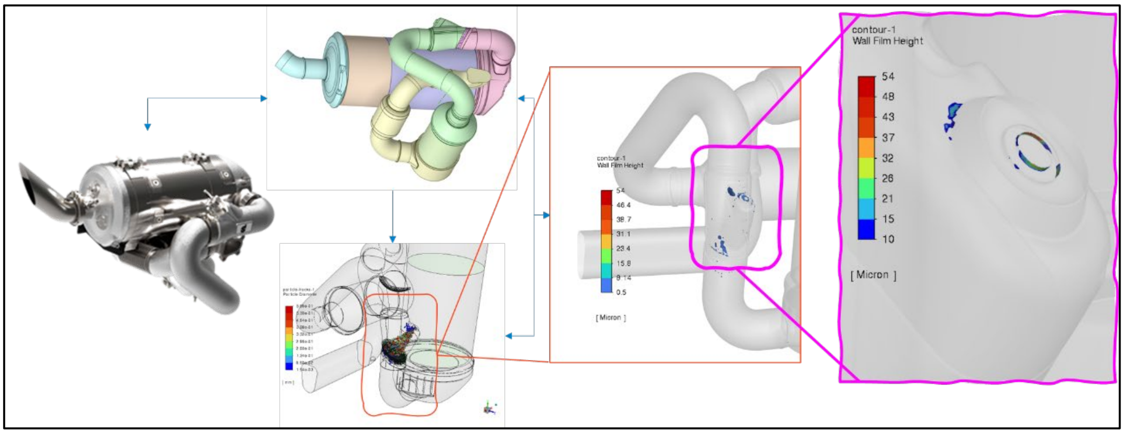
contour-1
Wall Film Height
54
46.4
38.7
31.1
23.4
15.8
8.14
0.5
[ Micron ]
contour-1
Wall Film Height
54
48
43
37
32
26
21
15
10
[ Micron ]

**Fig. 11.** Wall wetting and deposit study across full EAT system

To achieve this, we have conducted extreme correlation runs back-to-back between our burner labs and CFD. This allowed us to arrive at the CFD binning methodology. In this method, we conduct injection-based deposit study to observe wall film formation and have a mass balance between injected urea over a certain time and amount of non-evaporated mass that stays in the system. This delta in mass balance, indicated the potential risk of deposits. With our correlation back up, we scale down the mass and bin them based on their film thickness.

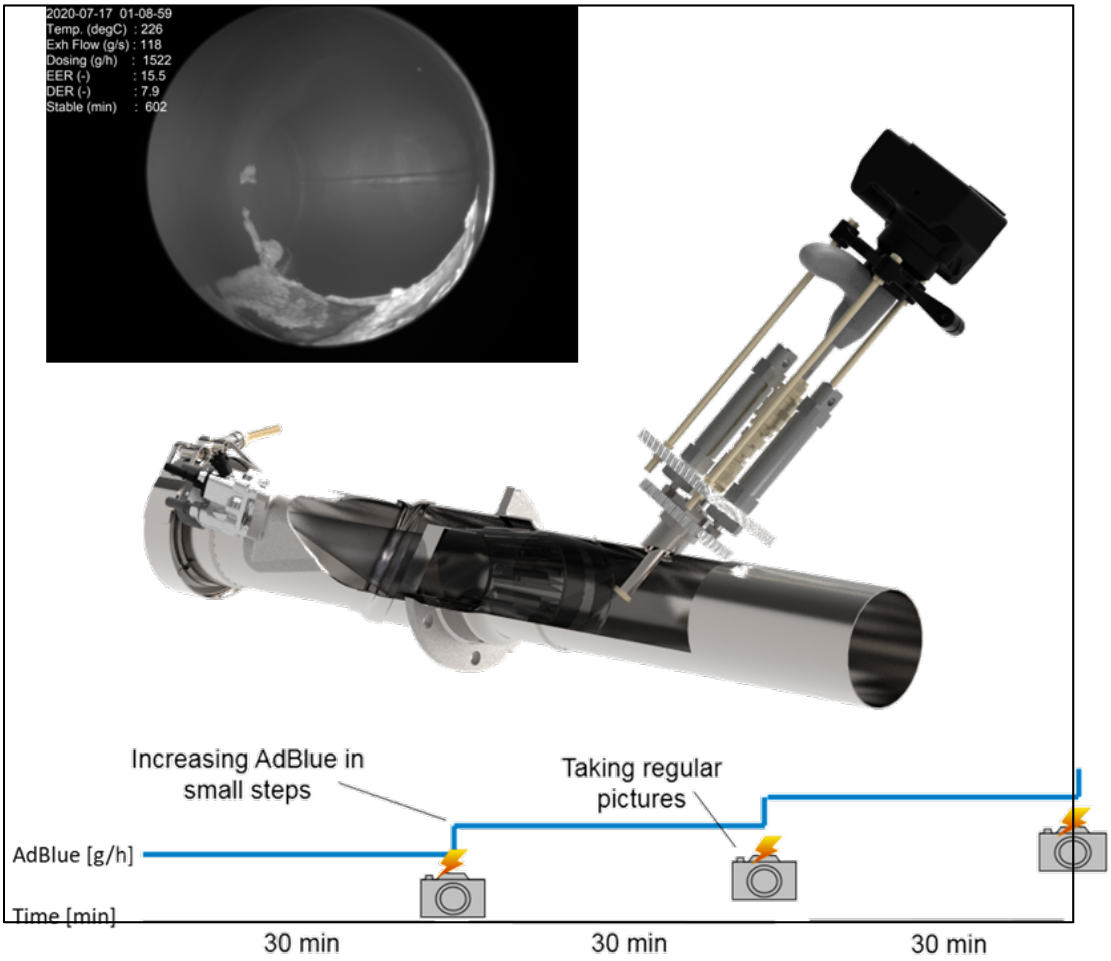
2020-07-17 01-08-59
Temp. (degC) : 226
Exh Flow (g/s) : 118
Dosing (g/h) : 1522
EER (-) : 15.5
DER (-) : 7.9
Stable (min) : 602
Increasing AdBlue in small steps
Taking regular pictures
AdBlue [g/h]
Time [min]
30 min
30 min
30 min

**Fig. 12.** Donaldson in-house developed deposit imaging system used for CFD correlation

After such binning, we can clearly identify, where reversible crystals will form, during what loads, at what rate and identify critical zones in mixers where irreversible deposits are foreseen. None of Donaldson design, would have a development go-ahead after a critical [red zone] is identified by CFD. We ensure to keep the mixers in low-risk zone before design freeze.

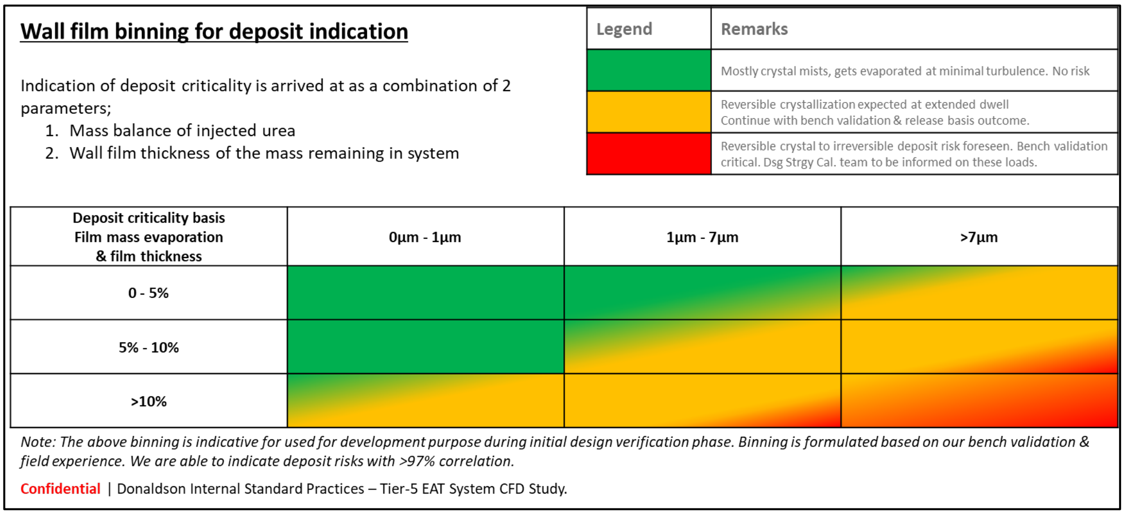

**Wall film binning for deposit indication**

Indication of deposit criticality is arrived at as a combination of 2 parameters;

1. Mass balance of injected urea
2. Wall film thickness of the mass remaining in system

| Legend | Remarks |
|---|---|
| 🟩 | Mostly crystal mists, gets evaporated at minimal turbulence. No risk |
| 🟨 | Reversible crystallization expected at extended dwell<br>Continue with bench validation & release basis outcome. |
| 🟥 | Reversible crystal to irreversible deposit risk foreseen. Bench validation critical. Dsg Strgy Cal. team to be informed on these loads. |

| Deposit criticality basis Film mass evaporation & film thickness | 0µm - 1µm | 1µm - 7µm | >7µm |
|---|---|---|---|
| 0 - 5% | 🟩 | 🟩 | 🟩 🟨 |
| 5% - 10% | 🟩 | 🟩 🟨 | 🟨 🟥 |
| >10% | 🟩 🟨 | 🟨 🟥 | 🟨 🟥 |

*Note: The above binning is indicative for used for development purpose during initial design verification phase. Binning is formulated based on our bench validation & field experience. We are able to indicate deposit risks with >97% correlation.*

**Confidential** | Donaldson Internal Standard Practices – Tier-5 EAT System CFD Study.

**Fig. 13.** Donaldson in-house developed deposit binning method used in CFD development reports

### 3.1.6 Sensor packaging

From Stage V/Tier4F, the EAT systems are included with close loop calibration for regeneration and dosing strategy to ensure effective NOx conversions. Such close looping is critical to have instantaneous feedback loops which are sensor driven. This puts critical need for the sensor, to be packaged to indicate the right references. Donaldson by extensive discussions and iterations with our sensor suppliers, have ensure the necessary packaging guidelines are respected in the CAD level and sensor evaluation procedures are conducted to understand sensitivity study.

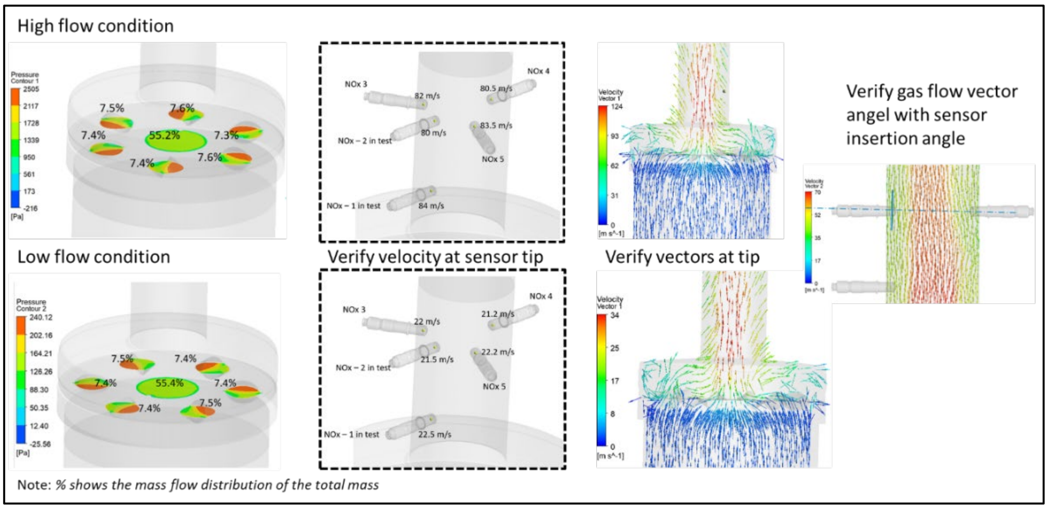
High flow condition
Pressure Contour 1
2505
2117
1728
1339
950
561
173
-216
[Pa]
7.5%
7.6%
7.4%
55.2%
7.3%
7.4%
7.6%
NOx 3
82 m/s
80.5 m/s
NOx 4
NOx – 2 in test
80 m/s
83.5 m/s
NOx 5
NOx – 1 in test
84 m/s
Velocity Vector 1
124
93
62
31
0
[m s^-1]
Verify gas flow vector angel with sensor insertion angle
Velocity Vector 2
70
52
35
17
0
[m s^-1]
Low flow condition
Verify velocity at sensor tip
Verify vectors at tip
Pressure Contour 2
240.12
202.16
164.21
126.26
88.30
50.35
12.40
-25.56
[Pa]
7.5%
7.4%
7.4%
55.4%
7.4%
7.4%
7.5%
NOx 3
22 m/s
21.2 m/s
NOx 4
NOx – 2 in test
21.5 m/s
22.2 m/s
NOx 5
NOx – 1 in test
22.5 m/s
Velocity Vector 1
34
25
17
8
0
[m s^-1]

Note: *% shows the mass flow distribution of the total mass*

**Fig. 14.** Sensor packaging and sensitivity evaluation [reference for NOx sensor]

This is ensuring first level confidence on sensor packaging, which at later stage supports the calibration team to have effective indication from the validated sensor locations. Sensor packaging and verifications methods are developed, validated, and not effectively included into our development reports for temperature, pressure, and NOx sensors. Correlation buildup is ongoing for PM sensors, which can find its need with implementation of OBD-2.

### 3.1.7 Readiness for beyond Stage V

With continuous learning and improvement inculcated within the engineering principle and having close working relationship with our customer and technology partners, we have effectively invested pour resources to ensure CFD methods are adept to suit future EAT system evaluation.

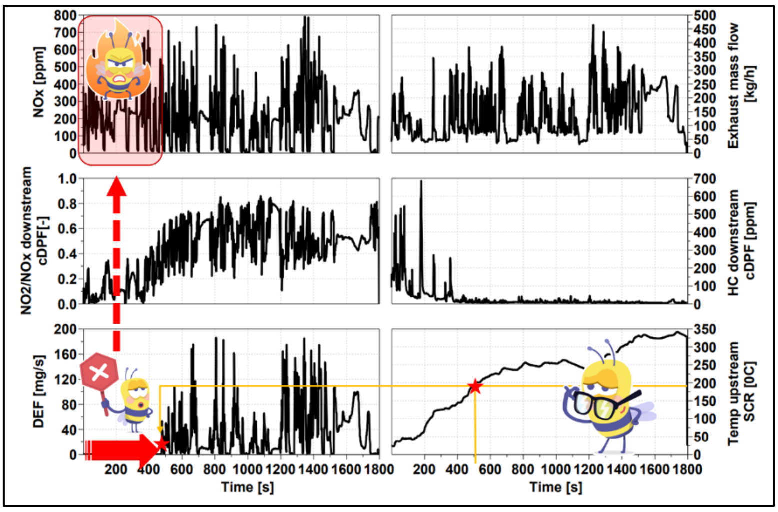

**Fig. 15.** Cold start explained over a OHW-Stage V NRTC Cycle

We have effectively completed 2 rounds of correlation runs based out of Donaldson internal demonstrator Tier-5 EAT systems.

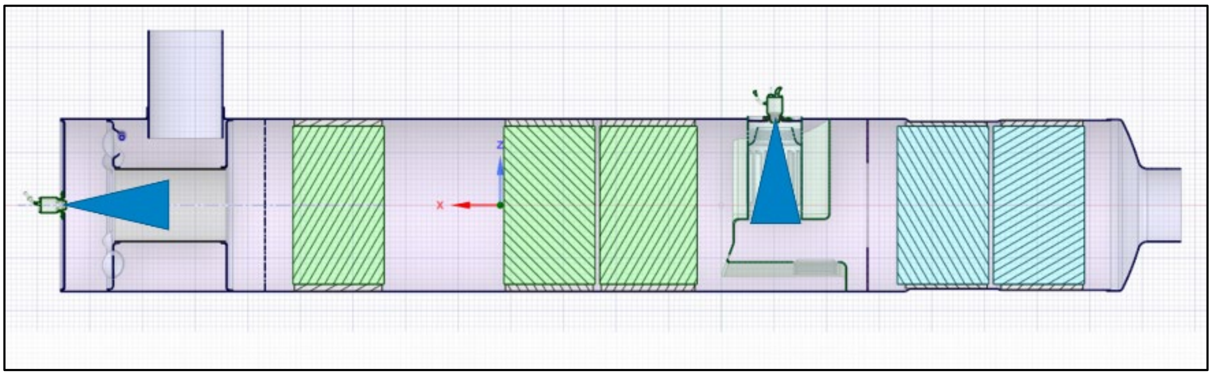

**Fig. 16.** Donaldson Internal Tier-5 Demonstrator [HC injection, eHeater, 2 urea injectors – dual dosing system]

These demonstrators EAT systems had 3 dosing injections, 1st urea injector for a close coupled SCR, 2nd HC injector for rapid heat up setup combined with a HC mixer, 3rd injector is also a urea injector for the main SCR setup packaged away from engine.

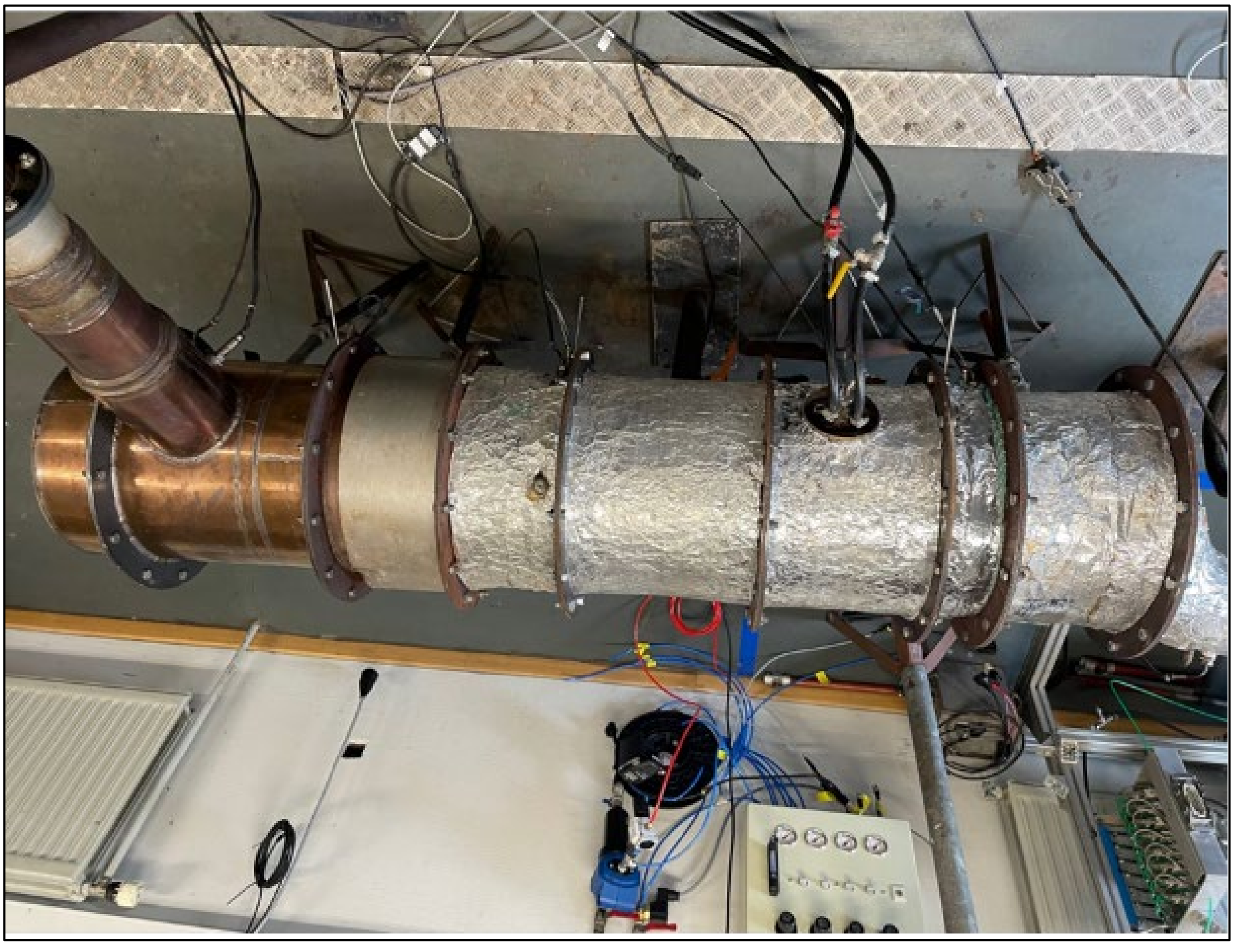

**Fig. 17.** Development correlation >97% achieved for Tier-5 internal demonstrator

## 4. Conclusion

Like any ideal product development team, Donaldson emission primarily focused on design verification, design optimization and design release for proof of concept based on flow simulations. With a customer first focus and our development strategy to ensure emission systems for performance and emission team's ease, we included the detailing of KPI of each technology and found ways to integrate those latent KPIs into our development study. This approach, has proven effective with excellent feedback of systems form field, meeting functional KPIs at all operating loads. Importantly, the design revision loops have come close to negligible from functional requirements. We continue with our focus of development for emission systems to meet calibrator's close loop requirements and ensure continuous improvements and correlation to our verification methods. Our CFD engineers are trained extensively on system performance and real-life applications. Their involvement in correlation runs from internal engine bench tests help understand and bridge gaps wherever necessary. With such close-knit work package, within Donaldson emissions, we can deliver, fully verified emission systems which can meet functional targets and behavior expectations of emission calibration team, with a first-time right approach. Our flow study correlation across system remains at >98% for pressure drop and uniformity indices. NH3 injection-based uniformity correlation is >98% and crystallization prediction is >97%. We have extensively invested in thermal CFD to support future emission system development to predict substrate heat up time by including substrate and EAT thermal inertia. Present level of maturity for skin temperature indication is >98%. Temperature predictions across EAT in steady state is >96% and transient legal cycles for each point across EAT is >94%. With gaps identified and maturity possibility in place, we are progressing well with our correlation runs and have plans to achieve higher correlation for thermal CFD also. This way, we would be able to deliver excellent thermal prediction for future Tier-5 emission systems, indicating at a very early stage regarding h4e cold start performance of the concept designs.

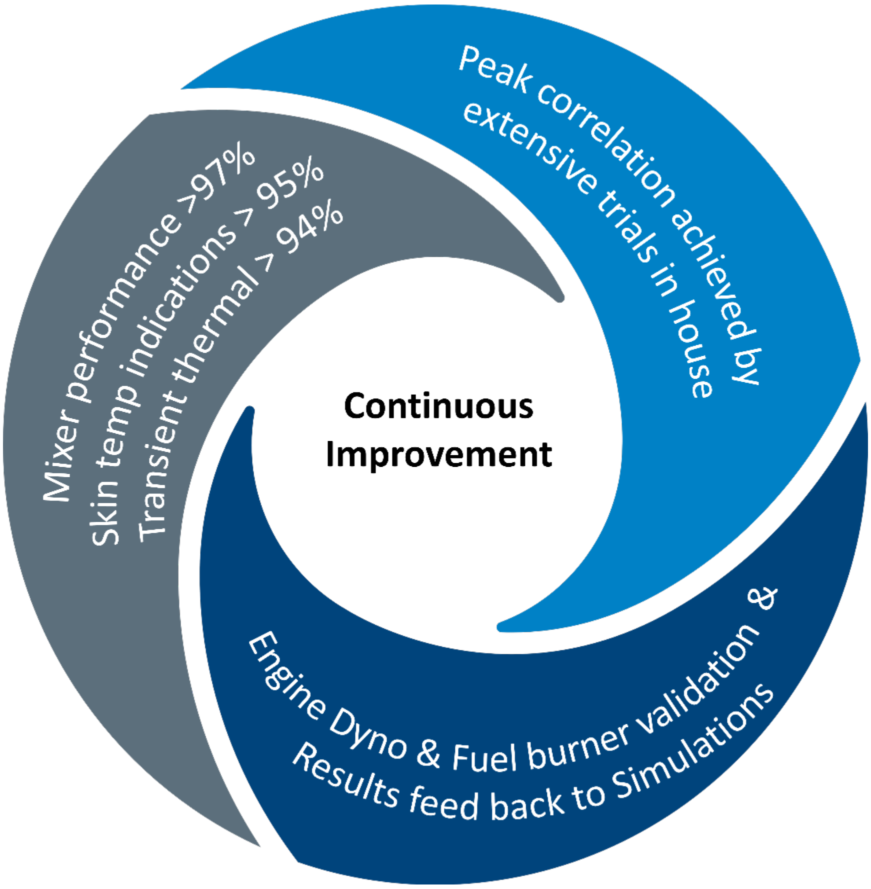
Peak correlation achieved by extensive trials in house
Continuous Improvement
Engine Dyno & Fuel burner validation & Results feed back to Simulations
Mixer performance >97%
Skin temp indications > 95%
Transient thermal > 94%

## Reference

1) EATS development for H2-ICE in off-road application [20th FAD conference 2023 - Dresden, 08-11-2023] -Liebherr Machines Bulle.
2) Ke Sun, Haiyang Zhao, Kui Zhao, Da Li, and Shuzhan Bai* - Optimization of SCR inflow uniformity based on CFD simulation [https://doi.org/10.1515/phys-2020-0221 received October 26, 2020; accepted November 26, 2020]
3) Praveena V, Martin MLJ. A review on various after treatment techniques to reduce NOx emissions in a CI engine. J Energy Inst. 2018;91(5):704–20. doi: 10.1016/j.joei. 2017.05.010.
4) Nishad K, Sadiki A, Janicka J. Numerical investigation of adblue droplet evaporation and thermal decomposition in the context of NOx-SCR using a multi-component evaporation model. Energies. 2018;11(1). doi: 10.3390/en11010222.
5) Tanner P, Gorman J, Sparrow E. Flow-pressure drop characteristics of perforated plates. Int J Numer Methods Heat Fluid Flow. 2019;29(11):4310–33. doi: 10.1108/HFF-01-2019-0065
6) Jongen T. Simulation and modeling of turbulent incompressible flows [dissertation]. Lausanne: EPFL; 1998.
7) Wolfstein M. The velocity and temperature distribution in onedimensional flow with turbulence augmentation and pressure gradient. Int J Heat Mass Transf. 1969;12:301–18. doi: 10.1016/0017-9310(69)90012-X
8) Rodi W. Experience with two-layer models combining the k-epsilon model with a one-equation model near the wall. 29th Aerospace Sciences Meeting. Reno, NV: AIAA; 1991 January 7–10. doi: 10.2514/6.1991-216.
9) Capetillo AJ, Ibarra F, Stepniewski D, Vankan J. Multiphase modelling of SCR systems: using the taguchi method for mixer optimisation. SAE Int J Engines. 2017;10(1):61–71. doi: 10.4271/2017-26-0113.
10) www.theicct.org. ICCT’s COMMENTS AND TECHNICAL RECOMMENDATIONS ON FUTURE EURO 7/VII EMISSION STANDARDS, Berlin, May 7, 2021
11) California Air Resources Board, Heavy-Duty Omnibus Regulation | California Air Resources Board, *December 22, 2021*
12) US Environmental Protection Agency, “Mobile Source Air Toxics,” http://www3.epa.gov/otaq/toxics.htm, accessed Jan. 2016.
13) Naseri, M., Chatterjee, S., Castagnola, M., Chen, H. et al., "Development of SCR on Diesel Particulate Filter System for Heavy Duty Applications," SAE Int. J. Engines 4(1):1798-1809, 2011, doi:10.4271/2011-01-1312.
14) Bosch, H., and Janssen, F., “Catalytic reduction of nitrogen oxides: A review on the fundamentals and technology,” Catal. Today 2(4):369-532, 1988.
15) Ansys Fluent Theory Guide, 2023 R2.

## Session 2.3 THERMAL RUNAWAY

# Risk and Challenges in Thermal Runaway and Propagation in Automotive Li-Ion Battery Packs

J. San Primitivo[1]

[1]JLR – Jaguar Land Rover. Abbey Road, Whitley, Coventry, CV3 4LF, United Kingdom

E-mail: jsanprim@jaguarlandrover.com
Telephone: +(44) 7576812821

**Abstract.**

Transition in the automotive industry from conventional Gasoline and Diesel vehicles to Battery Electric Vehicles (BEV) represents a challenge to overcome the range anxiety from the customer. Cell capacity and energy density are two key factors to improve the range of BEV vehicles. Nowadays, the best cell technology to maximise these factors, are Lithium – Ion (Li-Ion) battery cells. Li - Ion battery cells can experience uncontrolled release of energy under abuse conditions, which can compromise the safety of the vehicle, the passengers and surrounding elements. The control and containment after a thermal event is key in the design of a BEV vehicle and it is getting more complex due to the energy density increase of the cells. Early design optimisation is critical to avoid late battery and vehicle design changes that could lead to potential programme delays and induce unexpected costs. In order to design a robust and safe solution it is essential to develop a hybrid approach maximising capabilities and limitations of virtual and physical techniques. On the one hand, early in the programme there is typically limited capability to physically test full battery packs with different design solutions. On the other hand, later in the programme, there are limitations of conducting enough number of physical tests to include all potential levels of variability. For this reason, it is required to develop a hybrid process where virtual and physical techniques come hand in hand to design a robust and safe solution. In this paper, risk and challenges of thermal runaway and propagation will be explained, and a hybrid virtual-physical development process will be proposed.

**Notation (optional)**

| | |
|---|---|
| *ARC* | *Adiabatic Rate of Calorimeter* |
| *BEV* | *Battery Electric Vehicles* |
| *Cp* | *Specific Heat* |
| *OEM* | *Original Equipment Manufacturer* |
| *JLR* | *Jaguar Land Rover* |
| *m* | *mass* |
| *Q* | *Heat release* |
| *SoC* | *State of Charge* |
| *T* | *temperature* |

## 1. Introduction

Thermal runaway is an uncontrolled release of energy in form of an explosion with flames, gases and particles from a cell in a battery pack. Thermal propagation is the extension of the thermal runaway of a cell into thermal runaway in any other cells within the battery pack. The management of Thermal runaway and propagation is a safety concern for every Original Equipment Manufacturer (OEM), including Jaguar Land Rover (JLR). The management of it has effects in the safety of the vehicle and the occupants and in the potential warranty of the vehicles and brand's reputation if the battery pack is not robustly designed.

The control of the thermal propagation is regulated by the Chinese authorities in the GB38031 legislation; legislation that states that after a thermal runaway event of a single cell, the battery pack shall not cause danger to the occupant compartment of the vehicle within five minutes after the thermal event is detected. JLR is committed to ensure the maximum safety of their vehicles and it is designing the battery packs not only to ensure that the legislation is accomplished but also to maximize the level of safety for its customers.

The recent challenges from customers to increase the energy density of the battery pack has increased the risks and challenges for designing safe and robust battery packs that can contain thermal runaway and control propagation. In order to optimize the design of the battery packs against thermal runaway and propagation, a hybrid development process between physical test and virtual analysis is developed to maximize development cost, time and robustness [1].

## 2. Hybrid development process

The hybrid development process is the approach required for the robust design of battery pack to avoid and control thermal propagation after a thermal runaway event. This process consists of combining simulation and physical testing for optimization of the system allowing reduction of risk and saving development time. In this process, a set of physical tests are executed in order to characterize and calibrate the digital twins to be able to predict the behavior of the cells during thermal runaway. A digital twin is a virtual model that is created to accurately reflect an existing physical unit. The digital twin represents an individual physical product or process and it is used to understand and predict the physical counterpart's performance characteristics. For thermal runaway and propagation, there are two key set of tests that are needed to be executed to calibrate through the physical behavior through digital twins (figure 1).

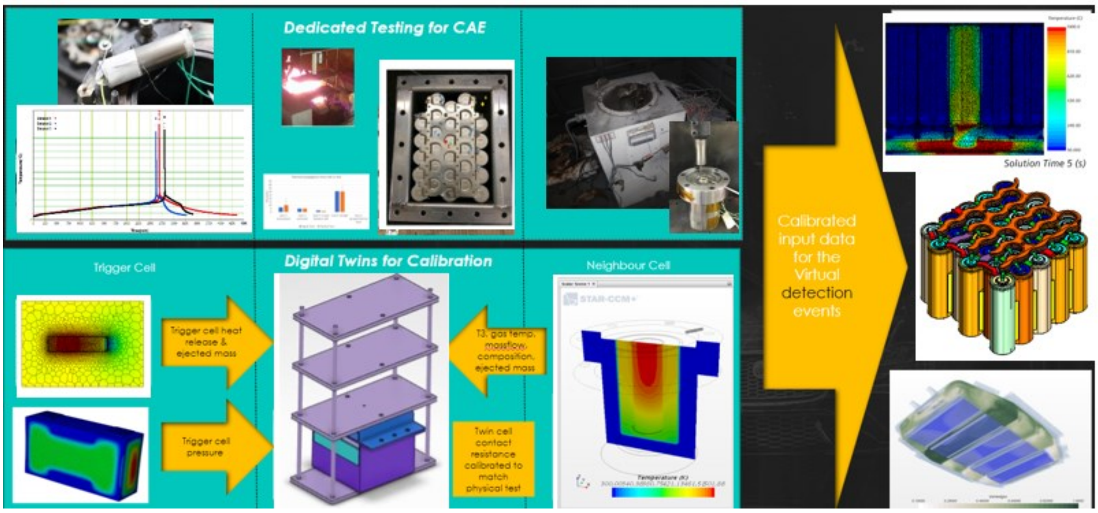
Dedicated Testing for CAE
Trigger Cell
Digital Twins for Calibration
Neighbour Cell
Trigger cell heat release & ejected mass
Trigger cell pressure
T3, gas temp, massflow, composition, ejected mass
Twin cell contact resistance calibrated to match physical test
STAR-CCM+
Temperature (K)
Calibrated input data for the Virtual detection events
Solution Time 5 (s)

**Fig. 1.** Hybrid development process

1. Trigger cell: heat release and cell expansion during thermal event based on the trigger method (figure 2); typically, a preferred triggered method is selected to assess the legislation. A bespoke test is executed with a high quantity of measurements to calibrate the heat release and heat transfer of the cell that is triggered. With this test, the heat release of the triggered cell is calibrated in the digital twin by matching thermal results from the test. Another test is required to assess the geometrical change of the cell due to expansion based due to the chemical reactions. The cell expansion can directly affect the heat transfer to neighbour cells and components depending on the design. A bespoke test is executed with a limited number of components but with same level of constraints as in the battery pack to assess the cell expansion. With this test, the thermal resistance as a function of time to the different components is calibrated in the digital twin. Both tests are repeated several times to obtain the variability based on cell-to-cell variation.

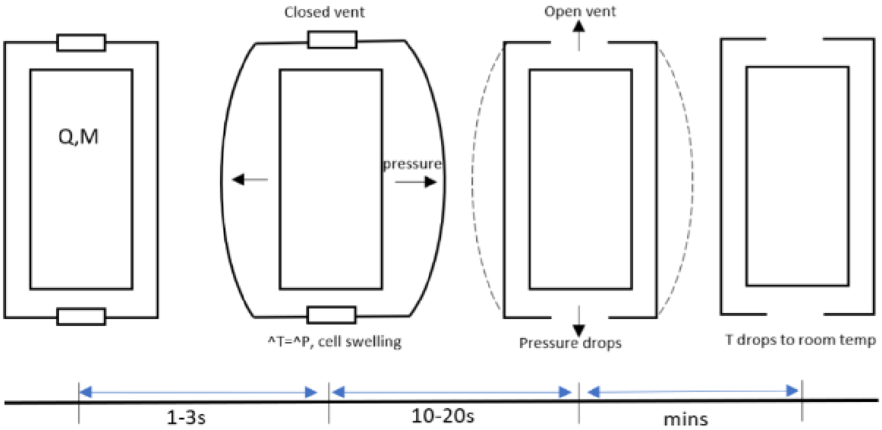

**Fig. 2.** Phases of the thermal runaway event for a typical automotive cell

2. Neighbour cell: heat up behavior of the neighbour cell due to heat transfer from the triggered cell. The test is typically executed in Adiabatic Rate of Calorimeter and the heat release of the neighbour cell is calibrated in the digital twin.

Once the model is calibrated, it is possible to assess the response of the battery pack to a thermal runaway event and support the optimization of the design to contain/prevent thermal propagation. To validate the virtual solutions, smaller rig configurations can be physically tested based on the design modifications assessed virtually to confirm the response before conducting costly full battery pack tests.

## 3. Thermal Runaway. Cell and energy Characterization

Thermal runaway in Li-Ion cells occurs due to the rupture of the separator between the cathode and anode which causes a short circuit within the cell. The failure of the separator can occur due to the separator collapsing, tearing or piercing. During thermal runaway, chemical reactions occur which result in the heat up of the cell material (within seconds) and the increase of the internal pressure, eventually causing the cell to rupture and mass ejection in the form of gases and particulates at high speed and temperature.

The energy released during the thermal runaway event is mainly due to the electric energy within the cell. In figure 3, it can be observed the different cell technology against energy density. In the last decade the specific energy has increased 50% from NMC111 to the latest NMC 900 series. For this latest type of cell, the specific energy can go up to 900 Wh/kg keeping a similar nominal voltage of 4V.

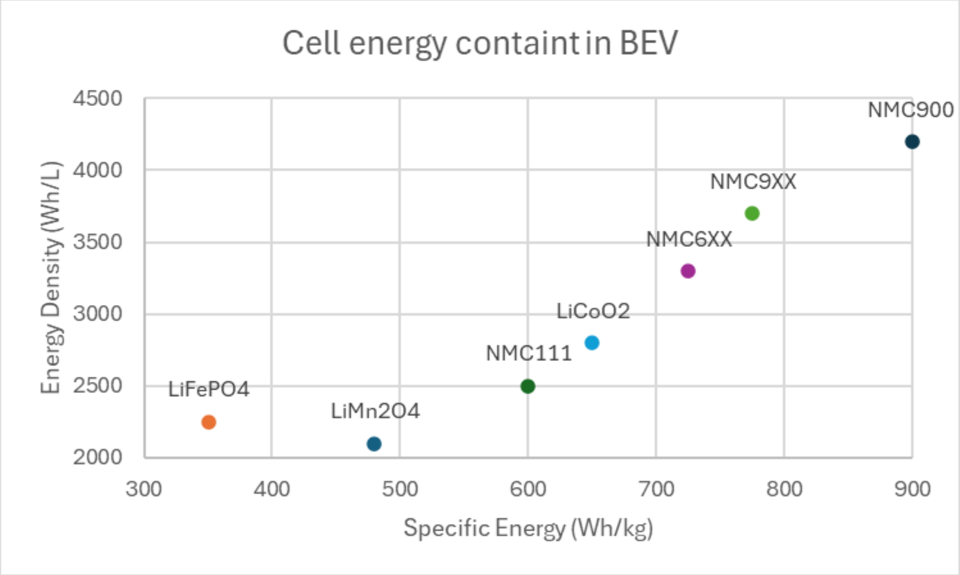

**Fig. 3.** Specific energy and energy density of Li Ion cells in automotive industry

Another factor that has improved the Energy Density and Specific Energy; apart from the chemistry, is the size of the cells, allowing to have higher capacity cells. The first generation of Tesla vehicles were using cylindrical cells with 3.1Ah capacity while today different cell suppliers and cell types (prismatic and pouch) allow cells up to 200Ah as shown in figure 4.

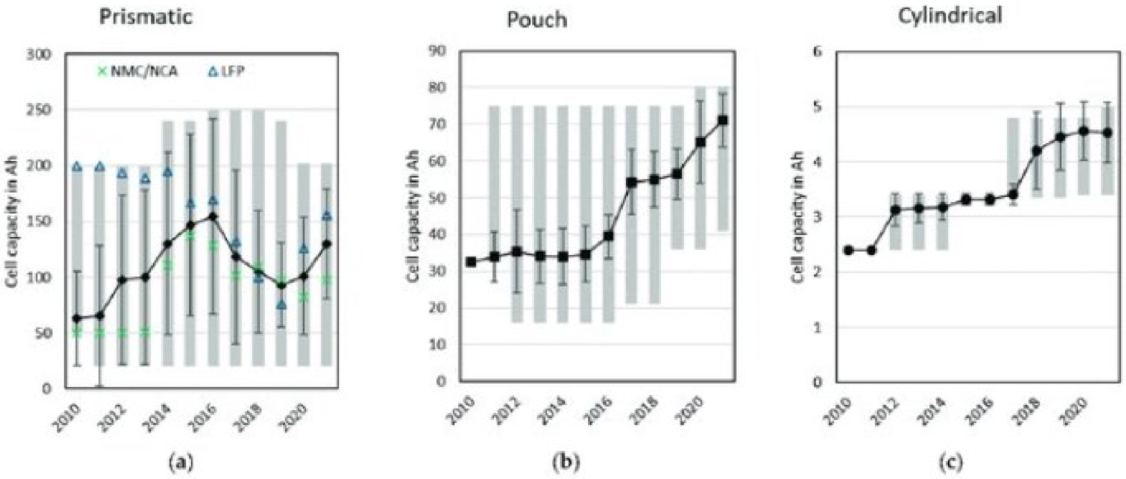

**Fig. 4.** Cell capacity evolution from 2010 to 2021 [2]

With the knowledge of the specific density, nominal voltage and the capacity, it is possible to calculate the total electric energy that is released in form of heat for a full State of Charge (SoC) cell using equation 1. For the high capacity cells, the energy can go up to 3MJ.

$$Q\,[J] = Capacity[Ah] \cdot Voltage\,[V] \cdot 3600$$

**Eq. 1.** Electric cell energy release after thermal runaway

In parallel, using equation 2, it is possible to obtain the typical cell weight of a single cell, weight that can go up to 3kg.

$$m\,[kg] = \frac{Capacity[Ah] \cdot Voltage\,[V]}{Specific\ density\,[\frac{Wh}{kg}]}$$

**Eq. 2.** Cell weight of latest BEV cells

With the knowledge of total energy release and the cell weight, using equation 3, it is calculated the temperature that the cell will be at after a thermal event that it will be around 1000-1200C depending of the cell specific heat ($C_p$) that is typically between 800-1000J/kgK.

$$\Delta T = \frac{Q[J]}{m[kg] \cdot Cp[\frac{J}{kgK}]}$$

**Eq. 3.** Cell Temperature after thermal event

### 3.1 Thermal Runaway energy distribution and trigger methods

During thermal runaway, there is heat up of the cell due to chemical reactions that occur inside the cell due to failure of the separator. The chemical reactions inside the cell increase the internal pressure. In order not to break the cell can from an uncontrolled location, the cells have venting pressure devices that break when the internal cell pressure increases to the vent device rupture limit. The rupture pressure is dependent on the type of cell and cell design but can be within the range of 3 to 10 bar. Through this venting device there are gases and particulates ejected into the battery pack what represents a challenge for the design. The gases are typically a mixture of combustible gases such as methane, hydrogen or carbon monoxide. These gases, if mixed in the correct conditions with air can result in flames what further increases the challenge of controlling a thermal runaway event. In parallel, the particulates are ejected from the cell at high speed and can cause erosion, impact damage and possible melting of structural components which can lead to flames outside of the battery pack compromising the safety of the battery design. Depending on how the separator fails the speed and behavior of the chemical reactions varies, leading to different distribution between percentage of mass retained within the cell and the; percentage of mass ejected in the form of gases and percentage of mass ejected in the form of particulates.

There are multiple reasons why the cell can fail, and there are equivalent trigger methods to induce the failure. The cell can fail due to separator collapsing, separator tearing or separator piercing. These 3 failures have their equivalent inducing method that are causing the failure of the cell due to over temperature, nail penetration or over-charge respectively. In parallel, these three failures are equivalent to field potential failures such as crush, internal short circuit and overheating during charging/traction respectively. The faster the thermal runaway happens; the more mass is ejected due to higher kinetic energy in the cell when the venting device fails. In table 1, it is shown the extreme of percentage distribution depending on the trigger method and the condition. The battery pack shall be designed for the worst condition of all three gases, particulates and mass retained.

**Table 1**. % of mass distribution after a thermal event

| | |
|---|---|
| Mass retained | 20-80% |
| Mass ejected (particulates) | 30-60% |
| Mass ejected (gases) | 10-15% |

In summary, for the latest cell technologies, it needs to be controlled after a thermal event up to almost 3MJ of energy release in terms of heat due to the electric energy; in addition, the gases can also combust increasing the risk of energy release and management. Finally, the distribution of energy between gas ejection, particles and mass retained in the cell differs based on cell design, cell state of charge, ambient conditions and cell failure method what makes more challenging the robust design of battery packs due to the multiple possible combinations. The extent of the of the variation can be observed in figure 5.

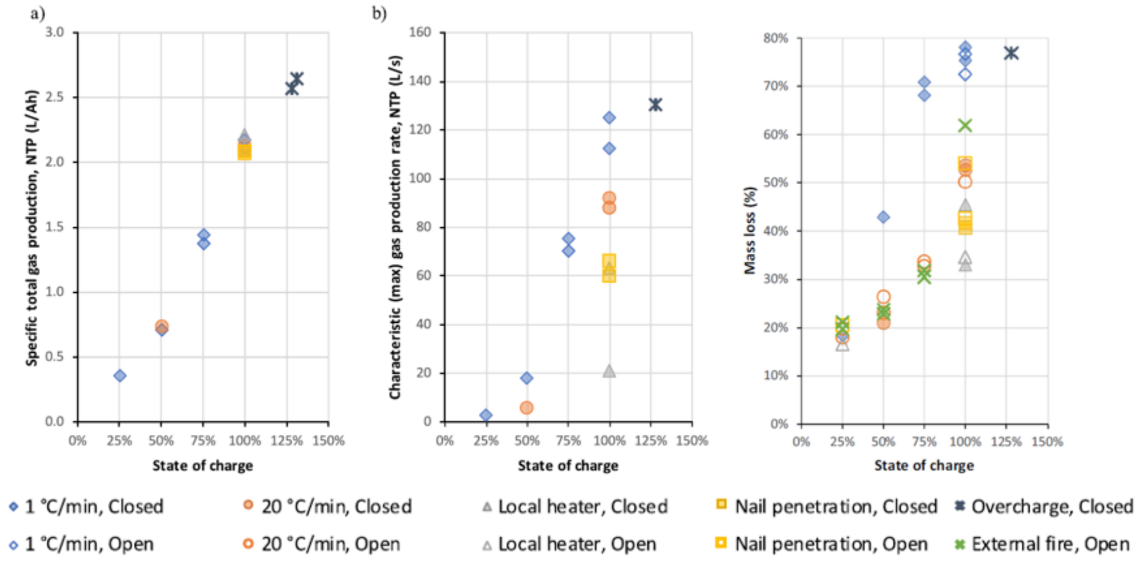

**Fig. 5.** Energy distribution as function of different trigger methods and external conditions [3]

### 3.2 Adiabatic Rate of Calorimeter (ARC)

The adiabatic Rate of Calorimeter (ARC) is the physical test used to characterize the behavior of a cell during thermal runaway. The ARC is a physical test that consists of introducing a charged cell in an adiabatic calorimeter. Afterwards, the cell is heated at constant rate (typically 5/10 degrees and letting the cell stabilize (heat and wait phase) until the cell start heating by itself (seek phase) at which the calorimeter follows the temperature of the cell until it goes to thermal runaway. In the heat up of the cell there are 3 main phases. In the first phase, up to $T_1$, there are no chemical reactions in the cell; at $T_1$, the chemical reactions start occurring, but the overall process is endothermic up to $T_2$. At $T_2$, the overall set of reactions become exothermic up to $T_3$ (Thermal Runaway temperature) that is when the thermal runaway event happens and there is a sudden increase in cell temperature with orders of 100s of degrees within seconds. It is important to mention that this $T_3$ varies based on separator design and can be between 150C to 200C, and there is a typical variation up to ±5 degrees for the same cell design. A schematic of the process can be observed in figure 6.

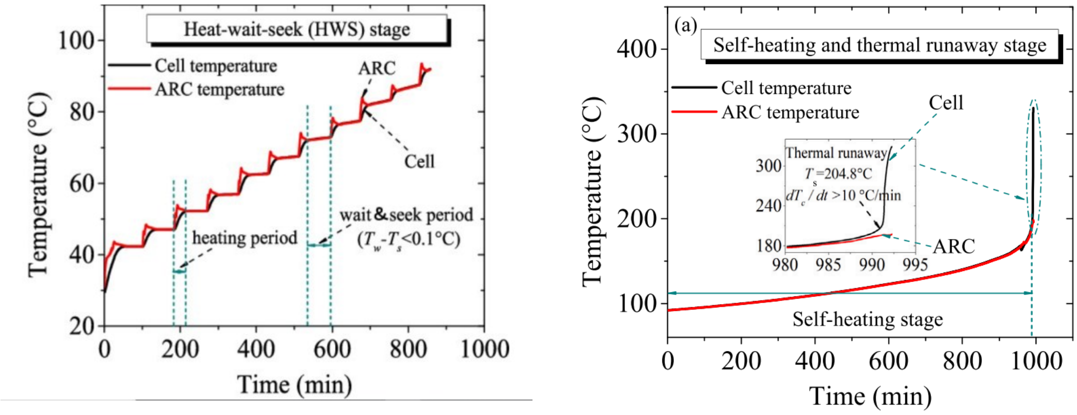

**Fig. 6.** ARC Process and phases [4]

The ARC data is the first key input of the hybrid development process as it is used to assess virtually if after a thermal runaway event in the triggered cell, there is propagation in any of the neighbours. It is necessary to build a digital twin of the ARC test and calibrate the virtual model to get the heat generation of the cell against temperature based on the physical test. This heat generation against temperature is what is used in the battery pack analysis as input to assess the propagation risk. The most important requirement in this calibration is to accurately capture the rate of heat ahead of the thermal event close to the thermal event as that will drive the predictability in cases where there is close risk to propagation. In figures 7, 8 and 9, a calibrated digital twin is shown for the thermal runaway of a Li-ion cylindrical cell [5]. The discrepancies shown after the thermal event in figure 6 are due to the fact that the ARC stops being adiabatic after the event while the digital twin is still adiabatic and, therefore, there is not heat loss; however, there is almost perfect match in the heat up section (figure 7).

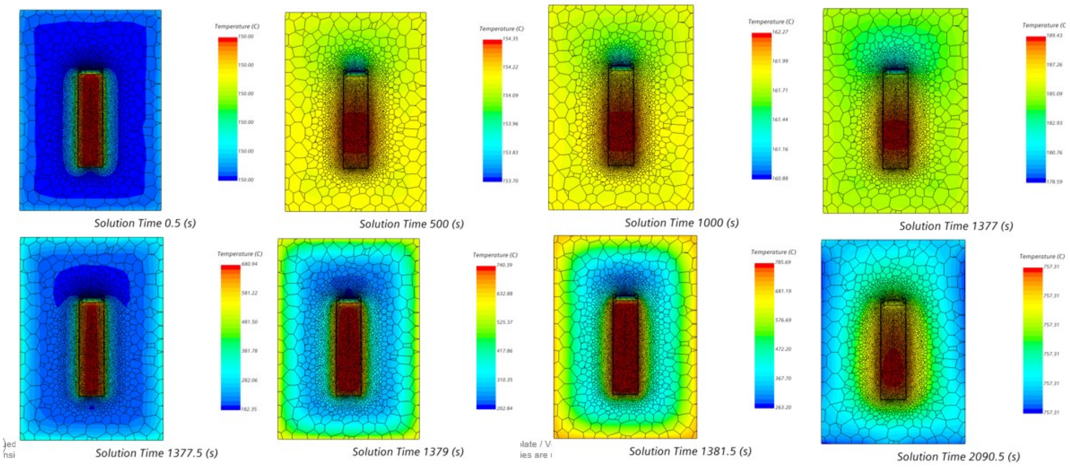

**Fig. 7.** Calibrated digital twin of a thermal runaway ARC test

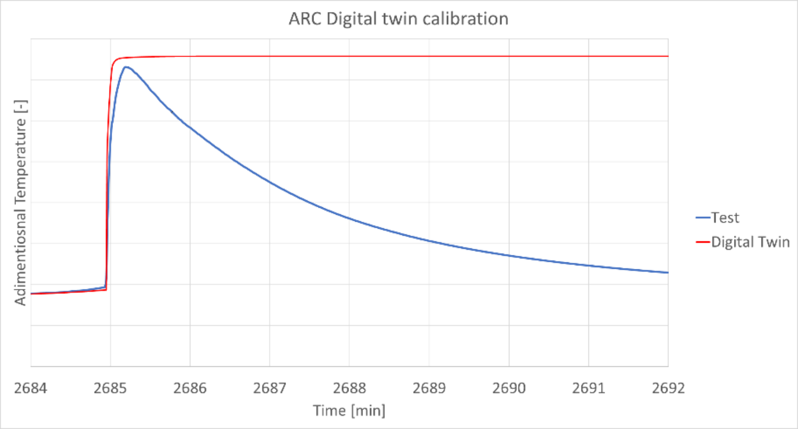

**Fig. 8.** Calibrate digital twin compared with physical test

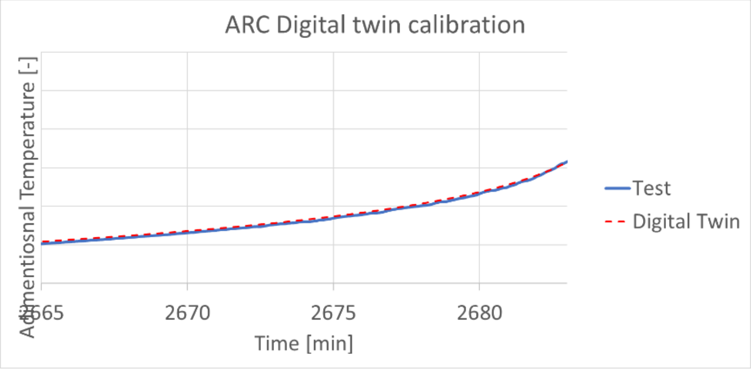

**Fig. 9.** Zoom in the heat up section of the ARC digital twin

## 4. Thermal Runaway and Propagation. Physics of failure

In order to design and optimize the battery pack to prevent thermal runaway and propagation, it is essential to firstly understand the challenges and risks that are required to be mitigated. To do so, 3 ideal functions are defined:

- Prevention of a secondary cell or more going into Thermal Runaway 'X' time (based on targets) after the initiator cell.
- Transportation and cooling the gas and particles from the trigger cell to the external atmosphere preventing flames existing pack (T < 500C) and avoiding damage to the pack components through erosion, melting & arcing.
- Warning of the driver of a thermal runaway event cascading timing requirement from the anti-propagation system

These 3 ideal functions allow the design team to understand the areas that the system needs to be controlled to control the risk after a thermal event to passengers and people around the vehicle.

### 4.1 Prevention of a secondary cell going into thermal runaway due to heat transfer

To prevent a neighbour cell from going into thermal runaway it is essential to design based on the different heat transfer mechanisms: conduction, convection and radiation. It is critical to ensure the avoidance of the overall heat but also potential local hotspots that can cause thermal propagation.

The conduction is the heat transfer occurring due to direct contact through the trigger cell. Cells are as packed as possible, to maximize the package space, to optimize weight and range. The heat transfer occurs through the structure, busbars, glues and other components in the battery pack. In order to control the conduction heat transfer, the battery packs are designed to guide the heat towards the paths that limit the heat transfer to the neighbor cell directly. Different materials are assessed to optimize the system. Another control parameter is the cooling system which can be used to extract the heat from the cell to the coolant fast and limit the total heat transfer to the rest of the structure. This heat transfer can occur as well due to particulates ejected landing into areas of the system close to neighbor cells. There are materials that are being optimized to control, delay and limit the heat transfer through conduction from these particulates. The convection is the heat transfer occurring from the hot gases ejected after the thermal event. These gases can enter in the air gaps between components and can cause localized heating that can induce cell propagation. In the pack design, it is essential to control and optimize the gas path to limit this heat source. Finally, radiation is another critical heat source due to the high temperature that the system gets to. In order to limit radiation effects, there are materials added to the system with low emissivity to control the radiation heat up effects. Virtual assessments are performed to optimize the system ahead of physical tests. An example of this optimization can be observed in figure 10, where different material selection based on diffusivity between cells can change considerably the neighbour cell temperature and, therefore, the risk of propagation. The best material is selected based on safety, cost and weight.

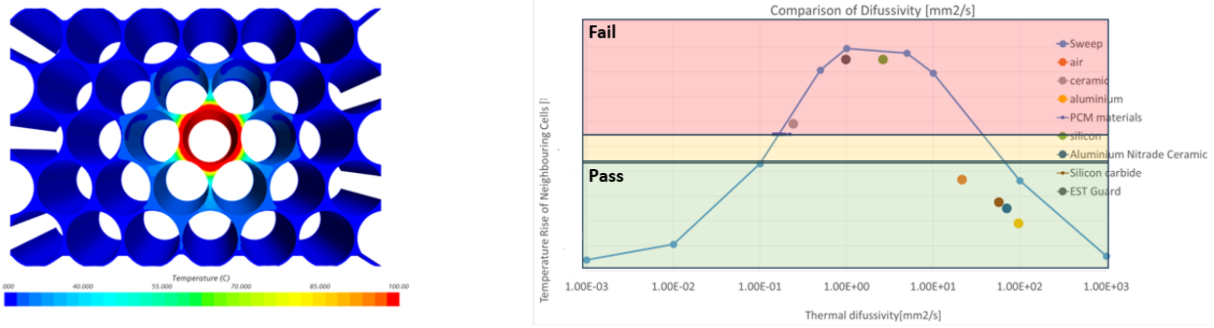

**Fig.10.** Effect of material selection between cell for thermal propagation risk

### 4.2 Prevention of a secondary cell going into thermal runaway due to arcing

Thermal propagation can occur due to the arcing. Arcing occurs when electricity jumps from one high voltage connection to another. This can happen due to an electrical breakdown of conductive gas/solid that produces an electrical discharge. As the particulates and the gases ejected from the trigger cell are electrically charged, there is risk of arcing what causes quick discharge of the cells and thermal propagation. The battery packs are designed against this failure mode by driving the gases and particulates away from critical areas. Besides, the critical high voltage components are usually protected with isolating materials and kept at enough distance to minimize the risk of this failure. Again, the system can be designed and tested virtually to minimize risk of arcing based on particulates and gases distribution.

### 4.3 Prevention of system failure due to gases causing flames outside the pack

The legislation specifies that the vehicle shall be safe after a thermal event and one of the requirements that get cascaded from it is that the gases need to be cool down inside the pack so that they are cold enough when they leave the pack so that they do not auto-ignite when mixing with air outside the pack. The requirements in terms of temperature based on the auto-ignition temperature of the gases ejected (hydrogen, methane and carbon monoxide mainly) is presented in figure 11. Typically, the structure and the gas path until the venting device is designed to absorb enough heat before the gas exit. Again, virtual analysis is executed to optimize the gas path for different cell locations to ensure that there is no risk of flames when physical test is executed.

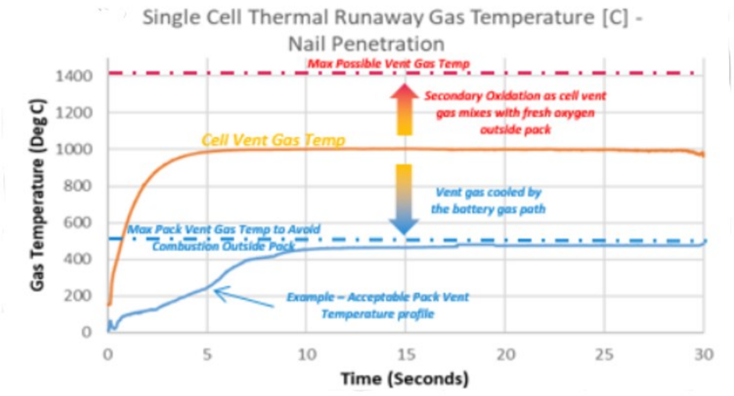

**Fig.11.** Thermal runaway gas temperature requirement at pack exit

### 4.4 Prevention of system failure due to structural integrity

During the thermal runaway, the ejection of gases and particulates can cause the failure of the structural integrity of the pack causing pack rupture and risk of flames outside the pack. The first reason of pack integrity failure is due to the increase of internal pressure of the pack due to the hot gases ejected that can cause the rupture of the lid, joints or sealings. In order to decrease this risk, it is typically introduced a venting device that opens after the event so that there is limited pressure increase allowing the system to keep its integrity. Knowing the gas ejection from physical test, it is possible to virtually assess the best location of this device and the mass flow requirements. The second reason for pack integrity failure is due to the melting caused by hot gases and particulates. One key set of components to focus Is the cooling pipes as melting these components can cause leakage of conductive coolant on the pack floor inducing a short-circuit and consequent thermal propagation. It is possible to virtually track the location of the particulates and gases and how they heat different components and protect any potential component that can be damaged, typically plastic components.

### 4.5 Prevention of failure due to thermal runaway detection

Finally, thermal runaway detection is a must condition in the design to be sure that the customer gets a warning signal after the thermal event to evacuate the vehicle. There are multiple types of sensors that can be used for detection due to the characteristics of the phenomenon. Depending on cost, robustness or reliability, it can be selected pressure, thermal or particle sensors (such as CO2 sensors) [6]. The number of sensors depends on the pack distribution as every cell in the pack needs to be able to trigger at least one of the sensors. However, extra robustness is typically added to have at least two sensors capturing the event. The selection of the sensor type, number of sensors and location is typically driven by virtual optimization. As it can be observed in figure 13, there are some parts of the pack where there is a low concentration of venting gases during the event what will increase the difficulty and delay of measuring the event and virtual analysis helps to position the sensors in ideal locations.

Concentration after 3s of thermal runaway

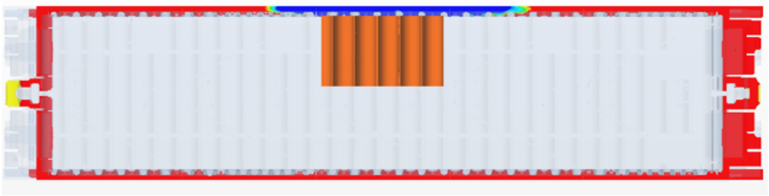

Concentration after 5s of thermal runaway

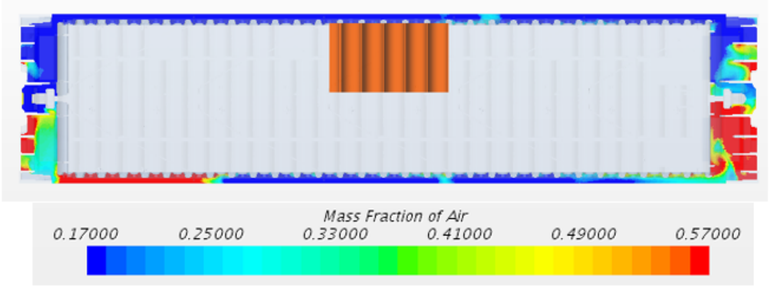

**Fig.12.** Virtual assessment of gas distribution in battery pack after a thermal event

## 5. Conclusions

As presented in this document, the design of battery packs against thermal runaway and propagation is one of the key safety and legislative requirements for BEV. The complexity of physics, the variability and the cost does not allow to develop the system against this requirement robustly using either physical or virtual techniques. For this reason, a hybrid development process is deployed, a process that allows to maximize the use of virtual techniques by calibration of key input data through physical tests and final verification in the test.

## References

[1] R. Spotnitz and J. Franklin, Abuse behavior of high-power, lithium-ion cells. Available from: https://doi.org/10.1016/S0378-7753(02)00488-3.

[2] Neef Christoph, Trends in Automotive Battery Cell Design: A statistical Analysis of Empirical Data. Available from: https://doi.org/0.3390/batteries9050261.

[3] Willstrand Ola, Pushp Mohit, Andersson Petra, Brandell Daniel, Impact of different Li-ion cell test conditions on thermal runaway characteristics and gas release measurements. Available from: https://doi.org/10.1016/j.est.2023.107785.

[4] He Xuanze, Zhao Chunpeng, Hu Zhenwen, Restuccia Francesco, Ritcher Franz, Wang Quingsong and Rein Guillermo, Heat transfer on accelerating rate calorimetry of the thermal runaway of Lithium-ion batteries. Available from: https://doi.org/10.1016/j.psep.2022.04.028.

[5] Robert Spottnitz, James Weawer, Gowri Yeduvaka, D.H. Doughty and E.P. Roth. Simulation of abuse tolerance of lithium. Available from: https://doi.org/10.1016/j.powsour.2006.10.013.

[6] Sascha Koch, Kay Peter Birke and Robert Kuhn. Fast Thermal Runaway Detection for Lithium-Ion Cell in Large Scale Traction Batteries. Available from: https://doi.org/10.3390/batteries4020016.

# Performance Comparison and Kinetic Mechanisms Evaluation of Thermal Runaway Prediction Accuracy of different Li-ion Battery Chemistry

S. Mehranfar[1] *, A. Mahmoudzadeh Andwari[1] *, J. Könnö[1], A. Garcia Martinez[2] and C. Mico Reche[2]

[1] Machine and Vehicle Design (MVD), Materials and Mechanical Engineering, Faculty of Technology, University of Oulu, FI-90014 Oulu, Finland
[2] CMT – Clean Mobility & Thermofluids. Universitat Politècnica de València. Camino de Vera s/n, 46022 Valencia, Spain.

*Corresponding Authors: Amin M Andwari, Sadegh Mehranfar
E-mail: Amin.M.Andwari@oulu.fi
Telephone: +358 29 448 1621
E-mail: Sadegh.Mehranfar@oulu.fi
Telephone: +358 50 4321302

**Abstract.** The trend toward electrification in powertrain systems and fast market uptake of electric vehicle (EV) batteries for reducing vehicle pollution underscore the growing importance of performance and safety in Li-ion batteries. Despite the outstanding status of Li-ion EV batteries in the market and rising energy density, significant safety concerns persist for battery manufacturers and EV drivers. Li-ion batteries are susceptible to various abuse conditions that can trigger exothermic chain reactions inleading to thermal runaway (TR), combustion of battery systems and EVs. Various battery TR kinetic mechanisms and models have developed to formulate the exothermic reactions occurring in batteries under critical operating conditions. Nevertheless, the application of TR models leads to different results which directly influence the predictability of TR process in the EVs. Accordingly, a comparative assessment of the most important kinetic mechanisms for different chemistries is necessary to facilitate the utilization of TR models in battery operation under the critical conditions. This study investigates different TR kinetic mechanisms by exploiting a battery 3D thermal model with the most common kinetic reactions in TR sub-model built in the COMSOL software. The research also examines the capability of the different kinetic mechanisms to reproduce the various reaction paths leading to TR for various battery chemistries. Additionally, the validation process of numerical studies against detailed 3D geometry compared to traditional 1D models is conducted to assess the reliability of results and provide a more in depth understanding of temperature evolution inside the cell. The results demonstrate that different cathode materials exhibit significantly different thermal behavior under abuse conditions including critical temperature of TR, maximum temperature and released heat. Moreover, different kinetic mechanisms and their ability to reproduce different reaction paths led to more accurate results.

## 1. Introduction

Electric vehicles have been increasingly growing in the last decade and are showing much more potential in the automotive industry due to their promising zero tailpipe emissions in the vehicle, excellent integration with renewable energy sources and superior performance in the electric powertrain systems. Despite the key role of batteries in electric vehicles, challenges toward the further development of Li-Ion batteries (LIBs) in EVs include, but are not limited to, increasing the energy density, improving lifetime, and enhancing the safety standards. Numerous attempts have been made to improve the safety standards of LIBs for further acceleration of EV global market and alleviating the remaining barriers in the development of next generations of LIBs [1].

The recent explosion of LIBs in EVs, smartphones and even in the transportation and storage process have caused extensive concerns in the public, with special safety issues in the EVs. LIBs can undergo a series of exothermic chain reactions called thermal runaway (TR) when triggered by thermal, mechanical, or electrical abuse conditions. Physical damage during car crashes, manufacturing faults, overcharging, and cooling insufficiencies are some of the examples of abuse conditions in the LIBs. The importance of TR comes from not only the high safety standards of EV and passenger, but also from the severity of event. EV battery packs contain hundreds to thousands of LIB cells and triggered cells can release a substantial amount of heat, resulting in the propagation of TR to the adjacent cells and threatening the whole vehicle and passengers. Thus, researchers have aimed at studying the thermal behavior of LIBs under different conditions and modelling of TR event with heat release rate and temperature increases of cell. Nonetheless, different TR models are developed for different chemistries and vary in terms of number of reaction and modelling approach, which limits their applicability in the real operating conditions [2].

Thermal abuse conditions trigger the decomposition of the chemical compounds and components inside the battery. The decomposition of different compounds is an exothermic reaction and leads to the elevated temperate, which could enable the decomposition of other compounds and form a series of chain reactions when temperature reaches a critical point. The significance of various paths that leads to thermal runaway and dominating routes correlated to the main components of batteries have resulted in the specification of different kinetic mechanisms [3]. Numerous reaction mechanisms have been proposed in the literature for different battery chemistries as new LIBs have been developed through years of investigations. Nonetheless, the application of different mechanisms leads to different results, hindering the utilization of TR kinetic mechanism in critical operation modelling [4]. As result, many efforts have been made to propose a detailed assessment of most common models for different cell chemistries to assess their capabilities for reproducing different reaction paths leading to thermal runaway condition and compare thermal behavior of different cells in critical conditions [5], [6].

Numerous investigations have focused on the definition of reaction paths for different chemistries. Wang et al. [7] studied the thermal stability of several commonly used organic solvents and electrolytes by micro calorimeter. Peng et al. [8] assessed the thermal safety of LIBs with various cathode materials. Kong et al. [6] compared the influence of lithiated graphite with lithiated $Li_4Ti_5O_{12}$ (LTO) as anode and concluded that LIBs with LTO anode show better thermal stability. Among those studies in the TR prediction of Li-ion cells, many researchers have tried to assess the TR of single cells by use of 3D models. Kim et al. [9] developed a 3D thermal abuse model for Li-ion cells in commercial software FLUENT. They compared the result of lumped model with 3D model for cell temperature, specific heat generation and nondimensional values. The results show the effect of nonuniform distribution effects and cell internal propagation of abuse reactions. Silva et al. [10] also compared the 0D and 3D TR models in MATLAB Simulink and Ansys Fluent and assessed the thermal runaway propagation in LIBs modules. Comparison of different studies indicates that 3D models show more reliable results by having the capability of addressing the effect of nonuniform thermal distribution inside cells and localized heating/cooling.

In this study, a comprehensive analysis of various TR kinetic mechanisms and various cathode materials in a Li-ion battery cell is conducted using a developed thermal model. Comparison is performed considering cell maximum temperatures, total heating power and integrated total energy, heating rates, integrated heat sources and average species during the TR event is done to gain a deeper understanding of different kinetic mechanisms and battery chemistries and reaction paths. Additionally, a 3D model is adopted to assess the temperature evolution of battery cell during the TR event. The core temperature of the cells provides profound insight for comparison with traditional 1D models in the developed kinetic mechanisms. The findings of this study facilitate the integration of kinetic mechanisms into battery modelling under critical operation and enhance the accuracy of the battery TR models in real-world scenarios for safer EV batteries.

## 2. Thermal model description

In this study, numerical analysis of the temperature dynamics in a cylindrical battery is performed after being placed in an oven. In TR phenomenon, as the temperature increases, various exothermal decomposition reactions are activated, which in turn results in further heating of the battery. TR is modelled by considering different reactions for decomposition of the different cell components, decomposition reaction rates and enthalpies.

A 3D model has been developed in the commercial software COMSOL Multiphysics by modelling of a single cell with the heat transfer governing equations and integrating the TR model to replicate the TR event inside of a LIB. The 18,650-cell geometry is selected, and the model was built in the software considering the jelly roll, still casing and mandrel. The geometry is defined in 2D and by the axial symmetry assumption to save the computational cost. Fig. 1 illustrates the simplified scheme of a battery cell and inner structure with model geometry of the present work. The model simulates the open circuit battery cell inside oven to replicate the accelerating rate calorimetry (ARC) test results and is validated to show the reliability of developed model. Main Li-ion cell properties are listed in Table 1 [9], [11].

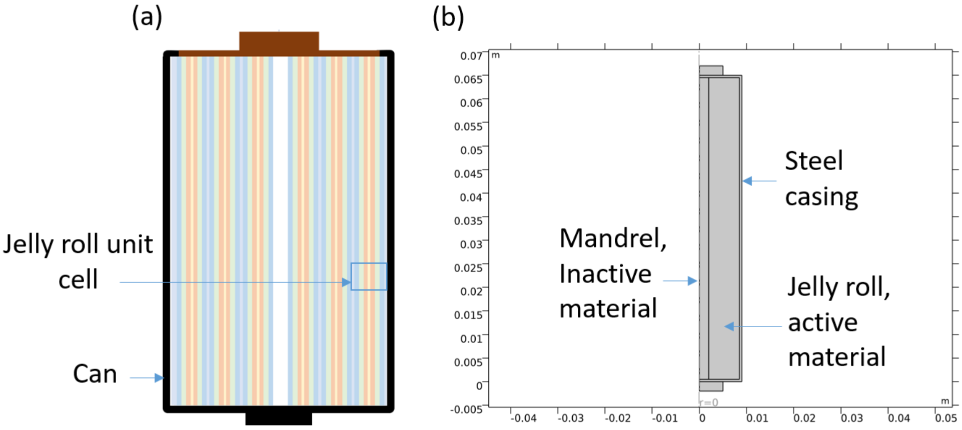

**Fig. 1.** A) Simplified scheme of a battery cell and inner structure B) Model Geometry of present work

**Table 1**. Major Li-ion cell properties

| Symbol | Description | Value |
|---|---|---|
| Cell format | 18,650 | - |
| Battery radius, m | r_batt | 0.009 |
| Battery height, m | h_batt | 0.065 |
| Thickness of battery can, m | d_can | 5E-4 |
| Mandrel radius, m | r_mandrel | 0.002 |
| Volumetric heat capacity of jellyroll, (J $m^{-3}$ $K^{-1}$) | RhoCp_batt | 2.789E6 |
| Average jelly roll radial thermal conductivity, W/cm K | kT_batt | 0.034 |
| Heat transfer coefficient, W/($m^2$·K) | h_conv | 7.17 |
| Positive electrode Thermal conductivity, W/(m*K) | K_cat | 1.58 |
| Negative electrode Thermal conductivity, W/(m*K) | K_an | 1.04 |
| Separator Thermal conductivity, W/(m*K) | K_sep | 0.344 |

The interplays of external heat transfer, decomposition reaction rates and enthalpies, and cell thermal mass balance determine the heating dynamics of a cell. The temperature of the oven is assumed to be constant in the present study. Li-ion cells reach the oven temperature due to heat transfer from the surrounding air. If the temperature of the oven is higher than the critical temperature for triggering the exothermic reactions of different cell components, the enthalpy from these reactions increases the temperature of the cell accordingly when heat generation is not compensated by the dissipated heat. Battery cell undergoes significant temperature increase, resulting in further temperature growth and TR.

To develop the proposed thermal model with TR mechanism, parameters of different reaction mechanisms, initial conditions and boundary conditions are specified for the model. Also, the TR heat of reaction for each component is introduced into the thermal model as a heat source and the numerical solution is calculated as a time dependent solution. The flow chart in Fig. 2. elaborates the key steps of the proposed model including the boundary conditions of thermal model and mechanisms parameters set up, calculation of the fraction of components, calculation of the heat of reaction, solving the energy equation, updating the temperature field and post processing the results of temperature plots and heat generation data along with temperature contours. Details of TR model coupled with the thermal model are given in the section 3.

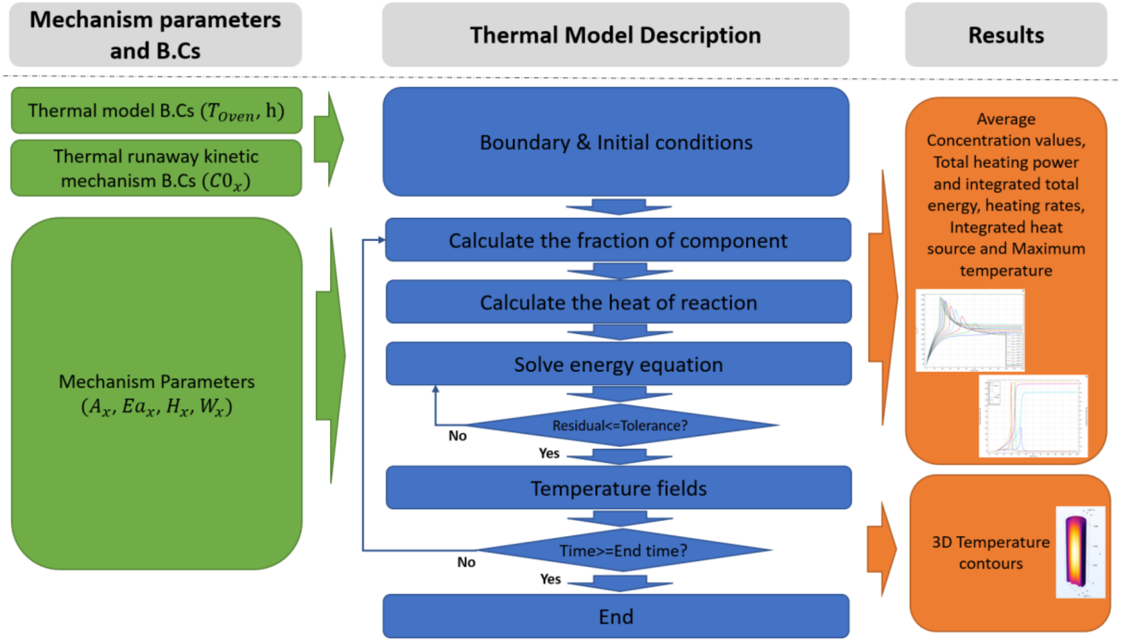
Mechanism parameters and B.Cs
Thermal Model Description
Results
Thermal model B.Cs ($T_{oven}$, h)
Thermal runaway kinetic mechanism B.Cs ($CO_x$)
Mechanism Parameters ($A_x$, $Ea_x$, $H_x$, $W_x$)
Boundary & Initial conditions
Calculate the fraction of component
Calculate the heat of reaction
Solve energy equation
Residual<=Tolerance?
No
Yes
Temperature fields
Time>=End time?
No
Yes
End
Average Concentration values, Total heating power and integrated total energy, heating rates, Integrated heat source and Maximum temperature
3D Temperature contours

**Fig. 2.** Thermal modeling flow work principle in correspondence with TR mechanism

The thermal model inside the battery is dominated by the conduction heat transfer. In addition, generated heat by reactions of kinetic mechanism in each cell component is imposed to the model as a heat source term. The heat sources are mostly exothermic and result in an increase of temperature. Furthermore, the temperature of the cell updates according to the Eq. (2) and heat of reaction changes due to the dependency on the temperature.

$$\frac{\mathrm{d}T_{\mathrm{Bat}}}{\mathrm{d}t} = \frac{Q_{\mathrm{gen}} - Q_{\mathrm{diss}}}{MC_p} \tag{1}$$

$$T_{\mathrm{Bat}}(t) = T_{\mathrm{Bat},0} + \int \frac{\mathrm{d}T_{\mathrm{Bat}}}{\mathrm{d}t}\,\mathrm{d}t \tag{2}$$

The generated heat is determined by the chemical reaction of TR which are mostly exothermic.

$$Q_{gen} = \sum \quad Q_i \tag{3}$$

where $Q_i$ represents generated heat of reaction for cell components. The interaction of battery with the surroundings is also modelled by the dissipation heat of convection and radiation as the following:

$$Q_{\mathrm{diss}} = Q_{\mathrm{conv}} + Q_{\mathrm{rad}} = h \cdot A \cdot (T_{\mathrm{ARC}} - T_{\mathrm{Bat}}) + \varepsilon\sigma(T_{\mathrm{ARC}}^4 - T_{\mathrm{Bat}}^4) \tag{4}$$

where $\varepsilon$ is the emissivity of the cell surface and $\sigma$ is the Stefan–Boltzmann constant. The oven is assumed to be an isothermal cavity. The oven plays as a heating device for battery up to the point of TR event, but battery acts as a heating component for the oven-cell system at the elevated temperature by omitting the excess heat of reactions.

## 3. Thermal runaway kinetic mechanism modeling

The basic kinetic mechanism equations of chemical reactions follow the Arrhenius equation form as the following:

$$\kappa_x = \frac{\mathrm{d}c_x}{\mathrm{d}t} = A_x (c_x)^{n_1} (1 - c_x)^{n_2} e^{\frac{E_{a,x}}{R_0 \cdot T}} \tag{5}$$

Where $\kappa_x$ is the reaction rate, $c_x$ is the normalized concentration, and $A_x$, $E_a$ and $g_x$ are the pre-exponential factor, activation energy and mechanism function respectively. The concentration of each species is under the following relationship with the reaction rate.

$$c_x = 1 - \int \kappa_x \, \mathrm{d}t \tag{6}$$

Furthermore, the heat release by each decomposition reaction is calculated by the multiplication of reaction rate, heating value of corresponding component ($H_x$) and total mass of that component ($m_x$).

$$Q_x = m_x \cdot H_x \cdot \kappa_x \tag{7}$$

Different kinetic mechanisms are developed by selecting various reaction paths in the TR process. Each of these models suggests several reactions with specific reaction rate, heating values and Arehenous model parameters. Two different kinetic mechanisms are adopted in this work to compare different reaction paths for TR process of LIBs.

## 3.1 Kim et al. kinetic mechanism

The source term $Q_{gen}$ in Eq.3 is associated with the abuse reaction and is determined by the sum of generated heat of SEI decomposition, negative-solvent reaction, positive-solvent reaction, and electrolyte decomposition, respectively (Eq. 8).

$$Q_{gen} = \sum Q_i = Q_{SEI} + Q_a + Q_c + Q_e \tag{8}$$

The generated heat of each reaction is then modeled based on the Arrhenius equation's reaction rate.

### 3.1.1 SEI reactions

The meta-stable SEI layer is formed from the first charging and protects anode form reaction with electrolyte. Identification of $(CH_2OCO_2Li)_2$ as meta-stable SEI layer and start of decomposition at around 90-110 ℃ is done by Richard and Dahn [12]. Energy release during reaction of SEI depends on the electrolyte composition and follows the Arrhenius equations reaction rate according to the following form [9], [11]:

$$R_{\mathrm{sei}}(T, c_{\mathrm{sei}}) = A_{\mathrm{sei}}(c_{\mathrm{sei}})^{m_{sei}} \exp\left[-\frac{E_{a,\mathrm{sei}}}{RT}\right] \tag{9}$$

The change in the reacting species is given by the Eq. (10). Furthermore, the generated heat is in proportion to the decomposition rate and heating value of reaction $H$ and mass of component $W$ following the Eq. (11) [9], [11]:

$$\frac{dc_{\mathrm{sei}}}{dt} = -R_{\mathrm{sei}} \tag{10}$$

$$Q_{\mathrm{sei}} = H_{\mathrm{sei}} W_a R_{\mathrm{sei}} \tag{11}$$

Where $c_{\mathrm{sei}}$ is dimensionless concentration of lithium containing meta stable species in the SEI, $H_{\mathrm{sei}}$ is Heat of reaction, $W_a$ is Volume-specific carbon content in the jelly roll. Model parameters for SEI reactions in Kim et al. [9] mechanism are listed in Table 2.

### 3.1.2 Anode reactions

Once SEI layer decomposed entirely, negative electrode is not protected against the contact with electrolyte and the intercalated lithium at electrode reacts exothermically according to the following reaction rate [9], [11]. The heat release per unit volume due to the decomposition of anode is calculated as Eq. (14).

$$R_a(T, c_a, t_{\mathrm{sei}}) = A_a(c_a)^{m_{a,n}} \exp\left[-\frac{t_{\mathrm{sei}}}{t_{\mathrm{sei,\,ref}}} - \frac{E_{a,a}}{RT}\right] \tag{12}$$

$$\frac{dc_a}{dt} = -R_a; \quad \frac{dt_{\mathrm{sei}}}{dt} = R_a \tag{13}$$

$$Q_a = H_a W_a R_a \tag{14}$$

Where $c_{\mathrm{a}}$ is dimensionless concentration of intercalated Li-species in the negative electrode and $t_{\mathrm{sei}}$ is dimensionless SEI layer thickness. Model parameters for anode reaction in Kim et al. [9] mechanism are presented in Table 2.

### 3.1.3 Cathode reactions

The positive active material reacts directly with electrolyte or decomposes exothermically and produce oxygen that can react with electrolyte. The reduction of positive active material is described in Eq (15). The heat release per unit volume for cathode decomposition is also determined according to the Eq. (17) [9], [11]:

$$R_c(T, \alpha) = A_c \alpha^{m_{c,p1}} (1-\alpha)^{m_{c,p2}} \exp\left[-\frac{E_{a,c}}{RT}\right] \tag{15}$$

$$\frac{d\alpha}{dt} = R_c \tag{16}$$

$$Q_c = H_{\mathrm{c}} W_c R_c \tag{17}$$

Where $\alpha$ is Degree of conversion of positive electrode material and $W_c$ is Volume-specific positive-active content in the jelly roll. Model parameters of cathode reactions in Kim et al. [9] mechanism are listed in Table 2.

### 3.1.4 Electrolyte reactions

Electrolyte can also decompose exothermically in addition to reacting with anode and cathode. The reaction rate is expressed as the Eq. (18) and (19) [9], [11]. The heat release per unit volume for electrolyte decomposition is also determined according to the Eq. (20):

$$R_{\mathrm{e}}(T, c_e) = A_{\mathrm{e}} c_e \exp\left[-\frac{E_{a,\mathrm{e}}}{RT}\right] \tag{18}$$

$$\frac{dc_e}{dt} = -R_{\mathrm{e}} \tag{19}$$

$$Q_e = H_{\mathrm{e}} W_e R_{\mathrm{e}} \tag{20}$$

Where $c_e$ is Dimensionless electrolyte concentration and $W_e$ is volume-specific electrolyte content in the jelly roll. Model parameters of electrolyte reactions for Kim et al. [9] mechanism are collected in Table 2.

**Table** 2. Model parameters for Kim et al. [9] mechanism.

| Symbol | Description | Value |
|---|---|---|
| Reaction heat, J·kg^(-1) | H_sei | 2.57×10^5 |
| | H_a | 1.714×10^6 |
| | H_e | 1.55×10^5 |
| Reaction frequency factor, s^(-1) | A_sei | 1.667×10^15 |
| | A_a | 2.5×10^13 |
| | A_e | 5.14×10^25 |
| | Ea_sei | 1.3508×10^5 |
| Reaction activation energy, J·mol^(-1) | Ea_a | 1.3508×10^5 |
| | Ea_e | 2.74×10^5 |
| Initial value, dimensionless | c0_sei | 0.15 |
| | c0_a | 0.75 |
| | α0 | 0.04 |
| | c0_e | 1 |
| Reaction order | m_sei | 1 |
| | m_a, n | 1 |
| | m_c, p1 | 1 |
| | m_c, p2 | 1 |
| | m_e | 1 |
| | t0_sei | 0.033 |
| Volume-specific content of reacting material, kg·m^(-3) | W_a | 610 |
| | W_e | 406 |

Cathode materials change significantly in terms of chemical components between different cell chemistries, influencing the thermal characteristics of Li-ion cells during TR. Model parameters for different cathode materials are collected in Table 3.

**Table 3**. Model parameters of different cathode materials for Kim et al. [9] mechanism. and thermophysical properties of other cathode materials [8]

| Parameter | $LiCoO_2$ | $Li_{1.1}(Ni_{1/3}Co_{1/3}Mn_{1/3})_{0.9}O_2$ | $LiFePO_4$ | $LiNi_{0.8}Co_{0.15}Al_{0.05}O_2$ |
|---|---|---|---|---|
| H_c | 3.14×10^5 | 7.9×10^5 | 1.947×10^5 | 2.18×10^5 |
| A_c | 6.667×10^13 | 2.25×10^14 | 2.0×10^8 | 7.25×10^16 |
| E_c | 1.396×10^5 | 1.54×10^5 | 1.03×10^5 | 1.3×10^5 |
| W_c | 1.3×10^3 | 1.293×10^3 | 0.96×10^3 | 1.274×10^3 |

## 3.2 Ren et al. mechanism

Ren et al. [13] mechanism proposed six reactions to address TR process in NMC cell chemistries. In Ren's mechanism two reactions for anode, one for cathode, two for binder and one for cathode-anode interaction are considered according to Table 4. The predictive TR kinetic mechanism by Ren et al. is established by superimposing the chemical kinetics equations of these six exothermic reactions and fits well with the oven tests results of a NMC Li-ion battery as one of the most popular cathode chemistries. The model parameters of the Arrhenius type equation (Eq. 5) is included in Table 4. and 5.

**Table 4**. Model parameters for Ren et al. [13] mechanism.

| Reaction | x | A_x [1/s] | E_(a,x) [kJ/ mol] | n_1 - | n_2 - | H_x [J/g] | g_x - |
|---|---|---|---|---|---|---|---|
| SEI decomp | Sei | 6.3623×10^9 | 109.6 | 5.5 | 0 | 578.7 | 1 |
| An+Ele | An | 5.151×10^17 | 200.77 | 1 | 0 | 253.2 | 1 |
| An + Bin decomp | BinAn | 4.9679×10^15 | 195.49 | 1 | 0 | 108.5 | 1 |
| Cat decomp | Cat | 5.3481×10^5 | 109.34 | 1.5 | 0 | 434 | 1 |
| Cat + Bin decomp | Bin-Cat | 6.5429×10^13 | 177.85 | 2 | 0 | 452.1 | 1 |
| Cat + An | An | 2.4262×10^13 | 162.01 | 1 | 0 | 560.6 | 1 |

**Table 5**. Initial concentrations and reaction rates for each component in Ren et al. [13] mechanism.

| Component | Initial concentration | dc/dt |
|---|---|---|
| Anode | 1 | -Ran-Rcatan |
| Cathode | 1 | -Rcat |
| Electrolyte | 1 | -Re |
| SEI | 1 | -Rsei |
| t_sei | - | - |
| Binder | 1 | -(γ/(γ+1))RbinAn-(1/(γ+1))RbinCat (Where γ=0.56) |
| BinAn | 1 | -RbinAn |
| BinCat | 1 | -RbinCat |

Validations of the TR simulations are performed by comparing the temperature evolution profiles with the experimental results. The results have shown to be in great agreement with the reference data as shown in Fig 3 which indicates the robustness of the simulation.

The source of validation data for Kim et al. is temperature vs. time plot for oven temperature of 155 ℃ and the source experimental data for Ren et al. is the prediction of battery behaviors under 150 ℃ oven test.

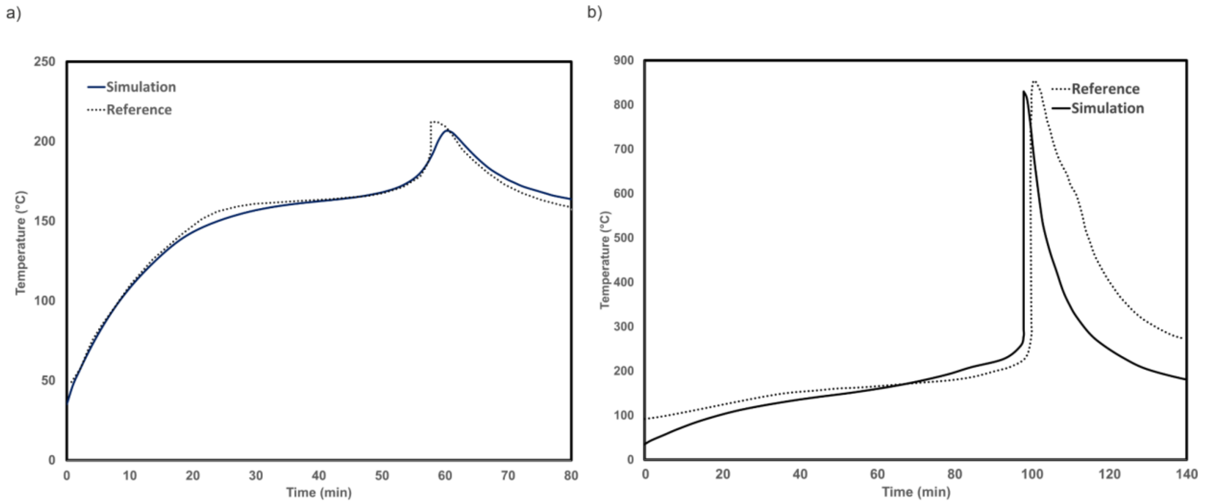

**Fig. 3.** Comparison of the simulated temperature and the reference temperature for: A) Kim et al. [9] and B) Ren et al. mechanism [13].

## 4. Results and discussion

The results of Kim et al. kinetic mechanisms for $LiCoO_2$ battery chemistry are illustrated in Fig. 4. The simulation result is performed by sweeping the oven temperatures from 150 to ℃ 200 ℃ in 5 ℃ steps. The results indicate that at low oven temperatures (150 ℃) the battery does not enter the TR process and the energy released in the process is absorbed by the oven. Nonetheless, the species decompositions lead to significant temperature increases when the oven achieves the critical temperature of 155 ℃. This abrupt increase in temperature is observed in the temperature-time plots and is more dramatic in higher temperatures. This can be attributed to the fact that total heat released follows an exponential pattern and is significantly higher in higher oven temperatures. The maximum battery temperature can reach to almost 315 ℃ for oven temperatures of 200 ℃ in $LiCoO_2$ batteries.

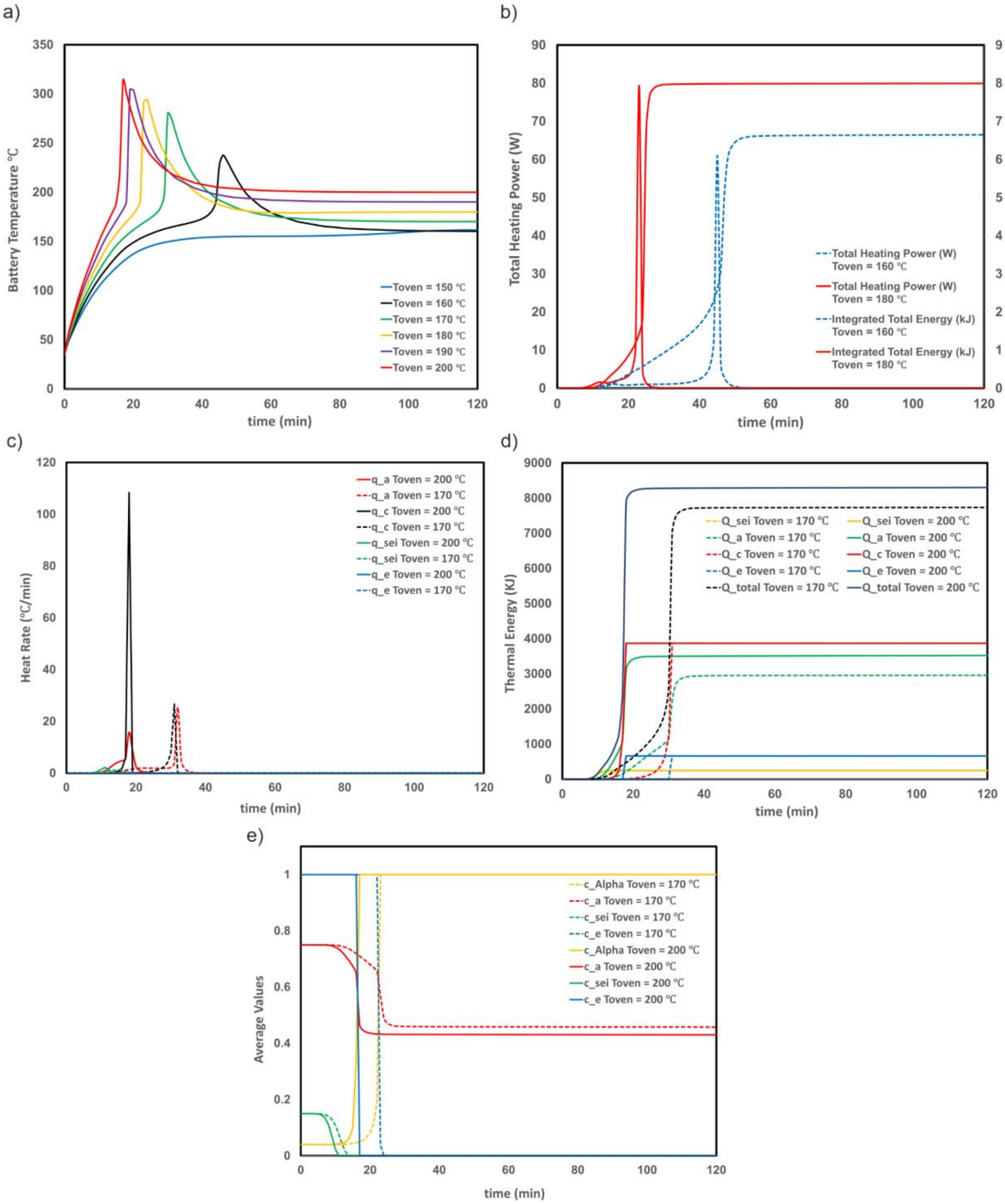

**Fig. 4.** Kim et al. kinetic mechanisms for $LiCoO_2$ battery. A) Maximum temperature for Oven_T 150-200 B) Total heating power and integrated total energy for Oven_T 160, 165 and 170 C) Heating rate for Oven_T 160 and 165 D) Integrated heat source for Oven_T 160 E) Average values and temperature for Oven_T 160 and 165

The results of Kim et al. kinetic mechanisms for $Li_{1.1}(Ni_{1/3}Co_{1/3}Mn_{1/3})_{0.9}O_2$ battery chemistry are illustrated in Fig. 5. The simulation is performed by sweeping the oven temperatures from 165 to ℃ 180 ℃ in 5 ℃ steps. Results indicate that at oven temperatures lower than 170 ℃ the battery does not enter the TR process. However, the species decompositions lead to significant temperature increases when the oven achieves the critical temperature of 175 ℃. This abrupt increase in temperature is observed in the temperature-time plots and can reach to 370 ℃. The results indicate that $Li_{1.1}(Ni_{1/3}Co_{1/3}Mn_{1/3})_{0.9}O_2$ batteries show more abrupt temperature growth and more severe energy release during the TR process compared to $LiCoO_2$ batteries.

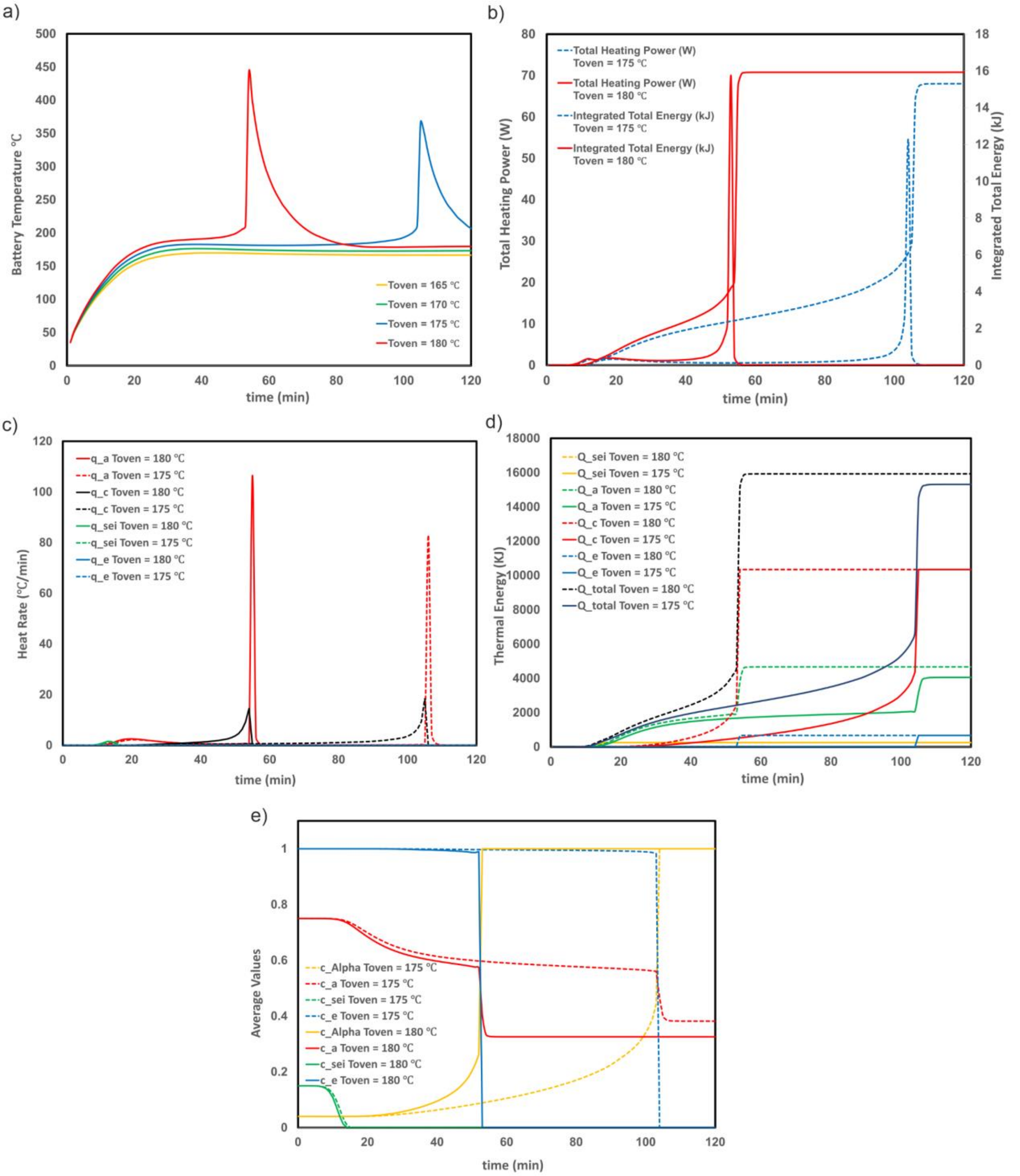

**Fig. 5.** Kim et al. kinetic mechanisms for $Li_{1.1}(Ni_{1/3}Co_{1/3}Mn_{1/3})_{0.9}O_2$ battery. A) Maximum temperature for Oven_T 165-180 B) Total heating power and integrated total energy for Oven_T 175 and 180 C) Heating rate for Oven_T 175 and 180 D) Integrated heat source for Oven_T 180 E) Average values and temperature for Oven_T 180

Kim et al. kinetic mechanisms for $LiFePO_4$ battery chemistry is also shown in Fig. 6. The simulation result is performed by sweeping the oven temperatures from 200 ℃ to 300 ℃ in 20 ℃ steps. At low oven temperatures (200 ℃) the battery does not enter the TR process and the energy released in the process is absorbed by the oven. Nevertheless, the species decompositions lead to significant temperature increases at the oven critical temperature of 220 ℃. This increase in temperature is observed in the temperature-time plots and is less dramatic in comparison to other cell chemistries.

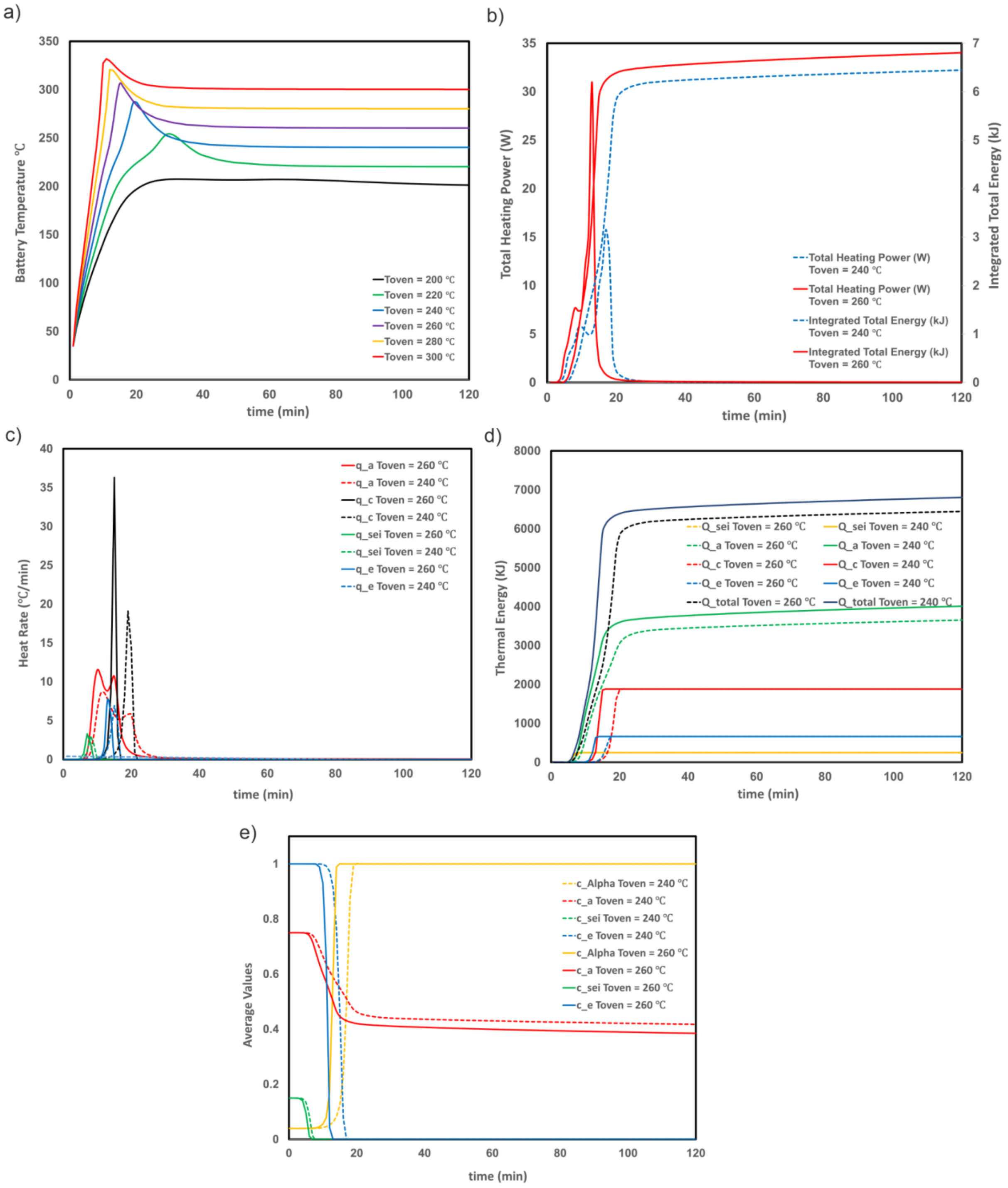

**Fig. 6.** Kim et al. kinetic mechanisms for $LiFePO_4$ battery. A) Maximum temperature for Oven_T 200-300 B) Total heating power and integrated total energy for Oven_T 240 and 260 C) Heating rate for Oven_T 240 and 260 D) Integrated heat source for Oven_T 260 E) Average values and temperature for Oven_T 260

The results of Kim et al. kinetic mechanisms $LiNi_{0.8}Co_{0.15}Al_{0.05}O_2$ battery chemistry are illustrated in Fig. 7. The simulation result is performed by sweeping the oven temperatures from 260 to ℃ 290 ℃ in 10 ℃ steps. The results indicate that at low oven temperatures (260 ℃) the battery does not enter the TR process and the energy released in the process is absorbed by the oven. Nonetheless, the species decompositions lead to significant temperature increases when the oven achieves the critical temperature of 270 ℃. This abrupt increase in temperature is more dramatic in higher temperatures which can be attributed to the fact that total heat released is significantly higher in higher oven temperatures. The maximum battery temperature can reach to almost 395 ℃ for oven temperatures of 290 ℃ in $LiNi_{0.8}Co_{0.15}Al_{0.05}O_2$ batteries.

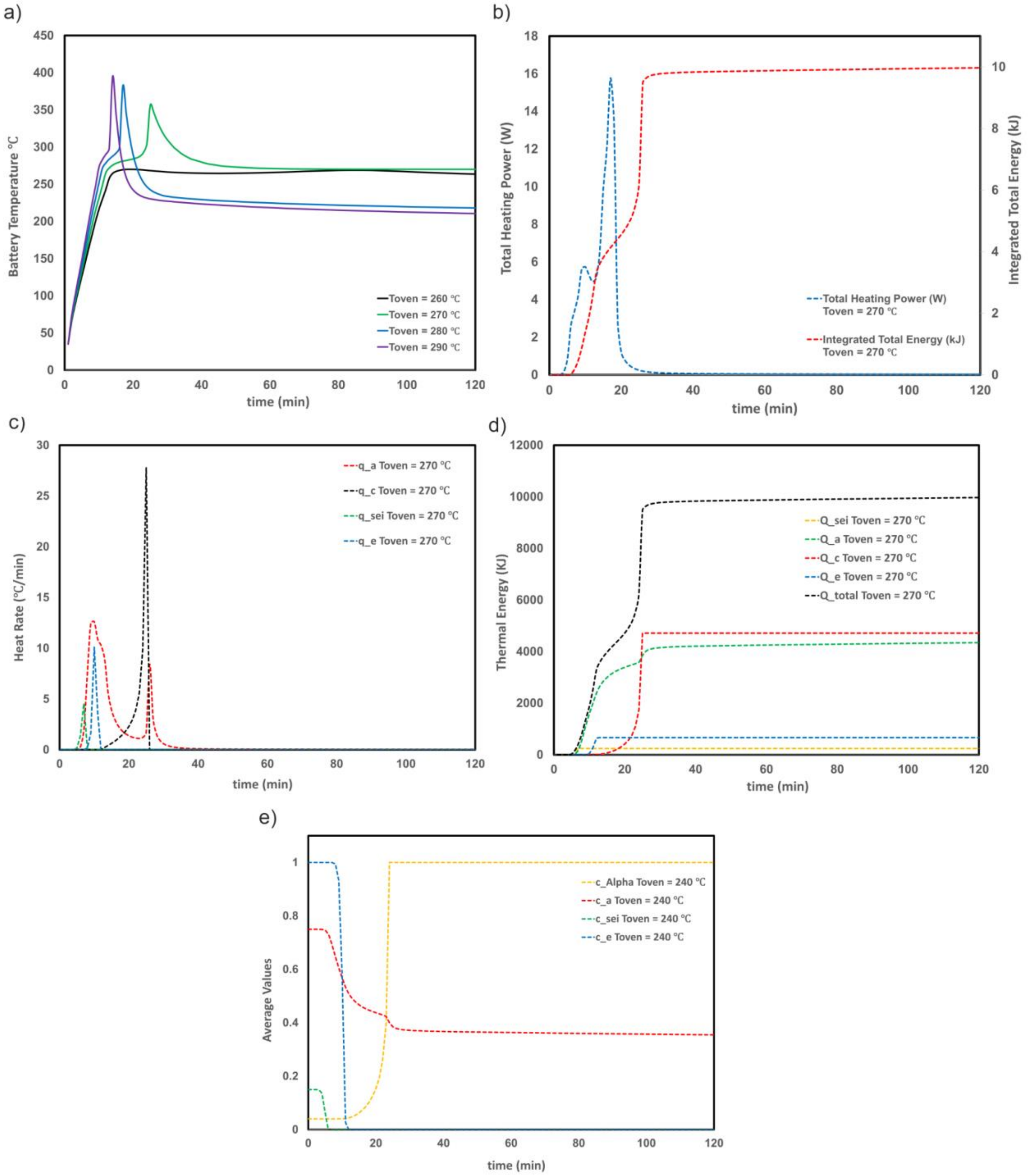

**Fig. 7.** Kim et al. kinetic mechanisms for $LiNi_{0.8}Co_{0.15}Al_{0.05}O_2$ battery. A) Maximum temperature for Oven_T 260-290 B) Total heating power and integrated total energy for Oven_T 270 C) Heating rate for Oven_T 270 D) Integrated heat source for Oven_T 270 E) Average values and temperature for Oven_T 270

Furthermore, the results of Ren et al. kinetic mechanisms for NMC 111 cathode battery chemistry are illustrated in Fig. 8. The simulation result is performed in the oven temperatures of 150 ℃ and the maximum battery temperature can reach to almost 950 ℃ which is exceptionally higher than other cell chemistries. This is attributed to the fact that NCM 111 cathode chemistry is more reactive than other chemistries and undergoes a more dramatic TR process. The results of total heating power, integrated total energy, integrated heat source and Average values are presented in Fig. 8.

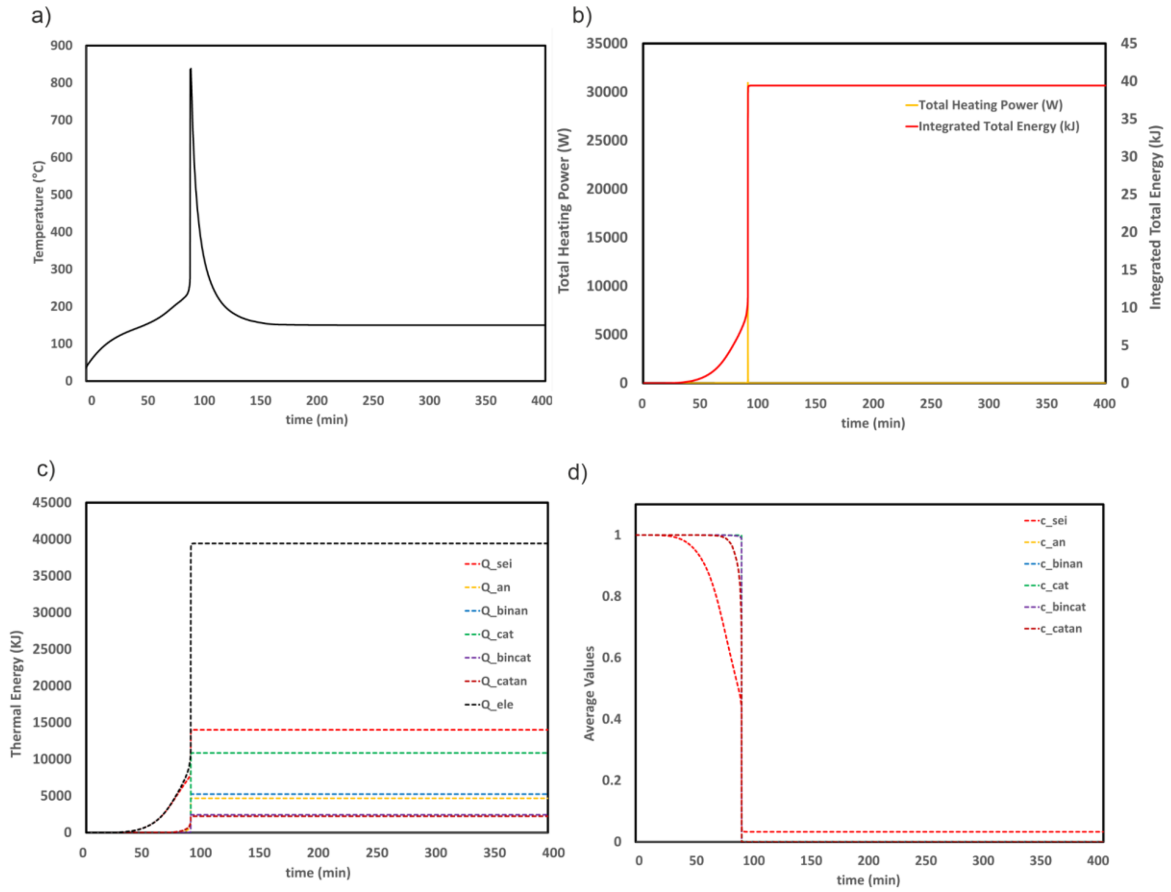

**Fig. 8.** Ren et al. kinetic mechanisms for NMC 111 battery. A) Maximum temperature for Oven_T 150 B) Total heating power and integrated total energy for Oven_T 150 C) Integrated heat source for Oven_T 150 D) Average values and temperature for Oven_T 150

In order to evaluate different mechanism and cell chemisteries, Fig. 9. compares emperature evolution of battery cells during thermal runway for different mechanism and cell chemistries. Maximum and minimum temperature have been presented in different times to assess the temperature evolution of battery cells. Furthermore, Table 6 compares maximum cell temperature during thermal runaway along with corresponding oven temperature, which shows the severity of TR event in different cases.

**Table 6**. Comparison of maximum cell temperature during thermal runaway along with corresponding oven temperature

| Mechanism | Chemistry | Maximum cell temperature during TR process | Corresponding oven temperature |
|---|---|---|---|
| Kim et al. Mechanism | $LiCoO_2$ | 237.43 | 160 |
| | $Li_{1.1}(Ni_{1/3}Co_{1/3}Mn_{1/3})_{0.9}O_2$ | 367.05 | 175 |
| | $LiFePO_4$ | 254.29 | 220 |
| | $LiNi_{0.8}Co_{0.15}Al_{0.05}O_2$ | 356.65 | 270 |
| Ren et al. Mechanism | NMC 111 | 836.56 | 150 |

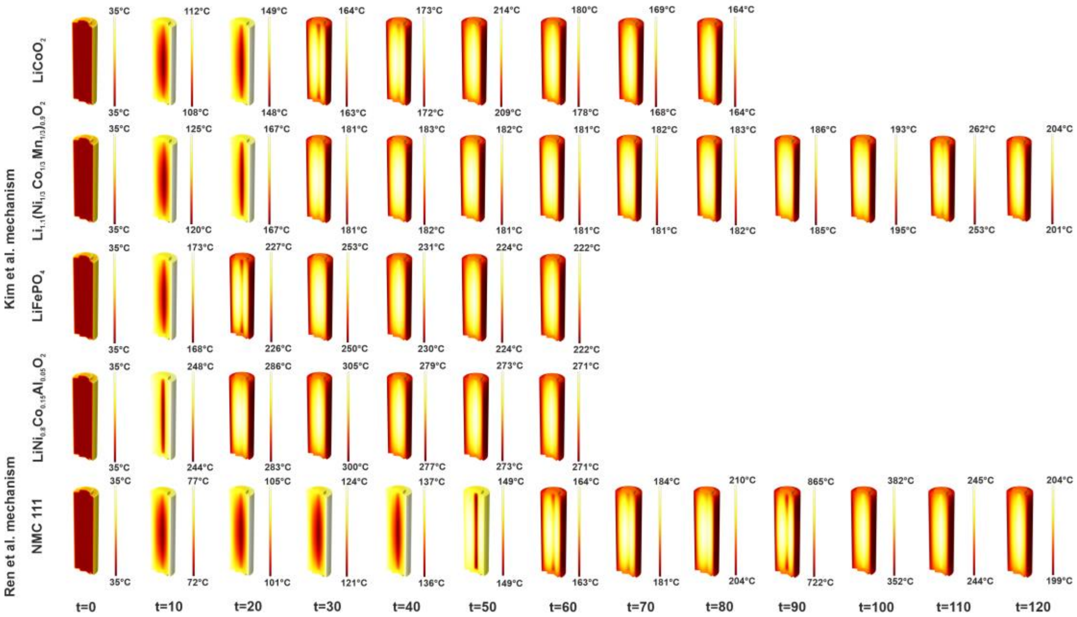

**Fig. 9.** Temperature evolution comparison of battery cells during thermal runway for different mechanism and cell chemistries

## Conclusions

A comprehensive analysis of various TR kinetic mechanisms and various cathode materials is performed using a detailed thermal model of Li-ion cell. this study evaluated two well-stablished mechanisms proposed by Kim et al. and Ren et al. and compared cell maximum temperatures, total heating power and integrated total energy, heating rates, Integrated heat sources and average species during the TR event. The results indicated that the Ren et al. mechanism offered a better understanding of TR process by addressing more comprehensive TR kinetic reactions. Furthermore, different battery chemistries exhibited distinct thermal behavior. Results indicated a significant peak temperature in NMC batteries, while TR phenomena are less severe in $LiCoO_2$, $Li_{1.1}(Ni_{1/3}\ Co_{1/3}\ Mn_{1/3})_{0.9}O_2$, $LiFePO_4$ and $LiNi_{0.8}Co_{0.15}Al_{0.05}O_2$ cell chemistries accordingly. This is attributed to the difference between the heat of reactions for different cathode materials. The developed 3D model provided good accuracy and reliability in simulation of TR process. These findings suggest further exploration into integrating kinetic mechanisms into battery modelling under critical operation conditions focusing on the temperature dynamic of cell components. It is noted that the core temperature of the cells significantly influences the prediction of the TR process.

## References

[1] X. Feng, M. Ouyang, X. Liu, L. Lu, Y. Xia, and X. He, “Thermal runaway mechanism of lithium ion battery for electric vehicles: A review,” *Energy Storage Materials*, vol. 10, pp. 246–267, Jan. 2018, doi: 10.1016/j.ensm.2017.05.013.

[2] Y. Wang, X. Feng, W. Huang, X. He, L. Wang, and M. Ouyang, “Challenges and Opportunities to Mitigate the Catastrophic Thermal Runaway of High-Energy Batteries,” *Advanced Energy Materials*, vol. 13, no. 15, p. 2203841, 2023, doi: 10.1002/aenm.202203841.

[3] T. Katrašnik, I. Mele, and K. Zelič, “Multi-scale modelling of Lithium-ion batteries: From transport phenomena to the outbreak of thermal runaway,” *Energy Conversion and Management*, vol. 236, p. 114036, May 2021, doi: 10.1016/j.enconman.2021.114036.

[4] A. García, J. Monsalve-Serrano, R. Lago Sari, and Á. Fogué Robles, “Numerical analysis of kinetic mechanisms for battery thermal runaway prediction in lithium-ion batteries,” *International Journal of Engine Research*, vol. 23, no. 10, pp. 1691–1707, Oct. 2022, doi: 10.1177/14680874211029902.

[5] A. García, J. Monsalve-Serrano, R. L. Sari, and S. Martínez-Boggio, “Thermal runaway evaluation and thermal performance enhancement of a lithium-ion battery coupling cooling system and battery sub-models,” *Applied Thermal Engineering*, vol. 202, p. 117884, Feb. 2022, doi: 10.1016/j.applthermaleng.2021.117884.

[6] D. Kong, G. Wang, P. Ping, and J. Wen, “Numerical investigation of thermal runaway behavior of lithium-ion batteries with different battery materials and heating conditions,” *Applied Thermal Engineering*, vol. 189, p. 116661, May 2021, doi: 10.1016/j.applthermaleng.2021.116661.

[7] Q. Wang, J. Sun, X. Yao, and C. Chen, “Micro calorimeter study on the thermal stability of lithium-ion battery electrolytes,” *Journal of Loss Prevention in the Process Industries*, vol. 19, no. 6, pp. 561–569, Nov. 2006, doi: 10.1016/j.jlp.2006.02.002.

[8] P. Peng and F. Jiang, “Thermal safety of lithium-ion batteries with various cathode materials: A numerical study,” *International Journal of Heat and Mass Transfer*, vol. 103, pp. 1008–1016, Dec. 2016, doi: 10.1016/j.ijheatmasstransfer.2016.07.088.

[9] G.-H. Kim, A. Pesaran, and R. Spotnitz, “A three-dimensional thermal abuse model for lithium-ion cells,” *Journal of Power Sources*, vol. 170, no. 2, pp. 476–489, Jul. 2007, doi: 10.1016/j.jpowsour.2007.04.018.

[10] G. M. da Silva, T. J. Lima, D. D. da Silva, and I. B. Henriques, “Assessment of Thermal Runaway propagation in lithium-ion battery modules with different separator materials,” *International Journal of Thermal Sciences*, vol. 197, p. 108836, Mar. 2024, doi: 10.1016/j.ijthermalsci.2023.108836.

[11] T. D. Hatchard, D. D. MacNeil, A. Basu, and J. R. Dahn, “Thermal Model of Cylindrical and Prismatic Lithium-Ion Cells,” *J. Electrochem. Soc.*, vol. 148, no. 7, p. A755, Jun. 2001, doi: 10.1149/1.1377592.

[12] M. N. Richard and J. R. Dahn, “Accelerating rate calorimetry study on the thermal stability of lithium intercalated graphite in electrolyte. II. Modeling the results and predicting differential scanning calorimeter curves,” *Journal of The Electrochemical Society*, vol. 146, no. 6, p. 2078, 1999.

[13] D. Ren *et al.*, “Model-based thermal runaway prediction of lithium-ion batteries from kinetics analysis of cell components,” *Applied Energy*, vol. 228, pp. 633–644, Oct. 2018, doi: 10.1016/j.apenergy.2018.06.126.

# Experiments and Simulations on Internal Temperature Monitoring for Batteries Subjected to Significant AC Current Ripples through Impedance Analysis

J. Salvador[1]

[1]TAE Power Solutions. 1 Vanderbilt, Irvine, CA 92618, USA.

E-mail: jsalvador@tae.com
Telephone: +1 949 830-2117

**Abstract.** The widespread adoption of batteries in many applications goes hand in hand with the need to ensure safe and efficient battery system operation through proper thermal management. Battery behavior is strongly influenced by internal temperature, which can significantly differ from surface temperatures. In this study, battery impedance analysis was investigated as a non-invasive technique to estimate the average jelly roll temperature. The conditions under study were representative of a modular multilevel power conversion system that supplies single-phase AC at the battery module level, inducing high-amplitude AC current ripples in the battery. In a lab experiment, the voltage response was measured on a battery module undergoing significant AC current ripples at controlled temperatures. Then, the voltage and current ripples were analyzed to determine the battery impedance for the different operating points. Subsequently, impedance was correlated with temperature to populate temperature look-up tables as a function of the impedance modulus and the ripple frequency, which exhibited an uncertainty of less than 1°C. An applicability study was performed in a virtual environment, combining a validated electrochemical model coupled with a thermal model to simulate a mobile power supply use case. The battery temperature monitoring capability using impedance analysis was demonstrated, achieving a mean tolerance of 0.46°C with respect to the average internal temperature. Detailed data analysis showed that reliable temperature estimation required high-accuracy current and voltage ripple measurements, preferably using frequencies under 300 Hz.

## Notation

| | |
|---|---|
| *AC* | *Alternating Current.* |
| *BMS* | *Battery Management System.* |
| *Cp* | *Specific Heat Capacity.* |
| *DC* | *Direct Current.* |
| *DCIR* | *Direct Current Internal Resistance.* |
| *EIS* | *Electrochemical Impedance Spectroscopy.* |
| *HPPC* | *Hybrid Pulse Power Characterization.* |
| *Im* | *Imaginary part of a complex number.* |
| *Re* | *Real part of a complex number.* |
| *SoC* | *State-of-Charge.* |
| *SoH* | *State-of-Health.* |
| *T* | *Temperature.* |
| *Z* | *Impedance.* |

## 1. Introduction

For years, technical and cost improvements in lithium-ion battery technology have driven the development of battery solutions to satisfy societal needs [1]. For example, in the mobility space, battery technologies are being adopted to mitigate pollutant concentrations in densely populated areas [2]. In stationary markets, the growth in both residential and large-scale renewable energy generation has created a demand for battery energy buffers due to the intermittent nature of renewable energy production [3]. Furthermore, battery systems are essential in backup power supply and in portable devices.

Battery packs incorporate thermal management systems to ensure proper heat dissipation and to maintain an adequate battery performance [4,5]. For control purposes, thermal management systems require temperature input that can be collected using different sensors [6]. Besides, several metrics for battery temperature can be identified. Cell surface temperature is the most straightforward metric. Although surface temperatures are the easiest to measure, they can significantly differ from internal temperatures that are more representative of battery operating conditions [7]. For example, Anthony et al. measured a temperature difference of 10ºC between the can and the core of a cylindrical 26650 cell during a 10C discharge using an embedded thermocouple [8]. Regarding internal temperatures, the crucial metric for safety applications is the cell's maximum temperature. However, it can be challenging to determine its location and to measure it [9]. Moreover, internal temperatures can be far from uniform. Significant thermal gradients can be found within a cell or among the cells in a battery module [10]. Thermal gradients have been linked to faster degradation and state imbalances [11,12]. Furthermore, it is more complicated to obtain a temperature metric that is representative of the average state of the battery using localized measurements if the temperature distribution is uneven. Noticing the strong interdependence between battery temperature and performance, researchers have proposed battery response analysis as a technique for monitoring temperature [13,14]. Analyzing the battery electrical response provides metrics that are related to the average internal state of the battery and the average state across all cells in a system. It has been proposed that the temperature derived from analyzing the battery response represents the average temperature of the jelly roll [15]. Therefore, the average temperature is the most suitable temperature to study battery performance and battery health, and it is also relevant for safety. The battery electrical response can be analyzed by measuring AC impedance or DC resistance [16]. Both methods are non-invasive. In this study, the impedance technique was chosen because the resulting datasets are richer as they contain information associated with excitation frequencies.

Impedance analysis is used as a method to gain insight into battery internal states. Advantageously, battery impedance can be calculated by analyzing current and voltage ripples while the battery is in operation [17]. The prime example of impedance analysis methods for in-lab testing is EIS. Galvanostatic EIS uses small current excitations -typically, sinusoidal signals- to generate low-amplitude voltage ripples. Extrapolating EIS impedance to higher excitation amplitudes is a very complex problem [18]. Kim et al. used a custom-made system to superimpose 0.1C sinusoidal current ripples to a 1C DC current offset capable of charging and discharging a battery cell [19]. They were able to obtain impedance traces for different frequencies in full charge and discharge tests, and they were also able to find a linear correlation between impedance and SoH. Despite SoH estimation being the most remarkable research focus, many research groups have applied impedance analysis to internal temperature estimation as well, studying different impedance parameters, frequency ranges, cell chemistries, and estimator types [6,16]. The studies performed on systems of multiple cells are of particular interest. Beelen et al. performed EIS-based temperature estimation on two cells simultaneously and studied the crosstalk interferences [20], while Ströbel et al. applied the technique to a 6-cell series-parallel system [21]. In both works, impedance was measured on each cell. Most studies used dedicated excitation devices to generate current ripples in the batteries. In contrast, Amamra et at., analyzed low-amplitude current ripples inherently induced by motor and inverter operation [22]. Howey et al. generated a 0.07C excitation current with a motor controller and measured impedance on a series array of 4 cells [23].

With regards to the development of novel battery systems, modular multilevel power conversion architectures have been proposed as a concept to improve efficiency and battery life [24,25]. Modular multilevel power conversion systems can supply AC at the battery module level, enabling more precise SoC balancing among the modules which could lead to higher energy utilization, more uniform aging and therefore the extension of the overall system life, no longer limited by the most degraded module [26]. A property of distributed power conversion systems is that generating single-phase AC at the module level induces high-amplitude current ripples in the battery. The induced ripples are an integral part of the current and are able to charge and discharge the battery. In these systems, no dedicated device is needed to produce the current ripples, since they are inherent to battery operation.

Based on the surveyed literature, it can be concluded that jelly roll temperature estimation using impedance measurements has been extensively explored for battery cells, but not for battery modules. Moreover, previous studies have generally focused on artificially generated current ripples that require dedicated excitation devices, or non-purposedly induced ripples that have low amplitude. The goal of this study is to assess the applicability of impedance-based temperature estimation to battery modules when significant AC current ripples are induced due to the module being part of a distributed power conversion system. This technique has the potential to reduce the number of sensors and to simplify temperature monitoring by taking advantage of the intrinsic properties of the system architecture. This paper is organized as follows. First, the experimental, analytical, and modeling methods used to obtain the measurements, processed data, and models are described. Then, the procedure for obtaining a temperature look-up table as a function of impedance and frequency is explained. A coupled battery electrochemical and thermal model formed the virtual environment in which the temperature monitoring approach was evaluated, allowing to compare the battery simulated internal temperature to the estimated temperature. Finally, the final case study is presented, and the simulation results are discussed to demonstrate the feasibility of using the temperature monitoring technique in a relevant application.

## 2. Methods

### 2.1 Impedance data collection

**Table 1**. Battery module specifications

| | |
|---|---|
| Cell configuration | 12s1p |
| Nominal capacity | 51 Ah |
| Nominal energy | 2.2 kWh |
| Nominal voltage | 43.8 V |
| Cycle life (1C/1C to 80% SoH) | 1500 cycles |

**Fig. 1.** Battery module and battery cell under study

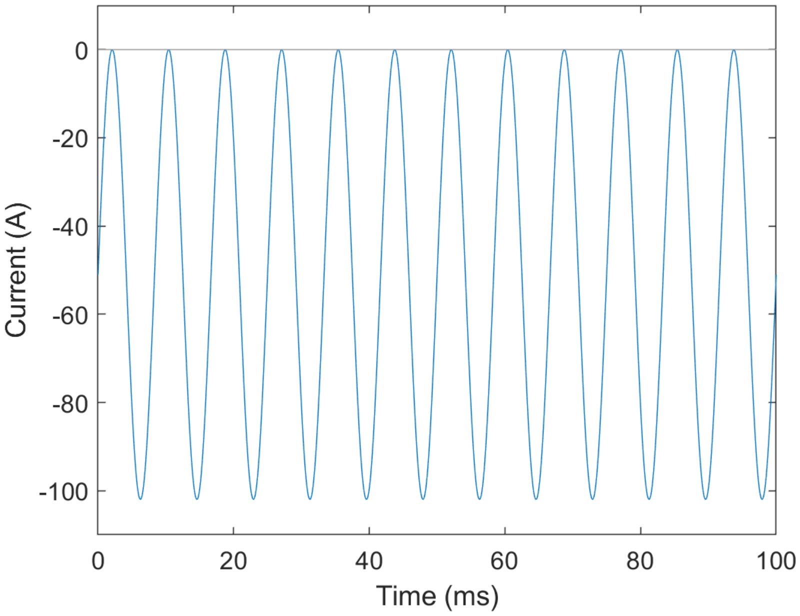

**Fig. 2.** Waveform for an 1C sinusoidal discharge current with an 1C offset

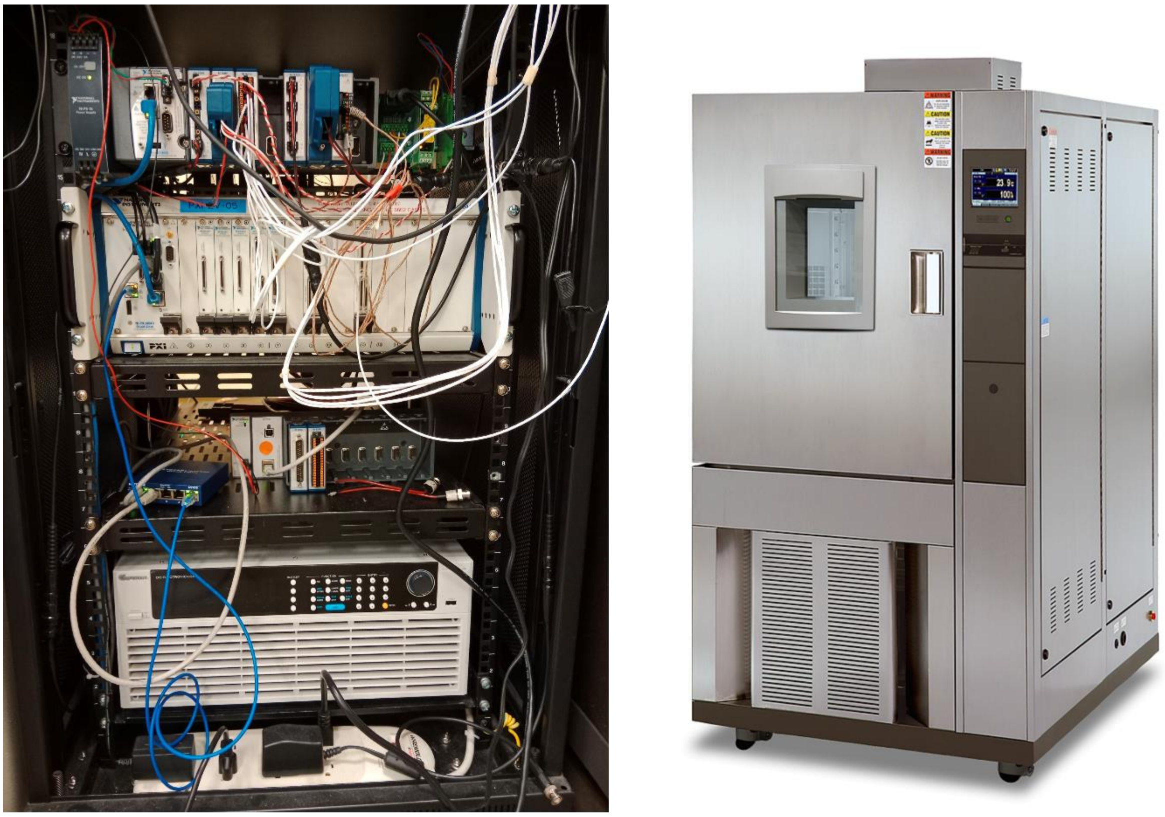

**Fig. 3.** Left: test equipment. Right: thermal chamber

The battery module under study was manufactured by Elring Klinger. The module specifications can be seen in Table 1. The module contains 12 Lishen LP2714897-51Ah cells connected in series. The cells are prismatic and have a Lithium/NMC111 cathode and a graphite anode. Pictures of a module and a cell are shown in Fig. 1.

An experimental setup was prepared to collect impedance data from the battery module. The goal was to investigate different conditions, including C-rates that were capable of realistically discharging the battery, various temperatures, and excitation frequencies. As mentioned in the introduction, extrapolating impedance spectra measured through EIS to conditions involving significant currents is problematic, with the additional challenge that the device under test was a battery module, but EIS tests are usually performed on cells. For these reasons, the chosen approach for this study was to run dedicated lab tests for relevant operating conditions, applying significant sinusoidal currents and measuring the induced voltage ripples. The ripples were then analyzed to determine the impedance for each operating point. To discharge the battery, the sinusoidal currents had an offset as in the example shown in Fig. 2. This waveform is representative of currents in a distributed power conversion system. Running the tests directly on the module meant that the contribution of bus bars and weld points to the measured impedance was considered.

The sinusoidal discharge currents with an offset were generated using a custom test setup shown in Fig.3 (left). The battery module was connected to a Chroma 63206A electronic load. The load was set to follow the waveform provided via an analog input port. An NI-9269 analog output module generated the physical sinusoidal voltage signal with an offset which had the desired waveform for the current. The system was controlled through a custom LabView application running on an NI PXI-8840 Quad Core controller. An NI-9149 Ethernet cRIO expansion chassis held the control modules, including the aforementioned NI-9269, an NI-9223 for reading current and voltage, and an NI-9210 for the thermocouple input. The tests were performed in a controlled temperature environment inside an ESPEC EPL-2H thermal chamber (Fig.3, right).

**Table 2**. Test matrix for impedance characterization

| | |
|---|---|
| Frequency (Hz) | 120, 300, 600, 800, 1000 |
| Temperature (ºC) | 0, 25, 40 |
| C-rate ($h^{-1}$) | 0.5, 1 |
| Repetitions | 2+ |

The full factorial experiment comprised 5 different frequencies, 3 different temperatures and 2 different C-rates. In total, 30 operating points were tested, and at least 2 repetitions for each point were measured. The test matrix is shown in Table 2. All measurements were made at a similar SoC in the 76 to 79% range. Each test ran for 2 seconds which was long enough to stabilize the electrical response but not too long to significantly reduce the SoC or increase temperature. The data acquisition rate was 35 kHz, which provided sufficient resolution for the highest signal frequency of 1 kHz. The lowest point in the frequency range was 120 Hz, which is twice the power grid frequency in many parts of the world. In stationary applications, a single-phase power converter operating close to a battery module in a distributed power conversion system will induce 120 Hz AC ripples in the battery. With regards to temperature, it was necessary to ensure thermal stability and uniformity during the tests. The battery module was put in the thermal chamber and then soaked at the temperature under study for three hours before the tests. The module then remained in the chamber during the tests. The short duration of the tests and the 30 minute or longer rest between test runs assured that the battery temperature was equal to the setting for each test. This was verified by a thermocouple attached to the bottom of the module, in contact with one central cell.

After collecting the measurements, the electrical response data was processed to calculate the battery impedance. The impedance was defined according to Eq. 1 [18]:

$$Z(j\omega) = \frac{\Delta V(j\omega)}{\Delta I(j\omega)} = \frac{\hat{V} \cdot e^{j\varphi_V}}{\hat{I} \cdot e^{j\varphi_I}} = |Z| \cdot e^{j\varphi_Z} = Re(Z) + j \cdot Im(Z) \qquad \textbf{(Eq. 1)}$$

where Z is impedance, ΔI is current excitation, ΔV is voltage response, ^ denotes amplitude, φ denotes phase, and | . | denotes modulus. The current and voltage data was split in portions of 10 cycles. Then, each portion was fitted to a sinusoidal curve using the sineFit function for MATLAB developed by Peter Seibold [27]. The function determined the amplitude, frequency and phase corresponding to the largest peak of the fast Fourier transform. Subsequently, the impedance modulus, phase delay, real and imaginary parts were calculated for each data portion using Eq. 1.

## 2.2 Coupled electrochemical and thermal modeling

As discussed in the introduction, measuring battery temperature is a complex problem. In this investigation, the temperature of interest was a representative temperature for the average electrical performance of all battery cells in a module. Simulation is a means to access internal temperature data while facilitating the exploration of multiple operating conditions. For this reason, the applicability study was performed in a virtual environment. AVL Cruise™ M was used as multiphysics simulation platform [28].

A Doyle-Fuller-Newman model was parametrized to simulate the battery cell electrochemistry [29,30]. A validation against experimental data, with special focus on the most relevant ripple characteristics, was conducted and is discussed in section 3.2.2. Regarding the thermal submodel, it was based on the heat balance equation with contributions from thermal inertia, thermal conduction, ohmic heat produced by ion transport [31], irreversible heat caused by interface currents [32], and reversible heat due to reaction entropy change during intercalation [32]. Cell thermal properties were defined in the model. The specific heat capacity was determined using a method known as thermal relaxation or cooling transient [33,34] at different environment temperatures. Fig. 4 (left) shows the cell temperature curves for the case in which the chamber temperature was 5ºC. A model using a constant, temperature-independent specific heat capacity value achieved a good agreement with all temperature relaxation curves. Thermal conductivity was estimated using the guarded heater method [33,35] in two different directions to consider the jelly roll anisotropy [34,36] and it was approximated by a linear fit as a function of temperature. In Fig. 4, (right) the collected data points and the resulting linear fits can be seen. To calculate the battery internal temperature evolution, a simple thermal model was coupled to the electrochemical model following the lumped parameter paradigm [37,38]. The thermal model consisted in a heat convection element connected to a temperature boundary representing the changing environmental temperature.

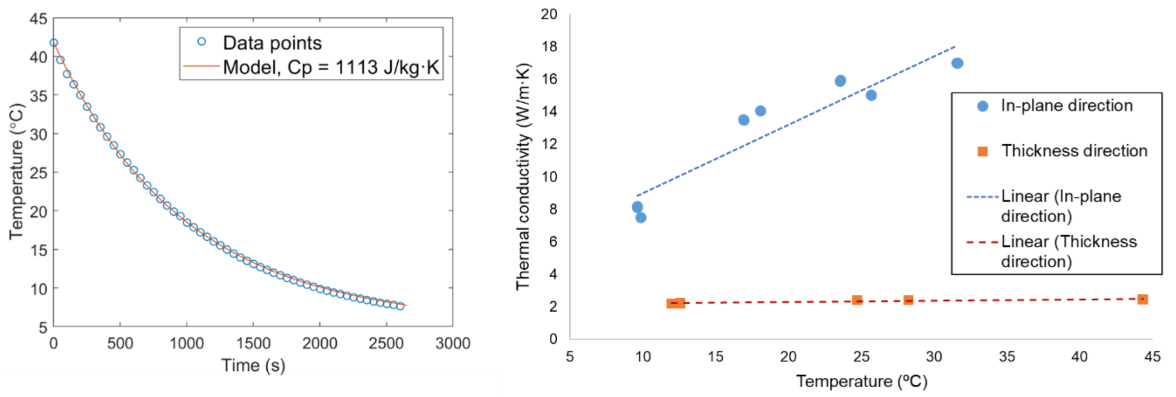

**Fig. 4.** Left: measured vs modeled temperature using the specific heat capacity of the cell. Right: cell thermal conductivity against temperature

# 3. Results

## 3.1 Correlation between temperature and impedance

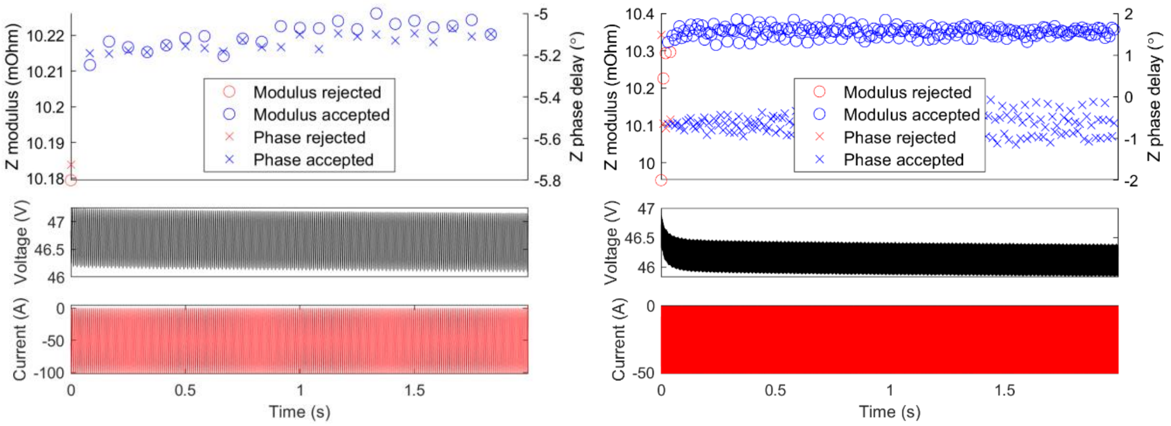

**Fig. 5.** Impedance calculation through current and voltage signal processing. Left: 120 Hz, 24ºC, 1C. Right: 1000 Hz, 0ºC, C/2

Fig. 5 shows the impedance calculation results for two operating points. As mentioned in Section 2.1, one impedance value was calculated for each 10-cycle segment in each test. The transient duration was short, and the impedance characteristics quickly stabilized. A point was considered an outlier if it deviated more than three scaled median absolute deviations from the mean, and it was removed. If the modulus was an outlier, the corresponding phase delay was also removed and vice versa. Outliers were concentrated in the initial transient phase. For the case in Fig. 5, right, the impedance stabilized after 41 ms. The slowest stabilization was 167 ms, observed in the 120 Hz, 0ºC cases. The mean value and the standard deviation of the remaining points were stored for the next steps.

Fig. 6 shows the Bode plot with all the test points measured in the experiment. Each marker represents the mean value while the associated error bar is the standard deviation over each 2-second test. The standard deviations are low, indicating that 2 seconds was long enough to stabilize the impedance measurement. The impedance points are shown in the Nyquist plot in Fig. 7, for the frequency range under study. Typical trends of increasing real and imaginary components as temperature decreases can be observed.

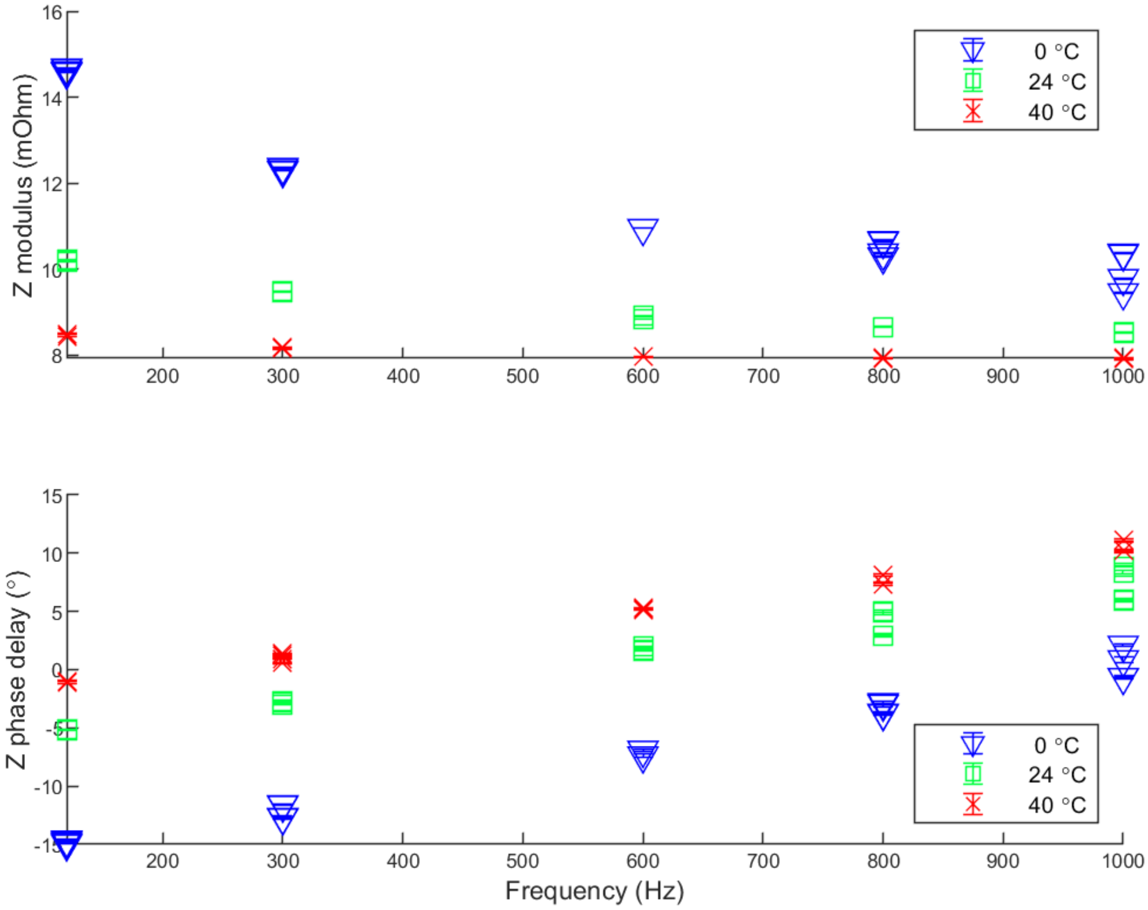

**Fig. 6.** Bode plot for module impedance at different temperatures

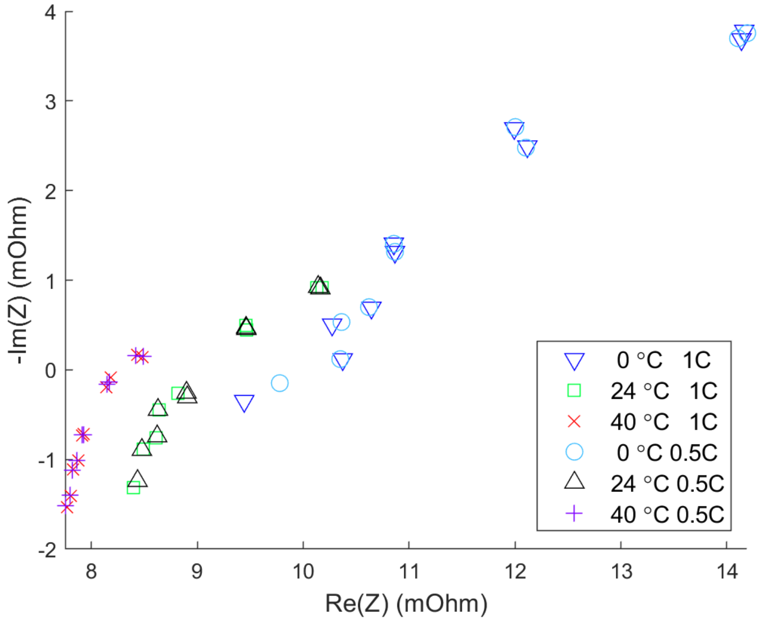

**Fig. 7.** Nyquist plot for module impedance at different temperatures and C-rates

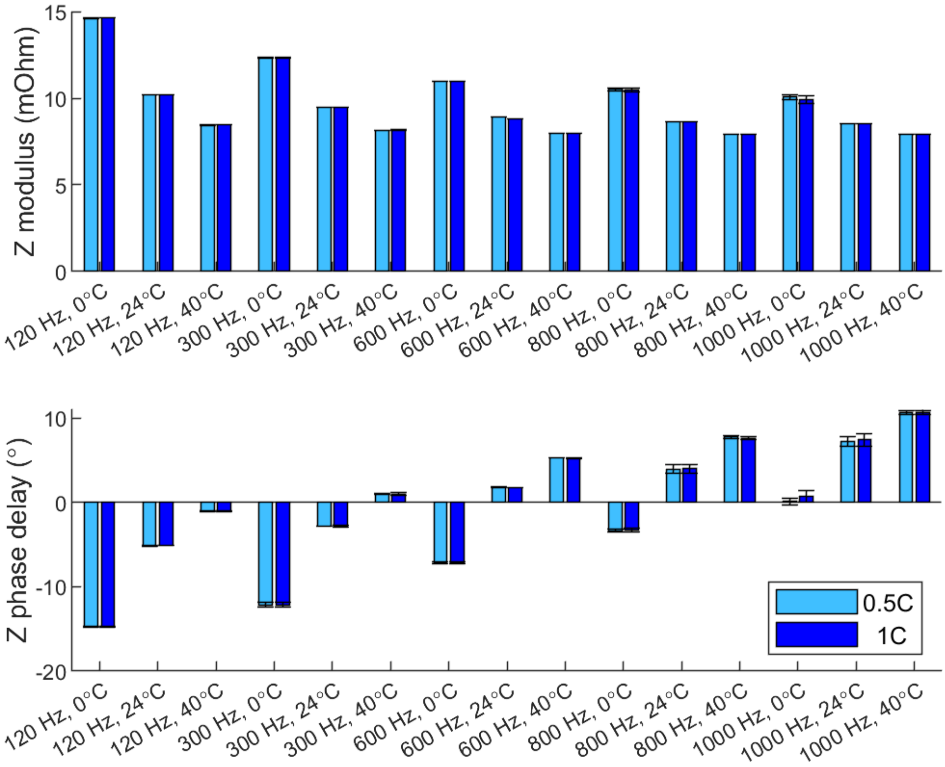

**Fig. 8.** Module impedance for every operating condition under study

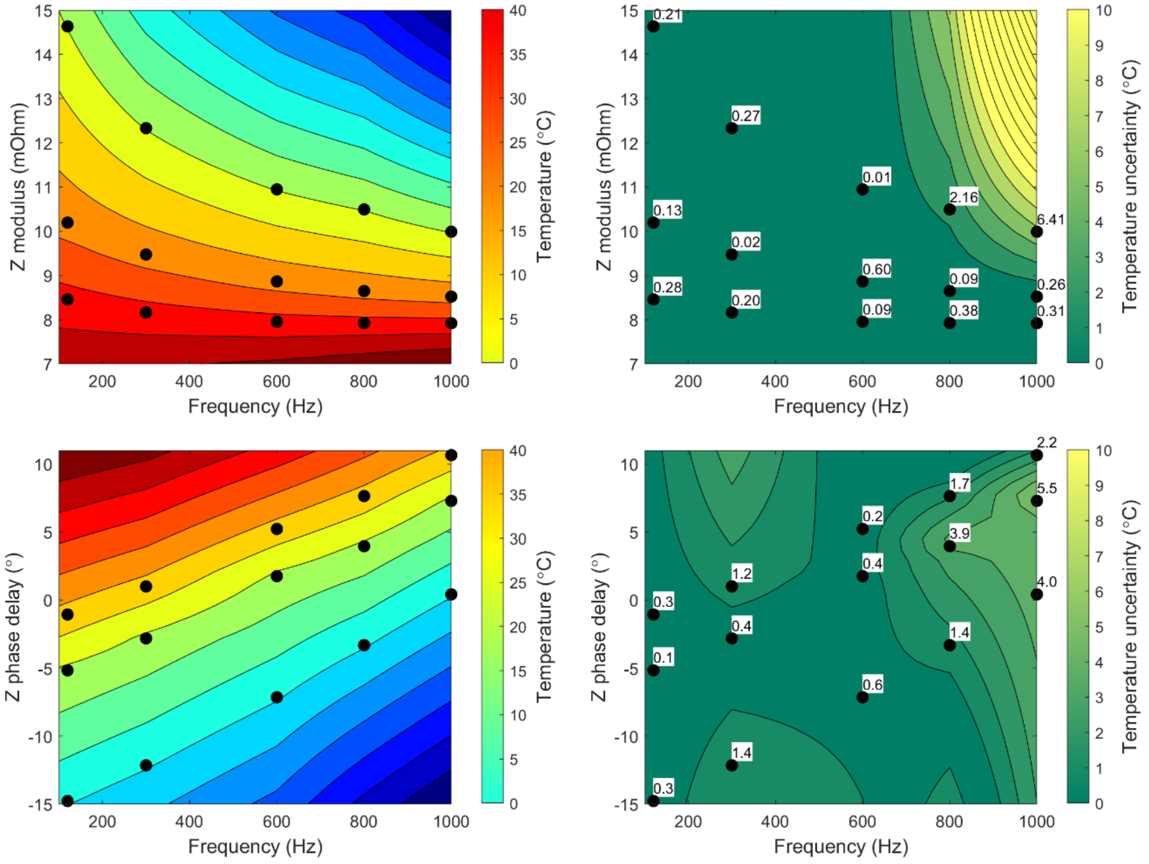

**Fig. 9.** Top left: temperature contours as a function of impedance modulus and frequency. Bottom left: temperature contours as a function of impedance phase delay and frequency. Right: corresponding temperature uncertainty contours

An examination of the Nyquist plot in Fig. 7 and the bar plot in Fig. 8 revealed the weak influence of C-rate on measured impedance in contrast to the significant influence of temperature and frequency. Moreover, it can be seen, especially in the Bode plot in Fig. 6, that the temperature influence on impedance was sensitive to frequency. Therefore, it was concluded that the data set was appropriate for populating a temperature look-up table as a function of frequency and impedance.

In the next step, the data points for a given temperature and frequency were grouped together disregarding the C-rate. Then, the mean and the standard deviation of the impedance for a given temperature and frequency combination were calculated using the data points in each group. Finally, the data was rearranged though linear interpolation within the range of measured impedance values to populate the temperature look-up tables. The two plots on the left side of Fig. 9 show the temperature contours resulting from the look-up tables that were a function of the impedance modulus (top) and the impedance phase delay (bottom) as well as the frequency. The original operating points were plotted as black dots. Regarding the right side of Fig. 9, the standard deviation for each operating point allowed to calculate the temperature uncertainty associated with the impedance variation across the data points (at least 4) that were grouped for each temperature and frequency combination. Eqs. 2 and 3 were used to calculate the temperature uncertainty:

$$\Delta T_{|Z|} = |\bar{T}(|Z| + 0.5 \cdot \sigma_{|Z|}, \nu) - \bar{T}(|Z| - 0.5 \cdot \sigma_{|Z|}, \nu)| \qquad \textbf{(Eq. 2)}$$

$$\Delta T_{\varphi_Z} = |\bar{T}(\varphi_Z + 0.5 \cdot \sigma_{\varphi_Z}, \nu) - \bar{T}(\varphi_Z - 0.5 \cdot \sigma_{\varphi_Z}, \nu)| \qquad \textbf{(Eq. 3)}$$

where ΔT is the temperature difference used as temperature uncertainty, T are the temperatures extracted from the look-up tables as a function of impedance and frequency, |Z| is impedance modulus, $\varphi_Z$ is impedance phase, v is frequency, | . | denotes absolute value, ‾ denotes mean value, and σ denotes standard deviation.

For the modulus, the temperature uncertainty was very low for every condition except the lower temperature, higher frequency combinations. Regarding the phase delay, the uncertainty was distributed in a complex manner between 0 and 6ºC. For the subsequent applicability study, it was decided to discard the impedance phase delay look-up table and to exclusively use the impedance modulus look-up table in the 100 to 600 Hz frequency range to achieve a high level of confidence. In the 100 to 600 Hz frequency range, the highest temperature uncertainty was 0.92ºC for the combination of 600 Hz and 15 mOhm, corresponding to an absolute temperature of -47ºC. The impedance modulus range for the look-up table was 7 to 15 mOhm and the covered temperature range was -47 to 57ºC temperature for 600 Hz.

To finalize the experimental data discussion, the influence of SoC on impedance was examined. In the experiment, the SoC was kept within a narrow window to exclude SoC effects. Therefore, applying the temperature look-up table to an extended discharge cycle required the assumption that a change in SoC did not have a significant effect on the impedance modulus. Evidence supporting this assumption for a specific SoC range can be seen in Fig. 10. The top plots show EIS data from the battery cell. For the temperatures and frequencies under study, SoC between 25 and 75% did not have a significant influence on impedance. Although EIS data for a battery cell cannot be directly extrapolated to a module and to higher currents, this analysis suggested that impedance was insensitive to SoC in that range. Furthermore, the bottom plot shows DCIR measurements extracted from HPPC tests on the battery module at the temperatures under study. The DCIR was evaluated 1 second after applying charge and discharge pulses with different step amplitudes between C/4 and 4C. It can be seen that the module's internal resistance remained almost constant for the range between 25 and 95% SoC.

In conclusion, for the applicability study it was decided to use the look-up table correlating temperature with impedance modulus and frequencies between 100 to 600 Hz during discharge in the 25 to 95% SoC range. However, based on strictly available data, only the impedance measured between 75 and 80% SoC provided the highest degree of confidence.

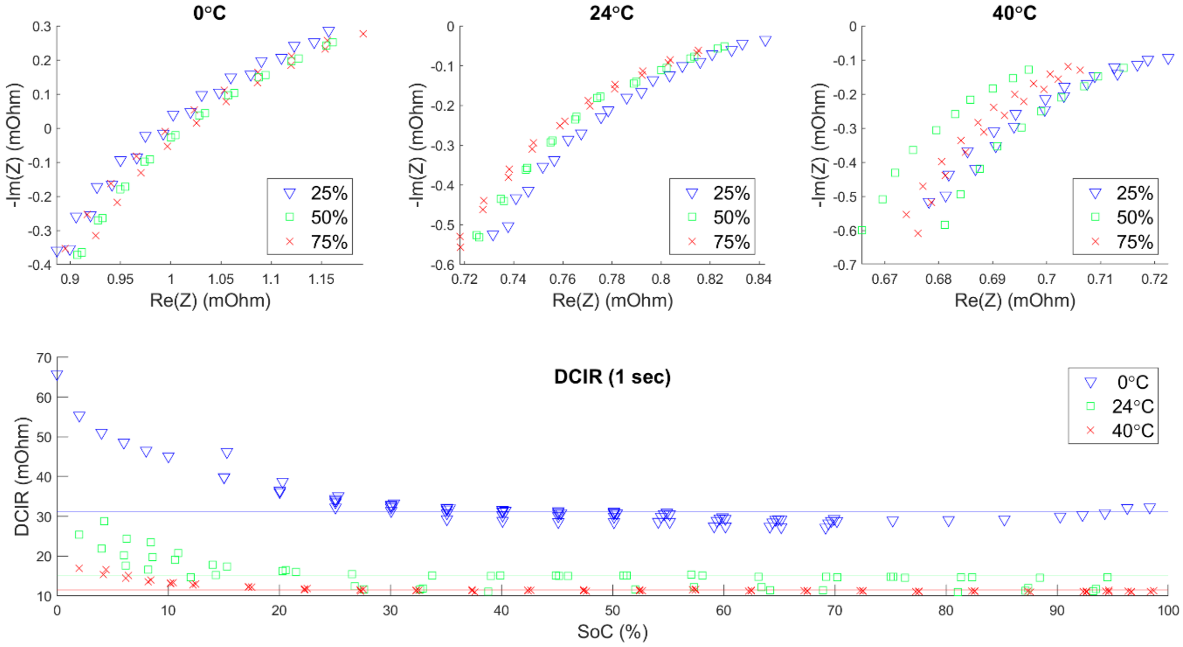

**Fig. 10.** SoC influence on impedance. Top: cell EIS impedance for different SoC and temperatures. Bottom: module DCIR against SoC for different temperatures

## 3.2 Models

### *3.2.1 Time step sensitivity study*

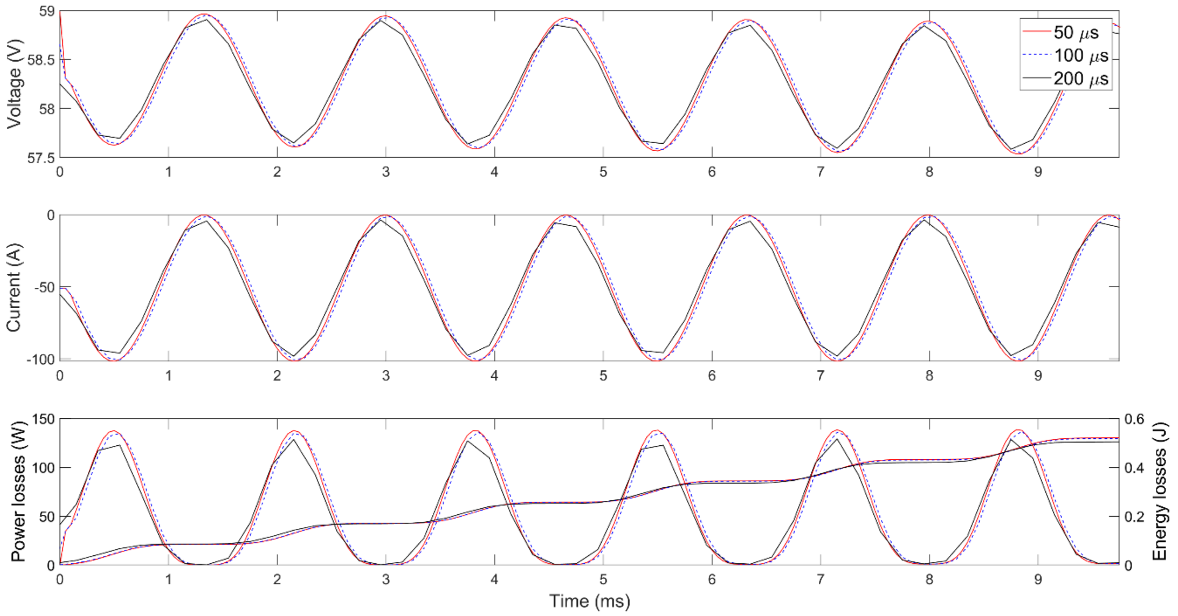

**Fig. 11.** Time step sensitivity study for the most demanding case

A sensitivity study was conducted to determine the optimal simulation time step. The most demanding condition was the combination of the highest current ripple frequency, the lowest temperature, and the highest C-rate under study, i.e., 600 Hz, 0ºC, and 1C. This combination produced the fastest voltage ripples with the largest amplitude. Fig. 11 shows voltage, current, and power losses for three different time steps. It can be seen that a 100 μs time step produced identical results to a 50 μs time step. However, if a bigger time step of 200 μs was used to simulate a 600 Hz signal, the waveform resolution was reduced, which would have led to a different impedance result. More critically, in the long term, the observed discrepancy in a cumulative amount such as energy losses would have resulted in a different temperature evolution. Consequently, a 100 μs time step was chosen for simulation.

### *3.2.2 Electrochemical model validation*

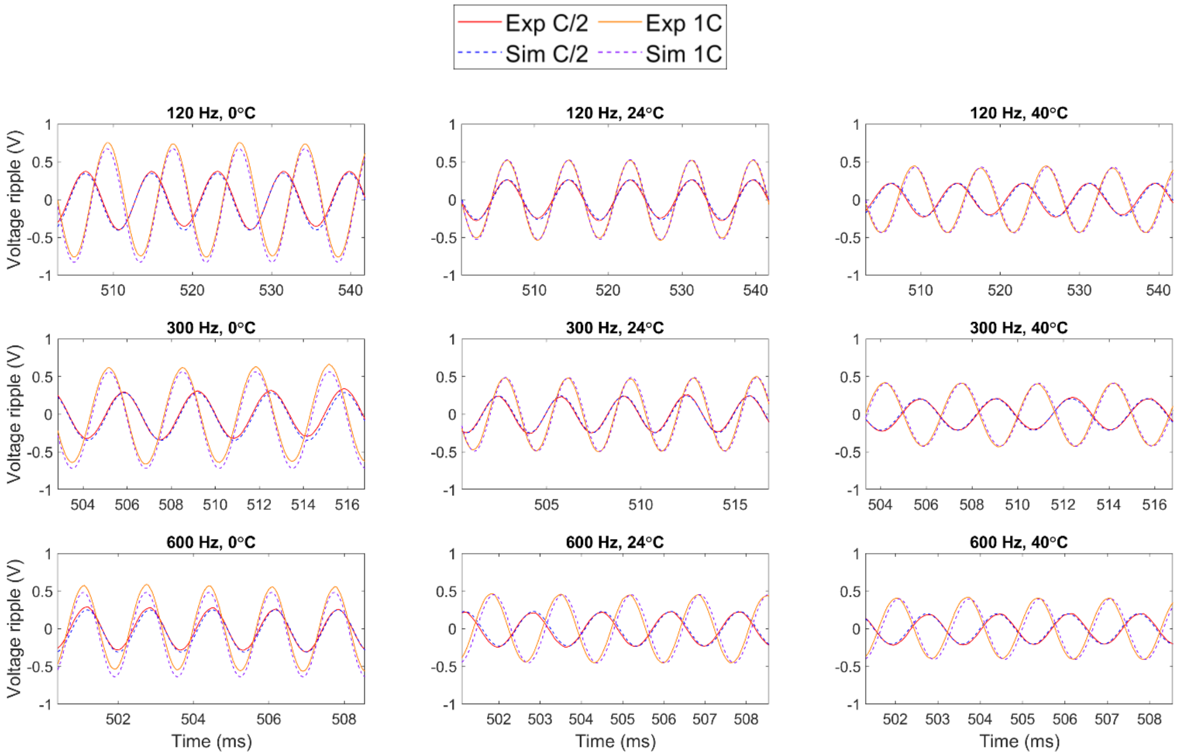

**Fig. 12.** Discharge voltage ripple validation for the operating conditions under study

**Table 3**. Modeled minus experimental voltage ripple amplitude, maximum (mV)

| Ripple amplitude difference (mV) | | Temperature (ºC) | | |
|---|---|---|---|---|
| **Frequency (Hz)** | **C-rate ($h^{-1}$)** | **0** | **24** | **40** |
| **120** | **0.5** | 2.2 | -0.6 | 1.1 |
| **120** | **1** | 0.4 | 4.6 | 0.6 |
| **300** | **0.5** | 0.4 | -0.8 | -0.6 |
| **300** | **1** | 3.1 | 3.6 | -0.7 |
| **600** | **0.5** | 0.1 | 1.2 | -0.6 |
| **600** | **1** | -1.7 | 0.8 | -1.6 |

**Table 4**. Maximum temperature difference resulting from modeled versus experimental impedance difference (ºC)

| Temperature difference (ºC) | | Temperature (ºC) | | |
|---|---|---|---|---|
| **Frequency (Hz)** | **C-rate ($h^{-1}$)** | **0** | **24** | **40** |
| **120** | **0.5** | -0.48 | 0.13 | -0.41 |
| **120** | **1** | -0.04 | -0.51 | -0.11 |
| **300** | **0.5** | -0.12 | 0.28 | 0.31 |
| **300** | **1** | -0.51 | -0.59 | 0.16 |
| **600** | **0.5** | -0.03 | -0.66 | -0.42 |
| **600** | **1** | 0.38 | -0.24 | -0.56 |

To ensure that the impedance modulus in the simulation matched the experimental measurements, a validation study based on the test cases was conducted. The impedance modulus is related to the amplitude of the current and voltage ripples. To simulate the test cases, the experimental currents were replicated and used as an input to the battery electrochemical model. Then, the resulting voltage ripple was analyzed and plotted against the measured voltage ripple. This was done for the three remaining frequencies, for the three temperatures and for the two C-rates under study. As previously mentioned, the SoC was between 76 and 79%. Fig. 12 shows the validation results. The plots show a representative time period around 500 ms after the start of the test, past the transient response. For both data sources, the ripple was calculated as the voltage minus its moving average. A good agreement between simulated and measured ripples was obtained for all operating points. The maximum amplitude differences between modeled and experimental voltages corresponding to the plots in Fig. 12 can be seen in Table 3. All differences were below 5 mV. Table 4 shows the maximum temperature differences resulting from the differences between the modeled and experimental voltage signals. The temperatures were obtained through the impedance modulus and the temperature look-up table created in Section 3.1. The errors were lower than 0.7ºC. The highest temperature difference, 0.66ºC, corresponded to the 600 Hz, 24ºC, 0.5C operating point and it was caused by a minor 1.2 mV difference. That was due to the high sensitivity of impedance to voltage variations and to the comparatively small sensitivity of impedance to temperature for 600 Hz frequency, as was seen in Fig. 9 (top left). For the 120 Hz, 24ºC, 1C operating point, the significantly higher 4.6 mV difference produced a lower 0.51ºC difference because the impedance modulus was more sensitive to temperature at 120 Hz than at 600 Hz. Accuracy concerns could compromise the adoption of impedance-based temperature monitoring, as real-world sensors can have issues such as limited accuracy, significant noise-to-signal ratios, or sensor drift.

A full discharge test using sinusoidal currents with an offset was simulated to validate the model performance in a longer time frame. The current had a frequency of 120 Hz. Sine amplitude was 1C and offset was 1C. During the test, the module was kept at 24ºC in the thermal chamber. In Fig. 13, it can be seen that the temperature oscillated less than 1ºC during the test. Regarding the voltage, the figure shows good agreement between the experimental and the simulated curves. The mean error between center lines was 117 mV for the duration of the test. The voltage ripple is visible in the main plot. Closer views for 25% and 60% SoC, respectively, are provided in the bottom plots. For the simulation curve, the ripple was calculated as the voltage minus its moving average. For the experiment, the 20 Hz sampling rate did not allow to visualize every individual ripple. Instead, the voltage range within a 2-second window was plotted as a band. For both SoC, the simulated ripple amplitude matched the experimental range. Furthermore, the electrochemical model did not produce significantly different ripple amplitudes across the SoC range. The experimental measurement suggested a similar behavior. This observation supported the assumption that the temperature look-up table as a function of the impedance modulus that was created in previous sections was valid for the whole SoC range under study, 25 to 95%.

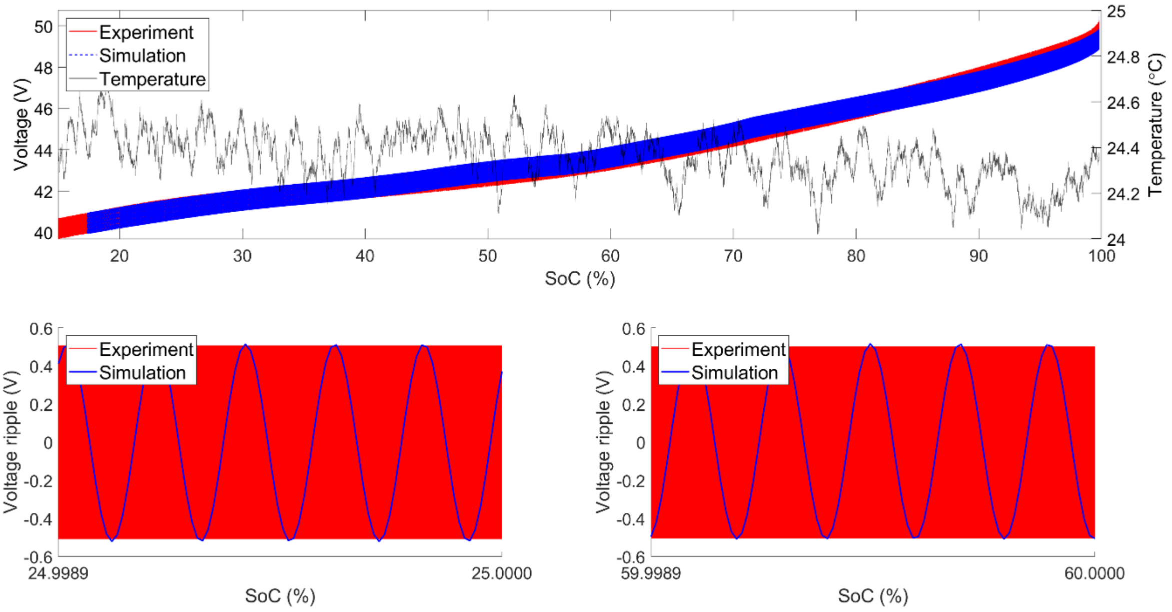

**Fig. 13.** Discharge cycle validation at 24ºC using a sinusoidal current with 120 Hz frequency, 1C offset and 1C amplitude. Top: full cycle. Bottom left: voltage ripple around 25% SoC. Bottom right: voltage ripple around 60% SoC

### 3.3 Temperature monitoring study

**Table 5**. Use case workload schedule

| Time | Usage | Power (W) | Frequency (Hz) |
|---|---|---|---|
| 6 am to 7 am | AC discharge | 1800 | 120 |
| 7 am to 7:30 am | Rest | 0 | - |
| 7:30 am to 9:30 am | AC fast charge | 900 | 120 |
| 9:30 am to 11:30 am | AC discharge | 600 | 300 |
| 11:30 pm to 2 pm | AC slow charge | 450 | 120 |
| 2 pm to 3:30 pm | AC discharge | 600 | 600 |
| 3:30 pm to 4:30 pm | Rest | 0 | - |
| 4:30 pm to 5:30 pm | AC discharge | 900 | 120 |
| After 5:30 pm | AC slow charge | 450 | 120 |

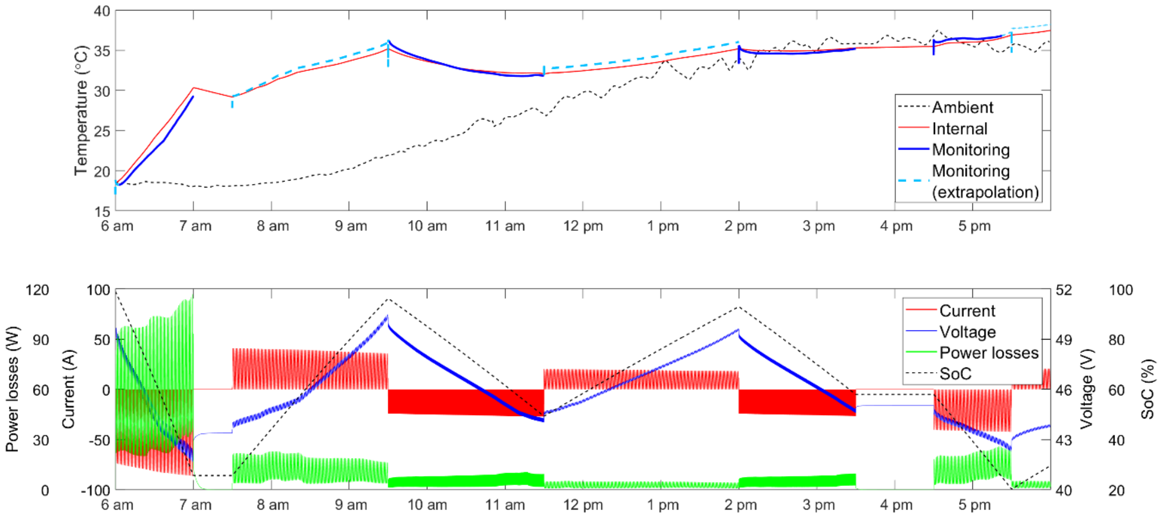

**Fig. 14.** Evolution of the battery module state for the 12-hour case study

To investigate the applicability of the impedance-based temperature monitoring technique, a use case was simulated using the model and the look-up table described in the previous sections. The use case represented a mobile battery power supply used for daily activities on a construction site. A representative battery module equal to the one studied in the previous sections of this paper was simulated. Battery operation during the working period between 6 am and 6 pm was simulated, and the battery internal temperature was monitored. The workload schedule is listed in Table 5. For simplicity, all usages were constant power applications. One usage type represented tools and machinery operating at 60 Hz, which produced 120 Hz sinusoidal currents with varying offsets in the battery. The current ripple amplitudes and offsets depended on the power demanded by the load and the voltage supplied by the battery. In all cases, the current ripple amplitude was equal to the offset as in the waveform shown in Fig. 2 that has been used throughout this study. For the first usage type, the load was 1.8 kW per battery module between 6 am and 7 am and 900 W per module between 4:30 pm and 5:30 pm. Two more usage types represented turning a motor that used 600 W per battery module and induced 300 Hz in the battery between 9:30 am and 11:30 am, and 600 Hz ripples between 2 pm and 3:30 pm. Charging periods were also simulated assuming AC currents from the grid at 60 Hz, producing 120 Hz ripples in the battery. Two charging modes were considered: one representing fast charging that applied 900 W per module, and one representing slow charging that applied 450 W per module. The battery started the day at 6 am fully charged and at ambient temperature. The ambient temperature, used as a boundary condition, increased during the day. The profile was extracted from a paper that reported a study conducted on an outdoor energy generation site [39].

The simulation results can be seen In Fig. 14. The bottom plot shows current in red, voltage in blue, power losses in green and SoC in black. Discharging currents are shown with negative sign and charging currents with positive sign. Current and voltage ripples could be observed while the battery was under operation. The ripple data was used to calculate impedance and estimate battery temperature throughout the simulation. Temperatures are shown in the top plot. The estimated temperature is shown in dark blue color when the conditions reported in the previous sections to populate the look-up table were met, i.e., 25% to 95% SoC in discharge (monitoring). Meanwhile, the estimated temperature is shown in light blue and dashed lines when SoC was off limits or during charging operation (monitoring - extrapolation). Lower reliability was expected under the latter conditions. The reference battery internal temperature was extracted from the model and plotted in red color. The ambient temperature was plotted as a black dashed line. In general, the estimated temperature was a good predictor for internal temperature. The mean temperature difference between the internal temperature curve and the monitoring curve was 0.46ºC under regular conditions and 0.63ºC under extrapolated conditions. Predictions deteriorated during transients which lasted between 0.3 and 0.8 seconds, highlighting the need for input stabilization. Battery temperature trends were influenced by the operation, and they were significantly different from ambient temperature trends, especially during the first half of the day. Therefore, in this scenario, ambient temperature would not have been a good estimator for battery temperature. This finding showcased the advantage of the monitoring technique.

## Conclusions

As battery systems technology develops, certain monitoring techniques become relevant for applicability studies. On the one hand, given the impact of temperature on battery health and performance, establishing correlations between electrochemical response and temperature is a plausible strategy that can be used for temperature monitoring. On the other hand, modular power conversion technologies that supply single-phase AC at the battery module level inherently induce current and voltage ripples in the battery, without the need for dedicated excitation devices. The ripples can be analyzed to determine the impedance. In this study, the applicability of impedance-based temperature monitoring was investigated for a battery module undergoing significant AC current ripples.

First, an experiment allowing to collect impedance data for different temperatures, frequencies and C-rates was described. Next, the analytical process used to calculate impedance from rippling signals was explained. The impedance results were discussed, leading to the creation of a temperature look-up table as a function of the impedance modulus for the battery module and the frequency of the corresponding AC current ripples. The temperature uncertainty was lower than 1ºC across the entire table. The impedance modulus range covered in the table was 7 to 15 mOhm, the frequency range was 100 to 600 Hz, and the widest temperature range was -47 to 57ºC for 600 Hz.

Once the temperature look-up table was complete, an applicability study was set up in a virtual environment. To this end, an electrochemical model for the battery under study was built and validated using experimental data. The model showed very high fidelity, capturing the voltage ripple with a maximum error lower than 5 mV and the voltage center line with a mean error of 117 mV. It is important to note the very high sensitivity of the estimated temperature to voltage, as the highest temperature difference between the model and the experiment, 0.66ºC, was caused by just 1.2 mV of difference in ripple amplitude. A thermal model was coupled with the electrochemical model and its characteristics were described. Finally, a use case was simulated, representing a mobile power supply on a construction site during working hours. A mean tolerance of 0.46ºC with respect to the average internal temperature was observed, showcasing the battery temperature monitoring capability using impedance analysis.

In conclusion, the study showed that the technique under study was conceptually feasible. In a system undergoing significant AC current ripples, the battery impedance could be monitored using high-accuracy sensors. Subsequently, the average jelly roll temperature could be estimated based on pre-populated look-up tables and used for safety and performance control. Although the topic of battery health was not investigated in this study, it is known that the correlation between temperature and impedance varies as the battery ages [40,41]. Therefore, look-up tables adapted to the declining SoH are needed in a real-world application. That is a challenge because a battery can age in different ways depending on operating and environmental conditions, differently impacting the impedance. Aging could also exacerbate disparities among the impedance of different modules [42]. On the other hand, the fact that battery impedance is sensitive to SoH means that impedance analysis can be applied to SoH estimation in a similar fashion to temperature estimation. As shown and discussed in Sections 3.1 and 3.2.2., battery impedance is more sensitive to temperature for low frequency measurements. To obtain reliable results, it is advisable to use low frequency measurements, despite the longer measurement times. Even at low frequencies, signal fidelity requirements are strict. Depending on practical considerations, such as sensor costs or noise-to-signal ratios, the temperature monitoring technique could be implemented on an on-board BMS, on a dedicated battery monitoring chip, or it could be part of a test rig. By leveraging this technique, a lower number of physical temperature sensors would be needed, and the remaining sensors could be relocated to measure temperatures that are more critical for safety.

## References

[1] M. Bielewski, A. Pfrang, D. Quintero-Pulido, et al. Clean Energy Technology Observatory: Battery technology in the European Union - 2023 status report on technology development trends, value chains and markets. Publications Office of the European Union, Luxembourg, 2023, doi:10.2760/52259

[2] J. Liu, J. Cui, Y. Li, Y. Luo, Q. Zhu, Y. Luo. Synergistic air pollutants and GHG reduction effect of commercial vehicle electrification in Guangdong's public service sector. Sustainability 2021, 13(19), 11098, doi:10.3390/su131911098

[3] U. Datta, A. Kalam, J. Shi. A review of key functionalities of battery energy storage system in renewable energy integrated power systems. Energy Storage 2021; 3:e224, doi:10.1002/est2.224

[4] M. Ahmadian-Elmi, P. Zhao. Review of thermal management strategies for cylindrical Lithium-ion battery packs. Batteries 2024, 10, 50, doi:10.3390/batteries10020050

[5] A. Broatch, P. Olmeda, P. Bares, S. Aceros. Integral thermal management studies in winter conditions with a global model of a battery-powered electric bus. Energies 2023, 16, 168, doi:10.3390/en16010168

[6] L.H.J. Raijmakers, D.L. Danilov, R.-A. Eichel, P.H.L. Notten. A review on various temperature-indication methods for Li-ion batteries. Applied Energy 240 (2019) 918–945, doi:10.1016/j.apenergy.2019.02.078

[7] R. Srinivasan. Monitoring dynamic thermal behavior of the carbon anode in a lithium-ion cell using a four-probe technique. Journal of Power Sources 198 (2012) 351–358, doi:10.1016/j.jpowsour.2011.09.077

[8] D. Anthony, D. Wong, D. Wetz, A. Jain. Non-invasive measurement of internal temperature of a cylindrical Li-ion cell during high-rate discharge. International Journal of Heat and Mass Transfer 111 (2017) 223-231, doi:10.1016/j.ijheatmasstransfer.2017.03.095

[9] R.R. Richardson, P.T. Ireland, D.A. Howey. Battery internal temperature estimation by combined impedance and surface temperature measurement. Journal of Power Sources 265 (2014) 254-261, doi:10.1016/j.jpowsour.2014.04.129

[10] T. Waldmann, G. Bisle, B.-I. Hogg, et al. Influence of cell design on temperatures and temperature gradients in Lithium-ion cells: an in operando study. Journal of The Electrochemical Society, 162 (6) A921-A927 (2015), doi:10.1149/2.0561506jes

[11] M. Fleckenstein, O. Bohlen, M.A. Roscher, B. Bäker. Current density and state of charge inhomogeneities in Li-ion battery cells with LiFePO4 as cathode material due to temperature gradients. Journal of Power Sources 196, 10 (2011) 4769-4778, doi:10.1016/j.jpowsour.2011.01.043

[12] X. Du, Y. Hu, M. Song, et al. Experimental studies of effects of temperature gradients on performance of pouch type large format NMC/C lithium-ion battery. Journal of Power Sources 587 (2023) 233688, doi:10.1016/j.jpowsour.2023.233688

[13] R. Srinivasan, B.G. Carkhuff, M.H. Butler, A.C. Baisden. Instantaneous measurement of the internal temperature in lithium-ion rechargeable cells. Electrochimica Acta 56(17) (2011) 6198-6204, doi:10.1016/j.electacta.2011.03.136

[14] J.P. Schmidt, S. Arnold, A. Loges, et al. Measurement of the internal cell temperature via impedance: Evaluation and application of a new method. Journal of Power Sources 243 (2013) 110-117, doi: 10.1016/j.jpowsour.2013.06.013

[15] S. Ludwig, M. Steinhardt, A. Jossen. Determination of internal temperature differences for various cylindrical lithium-ion batteries using a pulse resistance approach. Batteries 2022, 8(7), 60, doi:10.3390/batteries8070060

[16] Y. Zheng, Y. Che, X. Hu, et al. Thermal state monitoring of lithium-ion batteries: progress, challenges, and opportunities. Progress in Energy and Combustion Science 100 (2024) 101120, doi:10.1016/j.pecs.2023.101120

[17] N. Hallemans, D. Howey, A. Battistel, et al. Electrochemical impedance spectroscopy beyond linearity and stationarity - A critical review. Electrochimica Acta 466 (2023) 142939, doi:10.1016/j.electacta.2023.142939

[18] R. Koch. On-line electrochemical impedance spectroscopy for Lithium-ion battery systems. PhD Thesis (2017) Technische Universität München, url:https://mediatum.ub.tum.de/doc/1343447/1343447.pdf

[19] J. Kim, L. Krüger and J. Kowal. On-line state-of-health estimation of Lithium-ion battery cells using frequency excitation. Journal of Energy Storage 32 (2020) 101841, doi:10.1016/j.est.2020.101841

[20] H. Beelen, K. Mundaragi Shivakumar, L. Raijmakers, et al. Towards impedance-based temperature estimation for Li-ion battery packs. International Journal of Energy Research 2020, 44, 2889–2908, doi:10.1002/er.5107

[21] M. Ströbel, V. Kumar, K.P. Birke. Temperature estimation in Lithium-ion cells assembled in series-parallel circuits using an artificial neural network based on impedance data. Batteries 2023, 9, 458, doi:10.3390/batteries9090458

[22] S.-A. Amamra, Y. Tripathy , A. Barai, A.D. Moore, J. Marco. Electric vehicle battery performance investigation based on real world current harmonics. Energies 2020, 13, 489; doi:10.3390/en13020489

[23] D.A. Howey, P.D. Mitcheson, V. Yufit, G.J. Offer, N.P. Brandon. Online measurement of battery impedance using motor controller excitation. IEEE Transactions on Vehicular Technology, 63(6), 2557-2566 (2014), doi:10.1109/tvt.2013.2293597

[24] D. Ronanki, S.S. Williamson. Modular multilevel converters for transportation electrification: challenges and opportunities. IEEE transactions on transportation electrification 4(2) 399-407 (2018) doi:10.1109/TTE.2018.2792330

[25] A. Kersten, M. Kuder, E. Grunditz, et al. Inverter and battery drive cycle efficiency comparisons of CHB and MMSP traction inverters for electric vehicles. 2019 21st European Conference on Power Electronics and Applications (EPE '19 ECCE Europe), Genova, Italy, P.1-P.12, doi:10.23919/EPE.2019.8915147

[26] X. Han, L. Lu, Y. Zheng, et al. A review on the key issues of the lithium ion battery degradation among the whole life cycle. eTransportation 1 (2019) 100005, doi:10.1016/j.etran.2019.100005

[27] P. Seibold, sineFit version 3.2.1, url:https://www.mathworks.com/matlabcentral/fileexchange/66793-sine-fitting

[28] J. Wurzenberger, M. Jelovic, M. Šimundić, et al. Battery thermal management simulation - 1D+1D electrochemical battery and 3D module modeling on vehicle system level. SAE Technical Paper 2021-01-0757 (2021) doi:10.4271/2021-01-0757

[29] M. Doyle, T.F. Fuller, J. Newman. Modeling of galvanostatic charge and discharge of the Lithium/polymer/insertion cell. Journal of The Electrochemical Society 140(6), 1526 (1993), doi: 10.1149/1.2221597

[30] A. García, J. Monsalve-Serrano, R. Lago Sari, S. Martínez-Boggio. Thermal runaway evaluation and thermal performance enhancement of a lithium-ion battery coupling cooling system and battery sub-models. Applied Thermal Engineering 202 (2022) 117884, doi:10.1016/j.applthermaleng.2021.117884

[31] T.R. Ashwin, Y.M. Chung, J. Wang. Capacity fade modelling of lithium-ion battery under cyclic loading conditions. Journal of Power Sources 328 (2016) 586-598, doi:10.1016/j.jpowsour.2016.08.054

[32] T. Katrašnik, I. Mele, K. Zelič. Multi-scale modelling of Lithium-ion batteries: from transport phenomena to the outbreak of thermal runaway. Energy Conversion and Management 236 (2021) 114036, doi:10.1016/j.enconman.2021.114036

[33] L. Sheng, L. Su, H. Zhang. Experimental determination on thermal parameters of prismatic lithium ion battery cells. International Journal of Heat and Mass Transfer 139 (2019) 231–239, doi:10.1016/j.ijheatmasstransfer.2019.04.143

[34] H. Maleki, S. Al Hallaj, J.R. Selman, R.B. Dinwiddie, H. Wang. Thermal properties of Lithium-ion battery and components. Journal of The Electrochemical Society, 146 (3) 947-954 (1999), doi:10.1149/1.1391704

[35] M. Steinhardt, E.I. Gillich, M. Stiegler, A. Jossen. Thermal conductivity inside prismatic lithium-ion cells with dependencies on temperature and external compression pressure. Journal of Energy Storage 32 (2020) 101680, doi:10.1016/j.ijheatmasstransfer.2019.04.143

[36] D. Werner, A. Loges, D.J. Becker, T. Wetzel. Thermal conductivity of Li-ion batteries and their electrode configurations - A novel combination of modelling and experimental approach. Journal of Power Sources 364 (2017) 72-83, doi:10.1016/j.jpowsour.2017.07.105

[37] J. Salvador-Iborra, J. Schneider, R. Tatschl. Automatic conversion of a 3D thermal model of a battery cell into a 1D lumped-element network. 2020 IEEE Vehicle Power and Propulsion Conference (VPPC), Gijón, Spain, doi:10.1109/VPPC49601.2020.9330842

[38] A. Broatch, P. Olmeda, X. Margot, L. Agizza. A generalized methodology for lithium-ion cells characterization and lumped electro-thermal modelling. Applied Thermal Engineering 217, 2022, 119174, doi:10.1016/j.applthermaleng.2022.119174

[39] I. Santiago, J.L. Esquivel-Martin, D. Trillo-Montero, R.J. Real-Calvo, V. Pallarés-López. Classification of daily irradiance profiles and the behaviour of photovoltaic plant elements: the effects of cloud enhancement. Applied Sciences 2021, 11, 5230, doi:10.3390/app11115230

[40] S. Ludwig, I. Zilberman, A. Oberbauer, et al. Adaptive method for sensorless temperature estimation over the lifetime of lithium-ion batteries. Journal of Power Sources 521(15) (2022) 230864, doi:10.1016/j.jpowsour.2021.230864

[41] M.S. Hosen, R. Gopalakrishnan, T. Kalogiannis, et. al. Impact of relaxation time on electrochemical impedance spectroscopy characterization of the most common Lithium battery technologies—experimental study and chemistry-neutral modeling. World Electric Vehicle Journal 2021, 12, 77, doi:10.3390/wevj12020077

[42] S.J. Harris, D.J. Harris, C. Li. Failure statistics for commercial lithium ion batteries: A study of 24 pouch cells. Journal of Power Sources 342 (2017) 589-597, doi:10.1016/j.jpowsour.2016.12.083

# Session 2.4 DATA-DRIVEN CONTROL AND OPTIMIZATION

# Optimization of the Combustion System and Control Strategy for the New Hybrid-Dedicated 2.5L TGDI Engine

J. Park, H. Oh*, H, Im, J. Kim and H. Im

Hyundai Motor Company, Republic of Korea.

E-mail: disi@hyundai.com
Telephone: +(82) 032 360 5224

**Abstract.** HEV (hybrid electric vehicle) is a promising mid-term solution in mitigating greenhouse gas emissions and advancing vehicle electrification. This research focuses on optimizing various component technologies for developing a novel hybrid-dedicated 2.5L, 4-cylinder engine equipped with a turbocharger and gasoline direct injection technology. The study presents optimizing the combustion system and control strategy for improved fuel efficiency and sufficient power performance. The combustion system has been optimized to balance improved engine efficiency with acceptable performance compromise. The intake cam closing timing and geometric compression ratio were tuned to implement the Atkinson cycle, resulting in an increased expansion ratio and reduced effective compression ratio. Under low-speed and high-load engine conditions frequently operated in HEVs, a multiple injection strategy, including late injection during compression stroke and a diluted combustion strategy employing LP-EGR (Low-Pressure Exhaust Gas Recirculation), was employed to mitigate undesirable knocking combustion and to optimize combustion phasing further. The engine test results demonstrated a noteworthy 5% enhancement in fuel consumption within the frequent engine operation points in HEVs. The optimized engine also exhibited sufficient power and torque, making it suitable for midsize SUVs combined with hybrid motor systems. The newly designed piston geometry and the optimized injection strategy enable improved catalyst heating and reduced engine-out raw emissions compared to the base engine. The proposed new hybrid system, featuring two motors and a hybrid-dedicated engine, demonstrated superior system response through effective cooperative control among its components. The new engine will contribute to advancing the efficiency and performance of larger-size HEVs and serve as a compelling solution for a sustainable and environment-friendly future powertrain.

## 1. Introduction

The automotive industry is trying to reduce greenhouse gas (GHG) emissions and address global climate change. One of the most essential actions that put the most effort into is vehicle electrification, represented by the deployment of electric vehicles (EV). [1-3] All automotive manufacturers have recently been working hard to develop advanced EV technologies and present future strategies with extended EV lineups. EVs appear to significantly reduce GHG emissions, as no exhaust emissions are emitted during driving. However, eco-friendly infrastructure for power generation and the charging grid should be provided to support such an effort. Therefore, GHG reduction strategies based on deploying EVs are actively taking place among developed countries where the infrastructure is ready or near-term planned.[4-5] Many previous life cycle assessment (LCA) studies support the idea that EVs can be the most effective method for reducing GHG emissions in these regions. [6-7]

Meanwhile, some manufacturers propose future strategies, including hybrid electric vehicles (HEVs), in their portfolios.[8-9] In particular, they emphasize that a diversified powertrain strategy is advantageous over an EV-only approach by providing various GHG reduction solutions tailored to customers in multiple markets and regions. The propulsion system of HEV has an internal combustion engine and an electric motor(s) that enable the recovery of braking energy and optimize the engine's operating point. As a result, HEVs show significantly reduced GHG emissions during vehicle operation compared to conventional internal combustion engine (ICE) vehicles.[10-12] In particular, based on a recent LCA study, GHG emissions from HEVs are analyzed to be similar to or even lower than those from BEVs in many regions, even in advanced countries.[13] In addition, when low-carbon intensity biofuel [14] or e-fuel [15] is applied to HEVs, GHG emissions from an HEV can be drastically reduced. Therefore, HEVs are another essential axis of electrification that reduces GHG emissions along with EVs.

Since the introduction of hybrid vehicles with the first-generation Prius in the late 1990s, dedicated hybrid engines have been developed to improve the fuel efficiency of vehicles. Vehicle hybridization allows the engine to operate more efficiently in specific operating ranges compared to traditional internal combustion engine (ICE) vehicles. This optimization aims to achieve higher thermal efficiency in a specific range rather than considering a wide range of operating conditions, leading to significant improvements in efficiency compared to conventional ICEs. Dedicated hybrid engines utilize a higher geometric compression ratio with an effective compression ratio reduction strategy to implement the Atkinson cycle or Miller cycle for efficiency improvement without sacrificing engine performance. Dilute combustion with exhaust gas recirculation (EGR) is also commonly used to optimize combustion and prevent knocking under high-load conditions. This requires expertise in design and optimization to develop competitive HEV-dedicated engines. In addition, developing hybrid powertrain systems should cover various components, such as the engine, motor, battery, transmission, and clutch, requiring a cooperative control of these elements and a complex integrated control strategy. HEV systems frequently switch between different driving modes, including EV mode, series HEV mode, parallel HEV mode, engine performance driving mode, and idle mode, making it challenging to control the engine and system torque output accurately. Designing and controlling hybrid powertrains must consider achieving technical goals, minimizing costs, and meeting stringent emission regulations. Therefore, the successful development of new hybrid powertrains and engines requires an efficient and effective development process involving a comprehensive review of various engine performances and requirements.

This study presents the optimization made to combustion systems and control strategies for a new hybrid dedicated engine system, a 2.5L, 4-cylinder turbocharged gasoline direct injection(T-GDI) engine for a midsize crossover SUV hybrid. The optimization process used a combination of combustion system and control strategy technologies to achieve maximum fuel efficiency with minimized engine performance compensation. Additionally, the study included the development of design and control strategies to meet stringent future emission regulations and optimize the hybrid system's control strategy for dynamic response. The primary objective of this paper is to demonstrate the latest engine technologies and optimization methodologies for new hybrid dedicated engines, which are supported by experimental results. The discussions and methodologies presented in this study will provide valuable insights for powertrain engineers working on advanced engines and hybrid vehicles who aim to develop cleaner and more sustainable propulsion systems.

## 2. Base engine and development target

### 2.1 Base engine

The base engine for the optimization is a 2.5L inline 4-cylinder engine applied in E-segment sedans and midsize crossover SUVs. The engine is equipped with continuous variable valve timing (CVVT) systems on both intake and exhaust camshafts, with the intake camshaft being actuated electrically while the exhaust hydraulically. A direct injection system with a maximum injection pressure of 350 bar is installed on the engine, with laterally mounted injectors on the combustion chamber. The engine has a boosting system of a twin-scroll turbocharger with an electrically actuated wastegate. Furthermore, an integrated thermal management system (ITM) is installed to improve engine cooling performance. This system provides separate cooling for the engine block and head, effectively controlling engine warming and cooling by directing heated coolant to various cooling circuits, including the heater, radiator, and oil cooler. The engine is equipped with a variable oil pump and low-friction lubrication system for friction reduction. Table 1 summarizes the key specifications of the base engine.

**Table 1**. Specification of the base engine

| | |
|---|---|
| Bore [mm] | 88.5 |
| Stroke [mm] | 101.5 |
| Compression ratio | 10.5 |
| Valvetrain | Ducal CVVT |
| Fuel | RON 92 Gasoline |
| Block | I4 |
| Injection | GDI+MPI |
| Max. injection pressure [bar] | 350 |
| Boosting | Turbocharged |
| Intercooler | Air-Air |
| Maximum Power | 281 PS @ 5800 rpm |
| Maximum Torque | 43 kgf.m @1700-4000 rpm |

### 2.2 Development target

Hybrid dedicated engines are integrated with one or more propulsion motors in their hybrid powertrain systems. This means that the demand for power performance is lower than that of engines for conventional ICE vehicles, as discussed in the Introduction. Therefore, optimization mainly focuses on efficiency in the performance-efficiency trade-off. To ensure the competitiveness of new hybrid vehicles, the engine must achieve high efficiency. This study aims to improve efficiency by more than 5% under main engine operating conditions during HEV operation. Moreover, this engine will be equipped with a midsize crossover SUV, and sufficient power, considering vehicle size, is necessary. However, the base engine already has applicable power for midsize crossover SUVs. With the addition of electric motors in the hybrid powertrain system, a slight decrease in performance compared to the base engine will be acceptable. Additionally, new HEV vehicles must comply with increasingly stringent future emissions regulations. Therefore, low engine-out emissions, reliable after-treatment systems, and related control operations should be secured. Another development target is the dynamic response of transient operation. Since HEV performs EV-HEV mode transition frequently during the driving, to provide a fun-to-drive experience to the driver, a seamless transient response of the engine under dynamic conditions should be secured. Implementation and optimization of component technologies and control strategies have been conducted to meet these technical goals. Figure 1 provides schematics of the newly developed hybrid dedicated engine. A detailed discussion of the applied technologies and their effects will be followed in the next chapter.

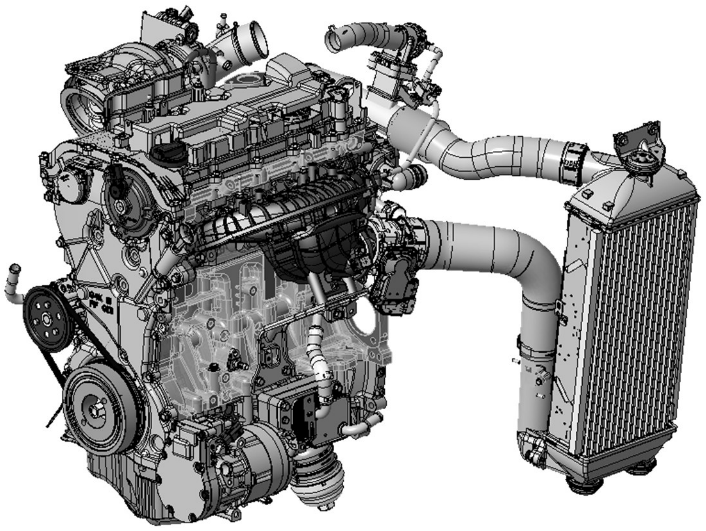

**Fig. 1.** Schematics of the newly developed hybrid dedicated engine

## 3. Optimization of System and Control

This chapter explains the optimizations to develop the new engine. First, the thermodynamic optimization of the combustion system to balance improved engine efficiency with acceptable performance degradation will be discussed. The optimization involved implementing the optimal Atkinson cycle by experimentally determining various intake cam closing timings and geometric compression ratios. The second topic covers applying and optimizing the multi-injection strategy and LP-EGR for improved fuel efficiency and performance under higher-load engine operating conditions. Next, optimization of the piston geometry design and injection strategy for the improved catalyst heating performance will be discussed. Finally, the optimization of the advanced engine control strategy will be discussed, and the improvement in system response under highly dynamic driving conditions through the newly proposed strategies will be demonstrated.

### 3.1 Thermodynamic optimization

As discussed in the Introduction, many hybrid dedicated engines adopt the Atkinson cycle. The Atkinson cycle implements the late intake valve closing (LIVC) to reduce the effective compression ratio, which minimizes the drawbacks of combustion phasing retardation due to knocking while maintaining a high expansion ratio to increase thermodynamic efficiency.[10] However, there are some limitations and drawbacks to using the Atkinson cycle. For instance, it can reduce volumetric efficiency and has limitations in knocking mitigation under high-speed operating conditions due to the ram effect. In detail, at low and middle engine speeds, the LVIC strategy can reduce the effective compression ratio by keeping the intake valve open during the compression stroke. This allows fresh charge to flow into the intake mani-fold from the cylinder as the piston rises during the delayed IVC period. However, at higher engine speeds, the inertia of the gas and increased pressure in the port prevent the reverse flow, making the LVIC strategy unable to control the effective compression ratio. Therefore, evaluating whether the powertrain performance meets the vehicle's requirements is essential. This study also adopted the Atkinson cycle and aimed to optimize fuel economy and power performance by testing different combinations of compression ratios and LIVC levels. Four combinations were tested, ranging from a compression ratio of 12 with a mild LIVC to 12.5 with an aggressive LIVC. The fuel economy evaluations were conducted on eight selected conditions, which are frequently operated engine conditions in midsize SUV hybrid vehicles. The result of the engine test showed that Case 2 consisted of a compression ratio of 12, and the intermediate level of LIVC strategy showed the best fuel economy improvement, as depicted in Figure 2. Fuel economy improvement was less in cases with higher compression ratios due to deteriorating knocking characteristics. A compression ratio of 12.5 resulted in relatively significant performance degradation, especially in Case 4, which had the most aggressive LIVC strategy combined with deteriorated volumetric efficiency. As a result, Case 2 was selected as the most optimal when consid-ering the trade-off between fuel economy improvement and performance. Figure 3 illustrates the fuel economy improvement ratio compared to the base engine when Case 2 is applied. Brake-specific fuel consumption (BSFC) improved by 2-4% in main engine operating conditions during the FTP vehicle test cycle. However, mid-to-high load conditions showed minimal fuel economy improvement or even deterioration due to reduced volumetric efficiency and increased knocking combustion caused by the implementation of the LIVC and increased compression ratio. Therefore, additional fuel economy improvement strategies are needed, mainly focusing on high-load conditions.

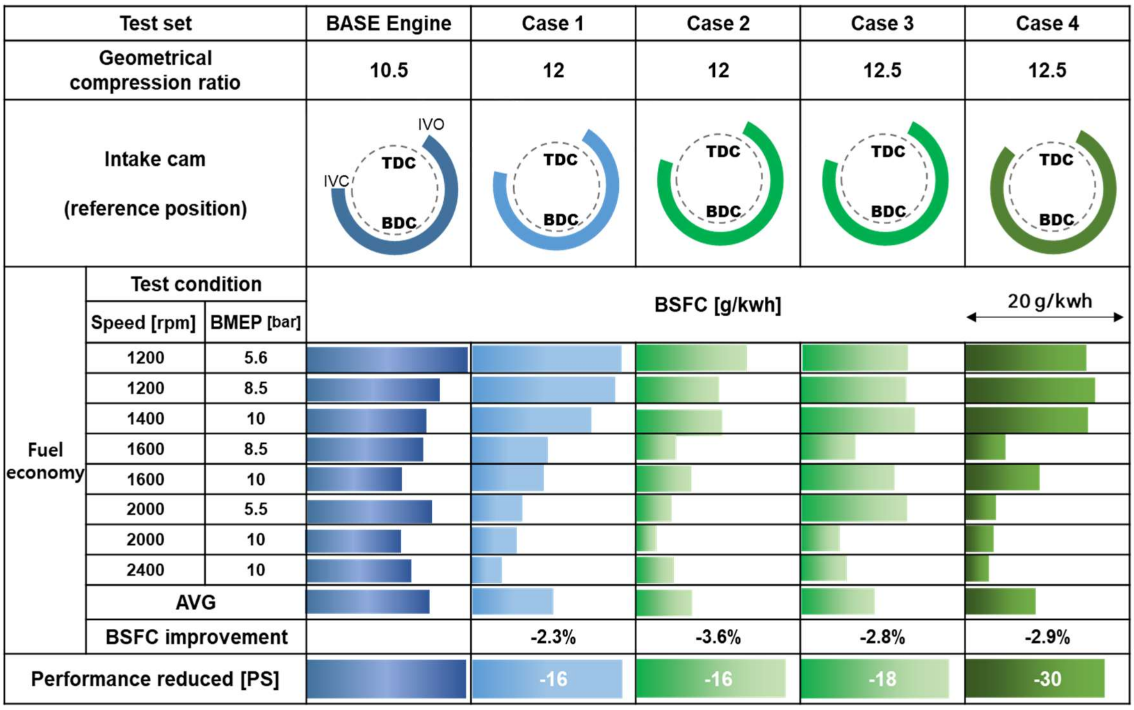

| Test set | | | BASE Engine | Case 1 | Case 2 | Case 3 | Case 4 |
|---|---|---|---|---|---|---|---|
| Geometrical compression ratio | | | 10.5 | 12 | 12 | 12.5 | 12.5 |
| Intake cam (reference position) | | | | | | | |
| Fuel economy | Test condition | | BSFC [g/kwh] | | | | 20 g/kwh |
| | Speed [rpm] | BMEP [bar] | | | | | |
| | 1200 | 5.6 | | | | | |
| | 1200 | 8.5 | | | | | |
| | 1400 | 10 | | | | | |
| | 1600 | 8.5 | | | | | |
| | 1600 | 10 | | | | | |
| | 2000 | 5.5 | | | | | |
| | 2000 | 10 | | | | | |
| | 2400 | 10 | | | | | |
| | AVG | | | | | | |
| | BSFC improvement | | | -2.3% | -3.6% | -2.8% | -2.9% |
| Performance reduced [PS] | | | | -16 | -16 | -18 | -30 |

**Fig. 2.** Optimization of LIVC strategy and geometric compression ratio (experimental results)

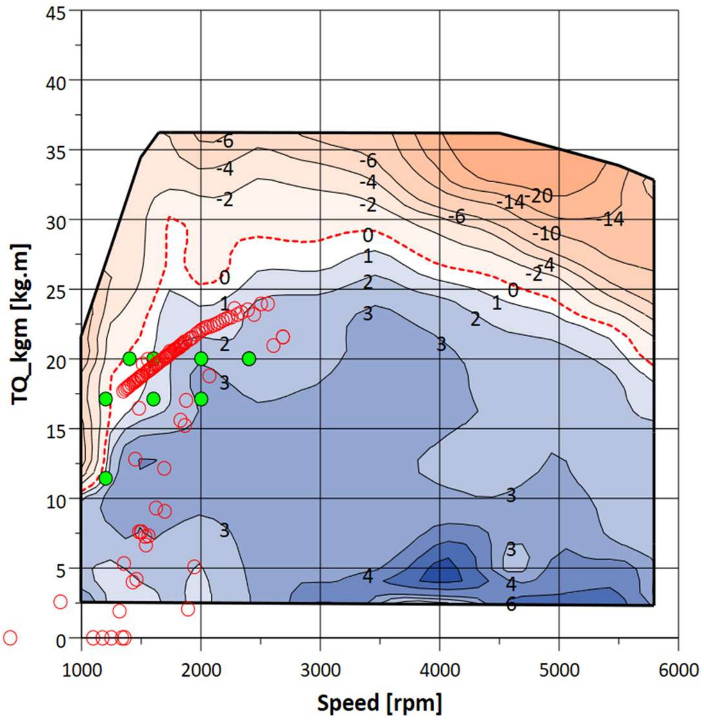

**Fig. 3.** Improvement in BSFC by the implementation of the Atkinson cycle

(red circle: engine operating points during FTP test cycle, green dots: engine test points for fuel consumption evaluation shown in Fig.2)

### 3.2 Multiple injection and LP EGR

In the new engine, a triple injection strategy has been implemented to improve both efficiency and performance under high-load conditions. In the previous engine, double injection was performed during the intake stroke to enhance mixture homogeneity under low-speed, high-load conditions. Adding additional late injection at the end of the compression stroke can improve combustion speed by enhancing the in-cylinder flow of the combustion chamber by the spray momentum. On the other hand, the late injection at the compression stroke could worsen mixture homogeneity, leading to a deterioration in combustion efficiency. In the newly developed engine, injection at the end of the compression stroke could be implemented with the minimized fuel quantity. Therefore, adverse effects of late injection could also be minimized while increasing combustion speed could be realized. This was achieved through improved injection quantity control and the quality management of the injector manufacturing [19]. Figure 4 (a) shows double and triple injection strategies that are applied in previous and new engines respectably, and (b) illustrates the comparison of combustion characteristics for different injection strategies. In figure 4 (b), the ignition timing was set to MBT or knock boundary for each condition. As shown in Figure 4 (b), the triple injection could significantly increase combustion speed, leading to mitigation in knocking and advancement in combustion phasing. Through the application of the triple injection, BSFC could be improved by about 4% additionally under high-load conditions.

In addition, low-pressure exhaust gas recirculation (LP-EGR) was applied to improve thermal efficiency further. Although LP-EGR presents technical challenges, such as high control complexity and durability issues like condensation water and fouling, it has significant advantages compared to HP-EGR. Specifically, LP-EGR enables a higher EGR rate, which is helpful in improving combustion phasing and efficiency [20]. As shown in Figure 5, the application of LP-EGR compensates for the reduction in fuel efficiency caused by the use of a high compression ratio. Figure 5(a) shows the rate of LP-EGR used in this study, and in (b), the combustion characteristics are compared before and after LP-EGR was applied. With LP-EGR, auto-ignition reactivity could be controlled, and combustion phasing (mass fraction bunt 50%: MFB50%) could be advanced by around five crank angle degrees (CAD) at maximum, as shown in Figure 5 (b). The implementation of LP-EGR resulted in a significant improvement in fuel efficiency under higher-load operation conditions, although the average fuel consumption improvement under representative eight test conditions was approximately 2%, less than in higher-load conditions.

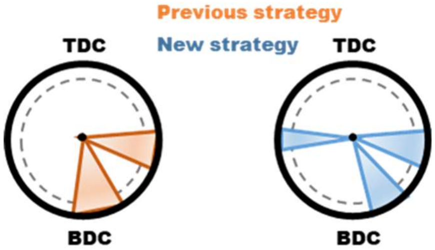
Previous strategy
New strategy
TDC
TDC
BDC
BDC

(a) Comparison of injection strategies

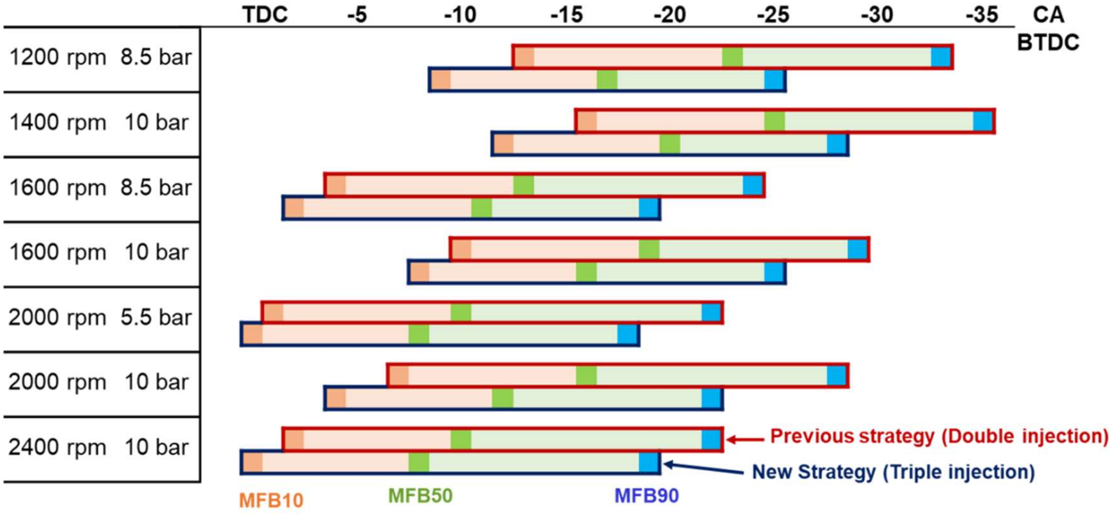

(b) Comparison of combustion phasing and speed (Experimental results)

**Fig. 4.** Effect of triple injection strategy

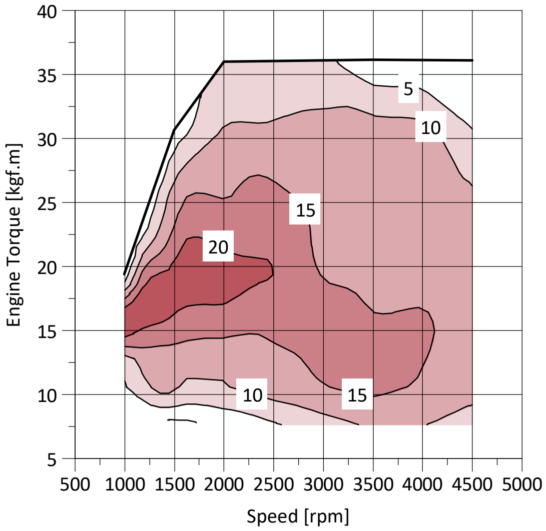

(a) EGR rate map of the new engine

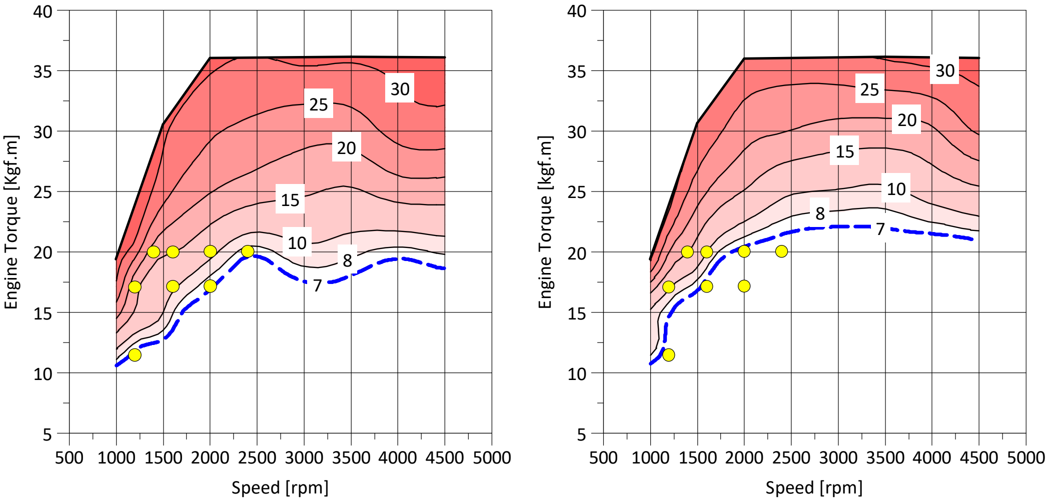

(b) Comparison of mass fraction burnt 50% (left: no EGR, right LP-EGR implemented, experimental results)

**Fig. 5.** Effect of LP-EGR

### 3.3 Optimized catalyst heating

Global emission regulations are becoming stricter, which makes it harder to introduce new engine-powered vehicles to the market. For example, the United States Environmental Protection Agency (EPA) regulates non-methane organic gases (NMOG) and nitrogen oxides (NOx) from light-duty vehicles. These emissions should decrease to an average fleet level of 12 mg/mi by 2032, with a challenging particulate matter (PM) emissions limit of 0.5 mg/mi. Optimizing the catalyst heating operation after a cold start is crucial to meet future exhaust regulations. This optimization aims to reduce the "light-off" time, during which most tailpipe emissions are emitted, and to minimize raw emissions during this period. Since the new engine uses the LIVC strategy, it is expected to experience reduced intake flow during the compression stroke, resulting in less favorable in-cylinder tumble flow and turbulent intensity. In catalyst heating conditions, the ignition timing is retarded as much as possible to deliver high heat to the exhaust catalyst, limited by the maximum available cyclic variation. However, this operation may be affected by reduced tumble flow and the deteriorated of cyclic variation. Therefore, improvements have been made in both design and injection control to compensate for this.

Figure 6(a) shows how the new engine's piston shape has been modified to enhance the intensity of the tumble flow. These design enhancements were specifically made to improve the tumble flow's intensity. Figure 6(b) presents the results of a Computational Fluid Dynamics (CFD) simulation carried out using STAR-CD CFD software. The simulation was performed at 1500 rpm under motoring conditions, focusing solely on the influence of intake flow and excluding the effect of fuel injection. The x-axis represents the crank angle, and the y-axis represents the spatially averaged turbulent kinetic energy around 10mm from the spark plug. The improved piston shape has increased the intensity of tumble flow compared to the flat piston, indicating that the in-cylinder flow is similar to the base engine under catalyst heating conditions. Combined with the increased compression ratio, which helps the mixture achieve faster laminar flame velocity, the enhanced in-cylinder flow characteristics of the new engine could prevent the deterioration of exhaust heat flux and light-off time compared to the base engine.

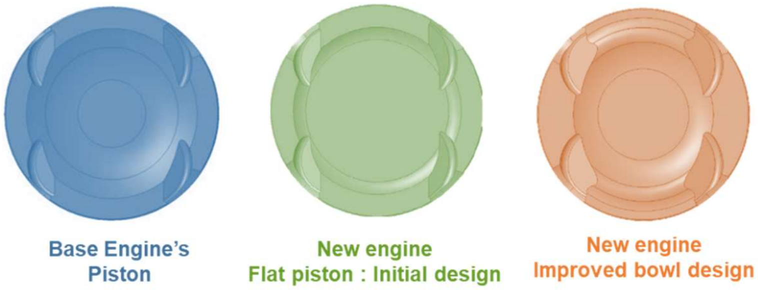
Base Engine's Piston
New engine Flat piston : Initial design
New engine Improved bowl design

(a) Comparison of piston bowl design

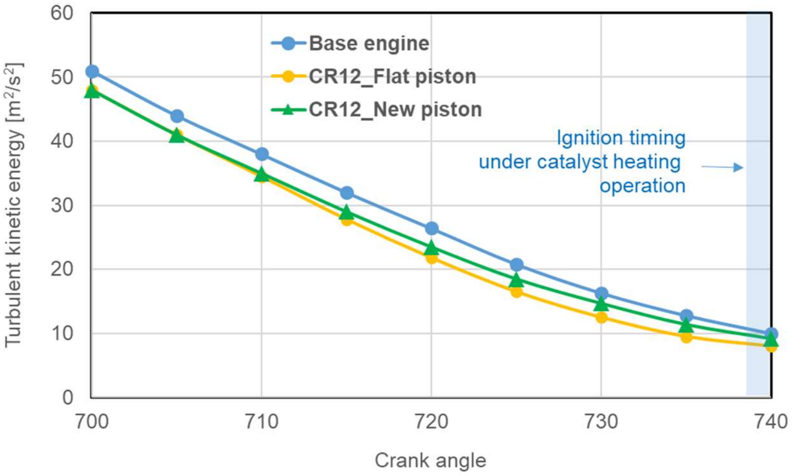

(b) Comparison of turbulent kinetic energy (CFD results using STAR-CD software)

**Fig. 6.** Effect of improved piston bowl design

In addition to the new design of the piston bowl geometry, optimization of injection strategies was also performed to improve catalytic heating performance. Similar to Chapter 3.2, triple injection, including late injection during the compression stroke, was applied to improve in-cylinder flow by spray momentum. The third pulse was optimized to enhance in-cylinder flow due to the spray momentum while minimizing the side effects of mixture inhomogeneity. During this process, optimization of the timing and ratio of the first and second injections is also required to maximize the mixture's homogeneity and avoid undesired spray impingement. Figure 7(a) compares the optimized injection timing, while Figure 7(b) compares the catalyst heating performance between the base and newly developed engines. As a result of the optimization, the catalyst heating performance of the new engine showed equivalent heat flux and slightly superior cyclic variation compared to the base engine, with equivalent HC emissions and superior NOx and PM emissions. These results confirm that the capability to meet the latest regulations, such as LEV-III SULEV30, has been sufficiently secured. It is also expected that compliance with future regulations such as CARB ACC-II and EPA tier 4 will be feasible with improved exhaust after-treatment systems.

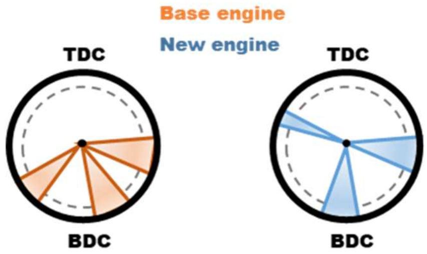

(a) Comparison of injection strategies

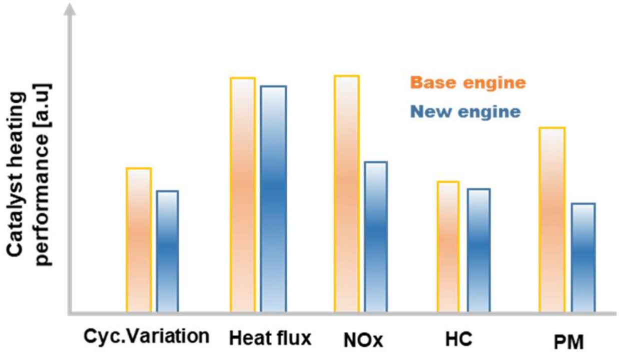

(b) Comparison of catalyst heating performance (experimental results)

**Fig. 7.** Optimization of catalyst heating operation

### 3.4 Improvement of engine dynamics

Hybrid engines generally operate cooperatively with motors, so the requirement for dynamic response seems less significant than conventional internal combustion engine vehicles. However, when a vehicle transitions between EV and HEV modes under dynamic drive conditions, the engine must go through various mode transitions to meet driver demands seamlessly. Therefore, it is essential to ensure that hybrid power systems provide better dynamic response than conventional ICEV.

Figure 8(a) displays a schematic of Hyundai's new hybrid system, which includes the engine, engine clutch, two motors, and transmission. Figure 8(b) depicts how the engine operates during dynamic acceleration. When the driver inputs the accelerator pedal while the vehicle is stationary, propulsion starts with the P2 motor, and the P1 motor spins the engine to start it. As the engine speed reaches an idle RPM, fuel injection initiates, and the engine speed further increases to synchronize with the P2 motor's speed. Once the engine speed aligns with the P2 motor's speed and the torque sum from the engine and P1 motor becomes zero, the clutch engages. These sequential processes greatly impact the vehicle's dynamic performance during acceleration. The air mass flow rate depicted in Figures 8 is a modeled value in the ECU calculated based on various sensor readings. It is measured in mg/stroke and indicates the mass of gas trapped in the cylinder at that specific point. Therefore, it's important to note that it can have a specific value even when the engine is not running.

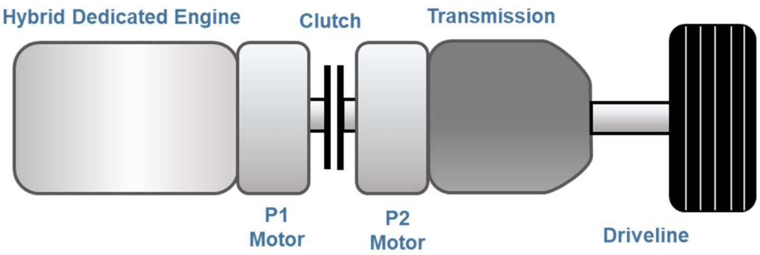

(a) Schematics of Hyundai's new hybrid system

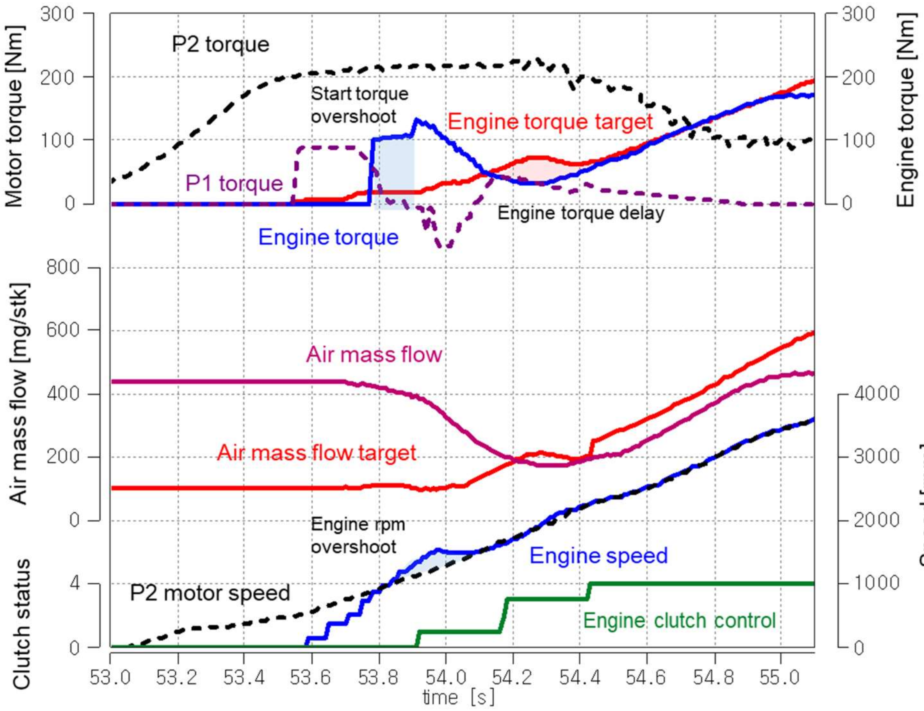

(b) Cooperative control of hybrid system during acceleration

**Fig. 8.** Schematics and operation of hybrid propulsion system

To enhance the control of the hybrid powertrain system for improved dynamic performance, it is crucial to ensure a reliable engine start as the initial step. Conversely, it is important to avoid engine speed and torque overshooting. This can be accomplished by fine-tuning the control parameters for engine start. In this study, the intake cam, throttle opening, ignition timing, and injection timing were optimized to refine the engine starting process. The ignition timing and intake cam advance level were adjusted to balance engine torque overshoot and starting stability. The throttle opening angle was modified to enhance the engine's ability to reach the desired torque immediately after starting. The injection timing was optimized to minimize emissions during frequent starts in HEV operations. Figure 9 demonstrates the outcome of the optimization of engine start parameters, showing a reduction in engine torque overshoot, leading to more precise torque control immediately after starting. The significantly reduced engine rpm overshoot can contribute to swift clutch engagement and improved system response.

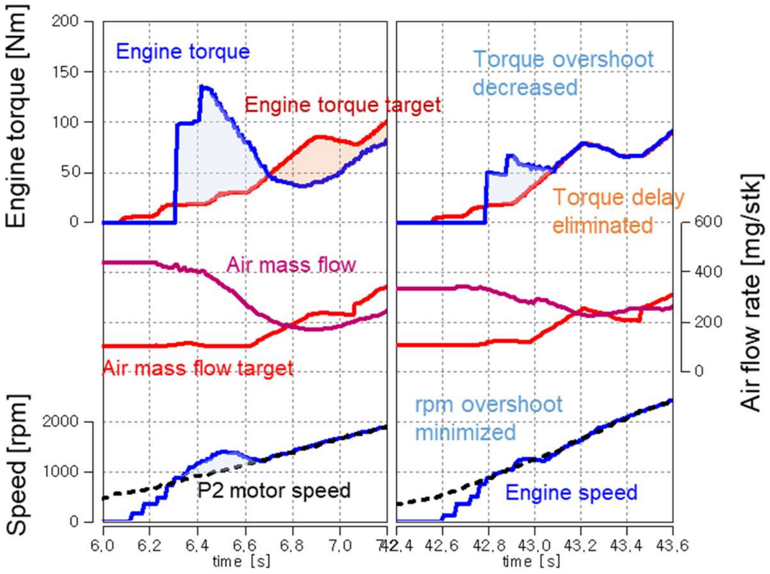

**Fig. 9.** Optimized engine start (left: before optimization, right: after optimization, experimental results)

Once the clutch is engaged, the engine and motor work together to fulfill the driver's torque request through a process called torque blending. Initially, the engine operates at low load. As the engine and motor speed increases, the motor's torque is limited due to its constant power characteristic. This means the engine must quickly accelerate from low to higher load. To achieve dynamic performance, two strategies were implemented in this study. The first strategy, called the dynamic throttle strategy, compensates for any shortfall in the current air quantity by adding a feed-forward compensation value to the throttle opening target calculated from the current air quantity. This ensures precise torque control despite excess air quantity, although it may slightly decrease efficiency in short transient or highly dynamic driving conditions. The second strategy is the transient cam strategy. Under steady-state conditions, the intake cam operates with maximally retarded intake valve closing (IVC) timing to avoid high effective compression ratios while supplying the required air quantity through boosting. However, to rapidly increase the load, advancing the intake cam can improve dynamic response by reducing dependence on boosting, which may decrease efficiency but only in short transient conditions during dynamic driving. Figure 10 shows the effects of applying these strategies, which have significantly improved powertrain system response and are expected to meet customers' dynamic requirements.

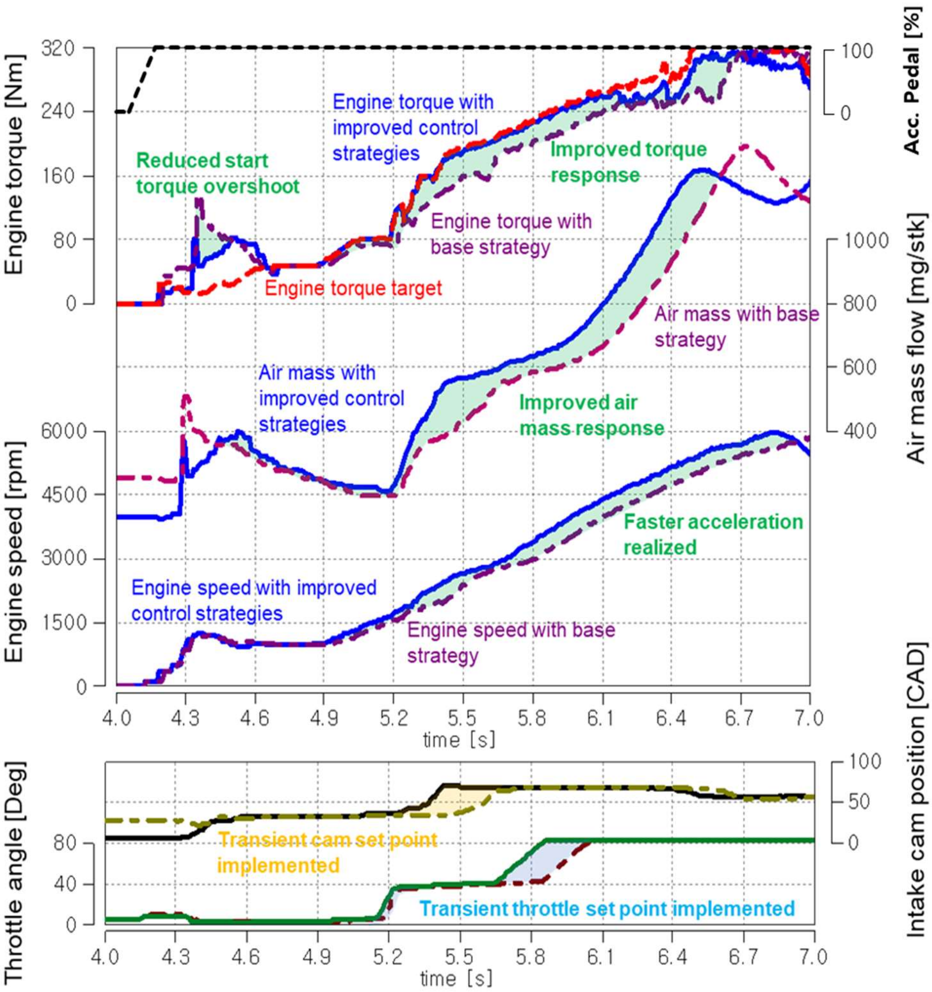

**Fig. 10.** Effect of dynamic throttle and transient cam strategy on dynamic response under acceleration condition (experimental results)

## Conclusions

The study presents a newly developed 2.5L, 4-cylinder turbocharged gasoline direct injection engine optimized for optimal fuel efficiency and minimized performance degradation. By optimizing engine combustion systems and control strategies, the engine achieves thermal efficiency approaching 40%, satisfying customers' dynamic driving performance expectations and meeting future emissions regulations. Details on optimizations follow.

- The Atkinson cycle with late intake valve closing (LIVC) was implemented to optimize fuel economy. Testing various compression ratios and LIVC levels revealed that a compression ratio of 12 with an intermediate LIVC level provided the best fuel economy improvement with the minimized compensation of engine performance. However, higher compression ratios led to deteriorated knocking characteristics, particularly at higher loads, indicating a need for additional fuel economy strategies.

- A triple injection strategy was implemented to enhance efficiency and performance under high-load conditions, with late injection at the end of the compression stroke improving combustion speed without compromising mixture homogeneity, resulting in a 4% improvement in BSFC at maximum under high-load conditions. Additionally, low-pressure exhaust gas recirculation (LP-EGR) was also employed to further enhance thermal efficiency, resulting in advanced combustion phasing by five crank angles at maximum under high-load conditions.

- For the catalyst heating operation under the cold start idle condition, newly designed piston shapes and optimized triple injection with late injection were applied. Despite the degradation in cylinder flow caused by the implementation of the LIVC strategy, the new engine exhibits a significantly improved catalyst heating performance compared to the base engine.
- Control strategies for the hybrid powertrain system were optimized to enhance dynamic performance. The optimized engine start control method significantly reduced engine torque and rpm overshoot, leading to more precise torque control and faster system response. Advanced transient strategies, such as dynamic throttle and transient intake cam control, were implemented and successfully improved the system's dynamic response without significantly affecting overall vehicle efficiency.

## References

[1] International Energy Agency, “Energy technology perspectives 2023,” Paris, France, 2023, https://iea.blob.core.windows.net/assets/a86b480e-2b03-4e25-bae1-da1395e0b620/EnergyTechnologyPerspectives2023.pdf

[2] Hyundai Motor Company, “Road to Sustainability - 2023 Sustainability Report,” 2023, https://www.hyundai.com/content/hyundai/ww/data/csr/data/0000000051/attach/english/hmc-2023-sustainability-report-en-v5.pdf

[3] International Energy Agency, "Global EV Outlook 2024: Moving towards increased affordability," https://iea.blob.core.windows.net/assets/72e8cec8-c4d3-445f-a6df-28b827a31666/GlobalEVOutlook2024.pdf

[4] Dornoff, J., Mock, P., Baldino, C., Bieker, G. et al., “Fit for 55: A review and evaluation of the European Commission proposal for amending the CO2 targets for new cars and vans,” ICCT BRIEFING, Sep. 2021, https://theicct.org/wp-content/uploads/2021/09/fit-for-55-review-eu-sept21-2.pdf

[5] J. C. Kelly, T. Kim, C. P. Kolodziej, R. K. Iyer, S. Tripathi, A. Elgowainy, A. and M. Wang, "Comprehensive Cradle to Grave Life Cycle Analysis of On-Road Vehicles in the United States Based on GREET," SAE Technical Paper 2024-01-2830, doi:10.4271/2024-01-2830

[6] T. R., Hawkins, B. Singh, G. Majeau-Bettez, and A. H. Strømman, "Comparative environmental life cycle assessment of conventional and electric vehicles." J. Ind. Ecol 17(1): 53-64, 2013, doi:10.1111/j.1530-9290.2012.00532

[7] R. Kawamoto, H. Mochizuki, Y. Moriguchi, T. Nakano, T. "Estimation of CO2 Emissions of Internal Combustion Engine Vehicle and Battery Electric Vehicle Using LCA," Sustainability 11(9):2690, 2019, doi:10.3390/su11092690

[8] K. Kaita, “Diversified Electrification–The Key for Toyota’s Challenge towards a Sustainable Society,” The 40th International Vienna Motor Symposium. 2019. Vienna. Austria. 15-17 May.

[9] T. Tsurushima, “Future Internal Combustion Engine Concept Dedicated to NISSAN e-POWER for Sustainable Mobility,” The 29th Aachen Colloquium Sustainable Mobility. 2020. Aachen. Germany, 5-7 October.

[10] S. Abe, S. Sasaki, H. Matsui, and K. Kubo, “Development of Hybrid Systems for Mass Productive Passenger Car,” JSAE Proceeding 9739543:21-24, 1997

[11] Y. Kim, B. Min, and H. Sim, “Sonata Hybrid the First Full Hybrid Electric Vehicle from Hyundai,” ATZ Autotechnol 11 10–17, 2011, doi:/10.1365/s35595-011-0005-8

[12] S. Hirota, T. Kikuchi, and T. Katanoda, “Development of the New 2.0L Hybrid System for Prius,” SAE Technical Paper 2023-01-0474, doi:10.4271/2023-01-0474

[ 13] T. Burton, S. Powers, C. Burns, G. Conway, "A Data-Driven Greenhouse Gas Emission Rate Analysis for Vehicle Comparisons," SAE Int. J. Elec. Veh. 12(1):91-127, 2023, doi:10.4271/14-12-01-0006

[14] Ö.Andersson and P.Börjesson, "The Green House Gas Emissions of an Electrified Vehicle Combined with Renewable Fuels: Life Cycle Assessment and Policy Implications." Applied Energy 289(2021): 116621, doi: 10.1016/j.apenergy.2021.116621

[15] A. Soler, V. Gordillo, W. Lilley, P. Schmidt, et al., “E-Fuels: A techno-economic assessment of European domestic production and imports towards 2050,” Concawe, Brussels, Nov. 2022, https://www.concawe.eu/wp-content/uploads/Rpt_22-17.pdf

[16] J. B. Heywood, "Internal Combustion Engine Fundamentals the 2nd Edition", McGraw-Hill Education, New York, 2019.

[17] K. Hwang, I. Hwang, H. Lee, H. Park, H. and Choi, Ket al, "Development of New High-Efficiency Kappa 1.6L GDI Engine," SAE Technical Paper 2016-01-0667, 2016, doi:10.4271/2016-01-0667.

[18] H, Oh, J, Lee, S, Woo and H, Park, "Effect of synergistic engine technologies for 48 V mild hybrid electric vehicles," Energy Convers. Manag., 244 (2021): 114515, doi:10.1016/j.enconman.2021.114515

[19]. S Moon, O. F. Atac. G. Bae and H. Oh, "Correlating armature and needle dynamics with voltage waveforms of solenoid-actuated GDI injector," Flow Meas. Instrum. 92(2023):102391, doi:10.1016/j.flowmeasinst.2023.102391

[20] D. Takaki, H. Tsuchida, T. Kobara, M Akagi, et al., "Study of an EGR System for Downsizing Turbocharged Gasoline Engine to Improve Fuel Economy," SAE Technical Paper 2014-01-1199, 2014, doi:10.4271/2014-01-1199

[21] United States Environmental Protection Agency, "Multi-Pollutant Emissions Standards for Model Years 2027 and Later Light-Duty and Medium-Duty Vehicle," Federal Register, Vol. 89, No. 76:27842-28215, 2024, https://www.govinfo.gov/content/pkg/FR-2024-04-18/pdf/2024-06214.pdf

# Application of Data-driven Approaches to Efficient Knock Prediction in Engine Development

C. Laubichler[1], S. Posch[1], C. Gößnitzer[1], T. Oppl[1], G. Pirker[1], A. Wimmer[1,2]

[1]LEC GmbH, Austria;

E-mail: office@lec.tugraz.at
Telephone: +43 316 873 30101

[2]Institute of Thermodynamics and Sustainable Propulsion Systems, Graz University of Technology, Austria

E-mail: institut@ivt.tugraz.at
Telephone: +43 316 873 30001

**Abstract.** Designing environmentally sound, efficient, and robust large internal combustion engines involves balancing a large number of desirable and undesirable combustion properties. Knocking—a phenomenon of uncontrolled and abnormal combustion—is one such undesirable characteristic of spark-ignited engines. During the design process, it is therefore necessary to determine the knock tendency in relation to the corresponding engine operating point. To this end, single-cylinder engine tests are important as they allow the evaluation of a variety of engine operating points for knocking under controlled conditions. But even with single-cylinder engine testing, experimental resources are limited. For this reason, a well-structured approach is required in order to efficiently determine the knock tendency. This study presents a method for predicting the engine knock probability of an operating point based on a limited amount of measurement data. A regression model is built that describes the (empirical) knock probability as a function of knocking-relevant control variables and additional relevant engine operating parameters. The required training data is generated from engine measurements that also determine the parameter space limits of knocking-relevant control variables such as ignition timing or charge air pressure. Eventually, this model allows prediction of the knock probability of operating points that are not studied during the engine tests. The presented method is verified by multiple engine tests on a large single-cylinder engine fueled with natural gas or hydrogen. The high prediction accuracy of the empirical knock probability for unseen points demonstrates the potential benefit of the approach. Since it is not tied to a specific engine size or type, this method can be used in the design process of other engines as well.

**Keywords**
large internal combustion engine, knock probability, zero-inflated beta regression,
engine design process

## 1. Introduction

Increasing efficiency and consequently reducing $CO_2$ emissions are two of the main research objectives in the development of internal combustion engines (ICEs). Thus, high-load operating points with high compression ratios are becoming increasingly important. However, these conditions significantly promote “knocking combustion,” which refers to an abnormal combustion event in spark-ignited (SI) ICEs due to auto-ignition of the in-cylinder end gas before the flame front reaches it. It can lead to serious damage to the engine from high-frequency pressure oscillations and propagating shock waves. Since the suppression of knocking combustion usually results in efficiency losses, comprehensive research that aims to understand, accurately detect and predict this phenomenon has been carried out over the last few decades as summarized in the review of Wang et al. [1].

The accurate detection of engine knocking with a focus on engine monitoring and control is essential to ensure optimal performance by preventing potential damage. Many common knock detection algorithms implemented in today’s engine control architectures are based on threshold methods [2,3]. These methods use distinct knock intensity measures such as the maximum amplitude pressure oscillation (MAPO) or the signal energy pressure oscillation (SEPO) criterion to label an engine cycle as knocking or non-knocking if a predefined threshold value is exceeded [4]. Although the use of these approaches is straightforward, significant calibration effort is required to cover the entire range of knock-relevant engine operating conditions. Recent research activities have focused on incorporating machine learning (ML) methods to enhance the detection of knocking cycles and potentially enable their forecast. Due to the complex nature of the phenomenon and the vast array of influencing factors, ML offers a sophisticated approach to enhance the understanding of knocking combustion in SI ICEs and the capability to predict it. Aramburu et al. [5] applied two different ML techniques to classify combustion cycles of a heavy-duty engine based on knock sensor signals. After the data was processed by applying a short-time Fourier transform, a one-class support vector machine representing an unsupervised ML method and a convolutional neural network (CNN) representing a supervised ML method were used for classification. By comparing the results with in-cylinder MAPO criteria, the authors reported that these methods are able to detect knocking cycles successfully and allow the evaluation of sensor position sensitivity. Similar work was conducted by Pla et al. [6]. Kefalas et al. [7] combined continuous wavelet transformation and CNN to develop a generalized knock detection method. They classified the engine cycles using a 2D-CNN on scalograms representing the energy spectrum of the in-cylinder pressure. The comparison of ML model results to expert labeled data from different engine configurations yielded high agreement. In a similar study by Ofner et al. [8], the in-cylinder pressure trace was directly fed into a 1D-CNN to classify knocking and non-knocking engine cycles. The kernel size of the first CNN layer was adapted to take into account the resonance frequency of the investigated engine. Their results revealed high accuracy compared to basic threshold-based methods and furthermore indicated the advantage of this approach in terms of generalization across different engine types. Cho et al. [9] used a deep neural network that processes the in-cylinder pressure directly to predict the knock onset (i.e., the timepoint when knocking begins). The results of the ML method were compared to manually labeled data that showed satisfactorily results. Common deterministic control strategies for keeping engine knock at an acceptable level adapt the spark timing if a knock event is observed by delaying it and then advance again it for engine efficiency improvement until the next knocking cycle occurs [3]. Since this approach is inflexible and inefficient and does not account for any stochastic behavior of the knock phenomenon, advanced approaches have been explored. Selmanaj et al. [10] developed a control strategy based on a logarithmic increase in the spark timing after a knocking cycle combined with additional parameters representing stochastic information. Their advanced control method outperformed conventional deterministic strategies in both simulation and experimental tests. Maldonado et al. [11] investigated the application of ML methods, specifically artificial neural networks, for the in-cycle prediction of knocking events. Since the desired prediction of knocking events would be at least at spark timing to allow control actions for the current cycle, the authors also explored in-cylinder data from the previous cycle until ignition timing of the current cycle. The results indicated that the information content in this signal range is not sufficient for predicting engine knock accurately. Thus, the authors concluded that cycle-to-cycle knock event prediction is unlikely. This is underlined by the investigations of Ghandhi and Kim [12], who conducted a statistical analysis of the knock intensity of three engine cycles sharing the same thermochemical time history. They came to the conclusion that engine knock is not uniquely defined by the time history of the end gas, which reflects the random nature of this phenomenon.

In contrast to the cycle-based knock detection methods outlined above, Zhao and Shen [13] proposed a statistical knock control method based on a Bayesian knock probability estimation in which the logarithm of the knock intensity is assumed to follow a normal distribution. The authors argued that the use of knock intensity in combination with probability estimation yields advantages for knock control since information is provided of how far the current control settings are from knock borderline conditions, which is not the case for binary knock event signals. Similarly, Zhao et al. [14] proposed a control approach that targets the knock probability estimation based on binary knock event signals determined by a knock intensity threshold. Their study uses a beta distribution as the initial probability distribution for the Bayesian probability estimation method. Based on this approach, Zhao and Shen [15] developed a map learning procedure (spark advance and TA throttle angle) that describes knock probabilities with uncertainties for determining the next engine operating points during test bed operation.

Compared to these methods that focus on online knock controls, the method proposed in the present study aims to predict the knock probability as a function of knocking-relevant control variables and additional relevant engine operating parameters. Such a model could help engineers to efficiently research and design new ICE configurations or combustion concepts. Given the underlying knock probability properties, a so-called zero-inflated beta regression is applied. This approach permits the modeling of the knock probability over the entire engine operation range from a limited number of operating points. The proposed method has been tested on two different large engine configurations operated by natural gas and hydrogen, respectively, and yielded satisfactorily results.

## 2. Methodology

### 2.1 Knock determination

The most common time-domain method for characterizing engine knock events employs the MAPO criteria. The MAPO value describes the maximum amplitude of the high- or band-pass filtered in-cylinder pressure on a cyclic base given by

$$MAPO := \max(p_{filt}),$$

where the filtering of the pressure trace allows the elimination of the low-frequency content of the signal related to compression and standard flame propagation [4]. In order to classify a combustion cycle as knocking or non-knocking, the threshold value exceed method is applied. For the MAPO value of a single combustion cycle, this can be noted as the indicator function

$$\mathbf{1}_{MAPO \geq MAPO_{crit}} := \begin{cases} 1, & if\ MAPO \geq MAPO_{crit} \\ 0, & if\ MAPO < MAPO_{crit} \end{cases},$$

where $MAPO_{crit}$ denotes the threshold value. Since the definition of such a threshold strongly depends on various factors such as engine type and operation, specific domain knowledge is required.

During the engine design process supported by engine tests, the focus is usually not on single-cycle phenomena but rather on entire engine operating points (OPs). In order to evaluate the knock tendency of an OP, the empirical knock probability is considered. For $i = 1, \dots, n$ OPs, the empirical knock probability of OP $i$ $P'_i$ is given by

$$P'_i = \frac{number\ of\ knocking\ cycles\ observed\ for\ OP\ i}{total\ number\ of\ cycles\ from\ OP\ i} = \frac{\sum_{j=1}^{n_i} \mathbf{1}_{MAPO_j \geq MAPO_{crit}}}{n_i},$$

where $n_i$ denotes the number of cycles observed with OP $i$. The empirical knock probability of OP $i$ strongly depends on certain engine operating parameters, $x_{i1}, \dots, x_{ip}$, that represent knocking-relevant engine control variables and additional relevant parameters. This set of engine operating parameters inherently depends on the investigated engine configuration and combustion concept. Nevertheless, it is possible in principle to describe this relationship using a regression approach that models the (empirical) knock probability as a function of the engine operating parameters (also features)—even with a limited amount of measurement data available. Since test bed time is often limited in practice, such a model would allow an engineer to predict the (empirical) knock probability of new/unseen OPs.

### 2.2 Knock probability model

In theory, $P'_i \in [0,1]$, i.e., zero to all cycles of OP $i$ knock. In practice, it is usually sufficient to assume that not every cycle of OP $i$ knocks, $P'_i \in [0,1)$, i.e., to neglect highly unwanted OPs. A suitable data-driven approach is required in order to build a proper regression model for a dependent variable (also response or target) such as the knock probability.

The so-called beta regression [16,17] is a well-established statistical regression method that assumes that the target variable follows a beta distribution. The beta distribution is a very flexible distribution with two parameters, but it is only defined on the open interval $(0,1)$. To model OPs without a knocking cycle, an extension of the beta distribution, the so-called zero-inflated beta distribution, and its corresponding regression variant [18] can be applied, where the probability at zero is additionally modeled via a third parameter. Fig. 1 illustrates some of the potential shapes of the beta distribution and the zero-inflated beta distribution. Formulated as a so-called generalized additive model for location, scale, and shape (GAMLSS) [19], the three parameters of the zero-inflated beta regression can be flexibly modeled using the model features [18], i.e., the engine operating parameters. The mathematical details of the zero-inflated beta regression and its GAMLSS-based R implementation can be found in [18] and [20–23], respectively. In the present study, the default preferences of the GAMLSS R implementation for the zero-inflated beta regression are used, with the model formula later specified in each investigation used for both the beta regression and the zero-inflated component of the overall model.

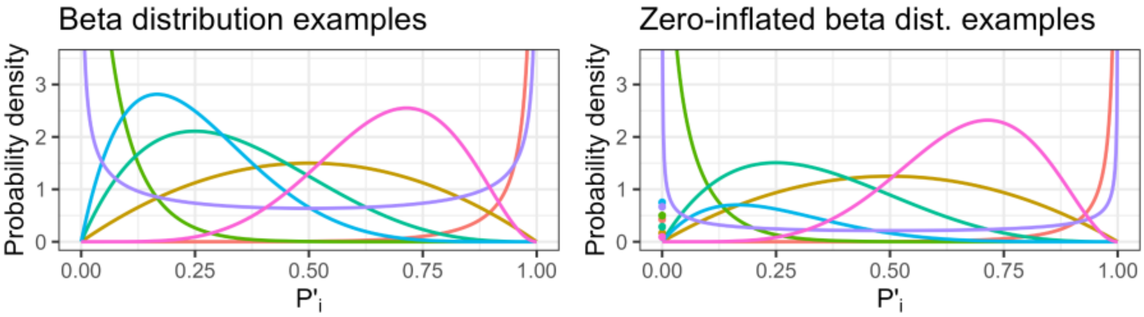

**Fig. 1.** Examples of beta distribution and zero-inflated beta distribution shapes

In summary, the knock probability model represents the empirical knock probabilities $P'_i$ of all considered operating points $i = 1, .. n$, jointly with a zero-inflated beta regression model in which the engine operating parameters $x_{i1}, \ldots, x_{ip}$, $i = 1, \ldots, n$, serve as model features. Depending on which data basis is considered, the regression model formula concerning the features (i.e., the right-hand side of the regression model formula) can be adapted.

One critical aspect of developing data-driven methods is model validation. Since the number of OPs available is rather small for both investigated large engine configurations, the model performance is evaluated on unseen data using a so-called leave-one-out cross-validation (LOOCV). With this resampling method, iteratively $n - 1$ OPs are used for model building while the remaining OP serves for validation. Thus, essentially $n$ different models (using the identical model structure) are fit. The LOOCV reflects the situation in which a certain OP would not have been measured during experimental investigations in a straightforward way—for whatever reason.

### 2.3 Experimental data

The data for the development of the knock probability model were obtained through experimental investigations on a single-cylinder research engine (SCE) at the Large Engine Competence Center (LEC) in Graz, Austria. Two different engine configurations operated by natural gas (available from the public gas network) and hydrogen, respectively, are considered. Although knocking was not the primary reason for these studies, the data collected is very well suited to demonstrate the approach presented for modeling the (empirical) knock probability.

Both configurations were investigated on the same SCE, which is a direct ignited high-speed large bore gas engine. In each case, a lean burn, high swirl combustion concept with Atkinson cam timing and a bowl-in piston was employed. All tests were carried out at a nominal engine speed of 1500 rpm. Table 1 shows the specifications and characteristics of the engine used. A more detailed description of the engine layout and test bed infrastructure is found in [24]. State-of-the-art equipment for crank-angle resolution and time-based measurements was used for data acquisition. [24] describes the data acquisition system in detail. A Venturi gas mixer located well upstream of the cylinder head provided the most homogeneous mixture of fuel gas and combustion air in the combustion chamber for the experimental investigations. The test bed infrastructure included a multicomponent gas mixer, which supplied fuel gases of different gas qualities indicated by the methane number (MN) of the fuel gas. The multicomponent mixer allows the supply of fuel gases with methane numbers between zero (pure hydrogen) and 100 (pure methane).

**Table 1.** Technical specifications of the research engine for the natural gas and hydrogen investigations

| | Natural gas investigations | Hydrogen investigations |
|---|---|---|
| Displacement | 3 dm³ | |
| Bore | 145 mm | |
| Stroke | 185 mm | |
| Nominal engine speed | 1500 min$^{-1}$ | |
| Compression ratio | 11.8 | |
| Number of inlet/exhaust valves | 2/2 | |
| Charge air conditioning | SCE charge air supply with pressure up to 10 bar (external compressor); compressed air dehumidified; water from a steam generator added to the dry air to obtain the desired humidity | |
| Balance of inertia forces | Four balancing shafts to compensate for first and second-order inertia forces | |

### 2.3.1 Natural gas investigations

The engine measurements with natural gas were principally performed with the goal of obtaining simulation data for advanced three-dimensional computational fluid dynamics (CFD) simulation analysis. Engine test bed operation usually specifies engine load, emission levels and variations thereof, and the result is the required fuel mass fraction (air excess ratio), ignition timing, and pressures at intake and exhaust. However, this approach is suboptimal for CFD since engine load and emission levels are results of these simulations. Thus, the measurement campaign focused on variations in ignition timing (IT), excess air ratio (λ), and pressure levels at intake (p2) and exhaust (p3) so that engine load and emissions become results, not input. In addition, data were generated for lean-limit operation and knock-limit operation. Indicated mean effective pressures (IMEP) of 12–24 bar and $NO_x$ emissions of 250–5000 mg/Nm³ were investigated. A total of 230 different OPs are available for modeling the knock probability. For each OP, 608–800 consecutive cycles were observed and the empirical knock probabilities were calculated. The following parameters/features are considered for building the regression model: IT, λ, p2, (p2−p3), and MN. Fig. 2 shows the observed distributions of the empirical knock probability and the features.

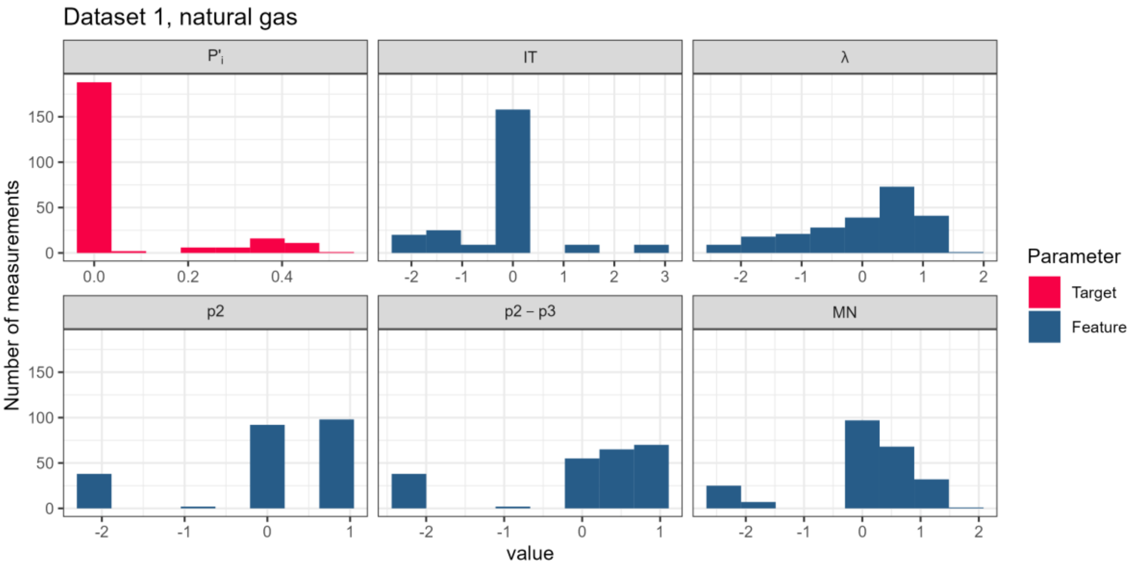

**Fig. 2.** Dataset 1: Data from natural gas SCE investigations (feature values are shown on a standardized scale)

### *2.3.2 Hydrogen investigations*

The experimental investigations with pure hydrogen were carried out with the objective of identifying the operating limits of the engine using existing hardware components of a natural gas combustion concept (identical to the hardware used for the natural gas investigations). Even with the most homogeneous cylinder charge possible, sporadic intake manifold deflagration occurred when the engine was operated on pure hydrogen. To ensure consistent boundary conditions, dehumidified combustion air was used for the hydrogen measurements as the intake manifold deflagrations made it impossible to measure and therefore control the humidity of the combustion air. The hydrogen measurement database mainly in-cludes variations in the excess air ratio at different ignition timings and loads. The excess air ratio was progressively varied within the knock and misfiring limits. In order to obtain robust results, the hydrogen measurement campaign varied only one engine operation parameter at a time. The dataset considered for modeling the knock probability corresponds to IMEP values of 10–13 bar and consists of 105 OPs that were each observed for 100 to 400 cycles. Similarly to the natural gas data, the following parameters/features are considered in the building of the regression model: IT, λ, p2. The observed distributions of the empirical knock probability and the features are shown in Fig. 2.

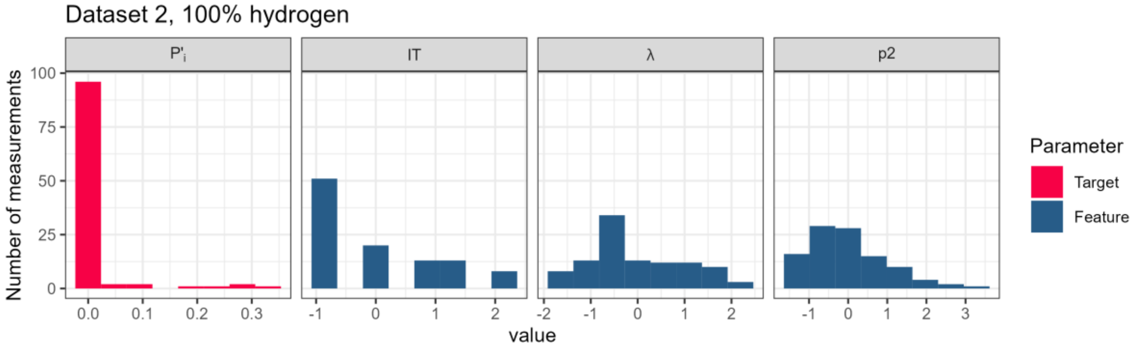

**Fig. 3.** Dataset 2: Data from hydrogen SCE investigations (feature values are shown on a standardized scale)

## 3. Results and Discussion

For both datasets, the modeling results from the LOOCV are evaluated as follows:

1. The classification accuracy as to whether a validated OP knocks or not ($P'_i > 0$ vs. $P'_i = 0$) is analyzed using a class assignment contingency table (also called the confusion matrix) and the Matthews correlation coefficient (MCC) [25] of all validations is calculated. The MCC ranges from -1 to 1, where an MCC of 0 indicates random class assignment and MCCs of -1 and 1 indicate perfect negative and perfect positive correlation, respectively.
2. For truly knocking OPs or those that are wrongly predicted as knocking (cf. Step 1.), the prediction accuracy of $P'_i$ is analyzed graphically using a scatterplot and with the root mean squared error (RMSE) of the predicted and actual target values (i.e., the empirical knock probability).

### 3.1 Natural gas investigations

The empirical knock probability of the natural gas investigations is modeled by applying a model structure/formula that contains each feature as a linear effect. All two-way interactions of λ, p2, (p2−p3), and MN are also modeled. As the confusion matrix in Table 2 shows, this modeling approach is able to correctly classify almost all OPs in the course of the LOOCV. This is also represented by the very high MCC of 0.971. Both wrongly classified OPs either have a very low observed/true empirical knock probability or the model predicts a very low knock probability.

**Table 2**. Confusion matrix of knock class predictions for dataset 1, natural gas

| | | OP predicted knocking | |
|---|---|---|---|
| | | False | True |
| OP truly knocking | False | 186 | 1 |
| | True | 1 | 42 |

As shown in Fig. 4, the modeling approach is capable of predicting the actual empirical knock probabilities during the LOOCV with sufficient accuracy. These results correspond to a RMSE of 0.0299. Given the stochastic nature of the knocking phenomenon, such accuracy in predicting the knocking probability of new OPs is more than sufficient. Therefore, the potential benefit of the approach presented in this study for the natural gas investigations is clearly demonstrated.

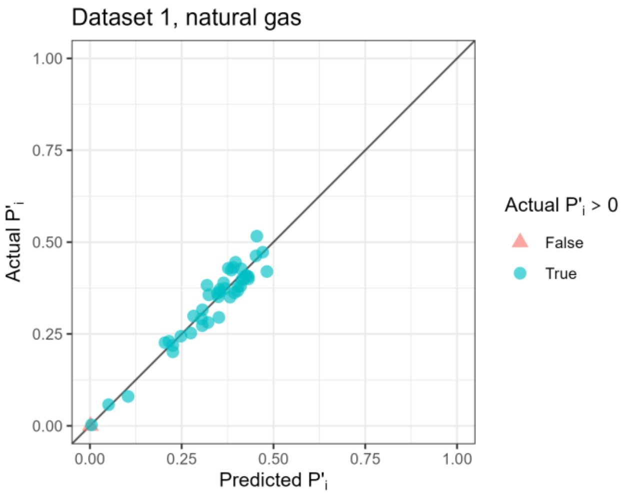

**Fig. 4.** Actual versus predicted empirical knock probability for dataset 1, natural gas

### 3.2 Hydrogen investigations

The empirical knock probability of the hydrogen investigations is modeled by applying a model structure/formula that contains each feature as a linear effect. All two-way interactions of IT, λ, and p2 are also modeled. As the confusion matrix in Table 3 shows, this modeling approach is able to correctly classify almost all OPs in the course of the LOOCV. Compared to the natural gas investigations, slightly more OPs are wrongly classified. Therefore, the MCC of the LOOCV results equals 0.740. Nevertheless, this demonstrates the overall high accuracy of the knock class predictions. Again, the five OPs that are incorrectly predicted as not knocking have a very low observed/true empirical knock probability.

**Table 3**. Confusion matrix of knock class predictions for dataset 2, 100% hydrogen

| | | OP predicted knocking | |
|---|---|---|---|
| | | False | True |
| OP truly knocking | False | 86 | 2 |
| | True | 5 | 12 |

Fig. 5 shows the results of predicting the actual empirical knock probabilities during the LOOCV. Compared to the natural gas results, there is more scatter visible, which also yields a higher RMSE of 0.0813. Nevertheless, the results indicate the basic ability of the modeling approach to correctly describe the knock probability based on engine operating parameters. Due to the stochastic nature of the knocking phenomenon, the considerably fewer cycles per OP observed for the hydrogen investigations may already introduce a higher uncertainty in the "true" empirical knock probabilities. Even though the predictions for the unseen OPs are not as accurate as in the natural gas investigations, the prediction accuracy observed seems to be sufficient to support the engine design process, yet again demonstrating the potential benefit of this approach.

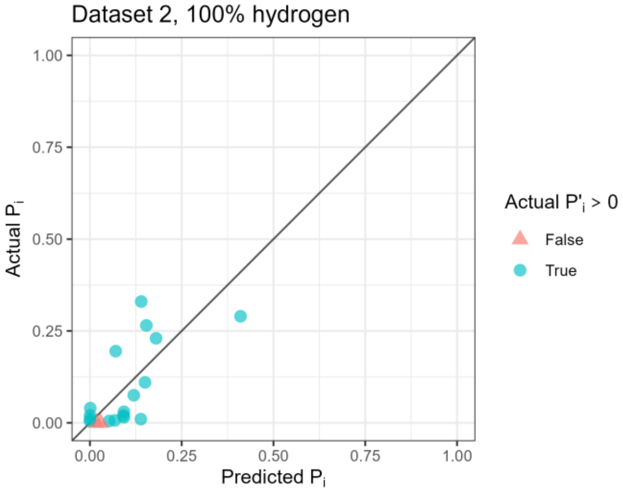

**Fig. 5.** Actual versus predicted empirical knock probability for dataset 1, 100% hydrogen

## 4. Summary and Conclusions

This study presents an approach to modeling the (empirical) knock probability of an engine OP using a zero-inflated beta regression. This approach allows direct modeling of the knock probability of non-knocking OPs (probability equals zero). Validation of the approach and results was based on data from two different combustion concepts investigated on a large-bore SCE research engine. While the regression model for natural gas operation relied on ignition timing, excess air ratio, pressure levels at intake and exhaust, and methane number, the regression model for 100% hydrogen operation involved ignition timing, excess air ratio, and pressure level at intake. In both application cases, the approach provided accurate results and thus can be considered a valuable support during the engine design process. The GAMLSS representation of the zero-inflated beta regression modeling approach allows flexible modeling of the empirical knock probability and customized solutions for other combustion concepts or datasets. The approach has been used post hoc with data obtained mainly for other research reasons. Eventually, knock relevant control variables and additional relevant engine operating parameters could be employed in a design of experiments approach in conjunction with the presented modeling approach. In this way, the knocking tendency of OPs can be specifically modeled and investigated on the basis of a few characteristic engine operating parameters.

## References

[1] Z. Wang, H. Liu, R.D. Reitz, Knocking combustion in spark-ignition engines, Progress in Energy and Combustion Science 61 (2017) 78–112. https://doi.org/10.1016/j.pecs.2017.03.004.

[2] J.C. Peyton Jones, J.M. Spelina, J. Frey, Optimizing knock thresholds for improved knock control, International Journal of Engine Research 15 (2014) 123–132. https://doi.org/10.1177/1468087413482321.

[3] P. Bares, D. Selmanaj, C. Guardiola, C. Onder, A new knock event definition for knock detection and control optimization, Applied Thermal Engineering 131 (2018) 80–88. https://doi.org/10.1016/j.applthermaleng.2017.11.138.

[4] A.J. Shahlari, J.B. Ghandhi, A Comparison of Engine Knock Metrics, in: 2012: pp. 2012-32–0007. https://doi.org/10.4271/2012-32-0007.

[5] A. Aramburu, C. Guido, P. Bares, B. Pla, P. Napolitano, C. Beatrice, Knock detection in spark ignited heavy duty engines: An application of machine learning techniques with various knock sensor locations, Measurement 224 (2024) 113860. https://doi.org/10.1016/j.measurement.2023.113860.

[6] B. Pla, J. De La Morena, P. Bares, A. Aramburu, An unsupervised machine learning technique to identify knock from a knock signal time-frequency analysis, Measurement 211 (2023) 112669. https://doi.org/10.1016/j.measurement.2023.112669.

[7] A. Kefalas, A.B. Ofner, G. Pirker, S. Posch, B.C. Geiger, A. Wimmer, Detection of Knocking Combustion Using the Continuous Wavelet Transformation and a Convolutional Neural Network, Energies 14 (2021) 439. https://doi.org/10.3390/en14020439.

[8] A.B. Ofner, A. Kefalas, S. Posch, B.C. Geiger, Knock Detection in Combustion Engine Time Series Using a Theory-Guided 1-D Convolutional Neural Network Approach, IEEE/ASME Trans. Mechatron. 27 (2022) 4101–4111. https://doi.org/10.1109/TMECH.2022.3144832.

[9] S. Cho, J. Park, C. Song, S. Oh, S. Lee, M. Kim, K. Min, Prediction Modeling and Analysis of Knocking Combustion using an Improved 0D RGF Model and Supervised Deep Learning, Energies 12 (2019) 844. https://doi.org/10.3390/en12050844.

[10] D. Selmanaj, G. Panzani, S. Van Dooren, J. Rosgren, C. Onder, Adaptive and Unconventional Strategies for Engine Knock Control, IEEE Trans. Contr. Syst. Technol. 27 (2019) 1838–1845. https://doi.org/10.1109/TCST.2018.2827898.

[11] B. Maldonado, B. Kaul, J. Szybist, Artificial Neural Networks for In-Cycle Prediction of Knock Events, in: 2022: pp. 2022-01–0478. https://doi.org/10.4271/2022-01-0478.

[12] J. Ghandhi, K.S. Kim, A Statistical Description of Knock Intensity and Its Prediction, in: 2017: pp. 2017-01–0659. https://doi.org/10.4271/2017-01-0659.

[13] K. Zhao, T. Shen, Normal-gamma distribution–based stochastic knock probability control scheme for spark-ignition engines, Proceedings of the Institution of Mechanical Engineers, Part D: Journal of Automobile Engineering 234 (2020) 1986–2000. https://doi.org/10.1177/0954407019872649.

[14] K. Zhao, Y. Wu, T. Shen, Beta-Distribution-Based Knock Probability Estimation, Control Scheme, and Experimental Validation for SI Engines, IEEE Trans. Contr. Syst. Technol. 29 (2021) 918–925. https://doi.org/10.1109/TCST.2020.2980799.

[15] K. Zhao, T. Shen, Beta distribution-based knock probability map learning and spark timing control for SI engines, Proceedings of the Institution of Mechanical Engineers, Part D: Journal of Automobile Engineering 235 (2021) 1902–1919. https://doi.org/10.1177/0954407020983208.

[16] R. Kieschnick, B.D. McCullough, Regression analysis of variates observed on (0, 1): percentages, proportions and fractions, Statistical Modelling 3 (2003) 193–213. https://doi.org/10.1191/1471082X03st053oa.

[17] S. Ferrari, F. Cribari-Neto, Beta Regression for Modelling Rates and Proportions, Journal of Applied Statistics 31 (2004) 799–815. https://doi.org/10.1080/0266476042000214501.

[18] R. Ospina, S.L.P. Ferrari, A general class of zero-or-one inflated beta regression models, Computational Statistics & Data Analysis 56 (2012) 1609–1623. https://doi.org/10.1016/j.csda.2011.10.005.

[19] D.M. Stasinopoulos, R.A. Rigby, Generalized Additive Models for Location Scale and Shape (GAMLSS) in *R*, J. Stat. Soft. 23 (2007). https://doi.org/10.18637/jss.v023.i07.

[20] R.A. Rigby, D.M. Stasinopoulos, Generalized Additive Models for Location, Scale and Shape, Journal of the Royal Statistical Society Series C: Applied Statistics 54 (2005) 507–554. https://doi.org/10.1111/j.1467-9876.2005.00510.x.

[21] R.A. Rigby, M.D. Stasinopoulos, G.Z. Heller, F. De Bastiani, Distributions for Modeling Location, Scale, and Shape: Using GAMLSS in R, 1st ed., Chapman and Hall/CRC, 2019. https://doi.org/10.1201/9780429298547.

[22] M.D. Stasinopoulos, R.A. Rigby, G.Z. Heller, V. Voudouris, F.D. Bastiani, Flexible Regression and Smoothing: Using GAMLSS in R, 1st ed., Chapman and Hall/CRC, 2017. https://doi.org/10.1201/b21973.

[23] R: The zero-inflated beta distribution for fitting a GAMLSS, (n.d.). https://search.r-project.org/CRAN/refmans/gamlss.dist/html/BEZI.html (accessed April 10, 2024).

[24] A. Tilz, C. Kiesling, G. Meyer, A. Nickl, G. Pirker, A. Wimmer, Experimental investigation of the influence of ignition system parameters on combustion behavior in large lean burn spark ignited gas engines, Experimental Thermal and Fluid Science 119 (2020) 110176. https://doi.org/10.1016/j.expthermflusci.2020.110176.

[25] J. Gorodkin, Comparing two K-category assignments by a K-category correlation coefficient, Computational Biology and Chemistry 28 (2004) 367–374. https://doi.org/10.1016/j.compbiolchem.2004.09.006.

# Multi-Stage ECMS Considering Engine Dynamics and Start/Stop Strategy for Real-Time Application in Hybrid Electric Vehicles

A. Reig, G. Mancini, F. Mazza

RSEngineering Srl, Via Nazionale 12, Maranello, Italy.

E-mail: alberto.reig@rsengineering.org

**Abstract.** Equivalent Consumption Minimisation Strategy (ECMS) is a popular algorithm to determine the optimal blending between internal combustion engine and electric motors torque contribution on a hybrid electric vehicle. Given that it is a realisation of the Pontryagin Minimum Principle, it condenses driving mission's a priori information into one single factor, avoiding any need of detailed predictions. This allows real-time implementation, making ECMS the only pure optimal control strategy that can be realistically implemented onboard a real-life vehicle. Despite this advantage, ECMS is natively based on very simplified powertrain models with limited representation of its dynamics, it lacks the impact of transients on fuel efficiency, and misses the drivability factor on an ECMS-based vehicle.

This paper proposes a strategy to address these weaknesses in a hybrid electric vehicle featuring a spark ignited (SI) engine in two ways. On the one hand, the control problem is divided in three stages, each of them controlling a single feature of the powertrain with a dedicated ECMS implementation. These three features are: torque split target by actuating engine throttle, engine ignition retardation, and engine start/stop command. Motor torque requests are also coordinated within ECMS algorithms. Powertrain components feedback provides both a link between these three ECMS modules and align-ment with current powertrain conditions. On the other hand, the minimum search algorithm on ECMS cost function considers both engine dynamic response and vehicle dynamic constraints to guarantee consistent drivability.

The presented strategy has been implemented as core hybrid strategy in the vehicle control unit of a production vehicle. This strategy has been proven lighter and more accurate in terms of candidates' selection than conventional ECMS implementations, plus being fully real-time capable. The algorithm has been tested in different environments such as hardware- and driver-in-the-loop and, in all cases, it controlled the torque split in a smoother manner, respecting dynamic constraints, and reducing the num-ber of start/stop events, while providing charge sustaining operation and a near-optimal fuel economy.

## 1. Introduction

Since several decades ago, hybrid electric vehicles (HEV) have been one of the few alternatives to conventional engine-powered vehicles, and the natural step towards full electric powertrains [1]. Moreover, in the last years it has become a widely popular choice for both manufacturers and drivers [2] for a number of reasons: certain advantages in driving restrictions within populated areas thanks to their lower level of emissions [3], competitive price compared to electric vehicles due to the use of smaller batteries [4], and ride smoothness among many others.

The combined use of batteries, motors and an internal combustion engine brings many advantages as those mentioned above, but it increases the powertrain complexity and the possibilities to operate the multiple powertrain components at different modes to achieve the torque requested by the driver. In order to manage engine and motors operation, HEVs require complex and sophisticated control systems that coordinate and dictate what each component must do during driving. HEVs can maximise engine efficiency by performing load shift (blend engine and motors torque to shift engine operating point to a better efficiency one), and plug-in HEVs (PHEV) can also enjoy better figures by alternating hybrid and pure electric operation. But these efficiency gains strongly depend on the adequate combi-nation of electrical and thermal blending since an ineffective control can even worsen efficiency and emissions figures of a traditional engine-only powertrain [5]. The set of algorithms and strategies that dictate how much each component shall contribute to total powertrain torque over time make up the energy management strategy of a HEV/PHEV.

In general, there are two main types of energy strategies: rule-based, and model-based [6]. The first family rely on a complex set of empirical rules to dictate operating points, often based on experience or intensive calibration effort. The second family makes use of simplified models of part of the powertrain to somewhat estimate the most beneficial operating point based on physics and first principles. There are some model-based strategies that make use of mathematical optimisation techniques as well, to exploit those models and find minimum-cost operating conditions [7]. Among these optimal control strategies, one of the most common in HEV control is known as Equivalent Fuel Consumption Strategy (ECMS) [8], or in control theory terms, a realisation of Pontryagin Minimum Principle (PMP) [9].

ECMS benefits of a simple cost function definition and the condensation of lookahead information into a single energy factor, to find the engine/motors blending that minimises fuel consumption on any driving cycle. These facts facilitate the implementation of ECMS as an on-board, on-line, real-time capable, optimisation algorithm to control a hybrid powertrain [10].

However, ECMS has several weaknesses: flickering of solution [11] (especially in systems showing flat cost functions), lack of states beyond battery state of charge (SOC) [12], or absence of a formal method to estimate its co-state or energy factor [13]. Many studies in existing literature have addressed some of these issues, proposing adaptive strategies to estimate co-states [14], learning geo-located driving behaviour [15], predicting conditions over a certain horizon [16], or addressing the energy management analytically [17]. But many times, the classic methodology limits the possibility to apply ECMS in a production-intent control software.

This paper proposes a particular implementation of ECMS by applying its optimisation algorithm in three stages. The objective of this methodology is to provide a control structure capable of managing a real-world powertrain in a production software environment, satisfying certain requirements (such as drivability, ride comfort, durability, safe component operation, integration with other systems and interventions, ease of calibration) and, at the same time, basing the torque split in an optimisation algorithm that permits to operate the powertrain as efficiently as possible.

## 2. Multi-stage ECMS strategy

The Equivalent Consumption Minimisation Strategy (ECMS) is a model-based control algorithm widely used in literature to solve the energy management problem of a hybrid electric vehicle (HEV) [8], or in other words, to decide the torque split between engine and electric motors. Since ECMS is a particular application of the Pontryagin Maximum Principle (PMP) [9], it guarantees that the resulting torque split is optimal from a fuel consumption point of view, as long as certain problem convexity requisites are met [18].

ECMS is based on a simplified powertrain model where engine and motors operate in a quasi-steady fashion, and the only state of the system is the battery state of charge (SOC). ECMS defines the Hamiltonian cost function:

$$H = P_f + \mu \cdot P_b \tag{1}$$

where $P_f$ is the chemical power of the fuel burnt by the engine during one calculation step, $P_b$ the internal power delivered by the battery chemicals during over the same calculation step, and $\mu$ a constant energy factor, generally known as co-state, which is equivalent to the Lagrangian multiplier found in PMP theory [19]. ECMS aims to minimise total fuel consumption over a driving mission by evaluating the Hamiltonian function at regular calculation steps, and finding the torque split that minimises it at each step:

$$\hat{u} = \underset{u}{\operatorname{argmin}}\{H\} = \underset{u}{\operatorname{argmin}}\{P_f(u) + \mu \cdot P_b(u)\} \tag{2}$$

In this paper, engine torque $M_{ice}$ is chosen as the control variable $u$. Engine fuel consumption $\dot{m}_f$ is calculated by interpolating on a fuel consumption map $\dot{m}_f(\omega_{ice}, M_{ice})$. Similarly, total electrical power consumption at the DC bus $P_e$ is estimated, first by calculating the total electrical torque needed to follow the driver demand $M_{drv}$ including driveline losses, and then by adding motor and inverter power losses by interpolating on their corresponding losses map. Once the total electrical power is known, the internal battery power is calculated by solving an equivalent circuit consisting of an ideal battery and a resistor in series:

$$P_b = \frac{V_{oc}^2 - V_{oc}\sqrt{V_{oc}^2 - 4RP_e}}{2R} \tag{3}$$

with $R$ the internal resistance of the battery, taking different values for charge and discharge currents, and $V_{oc}$ the open circuit voltage of the battery. Both $R$ and $V_{oc}$ are calculated as a function of SOC.

The co-state can be calculated in many ways, such as using a PI controller [20], with a prediction of future driving conditions [16], or by learning from past drives among others [15]. Theoretically, μ shall be a constant calibrated to a value that allows achieving the desired final SOC value, but due to the uncertainty about the driver requests to come, some form of closed loop controller is needed. Since there are several methods already analysed in literature and the μ algorithm is not part of the scope of this paper, for the sake of simplicity, a PI-based controller is used in this work. A more elaborated μ controller may produce a steady-state torque split slightly closer to optimum, but the presented methodology and its benefits are completely independent of the accuracy on the μ estimation.

ECMS quasi-steady models are limited in the way they can represent powertrain and engine dynamics due to its mandatory simplifications. Typically, this leads to several issues such as flickering of optimal engine operating point or frequent and aggressive changes of torque [11], since transient cost, emissions increase, and discomfort are not considered in the algorithm. ECMS solution could be post-processed and filtered downstream as a workaround, but this would relegate ECMS to act as a supervisor with reduced authority and its optimality would vanish as its solutions gets manipulated.

In order to avoid the above issues, this paper presents an alternative application of ECMS by using three ECMS optimisers in parallel. Spark-ignited engines show two well differentiated dynamics, controlled by different actuators [21]: dynamics of the airpath, mainly driven by the actuation of the throttle position, also called slow-path, and dynamics of the in-cylinder combustion, controlled by the ignition timing, also named the fast-path. While both paths show significantly different time constants, the two can be seen as quasi-steady processes at their own time scale. The last control path that requires control is the pure electric configuration of the powertrain, i.e. when engine is shut down. While pure electric driving may not benefit of classic ECMS control due to the lack of additional degrees of freedom, ECMS does help to estimate the best sequence of hybrid (engine running) and electric (engine stopped) phases during a driving mission. Therefore, the three parallel ECMS optimisers are:

- Throttle stage (slow-path): it operates on the slow dynamics of the engine. Controls the throttle position and acts as a long-term, slow dynamics, optimiser. It sets the desired steady state setpoints of the powertrain components.
- Ignition timing stage (fast-path): it works on the fast dynamics of the engine. Controls the ignition timing and operates based on the current airpath conditions. It chooses the optimum ignition retardation, including the possibility to go in fuel cut-off.
- Running mode stage: it evaluates an ECMS optimiser on the pure electric operation the powertrain to decide the optimum running mode of the powertrain, i.e. engine running, or engine stopped.

The presented multi-stage ECMS (MS-ECMS) strategy allows accounting for spark-ignited engine dynamics as well as drivability and ride comfort, while still exploiting ECMS optimal characteristics. A descriptive diagram of the three stages is presented in figure 1. Further details on each of the three optimisation stages are given in the next section.

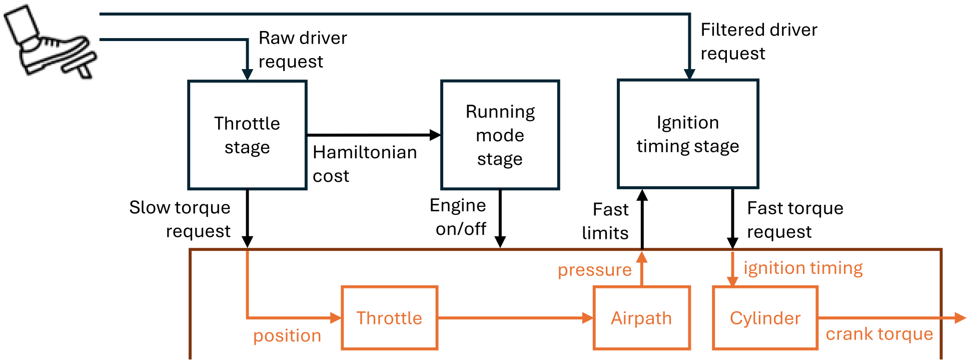

**Fig. 1.** Diagram showing the layout of the MS-ECMS optimiser, with its three stages and interface with the engine

## 3. Dynamics and drivability on the minimum search

All stages of ECMS optimisers, as described below, are constrained to operate within a space of feasible solutions, by respecting engine limits as communicated by the engine management system (EMS):

$$\underline{M}_{ice} \leq M_{ice} \leq \overline{M}_{ice} \tag{4}$$

motor limits published by inverters:

$$\underline{M}_{m} \leq M_{m} \leq \overline{M}_{m} \tag{5}$$

battery limits calculated at the battery management system (BMS):

$$\underline{P}_{b} \leq P_{b} \leq \overline{P}_{b} \tag{6}$$

and external interventions (such as a gear shift intervention), which generally apply as an additional EMS limitation. Solution candidates exceeding any of the above limits are rejected during the minimum search process.

Driver demand is the total torque that the entire powertrain shall be generated at the wheels:

$$M_{drv} = M_{ice} \cdot R_{ice} + \sum_{i} M_{m,i} \cdot R_{m,i} \tag{7}$$

where $R_x$ are total gear ratios of engine and motors to wheels. This paper differentiates two types of driver demand: raw driver demand, as calculated from the actual position of the accelerator pedal position, and filtered driver demand, calculated by applying several filters to the raw driver demand. The first serves as a setpoint for torque commands, while the second provides improved drivability levels to the vehicle due to smoother torque gradients. The filtered driver demand is also the actual torque that shall be generated at the wheels.

### 3.1 Throttle stage

This stage runs an ECMS optimiser to control the HEV torque split relative to the slow dynamics of the engine. The outcome is an engine torque which is later translated into an engine throttle position. The torques calculated by this ECMS stage are indeed the optimum torque split setpoint wished to be achieved once steady conditions are reached. The Hamiltonian function is evaluated by using the steady-state fuel consumption map of the engine, since this stage is driven by slow dynamics and transient effects are negligible. The torque coordination uses the raw driver demand, so ECMS can compensate the slow dynamics of the engine by generating airpath pressure before the filtered driver demand raises.

The ECMS algorithm is run twice at this stage. In the first run, named “global run” in this paper, the optimum solution of ECMS is allowed to lie anywhere between the minimum and the maximum steady-state torque capabilities of the engine. On the contrary, in the second run, named “local run”, optimum engine torque is constrained to be within a delta around the last engine torque request, as if it were a zoom-in around the current engine operating point. In practice, the local run acts as an engine torque filter within the ECMS optimiser. There are several reasons to have these two consecutive runs:

1. The fickleness of the optimum engine torque is constrained to a maximum gradient.
2. The local run provides a form of filter for improved drivability.
3. In embedded applications, the local run can provide much finer discretisation of candidates due to its limited range of solutions, bringing better accuracy to the solution.
4. In embedded applications, the computational effort and memory requirements can be reduced since a denser grid of candidates is only needed in the zoom-in provided by the local run. The total amount of candidates can be greatly reduced.

The evaluation of these two ECMS and the calculation of the corresponding optimal solution requires following several steps. The proposed methodology, named “marble strategy” in this paper, resembles a marble moving towards the bottom of a concave surface. First, the global run is evaluated, and its optimal engine torque $\hat{M}_{ice,glb}$ is calculated as per Eq. (2). Then, for the local run, engine torque is constrained by Eq. (4) with the following limits:

$$\underline{M}_{ice} = M_{ice,i-1} - \Delta \tag{8}$$

$$\overline{M}_{ice} = M_{ice,i-1} + \Delta \tag{9}$$

where $M_{ice,i-1}$ is the optimum engine torque from the previous calculation step, and Δ a maximum torque gradient that can be function of operating point, driver demand, and driving enthusiasm among others. Boundaries set in Eqs. (8) and (9) have been chosen for the sake of simplicity but, alternatively, complex filters for engine torque can be set instead, without changes on the presented algorithm.

Once the Hamiltonian in Eq. (1) is evaluated for all local run candidates, the minimum cost is chosen according to its Hamiltonian value and its distance from the seed $M_{ice,i-1}$, pretty much like the distance that a marble can cover downhill depends on the distance from its starting point and how steep the slope is. Following this comparison, the ECMS solution can only move a maximum distance from the seed, which is given by the slope of the Hamiltonian and the equation of a constant acceleration motion:

$$\overline{\Delta M} = \frac{1}{2} sin\,\alpha \cdot cos\,\alpha \cdot g \cdot T_s^2 \tag{10}$$

where α is the slope of the Hamiltonian between seed and the candidate, $T_s$ is the sample time, and $g$ is the "gravity" applied to the Hamiltonian minimum search. The value of this gravity term will affect to how quickly EMCS solution reacts to small cost differences. Among all candidates that are reachable in one sample time $T_s$, i.e. that their distance to the seed is below the limit determined by Eq. (10), the one with the minimum Hamiltonian cost is chosen as optimum solution of the local run. This strategy limits the amount of play in the system and effectively filters out unnecessary flickering of optimal solution for marginal cost benefits, and at the same time it promotes engine torque reaching the optimum torque split after a certain number of calculation steps.

There is a chance that the local run remains stuck around a local minimum, leaving the global and expectably better torque split solution out of its reach. In order to avoid this issue, it is possible to resort to the marble comparison once more. If the global run shows a candidate with a significantly lower Hamiltonian value, but this candidate is too far to stay within the range of the local run, the marble will need an external push to overcome the surrounding hills and roll down towards the lowest valley where the global optimum lies. To do this, the global run optimum needs to show a significant lower Hamiltonian value than that of the local run and to stay like that for a minimum time, otherwise a torque transient would be initiated for little to zero cost benefit. Eq. (10) can also be used to set a limit on how worth is to move to the global run optimum. The transition from local to global run optimum, if cost reduction is considered enough, is implemented with a similar rate transition to the limits in Eqs. (8) and (9).

### 3.2 Ignition timing stage

In this stage, the ECMS algorithm controls the fast dynamics of the HEV powertrain. The resulting optimum torque split includes torque requests to inverters and an engine torque that is later converted to an ignition timing. This stage calculates the actual torques that are generated at the wheels. The engine contribution to it, is limited by the current conditions of the airpath:

$$\underline{M}_{ice} = M_{ign,ret} \tag{11}$$

$$\overline{M}_{ice} = M_{ign,opt} \tag{12}$$

where $M_{ign,ret}$ is the engine torque corresponding to the most retarded ignition allowed (limited by heat and combustion stability reasons), and $M_{ign,opt}$ is the engine torque corresponding to the optimum ignition timing (limited by knock). These are the engine limits if fuel is burnt, but there is also the option to not inject any fuel at all, which brings a fuel cut-off engine torque $M_{fric}$. All these limits are dynamic since they are based on actual engine conditions and are a consequence of the throttle position chosen by ECMS in the throttle stage a few calculation steps before.

This stage also considers the multiple torque interventions $M_{itv,i}$ that are requested by external systems, such as during gear shifts, stability interventions, traction control events, or a mandatory torque reserve. These interventions constrain the maximum engine torque at Eq. (12):

$$\overline{M}_{ice} = min(M_{ign,opt}, M_{itv,1}, M_{itv,2}, \dots, M_{itv,i}) \tag{13}$$

Since a different ignition timing only degrades combustion efficiency but does not change the amount of injected fuel [22], it is evident that, in Eq. (1), the $P_f$ term of the Hamiltonian will not change. However, the $P_b$ term will increase due to a lower torque produced by the engine that needs to be compensated by an additional electrical contribution. It is trivial, then, that if engine burns fuel, the optimum torque is the limit on Eq. (13). However, depending on the SOC level, it may be more beneficial to go in fuel cut-off than keeping the engine firing.

Consequently, this ECMS stage evaluates only two candidates, $\overline{M}_{ice}$ and $M_{fric}$, keeping the algorithm light. The fuel cost for the first is calculated with a fuel map interpolated at $M_{ign,opt}$, while for the second the cost is zero.

This ECMS stage uses the filtered driver demand. As this is the actual torque that shall be generated at the wheels, the resulting torque split becomes the torque request to both engine and inverters.

### 3.3 Running mode stage

The last stage is in charge of commanding engine start and stop. It evaluates the Hamiltonian function assuming pure electric operation, i.e. engine stopped, and compares its value to the optimum Hamiltonian from the slow-path/throttle stage ECMS. This comparison shows which engine running mode is optimum for the current driving conditions, but it may bring three issues: lack of memory of previous running mode requests, possible flickering of optimum mode, and lack of a cost associated to the engine start process.

For the first, this paper suggests constraining the running mode to be held for a minimum time $t_{hold}$ before allowing a mode change. This can effectively reduce the number of engine cranking events and still track the optimum start/stop pattern once the time is over.

For the second, the proposal is to discard optimum mode changes that are held only for few samples. This avoids initiating an engine cranking or an engine stop procedure if the optimum mode is not stable or not significantly better than the current engine running mode.

For the third, an additional cost can be added to the slow-path Hamiltonian value. The energy spent to crank an engine that requires an equivalent fuel $m_{f,crk}$ to do so is:

$$E_{f,crk} = m_{f,crk} \cdot H_f \tag{14}$$

where $H_f$ is the petrol heating value. Assuming that the engine shall be running for a minimum time of $t_{hold}$, the minimum Hamiltonian cost difference that shall exist between slow-path and pure electric to make cranking worth, is:

$$P_{f,crk} = \frac{E_{f,crk}}{t_{hold}} \tag{15}$$

Therefore, for optimum Hamiltonian costs of $H_{slow}$ and $H_{ev}$, the running mode change criteria are:

$$\begin{cases} H_{slow} + P_{f,crk} < H_{ev}, & \text{if ICE off} \\ H_{ev} < H_{slow}, & \text{if ICE on} \end{cases} \tag{16}$$

## 4. Results

The multi-stage ECMS (MS-ECMS) algorithm has been implemented on a prototype Vehicle Control Unit (VCU), as part of the energy management and torque structure of a production-intent control software for a high-performance road-legal HEV.

The results shown below are part of a test campaign performed on a driver-in-the-loop (DiL) simulator. The configuration of this DiL consists of a real-time machine running a dynamic powertrain model, representative engine and transmission control units, inverters and BMS, a detailed lateral dynamics vehicle model, and a prototype VCU running the presented MS-ECMS algorithm. As part of the test campaign, various drivers performed several hot laps at Calabogie Motorsports Park, as well as city driving with traffic on an urban environment.

Overall, the driving perception feedback from the drivers was positive, highlighting the smoothness of torque blending, the natural correlation between engine torque (and sound) and accelerator pedal position, and the ability to perform charge sustaining laps with little calibration, as show in figure 2. A more disputed opinion was about commanded engine stops during a hot lap since the active driving mode did not force engine to stay on. As it could be expected, MS-ECMS opted for stopping the engine on the four longest braking zones of the track, as shown in figure 2. This helped to charge the battery a bit more as engine friction was avoided and contributed to achieve charge sustaining over the lap.

However, some drivers might not like engine stops during a hot lap, which can be sorted out by forcing Eq. (16) to always output engine on.

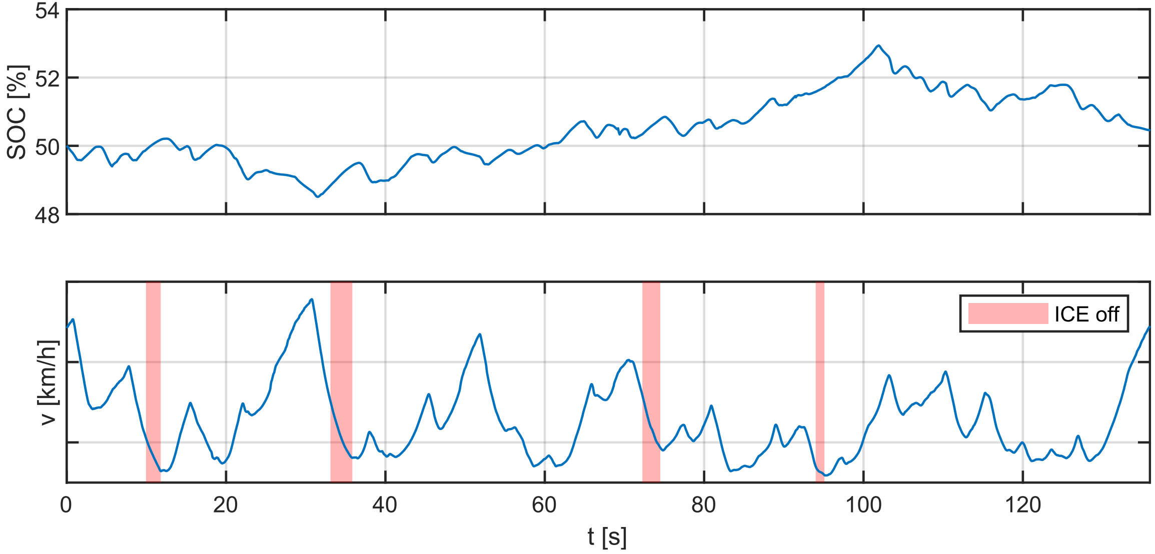

**Fig. 2.** Calabogie hot lap SOC and speed trace with highlighted engine off sections. Speed scale removed for confidential reasons

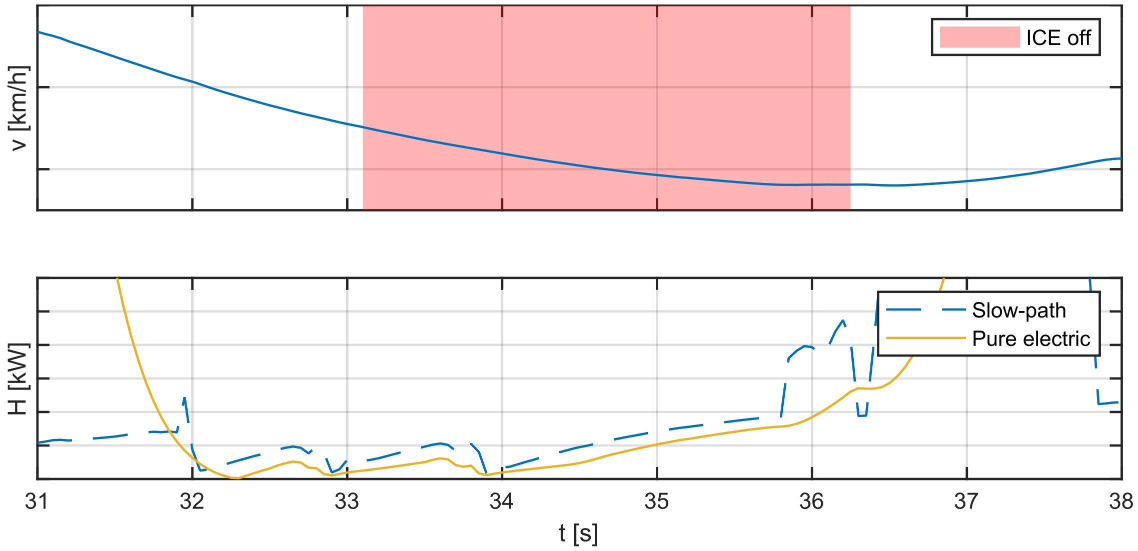

**Fig. 3.** Calabogie hot lap detail of an engine off event. Slow-path and pure electric operation Hamiltonian values are show for a comparison. Speed and cost scales removed for confidential reasons

The mechanisms in Eq. (16) controlling the running mode can be clearly distinguished in figure 3 where, at second 32, the pure electric Hamiltonian cost (bottom plot) becomes significantly cheaper than slow-path and, one second after (one second confirmation was set to filter out very short mode change requests), engine off is commanded. It is not until second 36.2 that slow-path Hamiltonian is the lowest and, therefore, engine is started again.

The join operation of throttle and ignition timing optimisation stages (sections 3.1 and 3.2) can be appreciated at figure 4. First, driver releases the accelerator pedal as the vehicle approaches a mid-speed corner. The raw driver demand drop that follows the pedal release produces a drop on the slow-path (in blue) engine request, closing the throttle. Then, a few tenths after, as the air pressure drops, fast-path limits (in red, dashed line) fall progressively. Fast-path ECMS stage opted to stay at maximum efficiency by operating at optimum ignition timing, even mid-corner, thanks to the slow-path ECMS stage that closed the throttle beforehand permitting to operate efficiently with a low torque output. This is particularly good for emissions, since avoiding fuel cut-offs helps reducing catalyst oxygen accumulation [23]. A bit further in the manoeuvre, when the driver gets back on the pedal, the slow-path ECMS stage local filtering described in Eqs. (8-10) is clearly visible on the ramp that the slow-path torque follows.

The reader may observe that this filtering seems to not be present during the pedal release. This is because the raw driver request drop is too steep for the motors to compensate any positive torque that the engine may produce while following a smooth filtering. Since driver demand takes precedence over filtering, the engine torque drops to the closest feasible candidate.

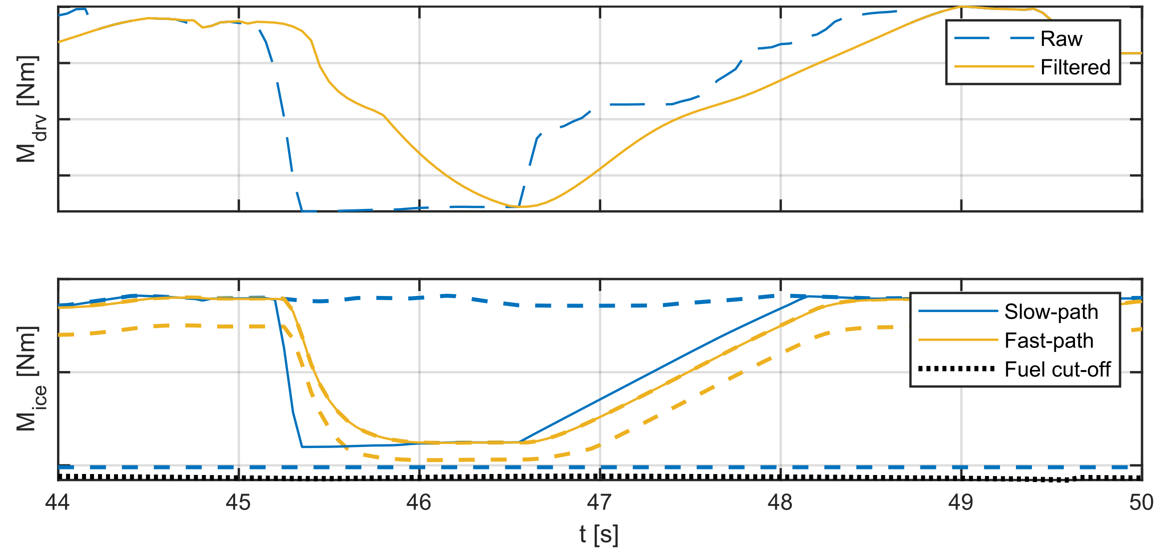

**Fig. 4.** Calabogie hot lap detail of a pedal release and tip-in, with slow (throttle) and fast (ignition timing) path optimum torques, and their limit values shown as dashed lines. Vertical scales removed for confidential reasons

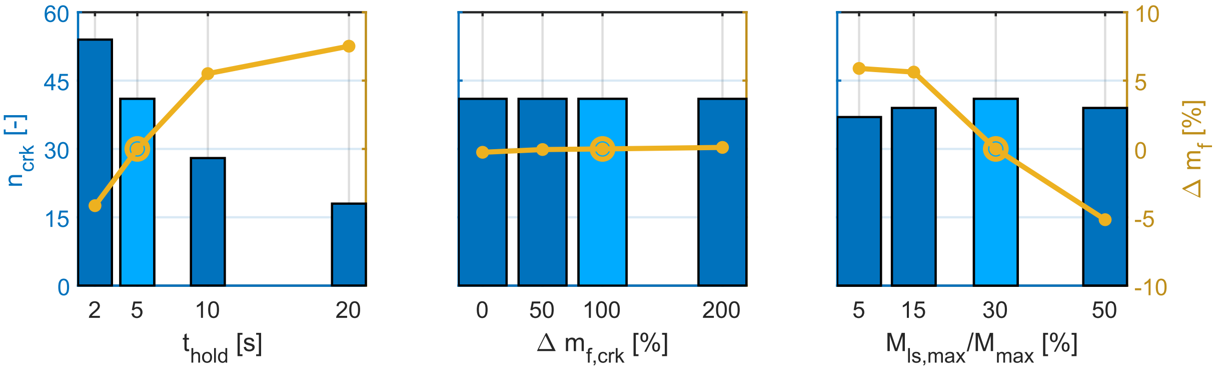

**Fig. 5.** Effect on total fuel consumption and number of engine start events of some calibratable parameters on a city driving cycle. From left to right: minimum time between engine mode changes, relative fuel cost assigned to the engine cranking procedure, maximum load shift percentage. Baseline calibration is in light colour. Positive fuel consumption increase means higher fuel consumption

The flexibility of the MS-ECMS during the calibration process is a strong point. Several strategy calibrations have been studied to analyse the effect on both fuel efficiency and number of engine start events on a city driving cycle. The analysed parameters are: the minimum time between two engine running mode changes $t_{hold}$ (section 3.3), the equivalent engine cranking fuel cost $m_{f,crk}$ shown in Eq. (14), and the maximum load shift (maximum engine torque relative to the driver demand). The advantage of MS-ECMS is that the strategy automatically re-adapts to these calibration changes without any need to retune other parameters, therefore facilitating the calibration process. Results in figure 5 show some interesting trends. An increase in the minimum time between engine on/off events as well as the reduction of the load shift limit, both constrain the algorithm producing a higher fuel consumption. In terms of number of cranking events, results are not so homogeneous: the increase of the time between on/off commands effectively reduces the total amount of engine starts, however the modification of the load shift limit shows mixed results. The increase of the engine start cost produced a slight increase on the fuel consumption but surprisingly it did not reduce the number of engine starts, which remained invariant. The reason is that in all 41 instances of an engine start, cranking the engine is much better than keeping it off according to the Hamiltonian value, beyond all tested values of engine start cost. The increase of engine start cost only delayed the engine cranking, reducing the amount of time taking advantage of engine running, thus producing a slight increase on fuel consumption.

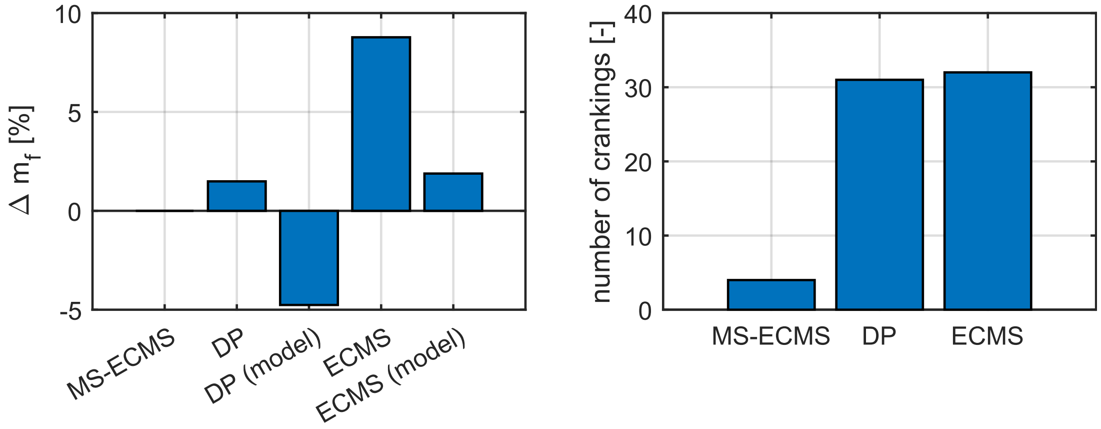

**Fig. 6.** Benchmark of MS-ECMS fuel consumption and cranking events against other methods of optimal control in a hot lap around Calabogie. Results tagged as "model" correspond to fuel consumption estimated by the optimisation algorithm, whereas the others are estimated by the powertrain model. Positive fuel percentage means higher fuel consumption

The presented MS-ECMS has been benchmarked against a classic ECMS [8] and Dynamic Programming (DP) [24] optimiser, to analyse its performance on a hot lap. Driver demand trace, gear number and vehicle speed have been extracted from the DiL test and have been used to define the optimisation problem for these two. DP and ECMS employed the same powertrain control model that MS-ECMS uses to keep test homogeneity. Given that these two optimisation methods do not consider the multiple simultaneous control paths that the MS-ECMS does, optimal solutions from ECMS and DP are a single torque command. This torque has been used as a target for the throttle position (equivalent to the command from MS-ECMS throttle stage in section 3.1). An additional controller for the ignition timing has also been placed downstream.

As revealed by figure 6, DP shows a 5% advantage in total fuel consumption according to the model used inside the optimiser (tagged as "model" in the figure). However, when ignition timing was also considered on the complete powertrain, DP shows a slightly worse fuel efficiency compared to MS-ECMS of about 1.5%, likely to be due to the lack of connection between DP optimiser and the fast-path of the powertrain. In addition to this, DP increased the number of cranking events of MS-ECMS by a factor of 8, which would expectedly worsen fuel consumption and emissions. Note that DP is an off-line algorithm that requires full knowledge of the driving mission beforehand [25] and, even though it is a valuable benchmark tool, its results cannot be translated to a real-time controller. Regarding classic ECMS, results in figure 6 shows that fuel consumption was worse than MS-ECMS in all situations, from about a 2% according to the optimisation model, to almost 9% increase in the complete powertrain model. The number of cranking events remains close to that of DP, far from the just 4 engine starts commanded by MS-ECMS during a hot lap.

## 5. Conclusions

The presented multi-stage ECMS (MS-ECMS) methodology proved to be able to control a HEV powertrain considering the different dynamics of the engine from an optimal perspective with success. It showed better fuel consumption figures and reduced number of engine start events than other methods such as the classic ECMS approach (MS-ECMS shows 9% lower fuel consumption and 8 times less engine starts) and a global off-line optimisation method like DP (MS-ECMS shows 1.5% lower fuel consumption and again 8 times less engine starts). This can be explained due to multiple cost function evaluations of MS-ECMS that look at different engine dynamics, embedding at a greater level with the engine controller, whereas classic ECMS and DP both work at a supervisory level.

MS-ECMS demonstrated to include drivability related constraints, such as torque filtering, with ease within the optimisation algorithm. These constraints provide stability of optimum torque split generation, a progressive and smooth torque command, and a torque split that correlates in a more natural manner with the accelerator pedal position. This contributes to improved ride comfort.

On the performed DiL test campaign, drivers valued the consistent performance of the vehicle, the predictable torque split and the capability to keep a charge sustaining balance during hot laps.

Several calibration parameters related to drivability and efficiency metrics were modified as part of a sweep analysis. MS-ECMS revealed to be easy to calibrate, as the modification of these calibrations did not impact on the optimality and stability of the control, since the strategy automatically adapts to a different calibration set.

The evaluation of the MS-ECMS impact on emissions is an interesting area to work in as a future step. Also, the integration of a pollutant emissions cost into the Hamiltonian function may bring additional benefits to the control of a HEV powertrain, in preparation for more stringent emissions regulations.

## References

[1] Conway, G., Joshi, A., Leach, F., García, A., & Senecal, P. K. (2021). A review of current and future powertrain technologies and trends in 2020. *Transportation Engineering*, *5*, 100080.

[2] European Environment Agency (2023). New registrations of electric vehicles in Europe.

[3] Mehdizadeh, M., & Shariat-Mohaymany, A. (2021). Who are less likely to vote for a low emission charging zone? Attitudes and adoption of hybrid and electric vehicles. Transportation Research Part A: Policy and Practice, 146, 29-43.

[4] Higueras-Castillo, E., Kalinic, Z., Marinkovic, V., & Liébana-Cabanillas, F. J. (2020). A mixed analysis of perceptions of electric and hybrid vehicles. Energy Policy, 136, 111076.

[5] Tran, D. D., Vafaeipour, M., El Baghdadi, M., Barrero, R., Van Mierlo, J., & Hegazy, O. (2020). Thorough state-of-the-art analysis of electric and hybrid vehicle powertrains: Topologies and integrated energy management strategies. Renewable and Sustainable Energy Reviews, 119, 109596.

[6] Xue, Q., Zhang, X., Teng, T., Zhang, J., Feng, Z., & Lv, Q. (2020). A comprehensive review on classification, energy management strategy, and control algorithm for hybrid electric vehicles. Energies, 13(20), 5355.

[7] Zhang, F., Wang, L., Coskun, S., Pang, H., Cui, Y., & Xi, J. (2020). Energy management strategies for hybrid electric vehicles: Review, classification, comparison, and outlook. Energies, 13(13), 3352.

[8] Paganelli, G., Delprat, S., Guerra, T. M., Rimaux, J., & Santin, J. J. (2002, May). Equivalent consumption minimization strategy for parallel hybrid powertrains. In Vehicular technology conference. IEEE 55th vehicular technology conference. VTC spring 2002 (cat. No. 02CH37367) (Vol. 4, pp. 2076-2081). IEEE.

[9] Serrao, L., Onori, S., & Rizzoni, G. (2009, June). ECMS as a realization of Pontryagin's minimum principle for HEV control. In 2009 American control conference (pp. 3964-3969). IEEE.

[10] Sciarretta, A., Guzzella, L., & Back, M. (2004). A real-time optimal control strategy for parallel hybrid vehicles with on-board estimation of the control parameters. IFAC Proceedings Volumes, 37(22), 489-494.

[11] Skugor, B., Ranogajec, V., & Deur, J. (2013, November). On smoothing HEV/EREV supervisory control action using an extended ECMS approach. In 2013 World Electric Vehicle Symposium and Exhibition (EVS27) (pp. 1-10). IEEE.

[12] Rezaei, A., Burl, J. B., & Zhou, B. (2017). Estimation of the ECMS equivalent factor bounds for hybrid electric vehicles. IEEE Transactions on Control Systems Technology, 26(6), 2198-2205.

[13] Guardiola, C., Pla, B., Onori, S., & Rizzoni, G. (2012). A new approach to optimally tune the control strategy for hybrid vehicles applications. IFAC Proceedings Volumes, 45(30), 255-261.

[14] Onori, S., & Serrao, L. (2011, December). On Adaptive-ECMS strategies for hybrid electric vehicles. In Proceedings of the international scientific conference on hybrid and electric vehicles, Malmaison, France (Vol. 67).

[15] Guardiola, C., Pla, B., Blanco-Rodríguez, D., & Reig, A. (2014). Modelling driving behaviour and its impact on the energy management problem in hybrid electric vehicles. International Journal of Computer Mathematics, 91(1), 147-156.

[16] Kazemi, H., Fallah, Y. P., Nix, A., & Wayne, S. (2017). Predictive AECMS by utilization of intelligent transportation systems for hybrid electric vehicle powertrain control. IEEE Transactions on Intelligent Vehicles, 2(2), 75-84.

[17] Luján, J. M., Guardiola, C., Pla, B., & Reig, A. (2018). Analytical optimal solution to the energy management problem in series hybrid electric vehicles. IEEE Transactions on Vehicular Technology, 67(8), 6803-6813.

[18] Mangasarian, O. L. (1966). Sufficient conditions for the optimal control of nonlinear systems. SIAM Journal on control, 4(1), 139-152.

[19] Pontryagin, L. S. (2018). Mathematical theory of optimal processes. Routledge.

[20] Kessels, J. T., Koot, M. W., Van Den Bosch, P. P., & Kok, D. B. (2008). Online energy management for hybrid electric vehicles. IEEE Transactions on vehicular technology, 57(6), 3428-3440.

[21] Guzzella, L., & Onder, C. (2009). Introduction to modeling and control of internal combustion engine systems. Springer Science & Business Media.

[22] Heywood, J. (1988). Internal combustion engine fundamentals. McGraw-Hill.

[23] Xin, B., Li, J., Wang, Q., & Sun, P. (2018). Emission control method for fuel cut-off condition of GDI engine. IFAC-PapersOnLine, 51(31), 158-161.

[24] Bellman, R. (1954). The theory of dynamic programming. Bulletin of the American Mathematical Society, 60(6), 503-515.

[25] Reig Bernad, A. (2017). Optimal control for automotive powertrain applications (Doctoral dissertation, Universitat Politècnica de València).

# A Reinforcement Learning Energy Management System for Off-Road Powertrain Application

F. Millo[1], L. Rolando[1], A. Vinogradov[1], N. Scinicariello[2], P. Fregni[2], D. Fantuzzi[2], S. Gaioli[2]

[1] Politecnico di Torino

[2] Kohler Engines

## Abstract

Likewise in the automotive field, off-road applications can benefit from powertrain hybridization to improve fuel consumption and/or machinery performance. Nevertheless, Non-Road Mobile Machineries (NRMMs) feature additional challenges such as the absence of common test cycles and the difficulty of setting up repeatable and accurate test procedures when a particular application is considered. This aspect significantly increases the complexity of the design of the Energy Management System (EMS).

In this context, Reinforcement Learning (RL) control techniques may have a huge potential thanks to their capability to self-learning the optimal control trajectory through a direct interaction with the environment.

Therefore, the present work assesses the performance of an EMS exploiting a Deep Q-Learning (DQL) agent and optimized for a parallel hybrid powertrain integrated in a skid steer loader (SSL). Initially, representative duty cycles were derived from the analysis of a wide set of experimental data measured in real-world operating conditions. Then a digital twin of the skid steer loader powertrain was used to train the DQL for the fuel consumption minimization. The performance of the proposed powertrain control strategy was finally benchmarked against the optimal solution provided by a Dynamic Programming (DP) optimization considering different mission profiles. The results of this comparison showed good robustness and a limited gap with respect to the DP reference across various mission profiles.

## 1. Introduction

In the last decades, the automotive industry proved the benefits of powertrain electrification and fostered its adoption in other fields such as Non-Road Mobile Machinery (NRMM). Nevertheless, in this sector, the impact of the hybridization may be significantly different according to the wide range of specific application. Among them, the construction industry may represent an early adopter as demonstrated by the increasing number of feasibility studies and prototypes. Commercially, Komatsu was the first to introduce a hybrid excavator, showing more than 25% fuel consumption gain alongside an overall performance improvement [1]. A key feature contributing to this significant enhancement is the electrification of the swing. By employing an Electric Motor (EM) rotation, the excavator can recover a significant portion of the inertial energy, while also offering precise control and responsiveness. In the construction industry, loaders and telehandlers could also represent promising applications for powertrain hybridization as demonstrated by the John Deere 644K Hybrid [2] or by the Dieci Mini Agri Hybrid Boost System [3]. Focusing on compact loaders, currently, only two examples of fully electric Skid Steer Loaders (SSLs) produced by Bobcat, i.e. the T7X and S7X, can be found in the market [4]. These versions entirely rely on electric power without any hydraulic systems for lifting tasks.

Despite this interest in hybrid NRMM, wider powertrain electrification of the off-road sector has to face some unique challenges. One of the most evident is the design of a hybrid architecture optimized for a high number of possible applications. Furthermore, at the beginning of the design process, it is necessary to clearly identify the additional loads beyond the traction (e.g. external hydraulic ancillaries), and a meaningful set of mission profiles. This second aspect is particularly relevant as it provides great opportunities to improve efficiency and performance. As a matter of fact, the power requirements of a specific vehicle task do not only depend on the application, but it can also be strongly affected by external conditions such as terrain, handled material, and driver behaviour. Thus, the definition of the duty cycle has great importance. Historically, there were no compelling reasons for a deep analysis of the mission profile since the engine selection was primarily dictated by the maximum torque request and by the packaging. However, with the advent of powertrain hybridization, the frequency and magnitude of the power peaks can significantly affect the size of the reversible Energy Storage System (ESS) and of the electric motor. Ultimately, the knowledge of the duty cycle is fundamental to develop a robust Energy Management Strategy (EMS).

Despite these challenges could restrain the widespread adoption of hybrid NRMMs, currently, the academic research is trying to tackle them from multiple perspectives such as the development of different architecture investigations [1], the analysis of innovative energy management strategies [5] and the design of specific components [6]. Concerning loaders, Fei et al. [7] summarized the energy savings potential of loaders, comparing both hydraulic and electric hybrids. In [8] Wang et al. analyzed the benefits of using a hydraulic accumulator to store energy and improve the overall fuel consumption. The same authors proposed in [9] the possibility of an electro-accumulator, which could achieve higher energy density of the storage and more freedom in the control strategy obtaining better fuel consumption and vehicle performance. Another interesting case study analyzed is the telehandler. In [10] an electro-hydraulic system was developed to enable an energy recovery through an EM coupled with a reversible pump and integrated within the hydraulic circuit of the powertrain. The developed system was able to recuperate up to 70% of the potential energy. A similar application was analyzed in [11] where a hydrogen ICE was hybridized. The work also addressed the definition of the duty cycle, by measuring power at different points of the transmission in order to separate the contribution of the traction and of working hydraulics. The study proved that the hybridization could reduce the engine-out NOx emissions and $H_2$ fuel consumption. In the case of Skid Steer Loaders, a significant contribution was provided by [12] where a numerical model was exploited to identify the most promising hybrid configurations. Furthermore, the division between lifting and traction indicated the importance of understanding and optimizing the energy flows associated with each task. The fuel consumption results showed significant variations ranging from 10% up to 30% reduction according to the different architectures.

Moving to the EMS, even if certain studies have addressed its design for hybrid NRMM applications [5], the automotive literature delves into the topic more comprehensively, as shown by the review [13] which analyzed over 250 EMS-related publications. Among the possible approaches, Rule-Based (RB) strategies are the most common. They rely on simplified rules the main parameters of which are empirically calibrated and stored in look-up tables. This aspect makes them easily implementable online, but they could frequently lack of robustness. On the contrary, the optimal solution could be found by exploiting Dynamic Programming (DP) [14], a global optimization algorithm which ensures the optimality, but it requires the a-priori knowledge of the complete duty cycle. Valid alternatives are local optimization methodologies such as the Equivalent Consumption Minimization Strategy (ECMS) [15] or Pontryagin's Minimum Principle (PMP) [16],and the Model Predictive Control (MPC) [17], which optimizes the power split over a short time horizon employing a simplified model of the powertrain.

More recently, Machine Learning (ML) techniques gained consensus in the automotive sector [13]. Among them, Reinforcement Learning algorithms seem to be one of the most promising solutions for planning and optimization tasks, since they can self-learn the optimal control solution through the experience directly interacting with the environment (vehicle, vehicle model, duty cycle). On the other side, during the learning phase, various parameters have to be calibrated making the training process quite tricky and time demanding. Moreover, the identification of the performance index, i.e. the RL reward, is a significant aspect and can highly influence the results. In a previous paper of the authors [18], potential agents and rewards suitable for the EMS design were extensively discussed. Among the various possibilities, Deep Q-Learning stands out for its simplicity and at the same time for its adaptability for EMS applications. For instance, DQL was employed for a series of HEV, with a reward structure designed towards fuel and electric energy costs in [19]. Another example is reported in [20] where a parallel hybrid electric bus demonstrated a 5.6% reduction in fuel consumption, by continuously penalizing the fuel consumption and the battery State of Charge (SoC) deviation.

In this context, the current work seeks to demonstrate, through numerical simulation, the fuel economy potential of a hybrid SSL and the feasibility of an Energy Management System based on an RL algorithm. An experimental campaign performed on a prototype of the vehicle allowed the definition of meaningful duty cycles for the training and the testing of the selected RL agent. A DQL agent was selected for this application and integrated into a virtual test rig of the hybrid powertrain for a Skid Steer Loader. The training process was targeted to the minimization of the fuel consumption and to the achievement of battery charge sustainability. The potential of the proposed hybrid architecture was assessed with respect to the performance of a conventional vehicle engine and benchmarked against the global optimum provided by Dynamic Programming.

The paper is structured as follows: the test case is presented in Section 2.1, while a discussion about the experimental campaign is performed in Section 2.2. Afterwards, the attention turns to the design of the energy management system (Section 3) and to the analysis of the results of the different working scenarios (Section 4). Finally, the paper summarizes the main findings of the research activity and describes its future developments (Section 5).

## 2. Case Study

### 2.1 Skid Steer Loader

A skid steer loader is a compact off-road machine primarily designed for the movement of material from one location to another, by pushing or gathering it into a bucket. Additionally, it is capable of grading or basement digging, and the number of working tasks can further increase with different attachments. Its main feature is the differential steering, which allows performing all operations in tight spaces through independent traction for the left and right tracks.

A simplified conventional powertrain of a skid steer is represented in Figure 1.a on the left. The propulsion is provided by two hydraulic motors. Each of them is connected to a variable displacement pump and, in turn, to a diesel Internal Combustion Engine (ICE). A third pump provides lifting power to the arm of the vehicle. As it can be observed from Table 1, where the main features of the vehicle and powertrain are reported, for a conventional architecture the displacement of ICE is relatively high because of the high low-end torque requirements of the operations performed by this type of machinery. The conventional powertrain considered is a 3.4 L - 80 kW diesel engine equipped with a Selective Catalytic Reduction (SCR) to be compliant with the Stage V NOx emission limits. It is noteworthy that many skid steer manufactures have chosen to limit the engine power to 55 kW to meet Stage V regulations, rather than implementing an SCR. Consequently, the proposed hybrid powertrain provides comparable power to a larger diesel engine avoiding complex aftertreatment systems. The hybrid powertrain integrates a 2.5 L - 55 kW diesel engine with a 48 V system comprising a peak 20 kW electric motor and an 8 kWh battery. The apparent oversizing of the 8 kWh battery was selected to provide margin for ancillary's electrification which at the present state was not considered. Moreover, the substantial battery capacity ensures greater durability by reducing the depth of discharge, thereby reducing aging effects.

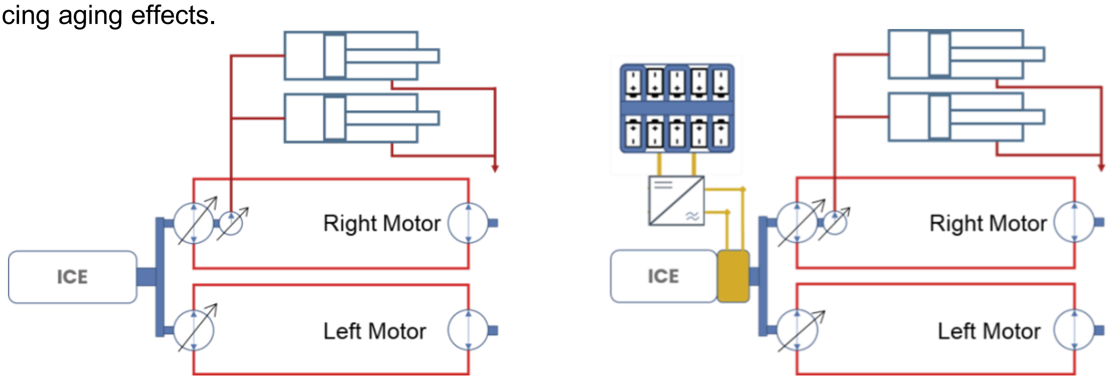

(a) (b)

Figure 1: (a): Simplified Conventional Powertrain for a Skid Steer Loader. (b): Hybrid Powertrain under analysis.

| | Conventional | Hybrid P1 |
|---|---|---|
| Lifting Capacity [kg] | 1000 – 1650 | 1000 – 1650 |
| Approximate Weight [kg] | 5700 | 5700 |
| Diesel Engine Displacement [cm$^3$] | 3400 | 2500 |
| Maximum Torque [Nm] | 470 | 450 |
| Maximum Power [kW] | 80 (w SCR) | 55 (+20 el.) |
| Nominal Working Speed [RPM] | 2300 | 2300 |
| Electric Motor Nominal/Peak Power [kW] | - | 16/20 |
| Battery Energy Capacity [kWh] | - | 8 |
| Battery Maximum Power [kW] | | 21 |

Table 1 Conventional and Hybrid Specifications of the SSL under analysis

As already discussed in the paper introduction, in the hybridization of any NRMM, the optimal topology depends on the vehicle usage. In an SSL, the implementation of the electric traction could be a promising solution since it allows decoupling the speed of the hydraulic pump from the engine operating conditions which, in turn, can be chosen to maximize the efficiency. Furthermore, the use of an electro-hydraulic system for the lifting of the arm could also be beneficial thanks to a partial recovery of energy used for the lifting.
However, the simultaneous use of the electric traction and of the electrohydraulic system may not be convenient from the economic perspective. As a matter of fact, an EM featuring high torque density would be necessary to move the vehicle in challenging terrains, while the concurrent use of an electro-hydraulic system requires the implementation of reversible hydraulic components or the increase of the circuit complexity. Therefore, in this study, the use of a parallel architecture (see Figure 1b), designed as a drop-in solution, may represent a cost-effective approach to enable the benefit of the hybridization on a skid steer loader. Indeed, it also allows the engine downsizing which can be beneficial in particular at high speeds and low loads. At the same time, the high torque levels requested at low speeds can be preserved through the combined use of the ICE and of the electric motor. Furthermore, this initial hybridization can improve fuel economy through features like start and stop and the electrification of auxiliaries such as cooling fan or air conditioning systems. The main technical specifications of the considered hybrid SSL are reported in the third column in Table 1.

### 2.2 Mission Profiles

As previously discussed, since the definition of a standard duty cycle is almost impossible, for the following analysis four different mission profiles were considered. The data were collected during an experimental campaign performed on an SSL prototype featuring the powertrain configurations depicted in Table 1. The first two duty cycles, in particular, were recorded on the conventional SSL while the others were measured on the vehicle equipped with the parallel hybrid powertrain. The engine operating variables such as speed and torque were derived from the ECU, while the electrical power was extracted from the Hybrid Control Unit. A unique aspect of hydraulic transmission is the request for a fixed engine speed to ensure a sufficient oil flow in all the operating conditions. The "Operating Speed" reported in Table 1 was derived from the experimental data which shows minor variations across the different duty cycles. The torque provided by the electric motor was estimated by combining electrical power and efficiency maps provided by the component supplier.

The experimental test focused on evaluating the SSL performance on four different working scenarios (see Table 2 and Figure 3). The first two involve the execution of a Y Cycle depicted in Figure 2, which is a typical SSL sequence of operations composed of the following phases:

1. Moving and boosting into a pile of material.
2. Reverse travel.
3. Steering and driving towards a truck.
4. Lift and dump the material into the truck.
5. Reverse driving and arm lowering.

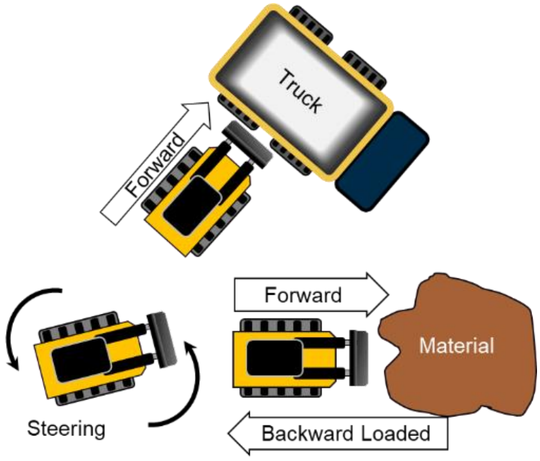

Figure 2 Schematic representation of the loading Y cycle

The *Y-Low-Load Cycle* is representative of the normal vehicle operations, and it was directly measured on the vehicle without any data post-processing. The *Y-High-Load*, on the contrary, features a significantly higher power request (see Table 2 and Figure 3) and it was created by combining the data obtained from separate measurements of the phases of a highly demanding Y-Cycle. In The *Field-Tracking* the Skid Steer performs a loop on an off-road track including an 18° degrees ramp. Finally, *the Basement-Dig* is an operation that involves the complete tilting of the SSL bucket towards the ground and then the use of traction to dig into the terrain to create a pit. Due to the strong influence of variables involving the resistance of the terrain, the periodicity of this duty cycle is less evident.

| | Y Low Load | Y High Load | Field Tracking | Basement Dig |
|---|---|---|---|---|
| Powertrain employed during testing | Conventional ICE 55 kW | Conventional ICE 55 kW | Hybrid 55 kW ICE + 20 kW Electric | Hybrid 55 kW ICE + 20 kW Electric |
| Average Load (with ref. to 55 kW) | 69 % | 84 % | 74 % | 82 % |
| Normalized Peak Torque [-] | 1 | 0.99 | 1.39 | 1.42 |
| Operating Speed [RPM] | 2400 | 2400 | 2000 | 2000 |
| Duration [seconds] | 220 | 1800 | 3860 | 1970 |

Table 2 Summary of Duty Cycles with some key parameters

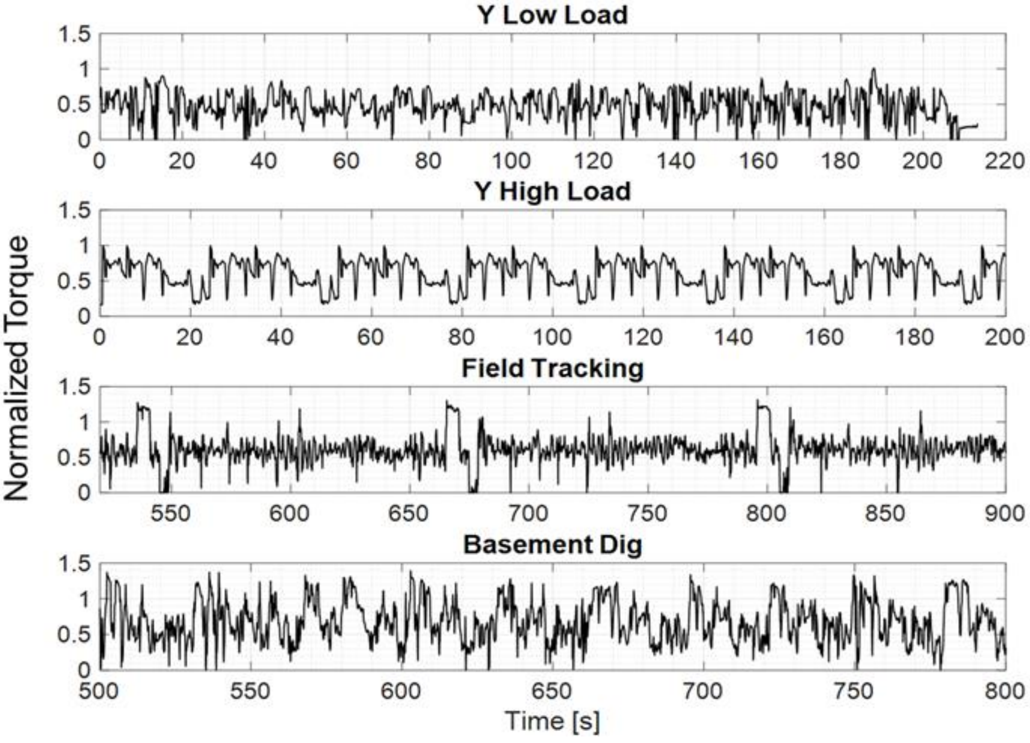

Figure 3 Experimental Duty Cycles

## 3.1 Energy Management System

The integration of a new energy source, i.e. the chemical battery, requires the definition of an Energy Management System (EMS) to split the power requests among the available actuators.

This is a typical optimal control problem whose objective is usually the minimization of the engine fuel consumption over a given mission profile. Alongside, the energy management must obey a set of local and global constraints such as physical limitations on the powertrain components and boundaries on the battery State of Charge respectively. These problems can be addressed through several methods which can differ in optimality and implementability.

In this work, Dynamic Programming (DP) was used as a benchmark to assess the potential of a Reinforcement Learning (RL) control technique. DP is based on the Bellman Optimality principle [14] which decomposes the decisional problem into a finite set of tail subproblems. The combined optimal solution of these subproblems provides the global optimal solution, but, since it requires the a-priori knowledge of the mission profile, is not implementable in a real Electronic Control Unit (ECU).

On the other side, recently, RL is raising as a promising solution for the EMS control problem. Alongside its real-time implementation, it is able to self-learn the optimal solution by directly interacting with the environment. The learning process is commonly referred to as the training phase. Figure 4 illustrates the working principle of RL training. At each time step, an agent selects an action *A*, based on the previous state of the environment *S*, and based on the reward *r*. The relationship between the states, the rewards, and the action to be taken, usually is called the policy $\pi$. During the training phase, any RL algorithm seeks to identify the optimal policy, $\pi^*$ which maximizes the return $g_t$, defined as a weighted sum of the temporal reward:

$$g_t = \sum_{k=0}^{inf} \gamma^k r_{t+k+1} \qquad 1$$

where $\gamma \in [0,1)$ is the discount factor, a parameter that determines the relative weights of future and current rewards [21]. When the discount factor, $\gamma$, is low, the present rewards have higher importance in the evaluation of the return.

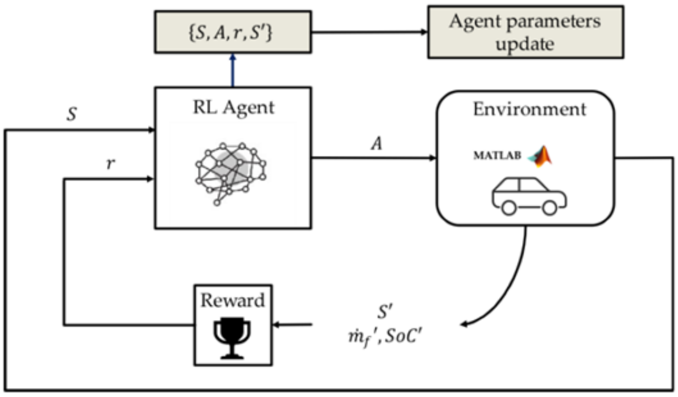

Figure 4 Schematic Representation of the RL Working Principle [18]

In the scientific literature, various types of agents have been presented. Among these, Q-Learning (QL) stands out as one of the most commonly employed thanks to its reduced complexity which makes it an ideal choice for a preliminary assessment of the Reinforcement Learning (RL) potential. The Q-value function represents a refined estimate of the expected future reward obtained by taking action *A* in state *S* and following a target policy from that point on. QL is a model-free agent, therefore it does not require the integration of any models of the environment. It is also value-based, meaning that the agent learns the Q-value function from any given state. Moreover, QL employs Temporal Difference (TD) learning [22], combining elements of both Monte Carlo (MC) methods [23] and DP. It should be noted that, like MC methods, TD can learn by directly interacting with the environment, without a model of the environment's dynamics while, similarly to the DP, TD employs a "bootstrapping" approach, i.e., it estimates the Q-value function based on estimates of successor state-action pairs.

The Q-value functions can be approximated through tables or Neural Networks (NNs). In the latter case, the agent is referred to as Deep Q-Learning (DQL) and, during the training process, two different NNs are used to enhance stability. The first one is called *behavior Q-value function* which generates the transition {S, A, r, S'}. The second one, called *target Q-value function* is updated with a customized frequency, and used by the trained agent. In order to explore the whole environment, during the training random actions must be taken to discover new state-action pairs that could lead to an improvement of the policy. A common exploration strategy is the ε-greedy [21] in which the action is randomly generated with a probability of ε, while in the other cases (with a probability of 1- ε) the action will be chosen to maximize the Q-value function. The value of ε is therefore commonly higher at the start of the training since, as the agent has limited experience with the system, and will be decreased over various episodes, to exploit the acquired knowledge.

As previously mentioned, during the training process, the RL algorithm updates the NNs parameters. Based on a taken action A, the agent collects a reward r, a new state S', and this information, related to a specific transition, is called experience. Technically, NNs parameters could be updated after each experience. However, to improve efficiency, the DQL relies on an off-policy approach where the experiences are collected in an experience buffer and in a subsequent moment, the parameters are updated using a random sampling of the experiences from the experience buffer.

### 3.2 Application to the Case Study

In this this study a Deep Q-learning agent was selected. It operates with the following states:

- Torque request to the powertrain.
- Engine speed.
- Battery State of Charge (SoC).
- Percentage of worked time, defined as the ratio between current time and duration. The percentage of worked time is necessary for maintaining charge sustainability. As the mission nears completion, the agent should aim to keep the battery level close to the target.

The action provided by the agent was the Engine Load, thereby the ratio between the actual ICE torque and the maximum value for the given engine rotational speed. Finally, since the Skid Steer Loader has to maximize both efficiency and productivity, the same reward defined in [18] was adopted. It is composed of two contributions: the instantaneous fuel consumption of the engine and a penalty considering the deviation between the initial and the final SOC.

$$r = k_1 - k_2 \dot{m}_f \Delta t - k_3 (SoC - SoC_{trg})^2 \qquad 2$$

Here $k_1$ serves as a null offset to make the reward positive. Meanwhile $k_2, k_3$ are used to balance the trade-off between fuel savings and SoC deviation. The SoC deviation is penalized in aiming to maintain charge sustainability during the duty cycle.

## 4. Simulation Results

This section presents the main findings of the research activities. The results of the training process will be presented first, while in the second part of the paragraph, the performance of the trained deep-Q learning algorithm will be benchmarked against the DP reference.

### 4.1 DQN Training

The DQL agent was trained on the *Y-Low-Load-Cycle* since it is representative of the average SSL operations. Figure 5 shows the averaged cumulative reward and the initial Q-value $Q_0$ which represent the sum of the rewards over one episode and the estimation for the expected reward at the beginning of each episode respectively. Typically, to consider the training acceptable, it is expected that both values reach a maintained stable value after a certain number of episodes, as it happens in this case.

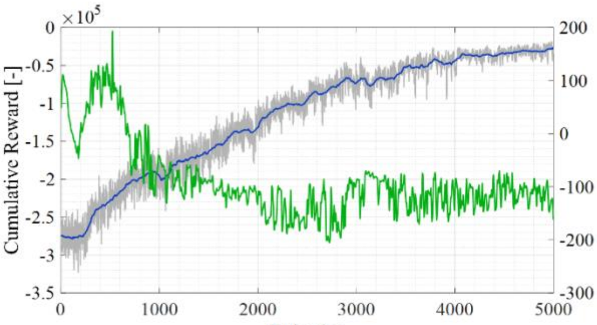

Figure 5: Training performance, average reward (blue) and Q-value (green).

In Figures 6 and 7, the behavior of the DQL agent can be observed in terms of SOC profile and torque split. The lower usage of the electric contribution in the DP optimal solution is evident with respect to the DQL agent. A peculiarity of the latter is the use of a limited number of actions, despite a wide range of candidates being available. This is evident from Figure 7a, where it is possible to observe how the ICE mainly switches between three main torque levels. This behavior of the agent may be intrinsic to the DQL framework, and it was already observed in a previous work of the authors [18]. Extensive testing with multiple action space grids and various neural network parameters yielded the same behavior. Nevertheless, this initial performance was considered satisfatory as a crucial intermediate step in the development of the framework and in evaluating the potential of reinforcement learning. On the contrary, the DP (Figure 7b) exploits the engine to cover most of the duty cycle while the electric motor provides assistance during highly demanding phases or to recharge the battery when the power request is low.

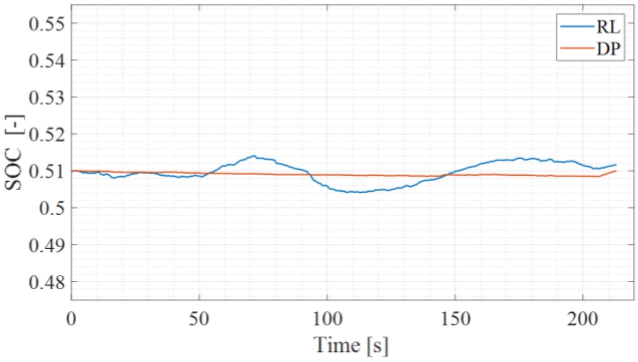

Figure 6: SoC profile during training compared against global optimum provided by the DP.

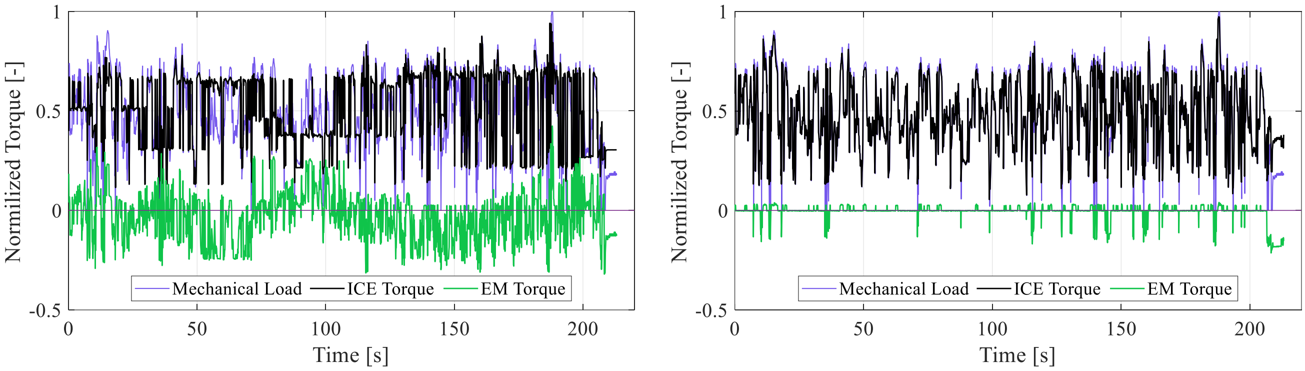

(a) (b)

Figure 7: Torque split on the Y Low Load Cycle.
On the left RL behavior, on the right the global optimum provided by DP.

### 4.1 Performance Assessment

The performance of the DQL agent was then assessed on the mission profiles not included in the training process. Figure 8 illustrates the SOC trajectory for the High Load Y cycle and it confirm the considerations made in the analyses of the training results. The DQL agent was able to achieve a final SOC quite close to the DP reference even if it showed a more oscillating behavior. During the whole mission profile, the RL tends to charge and discharge the battery according to the instantaneous power request since, differently from the DP, it has no a-priori knowledge of future operating conditions. Furthermore, the SOC swing indicates a higher exploitation of the electric components as it could be clearly identified in Figure 9, where the torque split is depicted. The RL control laws match quite well the DP reference, but the torque provided by the electric motor is significantly higher for the DQL Energy Management System. Such behavior also affects the time distribution of the engine operating points depicted in Figure 10. As a matter of fact, the Reinforcement Learning, keeps the ICE working at higher loads in comparison with the DP. Higher load operations seem to be quite efficient because the downsized engine presents the maximum efficiency close to the maximum torque value. Moreover, by contrasting the time allocation of the hybrid unit with that of the conventional unit (as depicted in Figure

10c), it is evident that less time is expended in regions of lower efficiency. This outcome can be directly attributed to the downsizing effect.

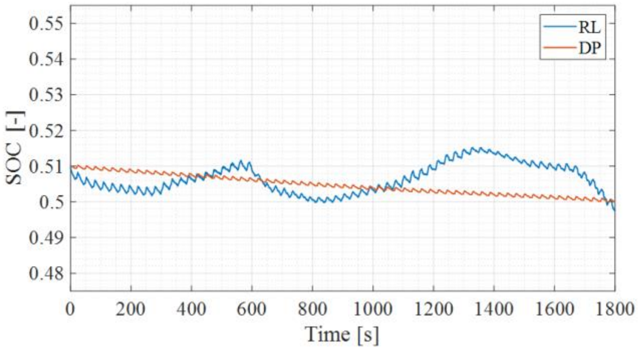

Figure 8 Comparison of SoC profile testing on Y High Load cycle against global optimum provided by the DP.

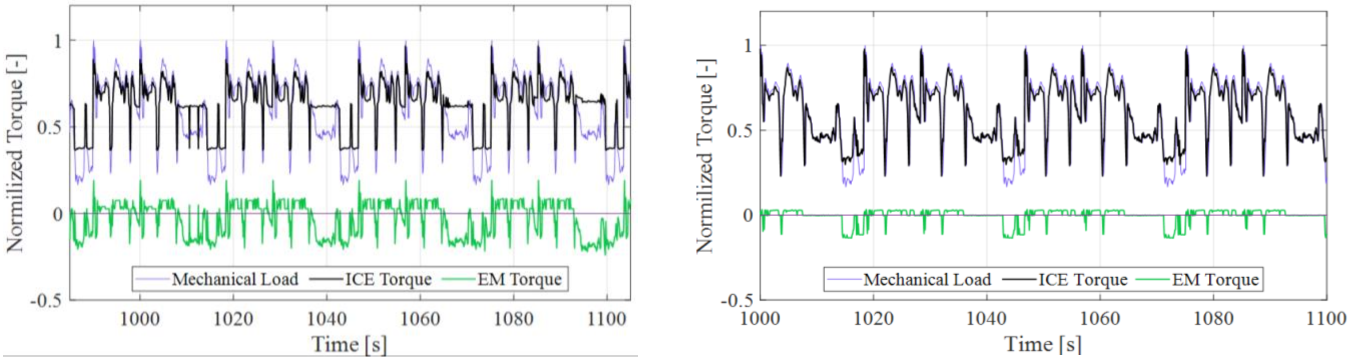

(a) (b)

Figure 9: Torque split on the Y High Load Cycle.
On the left RL behavior (a), on the right the global optimum provided by DP (b).

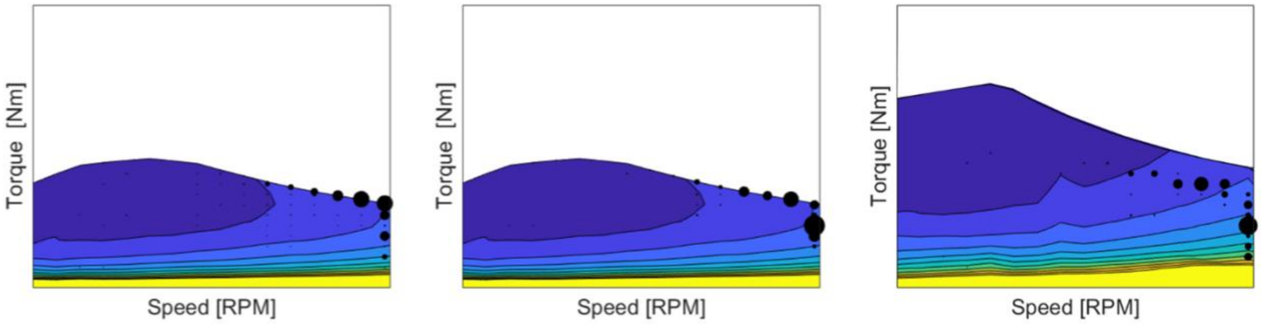

(a) (b) (c)

Figure 10: Time distribution of the engine operating points, on the Y High Load Cycle (a).
On the left RL distribution, on the right DP distribution (b). Conventional powertrain (c)

Analogous considerations could be applied to the final two duty cycles, which for the sake of conciseness are not included here. Nevertheless, it is worth to point out a peculiar behavior of dynamic programming in the early phases of the Field Tracking duty cycle (see Figure 11). During this period, the load of the powertrain is quite low since the SSL is simply moving towards the working field. The DP, therefore, thanks to its knowledge of the future driving conditions, performs a load point moving strategy in order to increase the engine efficiency and the energy stored in the battery. This reservoir is then exploited in the subsequent working phases saving a significant amount of fuel. The DQL, on the contrary, shows a limited SOC swing since it optimizes the powersplit based on the actual driving conditions.

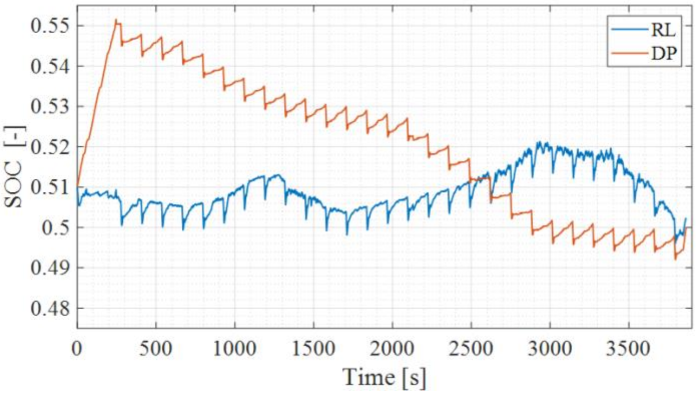

Figure 11: SoC profile during testing on Field Tracking cycle compared against global optimum provided by the DP.

From the fuel economy perspective, the performance of the DQL control algorithm is quite satisfactory. As previously mentioned, the 80 kW conventional powertrain was considered as a reference to perform a fair comparison, since in terms of performance and machine productivity the conventional 55 kW powertrain is outperformed by the hybrid one. The comparison reported in Figure 12 highlights an improvement with respect to the conventional powertrain up to 4% and a limited gap with respect to the DP benchmark (about 3-5%). The maximum reduction is achieved on the Y-cycles, and it is mainly produced by the engine downsizing. On the contrary, this effect is less evident on the last two mission profiles because of their higher load requirements. Indeed, this can be observed better in Figure 12b, which shows the brake specific fuel consumption relative to the provided mechanical power. On the *Basement-Dig*, in particular, the DP shows minimal potential, and RL is unable to enhance fuel economy with respect to conventional ICE even if the average load of this duty is quite close to the *Y-High-Load-Cycle* (see Table 2). This discrepancy can be motivated by the frequent peaks of the requested power which exceed the maximum torque of the ICE and require the support of the electric machine. Therefore, the efficiency drop produced by the double energy conversion of the series architecture could not be counterbalanced by the optimization of the engine operating point. Such a behavior is rarely present on the *Y-High-Load-Cycle* where the peaks of the load are always below the maximum ICE torque.

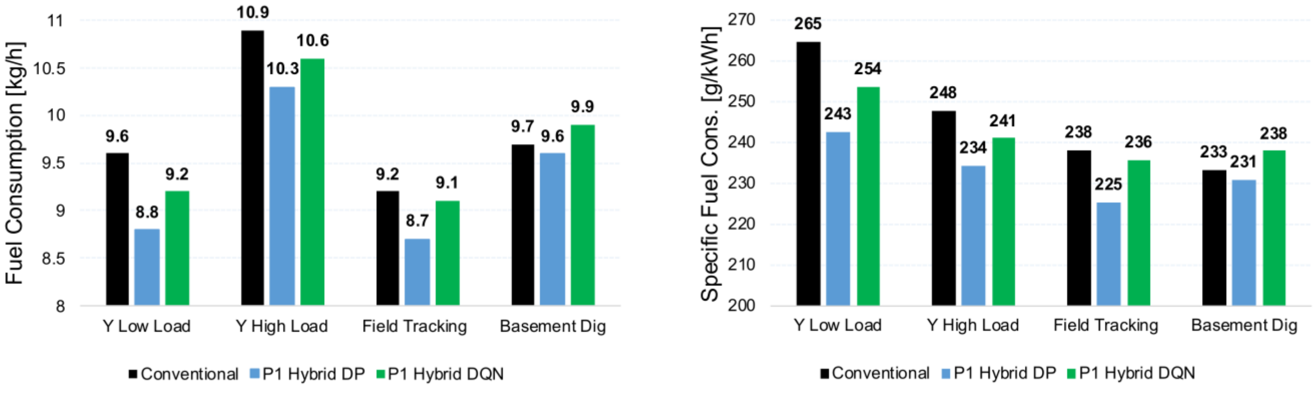

(a) (b)

Figure 12 Fuel consumption assessment for the different duty cycles (a). Specific fuel consumption for the different duty cycles (b)

## 5 Conclusions and Further Developments

In the present work, a Reinforcement Learning control algorithm was exploited to design the Energy Management System of a hybrid electric Skid Steer Loader. A Deep Q-Learning agent was trained and tested over relevant mission profile experimentally measured on a prototype of the considered vehicle.

The fuel economy of the hybrid SSL featuring the proposed control strategy was benchmarked against the performance of a conventional vehicle achieving a maximum improvement of 4%. Meeting the demands of critical duty cycles opens up promising opportunities for further fuel consumption reductions in mixed conditions. As a matter of fact, an average working day could feature long idling and lower loads during which the hybridization could be very beneficial. Indeed, fuel consumption can be improved since more intelligent control strategies could be implemented for start-stop operations and idling, as well as the electrification of the auxiliary systems like air conditioning and cooling fans. These additional capabilities will be examined in future phases of this research project.

The DQL is also able to mimic the control law of the dynamic programming with a limited gap in terms of average fuel consumption (+3-5%). However, a discrete behavior of the agent is observed during the training and testing phases, and it suggests the necessity of exploring a more responsive agent such as a Soft Actor Critic (SAC) in order to close the gap with the DP control law. Additional benefits could be also obtained including additional contribution in the RL reward, such as the minimization of the NOx Emissions which are critical for the compliance of the Stage V regulation.

Further analyses on the experimental data will be also performed to separate the contribution of traction power from the working hydraulics and to enable a refinement of the powertrain component design and the performance assessment of additional hybrid architectures.

## References

[1] J. Wang, Z. Yang, S. Liu, Q. Zhang, and Y. Han, “A comprehensive overview of hybrid construction machinery,” *Adv. Mech. Eng.*, vol. 8, no. 3, pp. 1–15, 2016, Doi: 10.1177/1687814016636809.

[2] J. Deere, “644K Hybrid Wheel Loader,” https://www.martinequipment.com/new-equipment/construction-equipment/wheel-loaders/644k-hybrid-wheel-loader/

[3] Dieci, “Dieci Mini Agri Hybrid Boost System,” https://dieci.com/web/en/eima-2022-hybrid-boost-system-de-dieci-conquiert-avec-la-technologie-green/

[4] Bobcat, “The word’s first all-electric compact loaders,” https://www.bobcat.com/na/en/equipment/future-products/t7x-s7x-all-electric-compact-loaders (accessed Jul. 05, 2024).

[5] W. Zhang, J. Wang, S. Du, H. Ma, W. Zhao, and H. Li, “Energy management strategies for hybrid construction machinery: Evolution, classification, comparison and future trends,” *Energies*, vol. 12, no. 10. MDPI AG, 2019. Doi: 10.3390/en12102024.

[6] D. Fassbender, V. Zakharov, and T. Minav, “Utilization of electric prime movers in hydraulic heavy-duty-mobile-machine implement systems,” *Autom. Constr.*, vol. 132, no. August, p. 103964, 2021, Doi: 10.1016/j.autcon.2021.103964.

[7] X. Fei, Y. Han, and S. V. Wong, “An Overview of and Prospects for Research on Energy Savings in Wheel Loaders,” *Automotive Experiences*, vol. 6, no. 1. Universitas Muhammadiyah Magelang, pp. 133–148, Jan. 01, 2023. Doi: 10.31603/ae.8759.

[8] F. Wang, M. A. Mohd Zulkefli, Z. Sun, and K. A. Stelson, “Energy management strategy for a power-split hydraulic hybrid wheel loader,” *Proc. Inst. Mech. Eng. Part D J. Automob. Eng.*, vol. 230, no. 8, pp. 1105–1120, Jul. 2016, Doi: 10.1177/0954407015600899.

[9] F. Wang, Z. Lin, B. Xu, and W. Fiebig, “An Electric-Hydrostatic Energy Storage System for Hydraulic Hybrid Wheel Loader,” *IEEE Trans. Veh. Technol.*, vol. 71, no. 7, pp. 7044–7056, Jul. 2022, Doi: 10.1109/TVT.2022.3167519.

[10] P. Ponomarev, R. Åman, H. Handroos, P. Immonen, J. Pyrhönen, and L. Laurila, “High power density integrated electro-hydraulic energy converter for heavy hybrid off-highway working vehicles,” *IET Electr. Syst. Transp.*, vol. 4, no. 4, pp. 114–121, Dec. 2014, Doi: 10.1049/iet-est.2013.0009.

[11] T. Aschauer *et al.*, “Hydrogen Hybrid ICE Powertrains with Ultra-Low NOx Emissions in Non-Road Mobile Machinery,” Apr. 2023. Doi: 10.4271/2023-01-0471.

[12] A. Bertini, M. Ceraolo, and G. Lutzemberger, “Systematic approach in the hybridization of a hydraulic skid loader,” *Autom. Constr.*, vol. 58, pp. 144–154, Aug. 2015, Doi: 10.1016/j.autcon.2015.07.013.

[13] A. Biswas and A. Emadi, “Energy Management Systems for Electrified Powertrains: State-of-the-Art Review and Future Trends”, *IEEE Trans. Veh. Technol.*, vol. 68, no. 7, pp. 6453–6467, 2019, Doi: 10.1109/TVT.2019.2914457.

[14] D. P. Bertsekas, *Dynamic programming and optimal control*. Athena Scientific, 2005.

[15] G. Paganelli, G. Ercole, A. Brahma, Y. Guezennec, and G. Rizzoni, “General supervisory control policy for the energy optimization of charge-sustaining hybrid electric vehicles,” *JSAE Rev.*, vol. 22, no. 4, pp. 511–518, 2001, Doi: https://doi.org/10.1016/S0389-4304(01)00138-2.

[16] L. S. Pontryagin, *Mathematical Theory of Optimal Processes*. 1987. Doi: doi.org/10.1201/9780203749319.

[17] C. E. García, D. M. Prett, and M. Morari, “Model predictive control: Theory and practice—A survey,” *Automatica*, vol. 25, no. 3, pp. 335–348, 1989, Doi: https://doi.org/10.1016/0005-1098(89)90002-2.

[18] L. Tresca, L. Pulvirenti, L. Rolando, and F. Millo, “Development of a deep Q -learning energy management system for a hybrid electric vehicle,” *Transp. Eng.*, vol. 16, no. March, p. 100241, 2024, Doi: 10.1016/j.treng.2024.100241.

[19] R. Zou, L. Fan, Y. Dong, S. Zheng, and C. Hu, “DQL energy management: An online-updated algorithm and its application in fix-line hybrid electric vehicle,” *Energy*, vol. 225, p. 120174, 2021, Doi: 10.1016/j.energy.2021.120174.

[20] J. Wu, H. He, J. Peng, Y. Li, and Z. Li, “Continuous reinforcement learning of energy management with deep Q network for a power split hybrid electric bus,” *Appl. Energy*, vol. 222, no. April, pp. 799–811, 2018, Doi: 10.1016/j.apenergy.2018.03.104.

[21] S. A. G. B. Sutton, Richard, *Reinforcement Learning: An Introduction*. 2018. [Online]. Available: http://incompleteideas.net/book/the-book-2nd.html

[22] L. P. Kaelbling and M. L. Littman and A. W. Moore, “Reinforcement Learning: A Survey,” 1996.

[23] N. Metropolis and S. Ulam, “The Monte Carlo Method,” *J. Am. Stat. Assoc.*, vol. 44, no. 247, pp. 335–341, Sep. 1949, Doi: 10.1080/01621459.1949.10483310.

# Session 3.1 SUSTAINABLE POWERTRAINS

# Exploring the Efficacy of Ether-based Ignition Improvers for Implementation of (M)Ethanol Mixing-Controlled Combustion

S. Lee and D. Lopez-Pintor

Sandia National Laboratories, 7011 East Ave, Livermore, CA 94550, USA.

E-mail: slee7@sandia.gov
Telephone: +(1) 925-230-7403

**Abstract.**

Methanol and ethanol are a promising alternative to fossil fuels for the decarbonization of the off-road and transportation sectors. Although methanol and ethanol are typically seen as fuels for spark ignition engines, mixing-controlled compression ignition combustion is typically preferred in most off-road and medium-and heavy-duty applications due to its high reliability, durability and efficiency. Among the various challenges to be addressed to implement ethanol/methanol combustion in mixing-controlled compression ignition engines, the primary hurdle is the low ignitability of the fuel. Blending reactive ignition improvers, such as 2-ethylhexyl nitrate, has demonstrated to achieve stable and efficient mixing-controlled compression ignition operation without major engine modification. However, the presence of the nitrate group in 2-ethylhexyl nitrate adversely affects the NOx emission characteristics. Conversely, ether-based molecules show significant potential as ignition improvers due to their high reactivity, and they can be directly produced from renewable sources. To assess the effectiveness of ether-based ignition improvers to enhance the reactivity of methanol and ethanol, experiments were performed in a single-cylinder medium-duty research engine and chemical kinetic simulations were performed using ANSYS CHEMKIN-PRO; and results were compared against previous data obtained with 2-ethylhexyl nitrate. Large amounts of dimethyl ether, diethyl ether and diethylene glycol diethyl ether were required to achieve a similar level of ignitability as demonstrated by 2-ethylhexyl nitrate because ethers predominantly yielded methyl, ethyl and atomic hydrogen radicals, whereas 2-ethylhexyl nitrate generated the more-reactive OH. Moreover, ethers formed radicals late during the ignition delay time whereas 2-ethylhexyl nitrate decomposed rapidly, thereby limiting the effect of ethers on methanol/ethanol reactivity. Results suggested that it may be more advantageous to introduce ether-based ignition improvers separately into the cylinder in a dual-fuel (m)ethanol/ether combustion strategy, which has been also explored in this study. Compression-ignition of port-injected ethers led to high-reactivity in-cylinder conditions to enable ignition of direct-injected methanol/ethanol, providing a viable approach for methanol/ethanol mixing-controlled compression ignition combustion.

## Notation

| | |
|---|---|
| *aTDC* | *After top dead center* |
| *CA50* | *Crank angle of 50% burn point* |
| *CAD* | *Crank angle degrees* |
| *CFD* | *Computational fluid dynamics* |
| *CN* | *Cetane number* |
| *CO* | *Carbon monoxide* |
| *COV* | *Coefficient of variation* |
| *DEE* | *Diethyl ether* |
| *DGE* | *Diethylene glycol diethyl ether* |
| $d_{hole}$ | *Injector orifice diameter* |
| *DME* | *Dimethyl ether* |
| *DOE* | *Duration of energizing* |
| *E85* | *Fuel with* $51\%_{vol}$ *to* $83\%_{vol}$ *ethanol content* |
| *EGR* | *Exhaust gas recirculation* |
| *EHN* | *2-ethylhexyl nitrate* |
| *FID* | *Flame ionization detector* |
| *Gge* | *Gasoline gallon equivalent* |
| *HCCI* | *Homogeneous charge compression ignition* |
| *HRR* | *Heat release rate* |

| | |
|---|---|
| *HTHR* | *High temperature heat release* |
| *ICE* | *Internal combustion engine* |
| *IMEPn* | *Net indicated mean effective pressure* |
| *ISCO* | *Indicated specific CO emissions* |
| *ISNOx* | *Indicated specific NOx emissions* |
| *ISPM* | *Indicated specific PM emissions* |
| *LTHR* | *Low temperature heat release* |
| *MCCI* | *Mixing controlled compression ignition* |
| *MFB* | *Mass fraction burned* |
| *MRMF* | *Most reactive mixture fraction* |
| *NOx* | *Nitrogen oxides* |
| *P* | *Pressure* |
| *PM* | *Particulate matter* |
| *RCCI* | *Reactivity controlled compression ignition.* |
| *RON* | *Research octane number* |
| *RoP* | *Rate of production* |
| *SOE* | *Start of energizing* |
| *T* | *Temperature* |
| *TDC* | *Top dead center* |
| $\varphi$ | *Equivalence ratio* |

## 1. Introduction

Ethanol and methanol are two of the most promising renewable liquid fuels for the decarbonization of the transportation sector, especially for hard-to-electrify applications where energy density is critical, such as many on-road medium and heavy-duty applications and most off-road applications including construction, agriculture, rail and marine. Some of the advantages of ethanol and methanol over other decarbonization strategies include:

- A very high production capacity of approximately 17.3 and 2.6 billion gallons per year for ethanol and methanol, respectively, only in the United States, which increases to 29.5 and 36.6 billion gallons per year worldwide [1].
- A well-stablished industry that can use the existing infrastructure [2]. For instance, E85 fuel (gasoline containing $51\%_{vol}$ to $83\%_{vol}$ ethanol) is widely available in the United States [3].
- A relatively high energy density of approximately 27 MJ/kg (21 MJ/L) and 22 MJ/kg (15.8 MJ/L) for ethanol and methanol [4], respectively, compared to other low-carbon technologies such as hydrogen (120 MJ/kg but only 5.6 MJ/L when compressed at 700 bar and room temperature [5]), or battery storage (1 MJ/kg for lithium-ion technology [6]).
- A much lower life-cycle carbon intensity than that of petroleum-derived fuels, from -47% to -90% (with carbon capture) for biomass-based production of ethanol or methanol using existing technology, and up to -92% in a renewable power grid scenario [7, 8].
- A competitive cost of \$2.69/gge and \$2.41/gge (gasoline gallon equivalent) for biomass-based production of ethanol and methanol, respectively [8], compared to \$2.28/gal and \$2.71/gal for petroleum-derived gasoline and diesel fuel in the United States, respectively [9].

Ethanol and methanol have demonstrated to be excellent fuels for spark-ignition engines mainly due to their very high laminar flame speed and octane number (research octane number, RON, of ethanol and methanol equal to 108.6 and 108.7, respectively [10]). However, mixing-controlled compression-ignition (MCCI) engines are desired for most heavy-duty and off-road applications due to their efficiency, reliability, robustness, durability and transient response. Unfortunately, the physicochemical properties of ethanol and methanol are not suitable for modern MCCI engines. Some of the technical challenges and barriers of implementing ethanol and methanol MCCI combustion include:

- Very low ignitability, with a cetane number (CN) of ethanol and methanol equal to approximately 8 and 3, respectively [11], compared to a minimum legal cetane number of 40 for diesel fuel in the United States [12].

- Lower energy density than conventional diesel fuel, meaning that a significantly higher mass of fuel injected per cycle is required to reach the same engine load. This can be achieved with longer injection durations or larger injector nozzle hole diameters, but these solutions may negatively impact the efficiency and emissions characteristics of the engine.
- Low viscosity and lubricity, with a kinematic viscosity of ethanol and methanol equal to 1.06 and 0.58 $mm^2/s$ at 40°C, respectively [13], compared to 1.3 – 4.1 $mm^2/s$ for diesel fuel [14], which makes the fuel incompatible with existing fuel-lubricated high-pressure pumps typically used in modern diesel engines. Lubricity additives for ethanol and methanol that can prevent wear problems with high-pressure fuel injection equipment exist and have been proved to work reasonably well at application-relevant conditions [15, 16].
- Material compatibility problems [17], especially with sealing rings and other rubber-made or plastic-made components.

Among these technical challenges, the low ignitability of ethanol and methanol is perhaps the most critical barrier for MCCI combustion. Different solutions have been proposed to overcome this barrier. The most straight-forward solution consists of increasing the in-cylinder reactivity by increasing the compressed-gas temperature [18]. This can be achieved by increasing the engine compression ratio, retaining hot residual gases or even using intake heaters for conditions where the enthalpy of the exhaust gases is not high enough to promote the ignition of the fuel (such at low engine loads or during cold starts) [19]. However, the transient response of the engine can be severely compromised by this approach due to the thermal inertia of the engine. An alternative solution consists of using ignition assistance devices such as glow plugs. However, glow plugs pose challenges with durability and energy consumption (up to 3%-unit engine efficiency penalty [20]), and more than one device may be required for reliable ignition of all the plumes to avoid combustion instabilities. Turbulent jet ignition of a direct-injection ethanol/methanol spray has been explored [21] and demonstrated to work well [22], but the required active pre-chamber increases the engine complexity and cost, poses durability concerns, and penalizes heat rejection and pumping work. Dual-fuel strategies where the ethanol/methanol spray is ignited by a highly reactive fuel have been reported in the literature. There are two main options for dual-fuel MCCI ethanol/methanol combustion. One approach consists of igniting the alcohol spray with a burning pilot injection of a highly reactive fuel [23]. However, two high-pressure injection systems are required in this approach, which increases engine cost and complexity. A different approach consists of direct-injecting the alcohol spray in a highly reactive mixture of partially-burned high-reactivity fuel, hot gases and radicals. Conceptually, this is equivalent to an inverted Reactivity Controlled Compression Ignition (RCCI) strategy [24], and it has been demonstrated experimentally [25]. However, a significant fraction of highly reactive fuel may be needed for low load operation, requiring regular refills of two fuels. Finally, autoignition reactivity improvers (also known as cetane improvers) can be blended with the ethanol/methanol to increase the ignitability of the fuel. This approach is followed by Scania in his DC9 E02 engine [26], which is fueled with ETAMAX (also known as ED95), a blend of 95% wet ethanol and 5% of an additive package that contains an ignition improver termed BERAID, a poly-ethylene-glycol derivative developed by Azko-Nobel. However, high engine compression ratios (between 25:1 and 28:1) are required to be able to operate the engine with additive levels equal to or below 5% at low engine loads.

From the previous literature review, it is clear that there are multiple approaches with potential to enable ethanol and methanol MCCI combustion. However, it is unclear what would be the best solution and significant research and development efforts are required to better understand the full potential of these strategies. In this paper, techniques based on blending ethanol/methanol with a highly reactive fuel or a cetane improver will be explored both experimentally in a single-cylinder research engine and numerically using chemical kinetic simulations. Cetane improvers are preferred by the authors over other strategies because they have been already proven commercially by Scania, with more than 600 buses supplied that operate with this technology. Moreover, no additional engine hardware is required for this strategy except an ethanol- or methanol-compatible fuel system, simplifying the engine design and opening the door for retrofitting of existing engines.

The potential of cetane improvers to enable ethanol [27] and methanol [28] MCCI combustion in a production-like medium-duty diesel engine has been previously evaluated by the authors. In both cases, the fuel was doped with 2-ethylhexylnitrate (EHN), a common and inexpensive cetane improver typically used with diesel fuel (around 50% of all the diesel fuel sold in the United States contains EHN) [29]. The engine was operated at low and medium loads with boundary conditions representative of diesel engine operation. Piston and injector were production parts, and the compression ratio (16:1) was the same as that of the production engine. MCCI combustion of ethanol and methanol was achieved in the experiments with an acceptable combustion control range that was limited by transition to kinetically-controlled combustion for very advanced injection timings and high cycle-by-cycle variability for very retarded injection timings. Medium load engine operation was achieved with 3%$_{vol}$ EHN, and ethanol and methanol combustion led to higher thermal efficiency values than those of diesel due to lower heat transfer losses and faster late mixing-control burning rates. At low loads ethanol and methanol combustion was only doable with 7%$_{vol}$ EHN and led to slightly lower efficiency values than those of diesel due to lower combustion efficiency. However, low load operation with 3%$_{vol}$ EHN was demonstrated by increasing the compression ratio from 16:1 to 20:1. Particulate matter emissions of ethanol and methanol combustion were much lower than the current U.S. Off-Road legal limit and the 2027 U.S. EPA Heavy-Duty limit, with NOx emissions within the range of those of diesel.

Despite the fact that these are encouraging results, it has been reported that around 30% of the nitrate group of EHN is converted to NOx [30], which motivates the exploration of alternative ignition enhancers. Ethers are interesting alternatives to traditional cetane improvers such as alkyl nitrates (e.g., EHN), peroxides or glycols. First, the cetane number of ethers is usually very high. Reported values include CN = 78 for dimethyl ether (DME) [11], CN = 160 for diethyl ether (DEE) [31] and CN = 140 for diethylene glycol diethyl ether (DGE) [32]. Second, ethers do not contain nitrogen, avoiding any contribution from the cetane improver to engine-out NOx emissions, and typically have low soot propensity. Finally, many ethers can be produced from renewable sources by dehydration of primary alcohols, such as ethanol or methanol, over acid catalysts at medium-to-high temperatures (above 240°C). In this process, two alcohol molecules combine to produce one molecule of ether and one molecule of water. The molecule of ether formed depends entirely on the alcohol used in the process. Thus, methanol dehydration leads to DME, ethanol dehydration leads to DEE, propanol leads to dipropyl ether, butanol leads to dibutyl ether, etc… Moreover, exhaust heat from the engine can be used to produce ethers on-board through this process [33, 34].

In this study, the potential of ethers to enable ethanol and methanol MCCI combustion was assessed. To do so, experiments with alcohol/ether blends were performed in a single-cylinder metal research engine, and the results compared with previous data obtained using EHN as ignition improver. Detailed chemical kinetic simulations were also performed to better understand the mechanisms that control the reactivity of alcohol/ether blends. Finally, dual-fuel alcohol-ether strategies were also explored numerically.

## 2. Methodology

### 2.1 Experiments

Engine experiments were performed in a 0.83 L single-cylinder medium-duty research engine based on an 8-cylinder 6.7 L Ford Scorpion engine and fueled with ethanol doped with three different ignition improvers: EHN, DEE and DGE. Engine specifications are shown in **Table 1**, and more details about the engine facility and operation can be found in [35].

**Table 1. Specifications of medium-duty single-cylinder research engine**

| | |
|---|---|
| Bore x stroke | 99 x 108 mm |
| Displacement volume | 0.8315 L |
| Compression ratio | 16.5: 1 |
| Swirl ratio | 1.7 |
| Valves | 4 |
| Fuel system | Common rail direct injection |
| Fuel injector | 8-hole piezo injector ($d_{hole}$= 138 μm) |

The experimental setup schematic is illustrated in **Fig. 1**. A high-pressure fuel-agnostic fuel system that uses a reciprocating pneumatic pump allowed reaching diesel-like injection pressures with ethanol without using lubricity additives. The intake airflow was precisely measured with sonic nozzles, the intake pressure was controlled by the intake airflow and the intake temperature was controlled by multiple electric heaters located in the intake line, plenum and runner. Exhaust gas pressure was controlled using a throttling valve within the exhaust flow to simulate the effect of turbocharging and aftertreatment systems. The coolant temperature was actively controlled with an external heating/cooling device, while engine oil temperature was not regulated. Synthetic exhaust gas recirculation (EGR), only used for baseline conventional diesel combustion experiments, is composed by a mixture of $N_2$ and $CO_2$ that reproduces the heat capacity of real EGR (estimated based on exhaust emission measurements and water formed during the combustion process).

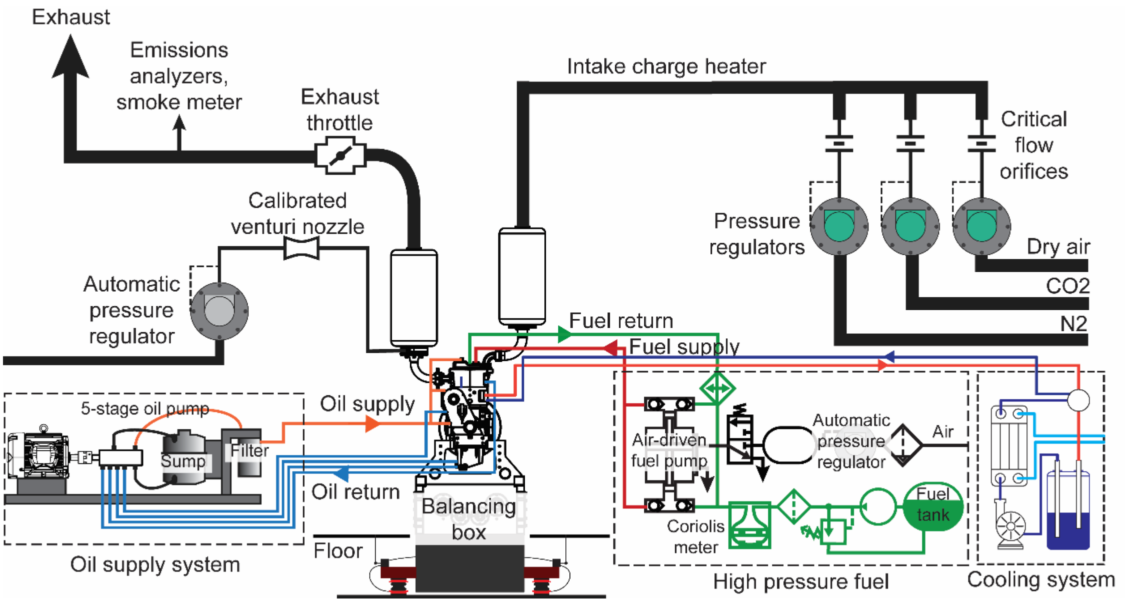
Exhaust
Emissions analyzers, smoke meter
Exhaust throttle
Intake charge heater
Critical flow orifices
Calibrated venturi nozzle
Pressure regulators
Dry air
CO2
N2
Automatic pressure regulator
Fuel return
Fuel supply
5-stage oil pump
Sump
Filter
Oil supply
Oil return
Balancing box
Floor
Oil supply system
Air-driven fuel pump
Automatic pressure regulator
Air
Fuel tank
Coriolis meter
High pressure fuel
Cooling system

**Fig. 1 Schematic of the experimental setup**

Engine experimental data were acquired and synchronized at intervals of every 0.25 crank angle degrees (CAD) utilizing an encoder with a resolution of 1440 pulses per revolution. Intake and exhaust pressures were measured using piezoresistive pressure transducers, while a piezoelectric pressure transducer was installed in the glow plug port to measure the in-cylinder pressure. Coolant and engine oil pressures and temperatures were continuously monitored. A Coriolis flow meter was installed along the fuel line after the low-pressure pump to measure fuel consumption, as shown in **Fig. 1**. Carbon monoxide (CO), nitrogen oxide (NOx), and smoke levels were measured from the exhaust flow line. Unburned hydrocarbons were not measured due to limitations of flame ionization detector (FID) in accurately measuring oxygenated hydrocarbons as those from (m)ethanol incomplete combustion. However, the composition of the exhaust stream was analyzed using gas chromatography with sampled exhaust gas.

Engine experiments were performed at low- and part-load conditions using laboratory-grade fuels and cetane improvers. A description of the engine operating conditions is provided in **Table 2**, and results for EHN-doped fuel were discussed in detail in [27, 28]. For ethanol doped with EHN, injection pressure was set at 882 bar and 1615 bar for low- and part-load conditions, respectively, which correspond with the injection pressure values used for diesel operation. However, recent results obtained with methanol showed that diesel-like injection pressures are not required to obtain ultra-low soot emissions and high late-stage mixing-controlled combustion rates with alcohols [28]. Therefore, new results with ether-based ignition improvers (DEE and DGE) presented in this paper were obtained with an injection pressure of 620 bar. A multi-injection strategy defined in [28] and described in **Table 3** was implemented in this study. Injection timing sweeps were performed by blockshifting the pilot and main injections within the stable combustion window (combustion stability limits defined by a coefficient of variation – COV – of the net indicated mean effective pressure – IMEP$_n$ – of 3% or by the occurrence of knock, whatever occurs first). The target IMEP$_n$ was achieved by adjusting the main injection duration at the different injection timings.

**Table 2 Engine operating conditions for low- and part-load**

| | Low-load | Part-load |
|---|---|---|
| Engine speed | 1200 rpm | 1600 rpm |
| IMEP$_n$ | 3.91 bar ± 0.1 bar (20% load) | 8.55 bar ± 0.1 bar (45% load) |
| Coolant temperature | 80 °C | 80 °C |
| Intake flow | 7.8 g/s | 14.9 g/s |
| Intake temperature | 90°C | 90°C |
| Intake pressure | 106 kPa | 137 kPa |
| Exhaust back pressure | 113 kPa | 146 kPa |
| Number of pilot injection | 2 pilot injections | 3 pilot injections |
| Rail pressure | 620 bar | |

**Table 3 Injection strategy for low- and part-load**

| | Low-load | Part-load |
|---|---|---|
| Duration of energizing (DOE)* of 1st pilot | N/A | 117 μs (1.12 CAD) |
| Dwell time between 1st and 2nd pilot | N/A | 1103 μs (10.59 CAD) |
| DOE of 2nd pilot | 160 μs (1.15 CAD) | 117 μs (1.12 CAD) |
| Dwell time between 2nd pilot and 3rd pilot | 1103 μs (7.94 CAD) | 883 μs (8.48 CAD) |
| DOE of 3rd pilot | 180 μs (1.30 CAD) | 200 μs (1.92 CAD) |
| Dwell time between 3rd pilot and main | 1380 μs (9.94 CAD) | 300 μs (2.88 CAD) |
| DOE of main | ≈ 690 μs (4.97 CAD) (adjusted to obtain 3.91 bar $IMEP_n$) | ≈ 1335 μs (12.82 CAD) (adjusted to obtain 8.55 bar $IMEP_n$) |

* DOE defined as the duration of the command signal sent to the injector driver.

A total of 500 consecutive cycles were acquired during steady-state operation and analyzed as detailed in [36]. Heat transfer losses were estimated by following two different approaches: (1) from an energy balance between the energy released by the fuel and work, exhaust gas enthalpy and heat transfer losses; and (2) by using the Woschni correlation [37] where the tuning parameters that define the film coefficient were calibrated for each operating condition using the approach described in [38]. The deviation between both methods was used as a metric for the uncertainty of the heat losses (reported as error bars in **Figs. 4** and **8**).

## 2.2 Chemical kinetic simulations

Chemical kinetic simulations were performed in ANSYS CHEMKIN-PRO using a comprehensive chemical kinetic mechanism for gasoline surrogates from Lawrence Livermore National Laboratory [39] (which contains the chemistry of methanol, ethanol and DME among many other fuels) combined with a detailed model for EHN decomposition [40] and with a detailed mechanism for DEE [41]. Unfortunately, the authors did not find a validated mechanism for DGE in the literature, so DGE was not included in the simulations. Alternatively, DME was evaluated as a potential ignition improver that can be obtained directly from methanol dehydration.

Two different approaches were investigated in this study. The first approach involves a single-fuel strategy where the ignition improver (EHN, DEE or DME) is blended with the alcohol fuel (ethanol or methanol). The 1-D spray model DICOM [42] was used to estimate the temperature and fuel distributions within the spray imposing boundary conditions from the experiments and assuming that the injection timing was fixed at top dead center (TDC). The model accounts for both fuel vaporization and mixing and takes into account the variation in physical properties between fuels. Then, the temperature and fuel distributions from the spray model were imposed in a 0-D constant-volume closed homogenous reactor in CHEMKIN to identify the most reactive mixture fraction (MRMF), which corresponds to the shortest ignition delay among the various temperature and equivalence ratio combinations. The MRMF was obtained for various amounts of DEE and DME and compared against that of (m)ethanol doped with $7\%_{vol}$ EHN, which has demonstrated robust combustion at both low- and part-loads experimentally. Rate of production (RoP) analyses were performed at MRMF conditions to understand the interactions between (m)ethanol and the ignition improvers.

The second approach consists of a dual-fuel strategy where the ignition improver is injected in the intake port followed by a direct-injection of (m)ethanol near TDC. A 0-D internal combustion engine (ICE) reactor that reproduces the single-cylinder engine of the experiments was used to simulate the decomposition process of the port-injected ignition improver during the compression and expansion strokes. The in-cylinder pressure, temperature and composition at the time of injection of the (m)ethanol direct-injection were obtained from the CHEMKIN ICE simulations and imposed in DICOM to obtain the temperature and fuel distributions within the alcohol spray. Then, results from DICOM were imposed in a 0-D constant-volume closed homogenous reactor in CHEMKIN to obtain the MRMF of the spray. It is noteworthy that the oxidizer in the ignition delay calculations was not pure air, but rather, the in-cylinder gas composition containing radicals derived from the ICE simulation. Calculations were performed at low load as this represents the most challenging condition for ignition due to the low in-cylinder reactivity.

The MRMF was obtained for various substitution ratios of ignition improver and for various injection timings of (m)ethanol, and compared with that of the single-fuel strategy with (m)ethanol doped with 7%$_{vol}$ EHN.

The simulation procedure for is summarized in **Fig. 2**.

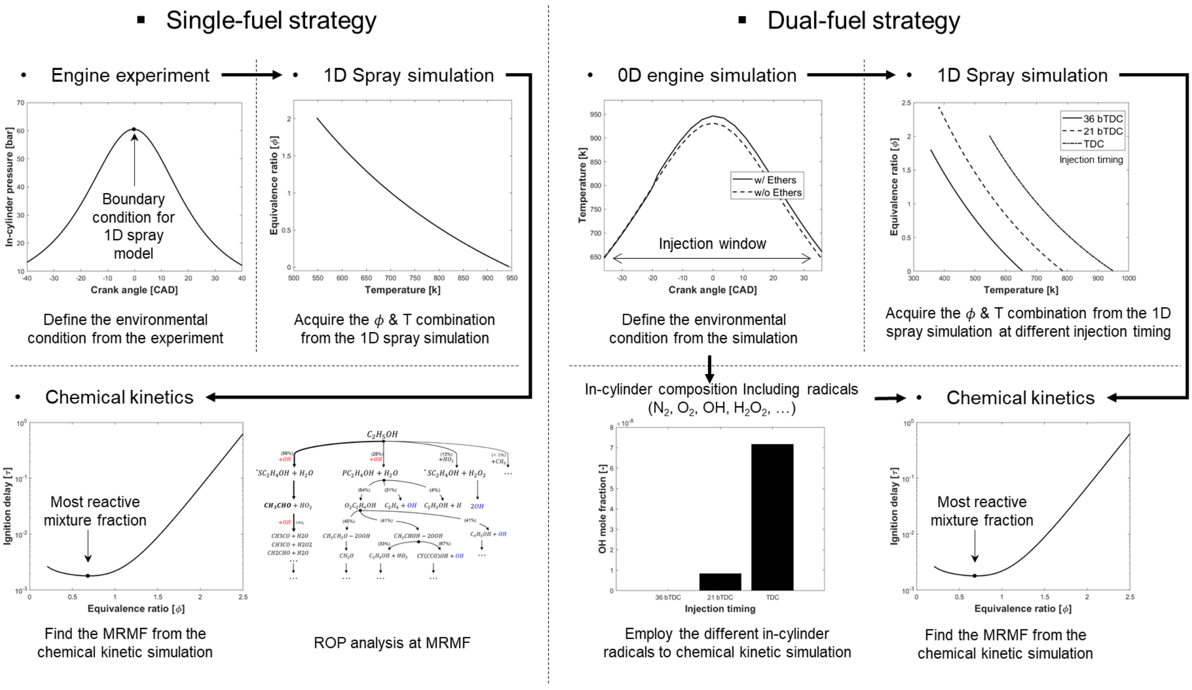
Single-fuel strategy
Dual-fuel strategy
Engine experiment
1D Spray simulation
0D engine simulation
1D Spray simulation
In-cylinder pressure [bar]
Crank angle [CAD]
Boundary condition for 1D spray model
Equivalence ratio [ϕ]
Temperature [k]
Temperature [K]
w/ Ethers
w/o Ethers
Injection window
36 bTDC
21 bTDC
TDC
Injection timing
Define the environmental condition from the experiment
Acquire the ϕ & T combination from the 1D spray simulation
Define the environmental condition from the simulation
Acquire the ϕ & T combination from the 1D spray simulation at different injection timing
Chemical kinetics
In-cylinder composition Including radicals (N2, O2, OH, H2O2, …)
Chemical kinetics
Ignition delay [τ]
Most reactive mixture fraction
Equivalence ratio [ϕ]
C2H5OH
OH mole fraction [-]
Injection timing
Find the MRMF from the chemical kinetic simulation
ROP analysis at MRMF
Employ the different in-cylinder radicals to chemical kinetic simulation
Find the MRMF from the chemical kinetic simulation

**Fig. 2 Numerical approached followed in this study**

## 3. Results and discussion

### 3.1 Ethanol MCCI combustion with ignition improver

The blending ratio of DEE and DGE was varied to enable MCCI combustion of ethanol. The engine totally misfired with 20%$_{vol}$ of both DEE and DGE, partially misfired with 30%$_{vol}$ of DEE and DGE and eventually stable combustion was achieved with 50%$_{vol}$ DGE. The minimum blending ratio of ether required for stable MCCI combustion was not optimized, but results suggested that the optimum amount is within the 35%$_{vol}$ - 45%$_{vol}$ range. In a previous investigation [27], the authors showed that stable ethanol MCCI combustion was achieved with 3%$_{vol}$ EHN at part-loads and 7%$_{vol}$ EHN at low-loads, indicating that ethers are significantly less effective in enhancing the ignitability of ethanol than EHN. In this section, experimental results of ethanol combustion with ether are compared against previous results obtained with EHN at both low- and part-load conditions.

#### *3.1.1 Low-load conditions*

**Fig. 3** shows the ignition delay, crank angle of the 50% burn point (CA50), and combustion stability (defined as COV of IMEP$_n$) of ethanol doped with 7%$_{vol}$ EHN and 50%$_{vol}$ DGE for an injection timing sweep at low load. In general, both ignition improvers showed similar ignition delay values at a given injection timing, with DGE being more reactive than EHN at the most advanced combustion timings. As explained in the *Methodology* section, the injection timing was varied within the stable combustion window, with the stability limit defined as COV of IMEP$_n$ = 3%. For EHN-doped ethanol, high COV of IMEP$_n$ values were obtained for injection timings of the 1st pilot injection more advanced or equal to -25.7 CAD aTDC and for injection timings of the 1st pilot injection more retarded or equal to -15.7 CAD aTDC, providing 7.1 CAD of CA50 control. For very advanced injection timings, combustion transitioned from MCCI to kinetically controlled combustion, leading to higher cycle-by-cycle variability, lower combustion stability, higher pressure rise rates, higher combustion noise and higher ringing intensity values. For very retarded injection timings, fuel ignitability was compromised due to the effect of the expansion on the in-cylinder temperature and pressure (and, therefore, on the in-cylinder reactivity), leading to combustion instabilities and lower combustion efficiency values. Compared to EHN, DGE showed a significantly wider stable combustion window with no combustion instability detected for the conditions tested in this study, providing 16.1 CAD of CA50 control. Moreover, combustion stability at a given injection timing was also higher with DGE than that of EHN. For DGE and EHN within the stable combustion window, the CA50 was linearly delayed as the injection timing delayed, indicating that the fuel burned in a MCCI combustion process. However, the same CA50 was obtained for the two most advanced injection timings of EHN (SOE of 1st pilot of -26.6 and -24.6 CAD aTDC), indicating a transition to kinetically controlled combustion where the CA50 advances instead of retarding as the injection timing retards [43].

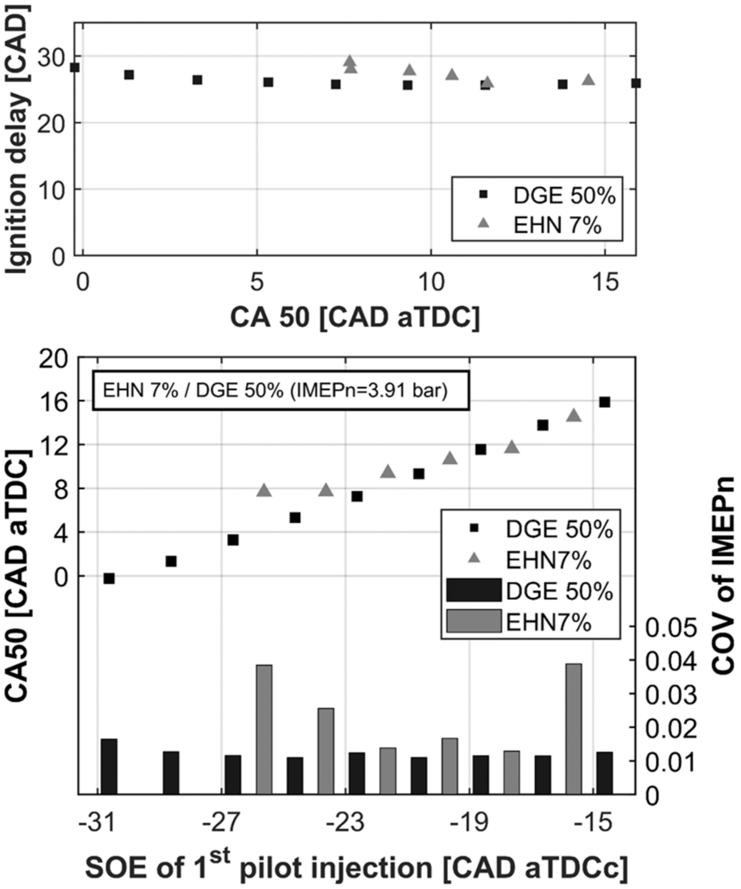

**Fig. 3. Ethanol ignition delay, CA50, and CoV of IMEP$_n$ with EHN and DGE against the SOE of 1st pilot injection at low-load conditions**

**Fig. 4** shows the indicated thermal efficiency and heat transfer losses for the same experiments shown in **Fig. 3**. Results from optimized diesel combustion operation with varying levels of EGR at 0%, 10%, and 20% were also included in the figure for completeness [44], and CA50 was used in the x-axis for a better comparison between fuels. At low-load conditions, DGE exhibited 1%-unit to 2%-unit lower thermal efficiency than both EHN and diesel, whereas EHN showed similar efficiency values as those of diesel. This is the result of a combination of multiple factors, including heat transfer losses, combustion efficiency and mixing-controlled burning rate. As shown on the right-hand side of **Fig. 4**, ethanol combustion with both DGE and EHN showed lower heat transfer losses than those of diesel due to a combination of lower adiabatic flame temperature, higher fuel vaporization cooling and much lower radiative heat losses due to ultra-low soot emissions (as will be shown later in **Fig. 6**), which would tend to increase efficiency. However, gas chromatography of the exhaust gases and CO emission measurements (discussed later and shown in **Fig. 6**) indicated that both DGE and EHN have lower combustion efficiency than diesel (note that combustion efficiency values were not reported here because unburned hydrocarbon emissions cannot be accurately measured with standard FID equipment), which would tend to decrease efficiency. Finally, **Fig. 5** shows the mass fraction burned (MFB) and heat release rate (HRR) for a CA50 of approx. 8 CAD aTDC and for ethanol doped with both EHN and DGE. DGE showed longer combustion duration and slower burning rate during the late-combustion stage, leading to lower degrees of constant volume combustion and explaining the lower thermal efficiency of DGE compared to EHN.

Interestingly, the HRR of DGE showed a combustion event associated with the pilot injections around TDC whereas the HRR of EHN did not. This pilot injection combustion enhanced the overall combustion stability by creating a more favorable environment for the ignition of the main injection, explaining the combustion stability results shown in **Fig. 3**. As mentioned before, DGE showed longer combustion duration and lower burning rate during the late-stage mixing controlled combustion process than EHN. For this late-stage combustion, burning rate is constrained by oxygen availability and air utilization. Replacing ethanol with an ignition improver resulted in a lower oxygen-to-carbon ratio, as ethanol inherently possesses a higher oxygen-to-carbon ratio than the ignition improvers (EHN and DGE have the same oxygen-to-carbon ratio equal to 0.375 vs. 0.5 for ethanol). Thus, the higher the cetane improver content, the lower the oxygen content of the fuel blend, which may impact negatively the burning rate.

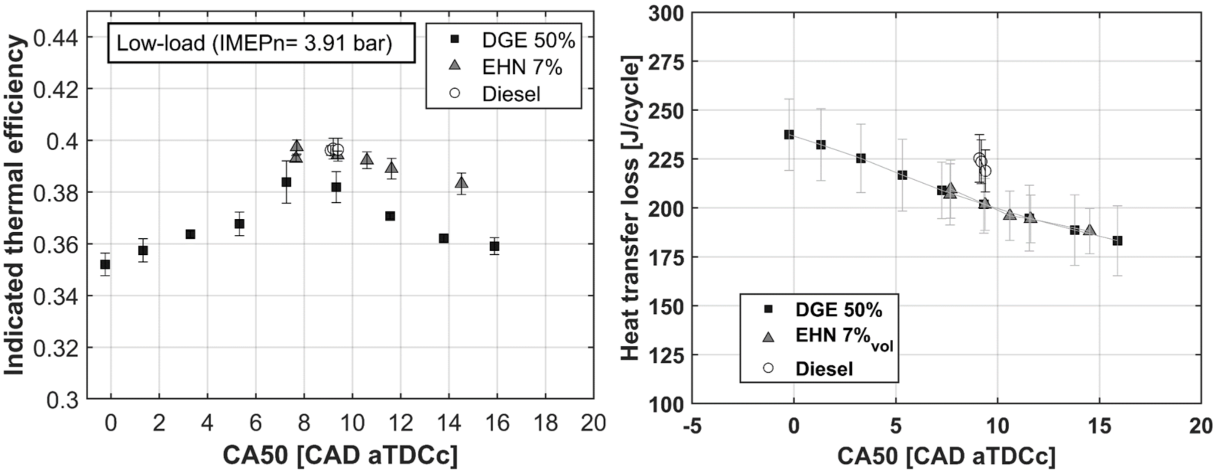

**Fig. 4 Indicated thermal efficiency (left) and heat transfer loss (right) with EHN, DGE and baseline diesel against CA50 at low-load conditions**

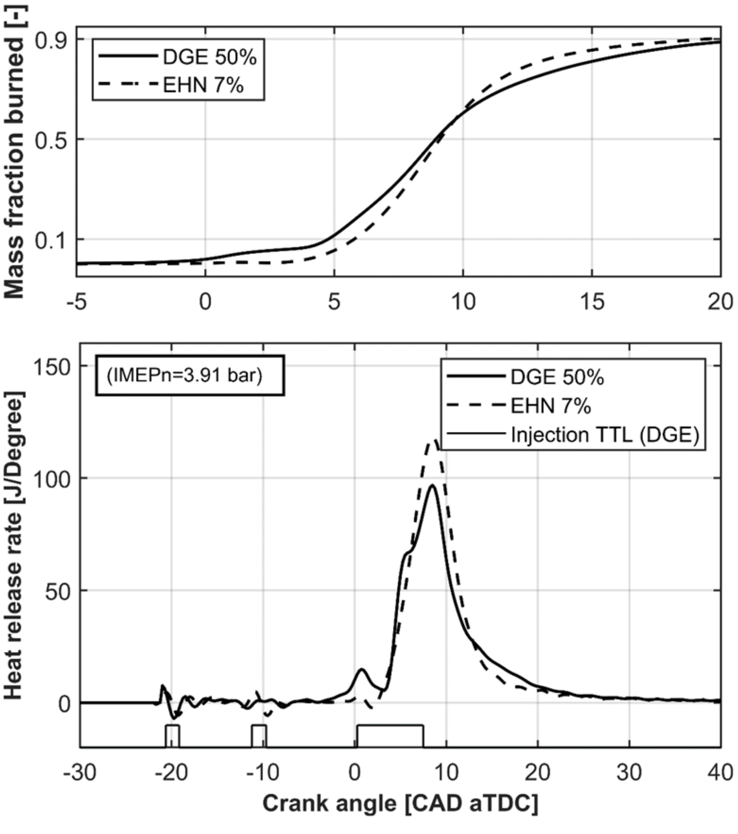

**Fig. 5. Mass fraction burned (top) and heat release rate (bottom) with EHN (SOE of the 1st pilot injection =-21.69 CAD aTDC) and DGE (SOE of the 1st pilot injection = -20.625 CAD aTDC) at low-load conditions**

**Fig. 6** shows the indicated specific CO emissions (ISCO), indicated specific NOx emissions (ISNOx) and indicated specific soot emissions (ISPM) against the SOE of 1st pilot injection for the same cases as those plotted in **Fig. 4**. Ethanol doped with EHN led to higher CO emissions than both ethanol doped with DGE and diesel fuel. As shown in **Fig. 5**, there is no specific combustion event associated with the pilot injections in the EHN cases, indicating lower reactivity compared to the DGE cases. Consequently, higher CO emissions were measured. Previous CFD results suggested that, at low-reactive conditions such, pilot injections may lead to overly lean regions that do not burn well, leading to high CO and unburned hydrocarbon emissions [45]. Although the calculation of an accurate combustion efficiency was not feasible due to the inability of standard FID equipment to measure oxygenated unburned hydrocarbons, ISCO data suggested that EHN exhibited poorer combustion efficiency compared to the other fuels. This may explain why EHN-doped ethanol had a similar thermal efficiency as that of baseline diesel despite showing less heat transfer losses and faster burning rates. The ISCO emissions of DGE were significantly lower as those of EHN and similar to those of diesel with 20% EGR. Regarding ISNOx emissions, DGE showed similar engine-out NOx as those of diesel with 10% EGR and less NOx than those of EHN probably due to the contribution of the nitrate group of EHN to engine-out NOx (it has been estimated that 30% of the nitrogen content of EHN leads to NOx [46]). The engine-out ISPM emissions from both EHN-doped and DGE-doped ethanol are extremely low, below the 2027 U.S. EPA heavy-duty legal limit.

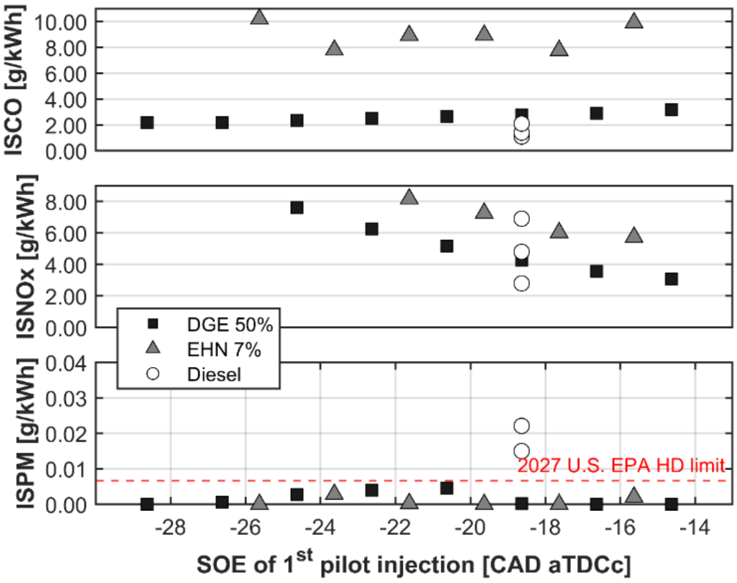

**Fig. 6. ISCO, ISNOx, and ISPM with EHN, DGE and baseline diesel against the SOE of 1st pilot injection at low-load conditions**

### *3.1.2 Part-load conditions*

**Fig. 7** shows the ignition delay, CA50, and COV of $IMEP_n$ of ethanol doped with $7\%_{vol}$ EHN and $50\%_{vol}$ DGE for an injection timing sweep at part-load conditions. The ignition delay of the DGE-doped cases barely changed with the injection timing, whereas the ignition delay of the EHN-doped cases significantly decreased as the injection timing retarded due to a better combustion of the fuel delivered by the pilot injections (see **Fig. 9**). Despite the fact that both DGE and EHN showed similar ignition delay times at low load, the DGE cases showed longer ignition delay times than the EHN cases at medium load, suggesting that the effect of DGE and EHN on the autoignition reactivity of ethanol may be sensitive to temperature and pressure, as also observed for EHN in [47]. Thus, the CA50 at a given injection timing is significantly more retarded for DGE than for EHN. Nevertheless, both DGE and EHN showed very robust combustion with COV of $IMEP_n$ values lower than 1.5%, providing wide CA50 control ranges. In both cases, the CA50 retarded linearly as the injection timing retarded, indicating MCCI combustion.

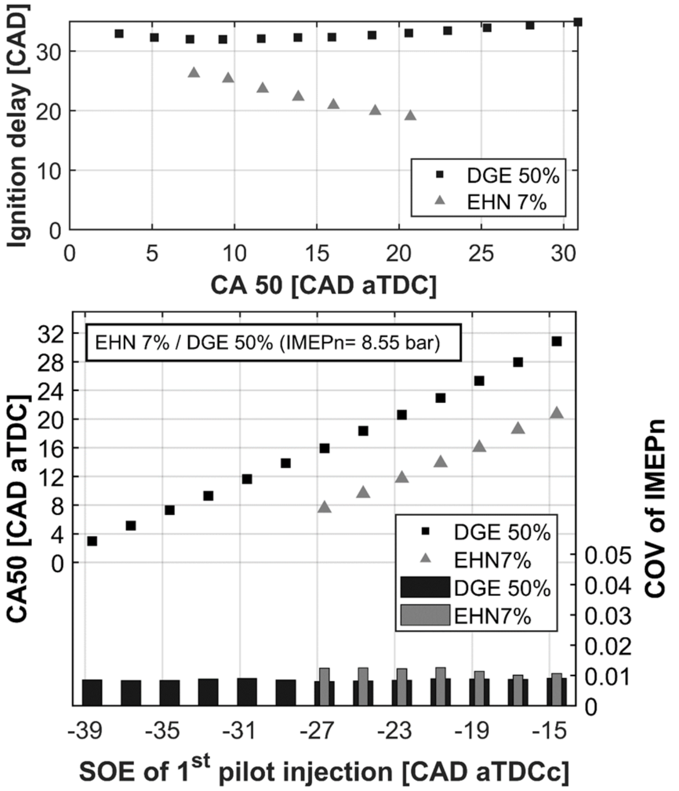

**Fig. 7. Ignition delay, CA50, and CoV of IMEP$_n$ with EHN and DGE against the SOE of 1st pilot injection at part-load conditions**

**Fig. 8** shows the indicated thermal efficiency and heat transfer losses for the same cases plotted in **Fig. 7**, whereas **Fig. 9** shows the MFB and HRR for two cases with approximately the same CA50 of 12 CAD aTDC. The thermal efficiency was higher with EHN compared to both DGE and diesel fuel due to a combination of reduced heat transfer losses and faster burning rates. Interestingly, ethanol doped with DGE showed higher heat losses as those of EHN and similar to those of the baseline diesel cases. Analysis of the HRR shown in **Fig. 9** revealed a predominance of longer diffusion burn behavior with DGE compared to EHN, particularly evident in the flat heat release region of DGE occurring approximately between 10 and 17 CAD aTDC. The higher proportion of diffusion burn and prolonged combustion duration associated with DGE compared to EHN indicates stronger flame impingement on the in-cylinder walls, which explains the higher heat transfer losses of DGE. Moreover, the MFB plot indicates that DGE has a lower burning rate than EHN during the late-combustion stage probably due to a combination of lower oxygen content and lower injection pressure.

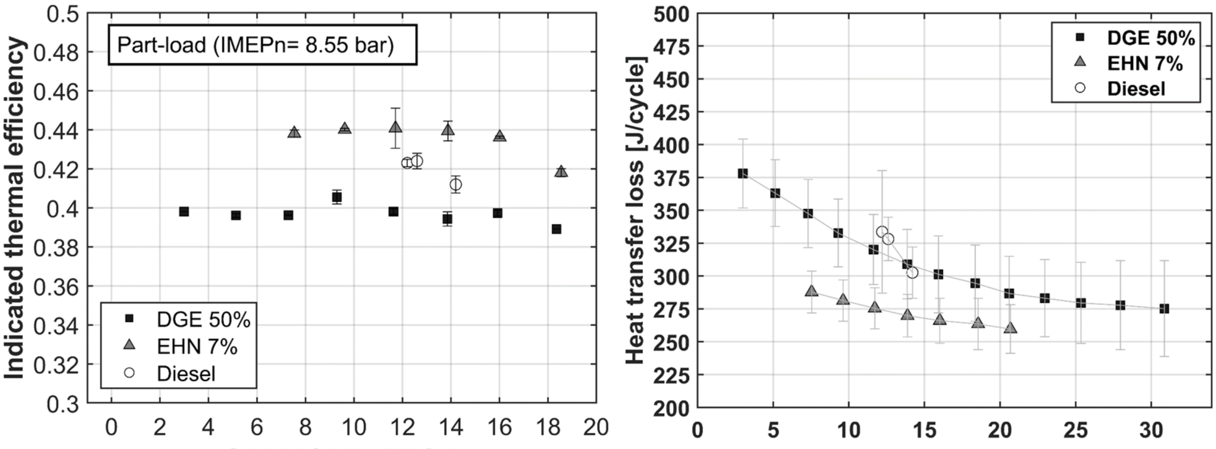

**Fig. 8. Indicated thermal efficiency (left) and heat transfer loss (right) with EHN, DGE and baseline diesel against on the CA50 at part-load conditions**

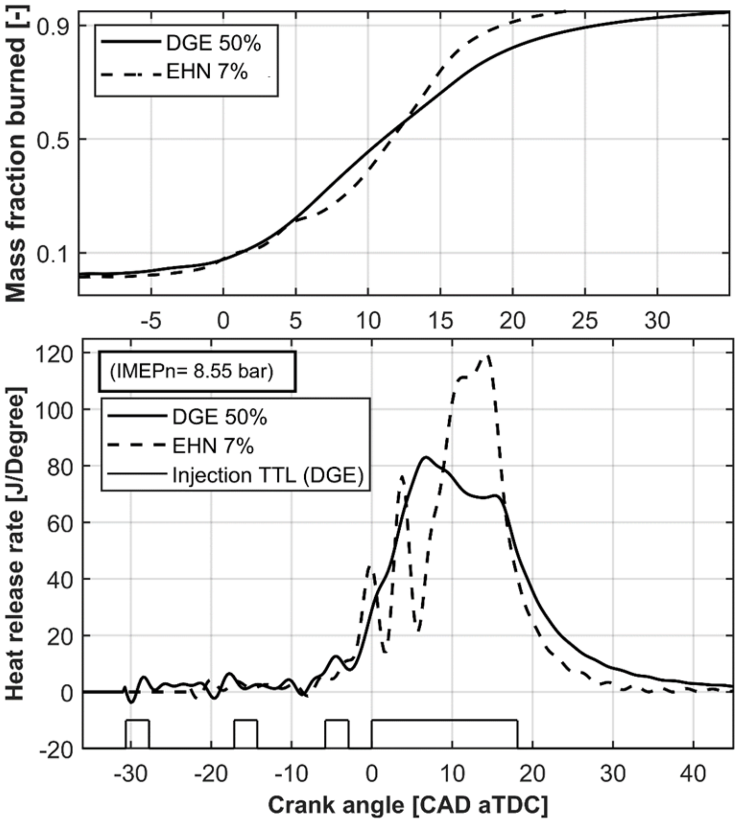

**Fig. 9. Mass fraction burned (top) and heat release rate (bottom) with EHN (SOE of the 1st pilot injection = -22.625 CAD aTDC) and DGE (SOE of the 1st pilot injection = -30.625 CAD aTDC) at part-load**

**Fig. 10** shows the ISCO, ISNOx, and ISPM against the SOE of 1st pilot injection for the same cases shown in **Fig. 8**. Significantly lower ISCO emissions are measured at medium load conditions compared to those at low loads due to the higher in-cylinder reactivity. This improvement is particularly noticeable for EHN, reinforcing the hypothesis that EHN is more effective at medium loads. Despite the prevalence of predominant diffusion burn with DGE, EHN still had higher NOx emissions, attributed to the nitrate content inherent to the molecule of EHN. Regarding ISPM, all results were found to comply with the U.S. EPA 2027 heavy-duty legal limits.

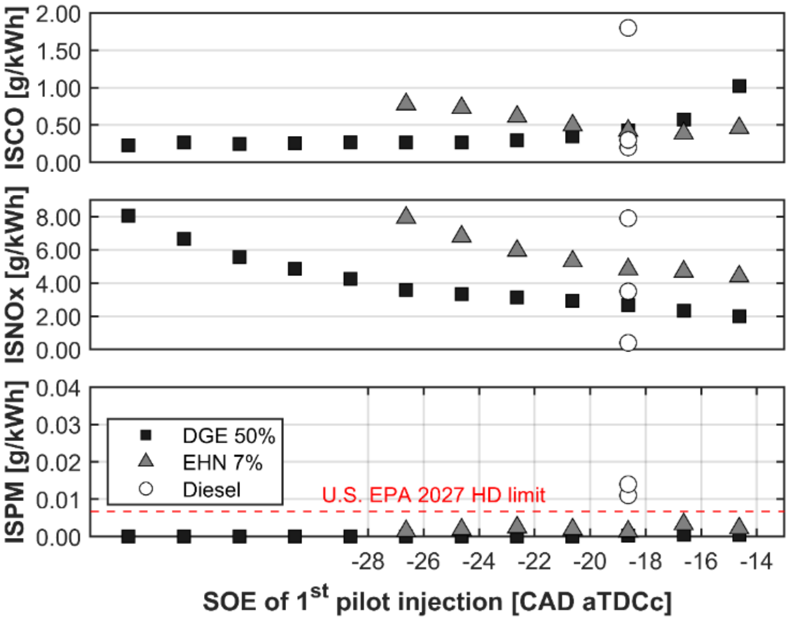

**Fig. 10 ISCO, ISNOx, and ISPM with EHN, DGE and baseline diesel against the SOE of 1st pilot injection at part-load conditions**

### 3.2 Chemical kinetics

Given the considerable amounts required to achieve stable combustion with DGE, it is evident that alkyl nitrates such as EHN are more effective ignition improvers for (m)ethanol than ethers. Chemical kinetic simulations were performed to gain a detailed understanding of the differences between ether- and alkyl nitrate-based ignition improvers and to better understand the mechanisms responsible for the lower efficacy of ethers. **Fig. 11** shows the RoP analysis of straight ethanol at its most-reactive mixture fraction (MRMF) obtained by following the methodology described in section 2.2. Ethanol decomposed into two main radicals, $SC_2H_4OH$ and $PC_2H_4OH$, via hydrogen abstraction reaction with hydroxyl radical (OH). The predominant radical formed was $SC_2H_4OH$ (71%) compared to $PC_2H_4OH$ (26%). Hydroxyl radicals are formed during the decomposition of $PC_2H_4OH$, as represented in blue in **Fig. 11**, aiding in the decomposition of ethanol. However, $SC_2H_4OH$ decomposed into acetaldehyde ($CH_3CHO$), which required additional hydroxyl radicals to decompose further. Therefore, both ethanol and acetaldehyde competed for hydroxyl radicals, with ethanol being more effective in reacting with OH. As a result and as shown in **Fig.12** (where the mole fractions of ethanol and acetaldehyde were shown against time divided by the ignition delay), acetaldehyde continuously accumulated as the mole fraction of ethanol decreased, acting as a bottleneck in the ethanol decomposition process. Moreover, it is noteworthy that hydroxyl radicals play a pivotal role in the overall reaction of ethanol. Previous research on the mechanism responsible for the effect of EHN on the autoignition reactivity of ethanol [48] showed that each mole of EHN formed 2 moles of hydroxyl radical early during the ignition delay process, mitigating the bottleneck for ignition of acetaldehyde decomposition and effectively enhancing the reactivity of ethanol even with relatively low EHN contents.

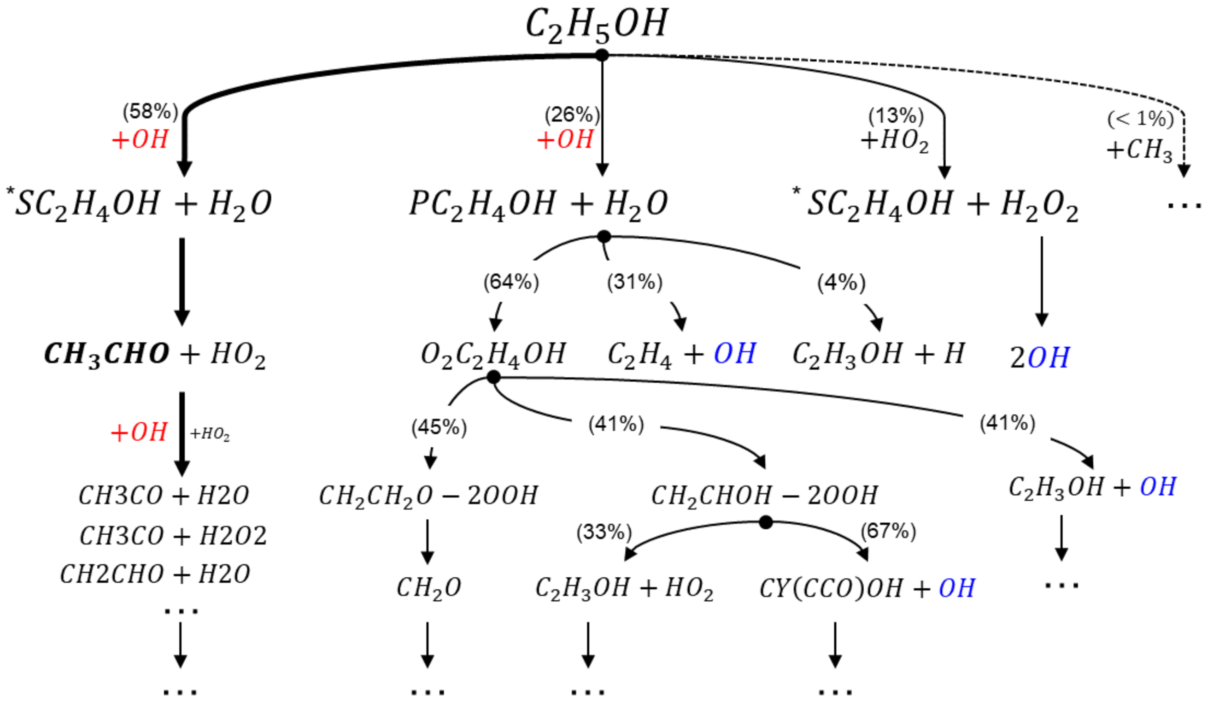

Fig. 11. Rate of production (RoP) analysis of straight ethanol under part-load condition at MRMF; $P_{amb}$ (60.51 bar), $T_{amb}$ (906.67 K) and $\phi$ (0.18)

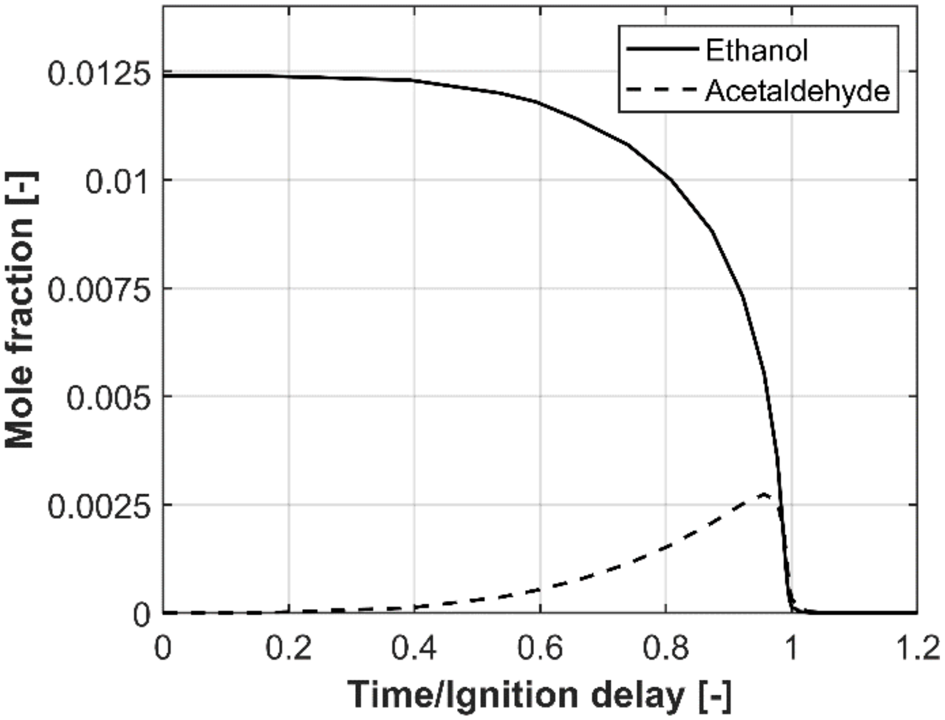

**Fig. 12. Mole fraction of ethanol and acetaldhyde against normalized time (time divided by the ignition delay) at MRMF; $P_{amb}$ (60.51 bar), $T_{amb}$ (906.67 K),= and $\phi$ (0.18)**

**Fig. 13** shows the RoP analysis of straight DEE at MRMF conditions obtained following an analogous approach as that used for straight ethanol. Unlike ethanol, which primarily requires hydroxyl radical for its decomposition, DEE decomposition is dominated by reaction with both hydroxyl radical and atomic hydrogen (H). The key focus is to determine whether DEE forms hydroxyl radical during the ignition delay process, which is essential for its role as an ignition improver of ethanol. The first step of DEE decomposition is mainly controlled by dehydrogenation to form $C_2H_5OC_2H_4$-A. Although small amounts of ketone radicals were formed by DEE thermal decomposition and by low-temperature branching of $C_2H_5OC_2H_4$-A, and ketones generate a significant amount of hydroxyl radicals, only a very small fraction of DEE underwent through this pathway. Results showed that acetaldehyde was the main intermediate species of DEE decomposition, suggesting that blending DEE with ethanol does not mitigate the main bottleneck for ethanol ignition. Thus, the little hydroxyl radical formation is a key reason for the limited effectiveness of DEE as an ignition improver for ethanol. Moreover, the formation of acetaldehyde during the DEE decomposition process can worsen the competition for hydroxyl radicals, because both ethanol and acetaldehyde require hydroxyl radical to be decomposed.

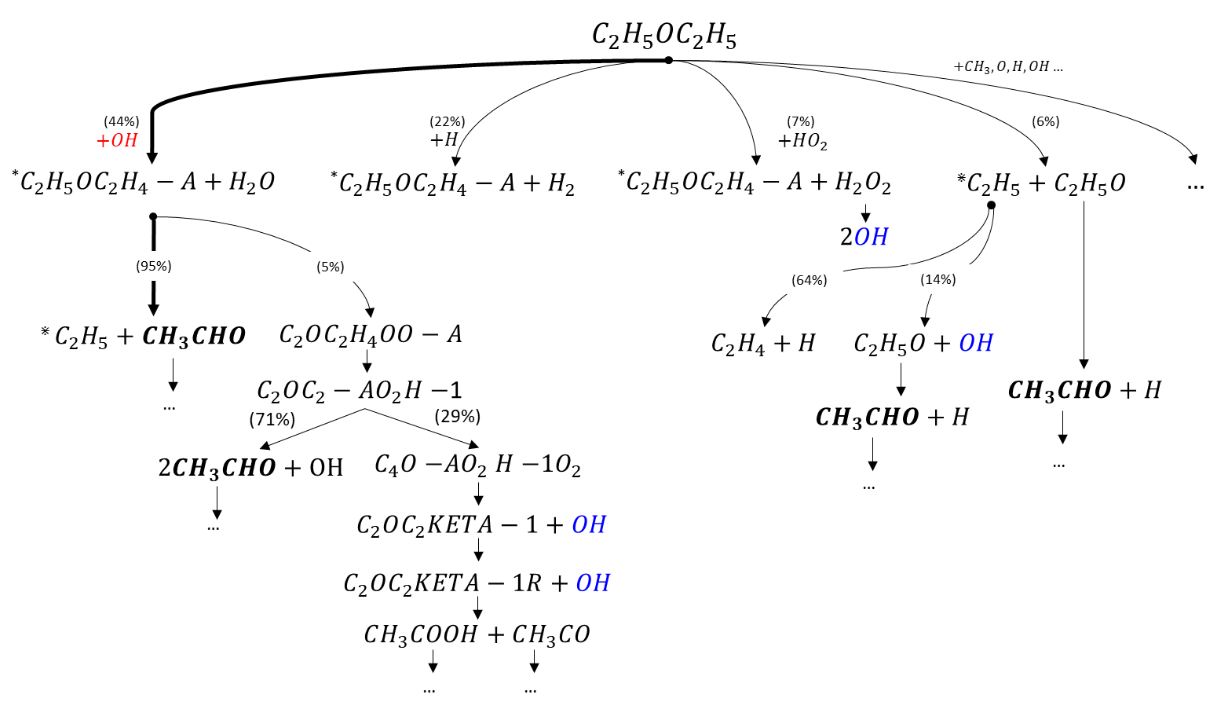
$C_2H_5OC_2H_5$
$+CH_3, O, H, OH ...$
(44%)
$+OH$
(22%)
$+H$
(7%)
$+HO_2$
(6%)
$^*C_2H_5OC_2H_4 - A + H_2O$
$^*C_2H_5OC_2H_4 - A + H_2$
$^*C_2H_5OC_2H_4 - A + H_2O_2$
$^*C_2H_5 + C_2H_5O$
...
$2OH$
(95%)
(5%)
(64%)
(14%)
$^*C_2H_5 + CH_3CHO$
$C_2OC_2H_4OO - A$
$C_2H_4 + H$
$C_2H_5O + OH$
$CH_3CHO + H$
$C_2OC_2 - AO_2H - 1$
(71%)
(29%)
$CH_3CHO + H$
$2CH_3CHO + OH$
$C_4O - AO_2H - 1O_2$
$C_2OC_2KETA - 1 + OH$
$C_2OC_2KETA - 1R + OH$
$CH_3COOH + CH_3CO$
...

**Fig. 13. Rate of production (RoP) analysis of DEE under part-load condition at MRMF; $P_{amb}$ (60.51 bar), $T_{amb}$ (769.68 K), and $\phi$ (1.50)**

**Fig. 14** shows the ignition delay of the MRMF at part-load conditions for ethanol doped with 7%$_{vol}$ EHN and with variable amounts of DEE (equivalent results obtained at low-load conditions). The chemical kinetic simulation results showed that approx. 32%$_{vol}$ DEE is required to match the reactivity of 7%$_{vol}$ EHN, which is consistent with the experimental findings, showing that 30%$_{vol}$ DEE led to partial misfires and 50%$_{vol}$ DGE was required to achieve stable combustion. Even though DEE has a very high CN of approx. 160, large amounts of DEE are required to increase the reactivity of ethanol due to the lack of hydroxyl radial production from DEE.

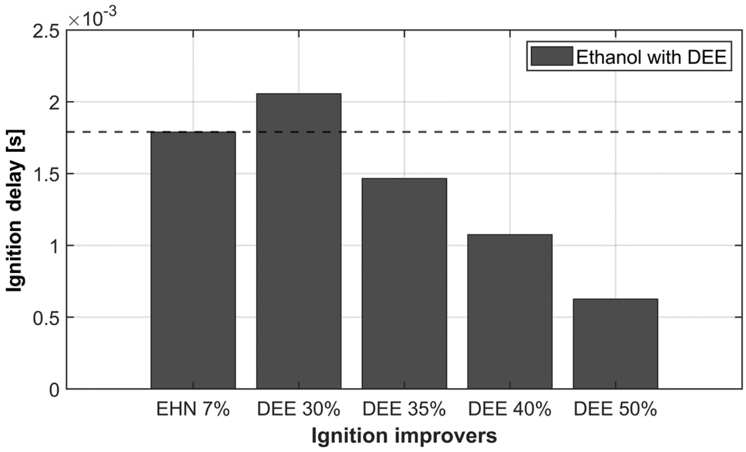

**Fig. 14. The ethanol ignition delay depending on the different blending ratio (volume-basis) of DEE under part-load at MRMF**

RoP analyses were performed for both ethanol with 7%$_{vol}$ EHN and ethanol with 35%$_{vol}$ DEE and for the MRMF at part-load conditions. **Fig. 15** shows the mole fraction of ethanol, acetaldehyde (main intermediate species of ethanol decomposition), hydroxyl radical and EHN (left) or DEE (middle) against time normalized by ignition delay. For EHN, rapid decomposition occurred at the beginning of the ignition delay, resulting in a rapid generation of hydroxyl radicals that attack ethanol. Acetaldehyde was formed from ethanol and accumulates during the ignition delay time, with the maximum accumulated mole fraction of acetaldehyde being approximately a quarter of the initial mole fraction of ethanol. A rapid increase in mole fraction of acetaldehyde observed early during the ignition delay indicates that ethanol was decomposed due to the reaction of hydroxyl radicals generated from EHN. For DEE, ethanol exhibited slow decomposition, gradually forming acetaldehyde over time, with the maximum mole fraction of acetaldehyde exceeding one third of the initial ethanol mole fraction. This indicates additional formation of acetaldehyde by DEE during the ignition delay, as confirmed by the RoP analysis of DEE. Although DEE forms important amounts of atomic hydrogen and ethyl radical during its decomposition, these radicals do not significantly affect the decomposition rate of ethanol when the blending ratio is low. Additionally, these radicals are not formed early in the ignition delay but rather near the ignition or during the high-temperature heat release rate. A clear difference was observed in the rate of hydroxyl radical production. To illustrate the rapid and abundant formation of hydroxyl radicals by EHN, the global production rate of hydroxyl radical is shown on **Fig. 15** –right. The production rate of hydroxyl radicals by EHN was three orders of magnitude higher than that of DEE (note that the DEE case was scaled up by a factor of 100).

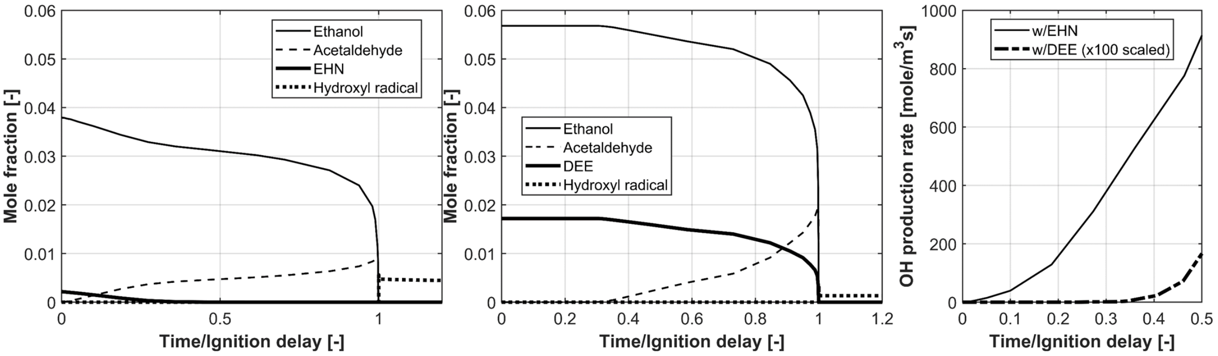

**Fig. 15. Mole fraction of ethanol, acetaldehyde and OH production rate (right) against to the normalized time with different ignition improvers EHN (left) and DEE (middle) at MRMF**

Analyses equivalent to those performed for ethanol doped with EHN and DEE were performed for methanol with EHN and DME. DME is used in the analysis because it can be formed directly from methanol dehydration (as DEE can be formed from ethanol dehydration). **Fig. 16** shows the ignition delay of the MRMF at part-load conditions for methanol doped with $7\%_{vol}$ EHN and with variable amounts of DME (equivalent results obtained at low-load conditions). Results showed that approx. $47\%_{w/w}$ DME is required to match the reactivity of $7\%_{vol}$ EHN. Similar results have been reported in the literature [49], indicating that the required amount of DME for auto-ignition of methanol in an HCCI engine ranged between $55\%_{w/w}$ to $78\%_{w/w}$. RoP analyses (not shown here for bevity's sake) showed that the main intermediate species of methanol decomposition is formaldehyde, which accumulated during the ignition delay due to the competition for hydroxyl radicals between formaldehyde and methanol. Thus, formaldehyde decompsoition by hydroxyl radicals is the bottleneck for methanol ignition. RoP analyses of DME showed that DME primarily formed methyl radicals ($CH_3$) and little hydroxyl radicals. Methyl radicals do not significantly affect the decomposition rate of methanol, explaining why large amounts of DME are required to enhance the ignitability of methanol sprays, despite its high CN.

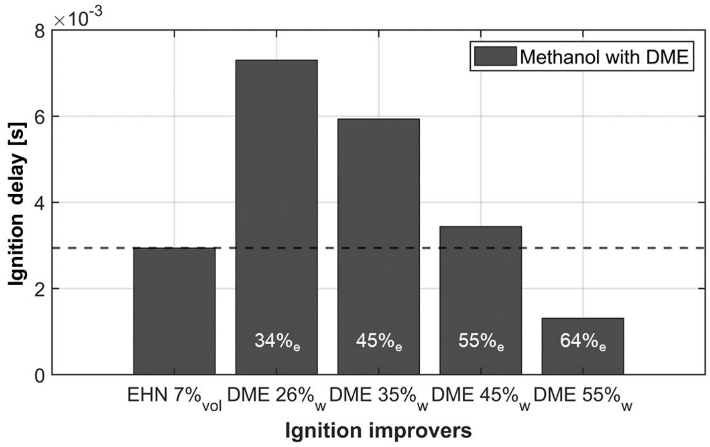

**Fig. 16 The methanol ignition delay depending on the different blending ratio of DME (mass-basis) at part-load (blending ratio indicated in the bar represents energy-based ratio)**

It is evident that blending a small amount of an ether-based ignition improver with methanol or ethanol was not a realistic approach to enable alcohol MCCI combustion due to the competition for hydroxyl radicals between the ether and the alcohol during the ignition delay. However, this competition between fuels may be avoided with dual-fuel strategies in which the ether is injected in the intake port of the engine and decomposed during the compression stroke and the alcohol is direct-injected near TDC. The potential of this strategy was investigated here following the methodology described in section 2.2. **Fig. 17** –left shows the ignition delay distribution within a spray of methanol injected at TDC into the products of DME decomposed during the compression stroke at low-load conditions, whereas **Fig. 17** –right shows the ignition delay of the MRMF for the same results shown in **Fig. 17** –left. Variable substitution ratios of DME (from 0% to 15% on an energy basis) were simulated, and results of a single-fuel strategy of methanol blended with 7%$_{\mathrm{vol}}$ EHN (equivalent to 11.6% on an energy basis) are included in the figure for completeness. As expected, the ignition delay within the spray decreased as the DME substitution ratio increased because DME releases heat and generates radicals during its decomposition. Interestingly, only 6%$_{\mathrm{w/w}}$ DME (equivalent to 7%$_{\mathrm{energy\text{-}basis}}$) was required to match the reactivity of 7%$_{\mathrm{vol}}$ EHN, compared to 47%$_{\mathrm{w/w}}$ DME (equivalent to 56%$_{\mathrm{energy\text{-}basis}}$) for a single-fuel strategy, suggesting that avoiding ether-alcohol competition for radicals by implementing a dual-fuel strategy is a promising approach to enable ether-assisted (m)ethanol MCCI combustion.

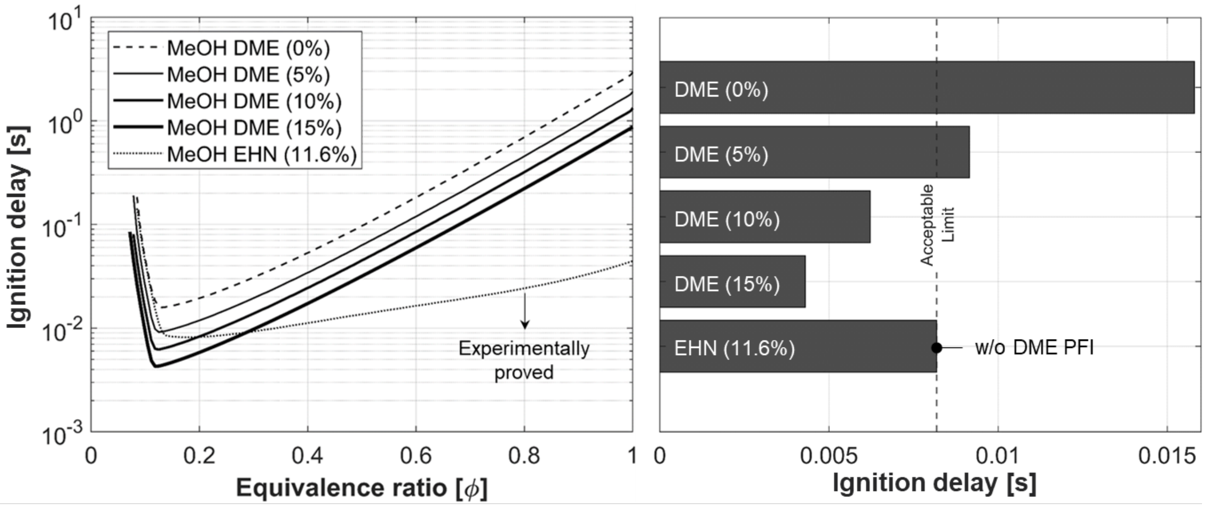

**Fig. 17 Ignition delay within a methanol spray for different DME substitution ratios (energy-basis) at low load condition (left) and ingition delay at MRMF (right); ambient conditions varied depending on the substitution ratio of DME**

As mentioned above, DME releases heat and generates radicals during the compression stroke, creating in-cylinder conditions suitable for methanol ignition. In order to understand the role of temperature vs. radicals in improving the ignitability of methanol, chemical kinetic simulations were performed to obtain the ignition delay distribution within a methanol spray at three different conditions: (1) no ignition improver (straight methanol), (2) in-cylinder thermodynamic conditions from DME decomposition but no radicals (ambient was air), and (3) in-cylinder thermodynamic conditions and radicals from DME decomposition. Results are shown in **Fig. 18** for a 10%$_{\mathrm{energy\text{-}basis}}$ DME substitution ratio. Both the effect of DME on the in-cylinder pressure and temperature and the radicals formed from DME decomposition contribute almost equally to shorten the ignition delay of a methanol spray. This is an intriguing result because RoP analyses showed that radicals formed by DME during the ignition delay are not effective in enhancing the reactivity of methanol. However, in this dual-fuel strategy, methanol is injected after the ignition of DME, suggesting that radicals formed after the ignition may be not only different from those formed during the ignition delay but also more effective in enhancing alcohol ignitability.

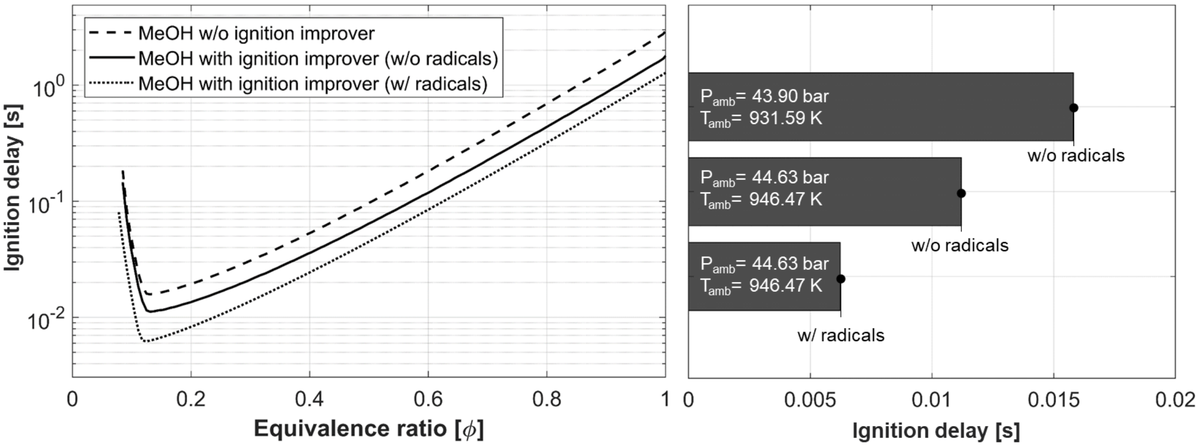

**Fig. 18 Ignition delay within a methanol spray (left) and ignition delay at MRMF (right)**

**Fig. 19** –left shows the normalized mole fraction of hydroxyl radical and hydrogen peroxide ($H_2O_2$) for engine simulations of port-injected DME at ϕ = 0.012 (equivalent to a 10%$_{\text{energy-basis}}$ DME substitution ratio at low load condition) and at ϕ = 1.0. For ϕ = 1.0, DME underwent a typical autoignition process where hydrogen peroxide accumulated before the ignition. At the time of ignition, each mole of hydrogen peroxide decomposed into two moles of hydroxyl radical, which rapidly attacked the fuel, triggering the high temperature heat release (HTHR). During the HTHR, hydroxyl radicals were formed and accumulated by the reaction between molecular oxygen and atomic hydrogen ($O_2 + H = OH + O$). Eventually, hydroxyl radicals recombined during the expansion stroke. However, for ϕ = 0.012, DME showed low-temperature heat release (LTHR) around -19 CAD aTDC, leading to a peak in hydroxyl radical concentration followed by rapid reduction. Subsequently, hydrogen peroxide accumulated steadily post-LTHR, persisting due to the absence of significant high-temperature heat release (HTHR). If (m)ethanol is direct-injected after the LTHR of DME, the alcohol spray will interact with the accumulated hydrogen peroxide, which decomposes into hydroxyl radicals, enhancing the ignitability of the spray. It is worth noting that the LTHR of ethers is suppressed by (m)ethanol in a single-fuel strategy.

**Fig. 19** –right shows the ignition delay of the MRMF of a methanol spray injected into the products of DME decomposition at different crank angle degrees. The ambient temperature and pressure were kept constant and equal to those of TDC in all cases, and only the radicals formed from DME decomposition were changed as a function of crank angle (isolating the effect of radicals from the effect of the in-cylinder thermodynamic conditions). The ignition delay of the MRMF of a spray of methanol doped with 7%$_{\text{vol}}$ EHN is also included in the figure as an acceptable limit for spray reactivity. Longer ignition delays were obtained when the methanol was injected before the LTHR of DME because of radical scarcity (note that the ambient pressure and temperature were maintained constant across all conditions). However, the ignition delay of the methanol spray significantly reduced for injection times equal to or more retarded than -19.4 CAD aTDC due to the presence of hydrogen peroxide. Notably, injection timing appears less pivotal for ignition with a dual-fuel strategy unless injections occur before the LTHR of the ignition improver.

In summary, a dual fuel strategy consisting in a port-injection of an ether-based ignition improver followed by a direct-injection of (m)ethanol near TDC is a promising approach to enable (m)ethanol MCCI combustion with low ether consumption. In this strategy, the competition for radicals between ether and (m)ethanol is avoided. For low ether concentrations, the ether reacts during the compression stroke of the engine, releasing energy (LTHR) and forming radicals that will assist the ignition of the (m)ethanol spray. Among those radicals, hydrogen peroxide, which is accumulated and persists during the expansion stroke due to the absence of HTHR, interacts with the direct-injected (m)ethanol generating hydroxyl radicals that enhance the ignitability of the alcohol spray. For this strategy to work, (m)ethanol shall be injected after the occurrence of the LTHR of the ether but, notably, injection timing is not pivotal for ignitability of the (m)ethanol spray because hydrogen peroxide (the key radical in assisting (m)ethanol ignition) persists in the cylinder during the compression stroke.

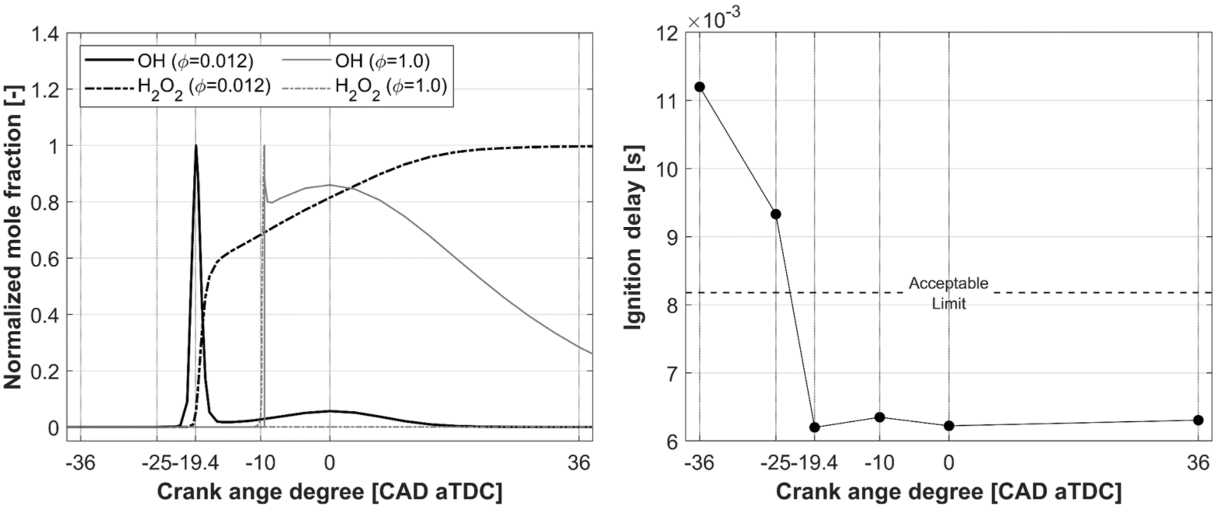

**Fig. 19. Normalized more fraction of OH and $H_2O_2$ at two different DME equivalence ratios from ICE simulations (left) and estimated ignition delay of a methanol spray at different injection timings under fixed ambient pressure and temperature conditions but different radicals (right, $\phi_{DME}$ = 0.012)**

## 4. Conclusions

To address the increasing demand for carbon-neutralization in hard-to-electrify industries, (m)ethanol was investigated as an alternative fuel for MCCI combustion engines using ignition improvers. The traditional cetane enhancer EHN proved to be effective as an ignition improver when blended with ethanol and injected in a single-fuel strategy. However, it led to high NOx emissions due to the nitrate group present in EHN. Consequently, ether-based ignition improvers were explored both experimentally and numerically as they can be easily produced through alcohol dehydration and do not contain nitrogen themselves. The key findings from this study are:

- Ignition improvers were demonstrated to enable stable ethanol MCCI combustion. However, the optimal blending ratio varied depending on the type of ignition enhancer used and the operating load conditions.

- Ethanol MCCI combustion with EHN resulted in higher thermal efficiency compared to using DGE due to reduced heat transfer losses and faster burning rate at the late-combustion stage. However, higher NOx emissions were observed with EHN, attributed to the presence of a nitrate group in the molecule.

- For a single-fuel strategy, high blending ratios (between $35\%_{vol}$ and $50\%_{vol}$) are required to achieve stable (m)ethanol combustion with ether-based ignition improvers because ethers primarily generate methyl/ethyl radical and atomic hydrogen, which are not effective at enhancing (m)ethanol reactivity. Moreover, both (m)ethanol and ethers produce similar intermediate species such as acetaldehyde and formaldehyde, which can act as bottlenecks in the (m)ethanol decomposition process due to competition with (m)ethanol for hydroxyl radicals.

- In contrast, EHN produces a significant amount of hydroxyl radicals, which are crucial for the decomposition of (m)ethanol. Consequently, much lesser amounts of EHN are required to enable MCCI combustion of (m)ethanol compared to ethers.

- Dual-fuel approaches where the ignition improver is premixed or injected in the intake port of the engine are promising strategies to enable ether-assisted MCCI combustion of (m)ethanol. This is because the low-temperature heat release from ether decomposition creates a favorable combustion environment (high temperature and radicals) for the ignition of a (m)ethanol spray. Moreover, this strategy avoids the competition for radicals between ethers and alcohols, which creates bottlenecks for ignition when the ether and the alcohol are blended in a single fuel.

- For the global equivalence ratios tested in this study, the port-fueled ignition improver did not undergo high-temperature ignition, accumulating significant amounts of hydrogen peroxide in the cylinder. This hydrogen peroxide significantly contributed to enhancing the ignitability of the (m)ethanol spray by generating hydroxyl radicals. Therefore, (m)ethanol needs to be injected after the low-temperature heat release of the ether-based ignition improver to actively utilize these radicals.

## Acknowledgments

The authors would like to thank Dan Pierce and Kyra Schmidt for their dedicated support of the Off-Road Mixing-Controlled Combustion Engine Laboratory, and Vishinu Radhakrishna for his technical review of this paper.

This work was performed at the Applied Combustion Research Department, Combustion Research Facility, Sandia National Laboratories, Livermore, CA. This Article has been authored by National Technology and Engineering Solutions of Sandia, LLC. under contract No. DE-NA0003525 with the U.S. Department of Energy/National Nuclear Security Administration. The United States Government retains and the publisher, by accepting the article for publication, acknowledges that the United States Government retains a non-exclusive, paid-up, irrevocable, world-wide license to publish or reproduce the published form of this manuscript, or allow others to do so, for United States Government purposes. The views expressed in the article do not necessarily represent the views of the U.S. Department of Energy or the United States Government.

## References

[1] U.S. Energy Information Administration, "Monthly Report of Biofuels, Fuels From Non-Biogenic Wastes, Fuel Oxygenates, Isooctane, and Isooctene." 2018.

[2] "Realising methanol's potential as a motor fuel – Analysis," *IEA*. [Online]. Available: https://www.iea.org/articles/realising-methanol-s-potential-as-a-motor-fuel. [Accessed: 20-Oct-2023].

[3] "Alternative Fuels Data Center: E85 (Flex Fuel)." [Online]. Available: https://afdc.energy.gov/fuels/ethanol_e85.html. [Accessed: 28-Mar-2024].

[4] B. Gainey and B. Lawler, "The role of alcohol biofuels in advanced combustion: An analysis," *Fuel*, vol. 283, p. 118915, Jan. 2021.

[5] N. Stetson and M. Wieliczko, "Hydrogen technologies for energy storage: A perspective," *MRS Energy & Sustainability*, vol. 7, no. 1, p. 41, Dec. 2020.

[6] F. M. N. U. Khan, M. G. Rasul, A. S. M. Sayem, and N. Mandal, "Maximizing energy density of lithium-ion batteries for electric vehicles: A critical review," *Energy Reports*, vol. 9, pp. 11–21, Oct. 2023.

[7] "U.S. DRIVE Net-Zero Carbon Fuels Technical Team Analysis Summary Report 2020," *Energy.gov*. [Online]. Available: https://www.energy.gov/eere/vehicles/articles/us-drive-net-zero-carbon-fuels-technical-team-analysis-summary-report-2020. [Accessed: 10-Oct-2023].

[8] B. Gainey, Z. Yan, J. Gandolfo, and B. Lawler, "Methanol and wet ethanol as interchangeable fuels for internal combustion engines: LCA, TEA, and experimental comparison," *Fuel*, vol. 333, p. 126257, 2023.

[9] "Gasoline and Diesel Fuel Update." [Online]. Available: https://www.eia.gov/petroleum/gasdiesel/index.php. [Accessed: 26-Sep-2023].

[10] I. Hunwartzen, "Modification of CFR Test Engine Unit to Determine Octane Numbers of Pure Alcohols and Gasoline-Alcohol Blends," presented at the SAE International Congress and Exposition, 1982.

[11] J. Yanowitz, M. A. Ratcliff, R. L. McCormick, J. D. Taylor, and M. J. Murphy, "Compendium of Experimental Cetane Numbers," National Renewable Energy Laboratory, NREL/TP-5400-67585, Feb. 2017.

[12] United States Environmental Protection Agency (EPA), "Diesel Fuel Standards and Rulemakings," *https://www.epa.gov/diesel-fuel-standards/diesel-fuel-standards-and-rulemakings*.

[13] "ILO-WHO International Chemical Safety Cards (ICSCs)." [Online]. Available: https://www.ilo.org/global/topics/safety-and-health-at-work/resources-library/publications/WCMS_113134/lang--en/index.htm. [Accessed: 28-Mar-2024].

[14] "Standard Specification for Diesel Fuel." [Online]. Available: https://www.astm.org/d0975-20a.html. [Accessed: 28-Mar-2024].

[15] W. H. Buck, J. R. Lohuls, and J. A. Murphy, "Lubrication Studies in a Methanol-Fueled Spark Ignition Engine," presented at the 1989 SAE International Fall Fuels and Lubricants Meeting and Exhibition, 1989, p. 892156.

[16] R. E. Bond, J. L. Loth, R. W. Guiler, N. N. Clark, and E. C. Heydorn, “Lubricity Problems and Solutions for a Methanol Fueled Gas Turbine,” presented at the ASME 2000 International Mechanical Engineering Congress and Exposition, 2021, pp. 55–58.

[17] T. Sathish Kumar and B. Ashok, “Material compatibility of SI engine components towards corrosive effects on methanol-gasoline blends for flex fuel applications,” *Materials Chemistry and Physics*, vol. 296, p. 127344, Feb. 2023.

[18] D. L. Siebers and C. F. Edwards, “Autoignition of Methanol and Ethanol Sprays under Diesel Engine Conditions,” presented at the SAE International Congress and Exposition, 1987.

[19] M. Svensson, M. Tuner, and S. Verhelst, “Low Load Ignitability of Methanol in a Heavy-Duty Compression Ignition Engine,” presented at the SAE Powertrains, Fuels & Lubricants Conference & Exhibition, 2022.

[20] C. J. Mueller and M. P. Musculus, “Glow Plug Assisted Ignition and Combustion of Methanol in an Optical DI Diesel Engine,” presented at the International Spring Fuels & Lubricants Meeting, 2001, pp. 2001-01–2004.

[21] A. Dempsey, M. Chowdhury, S. Kokjohn, and J. Zeman, “Prechamber Enabled Mixing Controlled Combustion - A Fuel Agnostic Technology for Future Low Carbon Heavy-Duty Engines,” presented at the WCX SAE World Congress Experience, 2022, pp. 2022-01–0449.

[22] A. Dempsey, J. Zeman, and M. Chowdhury, “Prechamber Enabled Mixing Controlled Combustion in a Heavy-Duty Flex-Fuel Engine – Experimental Results with Comparisons to Various Combustion Strategies,” presented at the DOE AEC Program Review Meeting, Oak Ridge National Laboratory, 2024.

[23] N. Giramondi, A. Jäger, S. K. Mahendar, and A. Erlandsson, “Combustion Characteristics, Performance and NO $_x$ Emissions of a Heavy-Duty Ethanol-Diesel Direct Injection Engine,” presented at the SAE Powertrains, Fuels & Lubricants Meeting, 2020, pp. 2020-01–2077.

[24] M. Chowdhury and A. Dempsey, “Inverted Reactivity Controlled Compression Ignition (iRCCI) with Methanol Fuel & amp; Reactivity Enhancers,” presented at the WCX SAE World Congress Experience, 2022, pp. 2022-01–0464.

[25] R. Rezaei, J. Dembler, D. Kovacs, G. Morris, W. Gottschalk, and T. Delebinski, “Gane Fuel - Introduction of an Innovative, Carbon-Neutral and Low Emission Fuel for HD CI Engines,” presented at the SAE Powertrains, Fuels & Lubricants Digital Summit, 2021, pp. 2021-01–1198.

[26] S. Velazquez, “Ethanol Usage in Urban Public Transportation - Presentation of Results,” *SAE Technical Paper Series*, pp. 0–21, 2010.

[27] S. Lee, D. Lopez Pintor, and S. Cho, “Enabling Ethanol Mixing-Controlled Compression-Ignition Combustion using 2-Ethylhexylnitrate in an Off-Road Engine,” *Applied Energy*, vol. In press, 2024.

[28] S. Lee, D. Lopez Pintor, and S. Cho, “Methanol Mixing-Controlled Compression Ignition with Ignition Enhancer for Off-Road Engine Operation,” *SAE Technical Paper 2024-01-2701*, 2024.

[29] P. Ghosh, “Predicting the Effect of Cetane Improvers on Diesel Fuels,” *Energy Fuels*, vol. 22, no. 2, pp. 1073–1079, Mar. 2008.

[30] A. B. Dempsey, N. R. Walker, and R. D. Reitz, “Effect of Cetane Improvers on Gasoline, Ethanol, and Methanol Reactivity and the Implications for RCCI Combustion,” *SAE Int. J. Fuels Lubr.*, vol. 6, no. 1, pp. 170–187, Apr. 2013.

[31] K. D. Vertin *et al.*, “Methylal and Methylal-Diesel Blended Fuels for Use in Compression-Ignition Engines,” presented at the International Fuels & Lubricants Meeting & Exposition, 1999.

[32] J. M. Herreros, K. Schroer, E. Sukjit, and A. Tsolakis, “Extending the environmental benefits of ethanol–diesel blends through DGE incorporation,” *Applied Energy*, vol. 146, pp. 335–343, May 2015.

[33] M. E. Karpuk and S. W. Cowley, “On Board Dimethyl Ether Generation to Assist Methanol Engine Cold Starting,” presented at the 1988 SAE International Fall Fuels and Lubricants Meeting and Exhibition, 1988.

[34] D. L. Horstman, D. L. Abata, and J. M. Keith, “On-Site DME Generation from Methanol for Pilot Injection in CI Engines,” presented at the SAE Powertrain & Fluid Systems Conference & Exhibition, 2003.

[35] A. Wu, S. Busch, F. Perini, S. Cho, D. Lopez Pintor, and R. Reitz, “Numerical and Experimental Studies of a Novel Dimpled Stepped-Lip Piston Design on Turbulent Flow Development in a Medium-Duty Diesel Engine,” presented at the WCX SAE World Congress Experience, 2022.

[36] S. Cho, A. Wu, and D. L. Pintor, “Understanding Hydrocarbon Emissions to Improve the Performance of Catalyst-Heating Operation in a Medium-Duty Diesel Engine,” *SAE Technical Paper 2023-01-0262*, Apr. 2023.

[37] G. Woschni, “A Universally Applicable Equation for the Instantaneous Heat Transfer Coefficient in the Internal Combustion Engine,” *SAE Paper no. 670931*, 1967.

[38] J. Dernotte, J. E. Dec, and C. Ji, “Energy Distribution Analysis in Boosted HCCI-like / LTGC Engines - Understanding the Trade-Offs to Maximize the Thermal Efficiency,” *SAE International Journal of Engines*, vol. 8, no. 3, pp. 956–980, 2015.

[39] S. Cheng *et al.*, “Autoignition and preliminary heat release of gasoline surrogates and their blends with ethanol at engine-relevant conditions: Experiments and comprehensive kinetic modeling,” *Combustion and Flame*, vol. 228, pp. 57–77, Jun. 2021.

[40] D. Lopez Pintor and J. E. Dec, “Development and validation of an EHN mechanism for fundamental and applied chemistry studies,” *SAE Int. J. Adv. & Curr. Prac. in Mobility*, vol. 4, no. 4, pp. 1198–1216, 2022.

[41] L.-S. Tran *et al.*, “Low-temperature gas-phase oxidation of diethyl ether: Fuel reactivity and fuel-specific products,” *Proceedings of the Combustion Institute*, vol. 37, no. 1, pp. 511–519, Jan. 2019.

[42] J. V. Pastor, J. M. Garcia-Oliver, J. M. Pastor, and W. Vera-Tudela, “One-dimensional diesel spray modeling of multicomponent fuels,” *Atomization and Sprays*, vol. 25, no. 6, pp. 485–517, 2015.

[43] D. Lopez Pintor, G. Gentz, and J. Dec, “Mixture Stratification for CA50 Control of LTGC Engines with Reactivity-Enhanced and Non-Additized Gasoline,” *SAE Technical Paper 2021-01-0513*, Apr. 2021.

[44] A. Wu, S. Cho, D. Lopez Pintor, S. Busch, F. Perini, and R. D. Reitz, “Effects of a CFD-improved dimple stepped-lip piston on thermal efficiency and emissions in a medium-duty diesel engine,” *International Journal of Engine Research*, p. 14680874221117868, Aug. 2022.

[45] D. Lopez-Pintor, S. Busch, A. Wu, T. Nguyen, J. Hwang, and S. Cho, “Catalyst-heating operation in compression-ignition engines: A comprehensive understanding using large eddy simulations,” *Applications in Energy and Combustion Science*, vol. 16, p. 100203, Dec. 2023.

[46] S. Cho and D. Lopez Pintor, “Understanding the effects of doping a regular E10 gasoline with EHN in an HCCI engine: Experimental and numerical study,” *Fuel*, vol. 329, p. 125456, Dec. 2022.

[47] S. Cho, D. Lopez-Pintor, and S. Goldsborough, “Chemical kinetic interactions and sensitivity analyses for 2-ethylhexyl nitrate-doped PRF91 using a reduced mechanism,” *Fuel*, vol. 329, p. 125503, Dec. 2022.

[48] U. Bin-Khalid, D. Lopez-Pintor, C. Micó, and S. Lee, “Potential of 2-ethylhexyl nitrate (EHN) and di-tert-butyl peroxide (DTBP) to enhance the cetane number of ethanol, a detailed chemical kinetic study,” *Fuel*, vol. 363, p. 130928, May 2024.

[49] Z. Zheng, M. Yao, Z. Chen, and B. Zhang, “Experimental Study on HCCI Combustion of Dimethyl Ether(DME)/Methanol Dual Fuel,” presented at the 2004 Powertrain & Fluid Systems Conference & Exhibition, 2004.

# Fuel Cell Humidity Control via Water Injection and its Influence on Root Compressor Performance

A. Plazas[1], P. Naghshtabrizi[1], R. Payri[2], P. Martí-Aldaraví[2] and A. Gómez-Vilanova[2]

[1]EATON Corporation. 26201 Northwestern Hwy, Southfield, MI 48076
E-mail: payamnaghshtabrizi@eaton.com
Telephone: +(1) 248-727-0281

[2]CMT – Clean Mobility & Thermofluids. Universitat Politècnica de València. Camino de Vera s/n, 46022 Valencia, Spain.
E-mail: pedmar15@mot.upv.es
Telephone: +(34) 963 877 650

**Abstract.** Hydrogen fuel cells offer a promising and environmentally friendly solution for future ground transportation systems, especially for heavy-duty truck applications. The fuel cell system generates electricity to power the vehicle by chemical reaction between hydrogen and oxygen in the fuel cell stack. The oxygen is provided by pumping compressed air into the fuel cell stack. To achieve optimal performance with minimal electrochemical losses, precise control of air and hydrogen flow within the fuel cell stack is crucial. One key factor affecting fuel cell performance is air relative humidity (RH). In this study, we focus on developing an efficient air humidity management system by directly injecting water into a twin vortices series compressor TVS R1320. The goal is to experimentally measure the effect of water injection on the efficiency of the compressor and attainable RH without water droplet formation at the inlet of the fuel cell stack. A simplex nozzle was positioned at the compressor inlet to inject water continuously. The experimental results show that for high air mass flow rate, the specific work, and mechanical power can be reduced by up to 7.83% and 2.3% respectively, while the System isothermal efficiency improved by 2.95%. However, the RH required by fuel cells cannot be achieved solely by direct water injection without water droplet formation that can cause fuel cell flooding. Other operating points will be discussed in detail.

## 1 Introduction

The transportation industry's increasing interest in alternative fuels and technologies reflects a broader paradigm shift toward environmental sustainability. As regulatory pressures intensify and societal expectations evolve, embracing cleaner energy solutions becomes not only a choice but a necessity for industries to research and develop new technologies in a rapidly changing global landscape. Some examples of this trend include the exploration and implementation of natural gas [1], hydrogen [2], oxy-combustion [3], Electric vehicles [4], and, as analyzed in this paper, the hydrogen fuel cell.

Proton-Exchange Membrane (PEM) Fuel cell technology has emerged as a promising alternative for clean and efficient energy in transportation, particularly for heavy-duty truck long-haul applications. The chemical reaction within a fuel cell involves combining hydrogen with oxygen to produce water and release electrons. These electrons generate an electrical current that powers electrical devices. Fuel cells offer high efficiency compared to internal combustion engines because they do not involve combustion processes and do not produce greenhouse gas emissions or atmospheric pollutants. The only byproducts are water and heat. Fuel cells are finding applications across various sectors, from transportation [5] to stationary power generation [6] and are considered a promising technology for reducing dependence on fossil fuels and mitigating the environmental impacts of energy production [7].

Several studies propose potential areas of improvement. Han et al. [8] proposed a technology study, identifying key research technological areas leading to promising improvements that could be implemented in the fuel cell. However, the efficient operation of fuel cells relies on the auxiliary systems and components of air and hydrogen loops called Balance of Plans (BOP) [9], [10]. Efficiency improvements in BOP components play a major role in minimizing parasitic power requirements, fuel consumption, and overall stack oversizing costs. Among these components, the air compressor stands out as a significant contributor to parasitic losses. Consequently, in this study, we explore reducing the compressor's power consumption by directly injecting water at the compressor inlet and leveraging the evaporative cooling effect. Also, previous research [11] has emphasized the critical role of humidity control in optimizing fuel cell performance, and emerging technologies [12] to address this need. Our approach enhances humidity levels and can significantly reduce (or eliminate) external humidification systems.

The US Department of Energy defined the Operating Points (OP) in Table 1, and we modified them slightly to meet the compressor requirements: idle, 50%, and 100% operating points (OPs). The boundary conditions for the air loop system to achieve the defined operating points were found based on the selected Ballard PEM fuel cell system that delivers a maximum of 300kW to a heavy-duty truck. For each OPs, we experimentally tested different conditions such as water injection rates and water temperature. Through comprehensive experimentation, we demonstrated that specific work is reduced by up to 7.83% due to water injection. However, the maximum achievable RH at the compressor outlet is limited because of the presence of liquid water at the outlet, which may compromise system integrity. In summary, this study sheds light on both the advantages and limitations of water injection at the compressor inlet for fuel cell applications. The findings provide valuable insights for optimizing fuel cell system components, aiming to enhance efficiency and performance in practical, real-world scenarios.

**Table 1.** Operating points definition

| Operating point | Dry Air Mass Flow [g/s] | Pressure [MPa] |
|---|---|---|
| OP1: Idle | 12 | 0.11 |
| OP2: 50% | 131 | 0.22 |
| OP3: 100% | 262 | 0.24 |

Section 2 will detail the experimental setup, providing insights into the configuration and components utilized. Concretely, it deals with the experimental methodology, delineating the specific procedures followed and the range of tests conducted. Subsequently, Section 3 will present the results and a thorough analysis of the water injection implications and different injection systems. The final section will encapsulate the key conclusions drawn from this study, offering insights into the implications of water injection at the compressor inlet for fuel cell applications and delineating potential avenues for future research and development in this domain.

## 2. Experimental Setup

The experimental bench was designed for testing Roots-type compressors to precisely measure airflow rate, pressure, and temperature at both the inlet and outlet sections of the compressor across various operating conditions. Additionally, humidity levels are monitored to assess the extent of evaporated water by comparing specific humidity values at the inlet and outlet sections. The experimental facility operates within a controlled environment to mitigate external factors that could impact test results. Rigorous ventilation and temperature control mechanisms maintain stable operating conditions throughout the testing process. This controlled setting facilitates precise data collection and analysis, crucial for evaluating the performance characteristics of the Roots-type compressor under investigation.

Figure 1 depicts the TVS R1320 compressor unit, highlighting the driveshaft, inlet, and outlet sections. Additionally, Figure 1 includes the visualization windows that connect the compressor inlet and outlet to the rest of the test setup. These visualization windows are crucial to assess water injection patterns at the inlet, and assessment of evaporation qualitatively at the outlet. Further details on the visualization techniques and the injection system are included in Sections 2.2 and 2.3. Figure 2 illustrates the overall experimental setup. The light blue color indicates the main air stream circuit, and the red color indicates the water injection circuit. The arrows indicate the air and water flow direction. The setup was instrumented with thermocouples (T), pressure transducers (p), two inlet mass-flow meters (M Air 1 and M Air 2), inlet and outlet relative humidity sensors (H), and the torque meter.

Two inlet lines are included to provide more flexibility in terms of mass flow ranges. For low flow operation points, one of the inlet branches is closed, so the mass-flow meter measurement is more robust. Otherwise, for high flow operation points, both inlet branches are opened, leading to a lower pressure drop at the inlet line. A heater and a cooler are included upstream of the compressor inlet to compensate for the daily temperature variability. An air-water separator has been installed downstream of the outlet visualization window to separate water droplets from the main vapor-air mixture. This water separator is a crucial component for robust measurement of outlet relative humidity, especially in scenarios where some water remains unevaporated at the compressor outlet. Composed of a series of fins, the separator changes the flow to a high-speed cyclone flow and separates water from the air phase with efficiencies exceeding 98%. Additionally, a backpressure valve is included at the compressor outlet, downstream of the outlet humidity sensor. This valve allows control of the compressor pressure ratio by adjusting its opening. For all air and water temperature measurements, type K thermocouples were

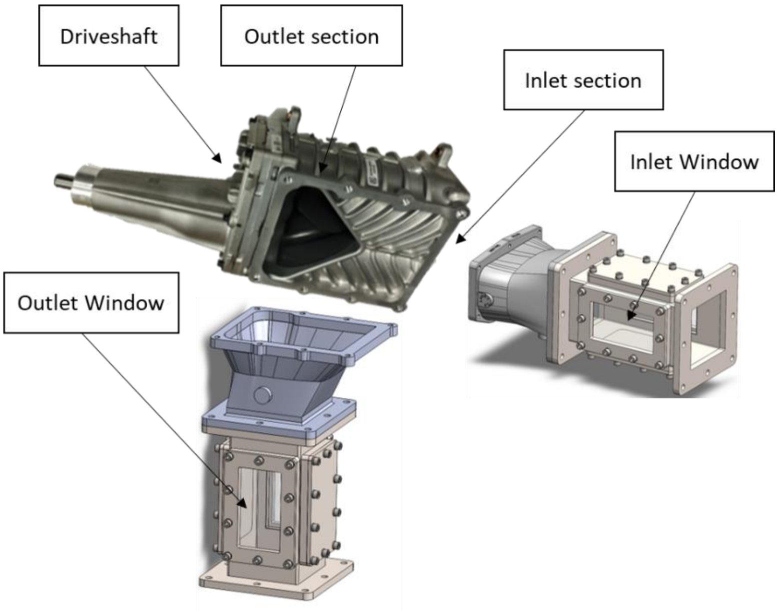
Driveshaft
Outlet section
Inlet section
Inlet Window
Outlet Window

**Fig. 1.** Roots compressor unit connection parts, inlet and outlet visualization windows

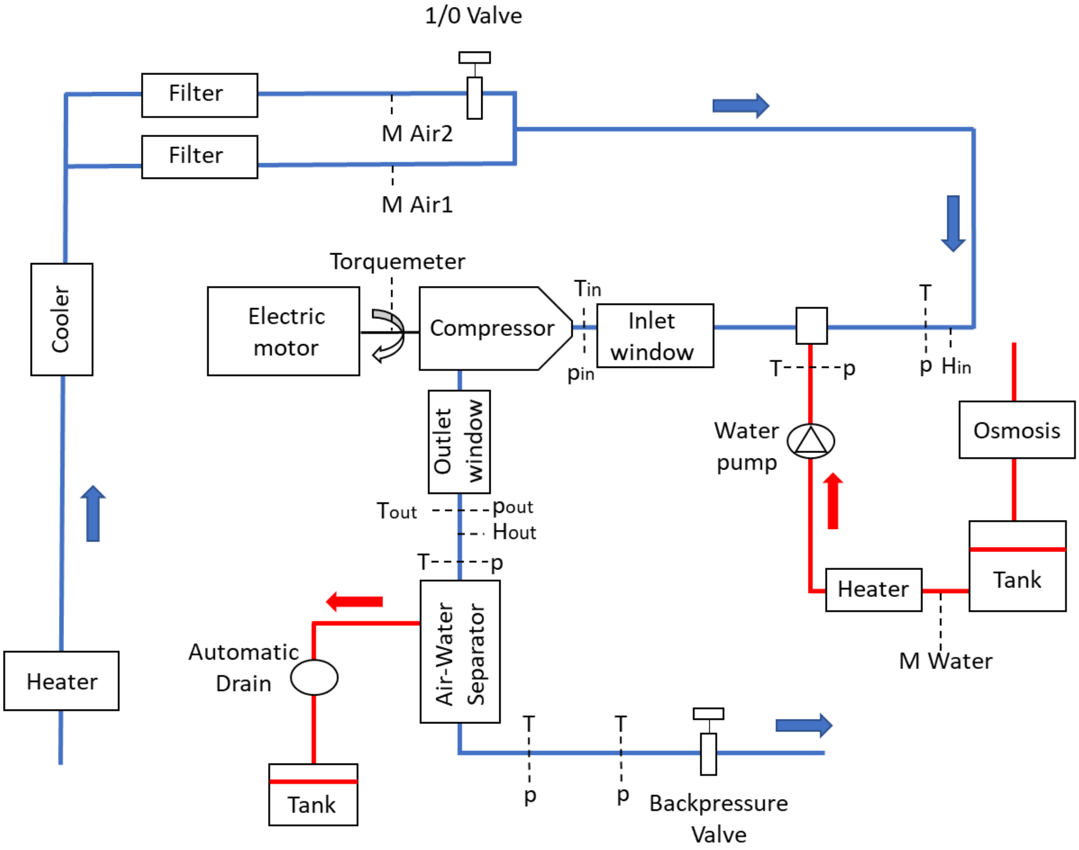
1/0 Valve
Filter
Filter
M Air2
M Air1
Torquemeter
Electric motor
Compressor
Tin
pin
Inlet window
T
p
Hin
T
p
Water pump
Osmosis
Cooler
Outlet window
Tout
pout
Hout
T
p
Heater
Tank
M Water
Automatic Drain
Air-Water Separator
Heater
Tank
T
p
T
p
Backpressure Valve

**Fig. 2.** Test cell diagram

The electric motor is connected to the compressor shaft using a 1:1 gear ratio depicted in Figure 3. The experimental setup includes a torquemeter to measure the torque applied to the compressor shaft during the test operation. The torquemeter is positioned in the transmission shaft, between the compressor and the electric motor. Additionally, the compressor speed is monitored considering the Variator signal. The power is calculated from measured torque and speed for each test point.

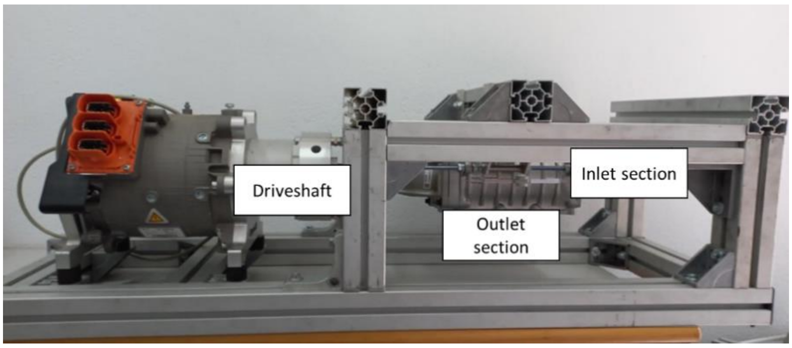

**Fig. 3.** Electric motor, driveshaft, and compressor assembly

The compressor efficiency map and the compressor speed map are depicted in Fig. ***4***.a and Fig. ***4***.b respectively. The OPs defined in Table 1 and analyzed in this study, are shown on the maps. For all these points, the impact of water injection mass and temperature will be analyzed.

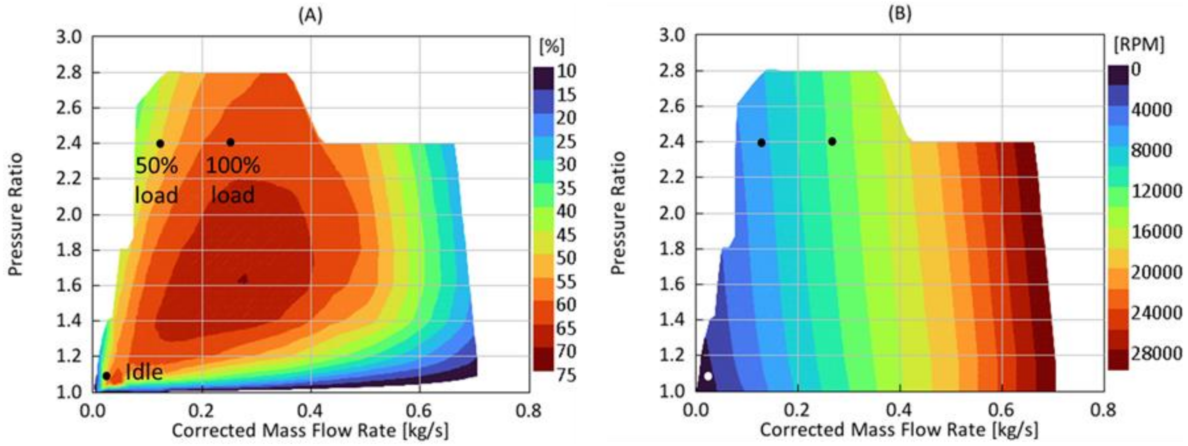

(a) Efficiency map

(b) Speed map

**Fig. 4.** Compressor maps and selected compressor operating conditions

Table 2 shows the initially planned test matrix. The maximum amount of water was estimated through preliminary 0D calculations for each of the Table 1 operating conditions, if 100% relative humidity is reached within the compressor. A higher compression ratio (so higher outlet temperature) allows more water to be evaporated as well as higher dry air mass flow. After the first set of experiments, a lower limit in the maximum amount of water that can be evaporated (see Sections 3.2 and 3.3) was identified (a 100% relative humidity could not be reached without water liquid at the outlet). Consequently, the test points indicated in red were not tested. For every test point, two repetitions were obtained. Every point was stabilized for 20-30 min in terms of gas temperature and outlet pressure. Next, the compressor performance was measured, and simultaneously the videos were recorded.

**Table 2.** Test matrix. The red font indicates test points that were not finally tested. $T_w$ is the water temperature with two values representing water at ambient temperature (under the hood) and generated by the fuel cell

| **OP1** | **Water injection** | | **OP2** | **Water injection** | | **OP3** | **Water injection** | |
|---|---|---|---|---|---|---|---|---|
| *Point* | *$T_w$ [K]* | *Flow [g/s]* | *Point* | *$T_w$ [K]* | *Flow [g/s]* | *Point* | *$T_w$ [K]* | *Flow [g/s]* |
| #01 | - | 0.00 | #06 | - | 0.00 | #15 | - | 0.00 |
| #02 | 313 | 0.25 | #07 | 313 | 2.00 | #16 | 313 | 3.00 |
| #03 | 313 | 0.35 | #08 | 313 | 4.00 | #17 | 313 | 6.00 |
| #04 | 353 | 0.25 | #09 | 313 | 6.00 | #18 | 313 | 9.00 |
| #05 | 353 | 0.35 | #10 | 313 | 8.00 | #19 | 313 | 12.00 |

| | | | | | |
|---|---|---|---|---|---|
| #11 | 353 | 2.00 | #20 | 313 | 15.00 |
| #12 | 353 | 4.00 | #21 | 353 | 3.00 |
| #13 | 353 | 6.00 | #22 | 353 | 6.00 |
| #14 | 353 | 8.00 | #23 | 353 | 9.00 |
| | | | #24 | 353 | 12.00 |
| | | | #25 | 353 | 15.00 |

**2.1 Water injection system** Fig. 5 shows the water injection system used for nozzle characterization and later in the experimental test cell. The water within the deposit comes from a reverse osmosis water filter system, effectively removing dissolved inorganic solids. The AEM rotary water pump with a maximum flow rate of 3.8 L/min and a maximum pressure of 1.4 MPa increases the fluid pressure based on the power consumption (set by a power unit) and the nozzle placed downstream the pump. To maintain a constant flow rate and dampen pressure oscillations, a large-volume reservoir is positioned between the pump and the nozzle. This reservoir serves as a heat exchanger, allowing control over the water temperature. Additionally, a Kistler pressure transducer (with a range of 0-5 MPa) and a K-type thermocouple were installed in the high-pressure line to monitor injected water pressure and temperature.

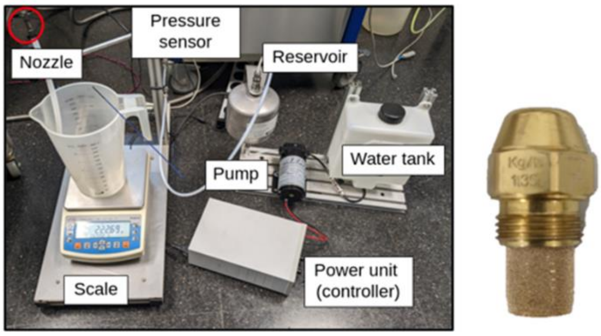

**Fig. 5.** The water injection system employed during the nozzle characterization

Three different Danfoss simplex nozzles (such as the one in Fig. ***5***) with a nominal opening angle of 80° but varying outlet diameters and consequently distinct maximum flow rates were utilized. Each nozzle was selected to match the requirement of the testing operating conditions (Table 2): (1) Small Nozzle with a maximum flow rate of 0.375 g/s for OP1. (2) Medium Nozzle with a maximum flow rate of 8.9 g/s for OP2. (3) Large Nozzle with a maximum flow rate of 15.7 g/s, for OP3. The water mass flow rate is determined based on:

$$\dot{m} = C_d \cdot A \cdot \sqrt{2 \cdot \rho \cdot \triangle p}, \qquad (1)$$

where $\triangle p$ [Pa] is the pressure difference between upstream the nozzle and discharge ambient pressure, $\rho$ [kg/m$^3$] is the water density, $A$ [m$^2$] is the nozzle outlet area, $C_d$ [-] is the nozzle discharge coefficient, and $\dot{m}$ [kg/s] is the water mass flow rate through the nozzle.

The experimental setup was used to characterize the nozzles to obtain: (1) power consumed by the water pump as a function of water mass flow and (2) nozzle discharge coefficients. The results of this characterization, with a maximum experimental uncertainty of about 5%, are summarized in Fig. ***6***. It is important to point out that the maximum power consumption of the water dosing system is 30 W, and it has negligible effect on the system efficiency that includes the water doser and the compressor.

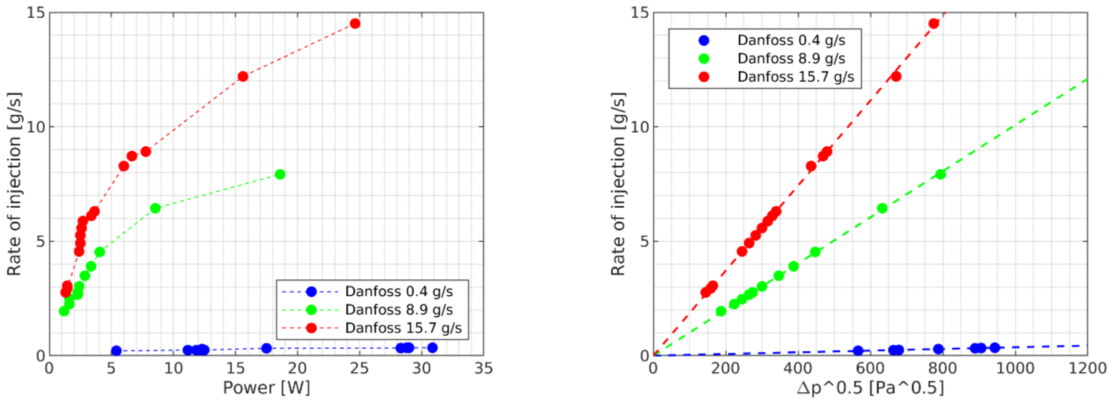

(a) Relationship between the water pump power consumption and the injected mass flow rate

(b) Relationship between the pressure drop through the nozzle and the injected mass flow rate

**Fig. 6.** Experimental characterization of the select Danfoss simplex nozzles

## 2.2 Visualization techniques and equipment

A picture of this visualization section is shown in Fig. **7**. A *25 cm* long section of a *15 cm* side square pipe is used to assemble the visualization window. On all sides, a rectangular cut is made, and a window holder is welded. Two opposite sides hold the *76 x 127 mm* laminated crystal windows, each *16 mm* thick. The remaining two sides hold metallic plates, with one of them supporting the nozzle holder. Two of these windows are assembled for upstream and downstream of the compressor visualization. Before installation in the test cell, static pressure tests were conducted to verify structural integrity and sealing. After welding the inner window support to the pipe and using double silicone seals for the rest of the windows and parts unions, no leakage occurred. Furthermore, no structural damage or cracks were observed when this section was subjected to pressures of 0.05-0.3 MPa inside the section.

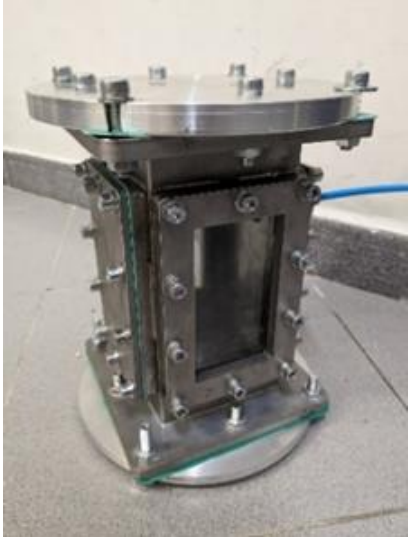

**Fig. 7.** visualization window under static pressure resistance and sealing

High-speed imaging is employed upstream and downstream of the compressor to assess qualitatively the flow state. Diffused Back-light Illumination (DBI) [12] technique is applied upstream of the compressor to identify and track the liquid water droplets injected into the pipeline. The corresponding setup is sketched in Fig. ***8***.a. A Dollar Jenner continuous light source emits the light that passes through a plane diffuser and a field lens to obtain a diffused light wide enough to cover the complete visualization area. When this light passes through the measuring section, one of three possibilities take place to the light:

- encounters liquid water on its path and therefore is blocked
- encounters vapor water and slightly deviates and attenuates
- passes through a zone where only the ambient air is present and therefore undisturbed.

After the visualization section, the light reaches a Photron Fastcam SA-Z high-speed camera equipped with a SIGMA lens of f2.8 aperture and variable 24-70 mm focal distance, where images are recorded. These images are a composition of black zones, with the light blocked by the liquid water, and white and gray zones, with the light undisturbed or slightly deviated by the vapor phase. In DBI technique, light is diffused, so no focusing is done to the light, and no cut-off device is mounted in front of the camera; the gray and white areas do not possess sufficient contrast to be distinguished.

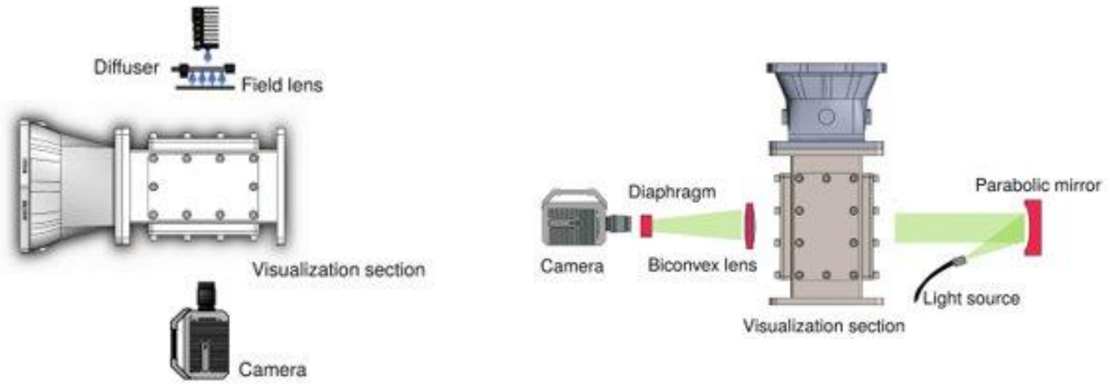

(a) DBI setup upstream the compressor (top view) (b) Schlieren setup downstream the compressor (side view)

**Fig. 8.** Schematics of the visualization techniques employed during the experimental campaign

The Single-pass Schlieren [13] technique is employed downstream of the compressor to detect and monitor the density gradients inside the pipeline at the compressor outlet. These density gradients can be due to temperature gradients but more importantly, they reflect the multi-phase composition of the flow consisting of both air and steam. As shown in Fig. ***8***.b, a punctual light source produced with a continuous Dollar Jenner lamp connected to an optical fiber expands until it reaches a parabolic mirror of 609.6 mm focus distance. Light is collimated in the mirror and redirected to the measuring section. The collimated (parallel) beams of light are subject to deviating from their original path by density gradients in the path traveled. After the visualization section, the light goes through a 450 mm focal length biconvex lens that focuses the light back to a point. In the focus of that lens, where the light point is formed, the shadowgraph cutting device (diaphragm) is mounted. This device provides direct control of the sensitivity of the technique. In this case, images are acquired by a Photron Fastcam SA5 high-speed camera. If liquid is present at the outlet section, it is also visualized as a black region in the images.

## 3. Results

Compressor performance results are first presented for the three different operating points and test conditions defined in Section 2.1. Subsequently, observations regarding the compressor performance are provided. Although water injection affects the pressure ratio, compressor speed, and air mass flow, the actuators were adjusted to maintain a constant pressure ratio and compressor speed. For each test point, the compressor power is calculated. However, comparing the compressor power does not provide any information regarding the impact of water, in terms of the compressor efficiency. Consequently, the specific work is calculated as the ratio between the compressor power and the total mass flow to assess the effect of water injection on the compressor performance as:

$$Compressor\ power = Torque * Speed \tag{1}$$

$$Specific\ work = \frac{Compressor\ power}{\dot{m}_{total}} \tag{2}$$

where $Torque$ [N·m] is the compressor torque, $rpm$ [rad/s] is the compressor speed, and $\dot{m}_{total}$ [kg/s] is the total mass flow rate. This parameter normalizes the compressor mechanical power by the total mass flow which in this study varies not only due to the water injection upstream but also to a variation in the compressor volumetric efficiency (see Section 3.2).

Moreover, the isothermal efficiency is utilized to assess the influence of water on the compression process, defined by:

$$\eta_{isothermal} = \frac{Isothermal\ work}{Specific\ work + \text{Injection system spcific work}} = \frac{R \cdot T_{in} \cdot \ln(\pi_c)}{\triangle h_{c+mech} + \frac{\dot{W_{inj}}}{\dot{m}_{total}}} \tag{3}$$

where $R = 287$ J/(kg·K) is the air gas constant, $T_{in}$ [K] is inflow gas temperature, $\pi_c$ [-] is the compression ratio, $\triangle h_{c+mech}$ [J/kg] is the sum of the compressor work and mechanical losses, $\dot{W_{inj}}$ [W] is the water injection system power consumption, and $\dot{m}_{total}$ [kg/s] is the total mass flow rate.

The water injection system power consumption is orders of magnitude lower than the compressor power and could be ignored. Injecting water upstream of the compressor inlet has two significant implications: firstly, the higher thermal inertia of water compared to air, which increases the overall mixture's thermal inertia, and secondly, water evaporation occurs. Both implications make the compression process more isothermal. The higher thermal inertia results in lower temperature change due to the compression process compared with the dry case. Moreover, due to water evaporation, the heat is absorbed from the air-water mixture keeping the system temperature constant (isothermal). In conclusion, injecting water should lead to an improvement (diminishment) of the specific work.

## 3.1 OP1 Idle operating condition

For this operating condition, despite water injection, the compressor performance parameters remain the same as in the dry condition (without water injection). Note that low inlet airflow lacks sufficient momentum to drag all the injected water inside the compressor. Consequently, most of the injected water does not even reach the compressor; instead, it accumulates at the inlet visualization section. Fig. **9**, captured during the experiments, illustrates how water thoroughly wets the visualization windows and settles at the bottom of the measuring section.

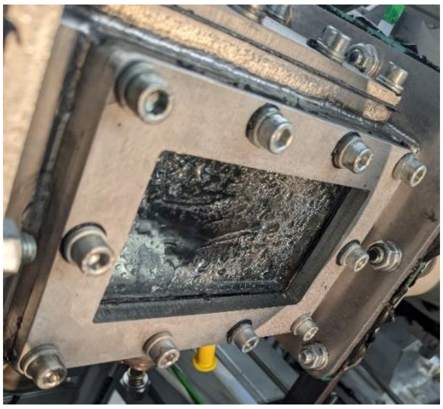

**Fig. 9.** Inlet visualization window during idle condition testing

Hence, the compressor power and specific work for all the OP1 test points slightly vary and are approximately 0.28 kW and 23 kJ/kg. At the outlet of the compressor without water injection, the relative humidity corresponds to the ambient value of 12-15%, depending on atmospheric conditions during testing. With water injection, the outlet humidity rises to 18-22% in test points #02 and #04, and to 21-25% in test points #03 and #05. This indicates that a small portion of the injected water evaporates within the compressor. The more water injected, the higher the humidity at the outlet, reflecting an increased amount of evaporated water.

## 3.2 OP2 50% load operating condition

Fig. ***10*** shows the inlet boundary conditions of the testing points corresponding to the 50% operating condition. Similar to the idle case, the inlet flow temperature after water injection is about 7 K lower than the temperature before the injection (Fig. ***10***.a) highlighting the evaporation cooling effect. This result could mean that a very small portion of the injected water is evaporated during the injection process. Fig. ***10***.b shows how the total mass flow increases because of the injected water, and how the dry air mass flow becomes also larger. This is assumed to occur because water injection and the corresponding evaporation within the compressor decrease the air-water mixture temperature, and since the pressure ratio and compressor speed are kept the same, the dry air mass flow can be increased, therefore improving the volumetric efficiency of the compressor.

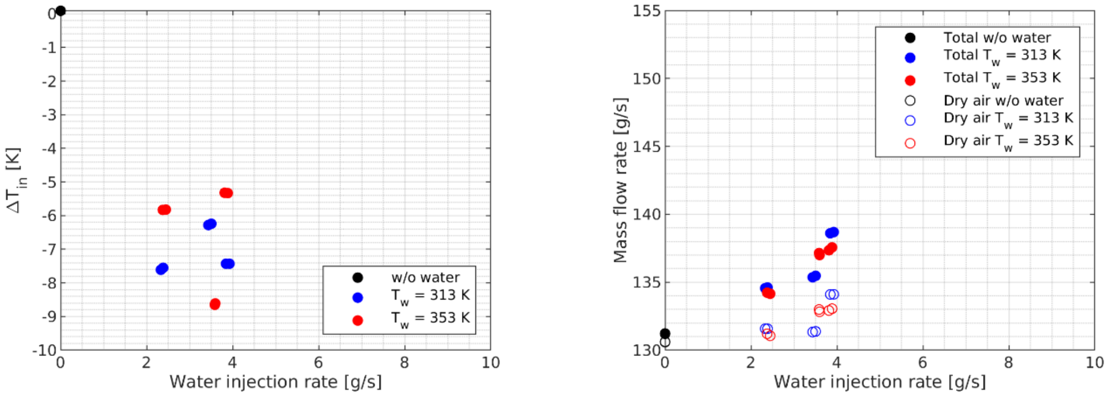

(a) Airflow temperature drop between after and before the water injection location

(b) Dry airflow and total mass flow through the compressor

**Fig. 10.** Inlet boundary conditions of all testing points corresponding to the 50% operating condition

Fig. ***11***.a shows the compressor power, which decreases after water injection. Due to the evap-oration that takes place within the compressor, the air-water mixture is at a lower temperature, and so the power required for reaching the same compression ratio is lower. In addition, the remaining liquid water is located next to the compressor walls, improving sealing, and thus reducing mechanical losses. Even though the total mass flow rate increases, Fig. ***11***.b shows a significant compressor specific work reduction of up to 7.5% with water injection of about 4 g/s. Indeed, Fig. ***11***.c shows the compressor isothermal efficiency that improves by increasing the water injection rate. The larger the amount of water injected, the greater the water mass being evaporated, and thus a compression process with a lower temperature increase is achieved. In other words, the compression process becomes more efficient (closer to the ideal isothermal process) as the amount of injected water is increased.

Test points corresponding to 313 K water temperature and 3.5 g/s injected water are out of the expected trend. See for instance Figure 11.b, where those conditions report a compressor specific work clearly above the 353 K conditions, around the same values of the conditions corresponding to 2 g/s of injected water. Those outlier results present measurement or control errors on the injected water quantity and should not be taken into consideration in analyzing compressor performance trends.

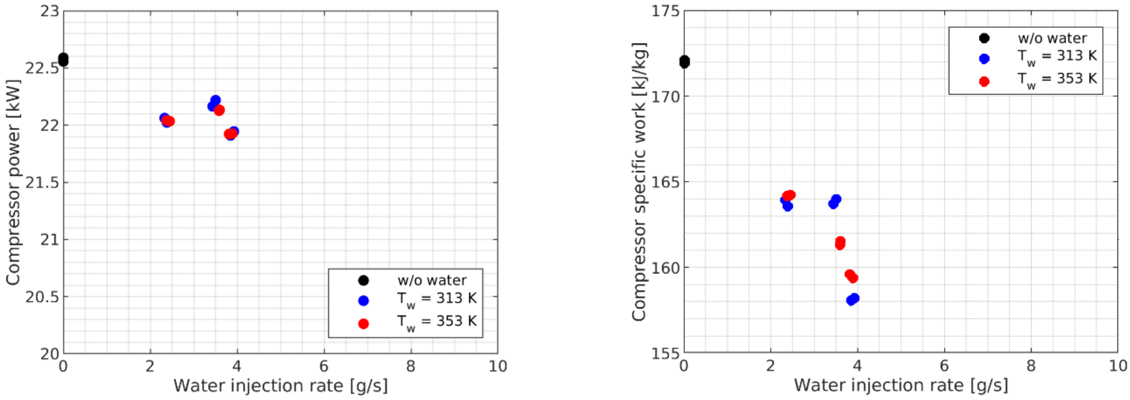

(a) Power

(b) Specific work

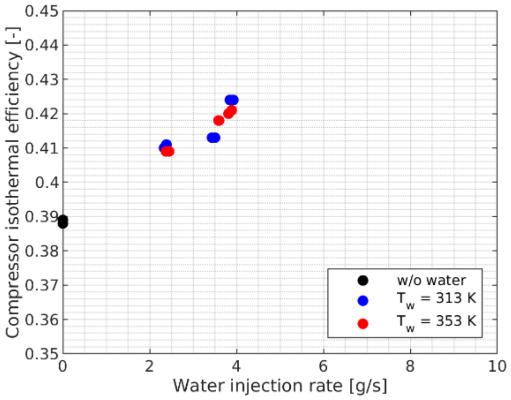

(c) Isothermal efficiency

**Fig. 11.** Compressor performance corresponding to the 50% operating condition

At the maximum tested value of the water injection rate, the relative humidity is still low (20-25%), although it reached the exponentially increasing region as shown in Fig. ***12***.b.

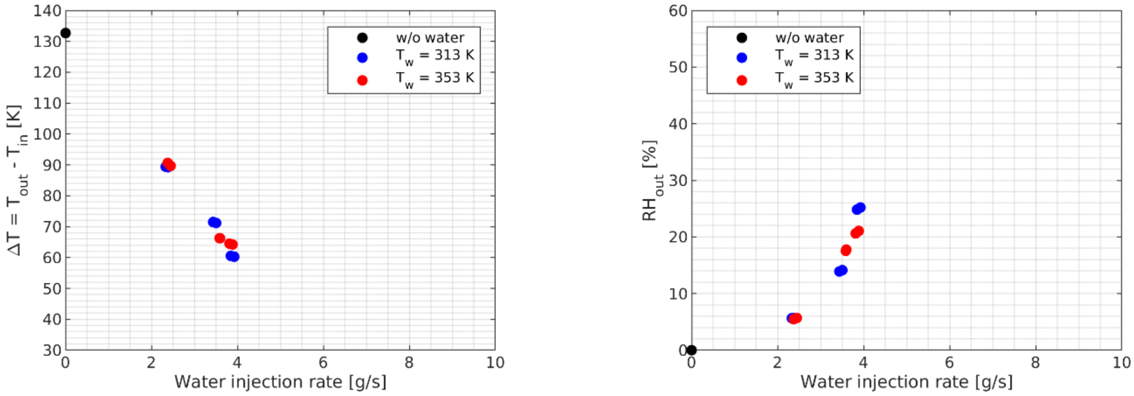

(a) Across Compressor temperature drop

(b) Relative humidity

**Fig. 12.** Compressor outlet measurements corresponding to the 50% operating condition

Liquid droplets coming out of the simplex nozzle impact the inlet visualization window under all test points and operating conditions. That makes the visualization and the corresponding postprocessing unreliable because part of the light is blocked by the water stagnating at the windows, disturbing the measurements. For example, in Fig. **13** the illuminated region is completely blurry due to wall wetting.

In addition to the test points listed in Table 2, extra points are measured with the goal of finding the maximum water injection rate upstream of the compressor that can be evaporated fully. Fig. ***14*** summarizes the corresponding results, obtained with the Schlieren technique downstream the compressor for 3 different water mass flow rates, 2 g/s (test #07), 3.5 g/s, and 4 g/s (test #08). This figure shows significant water formation at the outlet with 4 g/s (test #08). The water injection rate was reduced until no water droplet formation was reached. This limit of 3.5 g/s coincides with a temperature gradient of 70 K across the compressor (Fig. ***12***.a).

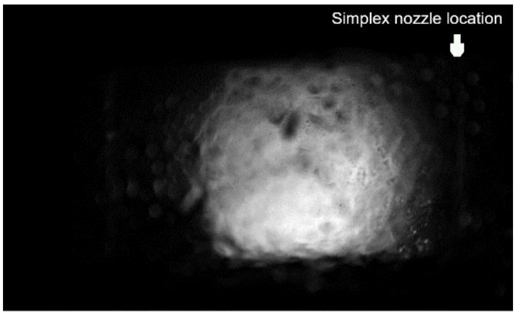

**Fig. 13.** Raw image from the DBI visualization during test #08

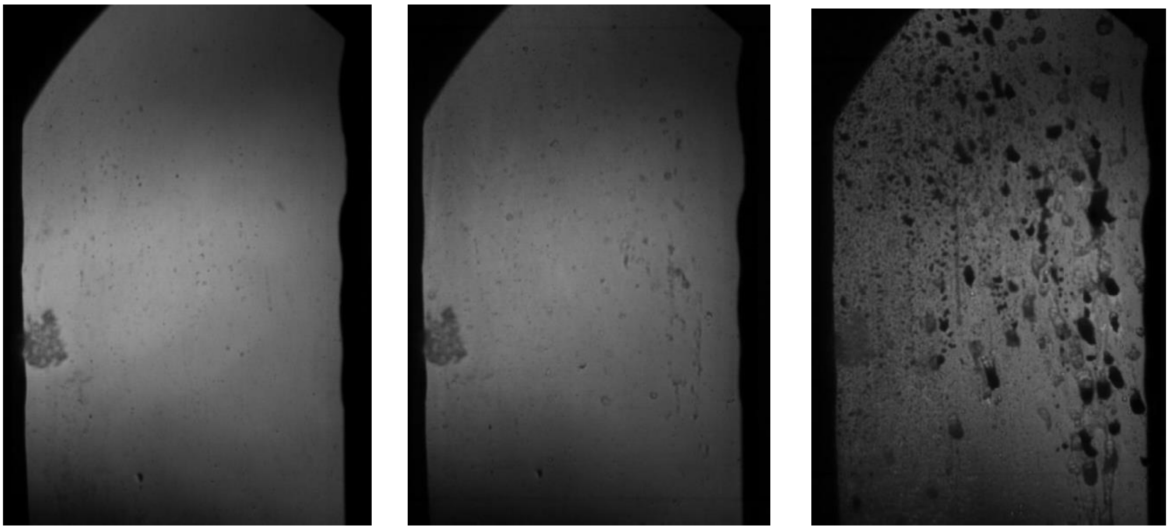

(a) 2 g/s (test #07)

(b) 3.5 g/s

(c) 4 g/s (test #08)

**Fig. 14.** Images from the Schlieren visualization during the 50% operating condition testing

### 3.3 OP3 100% load operating condition

Fig. ***15*** shows the inlet boundary conditions of the testing points corresponding to the 100% operating condition. The total air mass flow increases more (Fig. ***15***.b) compared with 50% operating condition (Fig. ***10***.b) due to a higher water mass rate injection.

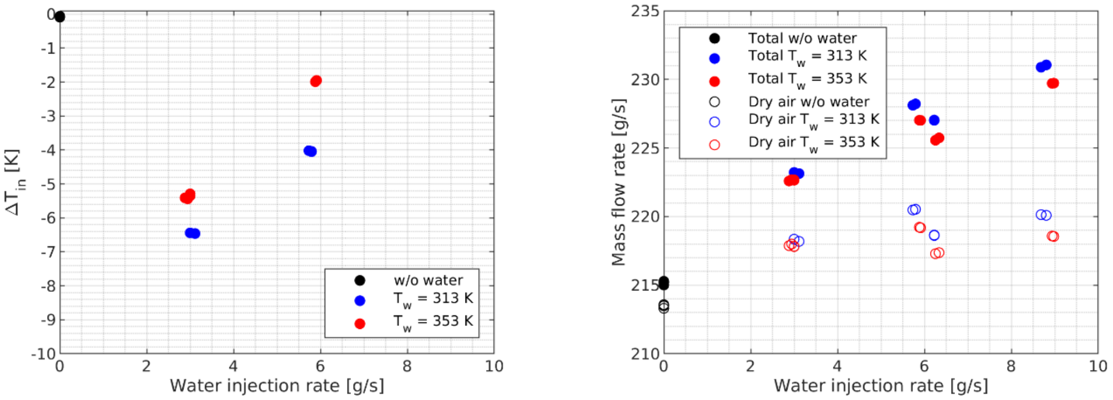

(a) Airflow temperature drop between after and before the water injection location

(b) Dry airflow and total mass flow through the compressor

**Fig. 15.** Inlet boundary conditions of all testing points corresponding to the 100% operating condition

Fig. ***16***.a shows compressor power which again decreases after water injection. The trend is almost linear (as observed in Fig. ***11***.a for the 50% operating condition) until a value of about 6 g/s of water mass flow rate. Fig. ***16***.b shows how the compressor specific work also decreases with increasing water mass flow rate, but with a clear change of trend at about 6 g/s. For higher mass flow rate values, not all the injected water is evaporated so the compressor power is not further reduced (it even increases with more water being injected), but as the total mass flow is increased the specific work is still slightly decreasing. Fig. ***16***.c shows the compressor isothermal efficiency that improves with the increase of water injection rate for all the tested points. In other words, the compression process becomes more efficient even though not all water is evaporated.

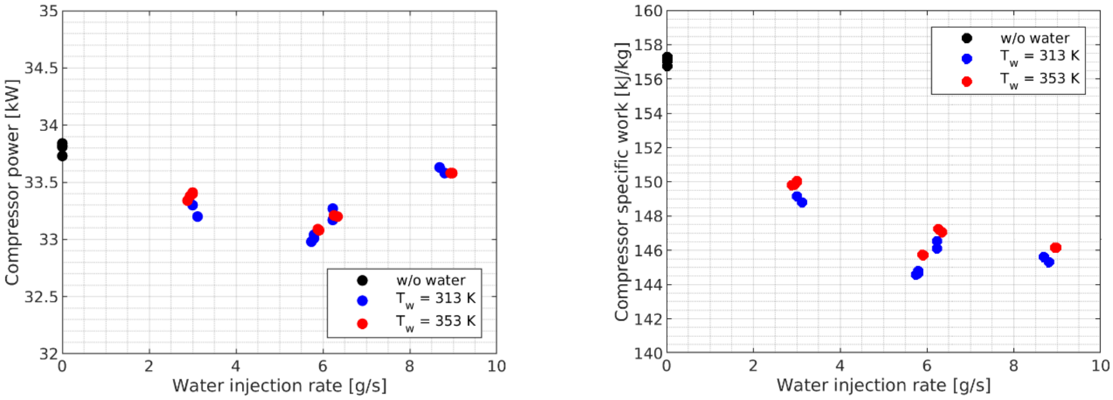

(a) Power

(b) Specific work

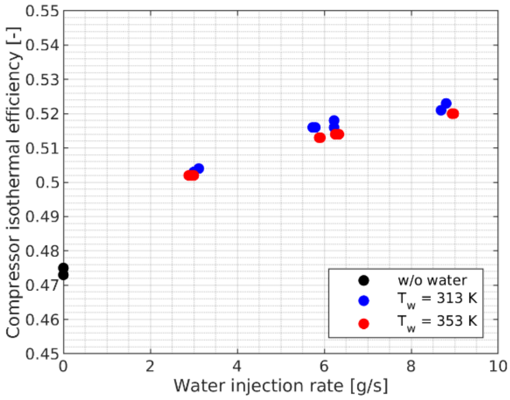

(c) Isothermal efficiency

**Fig. 16.** Compressor outlet measurements corresponding to the 100% operating condition

All the injected water is evaporated before the outlet visualization window and so relative humidity at the compressor outlet increases progressively within the water injection rate, water droplets start to be visible downstream the compressor with a water mass flow rate of around 6 g/s (in tests #17, #22,). At those test points the relative humidity, shown in Figure 16.b, is still very low (< 20%). With 9 g/s of water injection rate large liquid ligaments are visible at the outlet and the relative humidity is about 50-60% but its increasing rate is already exponential.

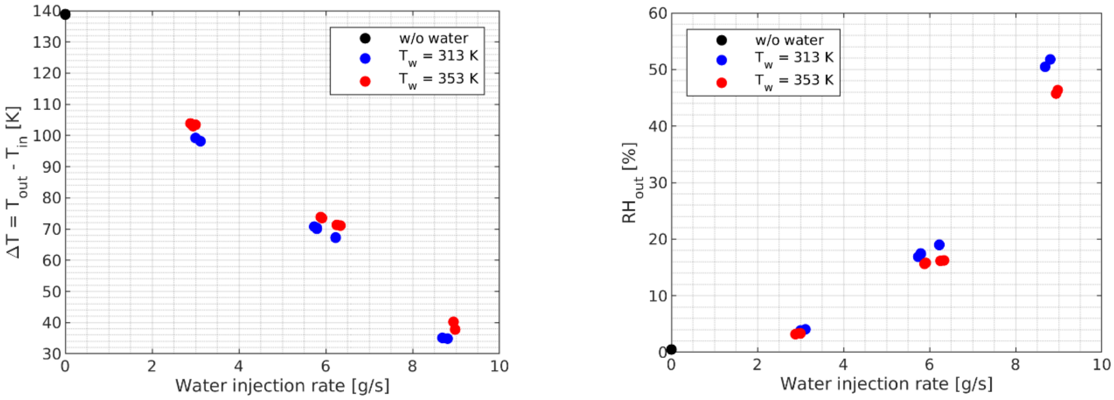

(a) Compressor outlet and inlet temperature drop

(b) Relative humidity

**Fig. 17.** Compressor outlet parameters of all testing points corresponding to the 100% operating condition

As for the 50% operating condition, extra testing points are measured to find the maximum amount of water that can be injected and fully evaporated inside the compressor. Schlieren visualization results are shown in Figure 17 (black spots in Figure 17.a correspond to liquid droplets on the windows which remain there from different test points). In this case, water droplets start to appear at the visualization window with almost 6 g/s, matching the conditions of test #17. For the 50% operating condition, the temperature drop in the compressor (Figure 14.a) is around 70 K for about 6 g/s of injected water. Figure17.c shows a completely wet window with a large liquid water stream coming out from the compressor and flowing on the left-hand side of the pipeline surfaces.

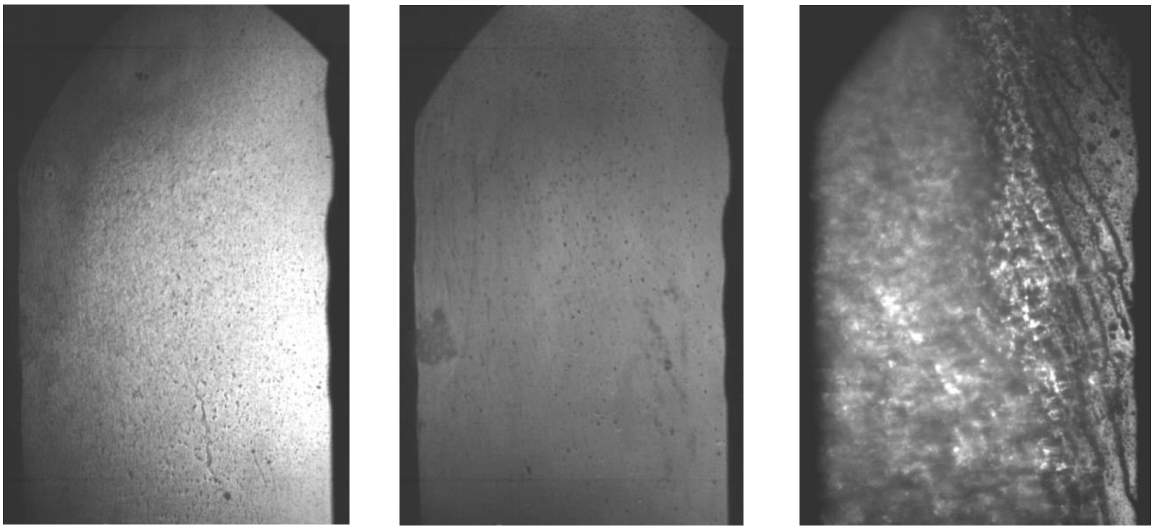

(a) 3 g/s (test #16)

(b) 6 g/s (test #17)

(c) 9 g/s (test #18)

**Fig. 18.** Images from the Schlieren visualization during the 100% operating condition testing and different mass flow rates injected upstream of the compressor

## 4 Conclusion and Future Work

The utilization of water injection at the compressor inlet to mitigate compressor energy consumption while enhancing humidity levels at the outlet for fuel cell applications has been investigated. A test cell has been designed and assembled to test a Roots-type compressor with a continuous flow water injection system and integrated visualization windows. The injected water mass flow rate can be controlled by adjusting the injection pressure (water pump power) and using different nozzles. The main findings of this experimental work are:

- At Idle conditions, the water must be injected directly into the compressor, or perfectly aligned with the airflow to increase the water ingested by the compressor and so the evaporated mass during the compressor. Otherwise, liquid water accumulates at the injection location.
- The evaporation process improves the system efficiency making the compression process more isothermal. This is assessed through isothermal efficiency.
- Mechanical power decreased by 2.65% and 2.3%, and specific work decreased by 7.83% and 4.7% for 50% and 100% operating points. These results are associated with the highest water injection rate that complete evaporation is guaranteed.
- Injected water temperature is not a significant parameter. In both 50% and 100% compressor operating conditions, the difference between results with 313 K and 353 K of water is negligible.
- Air mass flow increases with the injected water mass flow rate increase although the compressor speed and pressure ratio are constant which is evidence of volumetric efficiency improvement.
- Water evaporation within the compressor is not instantaneous and needs some time which is a function of temperature. The liquid droplets and ligaments appear at the compressor outlet when the outlet temperature is 263 K and RH reaches 25%.
- Outlet temperature or temperature drop along the compressor (Figures 12.a and 17.a) could be taken as a parameter to evaluate the evaporated quantity. A large temperature reduction across the compressor indicated that more heat is used for the evaporation process and more water is evaporated. In the test setup (Figure 2) an array of temperature sensors was used between the compressor outlet and separator inlet. It was observed that the temperature change across the sensor array is minor. Applying the same principle, test results suggest that negligible evaporation happens after the compressor outlet.
- To obtain these benefits, a complete injection system and its control are necessary. This definitively increases the complexity, weight, and maintenance costs. Furthermore, in a real-world application to prevent any unevaporated droplet from entering the fuel cell and damaging it, an additional control strategy or hardware is required.
- We assume an average 0.4 kW compressor mechanical shaft power reduction for a typical drive cycle of a linehaul truck enabled by a direct water injection system. Given 60% efficiency for a fuel cell system, 33 kWh/kg energy content of hydrogen, 10 $/kg cost of hydrogen, and 2000 hours of operation per year, the proposed system can potentially decrease the operation cost by $400 per year.

Potential future work includes investigating alternative injection systems techniques (such as pulsed injection using an electronically controlled injector) to improve water atomization and the evaporation process, thereby increasing the relative humidity at the compressor outlet. Validated 1D modeling and Computation Fluid Dynamics tools would be very beneficial to build a digital twin and thus accelerate the analysis of other strategies like injecting water in the compressor or downstream. Additionally, it is suggested to expand the range of operating points to areas with lower pressure ratios to evaluate if there are differences in achievable relative humidity at the compressor outlet.

## Acknowledgments

This work is a collaboration between Eaton Corporation and CMT-Clean Mobility & Thermofluids technicians for their collaboration and support during the development of the investigation. This project was funded by Eaton and provided invaluable information to the US Department of Energy (DOE) funded project "High Efficiency and Transient Air Systems for Affordable Load-Following Heavy-Duty Truck Fuel Cells", project award DE-EE0009618.

## References

[1] M. Xin, H. Gan, Y. Cong, and H. Wang, “Numerical simulation of methane slip from marine dual-fuel engine based on hydrogen-blended natural gas strategy,” Fuel, vol. 358, 2024, DOI: 10.1016/j.fuel.2023.130132.

[2] T. Su, C. Ji, S. Wang, L. Shi, J. Yang, and X. Cong, “Investigation on performance of a hydrogen-gasoline rotary engine at part load and lean conditions,” Applied Energy, vol. 205, pp. 683–691, 2017, DOI: 10.1016/j.apenergy.2017.08.049.

[3] J. R. Serrano, F. J. Arnau, L. M. García-Cuevas, and F. A. Gutiérrez, “Coupling an oxygen generation cycle with an oxy-fuel combustion spark ignition engine for zero NOx emissions and carbon capture: A feasibility study,” Energy Convers Management, vol. 284, 2023, DOI: 10.1016/j.enconman.2023.116973.

[4] S. Küfeoğlu and D. Khah Kok Hong, “Emissions performance of electric vehicles: A case study from the United Kingdom,” Appl Energy, vol. 260, Feb. 2020, doi: 10.1016/j.apenergy.2019.114241.

[5] Z. Wang, B. Dong, Y. Wang, M. Li, H. Liu, and F. Han, “Analysis and evaluation of fuel cell technologies for sustainable ship power: Energy efficiency and environmental impact,” Energy Conversion and Management: X, vol. 21, 2024, DOI: 10.1016/j.ecmx.2023.100482.

[6] M. T. Mehran et al., “A comprehensive review on durability improvement of solid oxide fuel cells for commercial stationary power generation systems,” Appl Energy, vol. 352, 2023, DOI: 10.1016/j.apenergy.2023.121864.

[7] L. Iannuzzi, J. A. Hilbert, and E. E. Silva Lora, “Life Cycle Assessment (LCA) for use on renewable sourced hydrogen fuel cell buses vs diesel engines buses in the city of Rosario, Argentina,” International Journal of Hydrogen Energy, vol. 46 (57), pp. 29694–29705, 2021, DOI: 10.1016/j.ijhydene.2021.01.065.

[8] F. Han, S. Yoon, N. Raghavan, B. Yang, and H. Park, “Technological trajectory in fuel cell technologies: A patent-based main path analysis,” Int J Hydrogen Energy, vol. 50, pp. 1347–1361, 2024, DOI: 10.1016/j.ijhydene.2023.10.274.

[9] J. L. Casteleiro-Roca, A. J. Barragán, F. S. Manzano, J. L. Calvo-Rolle, and J. M. Andújar, “Fuel cell hybrid model for predicting hydrogen inflow through energy demand,” Electronics (Switzerland), vol. 8, no. 11, Nov. 2019, doi: 10.3390/electronics8111325.

[10] T. Vidović, I. Tolj, G. Radica, and N. Bodrožić Ćoko, “Proton-Exchange Membrane Fuel Cell Balance of Plant and Performance Simulation for Vehicle Applications,” Energies (Basel), vol. 15, no. 21, Nov. 2022, doi: 10.3390/en15218110.

[11] C. W. Wu, W. Zhang, X. Han, Y. X. Zhang, and G. J. Ma, “A systematic review for structure optimization and clamping load design of large proton exchange membrane fuel cell stack,” Journal of Power Sources, vol. 476, 2020. DOI: 10.1016/j.jpowsour.2020.228724.

[12] F. C. Lee et al., “Optimization and characterization of graphene-based microporous layers for polymer electrolyte membrane fuel cells,” International Journal of Hydrogen Energy, vol. 51, pp. 1311–1325, 2024, DOI: 10.1016/j.ijhydene.2023.05.003.

[13] J. M. Desantes, J. M. García-Oliver, A. García, T. Xuan, “Optical study on characteristics of non-reacting and reacting diesel spray with different strategies of split injection”, International Journal of Engine Research, vol. 20 (6), pp. 606-623, 2019, DOI: 10.1177/1468087418773012.

# A Novel Method for Predicting Compressor Performance in the Vicinity of Surge

David Schwarz[1,2], Vivek Harsha[1], Somasekhar Reddy Dantla[1], Thikshana Reddy Yeruva[1], Galin Nakov[1], Ricardo Martinez-Botas[2]

[1] Daimler Truck AG, Fasanenweg 10, 70771 Leinfelden-Echterdingen, Germany
E-mail: contact@daimlertruck.com
Telephone: +49 711 8485-0

[2] Imperial College London, South Kensington Campus, London SW 7 2 AZ, United Kingdom
Telephone: +44 20 7589 5111

**Abstract.** Commercial Vehicle Turbocharger Compressors must achieve high efficiencies while maintaining a wide compressor map in order to fulfil increasing customer demands and emission regulations. These requirements push aerodynamic prediction methods to their limit, as they must provide accurate compressor maps in early design stages. With an emerging trend towards H2 combustion engines, surge prediction has become a major engineering challenge; traditional methods of turbocharger matching need to be extended to the new energy balance in the H2 engine inlet and outlet.

Metamodels, also known as surrogate models, can be helpful in the development of compressors, but are currently only of limited use due to the comparatively small design space available and the resulting numerical instabilities.

In this paper, a novel, metamodel-based approach is introduced that overcomes this limitation. The test-based metamodel is first numerically stabilized for low mass flow rates using an analytically derived boundary condition. In the second step, an analytically derived function is coupled with the metamodel to allow extrapolation towards lower mass flow rates where insufficient test data is available. The approach is compared with RANS, URANS and test bench data. Measurements show approximately 2% deviation in pressure ratio and approximately 2% efficiency deviation for the new approach compared to the test bench data at last stable point, while being of 4 orders of magnitude faster than a comparable URANS simulation.

This opens the way for early 1D engine surge simulations, which are especially important for the successful development of H2 combustion engines while at the same time this method supports current engine platforms.

## Notation

| | |
|---|---|
| *HGTR* | *Hot gas test rig* |
| $\dot{m}$ | *Mass flow rate* |
| $r$ | *Radius* |
| $R$ | *Gas constant* |
| $W$ | *Work* |
| $\gamma$ | *Ratio of specific heats* |
| $\eta$ | *Adiabatic efficiency* |
| $\Pi$ | *Pressure Ratio* |
| $\omega$ | *Angular velocity* |

Subscripts

| | |
|---|---|
| *ref* | *Referenced value* |
| *T* | *Total* |
| *1* | *Compressor inlet / wheel inner diameter* |
| *2* | *Compressor outlet / wheel outer diameter* |

## 1. Introduction

Compressor surge is a violent flow phenomenon that can severely damage the compressor, the piping system, and the surrounding components in flow systems such as turbochargers and gas turbines. Although research can be traced back to the 1920s, surge is still difficult to be accurately predicted [1].

Turbocharger compressors for heavy-duty diesel engines achieve adiabatic efficiencies of over 80% [2] but must become more efficient to meet fuel economy targets and emissions requirements. In general, improvements in efficiency result in a reduction in the surge margin. Consequently, surge margin has emerged as a significant challenge in the field of compressor development.

This is the case in the context of new green technologies such as H2 ICE, which must achieve an adequate level of efficiency from the outset to be attractive to customers. Due to restrictions like knocking sensitivity and air-fuel-mass ratio resp. emission limitations, hydrogen engines may not reach the specific torque level of diesel engines. Thus, they may require a wider engine speed range than diesel engines to ensure the same drivability. Therefore, the compressor map width has become even more important.

As the cost of computing power has decreased significantly and dozens of different compressors have been developed over the years, surrogate modelling, also known as metamodeling, has become a commonly used tool [3,4]. One of its major drawbacks is the lack of physical models embedded in the tools, which makes them less accurate. This is particularly when one gets closer to the limits of the design space or when there is not enough data available for training the tool. This can lead to undesirable response surface behaviour that prevents appropriate optimisation and use of the model. As surge is an inherent boundary of the design space, metamodeling could not be applied, thus precluding the use of 1D simulations of engine surge in the early design stages.

In this paper, a new method is proposed that overcomes this limitation by extending the design space with analytically derived boundary conditions. In the first section, the methodology is derived. Then, URANS simulations are performed to obtain additional points in the unstable region. Subsequently, the data is employed to substantiate the efficacy of the methodology and to ascertain its precision. Finally, the predictive capacity of the method is evaluated and compared with measurements obtained from the hot gas test bench.

## 2. Metamodeling

In the following sections, different (meta-)models are derived. All metamodels use the same test bench data as training data. The models are multi-dimensional and connect geometric parameters, tip speed and the mass flow rate with the corresponding output variable: $y = f(geometry,\, u_{tip},\, \dot{m})$ . Geometric input parameters were excluded from the model when no statistically relevant influence was found.

### 2.1 Compressor Designs and Data Acquisition

Two relevant geometries, Compressor A and B, are shown in Fig. 1. Both compressors deliver the same choke mass flow rate at maximum compressor speed and are designed for a 6 cylinder, 13l on-highway heavy-duty Diesel engine. Table 1 gives an overview of the compressor geometry characteristics.

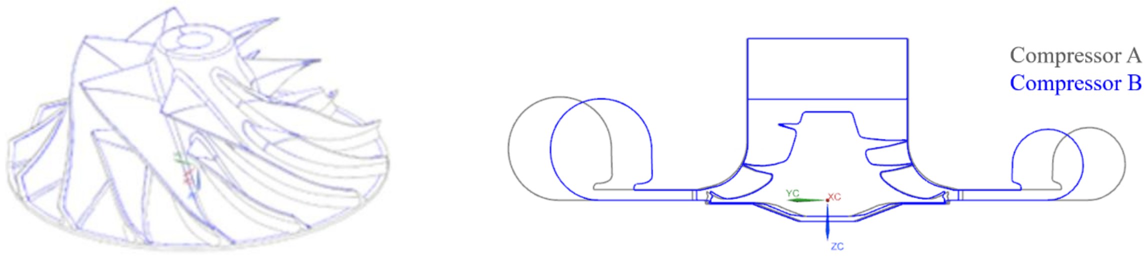

(a) Impellers A and B

(b) Cross-section fluid volume Compressor A and B

**Fig. 1**. Comparison of Compressor A and B

**Table 1**. Compressor geometry characteristics

| | Compressor A | Compressor B |
|---|---|---|
| Blades | 7+7 | 7+7 |
| Inlet diameter (mm) | 64 | 64 |
| A/R-Ratio | Linear | Linear |
| Design speed range (rpm) | 40.000-120.000 | 40.000-120.000 |
| Casing treatment | No | No |

All compressor performance data was measured at Daimler Truck AG´s internal Hot Gas Test Rig (HGTR). The HGTR is a fully automated, environment-controlled test rig allowing maximal repeatability which is compulsory for metamodeling. Surge is detected when the transient compressor outlet static pressure exceeds 5% of the sliding averaged value. During data acquisition, additional stability criterions such as temperature and speed are continuously monitored to assure a proper quasi-steady measurement. The HGTR is fully compliant to the measurement accuracies defined in SAE Standard J1826 [5].

## 2.2 Pressure Ratio Metamodel Stabilization

A metamodel, solely based on test bench data, is shown in Fig. 2 as grey speedlines. Its *Coefficient of Prognosis* (CoP) [6, 7] was found to be superior to other metamodels, although it was carefully checked that this was not due to overfitting.

The metamodel generally follows its training data ("Test" in the figure), but there are deviations in the choke mass flow. This is due to the steep slope of the compressor curve, which is a common problem in metamodeling. Choke is a crucial parameter in compressor design but can be accurately predicted using RANS. Hence, choke range is not of interest for the methodology presented here, and this effect is not investigated further.

On the left-hand side of the training data, or what can also be described as the unstable region of the compressor on the test bench, the metamodel estimates an increase in the pressure ratio before the typical positive slope develops. Any surge calculation based on this metamodel is therefore very inaccurate and not useful in any kind of development. To suppress the unphysical behaviour, additional support points must be added. This could be done by measurements in the unstable region. In the past, some authors [8, 9] have succeeded in achieving this for small automotive compressors. However, the compressors considered in this study are three times larger and Gharaibeh [10] concludes that measurements for such sizes are not feasible.

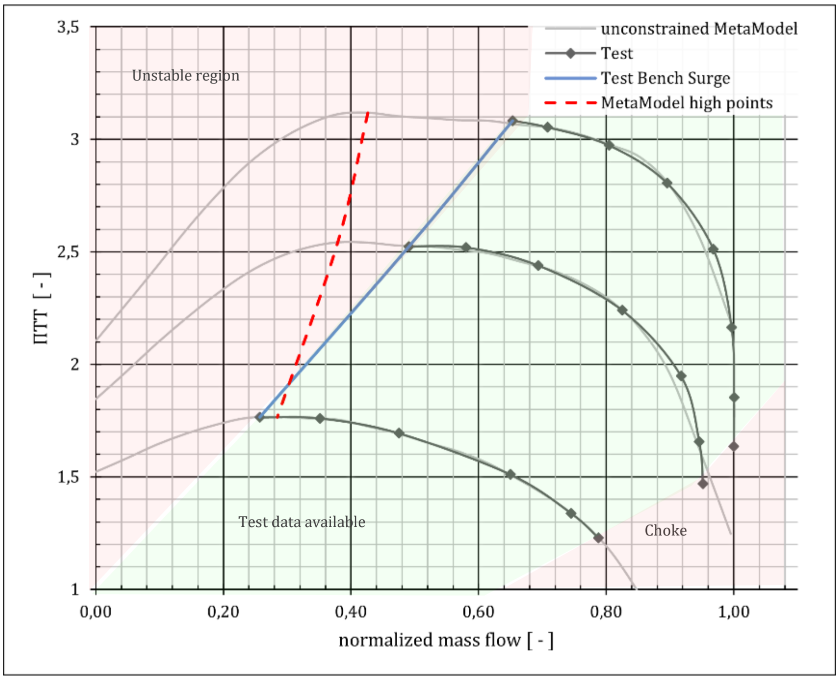

**Fig. 2** Test data and Metamodel- Compressor A

In the absence of experimental data, it is necessary to use data obtained by calculation. This is generally considered a poor approach, as the discrepancies between calculations and experiments degrade the accuracy of the metamodels. Consequently, the calculated support points should be situated at a considerable distance from the region of interest, in order to stabilise the metamodel without affecting its prediction accuracy in the region of interest.

The *Radial Equilibrium Theory* (RET) is employed by several authors [8, 11, 12, 13] to calculate the pressure ratio of the compressor at zero mass flow, as illustrated in Eqn. 1. Consequently, it can be regarded as a suitable boundary condition for the metamodel. Dehner et al. [13] propose the use of a constant multiplier $K$ to enhance the alignment between calculations and measurements.

$$\Pi_{TT,0} = K\,[1+\frac{\gamma-1}{2\gamma R T_1}\omega^2(r_2^2 - r_1^2)]^{\frac{\gamma}{\gamma-1}} \tag{1}$$

In the case of the metamodel, this parameter can additionally be used to improve its prediction accuracy. Therefore, an optimization, Eqn. 2,3, is introduced, with $f(\dot{m}_{ref}, K)$ being the metamodel and $g^{'}(\dot{m}_{ref})$ being the measured $\Pi_{TT}$ -curve. Figure 3 shows the optimization procedure.

$$\min_{K=0.9\ldots1.1}(|\Delta\dot{m}_{ref}|) \tag{2}$$

$$\Delta\dot{m}_{ref} = [f^{'}(\dot{m}_{ref}, K) = 0] - [g^{'}(\dot{m}_{ref}) = 0] \tag{3}$$

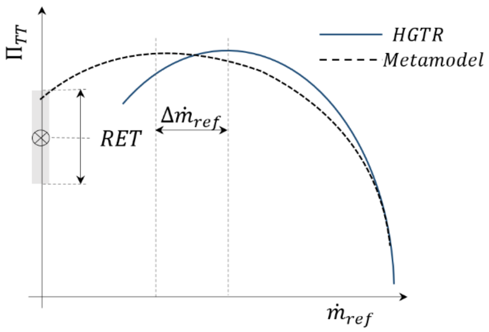

**Fig. 3** Metamodel optimization procedure

The procedure is implemented in Ansys OptiSlang and a variant of the Nelder-Mead SIMPLEX algorithm [14] is used to find the optimal solution. The programme flow chart is shown in the annex. The optimisation took 109 iterations to converge, with $\dot{m}_{ref}$ reduced to 35% of its original value. $K$ is 1.089, which is within the range of the work of Dehner et al. [13]. This indicates that the optimisation is not a tuning overfit, but rather based on physical effects that cannot be modelled with the RET. The optimised metamodel is depicted in green in Fig. 4. The graph illustrates how the applied boundary condition effectively suppresses the numerical overshoot in the unstable region. Instead of maintaining the negative slope, the metamodel develops a positive slope and drops almost linearly in the direction of the introduced boundary condition at a mass flow of zero.

The optimisation of $K$ also demonstrates the predicted enhancements in the precision of the metamodel within the stable operational range of the compressor. This is most apparent for the second speed line, where the prediction of the metamodel is well within the measurement accuracy of the test rig. Additionally, the general response surface has become more uniform.

At the highest speed line, an overshoot can be identified, which is attributable to the fact that $K$ is dependent on the compressor speed [13]. Nevertheless, the overshoot remains within 1.5% of the measured value, which is within the same range as the deviation of the unconstrained metamodel due to its coarser response surface.

### 2.3 Analytical Extrapolation

Although the metamodel has improved significantly, the response surface does not necessarily represent the true quasi-steady behavior. The few successful measurements of the unstable region indicate a third-order polynomial shape, with a low point at zero mass flow [8]. This observation contradicts the stabilized metamodel, which has an almost constant gradient. In certain applications, linear extrapolation is employed as it has minimal impact on the modelling of surge [15], but here the pressure ratio is later used to calculate the efficiency. Thus, the third-order polynomial equation (4) of Moore and Greitzer [16] is coupled with the tuned metamodel.

$$\Pi_{TT} = \Pi_{TT,0} + \beta\ [1 + 1.5\,(\frac{\dot{m}_{ref}}{\phi} - 1) - 0.5\,(\frac{\dot{m}_{ref}}{\phi} - 1)^3] \qquad (4)$$

Its determining parameters are calculated on the basis of the constrained metamodel and are individual for each compressor design. The final result can be seen as the dark blue line in Fig. 4.

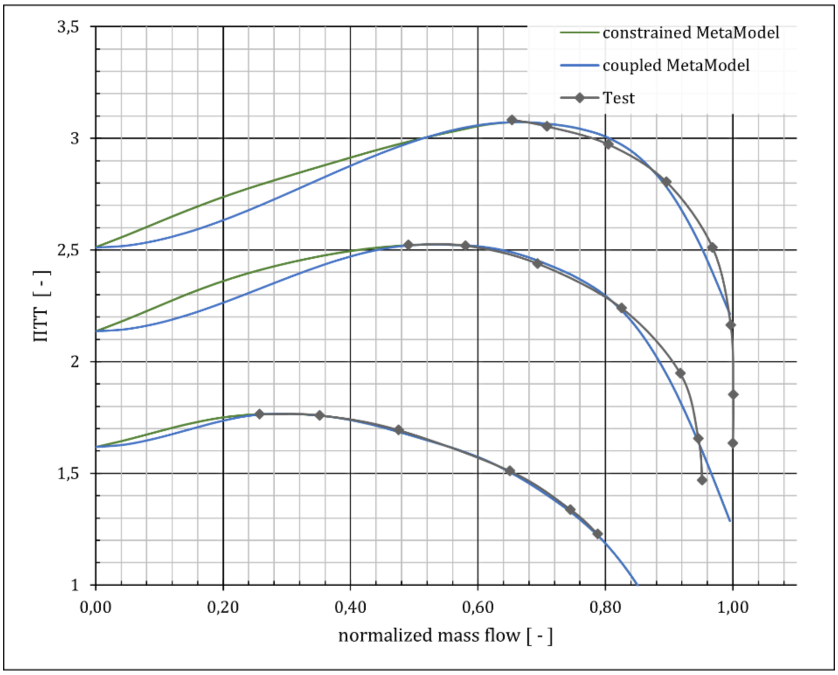

**Fig. 4** Constrained and coupled Metamodels- Compressor A

## 2.4 Efficiency Modeling

A metamodel of efficiency faces two significant challenges: firstly, the problem of identifying an appropriate boundary condition, and secondly, the difficulty of evaluating the overall shape of the response surface in the unstable region. As the value in question is the result of a calculation, it can be obtained from other, more direct parameters, which provide a more reliable and robust solution. Recalling Eqn. 5 for the isentropic efficiency and considering the metamodel for the pressure ratio, the only unknown variable is the total temperature at the compressor outlet, $T_{2T}$. However, this variable cannot be modelled directly, as $T_{2T}$ is not defined at a mass flow of zero. Nevertheless, it can be derived using the definition of shaft work, $W_{Shaft}$, as given in Eqn. 6. The equation for the shaft energy also provides a boundary condition for a mass flow of zero.

$$\eta = \frac{T_{1T}}{T_{2T}-T_{1T}}\,[(\frac{p_{2T}}{p_{1T}})^{\frac{\gamma-1}{\gamma}} - 1] \qquad (5)$$

$$W_{Shaft} = \dot{m}_{ref} c_p (T_{2T} - T_{1T}) \qquad (6)$$

The combination of Eqn. 5 and 6 leads to Eqn. 7. Since $c_p$ is dependent on $T_{2T}$, the equation is solved iteratively.

$$\eta = \frac{T_{1T}\dot{m}_{ref}c_p}{W_{shaft}}\,[\Pi_{TT}^{\frac{\gamma-1}{\gamma}} - 1] \qquad (7)$$

Several algorithms, including Polynomial Regression, Kriging and Deep Learning, were compared in terms of their CoP value and the general form of their response surface. The response of the metamodel and a comparison between predicted and measured shaft work is shown in Fig. 5.

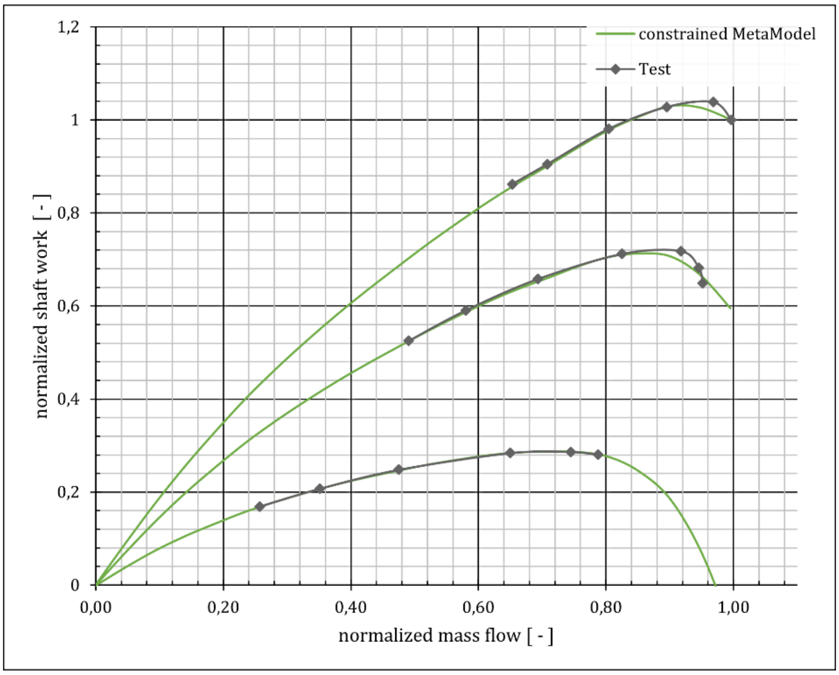

**Fig. 5.** Shaft work metamodel and HGTR measurement – Compressor A

As with the $\Pi_{TT}$- metamodel, the applied boundary condition stabilises the response surface over a wide range of the compressor map. If the deviations due to the steep gradient in the choke area are not taken into account, the metamodel is within the measurement accuracy of the test rig. Since the efficiency calculation is based on two metamodels, the final result is presented and discussed in Chapter 4.

## 3. URANS Simulation

The CFD URANS (unsteady RANS simulation) is set up on the basis of two criteria: computational complexity and accuracy. The aim is to achieve a good level of accuracy without making compromises, while taking into account the computational time required to achieve this accuracy. The Navier-Stokes equation is solved using the transient realisable $k - \epsilon$ RANS model.

The transient character of the model is defined by the temporal discretisation and the motion of the impeller. An implicit unsteady, second order temporal discretization scheme with 40 inner iterations is used. The time step for the simulation is a 10-degree rotation of the compressor, and the movement of the rotor is modelled with Rigid Body Motion (RBM) using a fixed mesh. This is due to the fact that the aim of the simulation is to capture global performance parameters in a compressor setup that is still stable due to its lack of up- and downstream volume.

The mesh discretizes the full-annulus model to approximately 8 million cells, with the critical regions around the impeller blades refined. Polyhedral volume mesh is used with a prism layer mesh for the boundaries. The wall y+ across the domain ranges between 30 to 80.

A mesh independence study is conducted to gain confidence in the sensitivity of the mesh to the performance parameters. The mesh sizes were varied by +34%, +16%, baseline, -10%, -16%. Figure 6 demonstrates that the performance parameters remain unchanged with different mesh sizes. These findings are in line with a previous investigation that uses the same spatial discretization method and extends the mesh size to more than 25 million cells [3].

The domain is divided into three main areas: axial (from inlet to rotor), rotor (impeller with casing), and radial (diffuser to outlet). The inlet is modelled as a pressure outlet and the outlet as a mass flow inlet, where the mass flow is defined as a boundary condition. For further details on the general setup, please refer to [3].

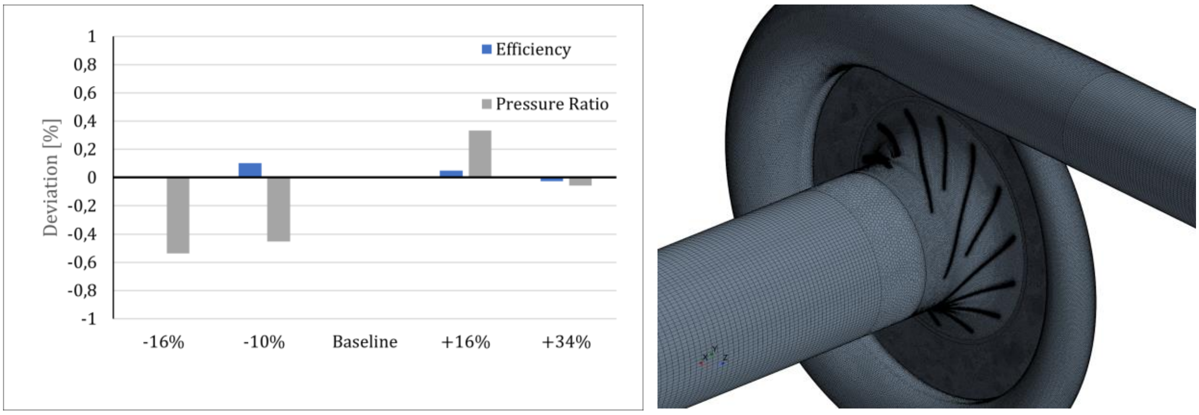

(a) Mesh independence study

(b) CFD mesh

**Fig. 6**. Computational domain and mesh independence study

To quantify the discrepancy between URANS and the measurement, a URANS simulation is conducted for compressor A at the last stable test bench point of the second speed line at a normalised mass flow of 0.255 and 76% compressor speed. The results indicate that the deviation in $\Pi_{TT}$ is -0.7% and in efficiency -3.1% (normalised), suggesting that URANS underestimates the performance of the compressor. These deviations can be most probably explained by the adiabatic modelling and the larger time step.

Four URANS simulations were conducted to assess the efficiency of the method, which is presented in the following two chapters. For compressor A, URANS No. 1 and No. 2 were performed for normalised mass flow rates of 0.38 and 0.47, respectively, with compressor speeds of 76% and 85%. For compressor B, URANS No. 3 and No. 4 were employed, with normalised mass flow rate of 0.22 and compressor speeds of 76% and 85%.

## 4. Validation of the Methodology

The methodology is validated by running the metamodel in regression mode, using Compressor A. This enables the prediction errors of the metamodel to be minimized and the coupling of the methods, their accuracy and form to be evaluated. Figures 7 and 8 show the metamodels and the URANS simulations in a pressure and efficiency map.

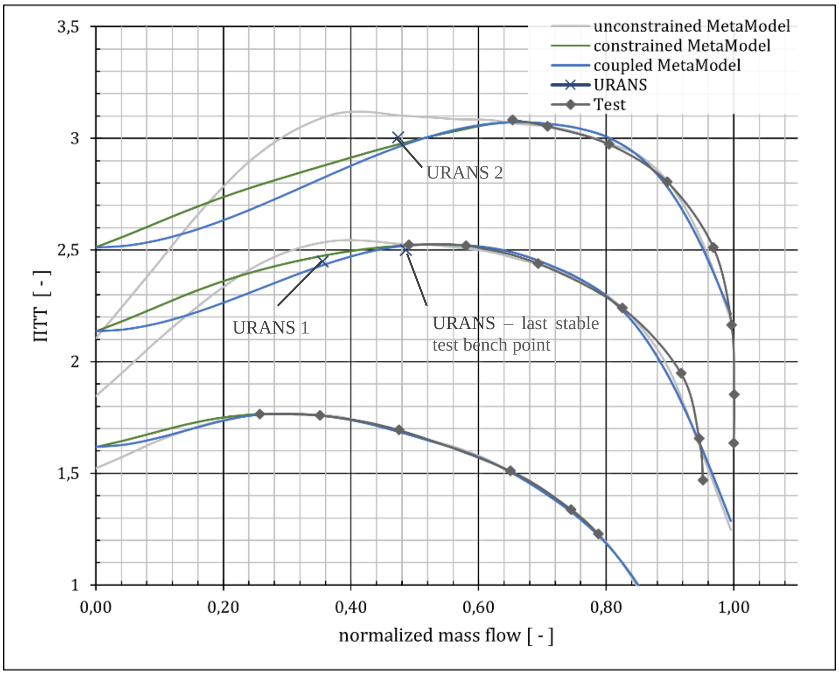

**Fig. 7.** Metamodel regression and HGTR result- pressure ratio, Compressor A

The derived $\Pi_{TT}$ -model follows the measurements within measurement accuracy for the second speed line. The transition point at which the metamodel transitions to the analytical equation is smooth and imperceptible. Furthermore, the calculated curve is within the measurement accuracy of the test rig results, thereby corroborating the validity of the coupling.

The URANS simulations, in which all downstream pipes were removed to obtain a "stable" solution in the otherwise unstable regime, demonstrate only minor differences in comparison to the new methodology. URANS No. 1 is almost on point with less than 1% deviation in the pressure ratio, while URANS No. 2 shows a deviation of 2%. This deviation is related to the fact that the metamodel for the high velocity is at the edge of its design space. This becomes clear from the difference between regression and measurement, leading to the conclusion that the methodology is valid for $\Pi_{TT}$.

The calculated efficiency exhibits a maximum deviation of 1.8% (normalized), which is observed at the optimal operating point. The error is reduced to the measurement accuracy at the last stable test bench point. Once more, the maximum deviation is observed at the highest compressor speed, which is related to the limitation of the $\Pi_{TT}$- metamodel design space. It is most accurate at the lowest speed.

The URANS simulations demonstrate a high degree of agreement with the extrapolation technique. The normalized deviation is 3% for the second speed line and 1% for the highest speed, which are within the deviation between URANS and the test rig at the last stable point.

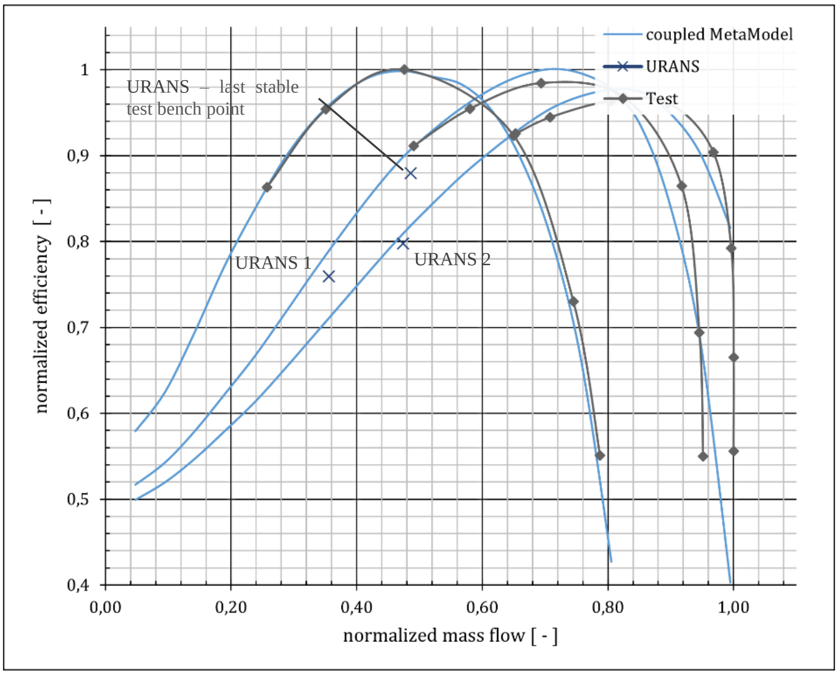

**Fig. 8.** Metamodel regression and HGTR result – efficiency, Compressor A

## 5. Suitability for Prediction

Following the confirmation of the model's regression capabilities, the prediction was tested with compressor B, which was excluded from the training data. This compressor design exhibits an improved surge margin and a distinctive bend in the surge line at higher speeds, which is generally considered to be a surge trigger switching point [17]. The results are presented in Fig. 9.

The constrained $\Pi_{TT}$-metamodel demonstrates a high degree of agreement with the measurements. The pressure ratio is slightly overestimated, but the constrained model follows the measurements with an almost constant offset in the area of interest. However, the constrained model does not agree well with the results of the URANS simulations, which is most obvious for the last speed line.

The coupled metamodel agrees well with the URANS results but shows an unfavorable slope in the surge critical region when compared to test bench data. This is most obvious for the second speed line, where the measured and predicted curve intersect. It is therefore concluded that the coupled metamodel should not be used in an attempt to improve the accuracy of the model in the most critical area for test bench and engine surge.

A speed line obtained by RANS CFD is also included in the figure. In the numerically stable region, the RANS speed line is comparable, or more accurate, than the model; the accuracy improves as the operating points shift closer to the compressors design point. Nevertheless, the RANS becomes numerically unstable for mass flows below 0.4, rendering it incapable of providing any useful information in the vicinity of surge.

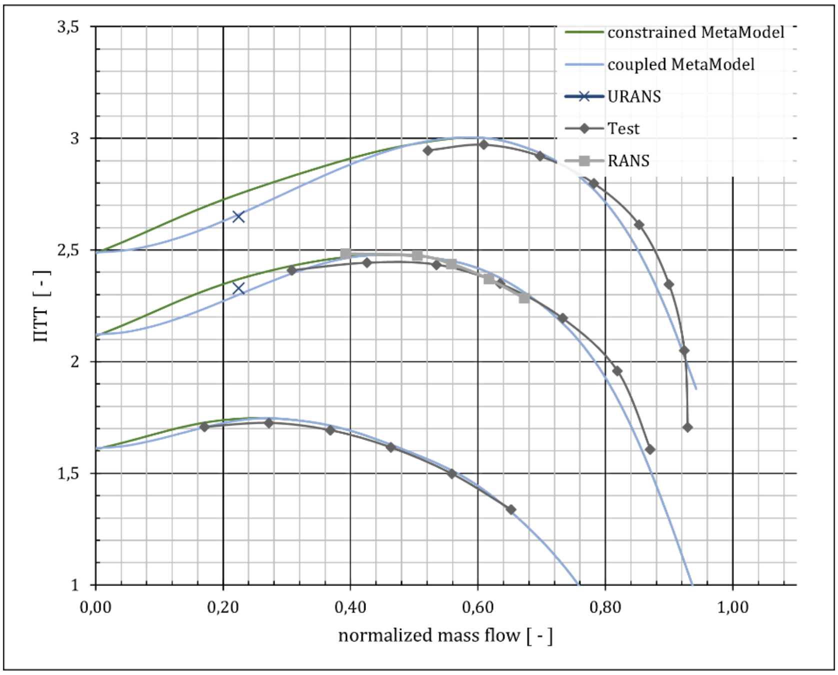

**Fig. 9.** Metamodel prediction and HGTR result- pressure ratio, Compressor B

The efficiency prediction based on the constrained metamodels is in good agreement with test data for the last two speed lines, but there is a discrepancy for the first one.

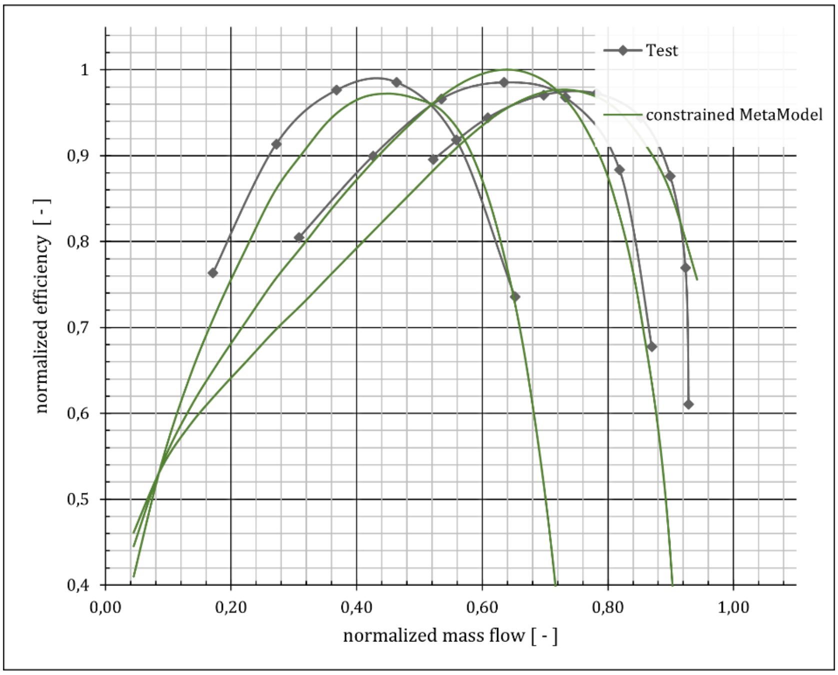

**Fig. 10**. Metamodel prediction and HGTR result- efficiency, Compressor B

An error analysis indicates that this is due to uncertainty in the shaft work metamodel, which overestimates the shaft work by 8% for the first speed line. Consequently, $T_{2T}$ is overestimated, resulting in a maximum decrease in normalized efficiency of 6%. The overestimation is a consequence of the diabatic nature of the test bench, which is most pronounced at low compressor speeds. This phenomenon has been demonstrated, among other studies, by Haug [18]. This, in turn, affects measurement accuracy and introduces noise into the training data, reducing the metamodels' accuracy. Nevertheless, it is notable that the shape of the response surface closely aligns with the measurements for all speed lines, particularly in the surge region.

## 6. Conclusions

This paper presents a method for extending the design space and hence the reliability of metamodels for compressor map prediction. The method is based on the RET and uses $K$ as an optimization parameter to stabilize the $\Pi_{TT}$-metamodel. It is further investigated whether an analytical function improves prediction accuracy. Compressor efficiency is calculated via shaft work, which provides a natural boundary condition for zero mass flow.

The findings indicate that the model is of order $O^4$ faster than a comparable URANS simulation and can predict compressor maps in less than a minute. Its accuracy is comparable to URANS simulations in the vicinity of surge, and, if the coupled model is considered, it is also comparable to URANS simulations in the deep unstable area. The analysis also showed that the RANS simulations were not able to capture the compressor characteristics in the vicinity of surge, thus significantly reducing their suitability as a source for engine surge simulations.

A comparison with test data showed that the method can accurately predict the pressure ratio. The efficiency prediction agrees well with the measurements. The slightly larger deviations compared to the pressure ratio prediction are due to an error summation of the two underlaying metamodels.

The coupled model was found to be accurate for standard high-efficiency compressors and showed little deviation to URANS simulations in the unstable area. However, it was observed that the use of surge-optimized geometries resulted in an unfavorable deviation. Consequently, it is recommended that the constrained metamodel be used, although this may introduce significant errors in the deep unstable area of the compressor.

Further work will be conducted on the implementation of the methodology into a one-dimensional engine simulation code and the validation of the model with transient engine test bench data.

## Acknowledgements

The Authors would like to thank Dr. Bernd Buettner from Ansys Germany GmbH for his support in OptiSlang.

## References

[1] Day, I. J. (October 13, 2015). "Stall, Surge, and 75 Years of Research." ASME. J. Turbomach. January 2016; 138(1): 011001. https://doi.org/10.1115/1.4031473

[2] Jürgen Lehmann, Peter Kozuch, and Kleffel, Jens, Lorenz, L.M. OM471 – Der maßgeschneiderte heavy-duty-Nutzfahrzeugmotor für den weltweiten Einsatz bei Daimler Trucks. Wiener Motorensymposium, 2022.

[3] Matthias Abel. Optimisation of a Turbocharger Compressor for Heavy-Duty Engines based on Aerodynamic Loss Analysis. Phd Thesis, Imperial College London, 2020.

[4] Michael Wöhr, Peter Wahl, Markus Schneid, Andreas Dillmann, and Markus Müller. Compressor Development at Daimler Trucks. In 23. Aufladetechnische Konferenz 2018, pages 143-165

[5] SAE International Technical Standard, Turbocharger Gas Stand Test Code, SAE Standard J1826_202204, Revised April 2022, Issued April 1989, https://doi.org/10.4271/J1826_202204.

[6] T. Most and J. Will. Metamodel of Optimal Prognosis - an automatic approach for variable reduction and optimal metamodel selection. In Proc. Weimarer Optimierungsund Stochastiktage 5.0, Weimar, Germany, November 20-21, 2008.

[7] T. Most and J. Will. Sensitivity analysis using the Metamodel of Optimal Prognosis. In Proc. Weimarer Optimierungsund Stochastiktage 8.0, Weimar, Germany, November 24-25, 2011.

[8] Galindo J., J. R. Serrano, H. Climent, and A. Tiseira. Experiments and modelling of surge in small centrifugal compressor for automotive engines. Experimental Thermal and Fluid Science, 32(3):818–826, 2008.

[9] Powers, KH, Kennedy, IJ, Brace, CJ, Milewski, PA, & Copeland, CD. Development and Validation of a Model for Centrifugal Compressors in Reversed Flow Regimes. Proceedings of the ASME Turbo Expo 2020: Turbomachinery Technical Conference and Exposition. Volume 8: Industrial and Cogeneration; Manufacturing Materials and Metallurgy; Marine; Microturbines, Turbochargers, and Small Turbomachines. Virtual, Online. September 21–25, 2020. V008T20A026. ASME. https://doi.org/10.1115/GT2020-16005

[10] Karim Gharaibeh. Experiments and modelling of surge in turbocharger compressors. Phd Thesis, Imperial College London, 2020.

[11] David Japikse. Centrifugal compressor design and performance. Concepts ETI Inc,Wilder, Vt, 1996.

[12] Theotokatos, G. and Kyrtatos, N., Diesel engine transient operation with turbocharger compressor surging, SAE Technical Paper 2001-01-1241, 2001, https://doi.org/10.4271/2001-01-1241.

[13] Rick Dehner, Ahmet Selamet, Philip Keller, and Michael Becker. Simulation of mild surge in a turbocharger compression system. SAE Int. J. Engines 3(2):197-212, 2010, https://doi.org/10.4271/2010-01-2142.

[14] J. A. Nelder, R. Mead, A Simplex Method for Function Minimization, The Computer Journal, Volume 7, Issue 4, January 1965, Pages 308–313, https://doi.org/10.1093/comjnl/7.4.308

[15] Gamma Technologies LLC. Gt suite: Flow theory manual. 2021

[16] F. K. Moore and E. M. Greitzer. A theory of post-stall transients in axial compression systems: Part I—development of equations. ASME. J. Eng. Gas Turbines Power. January 1986; 108(1): 68–76. https://doi.org/10.1115/1.3239887

[17] Hayashi, Y., and Cao, T. (November 25, 2022). "An Investigation of Non-Linear Surge Characteristic in a High-Speed Centrifugal Compressor." ASME. J. Turbomach. May 2023; 145(5): 051010. https://doi.org/10.1115/1.4056089

[18] Manuel Haug. Entwicklung eines diabaten Verdichterprüfstandmodells. Masterthesis,Universität Stuttgart, Stuttgart, 2024.

## Annex

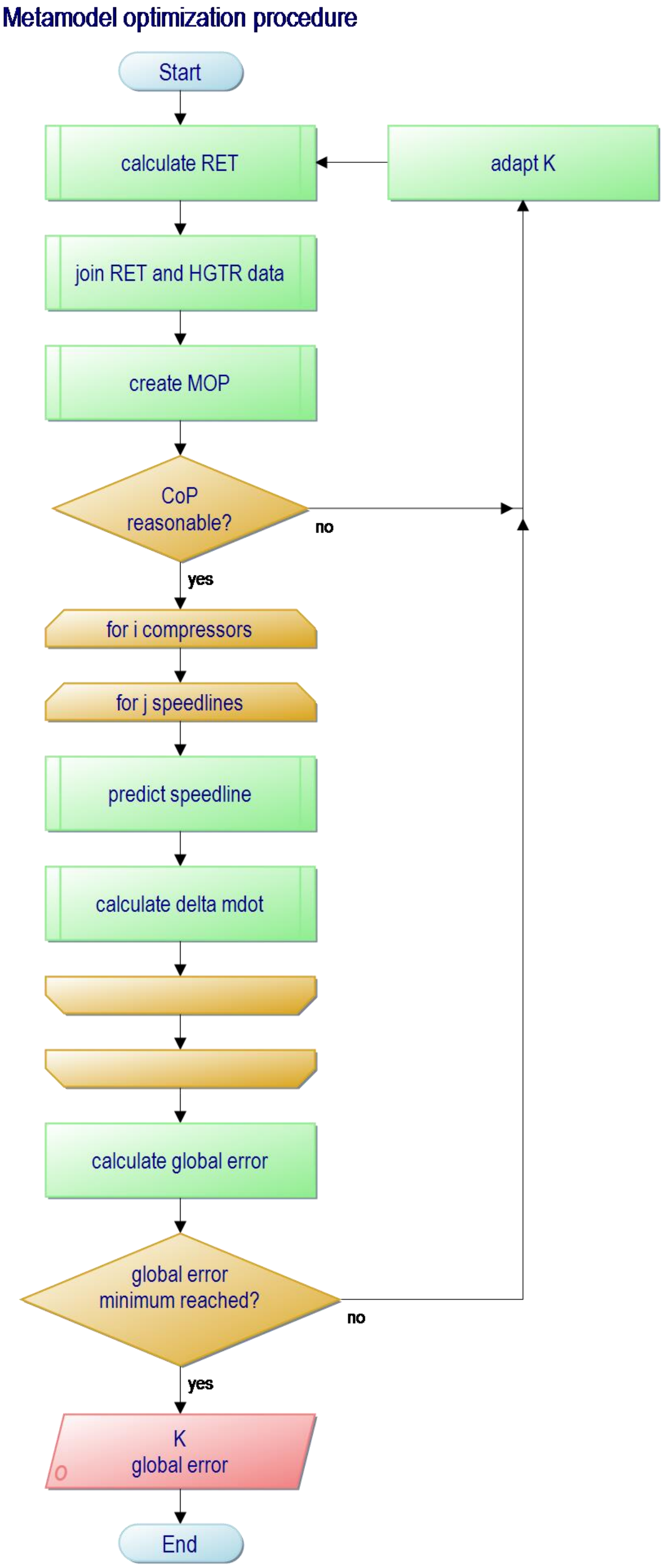
Metamodel optimization procedure
Start
calculate RET
adapt K
join RET and HGTR data
create MOP
CoP
reasonable?
no
yes
for i compressors
for j speedlines
predict speedline
calculate delta mdot
calculate global error
global error
minimum reached?
no
yes
K
global error
End

***Fig. 4*** *Metamodel optimization flow chart*

# Session 3.2 COMBUSTION EMISSIONS

# Soot Formation in OMEn Combustion in an Optically Accessible CI Engine

T. Fuyuto[1], Y. Mandokoro[1], T. Kondo[1], K. Nishikawa[1], R. Ueda[1], Y. Takatori[1], Y. Wakisaka[1], H. Kosaka[1]

[1]Toyota Central R&D Labs. Nagakute. Aichi. 480-1192. Japan.

E-mail: fuyuto@mosk.tytlabs.co.jp
Telephone: +(81) 561 71 7145

**Abstract.** Oxymethylene dimethyl ether ($OME_n$), if produced from a renewable source, can reduce “well-to-wheel” $CO_2$ emissions. In-cylinder optical imaging described in the recent literature showed that no bright luminous flames are observed in neat $OME_n$ combustion. On the other hand, some exhaust emission tests have reported that particulate matter (PM) can be detected after neat $OME_n$ combustion. Whether soot is formed from neat $OME_n$ combustion in diesel engines has been unclear. In this study, we examined the conditions under which soot is formed from neat $OME_{3\text{-}5}$ combustion in a diesel engine. To this end, we used in-cylinder imaging, 3-dimensional CFD simulation, and 0-dimensional detailed chemical reaction calculation. We compared two cases of pilot fuel injection; a base case (‘Base’), with a small amount of pilot fuel, and a second case (‘Soot’), in which the pilot fuel amount was quadrupled to raise the in-cylinder average temperature at the beginning of the main injection up to 1250 K. The CFD code AVL-FIRE with the improved ECFM-3Z+ combustion model was used to calculate the intermediate species ($C_2H_2$, polycyclic aromatic hydrocarbons (PAH), $H_2$, etc.) and correctly determine the trajectory of the fuel in the rich region on the $\phi$-T map. A detailed decomposition reaction model for $OME_3$ based on molecular dynamics and first-principles calculation was combined with detailed soot formation/oxidation models to determine the PAH formation on the grid points of the $\phi$-T map. In-cylinder imaging showed that luminous flames appeared in the Soot case but did not appear in the Base case. In the Soot case, the PAH distributions calculated using 3D-CFD were in good agreement with the measured luminous flame distributions. The calculated equivalence ratio and temperature in each cell were plotted on the $\phi$-T map of acepyrene formation determined by the 0D detailed chemical reaction calculation. In the Soot case, PAH is formed from $OME_{3\text{-}5}$ combustion if the trajectory of the fuel on the $\phi$-T map crosses the acepyrene formation region, while the trajectory of the fuel in the Base case does not cross the acepyrene formation region.

## 1. Introduction

E-fuels, which are manufactured using captured carbon dioxide together with hydrogen obtained from water split by sustainable electricity sources, have received considerable attention in recent years as an option for reducing transport-related $CO_2$ emissions. E-fuels are recognized as being a viable method of renewable energy storage over the medium and long term. $OME_n$ (Oxymethylene dimethyl ether) has been the subject of research as the e-fuel for diesel engines, especially in Europe. $OME_n$ is a hydrocarbon having the chemical structure $CH_3$-O-($CH_2$-O)$_n$-$CH_3$. $OME_{3\text{-}5}$, a mixture of $OME_n$ where n varies from 3 to 5, is liquid under normal atmospheric pressure, having similar evaporation characteristics to conventional diesel fuel. It also has a similar Cetane number to fossil diesel fuel. Several authors have reported that $OME_n$ can overcome the soot-NOx trade-off since $OME_n$ is an oxygenated fuel and it has a lower heating value (LHV) that is lower than that of diesel [1-4]. The authors also evaluated $OME_{3\text{-}5}$ fuel under middle-speed, medium-load conditions using a single-cylinder engine, and reported the simultaneous soot-NOx emission reduction, shown in Figure 1 [5]. Figure 2 compares the mass fraction distributions in a combustion chamber using $OME_{3\text{-}5}$ and diesel fuel with an EGR ratio = 0 on the $\phi$-T map, which explains the simultaneous soot-NOx emission reduction.

The literature reports that no luminous flame emitted by the formed soot was observed with $OME_n$ in either optically accessible engines or constant-volume vessels [6-10]. Pastor et al. observed the in-cylinder combustion of $OME_n$ fuel at 7.5 bar IMEP [6, 7]. They applied two-color pyrometry under the same exposure conditions as diesel fuel combustion, but no KL value was detected from the $OME_n$ combustion. Wiesmann et al. also observed the in-cylinder combustion of $OME_n$ in order to analyze the

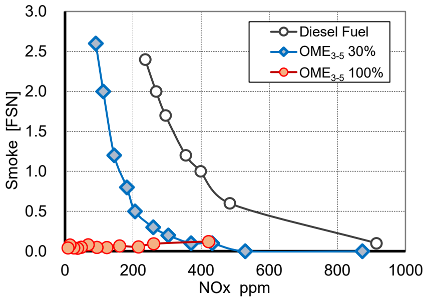

**Fig. 1.** NOx - Soot trade-off at speed = 2400 rpm and IMEP = 1.2 MPa, variation of EGR rate [5]

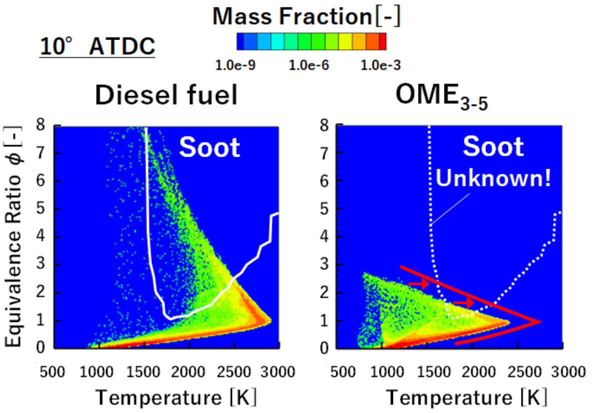

**Fig. 2.** Mass fraction distributions in combustion chamber using $OME_{3-5}$ and diesel fuel with EGR ratio = 0 on ϕ -T map [5]

ignition and combustion characteristics of $OME_n$. They applied multi-spectral high-speed imaging of the chemiluminescence which was captured simultaneously in the UV (OH*) and the blue (CH*) channel. Their analysis, coupled with 3D-CFD simulation, indicated that the soot production potential of OME is very limited [9]. On the other hand, some exhaust emission tests revealed that particulate matter (PM) can be detected after $OME_n$ combustion [1, 11]. Pellegrini et al. reported that PM emission was measured while the amount of PM decreased considerably from that produced by the combustion of diesel fuel [1]. Münz et al. carried out a comparison of particle size distribution for diesel fuel and $OME_n$ at 1500 rpm and 4 bar IMEP [11]. Their results showed that the number of particles of around 10 nm diameter produced from $OME_n$ was greater than that produced from diesel fuel. These measured PM (soot) emissions do not coincide with the in-cylinder observations made by Pastor et al. Whether soot is formed from $OME_n$ combustion in diesel engines has been unclear.

In the present study, we aimed to examine whether soot is formed from $OME_n$ combustion in diesel engines, and quantitatively detected the conditions under which soot is formed. We used in-cylinder imaging, 3-dimensional CFD simulation, and 0-dimensional detailed chemical reaction calculation. We compared two cases; a base case ('Base'), with a small amount of pilot fuel, and a second case ('Soot'), in which the pilot fuel amount was quadrupled to raise the in-cylinder average temperature at the main injection, which is illustrated by the red arrows and curves in Figure 2 (right). AVL-FIRE was used for the 3D-CFD simulation. The calculated equivalence ratio ϕ and temperature in each cell of the 3D-CFD simulation were displayed on the ϕ-T map. A modified ECFM-3Z+ combustion model was used to calculate the intermediate species (PAH, $H_2$, etc.) and correctly determine the trajectory of the fuel in the rich region on the ϕ-T map. A detailed decomposition reaction model for $OME_3$ based on molecular dynamics and first-principles calculation was combined with detailed soot formation/oxidation models to determine the PAH formation on the grid points of the ϕ-T map.

## 2. Methodology

### 2.1 In-cylinder Imaging

Table 1 lists the properties of the fuels tested in this study [5]. The mass composition of $OME_{3-5}$ is 58% $OME_3$, 29% $OME_4$, and 11% $OME_5$. A Bowditch-type optically accessible engine with an elongated piston [12] was used to visualize the combustion of $OME_{3-5}$. Table 2 lists the specifications of the optical engine which has the same bore and stroke as the metal single-cylinder engine for emission tests used in our previous study [5]. The compression ratio is 15.2, close to that of the metal engine (15.9). The same solenoid injector and nozzle were used. The engine speed was set to 1200 rpm to extend the duration around TDC to enhance the soot formation, while the engine speed in the previous study was 2400 rpm.

Figure 3 shows the optical system for the reflecting shadowgraph which visualizes the motion of the sprays. The bottom surfaces of the cylinder head and valves are chrome plated to reflect a parallel light beam which is transmitted through a flat bottom-view sapphire window (supplied by KYOCERA).

**Table 1.** Properties of the tested fuels [5]

| | Unit | $OME_{3-5}$ | Diesel fuel |
|---|---|---|---|
| Density | kg/m$^3$ | 1057.1 | 829.8 |
| Flash point | ℃ | 65.0 | >50℃ |
| Kin. Viscosity (40℃) | mm$^2$/s | 1.082 | 2.797 |
| Boiling Point | ℃ | 145-242 | 180-360 |
| HFRR (60℃) | µm | 320 | 338 |
| Oxygen content | mol % | 45.0 | - |
| Lower calorific value | MJ/kg | 18.66 | 41.81 |
| Cetane number (FIA) | - | 53.4 | 53.1 |

**Table 2.** Operating point and engine parameters

| | |
|---|---|
| Bore x Stroke | 86 x 96 mm |
| Compression Ratio | 15.2 |
| Nozzle | 0.119 mm x 9 hole |
| Engine Speed | 1200 rpm |
| Injection Pressure | 140 MPa |
| Fuel | $OME_{3-5}$ |
| EGR Rate | 0% |
| $P_{TDC}$ @Motoring | 6 MPa |

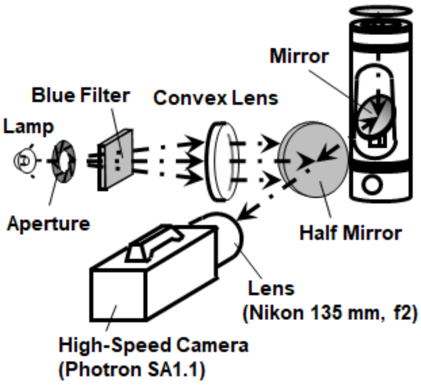

**Fig. 3.** Optical set-up for reflecting shadowgraph and direct photograph

Images were acquired using a high-speed camera (Photron SA1.1) operating at 20,000 fps. A halogen lamp was used as the source of the parallel light beam for the shadowgraph imaging. In addition to the shadowgraph imaging, a direct-photograph method was used to capture the natural chemiluminescence after ignition. Fuel injection was carried out over 20 cycles. A skip-firing operation was used to eliminate the effects of any residual gas: after each cycle in which fuel was injected, the optical engine was run without any fuel being injected for three cycles. The camera was triggered by the driving pulse of the first pilot injection. Images were averaged over 20 cycles at the same crank angle, to eliminate the cycle-to-cycle fluctuation.

### 2.2 3-dimensional CFD Simulation

AVL Fire v2020 was used to calculate the in-cylinder spray development and combustion process. The calculated equivalence ratio $\phi$ and the temperature in each cell of the 3D-CFD simulation are displayed on the $\phi$-T map. Table 3 shows the sub-models of 3D-CFD calculation. A combustion model for $OME_n$ has not been implemented in FIRE code, while detailed chemical reaction models of $OME_n$ consisting of hundreds of reactions have been proposed by some researchers [13-18]. We applied the ECFM-3Z+ combustion model coupled with the phenomenological soot kinetics (PSK) model, shown in Figure 4, to calculate the flame temperature accurately in the high equivalence ratio region on the $\phi$-T map. The carbon atoms of the fuel molecule are transformed into ethylene ($C_2H_4$), then acetylene ($C_2H_2$) is formed from $C_2H_4$. In our previous study using a 3D-CFD simulation of conventional diesel combustion using diesel fuel, we improved the ECFM-3Z+ model by replacing $CO + O_2 \Leftrightarrow CO_2 + O$ to $CO + OH \Leftrightarrow CO_2 + H$ [19]. In this study, the number ratio of C, H, O atoms in $OME_{3-5}$ and the standard enthalpy of formation were input as the model parameters of the ECFM-3Z+ model. The equivalence ratio for each cell was calculated from the number of C, H, O atoms in each cell using equation (1), thus taking the oxygen in the $OME_{3-5}$ fuel into account.

$$\phi = (2A_C + 0.5A_H)/A_O \qquad (1)$$

The phenomenological soot kinetics (PSK) model calculates the formation of polycyclic aromatic hydrocarbon (PAH) from $C_2H_2$, which is also one of the main chemical species of soot surface growth,

**Table 3.** Sub-models of 3D-CFD calculation

| | |
|---|---|
| Spray Break-up | Primary: Core Injection<br>Secondary: Wave |
| Evaporation | Dukowicz |
| Combustion | ECFM-3Z+ (Modified) |
| Soot Formation & Oxidation | Phenomenological Soot Kinetics (Modified) |

PAH Formation $C_2H_2 \leftrightarrow {}^{2}/_{25}\,PAH + H_2$

Soot Nucleation $PAH + PAH \rightarrow Soot$

Growth & Coagulation
$$\left\{\begin{array}{l} Soot + C_2H_2 \rightarrow Soot + H_2 \\ Soot + PAH \rightarrow Soot \\ Soot + Soot \rightarrow Soot \end{array}\right.$$

PAH Oxidation $PAH + {}^{25}/_{2}\,O_2 \rightarrow 25CO$

Soot Oxidation
$$\left\{\begin{array}{l} Soot + O_2 \rightarrow Soot + 2CO \\ Soot + OH \rightarrow Soot + CO + H_2 \end{array}\right.$$

**Fig. 4.** Phenomenological soot kinetics (PSK) model

is formed through the decomposition process of fuel. The PSK model does not calculate soot as particles but simply as a gas-phase species $C_{50}$, while the 0D detailed chemical reaction calculation, described later, calculates soot particle formation and oxidation. The PSK model treats PAH as a virtual gas-phase species $C_{25}$, while the 0D detailed chemical reaction calculation contains many types of PAH from 2-ring PAH up to 6-ring PAH, explained later. In our previous study addressing conventional diesel combustion using diesel fuel, the overestimated soot oxidation by $O_2$ was inhibited [19].

The flame temperature must be calculated correctly for the high equivalence ratio region on the ϕ-T map. Figure 5 illustrates the problems associated with the conventional soot-NOx ϕ-T map proposed by Akihama et al. [20]. The most significant problem is the overestimated flame temperature in the high equivalence ratio region calculated using KIVA code with a single-step combustion model in which the carbon atom in the fuel is directly transformed into $CO_2$. The temperature in a rich mixture is lowered by heat absorption by intermediate species, such as CO, $C_2H_2$, and $H_2$. This overestimated flame temperature makes the soot peninsula too narrow. The red curve in Figure 5a shows the estimated fuel trajectory considering intermediate species which does not pass through the outline of the narrow soot peninsula. The contour lines of the narrow soot peninsula gave rise to the misunderstanding that the amount of soot formed decreases as the $O_2$ concentration falls from 21% while a further decrease in soot oxidation increases the exhaust soot emissions. When the $O_2$ concentration falls from 21%, the trajectory of the fuel on the ϕ-T map shifts toward the lower temperature and the maximum altitude of the soot yield on the trajectory falls, regardless of which intermediate species are considered (Figure 5b). In reality, however, the amount of soot formed in the diesel spray flame increases as the $O_2$ concentration decreases from 21%. Figure 5c shows the soot (KL) distributions in a quasi-steady diesel spray flame as measured by two-color pyrometry [21]. Aronsson et al. showed that the amount of soot formed is

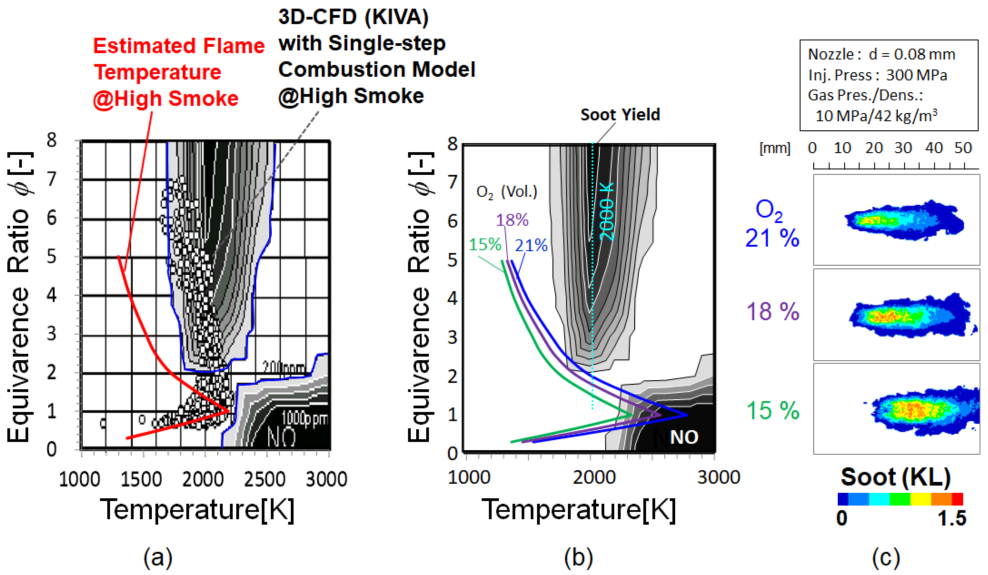

**Fig. 5.** (a) Conventional soot-NOx ϕ-T map devised by Akihama et al.[20]. The overlaid red curve shows the estimated flame temperature in which intermediate species are taken into account. (b) Problem with conventional soot-NOx ϕ-T map. The contours of the soot yield cannot explain the increase in the amount of soot formed by the spray flame as the oxygen concentration decreases (c) [21]

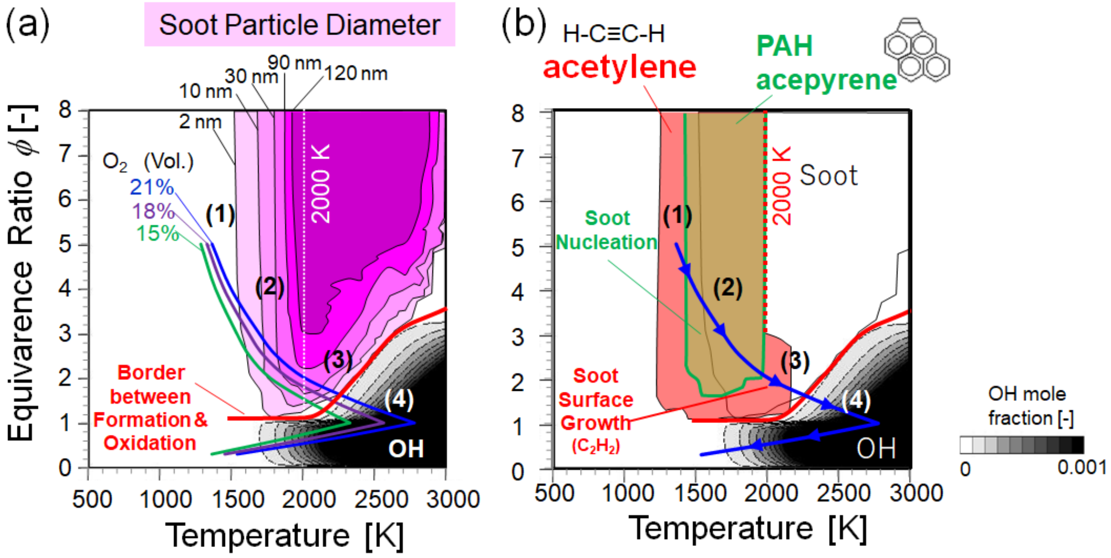

Fig. 6. (a) Improved soot ϕ-T map for soot formation/oxidation analysis [24]. The contours of the soot particle diameter and species mole fraction were determined from the ϕ-T map calculation by Akihama et al.[20], (b) Contours of acetylene ($C_2H_2$) and acepyrene (PAH)

proportional to the residence time of the fuel elements under the soot formation condition, and concluded that the residence time is more important than the soot formation rate and the soot yield on the ϕ-T map [22].

Therefore, the improved soot ϕ-T map shown in Figure 6 was proposed for the analysis of the soot formation/oxidation process in diesel combustion [23, 24]. To quantify the residence time of the fuel elements under the soot formation condition, the narrow soot peninsula was maximized by replacing the soot yield with the soot particle diameter. Instead of contour lines for the of NO mole fraction, contour lines for the OH mole fraction were implemented to show the border between the soot formation and soot oxidation on the ϕ-T map. The borderline between the soot formation and soot oxidation is clearly visible, consisting of a horizontal line in the lower-temperature region and a rising line in the higher-temperature region. Figure 6b shows the contours for $C_2H_2$ and acepyrene representing PAH. The contour for acepyrene, which indicates the soot nucleation, is to the left of the peak line of the soot peninsula, at 2000 K. The contour for $C_2H_2$ spreads on the upper-left side of the borderline between soot formation and oxidation, which indicates that soot surface growth by $C_2H_2$ continues until the fuel element reaches the borderline. The soot formation/oxidation processes can be divided into four stages along the flame temperature curve; (1) the over-rich stage in which soot cannot form due to the temperature being too low, (2) the soot formation stage in which soot formation overwhelms soot oxidation, (3) the competitive stage between soot formation and soot oxidation, (4) the soot oxidation stage, beyond the borderline, where only soot oxidation occurs. The process crossing the soot peninsula is divided into two stages by the peak line of the soot peninsula, at 2000 K.

Figure 7 shows the improvement in the fuel trajectory on the ϕ-T map resulting from improving the ECFM-3Z+ model. In our previous study [5], the 3D-CFD simulation shown in Figure 2 was carried out using the ECFM-3Z model which calculates the oxidation of the carbon atoms in two steps. The carbon atoms in the fuel are transformed into CO, then the CO is oxidized by OH. The ECFM-3Z model overestimates the temperature in rich mixtures, while it is lower than that calculated by the single-step reaction model. We switched the combustion model from the ECFM-3Z model to the ECFM-3Z+ model coupled with the PSK model. The improved ECFM-3Z+ model with a multi-step reaction can calculate better flame temperature in the rich mixture, as shown in Figure 7.

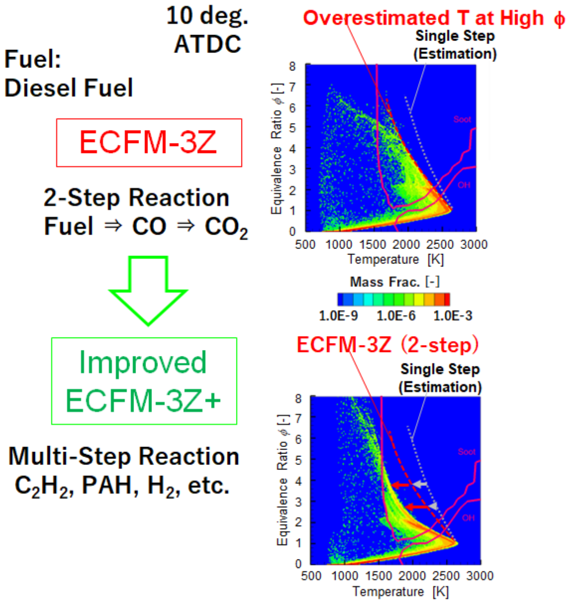

**Fig. 7.** Improvement of fuel trajectory on the $\phi$-T map resulting from improvements in ECFM-3Z+ model [19]

## 2.3 0-dimensional Detailed Chemical Reaction Calculation on $\phi$-T Map

Some detailed chemical reaction models for the oxidation of OME$_n$ fuels have been proposed, OME$_3$ by Sun et al. [13], OME$_3$ by Ren et al. [14], and OME$_{2\text{-}4}$ by Cai et al. [15]. As reviewed by Fenard et al. [25], these detailed OME$_n$ reaction models are based on extrapolations from the already-known DME and DMM reaction models. In our previous study, a detailed chemical reaction model for predicting the soot formation process from OME$_3$ was developed using molecular dynamic (MD) simulation based on the first-principles calculation [26]. The initial decomposition processes of OME$_3$ within 10 ns after the onset of combustion were calculated under various $\phi$-T conditions. An example of the initial conditions, shown in Figure 8, features a mixture of OME$_3$ and air including 240 OME$_3$ molecules and 144 O$_2$ molecules ($\phi = 3$) in a 130-Å cubic cell. The number of OME$_3$ molecules was increased to 240, which was determined to be sufficient. The mixture temperature condition was swept from 1600 to 3500 K. A detailed decomposition reaction model for OME$_3$ was extracted from the MD simulation and it was combined with the conventional soot formation/oxidation models [27] to form a soot formation/oxidation model for OME$_3$ as shown in Figure 9. Then, the calculation of PAH and soot formation from OME$_3$ by using this combined model was carried out on the grid points of the $\phi$-T map.

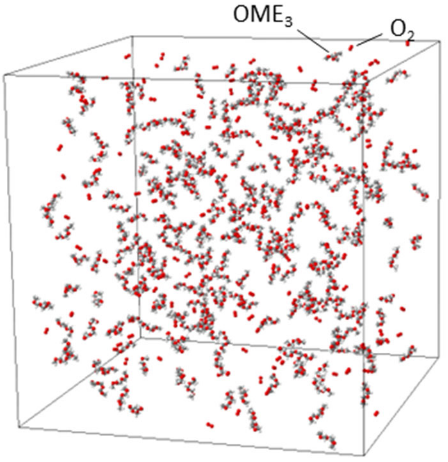

**Fig. 8.** Unit Cell of Molecular Dynamics (MD) Simulation [26]

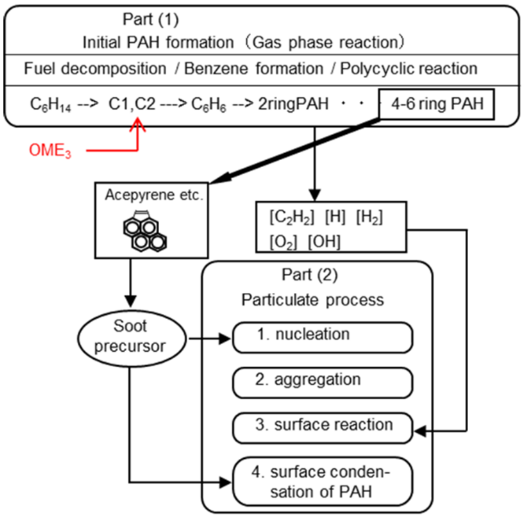
Part (1)
Initial PAH formation (Gas phase reaction)
Fuel decomposition / Benzene formation / Polycyclic reaction
C6H14 --> C1,C2 ---> C6H6 --> 2ringPAH · · 4-6 ring PAH
OME3
Acepyrene etc.
[C2H2] [H] [H2] [O2] [OH]
Part (2)
Particulate process
Soot precursor
1. nucleation
2. aggregation
3. surface reaction
4. surface condensation of PAH

**Fig. 9.** Outline of 0D Detailed Soot Formation Model [26]

## 3. Results

### 3.1 In-cylinder Imaging

The injection patterns in the two cases, namely, the Base and Soot cases, are shown in Figure 10 together with the histories of the in-cylinder pressure, heat release rate, and estimated temperature. The estimated temperature was calculated from the in-cylinder pressure and measured intake gas amount. In the Base case, which almost reproduced the in-cylinder condition at the start of the main injection of the experiment in our previous study [5], a single pilot fuel with 4 $mm^3$/st was injected at -20° ATDC. In the Soot case, the fuel amount of the 1st pilot injection was doubled to 8 $mm^3$/st and a 2nd pilot injection with the same amount of fuel was added. The total amount of pilot injections was quadrupled to raise the in-cylinder temperature at the start of the main injection, which enhances the soot formation. The main injection timing at -5° ATDC was optimized in our previous study. The fuel volume of the main injection (25 $mm^3$/st) was smaller than that used in our previous study. This was done for safety reasons, lessening the maximum in-cylinder pressure in the Soot case. The in-cylinder temperature at the start of the main injection in the Soot case was raised to 1250 K, while that in the Base case was 980 K.

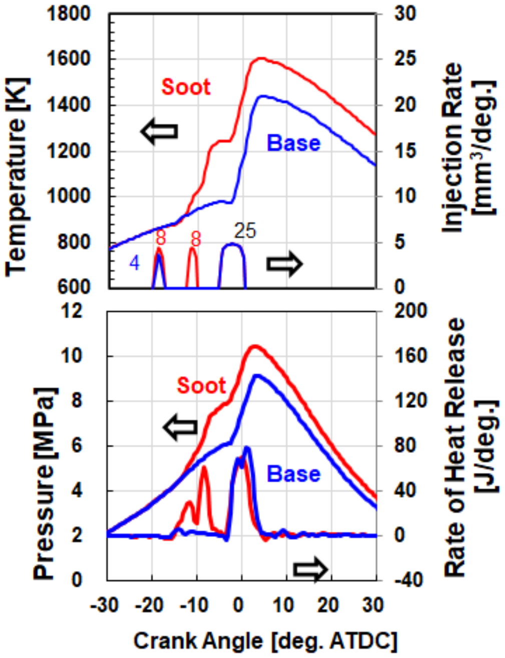

**Fig. 10.** Injection pattern, in-cylinder temperature, pressure, and rate of heat release in both cases (Experiment)

The results of shadowgraph imaging and natural luminescence imaging for the Base case are shown in Figure 11, which are averaged images for 20 cycles at the same crank angle. The crank angle is displayed above each image. Shadowgraph images show the spray motion of the 1st pilot and the main injection. After the ignition timing, the displayed images were switched from shadowgraph image to natural luminescence images. During the main combustion from -3.2 to 0.4°ATDC, there was no luminous flame emitted from the soot particles, and only a blue flame appeared.

Figure 12 shows shadowgraph images and natural luminescence images for the Soot case in which the pilot injections with the quadrupled fuel amount raised the in-cylinder temperature. Luminous flames emitted from the soot particles appeared during the main combustion after -3.9°ATDC. In addition, the red luminescence component emitted from the soot particles can be seen in the combustion flame of the 2nd pilot after -9.7°ATDC.

The amount of soot formed in the Soot case is only very slightly less than that formed from conventional diesel fuel. If the combustion of diesel fuel is observed in the same experimental and exposure conditions as those used in this study, a strong luminous flame appears immediately after ignition,

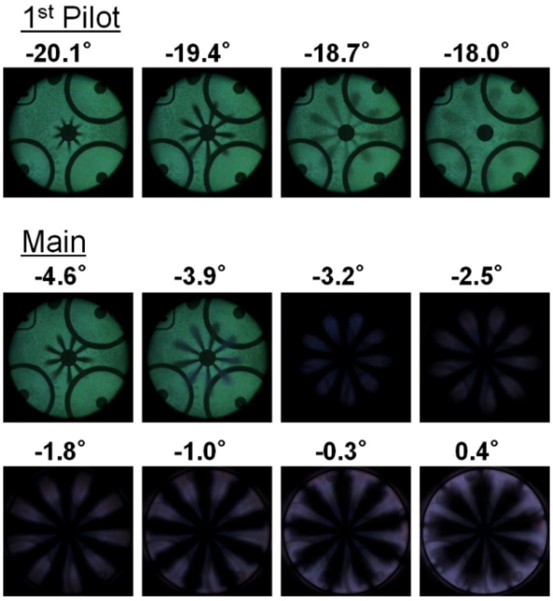

**Fig. 11.** Results of shadowgraph imaging and natural luminescence imaging (Base condition). 20-cycle average

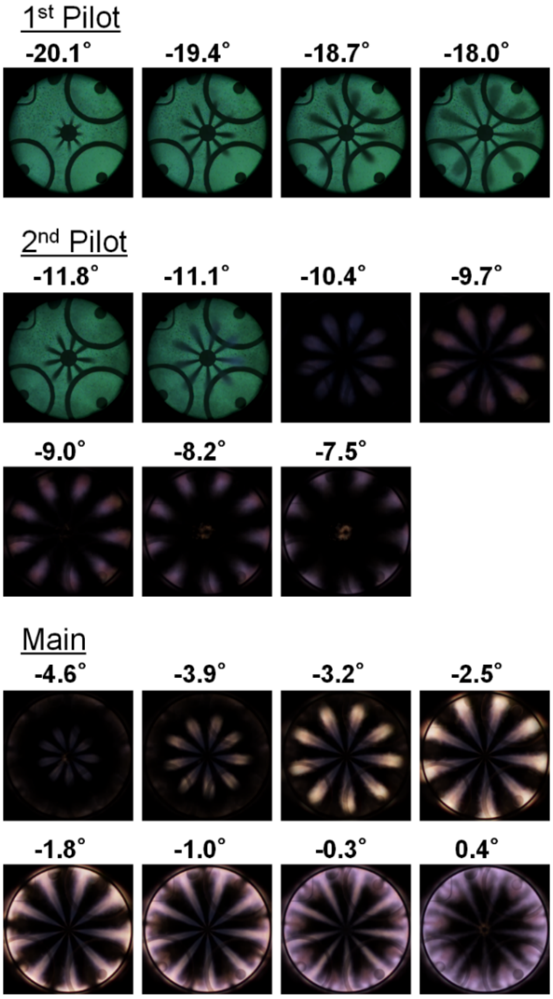

**Fig. 12.** Results of shadowgraph imaging and natural luminescence imaging (Soot formation condition). 20-cycle average

which induces halation throughout the observation field. The soot formed in the Soot case was oxidized quickly since the luminous flame disappeared rapidly as shown in Figure 12.

The difference between the Base and Soot conditions, shown in Figures 11 and 12, indicates that a borderline exists between these conditions which determines whether soot is formed. Next, this borderline will be analyzed quantitatively by 3-dimensional CFD simulation and 0-dimensional detailed chemical reaction calculation on the $\phi$-T map.

### 3.2 3D-CFD Simulation

The sub-model parameters for the spray break-up and combustion used with the AVL-FIRE code were adjusted to reproduce the measured rate of heat release (ROHR) in the Soot case, as shown in Figure 13. The simulated heat release rate was calculated from the in-cylinder pressure in the same way as in the experiment. The same model parameters were used for the Base case, such that the ignition timing could be reproduced. For the Base case, the peak value of the simulated ROHR was higher than that of the measured ROHR. This difference suggests that the simulated temperature distribution in the main spray flame is somewhat higher than in the actual main spray flame. Therefore, the trajectory of the fuel on the $\phi$-T map for the Base case would be shifted to the right, relative to the actual trajectory. The accuracy of the 3D-CFD simulation was validated by comparing with the results of the in-cylinder imaging. Figure 14 compares the spray flame motion by the simulation with the in-cylinder imaging in the Soot case, which shows good agreement as to the spray tip penetration and the shape of the spray flame. The 3D-CFD simulation was carried out for one sector of nine sprays. The horizontal cross-section of the one sector was duplicated in the circumferential direction, as shown in Figure 14. These results, shown in Figures 13 and 14, suggest that the calculated equivalence ratio $\phi$ and temperature in each cell of the 3D-CFD simulation have enough accuracy to be displayed on the $\phi$-T map to quantitatively analyze the soot formation condition from $OME_n$.

When the calculated equivalence ratio $\phi$ and temperature T in each cell of the 3D-CFD simulation are displayed on the $\phi$-T map, one more scalar can be displayed on the z-axis (contour line). The PSK model calculates the formation of PAH ($C_{25}$, a virtual species) from acetylene, as shown in Figure 4. The authors chose PAH to be displayed with the equivalence ratio $\phi$ (y-axis) and temperature T (x-axis). Soot ($C_{50}$) was not chosen because the quantitative accuracy of soot calculated with the PSK model has not yet been validated. The calculated in-cylinder PAH distributions were compared with the natural luminescence distributions, as shown in Figure 15. In the Soot case, the PAH distributions show good agreement with the acquired luminous flame distributions, while there were almost no PAH distributions in the Base case.

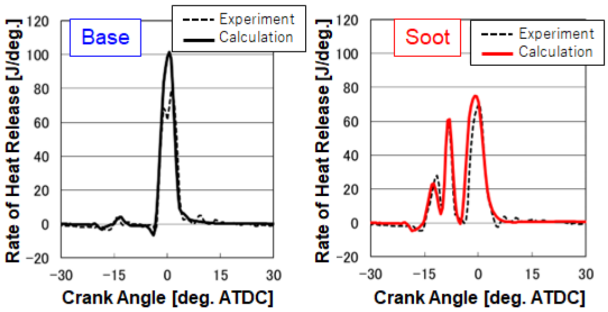

**Fig. 13.** Measured and simulated rate of heat release under both conditions

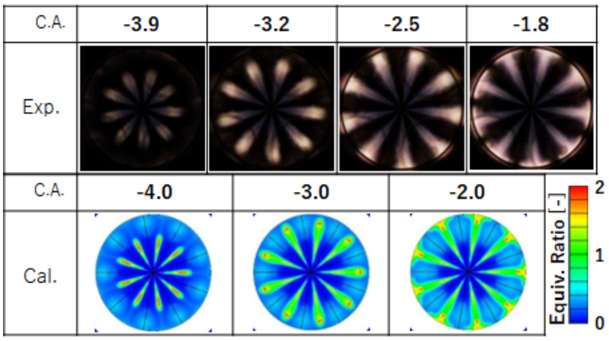

**Fig. 14.** Measured and simulated spray flame under soot formation condition

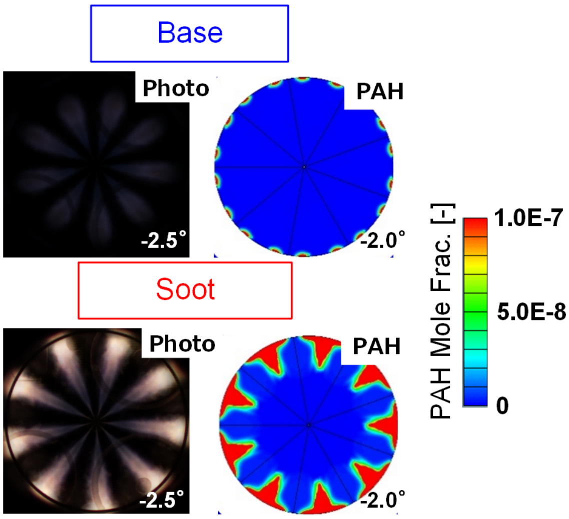

**Fig. 15.** Measured natural luminescence and calculated PAH distributions

### 3.3 Soot $\phi$-T Map Calculation

The $\phi$-T map of soot yields for $OME_3$, shown in Figure 16 (right), was calculated using the detailed chemical reaction model which was derived from the molecular dynamic simulation. It shows the results 1.0 ms after the start of the calculation under a pressure of 6 MPa. In comparison to the soot yield $\phi$-T map for n-hexane shown in Figure 16 (left), the peak height of the soot yield peninsula of $OME_3$ is lowered to one-third that of n-hexane, and the outline of the high soot yield region on the $\phi$-T plane became smaller. This suppression of the soot formation is caused by a lack of C-C bonds in the $OME_3$ molecule. Reaction path analysis revealed the formation of unsaturated $C_2$ species such as $C_2H_2$ which forms PAH, unlike with n-hexane [26].

In the cylinders of diesel engines, however, the trajectory of $OME_n$ fuel, shown by the red curve in Figure 16 (right), does not cross the high-soot region. This high soot yield region might induce misunderstanding which is explained in Figure 5. Therefore, we quantitatively analyzed the conditions under which soot is formed from $OME_n$ on the $\phi$-T map of other physical values except for soot yield.

Figure 17 shows two $\phi$-T maps for $OME_3$ calculated by the detailed chemical reaction model. Figure 17 (left) is the $\phi$-T map of acepyrene which is the representative 4-ring PAH. Figure 17 (right) shows the accumulated soot nucleation number from the start of the calculation to 1.0 ms, which shows a similar distribution to the acepyrene $\phi$-T map. The authors chose the formation region of acepyrene on the $\phi$-T map to quantitatively detect the soot nucleation condition from $OME_n$.

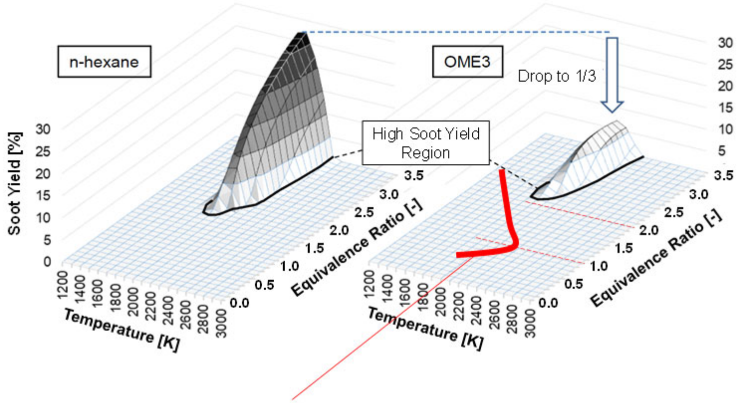

Trajectory of fuel does NOT cross the high soot yield region!

**Fig. 16.** Soot yield $\phi$-T map for n-hexane and $OME_3$ [26]

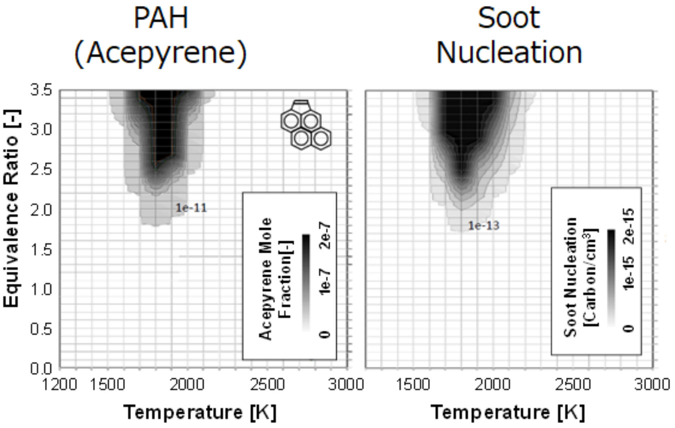

**Fig. 17.** Acepyrene and soot nucleation $\phi$-T maps

### 3.4 Soot Formation Condition for In-cylinder Combustion of $OME_n$

The calculated equivalence ratio $\phi$ and temperature T in each cell of the 3D-CFD simulation at 2.0°ATDC were plotted on the $\phi$-T map of the acepyrene formation region, as shown in Figure 18. The mole fraction 1.0 x $10^{-15}$ was selected for the outline of the acepyrene formation region to clearly show the difference between the Base case and the Soot case. The lower end of the acepyrene formation region reaches to $\phi = 1.5$, lower than $\phi = 2$ which is widely known as the lower end of the soot formation. In addition to $\phi$ and T, the calculated PAH mole fraction at each cell is displayed using color-scale shown at the right side of Figure 18. In the Soot case, where the increased fuel amount of the pilot injections raised the in-cylinder temperature, the trajectory of the fuel in the rich region ($\phi > 1$) goes across the acepyrene formation region. On the trajectory of the fuel in the rich region, PAH is formed in the 3D-CFD simulation. The natural luminescence image shows that soot was formed on the rich regions indicated by the red color in both the PAH distribution in the horizontal cross-section and the $\phi$-T map. On the other hand, in the Base case where no luminous flame from soot was observed, the trajectory of the fuel in the rich region does not go across the acepyrene formation region.

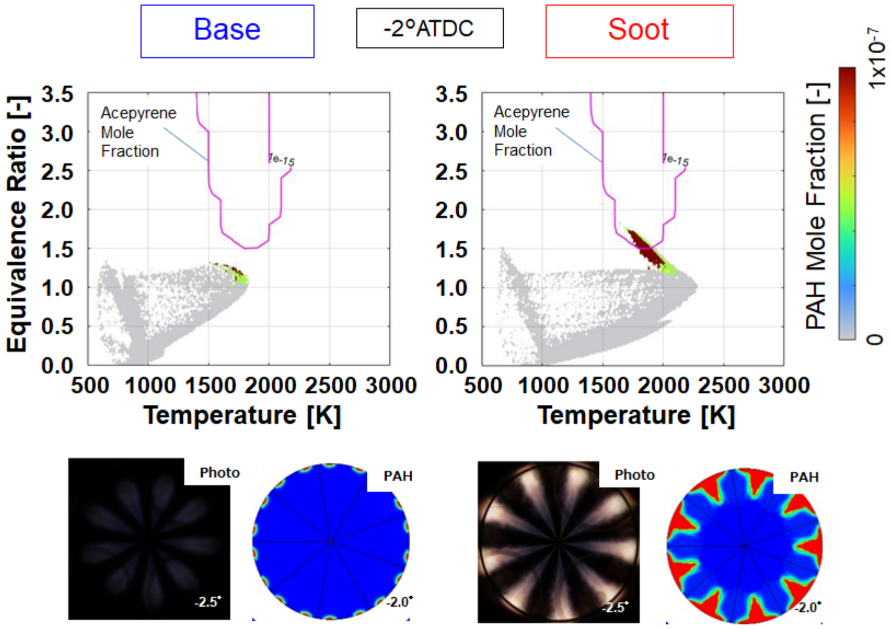

**Fig. 18.** $\phi$-T distributions of the results of 3D-CFD simulation on acepyrene $\phi$-T map calculated by the detailed chemical reaction model

## 4. Discussion

In this study, the results of in-cylinder imaging showed that soot can be formed from the combustion of neat $OME_{3-5}$ fuel under the condition that the in-cylinder temperature at the start of the main injection is raised. The reason why the in-cylinder imaging by Pastor et al. [6, 7] and Wiesmann et al. [9] showed no soot formation would be the shortage of the pilot fuel in comparison to this study. The low compression ratio (11) of the optical engine used by Pastor et al. is another reason for the insufficient temperature. The compression ratio (15) of the optical engine used by Wiesmann et al. [9] is very close to that of our optical engine (15.2). The in-cylinder pressure and temperature are 900 K and 6 MPa, respectively, which are similar to the Base case in this study. However, the maximum in-cylinder pressure was less than 8 MPa, lower than that of the Base case shown in Figure 10. This lower maximum in-cylinder pressure suggests that the in-cylinder temperature was not sufficient for soot formation. The oxygen concentration of 15% in bulk gas, lower than the 21% used in this study, would be one reason why the in-cylinder temperature did not increase sufficiently.

If neat $OME_{3-5}$ is used instead of diesel fuel, the injection duration of the main injection tends to be longer, especially under high-load conditions, since the lower calorific value is less than half that of diesel fuel, as shown in Table 1. Therefore, the soot formation from $OME_n$ fuel continues longer than with diesel fuel [5]. The late combustion after the end of main injection becomes shorter than that of diesel fuel because of the presence of oxygenated fuel [5]. However, soot formed from $OME_n$ at the latest timing would fail to be completely oxidized since the soot oxidation rate is relatively slower than that of a gas-phase oxidation reaction such as $CO + OH \Leftrightarrow CO_2 + H$. Soot particles smaller than 10 nm, which increased in the engine-out emissions in the experiments by Münz et al. [11], would be a new problem for the application of the neat $OME_n$ fuel.

The practical use of $OME_n$ fuel continues to present many problems. The energy efficiency, that is, the ratio of the fuel energy to the consumption energy for fuel production, of $OME_{3\text{-}5}$ is extremely low in comparison to the e-diesel fuel produced by the Fischer-Tropsch process [28]. The swelling of the sealing material is another serious problem which prevents $OME_n$ fuel from being a drop-in fuel for existing vehicles, in addition to the decrease in the energy density with an increase in the $OME_n$ blending ratio. Morita et al. [29] conducted an immersion test on rubber-based material with $OME_n$ blended diesel fuel and reported that the material was able to withstand an $OME_n$ blending ratio in excess of 10%. In their experiments, for a given torque, a 10% OME ratio in diesel fuel resulted in a deterioration in the thermal efficiency while the soot, HC, and CO emissions were reduced.

## 5. Conclusions

In-cylinder optical imaging described in the recent literature has shown that $OME_n$ combustion produced no luminous flames. On the other hand, some exhaust emission tests have reported that particulate matter (PM) can be detected after $OME_n$ combustion. Whether soot is formed as a result of $OME_n$ combustion in diesel engines has been unclear. In the present study, the conditions under which soot is formed as a result of $OME_{3\text{-}5}$ combustion in a diesel engine were evaluated quantitatively by conducting in-cylinder combustion imaging, 3-dimensional CFD simulation, and 0-dimensional detailed chemical reaction calculation on the $\phi$-T map. We compared two cases; a base case ('Base'), with a small amount of pilot fuel, and a second case ('Soot'), in which the pilot fuel amount was quadrupled to raise the in-cylinder average temperature at the main injection. Our major conclusions are as follows;

- In-cylinder imaging showed that luminous flames appeared during the main injection in the "Soot" case in which the in-cylinder average temperature at the main injection exceeds 1250 K. On the other hand, luminous flames did not appear in the Base case, in which the in-cylinder average temperature at the main injection is 980 K.
- In the Soot case, the PAH distributions calculated using 3D-CFD were in good agreement with the measured luminous flame distributions.
- The equivalence ratio and temperature in each cell of 3D-CFD calculation were plotted on the $\phi$-T map of PAH (represented by acepyrene) by the 0D detailed chemical reaction calculation. In the Soot case, PAH can be formed from $OME_{3\text{-}5}$ combustion if the trajectory of the fuel on the $\phi$-T map crosses the acepyrene formation region, while the trajectory of the fuel in the Base case does not cross the acepyrene formation region.

## Acknowledgements

The authors would like to thank Ms. Haruna Nakai of Gifu University for assistance with analysis of 3D-CFD simulation results on the $\phi$-T map during her internship at Toyota Central R&D Labs.

## References

[1] Pellegrini L, Marchionna M, Patrini R, et al. Emission Performance of Neat and Blended Polyoxymethylene Dimethyl Ethers in an Old Light-Duty Diesel Car. SAE Paper No.2013-01-1035, 2013.

[2] Pellegrini L, Patrini R, and Marchionna M. Effect of POMDME Blend on PAH Emissions and Particulate Size Distribution from an In-Use Light-Duty Diesel Engine. SAE Paper No.2014-01-1951, 2014.

[3] Deutz S, Bongartz D, Heuser B, Kätelhön A, et al. Cleaner production of cleaner fuels: wind-to-wheel – environmental assessment of CO2-based oxymethylene ether as a drop-in fuel. Energy & Environmental Science, 2018. 11(2): p. 331-343.

[4] Härtl M, Gaukel K, Pélerin D, and Wachtmeister G. Oxymethylene ether as potentially CO2-neutral fuel for clean diesel engines part 1: engine testing. MTZ worldwide, 2017. 78(2): p. 52-59.

[5] Kosaka H, Fuyuto T, Wakisaka Y, et al. Potential of Oxymethylene Dimethyl Ether for a Diesel Engine Improving Emission and Combustion Characteristics. Transactions of Society of Automotive Engineers of Japan, 2022. 53(6).

[6] Pastor J V, Garcia A, Micó C, et al. An optical investigation of combustion and soot formation in a single cylinder optical Diesel engine for different e-fuels and piston bowl geometries. Proceedings of THIESEL2020, 2020.

[7] Pastor J V, García A, Micó C, and Lewiski F. Simultaneous high-speed spectroscopy and 2-color pyrometry analysis in an optical compression ignition engine fueled with OMEX-diesel blends. Combustion and Flame, 2021. 230.

[8] Sasaki O, Higuma W, Sakaida S, et al. Observation of OME-diesel blends spray injected by a single-hole nozzle injector under engine relevant conditions. Transactions of the JSME, 2021. 87(895): p. 20-00361-20-00361, DOI: 10.1299/transjsme.20-00361.

[9] Wiesmann F, Bauer E, Kaiser S A, and Lauer T. Ignition and Combustion Characteristics of OME3-5 and N-Dodecane: A Comparison Based on CFD Engine Simulations and Optical Experiments. SAE Paper No.2013-01-0305, 2023.

[10] Xuan T, Li H, Wang Y, et al. A conceptual model of polyoxymethylene dimethyl ether 3 (PODE3) spray combustion under compression ignition engine-like conditions. Combustion and Flame, 2024. 261.

[11] Münz M, Mokros A, and Beidl C. OME in the Diesel engine – a concept for CO2 neutrality and lowest pollutant emissions. Internationaler Motorenkongress 2018, 2018. p. 445-458.

[12] Fuyuto T, Matsumoto T, Hattori Y, et al. A new generation of optically accessible single-cylinder engines for high-speed and high-load combustion analysis. SAE International Journal of Fuels and Lubricants, 2012. 5(1): p. 307-315.

[13] Sun W, Wang G Li S, et al. Speciation and the laminar burning velocities of poly (oxymethylene) dimethyl ether 3 (POMDME3) flames: An experimental and modeling study. Proceedings of the Combustion Institute, 2017. 36(1): p. 1269-1278.

[14] Ren S, Wang Z, Li B, et al. Development of a reduced polyoxymethylene dimethyl ethers (PODEn) mechanism for engine applications. Fuel, 2019. 238: p. 208-224.

[15] Cai L, Jacobs S, Langer R, et al. Auto-ignition of oxymethylene ethers (OMEn, n= 2–4) as promising synthetic e-fuels from renewable electricity: shock tube experiments and automatic mechanism generation. Fuel, 2020. 264: p. 116711.

[16] Niu B, Jia M, Chang Y, et al. Construction of reduced oxidation mechanisms of polyoxymethylene dimethyl ethers (PODE1–6) with consistent structure using decoupling methodology and reaction rate rule. Combustion and Flame, 2021. 232.

[17] Ngugi J M, Richter S, Braun-Unkhoff M, et al. A study on fundamental combustion properties of oxymethylene ether-2. Journal of Engineering for Gas Turbines and Power, 2022. 144(1): p. 011014.

[18] De Ras K, Kusenberg M, Vanhove G, et al. A detailed experimental and kinetic modeling study on pyrolysis and oxidation of oxymethylene ether-2 (OME-2). Combustion and Flame, 2022. 238: p. 111914.

[19] Fuyuto T, Ueda R, and Momose K. Improvement of Phenomenological Soot Model and ECFM-3Z+ Combustion Model Implemented to FIRE. AVL Simulation Conference, 2022.

[20] Akihama K, Takatori Y, Inagaki K, et al. Mechanism of the Smokeless Rich Diesel Combustion by Reducing Temperature. SAE Transactions, 2001. 110(3): p. 648-662.

[21] Fuyuto T, Mandokoro Y, Hattori Y, and Mashida M. Suppression of Soot Formation in Quasi-steady Diesel Spray Flame Produced by High-pressure Fuel Injection with Multi-orifice Nozzle. SAE Paper No.2019-01-2270, 2019.

[22] Aronsson U, Chartier C, Andersson Ö, et al. Analysis of EGR effects on the soot distribution in a heavy duty diesel engine using time-resolved laser induced incandescence. SAE International Journal of Engines, 2010. 3(2): p. 137-155.

[23] Fuyuto T. Borderline between Soot Formation and Soot Oxidation on phi-T Map. Proceedings of the 32nd symposium on internal combustion engines, Ota-city, Japan, 2021.

[24] Fuyuto T, Mandokoro Y, Tagita Y, and Umehara T. Axis-symmetric diesel spray flame model coupled with momentum flux distribution measurement and improved soot phi-T map. International Journal of Engine Research, 2023. 24(10): p. 4343-4361.

[25] Fenard Y, and Vanhove G. A Mini-Review on the Advances in the Kinetic Understanding of the Combustion of Linear and Cyclic Oxymethylene Ethers. Energy & Fuels, 2021. 35(18): p. 14325-14342.

[26] Takatori Y, Soot formation analysis of OME (oxymethylene dimethyl ether) using fuel decomposition model by molecular dynamics simulation. Transactions of the JSME, 2024. Advance Publication by J-STAGE No.23-00269, DOI: 10.1299/transjsme.23-00269.

[27] Takatori Y, Numerical analysis of the effects of H2O and CO2 additions on the chemical reaction of soot formation. Transactions of the JSME, 2021. 87(898): p. 21-00027, DOI:10.1299/transjsme.21-00027.

[28] Soler A, Gordillo V L, Schmidt W, et al. E-Fuels: A techno-economic assessment of European domestic production and imports towards 2050. Concawe report 2022. 17/22.

[29] Morita S, Okamoto T, Seto T, et al. Effect of blending OME with diesel fuel on fuel property and engine performance. Transactions of the JSME, 2021. 87(897): p. 20-00374-00320-00374, DOI: 10.1299/transjsme.20-00374.

# Fuel Property Impact on Soot Emissions in SI-Engines: A Comprehensive Analysis of Gasoline Blends in RDE-Testing

L. Heinz[1], U. Wagner[1] and T. Koch[1]

[1]IFKM – Institute of Internal Combustion Engines. KIT – Karlsruhe Institute of Technology. Rintheimer Querallee 2, 76131 Karlsruhe, Germany.

E-mail: lukas.heinz@kit.edu
Telephone: +(49) 721 608 48527

**Abstract**

In this study, the influence of fuel properties on the soot emissions of a spark ignition engine with direct injection was investigated. Eighteen fuel blends, including certification and acrylate fuel, as well as blends with different oxygenate and aromatic content and different boiling curves were compiled for this purpose. RDE tests were carried out on the highly dynamic test bench with cold and warm engine and the PN and PM emissions were measured in the raw exhaust gas using a particle spectrometer. The aim of the study is to analyze the relationship between known comparative indices such as the Yield Sooting Index (YSI), selected fuel properties and soot emissions in high-transient engine operation. For each fuel, 5 cycles were carried out with the engine cold and 5 cycles with the engine at operating temperature and the results were averaged to compensate for the scatter. The soot emission was then analyzed with regard to fuel properties and composition.

The experiments show that both the number of particles and the mass tendentially correlate with the comparative indices. While the addition of oxygenates such as ethanol and methanol to the reference fuel leads to a lower YSI, this can only be transferred to the test bench tests to a limited extent. This suggests that the influence of vaporization properties of a fuel, which are of great importance for mixture formation and therefore soot formation, are not sufficiently considered if only common indices are used for fuel characterization.

**Notation**

| | |
|---|---|
| $d$ | *Nozzle exit diameter.* |
| $D_{10}$ | *Arithmetic mean diameter of droplets.* |
| *DF* | *Density Factor* |
| $D_P$ | *Particle Diameter in nm* |
| *DVPE* | *Dry Vapor Pressure Equivalent* |
| *FBP* | *Final Boiling Point* |
| $m_p$ | *Particle Mass* |
| *PM* | *Particulate Matter* |
| *PM2.5* | *Particulate Matter with diameter* $< 2.5\ \mu m$ |
| *PN* | *Particle Number* |
| *RON* | *Research Octane Number* |
| *YSI* | *Yield Sooting Index.* |

## 1. Introduction

While electric drives are becoming increasingly important for newly registered vehicles in Germany, gasoline engines are still the most common drive type for passenger cars at over 62% [1]. The focus on reducing CO2 emissions while simultaneously increasing performance led to the introduction of turbocharged engines with direct injection. While these engines have advantages over units with intake manifold injection in terms of fuel consumption, the internal mixture formation leads to an increased formation of harmful particles. The mass of particulate matter (PM) emitted has therefore been limited by law since the introduction of the Euro 5 emissions standard for gasoline engines with direct injection [2,3]. Although the amount of particulate matter emitted has been decreasing since the introduction of particle filters, around 21% of PM2.5 near roads can be attributed to engine exhaust fumes [4]. As fine particles are considered to have a higher hazard potential, limit values for the number of particles in spark-ignition engines were introduced for the first time with the introduction of Euro 6 [5]. A further reduction of the particle size to be taken into account to 10 nm is being planned [6]. As particle filtration in the exhaust gas is always accompanied by more or less increased fuel consumption, the optimization of fuels to reduce the formation of particles is increasingly becoming the focus of development. Reduced raw emissions can minimize the increase in exhaust back pressure when the particulate filter is loaded as well as the frequency of regeneration.

### 1.1 Fundamentals of Particles (Characterization & Formation Mechanism)

Particles can be divided into volatile and non-volatile fractions. Sulphates, nitrates and organic compounds form the volatile particles, carbonaceous compounds and ash the non-volatile particles, whereby the carbonaceous fraction is generally referred to as soot. Due to the complex formation mechanisms, the composition depends on numerous influencing factors such as the combustion process, operating point, oil and fuel composition as well as the ambient conditions. [7] As ash is an incombustible component, a reduction can be achieved by avoiding such components in the fuel. The formation of soot, on the other hand, follows a complex formation path, so that these particles cannot be traced back directly to individual components, but instead require consideration of the fuel as a whole.

During the combustion of hydrocarbons, acetylene and other smaller hydrocarbon chains are formed through pyrolysis. Due to their structure, these species can combine to form aromatics. By combining with other aromatics or alkyls, larger, polyaromatic hydrocarbons (PAHs) are formed, which can form larger soot particles through agglomeration [8]. Due to the complexity of the formation mechanism, the formation of particles during the combustion of hydrocarbons cannot be completely avoided, but the formation of soot precursors can be reduced by selecting a suitable fuel.

The following fuel properties can be derived from this to reduce soot formation:

- Optimization of mixture formation through favorable evaporation behavior
- Avoiding the formation of soot precursors at the molecular level:
    - Avoidance of double bonds and ring structures

The influence of fuel on soot formation has been a subject of scientific interest for years. Aikawa et al. translated the observation that early-boiling fuel components as well as those with a low double bond equivalent (DBE) have a low soot tendency into a PM index and were able to show that this correlates with both PN and PM emissions [9]. In contrast, Dageförde et al. compared toluene with RON 95 and showed that the soot emission of the pure aromatic is above or below that of the reference fuel depending on the operating point. This is attributed to differences in mixture formation due to the lower calorific value and the associated longer injection times [10]. Although aromatics generally have the potential to form soot precursors due to their ring structure, the thesis is supported that only late-boiling aromatics favor an increase in PN emission. [10,11].

Leach et al. [12] developed a PN index which, in contrast to the PM index, uses the Dry Vapor Pressure Equivalent (DVPE) of the fuel for the calculation. Thus, a calculation from a standardized fuel analysis is possible. It was shown that the PN index correlates with the PN emission of a test engine with direct injection.

Ratcliff et al. [13] investigated the interaction between aromatics and ethanol in fuel. They were able to show that adding ethanol to the fuel can reduce PM formation by diluting and thus reducing the aromatics content. At the same time, the evaporation enthalpy of the alcohol can slow down the evaporation of low-boiling aromatics and thus increase their concentration in the last incompletely evaporated parts of the fuel jet. An admixture of alcohol can therefore have the opposite effect on soot formation than the oxygen content in the fuel would suggest. Similar effects were also described by Vuk [11] and Burke [14].

# 2. Experimental Setup

## 2.1 Engine and test bench setup

The engine tests were carried out on a turbocharged four-cylinder unit with direct injection. The exhaust gas aftertreatment and the control unit's configuration correspond to the standard Euro 6 specification. Ancillary units were also adopted from the standard version, as was the entire intake and exhaust gas section up to the catalytic converter and particulate filter. In order to ensure realistic heating behavior, additional oil conditioning was dispensed with and the coolant circuit was limited to a volume close to series production. The technical data of the unit is summarized in **Table 1**.

The number and size distribution of particles was recorded between the turbocharger and the gasoline particle filter using a DMS500 particle spectrometer from the manufacturer Cambustion. An external cooling water conditioning unit, cell ventilation and an additional air circulation fan enable the engine and cell to be conditioned to 20 °C between tests.
As there is no direct measurement of the particle mass, this is calculated from the particle number concentration and the mobility diameter. The calculation is carried out analogously to the manufacturer's specifications [15] according to **Equation** 1, assuming a spherical geometry for GDI engines. A power factor (PF) of 3 and a density factor (DF) of $5.2 \times 10^{-16}$ are therefore recommended.

$$m_p(\mu g) = DF \; x \; D_p{}^{PF}$$

**Equation** 1: Calculation of the particle mass

**Table 1**: Technical data of the test engine

| Number of cylinders | 4 | - |
|---|---|---|
| Effective capacity | 1998 | cm³ |
| Bore | 82.0 | mm |
| Stroke | 94.6 | mm |
| Compression ratio | 9.5 : 1 | - |
| Number of valves | 4 | - |

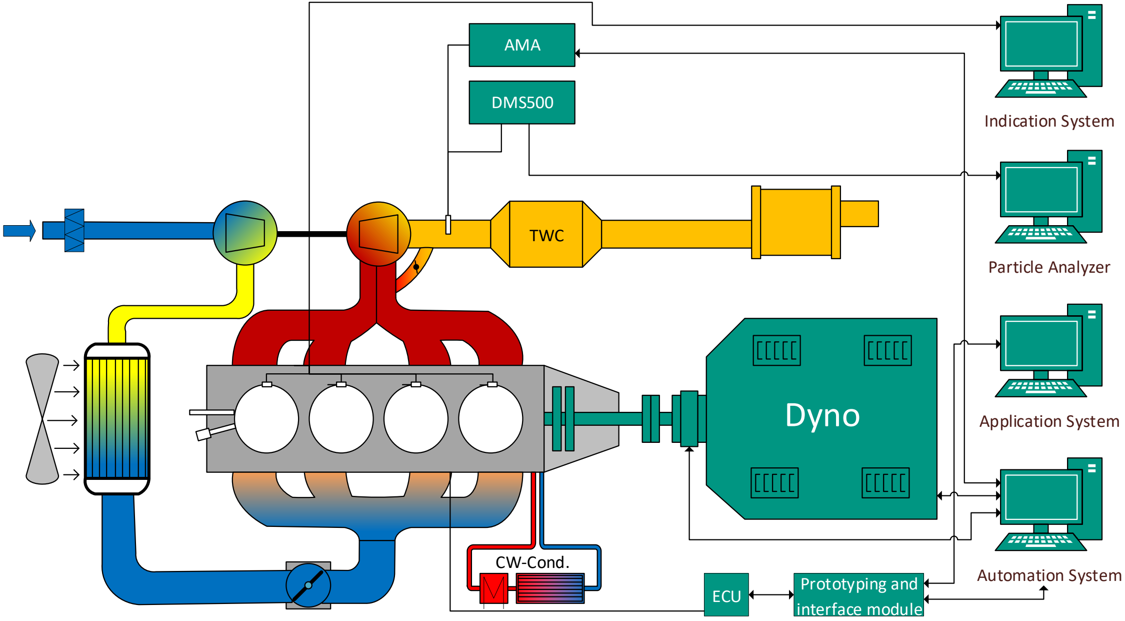

**Figure 1**: Test bench setup

## 2.2 Test Procedure

The test cycle used was derived from real driving data of a compact SUV with the same engine. Three sections of equal length were combined in the order of urban, interurban and highway driving. As the engine is preconditioned to 20 °C before each test, the start with a cold engine, catalytic converter heating phase and warm-up behavior are also taken into account. The test cycle is shown in Figure 2. Each test run was repeated 5 times under constant conditions and the average PN and PM emissions were calculated from the test runs with the same fuel. As there is no gravimetric measurement of the particle mass, this was calculated on the basis of the size distribution.

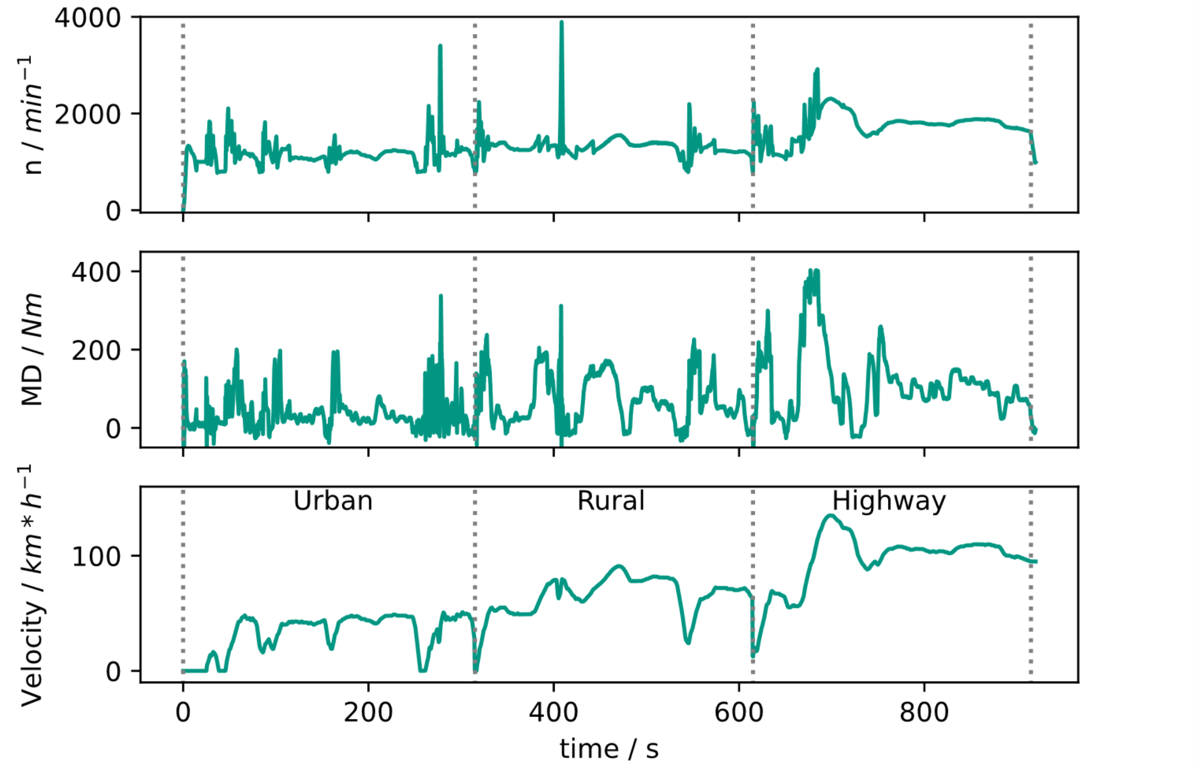

**Figure 2**: Test cycle sequence and segmentation

The measurement of the YSI was carried out by OWI Science for Fuels gGmbH. A steady flame co-flow burner according to Das et al. [16] was used. The unified YSI and the maximum soot volume fraction were determined for all fuels based on color pyrometry using the “peak-region” method described by Das et al. [17], where the mean soot volume fraction is determined by averaging over the sootiest parts of a doped methane flame. The robustness of this method proven by Montgomery et. al for various fuels and air to fuel ratios [18].

## 2.3 Tested Fuels

For the tests, 18 different fuels were selected to investigate the influence of the composition on soot emissions in the burner and engine tests. The aim is to vary the fuel properties relevant to soot formation as widely as possible. On the one hand, this includes a variation of the boiling behavior through different concentrations of low- and low-boiling components as well as a targeted adjustment of the chemical composition. For example, the proportion of aromatics overall, oxygenates and olefins was specifically changed. Since the number of carbon atoms within the aromatics group also has an influence on the soot tendency, the composition of the aromatics was also varied. A paraffinic base fuel (base low) with a low aromatics and olefin content was selected as the lower reference. The upper reference is a second base fuel (base high), which in contrast has a high content of aromatics greater than C7, olefins and a late end of boiling point. Based on these reference fuels, blends were produced with the alcohols methanol and ethanol as well as the aromatic toluene. In order to investigate the influence of boiling behavior and composition of the aromatic fraction, 5 additional fuels with variable boiling end and aromatic size, but comparable total aromatic, olefin and alcohol content were added. In addition, two regenerative fuel blends with 33 % and 85 % regenerative content and a Euro 5 certification fuel were investigated. The key fuel parameters are shown in **Table 2**.

**Table 2:** Properties of tested fuels

| No. | Name | T10 | T50 | T90 | FBP | Alcohols | Aromatics | Aromatics >C7 | Olefins | Oxygen |
|---|---|---|---|---|---|---|---|---|---|---|
| - | - | °C | °C | °C | °C | vol.-% | vol.-% | vol.-% | vol.-% | m.-% |
| 1 | Base High | 62.3 | 101.7 | 174.4 | 230.5 | 0.0 | 37.4 | 28.7 | 21.0 | 0.03 |
| 2 | Base Low | 55.9 | 82.5 | 111.9 | 182.9 | 0.3 | 0.7 | 0.7 | 0.3 | 2.51 |
| 3 | E10 High | 56.2 | 90.0 | 171.2 | 223.1 | 10.0 | 33.7 | 22.3 | 19.1 | 3.64 |
| 4 | E20 High | 57.9 | 71.9 | 168.6 | 216.4 | 19.7 | 29.9 | 19.8 | 17.1 | 7.12 |
| 5 | E30 High | 58.4 | 72.9 | 165.0 | 215.6 | 29.4 | 26.2 | 17.3 | 15.2 | 10.55 |
| 6 | M5 High | 47.7 | 103.9 | 172.2 | 223.1 | 5.2 | 34.6 | 30.9 | 18.5 | 2.71 |
| 7 | M15 High | 49.6 | 86.9 | 171.7 | 226.2 | 14.8 | 33.2 | 29.6 | 15.8 | 7.69 |
| 8 | T5 High | 64.0 | 102.7 | 172.5 | 225.3 | 0.0 | 40.1 | 23.7 | 20.3 | 0.03 |
| 9 | T10 High | 65.3 | 103.6 | 171.2 | 220.5 | 0.0 | 43.5 | 22.3 | 19.2 | 0.04 |
| 10 | T10 Low | 59.6 | 87.0 | 111.1 | 183.5 | 0.3 | 8.3 | 0.6 | 0.3 | 2.27 |
| 11 | FBP Var. 1 | 55.0 | 101.1 | 174.1 | 209.0 | 4.4 | 32.8 | 24.7 | 10.5 | 1.59 |
| 12 | FBP Var. 2 | 55.6 | 104.6 | 166.3 | 208.9 | 4.3 | 36.9 | 28.7 | 10.2 | 1.57 |
| 13 | FBP Var. 3 | 56.2 | 105.9 | 174.8 | 209.9 | 4.9 | 33.5 | 9.9 | 10.8 | 1.79 |
| 14 | FBP Var. 4 | 43.4 | 80.1 | 146.2 | 165.4 | 5.0 | 31.7 | 18.0 | 10.8 | 1.86 |
| 15 | FBP Var. 5 | 42.2 | 77.5 | 132.5 | 175.2 | 5.0 | 32.3 | 11.3 | 11.0 | 1.87 |
| 16 | G33 | 56.7 | 97.4 | 153.7 | 184.0 | 8.5 | 24.6 | 17.4 | 7.1 | 3.80 |
| 17 | G85 | 54.1 | 101.1 | 178.3 | 196.9 | 0.0 | 34.6 | 19.1 | 5.8 | 2.78 |
| 18 | EU5 | 66.7 | 105.6 | 145.3 | 165.3 | 5.0 | 32.4 | 19.3 | 1.3 | 1.82 |

## 3. Results

### 3.1 RDE-Results

The ambient and component temperature has a significant influence on particle formation, so that the particle concentration in the exhaust gas is significantly increased immediately after starting the engine [19,20]. Figure 3**:** Influence of oxygenate and toluene addition on cold start emissions shows the cumulative average PM emissions of various blends in comparison with their base fuels. All the investigated blends based on base-high lead to a significant reduction in soot formation compared to the base fuel. In the case of ethanol, an admixture of up to 20 percent leads to a 55% reduction in the cumulative particulate mass. A further increase in the ethanol content to 30%, however, leads to a flattening of the effect. The effect is more pronounced with methanol. While 5% methanol reduces PM emissions by about the same amount as adding 10% ethanol, a further increase in the methanol content leads to a further reduction in particle mass, but the effect also flattens out. Here, the mixture formation can be negatively influenced both by the lower density of the oxygenates and by an increased enthalpy of vaporization, so that a reduced soot tendency on a molecular basis of the blends is partially compensated. Toluene as a C7 aromatic, shows a comparatively high soot tendency in burner tests. As a result, in contrast to the alcohols, the calculated YSI of the toluene blends is above the base-high fuel. Nevertheless, a reduction in particulate mass is observed for both toluene blends when the engine is started. The T10-Low, on the other hand, shows a slight increase in particulate emissions compared to its base fuel. From this it can be concluded that the effect of small aromatics has a minor influence on a low-soot, aromatics-free fuel. In the case of the high-boiling aromatics base high fuel, on the other hand, dilution with smaller aromatics appears to be advantageous.

The results of the overall cycle are shown in **Figure 4**. It can be seen that the results of the start phase can differ significantly from a dynamic driving scenario depending on the fuel. While the same trends can be seen with toluene as with the starting phase, the effect achieved by adding alcohols is reduced and, in the case of methanol, can even lead to an increase in particle emissions. Since methanol has a low boiling point and at the same time a high enthalpy of vaporization, this can impair the vaporization of the late-boiling components. This phenomenon, already described by Ratcliff [13], appears to be further intensified in the case of the base high fuel, which is rich in late-boiling aromatics. A comparison with ethanol, on the other hand, shows that the enthalpy of vaporization alone does not adequately explain the effect. Although the mass-related enthalpy of vaporization of methanol is around 33% higher than that of ethanol, in the case of E10 this is compensated for by the double mass fraction compared to M5. In the case of ethanol, there is an increase in particle mass over the cycle of 3 %, which can possibly be attributed to increased enthalpy. However, the negative effect is limited exclusively to phases of higher load at the end of the cycle. In the urban and rural segment, the PM is reduced by 14 % and 2 %. With an increase to 20 or 30 % the effect of dilution appears to be dominant, so that there is again a decrease in particle output, even at higher loads. Overall, it can be seen for all oxygenate fuels that a significant reduction in particles can be achieved, particularly in the start phase and in the first 5 minutes of the cycle. The normalized, cumulative emissions are thus approximately at the level of the cold start. (48% for E30, 61% for E20 and 86% for E10). The differences decrease over the course of the cycle. On the one hand, this can be favored by the rising engine temperature and the associated better mixture formation for all fuels; on the other hand, errors in mixture formation, for example due to changes in the density of the fuel, are more significant at higher loads and due to longer injection times.

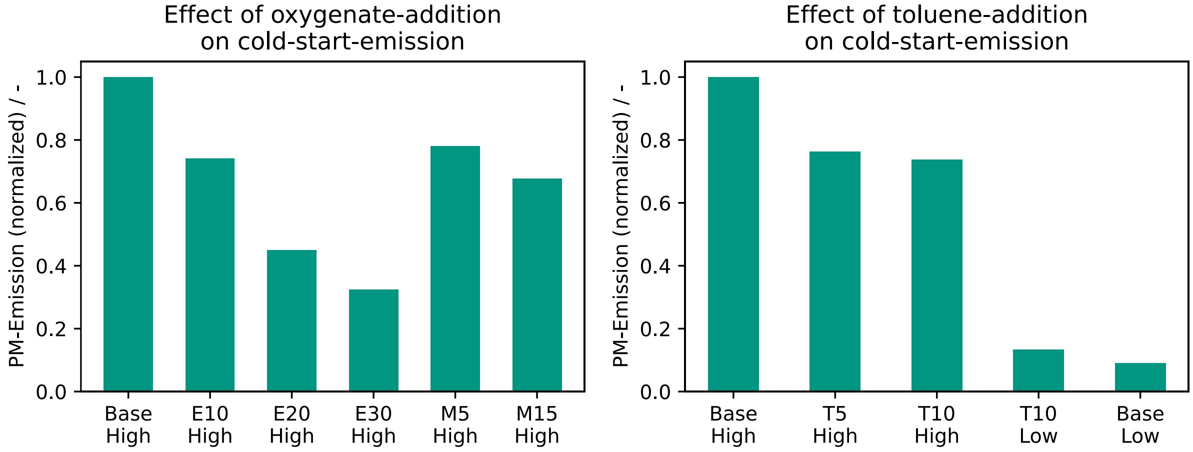

**Figure 3:** Influence of oxygenate and toluene addition on cold start emissions

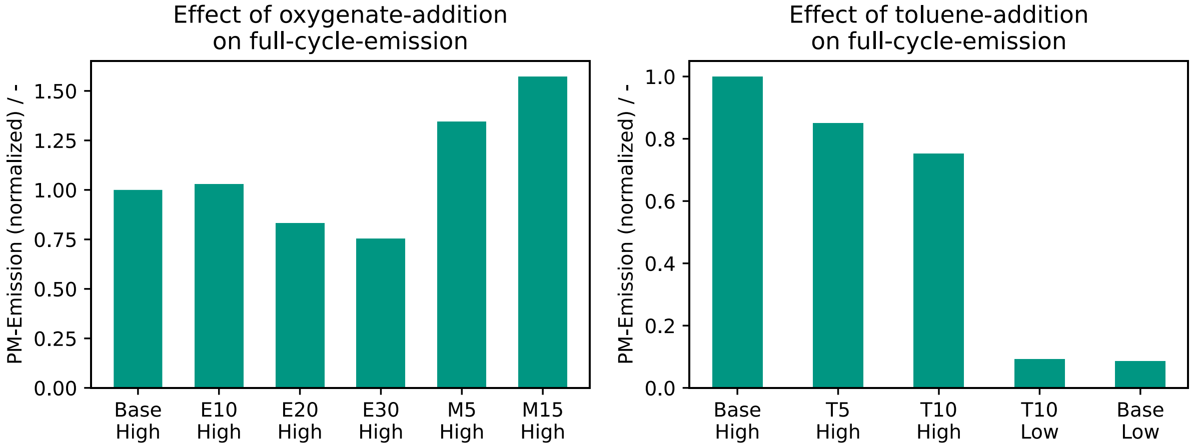

**Figure 4:** Influence of oxygenate and toluene addition on full cycle emission

Due to the lack of a carbon-carbon bond, methanol as a pure substance has hardly any potential to form soot, which is also reflected in a low YSI of 6.6 [17]. The molecular structure alone cannot therefore explain why the particle mass increases with increasing methanol content in the cycle. While a 32 % reduction in particle mass is achieved with M15 in the cold start (the measured YSI is 28 % lower than with base high), the particle mass emitted over the entire cycle is 57 % higher than with the reference fuel. Analysis of the data over time shows that these differences can only be attributed to a few cycle segments in the 50 to 75 % engine load range. Here, the particulate mass concentration is briefly 2 to 3 times higher than with the reference fuel. Due to the simultaneously occurring high exhaust gas mass flows, these segments are strongly taken into account in the overall result of the cycle. The cause of the short peaks cannot be identified with the measurement technology used, but optical recordings are planned to investigate possible anomalies.

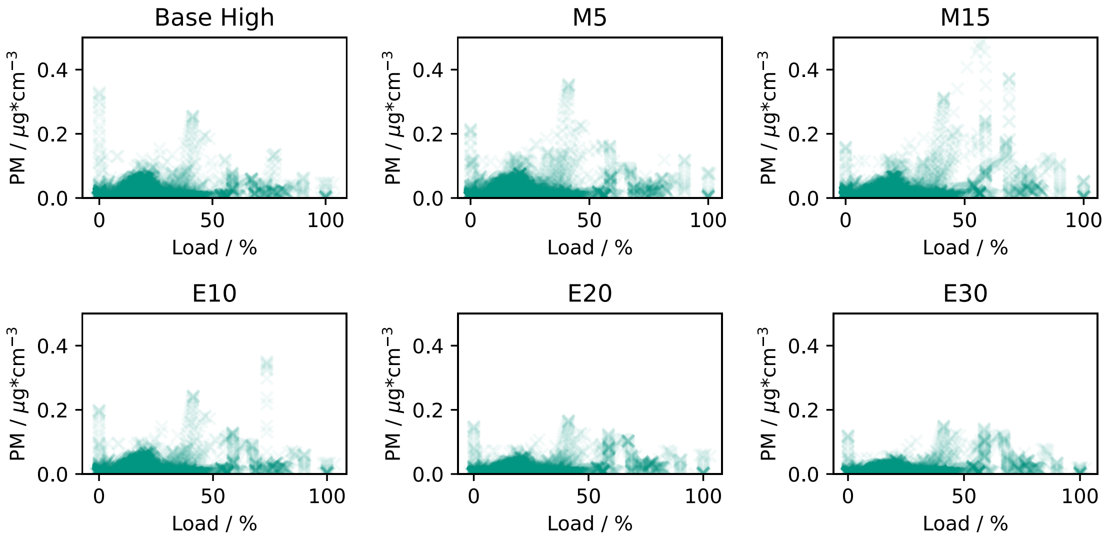

**Figure 5**: Distribution of PM concentrations by engine load for oxygenated fuels

The results from the YSI determination on the burner were compared with the measured particulate emissions below. For this purpose, the PN and PM emissions were cumulated for each segment of the test cycle and normalized to the respective result of the base-high fuel by dividing the cumulated PN or PM emission of the fuel by the cumulated result of the base high fuel. As the two methanol blends M5 and M15 lie outside the results of the other fuels across all segments, they are considered outliers and are not included in the calculation of the coefficient of determination. A linear relationship between the measured YSI and the PM emission can already be seen at engine start with subsequent idling phase in **Figure 6**. Although this decreases further as the cycle progresses, the correlation in the end-of-cycle results remains at a comparable level as the particulate emissions continue to decrease overall as the engine reaches operating temperature.

The PN10 emission, on the other hand, shows a reduced dispersion compared to the PM emission and therefore a stronger correlation in the urban to highway sections and therefore also in the end-of-cycle emissions. At engine start, on the other hand, there is no recognizable correlation between the two variables. However, this is due to the high number of particles in the ultrafine particle range. Here, the measurement stop of the strain gauge is reached shortly, so that no valid results can be obtained. As the particle mass is not measured directly, but is calculated from the particle size distribution, there are different effects at engine start and highway section. In principle, the particle mass is significantly influenced by the occurrence of larger particles. As the size ranges relevant for the particle mass are still within the measuring range when the engine starts, a comparison with the YSI is still possible here in contrast to the PN10 emission. In the further course, however, the particle number concentration in the exhaust gas tends to decrease. The signal to noise ratio therefore deteriorates for the already rare accumulation and coarse mode particles. At the same time, other factors such as the engine oil can influence the particle mass, particularly at high loads and with a warm engine. A clear separation is not possible based on the data.

Nevertheless, across all phases of the cycle, it is evident that the YSI is suitable for evaluating a fuel's soot generation. A linear relationship is recognizable for both the particle mass and the number of particles across all cycle phases.

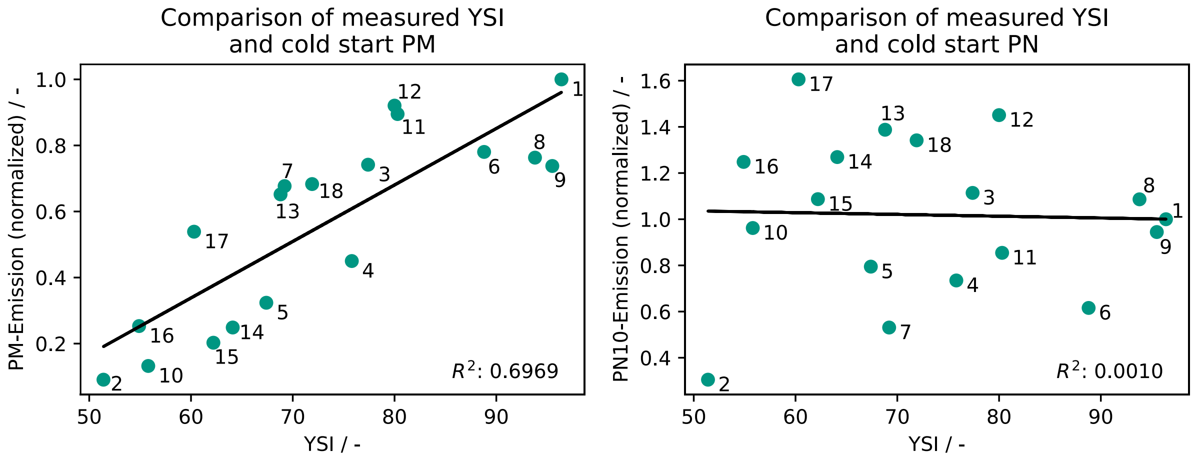

**Figure 6:** Correlation between cold-start PM-Emission and measured YSI

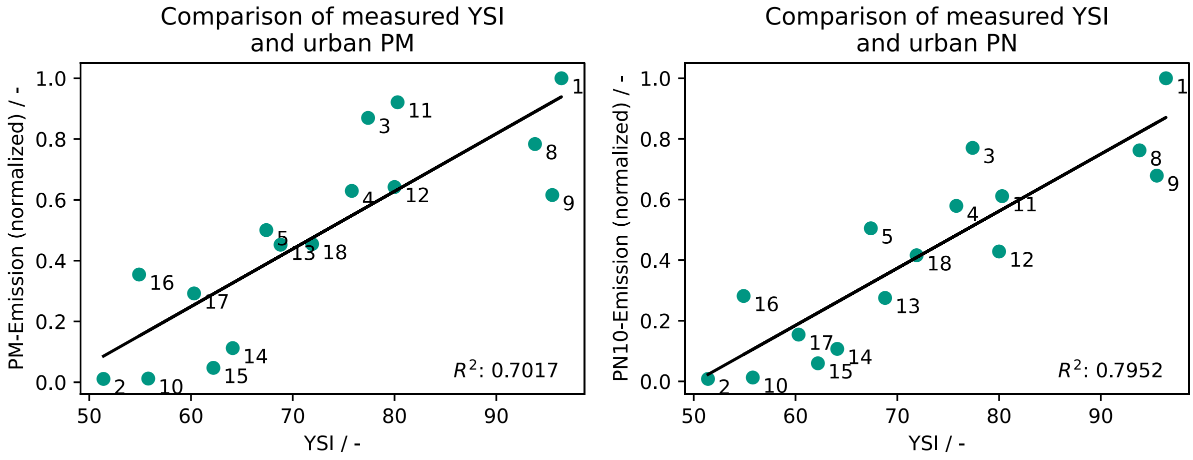

**Figure 7:** Correlation between urban PM-Emission and measured YSI

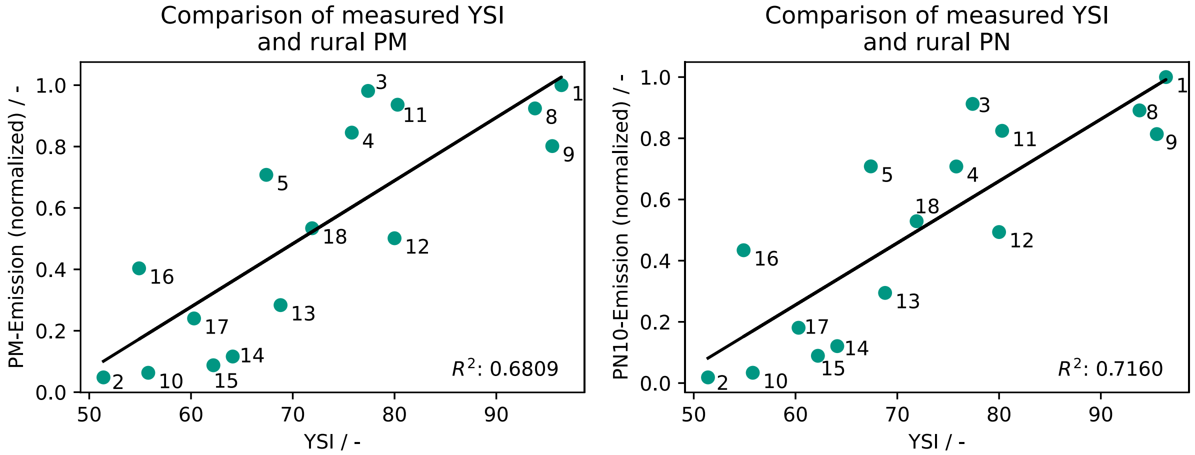
Comparison of measured YSI and rural PM

Comparison of measured YSI and rural PN

**Figure 8:** Correlation between rural PM-Emission and measured YSI

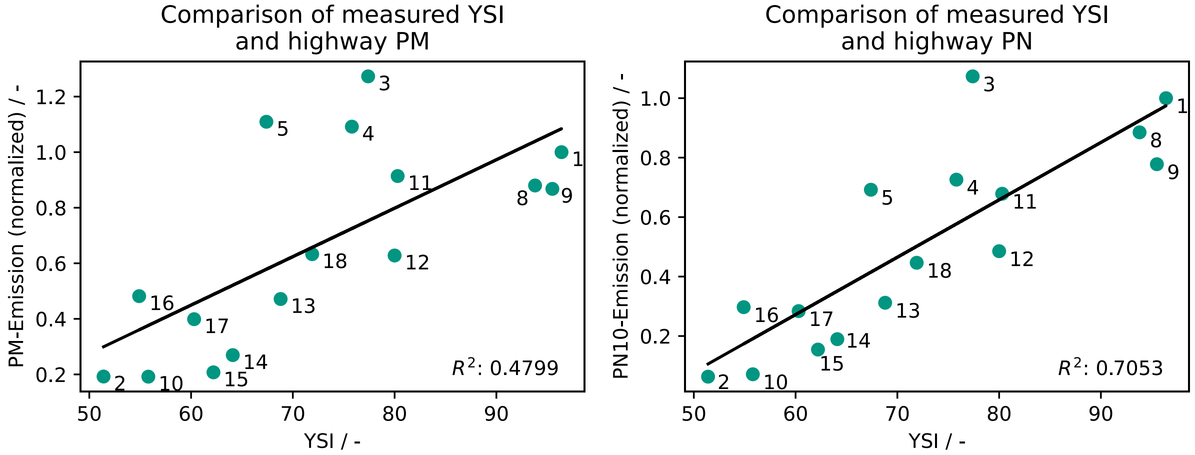
Comparison of measured YSI and highway PM

Comparison of measured YSI and highway PN

**Figure 9:** Correlation between highway PM-Emission and measured YSI

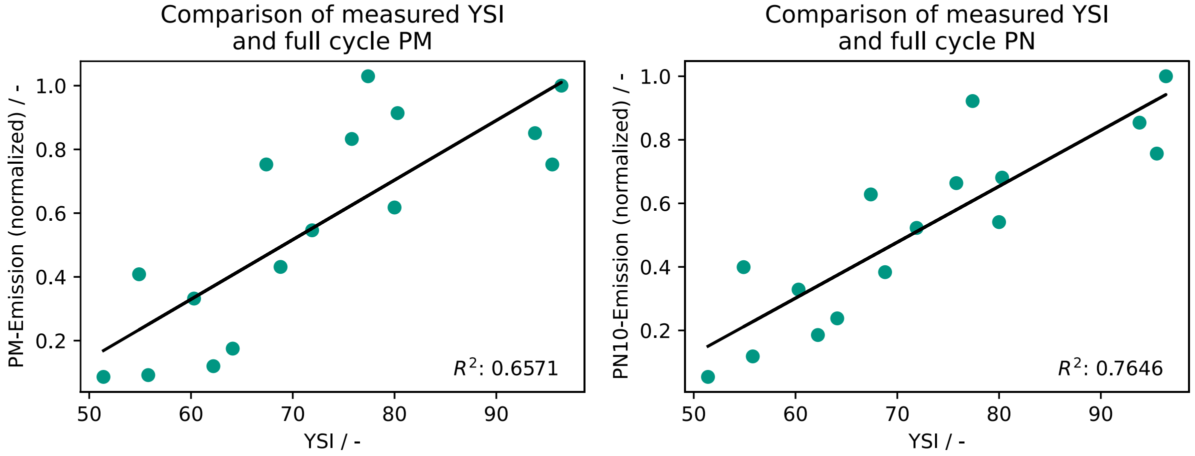
Comparison of measured YSI and full cycle PM

Comparison of measured YSI and full cycle PN

**Figure 10:** Correlation between full cycle PM-Emission and measured YSI

## 4. Conclusion

18 fuels were selected and examined on the basis of their properties. A fuel analysis was carried out for each fuel and the yield sooting index was determined on a laminar burner. The fuels were tested on the engine test bench with a production unit and the effects on PM and PN emissions in the raw exhaust gas were determined. It was shown that the YSI is suitable for a first suggestion of both the number of particles and the mass. The fuel with the lowest YSI compared to the base high fuel shows a 95% reduction in particle count and a 91% reduction in particle mass over the entire cycle. This shows that the selection of a suitable fuel also has a high potential for reducing pollutants in the existing fleet. While the YSI is by and large suitable for selecting such a fuel, there are nevertheless differences with regard to various fuels of comparable YSIs. For example, in the case of the blends investigated, an admixture of toluene leads to a higher YSI regardless of the fuel, while in the case of the base high fuel a reduction in particulate emissions is nevertheless achieved. Such opposing effects may occur in particular due to the interaction of late-boiling aromatics and early-boiling alcohols. Diluting an aromatic-rich fuel with ethanol or methanol leads to a reduction in YSI, but depending on the operating point, particle emissions can be increased. Particularly in the case of E10 and the methanol blends investigated, the PN emission are reduced when the engine is cold and under low load, but in the overall cycle the emission is higher than the base fuel, although the measured YSI indicates otherwise. This leads to the conclusion that for an evaluation of the soot potential of a fuel, further characteristic values such as the evaporation behavior should be taken into account. Since the multifactorial nature of the test setup makes it difficult to draw conclusions about individual causes, additional investigations are planned using 2d in-cylinder two-color pyrometry and an extended fuel matrix to consider the influence of individual fuel properties in particular.

## Acknowledgement

This report is the scientific result of a research project undertaken by the FVV eV and performed by the Institute of Internal Combustion Engines (IFKM) of the Karlsruhe Institute of Technology (KIT) under the direction of Prof. Dr. sc. techn. Thomas Koch and the OWI Science for Fuels gGmbH under the direction of Dr. Wilfried Plum.

The FVV would like to thank Professor Koch and Dr. Plum and their scientific research assistants – Lukas Heinz, M.Sc. (IFKM) and Dipl. Ing. Sebastian Feldhoff (OWI) for the implementation of the project. The project was conducted by a working group led by Dr. Jan-Hubert Wittmann (Freyberger engineering GmbH). We gratefully acknowledge the support received from the chairman and from all members of the project user committee.

In addition, we would like to thank the BMW AG and for the provision of the test engine and Aramco, Robert Bosch GmbH, Shell and Volkswagen AG for supplying the test fuels.

## References

[1] Kraftfahrtbundesamt, Bestand an Kraftfahrzeugen und Kraftfahrzeuganhängern nach Zulassungsbezirken, 1. Januar 2023 (FZ1), (2023). https://www.kba.de/DE/Statistik/Fahrzeuge/Bestand/Motorisierung/motorisierung_node.html;jsessionid=08D7BFCE8911BE239B233B3ADF0DE2B3.live21323 (accessed March 24, 2024).

[2] Das Europäische Parlament und der Rat der Europäischen Union, VERORDNUNG (EG) Nr. 715/2007 DES EUROPÄISCHEN PARLAMENTS UND DES RATES, 2007. https://doi.org/10.15358/9783800639366.

[3] Das Europäische Parlament und der Rat der Europäischen Union, VERORDNUNG (EU) 2021/1119 DES EUROPÄISCHEN PARLAMENTS UND DES RATES, 2021. https://eur-lex.europa.eu/legal-content/DE/TXT/PDF/?uri=CELEX:32021R1119&from=EN.

[4] V.N. Matthaios, J. Lawrence, M.A.G. Martins, S.T. Ferguson, J.M. Wolfson, R.M. Harrison, P. Koutrakis, Quantifying factors affecting contributions of roadway exhaust and non-exhaust emissions to ambient PM10–2.5 and PM2.5–0.2 particles, Science of The Total Environment 835 (2022) 155368. https://doi.org/10.1016/j.scitotenv.2022.155368.

[5] Die Kommission der Europäischen Gemeinschaft, VERORDNUNG (EG) Nr. 692/2008 DER KOMMISSION, 2008.

[6] Vorschlag für eine VERORDNUNG DES EUROPÄISCHEN PARLAMENTS UND DES RATES über die Typgenehmigung von Kraftfahrzeugen und Motoren sowie von Systemen, Bauteilen und selbstständigen technischen Einheiten für diese Fahrzeuge hinsichtlich ihrer Emissionen und der Dauerhaltbarkeit von Batterien (Euro 7) und zur Aufhebung der Verordnungen (EG) Nr. 715/2007 und (EG) Nr. 595/2009, 2022. https://eur-lex.europa.eu/legal-content/DE/TXT/HTML/?uri=CELEX:52022PC0586.

[7] P. Eastwood, Particulate Emissions from Vehicles, John Wiley & Sons, Chichester, England; Hoboken, NJ, 2008.

[8] I.M. Kennedy, Models of soot formation and oxidation, Progress in Energy and Combustion Science 23 (1997) 95–132. https://doi.org/10.1016/S0360-1285(97)00007-5.

[9] K. Aikawa, J.J. Jetter, T. Sakurai, Development of a Predictive Model for Gasoline Vehicle Particulate Matter Emissions, (2010).

[10] H. Dageförde, T. Koch, K. Beck, U. Spicher, Influence of Fuel Composition on Exhaust Emissions of a DISI Engine during Catalyst Heating Operation, (n.d.). https://doi.org/10.4271/2013-01-2571.

[11] C. Vuk, S.J. Vander Griend, Fuel Property Effects on Particulates In Spark Ignition Engines, in: 2013: pp. 2013-01–1124. https://doi.org/10.4271/2013-01-1124.

[12] F. Leach, R. Stone, D. Richardson, The Influence of Fuel Properties on Particulate Number Emissions from a Direct Injection Spark Ignition Engine, in: SAE International, 2013. https://doi.org/10.4271/2013-01-1558.

[13] M.A. Ratcliff, B. Windom, G.M. Fioroni, P. St. John, S. Burke, J. Burton, E.D. Christensen, P. Sindler, R.L. McCormick, Impact of ethanol blending into gasoline on aromatic compound evaporation and particle emissions from a gasoline direct injection engine, Applied Energy 250 (2019) 1618–1631. https://doi.org/10.1016/j.apenergy.2019.05.030.

[14] S.C. Burke, M. Ratcliff, R. McCormick, R. Rhoads, B. Windom, Distillation-based Droplet Modeling of Non-Ideal Oxygenated Gasoline Blends: Investigating the Role of Droplet Evaporation on PM Emissions, SAE Int. J. Fuels Lubr. 10 (2017) 69–81. https://doi.org/10.4271/2017-01-0581.

[15] Cambustion, ed., Application Note DMS01v06 - Real-time Mass Concentrations from Measured Size Distributions, (n.d.). https://www.cambustion.com/files/1606395876-dms01.pdf (accessed June 2, 2024).

[16] D.D. Das, J. Gau, C.S. McEnally, D. Giassi, N. Kempema, M. Long, Yale Coflow Diffusion Flames - Steady Flame Burner, (2014). http://guilford.eng.yale.edu/yalecoflowflames/steady_burner.html (accessed June 21, 2024).

[17] D.D. Das, P.C. St. John, C.S. McEnally, S. Kim, L.D. Pfefferle, Measuring and predicting sooting tendencies of oxygenates, alkanes, alkenes, cycloalkanes, and aromatics on a unified scale, Combustion and Flame 190 (2018) 349–364. https://doi.org/10.1016/j.combustflame.2017.12.005.

[18] M.J. Montgomery, D.D. Das, C.S. McEnally, L.D. Pfefferle, Analyzing the robustness of the yield sooting index as a measure of sooting tendency, Proceedings of the Combustion Institute 37 (2019) 911–918. https://doi.org/10.1016/j.proci.2018.06.105.

[19] D. Appel, F.P. Hagen, U. Wagner, T. Koch, H. Bockhorn, D. Trimis, Influence of Low Ambient Temperatures on the Exhaust Gas and Deposit Composition of Gasoline Engines, Journal of Energy Resources Technology 143 (2021) 082306. https://doi.org/10.1115/1.4050492.

[20] L. Chen, Z. Liang, X. Zhang, S. Shuai, Characterizing particulate matter emissions from GDI and PFI vehicles under transient and cold start conditions, Fuel 189 (2017) 131–140. https://doi.org/10.1016/j.fuel.2016.10.055.

# Experimental Investigation and Cyclic Emissions Characterization of Renewable Dipropyl Oxymethylene Ether - Natural Gas Dual Fuel Combustion at Low Load

Abhinandhan Narayanan[1], Giacomo Silvagni[2,*], Kalyan Kumar Srinivasan[1], Sundar Rajan Krishnan[1], Vittorio Ravaglioli[2], Fabrizio Ponti[2]

[1] *The University of Alabama, Department of Mechanical Engineering, (United States of America)*
[2] *Department of Industrial Engineering – DIN, University of Bologna (Italy)*
[*] *Correspondence: giacomo.silvagni2@unibo.it*

## 1. ABSTRACT

High efficiency natural gas dual fuel combustion is a promising low temperature combustion (LTC) concept capable of reducing greenhouse gas emissions in heavy-duty transportation and power generation applications. Viable strategies for reducing emissions in heavy-duty engines include the use of low carbon alternative fuels, with oxymethylene ethers (OMEs) as promising renewable low carbon fuels. In this study, dipropyl oxymethylene ether (P1P), larger alkyl group terminated OMEs, was tested as high reactivity fuel (HRF) along with Natural Gas (NG) as low reactivity fuel (LRF) in dual fuel combustion due to its excellent smoke and oxides of nitrogen (NOx) reduction potential. The experiments were performed on a single-cylinder heavy-duty engine operated at a nominal load of 5 bar IMEPg and 1339 RPM, and different strategies for emissions mitigation were investigated. The analysis of the combustion process along with the emissions and performance showed a good potential of dual fuel P1P-NG combustion achieving ultra-low NOx-soot trade-off (NOx lower than 0.1 g/kWh with no soot) and high efficiency (Indicated Fuel Conversion Efficiency of 46%). HC and CO trade-offs were also pointed out, providing a broad overview on the engine out emissions operating different strategies. Cycle-resolved HC and NOx emissions data were also acquired using fast flame ionization detector (FID) and fast chemiluminescence detector (CLD) analyzers aimed at highlighting the pollutant formation mechanisms in dual fuel combustion. By combining in-cylinder pressure data and the fast FID and CLD analyzers, two experimental correlations were found. The cycle-to-cycle variability, expressed by the variation of IMEPg, and combustion knocking, represented through the maximum value of the rate of heat release, were correlated with good accuracy to HC and NOx production, respectively. To easily compare the HC and NOx production tendency of P1P-NG with diesel-NG combustion in the same engine, the P1P-based correlations were normalized with respect to the chemical characteristics of the fuels, revealing a strong correlation.

## 2. INTRODUCTION

Heavy duty transportation is one of the most reliable methods for freight transportation in the United States as they move ~ 73% by weight of the nation's freight. They also contribute close to 3,132,411 million vehicle miles travelled as of 2021 [1]. Internal combustion (IC) engines are the most widely used prime movers in heavy duty trucks as close to 99.9% of commercial trucks are powered by diesel, natural gas or gasoline. According to the US Environmental Protection Agency (EPA) [2], heavy duty diesel vehicles produce ~ 8 grams per mile of NOx emissions and emitted 417 million metric tons of carbon dioxide equivalent as of 2021. As a result, the emissions regulations on heavy duty vehicles have gotten increasingly stringent, and with the push for decarbonization in the transportation industry gaining momentum, researchers are focusing their efforts on identifying sustainable pathways to reduce greenhouse gas and NOx emissions from heavy duty diesel engines. Two methods that have been widely researched to achieve these emissions reduction include identifying renewable low – carbon fuel substitutes to diesel and also through advanced combustion techniques that offer emissions reduction and performance improvement benefits [3-9]. Reactivity controlled compression ignition (RCCI) has been identified as one such advanced combustion technique that offers evident emissions reduction benefits without experiencing heavy efficiency penalties [10-14]. The RCCI combustion mode leverages the energy released from the combustion of a High Reactivity Fuel (HRF) to ignite a Low Reactivity Fuel (LRF). The HRF is typically a high cetane fuel which is easier to auto ignite when compared to a low cetane LRF, which is harder to auto ignite.

Liu et.al [15] studied the combustion characteristics of hydrogenated catalytic biodiesel – gasoline RCCI combustion to explore the challenges of combustion instability and misfires faced under low load operation. They performed experimental studies on an optical engine where they studied the effect of varying the LRF type and HRF injection timing on the combustion characteristics. The authors observed that increased ethanol blending on the HRF, caused increased ignition delay and delayed combustion phasing, and also identified that blending 10% ethanol with gasoline, enhanced the performance when compared to 0% or 100% ethanol blending. They also identified that late SOI timings led to improved stratification, which shortened heat release durations and reduced ignition delays.

Hariharan et.al [16] investigated multiple injection strategies on a heavy-duty single cylinder engine to reduce HC and CO emissions in diesel – methane dual fuel combustion. The authors were able to achieve ~50% IFCE with two injections (one early injection and one injection after TDC) and high injection pressures. The long dwell double injections also aided in reducing the HC and CO emissions by ~50%, when compared to a single injection baseline operating point. However, the long dwell injections caused an increase in the smoke emissions and a slight increase in the ISNOx emissions when compared to the single injection points.

Oxygenated fuels like oxymethylene dimethyl ether (OMEx) have exhibited excellent potential to mitigate soot emissions when used as the HRF in natural gas based dual fuel combustion, and due to its lower LHV than diesel, it also has the potential to aid in NOx reduction [17 - 19]. OMEx has exhibited great potential to replace diesel in dual fuel RCCI mode [20-21] as well as exhibit favorable blending properties with diesel to reduce NOx emissions in CI engines [22-23].

Benajes et.al [24] compared the performance and emissions of diesel – gasoline dual fuel combustion with OMEx – gasoline dual fuel combustion on a 6-cylinder, 7.7-liter engine with a compression ratio of 12.75:1. The authors observed that peak efficiencies from OMEx – gasoline combustion occurred at high load conditions when compared to diesel – gasoline combustion, where it occurred at medium load conditions. The peak IFCE from OMEx – gasoline dual fuel combustion was also found to be 2% greater. Near zero soot emissions were observed from OMEx – gasoline combustion, and BSNOx emissions were also close to 0.4 g/kWh when the BSNOx emissions from diesel – gasoline combustion went beyond the EURO VI limit. The authors also noted that at high load conditions the presence of EGR helped reduce NOx emissions. However, the authors observed that HC and CO emissions were high at low load conditions for both diesel – gasoline and OMEx – gasoline dual fuel combustion.

Hariharan et.al [25] observed a similar drawback of high HC and CO emissions at low load conditions for POMDME – NG dual fuel combustion, and the authors presented strategies to mitigate the increase in HC and CO emissions at low loads. Increased cyclic variations at the low load conditions could be attributed as one of the primary factors for increased HC emissions, direct linear correlations between increased variations in IMEPg to increased HC emissions were derived by Silvagni et.al [26]. Both close-to-TDC and early injection timings exhibited increased cyclic variations for diesel – NG and POMDME – NG dual fuel combustion [27], and HC emissions at these two timings were correlated with changes in IMEPg for diesel – NG dual fuel combustion. Silvagni et.al [26] observed a fairly linear correlation between HC emissions and change in IMEPg ($R^2$ = 0.86) for diesel – NG dual fuel combustion at these injection timings. Additionally, the authors also observed that NOx emissions also scaled fairly linearly with peak of the rate of heat release RoHR ($R^2$ = 0.82) for diesel – NG low load operation.

In the present work, dipropyl oxymethylene ether or P1P, was used as the HRF in NG based dual fuel RCCI combustion. P1P was found to have better properties than typical OMEx for blending with diesel, and also had a significantly higher LHV than OMEx [28, 29]. This meant that a much lower quantity of P1P had to be injected to derive the same energy output when compared to OMEx, which could lead to potential IFCE benefits. Our previous work evaluated the potential of P1P to substitute diesel as the HRF in RCCI combustion at high load operating conditions and identified pathways to achieve high IFCEs while maintaining low ISNOx emissions [30].

The objective of the present work is to identify a favorable tradeoff between emissions, efficiency and engine stability at low load operating conditions for P1P – NG dual fuel RCCI combustion, in addition to correlating HC and NOx emissions to variations in IMEPg and ROHR [31-33], by obtaining fast emissions data from Cambustion fast FID and NOx analyzers.

## 3. EXPERIMENTAL SETUP AND METHODS

Experimental testing was conducted on a single cylinder research engine (SCRE) platform, which had been modified from a production multi-cylinder heavy-duty diesel engine and had a compression ratio of 18.5:1. The engine specifications are provided in Table 1. The engine was coupled to a 393 HP AC dynamometer, which was controlled by a Dyne systems Inter-Loc V controller. Compressed air was provided at the inlet of the engine and the intake pressure was controlled using a Proportion Air QB1X pressure regulator. Intake air mass flowrate measurements were made using a Flowmaxx SN16 sonic nozzle, which was achieved by maintaining choked conditions at the throat of the nozzle. A common rail direct injection system was used for the management of the HRF injections, and pressurized fuel was supplied to the rail using a Delphi DFP5 fuel pump. Pressure at the common rail was regulated by controlling a solenoid actuated inlet metering valve, which was placed at the outlet of the fuel pump, and a pressure relief valve which was placed on the rail. The fuel injection system used stock components, including the injector and fuel pump, and was not modified to accommodate the injection of P1P. The fuel properties are shown in Table 2.

**Table 1.** Single Cylinder Research Engine (SCRE) specifications

| Parameter | Specifications |
|---|---|
| **Engine Type** | 4 stroke compression ignition |
| **Bore x Stroke** | 123 mm x 152 mm |
| **Displaced Volume** | 1806 cc |
| **Compression Ratio** | 18.5:1 |
| **Intake Valve Timings** | IVO = 710 CAD, IVC = 210 CAD |
| **Exhaust Valve Timings** | EVO = 490 CAD, EVC = 5 CAD |
| **Low reactivity fuel (LRF)** | Compressed city natural gas (~93% methane content by vol.) |
| **High reactivity fuel (HRF)** | P1P |
| **HRF system** | Common rail direct injection |

The LRF chosen for this study was compressed city natural gas, which had ~ 93% methane content by volume, and it was directly fumigated into the intake manifold. The mass flowrate of both the fuels were measured using CMFS015M319N0A2ECZZ Emerson Micromotion coriolis flowmeters used along with 2400SIA11B2EZZZ transmitters. Crank angle resolved cylinder pressure measurements were made using a Kistler 6124 A piezo electric transducer, which was coupled to a Kistler 5018 charge amplifier. A BEI XH25D-SS-3600-ABZC-28V/V-SM18 encoder was coupled to the crankshaft, which was used to trigger high-speed data acquisition, manage crank resolved actuations, and phase cylinder pressure data with respect to crank angle. **Figure 1** shows the schematic of the SCRE setup with various measurement and control devices. A National Instruments based data acquisition and controller system was used to acquire both high and slow speed data and was also used to control the actuators and injector used in the SCRE setup. The NI Direct Injector Control Module (DCM 2316) was used for rail pressure control and for actuating the direct injector at a commanded start of injection (SOI) angle. The NI PXIe 6356 module was used to record high speed analog input data, controlled by a PXIe 8840 quad core controller. The slow speed analog inputs and temperature data were measured using a NI 9205 module and a NI 9213 thermocouple module, which were attached to a NI cDAQ. A standard five gas emissions bench with Rosemount analyzers was used to measure steady state HC (FID), NOx (CLD), and CO and $CO_2$ emissions (NDIR). Crank angle resolved emissions measurements were performed using Cambustion fast emissions analyzers. A CLD500 analyzer which had a response time of 2 ms and an adjustable range up to 0 – 5000 ppm was used to measure instantaneous NOx emissions. A HFR400 analyzer which used the flame ionization detection method to measure HC was used to measure crank angle resolved hydrocarbon emissions. The fast pollutant measurements were sampled at 500 Hz and was provided as an analog input to the NI PXIe 6356 module.

**Table 2.** Fuel Properties

| | **Diesel** | **P1P** | **Natural Gas** |
|---|---|---|---|
| **Cetane/Octane Number** | CN – 46 | CN – 53.2 | ON – 110/120 |
| **Density (kg/m$^3$)** | 850 | 834 | 0.657 |
| **Lower Heating Value (MJ/kg)** | 43.4 | 32 | 49.229 |
| **H/C Ratio** | 1.8 | 12.3 | 3.8655 |
| **O/C Ratio** | 0 | 24.2 | 0.0029 |
| **N/C Ratio** | 0 | 63.5 | 0.0076 |

### 3.1 Experimental Methodology

Experimental studies were performed on the SCRE at a constant speed of 1339 RPM and IMEPg was maintained nominally at 5 bar which was representative of 25%-part load of the engine. Two types of test matrices were followed in this study to evaluate engine performance and emissions at low load for P1P – NG dual fuel combustion, and to correlate crank angle resolved emissions to cyclic variations in P1P – NG RCCI mode combustion. An SOI sweep was performed from a late SOI of -10 deg aTDC to an early SOI of -60 deg aTDC at a constant percentage energy substitution (PES) of the LRF of 80%, 1.5 bar intake pressure and 500 bar rail pressure, to highlight the typical behavior during the transition from dual stage heat release to single-stage Gaussian heat release. Table 3 shows the engine operating parameters of the SOI sweep.

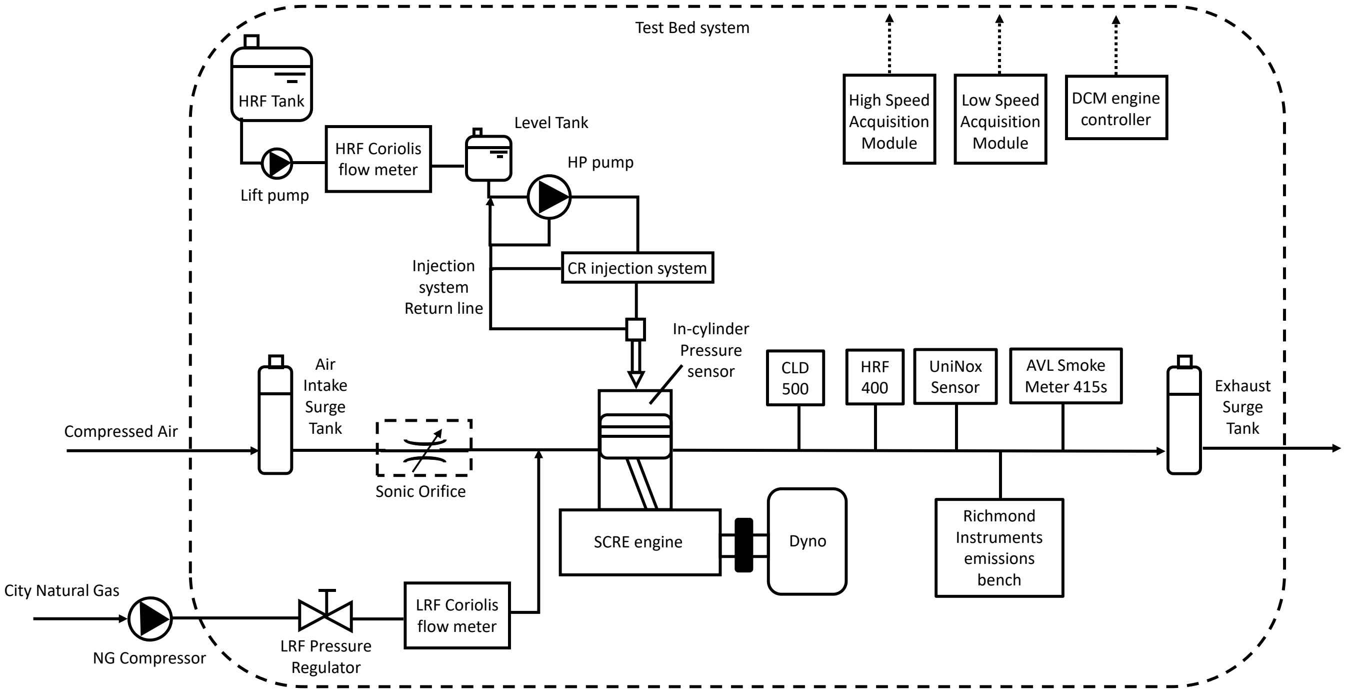
Test Bed system
HRF Tank
HRF Coriolis flow meter
Lift pump
Level Tank
HP pump
High Speed Acquisition Module
Low Speed Acquisition Module
DCM engine controller
Injection system Return line
CR injection system
In-cylinder Pressure sensor
Air Intake Surge Tank
Compressed Air
Sonic Orifice
CLD 500
HRF 400
UniNox Sensor
AVL Smoke Meter 415s
Exhaust Surge Tank
SCRE engine
Dyno
Richmond Instruments emissions bench
City Natural Gas
NG Compressor
LRF Pressure Regulator
LRF Coriolis flow meter

**Figure 1.** Schematic of the SCRE setup with locations of emissions measurement devices

The data points selected were also expected to exhibit a wide range of cyclic variability, which will aid in developing a correlation between the variations in IMEPg and peak ROHR with HC and NOx emissions.

A systematic parametric sweep was also performed in addition to the SOI sweep, to evaluate the emissions and efficiency benefits that each engine operating parameter had to offer, and the matrix was based on our previous work, published in Hariharan et.al [25]. At a nominal load of 5 bar IMEPg, Spray Targeted Reactivity Stratification (STARS) was achieved by adding a second injection and by sweeping the timing of the second injection. After identifying an optimum second injection timing, a PES sweep, intake pressure sweep, and injection pressure sweep were performed to achieve the various tradeoffs listed in Table 4.

**Table 3.** Engine operating parameters which were kept constant and controlled during the systematic parametric sweeps to improve the performance of dual fuel RCCI combustion.

| **Sweep** | **Constant** | **Control** | **Goals and Tradeoffs** |
|---|---|---|---|
| **SOI** | IMEPg, PES, $P_{rail}$, $P_{in,}$ Speed | Single injection SOI1 | Lowest NOx emissions |
| **STARS** | IMEPg, PES, $P_{rail}$, $P_{in,}$ Speed, SOI1 | SOI2 | HC, CO reduction and lower COV of IMEPg |
| **Coupled Injection** | IMEPg, PES, $P_{rail}$, $P_{in,}$ Speed, Dwell between SOI1 and SOI2 | Sweep SOI1 and SOI2 together | Improved stratification to achieve lower HC and CO emissions/ optimal CA50 to achieve higher IFCEs |
| **PES** | IMEPg, $P_{rail}$, $P_{in,}$ Speed, SOI1, SOI2 | PES | NOx vs HC |
| **$P_{rail}$** | IMEPg,$P_{in,}$Speed, SOI1,SOI2, PES | Rail pressure | NOx vs IFCE and lowering MPRR @ lower PES |
| **$P_{intake}$** | IMEPg,$P_{rail,}$ Speed, SOI1,SOI2, PES | Intake pressure | CO vs NOx w/ high IFCE |

### 3.2 Analysis of fast emissions data

The fast emissions data were resolved with respect to crank angle degrees using the BEI encoder and 1000 cycles of fast emissions data were obtained along with 1000 cycles of cylinder pressure data. The data were filtered using a third order Butterworth low pass filter with a cutoff frequency of 2.5 kHz, which was chosen to maintain uniformity as the same filter was applied to the cylinder pressure signal. Since the fast emissions probe were placed a few inches away from the exhaust manifold, a time delay was applied to the signal to compensate for the travel of exhaust gases from the exhaust port to the emissions analyzer's probes. **Figure 2** shows the hydrocarbon emissions in ppm from one engine cycle plotted along with the cylinder pressure trace. As marked in the figure, the substantial increase in HC emissions after the exhaust valve opens, corresponds to the exhaust gases flowing into the analyzer, from the current combustion cycle. After the exhaust valve closes, a portion of the sample remains in the analyzer, and after the next combustion cycle, the exhaust gases from that cycle flow into the analyzer, which leads to the HC emissions spiking. The Net Cyclic Hydrocarbon Emissions (NCHC) [26], which describes the difference between the peak in HC emissions ($HC_{cyclic}$ )and the residual average HC while the exhaust valve is closed ($HC_{residual}$) defined in Equation 1, was selected as a parameter to correlate the HC emissions with cyclic variations in IMEPg, and it can be defined as in Equation 1:

$$NCHC[ppm] = HC_{cyclic} - HC_{residual} \tag{1}$$

Additionally, as defined in Equation 2, the change in IMEPg, namely $\Delta IMEP$, was computed to be the difference between IMEP in cycles n and n-1:

$$\Delta IMEP\ [bar] = IMEP_{n_{th} cycle} - IMEP_{(n-1)_{th}\ cycle} \tag{2}$$

For correlating the NOx emissions with ROHR, the peak of the NOx emissions which was at the end of the expansion stroke (**Figure 3**), due to the time delay in transporting the exhaust gases from the exhaust manifold to the analyzer, was correlated with the peak ROHR [26]. The ROHR was computed from the well-known equation provided by Heywood [34] reported in Equation 3:

$$ROHR = \frac{1}{\gamma - 1} \cdot V \cdot \frac{dp}{d\theta} + \frac{\gamma}{\gamma - 1} \cdot p \cdot \frac{dV}{d\theta} \tag{3}$$

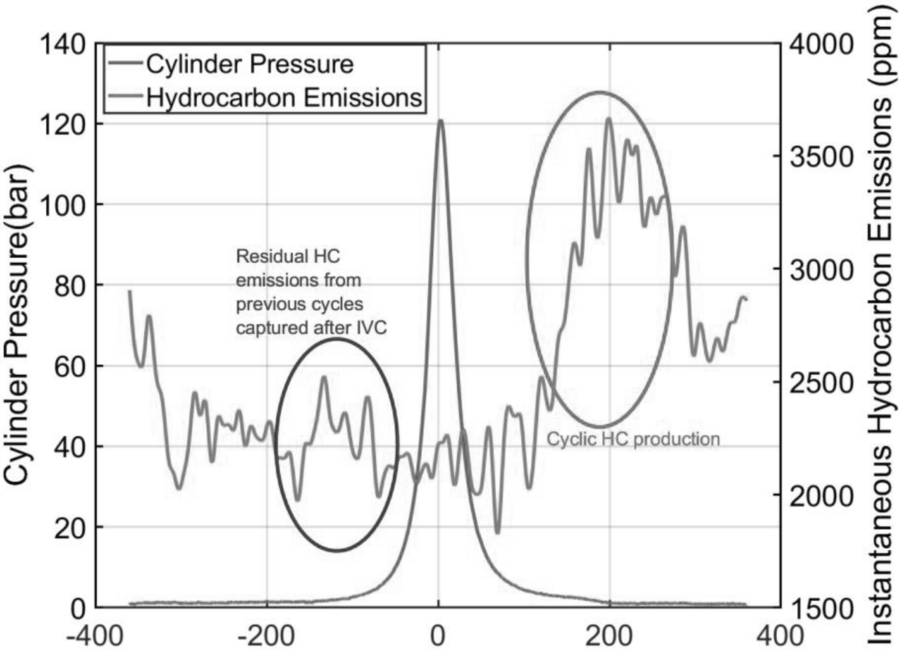

**Figure 2.** Hydrocarbon emissions signal received from the fast FID analyzer for one engine cycle, highlighting two important zones in the signal, plotted along with the cylinder pressure trace.

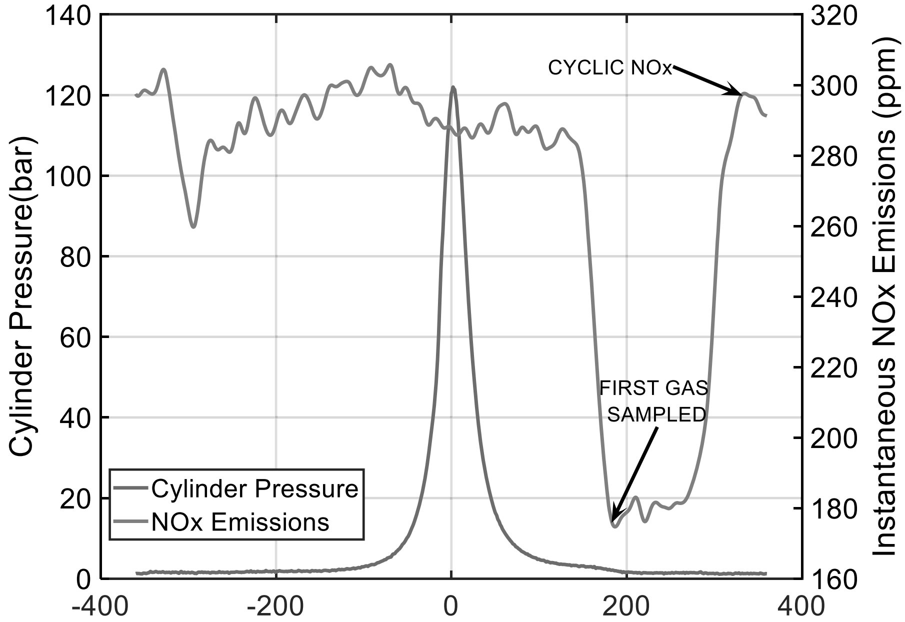

**Figure 3.** NOx emissions as a function of crank angle plotted along with the cylinder pressure trace to highlight the important zones of NOx production in a cycle

## 4. RESULTS AND DISCUSSION

### 4.1 Combustion characteristics during the SOI sweep

**Figure 4** shows the average CA50 as a function of SOI for the sweep performed at 5 bar IMEPg and 80% PES of natural gas. As observed in previous studies with diesel as HRF (cf. [26]), a distinct “switchback” is prevalent when the injection timing advances from – 10 deg aTDC to – 60 deg aTDC. The combustion phasing advances from 15 deg aTDC at -10 deg aTDC SOI to -3 deg aTDC at -30 deg aTDC SOI, indicating that the mixture stratification at those injection timings promotes faster burn rates and shorter ignition delays. However, as the injection timing is advanced from -30 deg aTDC to -60 deg aTDC, CA50 is delayed due to increased mixture homogeneity between air, LRF and HRF, and the unfavorable thermodynamic conditions for ignition within the combustion chamber at SOI. Both aspects cause an increased ignition delay retarding the whole combustion process.

This effect is also usually characterized by the transformation of the ROHR curve from a two – stage profile at late and intermediate injection timings, to a Gaussian single stage profile at early injection timings. Figure 5 shows the ROHR profiles for all the operating points of the SOI sweep, and it is evident that the transformation occurs between -30 deg aTDC SOI to -40 deg aTDC SOI, much like the transformation region observed with diesel – NG dual fuel combustion [35].

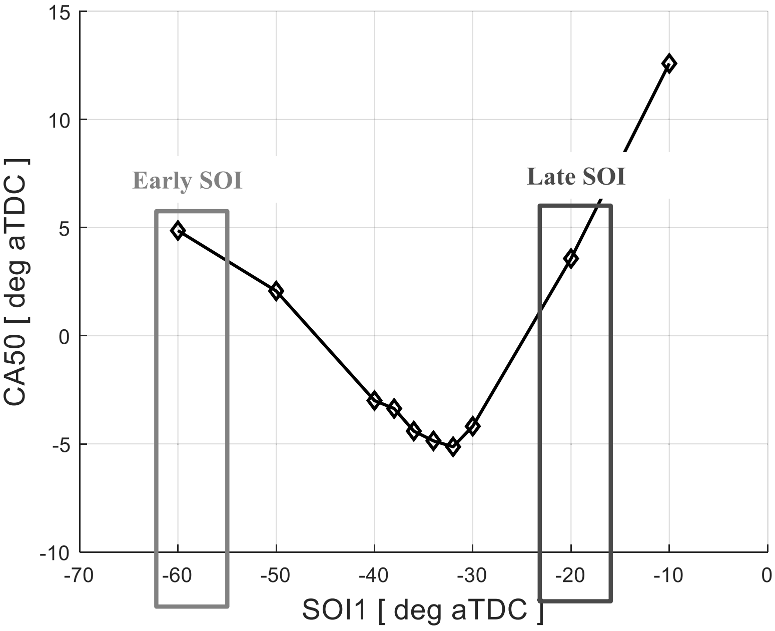

**Figure 4.** Average CA50 vs SOI for P1P - NG dual fuel combustion at low load conditions

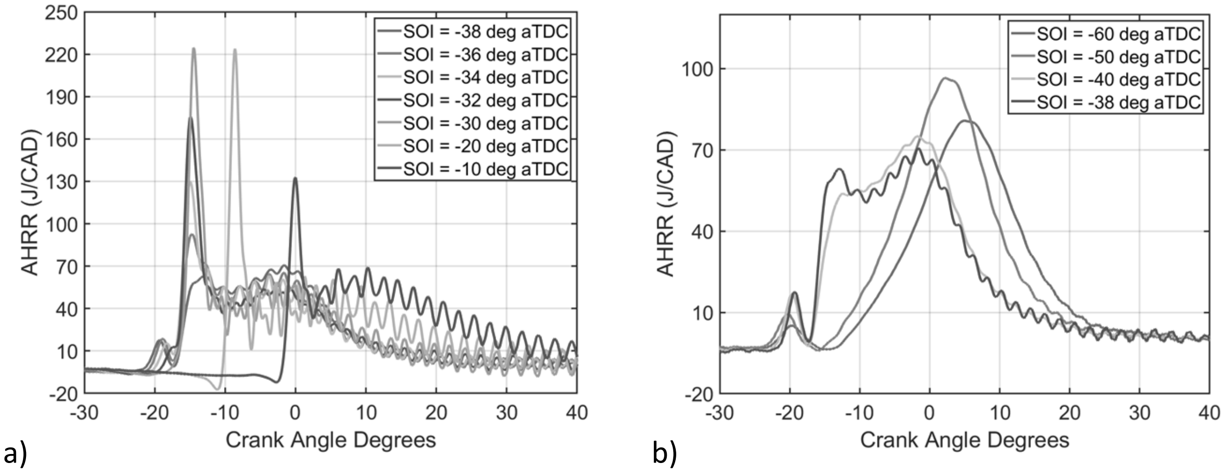

**Figure 5.** ROHR profiles for the SOI sweep for operating conditions with dual stage (A) and single stage (B) heat release profiles.

This transformation is also marked by a significant reduction in NOx emissions, which is caused likely due to the reduced stratification of the mixture at early injection timings, which might lead to lower local temperatures, as discussed in detail in Ref. [35]. **Figure 6** shows the indicated specific HC, CO and NOx emissions for the SOI sweep, highlighting the reduction in ISNOx from ~ 10 g/kWh at -30 deg aTDC SOI to < 0.1 g/kWh at an early injection timing of -50 deg aTDC (note the logarithmic scale for the ISNOx). Another feature of note is the increase in HC and CO emissions as the SOI is advanced, indicating incomplete combustion at these early SOIs. It is also noteworthy that the “near- zero” FSNs were measured using an AVL Smokemeter for all the operating points in this sweep.

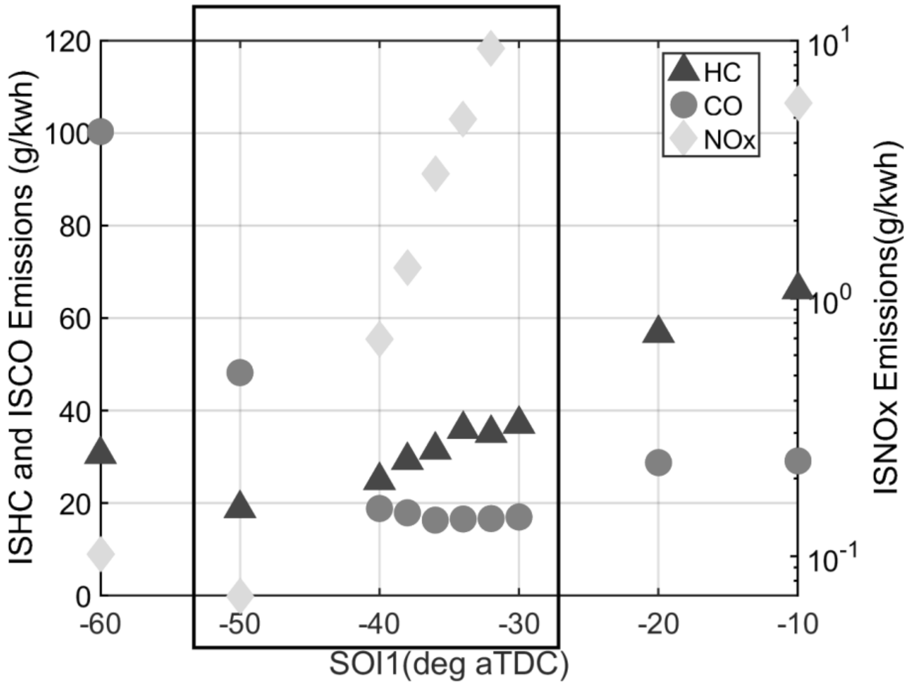

**Figure 6.** Steady state emissions measurements for the SOI sweep from a five - gas emissions bench highlighting the steep reduction in ISNOx (represented in log scale) as SOI advances from -30 deg aTDC to -50 deg aTDC.

**Figure 7** shows the Coefficient of variation (COV) of IMEPg for different SOIs, which was computed from 1000 cycles of experimental data at each SOI using Equation 4:

$$COV\ of\ IMEP_g = 100 * \frac{Standard\ Deviation\ of\ IMEP_g}{Mean\ of\ 1000\ cycles\ IMEP_g} \tag{4}$$

Higher COV of $IMEP_g$ values indicate higher cyclic variations. As the SOI advances from -10 deg aTDC to – 30 deg aTDC, a reduction in COV is observed, and as the SOI further advances the COV increases again. The peak COV of ~7% is observed at -60 deg aTDC SOI, which is likely due to less heterogeneity in fuel mixture reactivity, leading to potential partial misfires. On the other end of the spectrum, at late SOIs, the COV is lower than 5%, indicating more stable engine operation. This can also be attributed to the increased stratification at the late SOIs, where reduced ignition delays and faster burn rates mitigate the occurrence of misfires. The lowest COV, and consequently, the most engine operation is observed at the intermediate SOIs between -30 and -40 deg aTDC, with COV values of ~2%. To further establish the differences in cyclic variations of those operating conditions, ROHR profiles of 1000 cycles are plotted in **Figure 8** for both the late SOI and early SOIs. For the late SOI of -20 deg aTDC, the ROHR profiles show lower ROHR variations compared to the early SOI of ~60 deg aTDC. The first stage heat release profiles show minimal deviation from the ensemble averaged cycle, which is a sign of good combustion stability. The scatter of IMEPg, shown in the IMEP return maps are also more pronounced for the early injection timing than the late timing. From a nominal target IMEPg of 5 bar, the early injection timing had cycles which had a much lower IMEPg (~ 3 bar) and those cycles could be classified as cycles of deterioration. Cycles of deterioration refer to cycles which undergo partial or complete misfire, leading to a very low $IMEP_g$, and cycles of recovery refer to cycles that produce additional power by burning the residual unburnt fuel from a previous cycle of deterioration. These cycles have a much higher $IMEP_g$ than the nominal target value and tend to follow cycles of deterioration. To establish a correlation between HC emissions and $IMEP_g$, a late injection timing (-20 deg aTDC) and an early injection timing (-60 deg aTDC) were selected for further analysis of the crank-resolved fast emissions data, as they corresponded to stable and unstable engine operation, respectively.

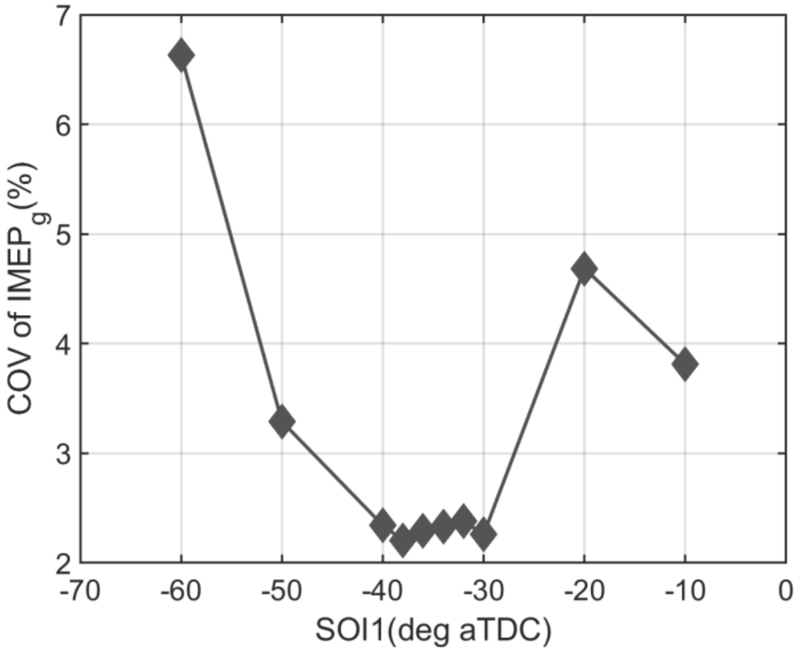

**Figure 7.** Variation of COV of IMEPg with SOI as it is advanced from -10 deg aTDC to -60 deg aTDC

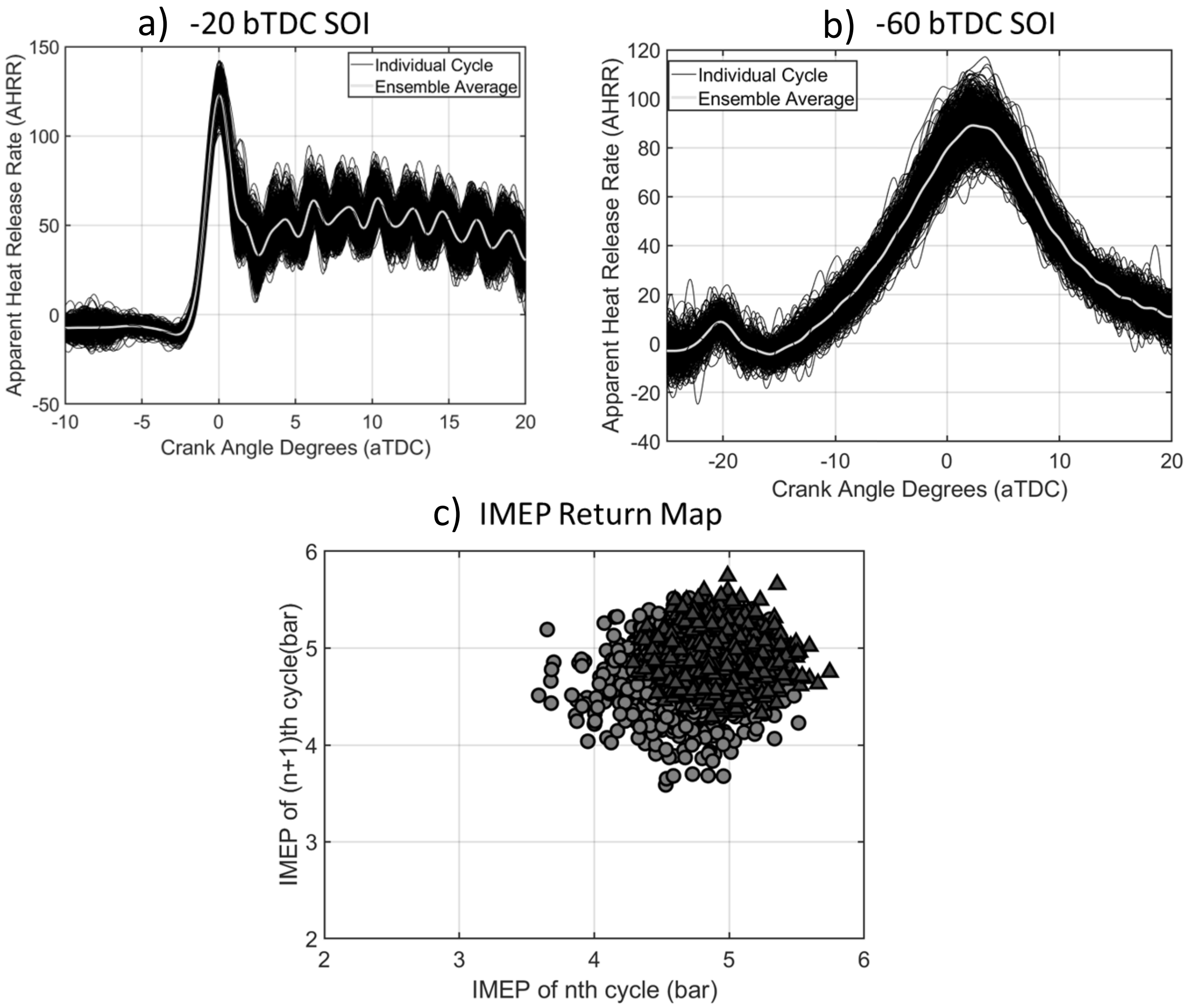

**Figure 8.** Comparison of individual cycle AHRR profiles at both late SOI a), and early SOI b), and the IMEP return maps c) of those SOIs to highlight the differences in cyclic variations of those conditions.

### 4.2 Correlating fast emissions with variations in combustion parameters.

Crank resolved emissions data for 1000 cycles were obtained using Cambustion fast FID and fast CLD analyzers to develop a correlation between HC emissions and $IMEP_g$ fluctuations, and NOx emissions and ROHR. The $\Delta IMEP_g$ and peak ROHR, the two parameters chosen for the correlations, were computed from the pressure data acquired by the cylinder pressure transducer. As specified in the previous sub-section, a late SOI and an early SOI were chosen to compare HC emissions and $\Delta IMEP_g$. **Figure 9.** (a) Net cyclic hydrocarbon emissions for each engine cycle compared with ΔIMEPg for an early and late SOI for P1P - NG dual fuel**Figure 9** shows the distribution of net cyclic hydrocarbon emissions with respect to the change in $IMEP_g$ for P1P – NG dual fuel combustion at -60 deg aTDC and -20 deg aTDC SOI for a nominal $IMEP_g$ of 5 bar. Additionally, the trendline observed for NCHC vs $\Delta IMEP_g$ from diesel – NG combustion investigated in [26] is presented in the image as well. A positive NCHC corresponds to an increased hydrocarbon production from a current cycle compared to the previous cycle, and this occurs predominantly when the $\Delta IMEP_g$ is negative, i.e., when the $IMEP_g$ of the current cycle is significantly lower than the nominal value. These cycles are likely to have had a partial or a complete misfire, and consequently have lower energy released from the cycle, which is reflected in the low IMEPg values. The NCHC emissions are significantly lower (closer to zero), when the $\Delta IMEP_g$ is closer to zero, further confirming that the cycles of deterioration have a likelihood of producing more HC emissions. A linear correlation between cyclic variability in $IMEP_g$ and HC emissions was obtained with an $R^2$ value of 0.92, which was marginally higher than the value obtained with diesel – NG ($R^2 = 0.86$). The slope of the linear correlation was also observed to be steeper for P1P – NG due to the difference in fuel properties, especially the difference in LHV. The zoomed version of the P1P – NG NCHC vs ΔIMEPg plot shown in Figure 9b, indicates that the highest HC production is at the cycles which have the highest deviation from nominal IMEPg. The zoomed-out version is shown in 9 (a) to accommodate the NCHC vs ΔIMEPg linear correlation for diesel – NG, which had ΔIMEPg greater than 4 bar.

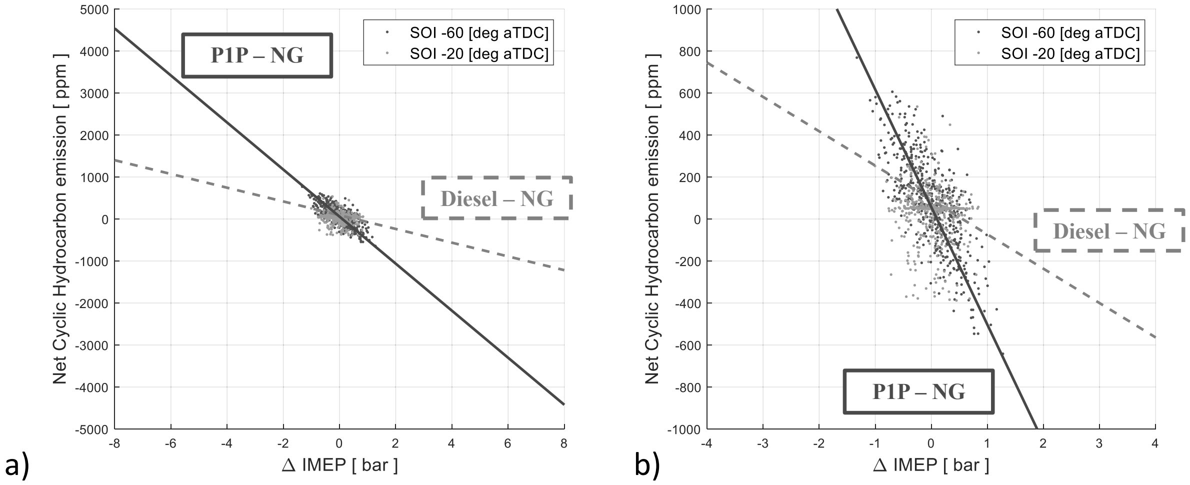

**Figure 9.** (a) Net cyclic hydrocarbon emissions for each engine cycle compared with ΔIMEPg for an early and late SOI for P1P - NG dual fuel combustion and the linear correlation comparison with diesel – NG and (b) a zoomed version of P1P – NG NCHC vs IMEPg scatter plot

However, the H/C ratio of the fuels are significantly different, and the hydrocarbon emissions are primarily dependent on the efficiency of the combustion process and the fuel properties of the HRF and LRF used. These factors necessitated the development of a normalization factor to further bolster the comparison between the NCHC vs $\Delta IMEP_g$ correlation of diesel – NG and P1P – NG. The load and intake pressures (and consequently, the intake mass flowrate) were constant at 5 bar IMEPg and 1.5 bar for both the studies, which enabled the normalization using the H/C ratio of the resulting HRF and LRF mixtures. Equation 5 and Equation 6 estimate the equivalent H/C ratio for the P1P – NG and the diesel – NG mixtures, respectively.

$$HC_{ratio\_eq\,P1P-NG} \approx \dot{m}_{P1P} HC_{ratio\,P1P} + \dot{m}_{NG} HC_{ratio\,NG} \tag{5}$$

$$HC_{ratio\_eq\,d-NG} \approx \dot{m}_{d} HC_{ratio\,d} + \dot{m}_{NG} HC_{ratio\,NG} \tag{6}$$

The NCHC emissions for diesel – NG and P1P – NG are then divided by their respective equivalent H/C ratio, yielding the normalized NCHC emissions shown in **Figure 10**. The slope of the diesel – NG correlation increased marginally with the normalized NCHC values, which range from -100 to 100, but it was still lower than the slope of the P1P – NG correlation. The higher volatility and lower LHV of P1P are potentially the most influential fuel properties for the difference in slope, as it may lead to higher production of HC when a misfire occurs. Nevertheless, advancing the SOI beyond the point where the ROHR transformation occurs from a two-stage profile to a Gaussian profile, led to increased fluctuations in $IMEP_g$, which proved to be the source of greater HC emissions for both diesel – NG and P1P – NG dual fuel combustion at low load conditions.

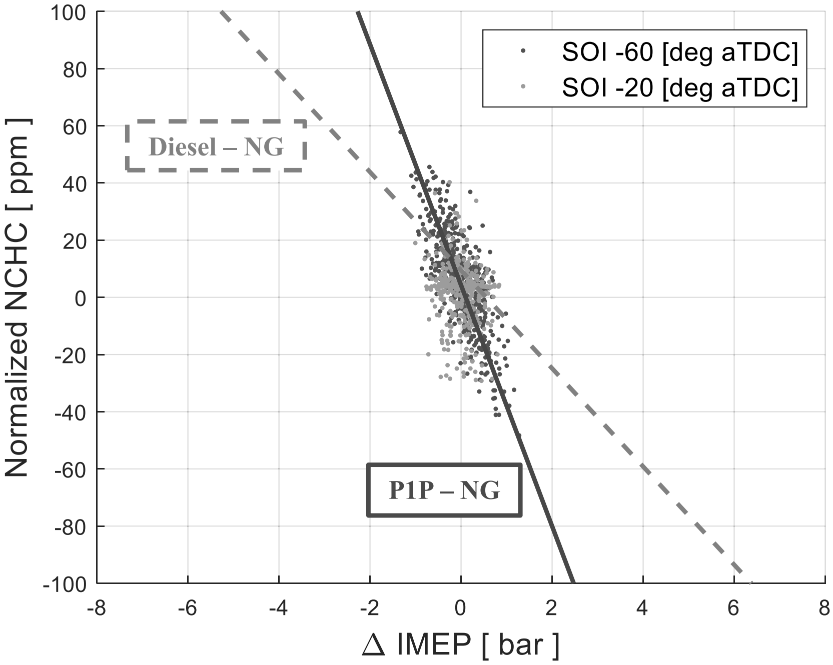

**Figure 10.** Normalized NCHC emissions vs IMEPg for diesel - NG and P1P - NG dual fuel combustion

According to the Zel'dovich mechanism, higher local temperatures are known to be the major contributor to increased NOx emissions and, in many cases, the local temperatures are likely to be higher when higher ROHR is achieved. Another factor that has a direct impact on the local temperatures is the local mixture stratification, and higher NOx emissions are likely at conditions where higher local mixture stratification is present [36, 37]. At late SOIs with dual fuel LTC, higher NOx emissions are expected, and it is confirmed by the linear correlation obtained between peak ROHR and peak NOx emissions shown in **Figure 11**. The peak NOx emissions from each cycle are compared with the peak ROHR for the SOIs which exhibit dual stage ROHR. At early SOIs, when the ROHR shape transforms into the single-stage Gaussian profile, the NOx emissions were too low to obtain a tangible correlation with peak ROHR. The link between NOx emissions and peak ROHR is confirmed by a strong linear correlation with an $R^2$ value more than 0.8. The highest NOx emissions of ~ 520 ppm were observed for cycles which had the highest ROHR of ~ 230 J/CAD for P1P – NG, and those cycles were all from the -30 deg aTDC condition which potentially has the highest stratification. Despite the correlation demonstrated above between peak ROHR and peak NOx emissions, it is important to remember that correlation does not always imply causation, especially between ROHR and NOx emissions. It must be noted that NOx is exponentially dependent on local temperatures, which are more dependent on local mixture stratification than ROHR, which is a more "global" calculated parameter from the entire cylinder pressure history.

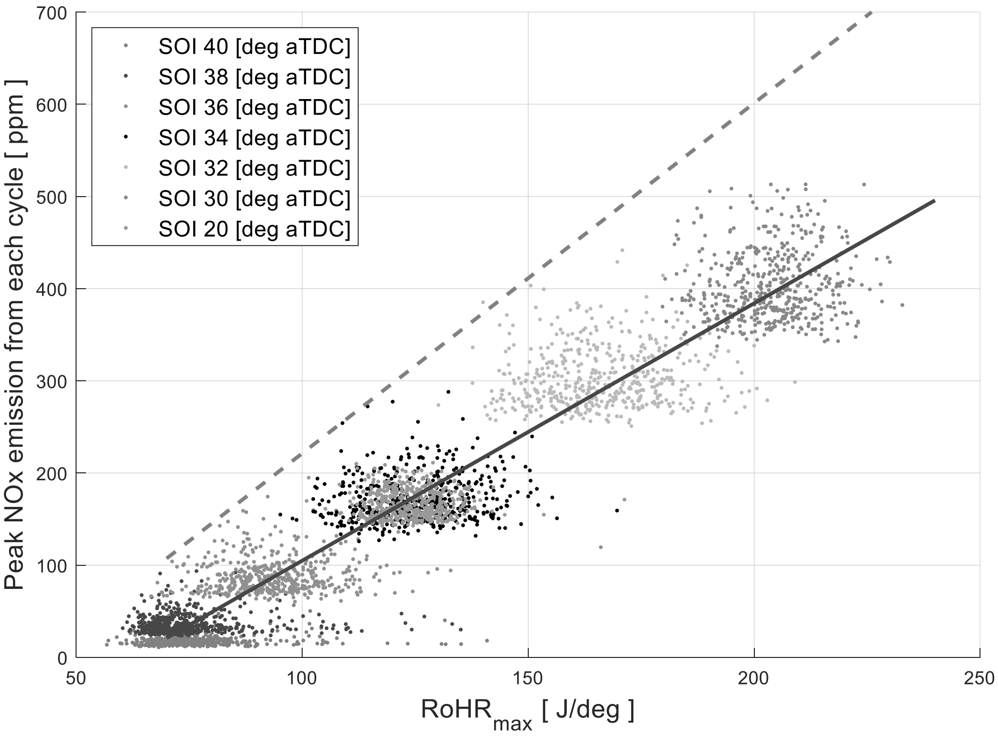

**Figure 11.** The linear correlation obtained between cycle resolved NOx emissions with cyclic peak ROHR at late SOIs for P1P – NG dual fuel combustion.

As with the HC emissions, the difference in fuel properties of diesel – NG and P1P – NG calls for a normalization to bolster the comparison of the correlation between NOx and ROHR. Since the LHV of P1P is significantly lower than that of diesel, this property was chosen to normalize the ROHR. The PES of both diesel and P1P were kept constant throughout the studies at 20%, with 80% of the energy provided by NG. Then the peak of RoHR can be normalized by the ratio of the LHV of the considered HRFs (diesel and P1P) obtaining the diesel equivalent-RoHRmax, as reported in Equation 7. The diesel equivalent ROHR-max was computed to eliminate the effect of fuel properties while comparing the NOx vs ROHR correlation for diesel – NG and P1P – NG dual fuel RCCI combustion and does not represent a physical/thermodynamic property of the fuel.

$$RoHR_{max\,d\_eq} \approx \frac{LHV_{diesel}}{LHV_{P1P}} RoHR_{max\,P1P} \tag{7}$$

**Figure 12** shows the correlation between NOx emissions and peak ROHR similar to Figure 11, with the addition of the P1P – NG diesel equivalent correlation. Both diesel – NG and P1P – NG combustion exhibit higher NOx production tendencies at SOIs which have two stage ROHR profiles. The slope of the linear correlation and the $R^2$ values are almost identical for both the fuel combinations, meaning that the shape of ROHR (and SOI consequently) impacts on the emissions with the same dynamics.

### 4.3 Tradeoffs in P1P – NG dual fuel combustion at Low Loads

The previous section highlighted the dependency of NOx and HC emissions on combustion parameters like $IMEP_g$ and ROHR for a single injection SOI sweep of P1P – NG dual fuel combustion, and it was observed that the late SOIs which had the tendency to produce low HC emissions, also resulted in high NOx emissions, and vice versa for the early SOIs. Various strategies that could be implemented to mitigate high HC emissions from dual fuel RCCI combustion of diesel – NG (low loads) and P1P – NG have been discussed in the literature [25, 30]. Similar strategies were adopted in this work to identify a better engine operating point at low load conditions (5 bar IMEPg) for P1P – NG dual fuel RCCI combustion, and the tradeoffs that were observed between engine performance and emissions are discussed in this section. Table 5 presents the engine operating parameters for the various sweeps presented in this section. The SOI1 for all the points were kept constant and -50 deg aTDC.

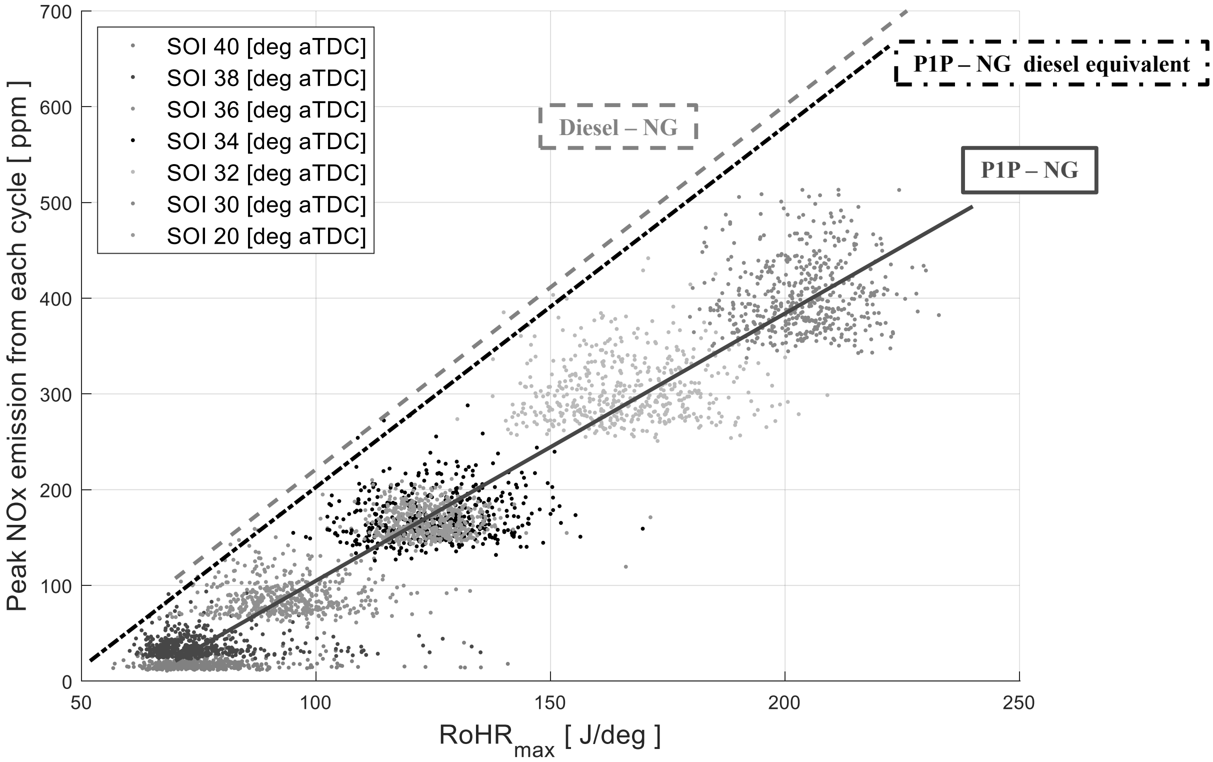

**Figure 12**. NOx vs $ROHR_{max}$ for 1000 cycles at SOIs ranging from -20 deg aTDC and -40 deg aTDC for P1P – NG dual fuel combustion at low loads. Additionally, the correlation for diesel – NG (magenta) and the diesel equivalent of P1P – NG dual fuel combustion (black) is shown for comparison.

**Table 4**. Operating points investigated in the single parameter sweep for P1P - NG combustion at 5 bar IMEPg

| **SOI2 Sweep** | | | | |
|---|---|---|---|---|
| **S.No** | **SOI 2 (deg aTDC)** | **PES of NG (%)** | **$P_{intake}$ (bar)** | **$P_{rail}$ (bar)** |
| 1 | -60 | 80 | 1.5 | 500 |
| 2 | -40 | 80 | 1.5 | 500 |
| 3 | -30 | 80 | 1.5 | 500 |
| 4 | -20 | 80 | 1.5 | 500 |
| 5 | -10 | 80 | 1.5 | 500 |
| 6 | 0 | 80 | 1.5 | 500 |
| **PES Sweep** | | | | |
| **S.No** | **SOI 2 (deg aTDC)** | **PES of NG (%)** | **$P_{intake}$ (bar)** | **$P_{rail}$ (bar)** |
| 1 | -40 | 50 | 1.5 | 500 |
| 2 | -40 | 60 | 1.5 | 500 |
| 3 | -40 | 65 | 1.5 | 500 |
| 4 | -40 | 70 | 1.5 | 500 |
| 5 | -40 | 85 | 1.5 | 500 |
| **Rail Pressure Sweep** | | | | |
| **S.No** | **SOI 2 (deg aTDC)** | **PES of NG (%)** | **$P_{intake}$ (bar)** | **$P_{rail}$ (bar)** |
| 1 | -40 | 70 | 1.5 | 300 |
| 2 | -40 | 70 | 1.5 | 700 |
| 3 | -40 | 70 | 1.5 | 900 |
| 4 | -40 | 70 | 1.5 | 1000 |
| 5 | -40 | 70 | 1.5 | 1200 |
| **Intake Pressure Sweep** | | | | |
| **S.No** | **SOI 2 (deg aTDC)** | **PES of NG (%)** | **$P_{intake}$ (bar)** | **$P_{rail}$ (bar)** |
| 1 | -40 | 70 | 1 | 1000 |
| 2 | -40 | 70 | 1.1 | 1000 |
| 3 | -40 | 70 | 1.26 | 1000 |
| 4 | -40 | 70 | 1.73 | 1000 |

Steady state emissions data and engine performance data were compared for each operating point to arrive at a tradeoff for a high efficiency, low emissions operating condition. **Figure 13** shows the indicated specific HC and CO tradeoffs with indicated specific NOx for all the operating points in the single parameter sweep. Spray Targeted Reactivity Stratification (STARS) was achieved by splitting the single injection and adding a second injection, which was swept from -60 deg aTDC to 0 deg aTDC. It was observed that close coupled injections were effective in reducing HC compared to the single injection SOI sweep, whereas an early first injection followed by a second injection close to TDC (i.e., “long dwell” injections) introduced more cyclic variability and consequently higher HC and CO emissions. The long dwell injection strategy also caused an increase in NOx emissions, and they were not chosen for optimizing the PES. The PES of NG was swept from 50 – 85% at injection timings of -50 deg aTDC and -40 deg aTDC, and it was observed that a lower PES of NG yielded lower ISHC emissions. The higher HRF quantities at lower PES enhances mixture stratification and promotes more complete combustion, resulting in lower HC emissions. ISHC emissions reduced from a baseline of 30 g/kWh for the single injection at -50 deg aTDC and 80% PES to 8 g/kWh at 50% PES and with STARS. Moreover, ISCO emissions also reduced by almost 50% at 50% PES when compared to the single injection baseline. However, the increased stratification is also likely to cause higher local temperatures and hence higher NOx emissions. A PES of 70% was chosen to proceed with the rail pressure and intake pressure sweep. Increased rail pressure contributed to reducing the ISNOx emissions at 70% PES operating condition from < 5 g/kWh to ~ 0.9 g/kWh, as higher rail pressures are likely to cause enhanced turbulent mixing, which reduces local stratification, leading to NOx reduction. Lower intake pressures at these higher injection pressures, on the other hand, promoted greater stratification and yielded the best efficiency-emissions tradeoff at low load. When the intake pressure was reduced, from 1.5 bar to 1 bar, ISHC and ISCO emissions decreased below 10 g/kWh, while the ISNOx emissions were maintained < 1 g/kWh. The operating condition which represented the best emissions tradeoff is marked with a red circle in Figure 13.

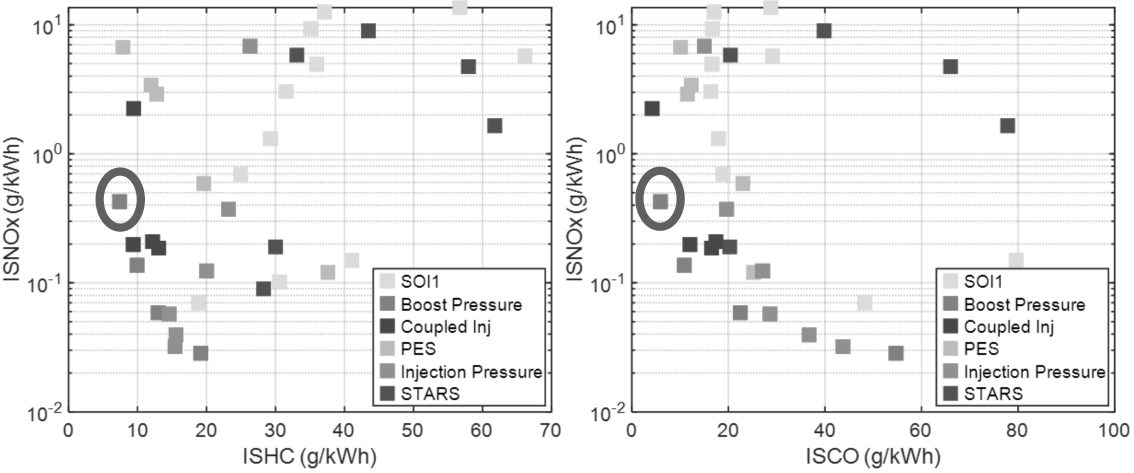

**Figure 13.** Indicated Specific HC and CO tradeoffs with Indicated specific NOx for P1P - NG dual fuel combustion at low loads.

**Figure 14** shows the indicated fuel conversion efficiency (IFCE) plotted against maximum pressure rise rate (MPRR) for the various single parameter sweeps of P1P – NG dual fuel combustion at low load conditions. Single injection SOI close to TDC and an SOI2 close to TDC yielded IFCEs < 30%, likely due to the suboptimal combustion phasing at those conditions. As the SOI and SOI2 were maintained in the region where single-stage Gaussian heat release can be obtained, IFCEs > 35% were observed. Closer to TDC injections also increased the MPRR which were close to the onset of knock and made the engine operation rougher. The peak IFCE of ~46% was observed at the lowest intake pressure of 1 bar, which had closed coupled injections with SOIs at -50 deg aTDC and -40 deg aTDC. The PES and injection pressure were maintained at 70% and 1000 bar respectively, and this point was also observed to offer an optimal emissions tradeoff. The CA50 of this operating condition was observed at 362 CAD, which is optimal for higher fuel conversion efficiencies, and the MPRR was < 5 bar/CAD which was well below the onset of knock limit for this engine. The low HC emissions and COV of IMEPg also indicate that this operating point guarantees good engine stability.

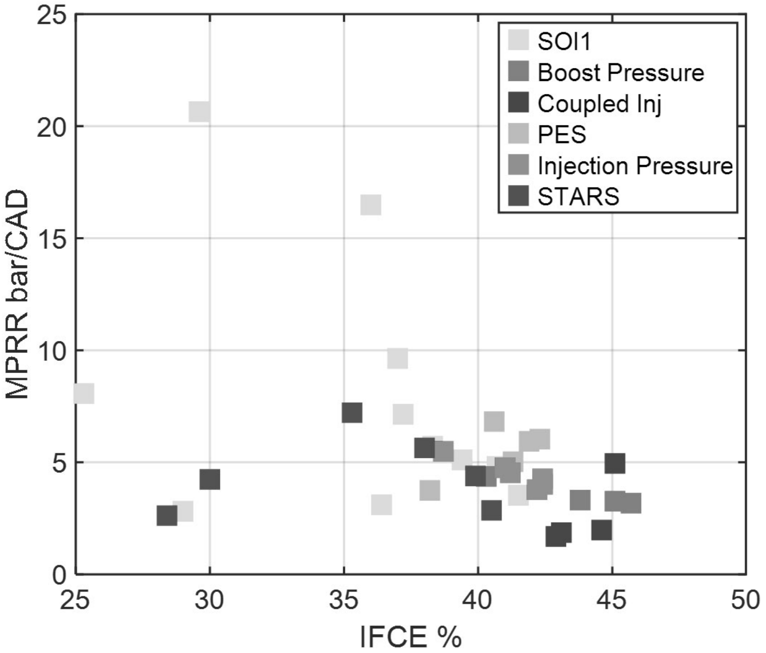

**Figure 14.** Indicated Fuel Conversion Efficiency (IFCE) vs MPRR tradeoff for P1P – GN dual fuel combustion at low loads.

## 5. CONCLUSIONS

An experimental investigation on the impact of cyclic combustion variations on unburned hydrocarbon (HC) and oxides of nitrogen (NOx) emissions was performed on a heavy-duty single cylinder engine, operating in the dual fuel RCCI mode with P1P as the HRF and NG as the LRF. Cycle resolved emissions from CAMBUSTION fast FID and fast NOx analyzers were obtained for 1000 engine cycles along with cylinder pressure data at each operating point for an SOI sweep ranging from – 10 deg aTDC to -60 deg aTDC. A two-stage ROHR was observed at late SOIs, like diesel – NG, and the transition from two-stage ROHR to single-stage Gaussian ROHR profiles occurred between -30 deg aTDC and -40 deg aTDC SOIs. Indicated specific NOx emissions significantly reduced as the SOI was advanced, but on the other hand, ISHC emissions were found to be higher from SOI -40 deg aTDC to -60 deg aTDC. Engine stability was also negatively impacted at early SOIs as COV of IMEPg increased to 7% at -60 deg aTDC.

A direct linear correlation was obtained between fluctuations in IMEPg and HC emissions, by comparing the net hydrocarbon emissions (NCHC) for each cycle with changes in IMEPg. The $R^2$ value obtained for P1P – NG dual fuel combustion was found to be marginally higher than the $R^2$ of diesel – NG combustion, indicating a stronger correlation between HC and ΔIMEPg. The HC emissions were normalized with respect to the differences in the H/C ratio of the fuels to achieve a more rational comparison, and from this the slope of the P1P – NG combustion was found to be steeper than that of the diesel – NG combustion. More unburned (NG) fuel emitted during misfiring cycles from P1P-NG combustion was likely a major contributor to the steeper slope.

At late injection timings, where the peak ROHR was observed to be high, higher NOx emissions were prevalent likely due to the increased local temperatures. A linear correlation between ISNOx emissions and peak ROHR was observed for P1P – NG dual fuel combustion similar diesel – NG combustion. For the NOx correlation, the normalization factor was based on the LHV of the fuels, as the lower heating value of P1P was 26% lower than that of diesel. At early injection timings, ISNOx emissions were too low to obtain a tangible correlation with peak ROHR.

Varying the single injection timings from close to TDC injection to early injection aided in ISNOx reduction but at the expense of higher HC emissions. To obtain a fruitful tradeoff between emissions and efficiency, a detailed single parameter sweep was performed at 5 bar IMEPg. A high injection pressure close coupled injection, with a slightly lower PES of NG, and intake pressure near atmospheric conditions yielded the best HC vs NOx tradeoff and the highest IFCE observed at low load conditions for P1P – NG dual fuel combustion. The optimal operating conditions and performance and emissions results for 5 bar IMEPg and 1339 RPM for this engine are summarized in Table 6.

**Table 5.** Operating conditions which yielded the optimum emissions-efficiency tradeoff from the single parameter sweep of P1P – NG RCCI combustion at low loads.

| Parameter | Value |
|---|---|
| **SOI 1 (deg aTDC)** | -50 |
| **SOI 2(deg aTDC)** | -40 |
| **PES (%)** | 70 |
| **$P_{intake}$ (bar)** | 1 |
| **$P_{rail}$ (bar)** | 1000 |
| **ISHC (g/kWh)** | ~8 |
| **ISNOx (g/kWh)** | ~0.8 |
| **ISCO (g/kWh)** | ~ 5 |
| **IFCE (%)** | ~46 |
| **MPRR (bar/CAD)** | 2.5 |
| **COV of IMEPg (%)** | 1.8 |

## 6. ACKNOWLEDGMENTS

This paper was developed based on funding from the Alliance for Sustainable Energy, LLC, Managing and Operating Contractor for the National Renewable Energy Laboratory for the U.S. Department of Energy (Prime Award # DE-AC36-08GO28308; Subaward # NHQ-9-82305-01). The authors gratefully acknowledge Prof. Paul Puzinauskas of The University of Alabama for his assistance with the Cambustion fast NOx and fast FID analyzers and Prof. Bret Windom of Colorado State University for providing the team with the P1P fuel used in these experiments.

## 7. REFERENCES

1. Federal Highway Administration, *Highway Statistics 2021,* 2022, Table VM-1.
2. Environmental Protection Agency, *Average In-Use Emissions from Heavy-Duty Trucks - Emission Facts*, 2021, Table 1.
3. Thring, R. Homogeneous-Charge Compression-Ignition (HCCI) Engines; SAE Technical Paper 892068; SAE: Warrendale, PA, USA, 1989.
4. Christensen, M., Johansson, B. Supercharged Homogeneous Charge Compression Ignition (HCCI) with Exhaust Gas Recirculation and Pilot Fuel; SAE Technical Paper 2000-01-1835; SAE: Warrendale, PA, USA, 2000.
5. Imamoto, T.; Kawahara, N.; Tomita, E. PREMIER combustion characteristics of a pilot fuel-ignited dual-fuel biogas engine with consideration of cycle-to-cycle variations. Fuel 2022, 314, 123049.
6. Azimov, U.; Tomita, E.; Kawahara, N.; Harada, Y. Premixed mixture ignition in the end-gas region (PREMIER) combustion in a natural gas dual-fuel engine: Operating range and exhaust emissions. Int. J. Engine Res. 2011, 12, 484–497.
7. Shin, J.; Choi, J.; Seo, J.; Park, S. Pre-chamber combustion system for heavy-duty engines for operating dual fuel and diesel modes. Energy Convers. Manag. 2022, 255, 115365.

8. Salahi, M.M.; Esfahanian, V.; Gharehghani, A.; Mirsalim, M. Investigating the reactivity-controlled compression ignition (RCCI) combustion strategy in a natural gas/diesel fueled engine with a pre-chamber. Energy Convers. Manag. 2017, 132, 40–53
9. Cung, K., Buffaloe, G., Briggs, T., Bitsis, C. et al., Engine and Emissions Performance of Renewable Diesel in a Heavy-Duty Diesel Engine: A Single-cylinder Engine Experiment, SAE Technical Paper 2023-01-0273, 2023, https://doi.org/10.4271/2023-01-0273.
10. Reitz, R.D., Duraisamy, G., Review of high efficiency and clean reactivity-controlled compression ignition (RCCI) combustion in internal combustion engines, Progress in Energy and Combustion Science, Volume 46, 2015, Pages 12-71, ISSN 0360-1285, https://doi.org/10.1016/j.pecs.2014.05.003.
11. Li, Y., Jia, M., Liu, Y., Xie, M., Numerical study on the combustion and emission characteristics of a methanol/diesel reactivity controlled compression ignition (RCCI) engine, Applied Energy, Volume 106, 2013, Pages 184-197, ISSN 0306-2619, https://doi.org/10.1016/j.apenergy.2013.01.058.
12. Benajes, J., Molina, S., García, A., Belarte, E., Vanvolsem, M., An investigation on RCCI combustion in a heavy-duty diesel engine using in-cylinder blending of diesel and gasoline fuels, Applied Thermal Engineering, Volume 63, Issue 1, 2014, Pages 66-76, ISSN 1359-4311, https://doi.org/10.1016/j.applthermaleng.2013.10.052.
13. Benajes, J., Molina, S., García, A., Monsalve-Serrano, J., Effects of direct injection timing and blending ratio on RCCI combustion with different low reactivity fuels, Energy Conversion and Management, Volume 99, 2015, Pages 193-209, ISSN 0196-8904, https://doi.org/10.1016/j.enconman.2015.04.046.
14. Silvagni, G.; Ravaglioli, V.; Falfari, S.; Ponti, F.; Mariani, V. Development of a Control-Oriented Ignition Delay Model for GCI Combustion. *Energies (Basel)* **2022**, *15*, 6470, doi:10.3390/en15176470.
15. Liu, X., Zhong, W., Jiang, P., Dai, L., He, Z., Wang, Q., Optimizing RCCI combustion for improved engine performance under low load conditions: Impact of low-reactivity fuel and direct injection timing, Fuel, Volume 351, 2023, 128871, ISSN 0016-2361, https://doi.org/10.1016/j.fuel.2023.128871.
16. Hariharan, D., Krishnan, S.R., Srinivasan, K.K, Sohail, A., Multiple injection strategies for reducing HC and CO emissions in diesel-methane dual- fuel low temperature combustion, Fuel, Volume 305, 2021, 121372, ISSN 0016-2361, https://doi.org/10.1016/j.fuel.2021.121372.
17. Dworschak, P., Berger, V., Härtl, M., and Wachtmeister, G., Neat Oxymethylene Ethers: Combustion Performance and Emissions of OME2, OME3, OME4 and OME5 in a Single-Cylinder Diesel Engine, SAE Technical Paper 2020-01-0805, 2020,doi:10.4271/2020-01-0805.
18. Iannuzzi, S.E., Barro, C., Boulouchos, K., and Burger, J., Combustion Behavior and Soot Formation/Oxidation of Oxygenated Fuels in a Cylindrical Constant Volume Chamber, Fuel 167:49-59, 2016, doi:10.1016/j. fuel.2015.11.060.
19. Härtl, M., Seidenspinner, P., Jacob, E., and Wachtmeister, G., Oxygenate Screening on a Heavy-Duty Diesel Engine and Emission Characteristics of Highly Oxygenated Oxymethylene Ether Fuel OME1, Fuel 153:328-335, 2015, doi:10.1016/j.fuel.2015.03.012.
20. Benajes, J., Garcia,A., Monsalve-Serrano, J., Potential of using OMEx as substitute of diesel in the dual-fuel combustion mode to reduce the global CO2 emissions, Transportation Engineering, Volume 1, 2020, 100001, ISSN 2666-691X, https://doi.org/10.1016/j.treng.2020.01.001.
21. Garcia, A., Monsalve-Serrano, J., Villalta, D., Sari., R., et.al., Potential of e-Fischer Tropsch diesel and oxymethyl-ether (OMEx) as fuels for the dual-mode dual-fuel concept, 2019, Applied Enery (253), https://doi.org/10.1016/j.apenergy.2019.113622.
22. Garcia, A., Antonio, G., Monsalve-Serrano, J., Sari., R., Martínez-Boggio, S., OMEx-diesel blends as high reactivity fuel for ultra-low NOx and soot emissions in the dual-mode dual-fuel combustion strategy, 2020., Fuel. 275. 117898. 10.1016/j.fuel.2020.117898.
23. Omari, A., Heuser, B., Pischinger, S., Potential of oxymethylenether-diesel blends for ultra-low emission engines, 2017,. Fuel. 209. 232-237. 10.1016/j.fuel.2017.07.107.
24. Benajes J., Garcia A., Monsalve-Serrano J., Sari R., Clean and efficient dual-fuel combustion using OMEx as high reactivity fuel: Comparison to diesel-gasoline calibration, Energy Convers Manage, 216 (2020), Article 112953

25. Hariharan, D. , Partridge, K. , Narayanan, A. , Srinivasan, K. , Krishnan, S. R. , and Anandaraman, N. , 2022, Strategies for Reduced Engine-Out HC, CO, and NOx Emissions in Diesel-Natural Gas and POMDME-Natural Gas Dual-Fuel Engine, https://doi.org/10.4271/2022-01-0460.
26. Silvagni, G., Narayanan, A., Ravaglioli, V., Srinivasan, K.K, Krishnan ,S.R., Collins N., Puzinauskas P., Ponti F., Experimental Characterization of Hydrocarbons and Nitrogen Oxides Production in a Heavy-Duty Diesel–Natural Gas Reactivity-Controlled Compression Ignition Engine. Energies. 2023; 16(13):5164. https://doi.org/10.3390/en16135164
27. Narayanan, A., Hariharan, D., Krishnan, S., and Srinivasan, K., An Experimental Comparison of Cyclic Variations in Diesel–Natural Gas and POMDME–Natural Gas Dual Fuel Combustion, ASME. J. Eng. Gas Turbines Power. October 2023; 145(10): 101005. https://doi.org/10.1115/1.4062901
28. Lucas, S. P., Chan, F. L., Fioroni, G. M., Foust, T. D., Gilbert, A., Luecke, J., McEnally, C. S., Serdoncillo, J. J., Zdanowicz, A. J., Zhu, J., & Windom, B. (2022). Fuel properties of oxymethylene ethers with terminating groups from methyl to butyl. Energy & Fuels, 36(17), 10213–10225. https://doi.org/10.1021/acs.energyfuels.2c01414
29. Bartholet, D. L.; Arellano-Treviño, M. A.; Chan, F. L.; Lucas, S.; Zhu, J.; St. John, P. C.; Alleman, T. L.; McEnally, C. S.; Pfefferle, L. D.; Ruddy, D. A.; Windom, B.; Foust, T. D.; Reardon, K. F. Property predictions demonstrate that structural diversity can improve the performance of polyoxymethylene ethers as potential bio-based diesel fuels, 2021, Fuel, 295, 120509, DOI: 10.1016/j.fuel.2021.120509.
30. Narayanan, A., Mundy, S., Thothadri, H., Gray, J., Baskara Babu, Y., Lucas, S., Windom, B., Krishnan, S., Srinivasan, K., Propyl Oxymethylene Ether-Ignited Natural Gas Dual Fuel Rcci Combustion – A Low Carbon Pathway for High Efficiencies and Low Emissions, ASME ICE Forward Conference 2023, ICEF2023-110454. https://doi.org/10.1115/ICEF2023-110454.
31. Peckham, M.; Hands, T.; Burrell, J.; Collings, N.; Schurov, S. Real Time In-Cylinder and Exhaust NO Measurements in a Production SI Engine; SAE Technical Paper 980400; SAE: Warrendale, PA, USA, 1998.
32. Leach, F., Davy, M., and Peckham, M. , Cycle-to-Cycle NO and NOx Emissions from a HSDI Diesel Engine, ASME. J. Eng. Gas Turbines Power. August 2019; 141(8): 081007.
33. Puzinauskas, P. V., Olsen , D. B., and Willson, B. D., Cycle-Resolved NO Measurements in a Two-Stroke Large-Bore Natural Gas Engine, ASME. J. Eng. Gas Turbines Power. April 2004; 126(2): 429–441. https://doi.org/10.1115/1.1635401
34. Heywood, J. Internal Combustion Engine Fundamentals; McGraw-Hill Education: New York, NY, USA, 1988.
35. Partridge, K.; Jha, P.; Srinivasan, K.; Krishnan, S. An experimental and computational analysis of combustion heat release transformation in dual fuel combustion, 2023, Fuel, 341, 127561.
36. Narayanan, A.; Hariharan, D.; Partridge, K.R.; Pearson, A.L.; Srinivasan, K.K.; Krishnan, S.R. Impact of Low Reactivity Fuel Type and Energy Substitution on Dual Fuel Combustion at Different Injection Timings. Energies 2023, 16, 1807. https://doi.org/10.3390/en16041807
37. Silvagni G., Moro D., Ravaglioli V., Ponti F., Corti E., Brusa A., Cavina N., Narayanan A., Srinivasan K. K., Krishnan S. R., “Analysis of the Vibrational Behavior of dual-fuel RCCI combustion in a Heavy-Duty Compression Ignited Engine fueled with Diesel-NG at Low Load”, J. Phys.: Conf. Ser., https://doi.org/10.1088/1742-6596/2648/1/012077.

# Performance and Regulated Emissions from Agricultural Engines Using 100% Renewable Fuel Hydrotreated Vegetable Oil (HVO)

F. Oliva[1], D. Donoso[1], J.A. Soriano[2], R. García-Contreras[2], O. Armas[2]

[1]Repsol Technology Lab, C/ Agustín de Betancourt s/n, Móstoles 28935, Spain

E-mail: david.donoso@repsol.com
Telephone: +(34) 638 339 173

[2]Universidad de Castilla-La Mancha, Campus de Excelencia Internacional en Energía y Medioambiente, Escuela de Ingeniería Industrial y Aeroespacial de Toledo, Real Fábrica de Armas, Edif. Sabatini, Av. Carlos III, s/n, Toledo 45071, Spain

E-mail: mariareyes.garcia@uclm.es
Telephone: +(34) 925 268 800

**Abstract.** Renewable liquid fuels are a sustainable alternative to power the agricultural sector, where electrification is still not possible. Hydrotreated vegetable oil, also known as HVO, is a potential drop-in biofuel to be used in heavy-duty engines. In this work, the performance and regulated emissions from two modern agricultural engines using pure HVO fuel and conventional diesel fuel were studied. Both agricultural engines comply with the latest EU Stage V / US Tier 4 emission regulation with different after-treatment system configurations, with and without using EGR system. In both technologies, similar engine performance was obtained with both fuels and reductions in mass fuel consumption were observed when using HVO fuel with respect to diesel fuel, being these reductions wider in the engine without EGR. When testing in the engine with EGR system, HVO fuel led to slightly higher engine out $NO_x$ emissions, because of its higher cetane number and the lower EGR rate, and lower opacity, due to the lower aromatic content and higher H/C ratio, compared to diesel fuel. When testing in the engine without EGR system, the trend in $NO_x$ and particle emissions is the opposite with respect to the engine with EGR, highlighting the trade-off between these emissions. Thus, different engine after-treatment system configurations and control strategies affect to HVO combustion performance and pollutant emissions formation, opening the possibility of further engine control improvements when using HVO fuel.

## 1. Introduction

Greenhouse gas emissions (mainly $CO_2$, and also $CH_4$ and $N_2O$) derived from combustion engines increase the climate change. Other pollutants ($NO_x$, THC, particle matter, carbonyls, and PAHs, among others) from combustion engines and further secondary reactions in atmosphere entail a big problem for human health. Several emission regulations have been approved to solve this global problem. In Europe, Stage V emission standard, formally adopted from Regulation (EU) 2016/1628 [1], apply to off-highway diesel engines used in non-road mobile machinery. This Stage V is the world's most tight emissions standard for these engines, even more than US Tier 4 standards. Both emission standards establish limits for gaseous emissions (CO, HC, $NO_x$) and particle emissions (PM, PN), depending on the engine power. In order to comply these limits, OEMs usually design after-treatment systems based on a combination of diesel oxidation catalyst (DOC), diesel particle filter (DPF) and selective catalyst reduction (SCR) system, in addition to exhaust gas recirculation (EGR) [2]. However, different configurations are used rather than the main trend (with all systems), such as full $NO_x$ emissions control with SCR system and without EGR system [3].

Agricultural vehicles are included within heavy-duty vehicles (HDVs), which are responsible for over 6 % of total GHG emissions in the European Union [4]. In the agriculture sector, $CO_2$ emissions from energy combustion (off-road vehicles, among others) are considered as a key source of agricultural emissions included in GHG inventories, apart from $CO_2$ from land use and methane ($CH_4$) and nitrous oxide ($N_2O$) from livestock and agricultural soils [5]. Thus, despite an exemption to the $CO_2$ reduction targets is applied to the heavy-duty vehicles used for agricultural purposes, incorporation of renewable fuels is a way of decarbonization. In this way, circular economy is promoted, using agricultural wastes for energy purposes.

Traditionally, fatty acid methyl ester (FAME), also called as biodiesel fuel, coming from transesterification of vegetable oil and/or animal fats has been used to partially substitute diesel fuel. However, hydrotreated vegetable oil (HVO) is a paraffinic advanced biofuel that has been tested as a better potential alternative, either in production costs, fuel compatibility with engine parts [6] or fuel properties, such as heating value, cetane number, cold flow properties, viscosity and oxidation stability [7][8]. Nowadays, some OEMs accept the use of 100 % HVO fuel in modern engines since HVO can completely replace diesel fuel without the need of doing engine changes complying the standard EN 15940, thus constituting a drop-in fuel [9]. Also, HVO fuel can be an advanced biofuel as established in Renewable Energy Directive 2018/2001 whether it is produced from raw materials included in Annex IX, part A [10].

For instance, the renewable fuel HVO used as drop-in fuel in diesel vehicles usually reports lower mass fuel consumption (2-5 % reduction) with respect to diesel fuel [11] due to its higher LHV in mass basis (typically, 44 vs 43 MJ/kg) [12], although higher volumetric fuel consumption (3-4 % increase) due to its lower density (typically, 765-800 vs 820-845 kg/m$^3$) [13]. In addition, slightly higher engine performance is typically obtained with HVO fuel due to its higher cetane number (>70 vs >51) [14] and practically nil oxygen content [15], in comparison with diesel fuel (which is usually blended with biodiesel). In overall, HVO fuel can reduce well-to-wheel $CO_2$ emission up to 90 % compared to diesel fuel [16], and up to 100 % $CO_2$ equivalent reduction, considering other production processes of renewable paraffinic diesel fuel according to the standard EN 15940 [17].

Related to gaseous and particle emissions, HVO fuel allows to significantly reduce CO [11][18] and HC [13][14] emissions with respect to diesel fuel, due to the higher cetane number and better ignition capability of this renewable diesel fuel [19][20]. Also, particulate matter is notably reduced when HVO fuel is used instead of diesel fuel [11][23], due to the nil aromatic content of HVO fuel because benzenic rings act as soot precursors [20][21]. However, a clear tendency in particle number emissions between HVO and diesel fuels remains unknown [11][18], because the effect of nil aromatic content is compensated with the high cetane number of HVO fuel, which implies higher local fuel/air ratio in premixed flames, as well as higher diffusive combustion [22]. On the other hand, differences in $NO_x$ emissions are also unclear [19], alternating between increase [14] and reduction [11] when HVO fuel is used instead of diesel fuel, since fuel properties, fuel atomization and injection and EGR strategies significantly influence in the $NO_x$ formation [14].

To the best of our knowledge, research about performance and pollutant emissions in agricultural engines are scarce. In this context, the purpose of this article is to evaluate the performance and emissions of two agricultural engines with different after-treatment systems (ATS) in common operating points, comparing renewable fuel HVO and the reference diesel fuel. Thus, a quantitative comparison between fuels is done for each off-highway engine. In parallel, a qualitative analysis between both engines with different ATS and control strategies when using HVO fuel is also carried out, which would help to a further engine optimization of renewable paraffinic fuels -according to EN 15940-.

## 2. Experimental facilities

### 2.1. Agricultural engines tested

The heavy-duty engines tested were compression ignition engines with different after-treatment systems (with and without EGR systems), whose main specifications are shown in Table 1. Both off-highway engines comply with the EU Stage V / US Tier 4 emission regulation. The engine with EGR system (namely engine w/EGR) was set in an engine test bench and coupled to a dynamometer brake D2T MDC 350, which was controlled by the system AVL PUMA 2.0, as can be seen in the Figure 1 (left). On the other hand, the engine without EGR system (namely engine w/o EGR) was set in an agricultural vehicle and also coupled to a dynamometer brake Froment Sigma 50, through the auxiliar power take-off, as shown in the Figure 1 (right).

**Table 1**. Specifications of the agricultural engines

| Characteristic | Engine with EGR system | Engine without EGR system |
|---|---|---|
| Cylinders / Valves | 4, in line / 8 | 6, in line / 24 |
| Displacement (cm$^3$) | 4483 | 6728 |
| Bore / Stroke (mm) | 106 / 127 | 104 / 132 |
| Compression ratio | 16.7:1 | 17.0:1 |
| Injection | Electronic high-pressure common rail direct injection | Electronic high-pressure common rail direct injection |
| Aspiration | Single waste gate turbocharged | Waste gate turbocharged |
| Power (max.) | 104 kW at 2400 rpm | 140 kW at 2200 rpm |
| Torque (max.) | 540 Nm at 1600 rpm | 770 Nm at 1500 rpm |
| Aftertreatment system | DOC, SCR, DPF | DOC, SCR, CUC |
| EGR | With cooled EGR system | Without EGR system |
| Emissions regulation | EU Stage V / US Tier 4 | EU Stage V / US Tier 4 |

DOC ≡ Diesel Oxidation Catalyst, SCR ≡ Selective Catalyst Reduction, CUC ≡ Clean-up Catalyst, DPF ≡ Diesel Particle Filter, EGR ≡ Exhaust Gas Recirculation

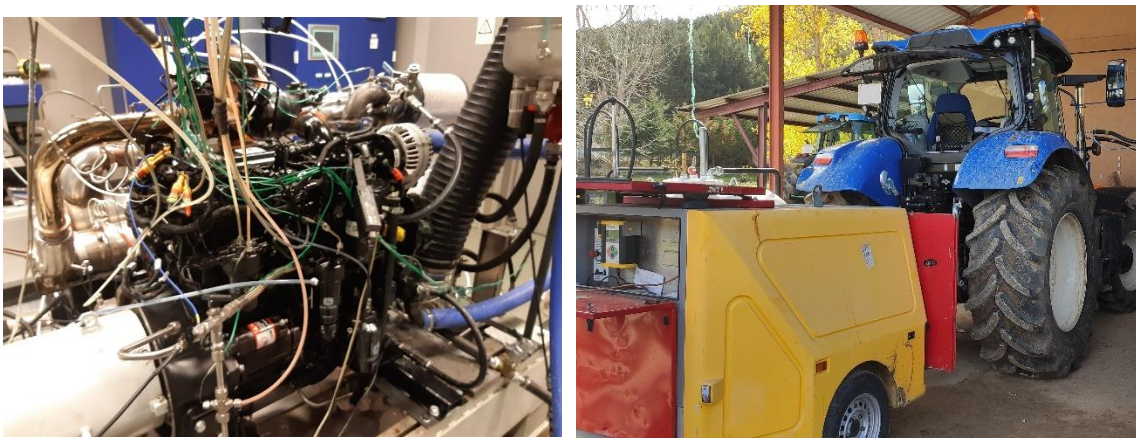

**Fig. 1.** Agricultural engines set in the engine test bench (left, engine w/EGR) and in the vehicle (right, engine w/o EGR)

## 2.2. Test procedures

The tests carried out with both agricultural engines were different. The engine with EGR system was submitted to different soiling stationary tests which consisted in repeating three times a sequence of three operating points: 1390 rpm - 100 Nm (1 h), 2220 rpm - 225 Nm (1 h) and 1650 rpm - 350 Nm (1 h). Then, results from these three operating points (namely, 1390x100, 2220x225 and 1650x350) in the last 5 min at steady conditions were analysed and discussed. On the other hand, the engine without EGR system was submitted to a sequence of ascending and descending load steps (engine load at 20, 58, 95, 70, 45, 15, 0 kW, taking 540 s for each position) at constant engine speed (1800 rpm) during 1 h. Previously, the engine was started, stabilized at idle speed (850 rpm) during 20 s, increased to 1800 rpm to connect power take off and stabilized at this engine speed during 120 s. This sequence was repeated three times. From the sequence of positive engine loads, results from three operating points at 120, 230 and 320 Nm, as well as 1800 rpm, were also examined. These quasi-stationary points are named here as 1800x120, 1800x230 and 1800x320. In summary, both sequences used with the two agricultural engines tried to simulate different load requirements applied in the routine work in the land.

## 2.3. Measuring equipment

In the tests on the agricultural engine w/EGR, torque and engine speed were obtained from a torquemeter located in the engine-brake connection. Air and fuel consumptions were measured with the equipment ABB Sensyflow P and the scale Mettler Toledo KCC300, respectively. Diesel emissions fluid (DEF) dosing was measured with the scale Mettler Toledo PBA430X-B150. In terms of emissions, the equipment Horiba Mexa-7170 DEGR was used to measure gaseous emissions, whereas AVL Opacimeter 439 allowed to measure opacity due to particle emissions. Both gaseous and particle emissions were measured upstream of the after-treatment system.

In the tests on the agricultural engine w/o EGR, the data acquisition system and the Electronic Control Unit (ECU) from the vehicle allowed to obtain the engine parameters through OBD port (including DEF dosing). However, in this case, fuel consumption was calculated from a balance of $CO_2$ emission. On the other hand, the equipment HORIBA OBS-ONE, an on-board modular measurement system (Portable Emissions Measurement System – PEMS), was used to measure gaseous and particle emissions downstream of the after-treatment system. In addition, $NO_x$ emissions were also measured upstream in the exhaust. More detailed information of this equipment can be found in previous works [12][23][24].

## 3. Fuels

The fuels tested were a hydrotreated vegetable oil (HVO) and a conventional diesel fuel (typically used in agriculture), which comply with the EN 15940 and EN 590 standards, respectively. The main properties of these fuels are detailed in Table 2.

**Table 2**. Main properties of tested fuels

| Property | HVO | Diesel |
|---|---|---|
| Density at 15ºC (kg/m$^3$) | 776 | 832 |
| Viscosity at 40ºC (mm$^2$/s) | 2.40 | 2.59 |
| Net heating value (MJ/kg) | 43.7 | 42.8 |
| Net heating value (MJ/L) | 33.9 | 35.6 |
| Flash point (ºC) | 59.0 | 65.5 |
| Cetane number | 76.6 | 54.2 |
| Oxidation stability (h) | 73.3 | 59.8 |
| Cold filter plugging point (ºC) | -10.0 | -11.0 |
| Sulphur content (mg/kg) | <1 | <1000 |
| C (wt. %) | 84.86 | 86.29 |
| H (wt. %) | 14.36 | 12.91 |
| H/C ratio | 2.03 | 1.80 |
| Molecular weight (g/mol) | 209.05 | 208.80 |
| Molecular formula | $C_{14.77}H_{29.78}$ | $C_{15.00}H_{26.74}$ |
| Stoichiometric ratio | 0.1401 | 0.1403 |

## 4. Results

The results obtained for HVO and diesel fuels using both agricultural engines are shown in parallel in graphs (which include the mean, shown in bars, and the standard deviation, indicated as error bars, from the three repeats of each engine sequence). Thus, the performance and emissions obtained with HVO, and diesel fuels are quantitatively compared for each heavy-duty engine. However, both engines are qualitatively compared in terms of performance and emissions because of the different after-treatment system configurations of the engines -according to EU Stage V and US Tier 4 standards- and due to the operating points tested are not exactly the same.

Figure 2 shows the results of fuel consumption (in mass basis) for HVO and diesel fuels using both agricultural engines. Same trend was observed with HVO, reducing fuel consumption versus diesel one. Slight differences were found in the engine w/EGR, being around 2 % lower with the renewable fuel. However, with the engine w/o EGR, fuel consumption using HVO was clearly lower (3-5 %).

Differences in fuel consumption between fuels in both technologies are consistent with fuel properties, due to the higher heating value (in mass basis, 2 % difference) and higher H/C ratio of HVO fuel versus diesel fuel, as observed in other research results using engines with EGR system [11] and engines without EGR system [12]. Nevertheless, slight differences in fuel consumption between engines are due to the different engine specifications and measuring equipment used. Then, since HVO fuel has 6.7 % lower density than diesel fuel, higher fuel consumption (in volume basis) of HVO is expected.

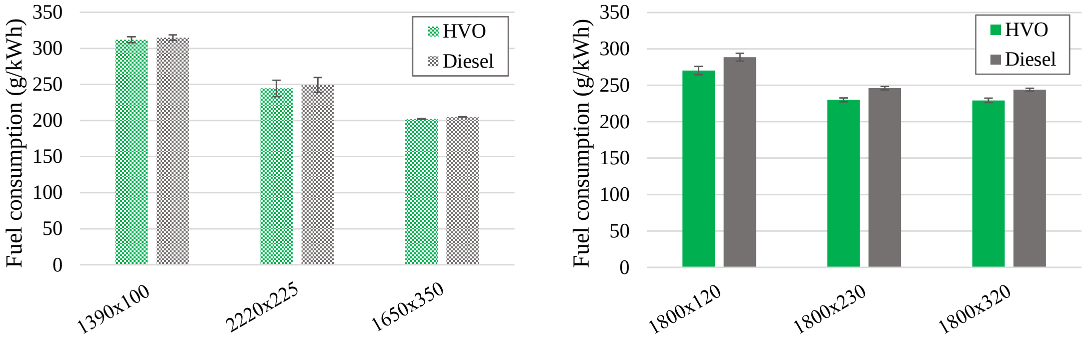

**Fig. 2**. Fuel consumption obtained for HVO and diesel fuels using the engine w/EGR (left) and the engine w/o EGR (right)

Figure 3 shows the results of equivalence ratio obtained with HVO and diesel fuels using both engines. The equivalence ratio was calculated dividing actual fuel/air ratio by stoichiometric fuel/air ratio. No clear trend was obtained between fuels on the agricultural engine w/EGR in this parameter, being almost equal in the three operating points studied (Figure 3, left). However, very slightly lower equivalence ratio was obtained with HVO fuel with respect to diesel fuel in the agricultural engine w/o EGR (Figure 3, right), in line with the lower fuel consumption since both fuels have similar stoichiometric ratio. Lower equivalence ratio was obtained in the engine w/o EGR because of higher air consumption and EGR absence with respect to the engine w/EGR.

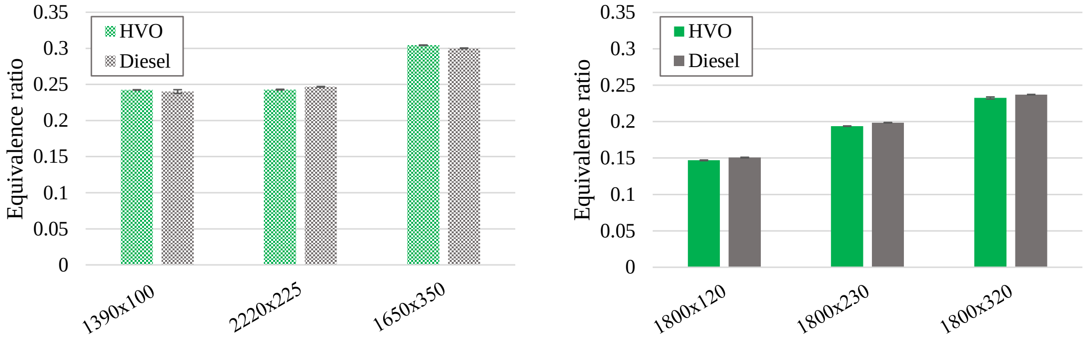

**Fig. 3**. Equivalence ratio obtained for HVO and diesel fuels using the engine w/EGR (left) and the engine w/o EGR (right)

Figure 4 shows the EGR rate obtained with HVO and diesel fuels using the engine w/EGR. No clear trend is observed between fuels when the three operating points are compared, whereas EGR rate was increased as load, AI50 and AI90 (crank angles of 50 and 90 % of integrated heat release, respectively) and exhaust manifold temperature (also referred here as exhaust temperature) did (see Figures S1, S2 and S3 in the Supplementary material, respectively). In the low load operating point (1390x100), EGR rate was clearly lower for HVO fuel compared to diesel fuel, as observed in other references [12], whereas the EGR rate was very similar between fuels in the other two points. On the other hand, the other engine has no EGR system, then it is not shown.

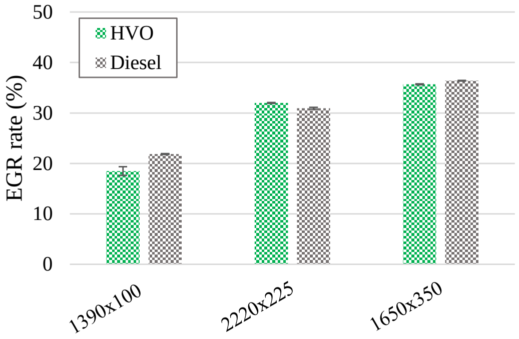

**Fig. 4**. EGR rate obtained for HVO and diesel fuels using the engine w/EGR

Related to engine performance (calculated from output power, fuel consumption and lower heating value of the fuel), Figure 5 shows the results obtained with HVO and diesel fuels using both engines. Same engine performance was obtained in the three operating points studied with the engine w/EGR (Figure 5, left) since no significant differences were observed in fuel consumption, equivalence ratio nor EGR rate. On the other hand, in the engine w/o EGR, engine performance is improved with HVO fuel (Figure 5, right) because the fuel consumption is notably lower using HVO with respect to diesel fuel providing the same output power (see Figure S4 in the Supplementary Material).

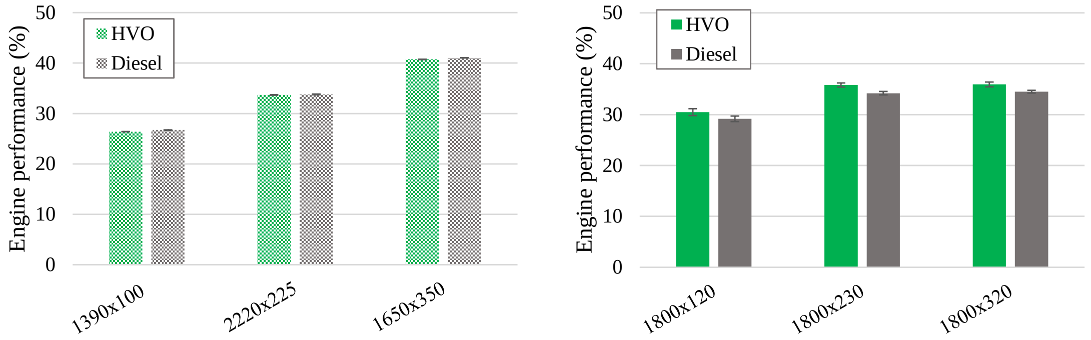

**Fig. 5**. Engine performance obtained for HVO and diesel fuels using the engine w/EGR (left) and the engine w/o EGR (right)

In terms of gaseous emissions, HVO led to lower $CO_2$ emissions than diesel fuel (Figure 6) in both the agricultural engines, in accordance with the lower fuel consumption (in mass) and its H/C ratio (Table 2), as observed in other experimental results [11][18]. However, lower difference in $CO_2$ emissions is observed between HVO and diesel fuels in the engine w/EGR (3-4 % lower; see Figure 6, left) with respect to the other engine w/o EGR (6-7 % lower; see Figure 6, right), corresponding with the differences in fuel consumption.

In both technologies, CO and HC emissions were very low (close to 0 and within detection limit of 20 ppm) for both fuels, due to the steady performance of the corresponding engines at warm conditions. In addition, the high efficiency of the oxidation catalyst (DOC) at warm conditions should be also considered in the engine w/o EGR since measurements were done downstream of ATS in this case.

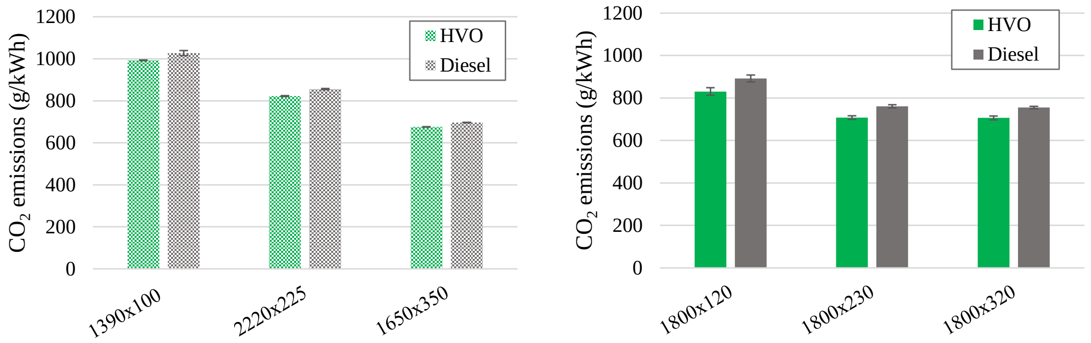

**Fig. 6**. $CO_2$ emissions obtained for HVO and diesel fuels using the engine w/EGR (left) and the engine w/o EGR (right)

$NO_x$ emissions (Figure 7) show a clear different behaviour between both engines when compared at the same point (upstream of ATS), which can be due to different combustion process between HVO and diesel fuels, as explained in [14]. These gaseous emissions were slightly higher for HVO fuel with respect to diesel fuel in the engine w/EGR (Figure 7, left) because of the lower AI50 and AI90 (see Figures S1 and S2 in the Supplementary material) in the three operating points due to its higher cetane number, as well as higher exhaust temperature (see Figure S3 in the Supplementary Material) and lower EGR rate in the low-load operating point. Similar conclusions were obtained by other researchers [13]. However, lower exhaust temperature was obtained in the other two operating points 2220x225 and 1650x350 for HVO compared to diesel. Whereas, the opposite trend was observed in $NO_x$ emissions between fuels in the other engine w/o EGR (Figure 7, right), which can be justified by the lower premixed combustion and thus slightly lower exhaust temperature obtained for HVO fuel, despite its higher cetane number. Comparing operating points in the engine w/EGR, higher $NO_x$ emissions were obtained for both fuels in the low-load operating point with respect to the other two medium-load points because lower AI50, AI90, EGR rate and output power was reached, despite showing lower exhaust temperature.

On the other hand, SCR strategy can be analysed by DEF dosing (Figure 8). In the engine with EGR, the control unit apply a lower DEF dosing because of the use of EGR system (Figure 8, left) in comparison with DEF dosing of the other engine without EGR system (Figure 8, right). Nevertheless, with the adjustment of the SCR strategy and the DEF dosing, $NO_x$ emissions using HVO fuel were almost equal to diesel fuel and close to zero at the exhaust pipe of the engine w/o EGR (see Figure S5 in the Supplementary material), denoting the high SCR efficiency at these operating points (over 95 % $NO_x$ reduction, as can be checked in Figure S6 in the Supplementary material) as the corresponding manufacturer claims to comply standard limits.

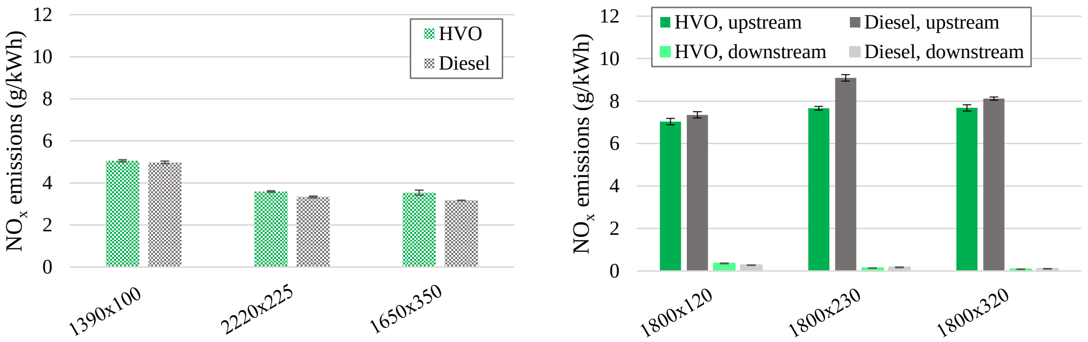

**Fig. 7**. $NO_x$ emissions obtained for HVO and diesel fuels using the engine w/EGR (left, upstream) and the engine w/o EGR (right, up- and downstream)

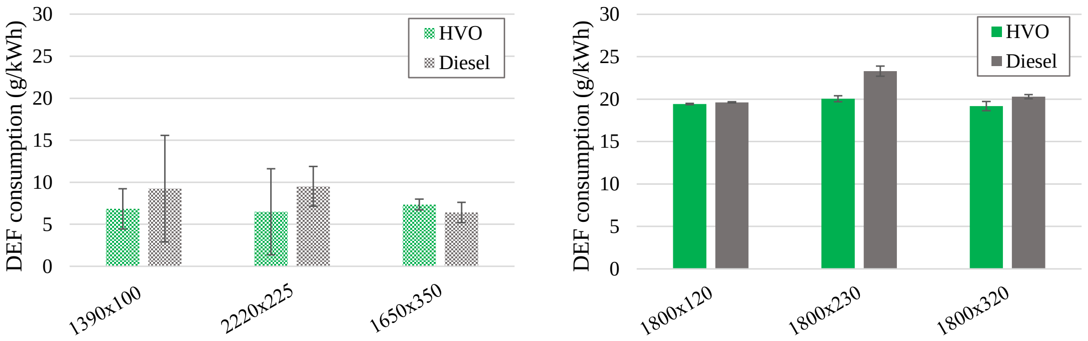

**Fig. 8**. DEF consumption obtained for HVO and diesel fuels using the engine w/EGR (left) and the engine w/o EGR (right)

Particle emissions were measured in a different way with both technologies. Opacity was measured in the engine w/EGR (upstream of ATS), whereas particle number was measured in the engine w/o EGR (downstream of ATS). Opacity was very low with both fuels, being slightly lower for HVO fuel in the two operating points with measurements (Figure 9, left), which can be due to the lower aromatic content, higher H/C ratio and lower volatile organic fraction (inferred from lower flash point) of HVO fuel with respect to diesel fuel, as explained in other references [25][26]. On the other hand, particle number emissions were higher when HVO fuel was used (Figure 9, right), although they were well below the certification limit ($1x10^{12}$ #/kWh). This difference between HVO and diesel fuel in terms of PN emissions is clearly discordant with respect to other references [27][28], which point out that HVO fuel produces lower particle number emissions in both modes (nucleation and cumulative), reaching up to 20 % reduction in PN tailpipe emissions [29]. However, some authors attained an increase in soot emissions when using HVO under some engine conditions [30]. Further research should be done to clarify the reason/s why this engine w/o EGR produces higher PN when running with HVO instead of diesel. Special attention should be put in combustion parameters (injection timing, injection pressure, temperature), fuel properties (aromatic content, H/C ratio, volatile organic fraction) and ATS parameters (urea injection timing, differential pressure in CUC), when comparing HVO fuel and diesel fuel in this engine w/o EGR.

When $NO_x$ and particle emissions are compared, a noticeable trade-off ($NO_x$-particles) is observed in the engine w/EGR. $NO_x$ emissions are slightly higher and opacity is lower when using HVO fuel compared to diesel fuel. This trade-off is observed in many other references [13][31][32]. On the other hand, the opposite trade-off is apparently checked in the engine w/o EGR, however, particle emissions were reduced by ATS, probably in different way between fuels.

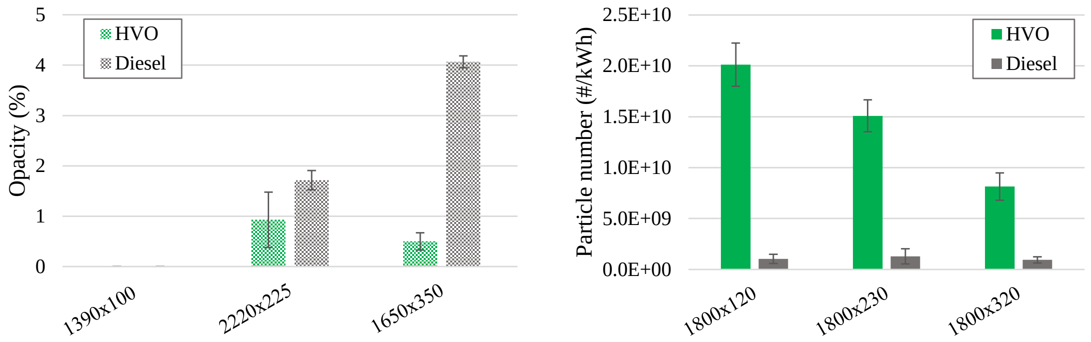

**Fig. 9**. Opacity using the engine w/EGR (left) and particle number using the engine w/o EGR (right) obtained for HVO and diesel fuels

## 5. Conclusions

The performance and emissions obtained with HVO and diesel fuels were quantitatively compared for two agricultural engines. In addition, both technologies were qualitatively compared to visualize how different engine configurations allows to comply with the same emission regulation (EU Stage V / US Tier 4). The renewable paraffinic fuel HVO led to lower fuel mass consumption (<2-5 %) with respect to diesel fuel in both engines. On the other hand, similar equivalence ratio and engine performance were obtained in the engine w/EGR, whereas slightly lower equivalence ratio and higher engine performance were attained using HVO fuel in comparison with diesel fuel in the engine w/o WGR. Differences between engines are attributed to different engine specifications and the measuring equipment used. In terms of emissions, $CO_2$ emissions followed the same tendency as fuel consumption, whereas CO and HC emissions were very low and within detection limit of 20 ppm for both fuels and both engines. $NO_x$ emissions showed a clear different behaviour between both technologies because of differences in engine calibration due to the use (or not) of EGR system. However, SCR allowed to greatly reduce these emissions through DEF dosing adjustment. Particle emissions were also different between engines. Opacity was lower using HVO fuel in the engine w/EGR due to its lower aromatic content and H/C ratio. Nevertheless, HVO fuel led to higher particle number emissions, although they were well below the certification limit, in the engine w/o EGR, which should be explained with further research. Therefore, diesel fuel can be substituted by HVO fuel in agricultural engines without the need of modifications, reaching similar engine performance and direct emissions, and potentially reducing well-to-wheel $CO_2$ emission up to 90 % compared to diesel fuel. However, the characteristic HVO combustion performance, due to its properties, makes possible a further optimization of the engine when renewable paraffinic fuels (EN 15940) are used. Then, a future project based on HVO engine optimization is recommended, independently of the ATS strategy defined.

## References

[1] Regulation (EU) 2016/1628 of the European Parliament and of the Council of 14 September 2016 on requirements relating to gaseous and particulate pollutant emission limits and type-approval for internal combustion engines for non-road mobile machinery, amending Regulations (EU) No 1024/2012 and (EU) No 167/2013, and amending and repealing Directive 97/68/EC. Official Journal of the European Union, 2016.

[2] Da Silveira, F.; Ruppental, J.E.; Lermen, F.H.; Machado, F.M.; Amaral, F.G. Technologies used in agricultural machinery engines that contribute to the reduction of atmospheric emissions: A patent analysis in Brazil. World Patent Information 2021, 64, 102023.

[3] McCaffery, C.; Yang, J.; Karavalakis, G.; Yoon, S.; Johnson, K.C.; Miller, J.W.; Durbin, T.D. Evaluation of small off-road diesel engine emissions and aftertreatment systems. Energy 2022, 251, 123903.

[4] European Comission. CO2 emission standards for heavy-duty vehicles, 2023. Last visit: 24/07/2023. Available in: https://ec.europa.eu/commission/presscorner/detail/en/qanda_23_763.

[5] European Environment Agency. Progress and prospects for decarbonisation in the agriculture sector and beyond, 2022. Last visit: 24/07/2023. Available in: https://www.eea.europa.eu/publications/Progress-and-prospects-for-decarbonisation.

[6] Stumborg, M.; Wong, A.; Hogan, E. Hydroprocessed vegetable oils for diesel fuel improvement. Bioresour. Technol. 1996, 56, 13–18.

[7] Dobrzy´nska, E.; Szewczy´nska, M.; Po´sniak, M.; Szczotka, A.; Puchałka, B.;Woodburn, J. Exhaust emissions from diesel engines fueled by different blends with the addition of nanomodifiers and hydrotreated vegetable oil HVO. Environ. Pollut. 2020, 259, 113772.

[8] Wei, X.; Meng, Q.; Kallio, K.J.; Olsson, R.T.; Hedenqvist, M.S. Ageing properties of a polyoxymethylene copolymer exposed to (bio) diesel and hydrogenated vegetable oil (HVO) in demanding high temperature conditions. Polym. Degrad. Stab. 2021, 185, 109491.

[9] No, S.Y. Application of hydrotreated vegetable oil from triglyceride-based biomass to CI engines—A review. Fuel 2014, 115, 88–96.

[10] Directive (EU) 2018/2001 of the European Parliament and of the Council of 11 December 2018 on the promotion of the use of energy from renewable sources, 2018. https://eur-lex.europa.eu/legal-content/EN/TXT/HTML/?uri=CELEX:32018L2001&from=EN (accessed 2023-07-24).

[11] Bortel, I.; Vávra, J.; Takáts, M. Effect of HVO fuel mixtures on emissions and performance of a passenger car size diesel engine. Renew. Energy 2019, 140, 680–691.

[12] Mata, C.; Cárdenas, D.; Esarte, C.; Soriano, J.A.; Gómez, A.; Fernández-Yáñez, P.; García-Contreras, R.; Sánchez, L.; Nogueira, J.I.; Armas, O. Performance and regulated emissions from a Euro VI-D hybrid bus tested with fossil and renewable (hydrotreated vegetable oil) diesel fuels under urban driving in Bilbao city, Spain. Journal of Cleaner Production 2023, 383, 135472.

[13] Aatola, H.; Larmi, M.; Sarjovaara, T.; Mikkonen, S. Hydrotreated Vegetable Oil (HVO) as a renewable diesel fuel: Tradeoff between NOx, particulate emission, and fuel consumption of a heavy duty engine. SAE Int. J. Engines 2009, 1, 1251–1262.

[14] Dimitriadis, A.; Natsios, I.; Dimaratos, A.; Katsaounis, D.; Samaras, Z.; Bezergianni, S.; Lehto, K. Evaluation of a Hydrotreated Vegetable Oil (HVO) and effects on emissions of a passenger car diesel engine. Front. Mech. Eng. 2018, 4, 7.

[15] Aatola, H.; Larmi, M.; Sarjovaara, T.; Mikkonen, S. Hydrotreated Vegetable Oil (HVO) as a renewable diesel fuel: Trade-off between NOx, particulate emission, and fuel consumption of a heavy-duty engine. SAE World Congress 2008, 2008-01-250.

[16] Hunicz, J.; Mikulski, M.; Shukla, P.C.; Gęca, M.S. Partially premixed combustion of hydrotreated vegetable oil in a diesel engine: Sensitivity to boost and exhaust gas recirculation. Fuel 2022, 307, 121910.

[17] Prussi, M.; Yugo, M.; De Prada, L.; Padella, M.; Edwards, R.; Lonza, L. JEC Well-to-Tank report v5, EUR 30269 EN, Publications Office of the European Union, 2020.

[18] Suarez-Bertoa, R.; Kousoulidou, M.; Clairotte, M.; Giechaskiel, B.; Nuottimäki, J.; Sarjovaara, T.; Lonza, L. Impact of HVO blends on modern diesel passenger cars emissions during real world operation. Fuel 2019, 235, 1427–1435.

[19] Hartikka, T.; Kuronen, M.; Kiiski, U. Technical performance of HVO (Hydrotreated Vegetable Oil) in diesel engines. SAE Tech. Paper 2012, 2012-01-1585.

[20] Azetsu, A.; Sato, Y.; Wakisaka, Y. Effects of aromatic components in fuel on flame temperature and soot formation in intermittent spray combustion. SAE Tech. Pap. 2003.

[21] Pflaum, H.; Hofmann, P.; Geringer, B.; Weissel,W. Potential of Hydrogenated Vegetable Oil (HVO) in a modern diesel engine. SAE Tech. Pap. 2010, 2010-32-0081.

[22] Dec, J. A. conceptual model of di diesel combustion based on laser-sheet imaging. SAE Tech. Pap. 1997, International Congress and Exposition, 90577.

[23] García-Contreras, R.; Soriano, J. A.; Fernández-Yáñez, P.; Sánchez-Rodríguez, L.; Mata, C.; Gómez, A.; Armas, O.; Cárdenas, M.D. Impact of regulated pollutant emissions of Euro 6d-Temp light-duty diesel vehicles under real driving conditions. Journal of Cleaner Production 2021, 286, 124927.

[24] Gómez, A.; Fernández-Yáñez, P.; Soriano, J. A.; Sánchez-Rodríguez, L.; Mata, C.; García-Contreras, R.; Armas, O.; Cárdenas, M. D. Comparison of real driving emissions from Euro VI buses with diesel and compressed natural gas fuels. Fuel 2021, 289, 119836.

[25] Lapuerta, M.; Armas, O.; Hernández, J.J.; Tsolakis, A. Potential for reducing emissions in a diesel engine by fuelling with conventional biodiesel and Fischer–Tropsch diesel. Fuel 2010, 89, 3106-3113.

[26] Calle-Asensio, A.; Hernández, J.J. Rodríguez-Fernández, J.; Lapuerta, M.; Ramos, A.; Barba, J. Effect of advanced biofuels on WLTC emissions of a Euro 6 diesel vehicle with SCR under different climatic conditions. International Journal of Engine Research 2021, 22, 3433-3446.

[27] Korhonen, K.; Kristensen, T.B.; Falk, J.; Malmborg, V.B.; Eriksson, A.; Gren, L.; Novakovic, M.; Shamun, S.; Karjalainen, P.; Markkula, L.; Pagels, J.; Svenningsson, B.; Tunér, M.; Komppula, M.; Laaksonen, A.; Virtanen, A. Particle emissions from a modern heavy-duty diesel engine as ice nuclei in immersion freezing mode: a laboratory study on fossil and renewable fuels. Atmospheric Chemistry and Physics 2022, 22, 1615–1631.

[28] Erkkilä, K.; Nylund, N.; Hulkkonen, T.; Tilli, A.; Mikkonen, S.; Saikkonen, P.; Mämkinen, R.; Amberla, A. Emission performance of paraffinic HVO diesel fuel in heavy duty vehicles. SAE Technical Paper 2011, 2011-01-1966.

[29] Gren, L.; Malmborg, V.B.; Jacobsen, N. R.; Shukla, P.C.; Bendtsen, K.M.; Eriksson, A.C.; Essig, Y.J.; Krais, A.M.; Loeschner, K.; Shamun, S.; Strandberg, B.; Tunér, M.; Vogel, U.; Pagels, J. Effect of renewable fuels and intake O2 concentration on diesel engine emission characteristics and reactive oxygen species (ROS) formation, Atmosphere 2020, 11, 641.

[30] Zubel, M.; Bhardwaj, O.P.; Heuser, B.; Holderbaum, B.; Doerr, S.; Nuottimäki, J. Advanced fuel formulation approach using blends of paraffinic and oxygenated biofuels: analysis of emission reduction potential in a high efficiency diesel combustion system. SAE Interantional Journal of Fuels and Lubricants 2016, 9, 481-492.

[31] Bohl, T.; Smallbone, A.; Tian, G.; Roskilly, A.P. Particulate number and NOx trade-off comparisons between HVO and mineral diesel in HD applications. Fuel 2018, 215, 90–101.

[32] Dimitriadis, A.; Seljak, T.; Vihar, R.; Žvar Baškovič, U.; Dimaratos, A.; Bezergianni, S.; Samaras, Z.; Katrašnik, T. Improving PM-NOx trade-off with paraffinic fuels: A study towards diesel engine optimization with HVO. Fuel 2020, 116921.

# Using Staged Combustion to Mitigate $NO_x$ Emissions from Ammonia

Md Nayer Nasim[1], Joshua Landis[1], Shubhra K. Das[1], Behlol Nawaz[1], J. Hunter Mack[1]

[1] Department of Mechanical & Industrial Engineering, University of Massachusetts Lowell, Lowell, Massachusetts, United States of America

Email: john_mack@uml.edu
Telephone: +(1) 978 934 5766

**Abstract.** While ammonia ($NH_3$) is largely viewed as a promising alternative fuel due to its lack of carbon, several issues need to be addressed prior to widespread adoption. In addition to infrastructure and materials compatibility, one particular risk is an increase in $NO_x$ and $N_2O$ emissions due to fuel-bound nitrogen. This study investigates the potential to reduce $NO_x$ emissions from $NH_3$ combustion through staging, which includes two distinct ignition events at disparate conditions; typically, a primary zone partially burns a fuel-air mixture prior to completing the combustion in a subsequent stage that may include the introduction of additional air. The process can be emulated in a constant volume combustion chamber (CVCC) by initially igniting a rich mixture, adding air to the combustion products, and then igniting a second time at a globally lean condition. This approach provides isolated insight into how changes in initial pressure and equivalence ratio (for both stages) affect the production of $NO_x$ emissions. Additional experiments with argon (Ar) as the working fluid are conducted in parallel to isolate the fuel-bound $NO_x$ production pathway. The experimental results indicate that a staged approach dramatically reduces $NO_x$ emissions, particularly in comparison to stoichiometric and lean ammonia combustion. Combustion of ammonia with argon as the working fluid generates only fuel-bound NOx while increasing the laminar burning velocity. The comparatively higher specific heat of argon stretches the flammability limit resulting in spherical flames even at low equivalence ratios with minimal buoyant forces. In comparison with other emissions control technologies, staged combustion provides a pathway to reduce $NO_x$ emissions from ammonia combustion for practical devices such as internal combustion engines and gas turbines.

## 1. Introduction

Significant pollution and greenhouse gas emissions are amongst the two most pressing downsides of using conventional fossil fuel as energy sources. Since approximately 79% of total U.S. energy production in 2022 came from fossil fuels, including 60% of electricity generation and 94% of the transportation sector [1], further adoption of renewable energy sources remains a global challenge. Hurdles remain around integrating intermittent renewable sources like solar and wind, especially with respect to specific sectors outside of large-scale grid implementation. Sustainable fuels could be better suited for applications requiring high energy densities such as aviation and heavy transportation [2]. For renewable fuels to be considered viable alternatives to fossil fuels, they must not only match or surpass the energy density and handling characteristics of conventional fuels but also achieve reduced, net-zero, or zero carbon emissions.

Ammonia ($NH_3$) is a potential zero-carbon fuel, which can be produced from renewable sources. Furthermore, ease of storage [3] and a high volumetric energy density in comparison to natural gas and hydrogen [4] has made $NH_3$ a promising candidate to replace fossil fuels. Furthermore, $NH_3$ has been used at industrial scales for decades with a well-established infrastructure producing more than 175 million tons globally every year [5]. Though it is primarily produced using nitrogen from air and hydrogen from fossil fuels [6], it can potentially be economically produced using hydrogen from renewable sources [7–9] or through direct photo-catalytic synthesis [10–12].

Unfortunately, $NH_3$ has some distinct implementation difficulties [13, 14] including low flammability [15], high corrosivity [14], and a low flame speed [16]. These issues need to be addressed before its widespread usage in practical systems such internal combustion engines and gas turbines. Additionally, the fuel-bound nitrogen in $NH_3$ leads to a substantial increase in $NO_x$ emissions during combustion [17–19]. In order to evaluate its potential as a zero-carbon fuel, extensive fundamental studies have been conducted on $NO_x$ formation from $NH_3$ combustion. Mashruk et al [20, 21] studied NOx and $N_2O$ generation from $NH_3$-$H_2$-air premixed swirl flames. The authors further investigated $NH_3$-$CH_4$-air flames at varying equivalence ratios and $NH_3$ fractions [22]. Zheng et al. simulated that the $NH_3$ flame speed can be increased through adding a small amount of active fuels (blends of $CH_4-H_2$) without increasing

NOx emissions [23]. The effect of OH*, $NH_2$*, NH* radicals on NOx formation have also been studied by researchers using large-eddy simulations of model flames [24] and chemiluminescence [25, 26]. The influence of combustor design on emissions has also been thoroughly investigated, including the use of swirl to stabilize the low flame speed [27], moderate or intense low oxygen dilution (MILD) combustion [28], the lean-burn dry-low emissions (DLE) technique [29],combustion at high initial pressures [27], steam addition [30] and staged combustion or rich-quench-lean (RQL) method [31, 32].

### 1.1 Staged Combustion

Natural gas fueled applications can minimize $NO_x$ emissions through the use of a 2-stage method that includes a controlled lean primary stage combustion to limit $NO_x$ production by maintaining low temperatures. The remaining fuel is ignited a second time, again at a lean condition, to minimize residence times at high temperatures [29]. However, combustors that use a fuel that contains nitrogen (such as $NH_3$) are more suited for the Rich-Quench-Lean (RQL) method, where a rich primary zone is followed by a lean secondary zone. Utilizing this concept, Pratt & Whitney have been able to develop reduced NOx combustors for aircraft gas turbine engines [33]. Recently, researchers have found success in achieving significantly less $NO_x$ production rates through the RQL configuration coupled with some other modifications when compared to a single stage burner operating at the same overall equivalence ratio. Wu et al. found that staged combustion can lower NOx emissions at high temperature and low overall equivalence ratios ($\Phi \leq 0.8$) [34]. Elevating the combustion temperature in a highly reducing atmosphere can boost H atom concentrations and alter the composition and magnitude of the radical pool, thereby promoting the conversion of NO to $N_2$. Simulations by Mashruk et al. [35] and Božo et al. [36] found that adding steam to the RQL system leads to lower NOx emissions due to the recombination of species and lower combustion temperatures. Okafor et al. found that it was necessary to have a sufficiently long fluid residence time in the primary combustion chamber to control unburned ammonia and $N_2O$ emissions in 2-stage RQL ammonia combustors [37]. A lower NOx generation rate was achieved by adding methane to the ammonia-air mixture while increasing the flame speed [38].

Internal combustion engines have also adopted concepts that borrow from staged combustion. At a basic level, exhaust gas recirculation can be viewed as partially staged combustion. In other instances, a pre-chamber has been used in conjunction with an internal combustion engine (ICE) for staged combustion [39, 40], showing both reduced $NO_x$ emissions and throtteless operation at ultra-lean conditions. Staged combustion has also been approximated in ICE applications using multiple injection events, often in systems that are compression ignited [41, 42]. Lastly, individual cylinders have been used for partial fuel-reforming and recirculated back to other cylinders [43]; this method starts to approach what could be implemented to achieve 2-stage combustion for $NO_x$ reduction in ammonia-fueled engines.

A two-stage rich-lean combustion approach has been suggested by the researchers to manage emissions from ammonia/air combustion. This method, while reducing NOx emissions, comes at the cost of increased unburned ammonia and hydrogen production resulting from ammonia breakdown. At this early phase of development, it remains unclear if modifications to combustor design and the use of two-stage combustion will sufficiently lower NOx emissions, potentially eliminating the need for additional NOx reduction equipment downstream [44, 45]. Many ongoing studies have attempted to determine the optimum operating conditions (initial equivalence ratio, pressure, and residence time) that enable the lowest achievable NOx emission rates [46–48].

This study investigates the reduction of $NO_x$ emissions from $NH_3$ combustion through staged combustion, emulated in a constant volume combustion chamber (CVCC) by initially igniting a rich mixture, adding air to the combustion products, and then igniting a second time at a globally lean condition. This approach provides isolated insight into how changes in the initial equivalence ratio and the amount of secondary air affect the production of $NO_x$ emissions. Unlike all other studies conducted before, both stages of the combustion experiments in this study were conducted inside a single CVCC. Single stage $NH_3$ combustion using argon (Ar) instead of nitrogen ($N_2$) as the diluent was also studied to isolate the controbutution of fuel-bound nitrogen without the influence of $N_2$ in the air. These experiments also provided insight into the effect of the Ar substitution on the laminar burning velocity of $NH_3$.

## 2. Methodology

Spherically expanding flames generated from 2-stage premixed combustion of $NH_3$ inside a CVCC were analyzed over two different initial equivalence ratios and a range of added secondary air. The amount of air inserted into the chamber after stage 1 determined the cumulative equivalence ratio of the mixtures after two stages of combustion events.

## 2.1 2-Stage Combustion inside CVCC

Figure 1 shows the experimental setup, consisting of a CVCC coupled with a Z-type schlieren imaging system, pressure transducers, data acquisition (DAQ) system, vacuum pump, gas cylinders, a centrally located spark ignition system, and a Fourier transform infrared (FTIR) spectroscopy system. The specifics of the CVCC and DAQ system has been presented in detail in a previous study [49].

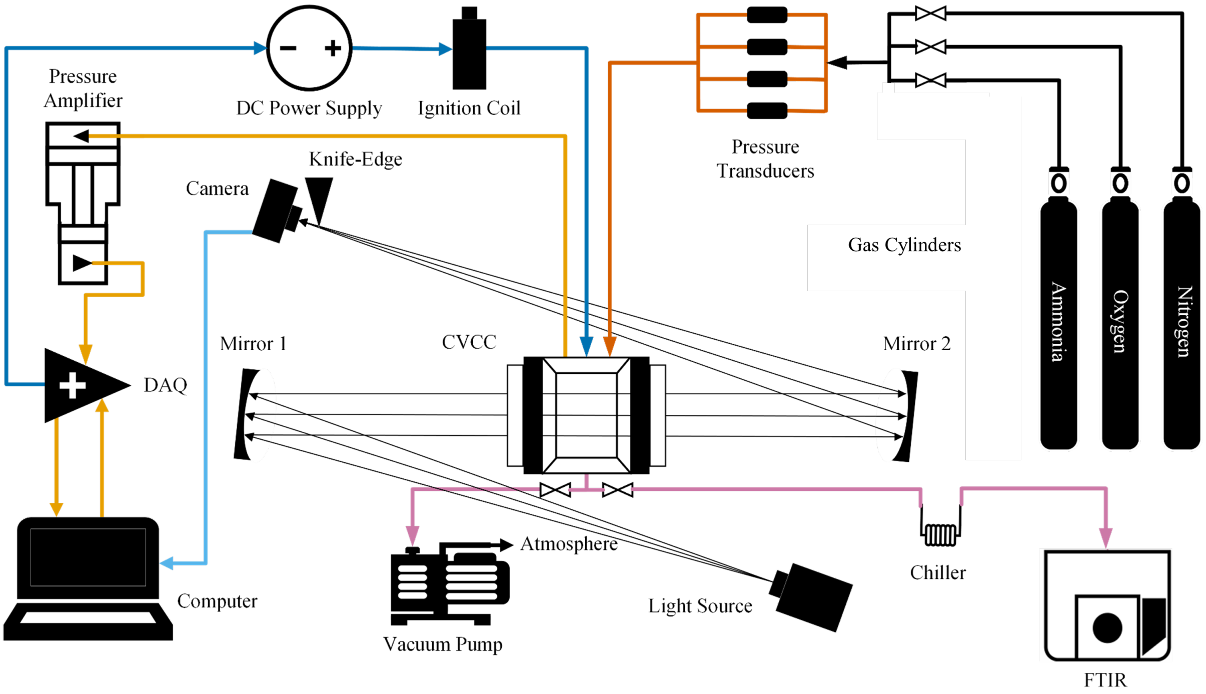

**Fig. 1:** Schematic of the experimental setup including the CVCC coupled with Z-type schlieren visualization, vacuum pump, ignition system, DAQ, and FTIR.

Before each combustion experiment, the combustion chamber and connected lines were evacuated to below 400 mTorr, ensuring no residual gasses from previous trials being present. The lines and chamber were then filled with research-grade gasses using the partial pressure method, monitored using the piezoresistive pressure transducers. This procedure established the desired equivalence ratio for the mixtures tested in the first stage of the experiment. Before ignition, the mixture was allowed to stabilize for three minutes. During these three minutes, the lines were then evacuated and subsequently filled with research-grade compressed air according to the partial pressures required to create the cumulative equivalence ratio desired for the second stage of combustion. The rich mixture was then ignited. The air from the lines was added to the chamber containing the initial combustion byproducts from the first stage. The amount of air introduced is carefully controlled based on the pressure in both the lines and the combustion chamber (air pressure in line was set at a higher pressure so that once the chamber is opened again, the air in-line enters the chamber and stabilizes). Once the desired pressure is reached, the cell is closed off from inlet lines and the products are ignited again. This mixture has a portion of its combustion products measured using an Fourier Transform Infrared (FTIR) spectrometer in order to analyse the level of $NO_x$ produced in the experiment. The different steps of the 2-stage combustion experiments conducted in this study have been explained in the process diagram in Figure 2.

It is worth emphasizing here that the above procedure was followed for the dual stage experiments where the first stage was rich and the second was lean. In the case of the single stage combustion of $NH_3$ with the $N_2$ in the air replaced by Ar ($NH_3$-$O_2$-Ar mixture), only the first part of the procedure was followed to create the mixture with the required equivalence ratio, followed by the wait period and ignition. There was no addition of additional air or a second combustion event.

The emissions results (NO, $NO_2$, $N_2O$) from the 2-stage combustion trials were compared against the $NO_x$ measurements from 1-stage combustion of a mixture with the corresponding lean equivalence ratio. The equivalence ratios tested have been presented in Table 1.

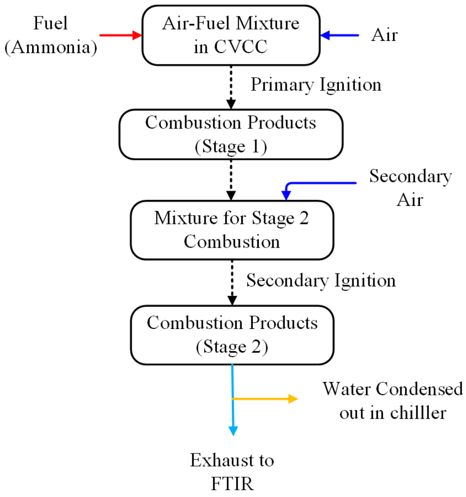
Fuel
(Ammonia)
Air-Fuel Mixture
in CVCC
Air
Primary Ignition
Combustion Products
(Stage 1)
Secondary
Air
Mixture for Stage 2
Combustion
Secondary Ignition
Combustion Products
(Stage 2)
Water Condensed
out in chilller
Exhaust to
FTIR

**Fig. 2:** Illustration of the steps required to perform staged combustion in the CVCC.

## 2.2 Exhaust Analysis with FTIR

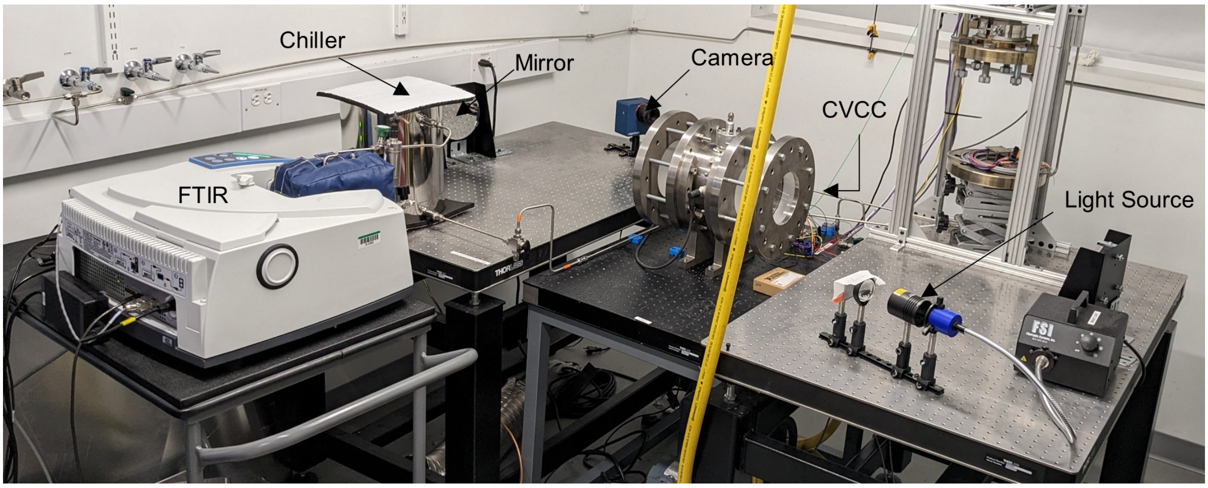
Chiller
Mirror
Camera
CVCC
FTIR
Light Source

**Fig. 3:** Experimental set-up including the CVCC with Z-type schlieren imaging and FTIR for exhaust characterization.

A Fourier Transform Infrared (FTIR) spectrometer (seen in Figure 3) was used to analyze the exhaust samples in this study. This method involves passing infrared radiation through a gas cell containing a known volume of gas. The gas absorbs radiation at specific wavelength ranges and at discrete quantities, creating a unique fingerprint for each exhaust product. A library of absorption spectra, collected at known gas concentrations, was used to generate calibration curves for each gas of interest by comparing the absorption curve intensity of each gas to the known concentration of each input gas analysed. By comparing exhaust spectra of unknown quantities against these calibration curves, the gases present and their concentrations can be determined [50]. More about the calibration matrix used in this experiment can be found in a a previous publication [16].

The exhaust gases from the CVCC experiments were directed to the FTIR (ThermoFischer Nicolet™ iS20) through $\frac{1}{4}$ inch stainless steel lines equipped with an integrated chiller. This chiller condensed the water vapor (and the absorbed $NH_3$) out of the gas stream. Removing water was necessary because its broad absorption spectrum interferes with key measurement regions for $NO_x$ species. Condensing out water is a common practice in emissions analysis protocols, such as when using a $NO_x$ analyzer with engines. After condensation, the gas flowed into a 200 ml gas cell with a 2 meter path length. Once in the cell, the gas pressure and temperature were recorded before collecting a spectrum (16 scans at 1 $\mathrm{cm}^{-1}$ resolution). The gas cell was maintained at 100°C to remain consistent with the gas calibrations used for quantification.

During the measurement process, there is a risk of NO and O2 reacting to form NO2 over time. To account for this potential issue, the combined concentration of NO and $NO_2$ ($NO_x$) is calculated and analyzed for each trial. The concentrations are determined from the spectra collected per trial using the OMNIC™software (version 9.12.1019) associated with the FTIR unit, along with the gas calibrations provided by the manufacturer.

**Table 1:** Initial and cumulative equivalence ratios used in the staged combustion experiments.

| Initial Equivalence Ratio ($\Phi_{S1}$) | Cumulative Equivalence Ratio ($\Phi_{S2}$) |
|---|---|
| 1.25 | 0.89<br>0.8<br>0.75 |
| 1.3 | 0.92<br>0.82<br>0.77<br>0.71 |

## 2.3 Laminar Burning Velocity (LBV)

In addition to the exhaust measurements which were carried out for all experiments, the laminar burning velocity (LBV also known as the unstretched flame speed) was calculated for single stage $NH_3$-$O_2$-Ar combustion experiments. This was done using the high speed schlieren images recorded at a frame rate of 8000 frames per second at a resolution of 384 x 384 pixels. The images were processed with a MATLAB code to calculate the instantaneous flame speed, $S_b$, was using Equation 1, where $r_f$ is the radius (cm) of the spherically propagating flame in each frame and $t$ is the time (s).

$$S_b = \frac{\mathrm{d}r_f}{\mathrm{d}t} \tag{1}$$

The corresponding flame stretch ($K$) values for the spherical flames were calculated using Equation 2. The flame stretch values were then extrapolated to calculate the flame speed at zero stretch.

$$K = \frac{1}{A}\frac{\mathrm{d}A}{\mathrm{d}t} = \frac{2}{r_f}\frac{\mathrm{d}r_f}{\mathrm{d}t} = 2\frac{S_b}{r_f} \tag{2}$$

Finally, the zero stretch flame speeds were corrected for density change between unburned and burned gas using Equation 3 to calculate the LBV.

$$S_u = \left(\frac{\rho_b}{\rho_u}\right)\frac{\mathrm{d}r_f}{\mathrm{d}t} \tag{3}$$

The methodology discussed here briefly for recording schlieren images and calculating the LBV is discussed in more detail in a previous publication [49].

## 2.4 Uncertainty Analysis

The major sources of errors present in this study could be divided into two categories: (1) experimental error introduced during mixture preparation and (2) repeatability error associated with conducting multiple trials at each mixture configuration.

With respect to the experimental error, piezoresistive pressure transducers (Omega PX419) with an uncertainty level of $\pm 0.08\,\%$ were used to fill up the chamber with gases that had a purity level of at least 99.999%. These error bars would be applicable along the X-axis representing the different equivalence ratios. For example, if gases were inserted into the CVCC to theoretically prepare a stoichiometric mixture of ammonia/air at an initial pressure of 1 bar, the value of $\Phi$ would fall between 0.9976 and 1.0024. Since this is very negligible, the error bars along the X-axis have not been presented in the plots.

The error bars along the Y-axis correspond to the variability detected in the exhaust of these combustion experiments at ppm level. The FTIR unit produced the standard error data for each species from each trial of the experiments. A single standard deviation (SD) was calculated from these three individual SD data points using Equation 4.

$$SD = \sqrt{\frac{(SD_1)^2 + (SD_2)^2 + (SD_3)^2}{9}} \tag{4}$$

The statistical SD was derived using the mean values from the three trials using Equation 5 where $N$ is the population size and $\overline{x}$ denotes the mean.

$$s = \sqrt{\frac{1}{N}\sum_{i=1}^{N}(x_i - \overline{x})^2} \tag{5}$$

The larger standard deviation was then selected to be the standard deviation of that specific experimental condition.

## 3. Results and discussion

### 3.1 Comparison between 2-stage and 1-stage ammonia combustion

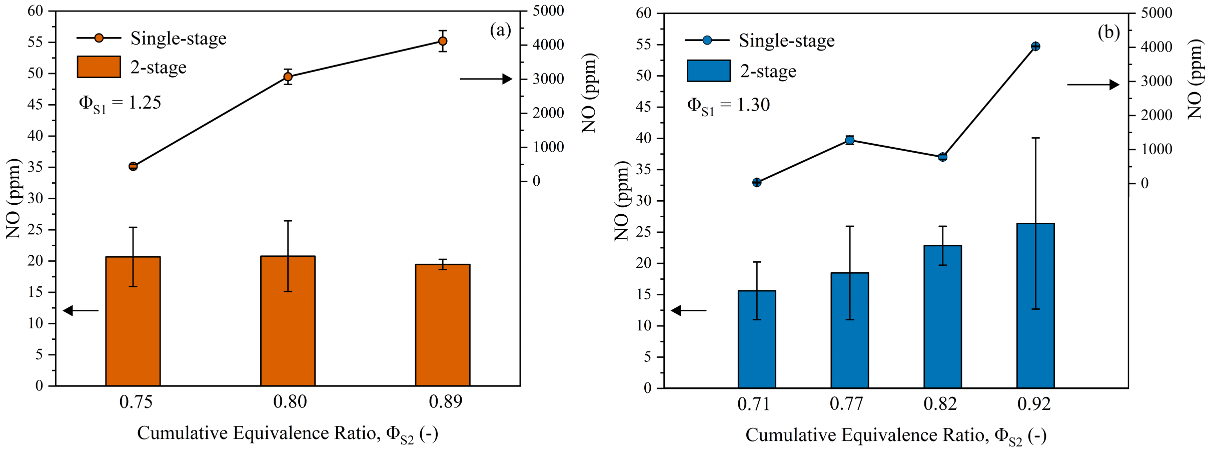

**Fig. 4:** NO concentration in the exhaust at varying initial ((a)$\Phi_{S1}$= 1.25, (b) $\Phi_{S1}$ = 1.3) and cumulative equivalence ratios with $N_2$ as the working fluid

.

Nitrogen oxides are generated through three different processes. The primary mechanism for $NO_x$ formation during combustion is thermal $NO_x$, which occurs due to the thermal dissociation of oxygen and nitrogen molecules and the subsequent reactions between them. The majority of $NO_x$ produced via this pathway happens in extremely high temperature zones. $NO_x$ production rates increase with higher oxygen concentrations, higher peak temperatures, and longer exposure times at the peak temperature. Staging the combustion of $NH_3$ can help reduce thermal $NO_x$ emissions because the primary combustion occurs in an oxygen deficit environment resulting in lower peak temperatures.

Figure 4 shows the amount of NO emissions for both 2-staged and 1-stage direct $NH_3$ combustion for the corresponding cumulative equivalence ratio. For NO emissions, as the amount of air added before the second stage combustion increases, a decreasing trend in NO values is observed when the initial equivalence ratio is $1.3$. But the amount of secondary air seem to have no significant effect on the NO measurements when the initial equivalence ratio was lowered down to $1.25$ (as seen in fig 4(a)). Regardless of the initial equivalence ratio or the amount of air entered in the second stage, all of the cases tested showed a drastic decrease (from 55% to 98%) in NO emissions compared to the combustion events where this amount of fuel and oxidizer were ignited in one stage. A similar trend was observed in the $NO_2$ emissions data shown in Figure 5, exhibiting a reduction in emissions from 1-stage direct combustion to 2-stage combustion.

From the time of the initial combustion event to the exhaust sent inside the gas cell for analysis, NO and $O_2$ potentially have time to form $NO_2$ [51]. To mitigate this effect, the combined concentration of NO and $NO_2$, (i.e., $NO_x$) has also been calculated and presented in the analysis for each trial. The combined $NO_x$ results presented in Figure 6 exhibits less variance amongst different initial equivalence ratios and secondary air amount (resulting in smaller sized error bars). Apart from showing a significant reduction in overall $NO_x$ emissions for a 2-stage $NH_3$ combustion, it also confirms to the findings reported by Nawaz

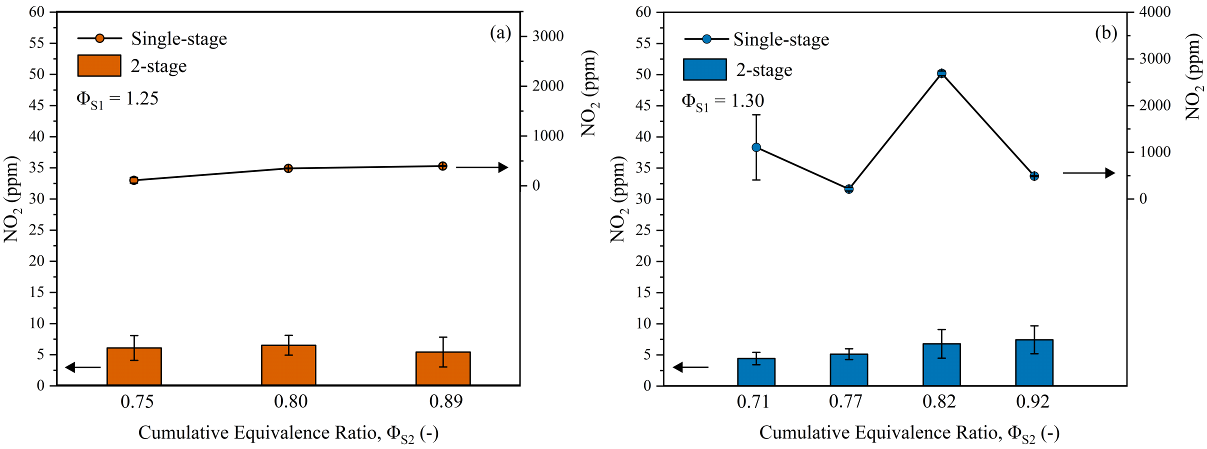

**Fig. 5:** $NO_2$ concentration in the exhaust at varying initial ((a)$\Phi_{S1}$ = 1.25, (b)$\Phi_{S1}$ and cumulative equivalence ratios with $N_2$ as the working fluid

.

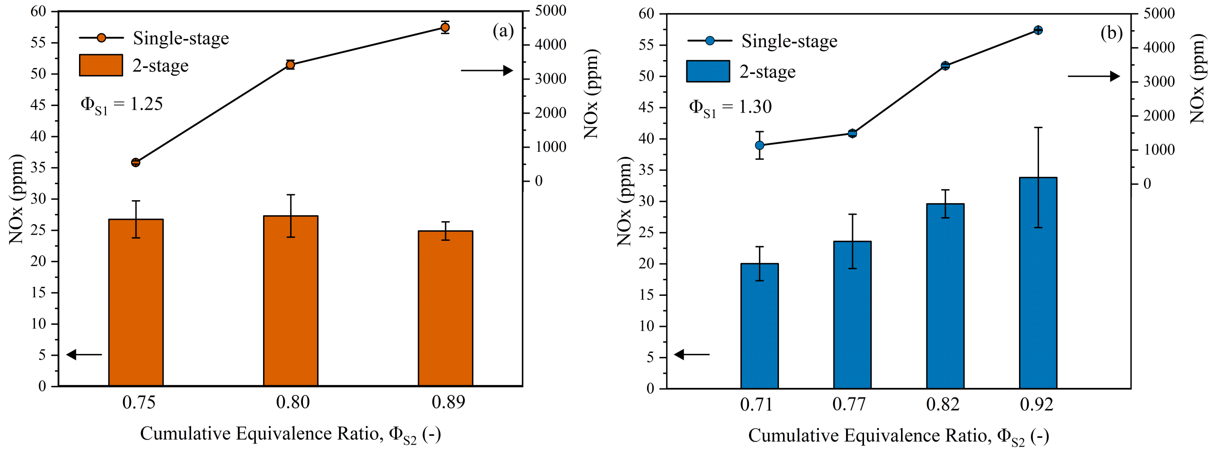

**Fig. 6:** $NO_x$ concentration in the exhaust at varying initial ((a)$\Phi_{S1}$ = 1.25, (b) $\Phi_{S1}$ = 1.3) and cumulative equivalence ratios with $N_2$ as the working fluid

.

et al. [16] where a reduction of $NO_x$ emissions was observed when the equivalence ratio of ammonia/air mixture decreased from $0.9$ to $0.7$.

Since NO is the dominant species that determines total $NO_x$ emissions, it is evident that anything that promotes NO relaxation will also reduce total $NO_x$ emissions. The unrelaxed NO produced in the primary stage is the dominant source of NO in final combustion products and this reduction is driven by longer residence time in combustors and higher pressures [47]. Since the first stage combustion in this study is conducted in a fuel rich region where the maximum pressure achieved during combustion is lower than that of a globally lean condition, a decrease in NO value is observed. At the second stage, the rise of pressure during combustion is even lower as the remaining fuel ignites amidst products from the first stage combustion. This results in a lower temperature during combustion that reduces the overall $NO_x$ production rates.

It has also been reported in literature that in rich ammonia flames (such as an initial equivalence ratio of 1.3), insufficient oxygen hinders nitrogen-containing radicals from bonding with O and OH, which encourages the production of $H_2$ and $N_2$ [29]. Furthermore, it is anticipated that when unburned ammonia recirculates, it may generate selective non-catalytic reactions within the flame, leading to the breakdown of NOx [29].

It has been reported in previous studies that as ammonia/air mixtures gets leaner, there is an increase in $N_2O$ concentration in the exhaust [16]. This trend is also observed in first stage experiments conducted in this study. Similar to the NO and $NO_2$ values, $N_2O$ also exhibit a decreasing trend upon switching to a 2-stage combustion method from a single stage combustion shown in fig 7.

The unburned ammonia left in the exhaust after each trial was also measured in the FTIR. For every

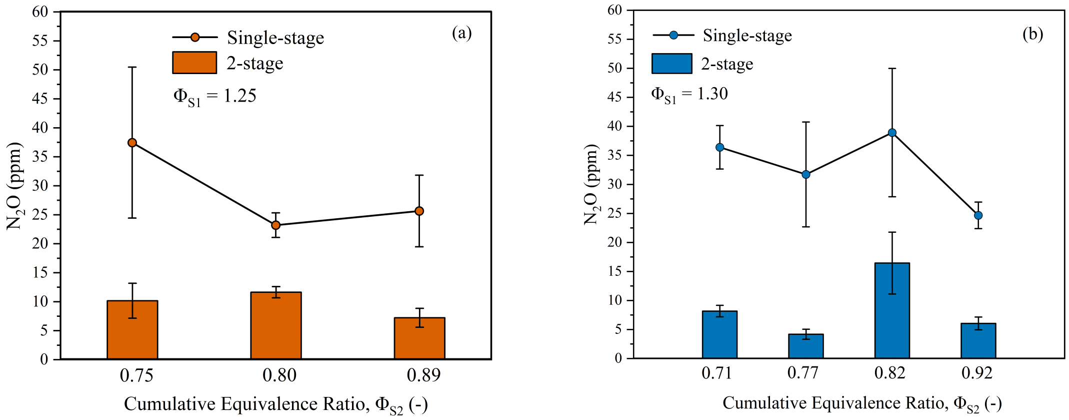

**Fig. 7:** $N_2O$ concentration in the exhaust at varying initial ((a) $\Phi_{S1}$ = 1.25, (b) $\Phi_{S1}$ = 1.3) and cumulative equivalence ratios with $N_2$ as the working fluid

.

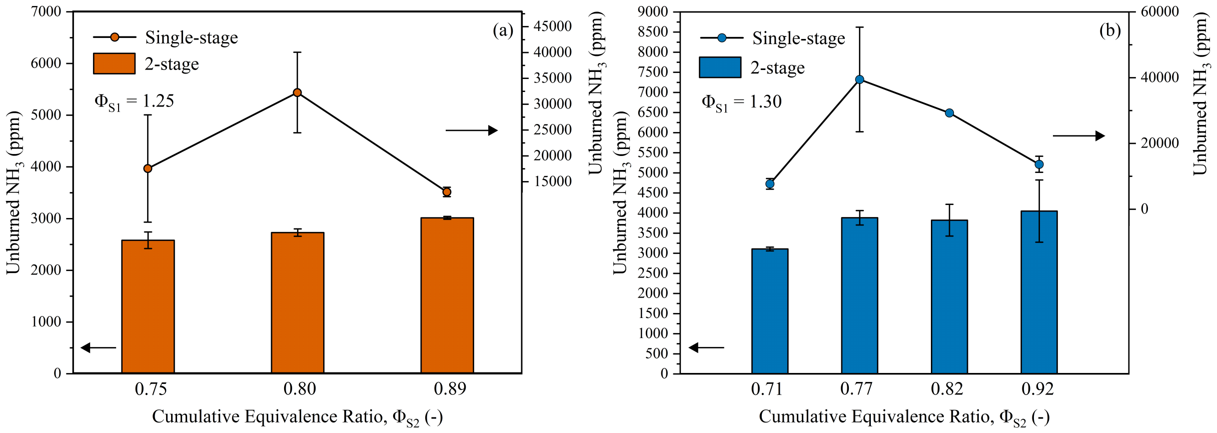

**Fig. 8:** Unburned $NH_3$ concentration in the exhaust at varying initial ((a) $\Phi_{S1}$ = 1.25, (b) $\Phi_{S1}$ = 1.3) and cumulative equivalence ratios with $N_2$ as working fluid

trial, regardless of the varying initial rich equivalence ratio the amount of unburned ammonia was always lower after the mixture went through two stages of combustion instead of being ignited at once which is also evident from Figure 8. Future studies have been planned to analyze the unburned fuel in detail for varying equivalence ratios of ammonia/air combustion.

### 3.2 Fuel bound $NO_x$ emissions from $NH_3$-Ar combustion

In addition to thermal $NO_x$ there is another significant pathway, known as fuel-bound $NO_x$, which results from reactions between oxygen and tthe nitrogen chemically bound within the fuel molecules. Unlike hydrocarbons, $NH_3$ contains a nitrogen atom in its molecule. As a result, fuel-bound $NO_x$ begins to contribute substantially to the overall $NO_x$ emissions.

Noble gases like Argon (Ar) have been utilized by researchers for enhancing thermal efficiency of the combustion process due to its higher specific heat ratio compared to nitrogen [52, 53]. In this study, nitrogen was replaced with argon as working fluid for ammonia combustion across different equivalence ratios. Due to the absence of environmental nitrogen, the $NO_x$ measured from $NH_3$-Ar experiments would only be generated by the fuel-bound mechanism. Upon comparing the emissions from $NH_3$-$N_2$ and $NH_3$-Ar mixtures (shown in Figure 9), it is evident that the mixtures with nitrogen as working fluid, generated an increased amount of $NO_x$ compared to the ones that contained argon. These mixtures did not only generate fuel bound $NO_x$ but also thermal $NO_x$ which resulted from the thermal dissociation of oxygen and nitrogen molecules and the subsequent reactions between them. Since this mechanism was neutralized in $NH_3$-Ar mixtures, they produced only the fuel bound $NO_x$. The difference between two emission values for a specific equivalence ratio shown in Figure 9 gives us an assumption of exactly how much of the $NO_x$ generated in ammonia combustion is from the thermal $NO_x$ mechanism.

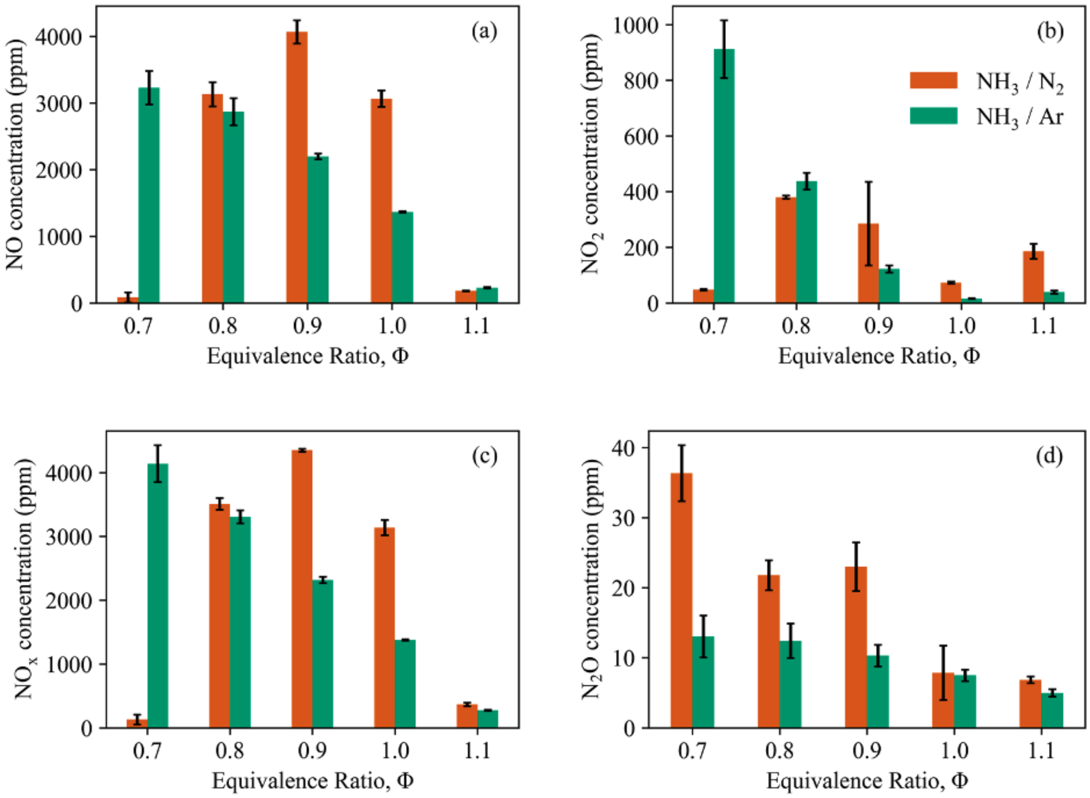

**Fig. 9:** Emission data from premixed $NH_3$-$N_2$ and $NH_3$-Ar flames across different equivalence ratios.

Regardless of the working fluid in use, NO, $N_2O$, and $NO_x$ showed an increasing trend as the mixture got progressively leaner. It is worth noting that there was a sharp decline $NO_x$ emission values as the equivalence ratio was changed from stoichiometry to $\Phi = 1.1$, primarily due to incomplete combustion.

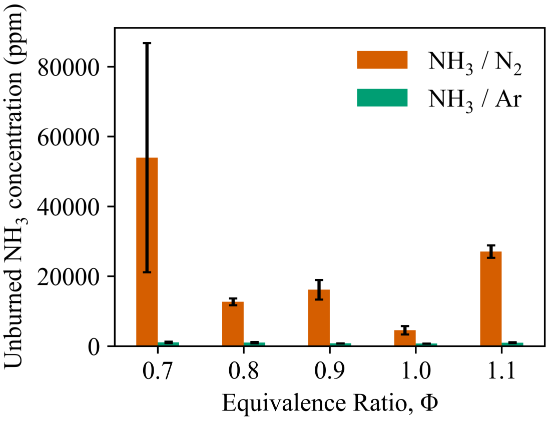

**Fig. 10:** Unburned ammonia from premixed $NH_3$-$N_2$ and $NH_3$-Ar flames at varying equivalence ratios

Emissions data from $\Phi = 0.7$ showed the opposite transition with changing working fluids where $NH_3$-Ar emissions were a lot higher than those of $NH_3$-$N_2$ mixture. At $\Phi = 0.7$, the mixture was extremely lean generating a floating shaped flame significantly influenced by buoyancy. This resulted in majority of the ammonia inside the CVCC (especially the lower region of the chamber) left unburned and generating such low emissions. This was not the case when argon was used as the working fluid and the flame generated at that particular mixture was free of any buoyancy effect. It can also be seen in Figure 10 where it shows the comparison between the unburned ammonia from argon and nitrogen experiments.

### 3.3 Laminar Burning Velocity

Laminar burning velocity (LBV) is a characteristic property of a fuel-mixture. It is a commonly used metric to validate chemical kinetic models while also giving insight into the pressure rise, heat release rate and the residence time inside a combustion chamber.

Apart from reducing thermal $NO_x$ emissions, combustion of any fuel with argon as working fluid can be utilized as a potential method of increasing flame speed. This works exceptionally well for fuels with low laminar burning velocities such as ammonia. Due to the smaller specific heat capacity of Ar (20.786 $\mathrm{J/mol-K}$) compared to $N_2$ (29.124 $\mathrm{J/mol-K}$), the mass burning flux of argon is higher than that of nitrogen, meaning that the flame generated by a fuel accompanied by argon would always have a higher adiabatic flame temperature when replaced with nitrogen resulting in comparatively increased laminar burning velocity [54].

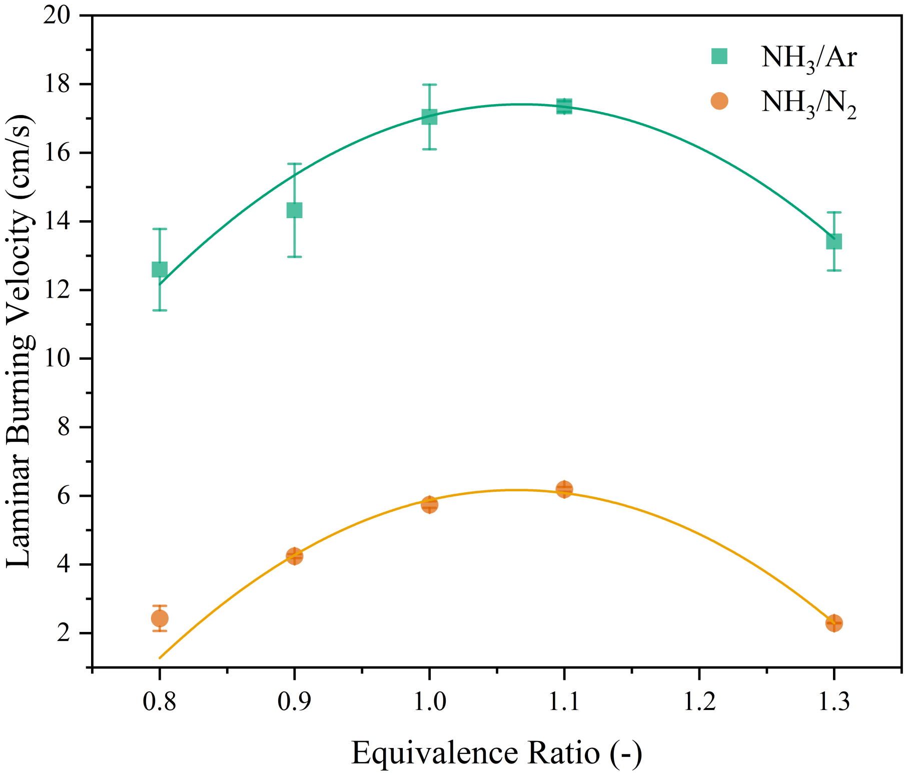

**Fig. 11:** Laminar burning velocity of premixed $NH_3$-$N_2$ and $NH_3$-Ar flames at varying equivalence ratios

Figure 11 shows the comparison between the laminar burning velocities of $NH_3$-Ar and $NH_3$-$N_2$ flames across varying equivalence ratios. As expected, $NH_3$-Ar flames exhibit increased LBVs across all of the equivalence ratios tested. Both Ar and $N_2$ mixtures achieve peak LBV at the equivalence ratio of $\Phi$ = 1.1 at then decreases gradually as the mixture equivalence ratio shifts away.

It is also important to know where does this shift of increased LBV stands with respect to the other methods of increasing ammonia's flame speed. Figure 12 compares the values found in this study with the values reported by Nawaz et al. [16] where hydrogen was added with ammonia in varying concentrations to increase the LBV.

Spherically expanding flames are heavily influenced by buoyant forces when the fuel mixture is close to its lower flammability limit. It can be seen that at fuel lean conditions, $NH_3$-Ar flames do not appear as floating flames like they do in corresponding $NH_3$-$N_2$ flames (shown is Figure 13). This implies that by replacing $N_2$ with Ar, it is possible to stretch the flammability limit of $NH_3$ combustion further (both on the lean and rich side). Since flammability limits of a fuel mixture are determined by the fuel chemistry, adiabatic flame temperature, pressure, and thermal radiation, switching the working fluid from nitrogen to argon can enable combustion of ammonia at even leaner conditions[55].

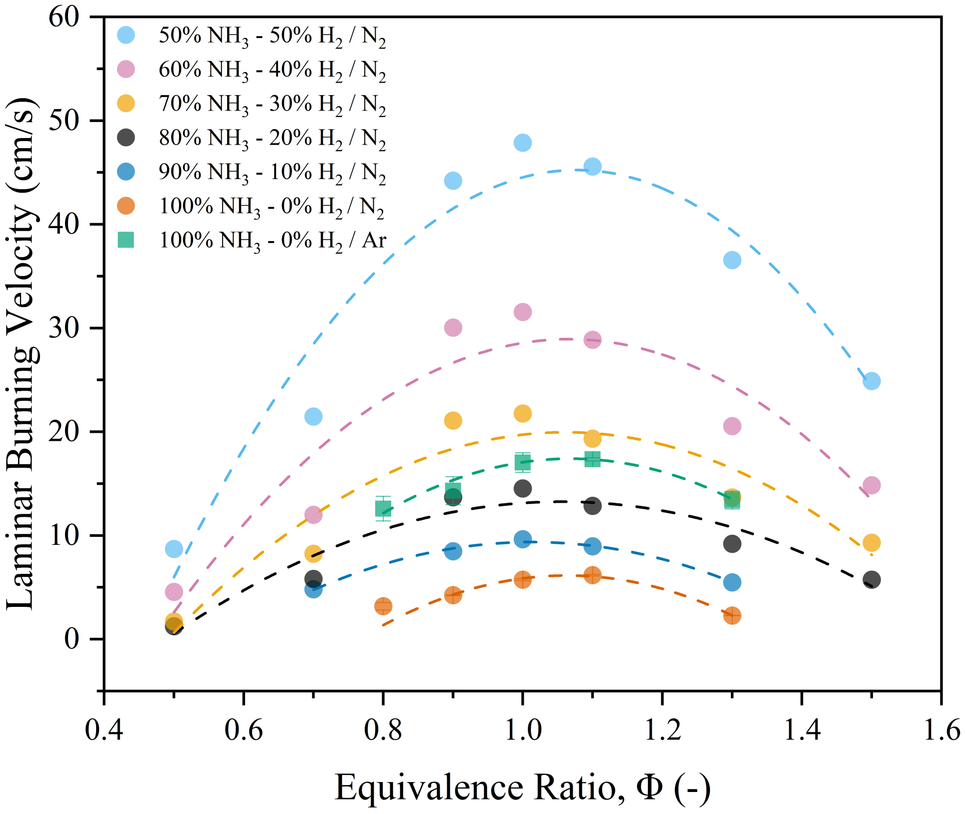

**Fig. 12:** Comparison between laminar burning velocity of premixed $NH_3$-Ar and different blends of $NH_3$-$H_2$-$N_2$ flames at varying equivalence ratios

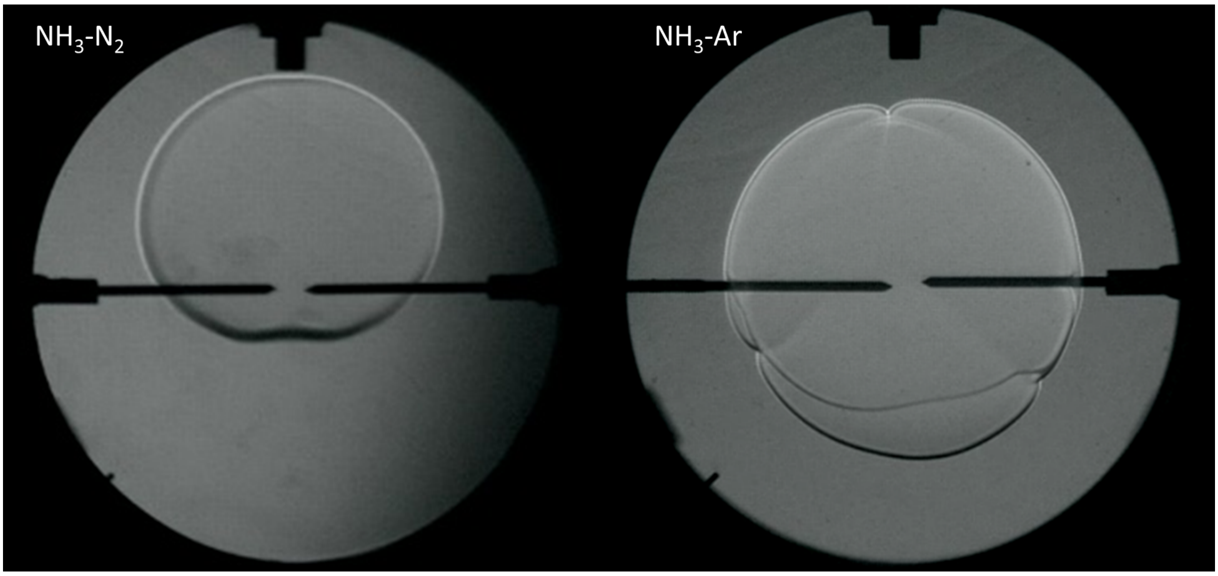

**Fig. 13:** Premixed (a) $NH_3$-$N_2$ and (b) $NH_3$-Ar flames at an equivalence ratio of $\Phi$ = 0.9

## 4. Conclusions

Staged combustion of $NH_3$ was tested inside a constant volume combustion chamber across various initial and cumulative equivalence ratios. An analogous ammonia/air mixture was prepared separately to match the cumulative equivalence ratio for each of the 2-stage mixtures tested and ignited directly. The exhaust generated from both these mixtures was sent to an FTIR spectrometer and analyzed for $NO_x$ emission data. Based on the schlieren images and spectra analysis obtained during the experiments, the following conclusions can be made.

- For an initial equivalence ratio of 1.3, a decreasing trend in NO emissions was observed as the secondary mixture got progressively leaner. This trend was not observed when the initial equivalence ratio was 1.25.
- NO is the dominant species in the total $NO_x$ emissions for all tested conditions.
- $N_2O$ and $NO_2$ emissions remained relatively constant with varying secondary air.
- Regardless of the initial or cumulative equivalence ratios tested, all of the exhaust showed a dramatic reduction in NO, $NO_2$, and $NO_x$ emissions (ranging from 55% to 98%) compared to direct one-stage combustion of mixtures at corresponding equivalence ratios.
- Similar observations were made for single-stage and 2-stage $N_2O$ measurements. The data showed a drop of 56% to 87% when burning $NH_3$ in staged combustion compared to a single-stage across all of the different conditions tested.
- Regardless of the working fluid (Ar or $N_2$) in use, NO, $N_2O$, and $NO_x$ showed an increasing trend as the mixture got leaner.
- Replacing nitrogen with argon as the working fluid results in an increase in the LBV across all of the tesetd equivalence ratios, with the highest value observed at $\Phi = 1.1$.
- Usage of argon as the working fluid stretches the range of flammability limit of ammonia flames, resulting in spherical flames even at low equivalence ratios with minimal buoyant forces.

In conclusion, employing a two-stage combustion procedure — initiating combustion in an oxygen-deprived environment followed by igniting the remaining ammonia in a fuel-lean mixture — demonstrates an overall reduction in NOx and $N_2O$ emissions compared to single-stage stoichiometric operation. It is important to note that the experimental methodology discussed here does not encompass applications, since specific factors such as residence times and wall temperatures will also affect emission pathways. Nevertheless, these findings underscore the potential of staged combustion for mitigating emissions in ammonia-based systems. Future research should focus on optimizing equivalence ratios for both stages to further minimize NOx emissions, while also exploring effective strategies for integrating this approach into gas turbines or internal combustion engines.

## References

[1] EIA Office of Energy Statistics, "US Energy Information Administration (EIA) Monthly Energy Review - May 2023," *US Department of Energy: Washington, DC, USA*, 2023.

[2] H. Stančin, H. Mikulčić, X. Wang, and N. Duić, "A review on alternative fuels in future energy system," *Renewable and Sustainable Energy Reviews*, vol. 128, p. 109 927, 2020.

[3] A. Hayakawa, T. Goto, R. Mimoto, Y. Arakawa, T. Kudo, and H. Kobayashi, "Laminar burning velocity and markstein length of ammonia/air premixed flames at various pressures," *Fuel*, vol. 159, pp. 98–106, 2015, ISSN: 0016-2361.

[4] J. Andersson and S. Grönkvist, "Large-scale storage of hydrogen," *International Journal of Hydrogen Energy*, vol. 44, no. 23, pp. 11 901–11 919, 2019.

[5] J. Lim, C. A. Fernández, S. W. Lee, and M. C. Hatzell, "Ammonia and nitric acid demands for fertilizer use in 2050," *ACS Energy Letters*, vol. 6, no. 10, pp. 3676–3685, 2021.

[6] A. Yapicioglu and I. Dincer, "A review on clean ammonia as a potential fuel for power generators," *Renewable and Sustainable Energy Reviews*, vol. 103, pp. 96–108, 2019.

[7] A. Nemmour, A. Inayat, I. Janajreh, and C. Ghenai, “Green hydrogen-based e-fuels (e-methane, e-methanol, e-ammonia) to support clean energy transition: A literature review,” *International Journal of Hydrogen Energy*, 2023, ISSN: 0360-3199.

[8] E. Latvytė, X. Zhu, L. Wu, R. Lan, P. Vale, and J. E. Graves, “A low-temperature ammonia electrolyser for wastewater treatment and hydrogen production,” *International Journal of Hydrogen Energy*, 2023, ISSN: 0360-3199.

[9] M. El-Shafie and S. Kambara, “Recent advances in ammonia synthesis technologies: Toward future zero carbon emissions,” *International Journal of Hydrogen Energy*, vol. 48, no. 30, pp. 11 237–11 273, 2023, ISSN: 0360-3199.

[10] A. Gupta, B. Likozar, R. Jana, W. C. Chanu, and M. K. Singh, “A review of hydrogen production processes by photocatalytic water splitting – from atomistic catalysis design to optimal reactor engineering,” *International Journal of Hydrogen Energy*, vol. 47, no. 78, pp. 33 282–33 307, 2022, ISSN: 0360-3199.

[11] S. Zhang, Y. Zhao, R. Shi, G. I. Waterhouse, and T. Zhang, “Photocatalytic ammonia synthesis: Recent progress and future,” *EnergyChem*, vol. 1, no. 2, p. 100 013, 2019, ISSN: 2589-7780.

[12] R. Lan, J. T. S. Irvine, and S. Tao, “Synthesis of ammonia directly from air and water at ambient temperature and pressure,” en, *Scientific Reports*, vol. 3, no. 1, p. 1145, Dec. 2013, ISSN: 2045-2322. (visited on 11/29/2022).

[13] H. Kobayashi, A. Hayakawa, K. K. A. Somarathne, and E. C. Okafor, “Science and technology of ammonia combustion,” *Proceedings of the Combustion Institute*, vol. 37, no. 1, pp. 109–133, 2019, ISSN: 1540-7489.

[14] J. Li, S. Lai, D. Chen, R. Wu, N. Kobayashi, L. Deng, and H. Huang, “A Review on Combustion Characteristics of Ammonia as a Carbon-Free Fuel,” *Frontiers in Energy Research*, vol. 9, p. 760 356, Oct. 2021, ISSN: 2296-598X. (visited on 11/15/2022).

[15] H. Haase, *Electrostatic hazards: their evaluation and control*, 1. Aufl. Weinheim ; New York: Verlag Chemie, 1976, 124 pp., ISBN: 978-3-527-25684-6.

[16] B. Nawaz, M. N. Nasim, S. K. Das, J. Landis, A. SubLaban, J. P. Trelles, D. Assanis, N. Van Dam, and J. H. Mack, “Combustion characteristics and emissions of nitrogen oxides (NO, NO2, N2O) from spherically expanding laminar flames of ammonia–hydrogen blends,” *International Journal of Hydrogen Energy*, vol. 65, pp. 164–176, 2024.

[17] A. M. Elbaz, S. Wang, T. F. Guiberti, and W. L. Roberts, “Review on the recent advances on ammonia combustion from the fundamentals to the applications,” *Fuel Communications*, vol. 10, p. 100 053, 2022.

[18] H. Kobayashi, A. Hayakawa, K. K. A. Somarathne, and E. C. Okafor, “Science and technology of ammonia combustion,” *Proceedings of the combustion institute*, vol. 37, no. 1, pp. 109–133, 2019.

[19] A. Valera-Medina, H. Xiao, M. Owen-Jones, W. I. David, and P. Bowen, “Ammonia for power,” *Progress in Energy and combustion science*, vol. 69, pp. 63–102, 2018.

[20] S. Mashruk, M. Kovaleva, A. Alnasif, C. T. Chong, A. Hayakawa, E. C. Okafor, and A. Valera-Medina, “Nitrogen oxide emissions analyses in ammonia/hydrogen/air premixed swirling flames,” *Energy*, vol. 260, p. 125 183, 2022.

[21] S. Mashruk, E. Okafor, M. Kovaleva, A. Alnasif, D. Pugh, A. Hayakawa, and A. Valera-Medina, “Evolution of N2O production at lean combustion condition in NH3/H2/air premixed swirling flames,” *Combustion and Flame*, vol. 244, p. 112 299, 2022.

[22] S. Mashruk, X. Zhu, W. L. Roberts, T. F. Guiberti, and A. Valera-Medina, “Chemiluminescent footprint of premixed ammonia-methane-air swirling flames,” *Proceedings of the Combustion Institute*, vol. 39, no. 1, pp. 1415–1423, 2023.

[23] M. Zhang, Z. An, L. Wang, X. Wei, B. Jianayihan, J. Wang, Z. Huang, and H. Tan, “The regulation effect of methane and hydrogen on the emission characteristics of ammonia/air combustion in a model combustor,” *International Journal of Hydrogen Energy*, vol. 46, no. 40, pp. 21 013–21 025, 2021.

[24] K. D. K. A. Somarathne, E. C. Okafor, D. Sugawara, A. Hayakawa, and H. Kobayashi, “Effects of oh concentration and temperature on no emission characteristics of turbulent non-premixed CH4-NH3-air flames in a two-stage gas turbine like combustor at high pressure,” *Proceedings of the Combustion Institute*, vol. 38, no. 4, pp. 5163–5170, 2021.

[25] D. Pugh, J. Runyon, P. Bowen, A. Giles, A. Valera-Medina, R. Marsh, B. Goktepe, and S. Hewlett, "An investigation of ammonia primary flame combustor concepts for emissions reduction with OH*, NH2* and NH* chemiluminescence at elevated conditions," *Proceedings of the combustion institute*, vol. 38, no. 4, pp. 6451–6459, 2021.

[26] M. O. Vigueras-Zúñiga, M. E. Tejeda-del-Cueto, S. Mashruk, M. Kovaleva, C. L. Ordóñez-Romero, and A. Valera-Medina, "Methane/ammonia radical formation during high temperature reactions in swirl burners," *Energies*, vol. 14, no. 20, p. 6624, 2021.

[27] A. A. Khateeb, T. F. Guiberti, G. Wang, W. R. Boyette, M. Younes, A. Jamal, and W. L. Roberts, "Stability limits and NO emissions of premixed swirl ammonia-air flames enriched with hydrogen or methane at elevated pressures," *International Journal of Hydrogen Energy*, vol. 46, no. 21, pp. 11 969–11 981, 2021.

[28] A. Mohammadpour, K. Mazaheri, and A. Alipoor, "Reaction zone characteristics, thermal performance and NOx/N2O emissions analyses of ammonia mild combustion," *International Journal of Hydrogen Energy*, vol. 47, no. 48, pp. 21 013–21 031, 2022.

[29] R. C. Rocha, M. Costa, and X.-S. Bai, "Combustion and emission characteristics of ammonia under conditions relevant to modern gas turbines," *Combustion Science and Technology*, vol. 193, no. 14, pp. 2514–2533, 2021.

[30] D. Pugh, P. Bowen, A. Valera-Medina, A. Giles, J. Runyon, and R. Marsh, "Influence of steam addition and elevated ambient conditions on NOx reduction in a staged premixed swirling NH3/H2 flame," *Proceedings of the combustion institute*, vol. 37, no. 4, pp. 5401–5409, 2019.

[31] Z. Li and S. Li, "Effects of inter-stage mixing on the NOx emission of staged ammonia combustion," *International Journal of Hydrogen Energy*, vol. 47, no. 16, pp. 9791–9799, 2022.

[32] E. C. Okafor, O. Kurata, H. Yamashita, T. Inoue, T. Tsujimura, N. Iki, A. Hayakawa, S. Ito, M. Uchida, and H. Kobayashi, "Liquid ammonia spray combustion in two-stage micro gas turbine combustors at 0.25 mpa; relevance of combustion enhancement to flame stability and NOx control," *Applications in Energy and Combustion Science*, vol. 7, p. 100 038, 2021.

[33] R. McKinney, A. Cheung, W. Sowa, and D. Sepulveda, "The Pratt & Whitney Talon X low emissions combustor: Revolutionary results with evolutionary technology," in *45th AIAA aerospace sciences meeting and exhibit*, 2007, p. 386.

[34] S. Wu, D. Che, Z. Wang, and X. Su, "NOx emissions and nitrogen fate at high temperatures in staged combustion," *Energies*, vol. 13, no. 14, p. 3557, 2020.

[35] S. Mashruk, H. Xiao, and A. Valera-Medina, "Rich-quench-lean model comparison for the clean use of humidified ammonia/hydrogen combustion systems," *International Journal of Hydrogen Energy*, vol. 46, no. 5, pp. 4472–4484, 2021.

[36] M. G. Božo, S. Mashruk, S. Zitouni, and A. Valera-Medina, "Humidified ammonia/hydrogen RQL combustion in a trigeneration gas turbine cycle," *Energy conversion and management*, vol. 227, p. 113 625, 2021.

[37] E. C. Okafor, M. Tsukamoto, A. Hayakawa, K. K. A. Somarathne, T. Kudo, T. Tsujimura, and H. Kobayashi, "Influence of wall heat loss on the emission characteristics of premixed ammonia-air swirling flames interacting with the combustor wall," *Proceedings of the combustion Institute*, vol. 38, no. 4, pp. 5139–5146, 2021.

[38] E. C. Okafor, K. K. A. Somarathne, R. Ratthanan, A. Hayakawa, T. Kudo, O. Kurata, N. Iki, T. Tsujimura, H. Furutani, and H. Kobayashi, "Control of NOx and other emissions in micro gas turbine combustors fuelled with mixtures of methane and ammonia," *Combustion and flame*, vol. 211, pp. 406–416, 2020.

[39] A. Jamrozik, W. Tutak, A. Kociszewski, and M. Sosnowski, "Numerical simulation of two-stage combustion in SI engine with prechamber," *Applied Mathematical Modelling*, vol. 37, no. 5, pp. 2961–2982, 2013.

[40] S. Szwaja, A. Jamrozik, and W. Tutak, "A two-stage combustion system for burning lean gasoline mixtures in a stationary spark ignited engine," *Applied Energy*, vol. 105, pp. 271–281, 2013.

[41] Y. Sun and R. D. Reitz, "Modeling diesel engine NOx and soot reduction with optimized two-stage combustion," SAE Technical Paper, Tech. Rep., 2006.

[42] S. Tanaka, F. Ayala, J. C. Keck, and J. B. Heywood, “Two-stage ignition in HCCI combustion and HCCI control by fuels and additives,” *Combustion and flame*, vol. 132, no. 1-2, pp. 219–239, 2003.

[43] L. Tartakovsky and M. Sheintuch, “Fuel reforming in internal combustion engines,” *Progress in Energy and Combustion Science*, vol. 67, pp. 88–114, 2018.

[44] X. Zhu, J. Du, Z. Yu, Y.-B. Cheng, and Y. Wang, “NOx emission and control in ammonia combustion: State-of-the-art review and future perspectives,” *Energy & Fuels*, vol. 38, no. 1, pp. 43–60, 2023.

[45] M. Alnajideen, H. Shi, W. Northrop, D. Emberson, S. Kane, P. Czyzewski, M. Alnaeli, S. Mashruk, K. Rouwenhorst, C. Yu, S. Eckart, and A. Valera-Medina, “Ammonia combustion and emissions in practical applications: A review,” *Carbon Neutrality*, vol. 3, no. 1, pp. 1–45, 2024.

[46] S. Gubbi, R. Cole, B. Emerson, D. Noble, R. Steele, W. Sun, and T. Lieuwen, “Air quality implications of using ammonia as a renewable fuel: How low can NOx emissions go?” *ACS Energy Letters*, vol. 8, no. 10, pp. 4421–4426, 2023.

[47] S. Gubbi, R. Cole, B. Emerson, D. Noble, R. Steele, W. Sun, and T. Lieuwen, “Evaluation of minimum NOx emission from ammonia combustion,” *Journal of Engineering for Gas Turbines and Power*, vol. 146, no. 3, 2024.

[48] S. Li, S. Zhang, H. Zhou, and Z. Ren, “Analysis of air-staged combustion of NH3-CH4 mixture with low NOx emission at gas turbine conditions in model combustors,” *Fuel*, vol. 237, pp. 50–59, 2019.

[49] M. N. Nasim, B. Nawaz, S. K. Das, A. SubLaban, L. M. G.-C. González, J. R. Serrano, and J. H. Mack, “Manipulating hydrogen oxy-combustion through carbon dioxide addition,” *Fuel*, vol. 357, p. 129 844, 2024, ISSN: 0016-2361.

[50] K. P. Horn, “Exhaust composition in a small internal combustion engine using FTIR spectroscopy,” Air Force Institute of Technology, Wright-Patterson AFB, Graduate School of Engineering and Management, Tech. Rep., 2015.

[51] H. S. Cole and J. E. Summerhays, “A review of techniques available for estimating short-term NO2 concentrations,” *Journal of the Air Pollution Control Association*, vol. 29, no. 8, pp. 812–817, 1979.

[52] F. Rahim, M. Elia, M. Ulinski, and M. Metghalchi, “Burning velocity measurements of methane-oxygen-argon mixtures and an application to extend methane-air burning velocity measurements,” *International Journal of Engine Research*, vol. 3, no. 2, pp. 81–92, 2002.

[53] M. Baghirzade, M. N. Nasim, B. Nawaz, J. Aguilar, M. Shahsavan, M. Morovatiyan, and J. H. Mack, “Analysis of Premixed Laminar Combustion of Methane With Noble Gases as a Working Fluid,” *ASME 2021 Internal Combustion Engine Division Fall Technical Conference*, vol. Internal Combustion Engine Division Fall Technical Conference, V001T04A005, 2021.

[54] Y. Li, M. Bi, K. Zhang, and W. Gao, “Effects of nitrogen and argon on ammonia-oxygen explosion,” *International Journal of Hydrogen Energy*, vol. 46, no. 40, pp. 21 249–21 259, 2021.

[55] A. Z. Mendiburu, J. A. Carvalho Jr, and Y. Ju, “Flammability limits: A comprehensive review of theory, experiments, and estimation methods,” *Energy & Fuels*, vol. 37, no. 6, pp. 4151–4197, 2023.

# Session 3.3 SPRAYS & COMBUSTION

# Infrared High-Speed Thermography of Wall Surface Impinged by Diesel Spray Flame:
# Effects of Inversed-delta Injection Rate Shaping using Heavy-Duty TAIZAC on Wall Heat Transfer

F. Shimizu[1], R. Yoshiuda[1], H. Kinoshita[1], T. Aizawa[1], T. Shimada[1],
K. Miyashita[2], A. Matsumoto[2] and R. Kitabatake[2]

[1] Graduated School of Science and Technology, Meiji University. 1-1-1 Higashimita, Tama, Kawasaki, Kanagawa, Japan
[2] Isuzu Advanced Engineering Center, LTD, Japan

E-mail: taizawa@meiji.ac.jp
Telephone: +(81) 44 934 7400
Fax: +(81) 44 934 7400

**Abstract.** As a potential strategy for thermal efficiency improvement of diesel engines, TAIZAC (TAndem Injector Zapping ACtivation) injectors have been developed with simple serial connection of the injectors in the authors' laboratory at Meiji University. "Inversed-delta" injection rate shaping (i.e., injection rate is ramped down during the injection period) can be easily realized using TAIZAC injectors and it has been expected to reduce late combustion and wall heat loss simultaneously. Varieties of TAIZAC injectors assuming passenger car engines have already achieved a cooling loss reduction in previous performance tests. However, it is not easy to elucidate the heat transfer phenomena on the diesel-flame-impinged wall surface, and the mechanism of cooling loss reduction by inversed-delta injection has not been clarified yet. In order to examine the effects of the inversed-delta injection on wall heat transfer in heavy-duty diesel engines, heavy-duty TAIZAC injectors were newly developed and high-speed infrared thermography of chromium coated quartz wall surface impinged by diesel spray flame was conducted in a constant volume combustion chamber. Regardless of the increased fuel amount and the change in the injection rate patterns between conventional rectangle and inversed-delta cases, the infrared radiation from the back surface of the chromium layer consistently exhibited distinct radially striped patterns similarly to the previous parametric studies with light-duty TAIZAC. With inversed-delta injection, heat flux on wall surface was successfully reduced compared to the conventional rectangular injection case, potentially due to reduced spray penetration and reduced flow velocity near the wall caused by the inversed-delta injection. In the conventional rectangular injection case, the advection speed of the radially striped pattern exhibited the first peak at the beginning of wall impingement and the second peak at the end of injection. This second peak was considered to be caused by the entrainment wave arising at the end of injection. In the inversed-delta injection cases, the second peak of advection speed became indistinct as the extent of the inversed-delta injection duration was increased. Interestingly, the heat flux did not show notable increase despite of advection speed increase and expected flame temperature increase at the end of injection. Possible explanations for this low correlation between the advection speed and heat flux at the end of injection might be reduced temperature difference between the flame and the wall in the later phase of combustion period and potential difference in the near-wall flow component vertical to the wall. Further examination of the results obtained in the present study is expected to contribute to better understandings of the wall heat transfer during diesel flame impingement.

## 1. Introduction

It is necessary to achieve carbon neutrality by 2050 all over the world [1]. Responding to the social demand, the automotive industry is rapidly accelerating the replacement of internal combustion engine vehicles with electrified ones. However, since $CO_2$ emissions come mostly from the burning of fossil fuels, global energy-related $CO_2$ emissions need to be reduced if we are to slow global warming [2]. Fossil fuel consumption still accounts for a significant portion of primary energy in most countries including Japan [3]. Under these circumstances, the reduction of $CO_2$ emissions through electrification of vehicles is limited.

According to the scenarios examined in BP's Energy Outlook2023 [4], the growth of the global economy requires more vehicles to transport goods, and even in the accelerated and Net Zero scenario

(NZE2050), medium- and heavy-duty vehicles will rely on oil products more than 65%. Among different types of internal combustion engines, the relative importance of diesel engines will not change in the carbon neutral society to come, mainly because of its inherently high thermal efficiency and high torque, and also for the best utilization of multiple distillate fractions from crude oil. It is also indicated that diesel fuel will likely be a significant part of the global energy economy well beyond 2050. Therefore, in order to realize the carbon neutrality in the global transportation sector, the maximum efforts have to be made both in the vehicle electrification and the thermal efficiency improvement of internal combustion engines, pursuing their best balance from the long-term perspective.

Multiple government-funded programs such as SIP Innovative Combustion Technology program in Japan [5] and SuperTruck II program in the U.S. [6] have demonstrated brake thermal efficiency over 50% for passenger diesel and close to 55% for heavy-duty diesel, respectively. Johansson et al and Uchida et al have recently been demonstrating brake thermal efficiency exceeding 55% with Double Compression Expansion Engine (DCEE) concept and/or an engine equipped with three injectors [7, 8, 9]. In order to improve the thermal efficiency of diesel engines, reduction of cooling loss has been attracting growing attention [10, 11, 12]. However, heat transfer from diesel flame to combustion chamber wall, known as a dominant factor in the cooling loss, is an extremely unsteady and spatially varying process. With conventional point-measurement heat flux sensors, it is extremely difficult to understand the spatial/temporal variation of heat flux distribution and its correlation with turbulent flame structure [13, 14, 15, 16, 17, 18]. The details of the process and its mechanism therefore remain unclear and relevant engine heat transfer models need further improvements.

As a new method to examine the extremely unsteady and spatially varying wall heat transfer phenomena on diesel engine combustion chamber wall, high-speed imaging of infrared thermal radiation from a chromium-coated glass wall surface impinged by a diesel spray flame has been explored and conducted in a constant volume combustion chamber by the authors using a high-speed infrared camera [19, 20]. Based on the previous reports, it was confirmed that the distributions of infrared radiation, temperature, and heat flux exhibited coherent and streaky structure with radially striped patterns extending and waving from a stagnation point likely reflecting the near-wall turbulent structure in a wall impinging diesel flame under parametric studies varying fuel injection pressure, ambient gas oxygen concentration, wall impinging distance, wall surface roughness, and wall materials, which corresponded to the actual diesel engine operating conditions.

In addition, authors have been proposing the use of progressive ramp-down or “inversed-delta” injection rate shaping as a potential strategy for thermal efficiency improvement of diesel engines, targeting simultaneous reduction of the late combustion and the wall heat loss [21, 22, 23, 26]. Figure 1 is a conceptual diagram for the inversed-delta injected diesel combustion based on the results of optical diagnostics [21, 23] and LES predictions of a diesel spray flame with detailed chemical kinetics [24, 25]. Compared to the conventional rectangular injection, the inversed-delta injection is predicted to enable;

1. suppressed catch up of following injected fuel to the preceding injected fuel and shift of the axial fuel distribution towards the upstream,
2. reduced flame tip penetration and flame impingement on the piston surface and thus reduced wall heat loss, and
3. enhanced growth and axial separation of large vortical structures enhancing air entrainment, mixing and thus reducing combustion duration.

For these features, inversed-delta injection is expected to reduce cooling loss by suppressing the wall impingement of the hot flame. In order to realize the above explained inversed-delta injection for experimental demonstrations, a new injector hardware with simple serial connection of injectors was developed in our laboratory and named as “TAIZAC (TAndem Injectors Zapping ACtivation)” [22, 26].

In our studies, TAIZAC can easily realize the progressive ramp-down or “inversed-delta” injection rate shaping as a potential strategy for thermal efficiency improvement of diesel engines, as demonstrated in our numerous previous publications on engine test results using TAIZAC injectors [22, 27, 28, 29]. For instance, the fourth-generation TAIZAC injector was applied to a single-cylinder engine and a cooling loss reduction of 2.2 pt was reported in a previous performance test [27]. Our numerous previous engine test results of TAIZAC have also shown that NOx and PM emissions are not worsen by the inversed-delta injection. The NOx emission level is around 1500ppm without EGR and PM emission level is 0.02-0.04 FSN both for conventional rectangle and inversed-delta cases [27]. However, it is not easy to elucidate the heat transfer phenomena on the diesel-flame-impinged wall surface with strong spatio-temporal variations using conventional measurement methods, and the mechanism of cooling loss reduction by inversed-delta injection is insufficiently clarified. In order to elucidate the heat transfer phenomena on the diesel-flame-impinged wall surface, we considered that the above method using the high-speed imaging of infrared thermal radiation from a chromium-coated glass wall surface impinged by a diesel spray flame would be effective.

The previous studies using TAIZAC injectors were conducted mainly on the assumption of passenger car engines. The authors have supposed that the effect of the inversed-delta injection described above is likely to be enhanced in heavy-duty diesel engines because they have relatively larger combustion chambers and longer injection periods compared with passenger car engines. We have newly developed heavy-duty TAIZAC injectors and have conducted some performance tests in single-cylinder engine and in constant volume combustion vessel. The purpose of this study is to examine the effects of the inversed-delta injection on wall heat transfer in heavy-duty diesel engines using a newly developed heavy-duty TAIZAC (TAndem Injector Zapping ACtivation) injectors, and high-speed infrared thermography of chromium coated quartz wall surface impinged by diesel spray flame was conducted in a constant volume combustion chamber.

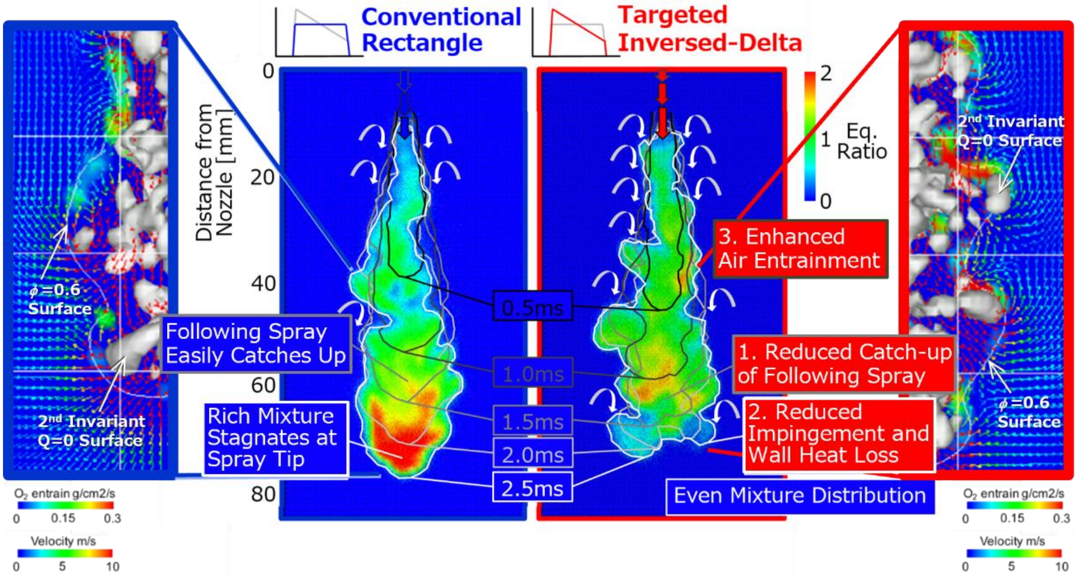
Conventional Rectangle
Targeted Inversed-Delta
Distance from Nozzle [mm]
0
20
40
60
80
2
1
0
Eq. Ratio
3. Enhanced Air Entrainment
0.5ms
1.0ms
1.5ms
2.0ms
2.5ms
Following Spray Easily Catches Up
Rich Mixture Stagnates at Spray Tip
1. Reduced Catch-up of Following Spray
2. Reduced Impingement and Wall Heat Loss
Even Mixture Distribution
φ=0.6 Surface
2nd Invariant Q=0 Surface
φ=0.6 Surface
2nd Invariant Q=0 Surface
O2 entrain g/cm2/s
0 0.15 0.3
Velocity m/s
0 5 10
O2 entrain g/cm2/s
0 0.15 0.3
Velocity m/s
0 5 10

**Fig. 1.** Conceptual diagram for the conventional rectangular and inversed-delta injected diesel combustion

## 2. Experimental methodology

### 2.1 Experimental Apparatus

The setup and conditions of the present study are similar to the ones of our previous study [19, 20] and details can be found in our previous publication [19, 20]. The high-speed imaging of infrared thermal radiation from the diesel-flame-impinged wall surface was conducted in a pre-combustion type optically accessible constant-volume combustion vessel as shown in Figure 2. The vessel has three identical optical window ports at both sides and the top with a view field of Φ35mm in a diameter. The window at the top was used for high-speed visualization of soot luminosity from a diesel spray flame using a high-speed camera (nac Image Technology Inc, GX-1, 10000fps, 464 × 464 pixels). One of the side ports was used for installing a heavy-duty TAIZAC injector, which is described in the following section, instead of a window and the other port on the opposite side was used for infrared high-speed imaging of the wall surface. The optical polished quartz patch was attached onto the inner surface of the window and coated with a 600 nm thick chromium layer and a protective 30nm SiO layer. This coating serves as a thermal radiator targeted for infrared high-speed imaging and also as a blocker for intense diesel flame soot luminosity. The 2mm thickness of the quartz window patch is estimated to be thick enough to cover the thermal penetration depth into the window patch during diesel flame impingement. The infrared radiation from the chromium-coated window surface heated by the diesel flame impingement was observed from back through the window using a high-speed infrared camera (Telops, Fast-IR M3k, 10000fps, 128 × 128 pixels). The resulting spatial resolution of the flame-impinged chamber wall images is approximately 0.27mm (35mm / 128 pixels).

The measured infrared radiation was converted to temperature by calibrating the infrared radiation intensity to temperature using an electric furnace. The chromium coated quartz window was placed in an electric furnace and the infrared radiation was imaged at known steady temperatures using the identical infrared high-speed camera [19, 20]. The heat flux distribution was obtained by numerically predicting the 3-D transient thermal conduction into the wall using the time-sequential wall surface temperature distributions as the boundary condition with the standard Fourier's law of thermal conduction provided in the ANSYS software [19, 20]. The model size was 34.944 × 34.944 × 0.23 mm, and the mesh was divided into 128 × 128 sections with the same spatial resolution as that of the infrared radiation image on the wall surface and into 10 sections using an unequally spaced mesh in the wall thickness direction with minimum mesh thickness of 0.3μm.

The injector nozzle has Φ0.143mm × 9 original orifices and an additionally drilled Φ0.143mm orifice on the nozzle axis. The nozzle was covered with a cap in order to extract only the axial spray by trapping fuel sprays injected from the other 9 orifices within the cap, which enables a simple experimental configuration with a single spray flame without interference by the other sprays [20]. The impinging distance from the axial hole to the wall surface is approximately 35 mm which is equivalent to the impinging distance between the nozzle and the piston cavity wall in heavy-duty diesel engines.

The experimental conditions are summarized in Table 1. The amount of injected fuel (Japanese JIS#2 diesel) from the additionally drilled axial orifice was 12.6 mg at an injection pressure of 150 MPa and 14.8 mg at an injection pressure of 200 MPa. A modern diesel equivalent ambient condition of ρ=23.8 kg/m3, Pa=4.8 MPa, Ta=1050 K, $O_2$=17% was achieved by premixed combustion of acetylene, oxygen, carbon dioxide and argon mixture. For the experimental safety reasons, carbon dioxide and argon were used to increase ambient density with reduced peak pressure mimicking the specific heat of nitrogen. For the wall condition, the vessel and the flame-impinged wall surface were electrically preheated to 373 K to prevent water condensation. The selection of the window material, the coating material, and the application process were all thoroughly detailed in earlier publication [19].

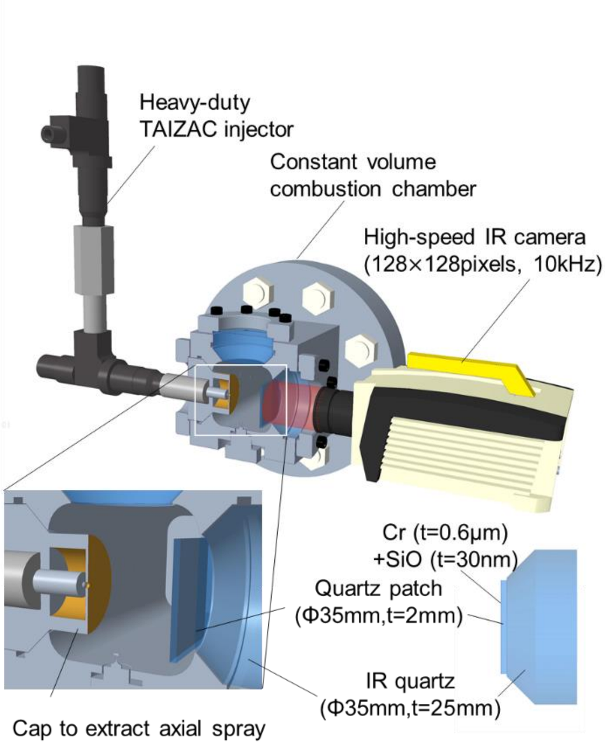

**Fig. 2.** Experimental Setup

**Table 1.** Experimental Condition

| **Injection Condition** | | | | |
|---|---|---|---|---|
| Nozzle | Φ0.143mm × (9+1 axial orifice) | | | |
| Fuel | JIS #2 | | | |
| Injection pressure | 150MPa | | 200MPa | |
| Injection quantity | 12.6mg | | 14.8mg | |
| Injection duration [ms] | Rect. | Inversed-delta | | Rect. |
| | 2.5 | 2.7-3.6 | 2.9 | 2.6 |
| Impinging distance | 35.8mm | | | |
| **Surrounding condition** | | | | |
| Gas density | 23.8kg/m³ | | | |
| Temperature | 1050K | | | |
| Pressure | 4.8MPa | | | |
| O2 concentration | 17 mass % | | | |
| Wall temperature | 373K | | | |
| **Imaging condition** | | | | |
| Camera | Fast IR M3k | | GX-1 | |
| Lens | 50mm+0.25 inch ext.ring | | 200-80mm | |
| Frame rate | 10000fps | | | |
| Exposure time | 10μs | | 2μs | |
| Pixels | 128×128 | | 464×464 | |

### 2.2 Development of Heavy-duty TAIZAC

Varieties of TAIZAC (TAndem Injector Zapping ACtivation) injectors have been developed in the authors' laboratory at Meiji University and have been successfully utilized in single-shot combustion vessel experiments [21, 22, 27, 28], performance tests on single- and multi-cylinder engines with hours of continuous and stable operation [21, 22, 27, 28, 29]. These previous studies, however, mainly conducted assuming passenger car engines. We have newly developed a heavy-duty TAIZAC injector with simple serial connection of solenoid-actuated heavy-duty G4S injectors (supplied by Isuzu Advanced Engineering Center, LTD, Japan). The upper injector is connected to a common rail system and the lower injector is injecting into the cylinder. The operation sequence of the inversed-delta injection is; 1) upper injector needle valve is opened with lower injector kept closed in order to accumulate the high pressure fuel into the injectors, 2) upper injector is closed in order to isolate the lower injector from the high pressure source (common rail system), 3) lower injector is opened in order to inject the fuel into the cylinder during which fuel pressure is released by the injection and continuously ramped down during the injection duration realizing the inversed-delta injection.

### 2.3 Flame Imaging Velocimetry (FIV) Analysis

Flame Imaging Velocimetry (FIV) analysis [30] was used to visualize and elucidate the velocity distributions from infrared high-speed thermography of the combustion chamber wall impinged by diesel spray flame. What is traced in the FIV analysis is not the near-wall flow velocity itself, but the advection velocity of the wall temperature distributions heated by a diesel spray flame impingement. In this study, wall temperature distribution is determined by the temperature of the gas near the wall, flow velocity, radiation heat transfer from the flame, and boundary layer conditions, etc. Although it is difficult to simply explain its physical meaning, it provides extremely important information about the gas flow near the wall surface.

The obtained high-speed infrared radiation images were analyzed with PIVlab, a Matlab-based open-source code for particle image velocimetry (PIV) applications. Masking for the specified region of interest (ROI) was performed prior to pre-processing the images with the Contrast-Limited Adaptive Histogram Equalization (CLAHE) filter. In this study, the images were processed with the optimized CLAHE filter size of 30 pixels, a four-step Discrete Fourier Transform (DFT) interrogation window size of 16, 16, 8, 8 pixels with the velocity limit for minimal interpolation counts.

## 3. Experimental results

### 3.1 Heat flux reduction by inversed-delta injection

Figure 3 shows that four-shot heat release rate profiles with thin lines and an ensemble averaged heat release rate and injection rate profiles with thick lines for conventional rectangular injection (blue line) and inversed-delta injection (red line) cases at an injection pressure of 200 MPa. The injection rate was measured with a Bosch long tube. The injection quantity from the axial hole was 14.8 mg. In order to examine only the effect of the gradual decrease in injection rate caused by inversed-delta injection, the dynamic pressure effect [22] was not used when the fuel flows into the lower injector from the upper injector, and the initial rise of the injection rate was matched to that of rectangular injection. Without dynamic pressure effect, injection always starts when the lower injector is filled with fuel, ensuring stable injection each time, even in single-shot combustion experiments using a constant-volume combustion vessel.

The difference in the initial heat release rate is not significant, however, the heat release rate differs after 2.5ms after start of injection between rectangular and inversed-delta cases. Inversed-delta cases exhibit notably higher heat release rate during diffusion combustion phase, which is consistent with our previous publications [21, 22, 26]. The total amount of heat release is almost the same for inversed-delta and rectangular injection cases, allowing a quantitative comparison of the effects of the injection rate pattern on wall heat transfer.

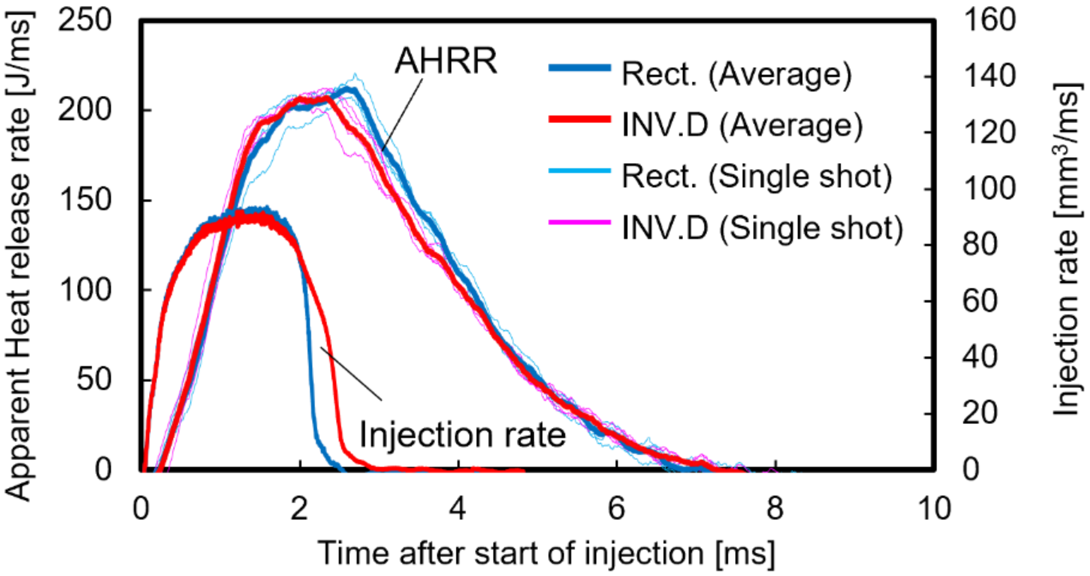

**Fig. 3.** 4-shot heat release rate and injection rate profiles for conventional rectangle and inversed-delta cases (injection pressure: 200MPa, injection amount: 14.8mg)

Figure 4 shows example high-speed images of diesel flame soot luminosity (side view), infrared radiation, and heat flux distributions for conventional rectangle (blue) and inversed-delta (red) injection cases. The heat flux distribution was obtained by numerically predicting the 3-D transient thermal conduction into the wall using the time-sequential wall surface temperature distributions as the boundary condition as already described in Sec.2.1.

Example high-speed images of soot luminosity shows that the diesel spray flame of rectangle injection disappeared more quickly than that of the inversed-delta injection. It was also observed in previous experiments using a light-duty TAIZAC [23, 26] for passenger cars. For both of rectangle and inversed-delta cases, the infrared radiation from the back surface of the chromium layer consistently exhibited distinct radially striped patterns similarly to the previous parametric studies [19, 20]. Compared to the previous experimental conditions using light-duty TAIZAC, the injection quantity was increased by a factor of about three, but no clear differences were observed in the width, spacing, or spatio-temporal behaviours of the radially striped patterns. In addition, it was qualitatively observed that the infrared radiation intensity of the inversed-delta injection case was lower than that of the rectangular injection case, indicating the lower wall surface temperature.

Figure 5 shows time-series plots of the infrared radiation intensity and the maximum and average heat flux within the view field for the conventional rectangle (blue) and inversed-delta (red) cases. In addition to the 4-shot ensemble averaged heat flux profile with a thick line, individual heat flux profiles are also shown with thin lines. The tinted area shows the cumulative heat flux value. These plots were obtained by spatially averaging the intensity within the view field, excluding the bright background flame luminosity at the outer edge of the circular view field. In the case of inversed-delta injection, the infrared radiation intensity increases moderately in the second half of the combustion period compared to the rectangular injection, and the averaged infrared radiation intensity is about 10% lower and about 17% lower at the maximum.

The heat flux in both injection patterns shows a maximum at around 0.6 ms after start of injection corresponding to the timing of the spray flame impingement. With inversed-delta injection, heat flux on wall surface was successfully reduced compared to the conventional rectangular injection case in almost all the time in spite of the variation of each shot. After 2 ms from the start of injection, while diffusion combustion is the main process, the average heat flux of the inversed-delta injection is about 5% lower than that of the rectangular injection, indicating that the wall heat transfer is successfully reduced potentially due to the reduction of spray penetration and flow velocity near the wall caused by the inversed-delta injection. We can see the variation of each shot is almost below the 5% observed deviation, except that only a shot in inversed-delta case shows over the deviation during injection period but below after 2 ms from the start of injection, while diffusion combustion is the main process.

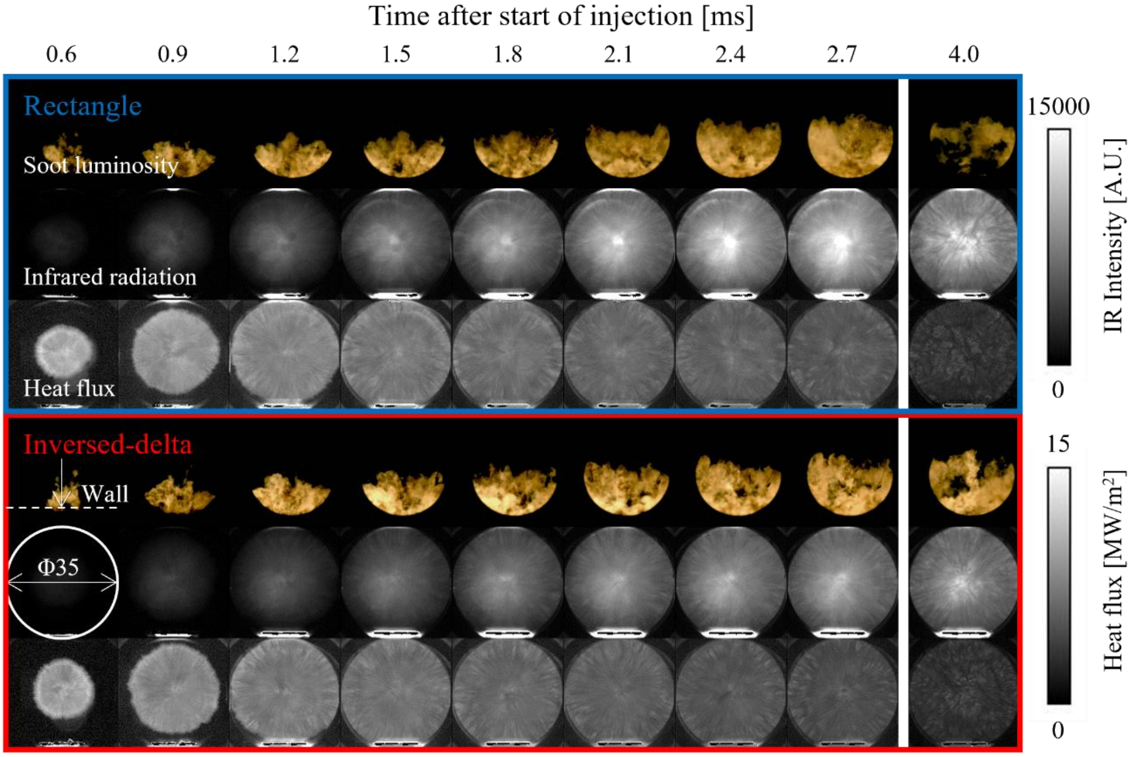
Time after start of injection [ms]
0.6
0.9
1.2
1.5
1.8
2.1
2.4
2.7
4.0
Rectangle
Soot luminosity
Infrared radiation
Heat flux
Inversed-delta
Wall
Φ35
15000
0
IR Intensity [A.U.]
15
0
Heat flux [MW/m²]

**Fig. 4.** Example high-speed images of side-view diesel flame soot luminosity (top), infrared radiation from chromium layer (middle), and heat flux (bottom) at injection pressure of 200MPa for conventional rectangle(blue) and inversed-delta(red) injection cases

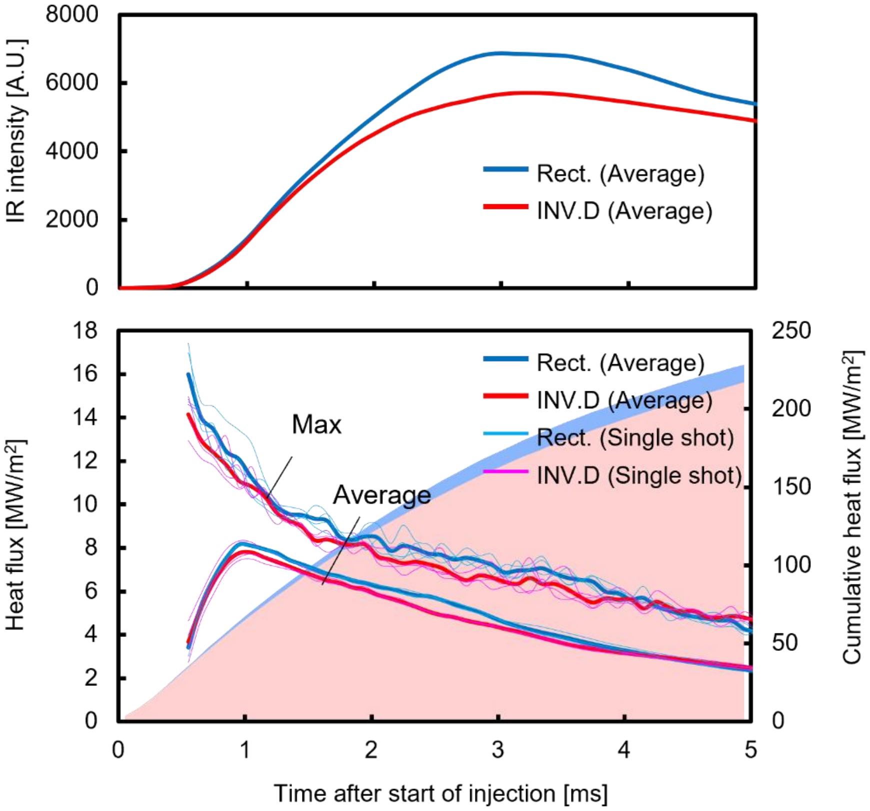

**Fig. 5.** Infrared radiation intensity (top) and maximum and average heat flux (bottom) profiles for the conventional rectangle (blue) and inversed-delta (red) injection cases (injection pressure: 200MPa, injection amount: 14.8mg)

### 3.2 Effects of inversed-delta injection on striped pattern advection velocity

In order to further investigate the effects of inversed-delta injection on near-wall flow and heat transfer phenomena, additional experiments were conducted with three different ramp-down rates of the inversed-delta injection pressure during the injection duration. Figure 6 shows 4-shot ensemble averaged heat release rate and injection rate profiles for conventional rectangle (blue) and 3 types of inversed-delta injection (Low: green, Middle: red, High: orange) cases. The injection pressure was 150 MPa and the injection fuel amount was set constant at 12.6 mg between the rectangle and inversed-delta injection cases in order to keep the total amount of heat release calculated by integrating each heat release rate. However, as shown in Figure 6, as the ramp-down duration of the inversed-delta injection pressure became longer, heat release rate gradually became lower after the upper injector needle valve of TAIZAC injector was closed and the injection rate ramp-down was started. This trend was not observed in the injection pressure of 200 MPa as mentioned in section 3.1, and the reason is under further examination. Therefore, it is difficult to quantitatively compare the heat flux for conventional rectangle and 3 types of inversed-delta injection cases, because the total amount of heat release is different by more than 10% from the rectangular (blue) to inversed-delta (orange) injection cases. On the other hand, it is still valuable to qualitatively discuss the trend of heat flux profiles and the effects of the injection rate patterns on the advection speed of infrared radiation patterns, which reflect the flow behaviours near the fuel-injected wall surface.

Figure 7 shows example high-speed images of soot luminosity (top), infrared radiation intensity from chromium layer (upper middle), heat flux distributions (lower middle), and advection speed of the striped pattern (bottom) at injection pressure of 150MPa for conventional rectangle and 3 types of inversed-delta injection cases. The advection velocity of the striped patterns was obtained by analysing the infrared radiation images with FIV (Flame Image Velocimetry) analysis [30] as mentioned in section 2.2.

Similarly to the result in Fig. 4, example high-speed images of soot luminosity shows that the diesel spray flame of rectangle injection disappeared more quickly than that of the inversed-delta injection and the infrared radiation from the back surface of the chromium layer consistently exhibited distinct radially striped patterns for both of rectangle and inversed-delta cases. Rectangle and Inv.D (low) cases exhibit relatively later and distinct transition from radially striped patterns to relatively random distributions around 3.0-3.5 ms, corresponding to the effects of the entrainment wave caused by the end of

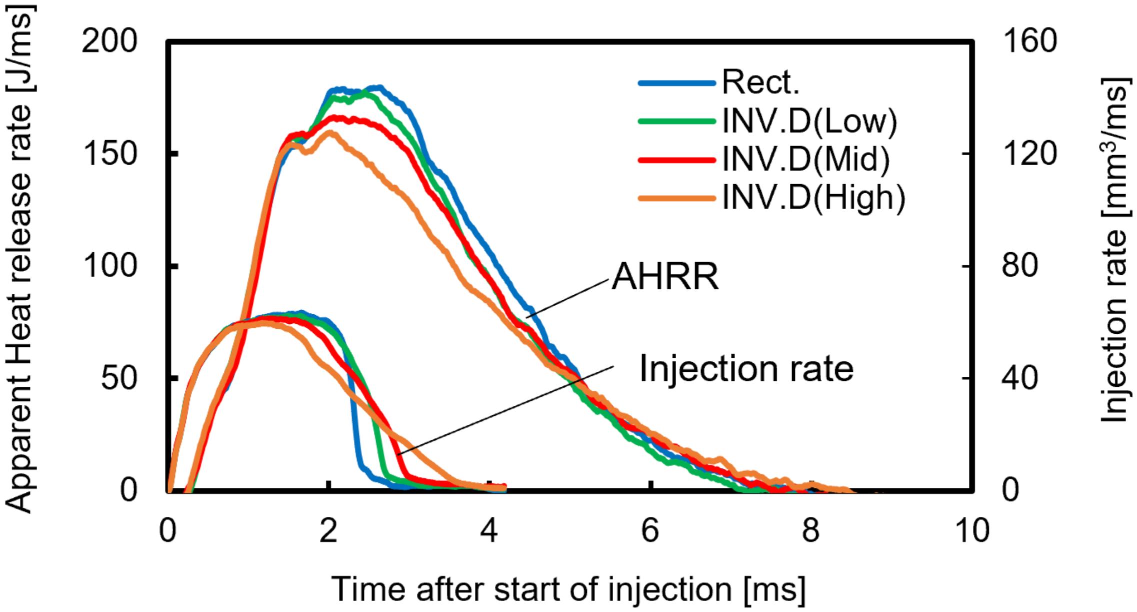

**Fig. 6.** 4-shot ensemble averaged heat release rate and injection rate profiles for conventional rectangle and 3 types of inversed-delta injection cases (injection pressure: 150MPa, injection amount: 12.6mg)

injection. In contrast, Inv.D (middle) and Inv.D(high) cases exhibit earlier and continuous transitions from radially striped patterns to relatively random distributions starting around 2.0-2.5ms, corresponding to the effects of turbulence promotion by the inversed delta injection rate shaping, which is consistent with the observations reported in our previous publication [26].

At 0.7ms after start of injection approximately corresponding to the timing of the spray flame impingement (arrow “a” in Fig.7), the advection velocity vectors exhibit strong local turbulence superimposed on the average velocity distribution radiating out from the central stagnation point. From 1.0 to 2.5 ms after start of injection, these local strong turbulences are decreased. From 3.0 to 3.5 ms after start of injection corresponding to the time after the end of rectangular injection (arrow “b” in Fig.7), strong turbulence appears again. On the other hand, in the case of inversed-delta injection, the turbulence after the end of inversed-delta injection is becoming unclear with the increase of the ramp-down duration of the inversed-delta injection from green to orange. Since this local strong turbulence after the end of injection becomes unclear as the stepwise decrease in injection rate at the end of injection is suppressed by inversed-delta injection, the turbulence is considered to be caused by an increase in flow velocity near the wall due to the entrainment wave effect associated with the end of injection [31].

In order to quantitatively compare the effect of the injection rate pattern on heat flux and advection velocity, Figure 8 shows heat flux (top) and advection speed (bottom) spatially averaged within the view field for conventional rectangle and 3 types of inversed-delta injection cases. For all the injection rate patterns, the heat flux sharply increases and the advection speed reaches its first peak at around 0.7ms after start of injection (arrow “a” in Fig.8) corresponding to the timing of the spray flame impingement. After 1.0 ms, the heat flux gradually decreases and the advection speed remains almost constant. In the rectangular injection shown in blue, the advection speed increases again from 2.5 to 3.5 ms (arrow “b” in Fig.8) corresponding to the end of fuel injection, and the second peak is observed. In contrast, in the cases of inversed-delta injection, the second peak of advection speed after the end of injection becomes indistinct with the increase of the ramp-down duration of the inversed-delta injection from green to orange. Interestingly, the heat flux is not notably affected by this increase in advection speed at the end of injection as seen in the cases of rectangular injection (blue) and low inversed-delta injection (green). Possible explanations for this low correlation between the advection speed and heat flux at the end of injection might be reduced temperature difference between the flame and the wall in the later phase of combustion period compared to the initial phase of flame impingement. However, it has been experimentally confirmed by the authors through diesel in-flame temperature measurements using a thin-wire platinum thermocouple [32] that the flame temperature notably increases in the tale of diesel flame after the end of injection due to the enhanced air entrainment caused by the entrainment wave. It is interesting to note that there is no sign of increase in heat flux despite of simultaneous increases in flame temperature and flow velocity near the wall.

Authors are considering the influence of the near-wall flow component vertical to the wall as one of the reasons for this low correlation between the advection speed and heat flux in the present experiments. The advection velocity discussed in this paper is expected to mainly reflect the flow component parallel to the wall surface. However, it might be more important to analyse the flow component vertical to the wall surface associated with the longitudinal vortex near the wall surface as the potential cause of the radially striped patterns of temperature and heat flux distributions. Further examination of the above explained results is therefore expected to contribute to better understandings of the wall heat transfer during diesel flame impingement.

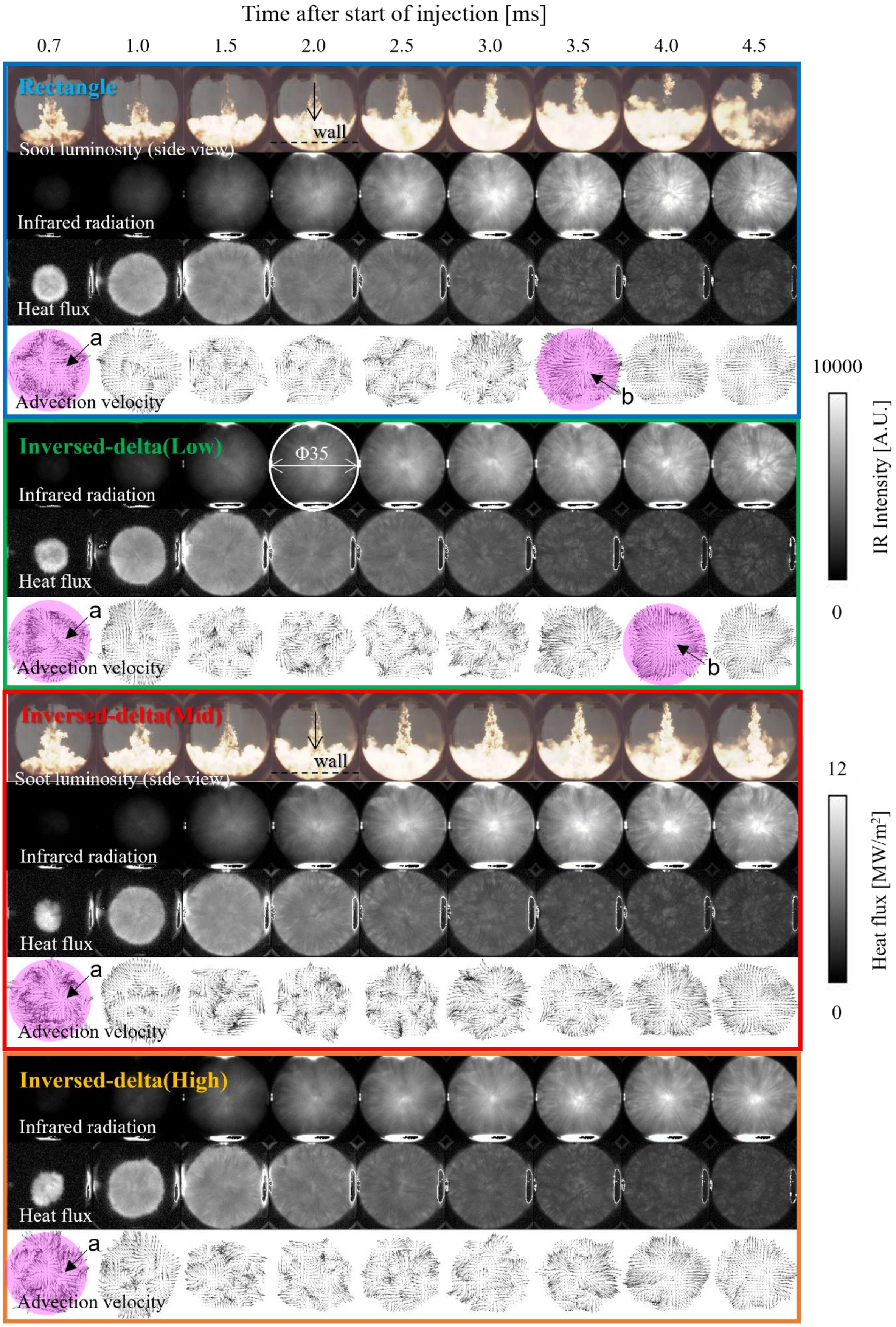
Time after start of injection [ms]
0.7
1.0
1.5
2.0
2.5
3.0
3.5
4.0
4.5
Rectangle
wall
Soot luminosity (side view)
Infrared radiation
Heat flux
a
Advection velocity
b
Inversed-delta(Low)
Φ35
Infrared radiation
Heat flux
a
Advection velocity
b
Inversed-delta(Mid)
wall
Soot luminosity (side view)
Infrared radiation
Heat flux
a
Advection velocity
Inversed-delta(High)
Infrared radiation
Heat flux
a
Advection velocity
10000
IR Intensity [A.U.]
0
12
Heat flux [MW/m²]
0

**Fig. 7.** Example high-speed images of soot luminosity (top), infrared radiation intensity from chromium layer (upper middle), heat flux distributions (lower middle), and advection speed of the striped pattern (bottom) at injection pressure of 150MPa for conventional rectangle and 3 types of inversed-delta injection cases

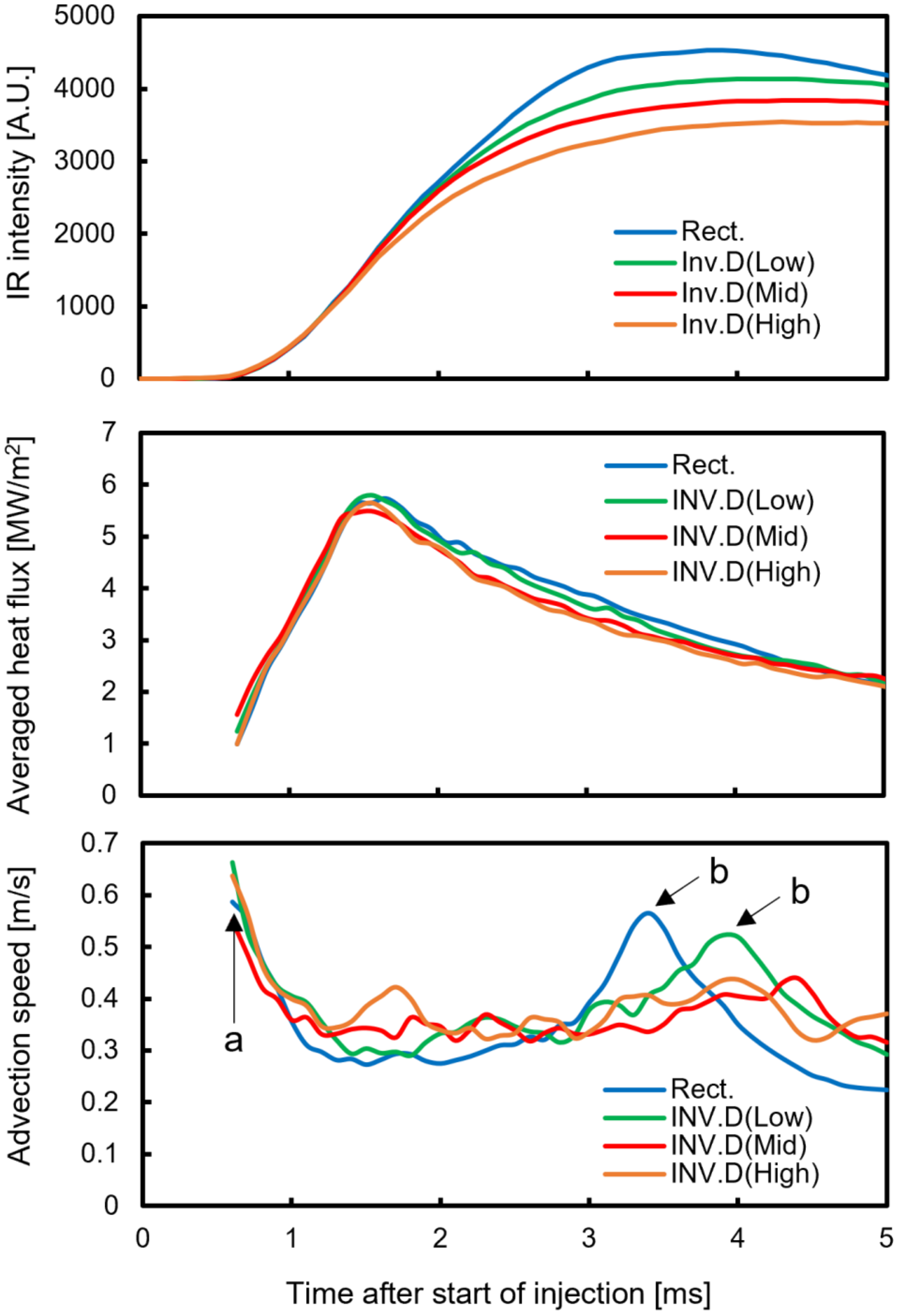

**Fig. 8.** Infrared radiation intens ity (top), averaged heat flux (middle) and advection speed (bottom) profiles for conventional rectangle and 3 types of inversed-delta injection cases (injection pressure: 150MPa, injection amount: 12.6mg)

## Conclusions

In order to investigate the effects of inversed-delta injection on wall heat transfer in heavy-duty diesel engines, a heavy-duty TAIZAC (TAndem Injector Zapping ACtivation) injector was newly developed and infrared high-speed thermography and time-series visualization of heat flux distribution on chromium coated quartz wall surface impinged by diesel spray flame was conducted in a constant volume combustion chamber. The obtained conclusions are summarized as follows;

1. For both of rectangle and inversed-delta injection cases, the infrared radiation from the back surface of the chromium layer consistently exhibited distinct radially striped patterns. Although the injection quantity was increased by a factor of about three compared to the previous studies using light-duty TAIZAC injectors, no clear differences were observed in the width, spacing, or spatio-temporal behaviours of the radially striped patterns.

2. With inversed-delta injection, heat flux on wall surface was successfully reduced compared to the conventional rectangular injection case, potentially due to reduced spray penetration and reduced flow velocity near the wall caused by the inversed-delta injection.

3. In the case of conventional rectangular injection, the second peak of advection speed was observed at the end of injection, which was considered to be caused by the entrainment wave arising at the end of injection. On the other hand, in the case of inversed-delta injection, the second peak of advection speed became indistinct with the increase of the ramp-down duration of the inversed-delta injection. The heat flux was not affected by the increase in advection speed and flame temperature at the end of injection. This may be caused by the reduction of the temperature difference between the flame and the wall in the later phase of combustion period and the effect of the near-wall flow component vertical to the wall.

## Acknowledgement

Authors are sincerely grateful to Niko Optics for their technical support in preparation of chromium coated windows, Tatsuya Tsuchihata, Ryo Shibata, Ryosuke Watanabe from Meiji University for their enthusiastic experimental support.

## References

[1] “COP26 Sustainability Report”, 2022 (Conference: UN Climate Change Conference - October/November 2021), https://unfccc.int/documents/617444

[2] International Energy Agency (IEA), “World Energy Outlook 2020”, https://www.iea.org/reports/world-energy-outlook-2020

[3] International Energy Agency (IEA), “Market Report Series - Renewables 2021”,

https://www.iea.org/reports/renewables-2021

[4] “bp Energy Outlook 2023”, https://www.bp.com/en/global/corporate/energy-economics/energy-outlook.html

[5] Ishiyama, T., Kawanabe, H. and Horibe, N., “Improvement of Thermal Efficiency in Passenger Cars' Diesel Engines -Research and Development for Diesel Combustion in SIP Innovative Combustion Technology,” JSAE20206022, (in Japanese).

[6] Mohr, D., Shipp, T., and Lu, X., “The Thermodynamic Design, Analysis and Test of Cummins’ Supertruck 2 50% Brake Thermal Efficiency Engine System,” SAE Technical Paper 2019-01-0247 (2019).

[7] Goyal, H., Nyrenstedt, G., Moreno Cabezas, K., Panthi, N. Im, H., Andersson, A., and Johansson, B., “A Simulation Study to Understand the Efficiency Analysis of Multiple Injectors for the Double Compression Expansion Engine (DCEE) Concept,” SAE Technical Paper 2021-01-0444 (2021).

[8] Nyrenstedt, G., Watanabe, K., Enya, K., Shi, H., Uchida, N., and Johansson, B., “Thermal Efficiency Comparison of Different Injector Constellations in a CI Engine,” SAE Technical Paper 2019-24-0172 (2019).

[9] Uchida, N., Galpin, J., Watanabe, K., Enya, K., Zaccardi, J., and Duffour, F., "Numerical and Experimental Investigation into Brake Thermal Efficiency Optimum Heat Release Rate for a Diesel Engine," SAE Technical Paper 2019-24-0109 (2019).

[10] Kawaguchi, A., Wakisaka, Y., Nishikawa, N., Kosaka, H., Yamashita, H., Yamashita, C., Iguma, H., Fukui, K., Takada, N., and Tomoda, T., "Thermo-swing insulation to reduce heat loss from the combustion chamber wall of a diesel engine", Int J Engine Res 2019; 20(7): 805–816.

[11] Harada, Y., Uchida, K., Tanaka, T., Sato, K., Zhu, Q., Fujimoto, H., Yamashita, H., and Tanahashi, M., "Wall heat transfer of unsteady near-wall flow in internal combustion engines", Int J Engine Res 2019; 20(7): 817–833.

[12] Uchida, N. and Watanabe, H., "A new concept of actively controlled rate of diesel combustion (ACCORDIC): part II—simultaneous improvements in brake thermal efficiency and heat loss with modified nozzles", Int J Engine Res 2018; 20(1): 34–45.

[13] Dejima, K., Nakabeppu, O., Nakamura, Y., Tsuchiya, T., and Nagasaka, K., "Three-point MEMS heat flux sensor for turbulent heat transfer measurement in internal combustion engines", Int J Engine Res 2019; 20(7): 696–705.

[14] Yokoyama, E., Shimura, M., Kamata, M., Nakabeppu, O., Yokomori, T., and Tanahashi, M., "Simultaneous High-speed and High-resolution PIV and Heat Flux Measurements near Piston Top under Tumble Enhanced Condition," Flow, Turbulence and Combustion, Published online on September 7, 2022.

[15] Dejima, K., Nakabeppu, O., Moussou, J., Pilla, G., "Application of a MEMS heat flux sensor to heat transfer research on an impinging diesel jet", International Journal of Engine Research, 23(3) (2022), pp.497-511.

[16] Dejima. K., and Nakabeppu, O., "Local instantaneous heat flux measurements in an internal combustion engine using a MEMS sensor," Applied Thermal Engineering 201, Part A, 117747, (2022).

[17] Li SW, Kamimoto, T., Kobori, S. and Enomoto, Y., "Heat transfer from impinging diesel flames to the combustion chamber wall", SAE technical paper 970896, 1997.

[18] Suzuki, Y., Shimano, K., Enomoto, Y., Emi, M., and Yamada, Y., "Direct heat loss to combustion chamber walls in a direct-injection diesel engine: evaluation of direct heat loss to piston and cylinder head", Int J Engine Res 2005, 6(2), 119–135.

[19] Aizawa, T., Kinoshita, T., Akiyama, S., Shinohara, K., and Miyagawa, Y., "Infrared high-speed thermography of combustion chamber wall impinged by diesel spray flame", Int J Engine Res 23(7), pp.1116-1130, 2021.

[20] Mahmud, R., Takahashi, T., Kinoshita, H., Shimizu, F., Naganawa, A., Morooka, M., and Aizawa, T., "Infrared high-speed thermography of combustion chamber wall impinged by diesel spray flame", SAE Technical Paper 2023-32-0087 (2023).

[21] Fareez, M., Akiyama, S., Kinoshita, T., Shimada, T., Aizawa, T., "Investigation of Inversed-Delta Injection Rate Shaping Diesel Spray Flame Structure and Combustion Characteristics Towards Thermal Efficiency Improvement," Applied Thermal Engineering 160 (2019): 113986.

[22] Aizawa, T., Akiyama, S., Shimada, T., Toyama, Y. Nishikawa, Y., Saruwatari, S., and Noguchi, Y., "TAIZAC-TAndem Injectors Zapping ACtivation-for Thermal Efficiency Improvement of Diesel Engine," SAE Int. J. Adv. & Curr. Prac. in Mobility 2, no. 1 (2019): 310-318.

[23] Kondo, K., Kuribayashi, M., Sakai, K., and Aizawa, T., "High-Speed Ultraviolet Chemiluminescence Imaging of Late Combustion in Diesel Spray Flame," International Journal of Engine Research 18, no. 1-2 (2017): 93-104.

[24] Adachi, T., Zhou, B., Kusaka, J., and Aizawa, T., "Numerical Analysis on Temporal and Spatial Distribution of Equivalence Ratio and Heat Release Rate in Diesel Spray Combustion by Using LES Coupled with Detailed Chemistry," in Proc. of JSAE Spring Congress, No.62-18, 1-6, 2018 (in Japanese).

[25] Zhou, B., Adachi, T., Kusaka, J., and Aizawa, T., "A Numerical Study on Correlation of Chemiluminescent Species and Heat Release Distributions Using Large Eddy Simulation," SAE Technical Paper 2018-32-0066 (2018).

[26] Aizawa, T., Kinoshita, T., Tanaka, Y., Takahashi, T., Miyagawa, Y., and Shimada, T., “Vortex Development and Heat Release Enhancement in Diesel Spray Flame by Inversed-Delta Injection Rate Shaping Using TAIZAC Injector,” SAE Technical Paper 2021-24-0037, (2021).

[27] Yoshiuda, R., Maruyama, Y., Yasui, H., Haga, N., Ikeda, R., Katayama, M., Gunawan, R., Shimada, T., and Aizawa, T., “Effects of Injection Rate Shaping using 3-Injector TAIZAC on Diesel Engine Performance”, Proc. of the 32nd internal combustion engine symposium, No. 32 (2021) (in Japanese)

[28] Maruyama, Y., Uematsu, K., Yokoe, T., Sato, K., Akiyama, S., Saruwatari, S., Shimada, T., and Aizawa, T., “Effects of Inversed-Delta Injection Using TAIZAC Injector on Diesel Engine Performance,” in Proc. of the 30th Internal Combustion Engine Symposium, Paper No.52, 2019 (in Japanese).

[29] Hasegawa, N., Horie, R., Shimada, T., Aizawa, T., Kuboyama, T., and Moriyoshi, Y., “Influence of Inversed Delta Injection Rate Shaping on Combustion of Multi-Cylinder Diesel Engine,” in Prof. of JSAE Fall Congress, No.123-17, 322-327, 2017 (in Japanese).

[20] Rao, L. and Kook, S., “Optimisation of Image Processing Parameters for Flame Image Velocimetry (FIV) Measurement in a Single-Cylinder, Small-Bore Optical Diesel Engine,” SAE Int. J. Advances & Curr. Prac. in Mobility 1(3):1311-1324, (2019).

[31] Musculus, M. and Kattke, K., “Entrainment Wave in Diesel Jets”, SAE Int. J. Engines 2(1), pp.1170-1193 (2009).

[32] Aizawa, T., Harada, T., Kondo, K., Adachi, T., Zhou, B., and Kusaka, J. “Thermocouple Temperature Measurements in Diesel Spray Flame for Validation of In-flame Soot Formation Dynamics”, International Journal of Engine Research 18(5-6), pp.453-466 (2017).

# Cycle Variations in Soot Formation and Oxidation for a Direct-Injection Compression Ignition Engine

R. Fitzgerald[1], P. Seiler[1], B. Hanks[1] and G. Martin[1]

[1]Caterpillar Inc. – Technical Center, 14009 Old Galena Rd., Chillicothe, IL 61552, USA.

E-mail: Fitzgerald_Russell_P@cat.com
Telephone: +(1) 309 266 4432

**Abstract.** Engine-out soot or particulate matter (PM) emissions are an unavoidable consequence for many direct-injection mixing-controlled compression-ignition engines. Understanding soot formation and oxidation processes is necessary for pollutant reduction and compliance with future Tier V emissions. Since nearly all exhaust PM measurements are averaged over many cycles, transient cycle variable behavior is generally unknown, and yet, awareness of these variations is essential for simulation and prediction. In this work, cycle soot variations are quantified and examined in a 2.53 L single-cylinder direct-injection compression-ignition engine using a novel laser-based extinction diagnostic in the exhaust runner. Measurement accuracy is better than 0.5 ppb exhaust soot volume fraction and temporal resolution is faster than 0.5 crank angle degrees (CAD). Exhaust soot volume fraction history is compared with cycle resolved apparent heat release rate to better understand in-cylinder processes that lead to PM formation.

Engine cycle soot variations are high, i.e., greater than 10% COV for a wide range of operating conditions. Minimum engine cycle PM variations are equal to injector shot PM variations for non-engine quiescent conditions without spray-wall interaction, suggesting that spray characteristics establish a governing baseline. For some engine operating conditions, exhaust averaged soot volume fraction can vary by as much as an order of magnitude from cycle to cycle. Skewed, non-normal cycle soot populations indicate instability and non-optimal operation points for the hardware employed, and thus, opportunities for improvement. Comparison of heat release rate (HRR) profiles for low- and high-soot cycles reveals statistically significant correlations between engine-out PM and specific combustion intervals. High-PM cycles generally exhibit common features, including: early ignition with advanced premixed burn, adverse spray-wall (piston and head) interactions with reduced heat release rates, and diminished late cycle burnout. This soot measurement and analysis approach represents a useful new tool for combustion system design, troubleshooting, and simulation validation.

## Notation

| | |
|---|---|
| AHRR | Apparent heat release rate |
| $\mathrm{AHRR}_p$ | Peak apparent heat release rate |
| aTDC | After top dead center |
| CA10 | Crank angle degree at 10% mass fraction burn |
| CA10-20 | Crank angle duration between 10-20% mass fraction burn |
| CAD | Crank angle degree |
| CI | Compression ignition |
| COV | Coefficient of variation |
| DFI | Ducted fuel injection |
| DME | Dimethyl Ether |
| ECN | Engine Combustion Network |
| EGR | Exhaust gas recirculation |
| EVO | Exhaust valve opening |
| FLEER | Fast laser extinction in the exhaust runner |
| FSN | Filter smoke number |
| $f_v$ | Soot volume fraction |
| HRR | Heat release rate |
| $I$ | Laser intensity |
| $I_o$ | Incident laser intensity |
| IAHRR | Integrated (cumulative) apparent heat release rate |

| | |
|---|---|
| $IAHRR_t$ | Total integrated apparent heat release rate |
| IMEP | Indicated mean effective pressure |
| IMEPg | Gross indicated mean effective pressure |
| $k_e$ | Dimensionless extinction coefficient |
| $L$ | Path length of extinction |
| LDM | Laser diode module |
| LLFC | Leaner lifted flame combustion |
| LOL | Lift of length |
| $\lambda$ | Wavelength of laser light |
| MCC | Mixing controlled combustion |
| MFB | Mass fraction burned |
| N | Number of cycles in a measured ensemble |
| NGR | Next generation research injector |
| NOx | Nitrogen oxides |
| O | Open Piston (Convention Tier IV Final) |
| PDF | Probability density function |
| PM | Particulate matter |
| PMBS | Premixed burn spike |
| PP | Pre-production injector |
| ppb | Part per billion |
| R | Re-entrant Piston |
| RPM | Rotations per minute |
| THC | Total hydrocarbons |
| TDC | Top dead center |

## 1. Introduction and Background

Mixing-controlled-combustion (MCC) by compression ignition (CI) of high cetane fuels is a robust, efficient strategy for heavy-duty power generation and propulsion, but it can suffer from unwanted emissions, including soot/particulate matter (PM), nitric oxides (NOx), and carbon-dioxide, especially for long-chain hydrocarbon fuels like diesel. The simultaneous injection and reaction of fuel in-cylinder enables an inherently stable, controllable, repeatable process with low cycle to cycle variations in heat release and high tolerance for varying fuel properties; however, this process introduces fuel rich regions upstream of the reaction zone or flame lift-off-length (LOL). If these fuel rich regions persist during high-temperature reactions, both PM and NOx will form. Although various operation strategies like EGR and high-pressure injection can abate the formation of these pollutants, they generally cannot be reduced simultaneously, as reduction of one (e.g., NOx by air dilution and lower flame temperature) tends to encourage persistence of the other (e.g., soot by lack of oxidation), resulting in the well-known soot-NOx trade-off. Consequently, the problem is often dealt-with by exhaust after-treatment, which is generally very effective but very costly.

Many strategies have been attempted to reduce in-cylinder PM with varying success. Leaner lifted flame combustion (LLFC), which attempts to enhance mixing prior to reaction by pushing the flame LOL further from the injector orifice [1], can significantly reduce PM emissions. This approach can work well for fewer (less than 8), small orifices (i.e., less than 150μm), but effectiveness and stability are limited, and such fuel systems are not well-suited for heavy-duty compression ignition engines [2-3]. Ducted fuel injection (DFI), which is a variant of LLFC, is another soot reduction strategy that shows promise for diesel MCC [4-5], but it also can exhibit high cycle variations [6], degraded performance at high-loads [7], and robustness challenges. Alternative oxygenated fuels (e.g., alcohols), represent another potential strategy for reducing PM [8]. Methanol, ethanol, and DME are also attractive because they are potentially renewable, lower-carbon intensity fuels. Nevertheless, these fuels can be more difficult to ignite [9] and generally require significantly higher quantities (due to their reduced lower heating values), both of which tend to diminish inherent benefits of traditional mixing controlled combustion. Practically employing any of these strategies requires detailed understanding of in-cylinder processes, reliable exhaust measurements, prediction of engine-out pollutants (including soot), and optimization of combustion system hardware, especially as more stringent pollutant regulations (e.g., Tier V) are on the horizon.

Understanding of in-cylinder soot formation and oxidation processes is currently lacking due to limited experimental characterization. Smoke meters represent a convenient means of monitoring engine-out soot emissions. Although generally accurate, these devices are slow, requiring seconds and hundreds of cycles to report the relative level of particulate matter in the exhaust – well downstream of the engine. If a few periodically occurring sooty (high PM) cycles are responsible for an elevated mean, no one is aware. No information is available about when soot leaves the engine during the exhaust portion of the cycle. From measured filter-smoke-number (FSN), there is no way to determine if soot emissions are high due to elevated formation or poor oxidation. Attempts to characterize *in situ* soot formation and oxidation are also quite challenging. Instantaneous PM measurements for burning diesel jets have been accomplished in combustion chambers via diffuse-back-illumination (DBI) [10] and by pointwise laser extinction measurements [11], but these are usually limited to static, quiescent conditions with little to no jet-wall interactions. Accurate, insightful optical engine measurements quantifying in-cylinder soot concentration during diesel combustion are challenged by optically thick conditions, evolving, uncertain soot optical properties [12], and complex analysis. A more practical approach is needed.

To address many of these PM measurement limitations, a high-speed laser-based soot extinction diagnostic was developed and previously applied in the exhaust runner of a heavy-duty optical engine [13]. In that work, soot detection limits of less than 0.2 ppb were demonstrated for a measurement frequency of less than 0.5 crank angle degrees (CAD) and absolute measurements of mean exhaust soot concentration were reconciled with measured FSN. The study revealed surprisingly high cycle soot variations for low-load (1.5 – 5.7 bar IMEP), skip-fired engine operation with a conventional six-orifice (116 µm exit diameter) diesel injector tip. For a single steady state operating condition, some cycles exhibited mean exhaust soot concentrations of nearly three times (3x) that of others with a 27% COV of PM while the COV of IMEP was low – a satisfactory 1.5%. A marked decrease in cycle soot variations with increasing injector hole quantity pointed toward inherent variations in individual burning sprays as a potential source/baseline for observed (multi-jet-summed or averaged-) behavior.

### 1.1 Objectives

In this work, soot formation and oxidation processes in a heavy-duty compression ignition engine are examined by correlating individual cycle apparent heat release rate (determined by measured cylinder pressure) with measurements of crank-angle resolved exhaust soot. The latter are determined by implementing the same laser-based soot extinction diagnostic [13] in the exhaust runner of a continuously fired single-cylinder conventional diesel engine operating over an extensive range of speeds, loads, injection pressures, and timings. The goals of the study are to better understand soot formation and oxidation processes in compression ignition engines to inform combustion system optimization and to improve predictive capability of computational simulation tools. Toward this end, we seek answers to the following:

- How much cycle soot variation is present in a conventional diesel engine and how much of that engine-out variation is due to injector spray variation?
- Are soot cycle distributions generally normal, or are they skewed or even bi-modal, suggesting potential combustion system design problems and/or paths for improvement?
- How does engine-out soot correlate with apparent heat release rate, and what does it reveal about soot formation and oxidation?
- How can this understanding be used to improve simulations and other design tools?

## 2. Methodology and Setup

### 2.1 Engine Hardware and Operating Conditions

#### 2.1.1 Engine Hardware

A 2.53 single cylinder engine based on the Caterpillar production C15 engine geometry has been employed for this work. While the critical combustion system components and specifications (as listed in Table 1) closely mimic those of the C15, the block, crankshaft, camshaft, and cylinder head have all been adapted to suit the needs of an engine research platform. Similarly, the fuel, lubricant and cooling systems are off-engine to optimize stability and control. Relatively large plenums (more than 10X displacement volume) in the intake and exhaust systems serve to regulate pressure dynamics and measurement of key state properties for subsequent analysis. Boosted intake manifold pressure is achieved by an upstream air compressor while the engine backpressure is controlled via parallel coarse and fine valves downstream of the exhaust plenum. Additional details are described in [14].

**Table 1.** Single Cylinder Engine Specifications

| | |
|---|---|
| Displace Volume: | 2.53 L |
| Bore / Stroke: | 137 mm / 171 mm |
| Connecting Rod Length: | 271 mm |
| Compression Ratio: | 16.4 |
| Valves: | 2-intake / 2-exhaust |
| Piston Bowl(s): | Conventional Open (O)<br>Re-entrant (R) |
| Swirl Number: | < 1 |
| Intake Valve Opening/Closing: | 324 / -154 CAD aTDC fired |
| Exhaust Valve Opening/Closing: | 127 / 354 aTDC fired |

Several combustion system configurations are employed to characterize engine performance and soot formation and oxidation in this work. Conventional open (O) Tier IV Final and re-entrant (R) piston bowl options enable different spray/wall interactions. These are combined with two different common-rail high-pressure direct-fuel-injector options as detailed in Table 2. These wall-guided configurations are designed to enhance mixing prior to the flame zone, efficiently utilize in-cylinder oxygen for complete combustion and low in-cylinder emissions. While performance differences were observed between the variant combustion geometries and injectors, they are not differentiated in this work, since the primary objective is to examine a wide range of soot formation and oxidation phenomena encompassing a comprehensive set of engine conditions. Delineated performance for different combustion systems is left for future work.

**Table 2.** Injector Specifications

| | NG Research Injector (NGR) | Pre-Production Injector (PP) |
|---|---|---|
| Steady Flow: | 2.5 kg/min @ 41MPa | 4.9 kg/min @ 41MPa |
| Number of Orifices | 5 | 7 |
| Orifice Exit Diameter | 228 µm | 254 µm |
| K-Factor / HEO | 0 / 0% flow gain | 2.2 / 20% flow gain |
| Included Angle | 130° | 125° |

A full array of instrumentation monitors and controls engine performance. Intake and exhaust manifold pressures are measured with Kistler 4045A transducers, with the latter mounted in a Kistler water cooled adapter. 0.1 CAD resolved in-cylinder pressure is monitored with a Kistler 6125C piezo-electric transducer. A Horiba MEXA 7100 DEGR measures a wide array of gaseous species including: NO, $NO_2$, CO, THC, and intake/exhaust $CO_2$ concentrations while an AVL415S smoke meter measures exhaust PM several meters downstream of the backpressure control valves. All channels including encoded engine crank angle location are recorded via Caterpillar low-speed and high-speed data acquisition systems (VDAQ/AVL).

The exhaust system has been substantially modified to enable crank-angle resolved soot measurements via Fast Laser Extinction in the Exhaust Runner (FLEER). About 500 mm downstream of the cylinder head, the exhaust is split into optical and bypass sections (see Figure 1). Each circuit includes a Caterpillar 3500 wastegate valve enabling flow to be temporarily diverted into the optical test section or to be normally bypassed, which prevents fouling of the test-section windows by particulates and other volatiles when soot is not being measured. The pneumatically actuated wastegate valves have water-cooled stems to prevent overheating of the actuator. The optical test section (also shown in Figure 1) houses quartz windows enabling laser light transmission, reflection, and detection. The housing is equipped with machined passages that admit pressurized inert nitrogen purge gas to continuously blanket the windows, so that soot deposition is minimized during measurements.

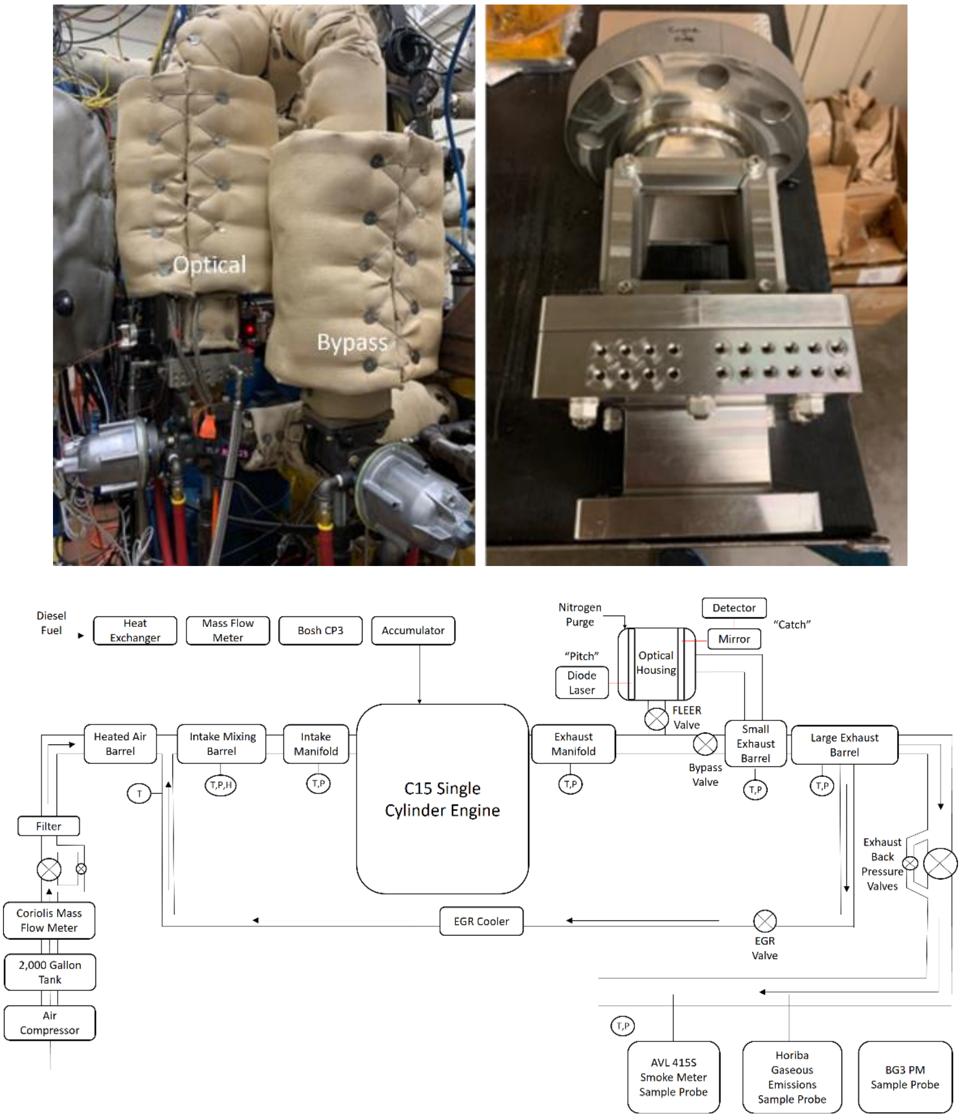
Optical
Bypass
Diesel Fuel
Heat Exchanger
Mass Flow Meter
Bosh CP3
Accumulator
Nitrogen Purge
Detector
"Catch"
Mirror
"Pitch"
Diode Laser
Optical Housing
FLEER Valve
Bypass Valve
Heated Air Barrel
Intake Mixing Barrel
Intake Manifold
C15 Single Cylinder Engine
Exhaust Manifold
Small Exhaust Barrel
Large Exhaust Barrel
T
T,P,H
T,P
Filter
Exhaust Back Pressure Valves
Coriolis Mass Flow Meter
EGR Cooler
EGR Valve
2,000 Gallon Tank
Air Compressor
AVL 415S Smoke Meter Sample Probe
Horiba Gaseous Emissions Sample Probe
BG3 PM Sample Probe

**Fig 1.** Images of split exhaust runner (top-left), optical window housing (top-right), and schematic (bottom)

### 2.1.2 Engine Operating Conditions

A wide range of engine loads, speeds, air-fuel ratios, and fuel injection parameters have been swept in this study (with more than 90 test points) to understand the full range of soot exhaust characteristics that may be observed in a heavy-duty direct-injection compression ignition engine (see Table 3). Acquiring soot extinction data is more difficult for high speeds and loads due to increased vibrations, beam steering, and beam clipping – which must be abated through careful adjustment of the initial laser pitch. Other conditions resulted in excessively high soot emissions (filter smoke number, FSN > 1), which tend to quickly foul the exhaust runner windows with particulates after a few minutes of operation. Consequently, more moderate operating conditions (1000 RPM and 5-10 bar IMEP) have been selected for the bulk of the investigation.

**Table 3**. List of comprehensive operating conditions tested in this work.

| | |
|---|---|
| Engine Speed | 1000-1800 RPM |
| IMEPg | 3.9 – 20 bar |
| Fuel Rate | 50-280 mg/str |
| Injection Pressure | 600 – 2100 bar |
| Commanded Injection Duration | 600 – 3000 µs |
| Injection Timing | -20 to 5 CAD aTDC |
| Air / Fuel Ratio | 27 – 84 [-] |
| EGR | 0 – 25% |
| Exhaust Valve Opening/Closing: | 127 / 354 aTDC fired |

Clear variations in exhaust soot properties were observed as engine operating conditions were varied; nevertheless, for this study, general observations and correlations are the focus. As the apparent trends in soot formation and oxidation are inferred from differences in heat release rate for low and high-soot cycles, the corresponding range of engine operating conditions will be reported for which the relevant phenomena are observed.

### 2.2 FLEER Optical Diagnostic Hardware

Optical diagnostic hardware required to measure instantaneous soot concentration in the exhaust runner is partially based on that originally employed in a skip-fired optical engine previously described in [13]. Implementation in a continuously fired single-cylinder heavy-duty diesel engine requires a few modifications to ensure robust measurement of laser light extinction over the full range of operation. Photographs of hardware used to introduce (pitch) collimated coherent light into the optical test section and hardware used to capture (catch) and measure transmitted light are shown in Figure 2.

The laser pitch (on the left) shows an opto-mechanical assembly rigidly mounted to a threaded breadboard integrated into the windowed-housing of the exhaust runner. (Flexible nitrogen hoses and fittings, which feed the window-purge circuit are also pictured). A 0.9 mW, 635nm (red) laser diode module (LDM – Edmund Optics #57-105) is integrated into a custom machined holder that is firmly secured into a 2-axis mirror mount, allowing remote beam steering during engine operation. The beam is pitched into the exhaust test-section through a 10 mm wide aperture past a high-temperature, highly reflective horizontal strip deposited on the near window. After spanning the 73.8 mm exhaust housing, the beam is reflected back and forth across the span between opposed windows via high-reflectance strips, covering nearly all of the exhaust cross-section orthogonal to the flow. This approach ensures a representative mean exhaust soot concentration is acquired and a sufficiently long extinction path is obtained to ensure high diagnostic accuracy.

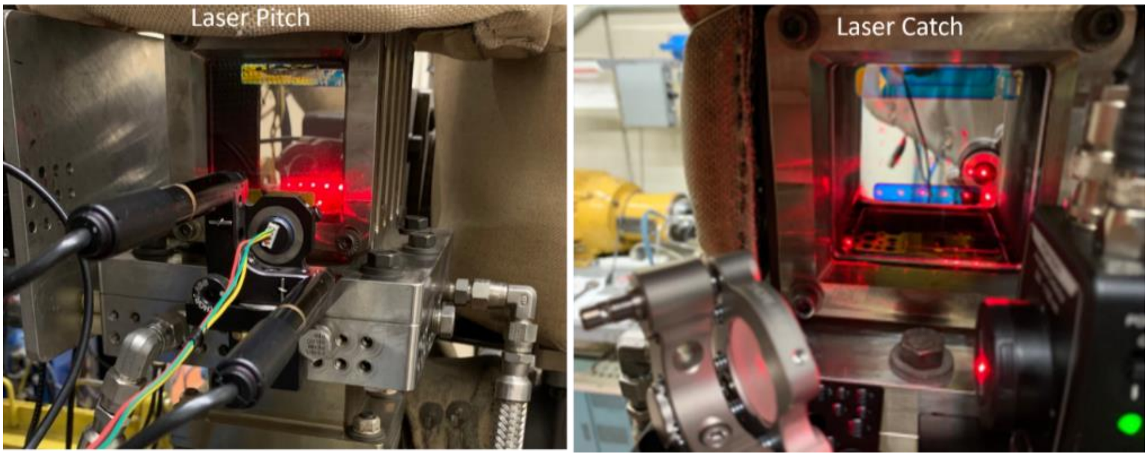

**Fig 2.** Photographs of the windowed optical exhaust runner with mounted diagnostic hardware, including that for the laser pitch (left) and the laser catch (right). Apparent red spots indicate beam reflections from the strategically located strips designed to create a long spatially averaged multi-pass extinction path length.

After the 2 mm diameter laser beam passes through the optical exhaust runner, it is captured by the 'laser catch' hardware pictured on the right side of Figure 2. After the beam leaves the optical runner via an aperture next to the reflective strip, it impinges on the center of a concave mirror, which corrects the beam direction/divergence and re-directs the transmitted light toward a switchable gain 10 V photodetector (Thorlabs PDA100A2), where the measured intensity is recorded and communicated to the high-speed data acquisition via a BNC cable.

### 2.3 Post-Processing

#### 2.3.1 Determining Exhaust Soot Volume Fraction

Exhaust soot volume fraction during the exhaust event is determined by meticulously analyzing transmitted laser intensity throughout each engine cycle. The instantaneous raw transmitted signal is measured by the photodetector and then normalized (as shown in Figure 3) for 200 consecutive cycles during fired engine operation when exhaust is permitted to flow through the optical exhaust runner. Gradual fouling of the windows and reflective coatings are corrected by renormalizing each cycle. The sudden instantaneous drop in signal after exhaust valve opening clearly indicates the onset of cycle soot extinction. About 30 crank angle degrees (i.e., time of flight) are required for the exhaust gases to reach the measurement volume. This signal shift is rectified by aligning the initial rapid drop (due to extinction) with the known exhaust valve opening (EVO) time indicated by the first (left) dashed vertical line in Figure 3. After the end of the exhaust period (indicated by the right dashed line), the signal slowly recovers to a quasi-steady value as the continually flowing nitrogen purges the exhaust runner of particulate matter. If the instantaneous signal level just prior to exhaust valve opening (after gas exchange) is used for normalization, the measured transmission and extinction can be computed for every cycle as shown. Note that the instantaneous average is plotted in red with all 200 cycles plotted in black. Deviations of black lines from the red line indicate cycle and instantaneous variations in soot.

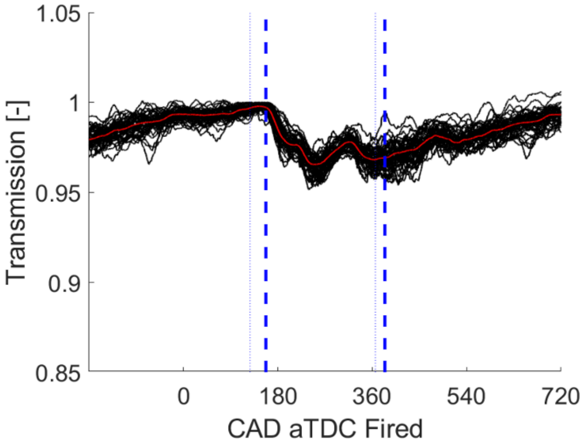

**Fig 3.** Plot illustrating the determination of cycle transmission from raw transmitted signal. Overlapping black lines represent data for 200 individual cycles. Red line represents instantaneous ensemble average. Left and right vertical blue dashed lines represent exhaust valve opening and closing, respectively.

A few additional computations are necessary to determine the mass-averaged soot volume frac-tion for each cycled. The normalized signal or transmission can be related to soot volume fraction ac-cording to the Beer-Lambert relationship:

$$f_v = -\frac{\lambda}{k_e L} ln\left(\frac{I}{I_o}\right) \tag{1}$$

for which $\lambda$ is the wavelength of attenuated light and $k_e$ is the dimensionless extinction coefficient. For red laser light near $\lambda$ = 635 nm, a value of 7.2 is assumed for $k_e$ in this work, based on measurements of the complex indices of refraction for soot by Skeen et al [12]. Since measurements are performed in the engine exhaust runner, intensity corrections for soot luminosity are unnecessary.

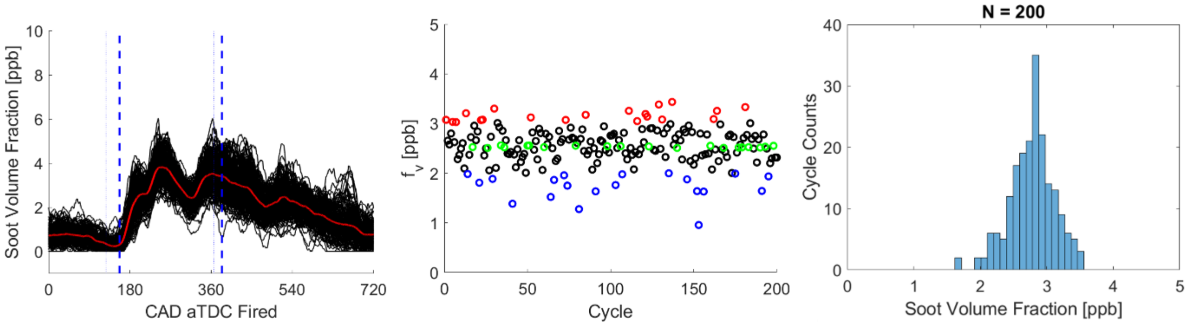

**Fig 4.** Crank-angle resolved soot volume fraction (left) as determine from the data in Figure 3. Mass-averaged values (center) for a 200 cycle ensemble are sorted by low (blue), median (green), and high (red) cycles. Corresponding probability density is plotted on the right.

The resulting instantaneous soot volume fraction during the exhaust is shown in the left plot of Figure 4 with peak measured concentrations of more than 5 ppb. This measured profile is indicative of a typical exhaust profile in which the bulk of exhaust mass leaves during the blowdown process immediately following EVO with an additional 30-40% leaving the cylinder as the piston pushes toward top-dead-center (TDC). Weighting the measured instantaneous soot volume fraction by the known exhaust flow and integrating allows computation of a mass-averaged soot volume fraction for each cycle as shown in the center of Figure 4. Note that the 20 cleanest (low soot) cycles are plotted in blue, the 20 median (mid) cycles are plotted in green, and the 20 highest soot cycles are plotted in red. Identification of these distinct cycles proves to be a powerful tool for analysing the heat release rate and identifying features of soot formation and oxidation (as will be shown in a later section). Constructing the cycle soot distribution as a probability density function as shown in the right image of Figure 4 is also helpful for understanding the statistical behavior of a particular operating condition.

### 2.3.2 Determination and Analysis of Apparent Heat Release Rate

Apparent heat release rate (AHRR) is determined from the high-speed cylinder pressure data using the well-known 1st law analysis presented in Heywood [15]. Measured cylinder pressure is first filtered and smoothed using a Fourier series low-pass filter with a Gaussian roll-off dropping to less than 1% above 2500 Hz. The resulting 0.1 CAD resolved scalar measurements indicate the net rate of heat release (chemical energy release minus heat transfer losses in J/CAD) for each individual cycle. Subsequently computing the integrated apparent heat release rate (IAHRR) at each CAD enables determination of total cycle heat release and individual burn durations. The former value - $IAHRR_t$ is generally represented by an asymptotic value reached prior to exhaust valve opening late in the expansion stroke. Normalization of $IAHRR_t$ and examination of the cycle times when 10, 20, 30% of the energy has been released allows the crank angles associated with these milestones (e.g. CA10, CA20, CA30) to be determined accordingly. Determination of the associated burn durations in crank angle degrees for each cycle (e.g., CA0-10, CA10-20, CA20-30, etc.) is then a simple matter of subtraction.

Subsequent analysis of cycle mass-averaged exhaust soot PM and the associated heat release durations can reveal interesting relationships. Correlative tests have been performed using the Matlab ‘corrcoef’ function [16], which returns a probability and coefficient for every metric and every test condition tested. True correlations are revealed if the probability of random correlation is less than 5%. Strength of correlation is represented by the correlation coefficient between cycle soot PM and burn duration metrics when a true correlation is identified. Results of this analysis will be shown later in more detail for particular cases of interest.

## 3. Results

### 3.1 Injector Performance and Quiescent Spray

Prior to engine testing, all injectors were tested to determine rates of delivery, hydraulic opening and closing delays, exit velocity, spray penetration, spreading angle, lift-off length, and soot mass formed from a quiescent spray at ECN diesel target conditions [17]. A few of these measurements are reported here as they indicate baseline variations that are expected when there is little ambient flow motion and no spray-wall interaction (i.e., contrary to typical engine conditions).

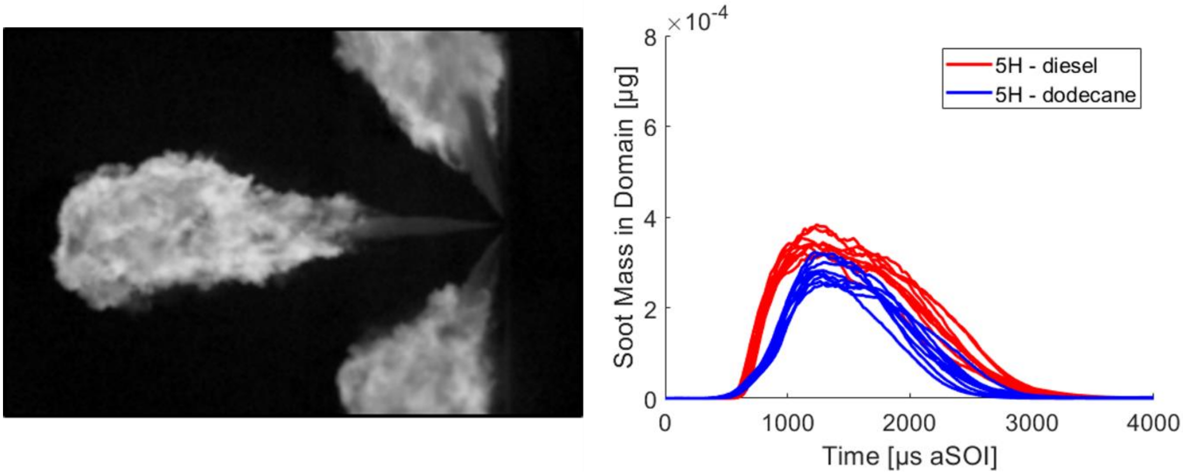

**Fig 5.** Image (left) of soot luminosity and scattering from NG research injector spray for quiescent reacting conditions. Measured soot mass (right) produced in quiescent conditions for two different fuels. Soot mass obtained using DBI imaging technique [19].

**Table 4.** Measured spray and combustion characteristics for injector operating under quiescent conditions.

| | **Mean** | **Coefficient of Variation [COV]** |
|---|---|---|
| Peak Velocity @ 1000 bar | 570 m/s | 1.0% |
| Spreading Angle | 18.7° | 7.0% |
| Lift-Off Length | 17.2 mm | 14.4% |
| Peak Soot Mass - Diesel | 3.40E-4 μg | 7.9% |
| Peak Soot Mass - Dodecane | 2.80E-4 μg | 10% |

Spray and combustion characteristics are listed in Table 4 for the NGR injector tested in this work, as it is representative. A representative spray image is shown in Figure 5. At an injection pressure of 1000 bar, the mean exit velocity is just below the expected Bernoulli velocity [18] with little shot to shot variation of 1%. When the spray is injected into engine representative ambient density (23 kg/m$^3$), the spreading angle is modest (18.7°) with shot- variations rising to 7%. For a 900 K reacting environment typical of engine start of injection (SOI), the lift-off length is 17.2 mm with a 14.4% coefficient of variation (COV). These variations manifest as shot-shot soot mass variations as listed in the table and shown in the right plot of Figure 5. The mean soot mass produced in the quiescent domain is measured using diffuse back illumination [19] of an isolated jet. For diesel fuel, the soot concentration in the jet is sufficiently high to 'saturate' the extinction such that the measured soot mass COV is artificially low at 7.9%. When a fuel with lower soot propensity is employed (i.e., dodecane), the mean soot measured in the domain is reduced, and the observed soot COV increases to 10%. This observed PM shot- variation serves as a reference against which engine-out PM variations may be compared to determine the effects of in-cylinder motion and spray-wall interactions.

### 3.2 Results: General Observations of Soot Variations and Apparent Heat Release Rate

Mass-averaged exhaust soot volume fraction and associated engine cycle variations are shown in Figure 6 for a wide variety of loads, speeds, air/fuel ratios and injection conditions. Mass-averaged exhaust soot varies significantly between 0.3 and 11.8 ppb, which is consistent with measured AVL filter smoke numbers varying between 0.1 and 1.0 [20]. Inspection of the cycle COV determined from 200 cycle ensembles collected for each operating point (middle) and ratio of max/min (right) exhaust soot cycles reveals that the amount of soot leaving one engine cycle can vary profoundly from that of another, even for quasi-steady operating conditions. For lower loads, when exhaust PM emissions are generally lower, soot volume fraction COV varies between 13-85% with max/min cycle soot ratios varying between 2 and 30. At higher loads, when exhaust PM is higher, variations diminish but remain between 10-40% COV with operating conditions frequently manifesting 5-15X max/min cycle soot variations.

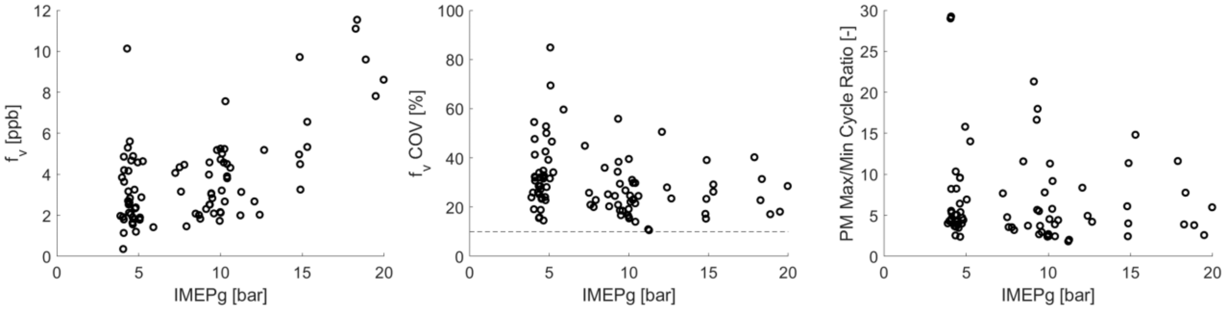

**Fig 6.** Measured engine-out soot volume fraction (left) and associated cycle variations (middle and right) over a wide range of engine loads. Coefficient of variation is plotted in the middle with a dashed line representing the measured baseline for quiescent non-engine test conditions. The ratio of maximum to minimum cycle averaged exhaust soot is plotted for different loads on the right.

For all engine conditions, exhaust soot cycle variations (COV) exceed the reference baseline quiescent spray variation represented by the horizontal dashed line (near 10%) plotted in the middle of Figure 6. Apparently, variations in the spray velocity, jet formation, and flame LOL manifest as baseline variations in soot formation as shot-shot spray mixing varies prior to the reaction zone in an 'undisturbed' jet (as detailed in Table 4). In the engine, variations in soot formation *and* oxidation manifest as even higher cycle soot variations as the burning jets encounter the piston bowl, engine head, and other jets. These previously unknown high levels of variation, which are generally not predicted by computational models of engine combustion, likely add to the elusiveness of accurate soot predictions for any conventional compression ignition combustion geometry.

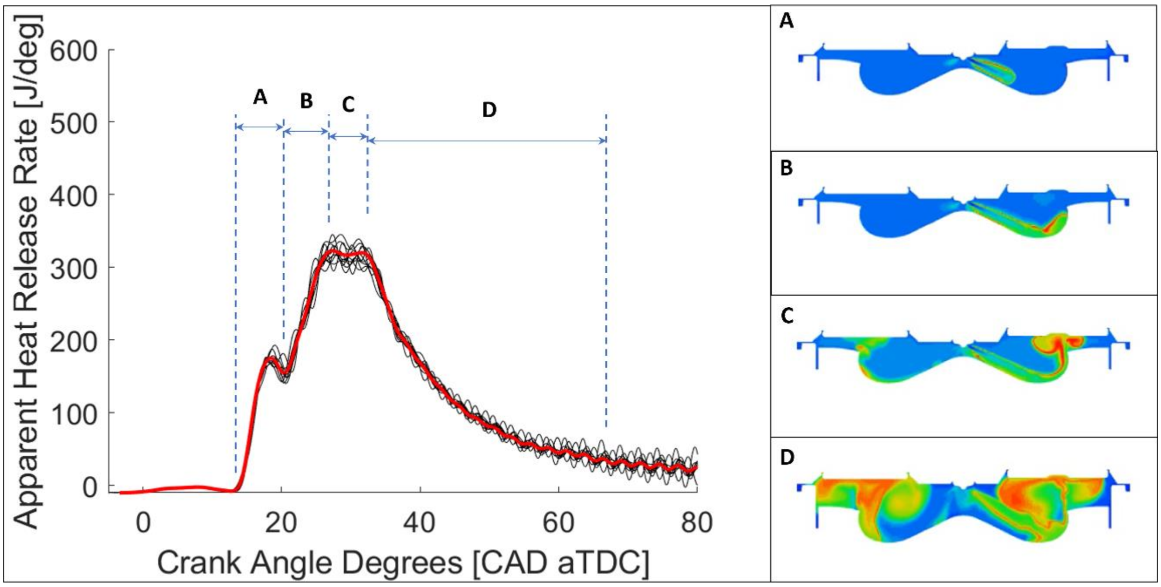

**Fig 7.** Apparent heat release rate (left) for 200 cycles (black) and the corresponding mean (red) for high load and relatively late injection timing. Four key combustion intervals are labeled with representative burning jet simulations (right) for a wall-guided combustion system illustrating the relevant spray-wall interaction during each interval.

That such high PM variations are not immediately obvious is not surprising given the relative invariance in cycle apparent heat release rate (and IMEP) as illustrated in Figure 7. The left plot reveals a relatively unchanging AHRR for which the cycle integrated totals and IMEP exhibit less than 2% COV. This contrasts with cycle PM variations for the same test condition of more than 25%. Nevertheless, scrutiny of the instantaneous heat release variations for low- and high-soot cycles during each of the labelled combustion intervals is revealing. In the following sections, the impact of each of four combustion intervals on soot formation and oxidation will be examined, including: A) jet formation and premixed burn, B) interaction of the burning jet with the piston bowl, C) interaction of the burning jet with the engine head, and D) burnout during late expansion. The set of images shown on the right side of Figure 7 from engine simulations of a similar re-entrant wall-guided system illustrates the known burning jet phenomena for each interval. The general timing and morphology of simulated spray-wall interactions have been verified by visualizing several sprays as they interact with a sector re-entrant piston in a quiescent test vessel [21-22].

### 3.3 Results: Mechanisms of Soot Formation and Oxidation as Revealed by Engine Exhaust Soot and Correlations with Apparent Heat Release Rate

A variety of test conditions (summarized in Table 5) are examined in the following sections to illustrate observed correlations between crank-angle and cycle resolved soot volume fraction and measured apparent heat release rates for each of the four combustion intervals shown on the right side of Figure 7. The listed test points/cases are by no means comprehensive (as many other conditions were tested and exhibited similar correlations). Some of the test conditions exhibit multiple correlative features of interest. For the sake of brevity, only a few representative cases are examined in this work to illustrate general trends. Soot measurements for each test condition are annotated in subsequent figures and are listed in the last three columns of Table 5.

It is noteworthy that measured filter smoke number (FSN) and mean soot volume fraction (measured in the optical exhaust manifold) do not always precisely agree. The former (FSN) is acquired far downstream at near atmospheric pressure while the latter is measured less than a meter downstream of the exhaust valves where the static pressure is elevated. A single FSN value is reported by the smoke meter as measured for thousands of cycles; whereas the mean soot volume fraction (measured by extinction) represents only one parameter of a non-gaussian, high-variance soot probability density function determined from a 200-cycle ensemble. Other potential sources of disagreement include poor sensitivity of the smoke meter at low levels and potential differences in volatiles as described in [14].

**Table 5.** Test conditions, hardware, operating parameters, and exhaust soot measurement summary

| Test Point | Piston / Injector | Speed [RPM] | IMEPg [bar] | Air/Fuel Ratio [-] | Injection Pressure [bar] | Injection Timing [CAD aTDC] | EGR [%] | FSN [-] | Mean Soot Volume Fraction [ppb] | Soot COV [%] |
|---|---|---|---|---|---|---|---|---|---|---|
| 46 | O / NGR | 1000 | 11.2 | 38 | 1050 | 1.7 | 0.9 | 0.06 | 2.0 | 11 |
| 65 | R / PP | 1000 | 5.2 | 66 | 580 | -14.4 | 3.9 | 0.38 | 2.9 | 47 |
| 45 | O / NGR | 1000 | 10.3 | 29 | 1050 | 1.8 | 0.8 | 0.14 | 2.4 | 30 |
| 67 | R / PP | 1000 | 4.9 | 66 | 580 | 0.5 | 3.8 | 0.51 | 4.9 | 39 |
| 87 | R / PP | 1000 | 18.2 | 29 | 780 | 4.8 | 1.5 | 0.38 | 11.1 | 23 |
| 5 | O / NGR | 1000 | 4.4 | 62 | 600 | -12.6 | 2.0 | 0.30 | 4.2 | 25 |
| 48 | O / NGR | 1000 | 12.4 | 44 | 1050 | -8.3 | 1.0 | 0.06 | 2.0 | 28 |

### 3.3.1 Impact of Ignition, Premixed Burn, and Lift-Off Length Establishment on Soot Formation

The early heat release period (indicated by interval ‘A’ in Figure 7) prior to spray-wall interaction and mixing controlled combustion is generally not expected to substantially affect soot formation. During this time, fuel that has mixed prior to ignition burns relatively quickly, resulting in a premixed burn spike (PMBS) or local maximum in the apparent heat release rate (as observed in Figure 8 for test point 46). Since the local equivalence ratio of premixed fuel is relatively low, the PMBS should not form much soot; however, conditions established during the early heat release period *may* lead to differences in soot formation throughout the rest of the burn as described below.

For a late injection, moderate load condition with relatively high rail pressure (represented by test point 46 in Figure 8), the exhaust soot is low (2.0 ppb, 0.06 FSN) with relatively low cycle to cycle soot variation (11% COV). Consequently, the cycle soot distribution or probability density function (PDF) shown in Figure 9 (left) is narrow. For all cycles, the soot exhausts uniformly, indicative of a uniform distribution of PM near the head, in the bowl, and in crevices as shown on the right side of Figure 9. Nevertheless, some cycles produce 1.5 ppb of soot while others produce 2.8 ppb. These cycle differences are not obvious from the AHRR (Figure 8 – left) and IAHRR (Figure 8 – right), but they become more evident upon closer inspection of the PMBS for all cycles (Figure 8 - middle).

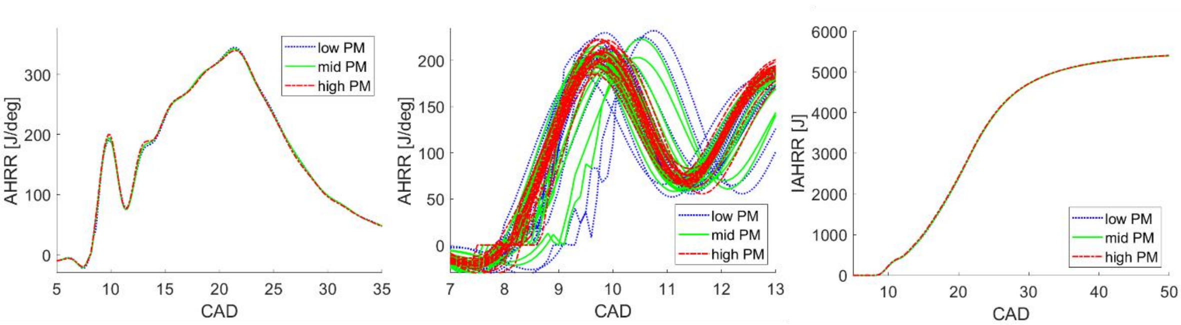

**Fig 8.** Plots of heat release rate vs. CAD for test point 46. Left and middle plots illustrate features of the premixed burn spike for low, mid, and high soot cases, while the right plot compares cumulative heat release. All cycles are explicitly represented in the middle plot; whereas, ensemble averages are shown on the left and right. Overall, the HRR shows very subtle differences between low- and high- sooting cycle ensembles.

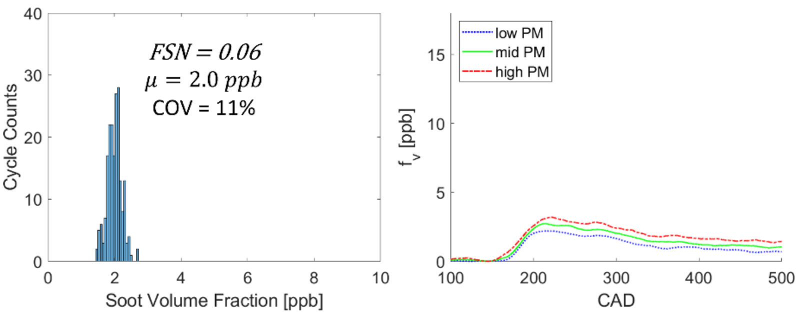

**Fig 9.** Plots of cycle soot distribution (left) and soot exhaust profiles (right) for low, mid, and high soot cycles of test point 46.

Most cycles in the middle of Figure 8 exhibit a consistent ignition timing, PMBS magnitude, and mixing-controlled burn, but clear differences in ignition delay are apparent for some of the mid- and low-PM cycles in the ensembles. These (blue and green) cycles with retarded ignition eventually produce less net soot in the exhaust. Although the cause for this phenomenon is uncertain, we speculate that the differences in exhaust soot are due to varying ignition location and lift-off length establishment. Delayed ignition means that the ignition location and initial flame lift-off length are further from the injector tip, allowing longer mixing residence time prior to reaction. Consequently, local equivalence ratios near the lift-off length would be lower, resulting in lower PM formation. Previous work by Pickett et al [1, 23] has shown (for a free jet in a quiescent vessel) that once the lift-off length establishes at a given location (in this case, near the time of ignition), it tends to remain there (even if reaction rates significantly change during the steady-flow mixing-controlled burn) because the characteristic time to relocate is much longer then the typical on-engine injection duration.

These small variations in cycle soot formation recall previous observations for baseline quiescent sprays as presented in section 3.1. Notice that the engine cycle soot COV for test point 46 is 11%, representative of the lowest value for any conditions tested (from Figure 6) and nearly equal to shot-soot variations observed for baseline injection into quiescent flow (Table 4). During the short interval ‘A,’ the jet propagates into an environment temporarily resembling quiescent flow for which there is little to no interaction of the newly formed burning jet with piston, liner, or cylinder walls (as illustrated by the top right image of Figure 7). Wider plume angles and slower jet head velocities apparent for some quiescent injections are likely to ignite sooner and produce more soot in the engine as well.

For many engine conditions, these correlative effects during interval ‘A’ are even more pronounced as shown for the low-load, low-injection-pressure, early-injection case shown in Figures 10 and 11 for test point 65. Despite a pronounced premixed burn spike (reaching nearly 250 J/deg), this case forms significantly more soot, likely because the injection pressure is less than 600 bar and the flame LOL is relatively short for all cycles, leaving little distance for mixing prior to reaction. The cycle soot distribution (shown on the left side of Figure 11) is also quite broad, with a COV of 47%. The low PM cycles exhaust less than 1 ppb of soot while high PM cycles exhaust nearly 6 ppb of soot. Although some of these cycle soot differences may be largely attributed to head interactions occurring later during interval ‘C’ (as discussed in the following sections), the same correlation between retarded ignition and lower soot as observed for test point 46 is also observed here. Low PM cases tend to exhibit later ignition with likely longer lift-off length until the end of injection.

Soot exhaust profiles (shown on the right side of Figure 11) offer additional clues about the in-cylinder processes affecting soot formation and oxidation. For this low-load case with lower injection pressure and shorter duration, much of the soot is concentrated in the bowl; consequently, soot levels are highest during the latter portion of exhaust when the piston is pushing out burned products from the bowl, consistent with previous observations by Koci [24-25].

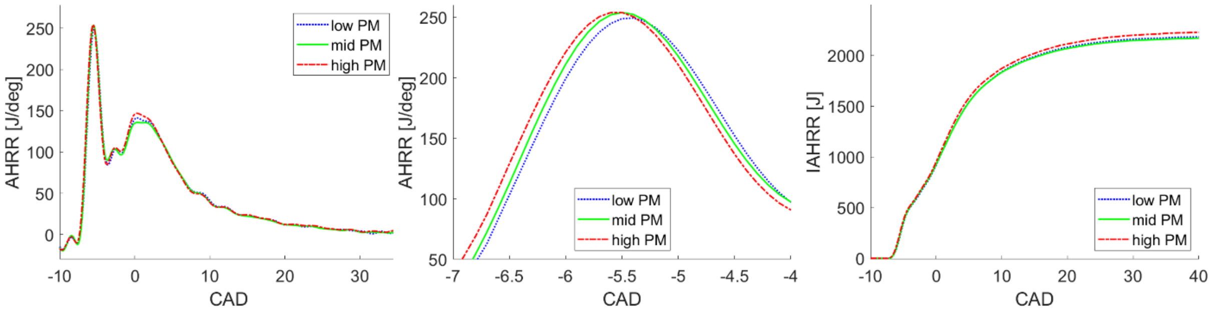

**Fig 10.** Plots of heat release rate vs. CAD for test point 65. Left and middle plots illustrate features of the premixed burn spike for low, mid, and high soot cases, while the right plot compares cumulative heat release.

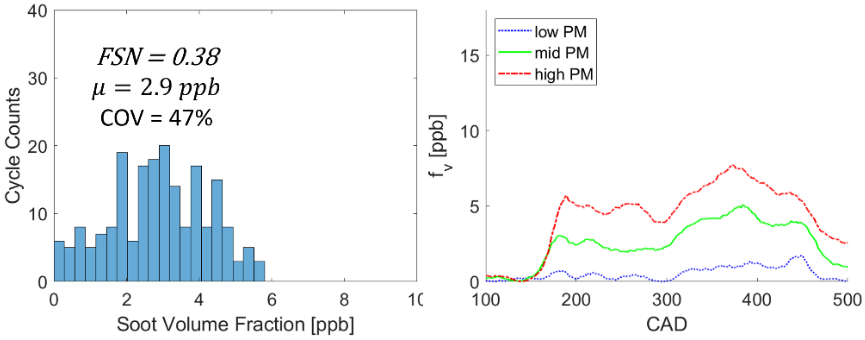

**Fig 11.** Plots of cycle soot distribution (left) and soot exhaust profiles (right) for low, mid, and high soot cycles of test point 65.

### 3.3.2 Impact of Spray-Bowl Interaction on Soot Formation and Heat Release Rate

After ignition and early jet penetration, as the burning spray interacts with the piston bowl, artifacts in the heat release rate and soot emissions are sometimes present (as shown in Figure 12 and 13). For this test point 45 with AFR = 29 (and relatively higher injection pressure), bulk temperatures are relatively high such that mean soot is relatively low (FSN = 0.14); however, some significant low-PM and high-PM cycle outliers are evident from the soot probability distribution shown in the bottom left of Figure 13, for which the soot COV is 30%. The magnified portion of AHRR corresponding to the spray-bowl interaction represented by interval 'B' exhibits a clear difference in the rising heat release rates for low- and high-PM cases (see middle of Figure 12). The measurably lower heat release rates (or higher heat loss) for high soot producing cycles during the spray-bowl interaction may be caused by reduced air entrainment as the jets encounter the solid piston boundary. We anticipate that some of the injections have lower velocity and speculate that the spray is occasionally directed toward the bottom of the bowl rather than along the piston pip. If this occurs, momentum and air-entrainment would be reduced for those cycles, resulting in lower rates of heat release and increased soot formation as local equivalence ratios remain higher. Previous spray visualization for similar hardware affirms that periodic spray axis deviations are probable. Local In-cylinder eddies may also be responsible for these phenomena. More investigation is needed.

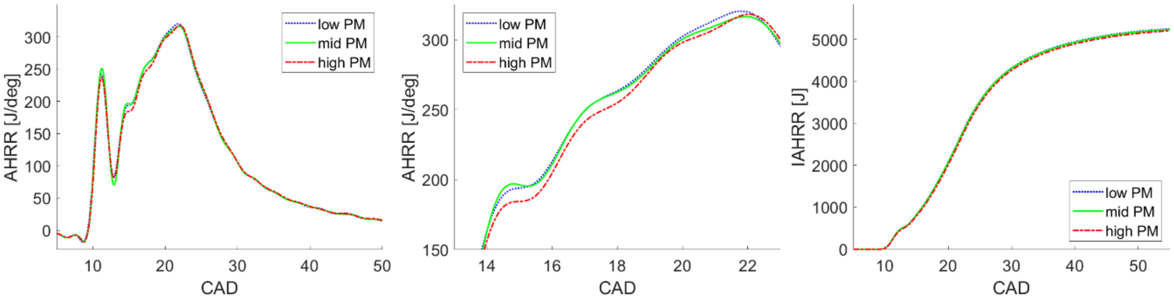

**Fig 12.** Rates of heat release for test point 45. Clear differences are observed between low and high PM cycles during interval 'B' (center) during which the spray interacts with the piston bowl.

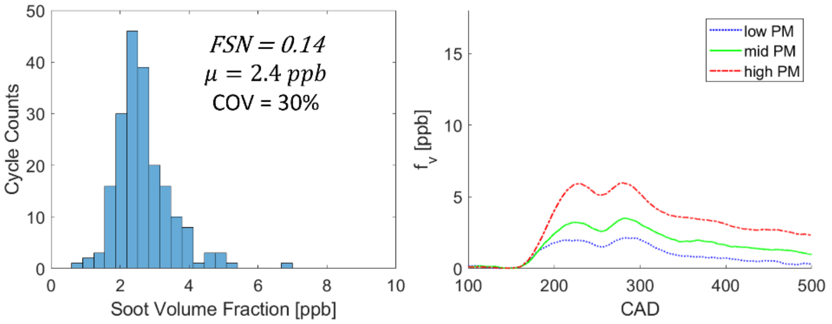

**Fig 13.** Cycle soot distribution (left) and soot exhaust profile (right) for test point 45.

These features of spray-bowl interaction are even more evident for low-load, late-injection cases as shown in Figures 14 and 15 for test point 67. The relatively low 580 bar injection pressure yields higher soot levels (4.9 ppb and 0.51 FSN) with high (39%) PM COV for which some of the cycles yield 9 ppb of exhaust soot while others yield less than 1 ppb. Close examination of the instantaneous heat release rate between 11 and 17 CAD aTDC indicates significant differences for low and high PM cycles immediately after the PMBS continuing into the spray-head interaction (see middle plot of Figure 14). The lowest sooting cases exhibit a bump in the heat release rate between 12-13 CAD aTDC followed by highest mixing controlled burn rate of 145 J/deg. The highest sooting cases indicate a very subdued bump after the PMBS followed by a measurably lower AHRR during early stages of MCC as the burning jet interacts with the bowl. Image 'B' in Figure 7 illustrates the significant spray wall interaction occurring during this period when the wall-guided spray is redirected by the bowl bottom toward the lip. Evidently, soot formed in the bowl tends to remain there until exhaust as the soot exhaust profiles in Figure 15 (right) indicate a high concentration of soot leaving the cylinder late during the exhaust stroke, well after initial blowdown. The relatively low-pressure injection is late and slow enough that it likely stagnates in the bowl rather than always following the piston pip to the bowl rim.

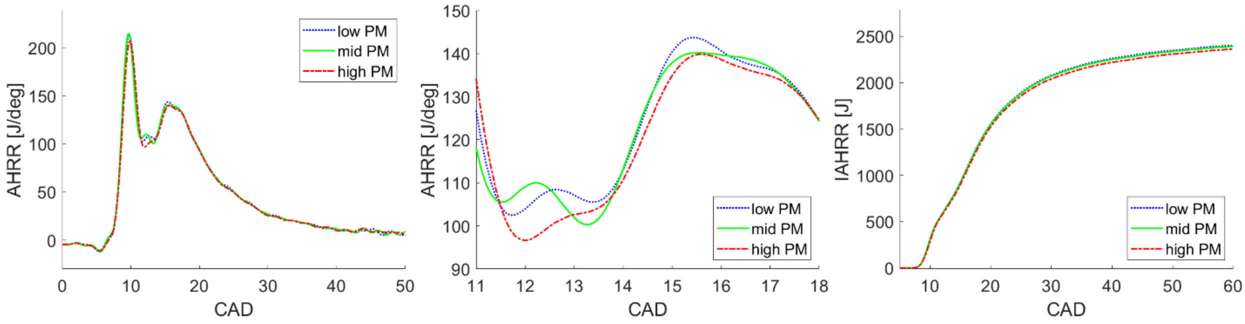

**Fig 14.** Rates of heat release measured for test point 67 showing clear differences between low and high PM cases during spray-bowl interaction.

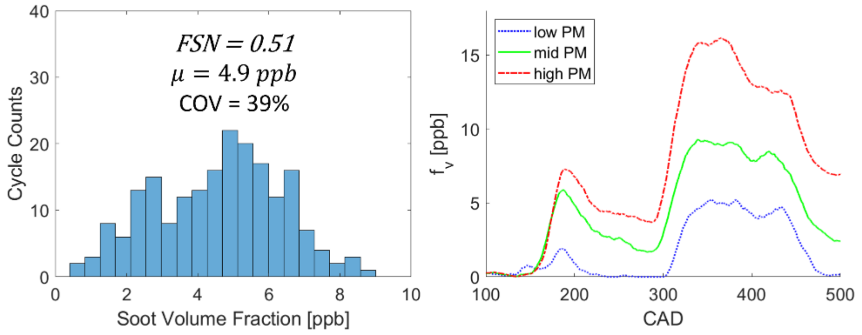

**Fig 15.** Cycle soot distribution (left) and soot exhaust profiles for test point 67. Soot formed in the bowl leaves late during exhaust.

Statistical evidence for these observed correlations between PM emissions and apparent heat release rate is presented in Figure 16. Each marker represents positive identification of a real (non-random) correlation between cycle PM and a particular burn rate metric, including peak heat release rate ($AHRR_p$), total integrated apparent heat release rate ($IAHRR_t$), CA0-10, CA10-20, etc. First evidence of burn duration correlation with PM is apparent for the CA20-30 interval when the mass fraction burned and net energy release progresses from 20 to 30% (between 11-14 CAD aTDC). The middle plot of CA20-30 vs. cycle PM annotated with low, mid, and high cycles, confirms the correlation with a measured coefficient of 0.25. The highest soot cycles require about 0.25 CAD duration longer than the lowest soot cycles to release the same amount of energy. Other correlations are evident later in the heat release and expansion; these will be addressed in subsequent sections.

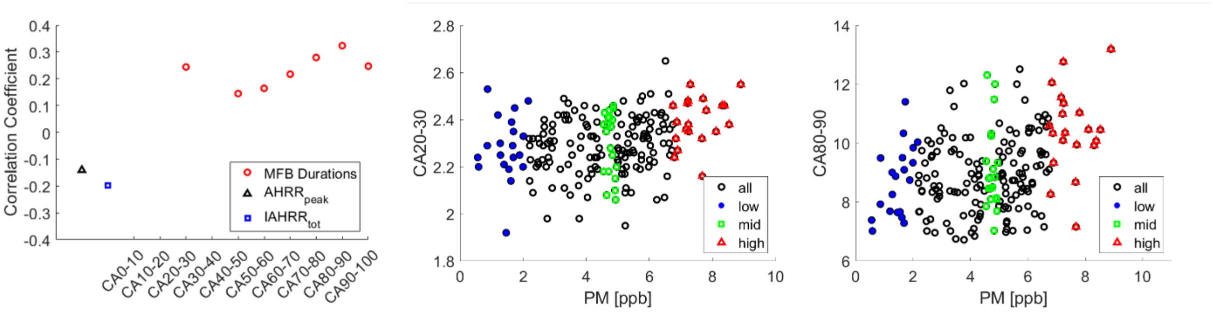

**Fig 16.** Evidence for PM and HRR correlations for test point 67. Left plot indicates real (>95% probability) correlations for each HRR interval with corresponding correlation coefficients. Middle plot illustrates the correlation of early burn duration, CA20-30, i.e., evidence of influence by spray-bowl interaction. Right plot indicates the correlation for late cycle burnout given by CA80-90.

The cycle PM/HRR correlations examined in this work are generally characterized by large cyclic variations in soot and *very subtle* (small) differences in measured apparent heat release rate. Consequently, one could be forgiven for skepticism. To reinforce the statistical significance of these measurable differences in heat release rate for low, mid, and high soot cycles, correlative tests have also been performed for PM and HRR from *different* (off) cycles (e.g., PM cycle N and HRR cycle N+10 or PM cycle N and PM cycle N+20). For all cases, statistically significant correlations and associated coefficient maxima were detected for *same* cycle parameters; whereas, real correlations generally disappeared for off-cycle parameters, thus bolstering confidence in this correlation detection approach and the associated conclusions.

### 3.3.3 Impact of Spray-Head Interaction on Soot Oxidation and Heat Release Rate

Many engine cases exhibit evidence of HRR and soot affected burning spray interactions with the engine head as illustrated in interval 'C' of Figure 7. During this time, the apparent heat release rate is generally tapering off or rising more slowly compared with earlier periods when the spray is interacting primarily with the piston bowl. This is apparent from the high-load, late-injection case represented by test point 87 as shown in Figures 17 and 18. Closer inspection reveals nearly invariant cycle heat release rates for this case (with 11.1 ppb mean soot with 23% PM COV) except during the time that the burning spray interacts with the head. Between 17-23 CAD aTDC, instantaneous heat release rates for high PM cases (>16 ppb in exhaust) are 3% lower than the cleanest cycles (<8 ppb). Near 18 CAD when the burning jet begins to interact with the head, the spray encounters the solid wall with reduced air entrainment and increased heat loss as evidenced by the HRR inflection point when the instantaneous HRR nearly levels off. For highest sooting cases, this interaction is more pronounced with measurably lower heat release rates. Due to these head interactions, soot formed upstream (where local equivalence ratio still exceeds two [26]) can escape the flame through disruption by the solid boundary, or it may encounter reduced air/reaction rates, all of which impede oxidation, depositing PM near the surface, where it lingers until exhaust valve opening. This is confirmed by initial concentrations of soot leaving the cylinder after EVO that are higher than at any other time during exhaust.

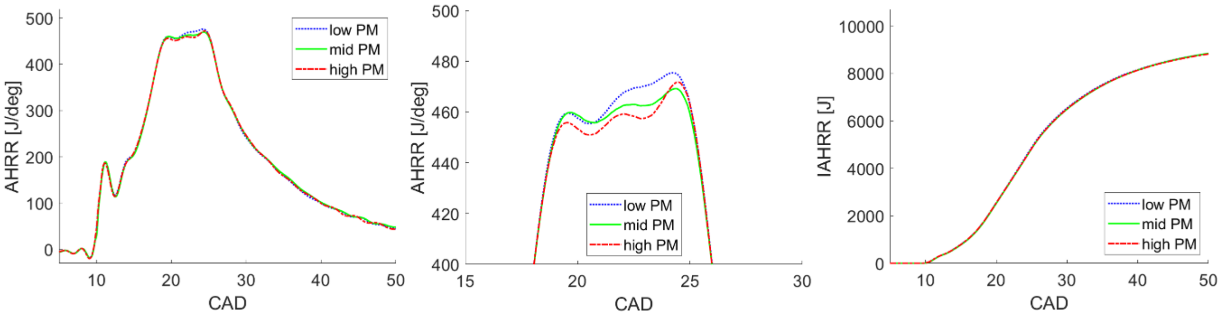

**Fig 17.** Heat release comparisons for test point 87. Observed variations between low and high PM are attributed to differences in spray-head interactions and effects on soot oxidation. A close comparison of AHRR during interval 'C' is shown in the center.

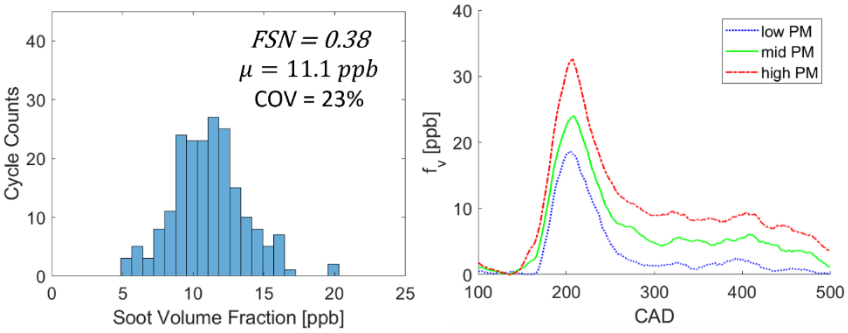

**Fig 18.** Soot cycle distributions (left) and exhaust soot profiles for low, mid, and high PM for test point 87.

Effects of spray-head interactions on PM oxidation and HRR have been observed for many test points over a wide variety of conditions, but, particularly for lower injection pressures. These include the low-load, early-injection case represented by test point 5 as shown in Figure 19-21. For this condition, a high premixed burn is followed by clear differences in the peak mixing controlled burn between 1-5 CAD aTDC for differently sooting cycles (see middle plot of Figure 19). Examination of the soot cycle probability density function (Figure 20 – left) reveals a non-gaussian, skewed soot distribution with a mean soot concentration of 4.2 ppb, but significant sooty cycle outliers. These may be partially attributed to a nearly 5% drop in AHRR when those cycles interact with the head. Additional causes for higher soot are evident from the soot correlation map shown on the left side of Figure 21. In addition to the mid cycle burn duration correlations observed for CA30-40 (associated with spray-head interactions), even higher correlations are observed later in the cycle as described in the next section.

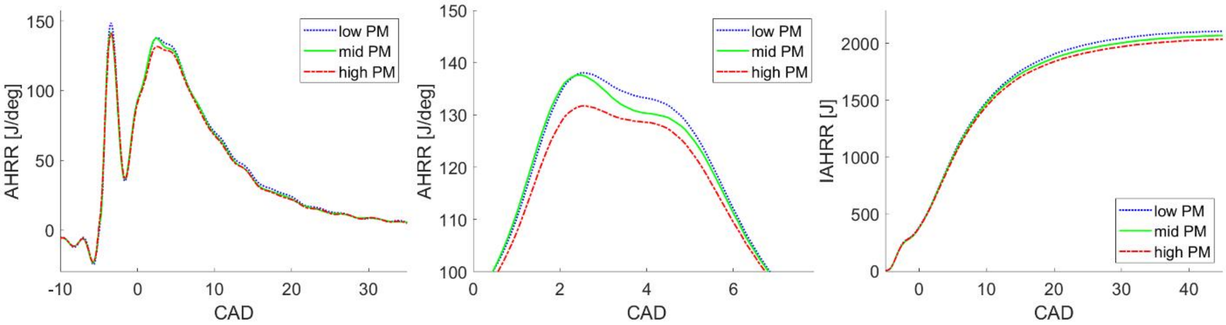

**Fig 19.** Heat release rate comparisons for test point 5 illustrating effects of spray-head interactions. A close comparison of AHRR during interval ‘C’ is shown in the center.

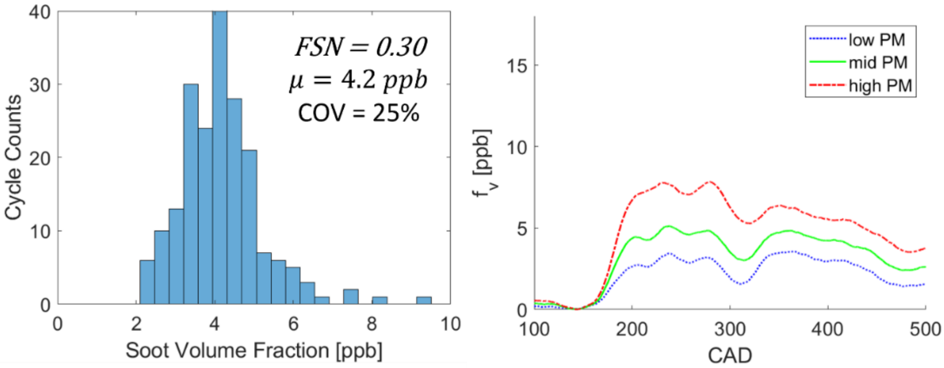

**Fig 20.** Exhaust soot cycle distribution (left) and exhaust profiles (right) for low, mid, and high PM cycles for test point 5.

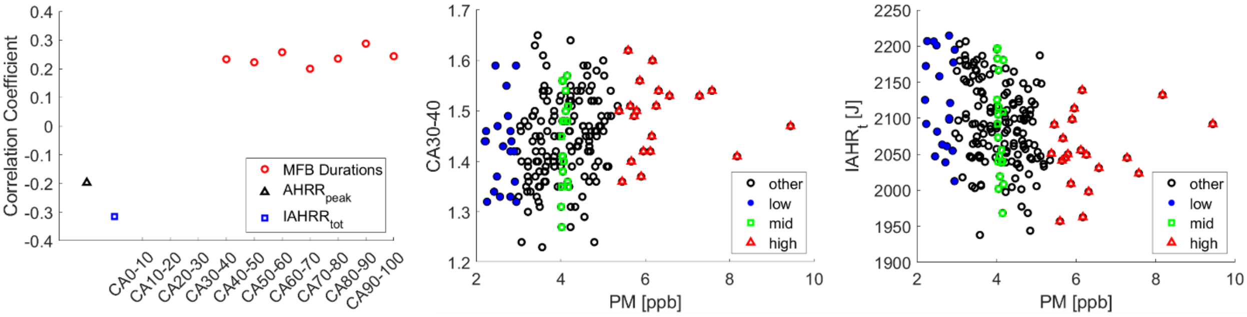

**Fig 21.** Evidence for PM and HRR correlations for test point 5. Left plot indicates real (>95% probability) correlations for each HRR interval with corresponding correlation coefficients. Middle plot illustrates the correlation of early burn duration, CA30-40, i.e., evidence of influence by spray-head interaction. Right plot indicates the correla-tion of cycle PM with total cycle heat release, $IAHRR_t$.

### 3.3.4 Impact of Late Cycle Burn-Out on Soot Oxidation

Many factors impact late cycle burnout and soot oxidation in an engine, including: spray wall interaction [27], engine swirl [28], flame recession [29-30], post-injections [31], and end of injection entrainment wave [32]. In this work, many of these factors are evident, demonstrating that low- and high- exhaust PM cycles are indeed associated with multiple phenomena in compression ignition engines. Several of test points that have already been analyzed are now revisited for evidence of late cycle burn-out on soot oxidation as observed during interval 'D' in Figure 7.

The low-load, late-injection engine condition described in Figures 14-16 (test point 67) exhibits high mean soot volume fraction with a very wide cycle soot distribution (COV = 39%). As mentioned previously, this is partially due to spray-bowl interaction observed between 11-15 CAD aTDC. More significant correlations (with higher correlation coefficients) are observed after the end of injection for late cycle burnout as observed for CA80-90 in the left and right plots of Figure 16. Despite significant scatter in the low- and high-PM bins represented by the blue circles and red triangles, the mean of each ensemble indicates a longer CA80-90 burn duration of 10.6 CAD for high soot cycles compared with 9 CAD for the low soot cycles. The right plot of Figure 14 further illustrates differences in cumulative heat release rate with clear separation between high- and low- sooting cycles beginning near 25 CAD aTDC and persisting to end of combustion near 50 CAD aTDC. Disturbances of the penetrating spray as it encounters the bowl are first manifest as higher soot formation associated with spray-wall interactions; these further manifest as poor late cycle PM oxidation with reduced late cycle burnout. That this trend occurs for low injection pressures (as for test point 67) is not surprising given the reduced momentum and spray penetration, which reduce access to air in the far reaches of the cylinder. Similar late cycle burnout and poor soot oxidation are evident in Figures 19-21 for case 5, which first exhibits effects of the burning spray interacting with the bowl.

Even cases with higher injection pressure as shown in Figures 22-24 for test point 48 can be impacted by late cycle burnout. For this moderate load (12 bar IMEPg) and moderate injection timing (-8.3 CAD aTDC), the mean soot is low (2 ppb, 0.06 FSN), but there is significant cycle variation. With a PM COV of 28% and a skewed soot distribution, low-soot cycles are less than 1 ppb while high soot cycles are more than 5 ppb (as shown in the left plot of Figure 23). Some of these differences may be attributed to spray-bowl interaction as evidenced by lower heat release rates between 4-10 CAD aTDC (middle plot of Figure 22) and high correlation coefficients for CA20-30 (middle plot of Figure 24). Nevertheless, differences in late cycle burnout are apparently a more likely cause for the high-PM outliers as indicated by longer CA90-100 (right plot of Figure 24), the negative correlation of high-PM with $IAHRR_t$, and the gradual divergence in cumulative heat release rate apparent after 20 CAD aTDC. (right plot of Figure 22). This poorer soot oxidation for high-PM cases finally manifests itself as high initial concentrations of soot lingering near the head that quickly exits the cylinder after EVO (as observed in the right plot of Figure 23).

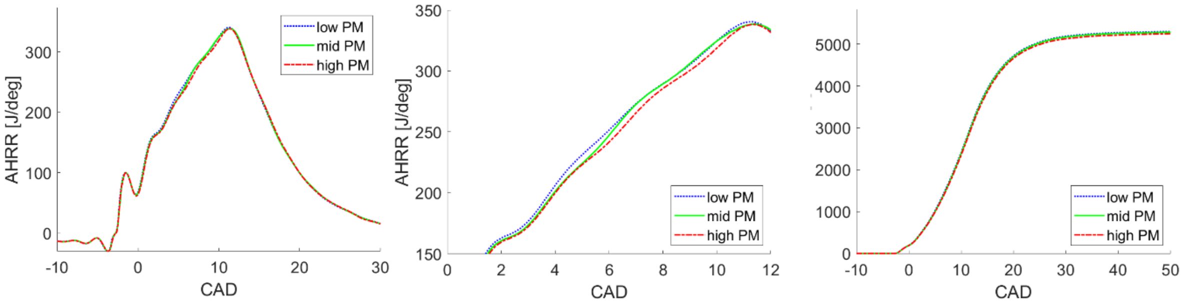

**Fig 22.** Plots of heat release rate vs. CAD for test point 48 illustrating effects of spray-bowl interaction and late cycle PM burnout.

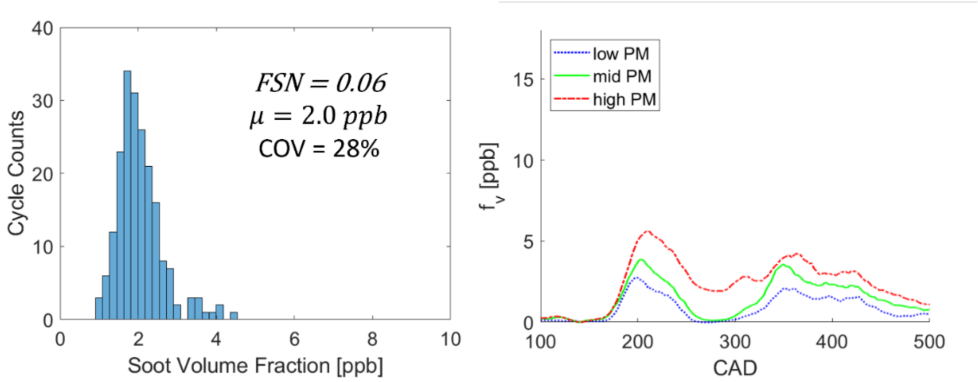

**Fig 23.** Soot cycle probability distribution (left) and soot exhaust profiles for test point 48.

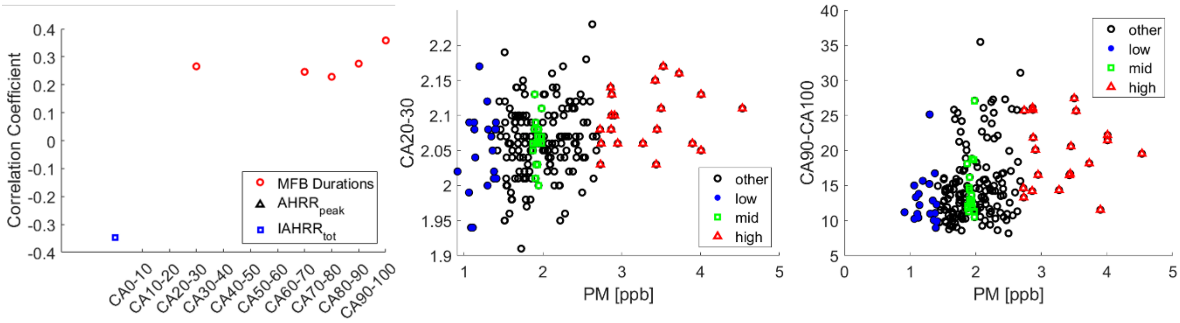

**Fig 24.** Evidence for PM and HRR correlations for test point 48. Left plot indicates real correlation coefficients for each HRR interval. Middle plot illustrates the correlation of early burn duration, CA20-30, i.e., evidence of spray-bowl interaction effects. Right plot indicates the correlation of cycle PM with CA90-100, confirming the role of late cycle burnout on PM emissions.

## 4. Discussion and Study Implications

The utility of a fast, crank-angle-resolved soot extinction technique capable of characterizing cycle PM emissions has been demonstrated by successful integration of the FLEER diagnostic with cylinder pressure sensing in a continuously fired metal engine. The measurement approach can reveal significantly more information about soot formation, oxidation, and rate of heat release than could ever be discovered using a simple exhaust smoke meter. FLEER can more accurately delineate combustion system performance, particularly, for points of instability (indicated by high COV and/or non-gaussian soot distributions), which could potentially be corrected and optimized by methodical study and iteration of injector and combustion system hardware. Although cycle soot variations are likely inescapable due to engine spray-wall interactions and baseline injector shot variations, improvements in spray formation (and repeatability) and charge motion (i.e., swirl and turbulence) could potentially reduce bulk soot emissions by minimizing high cycle soot variations. This approach may be particularly useful for meeting increasingly stringent PM emissions requirements like those expected for Tier V.

This approach for relating formation and consumption of specific pollutants to subtle differences in apparent heat release rate could be applied to engines operating on alternative fuels with concerns beyond PM emissions. Fuel slip for gaseous fuels (e.g., hydrogen and methane) could be studied using a similar approach. Unwanted pollutants like carbon monoxide, formaldehyde, and oxides of nitrogen could be measured in the same optical exhaust runner for various liquid fuels (e.g., methanol, ethanol, ammonia, and naphtha) to understand their relationship to apparent heat release rate and to pursue efficient abatement strategies.

Results of this study may have the most profound implications for engine combustion modeling and how engine-out emissions are predicted. Existing combustion models including soot formation and oxidation have not been privy to the cycle distribution information revealed by this study; therefore, they all rely on long time-integrated smoke meter data that is likely skewed by non-normal distributions. No wonder that such models often lack sufficient predictive capability for a wide variety of combustion geometries and operating conditions [33], especially as they are based on an average-cycle realizations. In many cases, they may be correctly simulating a particular mid-, high-, or low- sooting condition, while failing to capture quasi-stable or key cycle varying behavior as revealed in this work. Awareness of such significantly large cycle variations seems imperative to understanding and simulating bulk behavior. Multi-cycle realizations or some other statistical approach may be necessary. Finally, application of new understanding about how cycle soot formation and oxidation relate to heat release during each of the key intervals (ignition, premixed burn, LOL establishment, spray-bowl interaction, spray-head interaction, and late cycle burnout), may go a long way toward understanding model prediction gaps.

## Conclusions

A crank-angle resolved soot diagnostic has been successfully applied in the exhaust runner of a continuously fired single cylinder engine (based on a Caterpillar C15 production engine) to better understand cycle soot variations and relationships between soot formation and oxidation with apparent heat release rate. PM variations range between 11-80% COV with some cycles exhibiting more than an order of magnitude difference in engine out soot compared with other cycles. Lowest observed engine cycle soot variations are nearly equal to levels measured for the fuel injector spraying into quiescent conditions without piston or head jet interactions. In-cylinder motion and spray wall interactions only tend to increase these PM variations.

For several different hardware configurations and a wide range of engine operating conditions, exhaust soot variations are correlated with subtle differences in apparent heat release rates during four different intervals. During the ignition and premixed burn interval, flame lift-off length can establish closer to the injector tip (for some cycles) due to lower injection velocity or plume widening, resulting in an advanced premixed burn spike and elevated cycle soot emissions; this phenomenon is generally present for injection into quiescent conditions. When the burning spray interacts with the piston bowl, stagnation and markedly reduced air entrainment for some cycles can also lead to reduced heat release rates and elevated soot formation. Soot formed in the bowl is usually exhausted late. As the burning spray interacts with the engine head, for some cycles, reaction rates are lower and heat loss is higher, resulting in higher soot concentrations formed near the head; this soot tends to exhaust early. Many of these cases are coupled with reduced late cycle soot burnout/oxidation, especially for lower injection pressure when access to air/oxygen in far reaches of the cylinder is similarly diminished.

Application of the FLEER diagnostic technique has promise for aiding combustion system design and reducing mean cycle soot emissions by minimizing skewed (high-PM) cycles. Minimizing injector spray shot variations holds potential for reducing bulk soot emissions. Application of the technique to engines powered by alternative gaseous or liquid fuels could also help identify features of the heat release rate responsible for fuel slip and exhaust emission of other undesirable species. Understanding of soot formation and oxidation processes and their relationship to apparent heat release rate could be immediately used for combustion simulation validation and development. Significant changes in the soot simulation approach may be required to better predict such large cycle variations in soot for such subtle changes in AHRR. These may include multi-cycle realizations or another statistical approach.

## References

[1] Pickett, L., Siebers, D., and Idicheria, C., "Relationship Between Ignition Processes and the Lift-Off Length of Diesel Fuel Jets," SAE Technical Paper 2005-01-3843, 2005, https://doi.org/10.4271/2005-01-3843.

[2] Polonowski, C., Mueller, C., Gehrke, C., Bazyn, T. et al., "An Experimental Investigation of Low-Soot and Soot-Free Combustion Strategies in a Heavy-Duty, Single-Cylinder, Direct-Injection, Optical Diesel Engine," SAE Int. J. Fuels Lubr. 5(1):51-77, 2012, https://doi.org/10.4271/2011-01-1812.

[3] Bazyn, T. and Koci, C. ñThe Effect of Jet Spacing on the Combustion Characteristics of Diesel Sprays,òpresented at THIESEL Conference on Thermo- and Fluid Dynamic Processes in Direct Injection Engines 2014, Spain, September 9-12, 2014.

[4] Mueller C. J., Nilsen, C. W., Ruth, D. J., Gehmlich, R. K., Pickett, L. M., Skeen, S., ñDucted fuel injection: A new approach for lowering soot emissions from direct-injection engines, Applied Energy, 204(1): 206-220, 2017, https://doi.org/10.1016/j.apenergy.2017.07.001.

[5] Fitzgerald, R., Svensson, K., Martin, G., Qi, Y., and Koci, C., ñEarly Investigation of Ducted Fuel Injection for Reducing Soot in Mixing-Controlled Diesel FlamesòSAE International Journal of Engines, 11(6), 817ï 834, 2018, https://www.jstor.org/stable/26649132.

[6] Yraguen, B., Steinberg, A. M., Nilsen, C. W., Biles, D. E., and Mueller, C. J., ñParametric Evaluation of Ducted Fuel Injection in an Optically Accessible Mixing-Controlled Compression-Ignition Engine with Two- and Four-Duct Assembliesò, proceedings of THIESEL Conference on Thermo- and Fluid Dynamics of Clean Propulsion Powerplants, Spain, 2022.

[7] Svensson, K., Kim, C., Seiler, P., Martin, G. et al., "Performance and Emission Results from a Heavy-Duty Diesel Engine with Ducted Fuel Injection," SAE Technical Paper 2021-01-0503, 2021, https://doi.org/10.4271/2021-01-0503.

[8] Gehmlich, R., Dumitrescu, C., Wang, Y., and Mueller, C., "Leaner Lifted-Flame Combustion Enabled by the Use of an Oxygenated Fuel in an Optical CI Engine," SAE Int. J. Engines 9(3):1526-1543, 2016, https://doi.org/10.4271/2016-01-0730.

[9] Miller, S. and Savonen, C., "Development Status of the Detroit Diesel Corporation Methanol Engine," SAE Technical Paper 901564, 1990, https://doi.org/10.4271/901564.

[10] F. R. Westlye, K. Penney, A. Ivarsson, L. M. Pickett, J. Manin, and S. A. Skeen, ñDiffuse back-illumination setup for high temporally resolved extinction imaging,òAppl. Opt., vol. 56, no. 17, pp. 5028ï 5038, 2017, doi: 10.1364/AO.56.005028.

[11] Xuan, T., Cao, J., He, Z., Wang, Q., Zhong, W., Leng, X., Li, D., Shang, W., ñA study of soot quantification in diesel flame with hydrogenated catalytic biodiesel in a constant volume combustion chamberòEnergy, Vol. 145: 691-699, 2018, https://doi.org/10.1016/j.energy.2017.12.106.

[12] Skeen, S. A., Yasutomi, K., Cenker, E., Adamson, B., Hansen, N., & Pickett, L. M., ñStandardized Optical Constants for Soot Quantification in High-Pressure Sprays,òSAE International Journal of Engines, 11(6), 805ï 816, 2017, https://www.jstor.org/stable/26649131.

[13] Fitzgerald, R., Dempsey, A., Barlow, R., Nilsen, C. et al., "Fast Exhaust-Runner Soot Measurements in a Diesel Optical Engine," SAE Int. J. Engines 16(4):539-556, 2023, https://doi.org/10.4271/03-16-04-0032.

[14] Dempsey, A., Seiler, P., Svensson, K., and Qi, Y., "A Comprehensive Evaluation of Diesel Engine CFD Modeling Predictions Using a Semi-Empirical Soot Model over a Broad Range of Combustion Systems," SAE Int. J. Engines 11(6):1399-1420, 2018, https://doi.org/10.4271/2018-01-0242.

[15] Heywood, J. B., ñInternal Combustion Engine Fundamentals,òMcGraw Hill, New York, 1988.

[16] Mathworks documentation: https://www.mathworks.com/help/matlab/ref/corrcoef.html

[17] Pickett, L., Bruneaux, G., and Payri, R., ñEngine Combustion Network Special Issue.òInternational Journal of Engine Research 21(1): 11ï 14, 2020, doi:10.1177/1468087419882247.

[18] Payri, R., Molina, S., Salvador, F.J., “A study of the relation between nozzle geometry, internal flow and sprays characteristics in diesel fuel injection systems. KSME International Journal 18, 1222–1235, 2004. https://doi.org/10.1007/BF02983297.

[19] Maes, N., Skeen, S. A., Bardi, M., Fitzgerald, R. P., Malbec, L-M., Bruneaux, G., Pickett, L. M., Yasutomi, K., Martin, G., “Spray penetration, combustion, and soot formation characteristics of the ECN Spray C and Spray D injectors in multiple combustion facilities,” Applied Thermal Engineering, Vol 172, 2020, https://doi.org/10.1016/j.applthermaleng.2020.115136.

[20] AVL, “AVL 415S Variable Sampling Smoke Meter Operating Manual,” 2005.

[21] Koci, C., Martin, G., Kim, C., Seiler, P., Caliari, F., Saputo, J., Sampath, S., “Optical imaging for understanding of thermal barrier coated piston engine performance,” proceedings of THIESEL 2022 Conference on Thermo- and Fluid Dynamics of Clean Propulsion Powerplants, Valencia Spain, September 13-16, 2022.

[22] Svensson, K. and Martin, G., "Improved Method for Studying MCCI Flame Interactions with an Engine Combustion Chamber," SAE Technical Paper 2021-01-0507, 2021, https://doi.org/10.4271/2021-01-0507.

[23] Pickett, L. M., Kook, S., Persson, H., and Andersson, O., “Diesel fuel jet lift-off stabilization in the presence of laser-induced plasma ignition,” Proceedings of the Combustion Institute, 32(2): 2793-2800, 2009, https://doi.org/10.1016/j.proci.2008.06.082.

[24] Koci, C., Dempsey, A., Nudd, J., and Knier, B., "Understanding Hydrocarbon Emissions in Heavy Duty Diesel Engines Combining Experimental and Computational Methods," SAE Int. J. Engines 10(3):1093-1109, 2017, https://doi.org/10.4271/2017-01-0703.

[25] Koci, C., Fitzgerald, R., Ikonomou, V., and Sun, S., “The effects of fuel-air mixing and injector dribble on diesel unburned hydrocarbon emissions,” International Journal of Engine Research, 20(1): 105-127, 2019, https://doi.org/10.1177/1468087418821827.

[26] Pickett L. M., Siebers, D. L., “Soot Formation in Diesel Fuel Jets Near the Lift-Off Length,” International Journal of Engine Research. 7(2):103-130, 2006, doi:10.1243/146808705X57793.

[27] Pickett, L. and López, J., "Jet-Wall Interaction Effects on Diesel Combustion and Soot Formation," SAE Technical Paper 2005-01-0921, 2005, https://doi.org/10.4271/2005-01-0921.

[28] Jena, A., Singh, A. P., and Agarwal, A. K., “Optical and computational investigations of the effect of spray-swirl interactions on autoignition and soot formation in a compression ignition engine fuelled by diesel, dieseline, and dieseho1,” Applied Energy, 324(15), 2022, https://doi.org/10.1016/j.apenergy.2022.119677.

[29] Koci, C., Martin, G., Bazyn, T., Morrison, W., Svensson, K., and Gehrke, C., “The Influence of Diesel End-of-Injection Rate Shape on Combustion Recession, 8(2), 647-659, 2015.

[30] Knox, B., and Genzale, C. “Effects of End-of-Injection Transients on Combustion Recession in Diesel Sprays,” SAE International Journal of Engines, 9(2), 932–949, 2016, http://www.jstor.org/stable/26284870.

[31] O’Connor, J., and Musculus, M., “Post Injections for Soot Reduction in Diesel Engines: A Review of Current Understanding,” SAE International Journal of Engines, 6(1), 400–421, 2013, http://www.jstor.org/stable/26277626.

[32] Musculus, M. P. B., & Kattke, K. (2009). “Entrainment Waves in Diesel Jets,” SAE International Journal of Engines, 2(1), 1170–1193. http://www.jstor.org/stable/26308462.

[33] Dempsey, Adam, Seiler, P, Svensson, K., and Qi, Y., “Evaluation of the Two-Step Hiroyasu Soot Model over a Broad Range of Diesel Combustion Systems,” SAE International Journal of Engines, 11(6), 2018, 10.4271/2018-01-0242.

# Insights into Cycle-to-Cycle Variations: A Multi-Cycle LES Investigation of Knocking Combustion Initiation

M. Kircher[1], J. Schneider[2], A. Pati[3], M. G¿nther[4], C. Hasse[1]

[1]Technical University of Darmstadt, Department of Mechanical Engineering, Simulation of reactive Thermo-Fluid Systems, Otto-Berndt-StraÇe 2, 64287 Darmstadt, Germany

[2]FEV Europe GmbH, Propulsion Concepts, NeuenhofstraÇe 182, 52078 Aachen, Germany

[3]KTM Racing GmbH, Gewerbegebiet N 5, 5222 Munderfing, Austria

[4]RWTH Aachen University, Chair of Thermodynamics of Mobile Energy Conversion Systems, ForckenbeckstraÇe 4, 52074 Aachen, Germany

E-mail: kircher@stfs.tu-darmstadt.de

**Abstract**. Climate change requires a significant reduction in greenhouse gas emissions, with the optimization of existing technologies proving to be a promising path. In gasoline engines, the occurrence of knocking combustion is a key obstacle to further efficiency improvements. Here, the engine process exhibits cycle-to-cycle variations, which lead to differences in the combustion process and consequently may change the boundary conditions for knocking combustion initiation. The statistical nature of these variations poses a challenge for research and requires the application of appropriate methods and analytical approaches. While previous studies have found correlations between flow characteristics and the combustion process, the question of whether these correlations can be extended to the initiation of knocking combustion remains open and is addressed in the present study. Here, measurements of knocking combustion of a surrogate fuel in a single-cylinder research engine are used as a basis for subsequent numerical analysis. In a multi-cycle LES study, a recently developed precursor model with a detailed source term formulation is employed to predict the initiation of knocking combustion. The LES results are validated against the experimental data with regard to averaged combustion and knock quantities, taking into account cycle-to-cycle variations. In particular, it is shown that the experimentally determined knock initiation direction can be predicted very well by the simulation based on the spatial distribution of the auto-igniting mass. Furthermore, the cause-and-effect chain of knocking combustion initiation is investigated. Guided by correlation analyses the relationships among flow structures, flame propagation and the auto-ignition process are analyzed. Notably, large-scale flow structures are found to affect the early flame propagation, which subsequently influences the overall combustion process and local flame propagation. The latter, in turn, determines the local and global auto-ignition process. In summary, this study analyzes the complicated relationships among flow, combustion and auto-ignition process, providing valuable insights into the cause-and-effect chain of knocking combustion initiation.

## 1. Introduction

The use of carbon-based fuels in internal combustion (IC) engines produces greenhouse gases. A reduction of these emissions can be achieved by improving engine efficiency. Here, downsizing is a promising approach [1]. However, it poses the risk of knocking combustion [2, 3], which potentially can damage the engine. Consequently, in modern engines a knock control adjusts the spark timing to prevent the occurrence of knocking combustion. However, this limits the combustion efficiency.

In the past, different theories have been proposed to explain the occurrence of knocking combustion [2, 4, 5]. In the current understanding, knocking combustion is always initiated by auto-ignition events in the unburned mixture. These are ahead of the flame front and clearly separated spatially [6]. The knock limit is characterized by low-amplitude pressure oscillations. These result from a deflagrative mode in which the reaction front emerging from the auto-ignition is immediately separated from the respective pressure wave. Thus, the knock intensity depends primarily on the amount of auto-ignited mass [7, 8].

Knocking combustion has been investigated extensively both experimentally and numerically in the past as discussed in the review article by Wang et al. [3]. Experimental investigations of knocking combustion often use conventional gasoline fuels [9, 10]. However, the exact composition of gasoline is not standardized. Therefore, numerical studies consider surrogate fuels which consist of a reduced number of known components [11]. Common surrogates are Primary Reference Fuels (PRFs) which consist of isooctane and n-heptane and Toluene Reference Fuels (TRFs), where toluene is added. To account for the alcohol content of modern gasoline fuels, TRF+E surrogate fuels additionally contain ethanol [12]. For numerical investigations of knocking combustion, the auto-ignition delay times as well as burning velocity must be properly captured by the surrogate formulation. Alternatively, the experiments directly employ surrogate fuels to enable a comprehensive joint analysis with simulations.

The accurate prediction of the auto-ignition process of a surrogate fuel is a prerequisite for numerical investigations of knocking combustion initiation. There are two common modeling approaches: direct modeling and precursor models.

The high computational costs associated with direct modeling of the auto-ignition process can be reduced by simplified kinetic approaches [13, 14]. This was employed in several studies with finite-rate chemistry for the unburned gas for different surrogate fuels with reduced or skeletal mechanisms of varying complexity [15–19]. The pre-tabulation of chemistry is used in the tabulated kinetics of ignition (TKI) model [20–24]. This approach was employed for LES investigations of knocking combustion by Robert et al. [7, 9, 25].

In a precursor model, the evolution of a real or pseudo species is assumed to capture the auto-ignition process. In this regard, Livengood and Wu [26] proposed the knock integral method (KIM). For simplicity, a linear relation between the auto-ignition delay time and the precursor mass fraction is assumed. For the application in CFD simulations, empirical correlations [27, 28] or reaction mechanisms of varying complexity [29, 30] were used to calculate and tabulate the auto-ignition delay times, respectively. Linse et al. [31] developed the generalized knock integral method (gKIM), which incorporates the effect of turbulent fluctuations. Further adaption and application to a broader range of operating conditions demonstrated the capabilities of this approach [32]. Subsequently, the model was extended to surrogate fuels with negative temperature coefficient (NTC) behavior in an LES study [8].

The unsteady nature of spark-ignited IC engine operation is a particular aspect of knocking combustion. Even for nominal stable operation conditions cycle-to-cycle variations (CCVs) occur [33]. The combustion process differs from cycle to cycle [34] and so are related quantities such as cylinder pressure, heat release and thermodynamic conditions in the unburned gas, where auto-ignition may occur. The associated CCVs in the tendency of knocking combustion initiation pose a challenge for the investigation of knocking combustion.

There have been numerous numerical and experimental studies attempting to identify the causes and influencing factors of CCVs of combustion as summarized in the review articles by Young [34] and Ozdor [33]. Young [34] postulated that CCVs begin early in the cycle and that velocities in the spark region seem to have a significant influence. Ozdor [33] strengthened this hypothesis and identified the magnitude and direction of the local spark velocity as the main factors influencing the combustion process. This was subsequently further investigated in multiple experimental studies incorporating cylinder pressure measurements and imaging techniques for flow, spark and flame propagation [35–39].

In terms of numerical investigations, single cycles of multi-cycle LES studies allow the analysis and understanding of fundamental physics and the complex interactions between the different processes causing CCVs [40]. Respective LES studies [41–43] confirmed, that the local spark velocity is influencing the combustion process. Other studies identified the kinetic energy [44] or the location of coherent vortex structures [45] as influencing factors of CCV. Truffin et al. [42] emphasized that there is no universal hierarchy of influencing factors, but that they seem to depend on engine geometry and operating conditions.

Investigating knocking combustion, a deeper understanding of the CCVs, particularly at the knock limit, is important [33]. Recent LES studies [7, 9, 10, 19, 25, 46] demonstrated that by resolving CCVs, the influence of single cycles on the mean knock behavior can be investigated. In addition, correlations between physical phenomena can be analyzed. Here, Fontanesi et al. [10] and Robert et al. [9] found correlations between the flow velocity in the spark vicinity and the global burn rate. Robert et al. [25] presented a qualitative comparison of individual locations of auto-ignition. However, the global trend of these locations was attributed to heat transfer or residence times and the local randomness to turbulence, without further in-detail analysis. To the authors' knowledge, there is no systematic numerical study of the correlations of flow, combustion and auto-ignition.

Thus, this study conducts a systematic analysis of the cause-and-effect chain of knocking combustion initiation to investigate the causes of cycle-to-cycle variations. Focusing on the knock limit, an experimental campaign of a single-cylinder research engine provides data on the knocking behavior of a TRF+E surrogate fuel. In addition to conventional indicated in-cylinder pressure data, localized data is available through the employment of a fiber-optical spark plug. This data is used to validate the results of a multi-cycle LES study in which a previously developed precursor model [8] is employed for the prediction of auto-ignition. Subsequently, the LES data is used for the investigation of the cause-and-effect chain of knocking combustion initiation. Here, global and local correlation analyses are used to guide the analysis of the relationships between flow structures, flame propagation and the auto-ignition process.

The remainder of this paper is structured as follows. First, the experimental database is presented. Subsequently, the engine simulation framework and the applied modeling approaches are described. Thereafter, the results are discussed. The paper closes with a conclusion of the main findings.

## 2. Experimental database

The experiments are conducted employing a full-metal single-cylinder research engine (SCRE). The engine geometry and operating conditions are listed in Table 1. A schematic visualization of the combustion chamber is given in Fig. 1. More details on the engine can be found in previous studies [47–49].

Spark timing sweeps at the knock limit are conducted to vary the combustion phasing in terms of 50% fuel mass fraction burned (MFB50). Here, an engine speed of 1500 RPM and a load of 10 bar indicated mean effective pressure (IMEP) are chosen. The knocking combustion behavior is investigated under stoichiometric operating conditions for a TRF+E surrogate fuel that consists of 66.0 % iso-octane, 11.3 % n-heptane, 17.4 % toluene and 5.3 % ethanol by mass [8], [50]. A port-fuel injection (PFI) system is used for mixture generation. Valve timings of intake valve opening (IVO) and exhaust valve closing (EVC) are chosen to minimize valve overlap and internal exhaust gas recirculation (EGR) rate, which is around 4 %. Coolant and oil temperatures are conditioned to 90 °C.

The measurement signals are processed via Kistler 5064 charge amplifiers and an FEV combustion analysis system (FEVIS). The position of the crankshaft is measured with an optical encoder with a 0.1 °CA resolution. The engine is coupled to an eddy-current brake and an electric dynamometer to maintain the desired engine speed with an accuracy of ±1 RPM, regardless of the engine load. To ensure constant stoichiometric engine operation the relative air/fuel ratio $\lambda$ of the exhaust gas is derived according to Spindt [51] with the extension for oxygenated fuels by Bresenham et al. [52].

The pressures in the intake and exhaust manifolds are measured with Kistler 4045-A5 piezoresistive pressure transducers. The pressure in the cylinder is measured with two flush-mounted KistlerA6061B piezoelectric pressure transducers opposite each other in the combustion chamber roof between the intake and exhaust valves. The pressure values given refer to the average of both pressure transducers.

The auto-ignition of the unburned mixture induces high-frequency pressure oscillations that superimpose the mean pressure trace in the cylinder. Thus, the high-resolution pressure trace is used to characterize knock intensity. From the filtered high-frequency component of the cylinder pressure p, which is calculated by subtracting the weighted moving average low-pass filtered signal from the unfiltered signal, the characteristic value Knock-Peak-Peak (KPP) is determined. By averaging over the recorded 1000 cycles in one operating condition, the value KPP$_{\text{mean}}$ is calculated. Additionally, the filtered pressure signal is used to determine the crank angle of knock onset $\mathrm{CA}_{\mathrm{KO}}$. It is defined here as the crank angle at which the value of the high-frequency pressure oscillations exceeds a threshold of 0.25 bar for the first time considering only cycles with a KPP > 0.4 bar.

For the simulations, an operating point with a knock intensity KPP$_{\text{mean}}$ of 1.04 bar is considered. The respective spark timing of -6 °CA results in an MFB50$_{\text{mean}}$ of 14.0 °CA.

Additional signals are available based on the optical access through the insertion of a 40-channel fiber-optical spark plug (see Fig. 1) produced by AVL List GmbH. The optical data are acquired with a S1336-BQ photo-multiplier array from Hamamatsu Photonics. The spectral characteristics of the fiber system are only limited by the photomultiplier's spectral photosensitivity, which allows the detection of broadband light emission between 200–1100 nm with a peak sensitivity at 950 nm.

**Table 1**. Engine geometry and operating conditions

| | |
|---|---|
| Stroke | 90.5 mm |
| Bore | 75 mm |
| Compression ratio | 11.83:1 |
| Valve diameter (IV/EV) | 32/26 mm |
| Engine speed | 1500 RPM |
| IMEP | 10 bar |
| Fuel | TRF+E |
| IVO (1 mm lift) | 15 °CA |
| EVC (1 mm lift) | -26 °CA |

The optical signals track intensity peaks caused by auto-ignition events. These are processed in an indirect localization approach. The respective methodology described in Schneider et al. [53] is specifically developed for operating conditions with low knock amplitudes. Here, the individual signals of each of the 40 optical observation cones (see Fig. 1) are used to determine the most probable knocking combustion initiation direction. Thus, in addition to the global information provided by the pressure signals, local information is available to further characterize the observed knock event.

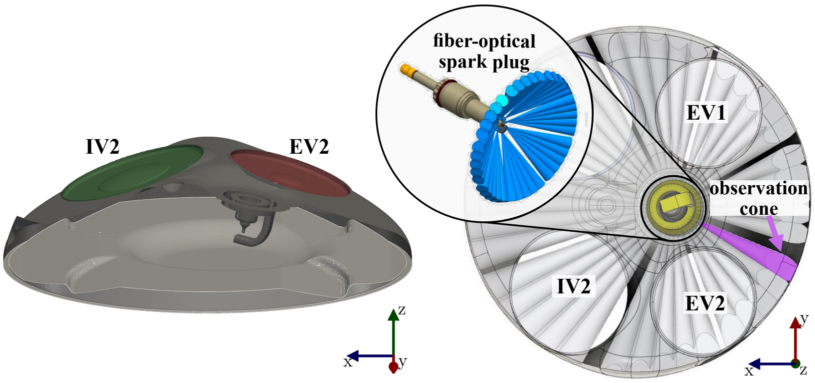

**Fig. 1.** The left side shows the combustion chamber geometry close to TDC. The cylinder head is cut at the symmetry (tumble) plane. On the right side, the fiber-optical spark plug is depicted. In addition, the 40 optical observation cones inside the combustion chamber are shown schematically (in transparent gray). Intake valves (IV) and exhaust valves (EV) are labeled for orientation

## 3. Engine simulation setup

The engine simulations are performed using *TFMotion* which is an *OpenFOAM*-based in-house framework developed for engine simulations [54]. The topological changes of the engine cycle are captured by a *key grid* approach [55] in a pre-processing step. The meshes are hexa-dominant structured grids. The base cell size in the cylinder is 0.5 mm, which is comparable to other engine LES studies [7, 8, 25, 42, 56]. To capture geometric features, a local refinement down to 0.125 mm is applied. The same refinement level Is used for a sphere of 2 mm around the spark position.

For the multi-cycle procedure (see schematic depicted in Fig. 2), the simulation is started in the early exhaust phase. The composition and temperature of the quiescent mixture in the cylinder and the exhaust port are set according to a burned state. Several realizations of the first combustion phase (*Cycle 0*) are simulated. Here, a numerical spark timing sweep is conducted to obtain different pressure traces. From these, three individual results are selected as initial conditions for the next cycle. From here on, three independent threads are executed in parallel. Individual consecutive full-cycle simulations are performed within each thread. With the simulation of the second combustion (*Cycle 1*) and subsequent gas exchange phases, initial conditions for the subsequent cycles (*Cycle 2*) are available and the initialization procedure is completed. Only results from here onwards are considered in the subsequent analyses.

### 3.1 Turbulent knocking combustion modeling

Knocking combustion results from auto-ignition events in a location ahead of the turbulent flame front. Thus, turbulent flame propagation and turbulent auto-ignition must be captured properly, which is incorporated by respective models. A detailed gasoline surrogate mechanism with 485 species and 2081 reactions [57] is used to describe the auto-ignition and combustion of the investigated surrogate fuel.

#### *3.1.1 Turbulent flame propagation modeling*

The modeling of the turbulent flame propagation is based on an algebraic flame surface density (FSD) model [58] coupled to a flamelet-based manifold. In the LES, a normalized reaction progress variable $\tilde{c}$ is defined based on the sum of mass fractions of carbon dioxide and carbon monoxide and a transport equation [59] is solved:

$$\frac{\partial(\overline{\rho}\tilde{c})}{\partial t} + \frac{\partial(\overline{\rho}\widetilde{u_i}\tilde{c})}{\partial x_i} = \frac{\partial}{\partial x_i}\left(\frac{\mu_{\mathrm{SGS}}}{\mathrm{Sc}_{\mathrm{SGS}}}\frac{\partial \tilde{c}}{\partial x_i}\right) + \rho_{\mathrm{u}} s_{\mathrm{L}} \Sigma\,. \tag{1}$$

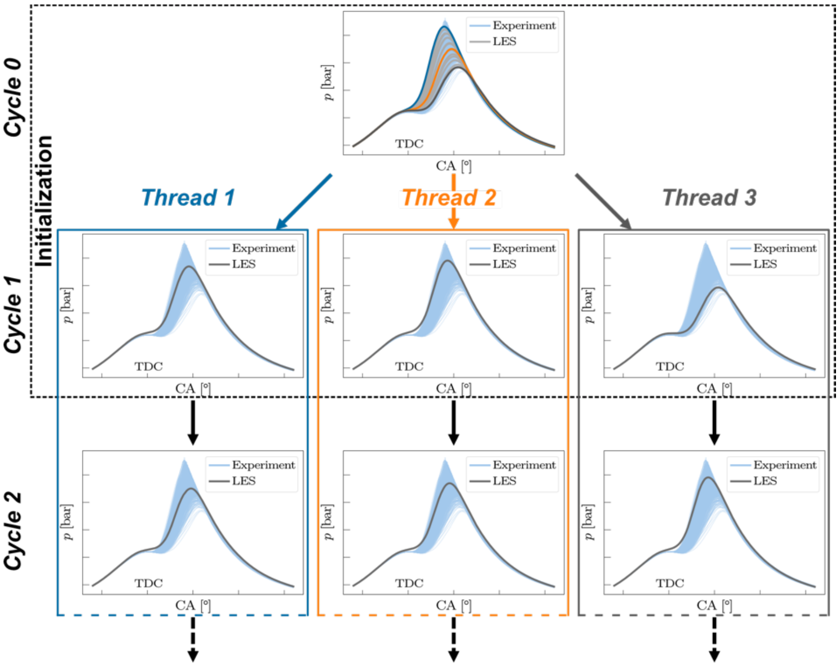

**Fig. 2.** Schematic visualization of the multi-cycle approach. *Cycle 0* and *Cycle 1* represent the initialization procedure. The arrows below *Cycle 2* indicate the extension of each thread by further cycles.

Here, $\rho_\mathrm{u}, \mu_\mathrm{SGS}, s_\mathrm{L}$ and $\Sigma$ denote the density conditioned upon the unburned state, sub-grid scale (SGS) eddy viscosity, laminar burning velocity and sub-grid flame surface density, respectively. For diffusion modeling, a unity Lewis number is assumed. A gradient assumption is used for turbulent flux closure, with the turbulent Schmidt number set to $\mathrm{Sc}_\mathrm{SGS} = 0.4$. The flame surface density $\Sigma$ is modeled by an algebraic relation [58]:

$$\Sigma = \left[ 1 + 0.46 \mathrm{Re}_\mathrm{SGS}^{0.25} \left( \frac{u'_\mathrm{SGS}}{s_L} \right)^{0.3} \left( \frac{p}{p_0} \right)^{0.2} \right] \left| \frac{\partial \tilde{c}}{\partial x_i} \right|, \tag{2}$$

where $\mathrm{Re}_\mathrm{SGS}$ and $u'_\mathrm{SGS}$ are turbulent Reynolds number and unresolved turbulent velocity fluctuation, respectively. The reference pressure $p_0$ is 0.1 MPa.

The combustion process is initiated by imposing a sphere of burned state ($\tilde{c}$ عي ρ, radius of 0.2ɑmm) in the spark plug gap at the numerical spark timing of -8.5ÁCA. The burned gas mass fraction of the previous cycle is taken into account by the passive scalar of exhaust gas recirculation $Y_\mathrm{EGR}$ and a respective transport equation is solved. Prior to exhaust valve opening (EVO), $\tilde{c}$ is mapped to $\tilde{Y}_\mathrm{EGR}$ and reset to zero [60].

During the simulation, a flamelet-based manifold is accessed to retrieve unknown quantities of the previous equations. In particular, $\rho_\mathrm{u}$ and $s_\mathrm{L}$ are tabulated. Additionally, the species composition is stored, from which transport and thermodynamic data are determined.

Utilizing the flamelet assumption [61] a set of 1-D laminar freely propagating flames is calculated with cantera [62]. As initial conditions, the pressure $p$, the unburned temperature $T_\mathrm{u}$ and the initial composition are varied (see Table 2). The latter is fixed to the stochiometric value but takes into account different exhaust gas recirculation (EGR) mass fractions $\Pi_{\text{Ác}\Pi}$ .

### 3.1.2 Turbulent auto-ignition modeling

Following Linse et al. [31], the auto-ignition process is modeled as a process separated from the turbulent flame. For that, a precursor is used to track the auto-ignition process in the unburned mixture [32]. The fuel consumption is used as a pseudo precursor species and determines the auto-ignition progress variable conditioned on the unburned state $Y_{c_{\mathrm{I,u}}}$. The transport equation of $\tilde{Y}_{c_{\mathrm{I,u}}}$ reads:

$$\frac{\partial \left( \overline{\rho} \tilde{Y}_{c_{\mathrm{I,u}}} \right)}{\partial t} + \frac{\partial \overline{\rho} \tilde{u}_i \tilde{Y}_{c_{\mathrm{I,u}}}}{\partial x_i} = \frac{\partial}{\partial x_i} \left[ \left( \overline{\rho} D + \frac{\mu_\mathrm{SGS}}{\mathrm{Sc}_\mathrm{SGS}} \right) \frac{\partial \tilde{Y}_{c_{\mathrm{I,u}}}}{\partial x_i} \right] + \overline{\rho} \tilde{\dot{\omega}}_{Y_{c_{\mathrm{I,u}}}} . \tag{3}$$

Here, a gradient assumption with a turbulent Schmidt number of $\mathrm{Sc}_{\mathrm{SGS}}$ = 0.4 is used for turbulent flux closure, and diffusion modeling assumes unity Lewis number.

The closure of this model is based on the determination of the unknown source term $\dot{\omega}_{Y_{c_{\mathrm{I,u}}}}$ from a flamelet-based auto-ignition manifold, which is generated based on homogeneous reactor calculations with the in-house solver ULF [63]. Variations of the pressure $p$, the unburned temperature $T_{\mathrm{u}}$ and the EGR mass fraction $Y_{\mathrm{EGR}}$ are taken into account (see Table 2). The mixture fraction is set to its stoichiometric value.

The source term $\dot{\omega}_{Y_{c_{\mathrm{I,u}}}}$ (see Equation 3) is based on the detailed non-linear auto-ignition evolution. Similar to existing modeling approaches, e.g., the TKI model [24], the source term is defined by the respective instantaneous reaction rates of the auto-ignition progress variable:

$$\dot{\omega}_{Y_{c_{\mathrm{I,u}}}} = \frac{\partial Y_{c_{\mathrm{I,u}}}}{\partial t}\,. \tag{4}$$

**Table 2**. Parameter variation of combustion and auto-ignition manifolds. Number of steps given in the second last (combustion) and last column (auto-ignition)

| Parameter | min. value | max. value | # steps (comb.) | # steps (auto-ign.) |
|---|---|---|---|---|
| $p$ | 0.8 bar | 70 bar | 20 | 18 |
| $T_{\mathrm{u}}$ | 300 K | 1000 K | 15 | 23 |
| $Y_{\mathrm{EGR}}$ | 0 | 1 | 11 | 10 |

In the post-processing, the conditional auto-ignition progress variable is normalized to $c_{\mathrm{I,u}} = Y_{c_{\mathrm{I,u}}}/Y_{c_{\mathrm{I,u,max}}}$, where $Y_{c_{\mathrm{I,u,max}}}$ is the value after auto-ignition. Assuming that no auto-ignition can occur in the burned gas [31], the auto-ignition progress variable is retrieved from $c_{\mathrm{I}} = (1-c)\cdot c_{\mathrm{I,u}}$ by taking into account the turbulent flame propagation $c$. Finally, the set $\Omega_{\mathrm{crit}}$, representing all computational cells that exhibit a critical auto-ignition state, is defined by $c_{\mathrm{I}} \geq \varepsilon$ = 0.95. Following previous works [8, 32], the mass represented by these cells is referred to as critical mass $ $%& hereafter and assumed to undergo auto-ignition. The knock onset $\mathrm{CA}_{m_{\mathrm{crit,max}}}$ is determined based on the peak in the temporal evolution of $m_{\mathrm{crit}}$ [8, 32].

## 4. Validation of the LES

The influence of cycle-to-cycle variations in flow and combustion on the knocking combustion initiation is investigated by employing a multi-cycle engine LES. The results of the simulations are validated against the experimental data. First, global combustion and knock quantities are considered. Thereafter, the fiber-optical signals are taken into account for the validation based on localized information. The validated LES data set is subsequently used for the investigation of the cause-and-effect chain of knocking combustion initiation.

### 4.1 Cycle-to-cycle variations of combustion

The cycle-to-cycle variations within the combustion process lead to different mass burning rates. These differences are associated with differences in heat release and thus result in different pressure traces $p_{\mathrm{exp}}$ as shown in Fig. 3. The $n$ cycles with the highest and lowest peak pressures are averaged as estimators for the 1-, 2- and 3-$\sigma$ intervals around the mean $\overline{p}_{\mathrm{exp}}$, where $n$ is 3, 46 and 318 respectively. Considering the extreme values of all 1000 cycles the peak pressures range from 43.3 to 65.2 bar. Within the 1-$\sigma$ interval, the peak pressures range between 51.0 and 58.7 bar

Pressure traces of experiments $p_{\mathrm{exp}}$ (gray) and LES realizations $p_{\mathrm{LES}}$ (green). In addition, the mean pressure traces $\overline{p}_{\mathrm{exp}}$ and $\overline{p}_{\mathrm{LES}}$ are shown (dark gray and dark green, respectively). The black lines indicate estimators for the experimental 1-, 2- and 3-$\sigma$ intervals (dash-dotted, dashed and dotted respectively).

The mean LES pressure trace $\overline{p}_{\mathrm{LES}}$ is in good agreement with the mean experimental pressure trace $\overline{p}_{\mathrm{exp}}$. The peak pressures of the 18 LES cycles conducted range from 46.8 to 58.9 bar. Thus, the multi-cycle LES study covers a substantial portion of the cycle-to-cycle variations observed in the experiments.

## 4.2 Cycle-to-cycle variations of knocking combustion initiation

The variations in combustion consequently lead to a variation in the knocking behavior of the 1000 individual experimental cycles. These variations are detectable both in the pressure indication data and in the optical signals.

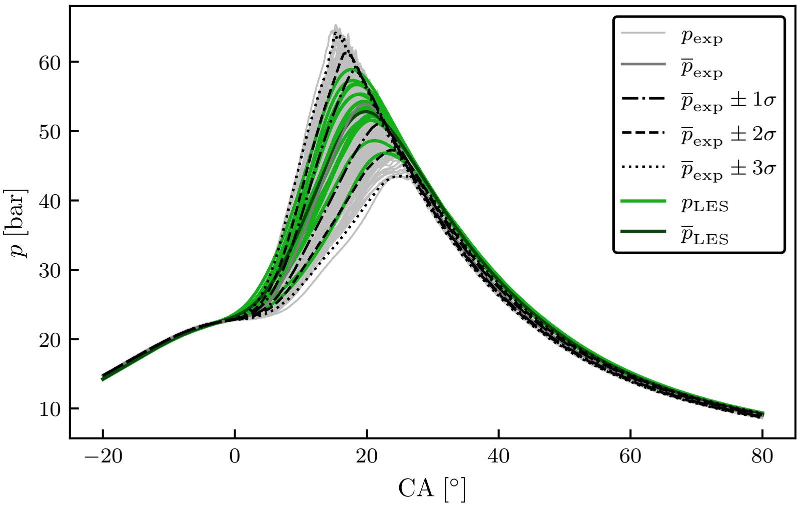

**Fig. 3.** Pressure traces of experiments $p_{\mathrm{exp}}$ (gray) and LES realizations $p_{\mathrm{LES}}$ (green). In addition, the mean pressure traces $p_{\mathrm{exp}}$ and $p_{\mathrm{LES}}$ are shown (dark gray and dark green, respectively). The black lines indicate estimators for the experimental 1-, 2- and 3-$\sigma$ intervals (dash-dotted, dashed and dotted respectively)

### *4.2.1 Pressure indication data*

Based on the signal of the in-cylinder pressure transducer, the knock amplitude KPP and the crank angle of knock onset $\mathrm{CA}_{\mathrm{KO}}$ are determined. Both $\mathrm{CA}_{\mathrm{KO}}$ and KPP vary from cycle to cycle as shown in Fig. 4. Each cycle has an individual value pair for KPP and $\mathrm{CA}_{\mathrm{KO}}$. While cycles with a KPP below the $\mathrm{KPP}_{\mathrm{mean}}$ of 1.04 bar show a wide range in $\mathrm{CA}_{\mathrm{KO}}$, higher KPP values only appear for earlier $\mathrm{CA}_{\mathrm{KO}}$.

For low knock intensities at the knock limit, mainly the mass consumed by the auto-ignition determines the knock intensity [8, 25]. For the auto-ignition model, this mass is reflected by the maximal critical mass $m_{\mathrm{crit,max}}$ [8, 32]. Due to the comparatively limited data set, it is not possible to conclusively assess whether the simulations can capture the trend toward higher knocking intensity with earlier knock onset. However, for the available samples, the lowest observed $m_{\mathrm{crit,max}}$ increases with earlier $\mathrm{CA}_{m_{\mathrm{crit,max}}}$. Here, the LES realizations capture variations in the knock intensity; different values of $m_{\mathrm{crit,max}}$ are observed for similar $\mathrm{CA}_{m_{\mathrm{crit,max}}}$. This suggests that local differences may contribute to variations in the global knock behavior, which is a particular focus of the subsequent analysis.

### *4.2.2 Fiber-optical signals*

The variations of knocking combustion discussed above show the global response to the local process of auto-ignition in the unburned gas. No local information is available in the usual solely pressure-based measurement campaigns. The use of a fiber-optical spark plug in this measurement campaign enables the determination of the most likely knocking combustion initiation direction for each cycle.

The respective circumferential distribution is shown in Fig. 5. For orientation purposes, the inlet valves (IV) and exhaust valves (EV) are shown in the illustration centered around the spark plug. The view is along the axis of the spark plug. Each bin reflects the acceptance cone of the corresponding optical channel (see Fig. 1). The height of each bar corresponds to the number of experimental cycles $N_{\mathrm{exp}}$ for which the respective knocking combustion initiation direction has been determined.

The knocking combustion initiation is not evenly distributed around the circumference of the engine. Most cycles show knocking combustion initiation between the exhaust valves (EV1 and EV2) and slightly fewer cycles between the intake valves (IV1 and IV2). In contrast, there are regions of less knocking combustion initiation between the exhaust valve and the intake valve on either side.

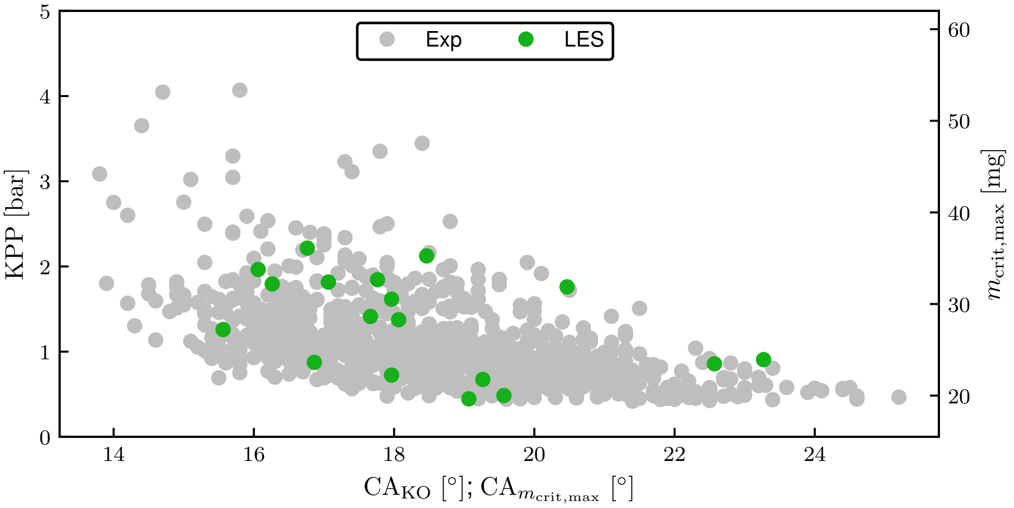

**Fig. 4.** Knock intensity KPP (experiments shown in gray) and maximal critical mass $m_{\mathrm{crit,max}}$ (LES, shown in green) as a function of knock onset $\mathrm{CA_{KO}}$ and $\mathrm{CA}_{m_{\mathrm{crit,max}}}$, respectively

For the LES, the data is transformed into cylindrical coordinates aligned with the experimental configuration of the fiber-optical spark plug. Instead of acceptance cones, wedges are used for circumferential binning. The auto-igniting mass at the time of knock onset is considered in the following analysis. The respective circumferential distribution of the critical mass of each LES realization is shown in Fig. 5. The bars are plotted with an alpha value of 0.2, so the overlap of 5 bars results in total opacity.

The individual bars indicate, that there is considerable auto-igniting mass all around the cylinder. However, the highest auto-igniting mass is observed between the exhaust valves. In addition, for the region between the intake valves, there are more cycles with higher auto-igniting mass than for the regions between the intake and the exhaust valves on either side. This agrees very well with the experimentally observed knocking combustion initiation directions. Thus, the circumferential distribution of the auto-igniting mass is a good indicator of the experimentally determined frequencies of knocking combustion initiation direction even with a low number of LES realizations.

In summary, the LES results exhibit good agreement with experimental trends in combustion and auto-ignition. Consequently, the LES data set proves valuable for further investigation of cycle-to-cycle variations in knocking combustion initiation.

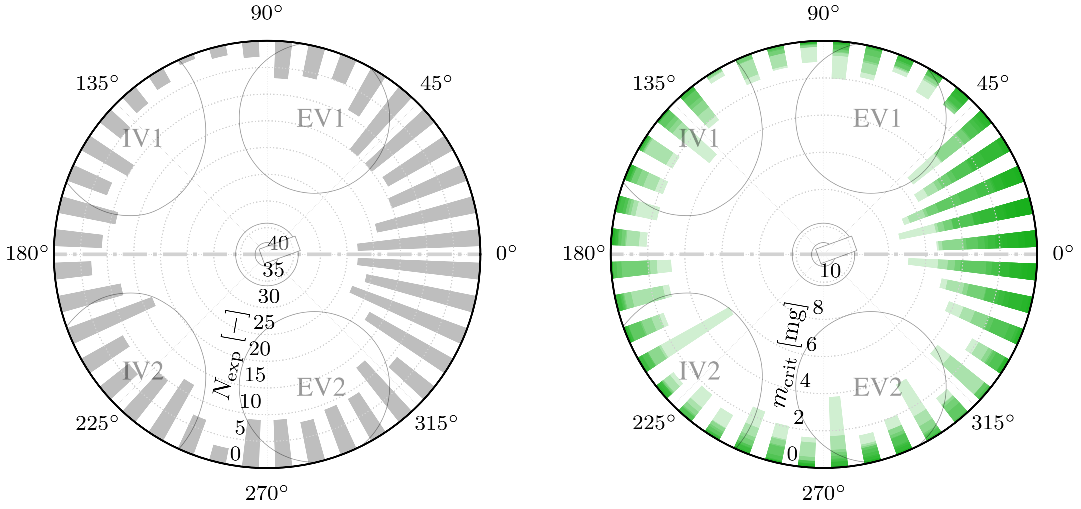

**Fig. 5.** Left: Circumferential distribution of knocking combustion initiation direction based on the fiber-optical investigations. Right: Circumferential distribution of critical mass at the time of knock onset of each LES realization. Individual bars have a transparency alpha value of 0.2. For orientation, intake valves (IV) and exhaust valves (EV) are shown in the illustration centered around the spark plug. The view is along the axis of the spark plug

## 5. Cause-and-effect chain of knocking combustion initiation

The cause-and-effect chain of knocking combustion initiation involves flow, combustion and auto-ignition. The subsequent analysis of these relationships is guided by a correlation analysis. For this, the Pearson correlation coefficient $R_{x,y}$ is used, which indicates correlations between feature $x$ and $y$:

$$R_{x,y} = \frac{\sum_{i=1}^{n} (x_i - \overline{x})\,(y_i - \overline{y})}{\sqrt{\sum_{i=1}^{n} (x_i - \overline{x})^2}\,\sqrt{\sum_{i=1}^{n} (y_i - \overline{y})^2}}\,. \tag{5}$$

Here, $x_i, y_i$ are individual samples and $\overline{x}, \overline{y}$ the respective means. Subsequently, features are defined based on the LES data. In the first step, this correlation analysis is used to identify global correlations. Thereafter, correlations of global features and LES fields are analyzed.

### 5.1 Global correlations of flow, combustion and auto-ignition

For the global correlation analysis, a distinct set of features is described for each of the aspects of flow, combustion and auto-ignition as listed in Table 3. A permutation is used to correlate each feature with all the others. The square of the correlation coefficient, $R^2$, is used hereafter as an indicator for a linear correlation between two features.

The flow features are based on the convective velocity Þ and turbulent kinetic energy $k$ in the spark plug gap vicinity (SP) at spark timing. These have been reported to influence the combustion process in several studies [9, 41ï 43, 64]. Following Truffin et al. [42], a radius of 1ɑmm around the spark plug gap center is considered for the calculation of the features. Both $u$ and $k$ are time-averaged with an interrogation window of 5ÁCA to smooth out small-scale turbulent structures.

The combustion features are divided into two groups distinguishing between the early and late combustion phases. The latter is taken into account by the feature of peak pressure $p_{\mathrm{max}}$. The early combustion phase is assumed to last until the time of TDC, at 0.0ÁCA. Here, the feature of mass fraction burned $\mathrm{MFB}^{0.0^{\circ}\mathrm{CA}}$ is used. Further features are based on the local field of the progress variable $\tilde{c}$ at TDC, consistently with the MFB feature. Two sample planes through the cylinder are considered as shown in Fig. 6. On the tumble plane (TP, blue) and middle plane (MP, red) the flame is approximated by the $\tilde{c} =$ πϑυ iso-line. Based on this, the distances $\Delta x$ and $\Delta y$, being the difference between the left-most and right-most point in the respective coordinate direction, are calculated as estimates for the flame width.

The auto-ignition features are based on the predictions of the auto-ignition model. The maximal critical mass $m_{\mathrm{crit,max}}$ and the respective crank angle $\mathrm{CA}_{m_{\mathrm{crit,max}}}$ are considered as indicators for the knock intensity and the knock onset, respectively.

**Table 3**. List of features used in the correlation analysis. The flow features are listed in the first segment, combustion features in the second segment and auto-ignition features in the last segment. In the following, the colors light gray, gray and dark gray are used to indicate the group to which the features belong

| | | |
|---|---|---|
| **flow** | $\lvert\overline{u}\rvert^{\mathrm{SP}}$ | Magnitude of velocity |
| | $\lvert\overline{k}\rvert^{\mathrm{SP}}$ | Magnitude of kinetic energy |
| **combustion** | $p_{\mathrm{max}}$ | Peak pressure |
| | $\mathrm{MFB}^{0.0^{\circ}\mathrm{CA}}$ | Fuel mass fraction burned at TDC |
| | $\Delta x_{\tilde{c}}^{\mathrm{TP},0.0^{\circ}\mathrm{CA}}$ | Flame width on tumble plane ($x$-direction) |
| | $\Delta y_{\tilde{c}}^{\mathrm{MP},0.0^{\circ}\mathrm{CA}}$ | Flame width on middle plane ($y$-direction) |
| **auto-ignition** | $m_{\mathrm{crit,max}}$ | Maximal critical mass |
| | $\mathrm{CA}_{m_{\mathrm{crit,max}}}$ | Crank angle of maximal critical mass |

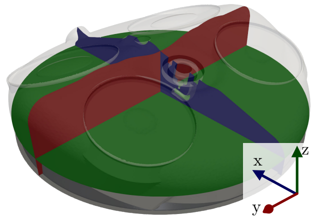

**Fig. 6.** Schematic of the two sample planes considered in the global correlation analysis: tumble plane (blue) and middle plane (red). The horizontal plane (green, $z$-value corresponds to TDC position) is considered in the analysis of local correlations in the next section

### *5.1.1 Results of the global correlation analysis*

The results of the feature permutation are presented in Table 4. The table is colored according to the shown $R^2$-value: values of $R^2 < 0.3$ are considered uncorrelated, from 0.3 to 1.0 the saturation of green increases linearly.

In the following, selected correlations are discussed segment by segment, i.e., first characteristics of the flow with those of combustion and auto-ignition, then those of combustion with those of auto-ignition and finally those of auto-ignition with itself. The respective scatters of the data and corresponding linear fits are shown in Fig. 8 and Fig. 9.

**Table 4**. Correlations of flow (light gray), combustion (gray) and auto-ignition (dark gray) features. The cells are colored according to the respective $R^2$-value: values of $R^2$ < 0.3 are white, and from 0.3 to 1.0 the saturation of green increases linearly

| | $\lvert\overline{u}\rvert^{\mathrm{SP}}$ | $\lvert\overline{k}\rvert^{\mathrm{SP}}$ | $p_{\max}$ | $\mathrm{MFB}^{0.0°\mathrm{CA}}$ | $\Delta x_{\tilde{c}}^{\mathrm{TP},0.0°\mathrm{CA}}$ | $\Delta y_{\tilde{c}}^{\mathrm{MP},0.0°\mathrm{CA}}$ | $m_{\mathrm{crit,max}}$ | $\mathrm{CA}_{m_{\mathrm{crit,max}}}$ |
|---|---|---|---|---|---|---|---|---|
| $\lvert\overline{u}\rvert^{\mathrm{SP}}$ | | 0.31 | 0.04 | 0.05 | 0.01 | 0.16 | 0.13 | 0.1 |
| $\lvert\overline{k}\rvert^{\mathrm{SP}}$ | 0.31 | | 0.0 | 0.02 | 0.01 | 0.03 | 0.04 | 0.01 |
| $p_{\max}$ | 0.04 | 0.0 | | 0.59 | 0.39 | 0.3 | 0.09 | 0.95 |
| $\mathrm{MFB}^{0.0°\mathrm{CA}}$ | 0.05 | 0.02 | 0.59 | | 0.51 | 0.31 | 0.05 | 0.59 |
| $\Delta x_{\tilde{c}}^{\mathrm{TP},0.0°\mathrm{CA}}$ | 0.01 | 0.01 | 0.39 | 0.51 | | 0.01 | 0.0 | 0.35 |
| $\Delta y_{\tilde{c}}^{\mathrm{MP},0.0°\mathrm{CA}}$ | 0.16 | 0.03 | 0.3 | 0.31 | 0.01 | | 0.48 | 0.4 |
| $m_{\mathrm{crit,max}}$ | 0.13 | 0.04 | 0.09 | 0.05 | 0.0 | 0.48 | | 0.2 |
| $\mathrm{CA}_{m_{\mathrm{crit,max}}}$ | 0.1 | 0.01 | 0.95 | 0.59 | 0.35 | 0.4 | 0.2 | |

**Correlations of flow features**

The lack of clear correlations between the flow and the combustion features is in contrast to the results of earlier studies [9, 41–43, 64]. However, it is important to emphasize that, e.g., Truffin et al. [42] found different relevance of the investigated features even on the same engine for different operating conditions. This indicates, that the found correlations are not universal and the detailed causes of CCV may vary between engines and operating conditions.

The engine investigated in studies by Enaux et al. [41] and Truffin et al. [42] featured a flat piston and a recess between the valves, which led to a tumble-induced vortex structure directly at the spark plug. For the engine investigated here, the piston and cylinder head geometries (see Fig. 1) lead to a different tumble flow. At spark timing, the ensemble-averaged velocity magnitude $\langle\overline{u}\rangle$ indicates that the mean tumble center is about 9 mm to the left of the spark plug gap as shown in Fig. 7.

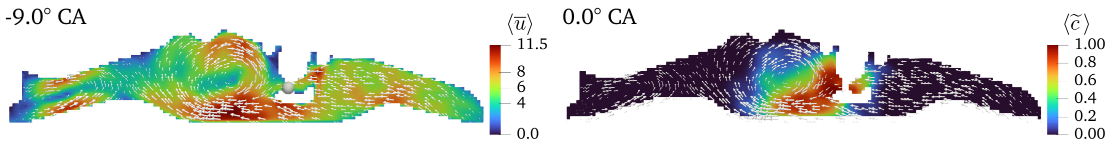

**Fig. 7.** The left side shows the ensemble average of the velocity magnitude $\langle\overline{u}\rangle$ at spark timing. The arrows indicate the velocity vector and their size is scaled with the velocity magnitude. The sphere considered for the determination of the spark plug features is shown in light gray. The right side depicts the ensemble average of the progress variable $\langle\tilde{c}\rangle$ at TDC. The velocity field at spark timing is indicated by the arrows for orientation

The influence of these flow structures on flame propagation is apparent considering the tumble plane at TDC. The ensemble-averaged progress variable $\langle \tilde{c} \rangle$ shown on the right of Fig. 7 is regarded as the flame probability. The mean flame is pushed towards the piston by the tumble motion (cf. the velocity arrows that indicate the velocity at spark timing). On the side of the spark plug gap facing away from the tumble vortex, only a small area shows a higher flame probability. With that, the convective flow in the spark plug gap seems to be of minor importance for the engine and operating conditions investigated. Additionally, it indicates that the tumble vortex has a higher influence on the early flame propagation and hence the burn rate.

Finally, no correlations are found between the selected flow and auto-ignition features. This is not surprising as auto-ignition occurs downstream of combustion and there are no clear correlations between flow and combustion features.

### Correlations of combustion features

It is known, that for an individual cycle, the early combustion phase determines the global combustion process [33, 34]. The indicator for early combustion progress $\mathrm{MFB}^{0.0^{\circ}\mathrm{CA}}$ ranges between 0.5 % and 1.5 % in this study. The correlation of $\mathrm{MFB}^{0.0^{\circ}\mathrm{CA}}$ to the later-stage combustion feature $p_{\max}$ is in agreement with the literature. However, the scatter around the linear fit (see Fig. 8) indicates, that there may be additional influencing factors after this very early combustion stage.

For the flame features based on the local progress variable field $\tilde{c}$, weak correlations exist between the global mass fraction burned $\mathrm{MFB}^{0.0^{\circ}\mathrm{CA}}$ and the flame widths $\Delta x_{\tilde{c}}^{\mathrm{TP},0.0^{\circ}\mathrm{CA}}$ and $\Delta y_{\tilde{c}}^{\mathrm{MP},0.0^{\circ}\mathrm{CA}}$. Fig. 8 exemplarily shows, that the relation between the mass fraction burned - &" 8 شرع and the flame width $\Delta x_{\tilde{c}}^{\mathrm{TP},0.0^{\circ}\mathrm{CA}}$ is scattered around the linear fit. With that, the local flame propagation differs for a comparable global combustion progress.

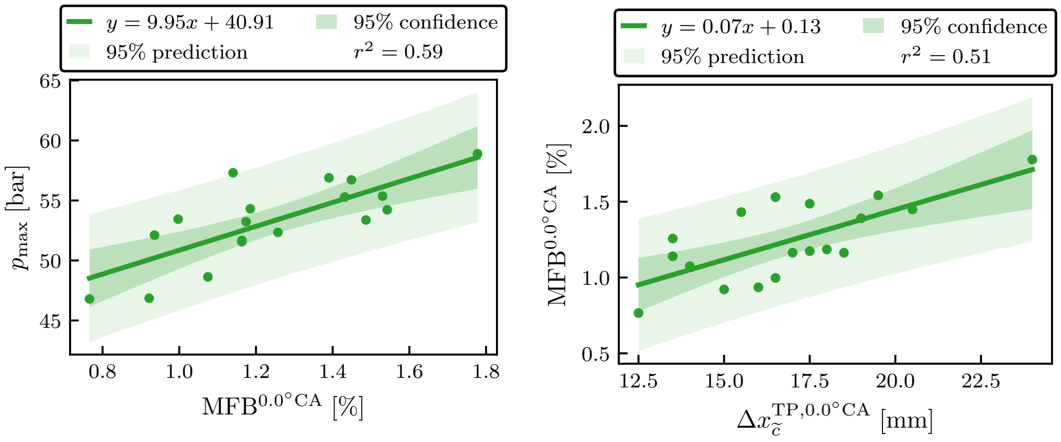

**Fig. 8.** Scatter and linear fit with confidence interval (very light green) and prediction interval (light green) for a combination of two combustion features (see Table 3). Left shows the mass fraction burned at TDC $\mathrm{MFB}^{0.0^{\circ}\mathrm{CA}}$ and peak pressure $p_{\max}$. Right shows the flame width on the tumble plane (Å-direction) at TDC $\Delta x_{\tilde{c}}^{\mathrm{TP},0.0^{\circ}\mathrm{CA}}$ and $\mathrm{MFB}^{0.0^{\circ}\mathrm{CA}}$

In the correlations to the auto-ignition features, the close relationship between the combustion process determining the boundary conditions and the auto-ignition is reflected in the correlation between all combustion features and the crank angle of knock onset $\mathrm{CA}_{m_{\mathrm{crit,max}}}$. In agreement with the previous findings, the correlation is high for the late combustion phase feature of $p_{\max}$ while it is weaker for the early combustion features $\mathrm{MFB}^{0.0^{\circ}\mathrm{CA}}$, $\Delta x_{\tilde{c}}^{\mathrm{TP},0.0^{\circ}\mathrm{CA}}$ and $\Delta y_{\tilde{c}}^{\mathrm{MP},0.0^{\circ}\mathrm{CA}}$.

However, the global combustion process (indicated by $p_{\max}$ and $\mathrm{MFB}^{0.0^{\circ}\mathrm{CA}}$) does not correlate with the auto-igniting mass $m_{\mathrm{crit,max}}$. The variations must therefore be caused by local processes. In this regard, the correlation between $m_{\mathrm{crit,max}}$ and the flame width in the y-direction projected on the middle plane at TDC $\Delta y_{\tilde{c}}^{\mathrm{MP},0.0^{\circ}\mathrm{CA}}$ is of interest. The linear fit shown in Fig. 9 suggests that higher early flame width in $y$-direction (perpendicular to the tumble plane) leads to higher critical mass at knock onset. This is further investigated in the local correlation analysis in the next section.

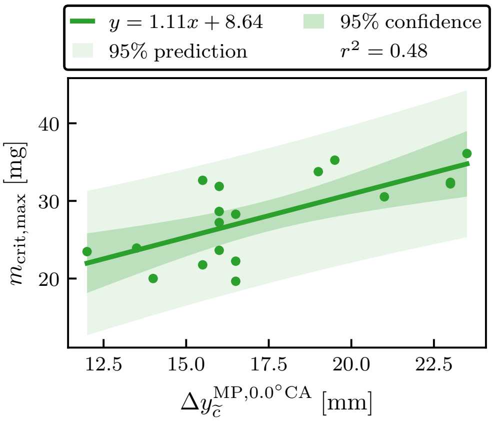

**Fig. 9.** Scatter and linear fit with confidence interval (very light green) and prediction interval (light green) for the flame width on the middle plane ($y$-direction) at TDC $\Delta y_{\tilde{c}}^{\mathrm{MP},0.0^\circ\mathrm{CA}}$ and the maximal critical mass $m_{\mathrm{crit,max}}$

### Correlations of auto-ignition features

The absence of linear correlations between the individual auto-ignition features (see Table 4) is expected and indicates potential limitations of the correlation method. It is well known that knock onset and knock intensity are not linearly related, however, higher knock intensities are only observed at earlier knock onsets (see Fig. 4). A careful manual inspection of all permutations is required as such trends cannot be captured with the linear fit applied.

Nevertheless, this correlation analysis provides a comprehensive global understanding of flow, combustion and auto-ignition for the operating conditions investigated. Additionally, it emphasizes the importance of local structures. In particular, the early-stage flame propagation perpendicular to the tumble plane correlates with the auto-ignition mass. This aspect is further investigated in the following by local correlation analysis.

## 5.2 Local correlations of flow, combustion and auto-ignition

In a further analysis, the previously described correlation analysis is extended. Now, the correlation coefficient $R$ (see Equation 5) is calculated for every cell of the 2-D domain resembling the horizontal plane shown in Fig. 6. In addition, a $H_0$-hypothesis test is performed based on the $t$-distribution of the test statistics. A significant correlation is assumed only for $p$-values lower than the significance level of 0.05. To further investigate the influence of early flame propagation on the auto-igniting mass, scalar features described in Table 3 are correlated to the field of auto-ignition progress $\tilde{c}_{\mathrm{I}}$ to identify local structures of correlations. Here, a time of 16.5° CA is considered, which is representative of the later combustion phase close to knock onset. First, the correlation between the local auto-ignition progress $c_{\mathrm{I}}$ and the flame width in $y$-direction on the middle plane $\Delta y_{\tilde{c}}^{\mathrm{MP},0.0^\circ\mathrm{CA}}$ is investigated, as latter was identified to correlate with the auto-igniting mass in the previous analysis. The respective correlation field $R_{\tilde{c}_{\mathrm{I}}\leftrightarrow\Delta y_{\tilde{c}}^{\mathrm{MP},0.0^\circ\mathrm{CA}}}$ is shown in Fig. 10.

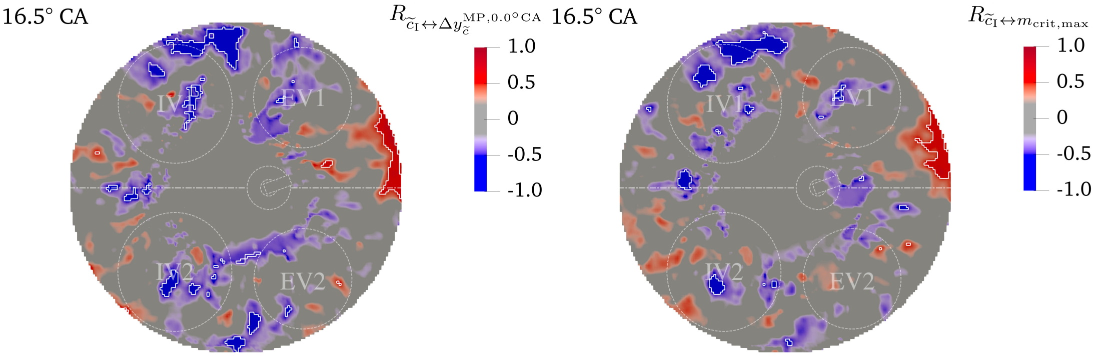

**Fig. 10.** Correlation coefficients $R_{\tilde{c}_{\mathrm{I}}\leftrightarrow\Delta y_{\tilde{c}}^{\mathrm{MP},0.0^\circ\mathrm{CA}}}$ (left) and $R_{\tilde{c}_{\mathrm{I}}\leftrightarrow m_{\mathrm{crit,max}}}$ (right) on the horizontal plane at 16.5° CA. The outlines of areas considered significantly correlated ($p$-value) are shown in white color. The view is in the direction of the cylinder head. Locations of the valves and the spark plug are illustrated for orientation. The dash-dotted line indicates the tumble plane

A distinct region of positive correlation is found between the exhaust valves (EV1 and EV2). Hence, a higher flame propagation perpendicular to the tumble plane in the early combustion phase correlates with higher auto-ignition progress in this region in the late combustion phase. Additionally, another distinctive area of correlation $R_{\tilde{c}_\mathrm{I}\leftrightarrow\Delta y_{\tilde{c}}^{\mathrm{MP},0.0^\circ\mathrm{CA}}}$ is found in the region between the intake and exhaust valve (IV1 and EV1, see Fig. 10). However, the sign is reversed, i.e., a higher flame propagation perpendicular to the tumble plane correlates with lower auto-ignition progress.

Interestingly, the local auto-ignition progress $\tilde{c}_\mathrm{I}$ in these regions also shows correlations with the global maximum critical mass $m_{\mathrm{crit,max}}$. This indicates, that the local auto-ignition progress in these regions determines the global auto-igniting mass. With that, a link to the previously discussed global correlation between $\Delta y_{\tilde{c}}^{\mathrm{MP},0.0^\circ\mathrm{CA}}$ and $m_{\mathrm{crit,max}}$ is found.

Further investigation of this relation is based on the comparison of two individual cycles (see Table 5). The cycles have the same $\mathrm{MFB}^{0.0^\circ\mathrm{CA}}$ of 1.2 % and a similar peak pressure (51.6 bar and 51.7 bar, respectively). Hence, the global combustion process is assumed to be comparable. However, they differ according to the previously found correlation. *Cycle B* has a higher flame width on the middle plane $\Delta y_{\tilde{c}}^{\mathrm{MP},0.0^\circ\mathrm{CA}}$ (19.5 mm and 15.5 mm, respectively) and show a higher $m_{\mathrm{crit,max}}$ (35.5 mg and 21.8 mg, respectively).

**Table 5**. Values of features of single cycles *A* and *B*.

| | $\mathrm{MFB}^{0.0^\circ\mathrm{CA}}$ [%] | $p_{\mathrm{max}}$ [bar] | $\Delta y_{\tilde{c}}^{\mathrm{MP},0.0^\circ\mathrm{CA}}$ [mm] | $m_{\mathrm{crit,max}}$ [mg] | $\mathrm{CA}_{m_{\mathrm{crit,max}}}$ [°] |
|---|---|---|---|---|---|
| *Cycle A* | 1.2 | 51.6 | 15.5 | 21.8 | 19.3 |
| *Cycle B* | 1.2 | 51.7 | 19.5 | 35.3 | 18.5 |

In Fig. 11, flame propagation and auto-ignition progress are compared based on the horizontal plane (see Fig. 6). Here, the time of the individual knock onset is considered. The flame front is defined by $\tilde{c} = 0.5$ and visualized as a white iso-line. The coloring of the auto-ignition progress variable $\tilde{c}_\mathrm{I}$ is adjusted to highlight solely the areas contributing to the critical mass ($\tilde{c}_\mathrm{I} \geq 0.95$).

The global flame propagation on the horizontal plane is comparable. However, the different local flame propagation leads to different locations and sizes of the pockets of unburned mixture ahead of the flame front. In the pockets in the direction of the exhaust valves and the intake valves, a substantial part of the unburned mixture is identified as auto-igniting. In contrast, the pockets towards the region between the exhaust and intake valve on either side contribute little to nothing to the critical mass despite their comparable size.

Consequently, the location of the pockets of unburned mixture in the late combustion phase and hence the local flame propagation influences the amount of unburned mixture undergoing auto-ignition. For the same global burn rate, faster flame propagation perpendicular to the tumble plane (in $y$-direction) leads to lower consumption of unburned mixture in the direction of the tumble plane ($x$-direction). Thus, pockets of unburned mixture with a relatively slow auto-ignition process (between the exhaust and intake valve on either side) are consumed while pockets of high reactivity persist (in the direction of the exhaust valves and intake valves). The correlation found between $m_{\mathrm{crit,max}}$ and $\Delta y_{\tilde{c}}^{\mathrm{MP},0.0^\circ\mathrm{CA}}$ indicates that this imbalance in flame propagation has already developed in the early combustion phase. Therefore, cycle-to-cycle variations in the local early flame propagation influence the cycle-to-cycle variations in the auto-ignition process. The early flame propagation, in turn, was previously found to be influenced by the tumble flow structure.

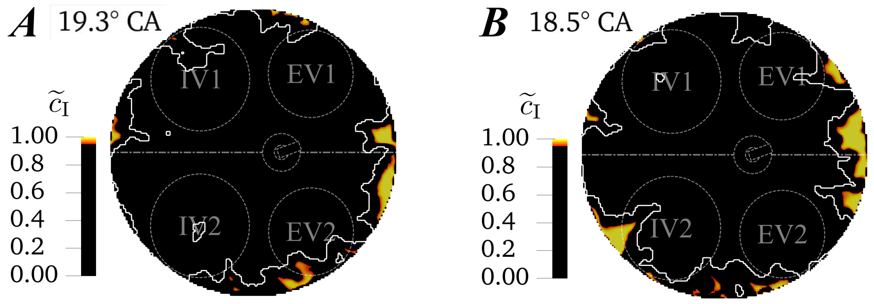

**Fig. 11.** Auto-ignition progress $\tilde{c}_I$ for two different LES realizations. Left shows Cycle A, right Cycle B (see Table 5). The time of individual knock onset is considered for the horizontal plane (see Fig. 6). The flame front defined by $\tilde{c} = 0.5$ is visualized as a white iso-line. For $\tilde{c}_I \geq 0.95$, colors are defined, and the values below are black. The view is in the direction of the cylinder head. Locations of the valves and the spark plug are illustrated for orientation. The dash-dotted line indicates the tumble plane.

## 6. Conclusions

In this work, the influence of cycle-to-cycle variations on knocking combustion initiation of a TRF+E surrogate fuel is investigated in a multi-cycle LES study. The LES results are validated against experimental observations, showing good agreement in capturing combustion and auto-ignition quantities, both in terms of main trends and cycle-to-cycle variations. In particular, the circumferential distribution of the auto-igniting mass predicted by the LES is identified as a good indicator of the experimentally determined knocking combustion initiation directions. Furthermore, the LES data is employed to investigate the cause-and-effect chain of knocking combustion initiation, which involves flow, combustion, and auto-ignition. Here, global and local correlation analyses are performed to assess the influence of flow structures on flame propagation and the auto-ignition process. The main findings are summarized as follows:

- The tumble position influences the local early flame propagation.
- The overall burn rate of an individual cycle is determined by the early combustion phase.
- The local early flame propagation perpendicular to the tumble plane correlates with the auto-igniting mass.
- The location of the pockets of unburned mixture in the late combustion phase is already decided by the imbalance of the early flame propagation direction.
- The reactivity and thus the auto-ignition progress within these pockets of unburned mixture varies.
- With that, the local flame propagation determines the local and global auto-igniting mass.

In summary, this study advances the understanding of knocking combustion initiation of surrogate fuels for operating conditions at the knock limit. The investigation of the cause-and-effect chain shows that cycle-to-cycle variations in the large-scale flow structures influence the local early flame propagation. The early combustion in turn influences the global burn rate. In the late combustion phase, the local flame propagation determines the subsequent local and thus the global auto-ignition process.

This shows that the downstream engine processes are influenced by upstream factors. For engine development, this finding suggests that a reduction of the knocking combustion tendency may be achieved by measures such as adjusting the in-cylinder flow. In this context, the investigation of further operating conditions or different fuels represents an interesting direction for future studies.

## Acknowledgments

The work of Magnus Kircher is supported by the Graduate School CE within the Centre for Computational Engineering at Technische Universität Darmstadt. Funded by the Deutsche Forschungsgemeinschaft (DFG, German Research Foundation) – Projektnummer 349537577.

## References

[1] N. Fraser, H. Blaxill, G. Lumsden, and M. Bassett, “Challenges for Increased Efficiency through Gasoline Engine Downsizing,” SAE International Journal of Engines, vol. 2, no. 1, pp. 991–1008, 2009.

[2] J. B. Heywood, Internal combustion engine fundamentals. New York: McGraw-Hill, 1988, pp. 26-0943-26-0943.

[3] Z. Wang, H. Liu, and R. D. Reitz, “Knocking combustion in spark-ignition engines,” Prog. Energy Combust. Sci., vol. 61, pp. 78–112, 2017, DOI: 10.1016/j.pecs.2017.03.004.

[4] W. E. Dalby, The internal combustion engine. Glasgow; Bombay: Blackie; Son Limited, 1922. DOI: 10.1038/110122a0.

[5] C. Miller, “Relation between spark-ignition engine knock, detonation waves, and autoignition as shown by high-speed photography,” NACA, 855, 1946.

[6] U. Spicher, H. Kröger, and J. Ganser, “Detection of knocking combustion using simultaneously high-speed schlieren cinematography and multi optical fiber technique,” SAE Tech. Pap., vol. 912312, no. 1991, pp. 569–588, 1991, DOI: 10.4271/912312.

[7] A. Robert, S. Richard, O. Colin, and T. Poinsot, “LES study of deflagration to detonation mechanisms in a downsized spark ignition engine,” Combust. Flame, vol. 162, no. 7, pp. 2788–2807, 2015, DOI: 10.1016/j.combustflame.2015.04.010.

[8] M. Kircher, S. Popp, S. Gierth, A. Pati, J. Schneider, M. G¿nther, and C. Hasse, ñInvestigation of Engine Combustion and Auto-ignition of a Multicomponent Surrogate Fuel with NTC Behavior Under Knocking Conditions,ò Flow, Turbul. Combust., vol. 110, no. 1, pp. 149ï 169, 2023, DOI: 10.1007/s10494-022-00351-9.

[9] A. Robert, K. Truffin, N. Iafrate, S. Jay, O. Colin, and C. Angelberger, ñLarge-eddy simulation analysis of knock in a direct injection spark ignition engine,ò Int. J. Engine Res., vol. 20, no. 7, pp. 765ï 776, 2019, DOI: 10.1177/1468087418796323.

[10] S. Fontanesi, A. DõAdamo, and C. J. Rutland, ñLarge-Eddy simulation analysis of spark configuration effect on cycle-to-cycle variability of combustion and knock,ò Int. J. Engine Res., vol. 16, no. 3, pp. 403ï 418, 2015, DOI: 10.1177/1468087414566253.

[11] S. M. Sarathy, A. Farooq, and G. T. Kalghatgi, ñRecent progress in gasoline surrogate fuels,ò Progress in Energy and Combustion Science, vol. 65, pp. 67ï 108, 2018, DOI: https://DOI.org/10.1016/j.pecs.2017.09.004.

[12] D. Kim, C. K. Westbrook, and A. Violi, ñTwo-stage ignition behavior and octane sensitivity of toluene reference fuels as gasoline surrogate,ò Combust. Flame, vol. 210, pp. 100ï 113, 2019, DOI: 10.1016/j.combustflame.2019.08.019.

[13] P. Eckert, S. C. Kong, and R. D. Reitz, ñModeling autoignition and engine knock under spark ignition conditions,ò SAE Tech. Pap., vol. 2003ï 1ï 0, 2003, DOI: 10.4271/2003-01-0011.

[14] M. A. Liberman, M. F. Ivanov, O. E. Peil, D. M. Valiev, and L. E. Eriksson, ñNumerical modeling of the propagating flame and knock occurrence in spark-ignition engines,ò Combust. Sci. Technol., vol. 177, no. 1, pp. 151ï 182, 2005, DOI: 10.1080/00102200590883813.

[15] L. Liang, R. D. Reitz, C. O. Iyer, and J. Yi, ñModeling Knock in Spark-Ignition Engines Using a G-equation Combustion Model Incorporating Detailed Chemical Kinetics,ò SAE Tech. Pap., vol. 2007ï 1ï 1, 2007, DOI: 10.4271/2007-01-0165.

[16] Z. Wang, Y. Wang, and R. D. Reitz, ñPressure oscillation and chemical kinetics coupling during knock processes in gasoline engine combustion,ò Energy and Fuels, vol. 26, no. 12, pp. 7107ï 7119, 2012, DOI: 10.1021/ef301472g.

[17] P. Pal, Y. Wu, T. Lu, S. Som, Y. C. See, and A. Le Moine, ñMultidimensional numerical simulations of knocking combustion in a cooperative fuel research engine,ò J. Energy Resour. Technol. Trans. ASME, vol. 140, no. 10, pp. 1ï 8, 2018, DOI: 10.1115/1.4040063.

[18] P. Pal, C. P. Kolodziej, S. Choi, S. Som, A. Broatch, J. Gomez-Soriano, Y. Wu, T. Lu, and Y. C. See, ñDevelopment of a Virtual CFR Engine Model for Knocking Combustion Analysis,ò SAE Int. J. Engines, vol. 11, no. 6, pp. 1069ï 1082, 2018, DOI: 10.4271/2018-01-0187.

[19] C. Chen, P. Pal, M. Ameen, D. Feng, and H. Wei, ñLarge-eddy simulation study on cycle-to-cycle variation of knocking combustion in a spark-ignition engine,ò Appl. Energy, vol. 261, pp. 1ï 33, 2020, DOI: 10.1016/j.apenergy.2019.114447.

[20] A. P. da Cruz, ñThree-dimensional Modeling of Self-ignition in HCCI and Conventional Diesel Engines,ò Combust. Sci. Technol., vol. 176, no. 5ï 6, pp. 867ï 887, 2004, DOI: 10.1080/00102200490428503.

[21] O. Colin, A. Pires Da Cruz, and S. Jay, ñDetailed chemistry-based auto-ignition model including low temperature phenomena applied to 3-D engine calculations,ò Proc. Combust. Inst., vol. 30 II, pp. 2649ï 2656, 2005, DOI: 10.1016/j.proci.2004.08.058.

[22] V. Knop, L. De Francqueville, F. Duffour, and F. Vangraefsch¯pe, ñInfluence of the valve-lift strategy in a CAI engine using exhaust gas re-breathing - Part 2: Optical diagnostics and 3D CFD results,ò SAE Tech. Pap., vol. 2, no. 1, pp. 271ï 288, 2009, DOI: 10.4271/2009-01-0495.

[23] V. Knop, B. Thirouard, and J. Ch®rel, ñInfluence of the local mixture characteristics on the combustion process in a CAI engine,ò SAE Int. J. Fuels Lubr., vol. 1, no. 1, pp. 1133ï 1149, 2009, DOI: 10.4271/2008-01-1671.

[24] V. Knop, J. B. Michel, and O. Colin, ñOn the use of a tabulation approach to model auto-ignition during flame propagation in SI engines,ò Appl. Energy, vol. 88, no. 12, pp. 4968ï 4979, 2011, DOI: 10.1016/j.apenergy.2011.06.047.

[25] A. Robert, S. Richard, O. Colin, L. Martinez, and L. De Francqueville, ñLES prediction and analysis of knocking combustion in a spark ignition engine,ò Proc. Combust. Inst., vol. 35, no. 3, pp. 2941ï 2948, 2015, DOI: 10.1016/j.proci.2014.05.154.

[26] J. C. Livengood and P. C. Wu, ñCorrelation of autoignition phenomena in internal combustion engines and rapid compression machines,ò in Symp. combust., 1955, pp. 347ï 356. DOI: 10.1016/S0082-0784(55)80047-1.

[27] F. A. Lafossas, M. Castagne, J. P. Dumas, and S. Henriot, “Development and validation of a knock model in spark ignition engines using a CFD code,” SAE Tech. Pap., vol. 111, no. 2002, pp. 1252–1263, 2002, DOI: 10.4271/2002-01-2701.

[28] A. P. Kleemann, P. Menegazzi, S. Henriot, and A. Marchal, “Numerical Study on Knock for an SI Engine by Thermally Coupling Combustion Chamber and Cooling Circuit Simulations,” in SAE tech. pap., 2003, pp. 821–831. DOI: 10.4271/2003-01-0563.

[29] A. Teraji, T. Tsuda, T. Noda, M. Kubo, and T. Itoh, “Development of a three-dimensional knock simulation method incorporating a high-accuracy flame propagation model,” Int. J. Engine Res., vol. 6, no. 1, pp. 73–83, 2005, DOI: 10.1243/146808705X7338.

[30] P. Jaworski, P. Priesching, A. Teodorczyk, and W. Bandel, “Validation of the Numerical Simulation of Iso-octane Auto-ignition Delay Time in Rapid Compression Machine with the Use of ECFM-3Z ( Extended Coherent Flame Model - 3 Zones ) Combustion Model Against Experimental Data,” Combustion, vol. 30, no. 1, pp. 1–14, 2010.

[31] D. Linse, A. Kleemann, and C. Hasse, “Probability density function approach coupled with detailed chemical kinetics for the prediction of knock in turbocharged direct injection spark ignition engines,” Combust. Flame, vol. 161, no. 4, pp. 997–1014, 2014, DOI: 10.1016/j.combustflame.2013.10.025.

[32] M. Kircher, E. Meindl, and C. Hasse, “Numerical and experimental study on knocking combustion in turbocharged direct-injection engines for a wide range of operating conditions,” Int. J. Engine Res., vol. 24, no. 2, pp. 652–671, 2023, DOI: 10.1177/14680874211060188.

[33] N. Ozdor, M. Dulger, and E. Sher, “Cyclic Variability in Spark Ignition Engines A Literature Survey,” in SAE tech. pap., 1994, pp. 1514–1552. DOI: 10.4271/940987.

[34] M. B. Young, “Cyclic dispersion in the homogeneous-charge spark-ignition engine—a literature survey,” SAE Transactions, vol. 90, pp. 49–73, 1981, DOI: 10.4271/810020.

[35] M. Buschbeck, N. Bittner, T. Halfmann, and S. Arndt, “Dependence of combustion dynamics in a gasoline engine upon the in-cylinder flow field, determined by high-speed PIV,” Exp. Fluids, vol. 53, no. 6, pp. 1701–1712, 2012, DOI: 10.1007/s00348-012-1384-3.

[36] A. Di Mauro, H. Chen, and V. Sick, “Neural network prediction of cycle-to-cycle power variability in a spark-ignited internal combustion engine,” Proc. Combust. Inst., vol. 37, no. 4, pp. 4937–4944, 2019, DOI: 10.1016/j.proci.2018.08.058.

[37] W. Zeng, S. Keum, T. W. Kuo, and V. Sick, “Role of large scale flow features on cycle-to-cycle variations of spark-ignited flame-initiation and its transition to turbulent combustion,” Proc. Combust. Inst., vol. 37, no. 4, pp. 4945–4953, 2019, DOI: 10.1016/j.proci.2018.07.081.

[38] D. Dreher, M. Schmidt, C. Welch, S. Ourza, S. Zündorf, J. Maucher, S. Peters, A. Dreizler, B. Böhm, and A. Hanuschkin, “Deep feature learning of in-cylinder flow fields to analyze cycle-to-cycle variations in an SI engine,” Int. J. Engine Res., vol. 22, no. 11, pp. 3263–3285, 2021, DOI: 10.1177/1468087420974148.

[39] A. Hanuschkin, S. Zündorf, M. Schmidt, C. Welch, J. Schorr, S. Peters, A. Dreizler, and B. Böhm, “Investigation of cycle-to-cycle variations in a spark-ignition engine based on a machine learning analysis of the early flame kernel,” Proc. Combust. Inst., vol. 38, no. 4, pp. 5751–5759, 2021, DOI: 10.1016/j.proci.2020.05.030.

[40] C. Hasse, “Scale-resolving simulations in engine combustion process design based on a systematic approach for model development,” Int. J. Engine Res., vol. 17, no. 1, pp. 44–62, 2016, DOI: 10.1177/1468087415597842.

[41] B. Enaux, V. Granet, O. Vermorel, C. Lacour, C. Pera, C. Angelberger, and T. Poinsot, “LES study of cycle-to-cycle variations in a spark ignition engine,” Proc. Combust. Inst., vol. 33, no. 2, pp. 3115–3122, 2011, DOI: 10.1016/j.proci.2010.07.038.

[42] K. Truffin, C. Angelberger, S. Richard, and C. Pera, “Using large-eddy simulation and multivariate analysis to understand the sources of combustion cyclic variability in a spark-ignition engine,” Combust. Flame, vol. 162, no. 12, pp. 4371–4390, 2015, DOI: 10.1016/j.combustflame.2015.07.003.

[43] L. Zhao, A. A. Moiz, S. Som, N. Fogla, M. Bybee, S. Wahiduzzaman, M. Mirzaeian, F. Millo, and J. Kodavasal, “Examining the role of flame topologies and in-cylinder flow fields on cyclic variability in spark-ignited engines using large-eddy simulation,” Int. J. Engine Res., vol. 19, no. 8, pp. 886–904, 2018, DOI: 10.1177/1468087417732447.

[44] L. Engelmann, J. Laichter, P. Wollny, M. Klein, S. A. Kaiser, and A. M. Kempf, “Cyclic Variations in the Flame Propagation in an Spark-Ignited Engine: Multi Cycle Large Eddy Simulation Supported by Imaging Diagnostics,” Flow, Turbul. Combust., vol. 110, no. 1, pp. 91–104, 2023, DOI: 10.1007/s10494-022-00350-w.

[45] H. Chu, C. Welch, H. Elmestikawy, S. Cao, M. Davidovic, B. Bºhm, A. Dreizler, and H. Pitsch, ñA Combined Numerical and Experimental Investigation of Cycle-to-Cycle Variations in an Optically Accessible Spark-Ignition Engine,òFlow, Turbul. Combust., vol. 110, no. 1, pp. 3ï29, 2023, DOI: 10.1007/s10494-022-00353-7.

[46] S. Fontanesi, S. Paltrinieri, A. DôAdamo, G. Cantore, and C. Rutland, ñKnock Tendency Prediction in a High Performance Engine Using LES and Tabulated Chemistry,òSAE Int. J. Fuels Lubr., vol. 6, no. 1, pp. 2013-01-1082, 2013, DOI: 10.4271/2013-01-1082.

[47] F. Hoppe, M. Thewes, H. Baumgarten, and J. Dohmen, ñWater injection for gasoline engines: Potentials, challenges, and solutions,òInt. J. Engine Res., vol. 17, no. 1, pp. 86ï96, 2016, DOI: 10.1177/1468087415599867.

[48] M. Thewes, M. Muether, S. Pischinger, M. Budde, A. Brunn, A. Sehr, P. Adomeit, and J. Klankermayer, ñAnalysis of the impact of 2-methylfuran on mixture formation and combustion in a direct-injection spark-ignition engine,ò Energy and Fuels, vol. 25, no. 12, pp. 5549ï5561, 2011, DOI: 10.1021/ef201021a.

[49] P. Burkardt, T. Ottenwªlder, A. Kºnig, J. Viell, A. Mitsos, C. Wouters, W. Marquardt, S. Pischinger, and M. Dahmen, ñToward co-optimization of renewable fuel blend production and combustion in ultra-high efficiency SI engines,òInt. J. Engine Res., 2021, DOI: 10.1177/14680874211040995.

[50] M. Kircher, J. Schneider, S. Popp, S. Gierth, M. G¿nther, and C. Hasse, ñExperimental and model-based analysis of combustion and auto-ignition of gasoline and three surrogate fuels in a single-cylinder research engine operated under knocking conditions,òInt. J. Engine Res., vol. 24, no. 6, pp. 2727ï2738, 2023, DOI: 10.1177/14680874221133143.

[51] R. S. Spindt, ñAir-fuel ratios from exhaust gas analysis,òSAE Tech. Pap., vol. 74, pp. 788ï793, 1965, DOI: 10.4271/650507.

[52] D. Bresenham, J. Reisel, and K. Neusen, ñSpindt air-fuel ratio method generalization for oxygenated fuels,òSAE Tech. Pap., vol. 107, pp. 2154ï2171, 1998, DOI: 10.4271/982054.

[53] J. Schneider, M. G¿nther, M. Kircher, and S. Pischinger, ñFiber-optical analysis of weak knock and pressure oscillations in a single cylinder research engine,òProc. Combust. Inst., vol. 39, no. 1, pp. 1387ï1395, 2023, DOI: 10.1016/j.proci.2022.09.005.

[54] A. Pati, ñNumerical investigation of the in-cylinder flow-spray-wall interactions in direct injection engines,òPhD thesis, TU Darmstadt, 2022.

[55] D. Paredi, T. Lucchini, G. DôErrico, A. Onorati, S. Golini, and N. Rapetto, ñGas Exchange and Injection Modeling of an Advanced Natural Gas Engine for Heavy Duty Applications,òSAE Tech. Pap., vol. 2017ïSeptember, 2017, DOI: 10.4271/2017-24-0026.

[56] J. Zembi, F. Mariani, and M. Battistoni, ñLarge Eddy Simulation of Ignition and Combustion Stability in a Lean SI Optical Access Engine,òSAE Tech. Pap., vol. 2019, 2019, DOI: 10.4271/2019-24-0087.

[57] L. Cai, A. Ramalingam, H. Minwegen, K. Alexander Heufer, and H. Pitsch, ñImpact of exhaust gas recirculation on ignition delay times of gasoline fuel: An experimental and modeling study,òProc. Combust. Inst., vol. 37, no. 1, pp. 639ï647, 2019, DOI: 10.1016/j.proci.2018.05.032.

[58] S. P. R. Muppala, N. K. Aluri, F. Dinkelacker, and A. Leipertz, ñDevelopment of an algebraic reaction rate closure for the numerical calculation of turbulent premixed methane, ethylene, and propane/air flames for pressures up to 1.0 MPa,òCombust. Flame, vol. 140, no. 4, pp. 257ï266, 2005, DOI: 10.1016/j.combustflame.2004.11.005.

[59] T. Poinsot and D. Veynante, Theoretical and numerical combustion. RT Edwards, Inc., 2005.

[60] P. R. Janas, ñLarge Eddy Simulation of In-Cylinder Phenomena in Spark Ignition Engines,òPhD thesis, Universitªt Duisburg-Essen, 2017.

[61] J. A. van Oijen and L. P. H. de Goey, ñModelling of premixed laminar flames using flamelet-generated manifolds,ò Combust. Sci. Technol., vol. 161, no. 1, pp. 113ï137, 2000, DOI: 10.1080/00102200008935814.

[62] D. G. Goodwin, H. K. Moffat, I. Schoegl, R. L. Speth, and B. W. Weber, ñCantera: An object-oriented software toolkit for chemical kinetics, thermodynamics, and transport processes.ò https://www.cantera.org, 2022. DOI: 10.5281/zenodo.6387882.

[63] A. Zschutschke, D. Messig, A. Scholtissek, and C. Hasse, ñUniversal Laminar Flame Solver (ULF).ò2017. DOI: https://DOI.org/10.6084/m9.figshare.5119855.v2.

[64] C. Welch, M. Schmidt, L. Illmann, A. Dreizler, and B. Bºhm, ñThe Influence of Flow on Cycle-to-Cycle Variations in a Spark-Ignition Engine: A Parametric Investigation of Increasing Exhaust Gas Recirculation Levels,ò Flow, Turbul. Combust., vol. 110, no. 1, pp. 185ï208, 2023, DOI: 10.1007/s10494-022-00347-5.

# POSTERS ABSTRACTS

# Development of a Tool to Optimize Demand Response in Thermal Powerplants. Simplex Method and GRG: Application to Island Power Systems

J.C. Lozano-Medina[2], V. Henríquez-Concepción[2], A. Ramos-Martín[2], C.J. Sánchez-Morales[2], F. León-Zerpa[1], C.A. Mendieta-Pino[1]

[1]Institute for Environmental Studies and Natural Resources (i-UNAT), University of Las Palmas de Gran Canaria (ULPGC)
E-mail: carlos.mendieta@ulpgc.es
Telephone: +34616221076

[2]Department of Process Engineering. University of Las Palmas de Gran Canaria (ULPGC)
E-mail: juancarlos.lozano@ulpgc.es
Telephone: +34609153268

**Abstract.** The penetration of renewable energies in island environments poses a series of challenges such as stability, demand response and guarantee of supply, among others. Throughout this work we will study the current conditions of electric energy demand in Gran Canaria and its electric production system. Based on the data and characteristics of the different combustion energy production equipment existing in the two power plants of Gran Canaria, a tool will be proposed to optimize the energy production system using combustion technology (non-renewable) and combine it with energy production using renewables that meet the expectations in terms of dynamic response, safety, scalability and integration with renewable energy systems, reduction of GHGs and reduction of production costs. This tool will be based on operational research, mathematical optimization methods, specifically on the simplex algorithm and the generalized reduced gradient (GRG) and will propose the different existing combinations in order to achieve energy production that satisfies the demand, minimizing fuel consumption and greenhouse gas (GHG) emissions, optimizing the power available in Gran Canaria.

## 1. Introduction

In previous studies such as, [1] and more recent ones such as [2], various scenarios are proposed that allow studying the transition and challenges faced by an island generation system in the implementation of a more sustainable generation and in parallel a promotion of a greater penetration of renewable energies with guaranteed supply [3]. On the other hand, and to mitigate the problems arising due to the weak or non-existent connectivity of the island energy systems [4], energy storage systems are proposed, [5], within which in the Canary Islands the implementation of Energy Storage Systems by hydroelectric pumping has been proposed [6] of which the PHE project "Chira-Soria" stands out as one of its greatest exponents. This system and its integration into the island energy system has been studied by [7], concluding that its implementation would maximize the integration of renewable energies, but detecting the need for the development of an advanced tool for the optimal selection of systems in the island energy mix. The methodology used in the analysis of generation in power generation systems has been studied at the continental level [8] or [9] or at the island level [10], by means of tools such as the Hybrid Optimization of Multiple Energy Resources (HOMER) model [1], which however does not consider other scenarios such as existing systems or the use of other types of renewable or lower emission fuels applied in conventional generation systems [2]. The objective of this work is to establish a tool that relates all the variables of energy production through thermal systems, minimizing costs and emissions and covering the energy demand that cannot be covered by energy production through renewables. For the application of this study, the 2021 energy data of the island of Gran Canaria and its generation system have been available [2]. This tool will optimize the energy production system using combustion technology (non-renewable) and combine it with energy production using renewables that meet expectations in terms of dynamic response, safety, scalability, and integration with renewable energy systems. The achievement of the objective will be based on operational research, mathematical optimization methods, namely the simplex algorithm [11] and the generalized reduced gradient (GRG) applied in various domains [12] and the different existing combinations will be proposed to achieve energy production that meets the demand while minimizing fuel consumption and greenhouse gas (GHG) emissions. As an application and validation of the model, it has been applied to the case of the electricity system of the island of Gran Canaria.

## 2. Methodology

The methodology followed for the achievement of the possible operational improvements sought in the energy generation process has been outlined in Figure 1:

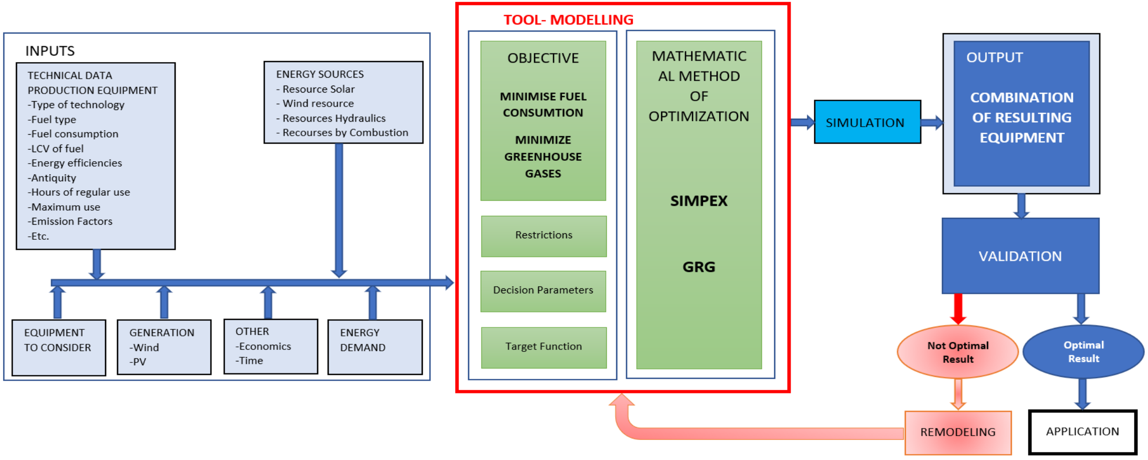
INPUTS
TECHNICAL DATA
PRODUCTION EQUIPMENT
-Type of technology
-Fuel type
-Fuel consumption
-LCV of fuel
-Energy efficiencies
-Antiquity
-Hours of regular use
-Maximum use
-Emission Factors
-Etc.
ENERGY SOURCES
- Resource Solar
- Wind resource
- Resources Hydraulics
- Recourses by Combustion
EQUIPMENT TO CONSIDER
GENERATION
-Wind
-PV
OTHER
-Economics
-Time
ENERGY DEMAND
TOOL- MODELLING
OBJECTIVE
MINIMISE FUEL CONSUMTION
MINIMIZE GREENHOUSE GASES
Restrictions
Decision Parameters
Target Function
MATHEMATICAL METHOD OF OPTIMIZATION
SIMPEX
GRG
SIMULATION
OUTPUT
COMBINATION OF RESULTING EQUIPMENT
VALIDATION
Not Optimal Result
Optimal Result
REMODELING
APPLICATION

**Figure 1.** Methodology.

## 3. Results and discussion.

### 3.1. Application of the tool to minimize hourly emissions of energy production equipment.

The developed tool is applied. It is analyzed 24 hours a day on August 17, 2021, the day when the highest annual energy demand occurred at 2:53 p.m., with 529.0 MW of instantaneous power. In this case, as already indicated, the tool seeks to minimize GHGs. As a result of this application, in the 24 hours we have a combination of power-producing equipment that makes emissions as low as possible, meeting the energy demand. The following graph shows, among others, the "GHG" curve that indicates the actual emissions produced during the 24 hours and the "GHG Minimized″ curve, emissions produced by the best combination of equipment based on the restrictions and methodology established by the tool.

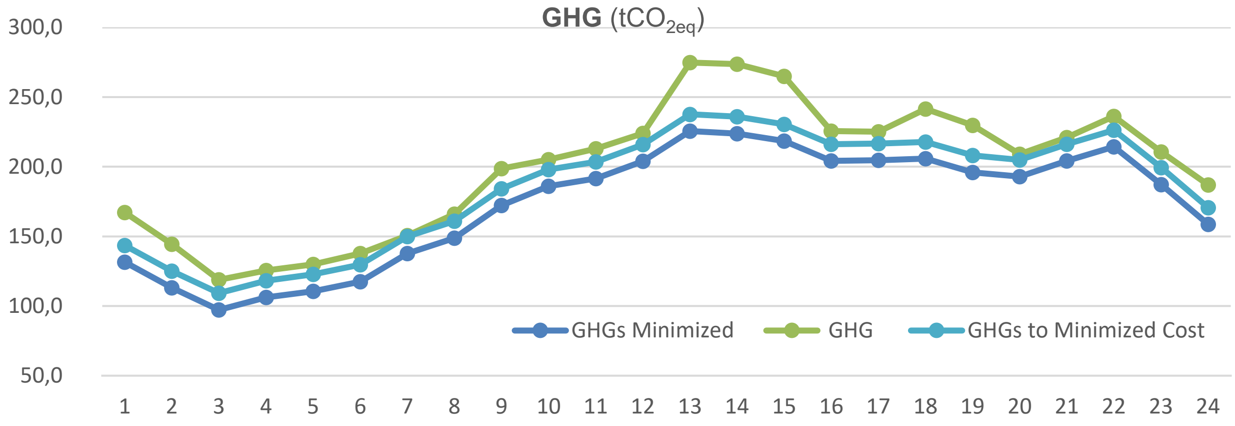

**Figure 2.** GHG emissions.

The algorithm established a new combination (it exclusively chose combined cycle technology for energy produc-tion), which decreases emissions in 24 hours by 388.0 $tCO_{2eq}$, (8.83%). In Figure 2, in addition to representing the two curves: "GHG", which are the actual emissions produced on August 17, 2021, and "*GHG Minimized*", which represent the emissions that would have occurred *on August 17, 2021* if the combination of equipment proposed by the algorithm to minimize GHGs had been used, The "GHG *for Minimized cost*" curve is also represented, which indicates the GHG emissions that would have occurred on August 17, 2021 if the combination of equipment proposed by the algorithm had been used to minimize costs. As will be seen in the corresponding section, cost minimization involves another combination of different equipment and therefore a different GHG production. This new combination of technologies results in a 24-hour decrease in GHGs by 338.3 $tCO_{2eq}$ (7.61%).

### 3.2. Application of the tool to minimize energy production costs

The developed tool is applied. In the case of the logarithmic objective function, coherent results are not obtained and it is not applicable to the system followed, so we will work with the potential objective function that did give good results. It is analyzed 24 hours a day on August 17, 2021, the day when the highest annual energy demand occurred at 2:53 p.m., with 529.0 MW of instantaneous power. In this case, as already indicated, the tool seeks to minimize the economic cost of energy production equipment depending on the installed power and/or production demanded. As a result of this 24-hour application, a combination of power-producing equipment is produced that makes the economic cost as low as possible while meeting the energy demand. The following graph shows, among others, two curves that indicate the real costs during the 24 hours and the costs established by the tool, algorithm, with its new combination of producing equipment.

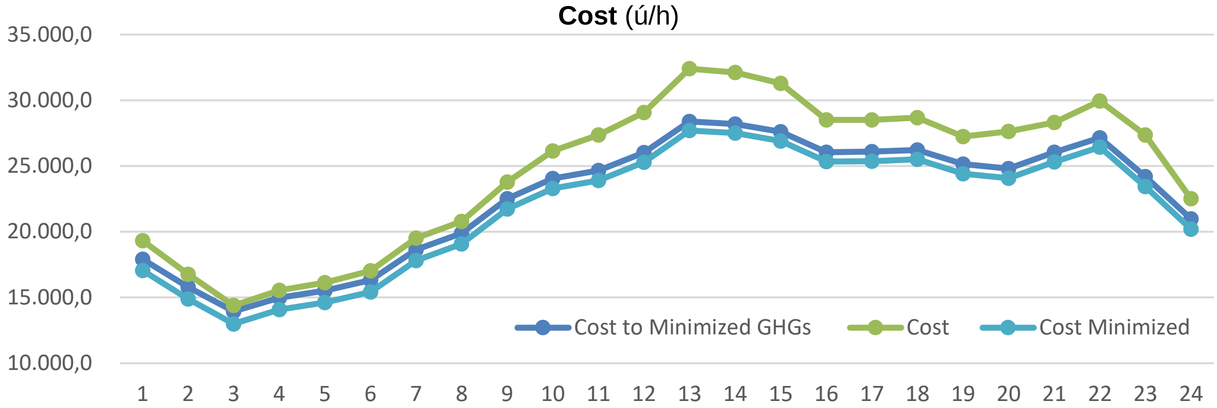

**Figure 3.** Economic costs.

The algorithm established a new combination (it chose the combined cycle and two-stroke diesel engine technol-ogies for energy production), which decreases the cost in 24 hours by €56,015.3, (10.48%). Figure 3, in addition to representing the "Cost" curves, which are the actual costs incurred on August 17, 2021, and the "*Cost* Mini-mized" curves, which represent the costs that would have occurred on August 17, 2021 if the combination of equipment proposed by the algorithm had been used to minimize them, the *"Cost to Minimized GHGs"* curve is also represented", which indicates the economic cost that would have occurred on 17 August 2021 if the combi-nation of equipment proposed by the algorithm had been used to minimize GHGs. As seen in previous sections, GHG minimization involves another combination of different equipment and therefore another production of dif-ferent costs. This new combination of technologies means a reduction in costs in 24 hours by €49,255.3, (9.10%).

## 4. Summary of applied methods

With all this, it is obtained, in summary, that the maximum daily cost savings in fuels in power production plants can be estimated for the day studied of approximately €85,000, if we choose exclusively to minimize the cost. And it has been obtained that the maximum daily decrease of GHGs in power production plants can be estimated to be approximately 388 $tCO_{2eq}$ for the day studied, if we choose exclusively to minimize GHGs as shown in Table 1.

**Table 1.** Result of GHG and Cost estimates for August 17, 2021 for different combinations of technologies.

| Algoritmo | Real data | Real Combination of Technologies simulated with the algorithm | | Combining technologies for get the Minimized Cost | | Combining technologies for obtain the Minimized GHG | |
|---|---|---|---|---|---|---|---|
| | amount | amount | % Difference from Actual | amount | % Difference from Actual | amount | % Difference from Actual |
| GEI ($tCO_{2eq}$) | 4.781,0 | 4,828.3 | 0.979 | 4,442,7 | 7.616 | 4.393,0 | 8.833 |
| Coste (€) | 590.416,9 | 592,532.9 | 0.357 | 534,401.6 | 10.482 | 541.161.7 | 9.102 |

## 5. Conclusions

The algorithm represents a valid tool for the management of production equipment, offering the best combination of these equipment for the best optimization of the variable under study. For the particular case analyzed, 24 hours on August 17, 2021, it can be summarized that the algorithm, tool, shows that there is an undoubted solution for the optimization of costs and a different solution for the reduction of GHGs. Both greatly improve the results of the equipment mix adopted by the production company. On the other hand, it has also served to seek a third compromise solution, consisting of one that encompasses the two joint optimizations, cost and GHG, resulting in a better compromise solution than the one applied by the producing company. This solution consists of another combination of equipment that provides the lowest economic cost, the Minimized COST curve represented in Figure 3, and which almost equals the combination of equipment that minimizes GHGs the most, being slightly above this minimum, the GHG curve for the Minimized COST represented in the one represented in Figure 2. and being well below the GHGs produced by the solution adopted by the producing company. With this algorithm and this methodology, it has been possible to solve the double problem posed, with Operations Research being the step prior to programming. Thanks to this mathematical tool, we have been able to understand how to develop our problem with continuous variables and linear constraints. It is true that, when it comes to solving these problems, other methods that can be applied analytically or graphically have been used. Possibly, the graphical method is one of the fastest and clearest methods when it comes to executing them, but it has the disadvantage that it can only be used when the problem has two variables and this situation in real life is almost impossible. That's where much of the relevance of both methods comes from. With this algorithm, we have been able to verify that, even if the number of variables is high, we will always obtain, if the problem has one, an optimal value. Therefore, we can conclude that thanks to the Simplex and GRG methods we can find an answer to the decision-making process because they always choose the sweet spot that gives the best value to the objective function.

**Funding:** This research was cofunded by the INTERREG V-A Cooperation, Spain–Portugal MAC (Madeira-Azores-Canaries) 2014–2020 program, MITIMAC project (MAC2/1.1a/263).

## References

[1] Vargas-Salgado C, Berna-Escriche C, Escrivá-Castells A, Alfonso-Solar D. Optimization of the electricity generation mix using economic criteria with zero-emissions for stand-alone systems: Case applied to Grand Canary Island in Spain. Progress in Nuclear Energy 2022;151:104329. https://doi.org/https://doi.org/10.1016/j.pnucene.2022.104329.

[2] Lozano Medina JC, Perez-Baez S, Leon-Zerpa F, Mendieta-Pino CA. Alternatives for the Optimization and Reduction in the Carbon Footprint in Island Electricity Systems (IESs). Sustainability 2024;16. https://doi.org/10.3390/su16031214.

[3] Qiblawey Y, Alassi A, Zain ul Abideen M, Bañales S. Techno-economic assessment of increasing the renewable energy supply in the Canary Islands: The case of Tenerife and Gran Canaria. Energy Policy 2022;162:112791. https://doi.org/https://doi.org/10.1016/j.enpol.2022.112791.

[4] Paspatis AG, Fiorentzis K, Katsigiannis I, Tsikalakis A, Karapidakis ES, Thalassinakis EJ, et al. Assessment of the required running capacity in weakly interconnected insular power systems. Electric Power Systems Research 2023;221:109436. https://doi.org/https://doi.org/10.1016/j.epsr.2023.109436.

[5] Mitali J, Dhinakaran S, Mohamad AA. Energy storage systems: a review. Energy Storage and Saving 2022;1:166–216. https://doi.org/https://doi.org/10.1016/j.enss.2022.07.002.

[6] Rehman S, Al-Hadhrami LM, Alam MdM. Pumped hydro energy storage system: A technological review. Renewable and Sustainable Energy Reviews 2015;44:586–98. https://doi.org/https://doi.org/10.1016/j.rser.2014.12.040.

[7] Lozano Medina JC, Mendieta Pino CA, Ramos Martín A, León Zerpa F. A Case Study of a Reverse Osmosis Based Pumped Energy Storage Plant in Canary Islands. Water (Basel) 2024;16. https://doi.org/10.3390/w16040515.

[8] Gkonis N, Arsenopoulos A, Stamatiou A, Doukas H. Multi-perspective design of energy efficiency policies under the framework of national energy and climate action plans. Energy Policy 2020;140:111401. https://doi.org/https://doi.org/10.1016/j.enpol.2020.111401.

[9] Gómez-Calvet R, Martínez-Duart JM, Serrano-Calle S. Current state and optimal development of the renewable electricity generation mix in Spain. Renew Energy 2019;135:1108–20. https://doi.org/https://doi.org/10.1016/j.renene.2018.12.072.

[10] Arévalo P, Cano A, Jurado F. Mitigation of carbon footprint with 100% renewable energy system by 2050: The case of Galapagos islands. Energy 2022;245:123247. https://doi.org/https://doi.org/10.1016/j.energy.2022.123247.

[11] Hardt M, Schraknepper D, Bergs T. Investigations on the Application of the Downhill-Simplex-Algorithm to the Inverse Determination of Material Model Parameters for FE-Machining Simulations. Simul Model Pract Theory 2021;107:102214. https://doi.org/https://doi.org/10.1016/j.simpat.2020.102214.

[12] Qiu R, Liu C, Cui N, Gao Y, Li L, Wu Z, et al. Generalized Extreme Gradient Boosting model for predicting daily global solar radiation for locations without historical data. Energy Convers Manag 2022;258:115488. https://doi.org/https://doi.org/10.1016/j.enconman.2022.115488.

# Drive Cycle Decomposition: Establishing the Trade-off Between ñCharacteristicò and ñDifficultò Sub-Samples of Real Driving Data For Multi-Objective Emissions Optimisation

J. Prior[1], J.A.C.Knowles[1], B. Mason[1], L. Bates[2], S. Whelan[2]

[1]Department of Aeronautical and Automotive Engineering, Loughborough University. Holywell Way, Loughborough, LE11 3TL.

E-mail: j.g.prior@lboro.ac.uk

[2] Intelligent Lab Team, HORIBA MIRA Ltd. Watling St, Nuneaton CV10 0TU

E-mail: steve.whelan@horiba-mira.com
Telephone: +44 24 7635 8010

## 1. Introduction

Calibration and optimisation of engine performance criteria such as fuel consumption and emissions continue to be an active area of research. The demand for robust calibration procedures is driven by a landscape of emissions validation standards such as Real Driving Emissions (RDE), which dramatically increase the range of conditions under which emissions are tested. Complexity is added by the competitive nature of these objectives (e.g. fuel consumption and Nitrogen Oxide emissions) and the procedure becomes a Multi-Objective Optimisation (MOO).

One approach to the MOO problem is to construct an empirical model of each objective according to key inputs and control parameters [1]. The advantage is that the model may be constructed directly from data collected under realistic operation, with key control parameters varied for a fixed transient that covers an area of the dynamic operating space. This may reduce the experimental burden compared to a steady-state approach.

The success of the model-based approach is contingent upon the selection/generation of this fixed transient. and thus is an open area of investigation. Approaches include decomposition of cycles into ñmicro-tripsò snippets of driving behaviour that connect two periods of engine idle [2]ï[4]. Other approaches generate bespoke signals, such as the use of Markov-Chain models that include vehicle velocity / acceleration as states [5], [6]. For purposes of engine characterisation, speed and torque profiles are necessary inputs. As such, other approaches seek to generate cycles which uniformly cover an engineœs dynamic speed-torque envelope [7]. In the original MOO optimisation work [8], an expertised basis is used to select a 2-minute sequence of the WLTC cycle for model characterisation. This sequence is chosen for its properties of being:

1. ñ*Characteristic*ò sweeping a broad area of the speed-load map in a manner that is representative of real usage conditions.
2. ñ*Difficult*ò contributing substantially to a minimisation objective such as cumulative NOx.

In the following work a framework is developed for metricising these two qualities for sequences of data collected under more varied driving conditions, including RDE. The resulting approach uses the Wasserstein Distance between a subsequenceœs speed-torque distribution and that of its parents cycle as a metric of characteristicness. Difficulty is represented as the cumulative sum of instantaneous objective values taken over the length of a sequence. The trade-off between these measures is established for all candidate sequences to establish their relationship as a function of sequence length.

## 2. Defining ñCharacteristicò and ñDifficultò Driving Sequences

In this work, the ñcharacteristicnessò of a sub-sequence $\mathbf{q}$ drawn from a drive cycle $\mathbf{p}$ is represented by their Wasserstein Distance $\mathcal{W}\ P\check{\imath}Q$ , otherwise known as the ñEarth-Moverœs Distanceò $P\ N\check{\imath}T$ and

$Q(N,T)$ are the respective speed-torque probability distributions of $\mathbf{p}$ and $\mathbf{q}$, and so $\mathcal{W}(P,Q)$ is a measure of statistical similarity. The Wasserstein Distance is given by:

$$\mathcal{W}(P,Q) = \left(\sum_{u=1}^{nm}\sum_{v=1}^{nm} \Theta_{uv}^{*}\,\mathbf{C}_{uv}\right)^{1/2}$$

Where $\Theta_{uv}^{*}$ is the optimal transport plan which minimizes the distance $\mathbf{C}_{uv}$ moved by a unit of probability mass from the $u$th value of $P$ to the $v$th value of $Q$. This plan is obtained via linear programming, subject to the constraint that all probability mass in $P$ is moved to $Q$. Wasserstein Distance assumes a value between 0 and 1, where lower values connote similar distributions. In this work a maximization objective termed the Wasserstein Similarity $\mathcal{S} = 1 - \mathcal{W}$ is introduced for consistency of metrics.

"Difficulty" of a sub-sequence in optimization is determined by its relative contribution to a minimization objective that accumulates over the cycle from which it is sampled. If a sub-sequence $\mathbf{q}$ has a start time $t_0$ and end time $t_q$ then the "Intensity Metric" that measures its relative contribution is:

$$\mathcal{I}(q) = \frac{\sum_{t=t_0}^{t_q} y(t)}{Y_p}$$

Where $y(t)$ is the instantaneous value of the objective function such as Nitrogen Oxide ($NO_x$) emissions at sample time $t$ within the sub-sequence $q$. This objective is summed over the duration of the sub-sequence and taken as a fraction of $Y_p$, the cumulative sum of the same objective over the full drive cycle. Sub-sequences that maximize $\mathcal{I}(q)$ are considered difficult "problem areas" within an existing engine calibration, and so are considered strong candidates for transients upon which to base the engine model.

## 3. Applying Metrics to All Sub-Sequences of Real Driving Data

As a demonstration, the previously introduced metrics have been applied to 100 minutes of real driving data collected by HORIBA MIRA Ltd, generated by driving a passenger vehicle instrumented with a HORIBA Portable Emissions Measurement System (PEMS) around Nuneaton, UK. The route satisfies RDE validation criteria including $va_{pos}[95]$: a limit on the 95th percentile of the velocity-acceleration product. Measurements include torque demand, engine speed and instantaneous engine-out $NO_x$ emissions in g/s, all sampled at a frequency of 10Hz.

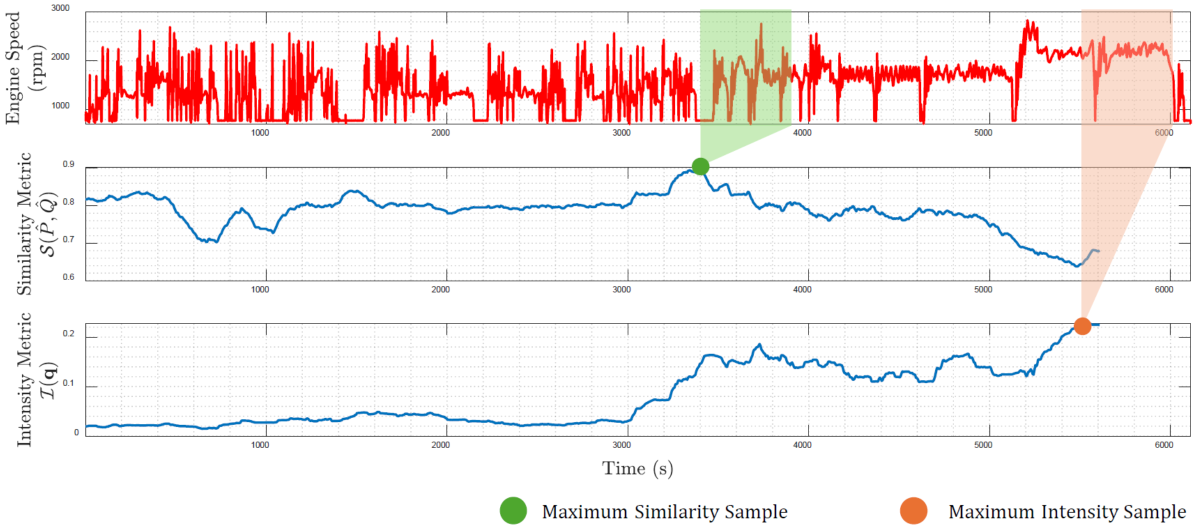

**Fig. 1:** Engine speed trace of driving data generated according to RDE specifications (top), The Wasserstein Similarity for every 500s subsequence taken (middle), The Intensity Metric for every 600s subsequence (bottom)

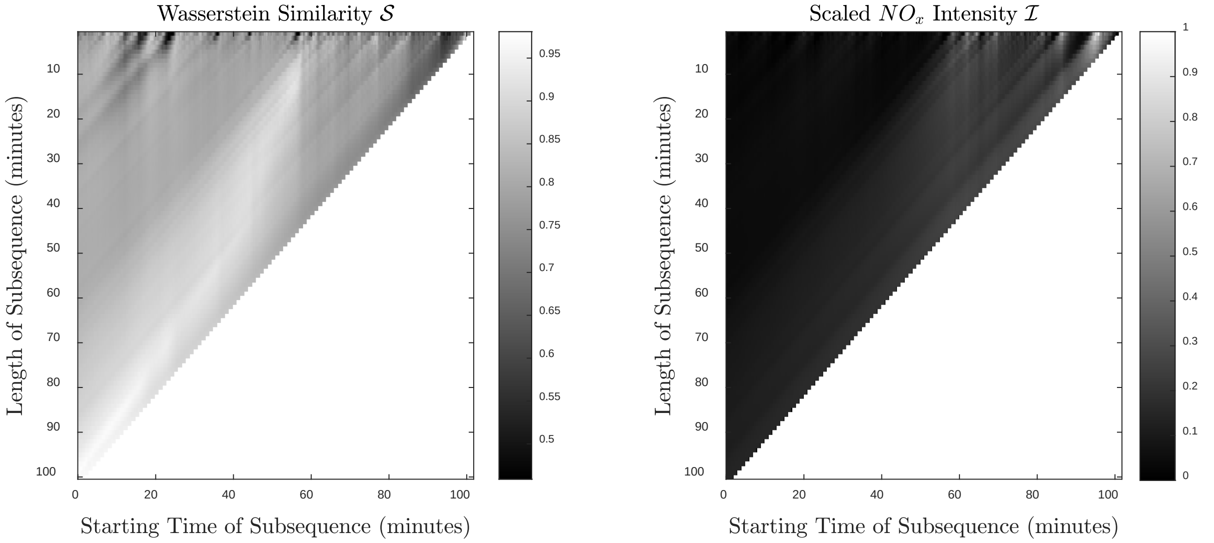

**Fig. 2:** Heat map of Wasserstein Similarity and NOx Intensity for all sub-sequences with duration between 1 and 100 minutes.

A sliding window analysis is conducted to extract all subsequences of length $l_q$ = 600 seconds from the drive cycle, whose engine speed trace can be seen in the upper plot of Fig. 1. The metrics $\mathcal{S}$ and $\mathcal{I}$ are computed for every sub-sequence $\boldsymbol{q}$ extracted by the sliding window and plotted as time series (middle and bottom of Fig. 1). Note that these time series are each 600s shorter than the drive cycle, ending at the start time $t_\pi$ of the final sub-sequence.

Highlighted for each signal is the sub-sequence that maximizes each metric. $\mathcal{I}_{max}$ coincides with a ramp to high speed-load under extra-urban conditions, an operating point that is correlated with high Nitrogen Oxide emission rates. $\mathcal{S}_{max}$ coincides with a series of rapid transients that oscillate between engine idle and various speed points, covering a wide area of the engine operating space in a short duration.

## 3. Assessing Trade-Off Of Metrics For All Subsequences

Fig. 2 extends the visualization to include subsequences for all $l_q$ in the range 1-100 minutes. For each of the heatmaps, warm colors represent subsequences that maximize each metric, valid only for points on the upper diagonal. In the right heatmap the intensity metric is scaled by the length of each subsequence, so that both long and short sequences may be compared. Thus, the trade-off $\mathcal{I}$ and $\mathcal{S}$ may be assessed for all possible subsequences.

Longer sequences that cover both the urban and extra-urban halves of the cycle account for most of the variation in speed-load, and so maximize $\mathcal{S}$. By contrast, the subsequences in the latter portion of the cycle contributes most to $NO_x$ due to the prevalence of high speed-load conditions and maximize. Thus the strong competition between $\mathcal{I}$ and $\mathcal{S}$ for a range of subsequence lengths is demonstrated.

A non-dominated sorting of all subsequences is used to ascertain a pareto front with respect to both $\mathcal{I}$ and $\mathcal{S}$. The pareto-optimal subsequences are presented in Fig 3 according to their starting position and length. Among the available solutions, shorter samples

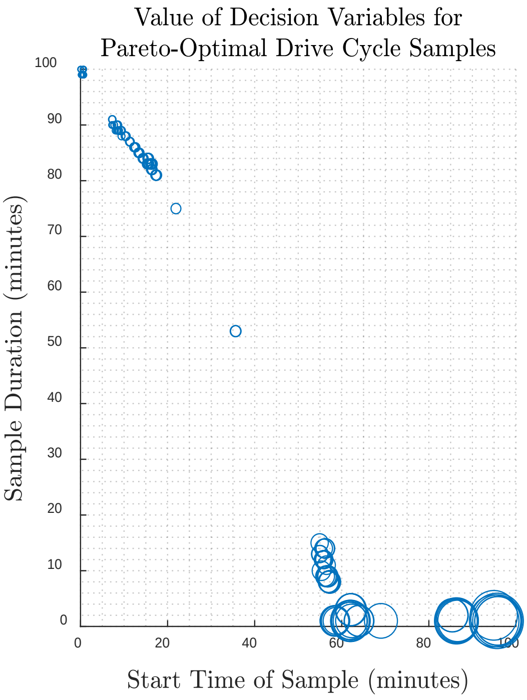

Fig. 3: Plot of start times and durations that most effectively trade-off similarity and intensity. Marker size corresponds to the magnitude of $\mathcal{I}$

(1-2 minutes) in the latter portion of the cycle prefer $\mathcal{I}$ (denoted by larger marker size) and are concentrated around extra-urban transients. A cluster of 8-16 minute samples that balance both metrics consist of medium-speed transients that transition between each half of the cycle. Longer samples beginning earlier in the cycle and covering much of its duration prefer $\mathcal{S}$, an intuitive result.

## 4. Discussion

By applying the two Wasserstein and Intensity-based metrics to all subsequences of an RDE-representative cycle, the ability to extract transients that are both characteristic and difficult is assessed. Due to the RDE cycle being constructed of multiple distinct operating modes, there are few single subsequences <8 minutes in duration that are similar according to Wasserstein Distance. To achieve high degrees of similarity, more than 50% of the cycle is required, traversing multiple distinct portions of the cycle. Subsequences of this duration are not efficient for designing characterization experiments.

If experimental limitations are strict and only ~2 minute transients may be used to train an optimization model, the best selection may be those that maximise contribution to the objective instead, such as high-speed extra-urban transients which weigh heavily in favour of the Intensity metric. This reproduces the “expertised basis” used by Le Corre et al [8].

Given the steep trade-off of the two metrics introduced, a potential next step of this work is to choose cycles that maximise each metric respectively and perform model based optimization using each. In doing so, their respective effect on the final calibration when validated upon longer drive cycles may be measured. This will therefore assist in deciding whether characteristic or difficult transients produce better calibrations in general.

The existence of a steep trade-off between the two metrics also reflects the heterogeneous nature of driving behaviour within a validation standard such as RDE. A further extension to the methodology may involve analysis of “combined transients”, taken from various stages of a cycle in a similar manner to Markov Chain methods.

## References

[1] S. D. Le Corre *et al.*, “Application of multi-objective optimization techniques for improved emissions and fuel economy over transient manoeuvres,” SAE Technical Paper, 2019.

[2] M. Montazeri-Gh and M. Naghizadeh, “Development of car drive cycle for simulation of emissions and fuel economy,” in *Proceedings of 15th European simulation symposium*, 2003.

[3] S. A. N. Prasad, M. Manickam, D. Balakrishnan, and N. Saravanan, “Development of Synthetic Drive Cycle for Fuel Economy Prediction,” SAE Technical Paper, 2012.

[4] Z. Yang, B. Mason, E. Winward, and M. Cary, “Two-Dimensional Transient Cycle Decomposition and Reduction (CDR) for Data Driven Nonlinear Dynamic System Modeling,” *IEEE Access*, vol. 12, pp. 37093–37102, 2024.

[5] T.-K. Lee and Z. S. Filipi, “Synthesis and validation of representative real-world driving cycles for plug-in hybrid vehicles,” in *2010 IEEE vehicle power and propulsion conference*, 2010, pp. 1–6.

[6] T.-K. Lee and Z. S. Filipi, “Synthesis of real-world driving cycles using stochastic process and statistical methodology,” *Int. J. Veh. Des.*, vol. 57, no. 1, pp. 17–36, 2011.

[7] E. Winward, Z. Yang, B. Mason, and M. Cary, “Excitation Signal Design for Generating Optimal Training Data for Complex Dynamic Systems,” *IEEE Access*, vol. 10, pp. 8653–8663, 2021.

[8] S. Le-Corre, “Multi-objective optimization and analysis of nonlinear dynamic systems using genetic algorithms.” Loughborough University, 2019.

# Variable Valve Actuation enabled Reactivity-Controlled Compression Ignition in a Natural-Gas/Diesel Marine Engine

J. Kim[1*], A. Kakoee[1], J. Hyvonen[2] and M. Mikulski[1]

[1]Efficient Powertrain Solutions (EPS) Research Group, School of Technology and Innovations, University of Vaasa, Wolffintie 34, FI-65200 Vaasa, Finland
*E-mail: jeyoung.kim@uwasa.fi
*Telephone: +(358) 29 449 8654

[2]Wärtsilä Finland Oy, FI-65170 Vaasa, Finland
E-mail: jari.hyvonen@wartsila.com
Telephone: +(358) 10 709 2311

**Abstract.** The present study numerically investigated two variable valve actuation (VVA) strategies – early intake valve closing (EIVC) and second exhaust valve re-opening (2EVO) with a large bore marine engine operating under natural-gas/diesel RCCI mode. A fully calibrated and validated 1D engine model was utilized for VVA simulation via commercial software, GT-Power. In order to capture RCCI combustion behaviour on VVA, a physic-based chemical kinetic multizone model (UVATZ) was directly coupled with GT-Power. The simulation results revealed that EIVC and 2EVO could control combustion phase and extend load range to some extent by controlling in-cylinder thermal condition right before the combustion initiates. EIVC retards combustion phase by decreasing compression temperature while 2EVO advances combustion onset by increasing in-cylinder temperature by trapping hot residual gases.

## 1. Introduction

Reactivity-controlled compression ignition (RCCI) is a promising option for maritime decarbonization, offering over 50% thermal efficiency and ultra-low emissions of $NO_x$ and soot [1]. This is achieved through lean combustion, rapid heat release, reduced heat rejection, and low combustion temperatures [1]. RCCI, a dual-fuel concept, can adapt to various zero-carbon fuels and is controlled by thermo-kinetic reactions and in-cylinder fuel stratification. Despite its advantages, RCCI faces challenges in real-world implementation due to limited load range, combustion stability, difficult transients, and poor exhaust thermal management [2]. Adjusting blend ratios or pilot injection timing can mitigate some issues, but RCCI remains sensitive to in-cylinder thermodynamic conditions, especially intake valve closing temperature. Variable valve actuation (VVA) enables ultra-efficient RCCI operation by regulating in-cylinder thermodynamic conditions flexibly [3]. This research examines two VVA strategies: EIVC and 2EVO and their impact on combustion using 1D engine simulation with a predictive multizone, kinetic-based combustion model.

## 2. Methodology – 1D engine simulation with multizone model (MZM)

The study is based on single cylinder version of a large bore medium speed marine engine. The engine specifications are presented in Table 1.

**Table 1**. Specifications of research engine and simulation condition

| | |
|---|---|
| Engine | Wärtsilä 31 DF |
| Displacement & nominal speed | 32.45 L & 720 rpm (4-stroke) |
| Stroke / bore | 1.39 |
| High reactivity fuel (HRF) | $nC_{12}H_{26}$ (ISO 8217 LFO) I Direct-injection |
| Low reactivity fuel (LRF) | Natural-gas (MN=80) I Port-injection |
| Valvetrain | Four valves with swirl & tumble ports |
| Reference operating point | 50% load I 0.108 (m/m) HRF/LRF I 49 AFR |

Since there is no commercial predictive combustion model for RCCI, a physic-based chemical kinetic multizone model (MZM) was utilized. In-house MZM code, known as UVATZ was originally developed by Vasudev et al. [1]. The UVATZ conceptual framework is illustrated in Figure 1 which is coupled with a one-dimensional (1D) engine model. The initial engine model was developed by Wärtsilä. Its general assumptions are listed in Table 2.

**Table 2**. Governing assumptions of in-house MZM (UVATZ)

| | |
|---|---|
| Source code | C++ & Cantera (thermo-kinetic library) |
| Reaction mechanism | Yao et al. [4] |
| Zonal configuration | Onion-skin (BL zone + crevice zone) |
| Interzonal mixing | Diffusion-based,<br>predictive turbulence model |
| Wall heat loss | Chang et al. [5]; zone dependent |
| Simulation time | < 3.5 min / cycle (coupled with GT) |
| HRF stratification | Generated from CFD simulations |

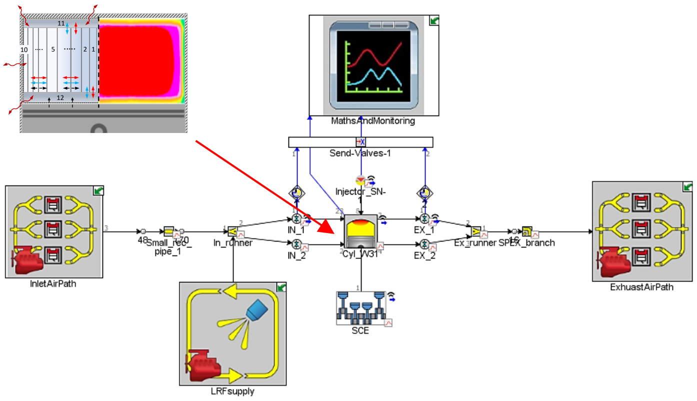
11
10
5
2
1
12
MathsAndMonitoring
Send-Valves-1
Injector_SN-1
InletAirPath
48
Small_rec_pipe_1
70
In_runner
IN_1
IN_2
Cyl_W31
EX_1
EX_2
Ex_runner
SPEX_branch
ExhuastAirPath
LRFsupply
SCE

***Fig. 1.*** *1D engine model coupled with in-house MZM (UVATZ)*

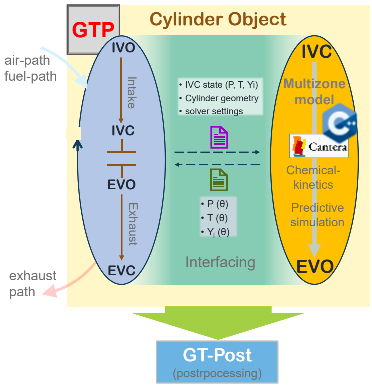
GTP
Cylinder Object
air-path
fuel-path
IVO
Intake
IVC
EVO
Exhaust
EVC
exhaust path
• IVC state (P, T, Yi)
• Cylinder geometry
• solver settings
• P (θ)
• T (θ)
• Y_i (θ)
Interfacing
IVC
Multizone model
Cantera
Chemical-kinetics
Predictive simulation
EVO
GT-Post
(postrpocessing)

***Fig. 2.*** *Coupling methodology between GT-Power and MZM [6]*

Figure 2 depicts how two models are coupled. From the perspective relevant to the present study, GT-Power handles airpath dynamics and gas exchange process during open cycle (IVO to IVC and EVO to EVC). It enables accurate estimation of in-cylinder conditions at IVC, while changing the valve profiles. UVATZ handles the combustion progress and emission calculation in the closed loop cycle (IVC to EVO), which affect the residual mass temperature and composition. The coupled simulation runs for several cycles until convergence in IMEP and CA50 is reached. The engine model was calibrated and validated with experimental data by Kakoee et al. [6]. The model presented less than 2% error in terms of in-cylinder/ air-path pressure and performance parameters. A mid-load RCCI operating point (where the model was calibrated) was used as reference for the present variable valve actuation study.

Two VVA strategies was investigated as shown in Figure 3. EIVC was realized by advancing IVC timing while maintaining IVO timing and exhaust profile. Three different IVC timings were examined by shifting -10/-20/-30 CAD from the baseline as shown in Figure 3-(a). 2EVO was implemented by re-opening exhaust valves during intake stroke as shown in Figure 3-(b). The opening duration was maintained (100 CAD) but the maximum lift was only varied to adjust hot residual fraction. During VVA simulation, only valve profiles were varied. The other parameters such as injection timing, amount of each fuel, and boost remain unchanged.

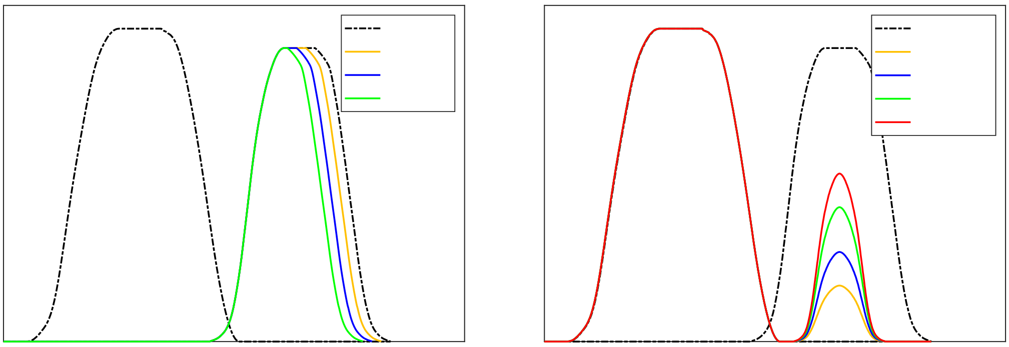

***Fig. 3.*** *Simulated VVA profiles: (a) EIVC; (b) 2EVO*

## 3. Simulation results and discussions

### 3.1 Effect of EIVC

Figure 4 shows simulation results of EIVC. With advancing IVC timings, peak of in-cylinder pressure ($P_{max}$) was reduced. It is mainly attributed to low effective compression ratio where compression pressure and temperature are decreased as shown in Figure 4-(a). In addition, low compression temperature leads to long ignition delay which could promote premixed combustion. However, CA50 is retarded due to delayed combustion onset due to low in-cylinder temperature. This relationship is clearly visible in Figure 4-(b). This also partially contributes to reducing peak of combustion pressure. However, IVC-30 incurs misfire since too low in-cylinder temperature is not able to initiate chemical reaction. For this reason, IVC modulation should be carefully implemented under safe boundary.

EIVC is more effective at high load where there is high temperature margin instead of low and mid load. In addition, the reduced $P_{max}$ and delayed combustion by EIVC allow to increase engine load further without exceeding $P_{max}$ limit. However, EIVC results in trapping less fresh charge by a short intake duration. In order to provide enough oxygen for high load operation, additional boost is necessary to maintain same lambda.

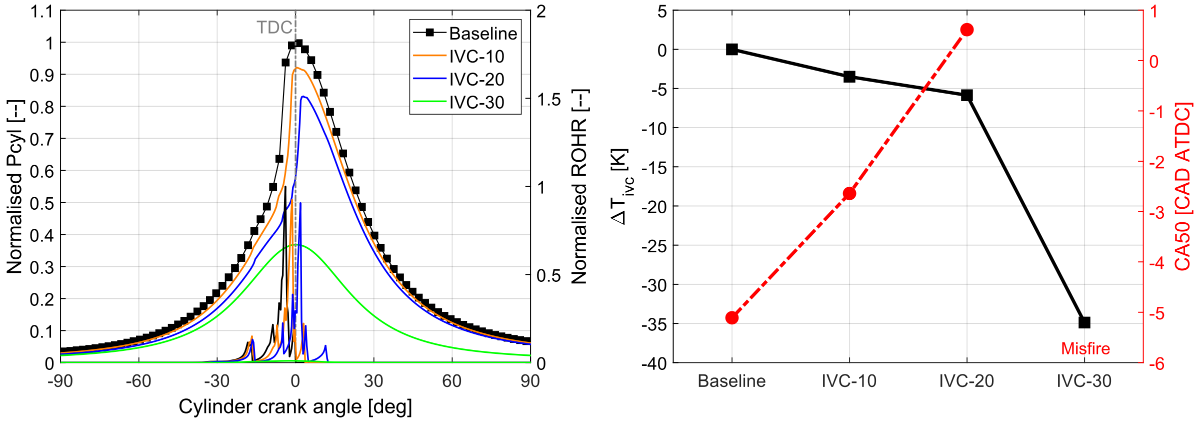

(a) (b)

***Fig. 4.*** *Simulation results of EIVC: (a) in-cylinder pressure ($P_{cyl}$) and rate of heat release rate (ROHR); (b) temperature at IVC ($T_{ivc}$) and CA50*

### 3.2 Effect of 2EVO

Figure 5 presents simulation results of 2EVO. Unlike EIVC, 2EVO increases $P_{max}$ as shown in Figure 5-(a). This is associated with increasing in-cylinder temperature. During 2EVO, there is backflow from exhaust to combustion chamber due to high back pressure ($P_{ex}>P_{in}$). This backflow allows to trap hot exhaust gases, known as internal EGR. The trapped hot exhausts gases elevate in-cylinder temperature directly. The higher lift admits more backflow and raises in-cylinder temperature ($T_{ivc}$) as shown in Figure 5-(b). In the end, this triggers early ignition and advances combustion phase (CA50) so that $P_{max}$ is increased.

Similar to EIVC, 2EVO also reduces intake fresh charge since the backflow suppresses incoming fresh charge during intake stroke. For this reason, this strategy is applicable at low load where there is less oxygen demand and could improve combustion capability suffering from relatively low in-cylinder thermal status. The improved combustion behaviour could reduce methane slip by improving combustion efficiency. Also, low trapped air mass could increase exhaust temperature due to reduced heat capacity effect [7] which is beneficial to increase conversion efficiency of aftertreatment system at low load operation.

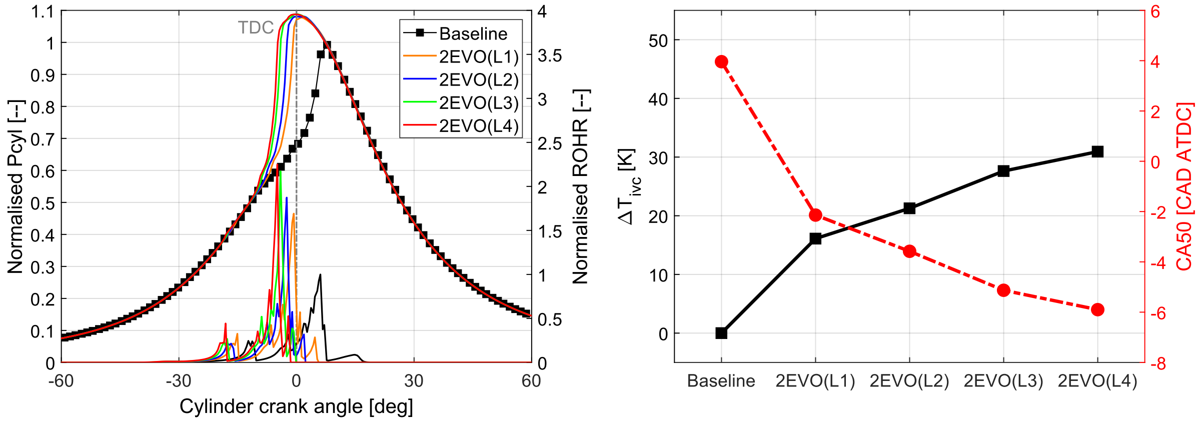

(a) (b)

***Fig. 5.*** *Simulation results of 2EVO: (a) in-cylinder pressure ($P_{cyl}$) and rate of heat release rate (ROHR); (b) temperature at IVC ($T_{ivc}$) and CA50*

## Conclusions

Two VVA strategies, EIVC and 2EVO were numerically examined with a large bore medium speed marine engine platform operating under natural-gas and diesel RCCI mode. The numerical simulation was conducted with GT-Power coupled with in-house multizone model (UVATZ). The multizone model is essential in this research to predict and capture RCCI combustion behavior with varying in-cylinder thermodynamic conditions by VVA. Both VVA strategies could be effective measures to control combustion and load extension by adjusting in-cylinder thermodynamic conditions. EIVC reduces in-cylinder temperature by reducing effective compression ratio which delay ignition and combustion. The reduced $P_{max}$ and pressure rise rate can be used for high load extension. 2EVO increases in-cylinder temperature by trapping hot exhaust gases which promote ignition and advance combustion onset. The capability to improve combustion is beneficial for low load operation/ extension. The additional benefit is low methane slip and better exhaust thermal management.

## Future works

Since the current study was carried out numerically, further experimental verification is required. This will be considered with an electronic-hydraulic valve actuation (EHVA) system in on-going research. Furthermore, systematic optimization will be performed for efficient RCCI operation.

## References

[1] A. Vasudev, et al. Thermo-kinetic multi-zone modelling of low temperature combustion engines. *Prog Energy Combust Sci, vol. 91, no. January, p. 100998, 2022, https://doi.org/10.1016/j.pecs.2022.100998.*

[2] X. Duan, et al. A review of controlling strategies of the ignition timing and combustion phase in homogeneous charge compression ignition (HCCI) engine. *Fuel, vol. 285, Feb. 2021, https://doi.org/10.10-16/j.fuel.2020.119142.*

[3] J. Kim et al. Variable valve actuation for next generation marine and off-road engines ï a comprehensive review oriented on meeting future emission legislation. *https://ssrn.com/abstract=4760136.*

[4] T. Yao, et al. A compact skeletal mechanism for n-dodecane with optimized semi-global low-temperature chemistry for diesel engine simulations. *Fuel, vol. 191, Mar 2017, https://doi.org/10.1016/j.fu-el.2016.11.083.*

[5] J. Yang and K. Martin. Approximate Solution ï One-Dimensional Energy Equation for Transient, Compressible, Low Mach Number Turbulent Boundary Layer Flows. *J. Heat Transfer. Aug 1989, 111(3): 619-624, https://doi.org/10.1115/1.3250727.*

[6] A. Kakoee, et al. A predictive 1D modeling framework for reactivity-controlled compression ignition engines, via a chemistry-based, multizone combustion object. *SAE Technical Paper 2023-24-0001, 2023, https://doi.org/10.4271/2023-24-0001.*

[7] J. Kim, et al. Variable valve actuation for efficient exhaust thermal management in an off-road diesel engine. *Appl. Therm. Eng. Vol. 246, June 2024, 122940, https://doi.org/10.1016/j.applthermaleng.2024.122940.*

# Energy-Free Compression and Storage System of Natural Gas for Small Vehicles Propulsion

M. Rudkowski [1], P. Iljaszewicz [2]

[1] NGV AUTOGAS sp. z o.o., ul. Kochanowskiego 3/1a, 31-127 Krak· w, Poland

E-mail: autogas@ngvautogas.com.pl
Telephone: +(48) 12 653 04 65

[2] CMT ï  Clean Mobility & Thermofluids. Universitat Polit¯cnica de Val¯ncia. Camino de Vera s/n, 46022 Valencia, Spain.

E-mail: piljasz@mot.upv.es
Telephone: +(48) 504 329 749

**Abstract.** Using CNG (compressed natural gas) as an automotive fuel has many benefits, however, due to its seasonal fluctuations in demand, is problematic in exploitation, as the pipeline networks do not operate in steady conditions and gas pressure must be reduced for the needs of distribution. The commonly performed method to compensate for it requires additional energy (used compressors are powered by external energy sources). The investigated compression station uses a reciprocating compressor driven by the energy of compressed gas taken from a medium or high-pressure transmission pipeline. After the compression work has been performed, gas from the compressor is directed to the low-pressure distribution pipeline, and compressed gas is stored in pressure tanks. During periods of increased gas demand the stored gas is expanded and directed to the transmission pipeline. The compression storage expansion installation is located at the network reduction station. It concerns the natural gas buffering system, i.e. eliminating temporary drops or surpluses in consumption from the network. By using dedicated boosters, it is possible to compress a certain volume of gas into storage energy-free (only the energy of the expanded gas is re-used). The stored compressed gas can be issued through a measuring distribution set directly as a CNG fuel for propulsion. It has already been done by the CERRAD group in Starachowice, Poland, where it successfully refuels approx. 40 CNG forklifts per day. The cost of such refuelling is limited to the costs of installation depreciation and minor services, but no electricity is needed. Hence, the carbon footprint of such a system is minimal.

In parallel, the new branch of investigation is to adjust the system to be used with compressed air to power pneumatic engines for light vehicles, for moving short distances (e.g. forklifts for unloading in closed warehouses). The method requires large-volume storage tanks or frequent refuelling, but is of high interest, as it could completely nullify the emission of greenhouse gases.

## 1. Introduction

Using CNG for propulsion offers numerous benefits, particularly in reducing environmental impact and improving economic efficiency. CNG combustion produces fewer greenhouse gases compared to conventional fuels, significantly lowering carbon emissions and contributing to cleaner air thanks to a reduction in ozone formation potential and maximum incremental reactivity. Specifically, CNG produces much smaller amounts of ozone during the chemically reactive process, even at similar non-methane organic gas levels, which is a crucial factor in reducing smog and improving air quality. [1] It is also more cost-effective, offering substantial savings in fuel expenses. Moreover, CNG has a high octane rating, which enhances engine performance and efficiency [2]. These advantages make CNG a viable alternative fuel for various vehicles, promoting sustainable and economically sound transportation solutions.

Compensating for fluctuations in natural gas consumption by network users ensures the smooth operation of gas distribution systems and reduces the load on gas pumping infrastructure. Utilizing the energy from expanded gas to compress CNG fuel can significantly lower energy consumption in facilities with gas installations. The proposed innovation addresses the challenge of periodic exceedances of contracted gas volumes in companies. This solution involves constructing installations that balance gas consumption (compressed gas storage), particularly for enterprises facing issues with fluctuating consumption from the transmission network. Implementing such a system within a company's operations can stabilize gas usage. Given the current technical limitations of gas transmission networks present in central European countries, maintaining a consistent gas consumption level is the primary technical challenge. Avoiding periodic surges in usage is crucial to prevent exceeding network capacity and causing excessive pressure drops. The proposed technological system harnesses the potential energy of expanded gas from medium or high-pressure transmission networks. This system compresses and stores a separated gas stream as CNG, which is then utilized during peak consumption periods. The approach is particularly beneficial for handling momentary and periodic consumption spikes associated with technological processes or refuelling CNG vehicles.

In the present socio-political situation, the embargo on Russian gas has imposed additional constraints on natural gas transmission networks available to the industry. [3] Sudden increases in consumption can lead to pressure drops below acceptable levels, causing technical issues for all users and financial penalties for excessive consumption. Traditional methods of refuelling CNG vehicles often result in periodic consumption spikes, which can exacerbate fluctuations in gas usage within global transmission networks. The solution outlined in this documentation addresses these fluctuations effectively. Implementing this technology has significant global market potential, as many enterprises face challenges related to stabilizing gas consumption from the network.

## 2. Proposed technological solution

To face the inconveniences, a new technological solution has been invented and applied. The method enables energy-free compression and storage of the compressed gas, especially in dispersed end zones of the transmission pipelines, where the gas pressure drops caused by the increased gas demand most often occur, assuring the correct operation of the gas network. At reduction stations, there are technical conditions for installing boosters that do not require external energy to drive them. The operating condition is the continuous receipt of gas into a medium or low-pressure gas pipeline. The working principle is similar to that of a pressure intensifier.

In the Fig. 1, the technological layout of the proposed installation can be seen. The numbers signify as follows: 1- transmission pipeline; 2, 6, 7, 8, 13, 15, 16, 18 – pipelines; 3 - network reduction station; 4 - distribution pipeline; 5- double-acting reciprocating compressor; 9- storage tank; 10- pipeline (for dispensing compressed gas as CNG fuel); 11- pressure reduction model; 12- measuring-distribution set; 14- gas liquefaction module (in the version of the natural gas liquefaction installation, which also includes a gas purification and cooling unit, based on the Joule-Thomson effect); 17- low-temperature storage tank; 19- evaporator; 20- measuring distribution set.

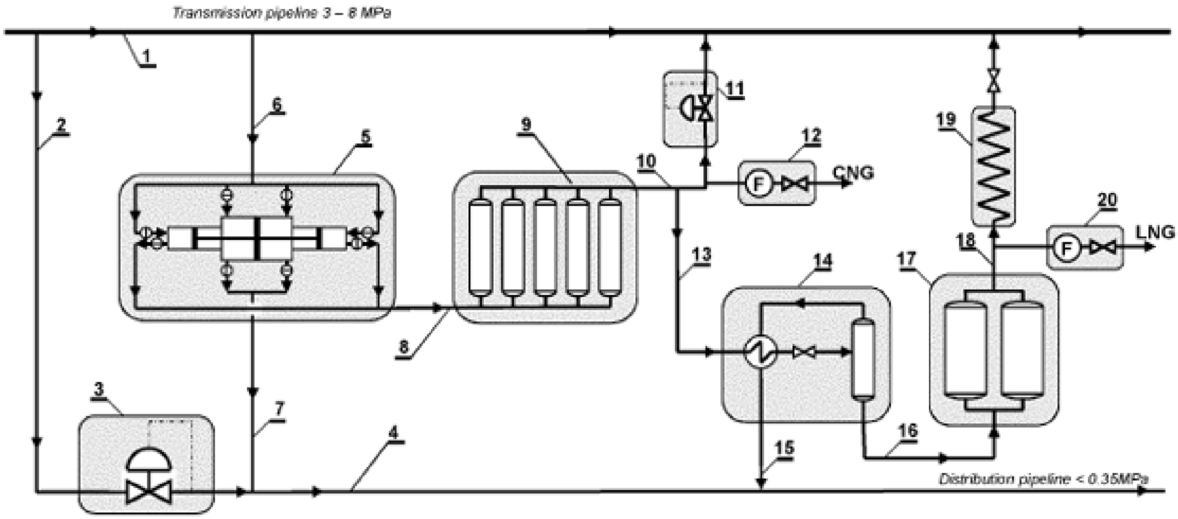
Transmission pipeline 3 – 8 MPa
1
2
6
5
9
10
11
12
F
CNG
19
20
F
LNG
18
13
14
17
8
3
7
4
15
16
Distribution pipeline < 0.35MPa

**Fig. 1.** Technological layout of the installation [4]

The operational method of an installation designed to compensate for fluctuations in gas demand within natural gas networks is: initially, natural gas is transported via a medium or high-pressure transmission pipeline (1), typically at pressures 3- 8MPa. The gas is then diverted to a network reduction station (3), where its pressure is reduced to below 0.35MPa before being directed into the distribution pipeline (4). Additionally, gas from the transmission pipeline (1) is routed to a double-acting reciprocating compressor (5). In this setup, a portion of the gas acts as a working medium; during its expansion, it compresses the remaining gas, which is typically pressurized to above 20MPa, most commonly 20-25MPa. The expanded gas is channeled into the distribution pipeline (4), while the compressed gas is stored in a storage tank (9) comprising parallel-connected pressure cylinders. During periods of increased gas demand, the compressed gas from the storage tank is routed through a pressure reduction module (11) back into the transmission pipeline (1). Alternatively, this compressed gas can be dispensed as CNG fuel via a measuring distribution set (12) or directed to a gas liquefaction module (14). In the liquefaction module, part of the gas is expanded using the Joule-Thomson effect, and the rest of the reduced-pressure gas, after the compression work has been performed, is directed to the distribution pipeline (4). The liquefied gas is directed to the low-temperature storage tanks (17). When gas demand spikes, liquefied gas from the storage tanks is evaporated (in 19) and redirected into the transmission pipeline. This liquefied gas can also be dispensed as LNG fuel through a measuring distribution set (20), providing a flexible and efficient method for managing gas demand fluctuations and ensuring a stable supply. [4]

The solution concerns the natural gas buffering system, i.e. eliminating temporary drops or surpluses in consumption from the network. By using boosters, it is possible to compress a certain volume of gas into storage without the need for additional energy (only the energy of the expanded gas is used for the compression), which can then be collected at increased consumption. In the Polish gas industry, where the invention is applied, this is a serious problem because increased gas consumption in weak networks causes a reduction in pressure, which in extreme cases may result in a periodic shutdown of the branch (the cut-off occurs in the reduction systems).

## 3. Cost-benefit analysis

A cost simulation has been conducted, taking into account the current conditions at the CERRAD group disposition in Starachowice, Poland, and after three years of utilization of the device. When estimating the savings, it was assumed that electricity consumption at the CNG station was completely reduced, and all the energy needed to refuel vehicles would be provided by decompressed gas. To drive the compressors at the indicated CNG station, located next to the reduction station, the electrical power requirement of 50-80kW (station capacity 500Nm$^3$/h) was determined. With twenty hours of daily operation, the energy consumption will be approximately 1,200kWh and in a month 36.000kWh, which, at the price of PLN 1 (0,23ú) for 1kWh, for the compressor, means savings of PLN 21.600 (5000ú) per month, which directly translates into a reduction in the costs of CNG gas compression. An additional saving is the reduction of implementation costs. By using an innovative booster design, investment outlays for the construction of a CNG station will be reduced from approximately PLN 1.2-1.5M (277-347Kú) to PLN 200-280K (46-65Kú), and for its operation from approx. PLN 150K (35Kú) decreased to PLN 15-20K (2.3 to 3.4 Kú) /year.

## 4. Future perspectives

The current research focuses on the potential of storing energy in compressed air, aiming to utilize the existing installation to compress air instead of gas. This compressed air could then be periodically used to drive pneumatic engines in power generators or vehicles equipped with pneumatic engines. The ongoing studies address the application of air compressed using renewable energy and enhanced by the technology, to power light vehicles such as golf carts. A key consideration for this application is the need for large-volume storage tanks, or composite tanks with high storage pressure, e.g. 700 bar (such as those currently used in hydrogen vehicles), as approximately 50 normal cubic meters of air are required to generate just 1 kWh of energy. Nonetheless, it holds an interesting possibility for ecological advancement.

## References

[1] K. Hamai, H. Mitsumoto, Y. Iwakiri, K. Ishihara, and M. Ishii, Effects of Clean Fuels (Reformulated Gasolines, M85, and CNG) on Automotive Emissions, SAE 1992 Transactions: Journal of Fuels & Lubricants-V101-4, 1992

[2] Z. Han, Z. Wu, Y. Huang, Y. Shi, and W. Liu, Impact of natural gas fuel characteristics on the design and combustion performance of a new light-duty CNG engine, International Journal of Automotive Technology, vol. 22, 2021

[3] M. Stuermer, F. Toscani, A. Pienkowski, A. Pescatori, K. Foda, M. Flanagan, and G. Di Bella, The potential impact of gas supply disruptions in Europe: An update, The economic consequences of war, VoxEU/CEPR Debate, 2022

[4] M. Rudkowski, J. Michalowski, Z. Borowiec, and D. Stasko, Installation for compensating fluctuations in gas demand in natural gas networks and the method of implementing this compensation, European patent no. EP 3 839 321 B1, 2021

# Thermal Loading in RCCI Marine Engine - A Study Using a Predictive Chemistry-Based Multizone Combustion Model and Wall-Thermal Solver

Alireza Kakoee[1], Maciej Mikulski[1], Alberto Cafari[2], Aneesh Vasudev[1], Jari Hyvºnen[2], Amin Mahmoudzadeh Andwari[3], Sadegh Mehranfar[3], Ben Smulter[2], Mahdi Salahi[3]

[1]School of Technology and innovation, University of Vaasa, Yliopistonranta 10, 65200 Vaasa,Finland
[2]Engine Research and Technology Development at Wªrtsila Marine solutions, Vaasa, Finland
[3]Machine and Vehicle Design (MVD), Materials and Mechanical Engineering, Faculty of Technology, University of Oulu, FI-90014 Oulu, Finland

**Abstract.** Energy transition drives rapid development in marine engine technology towards cleaner and more efficient low-temperature combustion concepts. Moving from conventional compression ignition, towards more control-challenging multi-fuel Reactivity Controlled Compression Ignition (RCCI) will increase the calibration complexity drastically. To resolve this complexity, fast and predictive quasi-dimensional combustion models such as the UVATZ, used in this study, re-gain attention as rapid calibration tools. The focus of the study is on thermal effects in diesel - natural gas RCCI engine by performing a close-coupling of the UVATZ combustion code with a finite element cylinder wall thermal solver of GT-Suite. The cylinder geometry and material data are based on the Wªrtsilª 31DF medium speed engine, and the data from a single cylinder research engine is used for model validation. Structural finite element method has been employed to calculate temperature loading on various engine parts such as cylinder head, piston section, liner, inlet and exhaust valves. All necessary boundary conditions have been adjusted according to coolant temperature (oil and water), material properties and geometry related aspects such as heat transfer coefficient and thickness. Postprocessing of results are according to the produced temperature data which were in contour format. Experimental thermal loading data are stored with specific equipment which corresponding points are selected from simulation data. Calibration of model is performed in combustion properties, engine outputs and thermal loadings. Results demonstrate that combustion phasing are in high level accuracy with less than 1 CAD error in CA10 and CA50. Accordingly, engine output specifications such as power, torque, IMEP, efficiency and volumetric efficacy are obtained with less than 3% deviation from where thermal loading on various parts also predicted with around 5% error.

## 1. Experimental setup

The studied RCCI data validation stems from the Wªrtsilª Mono single-cylinder research engine (SCRE) platform, mirroring the cylinder geometry of Wªrtsilª's 310 mm-bore dual fuel production engines. Test rig has been equipped with positioned twin-needle injector housed within the high-pressure common rail fuel system. This optimization is tailored for the utilization of light fuel oil (LFO) as the high-reactivity fuel (HRF) [1]. In RCCI injections, the smaller nozzle is utilized to enhance atomization of micro-injected quantities. Additionally, the narrow-cone injector tip facilitates reactivity stratification with early injection timings. Natural gas, employed as the low-reactivity fuel (LRF) in the test runs, is delivered through a multi-point gas injector positioned upstream of the intake valve. Notably, during dual-fuel mode, the smaller needle ensures precise delivery of minute pilot fuel doses, while the larger needle is exclusive to diesel-mode operation. The SCRE is equipped with a partially variable intake exhaust valvetrain. In contrast to a multi-cylinder engine, the SCRE doesn't incorporate a turbocharger, necessitating unique approaches to manage its charge air temperature and pressure. The comprehensive charge air system comprises two compressors, two buffer tanks, a charge air dryer, and two pressure-regulating valves. This setup is designed to control the charge air pressure and temperature effectively, stabilize airflow, and accurately simulate the exhaust system of a real production engine. High-frequency measurements of in-cylinder pressure (averaged over 300 consecutive cycles with a resolution of 0.20 CA) and pressure in the head ducts, both upstream and downstream of the combustion chamber, are recorded. Post-processing of pressure signals provides performance indicators such as indicated mean effective pressure (IMEP) and the crank angle of X% mass burned (CAX). Low-frequency measurements include the consumption of individual fuels (monitored using a Coriolis flow meter and gravimeter fuel balance for gaseous and liquid fuels, respectively), as well as receiver air. Furthermore, detailed thermal characterization of intake and exhaust ports, along with chamber surface temperatures of the piston top, liner, valves, and cylinder head, are documented for model validation purposes. Pentronic thermocouple K type has been used for component surface temperature measurement. Same thermocouple type, measurement depth and measurement principle considered for liner, flame plate (cylinder head) and piston top. Due to the large size of the pistons several thermocouples allocated consisting of eight thermocouples for cylinder head (flame plate), four for cylinder wall (liner), two of them in exhaust side and two for inlet side. Piston various temperature points has been measured by 16 sensors, Figure 1. Exhaust and inlet valves temperature have been measured with three sensors at each valve type. The results are transmitted by a telemetry system mounted on the piston alimented by battery. The measurement has been done during cycles with a 10Hz frequency.

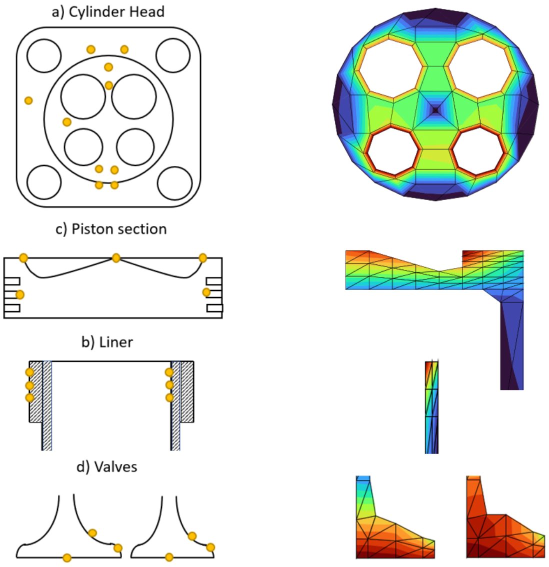

Figure 1 : Temperature sensor locations on various engine part and corresponding simulated thermal loads.

## 2. Simulation method

The UVATZ (University of Vaasa Advanced Thermo-kinetic multi-Zone) model, recently developed for in-cylinder combustion simulation, is utilized in this study, initially proposed by Vasudev et al. [2]. Specifically, it is tailored for natural gas and diesel-fueled RCCI combustion, accounting for key factors like fuel and thermal stratification, in-cylinder turbulence, IVC temperature, and residual burnt gas composition. This model comprehensively captures the complexities of low-temperature combustion concepts driven by chemical kinetics. The UVATZ model employs 12 zones, including disc-shaped zones representing the cylinder head and piston boundary layers, and annular zones capturing bulk inhomogeneity. Heat loss to walls and interzonal heat and mass flows are modeled using established correlations and gradient-based transport, with turbulence effects accounted for via a calibration constant, Chang et al [3]. Chemical reactions are handled using a mechanism accommodating 54 species and 269 reactions, developed by Yao et al [4], with high reactive fuel (HRF), stratification described by a simplified injection model. The surrogate for HRF is nC12H26, low reactive fuel (LRF) is defined as a mixture between $CH_4$ and $C_2H_6$. Further details of the governing equations and modeling assumptions are in the work by the A. Vasudev [2]. The entire model, implemented in C++, utilizes Cantera thermochemical libraries and the CVODES solver, requiring approximately three minutes per closed cycle simulation on an Intel(R) Core (TM) i7-10850H CPU @ 2.70GHz processor. The airpath model in GT-Power, based on the Wärtsilä SCRE, includes a multiple pulse injection rate map-based direct injector and a four-valve rotational position-based valve train. It employs a non-predictive combustion model and simplifies the gas supply system to a single injector component. Due to the absence of a turbocharger, the charge air system incorporates compressors, buffer tanks, a dryer, and pressure-regulating valves to regulate pressure and temperature, simulating a multi-cylinder engine's exhaust system and ensuring stable airflow [5]. The baseline airpath model undergoes calibration against experimental data from 40 operating cases, utilizing a three-pressure analysis (TPA) in GT-Power, renowned for its accuracy in postprocessing in-cylinder pressure data, implemented in A.Kakoee et. al. [5]. Calibration results show deviations from the ideal line (y = x), indicating a 0.4 bar error in BMEP, 4 g/kWh error in break specific fuel consumption, and ~1.7 CAD maximum error in combustion phasing (CA50). Additionally, the air mass flow rate deviates by 3%. Subsequently, six representative operating points from the calibration map were selected for model validation, both individually and in their coupled implementation [5]. A structured finite element method has been selected and adjusted to model heat transfer to various part of engine mainly, piston, cylinder head, cylinder wall(liner), valves and rings. In structural method the number of nodes and location of them is chosen by software. Material selection which consists of heat transfer specification have been adjusted for various mentioned parts. Comparison between experimental and simulated results has been done in various engine loads, 530 kW, 451 kW, 404 kW, 272 kW and 133 kW. Figure 2,a illustrates ratio of experimental and simulations data for various engine parts in all mentioned engine loads. Each part highlighted with different colour. Since exhaust valve had higher temperatures than other parts higher deviations from normal line was also for this part and mainly for seat points in lower loads. As expected, inlet valve had lower temperature than exhaust valves and simulations shown lower deviation for this part. Liner prediction had more precise than other parts. Piston data points almost were in good agreement with experimental data where higher deviation in this part were related to wall of the piston section. Cylinder head shows more deviations point to point although there are high accuracy points also.

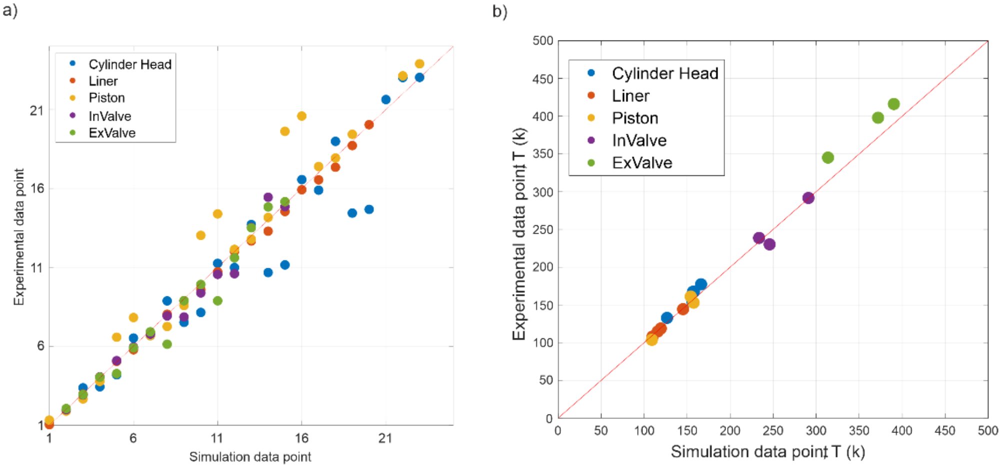

Figure 2: A) Point to point temperature comparison between experimental results and GT-TPA (BurnRate) simulation data points for various engine loads; B) Point by pint comparison of 25% load GT-UVATZ with corresponding experimental data

## 3. Coupling UVATZ and GT airpath model

Validation of GT-UVATZ model as newly obtained toolchain in this study has been performed with a 25% engine load. With considering thermal solver, calibration part contained three different scopes of study. At first combustion characteristics discussed entirely on various specifications such as in-cylinder pressure, cumulative heat release (CHR) and combustion timing. Going through it, Figure 3,a illustrates in-cylinder pressure curve compared with corresponding case in available experimental burn rate model described in section 1.2. Figure 3 also containes cumulative heat release rate comparison study. Comparing pressure curves in Figure 3,a demonstrates that the pressure curve followed the TPA model (as reference) specialty in the area of start of combustion and matched in peak pressure point. Calculation on the data have shown that simulation maximum pressure (Pmax) was about 123.2 bar which had around 0% error with experimental one which was 123.3 bar. Peak pressure for simulation was at 5.2 CAD aTDC where it was around 5.8 CAD aTDC for experimental data showing about 0.6 CAD error. In cylinder root mean square error (RMS) for point-to-point pressure curves calculated around 1.3 bar. Combustion phasing properties such as CA10 and CA50 have been calculated from CHR diagrams shown in Figure 3,b. For calculating CHR in this study, specific heat ratio (ɔ) has been considered contasnt, 1.364. Calculations on CHR have shown that CA10 in simulation accrued at -3.8 CAD bTDC where it was 5.4 CAD bTDC, about 1.6 CAD error on prediction. This difference was about 1 CAD between CA50 experimental and CA50 simulation. Point to point comparison on CHR shown RMS error about 9.4 kJ. Finally, net heat release (NHR) showed about 2.17% error. Validation of the GT-UVATZ model which was developed for thermal loading analysis continued by comparing engine out specifications. These properties consisted of mass flow rate specifications, fuel and air consumption, power specification and thermal properties. Figure 3,c illustrates all specifications those are automatically saved in GT-Post environment. Absolute error of all mentioned specifications has been illustrated in

Figure 3,c. Regarding to this figure, all specifications had below 4% deviation from reference data. In efficiency related specifications, volumetric efficiency had 0.1 % deviation indicated approximately same volume of fluid swept in the piston during combustions. This low error came from using the same airpath model in GT-UVATZ and TPA Gt-Suite models. Piston in operation were model with different method, as a result indicated efficiency shown higher amount of error with 1.8% but still in good agreement with reference data. Brake Efficiency, efficiency that calculated from crank shaft output, have shown higher error than previous due to have some deviations comes from additional parts than piston. Airpath dynamic model specifications such as air fuel ratio (A/F) error was about 0.0% and trapping ratio error was approximately zero percent indicated the accuracy in airpath dynamic parts. In this category fuel and air consumption showed higher error than other specification in mass flow rate properties. This error is mainly shown using different combustion model in simulation methods used in this study. Indicated specific fuel consumption (ISFC) error was about 2.5% where this specification for air consumption (ISAC) deviation was around 2.2%.

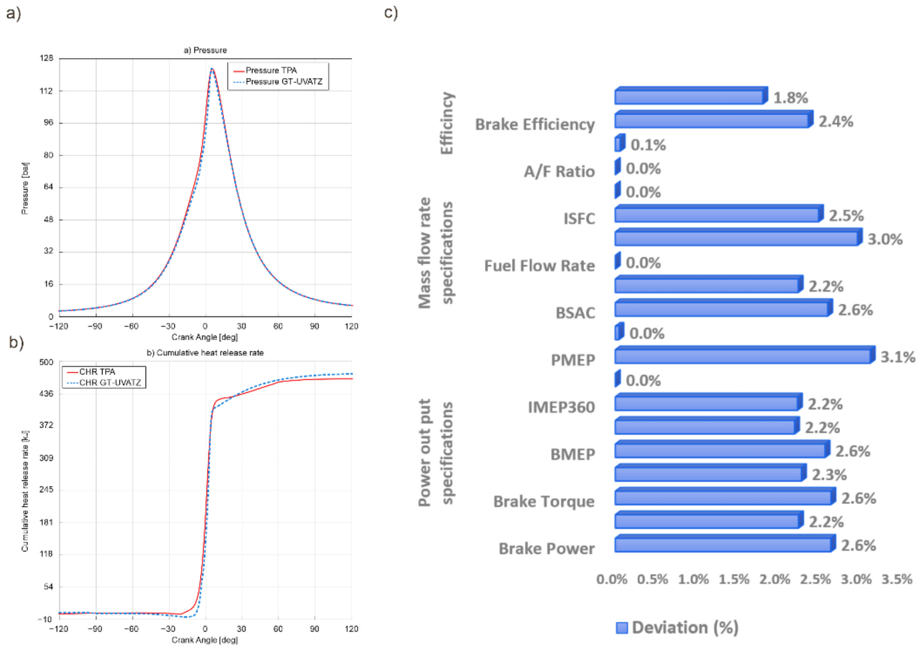

Figure 3: A) Pressure and cumulative heat release (CHR) simulated in GT-UVATZ toolchain compared with experiment TPA model, 25% load; B) Simulation deviation from reference data accrued in GT-UVATZ simulation in 25% load

Prediction of engine output specifications show high accuracy in the model predictivity. IMEP gross and full (360 and 720) has demonstrated the accuracy of 2.2% and 2.2% respectively where the accuracy in predicting brake mean effective pressure (BMEP) was obtained with by only 2.6% error. High accuracy in indicated power and brake power prediction also was achieved also by 2.2 and 2.6 percentage error. Till this point, GT-UVATZ simulation tool has shown good accuracy in predicting in-cylinder combustion properties and full cycle engine output specifications. Another main characteristic of engine operation which investigated as the main focus of this study was thermal loading on cylinder parts. Cylinder head, piston wall, cylinder wall (liner) and valves were selected as important parts in this study. The output results on parts thermal loading have been saved in contour format. For both GT-UVATZ and GT model simulation has been done by 25 cycles, about 4 second of engines operation. Although both models gone in steady state after approximately 12 cycles, this simulation continued to save more thermal data until 25 cycles. Thermal data has been saved at each second (6 cycles) of engine operation. As it was mentioned a 25% load case has been selected for the validation part. To do validation part on thermal loading issue, all mentioned parts have been investigated. All corresponding points temperature has been measured according to the output contour data. Comparison has been done point to point for each part. Figure 2,b depicted comparison of GT-UVATZ extracted temperatures with available measured data from the engine setup. In this figure deviations have been illustrated with respect to line x=y. According to these deviations, it is conceived that exhaust valves shown high error than other parts where cylinder head, piston and liner shown higher accuracy. Furthermore, intake valve temperature predictions had also lower deviation from reference data.

## References

[1] Jay, D. CR development in the last decade in Wª rtsilª . 28th CIMAC world congress, Helsinky, Finland, 2016, p. 6--10.

[2] Vasudev A, Mikulski M, Balakrishnan PR, Storm X, Hunicz J. Thermo-kinetic multi-zone modelling of low temperature combustion engines. Progress in Energy and Combustion Science 2022;91:100998. https://doi.org/10.1016/j.pecs.2022.100998.

[3] Chang J, G¿ralp O, Filipi Z, Assanis D, Kuo T-W, Najt P, et al. New Heat Transfer Correlation for an HCCI Engine Derived from Measurements of Instantaneous Surface Heat Flux. SAE Transactions 2004;113:1576ï 93.

[4] Yao T, Pei Y, Zhong B-J, Som S, Lu T, Luo KH. A compact skeletal mechanism for n-dodecane with optimized semi-global low-temperature chemistry for diesel engine simulations. Fuel 2017;191:339ï 49. https://doi.org/10.1016/j.fuel.2016.11.083.

[5] Kakoee A, Vasudev A, Smulter B, Hyvonen J, Mikulski M. A Predictive 1D Modeling Framework for Reactivity-Controlled Compression Ignition Engines, via a Chemistry-Based, Multizone Combustion Object, Capri, Italy: 2023, p. 2023-24ï 0001. https://doi.org/10.4271/2023-24-0001.

# Powertrain Design and Analysis of Electric Agricultural Vehicles

O. Fitter[1], T. Cavadino [1], A. Curness [1] D. Gilber[1], F. Salek [2], A. Mahmoudzadeh Andwari [3], J. Könnö [3] and M. Babaie[1*]

[1]School of Mechanical Engineering University of Leeds. United Kingdom

E-mail: M.Babaie@leeds.ac.uk
Telephone: +(44) 1133430234

[2]Faculty of Technology, Design and Environment, Oxford Brookes University. United Kingdom

E-mail: F.Salek@brookes.ac.uk
Telephone: +(44) 1865483622

[2]Machine and Vehicle Design (MVD), Materials and Mechanical Engineering, Faculty of Technology, University of Oulu. Finland

E-mail: M.Andwari@oulu.fi
Telephone: +(358) 294481621

**Abstract.** Electric vehicles are becoming more prominent due to increasing environmental concerns and legislation in different countries. Unlike vehicles in other sectors, the decarbonization of agricultural vehicles poses unique challenges and considerations, from the diverse range of tasks they perform to the re-mote and sometimes off-grid nature of farm operations. To develop a feasibility study for the electrification of a case study agricultural vehicle equivalent to a diesel-powered 127 kW tractor, AVL Cruise M software was employed to design and verify the powertrain for representative duty cycles. Four agricultural operations with associated drive cycles were selected for this study to assess the powertrain performance. The first selected farming drive cycle was ploughing, being the most common heavy-duty farming operation. The cultivator drive cycle was also selected, with the machinery resistance force profile. Finally, the Standard WHTC for general operation with no machinery attached, and the Modified WHTC representing typical transportation of goods, were considered. The batteries were parameterized and validated using experimental HPPC data for the equivalent circuit model (ECM). The operational range was evaluated by looping each drive cycle and running the model until the state of charge (SOC) dropped from 80% to 20%. The results showed that the chosen battery pack configuration, with a total capacity of 424.8 kWh, successfully achieved the required 5-hour operation time for ploughing. However, for cultivation, it was determined that a large battery pack with a total energy capacity of 1580 kWh would be necessary, and implementation of this larger battery pack would entail some challenges. Furthermore, level 3 charging could serve as a viable solution if cultivation tasks are required for this particular agricultural vehicle.

## 1. Introduction

The urgency of reducing greenhouse gases necessitates a fundamental transformation within the agricultural industry, with farming equipment producing 1.7% of total $CO_2$ emissions in the UK [1]. EU regulations aim to reduce the $CO_2$ emissions from heavy duty vehicles (HDV) by 90% by 2040 [2], with stringent measures targeting the environmental footprint of Non-Road Mobile Machinery engines. A promising solution towards sustainable farming is pure electric tractors (PETs) where the diesel engine is replaced by a battery pack and motor, offering no emissions and enhanced efficiencies [3]. Nonetheless, the principal disadvantage of current PETs is their limited operational range, stemming from the considerable power demands of agricultural tasks and their comparatively modest capacities compared to modern heavy-duty trucks [4]. Furthermore, PETs currently available in the market exhibit notable power deficiencies relative to conventional tractors, prompting market sentiment to suggest tractors surpassing the 200kW power threshold may need hybrid systems [5].

This study will therefore investigate the design of an electric powertrain for a case study tractor, to evaluate the suitability of larger battery pack PETs. An Equivalent Circuit Model (ECM) ensures that the dynamic behaviour of a cell can be appropriately captured, particularly important for vehicles, which have highly varying current demands. Hence, this model was created, validated, and used for developing the powertrain model within the AVL Cruise M software.

## 2. Methodology

Various battery modelling types are available such as electrochemical, data-driven black-box, and equivalent circuit model (ECM). Electrochemical method, such as the simplified electrochemical model, solve partial differential equations simultaneously and provide internal states, but at the cost of higher computational power. This model was successfully improved for higher C-rate applications, such as electric or hybrid vehicles. Data-driven method derives equations from empirical data. These can cause inaccuracies when a dynamic load is applied, which is inappropriate for electric vehicles. The latter model, ECM, is widely used for battery management applications due to its accuracy and ease to parametrize [6]. These models, also named lumped-parameter ECMs, use resistors and capacitors to mimic a battery's behaviour. Different arrangements of ECMs can be made for Li-ion batteries but the 2 RC (resistor-capacitor) model structure have the advantages of simplicity and acceptable accuracy [7]. In this study, a 3RC ECM was built using MATLAB Simulink to achieve better accuracy based on the Hybrid Pulse Power Characterisation (HPPC) data at three different temperatures (5˚C, 25˚C and 45˚C). and the components were parameterised using the Parameter Estimator App to match the HPPC experimental data from the literature [8]. For the purpose of the validation, R-squared value was calculated as suggested in the literature [8,9].

The mathematical modelling of the proposed electric powertrain was performed in AVL Cruise M software and the block diagram is shown in Figure 1. The body and powertrain parameters of the proposed electric tractor were selected for a suitable heavy-duty tractor [10]. 3 Ah cylindrical cells were selected for this study and the battery pack was modelled in AVL using the ECM parameters. The pack was connected in parallel to the INVO-Edu electric drive unit – an electric motor (EM) coupled to a continuously variable transmission (CVT) operating at optimal efficiency [11]. The model utilised four agricultural drive cycles to assess performance: cultivation, ploughing, modified WHTC - pulling a 6000kg trailer - and standard WHTC.

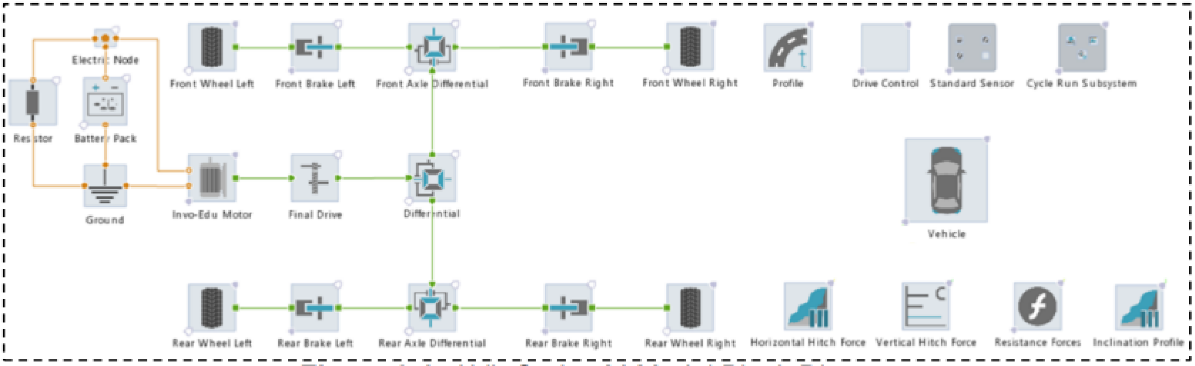
Electric Node
Resistor
Battery Pack
Ground
Front Wheel Left
Front Brake Left
Front Axle Differential
Front Brake Right
Front Wheel Right
Profile
Drive Control
Standard Sensor
Cycle Run Subsystem
Invo-Edu Motor
Final Drive
Differential
Vehicle
Rear Wheel Left
Rear Brake Left
Rear Axle Differential
Rear Brake Right
Rear Wheel Right
Horizontal Hitch Force
Vertical Hitch Force
Resistance Forces
Inclination Profile

**Fig. 1.** AVL Cruise M Model Block Diagram

## 3. Results

Investigations were conducted to find the most accurate ECM and parameterisation method possible while considering the computational demand for higher numbers of RC pairs. This gave a final method of the Simulink Parameter Estimator to create an ECM with 3 RC pairs. Figure 2 shows the complete HPPC test current input, the experimental voltage response, and the simulated voltage response at one temperature (5˚C). This shows that the data fits well for the majority of the HPPC test. Final R-squared values for each of these models were 0.99578, 0.99762 and 0.99684 for 5˚C, 25˚C and 45˚C respectively.

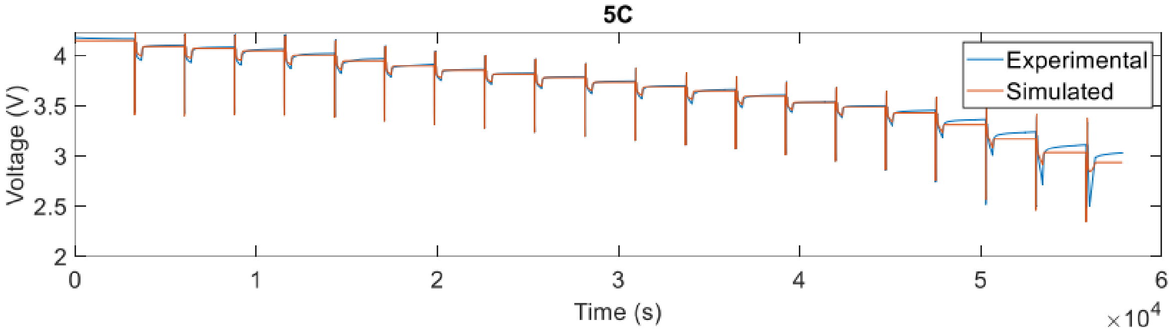

**Fig. 2.** HPPC simulated voltage response and experimental voltage response for 5C

The battery pack size and arrangement were determined in AVL Cruise M software and optimised for the space utilisation within the chassis. The final pack arrangement was 424.8 kWh considering all the space limitations and performance requirements. To assess the suitability of the electric powertrain design four agricultural drive cycle operations were selected for this study. For the verification purpose, the output vehicle velocity profile for each drive cycle from the simulation was compared with the desired drive cycle profile and it was demonstrated for one of cycles (Plough drive cycles) in Figure 3.

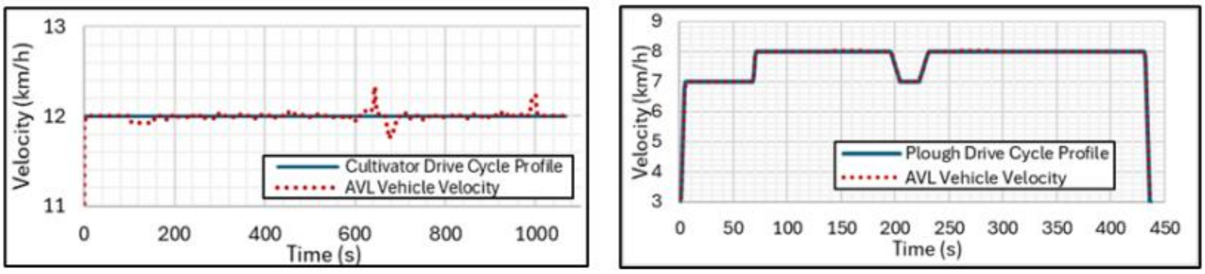

**Fig. 3.** Plough drive cycle and AVL model output vehicle velocity

Then, the total energy output, with the state of charge (SOC) dropping from 80% to 20%, was found to be 239.1 kWh. The cultivator had the highest average power demand at 158.8 kW, with the operating time lasting only 1hr 26min, covering 17.2 km. This was below the typical 5hr operation required in application. A small separate parametric study determined that the necessary battery size to meet this requirement would be about 1580 kWh, requiring an estimated volume of 3.762 $m^3$ - equivalent to raising the cabin height by 2.475 m. As clearly not feasible, heavy cultivation on a single discharge cycle was rejected. However, the ploughing time did exceed the 5-hr standard operational time by 7 minutes, reaching 39.6 km, and thus the powertrain design was deemed suitable for this farming task. It was also noteworthy that the tractor could reach 247.7 km with a 6000kg trailer and even 398.0 km without any equipment attached ï far greater than typical daily farming transport activity (19). It is important to note that the SOC window had been conservatively estimated at around 60% of the total pack capacity and could increase to about 95% for current EVs. Table 1 summarises the PET performance data for each of the selected driving cycles.

**Table 1**. Operational Time, Range and Average Power for each Driving Cycle

| Drive Cycle | Time (hr,min) | Range (km) | Average power (kW) |
|---|---|---|---|
| AVL Cultivator | 1hr 26min | 17.2 | 158.8 |
| AVL Plough | 5hr 7min | 39.6 | 46.4 |
| Modified WHTC - Trailer | 9hr 40min | 247.7 | 24.6 |
| Standard WHTC - No Trailer | 15hr 34min | 398.0 | 15.4 |

For the selected battery size, level 1 charging (36 kW) takes about 8hrs for a full charge with a current of 0.25A per cell. This level would therefore be suitable for overnight charging, minimising the degradation of the battery due to the low C-rate of the charging cycle. Meanwhile, level 3 (240 kW) would allow a farmer to significantly increase the maximum daily operational range of the tractor. For example, in a 12-hour day, a farmer could now plough for two 5hr shifts with an 1hr 36min charging break.

## Conclusion

To investigate the feasibility of agricultural vehicle electrification, a fully electric powertrain was modeled for a case study agricultural vehicle, equivalent to a diesel-powered 127 kW tractor. A mathematical equivalent circuit model (ECM) was developed and validated to accurately simulate the battery cells' behavior. This model was then combined with data for other powertrain components to create a comprehensive model of the case study tractor in AVL software. The results from the AVL Cruise M model demonstrated that the chosen battery pack configuration, with a total capacity of 424.8 kWh, successfully achieved the required 5-hour operation time for ploughing. However, for cultivation, it was determined that a battery pack with higher capacity would be necessary. Implementing this larger battery pack would entail significant chassis redesign. Alternatively, level 3 charging could serve as a viable solution if cultivation tasks are required for such a tractor.

## Acknowledgement

AVL List Gmb H support for proving the simulation tools through their University Partnership Program and Involution Technologies Limited (ITL) support in providing the technical data for INVO electric drive unit is greatly acknowledged.

## References

[1] DoEFRA. Agri-climate report 2021. [Online]. 2021. [Accessed 20 March 2024]. Available from: https://www.gov.uk/government/statistics/agri-climatereport-2021/agri-climate-report-2021#section-1-uk-agriculture-estimatedgreenhouse-gas-emissions

[2] EU, C. Reducing $CO_2$ emissions from heavy-duty vehicles. [Online]. 2024. [Accessed 20 March 2024]. Available from: https://climate.ec.europa.eu/euaction/transport/road-transport-reducing-co2-emissions-vehicles/reducingco2-emissions-heavy-duty-vehicles_en

[3] Li, T., Xie, B., Li, Z. and Li, J. Design and optimization of a dual-input coupling powertrain system: A case study for electric tractors. Applied Sciences. 2020, 10(5), p.1608. 4.

[4] Salek, F., Abouelkhair, E., Babaie, M., Cunliffe, F. and Zare, A. Assessment of the Powertrain Electrification for a Heavy-Duty Class 8 Truck for Two Different Electric Drives. SAE Technical Paper, 2022.

[5] Farmersweekly. Analysis: Is electric technology set to kill off diesel tractors? - Farmers Weekly. [Online]. 2017. [Accessed 25 March 2024]. Available from: https://www.fwi.co.uk/arable/analysis-electric-technology-set-kill-off-dieseltractors

[6] Lai, X., Zheng, Y. and Sun, T., 2018. A comparative study of different equivalent circuit models for estimating state-of-charge of lithium-ion batteries. Electrochimica Acta, 259, pp.566-577.

[7] Nejad, S., Gladwin, D.T. and Stone, D.A., 2016. A systematic review of lumpedparameter equivalent circuit models for real-time estimation of lithium-ion battery states. Journal of Power Sources, 316, pp.183-196.

[8] Salek, F., Azizi, A., Resalati, S., Henshall, P. and Morrey, D., 2022. Mathematical modelling and simulation of second life battery pack with heterogeneous state of health. Mathematics, 10(20), p.3843.

[9] Chicco, D., Warrens, M.J. and Jurman, G., 2021. The coefficient of determination Rsquared is more informative than SMAPE, MAE, MAPE, MSE and RMSE in regression analysis evaluation. Peerj computer science, 7, p.e623.

[10] Deere, J. 6195M | 6M Series | Tractors | John Deere UK & IE. [Online]. 2024. [Accessed 2 December 2023]. Available from: https://www.deere.co.uk/en/tractors/mid/6m-series/6195m/

# Recycling Food and Plastic Residues in Ternary Blends to Environmentally Friendly Power Diesel Engines

J. Tejada-Hernández[1], M. Carmona-Cabello[1], J.M. Herreros[2], M.P. Dorado[1], S. Pinzi[1]

[1]Dep. Physical Chemistry and Applied Thermodynamics, Ed. Leonardo da Vinci, Campus de Rabanales, Universidad de Córdoba, Campus de Excelencia Internacional Agroalimentario, ceiA3, 14071 Córdoba, Spain

E-mail: pilar.dorado@uco.es
Telephone: +(34) 957 21 83 32

[2]School of Engenieering, University of Birmingham, UK

E-mail: j.herreros@bham.ac.uk
Telephone: +(44) 0121 414 3344

**Abstract.** Organic waste contributes significantly to climate change. In Spain, 57% of this waste ends up in landfills, releasing $CO_2$ into the atmosphere. To address this situation, the EU is taking measures to reduce food waste in landfills. In addition, plastic waste poses an environmental problem due to its poor biodegradability. One possible solution is to produce biodiesel from this waste to fuel diesel engines, although it has a low cetane number and high kinematic viscosity. In contrast, eco-fuels produced from the pyrolysis of plastic waste show a lower kinematic viscosity and a higher cetane number than biodiesel based on food waste. This has led to the proposal of a new fuel that combines both components to achieve ideal fuel properties. In addition, the production of fuels from the trans-esterification of food waste (biodiesel) and the pyrolysis of plastic waste (ecofuels) adds value to this waste, supporting the circular economy.

In this study, both fuels are blended with diesel to achieve the optimum ternary blend to be used as an environmentally friendly fuel in commercial diesel engines. To determine the optimum blend, prediction models for kinematic viscosity, cold filter plugging point and cetane number were developed using the Derringer desirability function. These models were experimentally validated, resulting in a ternary blend that optimizes the physicochemical properties. In addition, the optimal blend meets the diesel standards, except for the flash point. In conclusion, the proposed ternary blend has proven to be a suitable fuel for diesel engines, thus preserving the environment within the framework of the circular economy.

## 1. Introduction

One of the most important challenges facing society today is the reduction of plastic consumption and the management of the plastic waste it generates. In Europe alone, 55.3 million tons of plastics were consumed in 2021, of which 90.1% were of fossil origin. Despite the increase observed in the recycling rate of plastic waste both at European level and in Spain (occupying third place with a higher recycling rate at European level), nowadays 36% of waste ends up in Spanish landfills without the possibility of being recycled. The reduction of this waste requires an increase in chemical recycling and energy recovery [1]. Pyrolysis of plastic waste (thermal degradation of the material in the absence of oxygen) is presented as the cleanest alternative, reducing the environmental impact by 50% compared to incineration [2]. The liquid fraction obtained within the pyrolysis products is composed of a mixture of hydrocarbons with characteristics similar to automotive gas oil (C5-C20) [3].

Another significant environmental challenge facing contemporary society is the recovery and reduction of organic food waste. It is estimated that about one third (1.3 billion tons per year) of the food produced worldwide is disposed of in landfills [4]. Recent studies have evidenced the feasibility of converting this waste into state-of-the-art biodiesel with high production yields [5], thus contributing to sustainable development within the framework of the circular economy [6].

In designing and developing new fuels for commercial automotive engines, physicochemical properties such as kinematic viscosity ($\nu$), that directly impact the injection system, or fuel cetane index and calorific value that influence fuel consumption and thermal efficiency, are key.

The objective of this study is to develop a predictive model for optimizing a ternary eco-fuel blend, which consists of pyrolytic oil derived from plastic waste (PP), biodiesel from food waste (FMWE), and ultra-low sulfur diesel fuel (ULSD). These fuel blends support the circular economy by reducing plastic and food waste, transforming these residues into valuable resources. The optimization of critical fuel properties as response variables ($\nu$, CI, and CFPP) has been conducted to design a fuel blend that is anticipated to enhance engine performance and reduce pollutant emissions.

## 2. Materials and methods

For the blends, commercial automotive ULSD (following UNE-EN 590 specifications) including up to 7% biodiesel was acquired. FWME complying with EN 14214 was supplied by Bio-Oils Huelva SLU (Huelva, Spain). PP was provided by Hintes Oil Europa (Almer²a, Spain).

The fuel chemical analysis was carried out according to EN-ISO 590:2022. Density was determined by the hydrometer method, described in ISO 3675. To measure kinematic viscosity ($\nu$), Cannon-Fenske viscosimeter Proton No. 75 (Barcelona, Spain) was used, according to ISO 3104. To obtain the distillation curve, according to ASTM D86 standard, the atmospheric distillation tester OptiDist by PAC (Houston, US) was used. Cetane index (CI) was calculated by the four-variable equation, described in ISO 4264. Cold filter plugging point (CFPP) was measured with automatic analyzer HCP 842 CFPP+ Herzog by PAC (Houston, US), as described UNE-EN 116. Flash point (FP) was measured by Setaflash Serie 3 by Stanhope-Seta (Chertsey, UK), following ISO 2719.

Statgraphics Centurion XVII$^{\text{È}}$ was software used to the statistic elaboration of mixture design of experiments (MODE) and Derringerôs desirability function. A minimum of 10% (v/v) and a maximum of 80% (v/v) were set for each of the three component fuels, since previous work [7] found that a percentage of pyrolytic fuel below 10% in the blend had a negligible effect on combustion pressure, which plays a critical role in engine performance.

## 3. Results and discussion

The values of $\nu$, CI and CFPP differ greatly between eco-fuels and diesel (Table 1). These differences could affect engine performance or the optimal operation of certain systems. Therefore, the limits established by the UNE EN 590 standard were considered in the optimization process.

**Table 1**. Physicochemical properties of pure fuels

| Properties | ULSD | FWME | PP | EN 590:2022 limits |
|---|---|---|---|---|
| Cold filter Pugging point (ÁC) | -16 | -6 | -7 | <-10ÁC for winter fuel |
| Cetane Index | 52.33 | 34.802 | 60.27 | >46 |
| Kinematic Viscosity (mm/s$^2$) | 3.08 | 4.91 | 2.04 | 2-4.5 (mm/s$^2$) |
| Density at 15ÁC (kg/m$^3$) | 830 | 874 | 784 | 820-845 (kg/m$^3$) |

As shown in Fig. 1 a), the cold behavior of the blends improved with the addition of ULSD, reaching up to -13ÁC. As for the IC, an increase directly proportional to the PP content of the mixture was observed (Fig. 1(b)). Therefore, combustion quality is expected to improve as the amount of PP increases. Finally, Fig. 1 c) shows a reduction in $\nu$ when the percentage of PP in the mixture increases, contrary to what occurs when the FWME content increases (kinematic viscosity increases). All the models used for the response surface study were previously validated by means of an analysis of variance (ANOVA), obtaining for all cases a P-value lower than 0.05, which guarantees the suitability of the model to predict the response variable.

The Derringer function method is based on defining a dimensionless desirability function for each response variable ($\nu$, CI and CFPP) to obtain a multiple response optimization. Table 2 shows the limiting values for each of the response variables as well as the objective value for each of the variables.

**Table 2**. Parameters of optimization desirability function

| Response | Low desirability | High desirability | Goal | Factor | Min. value | Max. value |
|---|---|---|---|---|---|---|
| CFPP (°C) | 2.00 | 4.45 | Minimize | ULSD% (v/v) | 10 | 80 |
| CI | 46.00 | 60.10 | Maximize | PP% (v/v) | 10 | 80 |
| ν (mm/s$^2$) | -13.00 | 7.00 | Minimize | FWME% (v/v) | 10 | 80 |

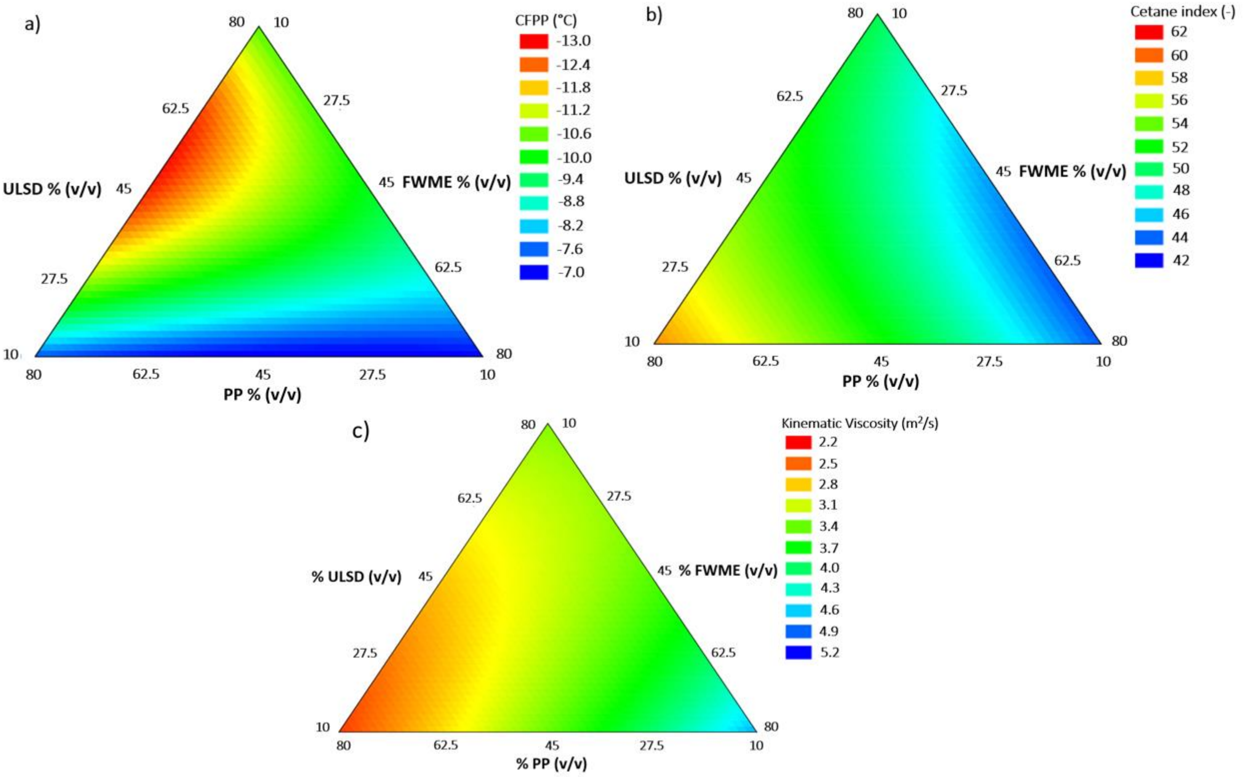

**Fig 1.** Estimated Response Surface Contours of a) Cold filter plugging point(°C); b) cetane index (-); c) kinematic viscosity (m$^2$/s)

The global desirability function was obtained as the product of the individual desirability functions of each response variable. The blend composed of 33% (v/v) ULSD, 57% (v/v) PP and 10% (v/v) FWME provided the highest value of the overall desirability function (0.7307). Therefore, this was considered as the optimal blend. Fig. 2 shows the value of the desirability function. The mixtures in the white area represent an overall desirability value of zero. This means that at least one of the analyzed response variables is outside the range established for its individual desirability function (Table 2). The area of the graph depicted in red contains the blends with the highest desirability.

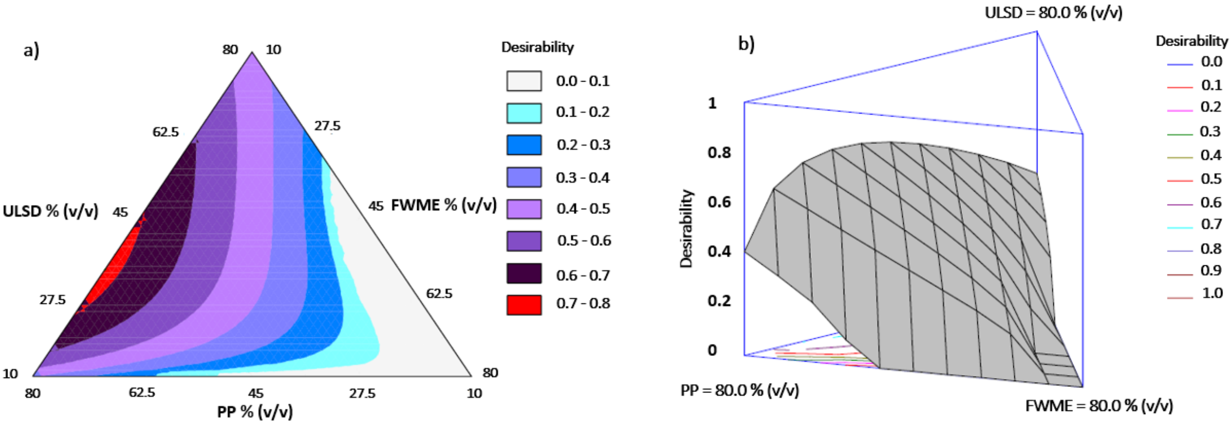

**Fig. 2.** Response Surface for Optimal Blend. a) Estimated Response Surface Contours b) Esimated Response Surface

## Conclusions

The composition of a ternary fuel blend, composed of diesel, biodiesel from food waste oil and pyrolytic oil from plastic waste, has been optimized. The optimization process focused on three key physicochemical properties: kinematic viscosity, cetane index and cold filter plugging point (CFPP).

The prediction of the kinematic viscosity of the blend was fitted to a quadratic model. It was observed that a higher percentage of biodiesel in the blend increased the kinematic viscosity, while a higher proportion of pyrolytic fuel decreased it. The cetane index showed an increase with the presence of pyrolytic fuel, which is beneficial for improving the self-ignition of the fuel. The CFPP was also fitted to a quadratic model, although the effect of renewable fuels on this parameter was not evident initially, as the CFPP of both fuels is very similar. Using the quadratic models obtained, an optimization was performed using the Derringer desirability function, with the objective of obtaining a blend that maximized the cetane index and minimized both kinematic viscosity and CFPP.

The results of the optimization of the ternary mixture were experimentally validated in the laboratory. The optimal blend complies with the UNE EN 590 standard, except for the flash point. It shows a slight increase in calorific value and cetane number compared to diesel. However, given that the mixture's flash point is below the lower limit established by the standard, it could pose problems in the handling and storage of the fuel.

It is concluded that the combination of fuels derived from plastic and food waste constitutes a viable alternative to replace fossil fuels in diesel engines. A fuel blend with a high content of fuels from waste is proposed, thus promoting a circular economy approach.

## References

[1] PlasticEurope, “Plastics – the Facts 2022,” 2022.

[2] H. Jeswani et al., “Life cycle environmental impacts of chemical recycling via pyrolysis of mixed plastic waste in comparison with mechanical recycling and energy recovery,” Sci. Total Environ., vol. 769, 2021, doi: 10.1016/j.scitotenv.2020.144483.

[3] D. Damodharan, B. Rajesh Kumar, K. Gopal, M. V. De Poures, and B. Sethuramasamyraja, “Utilization of waste plastic oil in diesel engines: a review,” Rev. Environ. Sci. Biotechnol., vol. 18, no. 4, pp. 681–697, 2019, doi: 10.1007/s11157-019-09516-x.

[4] Food and Agriculture Organization of the United Nations, “Pérdida y desperdicio de alimentos | FAO | Organización de las Naciones Unidas para la Agricultura y la Alimentación,” 2021.

[5] M. Carmona-Cabello, I. L. García, J. Sáez-Bastante, S. Pinzi, A. A. Koutinas, and M. P. Dorado, “Food waste from restaurant sector – Characterization for biorefinery approach,” Bioresour. Technol., vol. 301, no. January, p. 122779, 2020, doi: 10.1016/j.biortech.2020.122779.

[6] HLPE, “Los biocombustibles y la seguridad alimentaria. Un informe del Grupo de alto nivel de expertos en seguridad alimentaria y nutrición del Comité de Seguridad Alimentaria Mundial,” 2013.

[7] M. Karagöz, Ü. Ağbulut, and S. Sarıdemir, “Waste to energy: Production of waste tire pyrolysis oil and comprehensive analysis of its usability in diesel engines,” Fuel, vol. 275, p. 117844, Sep. 2020, doi: 10.1016/J.FUEL.2020.117844.

# Combustion and Emissions of Unblended Fast Pyrolysis Oils and Blends with HVO and EN590-B0 Diesel in a Heavy-Duty Diesel Engine

S. Sisodiya[1], A. Kittoe[2], C. Webb[2], N. Ladommatos[1] and P. Hellier[1]

[1]UCL Mechanical Engineering. Roberts Engineering Building, University College London, Torrington Place, London WC1E 7JE, United Kingdom.
E-mail: sunita.sisodiya.20@ucl.ac.uk
Telephone: +44(0)2076792850 Ext.32850

[2]bp plc, Fuels and Lubricants Research, Technology Centre, Whitchurch Hill, Pangbourne, Reading RG8 7QR, United Kingdom.

E-mail: amy.kittoe@castrol.com
Telephone: +44(0)2034 015630

## Abstract

Heavy-duty transportation is a sector that requires urgent decarbonisation due to significant $CO_2$ emissions from burning of fossil fuels, particularly road freight which accounts for the majority of transport emissions within the European Union [1]. Lower carbon fuels, such as fast-pyrolysis oil (FPO) and hydrotreated vegetable oil (HVO), are regarded as promising drop-in fuels that are compatible with existing infrastructure and vehicular hardware. Fast pyrolysis technology converts a wide variety of inedible biological feedstocks into bio-oil. Feedstocks can range from lignocellulosic biomass sourced from agricultural or forestry waste, making pyrolysis oils second generation biofuels that, in contrast to first generation biofuel, do not compete with global food security. Additionally, the impact of future transportation fuels on global air quality requires further investigation.

Bio-oil can be upgraded into renewable fuel via sequential processing stages that improve fuel properties. However, additional processing can consequently increase energy and resource usage that are already otherwise limited. Evaluating the feasibility of less refined FPO as drop-in fuels through investigating combustion characteristics and emissions formation could therefore reduce lifecycle greenhouse gas emissions.

In the present study, two commercially available grades of FPO, stabilised deoxygenated pyrolysis oil (SDPO) and a more refined hydrotreated pyrolysis oil (HPO) were tested in a heavy-duty diesel engine both as pure components and 50% blends (volume/volume) with two different base fuels: HVO and EN590 petroleum-derived diesel (B0). The combustion characteristics and pollutant emissions of the fuels was investigated at constant speed and load in a six-cylinder Volvo 7.7L d8k compression-ignition engine specially modified for prototype fuels research (Figure 1) [2]. Experiments were undertaken at constant start of injection (SOI) and constant start of combustion (SOC) conditions to distinguish between direct chemical fuel effects and those arising via the influence of combustion phasing.

Test fuels were supplied to the research cylinder via an ultra-low volume fuel system, described previously by Hellier (2013) [3]. The semi-isolated fuel delivery system allowed for operation of the research cylinder on test fuels available at only low quantities or of properties significantly beyond current fuel specifications. In-cylinder pressure during combustion was measured by a Kistler type 6052C high temperature pressure sensor relative to a crankshaft encoder of resolution 0.1 crank angle degrees (CAD). Integrated data acquisition and control of the experimental facility was developed in-house with a custom LabView (National Instruments) code [2]. Apparent net heat release rates were calculated from in-cylinder pressure data using a single zone model and assuming no heat transfer following the method outlined by Heywood (2018) [4]. Gaseous exhaust emissions were measured using a Horiba MEXA 9100 HEGR, including nitrous oxides (NOx). Particle size distributions (5-1000 nm) was measured by a Cambustion DMS500 fast particle analyser (Figure 1).

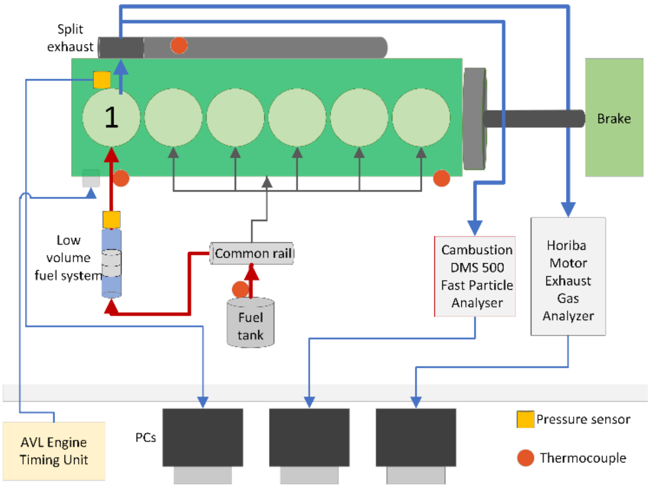
Split exhaust
1
Brake
Low volume fuel system
Common rail
Fuel tank
Cambustion DMS 500 Fast Particle Analyser
Horiba Motor Exhaust Gas Analyzer
AVL Engine Timing Unit
PCs
Pressure sensor
Thermocouple

*Figure 1: Schematic of heavy-duty engine test facility*

Both FPO displayed stable combustion as neat fuels at constant SOC injection timing. However, the less refined SDPO did not ignite at constant SOI injection timing. Both FPO increased the duration of ignition delay (ID), with HPO exhibiting a shorter ID than SDPO (Figure 2). The 50% (v/v) blend of HPO/HVO exhibited a similar ID to that of B0 reference diesel. Addition of 50% (v/v) of HPO to HVO increased the duration of ignition delay compared to neat HVO and resulted in an ID closer to that of B0 reference diesel in agreement with Han *et al* [5].

Additionally, the SDPO/B0 50% blend and unblended HPO also exhibited a similar ID. The less refined SDPO blended with B0 exhibited an appreciably longer ID than that of the HPO and B0 blend, but when SDPO was blended with HVO an approximately equivalent ID as that of the HPO/ B0 blend was observed. This is due to HVO exhibiting a shorter ID than B0 and offsetting the lower ignition quality of SDPO relative to HPO.

Both FPO produced significantly higher apparent heat release rates compared to that of the HVO and B0 base fuels, with the less refined SDPO producing the highest apparent peak heat release rate (Figure 3). Similarities in ID trends were reflected in the heat release profiles such as 100% HPO and 50% SDPO/B0 as well as 50% HPO/ HVO and 100% B0. A longer ID resulted in a higher premix burn fraction for the FPO blends, consistent with previous observations for HPO addition [6]. Conversely, 100% HVO and 50% HVO/B0 appeared to exhibit a larger mixing-controlled combustion relative to the premix burn fraction.

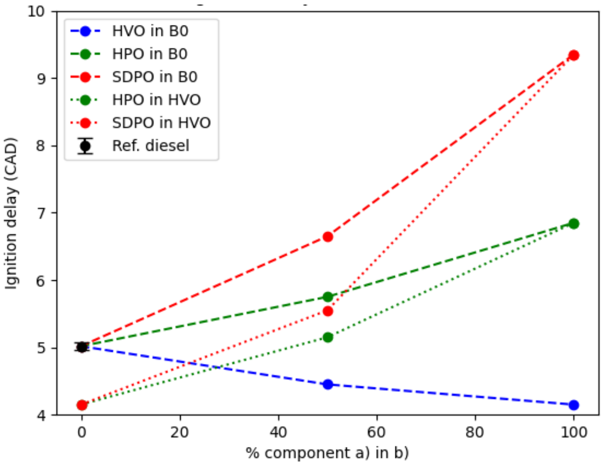

*Figure 2: Ignition delay for unblended FPO and FPO blends at const. SOC*

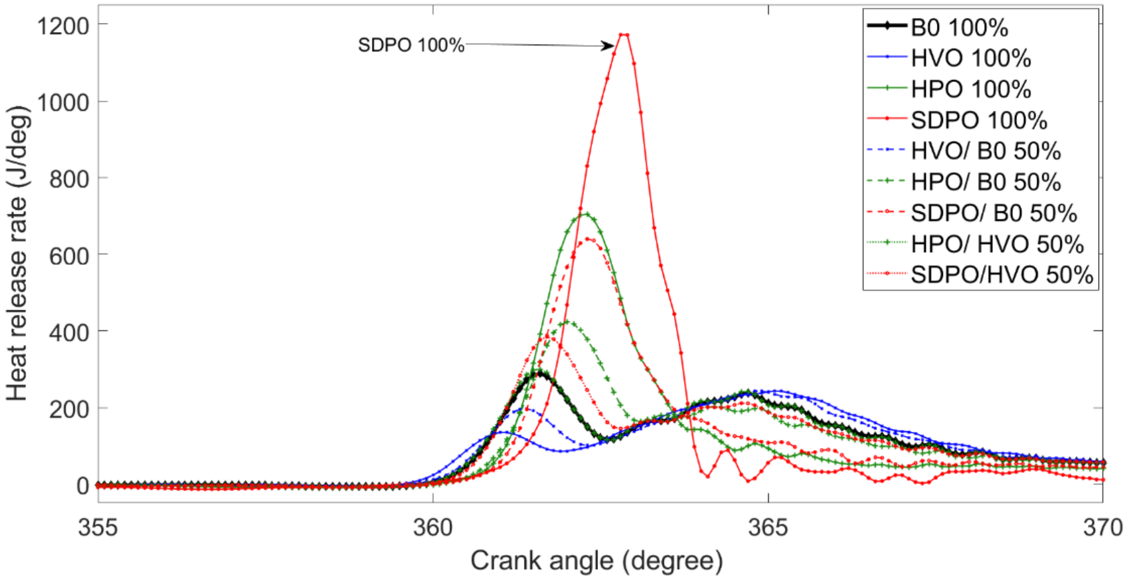

*Figure 3: Apparent heat release rates for unblended FPO and FPO blends at const. SOC*

FPO addition appeared to increase NOx emissions which is likely attributed to higher maximum in-cylinder temperatures (Figure 4). HVO addition to both FPO and B0 resulted in reduced NOx emissions. Similar maximum in-cylinder temperatures were determined for the HPO/HVO blend, 100% HVO and B0 reference diesel. However, despite the similar magnitudes of calculated in-cylinder maximum global temperature NOx levels for these fuels appeared to vary significantly. Maximum in-cylinder temperatures may have been reached at different times such that for B0, this was determined by the premix burn fraction and for HVO, the diffusion-controlled fraction. Therefore, in the case of 100% HVO, NOx formation may have occurred later and within a shorter period prior to the expansion stroke in which in-cylinder temperature reduces.

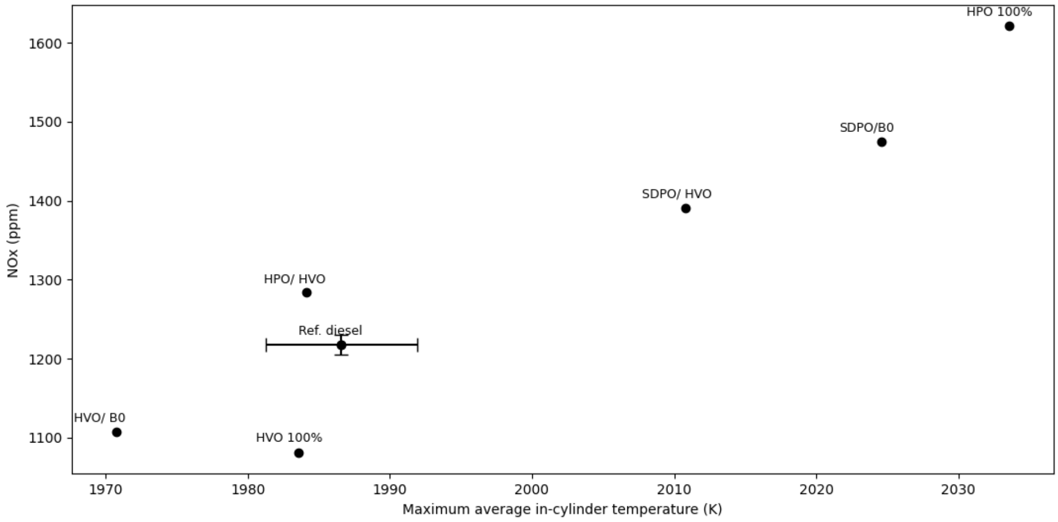

*Figure 4: NOx emission for unblended FPO and FPO blends at const. SOC*

Both FPO increased total particle number (PN), with the less refined FPO, SDPO, emitting the highest total PN (Figure 5). Similar total PN was observed for 50% HPO/B0 and 50% SDPO/HVO blends. However, the PN size distribution of SDPO/HVO was shifted towards smaller particles compared to 50% HPO/B0 (Figure 6). All fuels produced a peak in the ultrafine region (<100nm). However, both FPO exhibited larger peaks, representing an increase in the number of ultrafine particles. Increased PM emissions have previously been reported for HPO, potentially due to the presence of aromatic species [7]. SDPO as a 50% blend produced peaks of similar magnitude regardless of the base fuel used. Conversely, the peak for 50% HPO blend with HVO was significantly lower than that observed for the 50% HPO/ B0 blend, resulting in a PN size distribution comparable to that of 100% B0.

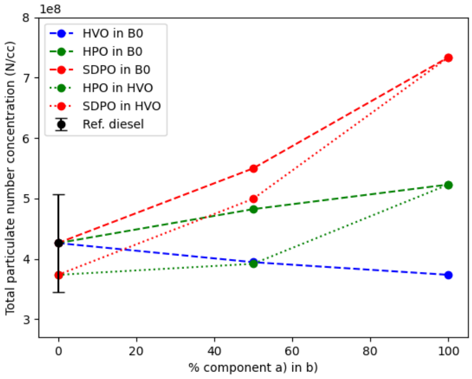

*Figure 5: Total particle number concentration for unblended FPO and FPO blends at const. SOC*

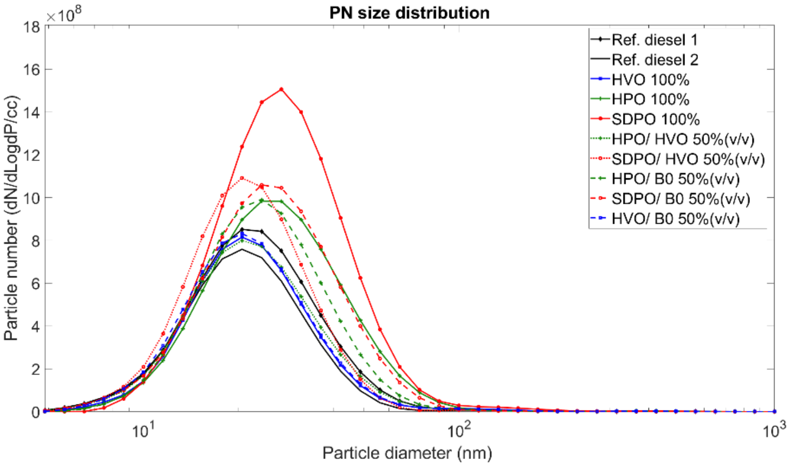

*Figure 6: Particle number size distribution for unblended FPO and FPO blends at const. SOC*

In conclusion, both FPO displayed stable combustion as neat fuels. However, unblended HPO and more so, SDPO exhibited longer durations of ignition delay, higher apparent heat release rates, increased NOx emission compared to B0 and HVO. At 50% blend level, similar trends were observed in the combustion characteristics and particle number size distributions of 100% HPO and 50% SDPO/B0 in addition to 50% HPO/ HVO and 100% B0. Both grades of FPO offer potential as drop-in fuels with HVO and B0, subject to further investigation to determine optimum blend levels.

## References

[1] EEA. (2022). Reducing greenhouse gas emissions from heavy-duty vehicles in Europe. doi:10.2800/066953

[2] Deehan, T. (2023). Investigating the combustion and emission characteristics of lignocellulosic derived future fuels with novel chemical reactivity in a heavy-duty compression ignition engine.

[3] Hellier, P. R. (2013). The Molecular Structure of Future Fuels.

[4] Heywood, J. (2019). Internal combustion engines fundamentals - 2nd edition, McGraw-Hill Education.

[5] Han, J., Wang, Y., Somers, L. M. T., van de Beld, B. (2022). Ignition and combustion characteristics of hydrotreated pyrolysis oil in a combustion research unit. Fuel, 316, 123419. https://doi.org/10.1016/J.FUEL.2022.123419

[6] Han, J., Somers, L. M. T., van de Beld, B. (2024). Experimental investigation performance and emission of hydrotreated pyrolysis oil in a heavy-duty engine with EGR. Fuel Processing Technology, 255. https://doi.org/10.1016/j.fuproc.2024.108061

[7] Han, J., Somers, L. M. T., van de Beld, B. (2023). Combustion and emission characteristics of hydrotreated pyrolysis oil on a heavy-duty engine. Fuel, 351, 128888. https://doi.org/10.1016/J.FUEL.2023.128888

# Design of Experiments Optimized Combustion and Emissions for OME$_x$-Diesel Blends on a Heavy-Duty Engine

Zhongcheng Sun[1], Harold van Beers[1], Michel Cuijpers[1], Bart Somers[1], Noud Maes[1]

[1]Department of Mechanical Engineering, Eindhoven University of Technology, Eindhoven 5600 MB, Netherlands

E-mail: z.c.sun@tue.nl

**Abstract.**

Oxymethylene dimethyl ethers (OME$_x$) as a renewable bio- or E-fuel provides huge potential for simultaneous soot and NO$_x$ reduction on heavy-duty engines. The optimization of combustion and emissions of OME$_x$-diesel blends has been investigated on a single-cylinder heavy-duty research engine with different operating strategies using the design of experiments (DOE) method. An engine speed of 1425 RPM with 30% load was targeted because of the relatively high specific particulate matter (PM) emissions with regular B7 diesel. The response surface of emissions based on experimental data indicates that PM is strongly correlated to OME$_x$ content, satisfying EU VI regulations without after treatment when OME$_x$ content surpasses 17% at a calibrated reference condition. While OME$_x$ concentration has a negative effect on NO$_x$, these emissions can be significantly reduced with increasing exhaust gas recirculation (EGR) ratios. Like PM emissions, CO and unburned hydrocarbon are also effectively reduced with OME$_x$ addition. The required injection duration at a fixed load increases with OME$_x$ addition because of its reduced lower heating value. This is accompanied by a diminished interval between ignition delay and the end of injection timing, limiting the amount of mixing before ignition and resulting in a reduced premixed heat release peak. In general, the ignition delay itself becomes shorter with increasing OME$_x$ content because of its higher reactivity. Still, at this relatively low-load condition, the burn duration is inversely proportional to OME$_x$ addition, and independent of injection duration because combustion is predominantly premixed. Because of these reasons, the combustion phasing (CA50, the crank angle where 50% of the heat has been released) is advanced with increasing OME$_x$ at this operating point.

## 1. Introduction

Global climate change has emerged as enormous challenges in recent years. The most promising approach for the transportation sections in the short term is to adopt cleaner fuels to achieve substantial reductions in emissions. OME$_x$ is characterized by a lack of C-C bonds and high oxygen content, effectively preventing soot formation during combustion. It also provides potential to break the soot-NO$_x$ trade-off by employing high EGR. Considering the compliance with EN590 standards, OME$_x$ is selected to conduct engine experiments without major modifications.

OME$_x$/diesel blends exhibit distinguished engine performance differences in previous literatures, considering the distinct engine specifications and tested conditions [1]. This work is aimed at investigating combustion and emissions characteristics of a wide range of OME$_x$ ratios in a heavy-duty test engine with variations in EGR and injection timing at low load using a DOE approach. This targets further understanding of multifactor engine operating strategies and their associated interactions in the complex environment. Finally, an effective operational strategy is proposed to achieve compliance with European emissions limits.

## 2. Experimental approach

Experiments are conducted on a modified single-cylinder research engine, based on a PACCAR MX13 heavy-duty engine, described in previous research [2]. The displaced volume of the engine is 2.15 L, with a bore diameter of 130 mm and a stroke length of 162 mm, and the compression ratio is 17.2. The engine schematic diagram is depicted in Fig.1. This engine features a common rail system equipped with a Delphi DFI21 injector. Note that the oxygenated OME$_x$ fuel used in this study consists of 47.65% OME$_3$, 29.7% OME$_4$, 16.98% OME$_5$, and 5.67% OME$_6$. The data is measured with a resolution of 0.2 CAD for 200 consecutive tested cycles. Exhaust gas emissions are recorded by a Horiba MEXA 7100 system. Additionally, the PM is quantified using an AVL 415s and an EEPS spectrometer TSI 3090. The test matrix is established using a DOE approach, where the tested factors consist of OME$_x$ content (8.1~11.5 bTDC), EGR ratio (19.3~52.9%), and injection timing (8~92 vol%), as shown in Fig. 2. The axial point α is equal to 1.68.

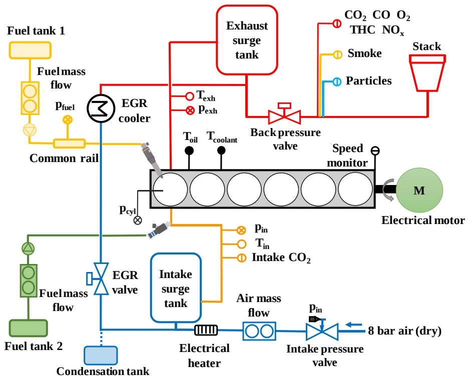
Fuel tank 1
Fuel mass flow
$p_{fuel}$
EGR cooler
Common rail
Exhaust surge tank
$CO_2$ CO $O_2$
THC $NO_x$
Smoke
Particles
Stack
$T_{exh}$
$p_{exh}$
Back pressure valve
$T_{oil}$ $T_{coolant}$
Speed monitor
M
Electrical motor
$p_{cyl}$
$p_{in}$
$T_{in}$
Intake $CO_2$
EGR valve
Intake surge tank
Fuel mass flow
Fuel tank 2
Air mass flow
$p_{in}$
8 bar air (dry)
Electrical heater
Intake pressure valve
Condensation tank

**Fig. 1.** MX13 heavy-duty engine schematic.

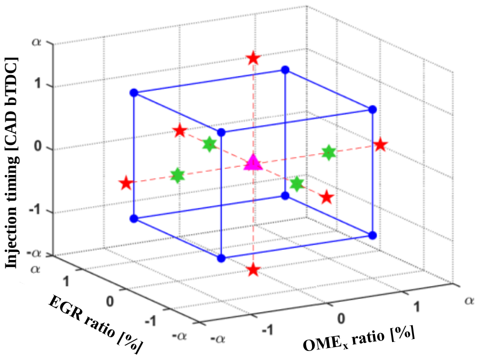
Injection timing [CAD bTDC]
α
1
0
-1
-α
EGR ratio [%]
OMEx ratio [%]

**Fig. 2.** Schematic diagram of the test matrix.

## 3. Results

### 3.1 Combustion characteristics analysis

The in-cylinder pressure trace and apparent rate of heat release (aROHR) of different $OME_x$ ratio blends are depicted in Fig. 3, at the center test point of the DOE matrix. The corresponding increased injection current signals with increasing $OME_x$ content are presented at the bottom of this figure as well, due to the reduced LHV. Shorter ignition delays are evident with higher $OME_x$ ratios, attributed to the elevated fuel reactivity. Despite the reduced LHV of the blends, higher heat release values are realized in the diffusive combustion phase with longer injection duration, elevating maximum pressures.

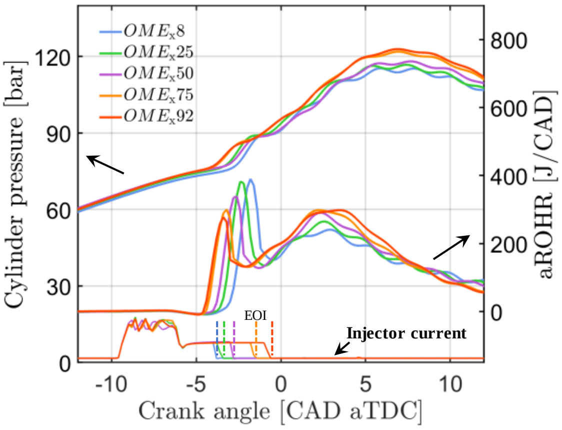

**Fig. 3.** Combustion characteristics comparison between different $OME_x$ content at the center test point (36.1% EGR & 9.8 CAD bTDC injection timing).

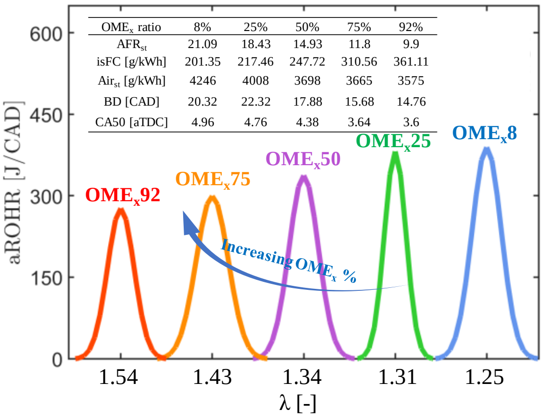

| $OME_x$ ratio | 8% | 25% | 50% | 75% | 92% |
|---|---|---|---|---|---|
| $AFR_{st}$ | 21.09 | 18.43 | 14.93 | 11.8 | 9.9 |
| isFC [g/kWh] | 201.35 | 217.46 | 247.72 | 310.56 | 361.11 |
| $Air_{st}$ [g/kWh] | 4246 | 4008 | 3698 | 3665 | 3575 |
| BD [CAD] | 20.32 | 22.32 | 17.88 | 15.68 | 14.76 |
| CA50 [aTDC] | 4.96 | 4.76 | 4.38 | 3.64 | 3.6 |

**Fig. 4.** Premixed heat release fits (Gaussian) for the blends at the center test point as function of global ə. Corresponding parameters are given in the inset.

The premixed combustion peaks are attenuated with $OME_x$ addition, better illustrated by the fitted Gaussian profiles in Fig. 4. This attenuation is ascribed to the reduced ignition delay with $OME_x$ addition resulting in less time for air-fuel mixing, coupled with the reduced LHV of the blends. However, this does not imply larger fuel-rich regions, despite the extended injection duration with $OME_x$ addition. In fact, the in-cylinder excess air-fuel ratio (ə) is increased with $OME_x$ addition because of its high oxygen content, leading to a lower stoichiometric air-fuel ratio ($AFR_{st}$, inset table in Fig. 4). The required stoichiometric air mass ($Air_{st}$, obtained via $AFR_{st}$ and the indicated specific fuel consumption, isFC), of $OME_x92$ is reduced by 15.8% when compared to $OME_x8$. Therefore, $OME_x$ fuel promotes more reactive mixtures while preventing excessive rich-fuel conditions, consistent with simulations in literature [3].

### 3.2 Global emissions analysis

Fig. 5 provides a comprehensive evaluation map, which illustrates the percentual differences in emissions for PM, $NO_x$, and CO, compared to diesel at the tested conditions. Injection timing is optimized at 10.5 CAD bTDC. Notably, the blends with $OME_x$ exhibit significant potential for soot reduction compared to diesel (black isoline with zero difference) across EGR variations. There is even a substantial region where engine-out soot emissions fall below Euro VI regulations. With EGR ratios above 36.1%, soot emissions start to increase. The $NO_x$ reduction mainly depends on EGR, while the $OME_x$ ratio has a minor negative impact, predominantly observed when EGR is below 31%. Noticeable, the $NO_x$ emissions satisfy with Euro V regulations EGR is over 36%, as indicated by the light-blue gradients in vertical direction. Thus, it becomes possible to mitigate the conventional soot-$NO_x$ trade-off by implementing $OME_x$-diesel blends, based on a high EGR tolerance for $OME_x$ fuel without observed PM emissions as mentioned above. Additionally, the CO emission also complies with EU VI regulations. Overall, the engine-out emission profiles comply with EU regulations (PM within EU VI and $NO_x$ within EU V) when the $OME_x$ ratio is above 24.1% and EGR surpasses 37.2%, as indicated by the magenta star. Remarkably, THC emission is not specifically highlighted on this map, as it falls within the Euro VI and is considerably lower than that of diesel. Finally, the soot-$NO_x$ trade-off relationship for the tested fuels with EGR variations is demonstrated in Fig. 6. The addition of $OME_x$ fuel again highlights its significant potential to break the traditional soot-$NO_x$ trade-off relationship.

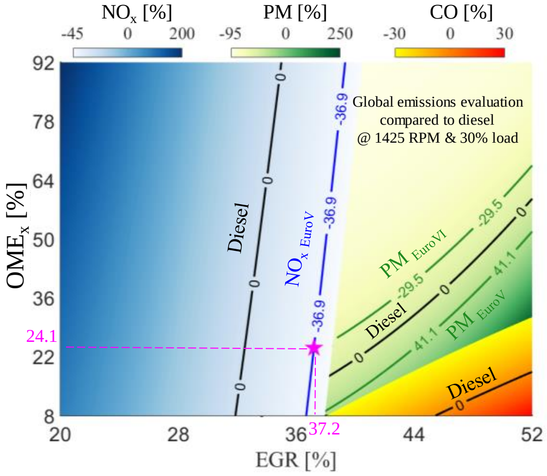

**Fig. 5.** Response surface with percentual differences of PM, $NO_x$, and CO, compared to that of diesel, as a function of $OME_x$ & EGR ratios. Injection timing is set to 10.5 CAD bTDC.

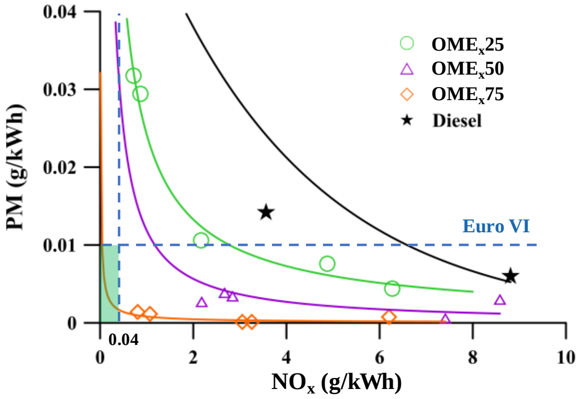

**Fig. 6.** Soot-$NO_x$ trade-off relationship for the tested fuels with EGR variations.

## Conclusions

The premixed combustion heat release peak is attenuated with $OME_x$ addition, ascribed to the reduced LHV, as well as the shorter ignition delay limiting mixing prior to ignition. Conversely, the overall excess air-fuel ratio increases with $OME_x$.

$OME_x$ content plays a significant role in soot reduction when EGR is below 36.1%, while soot emissions rise steeply above this value. While $NO_x$ emissions increase with $OME_x$ addition, they are efficiently curbed by higher EGR ratios within the operational range. $OME_x$ significantly contributes to the reduction of CO emissions across the studied parameters.

A comprehensive global emissions map is created, which suggests that $OME_x$ has great potential to break the soot-$NO_x$ trade-off relationship encountered with diesel combustion, complying with emission regulations when the $OME_x$- and EGR-ratio are above 24.1% and 37.2% respectively, with an injection timing of 10.5 CAD bTDC.

## References

[1] Omar Awad, et al. Overview of polyoxymethylene dimethyl ether additive as an eco-friendly fuel for an internal combustion engine: Current application and environmental impacts. Science of the total environment, 715, pp. 136849, 2020.

[2] Z. Sun, et al. The impact of exhaust gas recirculation calibration on emissions and efficiency with GTL and GTLB30 fuels on a heavy-duty diesel engine, submitted for review.

[3] J. García-Oliver, et al. A numerical investigation of the performance of oxymethylene ethers blended with fossil diesel to reduce soot emissions in compression ignition engines, Fuel, 324, pp.124768, 2022.

# Impact of a Neat 100% Renewable Diesel Fuel on Performance and Regulated Pollutant Emissions of a Catamaran for Passenger Transportation toward the Atlantic Islands National Park (Spain)

R. Garc²a-Contreras[1], J. A. Soriano[1], L. S§nchez[1], O. Armas[1], F. Oliva[2], M.D. C§rdenas[2].

[1]Universidad de Castilla-La Mancha, Campus de Excelencia Internacional en Energ²a y Medioambiente, Escuela de Ingenier²a Industrial y Aeroespacial de Toledo, Real F§brica de Armas, Edif. Sabatini, Av. Carlos III, s/n, Toledo, 45071, Spain.

E-mail: octavio.armas@uclm.es
Telephone: +(34) 926 29 54 62

[2]Repsol Tech Lab. Spain.

E-mail: mdcardenasa@repsol.com
Telephone: +(34) 917 53 80 00

**Abstract.** The use of 100% renewable fuels, as drop in fuel, in different propulsion systems is a reasonable alternative to achieve the sustainability of means of transportation. In this case, a renewable fuel Hydrotreated Vegetable Oil (HVO) compared to a fossil diesel fuel are tested. This experimental work was done on a catamaran, with capacity to transport up to 250 passengers, along the Vigo estuary, on the Cangas-Vigo-Cies Island marine circuit in Galicia (Spain), within an environmentally protected geographical area. The catamaran, powered by compression ignition engines which complies the International Marine Organization TIER II emission standard, was instrumented with a Horiba-OBS ONE analysers for measuring regulated gaseous emissions and with a diagnosis tool, developed by engine manufacturer, for registering different parameters from the Electronic Control Unit. The obtained results show excellent performance with HVO fuel compared to Diesel fuel. In most of cases, slight direct reduction of carbon dioxide emissions was observed when the renewable fuel is used. Hydrocarbons and nitrogen oxides specific emissions produced by HVO fuel were always lower than those produced by Diesel fuel, with around 35 and 18% average reduction respectively. Also, around 35% average reduction of carbon monoxide was observed. Obtained results show the potential of the 100% renewable fuel to be used even in an engine without modern aftertreatment devices.

## 1. Introduction

The use of 100% renewable fuels is a tangible reality that is reaching different means of land transportation [1], agricultural machinery [2] or even in more basic studies in test conditions that reproduces the operation of unmanned aerial vehicles [3]. In the first of the works, the effect on performance and regulated pollutant emissions on an urban passenger bus is evaluated and where a clear positive effect of the use of HVO fuel was observed. In the second of the works, results of the use of this same type of fuel obtained with two agricultural tractors of different make and models are compared, also observing a positive effect compared to fossil diesel fuel. Finally, in the third of the works it is revealed that this type of renewable fuel behaves in a similar way during the injection process in the engine.

The present work describes the comparative experimental work done on a marine vessel (catamaran for 250 passengers), equipped with Diesel engines which meet the International Marine Organization (IMO) TIER II. This vessel is used for the touristic transportation along the Vigo estuary between three ports: Cangas do Morrazo, Vigo and Cies Island, these last as part of the National natural park Atlantic Islands in the south coast of Galicia community, Spain.

## 2. Experimental work

### 2.1 Test vessel and engine

A catamaran managed by the shipowner NABIA, was used as test marine vessel. Its propulsive system equips 2 MAN turbocharged Diesel engines. Main characteristics of the catamaran and its engines are shown in Table 1.

**Table 1**. Main characteristics of the vessel and engine used for testing.

| Vessel | | Engine | |
|---|---|---|---|
| Definition | Characteristic | Definition | Characteristic |
| Type | Catamaran | Make | MAN |
| Name | Piratas de Cíes | Model | D2862LE433 |
| Marine Mob. Serv. Identity | 224924990 | Type | Turbocharged (HP EGR) |
| Callsign | EAXV | Inyection / Fuel | Common rail / Diesel |
| Business group | Acuña group | Cylinders / Arrangement | 12 / V |
| Shipowner | NABIA | Diameter (mm) | 128 |
| Construction year | 2010 | Stroke (mm) | 157 |
| Length (m) | 25.8 | Displacement (L) | 24.24 |
| Beam (m) | 8.5 | Rated power (kW) | 1324@2300 min$^{-1}$ |
| Dry weight (kg) | 63000 | Rated torque (Nm) | 6020@1200...2100 min$^{-1}$ |
| Passengers + crew | 250 + 5 | Compression ratio | 17:1 |
| Flag | Spanish | Emission standard | IMO Tier II |

### 2.2 Test fuels

In Table 2 are presented the main properties of fuels tested. Both fuels were supplied by REPSOL Tech Lab. As mentioned, the catamaran was firstly tested with Diesel fuel (EN5950) and later with neat 100% renewable hydrotreated vegetable oil (HVO) (EN 15490).

**Table 2**. Main properties of tested fuels.

| Property | Fuel | |
|---|---|---|
| | Diesel (EN590) | HVO (EN15940) |
| Density @ 15°C & 1 bar (kg/L) | 0.83 | 0.78 |
| H/C | 1.927 | 2.06 |
| O/C | 0.016 | 0 |
| Low heating value (kJ/kg) | 43500 | 43950 |
| Low heating value (kJ/L) | 36105 | 34281 |
| Cetane number | > 49 | > 70 |

### 2.3 Test routes, experimental tools, and procedure

The catamaran was tested along four routes. The order of testing was: 1) Cangas do Morrazo – Vigo (~25 min), 2) Vigo – Cies Island (–40 min), 3) Cies Island – Vigo (~40 min) and 4) Vigo – Cangas do Morrazo (~25 min). These four routes were tested, at least, three times a day and four days a week with each fuel. Figure 1 shows three repetitions of each route tested. The tests always began around 08.30 hours and finished around 18.00 hours. In any case, it is important to remark that the tests were carried out during the actual work of the vessel, which was conditioned by compliance with schedules for the transfer of tourists and the coordinated operation with vessels from other companies on arrival and departure of each port. A portable emission measurement system (PEMS) Horiba OBS One was used for measuring concentration of gaseous regulated emissions such as total hydrocarbons (THC), carbon monoxide (CO), nitrogen oxides (NOx) and carbon dioxide ($CO_2$). With an integrated global positioning system, the catamaran speed at the sea level was registered. The sondes of the Horiba OBS One were connected to the exhaust pipe, after the turbocharger of the engine. For registering different engine operating parameters such as engine throttle position (%), engine speed (min$^{-1}$), intake pressure (bar) and temperature (ºC), and volumetric fuel flow rate (L/h), a diagnosis tool, supplied by the original engine manufacturer, was used. This tool was connected to the electronic control unit (ECU) of the engine tested. In both cases, the Horiba OBS One analyzer and the diagnosis tool were connected to only one of the engines, the catamaran port side engine.

According to the time evolution of both, the engine, and emissions raw data, registered from the ECU and PEM respectively, was possible to identify three types of time periods of work: Departure (Initial), characterized by a progressive increase of engine parameters; Journey (Intermediate), characterized by an engine steady state work and Arrival (final), characterized by a progressive decrease of engine parameters. This work distribution was similar between the test routes.

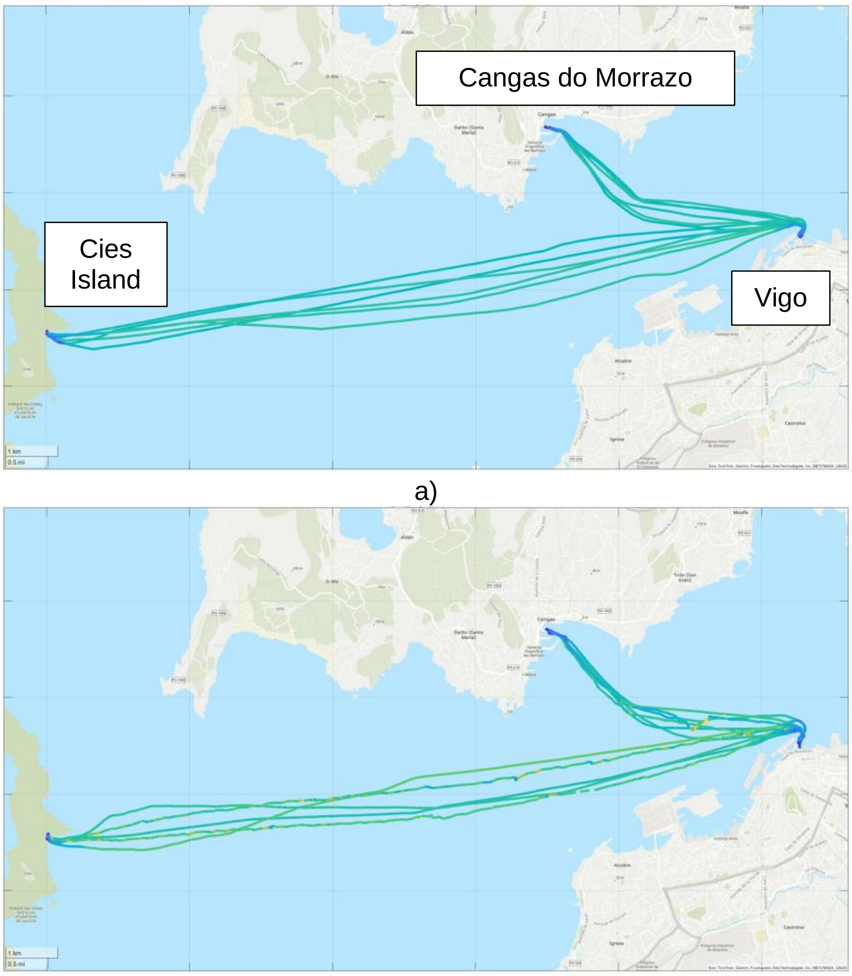

a)

b)

**Fig. 1.** Routes tested along the Vigo estuary with both fuels, a) Diesel fuel, b) HVO fuel.

## 3. Main results

Figure 2 shows the relative differences observed when testing both fuels in the marine vessel during the Journey (Intermediate) part of the different routes tested. The obtained results show excellent performance with HVO fuel compared to Diesel fuel. Those blue colour bars are positive for HVO fuel. In most of cases, slight direct reduction of $CO_2$ emissions was observed when the renewable fuel is used. THC and NOx specific emissions produced by HVO fuel were always lower than those produced by Diesel fuel, with around 35 and 18% average reduction respectively. Also, around 35% average reduction of CO was observed. Obtained results show the potential of the 100% renewable fuel to be used even in an engine without modern aftertreatment devices.

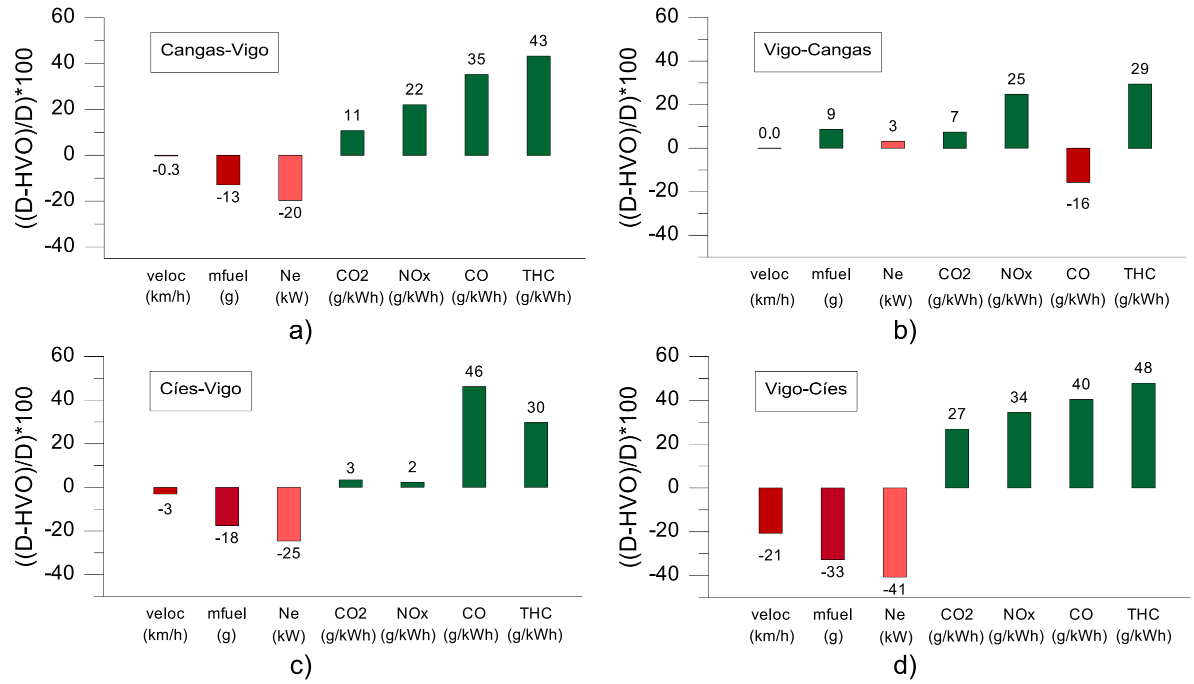

**Fig. 2**. Average relative differences of: vessel speed (km/h), cumulated consumed fuel mass (g), estimated power (kW) and specific gaseous emissions (g/kWh), determined between fuels tested during intermediate part of tested routes.

## Conclusions

According to the results obtained the following main conclusions can be drawn:

i) From the point of view of performance and regulated emissions, the use of 100% renewable fuels as drop-in fuel, such as HVO fuel, has positive effect in an engine used of catamaran vessel which meet the IMO TIER II standard.
ii) In most of tests, a direct reduction of $CO_2$ specific emissions was observed when the HVO fuel was tested. This contributes to the reduction of the net emissions of this greenhouse compound.
iii) The passenger transportation along the Vigo estuary is more environmentally friendly when the HVO fuel is used compared to Diesel fuel.

## References

[1] Mata C., Cárdenas D., Esarte C., Soriano J. A., Gómez A., Fernández-Yáñez P., García-Contreras R., Sánchez L., Nogueira J. I., Armas O. Performance, and regulated emissions from a Euro VI-D hybrid bus tested with fossil and renewable (hydrotreated vegetable oil) diesel fuels under urban driving in Bilbao city, Spain. Journal of Cleaner Production, Vol. 38310, 135472, 2023.

[2] F. Oliva, D. Donoso, J.A. Soriano, R. García-Contreras, O. Armas. Performance and regulated emissions from agricultural engines using 100% renewable fuel hydrotreated vegetable oil (HVO). THIESEL 2024 Conference on Thermo- and Fluid Dynamics of Clean Propulsion Powerplants. Valencia, Spain.

[3] L. Corral-Gómez, O. Armas, J.A. Soriano, J.I. Nogueira, G. Bracho. Spray Momentum Flux Novel Estimation Procedure through the Fuel Rate of Injection Using Hydrogenated Fuels with Single Hole Nozzle Diesel Injector. ACS Omega, 8, 50, 48071-48080, DOI: 10.1021/acsomega.3c06917, 2023.

# Crank-Angle-Resolved HR-TEM Analysis of Aggregation Process and Nanostructure of GDI In-Cylinder Soot Particles

T. Aizawa, S. Noguchi, Y. Hojo, T. Akayama, S. Yamamoto, H. Shaohang, T. Shimada

Dept. of Mechanical Engineering Informatics, School of Science and Technology, Meiji University,
1-1-1 Higshi-mita, Tama-ku, Kawasaki, Kanagawa, 214-8571 Japan.
E-mail: taizawa@meiji.ac.jp
Telephone: +(81) 44 934 7400

**Abstract.** In order to clarify details of the aggregation process of Gasoline Direct Injection (GDI) in-cylinder soot and thus to provide comprehensive quantitative experimental database required for development and validation of the PM/PN prediction models, Diffused Back Illumination (DBI) laser extinction measurements, crank-angle-resolved total in-cylinder gas/particles sampling, filter gravimetry, High-Resolution Transmission Electron Microscopy (HR-TEM) observation and analysis of morphology and nanostructure of in-cylinder soot particles using a Rapid Compression and Expansion Machine (RCEM) were conducted. Crank-angle-resolved total mass, aggregate size distribution, primary particle size distribution, fractal dimension, nanostructure and porosity of in-cylinder soot particles were successfully obtained.

## 1. Introduction

Alongside overcoming challenges of BEV including long charging time, short range, and the shortage of lithium and cobalt supply, the role of HEV/PHEV as a rational choice is expected to continue, and thus improving the thermal efficiency of gasoline engines remains an important technological challenge. For further improvement of thermal efficiency and drivability of gasoline engines, gasoline direct injection (GDI) has increasingly been adopted [1]. In order to meet stringent exhaust regulations of particulate matter (PM) and particulate number (PN) emissions, after-treatment devices such as Gasoline Particulate Filters (GPF) is being considered. However, deterioration of fuel efficiency due to pressure loss and filter regeneration are problematic and it is desirable to minimize engine out emissions. The process of PM/PN generation within GDI engine cylinder is a highly complex phenomenon [2, 3, 4]. This necessitates highly accurate PM/PN models based on detailed understanding of the phenomena. While models capable of reproducing trends with varying driving conditions are being developed [5, 6], there is a significant lack of crank-angle-resolved quantitative data of in-cylinder soot aggregation process during the combustion cycle necessary for detailed understanding of in-cylinder phenomena and model validation [7]. Particularly, nanostructure and porosity of young soot particles as small as 10nm initially formed in GDI engine cylinder, which are expected to significantly affect the particle size distribution [8], have never been experimentally investigated to the best of the authors' knowledge. Therefore, in the present study, laser extinction measurements, crank-angle-resolved total in-cylinder gas/particles sampling, filter gravimetry, HR-TEM observation and analysis of morphology and nanostructure of in-cylinder soot particles are conducted using a rapid compression and expansion machine (RCEM), in order to clarify details of the aggregation process of GDI in-cylinder soot.

## 2. Experimental Method

A direct-injection, spark-ignited and single-shot combustion event was achieved in the RCEM shown in Fig.1. The details are found in our previous publications [3, 4]. For optical diagnostic experiments, sapphire windows are installed in the head and the piston for in-cylinder soot measurements. For soot sampling experiments, the sapphire head window is replaced with a total cylinder sampling unit composed of a diaphragm and an air-actuated rupturing blade. For TEM observation and analysis, the soot particles were sampled onto copper or molybdenum TEM grids by exposing the grids directly to the soot laden gases. Two different soot sampling procedures at different locations, ñsemi crank-angle-resolved samplingò and ñsecondary-agglomeration-assisted samplingò, were selected depending on the purposes of the experiments.

With the ñsemi crank-angle-resolved samplingò, the TEM grids were placed directly on the piston surface to avoid secondary soot agglomeration in the expansion tank. With this sampling procedure, the soot particles existed near the grid surface from the start of in-cylinder soot formation to the evacuation of the in-cylinder gases due to diaphragm rupture are all deposited and mixed successively onto the grid

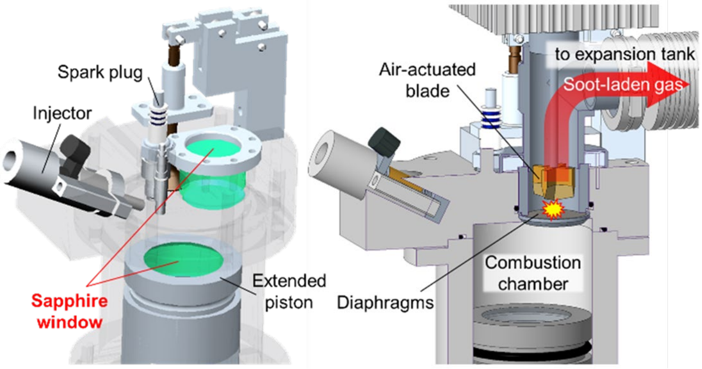

**Fig.1.** RCEM setup for optical diagnostics (left) and in-cylinder soot sampling (right)

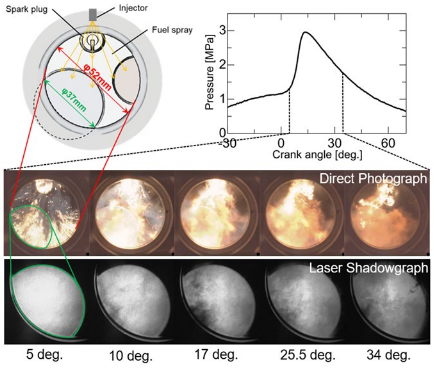

**Fig.2.** Example cylinder pressure, high-speed direct photographs and laser shad-owgraphs

surface. However, thanks to the progressive increase in the amount of in-cylinder soot during the combustion cycle, the variation of soot aggregate size, soot primary particle size and fractal dimension along coarsely divided crank angle resolution of the combustion cycle among early, middle and late phases can reasonably be quantified.

With the "secondary-agglomeration-assisted sampling", the soot particle samples for HR-TEM nanostructure observation were intentionally kept in the expansion tank for few minutes to let them secondary agglomerate and then deposited onto the lacey grid, in order to effectively facilitate the identification of very sparsely scattered young soot particles on the TEM grids in low-magnification wide-field TEM observations and the selection of primary particles that do not overlap with the lacey carbon on the TEM grid in high-magnification nanostructure observations.

## 3. Results

### 3.1. In-Cylinder Soot Mass via Laser Extinction and Filter Gravimetry

Figure 2 shows examples of cylinder pressure history, high-speed direct photographs and DBI laser shadowgraphs. The crank-angle-resolved in-cylinder soot amount can be obtained from the laser shadowgraphs by spatially integrating the line-of-sight laser transmissivity based on the Lambert-Beer law [3]. Figure 3 shows a comparison among cylinder pressure histories with (blue) and without (black) diaphragm rupture at three different rupture timings, in-cylinder soot mass by filter gravimetry (red plots) and by DBI laser extinction (green line). The in-cylinder soot mass rapidly increases right after the ignition and continue to increase gradually after the cylinder pressure peak. The in-cylinder soot mass at the end of the cycle stabilizes around 0.2mg.

### 3.2. Soot Morphology via Semi Crank-Angle-Resolved Sampling and TEM Analysis

Figure 4 shows the experimental setup for the semi time-resolved in-cylinder soot sampling and example TEM images of sampled soot. The sampled soot from different locations A, B and C exhibited notably different trends of fluctuation in their amount and morphology. Considering its relatively small fluctuation, soot sampled at location C was taken as the representative of in-cylinder soot for morphological analysis. Figures 5, 6 and 7 show aggregate gyration radius $R_g$, primary particle diameter $D_p$

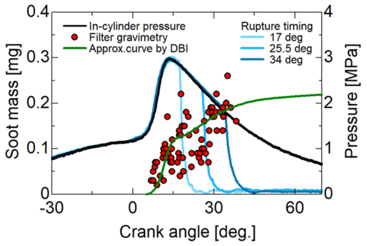

**Fig.3.** Cylinder pressure with and without diaphragm rupture, soot mass measured by filter gravimetry and DBI laser extinction

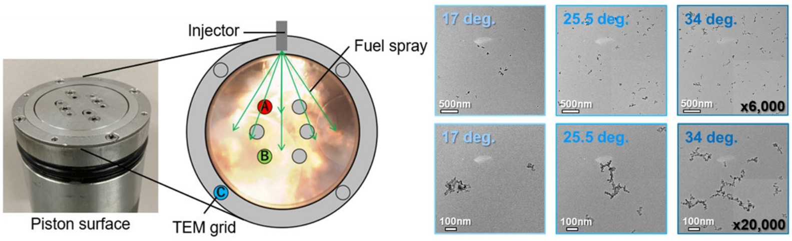

**Fig.4.** Experimental setup (left) and example TEM images of semi-time-re-solved in-cylinder soot sampling at location C (right)

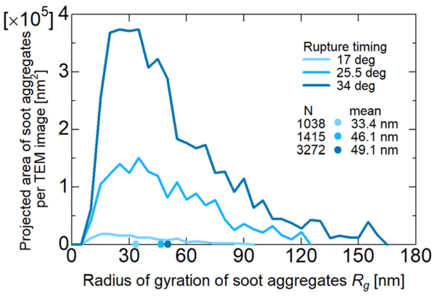

**Fig.5.** Projected-area-weighted gyration radius distri-bution of in-cylinder soot aggregates sampled at differ-ent timings

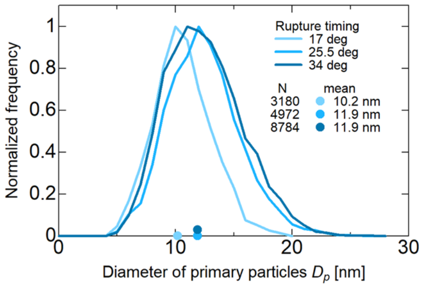

**Fig.6.** Primary particle diameter distribution of in-cyl-inder soot sampled at different timings

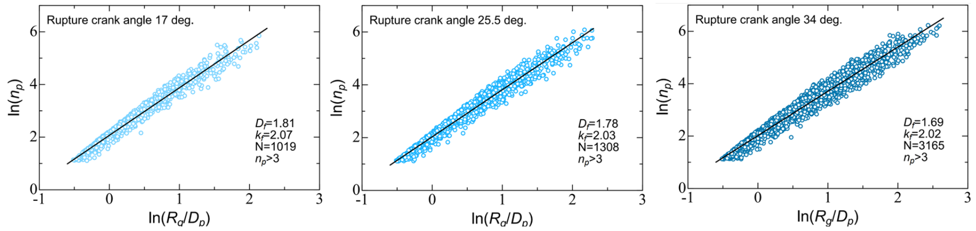

**Fig.7.** Logarithmic plots of $n_p$ vs. Rg/Dp for extraction of fractal dimension of in-cylinder soot aggregates sampled at different timings

and aggregate fractal dimension extracted from logarithmic plots of the number of primary particles within each aggregate $n_p$ vs. $R_g/D_p$, respectively. The total amount of soot aggregates, the amount of larger soot aggregates and their size significantly increase with the progress of combustion. The primary particle size notably increases from 17 deg to 25.5 deg, but not from 25.5 deg to 34 deg. The soot aggregate fractal dimension is decreasing from 1.81 to 1.69, indicating the extension of chain-like aggregate structure with the progress of combustion.

### 3.3. Porosity Estimation of In-Cylinder Soot based on HR-TEM Nanostructure Analysis

In the present study, soot porosity was estimated by normalizing the total length of carbon crystallites per unit area on the soot particle HR-TEM image by the graphite value. Figure 8 shows high magnification (2.5M and 1.25M) TEM images of in-cylinder soot particles in the early (7.5 deg) and late (31 deg) phases of the combustion cycle, two types of binarized crystallite images, MAX and MIN, manually extracted from these TEM images and the obtained soot porosity. Since manual extraction of crystallites from TEM images is affected by the operator's subjectivity, two types of extraction were performed on the same TEM image; MAX Extraction in which the area recognizable as crystallites is extracted to the maximum extent, and MIN Extraction in which the area recognizable as voids is extracted to the maximum extent. The maximum and minimum porosity values obtained from these analyses are indicated by the top and the bottom of the error bars, respectively. The average porosity was 39.4% for 7.5 deg

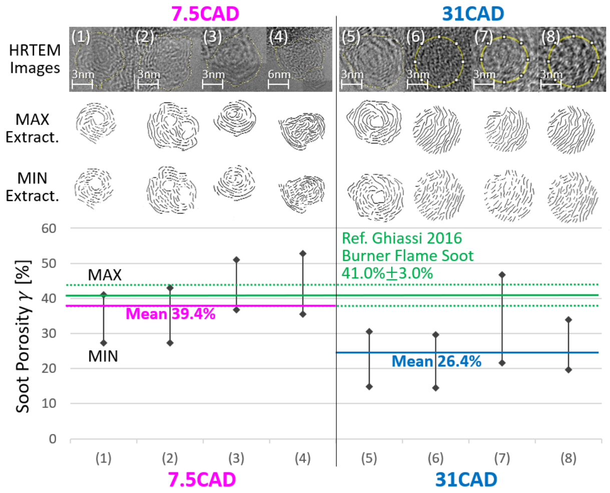

**Fig.8.** High magnification (2.5M and 1.25M) TEM images of in-cylinder soot particles in early (7.5 deg) and late (31 deg) phases of the combustion cycle, MAX and MIN manually extracted binarized crystallite images and obtained soot porosity

initially formed young soot and 26.4% for 31 deg late phase soot. The porosity values of the initially formed young soot obtained in the present study are reasonable and close to the porosity of relatively porous soot particles sampled in burner flame during oxidation [9], shown in green in Figure 8. In comparison, soot particles in the late phase of the combustion cycle show significantly lower values, indicating that the porosity of in-cylinder soot particles is high immediately after formation and decreases with the progress of combustion. These results are consistent with the results of a previous study on burner flames [8], which reasonably predicted a bimodal soot particle size distribution of the initially formed young soot particles due to their high porosity and low coagulation efficiency.

## 4. Conclusions

Crank-angle-resolved total mass, aggregate size distribution, primary particle size distribution, fractal dimension, nanostructure and porosity of GDI in-cylinder soot particles were successfully obtained. The quantitative data obtained in the present study are expected to facilitate the development and validation of GDI PM/PN prediction models.

## Acknowledgement

This paper is based on the results of JPNP21014, a project commissioned by the New Energy and Industrial Technology Development Organization (NEDO) and entrusted to The Research Association of Automotive Internal Combustion Engines (AICE). Authors would like to thank Tokyo Dylec Corporation for allowing us to borrow their real-time particle sizer for our experiments.

## References

(1) Kimura, K., Sakai, H., Omura, T., and Takahashi, D., “Development of 50% Thermal Efficiency S.I. Engine to Contribute Realization of Carbon Neutrality,” SAE Technical Paper 2023-01-0241, (2023).

(2) Xiong, Q., Gupta, A., Kuboyama, T., Moriyoshi, Y., Suzuki, H., Takeda, T., Akihama, K., Hashimoto, J., "Effects of Coolant Temperature and Fuel Properties on Soot Emission from a Spark-ignited Direct Injection Gasoline Engine," SAE Technical Paper 2019-01-2352, (2019).

(3) Maruyama, T., Sato, Y., Endo, K., Tsukamoto, T., Aizawa, T., “In-Cylinder GDI Soot via Visualization and Time-Resolved Total Cylinder Sampling,” SAE Int. J. Adv. & Curr. Prac. in Mobility, Vol.1, No.1, p.249-258 (2019).

(4) Miyashita, K., Tsukamoto, T., Fukuda, Y., Kondo, K., Aizawa, T., “High-Speed UV and Visible Laser Shadowgraphy of GDI In-cylinder Pool Fire,” SAE Technical Paper 2016-01-2165 (2016) .

(5) Hashimoto, J., Tokuyama, H., Imahara, T., “Development of a Prediction Model of Soot Particle Size Distribution Applicable for Design Calculations of Internal Combustion Engines (First Report) – Validation for iso-octane/n-heptane/toluene Blended Fuels,” Proc. of 2022 JSAE Annual Congress (Spring), No.20225150 (2022) (in Japanese).

(6) Hashimoto, J., Kuboyama, T., Akihama, K., “Development of a Prediction Model of Soot Particle Size Distribution Applicable for Design Calculations of Internal Combustion Engines (Second Report) – Effect of the Fuel Injection Timing on Soot Emissions,” Proc. of 2022 JSAE Annual Congress (Spring), No.20235140 (2023) (in Japanese).

(7) Kim, D., Kook, S., Kusakari, R., Shinohara, K., Iijima, K., Aizawa, T., “Soot particles in piston-top pool fires and exhaust at 5 and 15 MPa injection pressure in a gasoline direct-injection engine,” Proceedings of the Combustion Institute, Vol.38, p.5761–5768 (2021).

(8) Huoa, Z., Clearya, M.J., Sirignano, M., Masri, A.R., “A sectional soot formation kinetics scheme with a new model for coagulation efficiency,” Combustion and Flame Vol.230, 111444 (2021).

(9) Ghiassi, H., Toth, P., Jaramillo, I.C., Lighty, J.S., “Soot oxidation-induced fragmentation: Part 1: The relationship between soot nanostructure and oxidation-induced fragmentation,” Combustion and Flame Vol.163, pp. 179-187 (2016).

# NOx Measurement for PTI of SCR-Equipped Diesel Vehicles

Jacopo Franzetti[1,2], Tommaso Selleri[1,3], Natalia E. Fonseca Gonz§lez[2], Anastasios Melas[1], Roberto Gioria[1], Christian Ferrarese[1,2], , Barouch Giechaskiel[1], and Ricardo Suarez-Bertoa[1]

[1]European Commission, Joint Research Centre (JRC), 21027 Ispra, Italy;

E-mail: jacopo.franzetti@ec.europa.eu, anastasios.melas@ec.europa.eu, roberto.gioria@ec.europa.eu, barouch.giechaskiel@ec.europa.eu, ricardo.suarez-bertoa@ec.europa.eu.

[2]Mining and Energy Engineering School, Universidad Polit®cnica de Madrid, c/Rios Rosas 21, 28003, Madrid, Spain;

E-mail: natalia.fonseca@upm.es

[3]now at European Environment Agency (EEA), 1050 Copenhagen, Denmark;

E-mail: tommaso.selleri@eea.europa.eu

**Abstract.** The periodic technical inspections (PTI) for vehicles in the European Union aim at enhancing road safety and environmental protection. Malfunctioning deNOx aftertreatment systems can result in elevated NOx emissions with environmental and health impacts. Therefore, the current revision of the roadworthiness package by the European Commission considers the inclusion of a method to measure NOx during PTI (NOx-PTI), which is not included in current procedures. This study examined the effectiveness of an idling test in distinguishing between operational and malfunctioning SCR systems in light-duty Diesel vehicles. The results revealed a significant increase in NOx emissions over the regulatory homologation test cycle, ranging from 8 to 28 times, when the selective catalytic reduction (SCR) unit was not functioning. Additionally, the study evaluated methods for warming up the vehicleôs aftertreatment before the NOx-PTI idling test, such as urban speed drives. Furthermore, five different NOx analysers were compared to laboratory grade equipment. The results demonstrated the feasibility of the proposed method for measurements of NOX during vehicles PTI testing.

## 1. Introduction

Road transport is an important source of NOx [1], affecting air quality, health and the environment [2], [3]. Currently, all vehicles, light-duty (LD) and heavy-duty (HD), in the European Union are regularly checked during the mandatory periodic technical inspection (PTI) to ensure road safety and environmental protection. The specific requirements for these inspections are detailed in Directive 2014/45/EU [4], which is part of the ñso-calledò Roadworthiness Package that is currently undergoing revision. The European Commission investigates to include a new procedure to measure NOx during the vehiclesô PTI to verify the correct operation of the selective catalytic reduction (SCR) unit. A procedure has been developed and evaluated in a previous work [5] for Euro 6d-TEMP light-duty Diesel vehicles and newer models, which usually have SCR units installed [6]. It consists of an idling test, measuring the vehicle's NOx emissions at the tailpipe while idling after the vehicle has been warmed up. The warm-up process ensures that the SCR unit is at a temperature high enough to effectively sustain NOx reduction. If the SCR system malfunctions, it will result in high NOx emissions already at the beginning of the idling phase.

The current study focuses on some key elements needed for the idling test for NOx-PTI to be applicable in PTI stations. In particular, the research examines a warm-up method based on urban speed drives and analyses the impact of a malfunctioning Diesel Exhaust Fluid (DEF) injection system on PTI and NOx emissions. In addition, the performances of five NOx analysers designed for PTI use are investigated.

## 2. Experimental

Seven LD (LD1 to LD7) Diesel vehicles were tested at Vehicle Emissions Laboratories (VELA) of the Joint Research Centre (JRC) of the European Commission in Ispra (Italy). LD1-LD6 met the Euro 6d-

ISC-FCM standard, while LD7 was homologated as Euro 5. LD1 to LD5 were tested following the idling procedure described in [5]. They were then tested over the worldwide harmonized light vehicles test cycle (WLTC) with DEF injector/s disconnected in order to simulate a real-world example of SCR system malfunctioning. The emission factors in the two cases were calculated using bag measurement (EU Regulation 2017/1151), or from integrated instantaneous NOx mass emissions. The equipment used to measure NOx included a chemiluminescence detection (CLD) based analysers with a MEXA ONE (HORIBA, Kyoto, Japan), an AVL AMA i60 (AVL, Graz, Austria) and an AVL MOVE PEMS using a non-dispersive ultra violet (NDUV) analyser. Additional details on the equipment could be found at [5]. To gain insight into the warm-up time for the ATS, thirty real driving emissions (RDE) compliant tests from nineteen LD Diesel vehicles (tests part of Market Surveillance [7], [8]) were analysed. Cumulative NOx emissions were calculated for all tests, and various statistical measures computed (i.e. average, quartiles, etc.). The data was aligned based on engine speed signals, with the first second marking the engine start.

Five commercially available NOx-PTI analysers (#1 to #5) were assessed sampling from the tailpipe of LD6 and LD7. Analysers #1, #2, #4, and #5 used electrochemical sensors (ES), while analyser #3 was equipped with a CLD. The reference equipment used for these tests was an AVL MOVE PEMS. All analysers employed a technology to remove water condensate, and the reference values used were measured as dry. These measurements, averaged over 5-second intervals, were compared at varying concentration steps (0, 50, 100, >100 ppm).

## 3. Results and discussion

### 3.1 NOx-PTI idling test overview

LD1 to LD5 tested with DEF injector disconnected yielded emission factors over the WLTC that were 8 to 28 times higher when compared to those obtained with a working SCR system, see Table 1. These findings highlight the importance of deploying a NOx-PTI to pinpoint malfunctioning SCR unit, which might otherwise increase the NOx emissions released by the fleet into the environment.

**Table 1.** LD1 and LD5 NOx Emission Factors under WLTC with functional and malfunctioning SCR system. For LD4, it was not possible to perform the WLTC test simulating a malfunctioning of the SCR system.

| NOx (mg/km) | LD1 | LD2 | LD3 | LD4 | LD5 |
|---:|---:|---:|---:|---:|---:|
| WLTC[a] | 28 | 16 | 31 | 60 | 15 |
| WLTC sim. malfunctioning | 485 | 440 | 262 | - | 239 |

[a] Two tests per vehicle. The value reported is the average.

Figure 1 compares NOx emission profiles of a vehicle (LD1) with properly operating SCR unit (left panel) and with the DEF injector disconnected to simulate a malfunctioning, during the NOx-PTI idling test (right panel). When the SCR was functioning properly, the NOx concentration during the PTI test was zero and it remained at low levels for an extended period (1000 s for this specific case). It reached around 100 ppm at the end of the test. In the test with malfunctioning SCR, NOx concentrations were elevated immediately from the start of the idling phase. at around 100 ppm. In case of malfunction, $NO_2$ emissions reached ca. 80 ppm during the idling. Consistent results were obtained also for LD2 to LD5. These results complements the findings in [5], underscoring the capability of the NOx-PTI idling test to distinguish between operating and faulty SCR systems. These results also emphasize the importance of measuring NOx, and not just NO, during PTI to ensure the most accurate assessment of the vehicle's tailpipe emissions.

The ATS has to be warmed-up prior the idling test to ensure that the SCR unit temperature is sufficiently high to sustain NOx reduction activity. Urban speed drive (< 60 km/h) was assessed as ATS warm-up method, according to the methodology described in Section 2. Figure 2 shows (a) s-by-s NOx concentration and (b) cumulative NOx emissions during LD vehicle tests. These results show that after driving for 400 s (initial cold start peak) the vehicle can undergo an idling test at PTI because the SCR unit temperature would be adequate to maintain NOx reduction activity. NOx concentration was evaluated because SCR temperature was not available. It was assumed that the change from high to low NOx emissions during vehicle operation would indicate that the SCR unit reached a temperature high enough to effectively sustain NOx reduction.

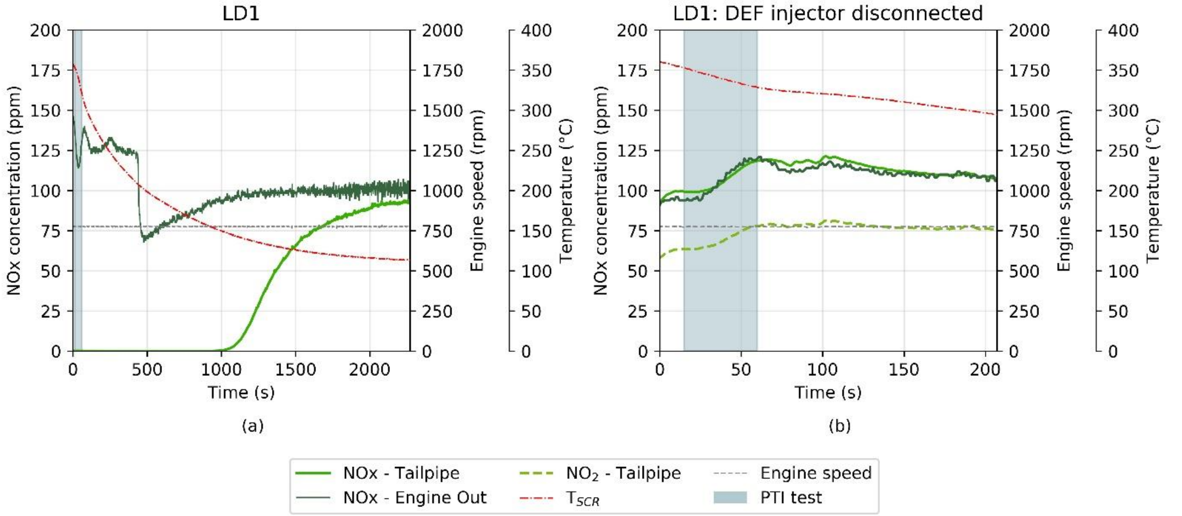

**Fig. 1.** NOx emission profiles of LD1 with (a) working SCR unit and (b) DEF injection malfunctioning. Time scale starts at the beginning of the idle test, immediately after the engine warmup. NOx-PTI measurement period is high-lighted. X-axis limit varies between the two subplots to effectively display the evolution of NOx concentration in (a)

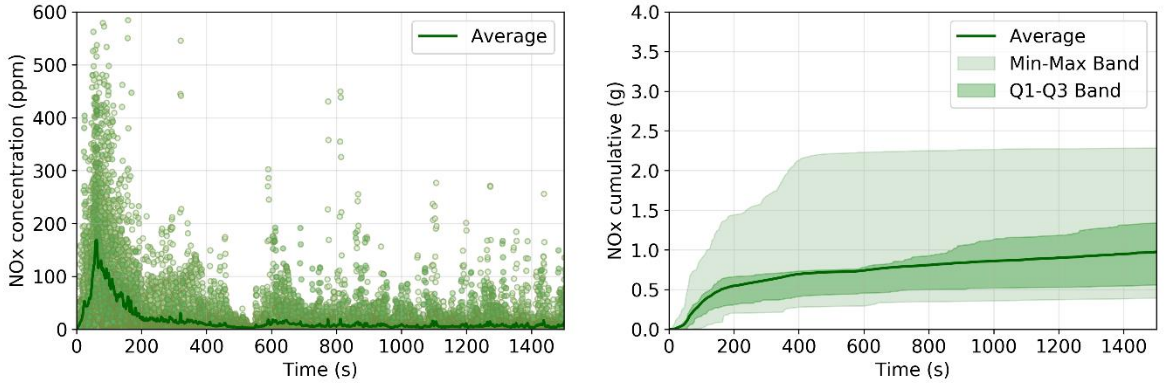

(a) (b)

**Fig. 2.** (a) NOx concentration and (b) cumulative NOx emissions for Diesel LD vehicles. Average of the calculated cumulative emissions is shown together with bands illustrating the minimum-maximum bandwidth and the 1st-3rd quartile bandwidth of cumulative NOx emissions for all tests. All graphs are zoomed on the first 1500 s of each test

### 3.2 NOx-PTI equipment validation

LD6 and LD7 were chosen to represent a functioning and malfunctioning SCR unit, respectively, to evaluate the performance of the PTI equipment in low and high NOx concentration scenarios. In addition, all the analysers were checked measuring a NOx span from a gas cylinder.

In Figure 3, the absolute and relative deviations of NOx concentration for LD6 and LD7 at idle and span gas, measured with the NOx-PTI analyzer, are presented in comparison to the reference equipment. PTI analysers demonstrated good linearity with the reference dry NOx. Across all PTI analyzers, relative differences ranged from -21% to +3% above 100 ppm reference NOx, and absolute differences ranged from -22 ppm to +2 ppm for reference NOx levels below 100 ppm. Most equipment displayed satisfactory differences. Analysers #1 and #3 had the greatest deviation.

## Conclusions

The introduction of a NOx-PTI test could identify vehicles with malfunctioning SCR systems, limiting their contribution to atmospheric NOx pollution. The measured NOx emissions from five tested light-duty Diesel vehicles with defective SCR systems were significantly higher, 8 to 28 times, compared to those with functioning SCR systems.

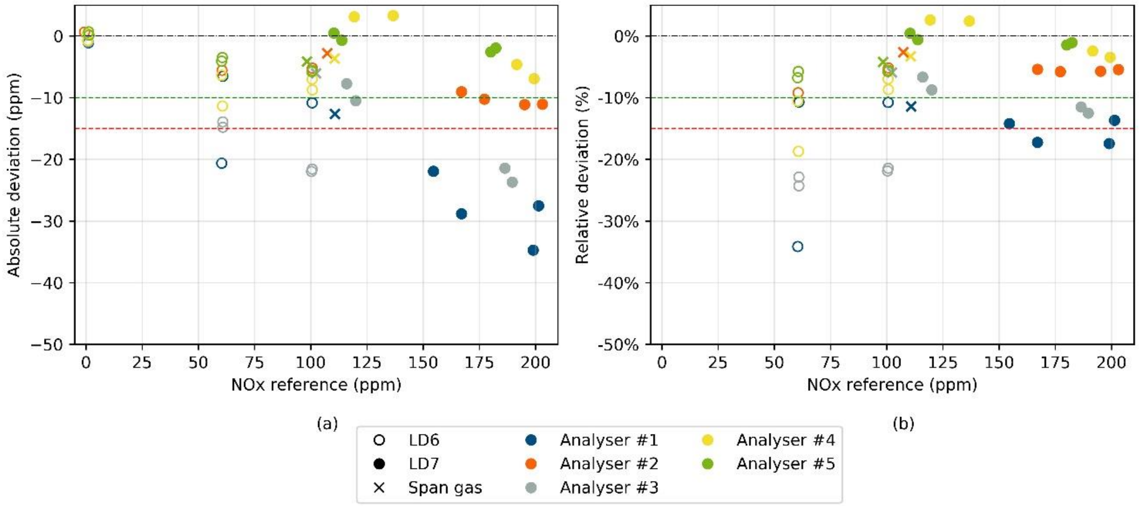

**Fig. 3.** Summary of the (a) absolute and (b) relative deviation of the PTI analysers plotted against the reference system. Green dashed lines indicate errors of 10 ppm and 10%, and red dashed lines 15 ppm and 15%. Empty and full circles used for LD6 and LD7 respectively, while 'x' marks for span gas check. *Analyser #1, #2 and #5 recorded NOx, analyser #3 and #4 only measured NO

For the proposed NOx-PTI procedure a warm-up of the vehicle with urban speed drives of at least 400 s, proved suitable for Euro 6d light-duty vehicles.

From the five commercially available NOx analysers for potential use in the NOx-PTI test, three gave differences of <10 ppm and two 20-30 ppm for concentrations 100-200 ppm. The results highlight the need for precise measurements of NOx, instead of solely measuring NO, as substantial $NO_2$ values were detected during PTI idle test, up to ca. 80 ppm, under conditions where the SCR system was malfunctioning.

## References

[1] European Environment Agency, *Air pollution in Europe: 2023 reporting status under the National Emission reduction Commitments Directive*. Luxembourg: Publications Office of the European Union, 2023.

[2] European Environment Agency, *Europe's air quality status 2021*. in EEA report (Online). LU: Publications Office, 2022. Accessed: Mar. 12, 2024. [Online]. Available: https://data.europa.eu/doi/10.2800/488115

[3] M. Kampa and E. Castanas, "Human health effects of air pollution," *Environmental Pollution*, vol. 151, no. 2, pp. 362–367, Jan. 2008, doi: 10.1016/j.envpol.2007.06.012.

[4] EP, "Directive 2014/45/EU of the European Parliament and of the Council of 3 April 2014 on periodic roadworthiness tests for motor vehicles and their trailers and repealing Directive 2009/40/EC Text with EEA relevance." Apr. 29, 2014. [Online]. Available: http://data.europa.eu/eli/dir/2014/45/oj

[5] J. Franzetti *et al.*, "Assessment of a NOx Measurement Procedure for Periodic Technical Inspection (PTI) of Light-Duty Diesel Vehicles," *Energies*, vol. 16, no. 14, p. 5520, Jul. 2023, doi: 10.3390/en16145520.

[6] T. Selleri, A. D. Melas, A. Joshi, D. Manara, A. Perujo, and R. Suarez-Bertoa, "An Overview of Lean Exhaust deNOx Aftertreatment Technologies and NOx Emission Regulations in the European Union," *Catalysts*, vol. 11, no. 3, p. 404, Mar. 2021, doi: 10.3390/catal11030404.

[7] P. Bonnel *et al.*, *European market surveillance of motor vehicles: results of the 2020-2021 European Commission vehicle emissions testing programme*. Luxembourg: Publications Office of the European Union, 2022.

[8] C. Gruening *et al.*, *European market surveillance of motor vehicles: results of the 2022 European Commission vehicle emissions testing programme*. Luxembourg: Publications Office of the European Union, 2023.

# Computational Analysis of Different Hydrogen Injector Characteristics in Wankel Rotary Engines

K. Moreno-Cabezas[1], R. Menaca[1], G. Vorraro[1], X. Liu[1], J. W.G. Turner[1] and H. G. Im[1]

[1]CCRC ï Clean Combustion Research Center. King Abdullah University of Science and Technology, Thuwal, Saudi Arabia.

E-mail: kevin.morenocabezas@kaust.edu.sa
Telephone: +(966) 54 410 8749

**Abstract.** The Wankel rotary engine is a viable alternative for some transportation applications due to its distinctive features of lightweight construction, small size and high-power density, and strong fuel adaptability. This study numerically explores and expands the characteristics and performance of the air-fuel mixing evolution in a hydrogen ($H_2$) Wankel rotary engine for different injector geometries commonly used in engine applications. 3D-CFD simulations were performed using CONVERGE. The modelled prototype engine is a 225 cc engine manufactured by Advanced Innovative Engineering UK. A validated engine and injection model are utilized as a basis to simulate the detailed direct injection (DI) of $H_2$ into the engine when using different injector geometries such as hollow- and solid single- and multi-cone injectors. Injecting the fuel into the chamber guarantees mixture enrichment for combustion and generates charge stratification that reduces heat release rate and improves power generation. The amount of mass trapped in the chamber after leakage through the crevices in the engine housing and the $H_2$ mixing quality distribution were compared in the different test cases. The results reveal that the solid-cone jet geometries hold a significant advantage, allowing faster mixing of $H_2$ with ambient gas as it reaches longer distances from the injector nozzles while interacting with rotor surfaces. Hollow-cone geometry also allows keeping a higher amount of fuel inside the chamber but generates higher mixture stratification. In summary, this study describes the mixing characteristics of $H_2$ direct injection fuelling within the Wankel engine. The study provides important insights for a richer and faster $H_2$ mixture formation.

## 1. Introduction

The need for a better world with clean air for future generations is an urgent concern, as human activities have led to emissions of NOx, particulate matter (PM), and greenhouse gases (GHGs). A significant portion of these emissions comes from the engines in the automobile sector, with over 99% of transport powered by combustion engines and more than 90% of transport energy derived from petroleum-based fuels [1]. Stringent regulations aimed at reducing these emissions have driven the development of electrification, non-conventional fuels, and technologies or engine concepts that enhance the efficiency of vehicle power systems. One promising technology is the Wankel rotary engine, which can utilize energy from renewable sources to produce alternative in the form of fuels like $H_2$ or sustainable liquid fuels known as electrofuels (e-fuels) suitable for internal combustion engines [2]. The Wankel rotary engine, first built in 1957 by Felix Wankel as an alternative to conventional reciprocating piston SI engines, features fewer components, making it simpler, lighter, easier to maintain, and compact, and it is also extremely well-balanced [3]. These characteristics make it ideal for applications such as aircraft or as a range extender in hybrid electric vehicles.

Among the alternative fuels proposed for internal combustion engines, $H_2$ is considered one of the most important and promising options due to its potential to be sourced from various green sources. $H_2$ is particularly suitable for operating the Wankel engine, as its high burning velocity and low extinction distance allow the flame to reach the crevices when the chamber narrows, thereby improving efficiency due to its high combustion rate [4]. Other studies have analysed the effects of injector location and nozzle diameter on gasoline combustion characteristics both experimentally [5] and using one-dimensional models [6]. Additionally, some researchers have applied Computational Fluid Dynamics (CFD) tools to include $H_2$ to enrich the mixture in varying amounts [7,8] and to analyse the orientation of the single-hole jet in the enriched mixture [9]. Building on this work, this research conducts a numerical study using CONVERGE CFD v3.1 [10] to investigate the mixing characteristics and performance of different direct injector designs for the operation of a $H_2$-dedicated Wankel rotary engine.

## 2. Experimental engine

The available experimental results [11] used to validate the proposed CFD model were previously obtained at the University of Bath with a 225 cm$^3$ Wankel rotary engine. Some of the technical specifications of the engine are presented in Table 1. These experiments were conducted using gasoline as the fuel and under stoichiometric conditions.

**Table 1.** Engine specifications [12].

| | |
|---|---|
| Engine Type | Wankel single rotor |
| Power output | 40 hp / 30 kW |
| Weight | 10 kg |
| Displacement | 225 cm$^3$ |
| Torque | 27 lb/ft @ 8000 rpm |
| Compression ratio | 9.6:1 |
| Ignition system | Twin spark plug |
| Generating radius | 69.5 mm |
| Eccentricity | 11.6 mm |
| Width of the rotor housing | 51.941 mm |

## 3. Computational CFD model

The governing equations that CONVERGE solves describe the conservation of mass, momentum, and energy. Some of the implemented submodels include the Reynolds-Averaged Navier-Stokes (RANS) Re-Normalisation Group k-ε for turbulence, SAGE as a detailed transient chemistry solver, Redlich-Kwong as the equation of state, and the extended Zeldovich for thermal NOx emissions. The experimental results used to validate the computational model in CONVERGE employ a chemical mechanism for Primary Reference Fuel (PRF) blends comprising 48 species and 152 reactions [13], as used in previous studies and publications by the authors [14]. The gasoline surrogate used in the validation corresponds to a Research Octane Number (RON) of 98 (PRF98), composed of 98% iso-octane and 2% n-heptane, being the same RON as the gasoline used in the experiments. Validation was performed by comparing the pressure trace from the model with the experimental data, corresponding to a Brake Mean Effective Pressure (BMEP) of 3 bar at 3000 rpm and Wide-Open Throttle (WOT). The good agreement between the experimental and simulation pressure data, as a representative sample of all the processes occurring in the engine, indicates that the model can predict the behavior and trends of using $H_2$ as a fuel in a rotary Wankel engine.

An initial study on the most appropriate injection strategy for $H_2$ injection in this rotary Wankel engine determined that aligning the injector with the major axis of the engine [14] is one of the easiest and most effective ways to achieve maximum power and lower emissions from $H_2$ combustion in this engine concept. To complement these results, different injector geometries were tested based on studies conducted in a constant volume chamber (CVC) [15]. The assessed geometries were based on the external geometry of the Bosch GDI injector HDEV4. This is a hollow-cone injector, but its geometry was simplified and modified to deliver the same mass flow rate with single-hole, four-hole, six-hole, and ten-hole configurations. The simplified geometry of the injectors and the nozzle diameters, designed to maintain a consistent mass flow rate, are shown in Fig. 1.

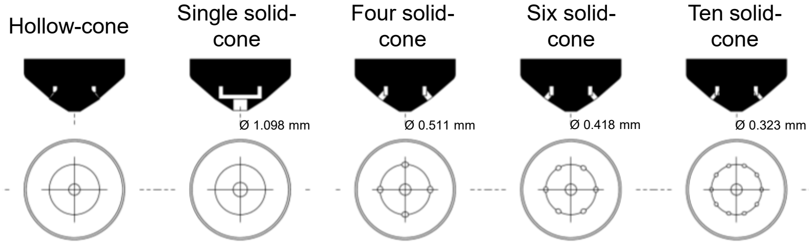

**Figure 1.** Injector geometry comparison.

## 4. Hydrogen injection and mixing

The simulations for the injection and mixing of $H_2$ were conducted using the thermodynamic and transport properties from the kinetic mechanism of H2/O2 developed by Burke [16]. The injection started at 330 degrees after $TDC_g$, when the intake port closes, and lasted for 68.38 degrees to ensure an equivalence ratio of $\varphi$ عي πδυ with an injection pressure of 20 bar. Figure 2(a) shows the increase in $H_2$ mass in the chamber over time, following a linear profile until 398.38 degrees after $TDC_g$, when the injection finishes for all injector geometries. After the injection ends, the leading apex of the rotor passes by the crevices generated by the spark plugs on the housing surface. Due to the interaction between the $H_2$ jet and the rotor surface, some of the fuel leaks through these crevices [14].

From the figure, it can be seen that the injector configuration with the highest fuel losses is the single-hole design, as the jet directly impinges on the rotor and is guided into the crevice. Following similar flow patterns observed in the CVC cases, the injector geometries that create an angle between the jet and the injector axis produce shorter penetration, which keeps the $H_2$ mass further from the crevices, thereby retaining more fuel inside the chamber. The figure shows that the hollow-cone configuration has the lowest losses through the spark plug crevices, followed by the four-hole, six-hole, and ten-hole configurations. Later, when the trailing apex of the rotor passes by the crevice generated by the injector, some additional $H_2$ leakage occurs into the following chamber, as indicated in the figure after 440 degrees. The amount of leaked fuel at this point depends on the level of mixing achieved up to that moment. Considering this, the higher leakage observed for the hollow-cone and four-hole configurations is due to a locally richer mixture near the injector tip. For other geometries, such as the single-hole, six-hole, and ten-hole configurations, the jets penetrate further, mixing more effectively with the bulk air.

The dynamics of the leakage through the crevices in the housing can be analyzed from Fig. 2(b), which shows the evolution of the equivalence ratio. An interesting observation from this figure is that after the injection, the equivalence ratio increases for all cases except the single-hole configuration, indicating that initially only air flows out of the chamber when the crevice opens. Shortly thereafter, some $H_2$ begins to leak as it starts to mix, as shown for the four-, six-, and ten-hole cases. Similarly, when leakage occurs through the injector crevice, the equivalence ratio increases for the single-hole, six-hole, and ten-hole cases, as the mixture is leaner locally near the spark plugs. In contrast, the opposite is observed for the hollow-cone and four-hole cases.

Figure 2(c) presents the fraction of fuel lost through the crevices and the $H_2$ left available in the combustion chamber. This figure indicates that the single-hole configuration has the lowest available fuel, with only 54.5% of the injected fuel retained, whereas the hollow-cone configuration retains 77.1% in the combustion chamber. As mentioned in Fig. 2(b), the hollow-cone and four-hole cases show 14.6% and 12.2% mass lost through the injector crevice, respectively, due to the stratification of the mixture during this process. The figure also shows that for the multi-hole configurations, such as the four-hole, six-hole, and ten-hole injectors, the amount of fuel lost through the injector crevices decreases as the number of holes increases, while the amount of fuel lost through the spark plug crevices increases, eventually reducing the total available fuel for the ten-hole case. These trends suggest that an excessive number of holes negatively affects fuel economy and overall operational efficiency.

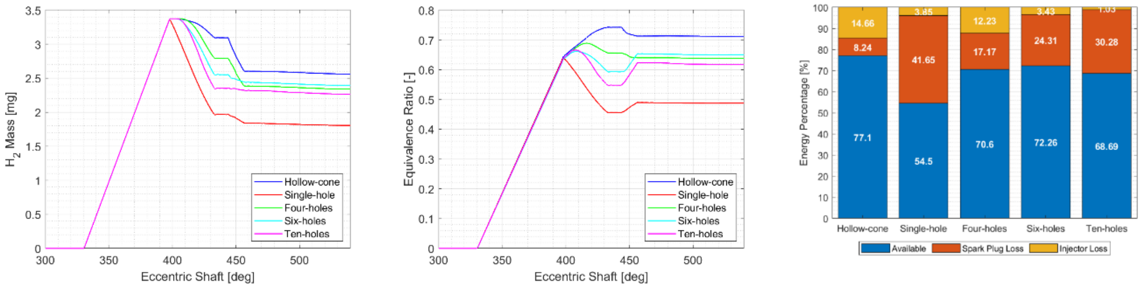

(a) (b) (c)

**Figure 2.** In-chamber mixture amount (a) $H_2$ mass (b) overall equivalence ratio (c) available injected $H_2$ and leakage at top dead center.

To expand the analysis on mixture formation and describe the mixing quality, the probability density function for the equivalence ratio inside the combustion chamber is shown in Fig. 3 for the different injector cases at top dead centre. From the figure, some geometries, such as the single-hole and four-hole configurations, exhibit a Gaussian distribution, indicating higher homogeneity of the mixture and higher probability values. In contrast, the single-hole, six-hole, and ten-hole configurations result in a more uneven and wider distribution, indicating lower mixing quality. According to the CVC results, all the solid-cone configurations generate similar mixing levels in a short time; however, implementing these injector geometries in the Wankel engine changes this result. This highlights the importance of the interaction between the jets and the bulk flow, as well as the moving walls, to improve $H_2$ diffusion and mixing.

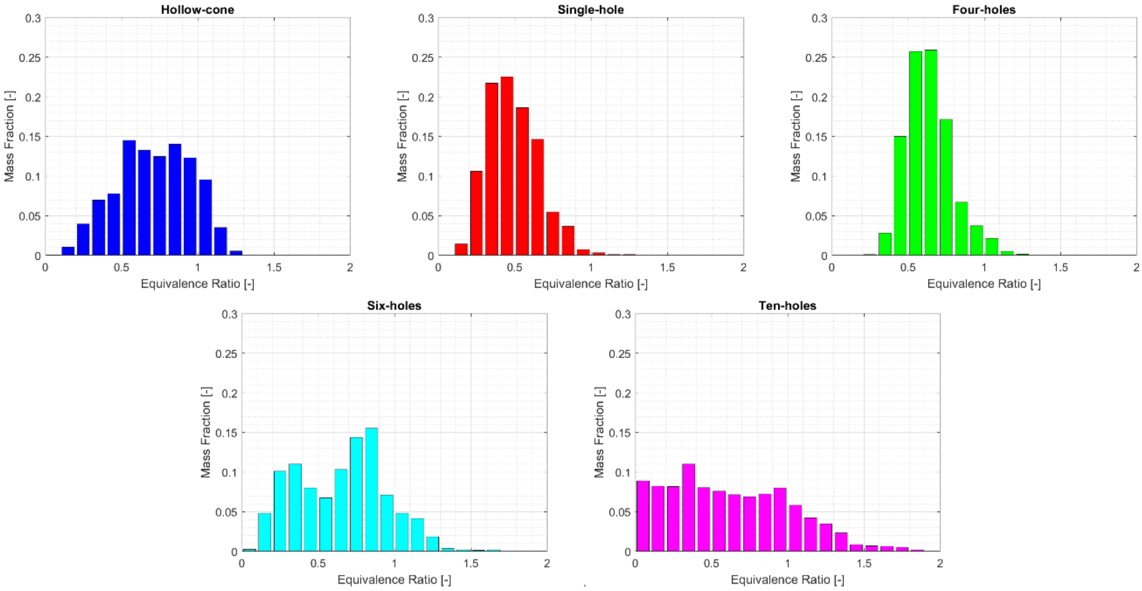

**Figure 3.** Probability Density Function distribution of the equivalence ratio in the combustion chamber for different injector designs at top dead center.

To quantify and summarize the information provided in the PDF plots, Table 2 presents the mean value and standard deviation of the equivalence ratio distribution for each injector geometry. The table shows that the richest mixture, with an equivalence ratio of 0.71, was achieved with the hollow-cone geometry. As mentioned before, the inhomogeneities in this configuration reduce $H_2$ losses through the spark plugs. In contrast, the single-hole case, with an equivalence ratio of 0.49, results in the most leakage occurring past the spark plugs. The homogeneity of the mixture, represented by the standard deviation in the table, shows a minimum value of 0.15 for the four-hole configuration, indicating the most homogeneous mixture. Conversely, the ten-hole configuration presented the most stratified mixture with a standard deviation of 0.40. Based on these results, the four-hole configuration is proposed as the optimum injector type for $H_2$ operation in a Wankel engine, as it minimizes fuel loss through the crevices in the engine housing while still generating a very homogeneous air-fuel mixture.

**Table 2.** Mean value and standard deviation of the equivalence ratio in the combustion chamber for different injector design at Top Dead Center.

| Injector Type | Hollow-cone | Single-hole | Four-holes | Six-holes | Ten-holes |
|---|---|---|---|---|---|
| Mean Equivalence ratio [-] | 0.71 | 0.49 | 0.64 | 0.65 | 0.62 |
| Standard Deviation [-] | 0.24 | 0.17 | 0.15 | 0.29 | 0.40 |

## 5. Conclusions

This study presented the $H_2$ injection and mixing characteristics in a Wankel engine concept with different injector geometries. Some of the main conclusions are:

- The location and size of essential components of an SI Wankel engine, such as spark plugs and fuel injectors, critically affect the mixing process of air and $H_2$ fuel due to local inhomogeneities in the mixture during the leaking process.
- Results showed that the single-hole configuration presents the highest initial $H_2$ leakage through the spark plug crevices as the $H_2$ jet impinges and is directed to the spark plug region of the combustion chamber.
- Opposite results are observed with the hollow-cone configuration, as the fuel remains near the injector region and further from the spark plug crevices.
- Subsequent leakage through the injector crevice is higher for geometries that generate higher stratification, such as the hollow-cone and four-hole configurations.
- The four-hole configuration resulted in the optimum geometry for $H_2$ injection in the Wankel engine, as it is one of the cases that presented a richer final mixture at TDC and exhibited one of the highest mixture homogeneities.

## 6. Acknowledgments

This work was funded by King Abdullah University of Science and Technology (KAUST) Competitive Center Funding (CCF). The simulations were conducted using the resources KAUST Supercomputing Laboratory. The authors also thank the licenses provided by Convergent Science.

## 7. References

1. Leach, F., Kalghatgi, G., Stone, R., and Miles, P., ñThe scope for improving the efficiency and environmental impact of internal combustion engines,ò Transportation Engineering 1:100005, 2020, doi:10.1016/J.TRENG.2020.100005.
2. Kalghatgi, G., ñIs it really the end of internal combustion engines and petroleum in transport?,ò Appl Energy 225:965ï 974, 2018, doi:10.1016/J.APENERGY.2018.05.076.
3. Ansdale, R.F. and Lockley, D.J., ñThe Wankel RC Engine. Design and Performance,ò Iliffe Books Limited, London, 1968.
4. Akal, D., ¥ztuna, S., and B¿y¿kakēn, M.K., ñA review of hydrogen usage in internal combustion engines (gasoline-Lpg-diesel) from combustion performance aspect,ò Int J Hydrogen Energy 45(60):35257ï 35268, 2020, doi:10.1016/j.ijhydene.2020.02.001.
5. JAVADZADEHKALKHORAN, M., KUTLAR, A., CĶHAN, ¥., and DOĴ AN, H.E., ñDetermination of the injector type and location for a direct injected Wankel engine,ò International Journal of Automotive Engineering and Technologies 11(4):129ï 139, 2022, doi:10.18245/ijaet.1179168.
6. Peden, M., Turner, M., Turner, J.W.G., and Bailey, N., ñComparison of 1-D Modelling Approaches for Wankel Engine Performance Simulation and Initial Study of the Direct Injection Limitations,ò SAE Technical Papers 2018-April:1ï 16, 2018, doi:10.4271/2018-01-1452.
7. Yang, J., Ji, C., Wang, S., Wang, D., Ma, Z., and Ma, L., ñA comparative study of mixture formation and combustion processes in a gasoline Wankel rotary engine with hydrogen port and direct injection enrichment,ò Energy Convers Manag 168:21ï 31, 2018, doi:10.1016/J.ENCONMAN.2018.04.105.
8. Yang, J., Ji, C., Wang, S., Wang, D., Shi, C., Ma, Z., and Zhang, B., ñNumerical study of hydrogen direct injection strategy on mixture formation and combustion process in a partially premixed gasoline Wankel rotary engine,ò Energy Convers Manag 176:184ï 193, 2018, doi:10.1016/J.ENCONMAN.2018.09.008.
9. Shi, C., Ji, C., Wang, S., Yang, J., Li, X., and Ge, Y., ñEffects of hydrogen direct-injection angle and charge concentration on gasoline-hydrogen blending lean combustion in a Wankel engine,ò Energy Convers Manag 187:316ï 327, 2019, doi:10.1016/J.ENCONMAN.2019.03.011.
10. Richard, K.J., Senecal, P.K., and Pomraning, E., CONVERGE 3.1 Manual, Convergent Science, Madison, WI, 2022.
11. Vorraro, G., Turner, M., and Turner, J.W.G., ñTesting of a Modern Wankel Rotary Engine - Part I: Experimental Plan, Development of the Software Tools and Measurement Systems,ò SAE Technical Papers 2019-Janua(January):1ï 16, 2019, doi:10.4271/2019-01-0075.
12. 225CS - 40BHP - Wankel Rotary Engine | Advanced Innovative Engineering (UK) Ltd, https://www.aieuk.com/225cs-40bhp-wankel-rotary-engine/, Feb. 2022.
13. Liu, Y.-D., Jia, M., Xie, M.-Z., and Pang, B., ñEnhancement on a Skeletal Kinetic Model for Primary Reference Fuel Oxidation by Using a Semidecoupling Methodology,ò Energy and Fuels 26(12):7069ï 7083, 2012, doi:10.1021/ef301242b.
14. Moreno Cabezas, K., Vorraro, G., Liu, X., Menaca, R., Im, H.G., and Turner, J.W.G., ñNumerical Analysis of Hydrogen Injection and Mixing in Wankel Rotary Engines,ò SAE Technical Paper Series, SAE International, 2023, doi:10.4271/2023-24-0069.
15. Moreno-Cabezas, K., Zaihi, A., Liu, X., Aljohani, B., Wu, H., Houidi, M. Ben, Roberts, W.L., and Im, H.G., ñNumerical Analysis of Different Hydrogen Injector Characteristics in a Constant Volume Chamber,ò SAE Technical Paper Series, SAE International, 2024, doi:10.4271/2024-01-2693.
16. Burke, M.P., Chaos, M., Ju, Y., Dryer, F.L., and Klippenstein, S.J., ñComprehensive H 2/O 2 kinetic model for high-pressure combustion,ò Int J Chem Kinet 44(7):444ï 474, 2012, doi:10.1002/kin.20603.

# Ultra-High Efficiency Hydrogen Fuelled Combustion Engine

Timo Janhunen

Aumet Oy, Huopalahdentie 6 a9, 00330 Helsinki, Finland

E-mail: timo.janhunen@aumet.fi
Telephone: +(358) 405026257

The pressure to reduce CO2 emissions has forced the car industry to make changes in the combustion engines, for example to use biofuels and hydrogen as fuel. Production of green hydrogen been increased in last years because of increased production of green electricity from wind turbines and solar cells. One problem in hydrogen fuelled passenger cars has been the high price of carbon fibre used in 700 bar high pressure hydrogen tanks. Now it seems that by using new production technologies and for example using lignin as raw material for carbon fibre manufacturing, it is possible to lower the price of 5 kg hydrogen tanks to about 1000 dollar in coming years [1].

According to MTZ (2-3/2023, p. 24-27) the drive shaft efficiency of fuel cells (including inverter and electro motor) is about 40 -50 % and its price is about 4 times higher than combustion engine. New methods to increase the efficiency of combustion engine are in research, for example a combination of Otto- and Rankine processes, having efficiency of up to 60% is possible [2].

Aumet Oy [3] has developed a 4-2 stroke valve-controlled hydrogen fuelled combustion engine with water injection, called Z-engine, working with Z-engine- Rankine combinate process. It has a very rapid highpressure gas exchange (tested with test engine) at 120-130 deg. ABDC. after the exhaust period between 30 deg. BBDC – 120 deg. ABDC has occurred. The intake air is compressed at full load with a turbo charger to 2.5 bar, then intercooled, then compressed to 10 bar and mixed with the remaining exhaust gases.

After the gas exchange the pressure in cylinder is about 15 bar and temperature 420K. After the gas exchange about 30% water of the gas mass of the cylinder is injected into the cylinder between 125 – 140 deg. ABDC, to cool the gas in the cylinder and to prevent too early ignition of the at 135 – 150 deg. ABDC injected hydrogen. As temperature in cylinder is quite low at this point and the pressure is quite high, the water droplets don’t evaporate, but they lower the end compression temperature and work.

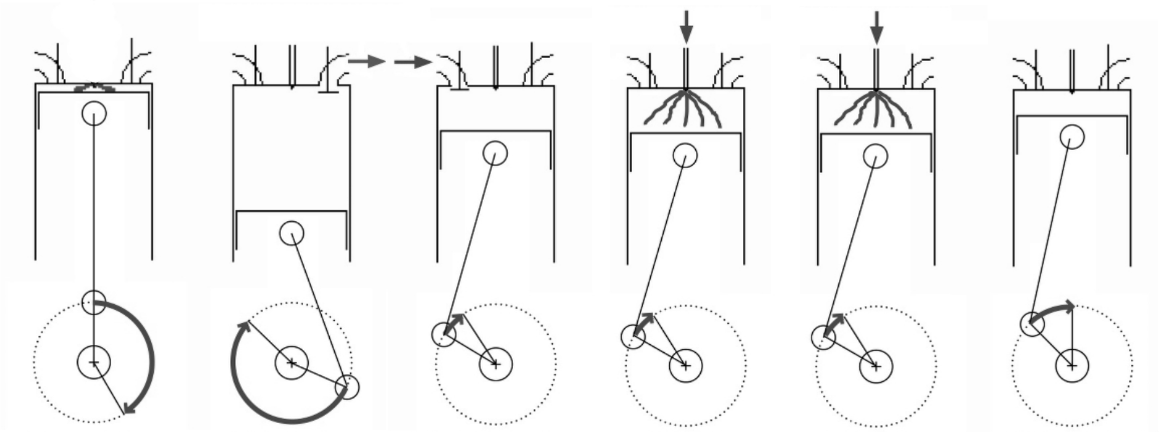

1. Ignition, combustion, water droplets evaporation and work cycle

2. Exhaust cycle

3. Very rapid intake, 10 bar. 12 degree, high turbulence

4. Water injection

5. Hydrogen injection

6. Final compression to TDC

**Fig. 1.** The working principle of the Z-engine

The high turbulence after the gas exchange mixes well the gases in cylinder and increases the cooling effect of the water droplets, lowering the compression work and pressure. The water droplets stay liquid until the spark ignition has occurred at about 15 deg. ATDC at full load. As the water droplets stay liquid, they act as neutral particles, and they don't have any effect to the ignition of the mixture. After the evaporation of water droplets during combustion, they increase the volume of the working gas at about 30%. The needed injected water is condensed is from exhaust gases.

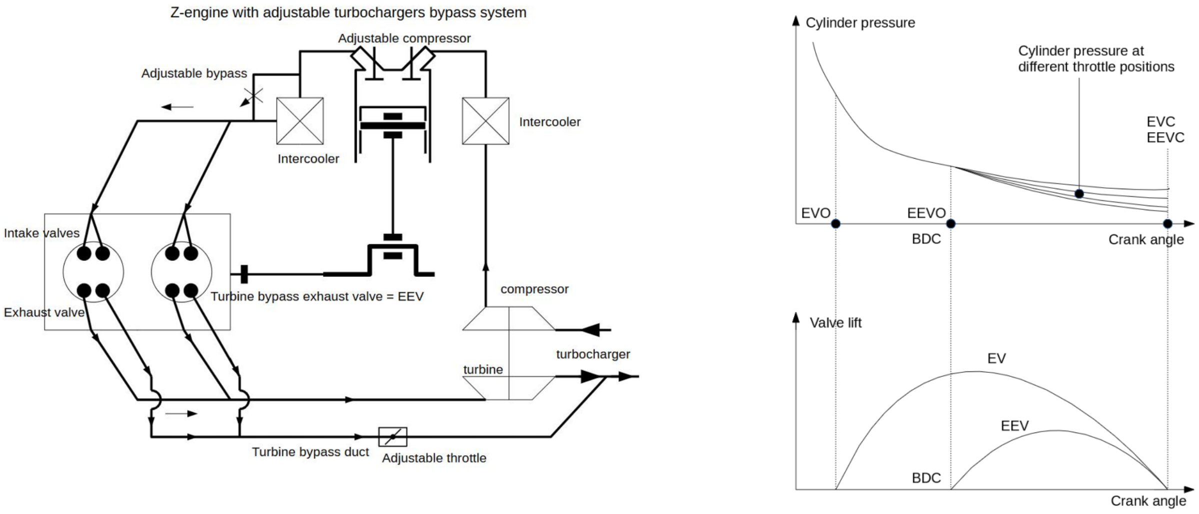
Z-engine with adjustable turbochargers bypass system
Adjustable compressor
Adjustable bypass
Intercooler
Intercooler
Intake valves
Exhaust valve
Turbine bypass exhaust valve = EEV
compressor
turbocharger
turbine
Turbine bypass duct
Adjustable throttle
Cylinder pressure
Cylinder pressure at different throttle positions
EVC
EEVC
EVO
EEVO
BDC
Crank angle
Valve lift
EV
EEV
BDC
Crank angle

**Fig. 2a and 2b.** The Z-engine with adjustable turbine bypass valve

The adjustable turbine bypass system allows the control in cylinder remaining amount of combustion gases and thus the temperature in cylinder during compression phase. The p-V diaphragm shows the situation at full load in cylinder. In order to avoid too high cylinder pressure, ignition is made quite late, about 15 deg. ATDC. The rapid downward moving piston limits pmax.

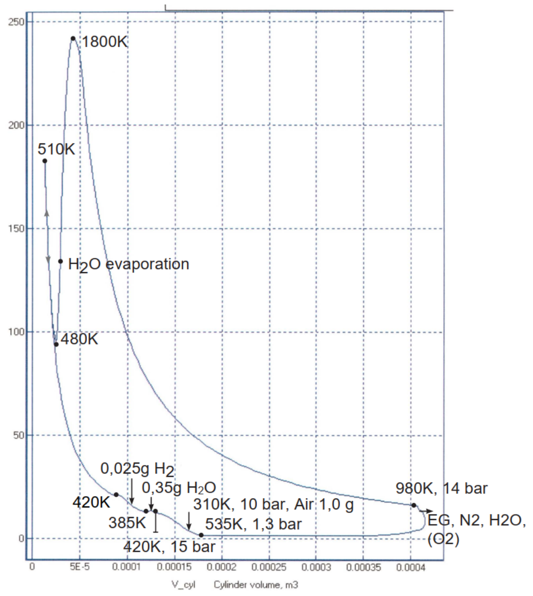

**Fig. 3.** P-V diagram of the Z-engine at full load

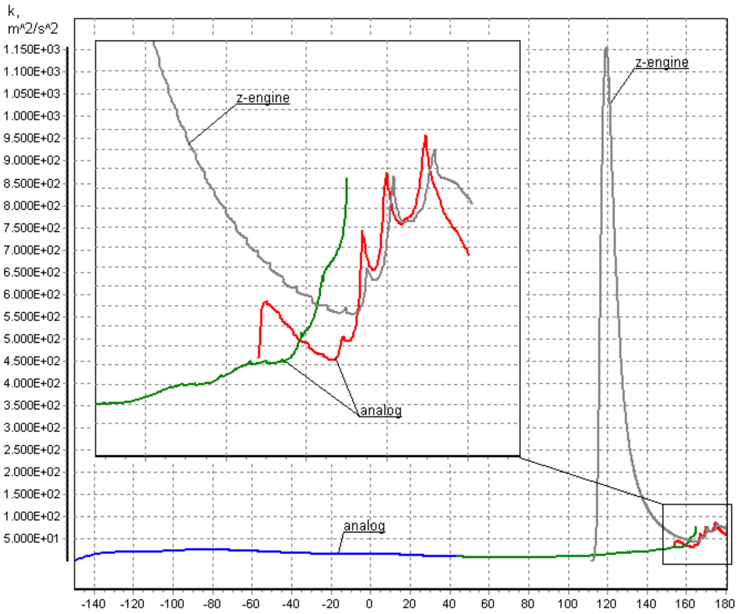

**Fig. 4.** Turbulence energy in cylinder of the Z-engine

The combustion duration at full load is 15 deg., max. pressure is 240 bar, max. temperature is 1780K, BTE 60%, Cr=32:1, lambda =1.0, BMEP = 47.5, 2 cylinder:80*80 mm, 2650 rpm, about 164 kW., expansion ratio at full load 13;1, at part load 32:1 At high loads the downwards moving piston lowers max. pressure and temperature when late ignition. Evaporation cooling from water droplets lowers max. temperature and Nox and heat losses. Evaporated water increases Cp after combustion in cylinder from about 1.4 to 1.75.

The high turbulence level in cylinder after the gas exchange mixes the gases well and increases the heat transfer between the water droplets and the gas in the cylinder.

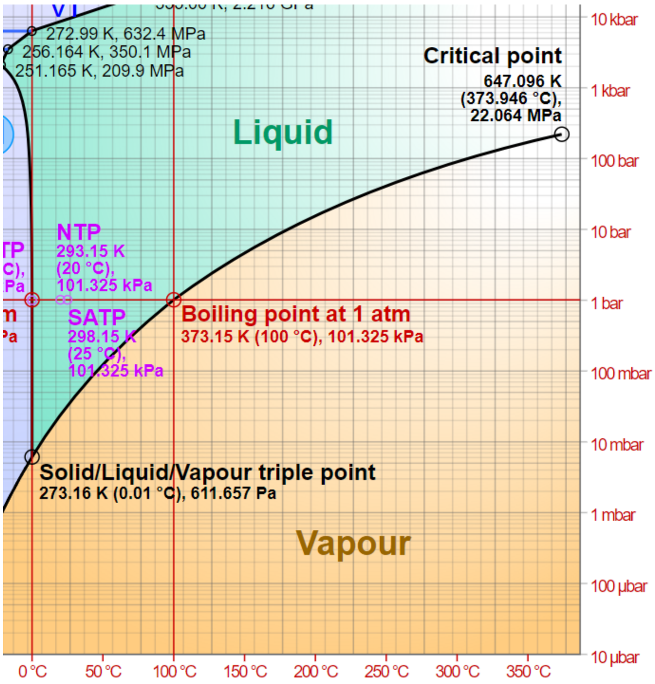

**Fig 5.** p-T diagram of water

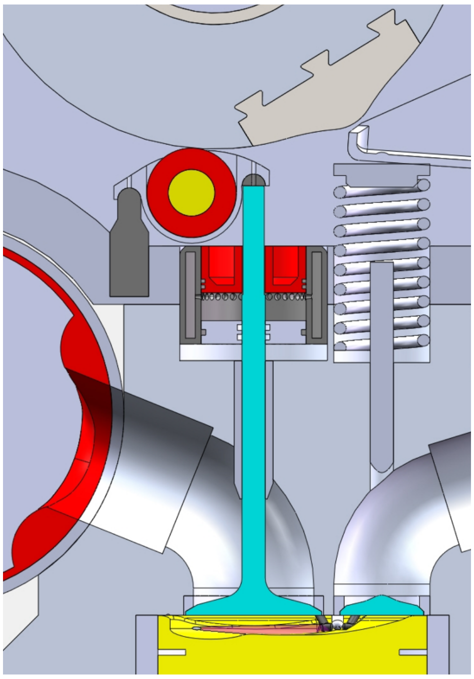

**Fig. 6.** The intake cam mechanism

Cronidur 30 steel is used in the valve mechanism in the cams and silicon nitride in cam follower rolls, max. contact pressure about 2 GPa., max. allowed contact pressure about 2.8 GPa. Modern simulation tools were used in this project, for example Diesel RK, Chemkin, GT-Power, Fluent etc.

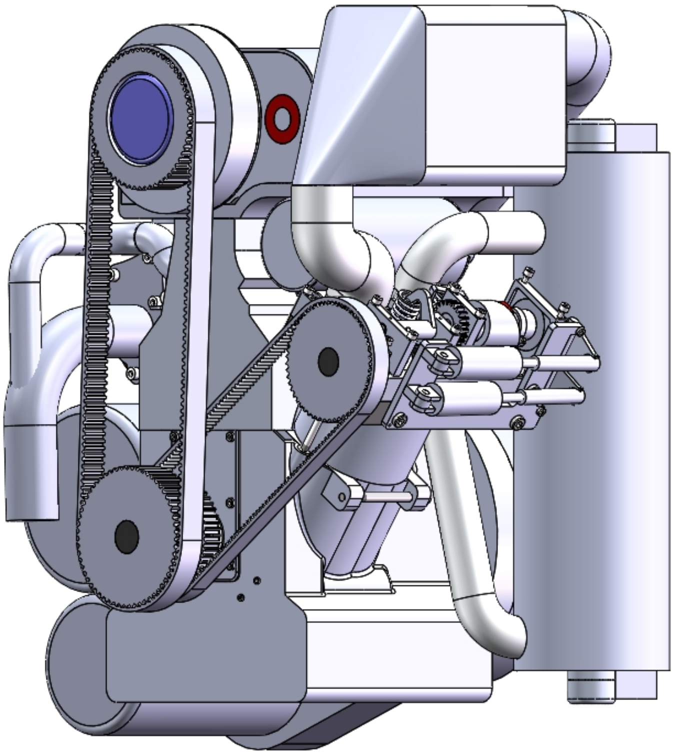

**Fig. 7.** The picture of the Z-engine with water-cooled compressor

## References

[1] H.K.Shin, S.K.Ha: A review of the Cost Analysis of Hydrogen Gas Storage Tanks for Fuel Cell Vehicles

[2] J. Wu, Z.Kang, Z.Wu: Thermodynamic Analysis of in-Cylinder Steam Assist Technology within an Internal Combustion Engine

[3] www.aumet.fi

# Effect of Compression Ratio Reduction and Water Injection on a Compression Ignition Engine Fueled with Straight Hydrogen

J.M. Rueda-Vázquez[1], J. Serrano[2], F. J. Jiménez-Espadafor[2] and M.P. Dorado[1]

[1]Department of Physical Chemistry and Applied Thermodynamics, Córdoba University, Spain.

E-mail: jmrueda@uco.es
Telephone: +(34) 957 212 080

[2]Department of Energy Engineering, Seville University, Spain.

**Abstract.** In this study, a modified compression ignition engine powered by hydrogen as the primary fuel, using diesel fuel merely as a pilot ignition source, was used to examine the combined effects of compression ratio (CR) and water injection (WI) on engine performance and $NO_x$ emissions. CR was reduced from 17.5 to 13.5, in steps of one point, forcing water and hydrogen into the intake manifold. The range of hydrogen energy share (HES) under different engine operating conditions varied from 0% to 85%. Results indicate that while $NO_x$ emissions rise with HES, CR reduction decreases $NO_x$ emissions by 50%. Additionally, WI results in an additional 50% reduction in $NO_x$ emissions. Experimental evidence shows that WI in conjunction with CR reduction can effectively decrease $NO_x$, attaining an efficiency above 35%. This strategy also decreases the maximum in-cylinder pressure, which allows an increase in turbocharger pressure and, consequently, engine specific power.

## 1. Introduction

To achieve carbon neutrality in the coming decades, the search for alternative fuels for Internal Combustion Engines (ICE) have been intensified. One of the most promising alternatives is provided by the use of $H_2$, due to its adaptability to existing infrastructure and potential to facilitate the transition to a hydrogen-based economy. $H_2$ has several benefits when combined with innovative technologies, providing flexibility to satisfy engine specifications, including:

- Zero carbon content (despite not existing freely in nature, hydrogen is the most abundant element in the universe).
- It can be produced from renewable energy sources, although currently, 95% of hydrogen is generated using methods based on fossil fuels.
- It possesses a very high energy density (120 MJ/kg), which is around 3 times that of hydrocarbon-based fuel.

Using $H_2$ to fuel ICE, combustion parameters differ from fuels based on hydrocarbons, since hydrogen burns quicker. Moreover, the high diffusivity of $H_2$ allows a perfect mixture with air, achieving almost complete homogeneity when introduced into the combustion chamber. Although $H_2$ can be used in compression ignition engines (CIE), it cannot be directly used due to its high self-ignition temperature (850 K). This would require either an impractically high CR or heating the intake air, which ultimately reduces both volumetric efficiency and engine power. However, using diesel fuel as ignition source, $H_2$ can be used in dual-fuel mode in CIE. However, the use of $H_2$ is directly related to a slight increase in $NO_x$ emissions, since their formation mechanism is mainly thermal (Zeldovich mechanism).

The objective of this research is to evaluate the influence of water injection (WI) on combustion and efficiency in a hydrogen-powered ICE. CR will be modified, while relying solely on diesel fuel for ignition, over a wide range of CR values. The reduction in $NO_x$ emissions will be also quantified.

## 2. Materials and methods

Renault 1.5 dCi k9k 766 engine (turbocharged, 63 kW rpm maximum power at 4000 rpm and 220 Nm maximum torque at 1800 rpm) was used. The engine has been modified to introduce $H_2$ and water into the intake manifold, as shown in Fig. 1. The engine configuration and timing were adjusted using the

Commander 4DE from Sybelle, which is the electronic control unit (ECU) that allows to modify most of the engine parameters. $NO_x$ exhaust gas emissions were measured using a Testo 350 XL.

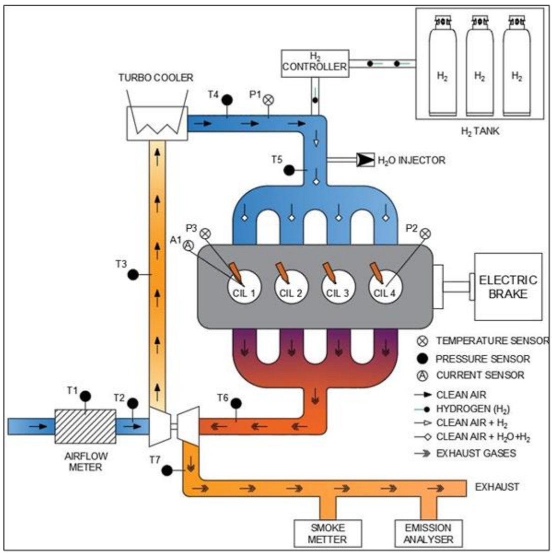
TURBO COOLER
$H_2$ CONTROLLER
T4
P1
$H_2$
$H_2$
$H_2$
$H_2$ TANK
T5
$H_2O$ INJECTOR
P3
A1
P2
T3
CIL 1
CIL 2
CIL 3
CIL 4
ELECTRIC BRAKE
TEMPERATURE SENSOR
PRESSURE SENSOR
CURRENT SENSOR
CLEAN AIR
HYDROGEN ($H_2$)
CLEAN AIR + $H_2$
CLEAN AIR + $H_2O$+$H_2$
EXHAUST GASES
T1
T2
T6
AIRFLOW METER
T7
EXHAUST
SMOKE METTER
EMISSION ANALYSER

**Fig. 1.** Schematic diagram of the experimental setup

In this study, a total of 469 tests have been conducted. These test have been carried out at five different CR (17.5:1, 16.3:1, 15.5:1, 14.5:1 and 13.5:1), four different engine speeds (1500, 2000, 2500 and 2750 rpm) and various SOI settings (+10º, +5º and 0º BTDC). At each of these test points, the amount of $H_2$ (0 - 2 kg/h) and water (0 - 48 kg/h) was varied.

## 3. Results and discussion

The rapid combustion of $H_2$ tends to elevate the gas temperature in the combustion chamber, thereby promoting the formation of $NO_x$. In this study, under identical operational conditions (engine speed, SOI, HES and water mass flow), $NO_x$ emissions decrease as the CR decreases, as expected. Fig. 2 shows the evolution of $NO_x$ emissions versus CR at different SOI and engine speed, while considering HES and WI as parameters.

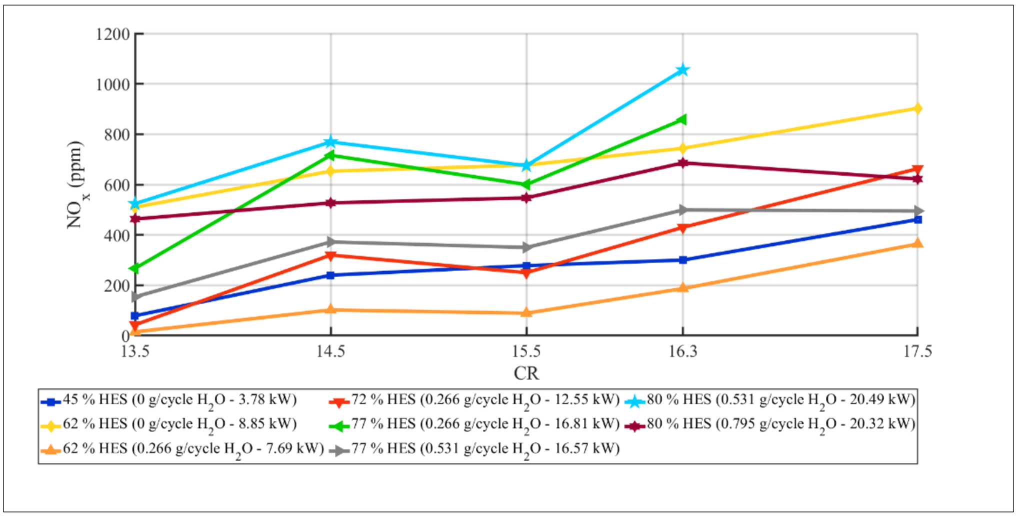

**Fig. 2.** $NO_x$ emissions *versus* CR at 2000 rpm and SOI 10ÜBTDC.

It can be seen that at CR 16.3 and 80% HES, $NO_x$ emissions decrease from 1050 ppm, with 0.531 g/cycle of water to 700 ppm, with 0.795 g/cycle of water. In this case, a 50% increase in WI leads to a 33% reduction in $NO_x$. A very similar behavior can be appreciated in all tested conditions.

WI reduces $NO_x$ due to the thermal mechanism, where two different steps occur. The first one increases the specific heat of gases, reducing the charge temperature during compression and combustion due to the water high thermal capacity compared to that of air. The second one is related to the phase change of water; most of the water that enters the cylinder is in a liquid state, although highly atomized. As the compression process advances and the temperature increases, the water undergoes a phase change from a liquid to a gas state and, therefore, it absorbs the energy required for the phase change.

Fig. 3 shows the relationship between $NO_x$ (in ppm) and the parameter α for all test conditions. This parameter was introduced by Serrano *et al* (2019) and relates the charge thermal capacity, in this case, air plus water, with to fuel power.

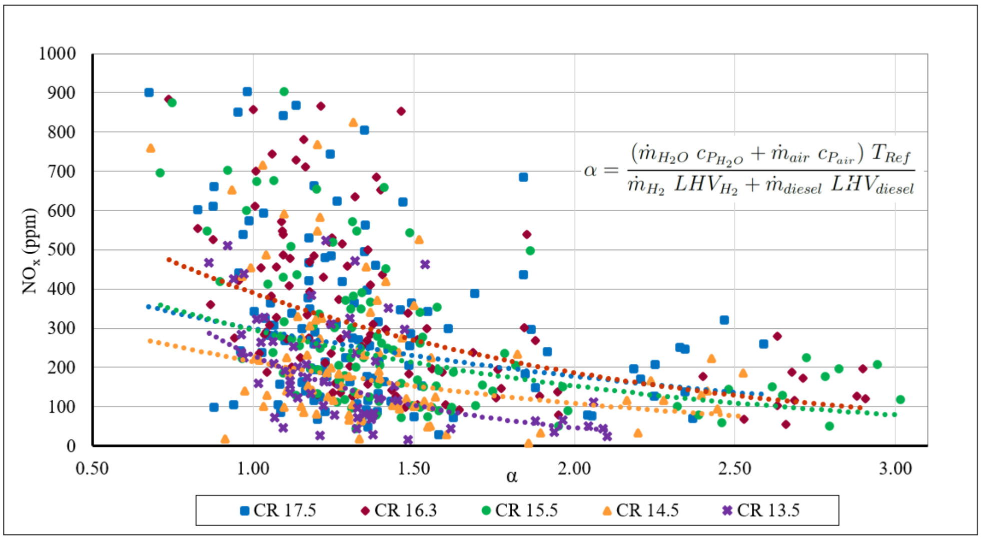

**Fig. 3.** $NO_x$ *versus* the parameter α.

For low α, in the range of 1.0–1.5, there is a dispersion in $NO_x$ emissions, indicating that multiple factors influence $NO_x$ formation, including thermal capacity, residence time and SOC. However, as α increases, this dispersion clearly diminishes. When α reaches approximately 2, $NO_x$ emissions achieve a minimum in an asymptotic manner, within a range between 200 and 50 ppm for different CR. This means that the thermal mechanism clearly dominates and provides a minimum value for $NO_x$, influenced by the load thermal capacity enhanced by water.

## Conclusions

The following conclusions can be drawn from this investigation:

- $NO_x$ emissions increase monotonically with HES for any CR, engine speed or SOI.
- The combination of different parameters, including WI, SOI and CR reduction, all managed simultaneously, shows a positive trend in $NO_x$ reduction.
- The parameter α has proven to be highly effective in determining the maximum amount of WI needed to control $NO_x$ emissions, ensuring that it meets the required limits.

## References

Rueda-Vázquez, J.M.; Serrano, J.; Jiménez-Espadafor, F.J.; Dorado, M.P. Experimental analysis of the effect of hydrogen as the main fuel on the performance and emissions of a modified compression ignition engine with water injection and compression ratio reduction. Applied Thermal Engineering (2024), 238, 121933.

Serrano, J.; Jiménez-Espadafor, F.J.; López, A. Analysis of the effect of different hydrogen/diesel ratios on the performance and emissions of a modified com-pression ignition engine under dual-fuel mode with water injection. hydrogen-diesel dual fuel mode. Energy (2019), 172, 702-711.

# Experimental Analysis of the Water Direct Injection Effects in a Hydrogen Direct Injection Spark Ignition Engine and its Application toward Load Extension

Seungil Lee[1], Seunghyun Lee[1], Seungjae Kim[1], Kiyeon Kim[2], Jeongwoo Lee[2], and Kyoungdoug Min *[1]

[1]Department of Mechanical Engineering, Seoul National University, Seoul 08826, Republic of Korea

E-mail: kdmin@snu.ac.kr
Telephone: +(82) 02 880 1661

[2]Department of Autonomous Vehicle System Engineering, Chungnam National University, Daejeon 34134, Republic of Korea

E-mail: jwoo@cnu.ac.kr
Telephone: +(82) 10 9460 7553

**Abstract.**

In this research, water direct injection into the combustion chamber along with hydrogen direct injection was systemically evaluated in a single-cylinder spark ignition engine. The result emphasized that 8 mg/cycle of water direct injection during compression stroke enhances 0.9 bar of nIMEP with reduced nitrogen oxide (NOx) emissions compared to that of base condition maintaining thermal efficiency. By employing 16 mg/cycle of water injection during compression, the engine's stability (i.e. cylinder pressure rise rate) was enhanced, leading to an increase in 16 % of gIMEP and a reduction in NOx emissions by approximately 20 %. Boosting, coupled with water injection, further enhances load expansion, and reduces knocking incidents, leading to significant improvements in engine performance and emissions.

## 1. Introduction

The reduction of NOx emissions by lowering the combustion temperature using water injection in hydrogen internal combustion engines were investigated by some researchers [1-4]. Nande et al. achieved a 1.4 % and 27 % improvement in efficiency and NOx emissions respectively over retarded ignition timing [2]. Younkins et al. compared with water injection to multiple injection and showed that water injection reduced NOx emissions by 87 % with a 2% fuel consumption penalty, while multiple injection reduced NOx emissions by 68% with a 6% fuel consumption penalty [3]. However, previous studies conducted experiment in the port water injection with hydrogen direct injection [1,2] or direct water injection with hydrogen port injection [3,4] system. This achieved a significant reduction in NOx emissions, but limited power output due to low volumetric efficiency.

The primary objective of this study was to reduce NOx emissions and increase the load while maintaining the efficiency of hydrogen direct injection engines with water injection. The effect of water injection was evaluated at 14 of compression ratio and 1500 rpm of engine speed. For hydrogen injection, the wall-guided injector was used at a pressure of 5 MPa and water was injected using diesel injector at 12 MPa. The basic parameters of the engine, such as water injection timing and water injection rate with the main aim of expend the load. Experimental studies were also conducted under boosting conditions to maximise the feasibility of water injection.

## 2. Experimental setup

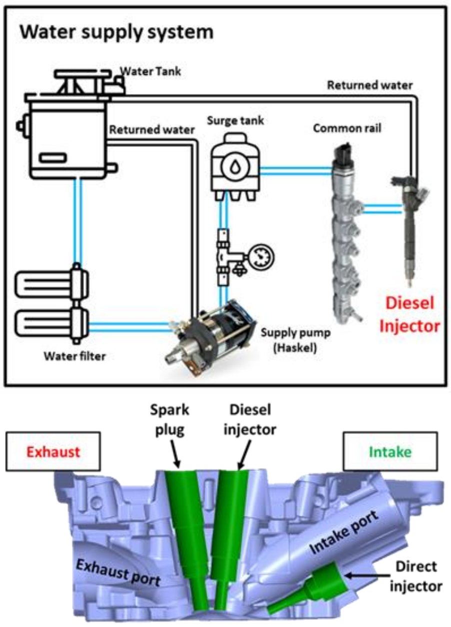

**Fig. 1.** Water injection system and engine head configuration

**Table 1**. Engine specifications and condition

| | |
|---|---|
| Engine speed [rpm] | 1500 |
| Stroke [mm] | 84.5 |
| Bore [mm] | 77.2 |
| Connecting rod [mm] | 140 |
| Displacement volume [cc] | 395.5 |
| Compression ratio [-] | 14 |
| Int/Exh valve duration [CA] | 224/232 |
| Tumble ratio | 1.1 |
| Hydrogen injector | Turbo-GDI injector (5 MPa) |
| Water injector | Diesel injector with common rail (5 MPa) |
| Hydrogen injection timing [CA bTDC] | 140, 160 |
| Water injection timing [CA bTDC] | 360 ~ -360 |

## 3. Results

### 3.1 Load expansion by water injection timing

In the water injection timing sweep experiment for load expansion, the water injection quantity was maintained at 8 mg/cycle, which was determined to be optimal for thermal efficiency. The water injection timing was varied bTDC from 360 to -360 °CA. The throttle was fully open, and hydrogen injection timing was fixed at bTDC 160 °CA which shows the highest load at the rich limit (i.e., knock incidence <20% or MPRR <5 bar/deg) in previous experiment. Since the load at the rich limit was explored under WOT conditions, the excess air ratio varied under all conditions, but was approximately between 1.4 and 1.62. The nIMEP, excess air ratio and $NO_x$ emissions in various water injection timing are illustrated in Fig. 2. For water injection during combustion, nIMEP was slightly increased but the nITE decreased due to the negative effect on combustion. For water injection in gas exchange stroke (i.e. intake and exhaust), nIMEP increased due to the denser fresh air resulting from the cooled residual gas and in-cylinder temperature.

It should be noted that the rich limit and the load were expanded the most at bTDC 140 °CA with water injection. The load expansion with water injection was remarkable in the compression stroke. Water injected at this timing directly lowers in-cylinder temperature. Both MPRR and knocking were reduced due to the lower initial pressure rise rate. After bTDC 140 °CA of water injection timing, the nIMEP slightly decreases because the decreasing in-cylinder volume increases wall wetting. Therefore, the NOx emissions were increased, mitigating the cooling effect of water injection.

### *3.2* Load expansion by water injection rate

Fig. 3 illustrates the result of gIMEP and NOx emissions at the rich limit at various water injection rates of 4,8,12 and 16 mg/cycle at 140 °CA bTDC, which shows the highest load expansion rate with reduced $NO_x$ emissions in Fig. 2. It was effectively suppressed with the approximately 5 bar/deg of MPRR, however, for knocking incidence, limited to 25.3 % in base condition (i.e. no water injection). Reduced both knocking incidence and pressure rise rate allowed a 1.22 bar increase in gIMEP from base condition at 16 mg/cycle. $NO_x$ emissions were effectively lowered by around 20 % due to the 63 K lower temperature at the start of combustion.

Fig. 3 also shows the retarded ignition timing which is a common method employed to mitigate knocking in conventional SI engines. The knocking incidence was 0 at both the result of retarding ignition timing and water injection 16 mg/cycle, but the load expansion rate of water injection was slightly higher than that of retarding ignition timing. Notably, the NOx was significantly reduced with water injection compared to retarding ignition timing case, and gIMEP was slightly enhanced. Furthermore, $NO_x$ emissions of the retarded ignition timing were higher and lower 1.45% nITE than the base condition, while the water injection strategy improved nITE by 0.64%.

### *3.3* Load expansion by boosting with water injection

The experimental results of load expansion by boosting and boosting with water injection are shown in Fig. 4. The hydrogen injection timing was fixed at 140 °CA bTDC, and the throttle was fully opened. The water injection timing was fixed at 140 °CA bTDC and the water injection rate was also fixed at 16 mg/cycle. Firstly, the boosting cases not only enhance air intake but also allow 3.8 bar of load expansion in intake pressure 1.6 bar condition by mitigating MPRR and knocking incidence. The knocking incidence was lowered by 25.3 %, 17.45 %, 14.53 %, and 5.32 % in base, 1.2 bar, 1.4 bar, and 1.6 bar boost-only conditions respectively as enhancing intake pressure, however, the knocking still occurred.

With water injection, knocking incidences were almost zero thanks to reduced in-cylinder temperature. To analyze the effect of water injection under boosting conditions, the spark timing was set to MPRR 5 bar/deg, and all other operating parameters were kept constant except for the spark timing during water injection. For boosting with water injection, the increase of 0.3 ~ 0.55 of gIMEP than only boosting condition was achieved. Finally, 13.69 bar was achieved retarding ignition timing in intake pressure 1.6 bar with 16 mg of water injection. In this condition, NOx emissions were reduced from 16.6 g/kwh to 12.0 g/kwh compared to the base condition.

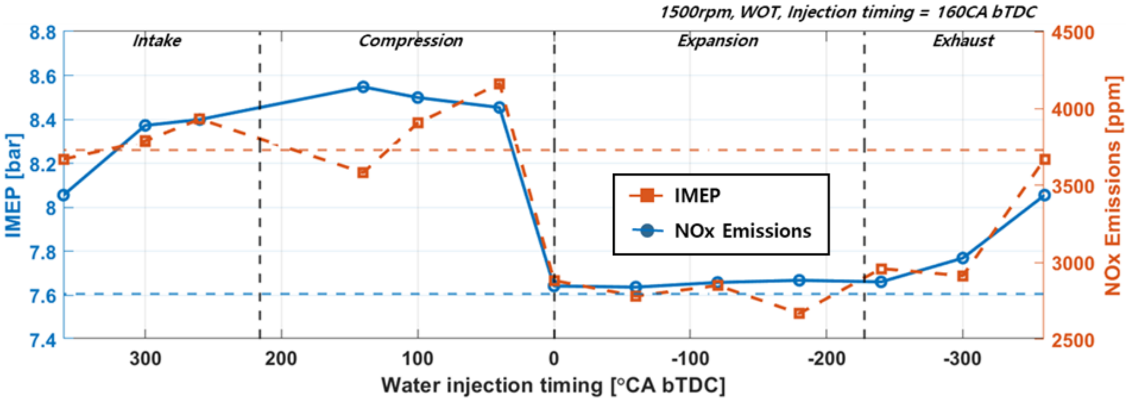

**Fig. 2.** Effect of water injection timing on nIMEP and NOx emissions

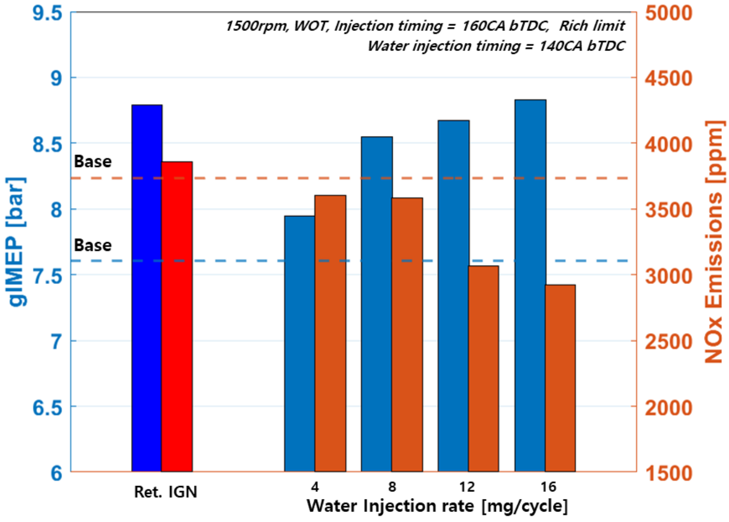

**Fig. 3.** Effect of water injection rate on gIMEP and NOx emissions

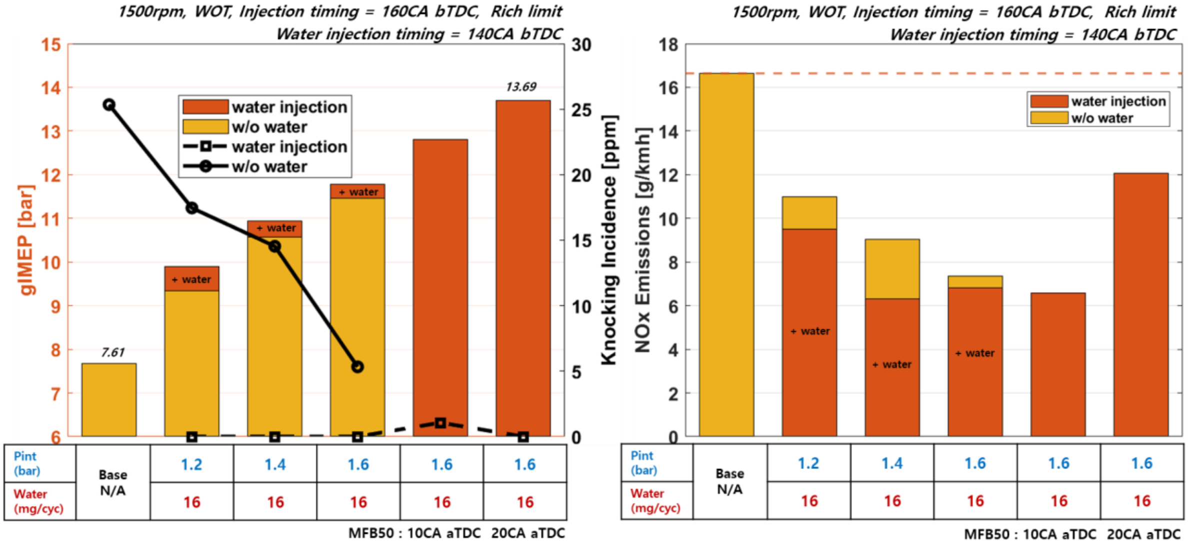

**Fig. 4.** Load expansion by boosting with water injection

## Conclusions

The experimental investigation of the effects of water direct injection as a strategy for improving load and reducing NOx in hydrogen fueled spark ignition engine. The water injection at compression stroke directly reduced the in-cylinder temperature, leading to notable load expansion due to reducing both MPRR and knocking. Water injection offers notable benefits in terms of increased engine stability including knocking and MPRR, enhanced load expansion rates, and reduced NOx emissions and these benefits were maximized as the amount of water increased. Moreover, when combined with boosting, water injection enabled achieving 78% of load expansion without encountering knocking issues compared to without both boosting and water injection condition.

## Acknowledgement

This research was partly supported by the Ministry of Trade, Industry and Energy of South Korea (MOTIE) (No. 20018473/Development of Direct Injection Hydrogen Engine Source Technology based on Carbon-Free Hydrogen Fuel), Korea Institute for Advancement of Technology(KIAT) grant funded by the Korea Government(MOTIE)(P0023684, HRD Program for Industrial Innovation) and the National Research Foundation of South Korea (NRF) (RS-2024-00335567/Research on the Energy Efficiency for the Integrated System of On-board Fuel Production/Reforming and xH2/Hydrogen Dual-fueled Engine on the Carbon Neutral-fueled Ship).

## References

[1] Subramanian V, Mallikarjuna J and Ramesh A. Effect of water injection and spark timing on the nitric oxide emission and combustion parameters of a hydrogen fuelled spark ignition engine. International Journal of Hydrogen Energy (32) 1159-1173. (2007).

[2] Nande AM, Wallner T and Naber J. Influence of water injection on performance and emissions of a direct-injection hydrogen research engine. Report no. 0148-7191, 2008. SAE Technical Paper.

[3] Younkins M, Wooldridge MS and Boyer BA. Port injection of water into a DI hydrogen engine. Report no. 0148-7191, 2015. SAE Technical Paper.

[4] Xu P, Ji C, Wang S, et al. Effects of direct water injection on engine performance in a hydrogen (H2)-fueled engine at varied amounts of injected water and water injection timing. International Journal of Hydrogen Energy (45) 13523-13534. (2020).

# LES-TFM Modeling of Hydrogen Combustion in Internal Combustion Engines

B. Mahmoodi[1], P. Tamadonfar[1], A. Bhattacharya[1] and O. Kaario[1]

[1]Department of Mechanical Engineering, School of Engineering. Aalto University. Otakaari 4, 02150 Espoo, Finland.

E-mail: bayazid.mahmoodi@aalto.fi
Telephone: +(358) 503 270 205

**Abstract.** The integration of hydrogen ($H_2$) as a fuel for internal combustion engines (ICEs) offers a promising avenue towards eco-friendly transportation. Despite having relatively simple combustion chemistry, $H_2$ combustion in ICEs needs to overcome challenges like high flame speed, wide flammability limits, extremely thin flame thickness, and thermo-diffusive instabilities (TDI). The scale-resolving 3-dimensional (3D) computational fluid dynamics (CFD) simulation of $H_2$ combustion at engine-relevant conditions is an accepted strategy for understanding these complex phenomena. Thus, to enhance the understanding of $H_2$ combustion in ICEs, this study presents an advanced numerical investigation of $H_2$ combustion within ICEs using Large Eddy Simulation (LES). The primary objective of this research is to investigate the crucial influence of TDI on the dynamics of $H_2$ flames under elevated temperatures and pressure conditions pertinent to ICEs. The simulation is carried out using StarCCM+ on a simplified piston-cylinder configuration, which accurately captures the key operational parameters of ICEs. For Turbulence-Chemistry Interactions (TCI), a dynamic Thickened Flame Model (TFM) is used. The combustion model is combined with Adaptive Mesh Refinement (AMR) within the reaction zone, where reaction sources are calculated using a detailed chemistry model. In order to consider suppressed TDI caused by artificial flame thickening, a TDI efficiency model is integrated into the TFM. The results of the TFM model have been validated against the established Turbulent Flame Speed Closure (TFC) model predictions for lean fuel-air combustion conditions. Quantitative comparisons reveal that the TFM results when integrated with the TDI efficiency model, align closely with those of the TFC model. Additionally, the TFM effectively captures the dynamics of $H_2$ flame propagation at high pressures.

**Bibliography**

| | |
|---|---|
| *CAD* | *Crank Angle Degree.* |
| *TDC* | *Top Dead Center.* |
| $\phi$ | *Fuel-air equivalence ratio.* |
| $c$ | *Progress variable (ranges from 0 to 1, where c=1 represents a completely burnt mixture).* |
| *TDI* | *Thermo-Diffusive Instabilities.* |
| *LES* | *Large Eddy Simulations.* |
| *TFM* | *Thickened Flame Model.* |
| *TFC* | *Turbulent Flame speed Closure.* |

## 1. Introduction

The use of $H_2$ as a fuel for ICEs offers a promising path towards environmentally friendly transportation. However, utilizing hydrogen in ICEs presents significant challenges due to its specific molecular transport properties compared to conventional hydrocarbon fuels. One major concern is the TDI of lean premixed hydrogen flames. This is caused by the difference between molecular and thermal diffusions, leading to low-Lewis number effects. Aniello et al. [1] recently addressed the TDI effects in the context of LES with TFM combustion model. They introduced an efficiency factor to increase the local reaction rate, compensating for the reduced TDI instabilities and flame acceleration due to thickening. They assumed a separation of scales between turbulent and TDI phenomena, as these occur at distinct scales, and proposed a TDI closure model based on direct numerical simulation (DNS) derived correlations for hydrogen-air mixtures, as indicated in [2].

This new model was tested for lean hydrogen-air combustion in an atmospheric swirled burner, revealing that TDI instabilities enhance local reaction rates in lean flame areas. However, the TFM-TDI model has only been tested under atmospheric conditions. Studies [2] show that TDI instabilities are significantly influenced by pressure variations. At higher pressures, the flame surface wrinkling structures resulting from TDI instabilities amplify, strongly affecting the overall flame propagation speed. Therefore, the main objective of this research is to investigate the TDI-TFM model under the high pressures relevant to ICEs.

## 2. Solution methodology and computational setup

In this study, turbulence combustion modelling is approached using LES. The set of transport equations is solved using the advanced commercial CFD solver StarCCM+ [3] in a simple piston-cylinder configuration, as detailed in [4].The chemistry is introduced using a detailed chemistry mechanism [5] within a multicomponent transport modelling framework, and the turbulent-chemistry interaction is modelled using TFC [6] and TFM [7] combustion models. The TDI effect is incorporated into TFM using an additional efficiency factor, following the correlation by Berger et al. [2] as detailed in [8]. To investigate the effect of TDI in TFM, two sets of TFM simulations, with and without TDI, are conducted, and the results are compared with the TFC model, which is widely used for hydrogen combustion simulations in ICEs [9], [10]. The cylinder region is resolved with more than $3.8\times10^6$grids, and in the case of TFM simulations, due to the dynamic resolution of the flame front using AMR, the grid count increases up to $65 \times10^6$. The TFM simulations are performed with a constant flame thickness of 0.25 mm, with the flame resolved by 8 cells. During combustion, the pressure increase inside the cylinder reduces the laminar flame thickness, resulting in large flame thickening factors of up to 30. These high flame thickening factors suppress hydrodynamic instability induced flame area enlargement and lead to an extreme underprediction of overall combustion speed. Therefore, in this study, the maximum flame thickening factor was limited to a value of 5. The validity of this assumption will be further evaluated in future studies. Further details about the engine setup and simulation conditions are provided in Table 1.

**Table 1**. Simulation setup specifications

| | |
|---|---|
| Stroke [mm] | 60 |
| Bore [mm] | 75 |
| Engine speed [RPM] | 560 |
| Compression ratio | 10 |
| Fuel | $H_2$ |
| Oxidizer | Air |
| Wall temperature [K] | 400 |
| Charge temperature [K] | 400 |
| Charge pressure [atm] | 1 |
| Spark time [CAD] | 3 before TDC |

## 3. Results and discussion

Figure 1 shows the performance of different combustion models and configurations by comparing the cylinder's mean pressure and mean fuel mass fraction predictions during combustion. Taking the TFC results as a reference, it is clear that the TFM simulations without the TDI effect significantly underpredict the pressure rise and fuel consumption rate. This discrepancy occurs because the thickening in TFM removes the TDI flame area enlargement effect, as the TDI wrinkling scales are of the same scale of the laminar flame thickness [8]. However, including the TDI effect in the TFM simulations using the TDI efficiency factor significantly improves the results, making them closely match the TFC results. This improvement is consistent with the findings in [8], which reported that the TDI effect in TFM increases the fuel consumption rate for lean hydrogen-air combustion under atmospheric conditions. These results extend this observation to high-pressure engine conditions, demonstrating a similar improvement.

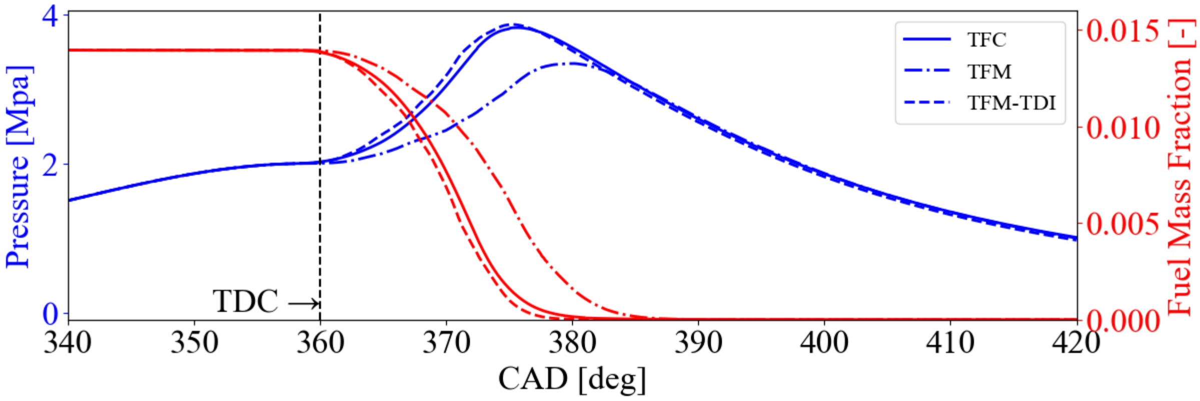

**Fig. 1.** Evolution of mean cylinder pressure and fuel mass fraction during Combustion with different modeling configurations.

Figure 2 illustrate the flame profiles obtained from TFM-TDI simulations at various CADs. The profiles are visualized using the progress variable isosurface at ($c$=0.9), colored by hydrogen mole fraction.

After ignition, a spherical flame expands until it contacts the cylinder head and piston walls, forming an annular shape within the cylinder. As the flame grows, it interacts with turbulent eddies, causing the flame surface to wrinkle. This wrinkling intensifies as the combustion process progresses due to ongoing interactions with turbulent eddies in the unburned regions. A detailed examination of Fig. 2. reveals two distinct scales of flame surface wrinkling. In addition to larger wrinkles induced by turbulence, smaller structures begin to develop and spread on the flame surface. As the flame propagates, these small structures grow and gradually extend across the entire flame surface, leading to further flame surface enlargement and resulting in flame front acceleration. These structures closely resemble the cellular patterns observed experimentally on the surfaces of expanding spherical hydrogen flames under high pressures by Tse et al. [11]. Similar patterns have also been reported in several DNS studies of spherical and cylindrical hydrogen flames [12], [13].

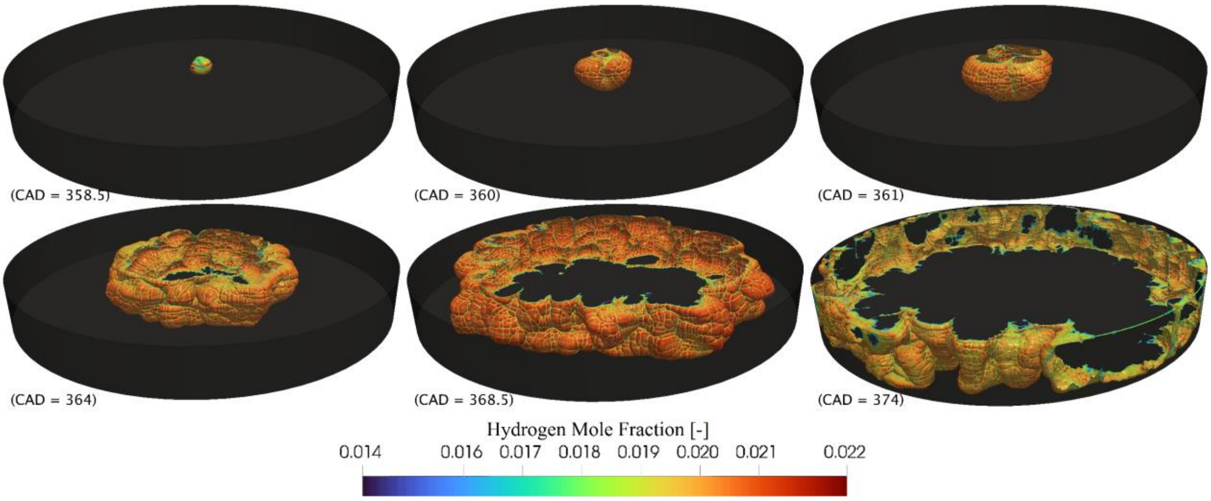

**Fig. 2.** Flame front evolution visualized by progress variable isosurface ($c$ = 0.9) across various CADs for lean ($\phi = 0.5$) TFM-TDI combustion simulation

## Conclusions

This research demonstrates that incorporating the TDI effect in TFM simulations significantly improves predictions of pressure rise and fuel consumption rate. This finding, consistent with previous studies under atmospheric conditions, also applies to high-pressure engine conditions, emphasizing the importance of including the TDI effect for accurate hydrogen combustion modeling in ICEs.

## Acknowledgments

This work is funded by the Henry Fordin Säätiö, Finland (grant numbers 700834 and 700851). BM expresses gratitude for the scholarships from the Merenkulun säätiö. The authors appreciate the computational resources supplied by the Aalto Science-IT project, Aalto Research Software Engineers (RSEs), and CSC (Finnish IT Center for Science).

## References

[1] A. Aniello, D. Laera, L. Berger, A. Attili, and T. Poinsot, “Introducing thermo-diffusive effects in large-eddy simulation of turbulent combustion for lean hydrogen-air flames,” *Proceedings of the 2022 Summer Program*, 2022.

[2] L. Berger, A. Attili, and H. Pitsch, “Intrinsic instabilities in premixed hydrogen flames: parametric variation of pressure, equivalence ratio, and temperature. Part 2 – Non-linear regime and flame speed enhancement,” *Combustion and Flame*, vol. 240, Jun. 2022, doi: 10.1016/j.combustflame.2021.111936.

[3] Siemens Digital Industries Software, “Simcenter STAR-CCM+ Theory Guide, version 2023.02,” 2023. Accessed: Jan. 23, 2024. [Online]. Available: https://docs.sw.siemens.com/en-US/doc/226870983/PL20221128664127487.starccmp_userguide_html?audience=external

[4] A. P. Morse, J. H. Whitelaw, and M. Yianneskis, “Turbulent Flow Measurements by Laser-Doppler Anemometry in Motored Piston-Cylinder Assemblies,” *Journal of Fluids Engineering*, vol. 101, no. 2, pp. 208–216, Jun. 1979, doi: 10.1115/1.3448937.

[5] T. Varga *et al.*, “Optimization of a hydrogen combustion mechanism using both direct and indirect measurements,” *Proceedings of the Combustion Institute*, vol. 35, no. 1, pp. 589–596, 2015, doi: 10.1016/j.proci.2014.06.071.

[6] P. D.-I. Flohr and H. Pitsch, “A turbulent flame speed closure model for LES of industrial burner flows,” 2001. [Online]. Available: https://api.semanticscholar.org/CorpusID:15328366

[7] O. Colin, F. Ducros, D. Veynante, and T. Poinsot, “A thickened flame model for large eddy simulations of turbulent premixed combustion,” *Physics of Fluids*, vol. 12, no. 7, pp. 1843–1863, Jul. 2000, doi: 10.1063/1.870436.

[8] A. Aniello, D. Laera, L. Berger, A. Attili, and D. T. Poinsot, “Introducing thermodiffusive effects in large-eddy simulation of turbulent combustion for lean hydrogen-air flames.”

[9] G. M. Kosmadakis, C. D. Rakopoulos, J. Demuynck, M. De Paepe, and S. Verhelst, “CFD modeling and experimental study of combustion and nitric oxide emissions in hydrogen-fueled spark-ignition engine operating in a very wide range of EGR rates,” *International Journal of Hydrogen Energy*, vol. 37, no. 14, pp. 10917–10934, Jul. 2012, doi: 10.1016/j.ijhydene.2012.04.067.

[10] U. Gerke and K. Boulouchos, “Three-dimensional computational fluid dynamics simulation of hydrogen engines using a turbulent flame speed closure combustion model,” *International Journal of Engine Research*, vol. 13, no. 5, pp. 464–481, Oct. 2012, doi: 10.1177/1468087412438796.

[11] S. D. Tse, D. L. Zhu, and C. K. Law, “Morphology and burning rates of expanding spherical flames in H2/ O2/inert mixtures up to 60 atmospheres,” *Proceedings of the Combustion Institute*, vol. 28, no. 2, pp. 1793–1800, 2000, doi: https://doi.org/10.1016/S0082-0784(00)80581-0.

# Visualization of Thermodiffusive Instabilities of the Early Flame in a Hydrogen-Fueled Spark Ignition Engine

Pedro Ye[1], Jannick Erhard[1], Cooper Welch[1], Hao Shi[1], Andreas Dreizler[1] and Benjamin Böhm[1]

[1]Technical University of Darmstadt, Department of Mechanical Engineering, Reactive Flows and Diagnostics, Otto-Berndt-Str. 3, 64287 Darmstadt, Germany

E-mail: ye@rsm.tu-darmstadt.de
Telephone: +(49) 6151 16-28907

**Abstract.** Lean hydrogen combustion is prone to thermodiffusive instabilities due to preferential diffusion leading to variations in the local equivalence ratio. This work investigates the prominence of such instabilities in internal combustion engine applications by studying planar flame images recorded in an optically accessible research engine using laser-induced fluorescence of inert $SO_2$ tracer gas. The comparison of mixtures with varying Lewis numbers shows that conditions with Lewis numbers far below unity have a higher number of cellular structures with smaller characteristic lengths along the flame front, indicating higher instabilities. This study reveals that thermodiffusive instabilities can be resolved under lean hydrogen-fueled conditions within the dynamic and highly turbulent environment of internal combustion engines.

## 1. Introduction

Hydrogen presents a promising alternative for reducing greenhouse gas emissions in internal combustion engines (ICEs). Unlike traditional hydrocarbon fuels, hydrogen has a higher diffusivity, which significantly affects flame propagation characteristics. In direct numerical simulations (DNS) it was shown for laminar flows that thermodiffusive instabilities occur in lean $H_2$ mixtures under the thermodynamic conditions prevailing in ICEs [1]. In turbulent flows, however, it is unclear whether the turbulent flow dominates the flame wrinkling or whether it promotes the thermodiffusive instabilities. Therefore, it is of high relevance to understand the possible influence of these instabilities on flame propagation in ICEs. To investigate these phenomena, this study focuses on visualizing the early flame under lean premixed hydrogen conditions using an optically accessible spark ignition engine and planar laser-induced fluorescence (LIF). Two reference conditions were used where thermodiffusive instabilities are not expected: one with hydrogen fuel and simulated exhaust gas recirculation (EGR) at stoichiometric conditions, and another with stoichiometric premixed methane. By examining these conditions, this work aims to identify and characterize the cellular structures associated with thermodiffusive instabilities. Shedding light on these structures is crucial for determining their influence on early flame propagation, ultimately providing valuable insights for accurately modeling and simulating hydrogen-fueled ICEs.

## 2. Methodology

### 2.1 Experimental Setup

The Darmstadt Engine is a single-cylinder optically accessible engine widely used as a reference for modeling and simulation [2–4]. In this work, the engine operating conditions were extended to include the use of premixed $H_2$. The fuel was injected well upstream of the intake valves to ensure homogeneous mixing of the air-fuel mixture. The engine has a compression ratio of 8.7, a spray-guided 4-valve pent-roof cylinder head, a centrally positioned spark plug, a quartz glass cylinder liner and a flat piston window. More detailed information on the engine and its flow characteristics can be found in [2,3].

Flame visualization was performed using sulfur dioxide ($SO_2$) LIF, a technique that has proven effective to resolve the flame front in previous research [5]. A 10 Hz LIF setup was used for different operating conditions to acquire one image per cycle using a frequency quadrupled Nd:YAG laser and an Imager M-lite (LaVision) coupled with an image intensifier (IRO, LaVision). The experimental setup is shown in Figure 1. The operating conditions are given in Table 1 where N is the engine speed in

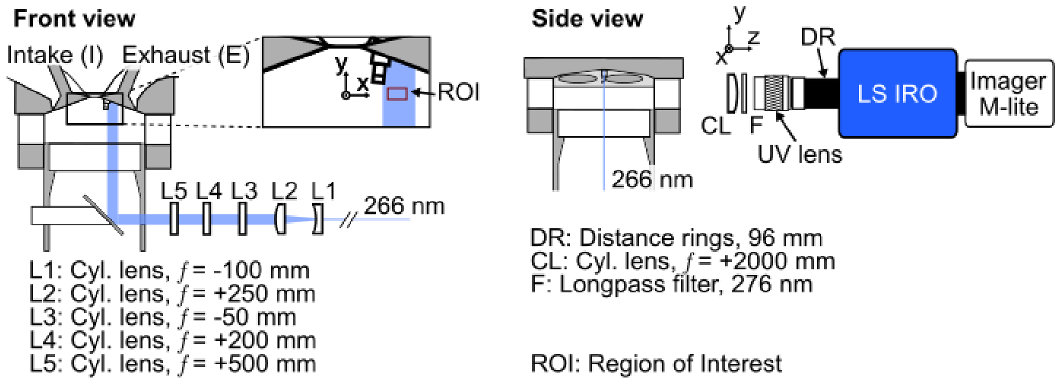
Front view
Intake (I)
Exhaust (E)
y
x
ROI
L5 L4 L3 L2 L1
266 nm
L1: Cyl. lens, f = -100 mm
L2: Cyl. lens, f = +250 mm
L3: Cyl. lens, f = -50 mm
L4: Cyl. lens, f = +200 mm
L5: Cyl. lens, f = +500 mm
Side view
y
z
x
DR
LS IRO
Imager
M-lite
CL
F
UV lens
266 nm
DR: Distance rings, 96 mm
CL: Cyl. lens, f = +2000 mm
F: Longpass filter, 276 nm
ROI: Region of Interest

**Figure 1.** Schematic of the experimental setup

rotations per minute (rpm), $p_{intake}$ is the intake pressure in bar, $t_{ign}$ and $t_{LIF}$ are the ignition and image timing in crank angle degree (°CA) and $\lambda$ is the air/fuel equivalence ratio. EGR was simulated by assuming nitrogen ($N_2$) as the only recirculated exhaust gas and by mixing it with air upstream of the intake pipe. The pressure at ignition $p_{ignition}$ is the average for all cycles of each condition and the temperature at ignition $T_{ignition}$ was calculated using an isentropic assumption following [6]. Although the complete pressure trace of the conditions varies, the initial conditions of ignition are the same except for the $H_2$ with EGR case, which has the ignition delayed to obtain similar combustion phasing as the other conditions. Additionally, the effective Lewis number ($\mathrm{Le}_{\mathrm{eff}}$) at the time of ignition for each condition was calculated according to [7,8] with the mechanisms of Burke et al. [9] for the $H_2$ conditions and GRI-Mech 3.0 [10] for the $CH_4$ conditions.

**Table 1.** Operating conditions. °CA: Crank angle degrees after compression top dead center (TDC)

| **N** [rpm] | $p_{intake}$ [bar] | $t_{ign}$ [°CA] | $t_{LIF}$ [°CA] | **Fuel** [–] | $\lambda$ [–] | **EGR** [%] | $p_{ignition}$ [bar] | $T_{ignition}$ [K] | $\mathrm{Le}_{\mathrm{eff}}$ [–] |
|---|---|---|---|---|---|---|---|---|---|
| 800 | 0.95 | -16.6 | -8.6 | $H_2$ | 2.56 | 0 | 13.3 | 775 | 0.397 |
| | | | | | 3.2 | | 12.8 | 775 | 0.368 |
| | | | | | 4.2 | | 12.7 | 775 | 0.346 |
| 800 | 0.95 | -8.8 | -5.2 | $H_2$ | 1 | 40 | 13.2 | 786 | 0.918 |
| | | -16.6 | -8.6 | $CH_4$ | 1 | 0 | 13.1 | 775 | 1.024 |

### 2.2 Flame Cell Detection

Flame cell detection was performed using a custom MATLAB script. The process starts by binarizing the raw images, whereby the images are background subtracted, energy corrected and filtered (gaussian filter with varying sigma determined by a sensitivity analysis). Then Otsu's method is applied and followed by a smoothing of the contours of the binarized flames. A curvature value was computed for each point along the flame front with negative curvature values assigned to points in concave segments. Points with curvature values less than -3 $mm^{-1}$ were identified as cusp regions. Furthermore, if a section between two cusps consisted entirely of points with negative curvature, all these points were classified as a single cusp together with the bounding cusps. Thus, a flame cell begins at the midpoint of one cusp and ends at the midpoint of the next cusp. Finally, sections bounded by only one cusp, such as segments in contact with the frame boundaries, were excluded from the analysis.

## 3. Results and Discussion

To visualize the flame differences between conditions without and with expected thermodiffusive instabilities, Figure 2 shows the normalized intensity and flame contour with each cell detected for a single cycle of the $CH_4$ with $\lambda = 1$ and $H_2$ with $\lambda = 2.56$ conditions. Although the images are manually selected, they serve to compare the differences between the flames of the two conditions. Different cell structures are shown as contours with different consecutive color segments. Flame intensity is normalized to the maximum intensity recorded for each condition. As the intensities are derived from $SO_2$-LIF signals, they are a representation of the gas temperature, with higher intensities indicating higher temperatures.

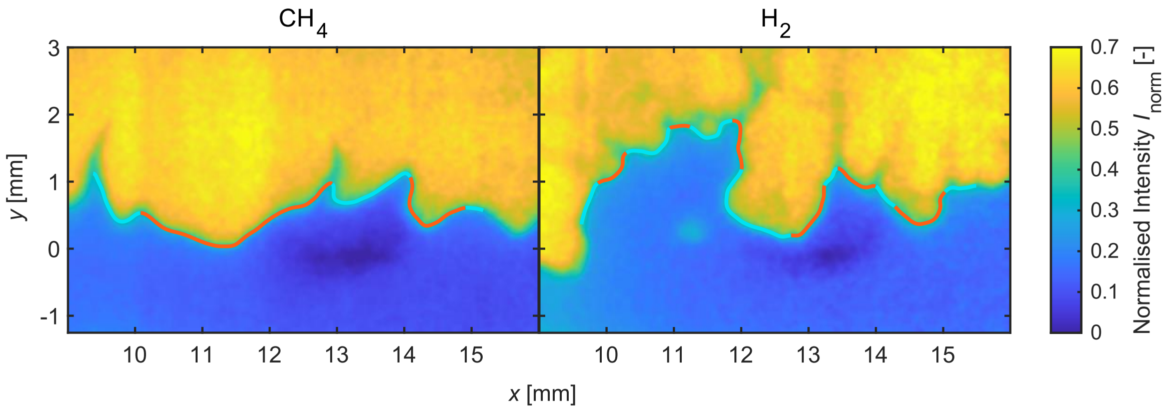

**Figure 2.** Instantaneous flame images and cells detected for individually selected cycles for $CH_4$ with $\lambda = 1$ and $H_2$ with $\lambda = 2.56$ each consecutive cell is colored separately. Images are taken at -8.6 °CA

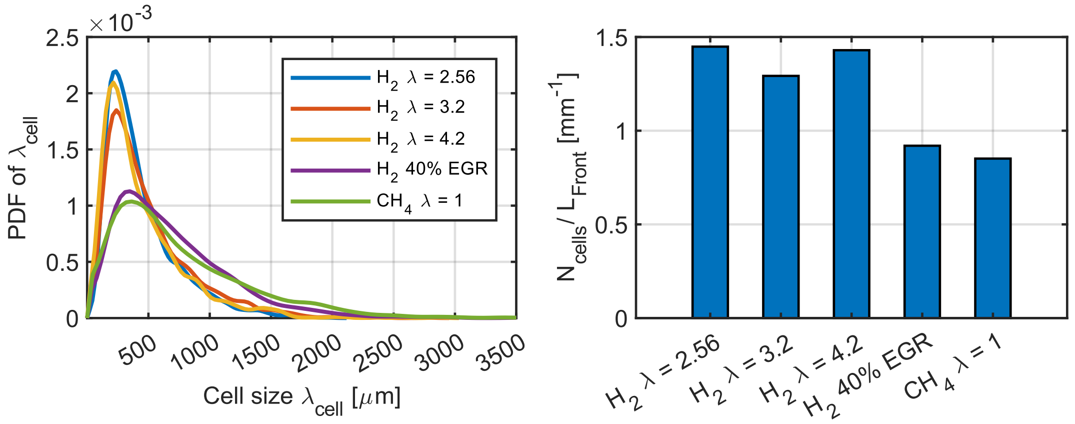

**Figure 3.** Cell size distribution and cell density. Data taken at -8.6 °CA for lean hydrogen and stoichiometric methane conditions; at -5.6 °CA for hydrogen with EGR condition

There is a clear contrast between the two conditions. While $CH_4$ flames have a more homogeneous intensity distribution within the burned gas region, the hydrogen flame shows more inhomogeneity. There are more gaps of lower intensity, which is also reflected in the flame front cell detection. In terms of the flame front, the $CH_4$ flame has a smoother front resulting in larger cells, while the $H_2$ flame front has a more cellular structure represented by the higher number of smaller cells. This cellular flame front is similar to canonical images of spherically expanding laminar flames with thermodiffusive instabilities [11], suggesting that the detected structures are indeed cells of thermodiffusive instabilities.

In order to quantify the trends found in the representative single cycles, Figure 3 shows the probability density function (PDF) of the cell size distribution for all images of the conditions studied. Assuming that each cell structure is a semicircle, the computed cell size $\lambda_{\mathrm{cell}}$ is taken as the diameter of such a semicircle. Although the cells are not exactly semicircular, this definition is retained to be consistent with the literature. The characteristic cell size for the lean $H_2$ flames is clearly separated from the characteristic cell size of the other conditions: the former is around 230 μm, while the latter is around 360 μm. Even though the obtained cell sizes are slightly higher than DNS studies of thermodiffusive instabilities [1], it is important to consider that these simulations are made in a two-dimensional domain under laminar conditions, while three-dimensional effects and turbulence can influence the cell sizes. The distribution of cell sizes is narrower for lean conditions compared to stoichiometric conditions, indicating a strong prevalence of smaller cells. Furthermore, the effective Lewis number has a clear correlation with the distribution of cell sizes. Cases with $\mathrm{Le}_{\mathrm{eff}} < 0.4$ show a narrower distribution shifted towards smaller values. In contrast, the distribution in the cases where $\mathrm{Le}_{\mathrm{eff}} \approx 1$ suggests that their structures are more likely associated with engine flow turbulence rather than thermodiffusive instabilities due to the lack of preferential diffusion. To account for the length of the flame front captured within the ROI for the different conditions, the number of cells detected ($N_{\mathrm{cells}}$) per flame front length ($L_{\mathrm{front}}$) is also shown on the right side of Figure 3. Conditions with thermodiffusive instabilities have a higher cell number density, with values close to 1.5 mm$^{-1}$. The other conditions have a lower cell number density, not even reaching 1 mm$^{-1}$, due to the larger size of the cells detected.

Therefore, evidenced by the single cycle images and the statistical analysis approach, cases with low $\mathrm{Le}_{\mathrm{eff}}$ contain flame cell structures typical of thermodiffusive instabilities. To the best of the authors' knowledge, this is the first time that such structures have been detected in ICE applications.

## 4. Conclusions

The cellular flame front of thermodiffusive instabilities has been visualized by $SO_2$-LIF inside an ICE. These instabilities were previously known to exist in more controlled laminar conditions and in DNS studies, but their impact on more practical applications within turbulent flows has been largely unknown. This demonstrates that although other processes such as turbulence, convection and volume confinement influence lean hydrogen combustion in ICEs, thermodiffusive instabilities also play a role in the early flame propagation. In order to characterize these instabilities, analysis techniques previously used for DNS of laminar cases were adopted to extract the cells size from the flame front of experimentally measured data. For lean $H_2$ conditions, where the effective Lewis number is far below unity and thermodiffusive instabilities are present, a characteristic cell size of $\approx 230$ µm was identified. In contrast, for conditions without thermodiffusive instabilities, larger and more widely distributed cell sizes were detected. This research contributes to a better understanding of the impact of thermodiffusive instabilities on early flame propagation, providing key insights that could improve the predictive accuracy of models used to simulate combustion in hydrogen-fueled engines.

## Acknowledgments

Support by Deutsche Forschungsgemeinschaft through FOR 2687 ‘‘Cyclic variations in highly optimized hydrogen-fueled spark-ignition engines: experiment and simulation of a multi-scale causal chain’’–project number 423224402 – is kindly acknowledged.

## References

[1] L. Berger, A. Attili, H. Pitsch, Intrinsic instabilities in premixed hydrogen flames: parametric variation of pressure, equivalence ratio, and temperature. Part 2 – Non-linear regime and flame speed enhancement, Combustion and Flame 240 (2022) 111936.
[2] E. Baum, B. Peterson, B. Böhm, A. Dreizler, On The Validation of LES Applied to Internal Combustion Engine Flows: Part 1: Comprehensive Experimental Database, Flow Turbulence Combust 92 (2014) 269–297.
[3] C. Welch, L. Illmann, M. Schmidt, B. Böhm, Experimental characterization of the turbulent intake jet in an engine flow bench, Exp Fluids 64 (2023).
[4] C. Geschwindner, P. Kranz, C. Welch, M. Schmidt, B. Böhm, S.A. Kaiser, J. de La Morena, Analysis of the interaction of Spray G and in-cylinder flow in two optical engines for late gasoline direct injection, International Journal of Engine Research 21 (2020) 169–184.
[5] R. Honza, C.-P. Ding, A. Dreizler, B. Böhm, Flame imaging using planar laser induced fluorescence of sulfur dioxide, Appl. Phys. B 123 (2017).
[6] S. Bürkle, L. Biondo, C.-P. Ding, R. Honza, V. Ebert, B. Böhm, S. Wagner, In-Cylinder Temperature Measurements in a Motored IC Engine using TDLAS, Flow Turbulence Combust 101 (2018) 139–159.
[7] J.K. Bechtold, M. Matalon, The dependence of the Markstein length on stoichiometry, Combustion and Flame 127 (2001) 1906–1913.
[8] J. Beeckmann, R. Hesse, S. Kruse, A. Berens, N. Peters, H. Pitsch, M. Matalon, Propagation speed and stability of spherically expanding hydrogen/air flames: Experimental study and asymptotics, Proceedings of the Combustion Institute 36 (2017) 1531–1538.
[9] M.P. Burke, M. Chaos, Y. Ju, F.L. Dryer, S.J. Klippenstein, Comprehensive H 2 /O 2 kinetic model for high-pressure combustion, Int J of Chemical Kinetics 44 (2012) 444–474.
[10] G.P. Smith, D.M. Golden, M. Frenklach, N.W. Moriarty, B. Eiteneer, M. Goldenberg, C.T. Bowman, R.K. Hanson, S. Song, W.C. Gardiner JR., V.V. Lissianski, Z. Qin, GRI-Mech 3.0, http://www.me.berkeley.edu/gri_mech/.
[11] S.D. Tse, D.L. Zhu, C.K. Law, Morphology and burning rates of expanding spherical flames in H2/O2/inert mixtures up to 60 atmospheres, Proceedings of the Combustion Institute 28 (2000) 1793–1800.

# Optical Multi-Spark Ammonia Combustion Engine: Numerical Analysis and Validation

Rafael Menaca[1,*], Mickael Silva[2], Kalim Uddeen[1], Fahad Almatrafi[1], Qinglong Tang[3], James W. G. Turner[1], Hong G. Im[1]

[1]CCRC, Physical Science and Engineering, King Abdullah University of Science and Technology, Thuwal (23955-6900), Saudi Arabia
[2] Aramco Americas: Aramco Research Center – Detroit
[3] Tianjin University, China
E-mail: rafael.menaca@kaust.edu.sa
Telephone: +(966) 565072780

**Abstract.** With the aim of achieving net-zero emission standards, internal combustion (IC) engines must enhance their efficiency and incorporate alternative fuels into their operations. Ammonia ($NH_3$) emerges as a promising fuel for IC engines due to its high hydrogen content and the well-established infrastructure for its production and transportation. Given the low flame speed of $NH_3$, it is essential to explore alternatives for accelerating the burning rate. One of the most promising methods to improve $NH_3$ engine performance is the use of multiple spark plugs to create ignition points at various locations within the combustion chamber, thereby facilitating faster combustion of the charge. In this study, optical experiments are employed to validate a 3D-CFD numerical model. The optical data is subsequently used to enhance the validation of a pure thermodynamic engine model, providing crucial insights into $NH_3$ flame development. This work establishes the groundwork for the best practices in CFD modeling to capture the complex interactions of $NH_3$ multi-flame dynamics, paving the way for future engine optimization studies.

## 1. Introduction

Meeting world energy demands relies primarily on the utilization of hydrocarbons. The transport sector represents about 20% of total energy consumption, with road mobility accounting for 72% of this fraction [1]. In the U.S., the transportation sector is the leading emitter of greenhouse gases [2]. To achieve established international environmental goals and net-zero targets, internal combustion (IC) engines must reduce their emissions. This can be accomplished either by enhancing engine efficiency or by utilizing alternative fuels. Ammonia ($NH_3$) emerges as a promising candidate for direct application in IC engines as a carbon-free fuel, benefiting from its high hydrogen content. The $NH_3$ production and transportation industry is well-established, reducing barriers for near-future deployment. Due to the high-octane number of $NH_3$, engines can operate at high compression ratios without safety concerns. One challenge of $NH_3$ combustion in IC engines is its very slow flame speed, even at high compression ratios, which limits the operation range. A conventional solution is the use of blends with faster-burning fuels like hydrogen to enhance the burning rate [3]. An innovative approach to boost the burning rate is operating the engine with $NH_3$ combustion using multiple spark plugs. This technique allows multiple flame kernels to grow, collapse, and cover the entire combustion chamber more quickly and stably, thereby improving efficiency and reducing variability [4, 5]. In this study, optical experiments are used to validate a numerical model for the SI multi-spark $NH_3$ engine operation. This work establishes the best strategies in CFD engine modeling for capturing the complex $NH_3$ multi-flame interactions, paving the way for future optimization investigations.

## 2. Optical experiments

The engine used in this study is a single-cylinder AVL CI optical research engine (AVL-2402), converted to SI mode. The engine piston is a flat-quartz, extended Bowditch piston for the optical access from the high-speed camera at the bottom. Four sparks are installed in a specialized metal liner in order to generate multiple kernels as shown in the schematic of the system in **Figure *1***. The original spark plug is kept with a top-central-mounted installation. As shown, there are 5 sparks that may be activated; in this case, the release of energy for the ignition initiation occurs simultaneously at -30 CAD in all the 5 different arcs. Moreover, some of the important engine specifications may be consulted in the following references: [4, 5].

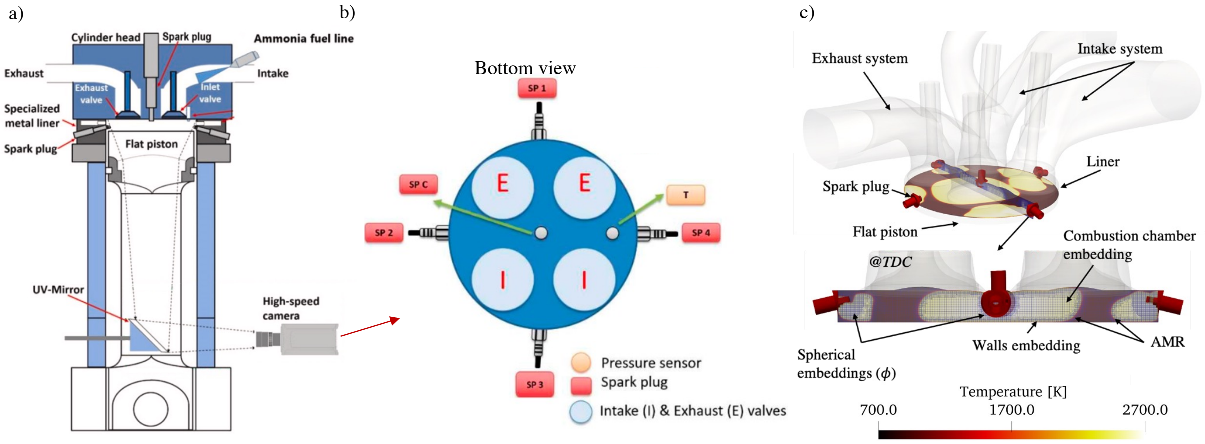

**Figure 1.** a) Schematic of the setup, b) bottom view of the combustion chamber arrangement, highlighting the multiple spark locations [4, 5], and c) computational domain and mesh features

## 3. Numerical approach

### 3.1 Numerical setup

The AVL optical engine was modeled and the numerical simulations were executed in the density-based finite volume CFD solver CONVERGE$^{TM}$ 3.0 due to its multi-physical capabilities. The computational domain is illustrated in **Figure *1*** c). As observed, the entire geometry was modeled, yet the analysis of the impact of considering the spark plug geometries on the model predictability will be discussed in the next section. The RNG $\kappa - \epsilon$ closure model is selected for the Reynolds-averaged Navier-Stokes turbulence modeling [6]. Pressure-implicit with splitting of operators' algorithm is employed to couple pressure and velocity dynamics [7]. Wall heat transfer is calculated with the O'Rourke and Amsden model [8]. The Redlich-Kwong equation of state is used along with real gas properties and mixture-averaged diffusion coefficients. Turbulent Prandtl and Schmidt numbers are set as 0.9 and 0.78, respectively. The multi-zone well-stirred reactor (MZ-WSR) SAGE combustion model is selected to solve for chemistry with the Zhang mechanism [9] for the homogeneous independent reactors on each element of the computational domain. Simulation starts at -175 CAD and last until 900 CAD covering a full cycle. Variable time-step algorithm is implemented with the minimum time step governed by the critical Courant-Friedrichs-Lewy number. Boundary conditions are adopted from experiments [4, 5]. The mixture composition is stoichiometric and assumed as a perfectly mixed inflow boundary condition. Constant Dirichlet pressure inlet and outlet boundary conditions are set, which simplifies the exchange gases process, yet capturing the correct delivered mass per cycle. Piston, liner and head walls are kept at 450 K, while the intake and exhaust systems temperatures are maintained at 333 K and 500 K, respectively. To mimic the spark, an energy source is set on each spark plug region. The source occurs in the spark plug gap in a spherical region. Mesh refinement techniques are applied in regions where strong gradient of variables are expected to occur. Moreover, walls embedding are adopted to capture near-wall physics. Spherical embeddings are implemented in the spark plug regions. Adaptive mesh refinement (AMR) is based on velocity and temperature. Mesh features are presented in **Figure *1*** c) bottom, and the details can be consulted in **Table *1*** for the five different evaluated configurations.

### 3.1 Validation stage and simulation strategy

The first step in the calibration of an engine model is related to the proper representation of the compression and expansion of the engine's work fluid. Optical engines experience large leakages due to the modifications and the setup configuration. Therefore, in order to assure a correct compression, crevices model is crucial in this type of computations. Based on literature [10], 7.5% of the total inducted mass per cycle is allowed to leak to the crankcase. The model was then calibrated targeting the squish distance, for which the geometrical compression ratio was set as CR = 12 to achieve the correct pressure evolution. Pressure traces in the motoring operation are then used to corroborate the results and the comparison is presented in **Figure *2*** a). With the motoring case adjusted, the combustion cycle is assessed. Aiming to understand the model sensitivity to mesh characteristics, different meshes are tested and the cases features are depicted in ***Table 1***. The baseline case setup is established based on literature [11], whereas the additional models attempt to improve the description of the initial kernel growth with the refinement of the mesh in the spark plug region. Additionally, a cylindrical embedding of the combustion chamber is explored to observe the keys aspects of the main chamber turbulence dissipation. Furthermore, AMR is used in meshes 3 and 4 to refine the zones where the flame is developing.

Finally, the geometry of all the spark plugs is introduced in mesh 4 and its effects on the combustion behavior will be explained in detail below.

**Table 1**. Mesh features in the mesh sensitivity analysis

| Refinement type \Case | Baseline | Mesh 1 | Mesh 2 | Mesh 3 | Mesh 4 |
|---|---|---|---|---|---|
| Spark spherical embedding* | $\phi = 5mm$<br>Level 2 | $\phi = 5mm$<br>Level 4 | $\phi = 10mm$<br>Level 4 | $\phi = 10mm$<br>Level 4 | $\phi = 10mm$<br>Level 4 |
| Cylindrical embedding Entire combustion chamber | No | No | No | Level 2 | Level 2 |
| Adaptive mesh refinement Based on velocity and temperature | No | No | No | Level 4 | Level 4 |
| Spark plug geometry | No | No | No | No | Five spark plugs |

*$\phi$: spherical embedding diameter.

## 4. Results and discussion

**Figure *2*** b) shows the pressure and heat release rate (HRR) evolution for the different evaluated cases. 100 combustion experimental cycles are used as benchmark for comparison. Upon initial observation, Baseline, Mesh 1 and 2 under-predict how combustion behaves and, although properly capturing the ignition delay (begin of HRR matching experiments), the rate is slower than the reported in the experiments. The observed behavior is a consequence of the coarse mesh in the spark plug region and the lack of AMR. The coarse mesh promotes a dissipation of the energy in a bigger volume, reducing the density in the release of energy. Furthermore, the flame grows towards a coarse zone (combustion chamber without refinements), catalyzing the same combustion response. On the other hand, Mesh 3 over-predicts the release of heat and the peak pressure reaches higher values when compared to experiments. Although the mesh in the spark plug surroundings is refined, as well as the combustion chamber, the ignition delay is shorter and a rapid raise of the in-cylinder pressure is appreciated. This behavior suggests an incorrect prediction of the thermodynamic state and fluid-dynamic conditions in the elements where ignition takes place. Therefore, the geometrical details of the spark plugs are included in the Mesh 4 model, aiming to improve the predictions in the local flow field. Remarkably, the ignition delay is improved and the overall engine performance is satisfactorily described by the numerical model. To further demonstrate the model prediction capabilities, the flame development and topology is analyzed in **Figure *3***. Upon initial assessment, the flame topology is closely captured. The multiple flame kernels are achieved in the computations and the evolution of the flame shows a similar topology to the optical images.

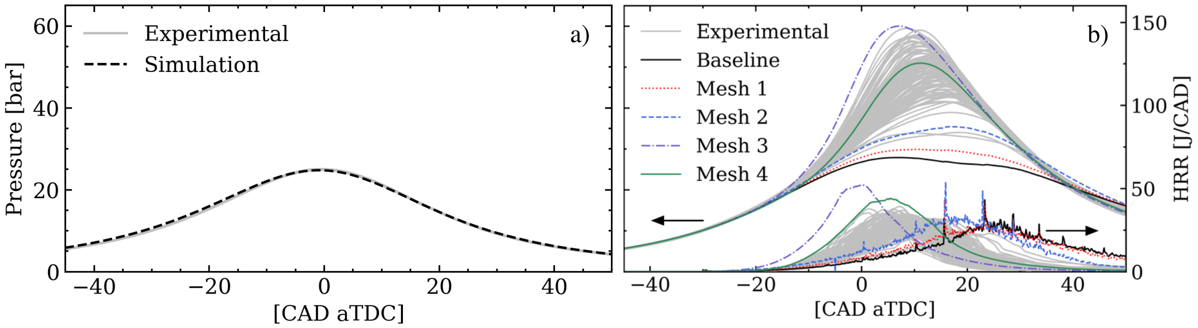

**Figure 2.** a) Pressure evolution for the motoring case validation and b) pressure and heat release rate comparison between numerical results and experiments for the different evaluated cases in the mesh sensitivity analysis

It is worth it to highlight the bottom flame (SP 3, **Figure *1*** b)). CFD results showcase very accurate qualitatively predictions in the flame development and the model is satisfactorily validated. Future studies exploring flame dynamics, interaction and engine optimization will be executed using this study as a benchmark.

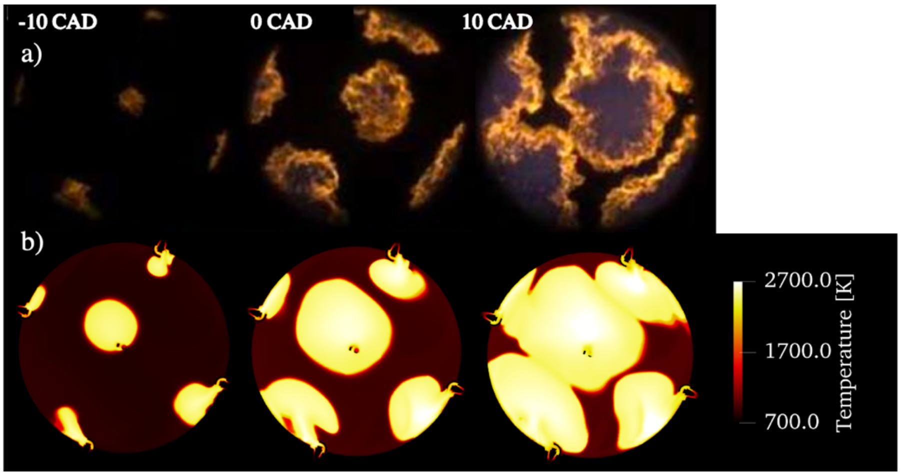

**Figure 3.** Flame development captured by a) optical experiments and b) numerical results with Mesh 4 model. Cross plane for the temperature profile at z = - 3 mm in the middle of the spark plugs gap

## Conclusions

This study delves into the development and validation of the SI multi-spark $NH_3$ CFD model. Advanced optical diagnostic techniques were employed as benchmarks for comparison, particularly in terms of flame development. Key features are identified for best practices in CFD modeling of $NH_3$ engines, such as the proper resolution of the mesh in the spark plug region to accurately capture ignition delay timings. Additionally, the incorporation of spark plug geometries enhanced the predictability of combustion by improving the predictions of the local flow field at the onset of ignition. Flame development showed a highly accurate qualitative agreement between the 3D-CFD results and optical experiments. Building on this foundation, future optimization studies are planned using the developed model.

## Acknowledgments

This work was funded by the King Abdullah University of Science and Technology in Saudi Arabia. The simulations were conducted using the high-performance computation resources of Shaheen supercomputer at KAUST Supercomputing Laboratory. The authors thank Convergent Science Inc. for providing the CONVERGE license.

## References

[1] Bilgen, SELÇUK. “Structure and environmental impact of global energy consumption.” Renewable and Sustainable Energy Reviews Vol. 38 (2014): pp. 890–902.

[2] “Fast Facts on Transportation Greenhouse Gas Emissions.” https://www.epa.gov/greenvehicles/fast-facts-transportation-greenhouse-gas-emissions. Accessed: 2024-04-02.

[3] Tornatore, Cinzia, Marchitto, Luca, Sabia, Pino and De Joannon, Mara. “Ammonia as green fuel in internal combustion engines: State-of-the-art and future perspectives.” Frontiers in Mechanical Engineering Vol. 8 (2022): p. 944201.

[4] Uddeen, Kalim, Tang, Qinglong, Shi, Hao, Magnotti, Gaetano and Turner, James. “A novel multiple spark ignition strategy to achieve pure ammonia combustion in an optical spark-ignition engine.” Fuel Vol. 349 (2023): p.128741.

[5] Uddeen, Kalim, Almatrafi, Fahad, Shi, Hao, Tang, Qinglong, Parnell, Jamie, Peckham, Mark and Turner, James. “Investigation into various strategies to achieve stable ammonia combustion in a spark-ignition engine.” SAE Technical Paper. 2023

[6] Z. Han and R. D. Reitz, “Turbulence modeling of internal combustion engines using rng κ-ε models,” Combustion science and technology, vol. 106, no. 4-6, pp. 267–295, 1995.

[7] R. I. Issa, A. Gosman, and A. Watkins, “The computation of compressible and incompressible recirculating flows by a non-iterative implicit scheme,” Journal of Computational Physics, vol. 62, no. 1, pp. 66–82, 1986.

[8] A. A. Amsden, P. J. O’Rourke, and T. D. Butler, “Kiva-ii: A computer program for chemically reactive flows with sprays,” tech. rep., Los Alamos National Lab.(LANL), Los Alamos, NM (United States), 1989.

[9] Zhang, X., Moosakutty, S.P., Rajan, R.P., Younes, M. et al., “Combustion Chemistry of Ammonia/Hydrogen Mixtures: Jet-Stirred Reactor Measurements and Comprehensive Kinetic Modeling,” Combustion & Flame (2021)

[10] Irimescu, Adrian, Tornatore, Cinzia, Marchitto, Luca and Merola, Simona Silvia. “Compression ratio and blow-by rates estimation based on motored pressure trace analysis for an optical spark ignition engine.” Applied Thermal Engineering Vol. 61 No. 2 (2013): pp. 101–109.

[11] Yang, Ruomiao, Yan, Yuchao, Liu, Zhentao and Liu, Jinlong. “Formation and evolution of thermal and fuel nitrogen oxides in the turbulent combustion field of ammonia internal combustion engines.” SAE Technical Paper. 2023.

# Influence of Ignition Improving Additives on Aqueous Ammonia and Diesel Dual-Fuel Combustion in a Single Cylinder Compression Ignition Engine

Y. Han[1], P. Hellier[1], N. Ladommatos[1] and A. Schönborn[2]
[1]UCL Mechanical Engineering – Torrington Place, London, WC1E 7JE, United Kindom

E-mail: yanlin.han.19@ucl.ac.uk Telephone: +44(0)7579854997

[2]World Maritime University, Fiskehamnsgatan 1, 211 18 Malmö, Sweden

E-mail: as@wmu.se

## 1. Introduction

The transition to sustainable energy sources is crucial for addressing the global challenge of climate change. Among various alternatives, hydrogen has emerged as a promising candidate due to its potential for zero-carbon energy production and utilization. However, the storage and transportation of hydrogen present significant challenges, which has led researchers to explore various hydrogen carriers. Ammonia, with its high hydrogen content and established industrial infrastructure, has gained attention as a potential vector for renewable hydrogen.

Ammonia ($NH_3$) is particularly compelling not only as a vector of renewably produced hydrogen, but also as a carbon-neutral fuel because it contains no fuel-bound carbon. This characteristic makes ammonia an attractive option for decarbonizing the transport sector, particularly as a fuel for diesel engines in road and marine transportation. Furthermore, ammonia can be synthesized using renewable energy sources through processes including electrolysis and the Haber-Bosch method, creating a sustainable cycle of production and utilization.

Despite these advantages, the use of anhydrous ammonia as a fuel is not without challenges. Its high volatility and toxicity make it dangerous and difficult to be handled safely. To address these issues, a water solution of ammonium hydroxide ($NH_4OH$) was proposed to investigate for potential use as a fuel in a diesel engine. Ammonium hydroxide, also referred to as aqueous ammonia, is simply synthesized by saturating water with ammonia, and is liquid phase under atmospheric conditions; therefore, the storage of such a fuel does not require high pressure. Previous work established that engine intake air aspirated ammonium hydroxide solution could contribute to energy release during co-combustion with direct injected fossil diesel fuel [1]. However, the presence of water was found to reduce the combustion stability and limit the extent to which aqueous ammonia could displace diesel fuel.

This study therefore explores the potential of ignition improving additives for ammonium hydroxide and fossil diesel dual-fuel combustion in a single-cylinder diesel engine. Tests were undertaken at constant engine work but with varying levels of displacement of diesel fuel by aspirated aqueous ammonia, with measurements of combustion characteristics and both gaseous and particulate exhaust emissions.

## 2. Methodology

Engine tests were undertaken using a pilot direct injection of diesel alongside the aspiration of the aqueous ammonia solution. The fossil diesel utilized was of zero FAME content, while the 28% ammonium hydroxide solution was sourced from Sigma-Aldrich, with a boiling point of 38 °C, a melting point of -58 °C, a density of 0.9 g/ml at 25 °C, and a vapor pressure of 2160 mm Hg at 25 °C. Two chemical additives, hydrogen peroxide and ammonium nitrate [2], were selected to blend with ammonium hydroxide at varied concentrations from 1000ppm to 5% molecular fraction.

As Fig. 1. shows, ammonium hydroxide was aspirated to the engine via port injection into the preheated air intake for all engine tests, while the fossil diesel fuel was direct injected by a Delphi six-nozzle injector and supplied by a conventional common rail circuit. A pressure vessel containing the ammonium solution was pressurized to 2 bar and connected via a short length of pipe to a Bosch gasoline fuel injector installed into the air intake of the diesel engine. Both additives were dissolved in the aqueous ammonia solution at varying concentrations and supplied via the port injection pathway.

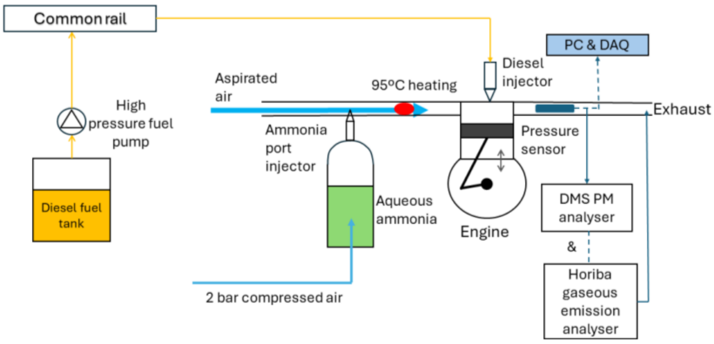
Common rail
High pressure fuel pump
Diesel fuel tank
Aspirated air
95°C heating
Diesel injector
PC & DAQ
Exhaust
Ammonia port injector
Pressure sensor
Aqueous ammonia
Engine
DMS PM analyser
&
Horiba gaseous emission analyser
2 bar compressed air

**Fig. 1.** Schematic of engine test facility and fuel supply

For all experiments reported in this work, fossil diesel was direct injected at a constant injection timing of 13° BTDC and 500±10 bar injection pressure, while the engine operated at a constant speed of 1200rpm. The injection duration of diesel and ammonium solution were controlled so as to maintain a constant total engine load of 5±0.05 bar IMEP. Table 1 summarizes the test conditions for the engine experiments. While the total IMEP was maintained at 5.0 bar, the relative contributions of both fuels varied. For example, when diesel fuel provided 4.5 bar IMEP, the ammonia contributed 0.5 bar IMEP, representing 10% of the total engine load. Similarly, ammonia contributions of 1.0 bar and 1.5 bar represented 20% and 30% of the total engine load, respectively.

**Table 1.** Test condition specifications

| Test | Diesel injection ($\mu$s) | Ammonia injection ($\mu$s) | Additive concentration | Diesel IMEP (bar) | Ammonia IMEP (bar) | Engine IMEP (bar) | Abbreviation |
|---|---|---|---|---|---|---|---|
| 1 | 485 | 0 | 0 | 5.00 | 0 | 5.00 | D5 |
| 2 | 442 | 2778 | 0 | 4.50 | 0.55 | 5.05 | 1-A0.5D4.5 |
| 3 | 410 | 5556 | 0 | 4.00 | 1.02 | 5.02 | 1-A1D4 |
| 4 | 380 | 3000 | 1000ppm $H_2O_2$ | 3.51 | 1.53 | 5.04 | 2-A1.5D3.5 |
| 5 | 410 | 1900 | 1000ppm $H_2O_2$ | 4.02 | 1.01 | 5.03 | 2-A1D4 |
| 6 | 380 | 2750 | 2000ppm $H_2O_2$ | 3.53 | 1.51 | 5.04 | 3-A1.5D3.5 |
| 7 | 380 | 2500 | 1% $H_2O_2$ | 3.50 | 1.54 | 5.04 | 4-A1.5D3.5 |
| 8 | 377 | 1944 | 5% $H_2O_2$ | 3.50 | 1.53 | 5.03 | 5-A1.5D3.5 |
| 9 | 410 | 4166 | 0.5% $NH_4NO_3$ | 4.02 | 1.00 | 5.02 | 6-A1D4 |
| 10 | 442 | 2083 | 0.5% $NH_4NO_3$ | 4.52 | 0.53 | 5.05 | 6-A0.5D4.5 |

In addition, Table 1 shows that the presence of the additives, regardless of their concentrations, resulted in an equivalent energy contribution by ammonia combustion with a reduced ammonia injection duration (test 4-10) compared to the combustion of aqueous ammonia without additives (test 2 and 3).

## 3. Result and discussion

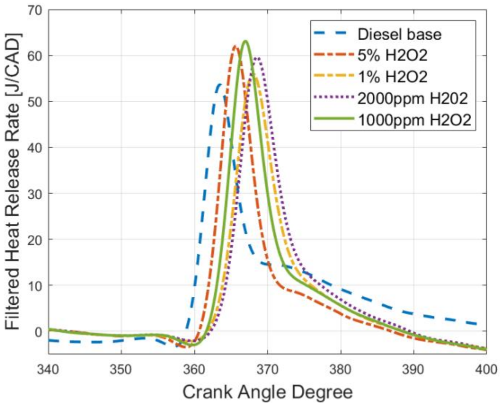

**Fig. 2.** Apparent net heat release rates of aqueous ammonia and diesel dual-fuel combustion providing 1.5 bar IMEP and 3.5 bar IMEP respectively and with varied concentrations of H2O2 additive

Fig. 2 shows the filtered heat release rate of aqueous ammonia and diesel dual-fuel combustion with varied concentrations of $H_2O_2$ additive from 1000ppm to 5%. The ammonia solution contributed 1.5 bar of the total IMEP, while diesel contributed 3.5 bar to the engine load (test 4, 6-8 in Table 1). It is immediately apparent that the injection of aqueous ammonia increased the ignition delay period compared to the diesel only combustion, which is attributed to the aspiration of water into the combustion chamber and the poor combustion characteristics of ammonia; however, the presence of high concentration of $H_2O_2$ additive (5%) reduced the ignition delay. Furthermore, the varying concentrations of $H_2O_2$ addition exhibited a non-linear effect on the ignition delay and the peak heat release rate.

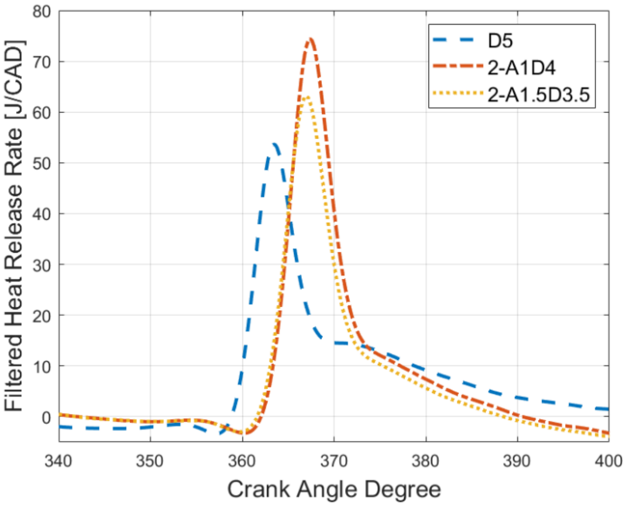

**Fig. 3.** Apparent net heat release rates of aqueous ammonia and diesel dual-fuel combustion with 1000ppm $H_2O_2$ additive and varying load contribution

Fig. 3 shows the comparison between test 4 (2-A1.5D3.5) and test 5 (2-A1D1) with 1000ppm $H_2O_2$ added to aqueous ammonia solution providing 30% and 20% of engine IMEP respectively. It is noted that as ammonia combustion contributed to a higher proportion of the total engine load, the peak heat release rate increased. In addition, it is interesting to see that the ignition delay of the test group where 30% engine IMEP was provided by aqueous ammonia (2-A1.5D3.5) was very similar to that with 20% aqueous ammonia (2-A1D1). This similarity could be related to the higher absolute amount of hydrogen peroxide present in the former case (2-A1.5D3.5).

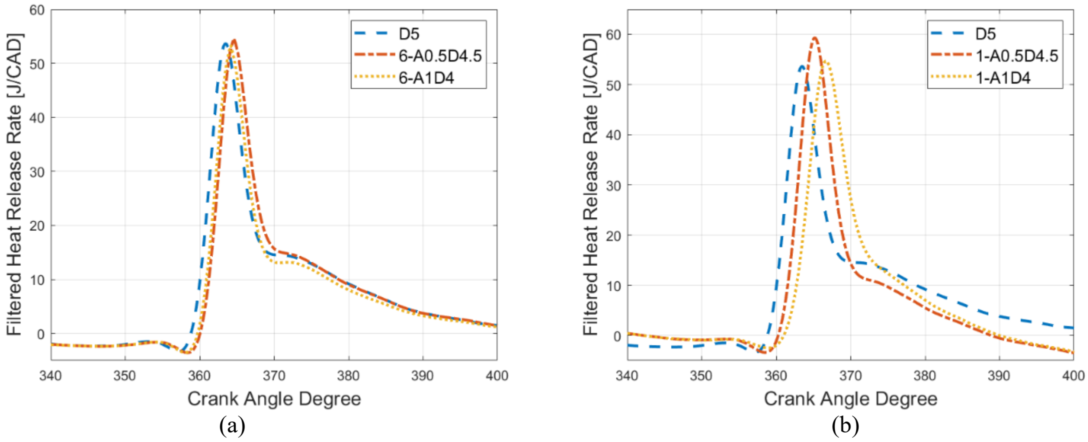

(a) (b)

**Fig. 4.** Apparent net heat release rates of aqueous ammonia and diesel dual-fuel combustion at varying load contributions with (a) 0.5% $NH_4NO_3$ additive; (b) no additive

Fig. 4.a shows the comparison between test 9 (6-A1D4) and test 10 (6-A0.5D4.5) with 0.5% $NH_4NO_3$ additive. Compared to adding $H_2O_2$ to the ammonia solution (Fig. 2), the addition of $NH_4NO_3$ does not significantly change the peak heat release rate (Fig. 4.a). However, when comparing Fig. 4.(a) and (b), it can be seen that the presence of 0.5 % $NH_4NO_3$ appears to offset the increases in ignition delay observed with an increasing contribution of aqueous ammonia to engine load.

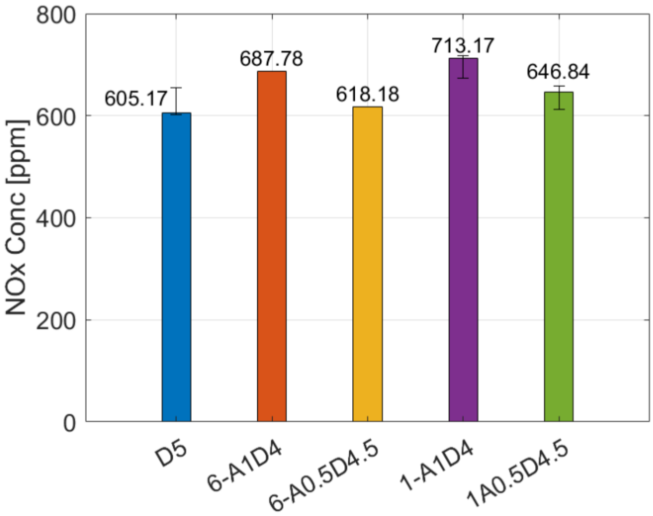

**Fig. 5.** Levels of exhaust $NO_X$ during ammonia and diesel dual-fuel combustion at varying load contribution and addition of hydrogen peroxide

Fig. 5 presents the $NO_X$ emissions during ammonia and diesel dual-fuel combustion in test 2 (1-A0.5D4.5), test 3 (1-A1D4), test 9 (6-A1D4) and test 10 (6-A0.5D4.5), while test 1 (D5) serves as a baseline reference. The error bars for tests 1, 2, and 3 represent plus and minus one standard deviation from the mean of 5 repeats. It is noticed that despite the presence of fuel-bound nitrogen, the ammonia combustion did not see a linear increase in the $NO_X$ formation relative to diesel only combustion. In addition, the presence of 0.5% $NH_4NO_3$ reduced the $NO_X$ levels compared to aqueous ammonia combustion without additive in tests 2 and 3.

## 4. Conclusions

The addition of $NH_4NO_3$ reduced the duration of ignition delay relative to aqueous ammonia and diesel co-combustion without additive, while the addition of $H_2O_2$ saw an overall increase in the peak heat release rate. Furthermore, the presence of both ignition improvers saw an equivalent energy release from aqueous ammonia achieved with a reduced injection duration. Meanwhile, despite the increase in fuel-bound nitrogen with the use of aqueous ammonia and ammonium nitrate, exhaust emissions of nitrous oxides did not linearly increase.

## References

[1] J. Frost, A. Tall, A. M. Sheriff, A. Schönborn, and P. Hellier, "An experimental and modelling study of dual fuel aqueous ammonia and diesel combustion in a single cylinder compression ignition engine," *International Journal of Hydrogen Energy,* vol. 46, no. 71, pp. 35495-35510, 2021, doi: https://doi.org/10.1016/j.ijhydene.2021.08.089.

[2] A. Schönborn, "Aqueous solution of ammonia as marine fuel," *Proceedings of the Institution of Mechanical Engineers, Part M: Journal of Engineering for the Maritime Environment,* vol. 235, no. 1, pp. 142-151, 2021, doi: 10.1177/1475090220937153.

# Characteristics of Ammonia Diffusion Combustion Based on Visualization Study Jointing LES Simulation

Dong Pengbo, Chen Weize, Zhang Zhenxian*, Tian Jiangping, Long Wuqiang

School of Energy and Power Engineering, Dalian University of Technology, Dalian, China

E-mail: pengbo.dong@dlut.edu.cn
Telephone: +86 15840682705

**Abstract.** Ammonia fueled engine applying diffusion combustion mode has the advantages in higher power density and thermal efficiency with cleaner exhaust emissions. However, liquid phase ammonia high-pressure spray has the difficulty in compression ignition, and there is a lack of fundamental studies about ammonia diffusion combustion characteristics. To clarify the ignition, combustion and emissions formation processes and mechanism of ammonia spray under diffusion combustion mode, a joint of fundamental optical diagnosis and large eddy simulation (LES) was conducted to establish the conceptual model of ammonia diffusion combustion ignited by diesel jet. The results show that entraining of the diesel flame and the rest ambient air in the effective ignition zone of the ammonia spray can realize stable and sustainable diffusion combustion. Moreover, substantial NO emission is generated and reduced during this process, while $N_2O$ is produced by NO at the forefront of the flame within a certain temperature range. Therefore, a conceptual model of ammonia diffusion combustion incorporating fuel/air mixing process, flame propagation and distribution of nitrogen oxides has been proposed, which is expected to provide effective theoretical guidance for the development of efficient and eco-friendly ammonia fuel engines.

**Notation**

| | |
|---|---|
| *LES* | *Large eddy simulation.* |
| *ASOAI* | *After start of ammonia injection.* |
| *STL* | *Stereolithography.* |
| *CFD* | *Computational fluid dynamics.* |
| *AMR* | *Adaptive mesh refinement.* |

## 1. Introduction

To address environmental pollution issues and the accompanying strict emission regulations, researchers are exploring the feasibility of using renewable low-carbon fuels in engines [1]. Ammonia, as a renewable zero-carbon fuel, has received attention and has been extensively studied in recent years, mainly focusing on ammonia in-port injection strategy [2-3]. To further improve the power performance and carbon reduction capabilities of engines fueled with ammonia, researchers explored the feasibility of the ammonia direct injection strategy. However, liquid phase ammonia high-pressure spray has the difficulty in compression ignition and there is a lack of the fundamental studies about ammonia diffusion combustion characteristics [4]. Therefore, it is necessary to conduct research on this issue to improve the basic combustion characteristics of ammonia direct injection strategy and enhance the feasibility of the application of ammonia high-pressure direct injection strategy engines.

## 2. Experimental and numerical setup

### 2.1 Experimental and numerical setup

The optical diagnostic experiments of ammonia fuel basic spray combustion characteristics were carried out based on the constant volume vessel [1]. High-pressure gas supply and electric heating wire are used to establish different environmental pressure and temperature conditions, simulating the thermal environment inside the engine cylinder. The temperature and pressure inside the vessel could reach up to 1000 K and 10 MPa. The top and surrounding regions of the volume vessel body are designed with mounting holes, which could be used to clamp components such as injectors and quartz glass. Generally, the mounting holes around are used as optical windows, which could be arranged according to different needs. The window is a 190mm x 90mm runway-type, with a large shooting range. The test device for exploring liquid ammonia diffusion combustion characteristics is shown in Figure 1. In this section, the development, interaction, ignition and combustion process of diesel and ammonia are photographed using the shadow method and the background light method.

According to the real structure of the experimental constant volume vessel, geometric model was established and imported into CONVERGE in STL format to perform three-dimensional CFD calculation. CONVERGE software has the advantages of auto-creating grides during the simulation of combustion and flow processes, which help to reduce the time of mesh preparation and improve simulation accuracy. The mesh algorithm implemented in the CFD model includes fixed embedding and AMR for the main field, the basic grid size was 2 mm, velocity field and temperature field AMR level were 4 and 3, fixed embedding level was 3. The initial condition in the vessel and injection parameters were consistent with experimental measurements.

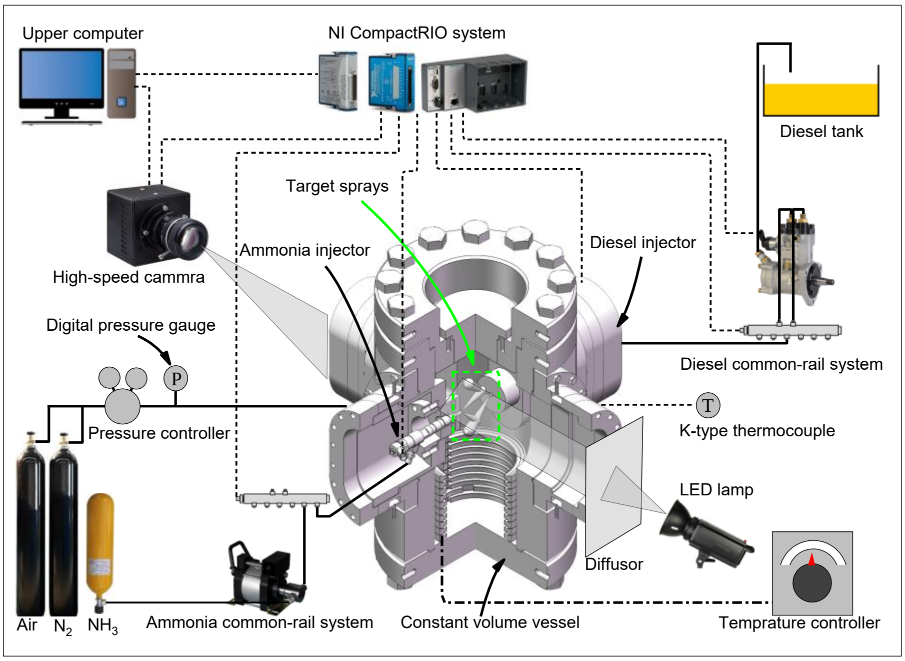
Upper computer
NI CompactRIO system
Diesel tank
Target sprays
Ammonia injector
Diesel injector
High-speed cammra
Digital pressure gauge
P
Diesel common-rail system
T
K-type thermocouple
Pressure controller
LED lamp
Diffusor
Air
$N_2$
$NH_3$
Ammonia common-rail system
Constant volume vessel
Temprature controller

**Fig. 1.** Schematic of experimental setup

## 3. Results and Discussion

### 3.1 Ammonia spray characteristics

The comparison between the simulation results of ammonia spray morphology based on LES and the experiment is shown in Figure 2 below. The stoichiometric ratio of ammonia combustion is 6.056, the equivalence ratio range of ammonia flammability limit is 0.63~1.40 [3], and the corresponding mass fraction is 9.42%~18.8%. The corresponding contour lines are plotted in the figure, indicating the combustible region of ammonia. With the advancement of spray process, the tail of spray is almost all ammonia concentration zone for a relatively long time in the ammonia injection phase (before 2.3 ms), and the mass fraction is higher than 18.8%. The liquid ammonia spray diffuses forward, and the concentration of premix gas at the head and edge is low, and it gradually becomes thinner with the development of spray. It is observed that the mass fraction of the mixture in the head and edge region of the ammonia spray is lower than 9.42%, and it gradually expands with the continuous injection of ammonia, and the ammonia concentration of this part of the premixed gas is lower than the combustion limit.

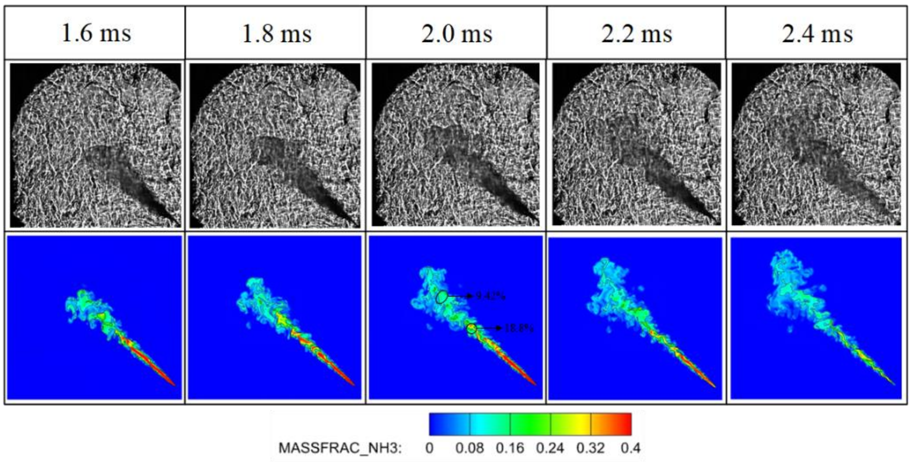

**Fig. 2.** Comparation between ammonia spray images in experiment and mass fraction distribution of vapor phase ammonia in simulation

### 3.2 Ignition and combustion characteristics of liquid ammonia diffusion combustion

The comparison between the simulation results of ammonia contour under combustion conditions based on LES and the experiment is shown in Figure 3 below. The hot flame reaction stage begins rapidly after the diesel ignition delay period ends. The light region in the 0.3 ms ASOAI corresponds to the diesel flame, which is generated by the incandescent emission of carbon particles inside the diesel flame, and the dark region corresponds to the high-temperature gas. The diesel spray is ignited and moves to the effective ignition region earlier than the liquid ammonia spray. After 0.7 ms ASOAI, the liquid ammonia spray passes through the diesel flame and is ignited. During the whole injection combustion process of liquid ammonia, the spray region in the figure is light or dark state of the corresponding flame and high-temperature gas, and there is no obvious unburned mixture region. Meanwhile, it could be observed that the region with ammonia mass fraction higher than 18.8% is the unburned region at 1.5~1.9 ms ASOAI, while the region with ammonia mass fraction between 9.42% and 18.8% is the obvious ammonia combustion region. The results show that the ammonia spray under diesel early injection condition is in the state of high-temperature gas.

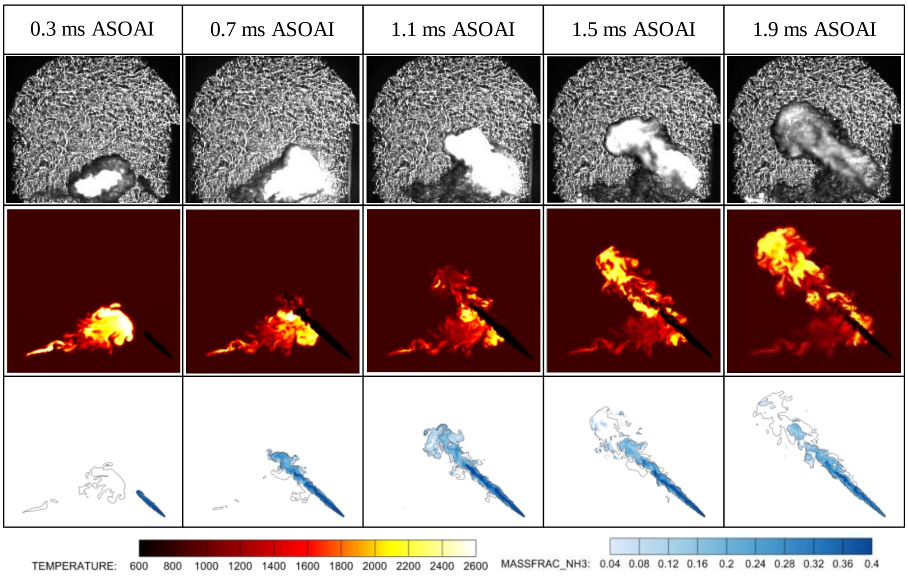

**Fig. 3.** Comparation between Combustion images in experiment and evolution of temperature and mass fraction of $NH_3$ in simulation

### 3.3 Emission characteristics of liquid ammonia diffusion combustion

The liquid ammonia is injected into the high-temperature and high-pressure environment from the injector, and forms ammonia-air combustible mixture through breaking up, collision, evaporation and mixing (hot air is entrained into the spray from the flame floating region). For the NO generated during the combustion of ammonia, including thermal NO and fuel NO, mainly fuel type NO. Fuel type NO is mainly generated by HNO generated by $NH_2$, which is ($NH_2$ → HNO → NO, $NH_2$ → NH → NO), therefore there is similarity in the distribution area of NO and $NH_2$. $N_2O$ is mainly generated by NO below 1400 K and reduced to $N_2$ in high-temperature environment [5]. Therefore, the main $N_2O$ should be distributed along the outer edge of the flame, as observed from the 2.5 ms SOAI.

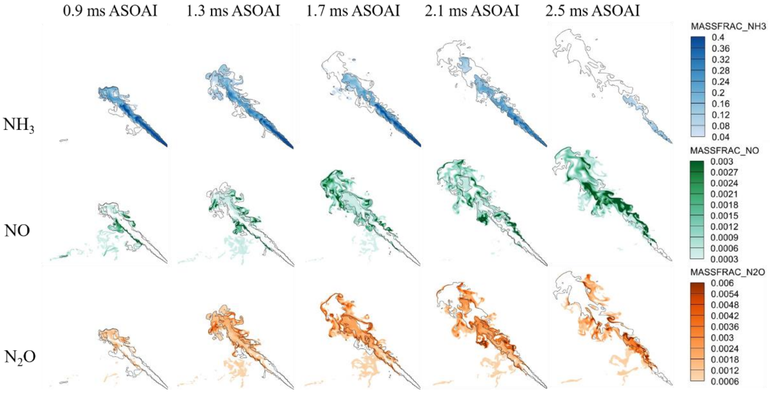

**Fig. 4.** Evolution of $NH_3$, NO and $N_2O$

## Conclusions

Optical diagnostic experiments and large eddy simulation were combined to establish a conceptual model of ammonia diffusion combustion ignited by diesel jet. The results show that stable and sustainable ammonia diffusion combustion could be achieved by entraining diesel flame and ambient air in the effective ignition zone of ammonia spray. In addition, a large amount of NO emission is generated and reduced due to the $DeNO_x$ reaction during this process, while $N_2O$ is produced by NO at the flame front within a certain temperature range. Therefore, a conceptual model of ammonia diffusion combustion combining fuel/air mixing process, flame propagation, and nitrogen oxide distribution has been proposed, which is expected to provide effective theoretical guidance for the development of efficient and environmentally friendly ammonia fuel engines.

## Acknowledgement

This research was supported by the National Key R&D program of China (No. 2022YFB4300700).

## References

[1] Kurien C, Mittal M. Review on the production and utilization of green ammonia as an alternate fuel in dual-fuel compression ignition engines[J]. Energy Conversion and Management, 2022, 251: 114990.

[2] Tay KL, Yang W, Li J, et al. Numerical investigation on the combustion and emissions of a kerosene-diesel fueled compression ignition engine assisted by ammonia fumigation[J]. Applied Energy, 2017, 204:1476-88.

[3] Chen Y, Zhang J, Zhang Z, et al. Effect of ammonia energy ratio and load on combustion and emissions of an ammonia/diesel dual-fuel engine[J]. Energy, 2024: 131860.

[4] Zhang Z, Long W, Dong P, et al. Performance characteristics of a two-stroke low speed engine applying ammonia/diesel dual direct injection strategy[J]. Fuel, 2023, 332: 126086.

[5] Wu B, Wang Y, Wang D, et al. Generation mechanism and emission characteristics of $N_2O$ and $NO_x$ in ammonia-diesel dual-fuel engine. Energy, 2023, 284, 129291.

# Towards Understanding the Optimal Conditions for Stable Ammonia Spray Flames

Santiago Cardona[1*], Thibault F. Guiberti [1,2]

[1]Clean Combustion Research Center, King Abdullah University of Science and Technology (KAUST), Thuwal 23955-6900, Kingdom of Saudi Arabia
[2] Mechanical Engineering Program, Division of Physical Science and Engineering (PSE), King Abdullah University of Science and Technology

*Corresponding author: santiago.vargas@kaust.edu.sa

**Abstract.** Ammonia is an attractive option to help decarbonize the global energy supply chain, supported by established production and distribution infrastructures. The use of ammonia combustion in its liquid state aims to reduce the costs associated with vaporization, storage, and compression. Additionally, liquid ammonia presents higher energy density and compatibility with high-pressure industrial environments. However, ammonia faces challenges as a fuel, including a low turbulent flame speed, NOx and unburned ammonia production, and high latent heat of vaporization that must be addressed before the completely implementation in combustion-based technologies. One possible approach to overcome these reactivity issues is to co-fire ammonia with a more reactive fuel, such as methane or hydrogen. This study aims to comprehensively investigate the characteristics of an ammonia spray flame co-fired with a premixed methane flame in a confined swirl burner through experimental methods, using optical techniques including chemiluminescence species imaging (NH, OH, CH and $NH_2$) and high-speed imaging to analyze and visualize the combustion process in detail. These methods provide insights into the interaction between the ammonia spray and methane flame, shedding light on their combustion behavior and flame structure.

## 1. Introduction

Stricter global regulations on emissions from conventional fossil fuels have prompted increased interest in alternative, carbon-free fuels. Ammonia ($NH_3$) has emerged as a promising candidate due to its carbon-free properties, relatively high energy density [1], and safe storage capabilities compared to hydrogen ($H_2$) [2]. However, challenges remain in utilizing $NH_3$ in combustion technologies, including its poor reactivity and flame speed [3], narrow flammability limits, and propensity to generate significant NOx emissions [4,5]. One strategy to address these challenges is co-firing $NH_3$ with more reactive fuels like methane ($CH_4$) or $H_2$ [6].

Research initially focused on gaseous $NH_3$, but its storage and distribution require liquefaction, making combustion in its liquid phase more practical by reducing the need for large-scale vaporizers and storage vessels. Using $NH_3$ in its gaseous form requires heating supply lines continuously to prevent condensation, leading to higher energy consumption and costs. However, liquid $NH_3$ ($LNH_3$) offers higher energy density and compatibility with high-pressure industrial conditions, making it a promising alternative for various industrial applications. Okafor et al. [7] reported the first successful study on liquid ammonia spray combustion in a swirl combustor, emphasizing the challenging factors for achieving a stable spray formation. Additionally, R. Pelé et al. [8] investigated the spray characteristics of ammonia under different air densities and temperatures in a constant-volume chamber, comparing the ammonia to biofuel, ethanol, and a common fuel, gasoline, through the Schlieren technique. The results showed that the spray geometry of ammonia differs from that of the other fuels and that its sensitivity is more significant to the air density and temperature. At flash boiling conditions at the ambient temperature, they found a wider spray at half-penetration length at phase change. Ichikawa et al. [9,10] explored the application of liquid $NH_3$ spray combustion in large two-stroke marine engines, employing a "three-layer $NH_3$ stratified injection" approach involving supporting fuel/liquid $NH_3$/supporting fuel. Recently, Yamashita et al. [11] conducted a comparative study on combustion characteristics using $LNH_3$ spray and $NH_3$ in a swirl combustor at atmospheric pressure. They found that the flame stability limits of $LNH_3$ spray combustion are narrower compared to $NH_3$ combustion, particularly under fuel-rich conditions. However, the addition of methane or hydrogen extends the flame stability limits of $LNH_3$ spray combustion, with hydrogen showing a more significant effect than methane. Despite ongoing research into liquid $NH_3$, further investigation into $LNH_3$ spray formation is necessary due to its complex and not fully understood nature.

The research employs optical techniques such as chemiluminescence species imaging (NH, OH, CH, and $NH_2$) and high-speed imaging to conduct a detailed analysis and visualization of the combustion process. Chemiluminescence species imaging allows for the real-time observation and quantification of reactive species like NH, OH, CH, and $NH_2$, providing valuable insights into their distribution and reaction pathways during combustion. Additionally, high-speed imaging captures rapid temporal changes in the flame structure and dynamics of the interaction between the ammonia spray and methane flame.

## 2. Material and methods

### 2.1 Experimental setup

Figure 1.a shows the laboratory-scale setup for characterizing $LNH_3$ spray. This included a precise $LNH_3$ supply system and an enclosed chamber. $LNH_3$ was sourced from an $NH_3$ dip tube cylinder and conveyed through a series of pipes to an electronic flow control valve (depicted as the flow control valve in Fig. 1), ensuring accurate injection timing. A secondary release valve (shown as the release valve in Fig. 1) was rapidly opened after the flow control valve closed to vent any residual $NH_3$ in the fuel line, preventing unnecessary cooling of the atomizer tip and halting $NH_3$ flow through the atomizer. To prevent $LNH_3$ evaporation, the supply lines were cooled to 279±2 K using a coaxial tube from the cylinder to the flow control valve upstream of the atomizer.

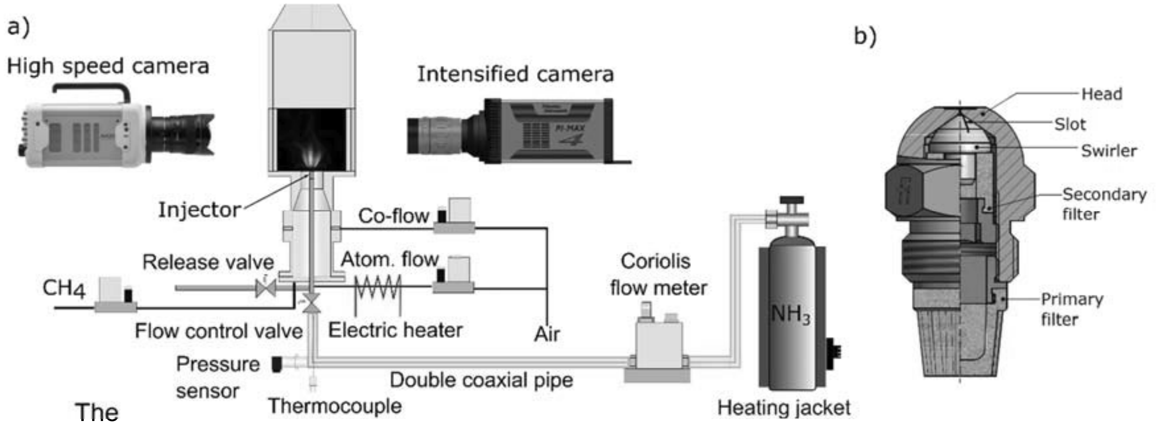

**Figure 1.**Experimental setup (a) and pressure swirl atomizer (b)

Ammonia spray flame was stabilized using a Delavan commercial pressure swirl atomizer (see Fig. 1.b), which had a spray opening angle of 60° and a standard mass flow rate of 1.18 kg/h at an injection pressure of 7 bar for standard fuel oil with a viscosity of 3.4 cSt and a density of 820 kg/m³.

### 2.2 Optical setup

NH, OH, and CH signals were captured using an intensified CCD camera (Princeton Instruments, PI-MAX4 1024EMB) equipped with UV lenses (Cerco, f = 100 mm, f/2.8) and set a recording speed of 10 frames per second (fps) and resolution of 512x512 pixels. For $NH_2$ signals, a PI-MAX4 camera with visible lenses (Nikon, f = 50 mm, f/1.4) was employed and set a recording speed of 14 frames per second (fps) and resolution of 512x512 pixels. High-speed imaging was conducted using a Photron SA4 model 500K-C1 color camera with visible lenses (Nikon, f = 50 mm, f/1.4), recording at 1000 frames per second (fps) with an exposure time of 1000 μs. The camera's resolution was set to 1024x1024 pixels, achieving a spatial resolution of 71 μm. Additionally, color images were recorded using a continuous 532 nm laser to scatter light off the ammonia droplets, enabling visualization of the liquid phase within the flame.

### 2.2 Experimental conditions

The $NH_3$ spray flame was tested with 3 different swirl angles (SA), 60°, 100° and 120° also changing the global equivalence ratio (1.5, 1.7 and 2) in order to assess their effect on the combustion performance and flame instability and tested until the flame blowout, all conditions. In addition, all experiments were conducted at atmospheric pressure and room temperature of 293 K. The conditions were chosen to ensure a stable $NH_3$ spray flame and to comprehensively evaluate the effects of swirl number, global equivalence ratio, and burner outlet shape on liquid ammonia combustion.

## 3. Results and discussion

Figure 2.a shows a time-resolved color image of this flame. This premixed co-flow flame surrounds the central ammonia jet, providing the heat needed for stabilizing the $NH_3$ spray flame. The flames exhibit the characteristic orange, and yellow hues typically associated with $NH_3$ combustion. The blue hues are indicative of the $CH_4$ premixed flame, while the green hue results from $NH_3$ Mie scattering excited by a 532 nm continuous-wave laser. On the other hand, Fig. 2.b depicts the averaged results from 500 images for two chemiluminescence species, $NH_2^*$ and $OH^*$. These species were selected for their distinct definition of the combustion regions: $NH_2^*$ is linked to $NH_3$ combustion, while $OH^*$ is associated with $CH_4$ combustion.

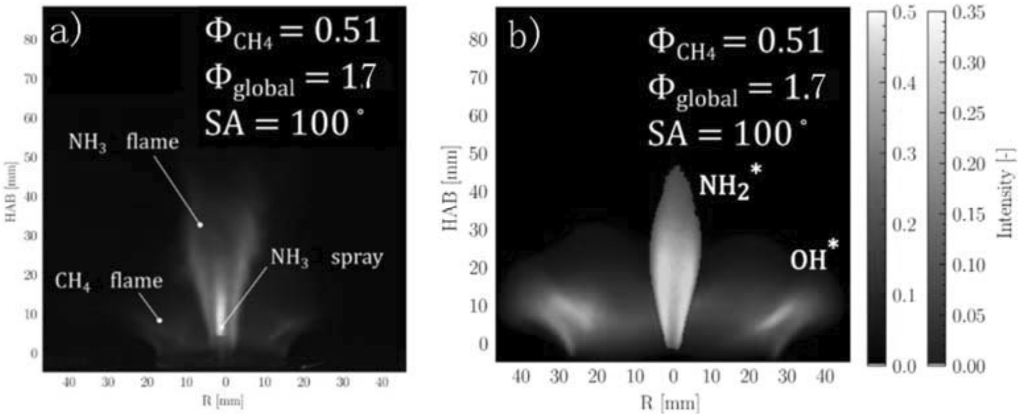

**Figure 2.** Ammonia spray flame cofired with a premixed methane flame (a) and averaged chemiluminescence images for $NH_2^*$ and $OH^*$ (b)

Figure 3.a illustrates the standard deviation derived from 1000 images captured by a high-speed camera along the central axis of the $LNH_3$ spray flame cofired with a swirl $CH_4$ flame. In the first region, specifically between 0 and 10 mm above the injector, it is evident that the swirl angle (SA) of 60° promotes the most stable geometric conditions for the $LNH_3$ spray flame. This behavior is likely due to swirler configuration with smaller swirl angle produces $CH_4$ flames that are less anchored to the burner root, thereby reducing injector heating and supporting stable $LNH_3$ atomization. However, this geometry struggles to sustain higher $LNH_3$ mass flow rates; increasing $LNH_3$ flow rates tend to extinguish flames with SA of 60° first.

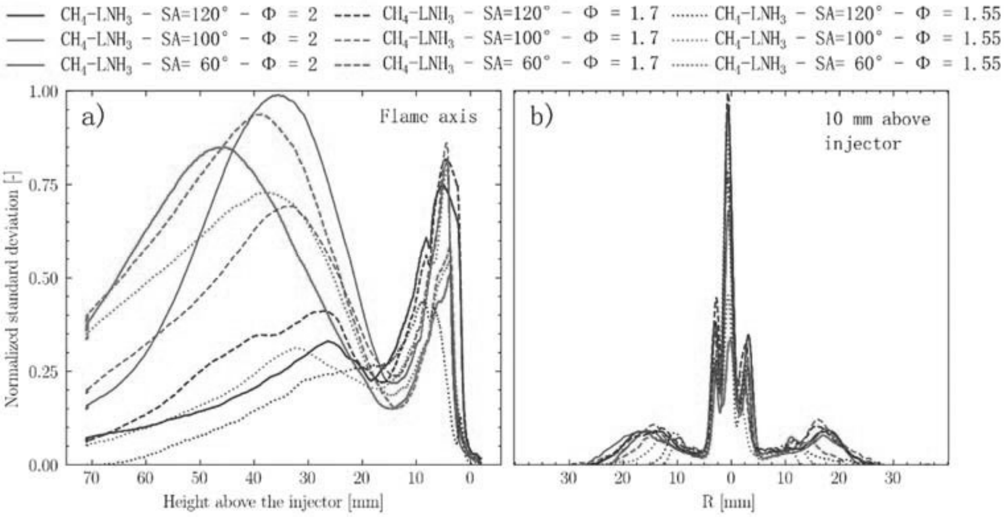

**Figure 3.** Frame to frame variation at the flame axis (a) and 10 mm above the injector (b)

Furthermore, in Figure 3.a, it is observed that SA values of 100° and 120° exhibit similar levels of frame-to-frame fluctuations, indicating that these anchored flames (with a characteristic "M" shape at lower flow velocities, as evidenced in chemiluminescence images) heat the injector more intensely and introduce instabilities in ammonia injection, leading to simultaneous expulsion of liquid and gaseous ammonia. However, particularly the swirler with the SA of 120° can support higher mass flow rates of $LNH_3$ in a more stable manner. As the $LNH_3$ mass flow rate increases, the flow effectively mitigate injector overheating challenges.

Figure 3.b depicts the frame-to-frame variation, represented as standard deviation in radial position at 10 mm above the injector. It is evident that the region closer to the central axis exhibits the most instabilities, coinciding with the presence of the $NH_3$ spray jet and combustion. Moving away from the center towards where $CH_4$ combustion occurs, the frame-to-frame variation diminishes. Additionally, similar behavior to Figure 3.a is observed along the spray flame axis, with less variation observed for the swirler with the smallest swirl angle, and similar variation observed for the other two swirler angles.

## Conclusions

This research combined optical methods, offering a comprehensive understanding of how $CH_4$ and $LNH_3$ interact and influence combustion behavior and flame structure. Such detailed observations are crucial for optimizing combustion processes and enhancing the efficiency and environmental performance of $LNH_3$-$CH_4$ co-firing technologies. The preliminary results revealed a crucial observation: the stability of the $NH_3$ spray flame is significantly influenced by the $CH_4$ flame under certain conditions that heat the injector, resulting in a highly unstable flame, often followed by a flame blowout. At specific $LNH_3$ mass flow rate, high swirl angles enhance the mixing of air and fuel, which can improve flame stability but may also increase the likelihood of upstream vaporization because it produces compact flames attached to the burner outlet, heating the injector. Similarly, conditions with high thermal power for a specific $LNH_3$ mass flow rate can cause ammonia vaporization upstream of the spray nozzle. Therefore, $LNH_3$ combustion is a complex process that requires a controlled heat source for efficient combustion. However, this heat source must be carefully controlled to prevent injector overheating that can cause fluctuations in the equivalence ratio, leading to an unstable combustion.

## References

[1] Zamfirescu C, Dincer I. Using ammonia as a sustainable fuel. J Power Sources 2008;185:459–65. https://doi.org/10.1016/j.jpowsour.2008.02.097.

[2] Klerke A, Christensen CH, Nørskov JK, Vegge T. Ammonia for hydrogen storage: challenges and opportunities n.d. https://doi.org/10.1039/b720020j.

[3] Hayakawa A, Arakawa Y, Mimoto R, Somarathne KDKA, Kudo T, Kobayashi H. Experimental investigation of stabilization and emission characteristics of ammonia/air premixed flames in a swirl combustor. Int J Hydrogen Energy 2017;42:14010–8. https://doi.org/10.1016/J.IJHYDENE.2017.01.046.

[4] Wang G, Guiberti TF, Cardona S, Jimenez CA, Roberts WL. Effects of residence time on the NOx emissions of premixed ammonia-methane-air swirling flames at elevated pressure. Proc Combust Inst 2022. https://doi.org/10.1016/J.PROCI.2022.07.141.

[5] Avila CD, Cardona S, Abdullah M, Younes M, Jamal A, Guiberti TF, et al. Experimental assessment of the performance of a commercial micro gas turbine fueled by ammonia-methane blends ☆. Appl Energy Combust Sci 2023;13. https://doi.org/10.1016/j.jaecs.2022.100104.

[6] Khateeb AA, Guiberti TF, Zhu X, Younes M, Jamal A, Roberts WL. Stability limits and exhaust NO performances of ammonia-methane-air swirl flames. Exp Therm Fluid Sci 2020;114. https://doi.org/10.1016/j.expthermflusci.2020.110058.

[7] Okafor EC, Yamashita H, Hayakawa A, Somarathne DKA, Kudo T, Tsujimura T, et al. Flame stability and emissions characteristics of liquid ammonia spray co-fired with methane in a single stage swirl combustor. Fuel 2020;287:119433. https://doi.org/10.1016/j.fuel.2020.119433.

[8] Pelé R, Mounaïm-Rousselle C, Bréquigny P, Hespel C, Bellettre J. First Study on Ammonia Spray Characteristics with a Current GDI Engine Injector. Fuels 2021;2:253–71. https://doi.org/10.3390/fuels2030015.

[9] Ichikawa Y, Niki Y, Takasaki K, Kobayashi H, Miyanagi A. NH3 combustion using three-layer stratified fuel injection for a large two-stroke marine engine: Experimental verification of the concept. Appl Energy Combust Sci 2022;10:100071. https://doi.org/10.1016/j.jaecs.2022.100071.

[10] Ichikawa Y, Niki Y, Takasaki K, Kobayashi H, Miyanagi A. Experimental study of combustion process of NH 3 stratified spray using imaging methods for NH 3 fueled large two-stroke marine engine. Appl Energy Combust Sci 2023;13:100119. https://doi.org/10.1016/j.jaecs.2023.100119.

[11] Yamashita H, Hayakawa A, Oku K, Colson S, Reibel G, Chen Y rong, et al. Visualization of liquid ammonia spray using 2p-SLIPI and comparison of liquid ammonia spray and gaseous ammonia combustion in a swirl combustor at atmospheric pressure. Fuel 2024;371:131833. https://doi.org/10.1016/j.fuel.2024.131833.

# AUTHORS' INDEX

Aizawa, Tetsuya 596, 689
Akayama, Tomoya 689
Alcove Clave, Silvia 193
Aljabri, Hammam 20
Almatrafi, Fahad 721
AlRamadan, Abdullah 20
An, Yanzhao 226
Andreoli, Silvia 332
Andwari, Amin Mahmoudzadeh 395, 665, 670
Armas, Octavio 570, 685
Babaie, Meisan 670
Bae, Choongsik 47
Balogun, Fatimoh 208
Bates, Luke 653
Bayet, Remi 76
Beers, Harold 682
Ben Houidi, Moez 20
Bhattacharya, Atmadeep 713
Böhm, Benjamin 717
Brinklow, George 193
Cafari, Alberto 665
Calvo Oliveira, Alejandro 146
Cárdenas Almena, María Dolores 685
Cardona Vargas, Santiago 733
Carmona Cabello, Miguel 674
Catapano, Francesco Concetto 146
Cavadino, T. 670
Cenker, Emre 20
Cerri, Tarcisio 61
Chaillou, Christophe 307
Chandelier, M. 89
Chen, Weize 729
Cova-Bonillo, Alexis 193
Cuijpers, Michel 682
Curness, A. 670
Dantla, Somasekhar Reddy 510
Das, Shubhra K. 580
de Paz Alcolado, Guillermo 76
D'Errico, Gianluca 61
Dober, G. 89
Dong, Pengbo 729
Donoso, David 570
Dorado Pérez, María del Pilar 674, 706
Dreizler, Andreas 717
Drevet, R. 89
Duffour, Florence 127
Eichlseder, Helmut 280
Eichmann, Simone 344
Erhard, Jannick 717
Fantuzzi, D. 461
Ferrarese, Christian 693
Fitter, O. 670
Fitzgerald, Russell 610
Fonseca González, Natalia E. 693
Franzetti, Jacopo 693
Fregni, Paolo 461
Frühwirth, Christian 280
Fuyuto, Takayuki 523
Gaioli, S. 461
Gallo, Alessandro 332
Garcia Martinez, Antonio 395
García-Contreras, Reyes 570, 685
Gastaldi, Patrick 89
Gautrot, Xavier 127
Gessaroli, Davide 115
Gianetti, Giovanni Gaetano 61
Giechaskiel, Barouch 693
Gilber, D. 670
Gioria, Roberto 693
Giuffrida, Vincent 127
Golisano, Roberto 115
Gómez Soriano, Josep 61
Gómez-Vilanova, Alejandro 496
Gößnitzer, Clemens 441
Guiberti, Thibault 733
Guilain, Stephane 76
Günther, Marco 631
Han, Yanlin 725
Hanks, Benjamin 610
Harsha, Vivek 510
Hasse, Christian 631
Heinz, Lukas 537
Hellier, Paul 354, 678, 725
Henríquez-Concepción, Vicente 649
Herreros Arellanos, José Martín 193, 674
Hinault, Julien 307
Hojo, Yudai 689
Hu, Zhichao 226
Hwang, Joonsik 47
Hyvonen, Jari 657, 665
Iljaszewicz, Paulina 661
Im, Hong G. 20, 697, 721

Im, Hyuk 428
Im, Hyunjun 428
Janhunen, Timo 702
Jiménez-Espadafor, Francisco J. 706
Kaario, Ossi 713
Kakoee, Alireza 208, 657, 665
Kärcher, Viktor 354
Kawaharazuka, Fumihiro 266
Khedkar, Nikhil 193
Ki, Youngmin 47
Kim, Jeyoung 657
Kim, Jinnam 428
Kim, Jungho Justin 47
Kim, Kiyeon 709
Kim, Seungjae 709
Kinoshita, Hiroyuki 596
Kircher, Magnus 631
Kitabatake, Ryo 596
Kittoe, Amy 678
Klenk, Dennis 344
Knowles, James 653
Koch, Thomas 537
Kondo, Teruaki 523
Könnö, Juho 395, 670
Kosaka, Hidemasa 523
Krishnan, Sundar 549
Kumar, D. 89
Ladommatos, Nicos 354, 678, 725
Laigle, Emmanuel 307
Landis, Joshua 580
Langridge, Simon 332
Larrieu, Clément 307
Laubichler, Christian 441
Lazzaro, Maurizio 146
Lee, Jeongwoo 709
Lee, Sanguk 474
Lee, Seong-Young 47
Lee, Seunghyun 709
Lee, Seungil 709
León Zerpa, Federico 649
Li, Shiyutian 173
Liu, Haoyu 173
Liu, L. 243
Liu, Long 156, 173
Liu, Xinlei 20, 697
Long, Wuqiang 729
Lopez Pintor, Dario 474
Lozano Medina, Juan Carlos 649
Mack, John Hunter 580
Maddineni, Ajay Kumar 368
Maes, Noud 682
Magnotti, Gaetano 20
Mahmoodi, Bayazid 713
Mancini, Giorgio 450
Mandokoro, Yoshiyuki 523
Martí-Aldaraví, Pedro 496
Martin, Glen 610
Martinez-Botas, Ricardo 510
Mason, Byron 653
Matsumoto, Atsushi 596
Mazza, Fabio 450
Medda, Massimo 2
Mehranfar, Sadegh 395, 665
Melas, Anastasios 693
Menaca, Rafael 20, 697, 721
Mendieta Pino, Carlos Alberto 649
Mico Reche, Carlos 395
Mikulski, Maciej 208, 657, 665
Milan, G. 89
Millington, Paul 193
Millo, Federico 461
Min, Kyoungdoug 709
Miyashita, Kazuya 596
Mohan, Balaji 20
Molina, Santiago 115
Moreno-Cabezas, Kevin 20, 697
Mortellaro, Fabio 2
Naghshtabrizi, Payam 496
Nakov, Galin 510
Narayanan, Abhinandhan 549
Nasim, Nayer 580
Nawaz, Behlol 580
Nishikawa, Kazuaki 523
Noguchi, Shoei 689
Norsic, Caroline 307
Novella, Ricardo 61
Oh, Heechang 428
Olcina-Girona, Miguel 115
Oliva Miñana, Fermín 570, 685
Onorati, Angelo 61
Oppl, Thomas 441
Pandey, Rangesh 368
Panithasan, Mebin Samuel 20
Panthi, Niraj 20
Park, Jongguk 428
Pati, Andrea 631

| | |
|---|---|
| Payri, Raúl | 496 |
| Pei, Yiqiang | 226 |
| Peng, Yan | 156 |
| Pesce, Francesco Concetto | 115 |
| Pinzi, Sara | 674 |
| Pirker, Gerhard | 441 |
| Plazas, Alejandro | 496 |
| Ponti, Fabrizio | 549 |
| Posch, Stefan | 441 |
| Préterre, David | 307 |
| Prior, Jack | 653 |
| Ramognino, Federico | 61 |
| Ramos Martín, Alejandro | 649 |
| Ravaglioli, Vittorio | 549 |
| Reig, Alberto | 450 |
| Roberts, William L. | 20 |
| Rolando, Luciano | 461 |
| Rudkowski, Marek | 661 |
| Rueda Vázquez, Juan Manuel | 706 |
| Sacco, Nicola Pio | 115 |
| Salahi, Mahdi | 665 |
| Salek, F. | 670 |
| Salvador, Josep | 410 |
| San Primitivo, Juan Antonio | 385 |
| Sánchez Morales, Carlos Jesús | 649 |
| Sanchez Rodríguez, Luis | 685 |
| Scalabrini, Stefano | 115 |
| Schlegel, Reto | 332 |
| Schneider, Jonathan | 631 |
| Schönborn, Alessandro | 725 |
| Schroeder, Matthias | 344 |
| Schutting, Eberhard | 280 |
| Schwarz, David | 510 |
| Scinicariello, Nicola | 461 |
| Seiler, Patrick | 610 |
| Selleri, Tommaso | 693 |
| Sementa, Paolo | 146 |
| Serrano Reyes, Javier | 706 |
| Serrano, David | 127 |
| Sforza, Lorenzo | 61 |
| Shaohang, Han | 689 |
| Shi, Hao | 717 |
| Shimada, Taizo | 596, 689 |
| Shimizu, Fumika | 596 |
| Silva, Mickael | 721 |
| Silvagni, Giacomo | 549 |
| Sirviö, Katriina | 208 |
| Sisodiya, Sunita | 678 |
| Smulter, Ben | 665 |
| Somers, Bart | 156, 682 |
| Soriano García, José Antonio | 570, 685 |
| Sridharan, Naveen | 368 |
| Srinivasan, Kalyan Kumar | 549 |
| Su, Zhanwang | 226 |
| Suarez-Bertoa, Ricardo | 693 |
| Suatean, Bogdan | 76 |
| Sun, Zhongcheng | 682 |
| Takatori, Yoshiki | 523 |
| Tamadonfar, Parsa | 713 |
| Tang, Qinglong | 721 |
| Tejada Hernández, Jesús | 674 |
| Terekhov, A. | 243 |
| Thorsen, Lauge | 146 |
| Tian, Jiangping | 729 |
| Tonelli, Roberto | 2 |
| Tornatore, Cinzia | 146 |
| Tsolakis, Athanasios | 193 |
| Turner, James W.G. | 20, 697, 721 |
| Uchida, Noboru | 266 |
| Uddeen, Kalim | 721 |
| Ueda, Reiko | 523 |
| Valin, Thomas | 127 |
| Vassallo, Alberto Lorenzo | 115 |
| Vasudev, Aneesh | 208,665 |
| Viglione, Ludovico | 146 |
| Vinogradov, Afanasie | 461 |
| Vorraro, Giovanni | 697 |
| Wagner, Uwe | 537 |
| Wakisaka, Yoshifumi | 523 |
| Wang, Yang | 173 |
| Warnberg, D. | 243 |
| Watanabe, Kazumasa | 266 |
| Webb, Cameron | 678 |
| Welch, Cooper | 717 |
| Whelan, Steve | 653 |
| Wimmer, Andreas | 441 |
| Wu, Bin | 20 |
| Wu, Hao | 20 |
| Wu, Mengda | 193 |
| Wu, Yue | 156 |
| Yamamoto, Sosuke | 689 |
| Ye, Pedro | 717 |
| Yeruva, Thikshana Reddy | 510 |
| York, Andrew P.E. | 193 |
| Yoshiuda, Ryogo | 596 |
| Zaihi, Abdullah | 20 |

Zeraati Rezaei, Soheil 193
Zhang, Liwen 243
Zhang, Zhenxian 729
Zhao, Deyang 226
Zhao, Hua 226
Zhao, Peng 243

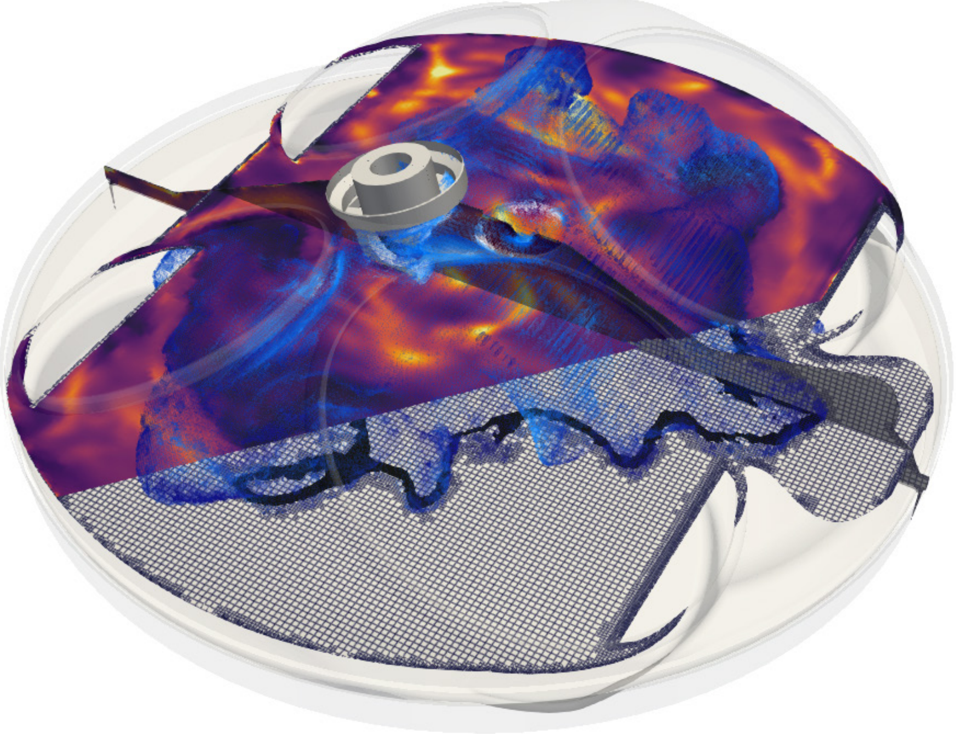

**CMT-Clean Mobility & Thermofluids**
Universitat Politècnica de València
Camino de Vera s/n · 46022 Valencia. Spain
Tel.: +34 96 387 76 50 · cmt@mot.upv.es · www.cmt.upv.es

**SCIENTIFIC EDITORS**

Xandra Margot
Raúl Payri
José Ramón Serrano

**PUBLISHER**
**edUPV, 2024**
www.lalibreria.upv.es / Ref.: 6796_01_01_01
ISBN: 978-84-1396-275-7
DOI: http://dx.doi.org/10.4995/Thiesel.2024.679601